PHYSICS AND APPLICATIONS OF GRAPHENE - EXPERIMENTS

Edited by **Sergey Mikhailov**

INTECHWEB.ORG

Physics and Applications of Graphene - Experiments
Edited by Sergey Mikhailov

Published by InTech
Janeza Trdine 9, 51000 Rijeka, Croatia

Publishing Process Manager Ivana Lorkovic
Technical Editor Teodora Smiljanic
Cover Designer Martina Sirotic
Image Copyright Blaz Kure, 2010. Used under license from Shutterstock.com

First published March, 2011
Printed in India

A free online edition of this book is available at www.intechopen.com
Additional hard copies can be obtained from orders@intechweb.org

Physics and Applications of Graphene - Experiments, Edited by Sergey Mikhailov
p. cm.
ISBN 978-953-307-217-3

Contents

Preface

The Stone Age, the Bronze Age, the Iron Age ... Every global epoch in the history of the mankind is characterized by materials used in it. In 2004 a new era in the material science was opened: the era of graphene or, more generally, of two-dimensional materials [K. Novoselov, A. Geim et al. Science 306, 666 (2004)]. Graphene is the one-atom thin layer of sp^2-bonded carbon atoms arranged in a honey-comb lattice. It possesses the unique physical properties: graphene is the strongest and the most stretchable known material, has the record thermal conductivity and the very high intrinsic mobility and is completely impermeable. The charge carriers in graphene are the massless Dirac fermions and its unique electronic structure leads to a number of interesting physical effects, such as the minimal electrical conductivity, anomalous quantum Hall effect, Klein tunneling, the universal optical conductivity and the strong nonlinear electromagnetic response. Graphene offers and promises a lot of different applications, including conductive ink, terahertz transistors, ultrafast photodetectors, bendable touch screens, strain tensors and many other. In 2010 Andre Geim and Konstantin Novoselov were awarded the Nobel Prize in Physics "for groundbreaking experiments regarding the two-dimensional material graphene".

Nowadays, graphene is in the focus of research activity of condensed matter physicists in the whole world. Research articles reporting on different aspects of graphene studies are collected in the present two volumes "Physics and Applications of Graphene". These books cover a broad spectrum of experimental and theoretical studies of graphene and present contributions from research groups and laboratories from the North and South America, Europe, Asia and Australia.

The contributed articles are presented in two volumes. The first volume contains experimental papers, divided into three Sections. Section I describes the methods of the synthesis and fabrication of graphene films and related materials, in Section II the electronic properties of graphene are discussed and Section III is devoted to its electronic, chemical and biosensing applications. The readers interested in theoretical studies of graphene are referred to the second volume.

Sergey Mikhailov
University of Augsburg
Germany

Part 1

Synthesis and Fabrication

1

Nano-Engineering of Graphene and Related Materials

Zhiping Xu
Tsinghua University
China

1. Introduction

Graphene is the ultimately monolayer material with single-atom thickness. It possesses many fascinating properties including massless Dirac electronic structure, anomalous quantum Hall effects, high mobility, extraordinary high thermal conductivity, stiffness and strength (*see other chapters in this book*). Impressively, these properties have remarkable dependence on its morphology and atomic structure, e.g. its size and shape (Fig. 1, Xu & Buehler, 2010a). Moreover, interior and exterior doping effects from defects, molecular adsorptions or electromagnetic fields are also significant. For example, hydrogenation, oxidation and electrical field significantly tune its structural, mechanical, thermal, electronic and optical structures, which is controllable and even reversible. These sensitive responses of a graphene sheet to structural and environmental cues enable us opportunities to engineer its physical and chemical properties at nanoscale.

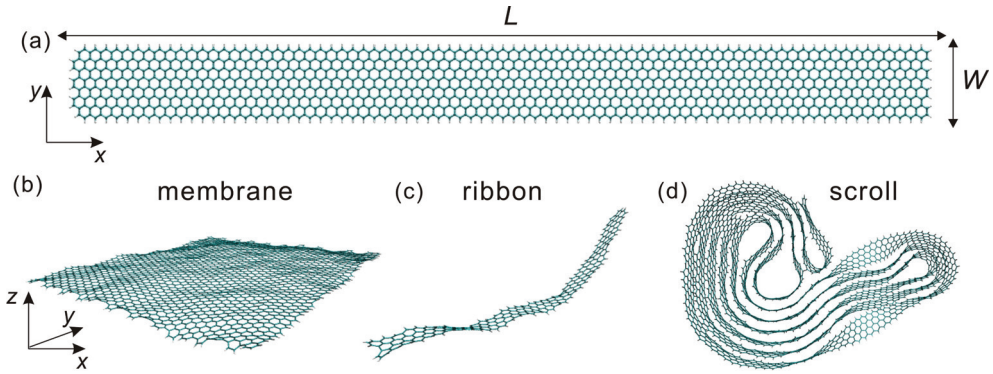

Fig. 1. A phases diagram for graphene sheets as a function of their geometric parameters: (a) a graphene sheet with length L and width W; (b) a two-dimensional membrane with ripples from thermal fluctuation as $L \sim W$; (c) a fluctuating one-dimensional ribbon while it has apparent aspect ratio $n = L/W$; (d) a nanoscroll after a ribbon self-folds due to the van der Waals interactions between adjacent graphene sheet. (Xu & Buehler, 2010a)

2. Nano-engineering by tailoring nanostructures

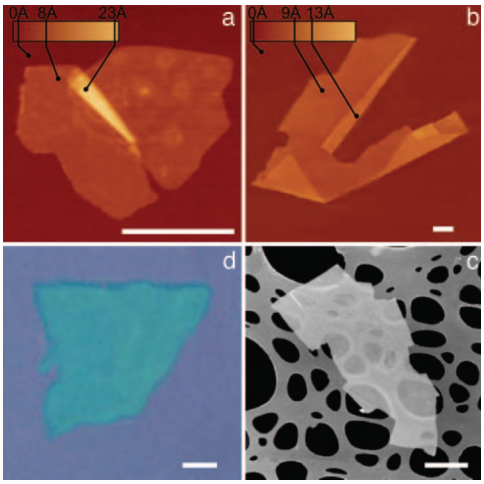

Fig. 2. Two-dimensional monolayer crystallites of $NbSe_2$ (a), graphite (b), $Bi_2Sr_2CaCu_2O_x$ (c) and MoS_2 (d) as prepared by the mechanical exfoliation technique and visualized by atom force microscopy (AFM) (a and b), scanning electron microscopy (c) and optical microscope (d). (All scale bars: one micrometer) (Novoselov et al., 2005)

Back to year 2004, the first experimental establishment of producing graphene sheets is achieved by Andre Geim and Konstantin Novoselov of the University of Manchester, through a so-called "scotch-tape" technique (Novoselov et al., 2004). In this approach, single- or few-layered graphene sheets can be obtained by repeatedly peeling highly oriented pyrolytic graphite (HOPG) using scotch tapes. Although the graphene sheets thus produced are poor in the production yield and controllability on the geometry, this mechanical exfoliation technique features high reliability and offers graphene sheets of very high quality. Even at present, the simple but efficient "scotch-tape" technique is still a common one to fabricate high-quality samples. This seminal work is our first time to fabricate and observe two-dimensional crystalline materials. Geim and Novoselov are thus awarded the 2010 Nobel Prize in physics. In prior to their work, physicists believed that two-dimensional crystals couldn't sustain stabilities in ambient environment at finite temperature. Early work based on elasticity theory shows that the out-of-plane displacement field diverges for infinite large two-dimensional crystals (Mermin & Wagner, 1966). However, the observation of stable graphene, BN, MoS_2 and other monolayers (Fig. 2) gives rise to a the contradiction to the theoretical prediction. It is realized later that the monatomic layers are stablized by the anharmonic coupling between bending and stretching modes in the graphene sheet, i.e. forming out-of-plane ripples and wrinkles on the graphene sheet maintains its planar morphology (Fig. 1(b)) and avoids collapsing into folds and scrolls (Fig. 1(d)). The morphology of graphene sheet are thus determined by the size, shape, temperature and boundary conditions. Recent atomistic simulations (Fasolino, Los & Katsnelson, 2007; Xu & Buehler, 2010a) and experiments (Meyer et al., 2007) clarify the underlying mechanism and predict the morphology phase diagram for graphene.

Inspired by this exciting discovery and novel physics uncovered in subsequent experiments, numerous efforts have been made to fabricate graphene sheets of high quality, and low price in parallel. In addition to mechanical exfoliation technique that produces micron-sized graphene flakes, chemical vapour deposition (CVD) on metal surface has also been successfully applied to synthesize single- and few-layer graphene sheet with areas of square centimetres (Bae et al., 2010). However, the most popular method for mass production at present is the chemical reduction technique, where graphite is firstly exfoliated in an oxygen-rich environment. The intermediate product, graphene oxide, is subsequently reduced to recover bare graphene sheet. In addition, there are also several novel approaches available now, such as cutting single-walled carbon nanotubes (Kosynkin et al., 2009; Jiao et al., 2009) and bottom-up assembling from organic molecules (Yang et al., 2008; Cai et al., 2010).
The bulk graphene sheet is a semi-metal with a linear dispersion around the Dirac point. However when one of the in-plane dimensions reduces below 20 nm while maintaining the other dimension, the graphene ribbon (Fig. 1(c)) will feature an edge-dependent electronic structure due to the quantum confinement and lattice symmetry (Son, Cohen & Louie, 2006a and 2006b). Armchair-edged graphene nanoribbons (AGNR) have width-dependent energy gaps, while a zigzag-edged nanoribbons (ZGNR) is always metallic with a localized state at the edge when the spin is unpolarized. This unique structure-property relationship suggests that simple geometrical tailoring could realize effective modification on the properties of graphene.

2.1 Graphene nanostructures as building blocks for nanoelectronics

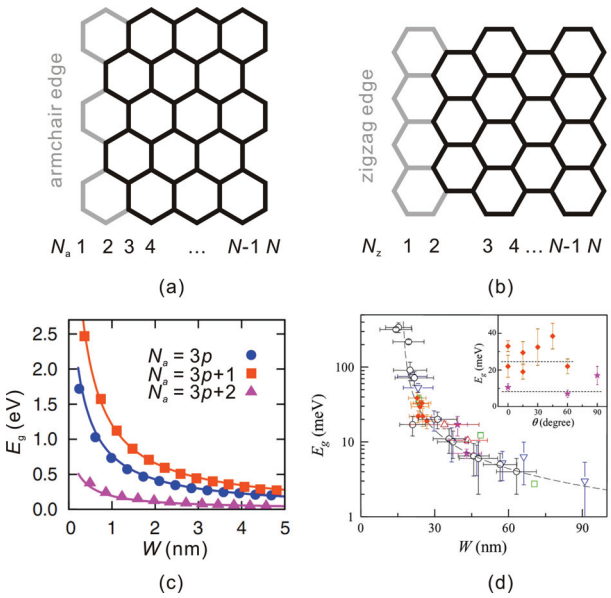

Fig. 3. (a) and (b) Atomic structures of armchair and zigzag GNRs; (c) Bandgap of armchair graphene nanoribbons calculated from density functional theory (Son, Cohen & Louie, 2006); (d) Experimental measured bandgaps of graphene nanoribbons and their dependence on the orientation of crystalline lattice (Han et al., 2007).

As illustrated in Fig. 3, the width of AGNR structure can be denoted by the number N_a. Tight-binding analysis shows that (Ezawa, 2006; Son, Cohen & Louie, 2006a and 2006b) when N_a is $3p$+2 (where p is a positive integer), the AGNR is metallic. While when N_a is $3p$ or $3p$+1, the bandgap of AGNR is inversely proportional to its width ($E_{g(3p)} \geq E_{g(3p+1)}$). These results are consistent with density functional theory (DFT) calculations based on local density approximation (LDA). The only difference is that in the DFT simulation, the reconstruction of structure and electron density at ribbon edge opens small gap for N_a = $3p$+2, and decreases (increases) the gaps of $3p$ ($3p$+1) AGNRs.

The structure of ZGNR is shown in Fig. 3(b). Simple analysis from the tight-binding picture predicts that the spin-unpolarized eigenstates of ZGNRs near E_F have a peculiar edge-state structure. There are two edge states decaying into the center of ZGNRs with a profile depending on their momentum. This can be seen from the flat bands in Fig. 3 for $k > 2\pi/3$, which give rise to a very large density of states at E_F and infinitesimally small on-site repulsion, could make the ZGNRs magnetic (Fujita et al., 1996; Nakada et al., 1996). Son, Cohen and Louie further find that when a transverse electric field is applied, an energy gap is opened for one spin channel while the other remains metallic (Son, Cohen & Louie, 2006a and 2006b).

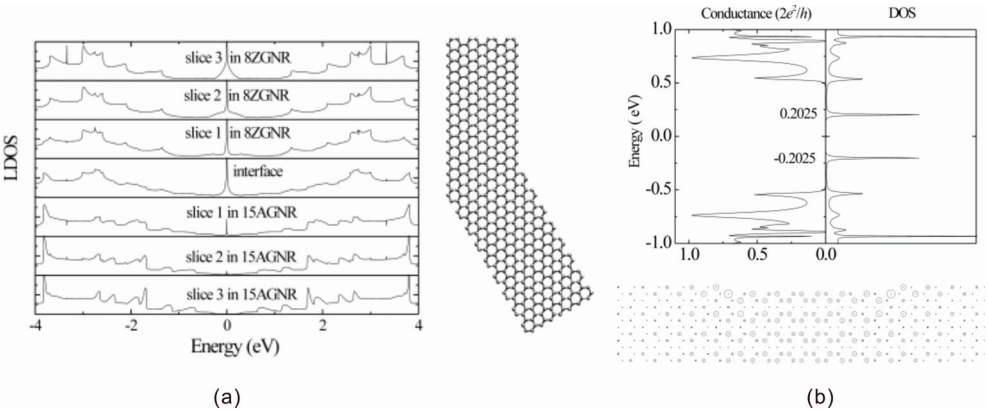

Fig. 4. GNR junctions based building blocks for nanoelectronics: (a) a junction connecting metallic ZGNRs and semiconducting AGNRs form a Schottky barrier at the interface; (b) a sandwich AGNR structure with varying width behaves as a quantum dot, the energy levels are tunable through varying the width of the central GNR (Xu, Zheng & Chen, 2007).

The width-dependence energy gaps in AGNR are soon verified by experiments (Chen et al., 2007; Han et al., 2007). Interestingly, Han et al. also find that the bandgap E_g shows no direct dependence on the crystallographic direction (Han et al., 2007). Actually during the fabrication processes or during the self-passivating process after the structure is formed, the edge shape (armchair or zigzag) can reconstruct (Jia et al., 2009; Girit et al., 2009) and this may cause the bandgap to appear for graphene nanoribbons with any crystalline orientation.

As mentioned above, graphene nanoribbons feature remarkable size- and edge-dependent electronic properties. Elementary building blocks for nanoelectronics, such as metal/semiconductor junctions and quantum dots, thus can be constructed through a combination of these structural patterns (Xu, Zheng & Chen, 2007). As shown in Fig. 4(a), a junction combining metallic and semiconducting GNRs is easy to form. By design a

sandwich structure as shown in Fig. 4 (b), a quantum dots with tunable energy levels can also be achieved.

Moreover, Finite-sized graphene nanodisk is another graphene derivative with close edges. They feature similar electronic structure as the GNRs. The triangular zigzag nanodisk can be interpreted as a quantum dot with an internal degree of freedom. Ezawa find that its ground state is a quasi-ferromagnet, which is a ferromagnetic-like state with a finite but very long lifetime. A combined system including nanodisks and leads can find applications in spin filters, amplifiers and diodes (Ezawa, 2009). Kaxiras's group also investigate arbitrarily shaped graphene nanoflakes with focuses on the spin properties and propose spintronic nanoscale devices by sculpting graphene fragments and exploiting the shape dependence of magnetic properties (Wang et al., 2007). Other nanostructures of graphene such as twists (Bets & Yakobson, 2009; Gunlycke et al., 2010) and scrolls (Xie et al., 2009; Shi et al., 2010) also have interesting electronic properties and potential applications.

2.2 Synthesis and fabrication of graphene nanostructures

To achieve a rational design of graphene nanostructures as suggested in Section 2.1, experimental techniques such as catalytic hydrogenation based nanocutting method are proposed to fabricate graphene nanostructures with specific geometry.

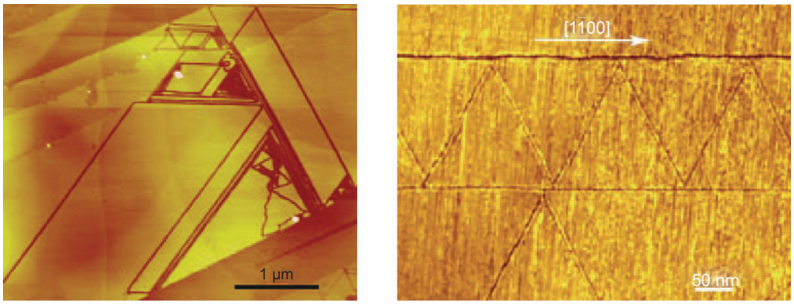

Fig. 5. Graphene nanostructures fabricated by catalytic hydrogenation: (a) an AFM images of graphene nanoribbons with different sizes and shapes; (b) STM image of equilateral triangle shaped graphene flakes formed by channels along [1-100] orientation (Ci et al., 2008).

Ci et al. (Ci et al., 2008) report a controlled cutting process for graphene sheets, using nickel nanoparticles as a knife that cuts with nanoscale precision (Fig. 5). The cutting proceeds via catalytic hydrogenation of the graphene lattice, where carbon atoms in graphene react with hydrogen into hydrocarbon and the catalytic nanoparticles continue to move due to the adhesion from remainder carbon atoms in graphene. This cutting process generates graphene pieces with specified zigzag or armchair edges. The size of the nanoparticle dictates the width of etched channel and edge structure that is produced during the cutting. The cutting occurs along straight lines and along symmetry lines, defined by angles of 60^{o} or 120^{o}, and is deflected at free edges or defects, allowing practical control of graphene nano-engineering. DFT calculation shows that the reaction barrier to remove carbon atoms and leave zigzag edges is much higher than armchair edges. This explains the experimental observation where zigzag edges are dominant.

Kinetic Monte Carlo method based on DFT results is applied to simulate the cutting dynamics. The result indicates that the nickel nanoparticle prefers to keep a straight trajectory. However when it encounters a void or open edge, the cohesion between carbon and nickel atoms force it to turn or retract back into the graphene. Thus with predefined voids or channels, specific cutting patterns can be created. Example nanostructures as fabricated using this technique, such as triangular and rectangular graphene sheets, are shown in Fig. 5.

Scanning tunnelling microscope lithography is also used to patterning graphene sheets into nanoribbons, bent junctions with nanometer-precision, well-defined widths and predetermined crystallographic orientations (Tapasztó et al., 2008). Furthermore, oxidation induced epoxy group can assist the lithography further (Fujii & Enoki, 2010).

Back to the "scotch tape" approach, as the armchair edge has lower energy than the zigzag edge, thus tearing the graphene sheet along either armchair or zigzag direction will be self-directed to leave armchair edges (Kawai et al., 2009). If the graphene sheet is attached to an adhesive substrate, the peeling process and edge geometry are then determined by both the tearing direction and substrate cohesion (Sen et al., 2010).

It is observed that the nanostructures thus fabricated have their confinement gaps opened up to 0.5 eV, enabling room-temperature operation of graphene nanoribbon-based devices.

The methods introduced above are all top-down approaches. These methods avoid the difficulties of assembling nanoscale components and may prove useful in the realization of complete integrated circuits, operating as room-temperature ballistic electronic devices. However, recent progresses also show that chemical methods that based on self-assembly reaction of monomers are also feasible. Using building blocks such as 10,10′-dibromo-9,9′-bianthryl, graphene nanoribbons with atomic precision can also be synthesized (Yang et al., 2008; Cai et al., 2010).

3. Molecular doping on the graphene sheets

In comparison to three-dimensional bulk semiconductors such as silicon, the two-dimensional morphology and single-atom thickness offer the graphene sheet more activity flexibility in response to either interior defects or exteriorly physical or chemical adsorptions. In graphene, each carbon atom is exposed to the environment with a dangling π bond, and thus is amiable to molecular functionalization on the basal plane. It is remarkable that the functionalization process could be reversed by breaking the bonding between adsorptions and graphene sheet. For example, in the chemical reduction process for producing graphene sheets, graphene monolayers are firstly exfoliated from graphite by oxidation, where the epoxy and hydroxyl binding on the basal plane of graphene break the interlayer binding. The oxidation groups are subsequently reduced to recover graphene sheets. Recently there are arising efforts in engineering the physical chemistry of graphene by functionalization, especially in the extent of molecular doping, covalently or non-covalently. In addition to the approaches in bulk materials such as substitutions, vacancies and interstitials, the notion of doping has been renovated here in a controllable and even reversible manner thanks to the coexistence of chemical inertness of sp^2 carbon network and relative activity of the p_z electrons therein.

3.1 Molecular doping on the basal plane of graphene sheets

Non-covalent functionalization, or physisorption refers to the process in which the electronic structure of graphene is barely perturbed. The weak binding nature can be established through forces such as van der Waals or electrostatic dipole-dipole interactions.

These functionalizations, especially those are weak in mechanical binding but strong in electronic coupling, hold great promises in the various applications such as chemical sensors, molecular switches and transistors.

The fundamental limit for these applications is the fluctuations due to thermal motion of charges and defects that lead to intrinsic noise exceeding the responsive signal from individual adsorption molecules. Impressively, gaseous non-covalent dopants, such as the water molecule, N_2, NO_2 and NH_3, can be adsorbed physically on the basal plane of graphene. These adsorptions, although interacting weakly with graphene, have remarkable impacts on the intrinsic electronic properties of graphene. The Hall measurements show that NO_2, H_2O and iodine act as acceptors whereas NH_3, CO and ethanol are donors. They contribute to a resistivity change up to 4 percent at zero magnetic field (Schedin et al., 2007). The adsorbed molecules change the local carrier concentration in graphene one by one electron, and lead to step-like changes in resistance. The micro-sized graphene thus can detect individual events when a gas molecule attaches to or detaches from its surface. Chemical sensors and non-volatile memories can be directly designed following this concept.

Similarly, the non-covalent binding of 2,3-dichloro-5,6-dicyano-1,4-benzoquinone (DDQ) and tetrathiafulvalene (TTF) on graphene sheet induce the hybridization between the molecular levels and graphene valence bands, and transform the zero-gap semiconducting graphene into a metallic graphene. However, The functionalizations by non-covalent organic molecules physisorptions cannot lead to significant response in the transport property for sensory applications. Instead, by introducing metal atoms to intercalate between the molecules and graphene sheet, a two-order higher response can be achieved (Zhang et al., 2009).

Not only non-covalent adsorptions, but also some chemisorptions that forming covalent bonds with carbon atoms on the basal plane of graphene can tune its properties in a controllable manner. Hydrogenation and oxidation are two of the most noticeable approaches in the covalent context. Electrochemical modification of graphene can be induced by chemical reactions of graphene with proton and hydroxyl that are catalytically generated from water molecules in the gate dielectrics, making the graphene nonconductive. Notably, this process can subsequently be reversed by short current pulses that cause rapid local annealing (Echtermeyer et al., 2007). Experimental studies also reveal the semimetal-insulator transition in graphene after hydrogenation, which is then recoverable through structural annealing (Elias et al., 2009). When rationally designed, this reversible engineering on graphene has further potential applications in designing functional nanoscale materials and devices, such as hydrogen storage materials and patterned nanoelectronics (Singh & Yakobson, 2009; Lee & Grossman, 2010). The fully hydrogenated graphene – graphane – offers a high hydrogen storage weight ratio up to 7.7 wt % that is able to meet US Department of Energy (DOE)'s 2010 goal (6 wt %).

Oxidation of graphene sheet has been widely utilized in fabricating graphene sheet in the chemical reduction method to exfoliate monatomic layer from graphite. The most notable structure for the intermediate product, graphene oxide, proposed is the Lerf–Klinowski model on the basis of NMR spectroscopy data, which contains epoxy and hydroxyl groups on the graphene sheets or at their edges (Lerf et al., 1998). Whereas hydroxyl groups are easy to be removed under annealing, the epoxy groups are much more stable. Experimentally, fault lines in graphene are observed experimentally in oxidized graphene, where epoxy group unzip the sp^2 carbon-carbon bonds beneath (Li et al., 2006). This is explained as adsorbed epoxy groups that tend to line up cooperatively for lower formation

energy. In contrast, a recent ultrahigh vacuum scanning probe microscopy (UHV STM) study reveals locally periodic structures where the hexagonal lattice of graphene is only distorted slightly. The atomic structure is identified as an oxygen atom lattice bound to the graphene sheet with a high density of n_O:n_C = 1:4, where n_C and n_O is the number of carbon and oxygen atoms (Pandey, Reifenberger & Piner, 2008).

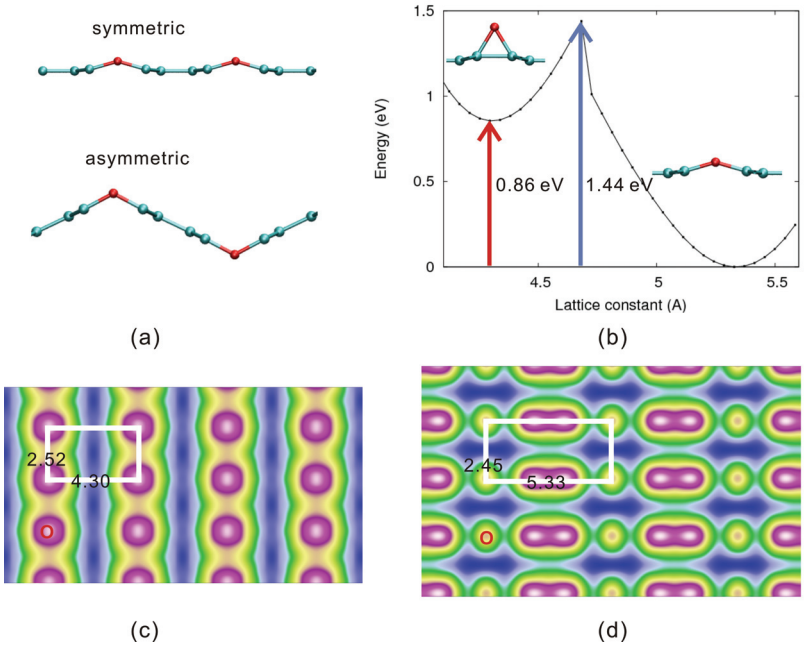

Fig. 6. (a) Optimized symmetric and antisymmetric structures for C_8O, projected along the epoxy line direction; (b) Energy landscape for graphene epoxide C_4O as changing the lattice constant along the *x* direction: insets show its metastable clamped (left) and unzipped (right) structures; (c) and (d) Simulated STM image for clamped (c) and unzipped (d) graphene oxide where epoxy groups bind on the same side. For the clamped phase, the simulated image and lattice constants (a = 4.30 Å and b = 2.52 Å) are consistent with experimental observations (Pandey, Reifenberger & Piner, 2008; Xu & Xue, 2010).

To clarify this inconsistence, DFT calculations are performed for graphene epoxide. The results show that in graphene epoxide C_4O, when oxygen atoms bind on the same side (symmetric structure in Fig. 6(a) and (b)), two distinct phases—metastable clamped and stable unzipped structures—are observed consistent with the two experimental observations (Fig. 6(b)). In the clamped structure, oxygen atoms form a regular lattice on the graphene sheet. This metastable structure is stabilized by an energy barrier of 0.58 eV. The simulated STM images (Fig. 6(c) and (d)) reproduce corresponding structures observed in the experiments. Furthermore, if both sides of the graphene are exposed for oxidation, neighboring epoxy groups can reside also on opposite sides to form the so-called antisymmetric structure. The formation energy of graphene epoxide in this symmetry is lower in unzipped phases (Fig. 6(b)). In the antisymmetric structures, the planar structure of the graphene part between epoxy groups is well kept and there is negligible lattice

distortion in the graphene sheet. The final structure is optimized in a zigzag shape, where neighbouring epoxy groups hinge planar zigzag graphene ribbons.

3.2 Coupling between graphene sheets and substrates

Although suspended and freestanding graphene can be established by deposit graphene sheet on scaffolds or nano-pores, most applications require that graphene is supported by a substrate, which has a stable and planar morphology and is easy to pattern. Substrates with mismatched lattice constants and strong adhesion could induce ripples of several Angstroms in the graphene sheet. While those with similar lattice constants, e.g. Ni, preserve its planar geometry. The substrates where graphene sheets are deposited offer another route to modulate the ground state and transport properties of graphene and related materials (Witterlin & Bocquet, 2009; Xu & Buehler, 2010b).

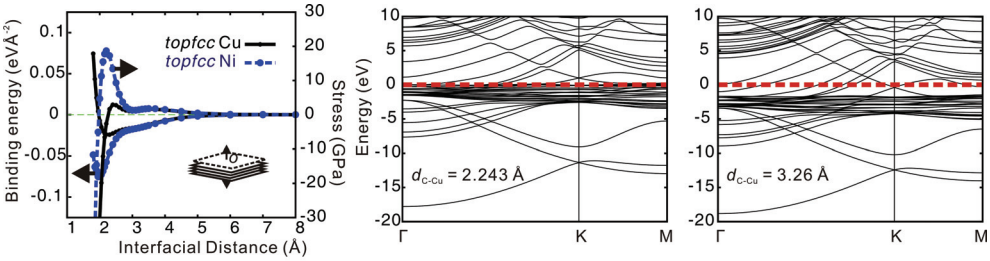

Fig. 7. (a) Interface binding energy and stress σ between graphene and the copper/nickel (111) surfaces. The binding energy E_b is -91.33 meVÅ^{-2} for nickel, higher than -24.81 eVÅ^{-2} for copper surface. Its tensile strength is 18.70 GPa, also much higher than 2.92 GPa as obtained for the copper surface; (b) and (c) Electronic band structures of the graphene-copper (111) hybrid system with interface distance $d_{C\text{-}Cu}$ = 2.243 Å (b) and 3.26 Å (c) (Xu & Buehler, 2010b).

The binding between graphene and metal substrates is generally weaker than a covalent bond, and can be classified into two groups. Al, Cu, Ag, Au and Pt have weak cohesion with graphene, while Co, Ni and Pd have strong cohesion (Giovannetti et al., 2008). DFT calculations on copper (111) and nickel (111) surfaces adhered to a monolayer of graphene show that their cohesive energy, strength and electronic structure correlate directly with their atomistic geometry. Due to the strong coupling between π-orbitals in graphene and open *d*-orbitals in metal, the nickel-graphene interface has much a stronger cohesive energy with graphene than copper (Fig. 7(a)). Interestingly, for both nickel and copper, the interface cohesive energy profile features a well-and-shoulder shape that cannot be captured by simple pair-wise models such as the Lennard-Jones potential. Band structure analysis shows that, the binding between graphene and metal substrate at the well and shoulder positions in the profile correspond to different electronic coupling at the interface. For example, at $d_{C\text{-}Cu}$ = 2.243 Å, the Fermi level (E_F = 0) of the hybrid system is pinned to the Cu bands and $d_{C\text{-}Cu}$ is close to the interlayer distance in graphite. While at $d_{C\text{-}Cu}$ = 3.26, the coupling between the p_z orbital of carbon atoms and the d_{z2} orbital of copper atoms is weak, the Fermi level is close to the crossing between graphene π and π* bands, and $d_{C\text{-}Cu}$ is close to the interlayer distance in copper crystal along (111) direction (Xu & Buehler, 2010b). These results provide a detailed understanding of the interfacial properties of graphene-metal systems, and help

to predict the performance of graphene based nanoelectronics and nanocomposites. The availability of structural and energetic data of graphene-metal interfaces could also be useful for the development of empirical force fields for molecular dynamics simulations that correctly characterize their structural and mechanical properties.
Intercalation of atoms (metal, hydrogen, oxygen, nitrogen oxide, etc.) between graphene sheet and the substrate is another novel route to modify the interfacial chemistry. The selective oxidation of ruthenium surface beneath graphene can lift the strong Ru-graphene coupling and restores characteristic Dirac cones of monolayer graphene sheet (Sutter et al., 2010). Hydrogen intercalation can also decouple graphene sheet from silicon carbide surface that is initially covalently bonded and produce quasi-free-standing epitaxial graphene sheet on large SiC wafers (Riedl et al., 2009).

3.3 Interior doping through defects

Creating defects, localized or extended, can also modify graphene and form nanostructures interiorly (Lusk & Carr, 2008; Bai et al., 2010), in comparison to the exterior doping as discussed previously. Grain boundaries introduced by extended local defects, such as Stone-Wales defects and divacancies, can alter the electronic structures of graphene sheet (Yazyev & Louie, 2010). A one-dimensional topological defect containing octagonal and pentagonal sp^2-hybridized carbon rings embedded in a perfect graphene sheet act as a quasi-one-dimensional metallic wire (Lahiri et al., 2010).

3.4 Effects of external fields

It is reported that the bandgap of bilayer graphene can be tuned by electric field in perpendicular to the basal plane, e.g. through gating. The symmetry of sublattice in AB stacking is broken upon electrical gating. The electrical displacement fields in different graphene layers produce two effects including a net carrier doping (shifting of the Fermi energy) and generation of a non-zero bandgap. The gate-tunable bandgap can reach 250 meV and has the unusually strong oscillator strength for the bandgap transitions. Thus bilayer graphene under electrical field tuning can enable novel nanophotonic devices for infrared light generation, amplification and detection. Using a double-gate configuration, an insulating state with large suppression of the conductivity in bilayer graphene can be further achieved (Zhang et al., 2009; Oostinga et al., 2008). In comparison to exterior dopants and defects, the advantage of this control method is that the control is non-contact and can be continuous tuned.

4. Strain engineering

Strain engineering, or more generally tuning material properties by applying mechanical loads or deformation, is a powerful strategy in improving material performance. In silicon-based semiconductor industry, strained silicon has much higher mobility, and thus much better chip performance and lower energy consumption. When material goes down to low dimension, the effects of strain become even more significant as directional load is more feasible. Also bending of two-dimensional membranes or one-dimensional ribbons can easily be excited at ambient condition, resulting in a significant local curvature. Recently, stretchable and flexible electronics have attracted many interests from various disciplines. Thus, a mapping between deformation of graphene and its impacts on the properties becomes extremely important.

As introduced in previous sections, molecular functionalization on graphene sheet usually induces structural distortion as it disturbs or breaks the underlying sp^2 bonding network and forms sp^3 bonds locally. Vice versa, mechanical deformation, which modifies the sp^2 bonds, provides another method to tune the graphene properties, reversibly. This approach, in combination with molecular doping, is expected to play a critical role in nano-engineering of graphene and related materials.

4.1 Structural and structural response to molecular doping

When graphene is hydrogenized by single hydrogen atom, the dangling p_z state of carbon is saturized by the proton. As a result the sp^2 network below is broken. Distortion is formed, tending to transform the planar morphology into tetrahedral lattice as in diamond. The fully hydrogenated graphane structure, as shown in Fig. 8, can take two forms with hydrogen binding on the same or alternating sides of A and B lattices. We call them symmetrical and anti-symmetrical graphane, respectively.

In comparison to pristine graphene where a_g=2.44 Å, consistent with experimental value 2.42 Å, these two graphane phases have lattice constants a_{sym}=2.79 Å and a_{asym}=2.5 Å, respectively. The antisymmetric phase is found to be energetically 1.8 eV (per carbon-hydrogen pair) more favorable than the symmetric one.

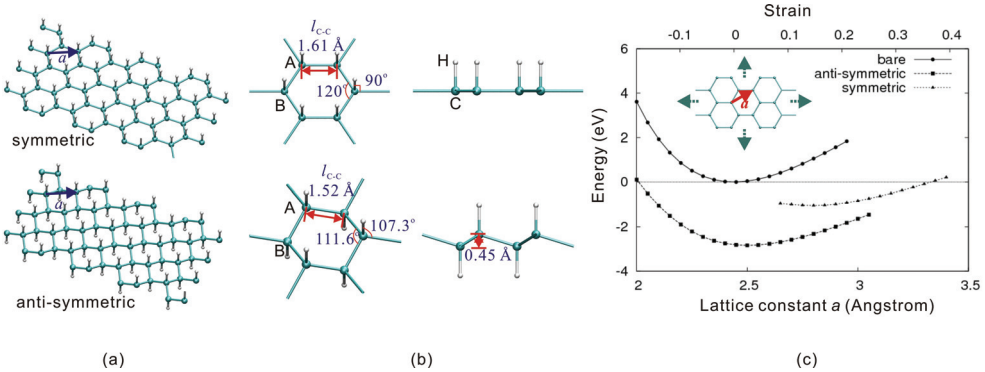

Fig. 8. (a) Optimized structures of symmetric and antisymmetric graphane. The unit cell contains two carbon atoms (A and B denote the two sublattices) as in graphene and two hydrogen atoms; (b) Local atomic structures; (c) Energies of pristine graphene (with additional energies from isolated hydrogen atoms) and graphane under biaxial strain loading showing the effects of strain engineering (Xue & Xu, 2010a).

In the symmetric phase (Fig. 8 a and b), binding of hydrogen atoms expands the lattice constant underneath hexagonal graphene lattice by 14%, while preserving the planar configuration. As evidenced by localized density of states close to the Fermi level, the planar symmetry preserves sp^2 characteristic in graphane. Total density of states is projected onto s and p atomic orbital on each carbon atoms. $p_z(l = 1, m = 0)$ orbital is distinct and contributes mostly near the Fermi level. Binding of hydrogen induces 0.14 electron transfer from hydrogen to carbon since carbon is slightly more electronegative than hydrogen. Also the hydrogenation through p_z orbital opens an energy gap E_g of 0.26 eV in comparison with the zero-gap nature of pristine graphene.

In antisymmetric phase (Fig. 8 a and b), symmetry breaking between the two representative carbon (hydrogen) atoms in a unit cell allows the transition from sp^2 (graphene-like)

hybridization to sp^3 (diamond-like) characteristics. The sp^3 hybridization induces out-of-plane corrugation of 0.45 Å and the carbon–carbon bond length is 1.52 Å, which is close to 1.54 Å in diamond. The bond angle $A_{C\text{-}C\text{-}C}$ = 111.6° and $A_{H\text{-}C\text{-}C}$ = 107.3° also resemble the tetrahedral angle 109° in diamond. The antisymmetric phase also opens a bandgap E_g of 3.35 eV, which is smaller than that in diamond (4.2 eV from DFT calculation).
In the symmetric structure, all the bond distortion has the same sign of curvature, thus forcing the sheet to bend towards the hydrogen-free side. This mechanism is proposed to form nanoscrolls or nanotubes by hydrogenating suspended graphene sheet (Yu & Liu, 2007). However, in the anti-symmetric graphane, although the structure is corrugated due to the torsion of carbon-carbon bonds, the whole structure keeps two-dimensional.
Oxidation by epoxy groups also induces significant change of the graphene structure as discussed in the previous section. For the symmetrical structure, the epoxy ring is close to an equilateral triangle in the metastable clamped phase. The adsorption of an oxygen atom stretches the lower C–C bonds by 5% but does not break the sp^2 carbon network (Fig. 6(b)). In the more stable unzipped structure, the angle C–O– C between two carbon–oxygen bonds in an unzipped epoxy ring is about 150°. The final C–C bond is broken with an extended distance of 2.5 Å (Fig. 6(a and b)), explaining the folds and wrinkles observed in graphene oxides due to sparse epoxy lines (Li et al., 2006).
In the unzipped phase, an epoxy group breaks the lower sp^2 bond and modifies the mechanical and electronic properties of graphene remarkably. The foldable epoxy ring structure reduces its Young's modulus by 42.4%, while leaving the tensile strength almost unchanged. As n_O:n_C is decreasing, the perturbation of epoxidation on the band structures depends on the density and symmetry of oxidation. These oxygenated monolayer sheets are structurally close to graphene and are expected to have similarly peculiar properties. One thus can functionalize graphene structures in a controllable manner through chemical oxidation and reduction (Xu & Xue, 2010).

4.2 Effects of structural deformation on the properties of graphene materials

Elastic strain can induce a shift of the Dirac point energy from local changes in electronic density. Moreover, it will also induce an effective vector due to the change of electron-hoppling amplitude between adjacent carbon atoms (Castro Neto et al., 2009). Local buckling, wrinkling and curving of graphene sheet also generate pseudoelectric and pseudomagnetic fields that modify its electronic structures and transport properties (Pereira et al., 2010; Bao et al., 2009). The charge carriers in graphene are expected to circulate as if under the influence of an applied out-of-plane magnetic field. It has recently been proposed that a modest strain field with triangular symmetry will give approximately uniform, quantizing magnetic fields upward of tens of Tesla (Levy et al., 2010).
The abrupt change in lattice constants and planar structure of graphene after hydrogenation in symmetric and antisymmetric phase suggests possible control of the hydrogenation process and the properties of graphane through applying mechanical deformation. Strain engineering is proposed to tune the hydrogenation process on graphene by applying deformation to graphene in prior to hydrogen binding or releasing. To quantify the binding strength between the hydrogen atoms and graphene sheet in terms of single carbon-hydrogen pair, the formation energy of graphane is defined as $E_f = E_{graphane} - (E_{graphene} + E_H)$, where $E_{graphane}$ and $E_{graphene}$ are the energy of graphane and pristine graphene, respectively. In absence of strain in the graphene lattice, symmetric and antisymmetric graphane phases (Fig. 8(a) and (b)) have binding strength E_f of -1.044 and -2.847 eV per C–H atom pair.

Fig. 8(c) show the effects of biaxial in-plane strain on the energies of both the types of graphane structures, and also the combined system of pristine graphene and isolated hydrogen atom. Pristine graphene has an optimized lattice constant a_g = 2.44 Å, while symmetric graphane has a_{sym} = 2.79 Å. The energy of both graphene (with additional constant energy terms from isolated hydrogen atoms) and symmetric graphane increases as the tensile strain is enhanced, When the lattice constant a exceeds 3.35 Å, the binding energy of symmetric graphane is larger than the value of undeformed system with pristine graphene and isolated hydrogen atoms. Also energy of nonhydrogenated system increases much faster than symmetric graphane. As a result, the binding energy of hydrogen is changed by 53.89% (with respect to the value without loading, a = 2.44 Å) when the graphene is under a prestrain of 10% (from a = 2.44 to 2.69 Å). The strain for sp^2 bond breaking in graphene is 18%, enabling a feasibly reversible control. On the other hand, if the graphene sheet is restrained at a_g = 2.44 Å against to in-plane expansion or the symmetric graphane is compressed from its equilibrium value to below 2.65 Å, repulsion between the carbon-hydrogen pairs will cause the hydrogenated structure to be mechanically unstable. The hydrogen atoms are repelled (released) from the graphene plane. The sensitivity of symmetric hydrogenation of graphene on strain observed here thus provides a flexible and reversible controllability by simply stretching or compressing the graphene sheet.

In antisymmetric phase, a remarkable dependence of the formation energy on the strain is also observed. Optimized lattice constant a_{asym} = 2.5 Å. In-plane tensile and compressive strain of graphene sheet up to 10% can change the binding strength remarkably by 23.56% and -2.9%. The structure breaks at a tensile strain of 22% or a compressive strain of 26%. In comparison with symmetric phase, the strain modification of hydrogen binding energy is less significant as it has similar optimal lattice constant as pristine graphene. Under tensile strain, due to the weaker interaction between adjacent carbon-hydrogen pairs on the opposite sides of graphene, the expansion of in-plane lattice constant is found to be able to reduce its out-of-plane corrugation slightly and partially recover the π electron characteristics of graphene.

In symmetric phase, carbon-hydrogen bond length l_{C-H} increases at either tensile or compressive strain. As a is reduced to be less than 2.6 Å, the carbonhydrogen bond is broken. Hydrogen atoms on graphene will be released from graphene sheet as discussed before. While at tensile strain and when the stress approaches the tensile strength and the in-plane sp^2 carbon network is about to be broken, l_{C-H} is elongated to the same value as in benzene or methane ($l_{CH\text{-}methane}$ = 1.096 Å). In antisymmetric phase, when tensile strain is applied, the planar configuration of graphene is partially recovered, suggesting emerging sp^2 feature. The carbon-hydrogen bond length decreases and approaches the value in sp^2 bonded symmetric phase in this situation. When antisymmetric structure is compressed, the sp^3 characteristic is enhanced and the carbon-hydrogen bond length also decreases toward the value in methane. As a result, the carbon-hydrogen bond length maximizes at the optimised lattice constant. These remarkable strain effects can further be extended to other nanostructures like carbon nanotubes and few-layer graphite (Xue & Xu, 2010a; Xue & Xu, 2010b).

5. Hierarchical structures of macroscopic graphene materials

Graphene and graphene nanoribbons present intriguing properties and thus have been suggested for a wide range of applications from nanoelectronics to nanoelectromechanical

systems. However, as introduced before (Fig. 1), the morphology of this monolayer material has large derivation from the native two-dimensional sheet at elevated structures, especially for the ribbon with high aspect ratio. Also entanglements and scrolls are easy to form at marked density, instead of the patterned or self-organized structures as required by industrial applications. To bridge the scales from their nanostructural geometry—the key for their unique properties—to the critical requirements for large-scale electronics and device applications, there we need a hierarchical approach to assembly macroscopic materials from functionalized graphene sheets or nanoribbons. This approach has to (1) be able to assemble the nanostructures into macroscopic assemblies, while (2) preserving their nanostructure-specific physical significance and novel properties at larger scales, such as its size- and shape-dependent electronic structures.

5.1 Hierarchical assembly of functionalized graphene nanostructures

As inspired by the hierarchical bonding networks in protein and nucleic acid materials (Fig. 9(a)), a bottom-up assembly or top-down lithography approach has been proposed by introducing hydrogen bonds between individual graphene nanoribbons (Fig. 2(b), Xu & Buehler, 2009). After substitutional doping by oxygen and nitrogen atoms on carbon atoms at edges of graphene ribbons, hydrogen bonds (–C=O…H-N- or –N…H-N-) are formed between each GNR monomer. DFT calculations show that a two-dimensional sheet consisting of GNR arrays can be stabilized through these directional weak bonds, mimicking the structure of beta-sheet proteins or base-pairs connecting DNA or RNA strands (Fig. 9(b)). The cohesive energy for each –C=O…H-N- hydrogen bond is 29.98 $kcalmol^{-1}$, which is considerably higher than the typical value 2.8 $kcalmol^{-1}$ in organics. This binding energy level resides in the realm of 'strong hydrogen bond' nature and reflects the cooperativity of periodic hydrogen bonds arrangements. The hierarchical structure is mechanically stablized by a tensile strength of 1.08 GPa in parallel to the hydrogen bond direction and a shear strength of 1.78 GPa across the hydrogen bond network.

Remarkably, these assemblies, as predicted by both first-principles calculations and molecular dynamics simulations, not only are energetically and mechanically stable, but also preserve the unique electronic properties of individual graphene nanoribbons in the bulk. Specifically, the energy gap of the bulk material shrinks as the width of the constituting graphene nanoribbon increases. For instance, the bandgap E_g and π-π^* energy gap for –C=O…H-N- assembly decreases from 1.5 and 0.5 eV at w = 1 nm to zero at 3.6 and 2.8 nm respectively (Fig. 9(c)). This tunability of bulk material properties through controlling the nanostructure enables the synthesis of a broader class of biomimetic multifunctional mechanomutable and electromutable nanomaterials for electromechanical applications. It's also notable that the localized density of states of valence and conduction bands locates at different spatial region in the assembly (Fig. 9(d)). Effective charge separation could thus be achieved by forming such junctions for photovoltaic applications.

5.2 Graphene based nanocomposites

Another class of macroscopic assemblies from graphene sheets are nanocomposites. Carbon materials, as special types of polymers, have been widely used as the filler phases to enhance the mechanical, thermal and electrical properties of polymers or metals. The carbon fiber is the most notable example of this material class, which has been developed and widely used from the 1960s and is still spreading in many industries today.

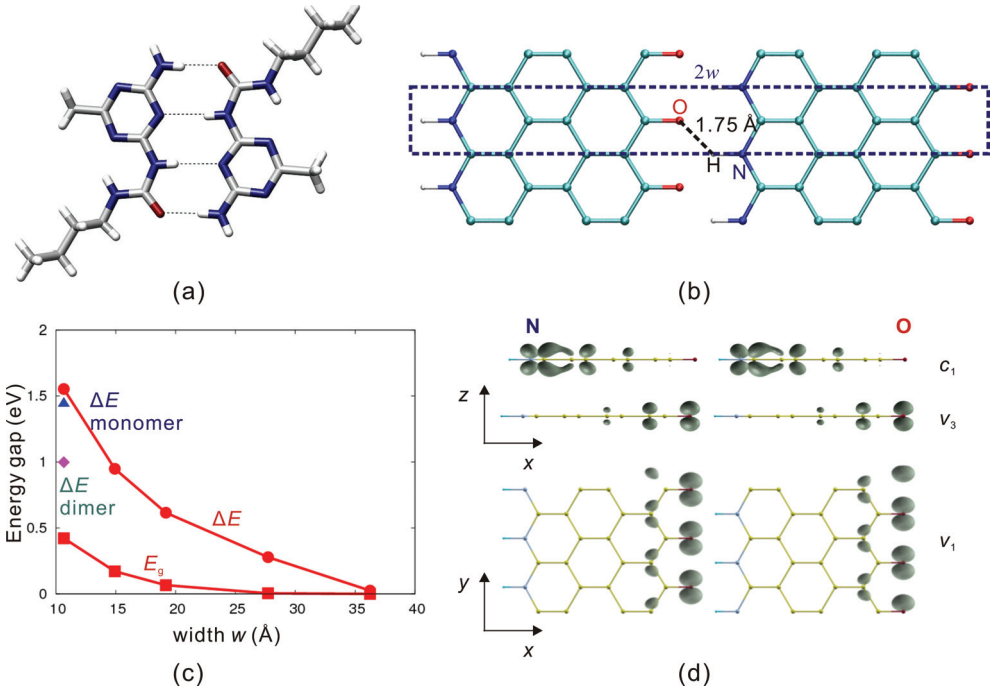

Fig. 9. (a) Hydrogen bond network in proteins; (b) Atomic structure of the assemblies, resembling the geometry of beta-sheet proteins. The dashed box shows a unit cell with width $2w$, where w is the width of individual GNR; (c) Energy gap E_g (circle line) and π–π* bandgap $\Delta E = E_{\pi^*} - E_{\pi}$ of monomer, dimer and hierarchical graphene nanoribbon assemblies through -C=O…H-N- hydrogen bonds (square line) with different widths; (d) Local densities of states for π* (c_1), π (v_3) and oxygen (v_1) states, which are all localized at the graphene edge and decay quickly into the ribbon (Xu & Buehler, 2009).

The key issues determining performance of these composites are to (1) effectively disperse the filler phase and (2) improve the load or energy transfer between filler and matrix. Graphene sheets have highly appreciated structural and thermal stability, outstanding mechanical and thermal, electrical transport properties. However, the cohesion between graphene sheets in graphite platelets and weak van der Waal binding between graphene and polymer matrix greatly prohibit the load transfer, distribution, and thus its application in high-performance nanocomposites.

However, recent progresses in functionalized graphene, such as graphene oxide nanocomposites, successfully solve these two critical issues. Firstly, the formation of epoxy, hydroxyl and other functional groups on the basal plane of graphene sheet expands the interlayer distances in graphite and avoids multiplayer aggregation. Secondly, through forming hydrogen bonds, metal-mediated bonds or polymerisation between the graphene oxide sheets and polymers, the performance can be effectively improved, thus providing in parallel excellent performance and cheap fabrication.

In comparison to the buckypapers consisting of carbon nanotubes and other carbon or clay-based papers, Ruoff's group find that the graphene oxide paper-like material possesses

unique layered structures where individual compliant graphene oxide sheets are interlocked/tiled together in a near-parallel fashion. Their atomic-scale corrugation, micro-scale wrinkled morphology and strong interlayer interactions results in a highly effected load distribution across the entire macroscopic sample and thus make the material more resilient than other papers (Dikin et al., 2007). Impressively, they find that the graphene oxides are feasible for further functionalization. Significant enhancements in mechanical stiffness (10 - 200%) and fracture strength (~ 50%) are achieved by introducing a small amount (less than 1 wt%) of divalent ions, e.g. Mg^{2+} and Ca^{2+} (Park et al., 2008). Chemical modification with alkylamines can also be established that directly introduces tunability of paper structures and tensile strength through the amine length (Stankovich et al., 2010).

6. Conclusion and perspectives

In this chapter, we outline recent research progresses on nano-engineering the graphene and related materials. The content is classified into four categories: structural tailoring, molecular doping, strain engineering and hierarchical assembling. Each of these categories is elaborated with both the general idea, related theoretical and experimental work. The topics selected here are those the author has been working on, to ensure we include as much exciting achievement as possible in this fertilized field.

Nevertheless, there are still several key issues expected to be resolved in the future development on the graphene nano-engineering:

Scalability – Most of the nano-engineering techniques modify the properties of graphene and related materials at the molecular level. However towards industrial applications, feasible scaling methods have to be developed, such as patterning and self-assembly. Unlike other self-assembly system, the scaling here on graphene sheet must be hierarchical, the layer-by-layer or scrolling organizing have to be exclude in the assembling process as they introduce interlayer coupling between graphene sheets. The controllable top-down lithography and bottom-up assembly directed by hydrogen bonds or covalent bonds that have orientation-specification are very promising in this direction.

Tunability – Multifunctional materials hold great potentials for the next-generation materials including high-performance composites, nanoelectronics, microfluidics, and other microelectromechanical systems (MEMS) or nanoelectromechanical systems (NEMS). The non-covalent functionalization methods treating gaseous molecules, metal atoms, or covalent functionalization that can be reversibly applied have great potentials for this issue.

Applications – The multifunctionality of graphene offers it numerous applications. Novel applications in emerging fields still need exploration, such as quantum information devices and sustainable energy applications where nanoscale engineering can play an important role. Moreover, the graphene flake, nanoribbon, sheet and graphite are representative zero-, one-, two- and three-dimensional materials. This unique feature suggests to use graphene related materials as platforms or model materials for basic research. Graphene is also a unique material standing between inorganic and organics materials. Combining materials engineering with synthetic biological methods also helps to select, design and produce new classes of materials designed from the molecular level upwards.

Finally, we close this chapter by calling upon researchers to pay attention to following key scientific problems.

Intermolecular interactions – The basic interactions between molecular dopants, functional groups, supporting substrates and graphene are still not clear. The physical and chemical

properties of interactions such as hydrogen bonds, electrostatic, hydrophobic forces, especially those involved in assembling processes, should be highlighted.

Nanoscale interfaces – The interface between graphene and various materials including semiconductors, metals and polymers dominates the performance of nanoelectromechanical devices and nanocomposites. However, it is not clear that if conventional interface theories still hold at this scale, especially those related to the energy transport processes across.

Multiphysics coupling – The research on graphene and related materials towards industrial applications are intrinsically multiphysical and multiscale. The interplay between structural, mechanical, electronic and optical properties, which shapes the unique features of these materials outperforming conventional materials, must be understood. Multiphysics and multiscale computational paradigm and experimental platforms are urged.

7. References

Bae, S. et al. (2010). Roll-to-roll production of 30-inch graphene films for transparent electrodes, *Nature Nanotechnology* 5, 8, 574-578

Bai, J. et al. (2010). Graphene nanomesh, *Nature Nanotechnology* 5, 3, 190-194

Bao, W. et al. (2009). Controlled ripple texturing of suspended graphene and ultrathin graphite membranes, *Nature Nanotechnology* 4, 9, 562-256

Bartels, L. (2010). Tailoring molecular layers at metal surfaces, *Nature Chemistry* 2, 2, 87-95.

Bets, K. and B. Yakobson (2009). Spontaneous twist and intrinsic instabilities of pristine graphene nanoribbons, *Nano Research* 2, 2, 161-166

Cai, J. et al. (2010). Atomically precise bottom-up fabrication of graphene nanoribbons, *Nature* 466, 7305, 470-473

Castro Neto, A. H. et al. (2009). The electronic properties of graphne, *Review of Modern Physics* 81, 1, 109-162

Chen, Z., et al. (2007). Graphene nano-ribbon electronics, *Physica E: Low-dimensional Systems and Nanostructures*, 40, 2, 228-232

Ci, L. et al. (2008). Nanocutting of graphene, *Nano Reseach* 1, 2, 116-122

Dikin, D. A. et al. (2007). Preparation and characterization of graphene oxide paper, *Nature* 448, 7152, 457-460

Echtermeyer, T. J. et al. (2007). A graphene-based electrochemical switch, *Arxiv :0712.2026*

Elias, D. C. et al. (2009). Control of graphene's properties by reversible hydrogenation: evidence for graphane, *Science* 323, 5914, 610-613

Ezawa, M. (2006). Peculiar width dependence of the electronic properties of carbon nanoribbons. *Physical Review B* 73, 4, 045432.

Ezawa, M. (2009). Spin filter, spin amplifier and spin diode in graphene nanodisk, *The European Physical Journal B* 67, 4, 543-549

Fasolino, A., Los, J. H. & Katsnelson, M. I. (2007). Intrinsic ripples in graphene, *Nature Materials* 6, 6, 858-861

Fujii, S. & Enoki, T. (2010). Cutting of oxided graphene into nanosized pieces, *Journal of the American Chemical Society* 132, 29, 10034-10042.

Fujita, M. et al. (1996). Peculiar localized state at zigzag graphite edge, *Journal of the Physical Society of Japan* 65, 7, 1920-1923

Giovannetti, G. et al. (2008) Doping graphene with metal contacts, *Physical Review Letters* 101, 2, 026803-4

Girit, Ç. Ö. et al. (2009). Graphene at the edge: stabilityand dynamics, *Science* 323, 5922, 1702-1708

Guinea, F. et al. (2010). Energy gaps and a zero-field quantum Hall effect in graphene by strain enginering, *Nature Physics* 6, 1, 30-33

Gunlycke, D. et al. (2010). Edges bring new dimension to graphene nanoribbons, *Nano Letters* 10, 9, 3638-3642

Han, M. Y. et al. (2007). Energy bandgap engineering of graphene nanoribbons, *Physical Review Letters* 98, 20, 206805-4

Jia, X. et al. (2009). Controlled formation of sharp zigzag and armchair edges in graphitic nanoribbons, *Science* 323, 5922, 1702-1705

Jiao, L. et al. (2009). Narrow graphene nanoribbons from carbon nanotubes, *Nature* 458, 7240, 877-880

Kawai, T. et al. (2009). Self-redirection of tearing edges in graphene: tight-binding molecular dynamics simulations, *Physical Review B* 80, 3, 033401-4

Kosynkin, D. V. et al. (2009). Longitudinal unzipping of carbon nanotubs to form graphene nanoribbons, *Nature* 458, 7240, 872-876

Lahiri, J. et al (2010). An extended defect in graphene as a metallic wire, *Nature Nanotechnology* 5, 5, 326-329

Lee, J.-H. & Grossman, J. C. (2010). Magnetic properties in graphene-graphane superlattices, *Applied Physics Letters* 97, 13, 133102-3

Lerf, A. et al. (1998). Structure of graphite oxide revisited, *Journal of Physical Chemistry B* 102, 23, 4477-4482

Levy, N. et al. (2010). Strain-induced pseudo-magnetic fields greater than 300 tesla in graphene nanobubbles, *Science* 329, 5991, 544-547

Li, J.-L. et al. (2006). Oxygen-driven unzipping of graphitic materials, *Physical Review Letters* 96, 17, 176101-4

Li, X. et al. (2008). Chemically derived, ultrasmooth graphene nanoribbon semiconductors, *Science* 319, 5867, 1229-1232

Lusk, M. T. & Carr, L. D. (2008). Nanoengineering defect structures on graphene, *Physical Review Letters* 100, 17, 175502-4

Meyer, J. C. et al. (2007). The structure of suspended graphene membrane, *Nature* 446, 7131, 60-63

Nakada, K. et al. (1996). Edge state in graphene ribbons: nanometer size effect and edge shape dependence, *Physical Review B* 54, 24, 17954-17961

Novoselov, K. S. et al. (2004). Electric field effect in atomically thin carbon films, *Science* 306, 5696, 666-669

Oostinga, J. B. et al. (2008). Gate-induced insulating state in bilayer graphene devices, *Nature Materials* 7, 2, 151-157

Pandey, D., Reifenberger, R. & Piner, R. (2008). Scanning probe microscopy study of exfoliated oxidized graphene sheets, *Surface Science* 602, 9, 1607-13

Park, S. et al. (2008). Graphene oxide papers modified by divalent ions – enhancing mechanical properties via chemical cross-linksing, *ACS Nano* 2, 3, 572-578

Pereira, V. M. et al. (2010). Geometry, Mechanics, and Electronics of Singular Structures and Wrinkles in Graphene, *Physical Review Letters* 105, 15, 156603-4

Riedl, C. et al. (2009). Quasi-free-standing epitaxial graphene on SiC obtained by hydrogen intercalation, *Physical Review Letters* 103, 24, 246804.

Schedin, F. et al. (2007). Detection of individual gas molecules adsorbed on graphene, *Nature Materials* 6, 9, 652-655

Sen, D. et al. (2010). Tearing graphene sheets from adhesive substrates produces tapered nanoribbons, *Small* 6, 10, 1108-1116

Shi, X. et al. (2010). Tunable water channels with carbon nanoscrolls, *Small* 6, 6, 739-744

Singh, A. & Yakobson, B. I. (2009). Electronics and magnetism of patterned graphene nanoroads, *Nano Letters* 9, 4, 1540-1543

Son, Y. W., Cohen, M. L. & Louie, S. G. (2006a). Half-metallic graphene nanoribbons, *Nature* 444, 7117, 347-349

Son, Y. W., Cohen, M. L. & Louie, S. G. (2006b). Energy gaps in graphene nanoribbons, *Physical Review Letters* 97, 21, 216803-4

Stankovich, S. et al. (2010). Systematic Post-assembly modification of graphene oxide paper with primary alkylamines, *Chemistry of Materials* 22, 14, 4153-4157

Sutter, P., Sadowski, J. T. & Sutter, E. A. (2010). Chemistry under cover : tuning metal-graphene interaction by reactive intercalation, *Journal of the American Chemical Society* 132, 23, 8175-8179

Tapasztó, L. et al. (2008). Tailoring the atomic structure of graphene nanoribbons by scanning tunneling microscope lithography, *Nature Nanotechnology* 3, 7, 397-401.

Wang, W. L. et al. (2007). Graphene nanoflakes with large spin, *Nano Letters* 8, 1, 241-245

Wintterlin, J. & Bocquet, M. L. (2009). Graphene on metal surfaces, *Surface Science* 603, 10-12, 1841-1852

Xie, X. et al. (2009). Controlled Fabrication of high-quality carbon nanoscrolls from monolayer graphene, *Nano Letters* 9, 7, 2565-2570

Xu, Z.; Zheng, Q. & Chen, G. (2007). Elementary building blocks of graphene-nanoribbon-based electronic devices, *Applied Physics Letters* 90, 22, 223115-3

Xu, Z. & Buehler, M. J. (2009). Hierarchical graphene nanoribbon assemblies feature unique electronic and mechanical properties, *Nanotechnology* 20, 37, 375704-8

Xu, Z. (2009). Graphene nanoribbon under tension, *Journal of Computational and Theoretical Nanoscience* 6, 3, 625-628

Xu, Z. & Xue, K. (2010). Engineering graphene by oxidation: a first principles study, *Nanotechnology* 21, 4, 045704-7

Xu, Z. & Buehler, M. J. (2010a). Geometry controls conformation of graphene sheets: Membranes, ribbons and scrolls, *ACS Nano* 4, 7, 3869-3876

Xu, Z. & Buehler, M. J. (2010b). Interface structure and mechanics between graphene and metal substrates, *Journal of Physics : Condensed Matter* 22, 48, 485301-5

Xue, K. & Xu, Z. (2010a). Strain effects on basal-plane hydrogenation of graphene: a first-principles study, *Applied Physics Letters* 96, 6, 063103-3

Xue, K. & Xu, Z. (2010b). Hydrogenation of carbon nanotubes: roles of symmetry and strain, *Journal of Computational and Theoretical Nanoscience* (in the press)

Yang, X. et al. (2008). Two-dimensional graphene nanoribbons, *Journal of the American Chemical Society*, 130, 13, 4216-4217.

Yazyev, O. V. and S. G. Louie (2010). Electronic transport in polycrystalline graphene, *Nature Materials* 9, 10, 806-809

Yu, D. & Liu, F. (2007). Synthesis of carbon nanotubes by rolling up patterned graphene nanoribbons using selective atomic adsorption, *Nano Letters* 7, 10, 3046-3050

Zhang, Y.-H. et al. (2010). Tuning the electronic structure and transport properties of graphene by noncovalent functionalization: effects of organic donor, acceptor and metal atoms, *Nanotechnology* 21, 6, 065201-7

Zhang, Y. et al. (2009). Direct observation of a widely tunable bandgap in bilayer graphene, *Nature* 459, 7248, 820-823.

2

Synthesis of Graphenes with Arc-Discharge Method

Nan Li, Zhiyong Wang and Zujin Shi
College of Chemistry and Molecular Engineering, Peking University
People's Republic of China

1. Introduction

Carbon is one of the elements which form life. It plays a key function in nature and is very crucial for human beings. Carbon has many different kinds of allotropes, some known for thousands of years (graphite and diamond) and some known for several decades (fullerenes and nanotubes). The amazing two-dimensional form, which named graphene, is generated only several years ago. Graphene has raised a new tidal wave of research among the whole globe since its discovery and become a dazzling star in nanoscience.

Graphene is one-atom-thick layer of sp^2-hybridized carbon tightly packed into a honeycomb lattice, and is a basic building unit for graphitic materials of all other dimensionalities (Geim et al., 2007). Over the past several years, a great deal of intensive research has been generated by graphene due to its unique electrical, thermal, mechanical, optical and other characteristics(Du et al., 2008; Booth et al., 2008). With the understanding of their physical properties, the promises for application are growing in areas of nanoelectronics, sensors, composites, batteries and hydrogen storage (Li et al., 2008).

Nevertheless, the large-scale production of high quality graphene is the principal question, which concerned with the graphene's successful applications. The methods for synthesis of graphene include exfoliation of graphite(Novolesov et al., 2004; Niyogi et al., 2006; Li et al., 2008), chemical vapor deposition(Chae et al., 2009; Yuan et al., 2009; Li et al., 2009; Dervishi et al., 2009), epitaxial growth on electrically insulating surfaces such as SiC(Emtsev et al., 2009; Juang et al., 2009), chemical reduction of graphite oxide and graphite intercalation compounds(McAllister et al., 2007; Fan et al., 2008; Zhu et al., 2010), arc-discharge method(Subrahmanyam et al., 2009; Li et al., 2010a; Wang et al., 2010), other chemical methods(Choucair et al., 2009) and so on. Among the above methods, the arc-discharge method has its unique advantages: no metal catalyst is used; the process is timesaving and facile; high quality graphene could be synthesized in decagram-scale in low cost. In the following section, we will introduce the massive synthesis of graphene through arc-discharge method, including experimental details, characterization and formation mechanisms.

2. Synthesis of graphene with arc-discharge method

2.1 Experimental details

Arc-discharge method was first used by Krastchmer and Hoffman to synthesize C_{60}(Krätschmer et al., 1990). In the last two decades, it was widely used to prepare carbon-

based nanomaterials(Li et al., 2010a; Xu et al., 2004; Xu et al., 2005; Li et al., 2010b). The electric arc oven for synthesis of graphene mainly comprises two electrodes and a steel chamber cooled by water. The cathode and anode are both pure graphite rods. The current in the discharge process is maintained at 100-150 A. Up to now, the atmospheres for arc evaporation of graphite rods are H_2, NH_3 and He, air. As the rods are brought close together, discharge occurs resulting in the formation of plasma. As the anode is consumed, the rods are kept at a constant distant from each other of about 1-2 mm by rotating the cathode. When the discharge ends, the soot generated is collected under ambient conditions. Only the soot deposited on the inner wall of the chamber is collected, avoiding the substance at the bottom of the chamber, for the latter tends to contain other graphitic particles. The arc-discharge method is useful to prepare pure, B- and N-doped graphene. B-doped graphene is obtained by carrying out the discharge in the presence of a mixture of a H_2 and B_2H_6(Subrahmanyam et al., 2009). N-doped graphene is obtained by carrying out the discharge in the mixing atmosphere of He and NH_3(Li et al., 2010a) or H_2 and pyridine(Subrahmanyam et al., 2009).

2.2 Characterizations of graphene

The graphene can be synthesized in three different kinds of atmospheres with arc-discharge method. We will introduce the characterizations of graphene according to the different atmosphere.

2.2.1 Graphene synthesized in the atmosphere of H_2

Subrahmanyam et al.(2009) first synthesized pure graphene(HG) with the arc-discharge method in the atmosphere of H_2. They also synthesized B-(BG) and N-doped graphene (NG) in the presence of B_2H_6 and pyridine. Fig. 2.1 is the transmission electron microscopy (TEM) images of the graphene. TEM image of HG shown in Fig. 2.1a reveals the presence of 2-4 layers. Fig. 2.2 shows typical atomic force microscopy (AFM) images with the height profiles. AFM images show the thickness to be generally around 0.7-1 nm corresponding to 2-3 layers, consistent with the TEM results.

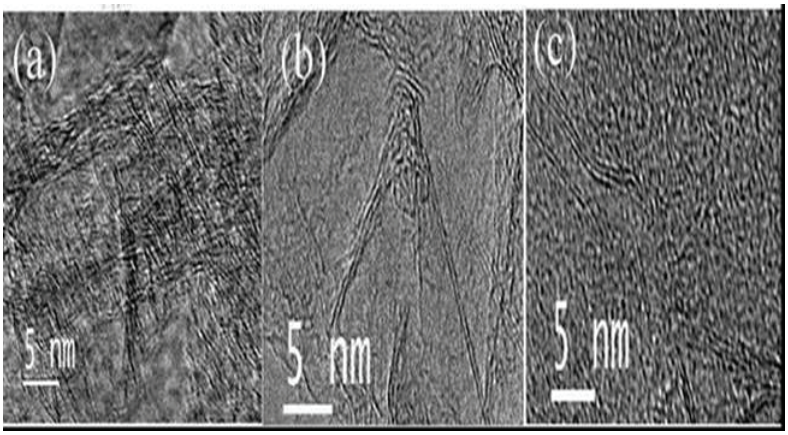

Fig. 2.1. TEM images of (a) HG and (b) BG and (c) NG graphenes. (Subrahmanyam et al. 2010. Reproduced by permission of The American Chemistry Society)

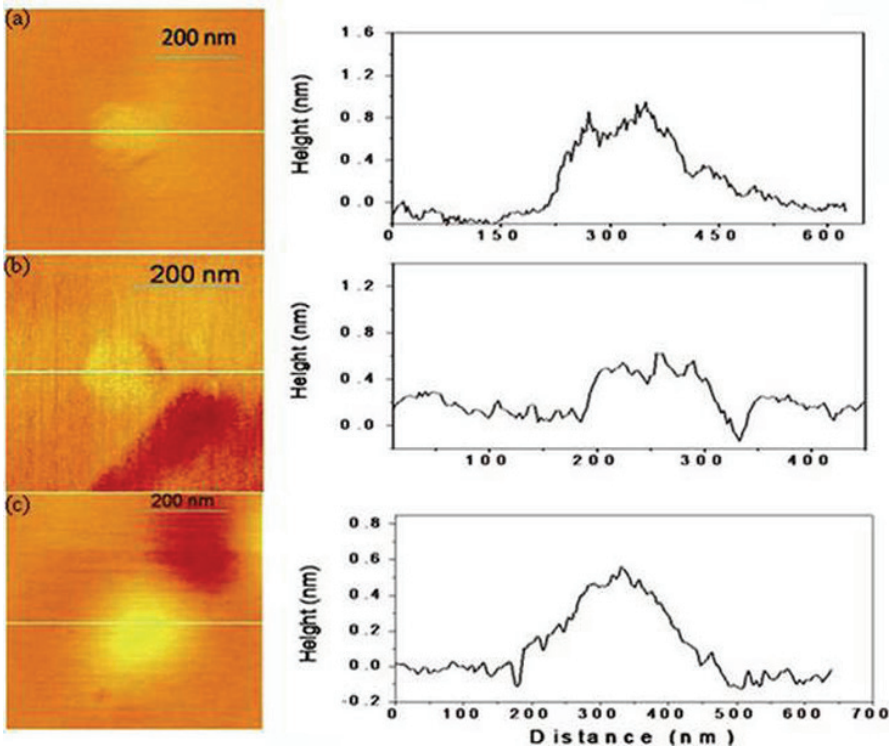

Fig. 2.2. Noncontact mode AFM images of (a, b) HG and (c) BG graphenes with height profiles. (Subrahmanyam et al. 2010. Reproduced by permission of The American Chemistry Society)

Fig. 2.3 shows the Raman spectra of HG, BG, and NG. The Raman spectrum of HG exhibits the characteristic D, G, and the 2D bands of graphene around 1323, 1569, and 2634 cm^{-1} respectively. It also shows the defect related G' band as a shoulder around 1600 cm^{-1}. Raman spectra of BG and NG show a blue-shifted G band (1576 and 1572 cm^{-1} in BG and NG, respectively) compared to HG (1569 cm^{-1}). BG and NG show a more intense D band and a less intense 2D band relative to HG. The area of the HG samples is generally in the range of 10-40×10^3 nm^2. The surface areas of the HG samples, determined by the Brunauer-Emmett-Teller (BET) method are in the range of 270-680 m^2/g. The synthesis, structure, and properties of BG and NG are being investigated in detail by Subrahmanyam et al.

2.2.2 Graphene synthesized in the mixing atmosphere of He and NH_3

Li et al.(2010a) synthesized N-doped multi-layered graphene in the mixing atmosphere of He and NH_3. Fig. 2.4 is the TEM image of multi-layered graphene, from which we can see large area of high purity multi-layer graphene with the size of 100~200 nm. Fig. 2.5a to 2.5c is the high resolution transmission electron microscope (HRTEM) images of multi-layered graphene with layer numbers of 2~4. According to the HRTEM observation, the multi-layered graphene are mainly of 2~6 layers. Fig. 2.6 is the X-ray diffraction (XRD) pattern of the graphene. It shows broad (002) reflection around 25° and overlapping (100) and (101) reflections around 45°.

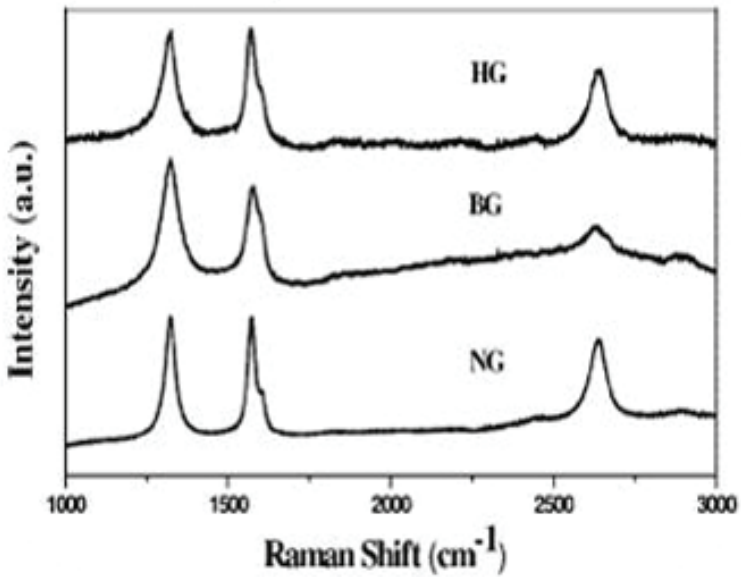

Fig. 2.3. Raman spectra of HG, BG, and NG graphene samples. (Subrahmanyam et al. 2010. Reproduced by permission of The American Chemistry Society)

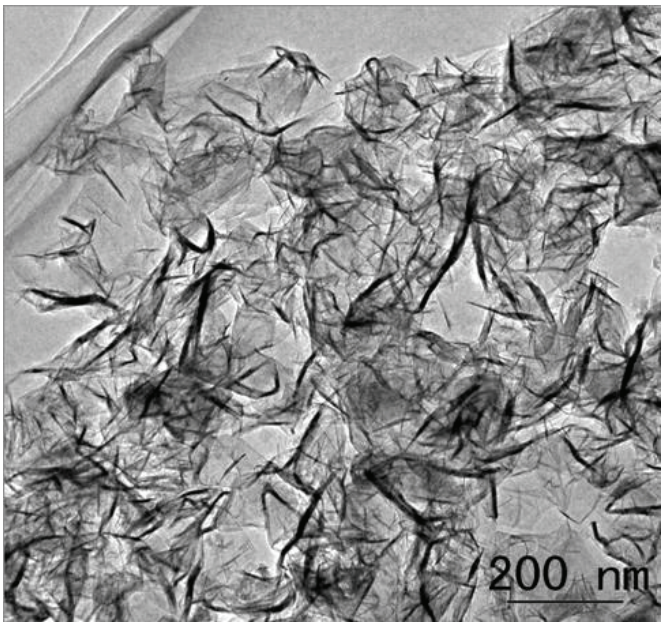

Fig. 2.4. TEM image of multi-layered graphene produced by arc-discharge method. (Li et al. 2010a. Reproduced by permission of Elsevier Limited)

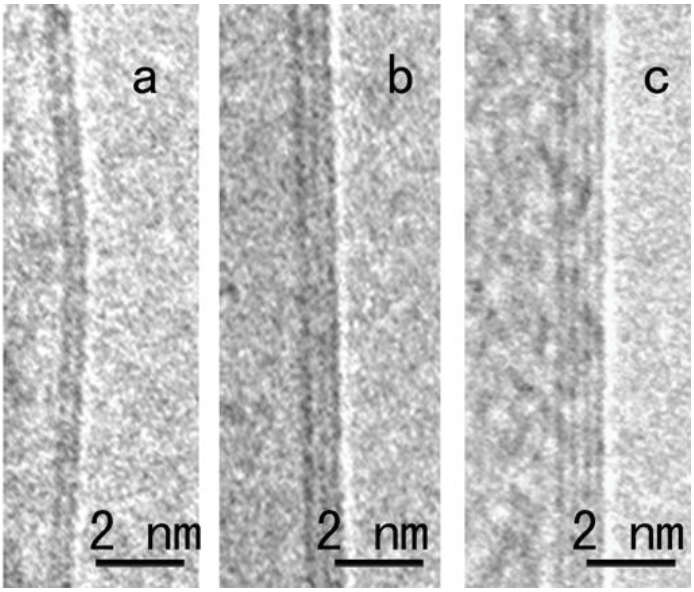

Fig. 2.5. HRTEM images showing the edge of multi-layered graphene consisting of two (a), three (b) and four (c) layers. (Li et al. 2010a. Reproduced by permission of Elsevier Limited)

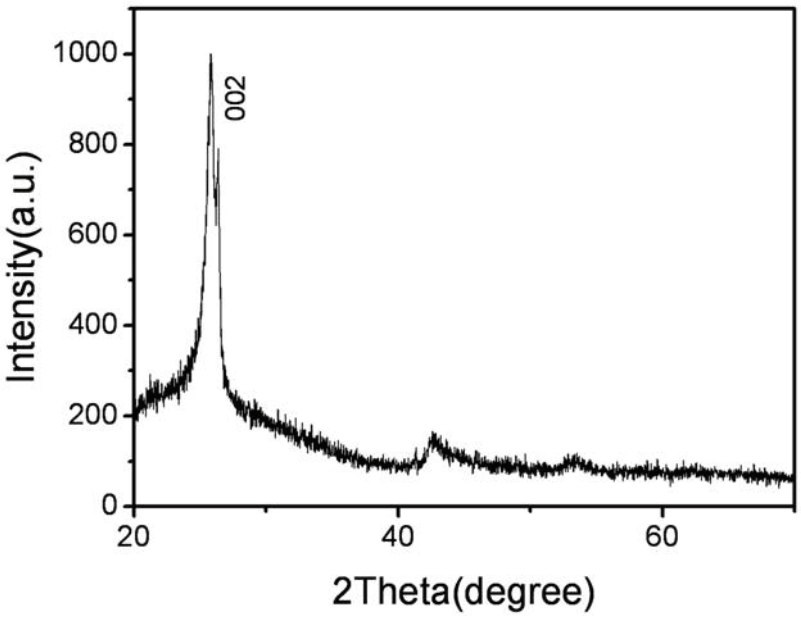

Fig. 2.6. XRD pattern of multi-layered graphene. (Li et al. 2010a. Reproduced by permission of Elsevier Limited)

Fig. 2.7 shows the Raman spectra of multi-layered graphene. There are three dominant peaks. The two most intense features are the G band at ~1560 cm^{-1} and the 2D band at ~2600 cm^{-1}. The peak at ~1350 cm^{-1} is the D band. The G band corresponds to the zone center E_{2g} mode(Ferrari et al. 2006) related to phonon vibrations in sp^2 carbon materials(Malesevic et al., 2008). The 2D band has nothing to do with the G band, but is an overtone of the disorder-induced D band, which is frequently observed in carbon materials(Parvizi et al., 2008). The D band arising from disorder is weak in a single-layer graphene and increases in intensity with the numbers of layers(Submanyam et al., 2008). The 2D band is also sensitive to the number of layers. The shape of the D and 2D band, more specially the absence of a typical graphite shoulder, is a characteristic feature of graphene. The intensity ratio of the D band to the G band is measured and denoted as the R value to analysis the structure of graphitic materials(Malesevic et al., 2008; Kastner et al., 1994). The I_G/I_{2D} is also changed with the layers of graphene(Reina et al., 2009). The R value is by definition inversely proportional to quality. The R value is ~0.26 (Fig. 2.7a) and ~0.23 (Fig. 2.7b) for the multi-layered graphene and the I_G/I_{2D} is ~1.90 and ~1.57. This indicates that the N-doped multi-layered graphene produced by arc-discharge method bear well crystalline structure and the number of graphene's layers is not influenced significantly by the content of NH_3.

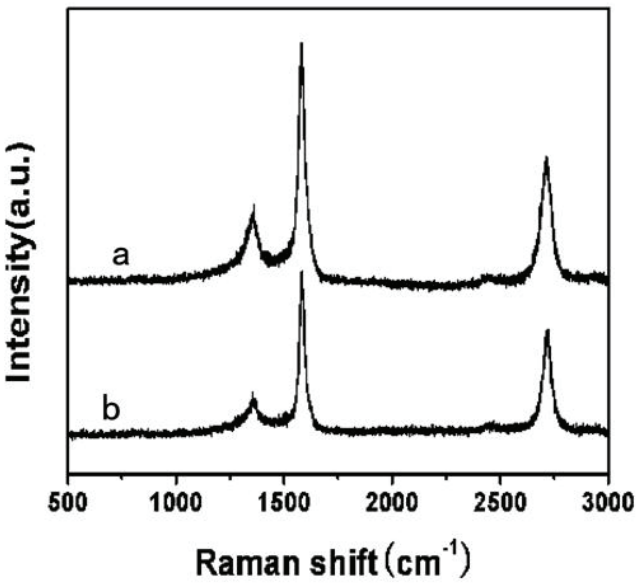

Fig. 2.7. Raman spectra of the two samples prepared in mixing atmosphere of NH_3 and He with the different ratio of NH_3/He (V/V): (a) NH_3: He =1:0; (b) NH_3: He=1:1. (Li et al. 2010a. Reproduced by permission of Elsevier Limited)

Fig. 2.8 shows the TGA curve of the N-doped multi-layered graphene. There are two significant drops in mass around 387 and 688 °C. The former is assigned to the oxidation of amorphous carbon, and the latter is attributed to the combustion of the carbon skeleton of graphene sheets. From the TGA curve, we can conclude that the N-doped multi-layered graphene is thermally stable and starts to lose mass upon heating at 500 °C and the content

of graphene in raw soot is ~79 wt.%. After the heat treatment at 450 °C for 1 h in the atmosphere of air, there was not any amorphous carbon in the soot (Fig. 2.9). From the experimental results we can see that the N-doped multi-layered graphene produced by arc-discharge method can be purified by a simple heat treatment process.

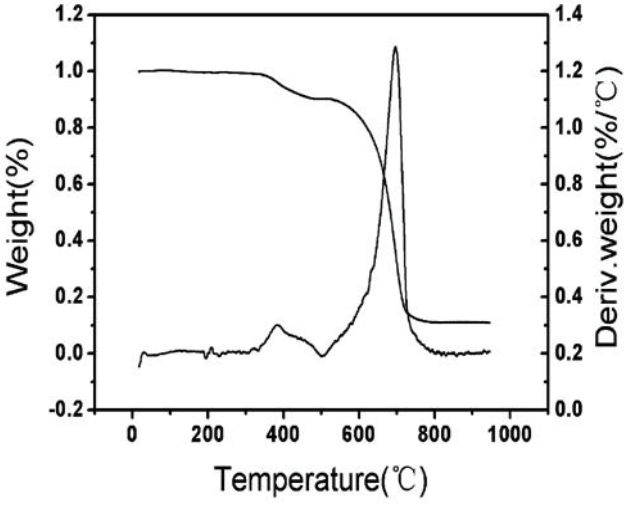

Fig. 2.8. TGA curve of N-doped multi-layered graphene. (Li et al. 2010a. Reproduced by permission of Elsevier Limited)

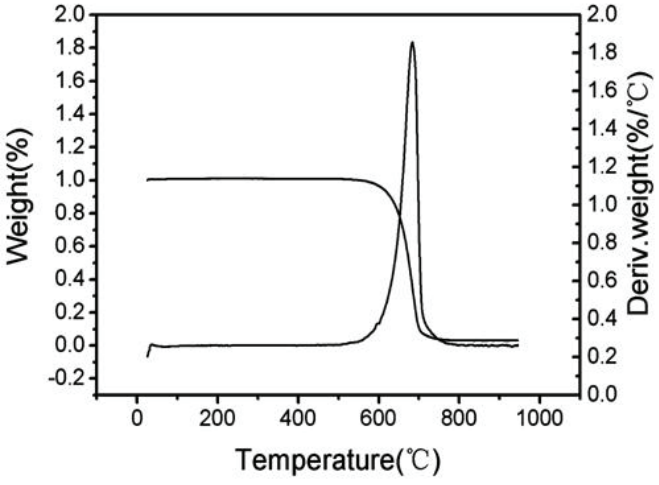

Fig. 2.9. TGA curve of multi-layered graphene sheets after heat treatment at 450 °C for 1h. (Li et al. 2010a. Reproduced by permission of Elsevier Limited)

The XPS results shown in Fig. 2.10 confirm the existence of N. The peaks appeared at 284.50, 399.59 and 532.70 eV can be assigned to C_{1s}, N_{1s} and O_{1s}. No extra peaks except C, N and O were observed, indicating the high purity of the product. Oxygen can be included due to exposure to the air. In graphene sheets, the C atoms are mostly constrained to a sp^2-hybridization. There are two types of N bonding for N-doped graphene(Ayala et al., 2001). One is substitutional doping, which N is bonded to three C atoms in a sp^2 configuration. The other is the pyridine-type doping, which N is bonded with two coordinated bondings. From the position of the N_{1s} level, we can distinguish the N-doping type. Fig. 2.11 is the high-resolution XPS spectra of N_{1s}. From it we can see that the N_{1s} core level lied at 399.59 eV is in good agreement with the spectral feature of pyridine-type N-doping(Gammon et al., 2003). Furthermore, element analysis was used to reveal the precise N content of the N-doped multi-layered graphene sheets. The result shows that the content of N is ~1% for the sample produced in the atmosphere of pure NH_3.

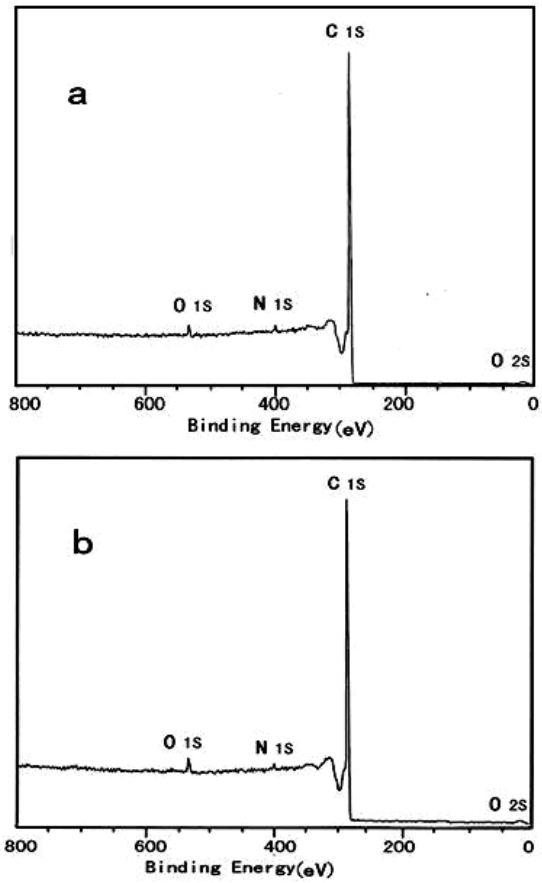

Fig. 2.10. XPS spectra of the two samples prepared in mixing atmosphere of NH_3 and He with the different ratio of NH_3/He (V/V): (a) NH_3: He =1:1; (b) NH_3: He=1:0. (Li et al. 2010a. Reproduced by permission of Elsevier Limited)

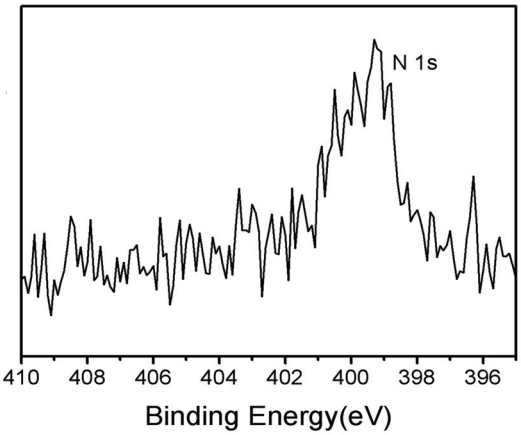

Fig. 2.11. High-resolution XPS spectra of N_{1s}. (Li et al. 2010a. Reproduced by permission of Elsevier Limited)

2.2.3 Graphene synthesized in the atmosphere of air

Wang et al.(2010) synthesized graphene in the atmosphere of air. The yield of their products was found to be strongly dependent on the initial air pressure. Fig. 2.12 shows the TEM images of the products corresponding to differing initial air pressure. When the initial air pressure is 1000 torr, the product is dominated by graphene nanosheets, and there are also small amounts of carbon nanohorns (Fig. 2.12a). Carbon nanohorns are single-layered tubular structures with horn-shape tips, which are frequently observed near the edge of the graphene nanosheets (a carbon nanohorn is indicated with an arrow in Fig. 2.12a). When the initial air pressure is decreased to 700 torr, the amount of graphene nanosheets is reduced and there are more carbon nanohorns in the products (Fig. 2.12b). Further decreasing of the air pressure to 400 torr leads to the formation of carbon nanospheres together with nanohorns (Fig. 2.12c). The carbon nanohorns can be removed by oxidation in air. After heat-treatment in air, most of the carbon nanohorns are oxidized to gases and graphene nanosheets with a high purity is obtained (Fig. 2.12d).

Based on TEM analysis, the width of the graphene nanosheets is mainly in the range of ~100-200 nm. This size range is similar to that of graphene nanosheets produced by arc discharge in H_2 (Subrahmanyam et al., 2009). The layer number of the graphene nanosheets produced in air atmosphere mainly ranges from 2 to 10. Typical high-resolution TEM images of graphene are shown in Fig. 2.13, in which the graphene layers of the nanosheets can be distinguished. Fig. 2.13a shows a graphene nanosheet with triple layers at the lower part and single layer at the upper part. The interlayer distance of the graphene nanosheets was determined to be 0.37-0.39 nm, which is larger than that of bulk graphite (0.34 nm).

Fig. 2.14 depicts the Raman spectra of the raw and purified graphene nanosheets produced with an initial air pressure of 1000 torr. Three dominant peaks at 1325, 1570, and 2646 cm^{-1}, known as the D band, G band and 2D band, are observed for the two samples. It is apparent that intensity ratio of D band to G band for the purified sample is significantly lower than that for the raw material. This difference is caused by the elimination of the carbon

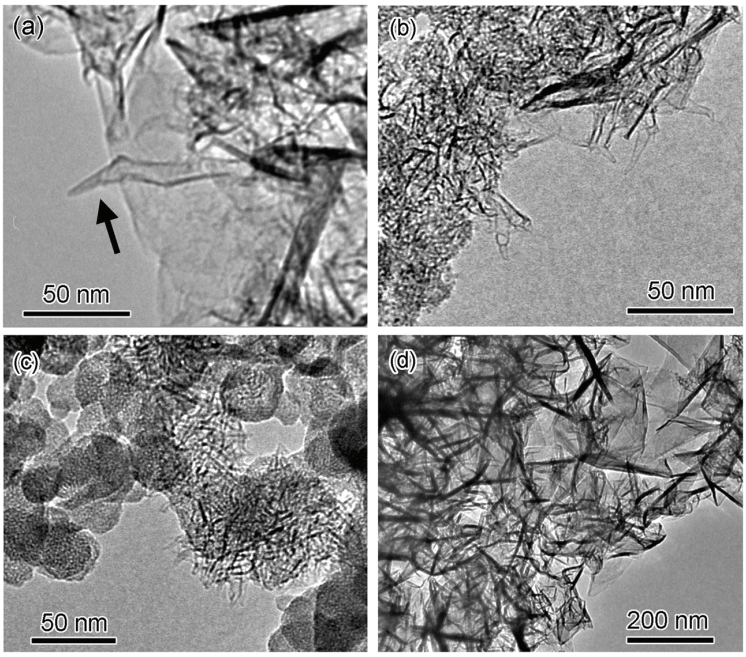

Fig. 2.12. (a-c) TEM images of the products for different initial air pressure of 1000, 700 and 400 torr, respectively. The arrow in (a) indicates the carbon nanohorn. (d) TEM image of products after oxidation in air. (Wang et al. 2010. Reproduced by permission of IOP Publishing Limited)

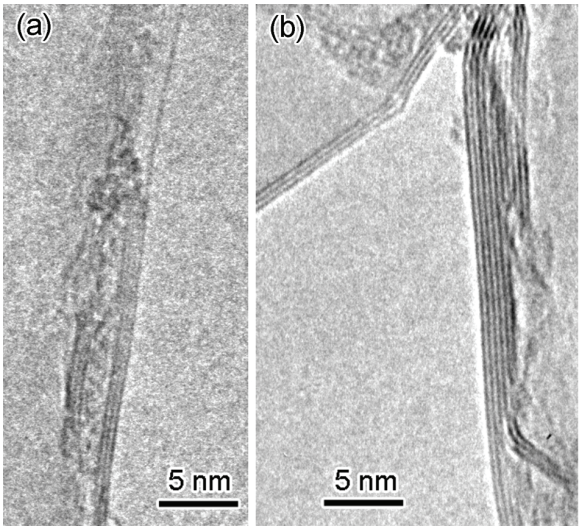

Fig. 2.13. (a, b) High-resolution TEM images of graphene nanosheets showing the edges of the graphene. (Wang et al. 2010. Reproduced by permission of IOP Publishing Limited)

nanohorns. It is known that the D band is related to disorder of carbon materials and the G band corresponds to the zone center E_{2g} mode. Because of the curvature and the coniform tips of the carbon nanohorns, the intensity of the D band for the carbon nanohorns is stronger than that for the flat graphene sheets. Therefore, the D band is depressed after the elimination of the carbon nanohorns. On the other hand, the position of the 2D band is associated with the thickness of the graphene sheets. The 2D band of graphite is located at 2685 cm^{-1}, while the 2D band of graphene with few (less than five) layers is in the range of ~2640-2680 cm^{-1} (with excitation wavelength of 633 nm). Thus the frequency of 2D band for the purified sample in the present study (2646 cm^{-1}) is a signature of few-layered graphene nanosheets.

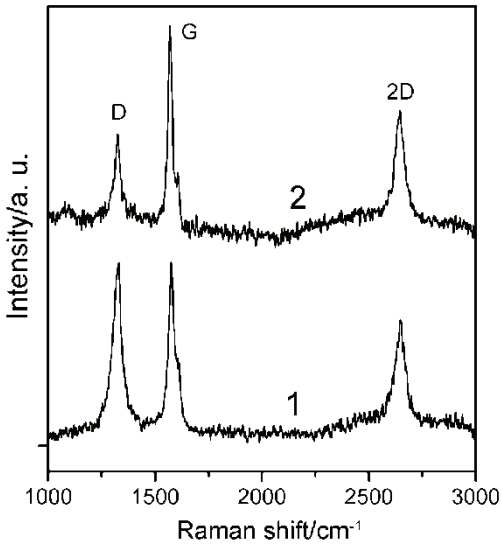

Fig. 2.14. Raman spectra of raw (curve 1) and purified (curve 2) graphene nanosheets. D, G and 2D bands are observed. (Wang et al. 2010. Reproduced by permission of IOP Publishing Limited)

3. Formation mechanisms of graphene with arc-discharge method

There are two formation mechanisms of graphene according to the atmosphere. In the atmosphere of H_2, it makes use of the knowledge that the presence of H_2 during the arc discharge process terminates the dangling carbon bonds with hydrogen and prevents the formation of closed structures(Wang et al., 1995). H_2 plays a key role in the formation of graphene by preventing the rolling of sheets into nanotubes and graphitic polyhedral particles. In the mixing atmosphere of NH_3 and He, the formation mechanism is similar to the atmosphere of H_2. NH_3 not only acts as the nitrogen source, but also suppresses the formation of fullerenes. NH_3 also plays another important role for the formation of N-doped graphene besides the as-described function. It decomposes to nitrogen and hydrogen under the high temperature during discharge process. The highly reactive hydrogen terminates the dangling carbon bonds at the edge of graphene sheets thereby preventing the graphene

sheets from closing(Maiti et al., 1995). At the same time, the high pressure of buffer gas and high current provide more energy to prompt the ionization of anode, which engenders bigger carbon clusters. This further guarantees the shape of graphene sheets(Kokai et al., 2004).

In the atmosphere of air, the pressure of the system is a critical factor that determinates the yield of graphene. As the graphene sheets are flat, the formation of graphene might be related to inhibition of the curvatures of graphene layers by high pressure of the system. The pressure-induced formation of graphene is different from the growth mechanism of graphene in H_2 and NH_3, when hydrogen atoms could terminate the dangling bonds on the edge of graphene sheets and thereby prevent their rolling into closed structures. The formation of graphene in H_2 and NH_3 is associated with the chemical activity of the atmosphere. On the contrary, pressure-induced formation of graphene is independent of the chemical activity of the buffer gas.

4. Summary

Graphene is an amazing new carbon nanomaterial, which possess distinct characteristics. The applications of graphene mainly focus on electronics, molecular gas sensors, and energy storage etc. To achieve these goals, the massive production of high quality graphene is the precondition. The production of graphene in decagram-scale with high purity has been achieved by the arc-discharge method. This has promoted further applications of graphene in many technological areas.

5. Acknowledgements

The work by the authors was supported by the National Natural Science Foundation of China (Nos. 20771010, 504371004 and 90206048) and the Ministry of Science and Technology of China (Grant 2006CB932701 and 2007AA03Z3110).

6. References

Ayala P, Grüneis A, Gemming T, Grimm D, Kramberger C, Rümmeli M H, Freive F L, Kuzmany H, Pfeiffer R, Barreiro A, Büchner B, Pichler T. (2007). Tailoring N-doped single and double wall carbon nanotubes from a mondiluted carbon/nitrogen feedstock. *J. Phys. Chem. C*, 111, 7, 2879-2884, ISSN.

Booth T J, Blake P, Rahul R N, Jiang D, Hill E W, Bangert U, Bleloch A, Gass M, Novoselov K S, Katsnelson M I, Geim A K. (2008). Macroscopic graphene membranes and their extraordinary stiffness. *Nano Lett.*, 8, 8, 2442-2446, ISSN.

Chae S J, Günes F, Kim K K, Kim E S, Han G H, Kim S M, Shin H J, Yoon S M, Choi J Y, Park M H, Yang C W, Pribat D, Lee Y H. (2009). Synthesis of large-area graphene layers on poly-nickel substrate by chemical vapor deposition: wrinkle formation. *Adv. Mater.*, 21, 22, 2328-2333, ISSN.

Choucair M, Thordarson P, Stride J A. (2009). Gram-scale production of graphene based on solvthermal synthesis and sonication. *Nat. Nanotechnol.*, 4,1, 30-33, ISSN.

Dervishi E, Li Z R, Watanabe F, Biswas A, Xu Y, Biris A R, Saini V, Biris A S. (2009). Large-scale graphene production by RF-Ccvd method. *Chem. Comm.*, 27, 4061-4063, ISSN.

Du X S, Yu Z Z, Dasari A, Ma J, Mo M, Meng Y Z, Mai Y W. (2008). New methods to prepare graphite nanocomposites. *Chem. Mater*., 20, 6, 2066-2068, ISSN.

Emtsev K V, Bostwick A, Horn K, Jobst J, Kellogg G L, Ley L, McChesney J L, Ohta T, Reshanov S A, Röhrl J, Rotenberg E, Schmid A K, Waldmann D, Weber H B, Seyller T. (2009). Towards wafer-size graphene layers by atmospheric pressure graphitization of sllicon carbide. *Nat. Mater*., 8, 3, 203-207, ISSN

Fan X B, Peng W, Li X Y, Wang S, Zhang G L, Zhang F B. Deoxygenation (2008). of exfoliated graphite oxide under alkaline conditions: a green route to graphene preparation. *Adv. Mater*., 20, 23, 4490-4493, ISSN.

Ferrari A C, Meyer J C, Scardaci V, Casiraghi C, Lazzeri M, Mauri F. (2006). Raman spectrum of graphene and graphene layers. *Phys. Rev. Lett*., 97, 18, 187401, ISSN.

Gammon W J, Kraft O, Reilly A C, Holloway B C. (2003). Experimental comparison of N(1s) X-ray photoelectron spectroscopy binding energies of hard and elastic amorphous carbon nitride films with reference organic compounds. *Carbon*, 41, 10, 1917-1923, ISSN.

Geim A K, Novoselov K S. (2007). The rise of graphene. *Nat. Mater*., 6, 3, 183-191, ISSN.

Juang Z Y, Wu C Y, Lo C W, Chen W Y, Huang C F, Hwang J C, Chen F R, Leou K C , Tsai C H. (2009). Synthesis of graphene on silicon carbide substrates at low temperature. *Carbon*, 47, 8, 2026-2031, ISSN.

Kastner J, Pichler T, Kuzmany H, Curran S, Blau W, Weldon D N, Delamesiere M, Draper S, Zandbergen H. (1994). Resonance Raman and infrared spectroscopy of carbon nanotubes. *Chem. Phys. Lett*., 221, 1-2, 53-58, ISSN.

Kokai F, Koshi A, Kasuya D, Hirahara K, Takahashi K, Nakayama A, Ishihara M, Koga Y, Iijima S. (2004). Three nanostructured graphitic particles and their growth mechanisms from high-temperature carbon vapor confined by Ar gas. Carbon, 42, 12-13, 2515-2520, ISSN.

Krätschmer W, Lamb L D, Fostiropoulos K, Huffman D R. (1990). Solid C_{60}: a new form of carbon. *Nature*, 347, 6291, 354-358, ISSN.

Li D, MÜller M B, Gilje S, Kaner R B, Wallace G G. (2008). Processable aqueous dispersions of graphene nanosheets. *Nat. Nanotechnol*., 3, 2, 101-105, ISSN.

Li X L, Wang X R, Zhang L, Lee S W, Dai H J. (2008). Chemically derived, ultra-smooth graphene nanoribbon semiconductors. *Science*, 319, 5876, 1229-1232, ISSN.

Li X S, Cai W W, An J, Kim S, Nah J, Yang D X, Piner R, Velamakanni A, Jung I, Tutuc E, Banerjee S K, Colombo L, Ruoff R S. (2009). Large-area synthesis of high-quality and uniform graphene films on copper foils. *Science*, 324, 5932, 1312-1314, ISSN.

Li N, Wang Z Y, Zhao K K, Shi Z J, Gu Z N, Xu S K. (2010a). Large scale synthesis of N-doped multi-layered graphene sheets by simple arc-discharge method. *Carbon*, 48, 1, 255-259, ISSN.

Li N, Wang Z Y, Zhao K K, Shi Z J, Gu Z N, Xu S K. (2010b). Synthesis of single-wall carbon nanohorns by arc-discharge in air and their formation mechanism. *Carbon*, 48, 5, 1580-1585, ISSN.

Maiti A, Brabec C J, Roland C, Bernholc J. (1995). Theory of carbon nanotube growth. *Phys. Rev. B*, 52, 20, 14850-14858, ISSN.

Malesevic A, Vitchev R, Schouteden K, Volodin A, Zhang L, Tendeloo G V, Vanhulsel A, Haesendonck C V. (2008). Synthesis of few-layer graphene via microwave plasma-enhanced chemical vapor deposition. *Nanotechnology*, 19, 30, 305604, ISSN.

McAllister M J, Li J L, Adamson D H, Schniepp H C, Abdala A A, Liu J, Herrera-Alonso M, Milius D L, Car R, Prud'homme R K, Aksay I A. (2007). Single sheet functionalized graphene by oxidation and thermal expansion of graphite. *Chem. Mater.*, 19, 18, 4396-4404, ISSN.

Niyogi S, Bekyarova E, Itkis M E, McWilliams J L, Hamon M A, Haddon R C. (2006). Solution properties of graphite and graphene. *J. Am. Chem. Soc.*, 128, 24, 7720-7721, ISSN.

Novolesov K S, Gleam A K, Morozov S V, Jiang D, Zhang Y, Dubonos S V, Grigorieva I V, Firsov A A. (2004). Electric field effect in atomically thin carbon films. *Science*, 306, 5296, 666-669, ISSN.

Parvizi F, Teweldebrhan D, Ghosh S, Calizo I, Balandin A A, Zhu H, Abbaschian R. (2008). Properties of graphene produced by the high pressure-high temperature growth process. *Micro& Nano Lett*, 3, 1, 29-34, ISSN.

Reina A, Jia X, Ho J, Nezich D, Son H, Bulovic V, Dresselhaus M S, Kong J. (2009). Large area, few-layer graphene films on arbitary substrates by chemical vapor deposition. *Nano Lett.*, 9, 1, 30-35, ISSN.

Subrahmanyam K S, Vivekchand S R C, Govindaraj A, Rao C N R. (2008). A study of graphemes prepared by different methods: characterization, properties and solubilization. *J. Mater. Chem.*, 18, 13, 1517-1523, ISSN.

Subrahmanyam K S, Panchakarla L S, Govindaraj A, Rao C N R. (2009). Simple method of preparing graphene flakes by an arc-discharge method. *J. Phys. Chem. C*, 113, 11, 4257-4259, ISSN.

Wang X K, Lin X W, Dravid V P, Ketterson J B, Chang R P H. (1995). Carbon nanotubes synthesized in a hydrogen arc-discharge. *Appl. Phys. Lett.*, 66, 18, 2430-2432, ISSN.

Wang X K, Lin X W, Mesleh M, Jarrold M F, Dravid V P, Ketterson J B, Chang R P H. (1995). The effect of hydrogen on the formation of carbon nanotubes and fullerenes. *J. Mater. Res.*, 10, 8, 1977-1983, ISSN.

Wang Z Y, Li N, Shi Z J, Gu Z N. (2010). Low-cost and large-scale synthesis of graphene nanosheets by arc discharge in air. *Nanotechnology*, 21, 17, 175602, ISSN.

Xu J X, L X, Zhou X H, He X R, Shi Z J, Gu Z N. (2004). Synthesis, Isolation and spectroscopic Characterization of Ytterbium-Containing Metallofullerenes. *Chem. Mater.*, 16, *15*, 2959-2964, ISSN.

Xu J X, Wang Z Y, Shi Z J, Gu Z N. (2005). Synthesis, Isolation and Spectroscopic Characterization of Yb-containing High Metallofullerenes. *Chem. Phys. Lett.*, *409*, 4-6, 192-196, ISSN.

Yuan G D, Zhang W J, Yang Y, Tang Y B, Li Y Q, Wang J X, Meng X M, He Z B, Wu C M L, Bello I, Lee C S, Lee S T. (2009). Graphene sheets via microwave chemical vapor deposition. *Chem. Phys. Lett.*, 467, 4-6, 361-364, ISSN.

Zhu C Z, Guo S J, Fang Y X, Dong S J. (2010). Reducing sugar: new functional molecules for the green synthesis of graphene nanosheets. *ACS Nano*, 4, 4, 2429-2437, ISSN.

3

Chemical Vapor Deposition of Graphene

Congqin Miao, Churan Zheng, Owen Liang and Ya-Hong Xie
University of California, Los Angeles
United States

1. Introduction

Graphene is a two-dimensional material composed of carbon atoms arranged in a hexagonal atomic structure. Tremendous amount of research has been done on digging out its excellent properties in future applications. However, the ability of fabricating large-area monolayer graphene is hindering its application. So far the graphene of the best electronic properties is synthesized by mechanical exfoliation from Highly Ordered Pyrolytic Graphite (HOPG), which is of tens of micrometers in size (Novoselov et al., 2004). Graphene can also be produced by chemical reduction of graphite oxide (Tung et al., 2009), high temperature annealing of single crystal SiC (Konstantin et al., 2009) and Chemical Vapor Deposition (CVD) on metal substrates (Reina et al., 2009). These techniques have been employed in demonstrating good quality graphene transistors. However the only one that has the promise of becoming a manufacturable technology is CVD, which has been one of the mostly used thin film fabrication techniques in silicon Very-Large-Scale Integration (VLSI).

2. CVD technology

CVD is a technique of thin solid film deposition on substrates from the vapor species through chemical reactions. The chemical reaction plays an important role and is thus one of the most distinctive features that CVD possesses compared with other film deposition techniques such as physical vapor deposition (PVD). Figure 1 shows the schematic drawing of a typical tube-furnace CVD system for graphene growth. It is composed with a gas deliver system, a reactor and a gas removal system. During the CVD process, reactive gas species are fed into the reactor by the gas delivery system that consists necessary valves, Mass Flow Controllers (MFCs) that manipulate the flow rates of the gases passing through, and a gas-mixing unit that is responsible for mixing the various gases uniformly before they are let in the reactor. The reactor is where the chemical reaction takes place and the solid materials are deposited on substrates as the purpose of the reaction. The heaters are placed surrounding the reactor to provide high temperatures for the reaction. Eventually the by-products of the reaction and non-reacted gases are removed by the gas delivery system that is made of one or more pumps that are not necessary for the CVD not operating at vacuum condition.
In contrast to the relatively unsophisticated setup, however, CVD is far away from an easy-to-control process. In addition to the control of regular parameters such as temperature, pressure, time and so on that other deposition techniques also inevitably encounter, there are other factors need to be considered carefully to conduct CVD. In a successful CVD process (Figure 2) the transport kinetics of gas species tends to be complicated with convection and

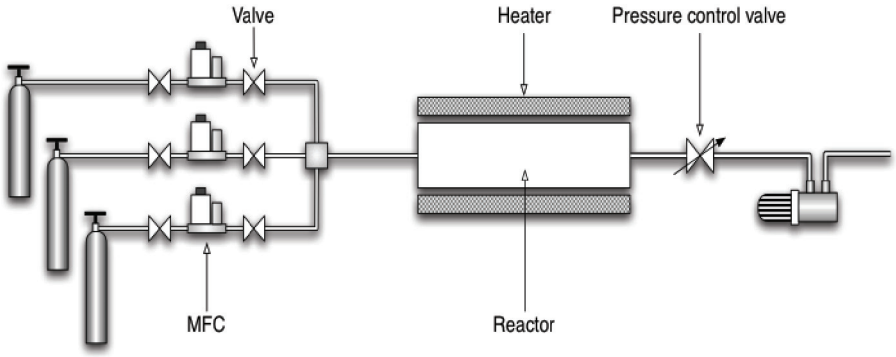

Fig. 1. The schematic diagram of a typical tube-furnace CVD system. Gas flows are regulated by MFCs, and fed into the reactor through a gas-distribution unit. Chemical deposition takes place in the reactor that is heated by the outside heaters. The exhaust gases are removed by vacuum pumps.

diffusion being dominating in different regions of a reactor. And the chemical reaction might be the most complicated because it usually involves many intermediate steps and one may not know the exact step-by-step reaction mechanism. The diffusion of reactive species to or from the substrates is also complicated in that a stagnant boundary layer of non-uniform thickness is formed above a fixed substrate surface based on the fluid dynamics (Figure 3). As a result the diffusion occurs slower at the thick boundary layer region, and results in deposition non-uniformity.

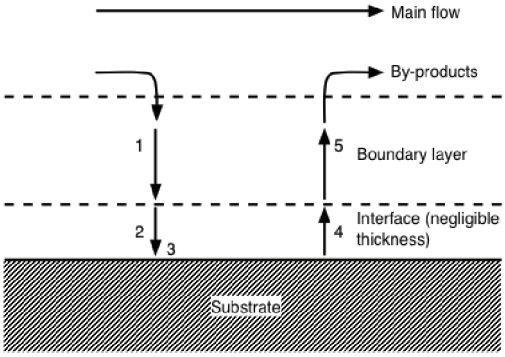

Fig. 2. The chemical deposition process in CVD. 1. Reactants diffuse through the boundary layer. 2. Reactants are adsorbed onto substrate surface. 3. Chemical reaction occurs on the surface. 4. The by-products of the reaction are desorbed from the surface. 5. The by-products diffuse through the boundary layer.

Another factor one must consider is the depletion of reactants from one end of the reactor to the other. Note that this is different from flow rate which as mentioned earlier does not affect the growth of the film; however if inert gas is hitting the wafer at the end of the reactor, then no chemical reaction will occur. This is because reaction will usually occur near the front end of the reactor and not near the end. To eliminate this issue, one can have increasing temperatures moving away from the location where reactant gas is flowed in which will cause a higher

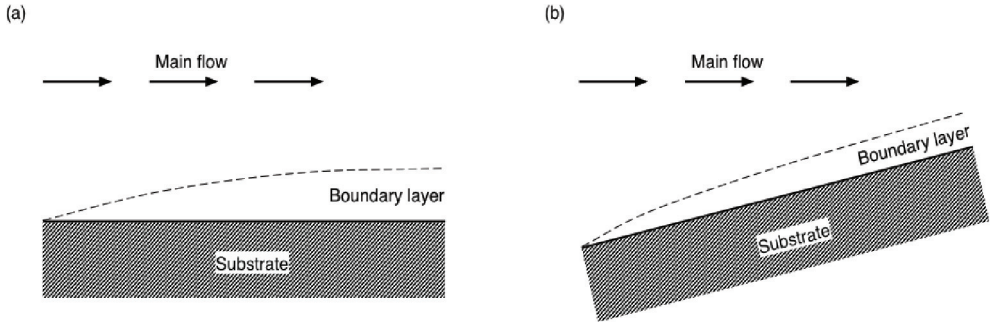

Fig. 3. An example of a boundary layer above the substrate surface. (a) The substrate surface is parallel to the main flow. (b) The substrate is tilted to enhance the thickness uniformity of the boundary layer based on fluid dynamics.

diffusion rate to occur near the end of the reactor; this leads to better throughput throughout the reactor.

All the factors in the CVD process are entangled with one another and it is extremely tedious work to single out one to look into its influence to the entire deposition process. Hence CVD is a more complex process than other processes and it is necessary that several test runs should be performed to calibrate the system before a successful deposition of thin film with desired thickness and quality.

3. Unique aspect of CVD graphene

3.1 Requirement of catalysts

Graphene deposition can be divided into two parts: precursor pyrolysis to carbon and the formation of graphitic structure from dissociated carbon atoms. The precursor dissociation should be done only on the substrate surface (i.e. heterogeneous reaction) to avoid the precipitation of carbon clusters in the gas phase which is typically in the form of carbon soot and sits on synthesized graphene, if any, to form graphene/soot mixture as well as on reactor walls. Although they are all made of carbon, the amorphous structure of carbon soot determines that their composite no longer retains the properties of monolayer graphene. To achieve the heterogeneous decomposition of precursors on surface, various catalysts of mostly elemental metals are typically used as catalysts. The function of catalysts is to lower the energy barrier of the reaction. In addition to the undesirable need for very high temperature, high energy barriers result in reaction rates to be sensitively dependent on temperature making it difficult to control the reaction rate. Because the film quality is determined by reaction kinetics, high energy barrier leads directly to the difficulty in controlling the film quality.

In the graphitic structure formation step, large area graphitic structure forms only when reaction temperature is raised to beyond 2500 °C without catalysts, which is too high that requires special setup of the deposition system and the substrate. In addition huge amount of energy consumption becomes a considerable issue. The introduction of catalysts lowers energy barriers not only for the pyrolysis of precursors, but also for the graphitic structure formation.

3.2 Impacts of catalysts

The usage of catalysts introduces new materials into the reactor chamber, leading to potential issues. Catalysts are usually metals, which may have finite carbon solubility. For example, Cu has almost zero carbon solubility (Lopez & Mittemeijer, 2004), and Ni has a non-negligible carbon solubility (Natesan & Kassner, 1973). During the growth at elevated temperature, dissociated carbon atoms on the catalyst surface may dissolve into the bulk due to the finite solubility. Things become worse when these dissolved carbon atoms precipitate back onto Ni surface as temperature drops and hence unwanted carbon deposition may occur from bottom. Different cooling rate suggests the different thickness of graphene, and one more freedom participates in the deposition process. Hence the control of deposition is of more difficulties. Figure 4 shows the schematic drawing of graphene grown on Ni with different cooling rate (Yu et al., 2008). Extreme fast cooling leads to little carbon precipitation, because not sufficient time is allowed for carbon to precipitate. Medium cooling gives graphene, and slow cooling has nothing on the surface in that carbon atoms diffuse deep into the bulk catalyst.

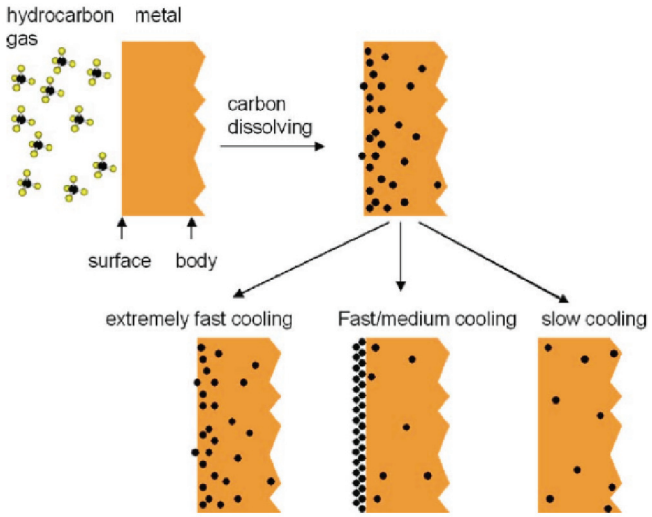

Fig. 4. Illustration of carbon segregation at metal surface (Yu et al., 2008).

Another issue with catalysts is the surface roughness, mainly due to the grain boundaries. When carbon precipitates out to the surface, they prefer to stay in the areas with higher surface energy, such as grain bounties, surface trenches and so on, for the reason that these areas have more atomic dangling bonds that could easily attract precipitated carbon atoms. Eventually the deposited graphene exhibits non-uniformity with thick graphene around grain boundaries and other surface defects, and thin sheet on the other areas. It is thus important to pre-anneal catalyst substrates in order to have large grains to reduce total length of grain boundaries, as well as other minor surface defects.

3.3 CVD graphene on Ni

Ni is one of the major catalysts that used in CVD growth of graphene. Growing graphene on Ni provides sufficient details of various concerns of deposition process with majority of this chapter being dedicated to it as a result.

The first successful graphene deposition via CVD was conducted using Ni as catalyst with the inspiration coming from the CNT growth where Ni is a well-known efficient catalyst. The crucial difference between graphene and CNT growth is that in graphene growth the precursor partial pressure is significantly reduced in that low growth rate is needed for the growth of graphene, a sub-nanometer film. High growth rate leads to over deposition. The prepared samples for graphene growth have structures show in Figure 5, i.e. $Ni/SiO_2/Si$, with SiO_2 as the diffusion barrier to prevent Ni from diffusing to Si substrate. The deposition parameters are set up as follows. After the prepared sample (Figure 5) is loaded into the furnace, the whole reaction chamber is pumped down with a vacuum pump (Figure 1) to the base pressure that should be much less than the deposition pressure for the purpose of reducing the probability of depositing residue gas molecules on graphene (i.e. graphene contamination or doping). When the base pressure is reached, hydrogen gas is let into the reaction chamber and the furnace is turned on to heat up to the deposition temperature. The temperatureis maintained for some time to anneal the catalyst Ni to initiate grain growth that may increase graphene uniformity eventually. Then the deposition begins, by letting in methane together with hydrogen. The whole chamber is then cooled down to the low temperature before taking out the sample. All the above steps are for Low Pressure CVD (LPCVD) growth. Note that graphene can also be fabricated via atmospheric pressure CVD, in which case a huge amount of argon gas is usually used to purge of the residue oxygen in the chamber to protect the metal surface from being oxidized, beside hydrogen gas, and to dilute the precursor to lower deposition rate.

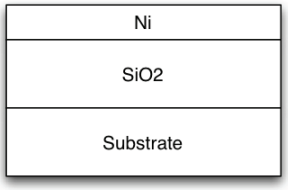

Fig. 5. Schematic diagram of the sample prepared for graphene growth. The top Ni layer is the catalyst, and the middle layer SiO_2 is the diffusion barrier layer to prevent Ni diffusion to the substrate that is usually silicon.

Figure 7 shows the images of the CVD graphene grown on Ni as deposited at 900 °C, 3 minutes and the corresponding spectra of Raman spectroscopy, which has been shown to be a valuable tool for characterizing graphene (Ferrari et al., 2006). Figure 6 shows the Raman spectra (2D peak) of graphene of different thickness (Ferrari et al., 2006). Graphene film grown on Ni is not uniform in thickness all over the substrate surface as indicated by the color contrast (the dark areas correspond to thick graphene). Instead, the monolayer areas are small in size and randomly distributed among the multilayer graphene regions. To better illustrate its morphology, graphene is transferred from Ni to SiO_2 oxide substrate of 300 nm thick on which graphene is visible under optical microscopeso one can observe its uniformity without the disturbance of Ni surface (Ni et al., 2007). Figure 8 shows the image of the transferred graphene on SiO_2 surface together with Raman spectra. In Figure

7 and 8, the upper-right Raman spectrum peak indicates a monolayer graphene, and the lower-right spectrum corresponds to a thick graphene layer, based on Raman spectrum analysis. Therefore, the graphene growth on Ni is confirmed to be non-uniform in thickness over a large area, but monolayer graphene can be found in small areas. One might notice that the backgrounds in Raman spectra are different when graphene is on Ni and on SiO_2. This is due to the interaction of graphene and its substrate (Wang et al., 2008).

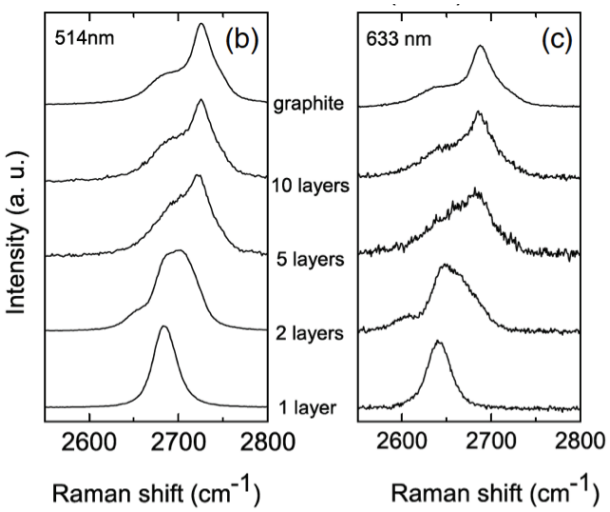

Fig. 6. Raman spectra of 2D peaks of graphene of different thickness (Ferrari et al., 2006).

Like CVD growth of CNTs, the achievement of graphene on nickel was not based on the solid understanding of the mechanism. It is proposed briefly (Li et al., 2009) that when the precursor decomposes into carbon ad-atoms on the Ni surface, they soon dissolve into the bulk Ni, because Ni has a finite solubility of carbon at high temperatures (e.g. 900 °C). At the cooling step, the bulk Ni is subject to temperature decrease, leading to the solubility reduction since the solubility of carbon in Ni is temperature-dependent, and hence the excessive dissolved carbon atoms have no way out but to precipitate back onto the top surface, where they form graphene sheet (Figure 9). The thickness of graphene is therefore controlled by the carbon solubility difference in Ni at the deposition temperature and the rate of cooling at the last growth step.When carbon atoms precipitate out, they do not arrange themselves uniformly on the Ni surface. Instead they precipitate onto the sites with high surface energy such as rough areas and grain boundaries. That is the reason why graphene sheets deposited on nickel is non-uniform as seen in Figure 7 and 8. In summary, this is a "bottom-up" process rather than a "top-down", leading to difficulties in control graphene thickness precisely.

3.4 Challenges of graphene synthesis on Ni

The first challenge comes from the pyrolysis of the precursor species. Hydrocarbon species are typically used as precursors for graphene growth, such as methane (CH_4), acetylene (C_2H_2) and so on. CH_4 is one of the most commonly used precursors, as it is comparatively stable (i.e. low pyrolysis rate) at high temperature (e.g. 800-1000 °C for most graphene growth)and has simple atomic structure. Most other hydrocarbons have a very high pyrolysis rate at high temperature, resulting in large amount of carbon deposition that is not preferred for

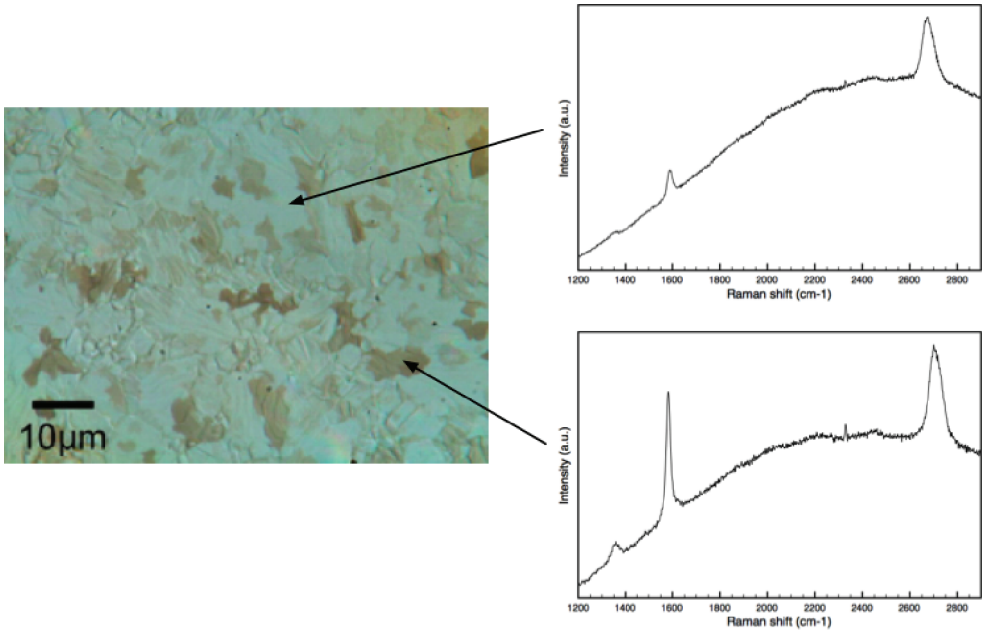

Fig. 7. Optical image of ad-deposited graphene on Ni (left). And the Raman spectra measured at certain points (see arrows). The dark areas correspond to the multilayer graphene, based on Raman spectroscopy analysis.

sub-nanometer graphene. However, even with CH_4, the process of how it is decomposed thermally is still not absolutely understood because of the intermediate steps in CH_4 pyrolysis. A possible dissociation path of CH_4 is CH_3-CH_2-CH-C. The more intermediate steps of the decomposition of the precursors, the more freedom get involved in supplying carbon atoms for the subsequent graphene formation. Hence difficulties inevitably arise to control the carbon supply rate.

The main challenge originates from the unique dimension of graphene. Graphene differs from other materials in a way that it is a sub-nanometer-thick material, whereas the typical CVD deals more with the film much thicker than graphene. The deposition technique of graphene should essentially provide extremely precise control of the thickness of the deposited film analogous to the atomic layer deposition (ALD) with the deposition resolution of a single atomic layer.Such high precision has never been achieved in the past in CVD, reasons being mentioned earlier, and thus raises great challenges. In details, the depositionmust be terminated right after the first layer of graphene is formed on the substrate. Over deposition leads to the undesired nucleation of the second layer graphene and eventually multilayer graphite, while insufficient deposition sparks off many isolated graphene flakes rather than a continuous sheet.In order to have perfect graphene sheet deposited, the deposition rate-limiting step needs to be seriously considered as the slow rate implies more control of graphene growth, which may not be good for the deposition of other thick films.Typically the deposition rate in CVD is limited either bychemical reaction rate or by mass transportation.

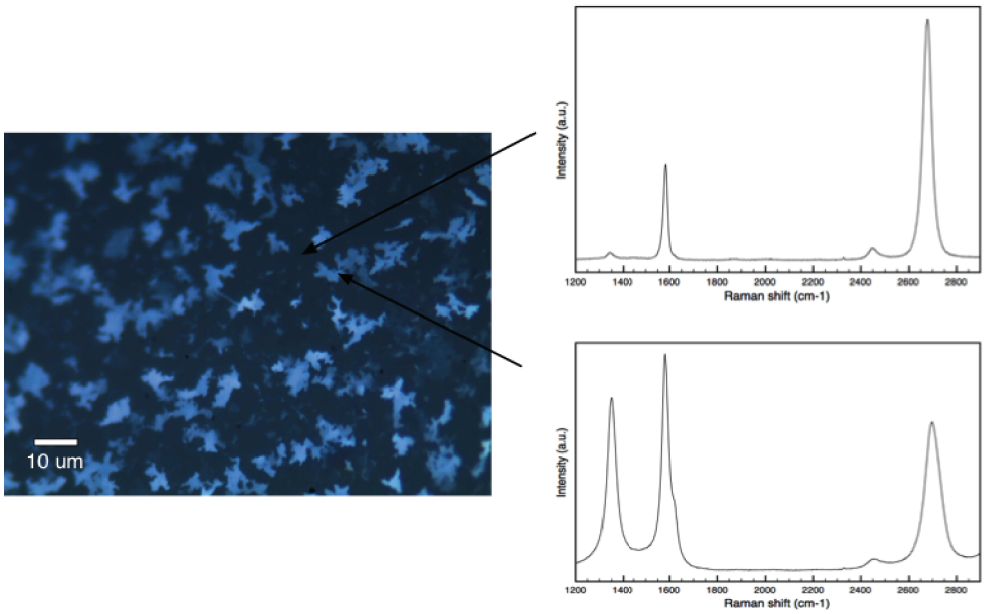

Fig. 8. Optical image of transferred graphene on SiO_2 of 300 nm thick. And the Raman spectra measured at certain points (see arrows). The bright areas correspond to the multilayer graphene, based on Raman analysis.

In the chemical reaction controlled process, the reaction rate is the limiting factor, which is related to the reaction temperature and the concentration of the reactants. Hence it is helpful to reduce the deposition temperature in case of graphene deposition with hydrocarbon pyrolysis, or to decrease the partial pressure of the precursor species from the perspective of the reaction kinetics. However, temperature affects not only the reaction rate, but also the microstructure of the deposited film. Low temperature leads to fine-grained graphene sheets, by decreasing the diffusion length of the dissociated carbon ad-atoms after the reactionaccording to the surface kinetics, which is desired for some film depositions, but not for the graphene. The low partial pressure has been widely applied in the recent graphene growths for this reason. In fact the total pressure during the CVD process is also decreased to minimizethe diffusion effect by minimizing the boundary layer above the substrate due to the inverse relation of the boundary layer thickness and the pressure, and enhance the graphene uniformity.

Besides the regular manipulation of the deposition parameters, the replacement of effective catalysts with low-efficient materials is a good idea in CVD growth of graphene by slowing down the pyrolysis of precursors. Ni significantly reduces the energy barrier to form graphene, but it also promotes the deposition rate. Recently the effort has been shifted to Cu partly because it is not as efficient as nickel in lowering the energy barrier, and the results were proved to be promising.

All the above measures are effective, but do not guarantee precise growth control in sub-nanometer scale. The most important reason encouraging people to use CVD to grow graphene is that the growth is a self-limiting process. Assuming a graphene sheet has

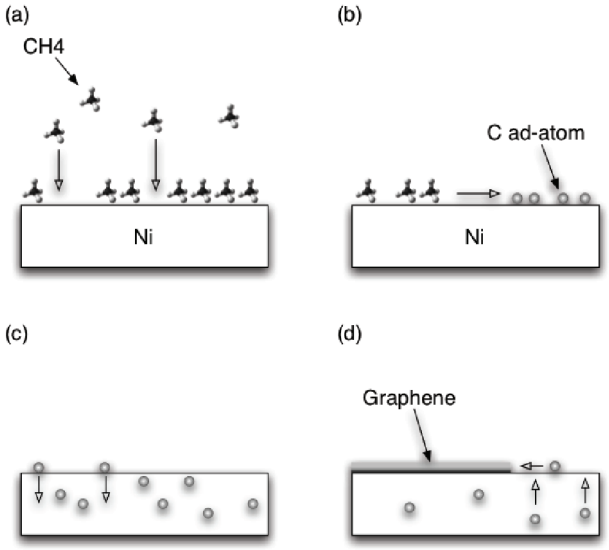

Fig. 9. Schematic drawing of the graphene growth mechanism with nickel as catalyst. (a) Methane molecules diffuse and adsorb on nickel surface. (b) Methane pyrolysis to carbon ad-atoms on nickel surface. (c) Carbon ad-atoms dissolve in bulk nickel. (d) Carbon atoms precipitate back to nickel surface at low temperature and graphene is formed.

been deposited on catalyst surface, the "catalyst-poisoning" effect (i.e. catalyst looses its catalytic feature) takes place because the catalyst is now hidden under the first-layer graphene, preventing the precursor species to access the catalyst. Hence the chemical deposition should stop automatically after the first layer is synthesized. This may be questionable, however, because the first layer graphene itself is a catalyst for the second layer to be deposited, which is true in the deposition of graphite via CVD. Compared with the origin catalyst, graphene is less effective, reason being that the energy barrier of the second-layer graphene nucleation is huge in that the second-layer nuclei are "floating" on the bottom graphene layer with the weak Van Der Waals force as the bonding force. In other words, the critical size of the nuclei is so huge that the probability of the second layer nucleation is negligible, especially with the limited super-saturation of carbon ad-atoms and the reasonable temperature. The CVD growth of graphite is a counter example where high temperature is preferred to initiate layer-by-layer growth. Therefore, as long as the partial pressure and temperature are controlled, the second layer growth could be minimized.

The mass transportation controlled process rarely is the case in graphene growth. Mentioned earlier, the low pressure is typically used, and hence precursor diffusivity to substrate surface is high because it is inversely related to the pressure.

The other challenge is the obscure mechanism. Using hydrocarbon precursor to grow graphitic materials has been studied for decades, but the secret of what is happening in the deposition process is never indeed revealed for the reason that it is a complex process as mentioned above. As a result, try-and-error method is commonly used to grow graphene and thus the production yield and repeatability are not so high as that of thick material deposition.

3.5 Graphene synthesis on Cu

While nickel encounters problems as a catalyst, the second-generation graphene was synthesized with Cu as catalyst. Cu has almost zero solubility of carbon even at 1000 °C, so the amount of carbon participating in dissolution-precipitation process is not sufficient to form a single layer of graphene. As a result, the dissolution-precipitation mechanism is negligible for Cu. The carbon atoms form a graphene sheet on the copper surface during the growth step directly. This mechanism suggests easier control over the deposition of graphene on the copper surface as the cooling rate at the last step does not affect the graphene thickness. One can roughly estimate the amount of precursor gas needed for monolayer graphene fabrication at a certain temperature and pressure, and then predict the CVD recipe to start with.

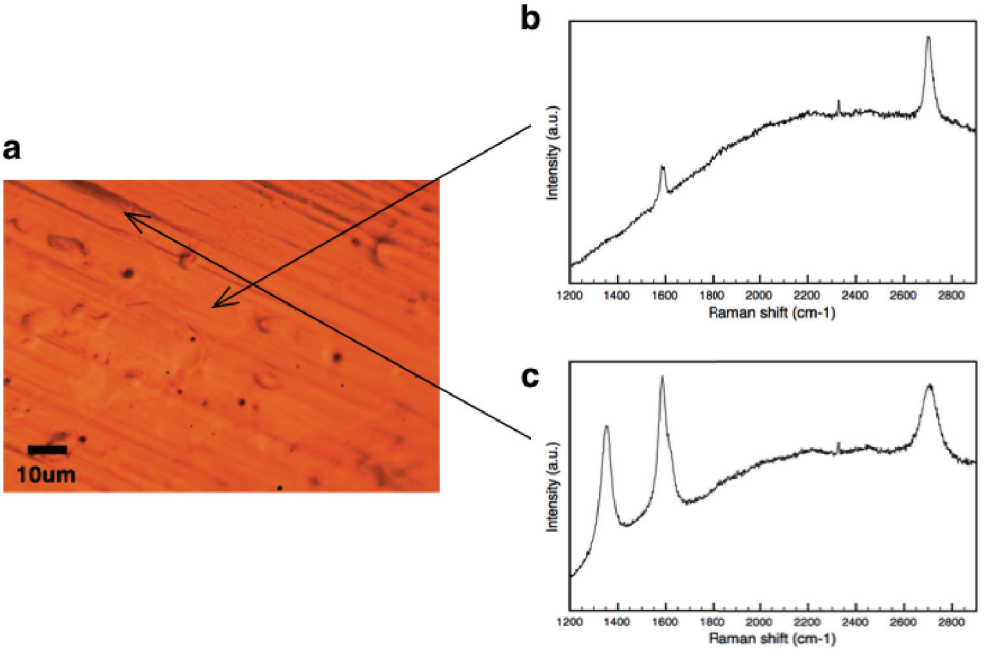

Fig. 10. (a) OM image of graphene growth on Cu foil surface. (b) and (c) Raman spectrum measure at the flat area (see arrow) and corrugated area at graphene surface, respectively.

Figure 10 shows the results of graphene deposition on copper foil surface. Different from the graphene on nickel, the graphene grown on copper has less obvious color contrast, indicating better uniformity in graphene thickness. The uniformity can also be seen on the transferred graphene on silicon oxide of 300 nm thick (Figure 11). According to the Raman spectra in most areas, graphene is monolayer. But on the rough surface areas, the graphene is thick and defective because the D peak is high and the G peak is higher than the 2D peak. One might want to polish the Cu foil surface before the deposition, but the thin dimension and softness of the foils are obstacles that render this not a good idea. In addition, the polishing will also introduce a lot of contaminates onto the copper surface. Fortunately, the artificial trenches and other textures are reduced in transferred graphene, meaning the pretreatment of polishing the

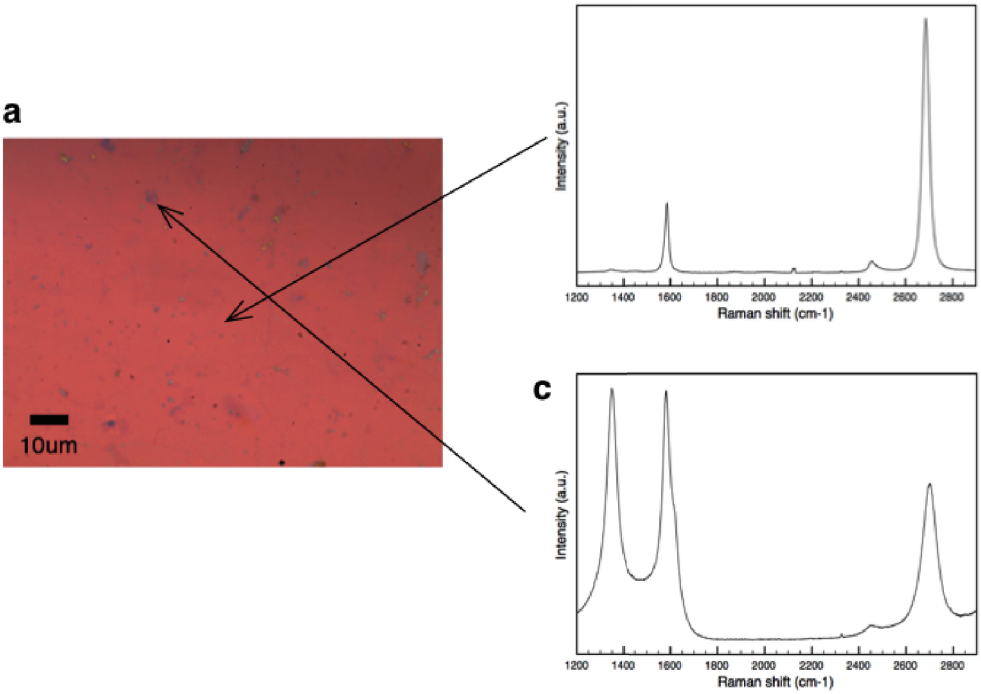

Fig. 11. (a) OM image of graphene transferred onto SiO_2. The graphene was initially deposited on Cu foils. (b) and (c) Raman spectrum measure at the flat area (see arrow), and non-uniform area at graphene surface, respectively.

copper foils may not be necessary if the transfer graphene is good enough for the potential applications.

So far most successful deposition of graphene on copper surface is done with copper foil, which is commercially available with a large size of grains, basically greater than 100 μm, one order of magnitude larger than that of typical copper thin film deposited via e-beam evaporation or sputtering. The large grain size guarantees more crystalline and higher average surface flatness, improving the synthesized graphene uniformity.

The largest production,roll-to-roll graphene production has been achieved (Bae et al., 2010) with Cu foil as catalyst (Figure 12), which shows that CVD is indeed a scalable technique capable of producing large-area graphene.

3.6 Challenges of graphene synthesis on Cu

Cu is a metal not so reactive as Ni. So attention needs to be paid during the deposition process to avoid it to be oxidized. It requires much lower base pressure of the system, and the lower temperature at which the sample could be unloaded after deposition. In the subsequent graphene transfer step (see next section), stronger etchants should be used to remove Cu, subject graphene to higher possibility to be damaged by the etchant. As a result, the properties of graphene might not be comparable to that synthesized with Ni.

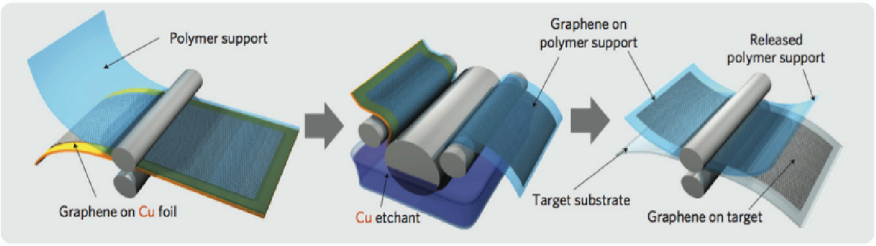

Fig. 12. Roll-based production of graphene films grown on a copper foil and graphene transfer process with thermal release tapes (Bae et al., 2010).

The second challenge is the crystalinity of as-deposited graphene, which is applied to both Ni and Cu. The graphene deposited via CVD is still far from the perfect crystalline materials. It has something to do with the catalysts. Catalysts like Ni and Cu are all metals, which are difficult to format to single crystalline materials. Instead, the catalysts deposited via a sputtering machine or an e-beam evaporator arenano-crystaline materials. Although the annealing treatment may induce grain growth that significantly enlarges the grains, the catalysts are still polycrystalline materials with many grain boundaries and different crystalline orientations on the surface. Consequently, graphene grows in a polycrystalline fashion, as illustrated in Figure 13. On the left side shows the carbon ad-atoms sitting on catalyst surface. The middle figure shows the nucleation of graphene occurring at certain points. One must know that the crystalline orientation of the nuclei may not be the same, which may be dependent on the crystalline structure of the catalyst they sit on. Finally when the nuclei keeps growing, the polycrystalline graphene is formed as shown in the image on the right side of Figure 13. It is also possible for a second layer nucleation to occur at some conditions (e.g. higher super-saturation).

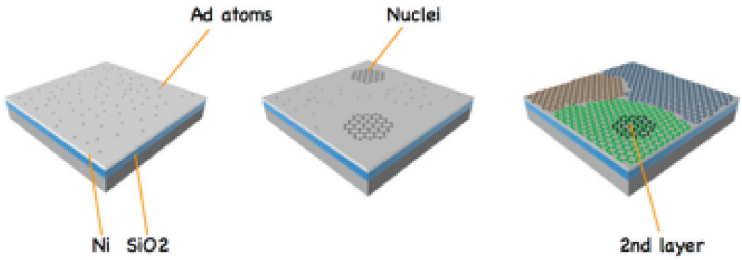

Fig. 13. Schematic diagram of carbon growth on catalyst forming polycrystalline graphene.

With all the challenges discussed, graphene growth by CVD is still a promising process compared with others. Its intrinsic properties stimulate more and more people to involve in the field of CVD graphene.

Although CVD of graphene has advantages such as low cost and scalable production, recall that graphene is deposited on metal catalysts. Since many applications of graphene (e.g. graphene MOSFET) require it to be on an insulator, the graphene needs to go through a transfer process to move graphene, without damaging or degrading its performance, to a

suitable insulator substrate; the current catalysts are not insulators. Therefore the transfer process plays an important role in graphene fabrication.

3.7 Growth mechanism comparison

To compare the growth mechanism on Ni and Cu straightforwardly, the Texas group has come up with a smart idea that utilities the characteristics of ^{13}C, an isotope of regular ^{12}C. During the growth, $^{12}CH_4$ and $^{13}CH_4$ are fed into the chamber in turns (i.e. $^{12}CH_4$ is fed in for 1 minute, followed by $^{13}CH_4$ for 1 minute and so on). Note that the Raman signatures of the two carbon isotopes are not exactly the same and the difference is distinguishable. Hence it is feasible to use Raman spectroscopy/mapping to tell ^{12}C- and ^{13}C-graphene patterns. If the clearly distinguished ^{12}C- and ^{13}C-graphene patterns are shown, the graphene must be formed immediately during the adsorption of carbon atoms onto the graphene nucleus edge (i.e. surface kinetics). And the randomly mixed ^{12}C- and ^{13}C-graphene patterns should be caused by the dissolution and surface segregation mechanism.

After the experiment, the grown graphene shows ^{12}C- and ^{13}C-graphene patterns separately in case of Cu, but they are uniformly distributed on the Ni surface (Figure 14) (Li et al., 2009). Hence it is suggested that graphene growth on Ni is through dissolution-precipitation mechanism, while graphene growth on Cu is a surface process.

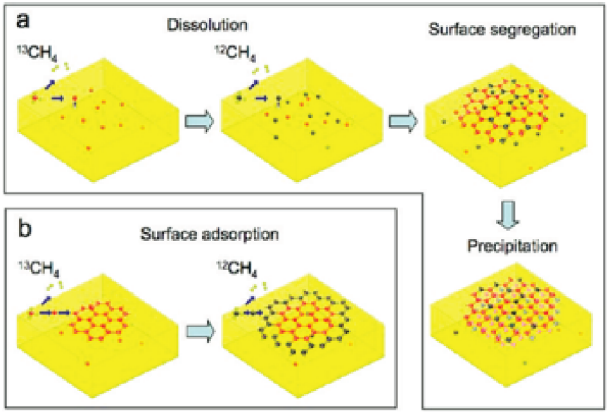

Fig. 14. Schematic diagram of the growth mechanism of graphene on metal catalysts (Li et al., 2009). (a) Graphene is grown with ramdomly distributed C isotopes due to surface segregation and/or precipitation. (b) Graphene is grown by surface adsorption where C isotopes is obviously seperated.

The second different between Ni and Cu is their chemical reactivity. Cu is more sensitive to O_2 to form Cu oxide than Ni, suggesting more attention needs to be paid when dealing with Cu. For example, after growth, graphene/Cu sample should be unloaded out of the reactor at room temperature, while graphene/Ni sample is safe to be taken out at 300 °C, as both Ni and graphene are of high oxidation resistance.The reactivity difference also affects the graphene transfer process that will be discussed later.

The third difference lies in their melting points. Cu has a relatively lower melting point 1083 °C and Ni 1453 °C. In the deposition process, Cu evaporation is more significant than that of Ni, leading to more deposition on reactor walls. Therefore the reactor should be cleaned more frequently with Cu. The high evaporation is not preferred for thin film deposition, owing to

the fact that evaporation of substrate material is a competing process with deposition of new material. In case of Cu, its high evaporation may result in the difficulty of graphene growth, especially for extreme thin film deposition.
The last difference is their catalytic capability. Ni is a widely used catalyst in CNT growth where high deposition rate is desired. From scientific perspective, Cu is not as effective as Ni to lower the overall energy barrier to form graphene. Hence it is suggested to use Cu as catalyst to lower the entire graphene deposition rate in growth of sub-nanometer material, so that one can gain more control.
It has to be mentioned that neither Ni nor Cu is an ideal catalyst for graphene growth, although they are most popular ones in the community of graphene deposition. The catalyst issue is the one that scientists have to face and seeking right catalyst is left as one of the future research topics.

4. Graphene transfer

The transfer of CVD-grown graphene films is very crucial, as we have mentioned previously; in order for electrical current to flow through graphene devices as opposed to being shorted out by a conducting substrate, graphene must be removed from the conducting catalyst surface and transferred onto an insulating surface (Kedzierski et al., 2009).
Not all the transfer techniques are applicable for CVD graphene. Graphene transfer techniques that are suitable for CVD graphene, are usually done by etching the underlying catalyst and then scooping the graphene directly or using some kind of media such as Poly(methyl methacrylate) (PMMA), Polydimethylsiloxane (PDMS) and thermal tape. Other techniques are not suitable such as mechanical exfoliation or chemical exfoliation dealing with multi-layer graphite as precursor material.

4.1 Direct transfer

The etching and scooping method is a straightforward transfer method to move graphene from the surface of metals to the target substrate. The key idea is to get rid of the catalyst film underneath the graphene so that the graphene sheet can be separated and scooped. An example process is shown in Figure 15. After the CVD growth, graphene is not isolated; it sits on the catalyst that is again on the substrate. The whole sample is submerged in an etchant, depending on the type of catalyst, to etch away the metal. After the catalyst is gone, the graphene sheet is floating on the liquid surface because of its hydrophobic nature (Leenaerts et al., 2009). One needs to be extremely careful to use the target substrate to scoop the floating graphene while letting the graphene sheet to sit uniformly on the surface. Finally after the graphene is dried, the transferred graphene is ready.
The advantage of this technique is that it is a simple process with few steps which reduces the possibility of introducing potential environment impacts. However, the direct scooping method requires high stability of the transferring setup to avoid the fragile graphene sheet from breaking during the process. Therefore it is of low yield. In addition, the etchant goes in between transferred graphene and its target substrate, which behaves as chemical dopants and enhances carrier scattering to degrade the electrical properties of graphene.

4.2 Transfer with media

To increase the throughput, a media is introduced to protect graphene. The mechanism is similar that the catalyst film underneath graphene is etched.Figure 16 shows an example of

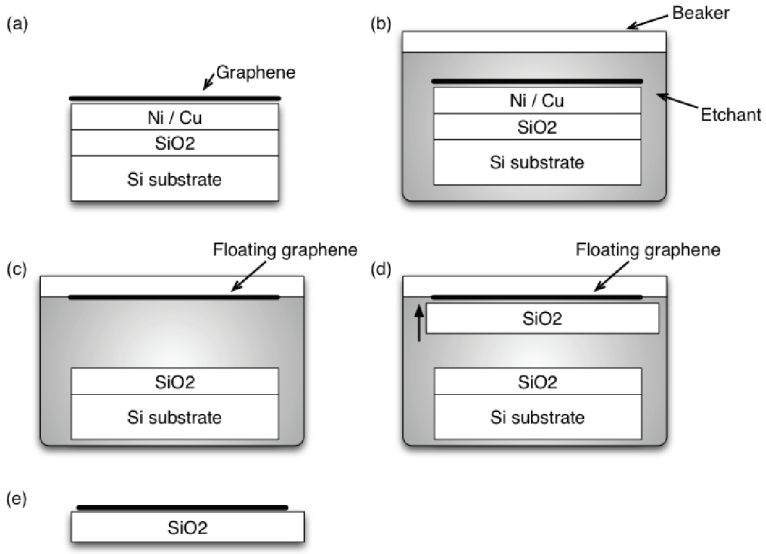

Fig. 15. Schematic diagram of the etching and scooping method without using a support. (a) The CVD-grown graphene on Ni or Cu catalyst. (b) The graphene sample is submerged into the metal (Ni or Cu) etchant. (c) The Ni or Cu is etched and the graphene is floating on the etchant surface, while the remaining SiO_2 and Si substrate sinks to the bottom of the beaker. (d) Another SiO_2 is used to scoop the floating graphene out of the etchant. (e) After drying, graphene is sitting on SiO_2, ready for future processing.

transfer graphene using PMMA as a media. Beside PMMA, PDMS and thermal release tape are commonly used as support materials too.

The only difference between PDMS and the other two is that PDMS and thermal tape are not dissolved at the last step (Figure 16f); instead they are pilled off by hand. It is crucial that the interface bonding between graphene and substrate is greater than that between PDMS and graphene to ensure graphene is left on substrate while being peeled off.However, the quantified values are unknown now. The current solution is that the PDMS stamp is applied onto graphene that is on catalyst surface when it is sticky, i.e. partially cured (Figure 16e). Then the PDMS is completely cured to reduce the adhesion before the PDMS stamp is peeled. It works because the adhesion strength of PDMS surface can be approximately linearly related to the degree of cross-linking of elastomers (Shanahan & Michel, 1991). Beside the effort on PDMS, the surface treatment on the substrates where graphene is transferred may be helpful by increasing its bonding strength with graphene, thus improving the yields. For example, surface activation with plasma, which is commonly done in wafer bonding for SOI fabrication, could be performed to help enhance the surface adhesion.

5. Summaries

Deposition of graphene on catalysts is demonstrated using thermal CVD process. Monolayer graphene is formed on catalyst through the surface catalytic pyrolysis of carbon-containing precursors, and it is transferred to arbitrary substrates via a transfer process with or without support media. Color contrast using optical microscope and Raman spectroscopy distinguish

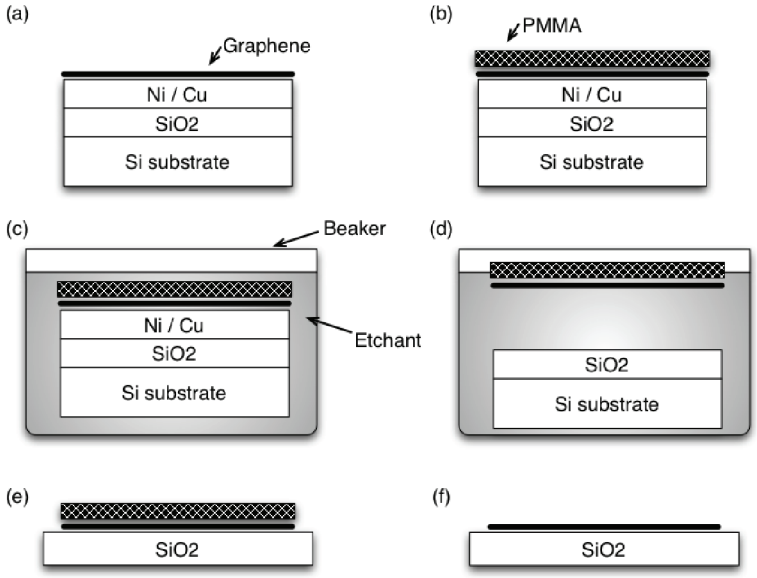

Fig. 16. Schematic diagram of graphene transfer with PMMA as a support. (a) The CVD-grown graphene on Ni or Cu catalyst. (b) A PMMA layer is spin-coated on top of graphene. (c) The graphene sample is submerged into the metal (Ni or Cu) etchant. (d) The Ni or Cu is etched and the graphene is floating with PMMA on the etchant surface, while the remaining SiO_2 and Si substrate sinks to the bottom of the beaker. (e) The floating graphene/PMMA is transferred onto a SiO_2 substrate. (f) The PMMA top layer is removed by acetone or other PMMA remover and graphene remains on SiO_2.

the number of graphene layers. It shows that the graphene morphology is closely dependent on the catalyst material, and thus the selection of right catalyst is crucial. Although the overall deposition process is not exactly scientifically known in terms of mechanism, the knowledge of the effect of carbon solubility in catalyst already leads to the upgrade of catalyst from Ni to Cu that significantly improves the surface uniformity of graphene.

CVD plays an important role in graphene fabrication, as the progress in development of graphene-based products is largely stalled by a lack of supply of high-quality large-size graphene sheets and CVD is a solution compatible with massive production. It is a milestone in CVD history that the fabrication of sub-nanometer materials has been successfully achieved.

6. References

Bae, S., Kim, H., Lee, Y., Xu, X., Park, J., Zheng, Y., Balakrishnan, J., Lei, T., Kim, H. R., Song, Y., Kim, Y., Kim, K., Ozyilmaz, B., Ahn, J., Hong, B. & Iijima, S. (2010). Roll-to-roll production of 30-inch graphene films for transparent electrodes, *Nat Nano* 5(8): 574–578.
URL: *http://dx.doi.org/10.1038/nnano.2010.132*

Ferrari, A., Meyer, J., Scardaci, V., Casiraghi, C., Lazzeri, M., Mauri, F., Piscanec, S., Jiang, D., Novoselov, K., Roth, S. & Geim, A. (2006). Raman spectrum of graphene and graphene layers, *Phys. Rev. Lett.* 97(18): 187401.

Kedzierski, J., Hsu, P.-L., Reina, A., Kong, J., Healey, P., Wyatt, P. & Keast, C. (2009). Graphene-on-insulator transistors made using c on ni chemical-vapor deposition, *Electron Device Letters, IEEE* 30(7): 745 –747.

Konstantin, E., Bostwick, A., Horn, K., Jobst, J., Kellogg, G. L., Ley, L., McChesney, J. L., Ohta, T., Reshanov, S., Rohrl, J., Rotenberg, E., Schmid, A., Waldmann, D., Weber, H. B. & Seyller, T. (2009). Towards wafer-size graphene layers by atmospheric pressure graphitization of silicon carbide, *Nat Mater* 8(3): 203–207.
URL: *http://dx.doi.org/10.1038/nmat2382*

Leenaerts, O., Partoens, B. & Peeters, F. (2009). Water on graphene: Hydrophobicity and dipole moment using density functional theory, *Phys. Rev. B* 79(23): 235440.

Li, X., Cai, W., An, J., Kim, S., Nah, J., Yang, D., Piner, R., Velamakanni, A., Jung, I., Tutuc, E., Banerjee, S., Colombo, L. & Ruoff, R. (2009). Large-Area Synthesis of High-Quality and Uniform Graphene Films on Copper Foils, *Science* 324(5932): 1312–1314.
URL: *http://www.sciencemag.org/content/324/5932/1312.abstract*

Lopez, G. A. & Mittemeijer, E. J. (2004). The solubility of c in solid cu, *Scripta Materialia* 51(1): 1 – 5.
URL: *http://www.sciencedirect.com/science/article/B6TY2-4C603D5-9/2/bf4550d41ac2d5011e7a34f4eba440d3*

Natesan, K. & Kassner, T. (1973). Thermodynamics of carbon in nickel, iron-nickel and iron-chromium-nickel alloys, *Metallurgical and Materials Transactions B* 4: 2557–2566. 10.1007/BF02644258.
URL: *http://dx.doi.org/10.1007/BF02644258*

Ni, Z., Wang, H., Kasim, J., Fan, H., Yu, T., Wu, Y., Feng, Y. & Shen, Z. (2007). Graphene thickness determination using reflection and contrast spectroscopy, *Nano Letters* 7(9): 2758–2763.
URL: *http://pubs.acs.org/doi/abs/10.1021/nl071254m*

Novoselov, K. S., Geim, A. K., Morozov, S. V., Jiang, D., Zhang, Y., Dubonos, S. V., Grigorieva, I. V. & Firsov, A. A. (2004). Electric field effect in atomically thin carbon films, *Science* 306: 666–669.

Reina, A., Jia, X., Ho, J., Nezich, D., Son, H., Bulovic, V., Dresselhaus, M. & Kong, J. (2009). Large area, few-layer graphene films on arbitrary substrates by chemical vapor deposition, *Nano Letters* 9(1): 30–35.
URL: *http://pubs.acs.org/doi/abs/10.1021/nl801827v*

Shanahan, M. & Michel, F. (1991). Physical adhesion of rubber to glass: cross-link density effects near equilibrium, *International Journal of Adhesion and Adhesives* 11(3): 170 – 176.
URL: *http://www.sciencedirect.com/science/article/B6TW7-482B0VF-5C/2/458993c18b2508bfaf4200536fa98199*

Tung, V. C., Matthew, M. J., Yang, Y. & Kaner, R. B. (2009). High-throughput solution processing of large-scale graphene, *Nat Nano* 4: 25–29.

Wang, Y., Ni, Z., Yu, T., Shen, Z., Wang, H., Wu, Y., Chen, W. & Wee, A. S. (2008). Raman studies of monolayer graphene: The substrate effect, *The Journal of Physical Chemistry C* 112(29): 10637–10640.
URL: *http://pubs.acs.org/doi/abs/10.1021/jp8008404*

Yu, Q., Siriponglert, S., Hao, L., Chen, Y. P. & Pei, S. (2008). Graphene segregated on ni surfaces and transferred to insulators, *Appl. Phys. Lett.* 93: 113103.

4

Epitaxial Graphene on SiC(0001): More Than Just Honeycombs

Lian Li
University of Wisconsin-Milwaukee, USA

1. Introduction

The growth of graphitic layers by the sublimation of Si from SiC substrates has been known since 1975 (van Bommel et al., 1975). The electronic properties of these materials are recently found to be similar to that of isolated graphene sheets (Berger et al., 2006; Castro Neto et al., 2009; Miller et al., 2009). Due to its compatibility with current standard semiconductor device fabrication technology, this process offers additional benefit of large-scale production of wafer-sized materials to facilitate the development of graphene electronics (Berger et al., 2004; Kedzierski et al., 2008; Lin et al., 2010).

Currently, 4H- and 6H-SiC polytypes are commercially available for the growth of epitaxial graphene. Because of the mismatch with the SiC, the physical and electronic properties of graphene films strongly depend on the polarity of the substrate. On the (000-1) C-face, graphene films typically grow in multiple layers with a "twisted" interface, which leads to the decoupling between different layers, and a carrier mobility comparable to that of exfoliated graphene (Hass et al., 2008a; Orlita et al., 2008; Sprinkle at al., 2009).

On the (0001) Si-face, on the other hand, the growth is self-limiting, where more uniform wafer-sized graphene films with controlled number of layers has been grown epitaxially (Emtsev et al., 2009). The graphitization has been known to start with a ($6\sqrt{3}$x$6\sqrt{3}$) (denoted "$6\sqrt{3}$" hereafter) structure, which remains at the interface during the growth of subsequent layers (van Bommel et al., 1975; Hass et al., 2008b). The interactions of this interfacial layer with the graphene above and SiC(0001) substrate below lead to giant inelastic tunnelling in scanning tunnelling spectroscopy (STS) (Červenka et al., 2010); modification of the dispersion about the Dirac point (Bostwick et al., 2007(a,b); and even gap opening in angle-resolved photoemission spectroscopy (ARPES) - a property crucial for its use in electronic devices – but found only for epitaxial graphene on the Si-face, and absent for the C-face and exfoliated graphene (Novoselov, 2007; Zhou et al., 2007).

Despite its impact on the electronic properties of graphene, the atomic structure of the $6\sqrt{3}$ layer remains controversial. Earlier studies have suggested that it consists of a graphene honeycomb layer weakly bonded to the SiC (1x1) surface (van Bommel et al., 1975; Tsai et al., 1992) or Si-rich interface layer (Northrup & Neugebauer, 1995; Forbeaux et al., 1998). More recent work indicates covalent bonding at the interface to the SiC (Seyller et al., 2008; Emtsev et al., 2008). Furthermore, most calculations, which are based on defect-free graphene covalently bonded to the SiC(0001) (1x1), indicate a metallic $6\sqrt{3}$ layer (Kim et al., 2008; Varchon et al., 2007), contrary to a semiconducting surface around K as observed in

ARPES (Emtsev et al., 2008; Seyller et al., 2008). A highly interacting graphene layer would yield a semiconducting gap (Rutter et al., 2007), but also requires Si adatoms and tetramers that are bonded to the SiC at the graphene/SiC interface, which are not seen in ARPES (Emtsev et al., 2008; Seyller et al., 2008).

By using functionalized W tips coated with transition metals such as Cr and Fe, we recently have found that scanning tunnelling microscopy (STM) imaging of the $6\sqrt{3}$ structure close to a few meV of the Fermi level is possible (Qi et al., 2010; Rhim et al., 2011). As a result, we have observed new details of the complex electronic properties of this interfacial graphene layer that were not detected by W tips in previous studies (Hass et al., 2008b; Li & Tsong, 1996; Lauffer et al., 2008; Mallet et al., 2007; Owman & Mårtensson, 1996; Riedl et al., 2007; Tsai et al., 1992). Aided with first principles calculations, we found that the unique properties of epitaxial graphene on Si-face arise from the distinct structure of the $6\sqrt{3}$ interfacial layer - a warped graphene layer resulted from the periodic inclusions of hexagon-pentagon-heptagon ($H_{5,6,7}$) defects in the honeycomb - to relieve the mismatch with the SiC substrate (Qi et al., 2010). The $H_{5,6,7}$ defects break the symmetry of the honeycomb, thereby inducing a gap: the calculated band structure of the proposed model along Γ-K is semiconducting with two localized states near K points below E_F, correctly reproducing the published photoemission and C *1s* core-level spectra. The 1st graphene layer assumes the defect-free honeycomb lattice; however, its interaction with the warped layer leads to deviations from the linear dispersion at the Dirac point.

On multilayer graphene films, we have found that the mismatch between the graphene and the SiC substrate can cause ridges and wrinkles, which introduce ripples in the otherwise atomically flat graphene sheet (Sun et al., 2009). These features can cause carrier scattering and decrease in mobility (Morozov et al., 2006). The origin of these ridges and wrinkles had previously been attributed to a number of causes such as the formation of carbon nanotubes (CNTs) on the surface (Derycke et al., 2002); condensation of mobile atoms that are present at the graphene/SiC interface during high temperature annealing (Luxmi et al., 2009); or compressive strain induced during cooling due to the difference in thermal expansion coefficients of graphene and SiC (Biedermann et al., 2009). We have found, by atomically resolved STM imaging, that these ridges and wrinkles are actually bulged regions of the graphene (Sun et al., 2009). We further have shown that the ridges can be manipulated, even created during STM imaging, indicating that the epitaxial graphene on SiC is still under compressive strain at room temperature (Ferralis et al., 2008; Ni et al., 2008). By minimizing this strain with decreased terrace size, nearly ridge-free graphene has been grown on vicinal SiC substrates.

2. Methods

Experiments were carried out on epitaxial graphene grown on N-doped 6H-SiC(0001), which was first etched in a H_2/Ar atmosphere at 1500 °C. After annealing at ~950 °C for 15 min in a Si flux to produce a (3x3) reconstructed surface, the SiC substrate was heated to 1100-1400 °C to grow graphene in ultrahigh vacuum (UHV) (Li and Tsong, 1996). Scanning tunnelling microscopy images were taken using W tips, as well as functionalized W tips by Fe(Cr) coating at room temperature followed by annealing at 500-700 °C in UHV (Bode, 2003; Qi et al., 2009; Rhim et al., 2011).

First-principles calculations using the Full-potential Linearized Augmented Plane Wave (FLAPW) method as implemented in *flair* (Weinert et al., 2009) model the substrate using a

3x3 6H-SiC(0001) 6-bilayer supercell, with a vacuum region of ~20-25 Å and a basis cutoff of ~195 eV. Because of the usual density functional theory underestimation of the gap (1.6 vs. 3.0 eV for 6H-SiC), comparisons of calculated density of states (DOS) and STM images are limited to biases within E_F±0.5 eV.

3. Results

3.1 STM imaging of the interface layer with W tips

Graphene growth on SiC(0001) follows the phase transitions from the Si-rich (√3x√3) (denoted "√3" hereafter), to (6√3x6√3), to 1st layer graphene (Hannon & Tromp, 2008). At the early stages, the √3 and 6√3 phases are often found to coexist; while at later stages, both the 1st layer graphene and 6√3 are observed, accompanied by pits of a few atomic layers in depth. Figure 1 presents STM images of the surface after growth at 1100 °C. The morphology is characterized by terraces of ~100 nm separated by mostly bilayer steps (Fig. 1(a)). On the terrace, two regions of different contrast are observed: a closed-pack structure in the brighter region *I*, and a honeycomb structure in the dimmer region *II* (Fig. 1(b)). Close inspection of an atomic resolution image of the structure in region *I* shown in Fig. 1(c) indicates a periodicity of 0.52 ± 0.01 nm, consistent with the (√3x√3) assignment, which consists of one Si adatom per unit cell (Northrup & Neugebauer, 1995). In addition, randomly distributed depressions are also found (circled), indicating desorption of the Si adatom at the site. Figure 1(d) is a filled-state atomic resolution image of the honeycomb structure observed in region *II*, showing that it consists of two major building blocks: two types of trimers pointing in opposite directions: marked blue are approximately 6 Å in size, and green 5 Å. These features distribute randomly without apparent order.

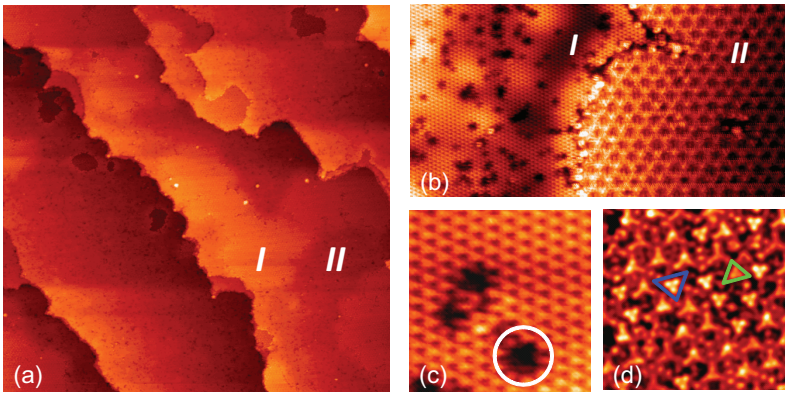

Fig. 1. (a) Topography image showing the step morphology of epitaxial graphene on 6H-SiC(0001) at 1100 °C (300x300 nm², V_s=-2.0 V, I_t=0.2 nA). (b) Close-up view of the two phases observed (50x25 nm²; V_s=-1.5V, I_t=1.2 nA). (c) Atomic resolution image of the (√3x√3) structure in region *I* (3.2x3.2 nm²; V_s=-1.5V, I_t=1.2 nA). (d) Atomic resolution image of the (6√3x6√3) structure in region *II* (12x12 nm², V_s=-1.4 V, I_t=1.2 nA).

To better understand this structure, filled- and empty-state STM images were taken, as shown in Fig. 2. Interestingly, in the empty-state image, the trimers pointing upward in filled state appear only as single bright spots, while the trimers pointing downward in filled-state now appear as featureless depressions. Note that the same trimers are identified by their relative positions to a commonly seen defect (circled).

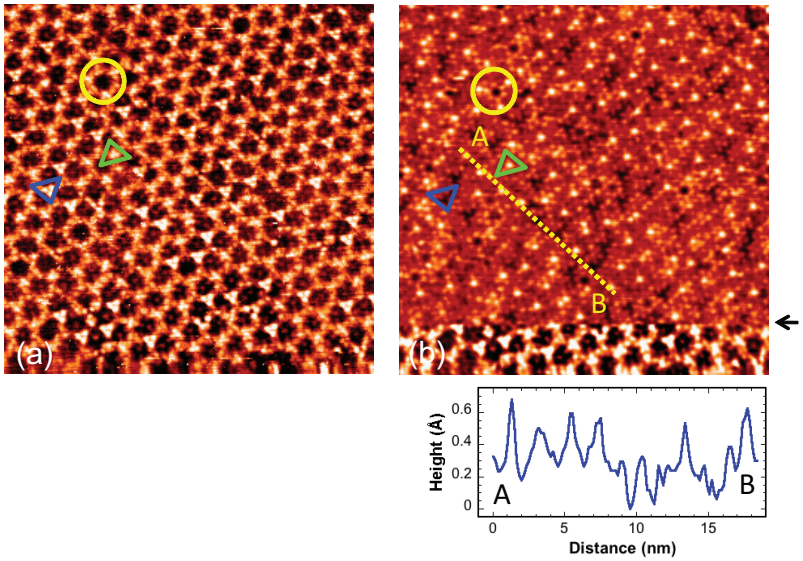

Fig. 2. STM images of the 6√3 structure taken with a W tip at the same location: (a) filled-state (35x35 nm², V_s=-1.5 V, I_t=0.3 nA); (b) empty-state (35x35 nm², V_s=+1.5 V, I_t=0.3 nA). The arrow indicates where the V_s is changed from -1.5V to +1.5V during imaging.

Small changes in heights and depressions are also observed along the line profile *AB* through six bright spots and three depressions in Fig. 2(b), confirming the fact that they do not line up perfectly as already evident visually. Detailed analysis of many line profiles indicates: 1) neighbouring trimers do not always fall on the same line; and 2) the spacing between the trimers is not uniform, with an average value of ~19 Å, i.e., about 6 times the (1x1) spacing of the SiC(0001) surface. These characteristics are consistent with earlier STM observations of the 6√3 structure (Li & Tsong, 1996; Lauffer et al., 2008; Mallet et al., 2007; Owman & Mårtensson, 1996; Riedl et al., 2007; Tsai et al., 1992).

Furthermore, the ratio of the larger to smaller trimers varies with growth conditions, with the later type always being more populated. For example, the ratio is found to be ~3:1 on a sample at the early stages of growth (Fig. 1(b)), where part of the surface is still covered with the √3 structure. And for a sample at later stages of growth where some regions are already converted to graphene (Fig. 2), the ratio is ~4:1.

Over all, these STM images of the 6√3 structure taken using W tips at larger bias (e.g., E_F±2.0 eV) are similar to earlier studies. Also similar is that imaging at energies closer to E_F (e.g., within ±0.1 eV) is challenging (Mallet et al., 2007; Lauffer et al., 2008; Riedl et al., 2007). Given that epitaxial graphene on SiC(0001) represents a system of a zero gap graphene supported on a wide bandgap semiconductor SiC, selective STM imaging with functionalized W tips (Deng et al., 2006), particularly near the Fermi level, may be necessary to unravel the atomic structure of the 6√3 interface layer, as discussed below.

3.2 STM imaging of the interface layer with (Fe, Cr) coated W tips

Using an Fe/W tip imaging at 1.0 eV below the E_F, the 6√3 structure appears similar to that of W tip (Fig. 3(a)). However, at E_F±0.5 eV, drastic differences are observed: the smaller up-

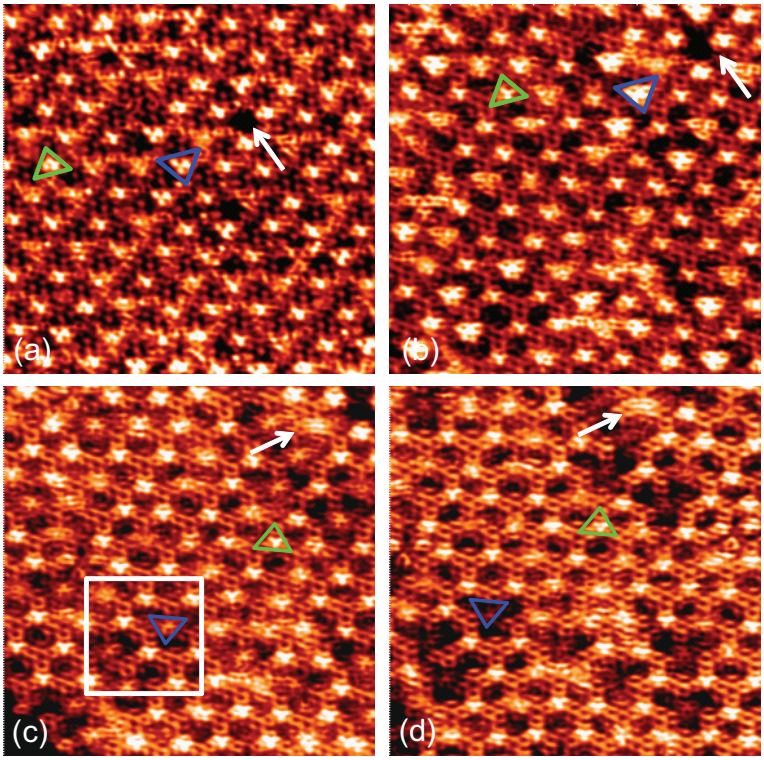

Fig. 3. Filled-stated STM images of the $6\sqrt{3}$ structure taken with an Fe/W tip at (a) V_s=-1.0 V; and (b) V_s=-0.5 V. I_t=0.3 nA. (c) Filled-state V_s=-0.1 V; and (d) empty-state V_s=+0.1 V; I_t=0.3 nA and image sizes are 20x20 nm^2 for all.

facing trimers (marked green) now face downwards, while the larger down-facing trimers (marked blue) now appear as six-fold rosettes. Again the same trimer and rosette are identified by their relative positions to a defect marked by an arrow in both images. (Note that the two images are taken sequentially, the slight change in position is a result of thermal drift.)

Interestingly, the trimers marked by green that appear as a single protrusion in the +1.5 eV image (Fig. 2(b)), are now better resolved to be a trimer facing downwards at +0.1 eV (Fig. 3(d)). The biggest change is seen for the trimers marked blue that appear as featureless depressions in the +1.5 eV image (Fig. 2(b)): at +0.1 eV (Fig. 3(d)), they appear as rosettes surrounded by depressions. In addition, while the appearance of the trimer is independent of bias, the contrast of the rosette is slightly less in empty-state images. In the case of Cr-coated W tips, imaging down to E_F±2 meV can be carried out, with results qualitatively similar to those shown in Fig. 3 (Rhim et al., 2011).

Figure 4(a) is an STM image of the 1st layer graphene taken with an Fe/Cr/W tip. At E_F-0.052 eV, a honeycomb structure characteristic of graphene is seen over the whole surface, with additional periodic modulations. Two of the brighter ones are marked by down-pointing triangles, and two slightly dimmer ones marked by up-pointing ones. At E_F-0.52 eV (Fig. 4(b)), the honeycomb structure is no longer seen, and the features marked by

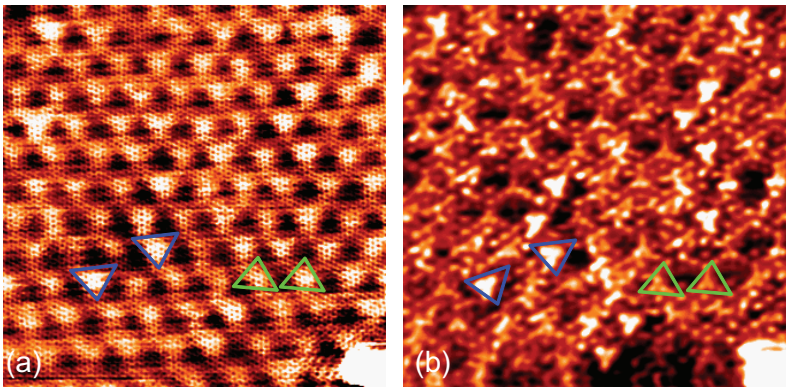

Fig. 4. STM images of the 1st graphene taken with an Fe/Cr/W tip at (a) V_s=-0.052 V; and (b) V_s=-0.52 V; I_t=5.3 nA and image sizes are 20x20 nm² for both.

triangles now appear as up- and down-pointing trimers similar to those seen by W tips (Fig. 1(d)). (Note that the large bright feature in the lower right hand corner is used to identify the features in discussion.) This confirms that the (6√3x6√3) layer remains at the interface after the growth of the 1st graphene layer, and is still accessible by electron tunnelling at 0.5 eV above and below E_F (Rutter et al., 2007).

Functionalization of W tips by transition metal coating has been typically used in spin-polarized tunnelling to probe spin dependent properties of magnetic heterostructures (Bode, 2003). The results presented here clearly show that these tips also facilitate the probing of electronic properties of the 6√3 interface layer that were not accessible using conventional W tips. To better understand this effect, we have modelled the Fe/W tips using a Fe pyramid on W(110), as shown in Fig. 5(a). The calculated density of states shown in Fig. 5(b) indicate that the apex Fe atom exhibits a large enhancement of magnetic moment (2.78 μ_B/atom) compared to that of bulk Fe, as well as the Fe atoms directly bonded to the W slab (2.1-2.3 μ_B/atom). The enhancement of magnetic moment of the topmost Fe atom is reminiscent of increased moments at surfaces and is due to a shift of peaks in DOS related to band narrowing. The minority spin channel has an especially sharp peak at ~0.5 eV below E_F (Fig. 5(b)). Electron tunnelling between graphene and these localized states enables the imaging of energy-dependent DOS not accessible with a W tip (Rhim et al., 2011).

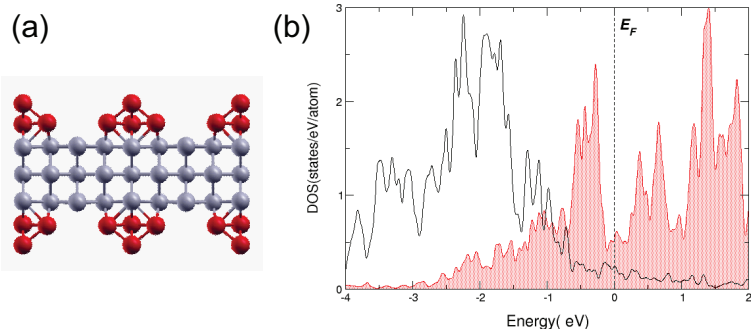

Fig. 5. (a) Ball-and-stick model used in the tip calculations. (b) Spin-resolved DOS for Fe/W(110); area shaded in red is for the minority and unshaded for the majority spins.

3.3 Proposed model of the interface layer

To account for these observations made taken with Fe/Cr coated W tips, which clearly reveal new details of the 6√3 structure, let's first consider the possible commensurate structures that can form when a layer of graphene is placed on top of the SiC(0001) (1x1) lattice. Among the possible phases, (13x13) graphene lattice is nearly commensurate to the (6√3x6√3) SiC(0001) (Tsai et al., 1992; Hass et al., 2008b), which results in two types of high symmetry positions: either a C atom or a graphene hexagon centred above a Si (Fig. 6(a)). Our calculations indicate that the in-plane graphene C-C bond is shortened from 1.67 to 1.42 Å. In addition, C atoms located directly above Si are pulled towards the SiC surface significantly such that the Si-C bond is shortened to 1.99 Å from 2.29 Å, consistent with other calculations (Mattausch & Pankratov, 2007; Varchon et al., 2008). Effectively, the graphene layer is broken.

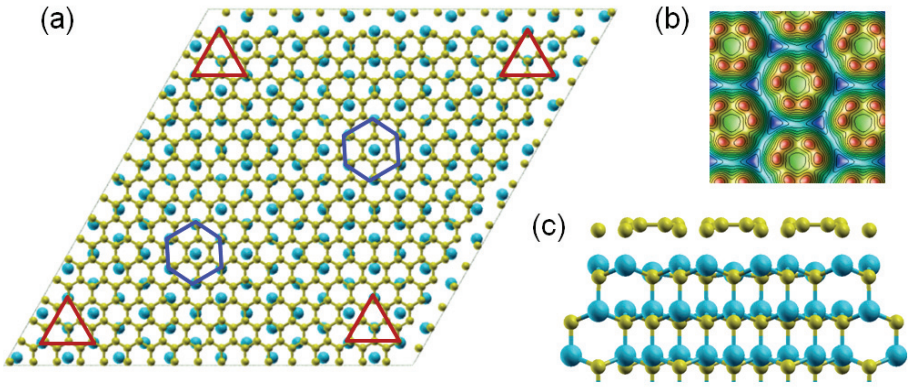

Fig. 6. (a) Ball-and-stick model of the graphene (13x13) on SiC(0001) 1x1 in plane-view (C: yellow balls; Si: blue balls). Red triangles and blue hexagons mark the two configurations of C atoms directly above Si atoms. (b) Calculated DOS at E_F+2 eV using a √3x√3 supercell and (c) ball-and-stick model in side-view, showing the distortions of the in-plane C-C bonds, and Si-C bonds at the graphene/SiC interface as a result of covalent bonding.

Alternatively, to better accommodate this bond distortion and retain the three-fold coordination for each C atom, let's now consider the inclusion of pentagons and heptagons – which cause positive and negative curvatures, respectively, when inserted into the honeycomb lattice (Charlier & Rignanese, 2001; Ihara et al., 1996). Furthermore, to preserve the long-range translational and rotational integrity of the graphene honeycomb, they can take the form of three pairs of alternating pentagons and heptagons around a rotated hexagon ($H_{5,6,7}$), which can be created by adding a C dimer to the graphene honeycomb lattice (Orlikowski et al., 1999).

As shown in Fig. 7, placement of the $H_{5,6,7}$ defects at the two high symmetry positions leads to two variants. At the "top" site, three Si atoms sit directly below the corners of the central hexagon of the $H_{5,6,7}$, with this hexagon centred above a C of the SiC substrate. At the "hollow" site, the central hexagon is centred over a Si and three Si atoms are now bonded to C atoms at the edge of the $H_{5,6,7}$ defect. Overall, this transformation decreases interfacial Si-C bonds from 6 (4) to 3 at the top (hollow) sites, further reducing the mismatch with the SiC substrate. The result is a warped graphene layer covalently bonded to SiC(0001) (1x1),

whose formation is favoured by ~0.1 eV/C compared to a perfect honeycomb structure. In addition, the top site is also found to be more stable than the hollow site by 0.03 eV/C. These results are in contrast to unsupported graphene where the $H_{5,6,7}$ defect formation energy is ~5.1 eV; the stability of the warped layer on SiC(0001) arise from its efficacy to accommodate the strain induced by the Si-C interactions at the interface. Furthermore, the spacing between the neighbouring $H_{5,6,7}$ defect sites is only approximately 6× the (1x1) lattice spacing of SiC(0001), consistent with the apparent slight disorder observed in STM images (Figs. 2 & 3).

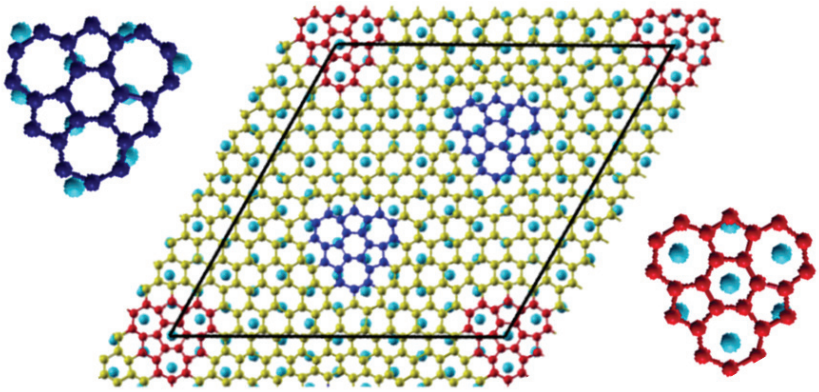

Fig. 7. Ball-and-stick model of the two placements of the $H_{5,6,7}$ defect on the SiC(0001): with the rotated central hexagon of the $H_{5,6,7}$ defect centered either above a first layer C atom (top site, marked red), or above a top layer Si (hollow site, marked blue).

To verify if these two $H_{5,6,7}$ variants on SiC would produce the complex electronic structures observed by STM, calculated local DOS isosurfaces, which resembles the STM constant current mode, are shown in Figs. 8 (a,b). For the top site, the six-fold symmetry of the centre hexagon is broken as a result of the formation of three Si-C bonds, leading to maxima at three adjacent alternating C atoms, appearing as a trimer of ~3 Å. For the hollow site variant, depressions are seen within the three heptagons as well as at the three C atoms at the tips of the three pentagons, resembling the six-fold depressions (marked by the hexagons) seen in STM. Because the six depression sites are inequivalent, they do not coincide perfectly with the hexagon of ~3 Å, also consistent with STM observations. In addition, the central three C atoms above the T_4 sites are slightly brighter, appearing as a upward trimer. Overall the main features seen in the STM images (e.g., Fig. 8(c)) at energies within E_F±0.5 eV using Fe(Cr)/W tips are well reproduced in the simulated images.

3.4 Electronic properties of the interface layer

The electronic properties of the resulting graphene structure is significantly altered due to the inclusion of the $H_{5,6,7}$ defects. Thus, experimental ARPES results provide a stringent test of our and other models. The calculated k-projected surface bands for the two $H_{5,6,7}$ variants are given in Figs. 9(a)-(c). Both variants show definite gaps, i.e., are semiconducting along Γ-K. Compared to defect-free graphene, the well-developed graphene-like σ bands are shifted to greater binding energy. Significant changes are seen in the π-band region with increased (diffuse) weight around Γ, and upward dispersing bands that do not reach E_F but are ~3 eV

below at K. In addition, there are defect-induced states (marked by arrows) with energies ε(K) of about -0.9 and -1.8 eV for the hollow and top configurations, respectively. The dispersions of these states (whose intensities decrease significantly away from K) have a tight-binding behaviour for a single band of localized orbitals, $\varepsilon(K)= \varepsilon_H$-A: the period of the oscillations seen in Figs. 9(b,c) reflect the 3x3 cell used in the calculations, while the amplitude A~0.3 eV about the "on-site" energies ε_H (indicated by the horizontal lines) is a measure of the interactions among the $H_{5,6,7}$ defects. Based on tight-binding scaling arguments, the use of larger $6\sqrt{3}x6\sqrt{3}$ (or 6x6) cells would result in a decrease in the interactions by at least an order of magnitude, i.e., we predict almost dispersionless states around K with energies $\varepsilon_H \approx$ -0.6 and -1.5 eV, in excellent agreement with the experimental values of -0.5 and -1.6 eV (Emtsev et al., 2008; Seyller et al., 2008).

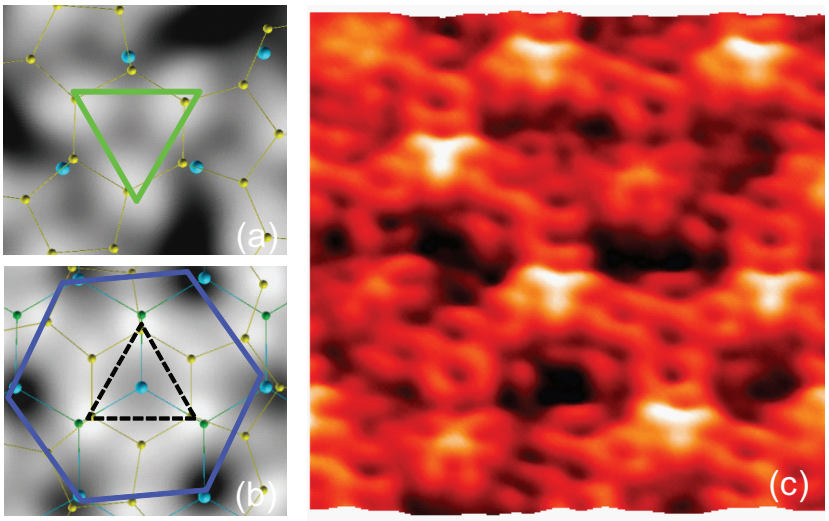

Fig. 8. Calculated DOS isosurfaces (10^{-6} a.u.$^{-3}$) for occupied states between -0.1 eV and the Fermi level for the (a) top and (b) hollow variants. Carbon and silicon atoms are represented by small and larger balls, respectively. (c) Expanded 3D STM view of the boxed region in Fig. 3(c) (5x5 nm^2).

The apparent inconsistency between a gap along Γ-K and STM imaging at very low bias can be understood by noting that STM probes the electronic states in the outer tails of the electronic distribution, whereas ARPES is sensitive to the overall wave function. In Figs. 9(d,e), the k-projected bands along Γ-M-K are shown for the two variants, but now weighted by the contributions in the vacuum region probed by STM. In both cases, the gap at K is still seen, but states elsewhere in the (1x1) zone cross E_F (such as those circled in Figs. 9(d,e)) are responsible for the contrast seen in STM images at low biases.

Calculated initial state C *1s* core level shifts, relative to C from the SiC substrate, are ~-1.1 eV for the $H_{5,6,7}$ defect, and ~-1.8 eV for the rest, which are also consistent with experimental results (Emtsev et al., 2008; Seyller et al., 2008). Overall, the warped graphene model provides a comprehensive explanation of the available experimental data on the defining properties of the $(6\sqrt{3}x6\sqrt{3})$ layer – the gap at K point, the overall dispersion, the two localized states near K, and the C core level shifts.

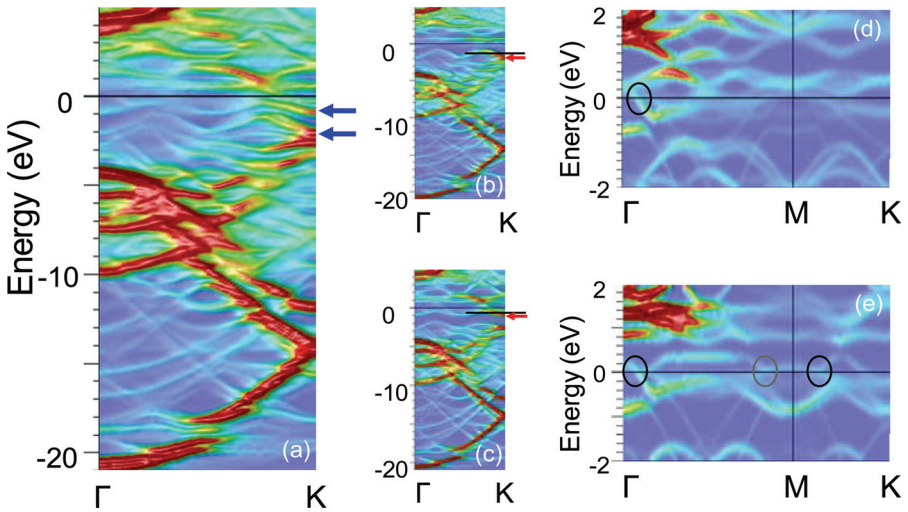

Fig. 9. Calculated k-projected surface bands (convoluted with a decaying exponential to account for the photoelectron escape depth) for the $H_{5,6,7}$ structure along Γ-K for (a) equal contributions of both variants, and (b) top and (c) hollow variants separately. Arrows mark the localized states at K and the lines in (b) and (c) indicate ε_H. Vacuum-weighted bands along Γ-M-K for (d) top and (e) hollow variants.

3.5 1st layer graphene

Calculations further indicate that the 1st layer graphene resumes the perfect honeycomb lattice with an interlayer spacing of 3.2 Å relative to the warped interface layer (Fig. 10(a)). The k-projected band structure for the interface + 1st layer graphene (Fig. 10(b)) shows almost perfect graphene bands, with the Dirac point below E_F. The bottom of the σ(π)-band at Γ is shifted upwards by about 1.3 (3.5) eV compared to the interface (Fig. 9), qualitatively consistent with the ARPES data (Emtsev et al., 2008; Seyller et al., 2008).

The downward shift of E_D = -0.4 eV indicates that the layer is n-doped, also consistent with experiment (Bostwick et al., 2007a; Zhou et al., 2007). Comparison of Figs. 10(d,e) reveals subtle, but distinct differences in the dispersions, especially above the Dirac point, as a direct consequence of the different interactions between the 1st graphene layer and the two $H_{5,6,7}$ variants. From inspection of the calculated eigenvalues and wave functions, the splitting of the Dirac states is only 33 meV. This is in good agreement with the estimated maximum value of 60 meV in one ARPES study (Bostwick et al., 2007b). Closely related is the misalignment of the bands above and below E_D, illustrated by the dotted lines in Figs. 10(c)-(e): the projections of the π states below E_D do not pass through the π* states above E_D, an observation previously attributed to electron-phonon or electron-plasmon interactions (Bostwick et al., 2007 (a,b)). Our results indicate that interactions of the π states with the $H_{5,6,7}$ defects contribute significantly to the observed dispersion at the Dirac point. Furthermore, the interactions also cause deviation from the linear dispersion of 1st graphene layer, leading to parabolic dispersion above the gap, and an apparent gap of ~0.25 eV (marked by the arrows in Fig. 10(c)), closely matched to the 0.26 eV gap assigned in separate ARPES studies (Zhou et al., 2007; Zhou et al., 2008; Rotenberg et al., 2008).

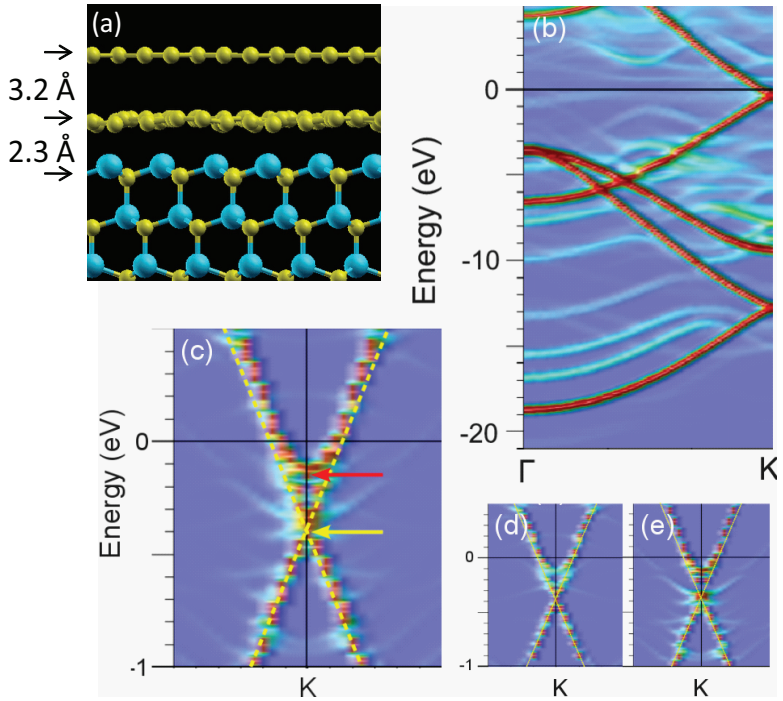

Fig. 10. (a) Ball-and-stick model, and (b) calculated k-projected surface bands of 1st layer graphene + the warped interface on SiC(0001). (c) Close-up view of bands around the Dirac point with equal contributions from (d) top and (e) hollow variants. The arrow at ~-0.4 eV marks the (split) Dirac point and dotted lines are guides for the linear dispersion.

3.6 Ridges on multilayer graphene

The morphology of the graphene grown at 1400 °C is shown in Fig. 11(a). The original SiC steps are no longer discernible. Instead, terraces with width varying from tens to hundreds of nanometers are present. On the terrace, a closed-pack lattice with a periodicity of 0.25±0.01 nm (Fig. 11(b)) is observed, indicating that multilayer graphene film is developed at this stage (Hass et al., 2008b; Lauffer et al., 2008). In addition, bright stripes along step edges and across terraces are clearly visible, with a typical size of ~1.5 nm in height and ~6 nm in width. Some of these features can terminate on a terrace, as the one circled in Fig. 11(a). Their initial density is estimated to be ~10/μm^2, though it may vary due to the creation of new ones during STM imaging (see discussion below). These features are consistent with the ridges and wrinkles reported in earlier studies (Biedermann et al., 2009; Derycke et al., 2002; Luxmi et al., 2009).

Figure 11(c) is an atomic resolution STM image of the tip of a ridge. A closed-pack lattice, same as those on the terraces, is clearly evident on top of the ridge. More importantly, no discontinuity is observed between the graphene film and the ridge both at its tip and at the boundary along either sides of the ridge. The closed-pack structure on the ridge suggests that the ridge consists of at least two graphene layers with *AB* stacking. However, the lattice constant on the ridge is measured to be 0.28±0.01 nm, slight larger than the graphene lattice

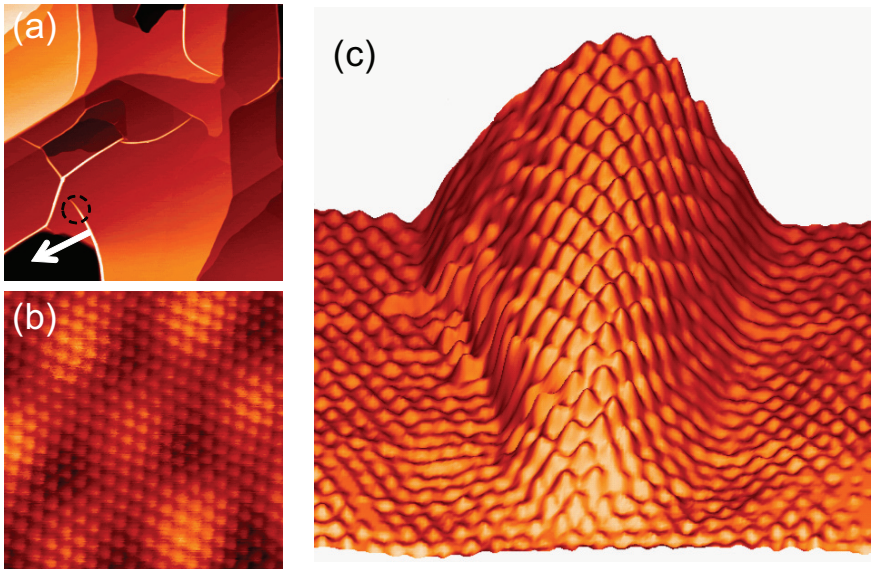

Fig. 11. (a) Topography of epitaxial graphene on 6H-SiC(0001) grown at 1400 ^{o}C taken with a W tip (1x1 μm^2, V_s = -2.0 V, I_t = 0.5 nA). The pit marked is 10 bilayers deep. (b) Atomic resolution image of the structure on the terrace (4.5x4.5 nm^2, V_s=-1.1 V, I_t=1.0 nA). (b) Atomic resolution image of the tip of a ridge in 3D view. (5x5 nm^2, V_s=-0.02 V, I_t=0.02 nA).

of 0.25±0.01 nm on the terrace, indicating that the lattice of the ridge is deformed due to bending. These findings clearly indicate that the ridges are neither CNTs nor domain boundaries as suggested previously (Derycke et al., 2002; Luxmi et al., 2009). They are in fact bulged regions of the graphene film, likely as a result of strain (Biedermann et al., 2009). Raman studies have indeed shown that the films are under compressive strain, which can be controlled by annealing time, reaching a theoretical limit of 0.8% (Ferralis et al., 2008; Ni et al., 2008).

In addition, we have found that their structure (e.g., length and orientation) can be manipulated by tip-surface interaction during STM imaging. In some cases, even new ridges can be created by such interactions. Shown in Fig. 12 are STM images taken sequentially at the same location, displaying the morphological evolution of the ridges. Several dramatic differences are seen. First, the ridge at location *A* grew much longer and now ran straight down across the whole terrace. Second, the ridge at *B* on the same terrace changed its direction from pointing-up to pointing-down. Third, the ridge at *C* along the step edge on the up terrace shrunk and became shorter. Fourth, a new ridge is formed on the up terrace at location *D*. Lastly, a new ridge is formed at *E* across two terraces. Manipulation of ridges using atomic force microscopy has also been reported previously (Derycke et al., 2002), where the growth of new ridges was attributed to subsurface segments of CNTs being moved to the surface. However, since our results clearly indicate that the ridges are bulged regions of graphene film, and not CNTs, it would also rule out this particular mechanism.

Through the close examination of many STM images, it is also found that the density of the ridges varies with the size of the terrace, where fewer ridges are found on smaller terraces. The question arises then if ridge-free graphene film can be grown on a surface consists of

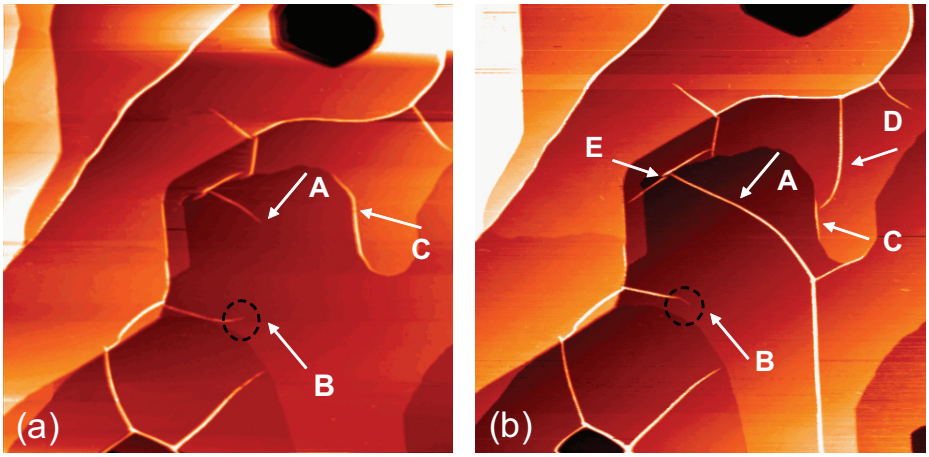

Fig. 12. STM images taken sequentially at the same location with a W tip. (a) V_s=-1.7 V, I_t=0.5 nA. (b) V_s=-2.2 V, I_t=0.5 nA. Image sizes are 1x1 μm² for both.

sufficiently small terraces, such as those of vicinal substrates. Shown in Fig. 13 is an STM image of epitaxial graphene film grown on a vicinal SiC substrate. As a result of step bunching, an average terrace width of ~80 nm is observed. Clearly, the density of ridges decreased significantly on this surface: only very few small ones are found on wider terraces, while the majority is found along the step edges. These observations indicate that the compressive strain in epitaxial graphene film is not sufficient to induce ridges on small terrace, but can still cause bending at step edges. From these results, we have estimated that a lower limit of the terrace size for ridge formation is ~80 nm.

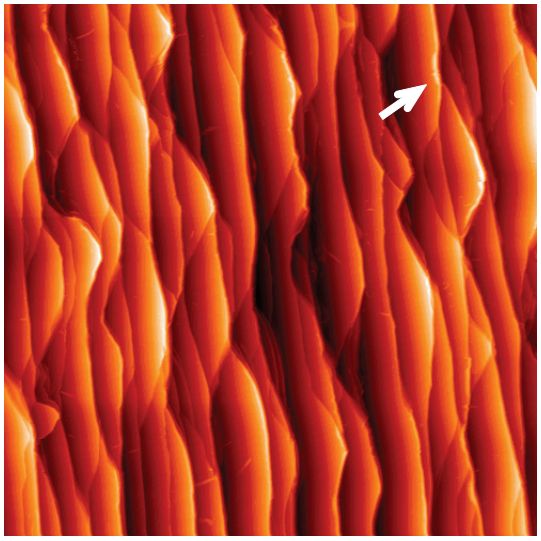

Fig. 13. STM image of epitaxial graphene film grown on vicinal 6H-SiC(0001) substrate (3.5° miscut angle), taken with a W tip (1x1 μm², V_s=-1.0 V, I_t=0.5 nA).

The picture that emerges from these results is that ridges are formed during cooling of the sample to room temperature to relieve the strain in the epitaxial graphene. On larger terraces, residual compressive strain still exists. Perturbation by the tip-surface interaction during STM imaging is clearly sufficient to initiate the creation of new ridges, as well as the growth of existing ones. Previous studies have shown that tip-surface interaction during STM imaging can exert a pressure of 5 MPa, which induces motion of subsurface dislocations on graphite (Snyder et al., 1993). The imaging conditions used in our studies are similar to those reported in these earlier studies, indicating that the pressure exerted can be of similar magnitude, sufficient to modify the ridge morphology.

4. Conclusions

In summary, using functionalized Fe(Cr) coated W tips, which facilitate the imaging of the graphene/SiC(0001) $6\sqrt{3}$ interface layer, we have found that it is a warped graphene layer resulted from the periodic inclusion of $H_{5,6,7}$ defects in the honeycomb lattice. The subsequent layer assumes the perfect honeycomb structure, though its interaction with the warped layer leads to deviations from the linear dispersion at the Dirac point. The presence of this interfacial layer alleviates the mismatch between the graphene and the SiC substrate, but also significantly modifies its electronic properties. This model provides a consistent and comprehensive explanation for the existing experimental data on the defining properties of the ($6\sqrt{3}$x$6\sqrt{3}$) layer: the gap at K point, the overall dispersion, the two localized states near K, and the C core level shifts, resolving a long-standing controversy regarding the interfacial structure of epitaxial graphene on SiC(0001).

On multilayer graphene films, we have found that ridges and wrinkles are in fact bulged regions of the graphene sheet, formed to relieve the compressive strain due to its mismatch with the SiC substrate. We can also manipulate these ridges and create new ones through tip-surface interactions during STM imaging. By minimizing this strain with decreased terrace size, nearly ridge-free graphene has been grown on vicinal SiC substrates.

5. References

Berger, C.; Song, Z.; Li, T.; Li, X.; Ogbazghi, A. Y.; Feng, R.; Dai, Z.; Marchenkov, A. N.; Conrad, E. H.; First, P. N. & de Heer, W. A. (2004). Ultrathin epitaxial graphite: 2D electron gas properties and a route toward graphene-based nanoelectronics. *J. Phys. Chem. B*, Vol. 108, 19912-19916, ISSN 1520-6106

Berger, C.; Song, Z.; Li, X.; Wu, X.; Brown, N.; Naud, C.; Mayou, D.; Li, T.; Hass, J.; Marchenkov, A. N.; Conrad, E. H.; First, P. N. & de Heer, W. A. (2006). Electronic confinement and coherence in patterned epitaxial graphene. *Science*, Vol. 312, 1191-1196, ISSN 0036-8075

Biedermann, L. B.; Bolen, M. L.; Capano, M. A.; Zemlyanov, D. & Reifenberger, R. G. (2009). Insights into few-layer epitaxial graphene growth on 4H-SiC(000-1) substrates from STM studies. *Phys. Rev. B*, Vol. 79, 125411 1-10, ISSN 1098-0121

Bode, M. (2003). Spin-polarized scanning tunnelling microscopy. *Rep. Prog. Phys.*, Vol. 66, 523-582, ISSN 0034-4885

Bostwick, A.; Ohta, T.; Seyller, Th.; Horn, K. & Rotenberg, E. (2007a). Quasiparticle dynamics in graphene. *Nature Phys.*, Vol. 3, 36-40, ISSN 1745-2473

Bostwick, A.; Ohta, T.; McChesney, J. L.; Emtsev, K. V.; Seyller, Th.; Horn, K.& Rotenberg, E. (2007b). Symmetry breaking in few layer graphene films. *N. J. Phys.*, Vol. 9, 385 1-22, ISSN 1367-2630

Castro Neto, A. H.; Guinea, F.; Peres, N. M. R.; Novoselov, K. S. & Geim, A. K. (2009). The electronic properties of graphene, *Rev. Mod. Phys.*, Vol. 81, 109-162, ISSN 0034-6861

Červenka, J.; van de Ruit, K. & Flipse, C. F. J. (2010). Giant inelastic tunneling in epitaxial graphene mediated by localized states. *Phys. Rev. B*, Vol. 81, 205403 1-5, ISSN 1098-0121

Charlier, J. -C. & Rignanese, G. -M. (2001). Electronic structure of carbon nanocones. *Phys. Rev. Lett.,* Vol. 86, 5970-5973, ISSN 0031-9007

Deng, Z. T.; Lin, H.; Ji, W.; Gao, L.; Lin, X.; Cheng, Z. H.; He, X. B.; Lu, J. L.; Shi, D. X.; Hofer, W. A. & Gao, H.-J. (2006). Selective analysis of molecular states by functionalized scanning tunneling microscopy tips. *Phys. Rev. Lett.*, Vol. 96, 156102 1-4, ISSN 0031-9007

Derycke, V.; Martel, R.; Radosavljević, M.; Ross, F. M. & Avouris, Ph. (2002). Catalyst-free growth of ordered single-walled carbon nanotube networks. *Nano Lett.,* Vol. 2, 1043-1046, ISSN 1530-6984

Emtsev, K. V.; Speck, F.; Seyller, Th.; Ley, L. & Riley, J. D. (2008). Interaction, growth, and ordering of epitaxial graphene on SiC{0001} surfaces: A comparative photoelectron spectroscopy study. *Phys. Rev. B*, Vol. 77, 155303 1-10, ISSN 1098-0121

Emtsev, K. V.; Bostwick, A.; Horn, K.; Jobst, J.; Kellogg, G. L.; Ley, L.; McChesney, J. L.; Ohta, T.; Reshanov, S. A.; Röhrl, J.; Rotenberg, E.; Schmid, A. K.; Waldmann, D.; Weber, H. B. & Seyller, Th. (2009). Towards wafer-size graphene layers by atmospheric pressure graphitization of silicon carbide. *Nature Mater.*, Vol. 8, 203-207, ISSN 1476-1122

Ferralis, N.; Maboudian, R. & Carraro, C. (2008). Evidence of structural strain in epitaxial graphene layers on 6H-SiC(0001). *Phys. Rev. Lett.*, Vol. 101, 156801 1-4, ISSN 0031-9007.

Forbeaux, I.; Themlin, J. M. & Debever, J. M. (1998). Heteroepitaxial graphite on 6H-SiC(0001): Interface formation through conduction-band electronic structure. *Phys. Rev. B*, Vol. 58, 16396-16406, ISSN 1098-0121

Hannon, J. B. & Tromp, R. M. (2008). Pit formation during graphene synthesis on SiC(0001): In situ electron microscopy. *Phys. Rev. B*, Vol. 77, 241404(R) 1-4, ISSN 1098-0121

Hass, J.; Varchon, F.; Millán-Otoya, J. E.; Sprinkle, M.; Sharma, N.; de Heer, W. A.; Berger, C.; First, P. N.; Magaud, L. & Conrad, E. H. (2008a). Why multilayer graphene on 4H-SiC(000-1) behaves like a single sheet of graphene, *Phys. Rev. Lett.*, Vol. 100, 125504 1-4, ISSN 0031-9007

Hass, J.; de Heer, W. A. & Conrad, E. H., (2008b). The growth and morphology of epitaxial multilayer graphene. *J. Phys.: Condens. Matter*, Vol. 20, 323202 1-27, ISSN 0953-8984

Ihara, S.; Itoh, S.; Akagi, K.; Tamura, R. & Tsukada, M. (1996). Structure of polygonal defects in graphitic carbon sheets. *Phys. Rev. B*, Vol. 54, 14 713-14719, ISSN 1098-0121

Kedzierski, J.; Hsu, P. –L.; Healey, P.; Wyatt, P. W.; Keast, C. L.; Sprinkle, M.; Berger, C. & de Heer, W. A. (2008). Epitaxial graphene transistors on SiC substrates. *IEEE Trans. Elec. Dev.*, Vol. 55, 2078-2085, ISSN 0018-9383

Kim, S.; Ihm, J.; Choi, H. J. & Son, Y. –W. (2008). Origin of anomalous electronic structures of epitaxial graphene on silicon carbide. *Phys. Rev. Lett.*, Vol. 100, 176802 1-4, ISSN 0031-9007

Lauffer, P.; Emtsev, K. V.; Graupner, R.; Seyller, Th.; Ley, L.; Reshanov, S. A. & Weber, H. B. (2008). Atomic and electronic structure of few-layer graphene on SiC(0001) studied with scanning tunnelling microscopy and spectroscopy. *Phys. Rev. B*, Vol. 77, 155426 1-10, ISSN 1098-0121

Li, L. & Tsong, I. S. T. (1996). Atomic structures of 6H-SiC (0001) and (000$\bar{1}$) surfaces. *Surf. Sci.*, Vol. 351, 141-148, ISSN 0039-6028

Lin, Y. -M.; Dimitrakopoulos, C.; Jenkins, K. A.; Farmer, D. B.; Chiu, H. -Y.; Grill, A. & Avouris, Ph. (2010). 100-GHz transistors from wafer-scale epitaxial graphene. *Science*, Vol. 327, 662-662, ISSN 0036-8075

Luxmi; Nie, S.; Fisher, P. J.; Feenstra, R. M.; Gu, G. & Sun, Y. G. (2009). Temperature dependence of epitaxial graphene formation on SiC(0001). *J. Elec. Mater.*, Vol. 38, 718-724, ISSN 0361-5235

Mallet, P.; Varchon, F.; Naud, C.; Magaud, L.; Berger, C. & Veuillen, J.-Y. (2007). Electron states of mono- and bilayer graphene on SiC probed by scanning-tunneling microscopy. *Phys. Rev. B*, Vol. 76, 041403(R) 1-4, ISSN 1098-0121

Mattausch, A. & Pankratov, O. (2007). Ab Initio study of graphene on SiC. *Phys. Rev. Lett.*, Vol. 99, 076802 1-4, ISSN 0031-9007

Miller, D. L.; Kubista, K. D.; Rutter, G. M.; Ruan, M.; de Heer, W. A.; First, P. N. & Stroscio, J. A. (2009). Observing the quantization of zero mass carriers in graphene. *Science*, Vol. 324, 924-927, ISSN 0036-8075

Morozov, S. V.; Novoselov, K. S.; Katsnelson, M. I.; Schedin, F.; Ponomarenko, L. A.; Jiang, D. & Geim, A. K. (2006). Strong suppression of weak localization in graphene. *Phys. Rev. Lett.*, Vol. 97, 016801, ISSN 0031-9007

Ni, Z. H.; Chen, W.; Fan, X. F.; Kuo, J. L.; Yu, T.; Wee, A. T. S. & Shen, Z. X. (2008). Raman spectroscopy of epitaxial graphene on a SiC substrate. *Phys. Rev. B*, Vol. 77, 115416 1-6, ISSN 1098-0121

Northrup, J. E. & Neugebauer, J. (1995). Theory of the adatom-induced reconstruction of the SiC(0001) $\sqrt{3}$x$\sqrt{3}$ surface. *Phys. Rev. B*, Vol. 52, R17001-R17004, ISSN 1098-0121

Novoselov, K. S. (2007). Graphene: Mind the gap. *Nature Mater.*, Vol. 6, 720-721, ISSN 1476-1122

Orlikowski, D.; Nardelli, M. B.; Bernholc, J. & Roland, C. (1999). Ad-dimers on strained carbon nanotubes: A new route for quantum dot formation? *Phys. Rev. Lett.*, Vol. 83, 4132-4135, ISSN 0031-9007

Orlita, M.; Faugeras, C.; Plochocka, P.; Neugebauer, P.; Martinez, G.; Maude, D. K.; Barra, A-L.; Sprinkle, M.; Berger, C.; de Heer, W. A. & Potemski, M. (2008). Approaching the Dirac point in high-mobility multilayer epitaxial graphene, *Phys. Rev., Lett.*, Vol. 101, 267601 1-4, ISSN 0031-9007

Owman, F. & Mårtensson, P. (1996). The SiC(0001) $6\sqrt{3} \times 6\sqrt{3}$ reconstruction studied with STM and LEED. *Surf. Sci.*, Vol. 369, 126-136, ISSN 0039-6028

Qi, Y.; Sun, G. F.; Weinert, M. & Li, L. (2009). Electronic structures of Mn-induced phases on GaN(0001). *Phys. Rev. B*, Vol. 80, 235323 1-5, ISSN 1098-0121

Qi, Y.; Rhim, S. H.; Sun, G. F.; Weinert, M. & Li, L. (2010). Epitaxial graphene on SiC(0001): More than just honeycombs. *Phys. Rev. Lett.*, Vol. 105, 085502 1-4, ISSN 0031-9007

Rhim, S. H.; Qi, Y.; Sun, G. F.; Weinert, M. & Li, L. (2011). Imaging epitaxial graphene on SiC(0001) using STM with functionalized W tips. *To be published.*

Riedl, C.; Starke, U.; Bernhardt, J.; Franke, M. & Heinz, K. (2007). Structural properties of the graphene-SiC(0001) interface as a key for the preparation of homogeneous large-terrace graphene surfaces. *Phys. Rev. B*, Vol. 76, 245406 1-8, ISSN 1098-0121

Rotenberg, E.; Bostwick, A.; Ohta, T.; McChesney, J. L.; Seyller, Th. & Horn, K. (2008). Origin of the energy bandgap in epitaxial graphene. *Nature Mater.*, Vol. 7, 258-259, ISSN 1476-1122

Rutter G. M.; Guisinger, N. P.; Crain, J. N.; Jarvis, E. A. A.; Stiles, M. D.; Li, T.; First, P. N. & Stroscio, J. A. (2007). Imaging the interface of epitaxial graphene with silicon carbide via scanning tunneling microscopy. *Phys. Rev. B*, Vol. 76, 235416 1-6, ISSN 1098-0121

Seyller, Th.; Bostwick, A.; Emtsev, K. V.; Horn, K.; Ley, L.; McChesney, J. L.; Ohta, T.; Riley, J. D.; Rotenberg, E. & Speck, F. (2008). Epitaxial graphene: a new material. *Phys. Stat. Sol. (b)*, Vol. 245, 1436-1446, ISSN 0370-1972

Snyder, S. R.; Gerberich, W. W. & White, H. S. (1993). Scanning-tunneling-microscopy study of tip-induced transitions of dislocation-network structures on the surface of highly oriented pyrolytic graphite. *Phys. Rev. B*, Vol. 47, 10823, ISSN 1098-0121

Sprinkle, M.; Siegel, D.; Hu, Y.; Hicks, J.; Tejeda, A.; Taleb-Ibrahimi, A.; Le Fe`vre, P.; Bertran, F.; Vizzini, S.; Enriquez, H.; Chiang, S.; Soukiassian, P.; Berger, C.; de Heer, W. A.; Lanzara, A. & Conrad, E. H. (2009). First direct observation of a nearly ideal graphene band structure. *Phys. Rev. Lett.*, Vol. 103 226803 1-4, ISSN 0031-9007

Sun, G. F.; Jia, J. F.; Xue, Q. K. & Li, L. (2009). Atomic-scale imaging and manipulation of ridges on epitaxial graphene on 6H-SiC(0001). *Nanotechnology*, Vol. 20, 355701 1-4, ISSN: 0957-4484

Tsai, M. –H.; Chang, C. S.; Dow, J. D. & Tsong, I. S. T. (1992). Electronic contributions to scanning-tunneling-microscopy images of an annealed β-SiC(111) surface. *Phys. Rev. B*, Vol. 45, 1327-1332, ISSN 1098-0121

van Bommel, A. J.; Crombeen, J. E. & van Tooren, A. (1975). LEED and Auger electron observations of the SiC(0001) surface. *Surf. Sci.*, Vol. 48, 463-472, ISSN 0039-6028

Varchon, F.; Feng, R.; Hass, J.; Li, X.; Ngoc Nguyen, B.; Naud, C.; Mallet, P.; Veuillen, J.-Y.; Berger, C.; Conrad, E. H. & Magaud, L. (2007). Electronic structure of epitaxial graphene layers on SiC: Effect of the substrate. *Phys. Rev. Lett.*, Vol. 99, 126805 1-4, ISSN 0031-9007

Varchon, F.; Mallet, P.; Veuillen, J. –Y. & Magaud, L. (2008). Ripples in epitaxial graphene on the Si-terminated SiC(0001) surface. *Phys. Rev. B*, Vol. 77, 235412 1-8, ISSN 1098-0121

Weinert, M.; Schneider, G.; Podloucky, R. & Redinger, J. (2009). FLAPW: applications and implementations. *J. Phys.: Condens. Matter*, Vol. 21, 084201 1-14, ISSN 0953-8984

Zhou, S. Y.; Gweon, G. –H.; Fedorov, A. V.; First, P. N.; de Heer, W. A.; Lee, D.-H.; Guinea, F.; Castro Neto, A. H. & Lanzara, A. (2007). Substrate-induced bandgap opening in epitaxial graphene. *Nature Mater.*, Vol. 6, 770-775, ISSN 1476-1122

Zhou, S. Y.; Siegel, D. A.; Fedorov, A. V.; El Gabaly, F.; Schmid, A. K.; Castro Neto, A. H.; Lee, D.-H. & Lanzara, A. (2008). Origin of the energy bandgap in epitaxial graphene. *Nature Mater.*, Vol. 7, 259-260, ISSN 1476-1122

5

Thermal Reduction of Graphene Oxide

Seung Hun Huh
Nanotechnology Convergence Lab,
Korea Institute of Ceramic Engineering and Technology (KICET),
South Korea

1. Introduction

In a two-dimensional carbon system for graphene (GP), three carbon electrons in four hybridized bonding electrons ($2s^1 2p_x^1 2p_y^1 2p_z^1$) form strong in-plane sp^2 bonds consisting of a honeycomb structure, and a fourth electron spreads out over the top or bottom of the layer as a π electron. The π electrons play an important role in the coupling interactions of multilayered GPs. A two-dimensionally spread C=C resonance structure and the hybridized electrons confined in GP are directly related to graphene's unique characteristics, such as its ballistic electron conduction, high thermal conduction, and high mechanical strength (Geim & Novoselov, 2007; Lee et al., 2008). These fundamental properties have been well studied using high-quality graphene produced by the "top-down" physical exfoliation (McAllister et al., 2007) and solvation-assisted exfoliation of graphite (Lotya et al., 2009) and GP thin films produced using chemical vapor deposition (Kim et al., 2009; Obraztsov, 2009).

Meanwhile, thermally reduced GP from graphene oxide (GO) (Gao et al., 2009; Jeong et al., 2009), produced from graphite using various chemical oxidation routes (Brodie, 1859; Hummers & Offerman, 1958; Hirata et al., 2004), has attracted considerable attention as a potential material for use in various industrial applications such as photovoltaic cells, capacitors, sensors, and transparent electrodes (Geim & Novoselov, 2007; Stoller et al., 2008; Wang et al., 2008; Liu et al., 2009). This is because of not only its potential in significantly lowering the cost of mass-produced graphene but also the simple, nonchemical, thermal conversion of GO powder or film to GP powder or film, respectively (Titelman et al., 2005; (a) Jeong et al., 2009; (b)). However, the thermal reduction of GO is a very complex phenomenon because of the thermal-energy-induced multistep removal processes of intercalated H_2O molecules and oxide groups of –COOH (carboxyl group), –OH (hydroxyl group), and >O (epoxy group). It should be noted that in chemical reduction, individual GO sheets in the solution phase are chemically reduced by the strong chemical base (Titelman et al., 2005; Ju et al., 2010). Therefore, the thermal reduction of GO and resultant GP needs to be studied in great detail.

In this research, X-ray diffraction (XRD) was used to probe the temperature-dependent evolution of the interlayer distance (d_{002}) of GO/GP films and powders within temperature ranges of room temperature (RT) to 1000°C and RT to 2000°C, respectively. XRD results show a detailed thermal reduction of GO with the removal of intercalated H_2O molecules and oxide groups, defect formation, lattice contraction and exfoliation mechanisms of the GO/GP sheets, the folding and unfolding of the GO/GP layers, and a bottom-up layer stacking toward bulk graphite.

2. Experimental

Graphene oxide was prepared using a modified Hummers' method (Hirata et al., 2004). First, 5 g of natural graphite (99.995%, Alfa), 3.75 g of $NaNO_3$ (99%, Aldrich), and 310.5 g of H_2SO_4 (96%) were mixed in a 10-L pyrex reactor with a water cooling system; this mixture was then stirred for 30 min. Next, 22.5 g of $KMnO_4$ (99%, Aldrich) was carefully added to this mixture for 1 h. The resultant mixture was stirred for 5 days at room temperature, after which 5 L of a H_2SO_4 aqueous solution (5%) was slowly added over a 1 h period. After stirring for 2 h, 150 g of H_2O_2 (30%, Aldrich) was added to the mixture. Upon centrifugation, the GO slurry at the bottom was washed with a 3%-H_2SO_4/0.5%-H_2O_2 solution and then rewashed with deionized water (Ju et al., 2010).

The final GO was obtained as a slurry or colloidal solution, which was then spin-coated on a flat Pt XRD holder and dried at RT. The GO thickness was approximately 300 to 500 nm. The GO film mounted on the Pt XRD holder was measured in situ in a vacuum (~10^{-3} torr, obtained with a rotary pump) at RT to 1000°C using a high-temperature XRD instrument (RIGAKU, D/MAX-2500, λ = 1.54056 Å (Cu K_α)). The heating rate was 5 °C/min.

To obtain the GO powder, the GO slurry was dried in a vacuum oven at 60°C for 24 h. Dried GO powder (the brown color in Fig. 1b) mounted on a crucible was introduced into a quartz furnace and thermally treated at RT to 2000°C for 1 h under a flow of laminar N_2 gas (99.999%). The heating rate and N_2 flow rate were 5 °C/min and 50 ml/min, respectively. GO and GP were further characterized using a field-emission scanning electron microscope (FE-SEM: JEOL, JSM 6700F), FE-transmission electron microscope (FE-TEM, JEOL, JEM-2000EX (200 keV)), Fourier transform infrared spectroscope (FT-IR; Jasco 4100), and a Cs-corrected FE-TEM (JEOL/CEOS) was used for measuring the in-plane carbon lattices. The obtained products are denoted as $GP_{temperature}$, e.g., GP_{200} or GP_{1000}. The interlayer distances (d_{002}) are denoted as $d_{temperature}$, e.g., d_{RT} or d_{2000}.

3. Results and discussion

3.1 XRD theory and concept of interlayer distances of graphene and graphene oxide

The principle of XRD for materials is based on Bragg's law (Cullity, 1978), and it is expressed by

$$n\lambda = 2d_{(hkl)}\sin\theta \quad (1)$$

where λ is the wavelength of the X-ray, θ is the scattering angle, n is an integer representing the order of the diffraction peak, d is the interplane distance of the lattices, and (hkl) are Miller indices. If (002) planes of graphite or multi-layered graphene are given as in Fig. 1a, the interlayer distance is denoted as d_{002}. The incoming X-rays are specularly scattered from each GP plane. Since the angle θ between the GP plane and the X-ray beam results in a path-length difference that is an integer multiple *n* of the X-ray wavelength λ, X-rays scattered from adjacent individual GP planes will combine constructively. Therefore, the XRD peak of the (002) facet of GP gives rise to a critical d_{002} value as well as the information required for the lattice size and quality. The GP thickness can be estimated using Sherrer's equation (Cullity, 1978), which is expressed by

$$D_{002} = K\lambda / B\cos\theta \quad (2)$$

where D_{002} is the thickness of crystallite (here, GP thickness), K is a constant dependent on the crystallite shape (0.89), λ is the X-ray wavelength, B is the full width at half maximum (FWHM), and θ is the scattering angle. From Sherrer's equation, the number of GP layers (N_{GP}) can be obtained using the following equation (Ju et al., 2010):

$$N_{GP} = D_{002} / d_{002} \quad (3)$$

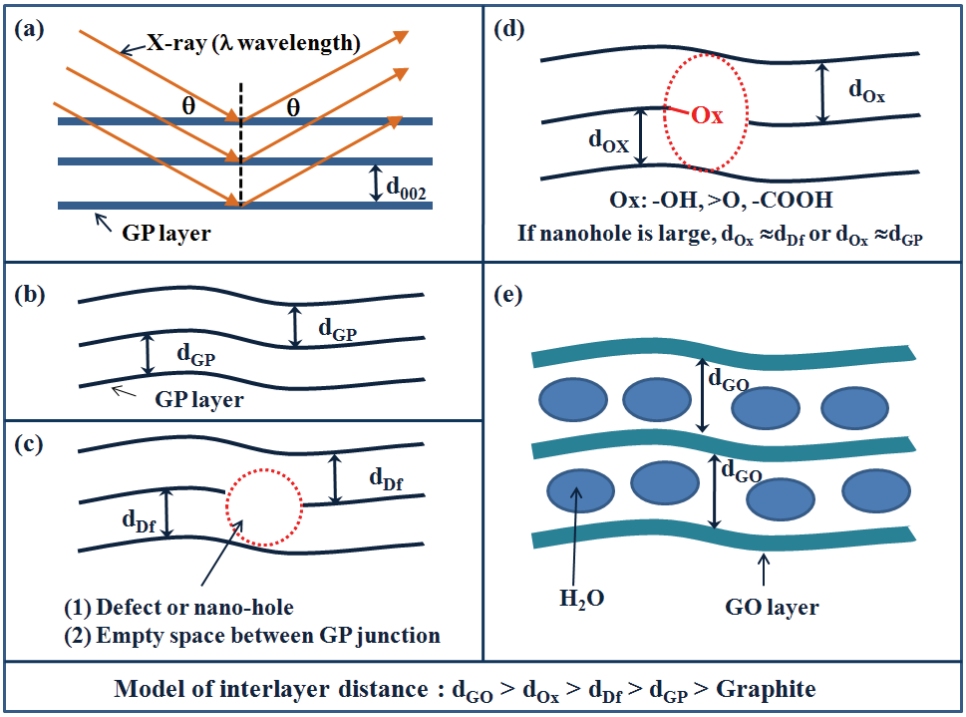

Fig. 1. Bragg's law for GP or graphite (002) planes (a), and models for d_{002} of GO (e) and thermally reduced GP (b-d). In this model, the order of interlayer distance becomes graphite < d_{GP} < d_{Df} < d_{Ox} < d_{GO}.

To understand the XRD pattern formed during the GO reduction as well as the resultant GP, a simple, intuitive concept for various types of interlayer distances of graphene and graphene oxide is considered, as shown in Figs. 1b through 1e. Because GP layers have intrinsic nanocurvature distortions (Fig. 1b) (Fujimoto, 2003; Li et al., 2007) existing in a two-dimensional single crystalline structure (McAllister et al., 2007; Gosselin et al., 2009), the interlayer distance of GP (d_{GP}) is slightly larger than that of bulk graphite. The reported d_{GP} and graphite are ~3.4 (Stankovich et al., 2007) and 3.348–3.360 Å (Li et al., 2007), respectively. Because GO has many defects or nanoholes, it is reasonable that thermally reduced graphene would also have many defects and nanoholes (d_{Df}) (Fig. 1c). Therefore, GO and GP can have oxide groups of C–Ox with an sp^3 bond in their defects and nanoholes (d_{Ox}) (Fig. 1d). Graphene oxide has the largest interlayer distance (d_{GO}) because of its intercalated H_2O molecules and various oxide groups (Fig. 1e). The d_{GO} value is in the range

of ~5 to 9 Å, depending on the number of intercalated water molecules. It is rational to assume that the interlayer distance order is $d_{GO} > d_{Ox} > d_{Df} > d_{GP}$ > graphite. If defects in the layer are sufficiently large, oxide groups and H_2O molecules can be considered to exist in the empty space; thus, the order is $d_{Ox} \approx d_{Df}$ or $d_{Ox} \approx d_{GP}$. On the basis of a model with various interlayers, we expect that graphene oxide has an intermediate structure with d_{Ox} and d_{Df} during thermal reduction, and through bottom-up layer stacking, the resultant graphene evolves toward graphite as crystal growth with the removal of d_{Ox} and d_{Df}.

3.2 Images of GO/GP film and GO/GP powder

Figure 2a shows a digital image of GO slurry. Figure 2b shows an FE-SEM image of a GO film with a thickness of ~300 to 500 nm, and demonstrating a soft carpet-like morphology (c). An FE-TEM image of a GO film coated on a Cu TEM grid (Fig. 2d) shows a layered AB-stacked structure. However, GP films obtained after thermal annealing at 1000°C have surface microcracks and a shrunken thickness, as shown in Figs. 2e and 2f, respectively. Figure 2g shows a digital image of dried GO powder. After undergoing thermal reduction at 1000°C, the brown-tinted GO lumps turn into fine black GP powder (Fig. 1h).

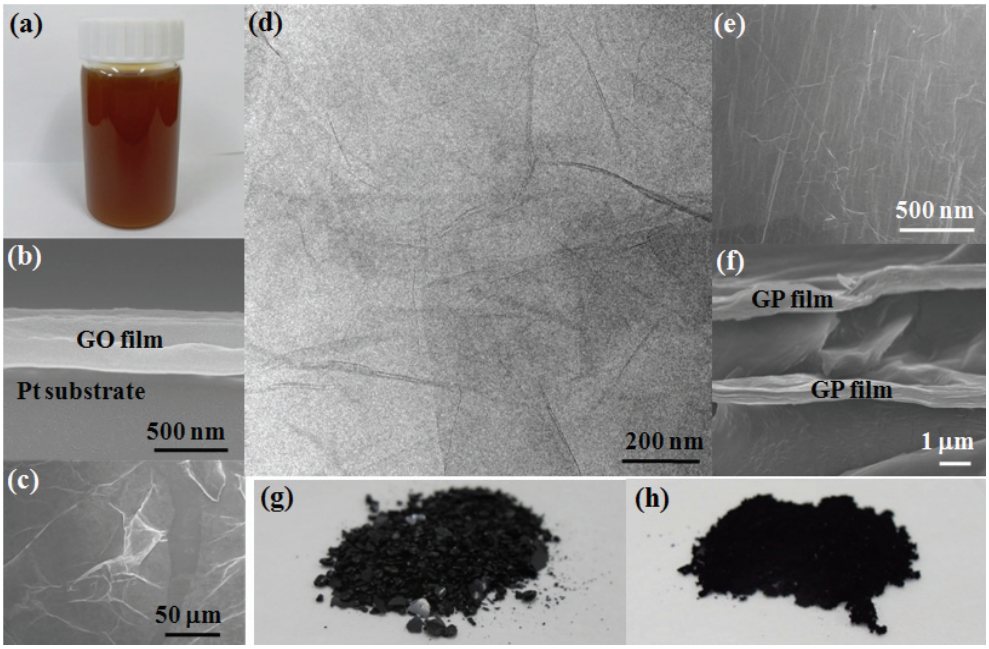

Fig. 2. A digital image of GO slurry (a), dried GO powder (g), and thermally reduced GP powder (h). FE-SEM images of GO films (b, c), thermally reduced GP films (e, f), and FE-TEM image of GO film (d).

3.3 Temperature-dependent XRD patterns of GO and GP films

All temperature-dependent XRD patterns of GO/GP films measured within the range of RT to 1000°C are completely plotted in Fig. 3. At increasing temperatures, the (002) peak of a GO film (left side) moves continuously toward the right with a variance of intensity and FWHM.

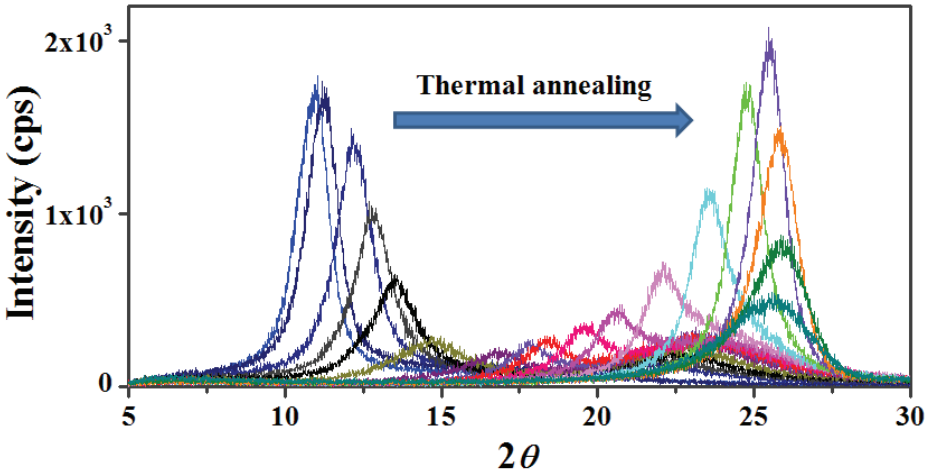

Fig. 3. Total plot for measured in situ XRD patterns of GO/GP films obtained at RT to 1000°C.

The individually-represented XRD spectrum shows important information regarding the detailed temperature-dependent evolution of (002) peaks, as shown in Fig. 4. A GO film with an AB stacked structure (Li et al., 2007; (b) Jeong et al., 2008) shows a typical XRD pattern with a strong and sharp (002) peak at 2θ = ~11° (Fig. 4a). The GO (002) peak gradually shifts to the right with an increase in temperature and yields three types of (002) peak series. The first peak series (Peak I) is the main change during the thermal reduction of graphene oxide and shows a gradual shift to the right. The d_{GO} and d_{1000} values for Peak I are 8.071 (Fig. 4a) and 3.453 Å (Fig. 4t), respectively. In the second peak series (Peak II), a peak at 2θ = ~24° emerges at 140°C (Fig. 4d), with a slight shift to the right within the temperature range of 140–600°C. Importantly, all Peak II values have a larger FWHM than those of Peak I. The d_{140} and d_{500} values for Peak II are 4.034 (Fig. 4d) and 3.602 Å (Fig. 4n), respectively. Significantly, Peak II is combined to Peak I at 600°C (Fig. 4o). The combined peak of GP_{600} is very sharp, and d_{600} is 3.593 Å. The combined GP_{600} is gradually moved to the right with an increase in temperature, along with a broadening FWHM. However, peaks above 700°C show a long-tailed structure because of small portions of peaks at 2θ = ~23–24°, which is denoted as a third peak series (Peak III). The centers of Peak III are changed slightly, and their d_{002} values are far from graphite d_{002}. From these results and from the fact that the intensities of all Peak III values are much lower (less than 100 cps) than those of Peak I and Peak II, it is assumed that Peak III is amorphous-like carbon comprising many defects, folding structures, impurities, and sp^1, sp^2, and sp^3 hybridization structures. It should be noted that GP_{1000} measured in situ at 1000°C (Fig. 4s) shows a very broad and left-shifting structure compared to GP_{800} because of typical Debye-Waller effects induced by atomic thermal vibration; thus, after the cooling of GP_{1000}, GP_{RT} is obtained after an XRD measurement at RT (Fig. 4t). The d_{002} and FWHM values, as well as induced errors, are summarized for both Peaks I and II in Appendix 1.

Figures 5a and 5b show a plot of the d_{002} and FWHM values for both Peak I (solid blue circles) and Peak II (hollow red circles), respectively, on the basis of the fitting (Lorentzian function) XRD patterns shown in Fig. 4. The plots show four temperature-dependent

tendencies: (1) RT–130°C, (2) 140–180°C, (3) 180–600°C, and (4) 600–1000°C. Within the RT–130°C zone, only Peak I appears. The mild reduction of d_{002} values and unchanging FWHM (or a very slight increase) are attributed to a mild vaporization of intercalated H_2O molecules. Within the 140–180°C zone, both Peaks I and II appear. For Peak I, the d_{002} values are largely reduced, and the FWHM values are maximally broadened. This is because of a drastic vaporization of intercalated H_2O molecules ((a) Jeong et al., 2009; (b)). In this process, the sizes of the GO crystals estimated using Sherrer's equation are reduced as the crystals are exfoliated during a drastic escaping of H_2O gases from stable GO-layered lattices, resulting in Peak II with very broad FWHM. For Peak II, the d_{002} and FWHM tendencies are similar to those of Peak I. Thus, partial H_2O molecules exist in the exfoliated GO and are then vaporized in a temperature range of 140–~180°C. Within the 180–600°C zone, the d_{002} and FWHM values are continuously reduced for both Peak I and Peak II. This is due to the removal of the main oxide groups of COOH. However, above 600°C, although the d_{002} values are continuously contracting and approaching graphite d_{002}, the FWHM values are gradually broadening. This is a very complex phenomenon related to lattice relaxation and disordering, which is detailed in section 3-5.

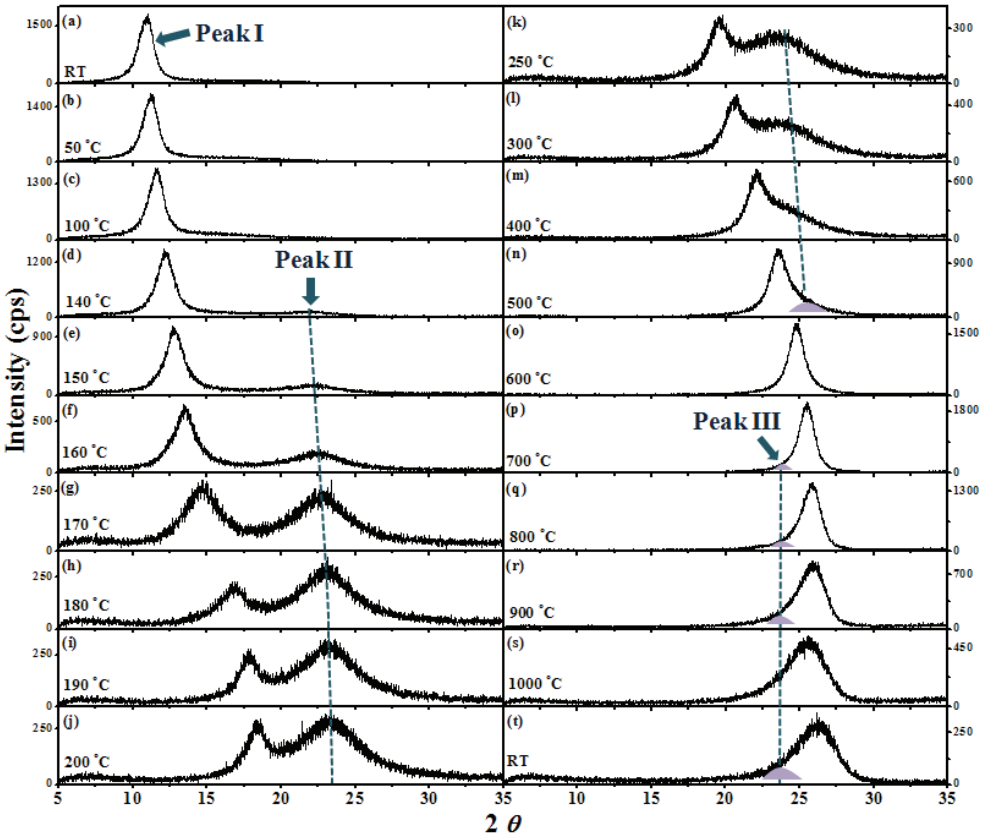

Fig. 4. Individual XRD plot for Fig. 3.

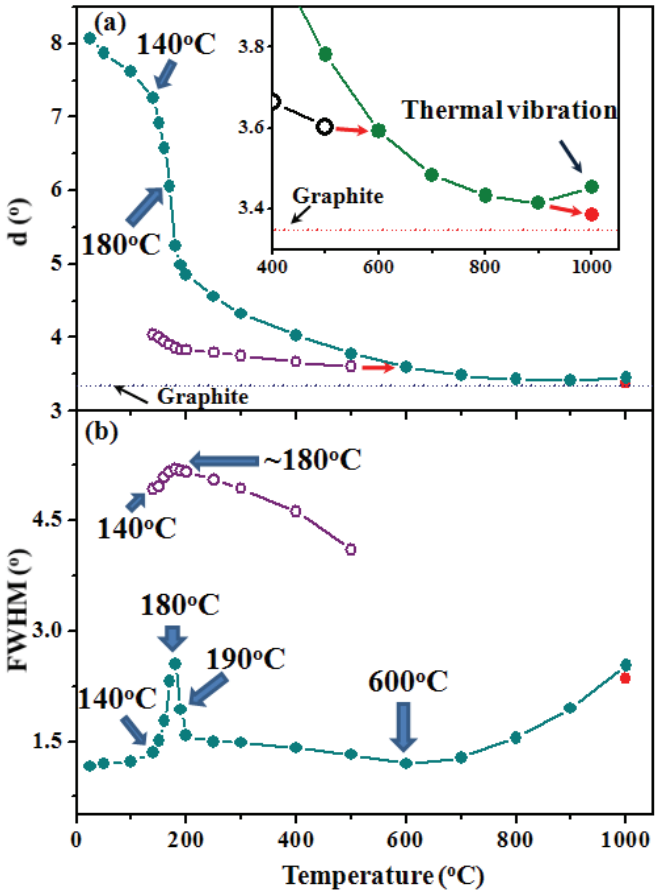

Fig. 5. FWHM (a) and d_{002} (b) plots for XRD patterns of Fig. 4. The inset shows a magnified image of (a).

3.4 Temperature-dependent XRD patterns of GO and GP powders

The XRD patterns of GO/ GP powders (Fig. 6) appear to be totally different from those of GO/GP films with a range of RT–1000°C because there is only one peak type with a broad FWHM. However, the peaks are very similar to Peak II of GO/GP films, as shown in the d_{002} and FWHM plots of Fig. 7. As a result, GP_{200} and GP_{400} have a fully exfoliated structure, such as that in Peak I. Full exfoliation of GO powder at a relatively low temperature of 200°C depends on the GO drying process. To obtain a GO powder, a GO slurry is extensively dried above 60°C in vacuum. The d_{002} value (7.131 Å) of the obtained GO powder is smaller than d_{100} (7.611 Å) and is similar to d_{140} (7.259 Å) of a GO film (note that Peak II emerges at 140°C in a GO film).

Therefore, extensively dried GO powder can be fully exfoliated when a large number of intercalated H_2O molecules escape at 200°C. Importantly, along with similar tendencies compared to a GP film, the temperature-dependent XRD patterns of thermally reduced GPs

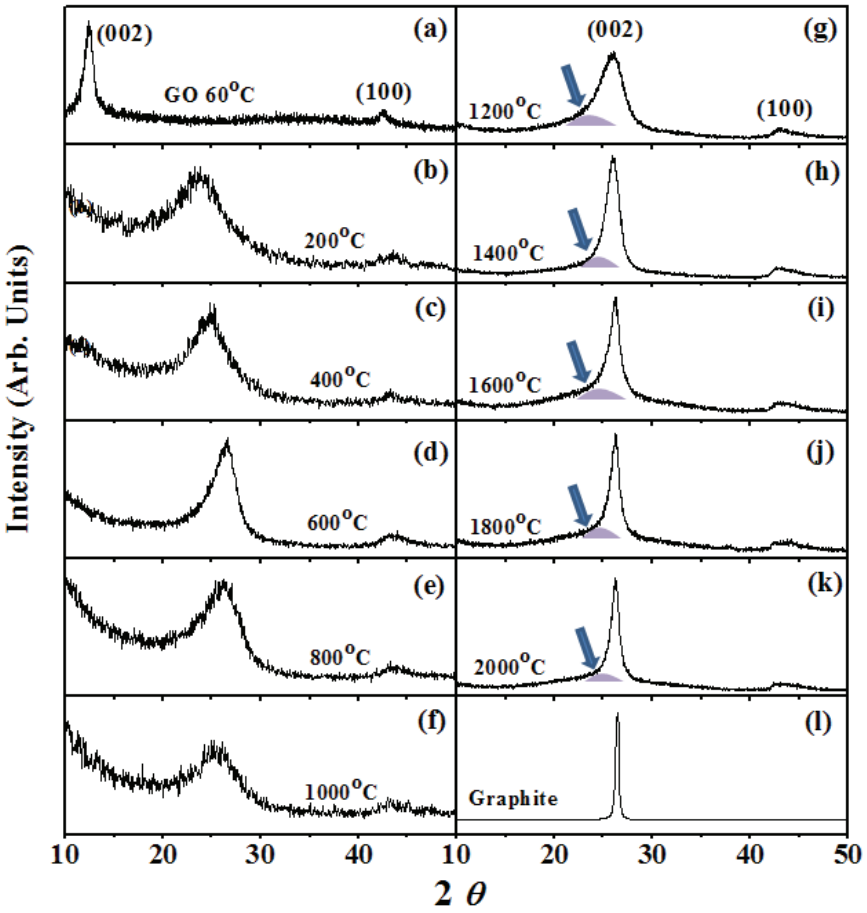

Fig. 6. XRD patterns of GO/GP powders obtained after thermal annealing at RT to 2000°C.

from RT to 1000°C have two different zones with their boundary appearing at 600°C in FWHM and d_{002} (Figs. 7a and 7b and Figs. 7c and 7d). FWHM sharpens as $GP_{200} \rightarrow GP_{400} \rightarrow GP_{600}$ and then broadens as $GP_{600} \rightarrow GP_{800} \rightarrow GP_{1000}$, shrinking as $GP_{200} \rightarrow GP_{400} \rightarrow GP_{600}$ and growing as $GP_{600} \rightarrow GP_{800} \rightarrow GP_{1000}$. Above 1000°C, the quality of thermally reduced GP powder increases because of the decreasing FWHM and d_{002} approaching bulk graphite. Furthermore, peaks above 1200°C show a long-tailed structure because of small portions of peaks at 2θ = ~23–26°, which is considered to be a similar structure as Peak III in GP films. The measured d_{002} and FWHM values, along with induced errors, are summarized in Appendix 1.

3.5 FT-IR, Raman, and FE-TEM results for GO and GP powder

From the FT-IR spectra of GO and GP powder (Fig. 8), typical peaks of intercalated free H_2O molecules are seen at ~3250 cm^{-1}, and those of bound H_2O molecules are observed at ~1612 cm^{-1} and ~1383 cm^{-1}; peaks corresponding to COOH, OH, and epoxide groups and in-plane

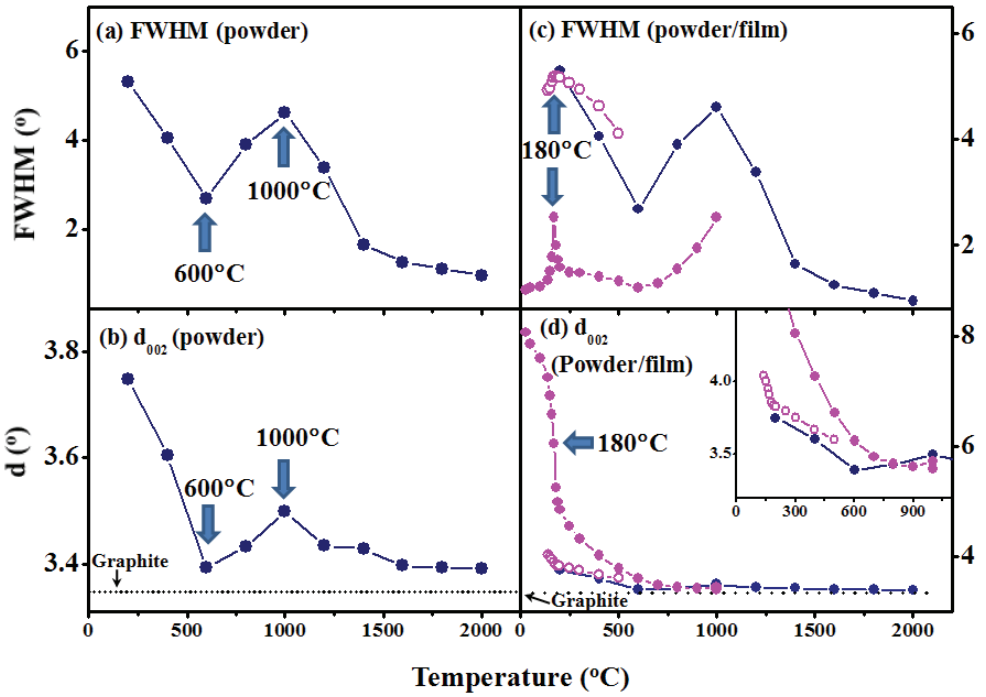

Fig. 7. FWHM (a) and d_{002} (b) plots, and FWHM (c) and d_{002} (d) co-plots for GO/GP films and powders. The inset shows a magnified image of (d).

C=C bonds are also observed at ~1730, ~1200, ~1040, and ~1510 cm^{-1}, respectively. FT-IR spectra indicate five types of GO and GP thermochemical reactions: (i) vaporization of intercalated water molecules at RT to 200°C, (ii) removal of most carboxyl groups (–COOH) at ~200–600°C, (iii) removal of residual carboxyl and partial hydroxyl groups (C–OH and O–H) at ~800°C, (iv) near removal of residual hydroxyl groups and partial removal of the epoxide group (>O) at ~1000°C, and (5) the removal (cracking) of aromatic C=C bonds at 1000°C.

Meanwhile, the Raman spectra (Fig. 9) show three different regimes of the D/G ratio (disorder/order carbon), with their boundaries between 800 and 1000°C (Fig. 10). This ratio remains at RT to 800°C and then drastically increases as GO/$GP_{200–800}$ (~1.5) → GP_{1000} (~2.1), which implies that the disordering portion of the two-dimensional carbon backbone is increased in this temperature range. The XRD patterns and Raman spectra taken together indicate that a change from $GP_{200–600}$ to GP_{800} with a decrease in d_{002} and an increase in FWHM is not related to the number of defects, whereas a change from GP_{800} to GP_{1000} with an increase in d_{002} and an increase in FWHM is largely affected by an increase in the number of disordered carbons.

Although GP_{600} has a partial carboxyl group and numerous hydroxyl and epoxide groups, as shown in the FT-IR spectra, it has high-quality crystallinity with d_{600} = 3.392 Å, which is closest to a typical GP (d_{002} = 3.4 Å). This means that most of the residual oxide groups exist on the edge or interlayer empty space of GP_{600}; therefore, the oxide groups are not largely

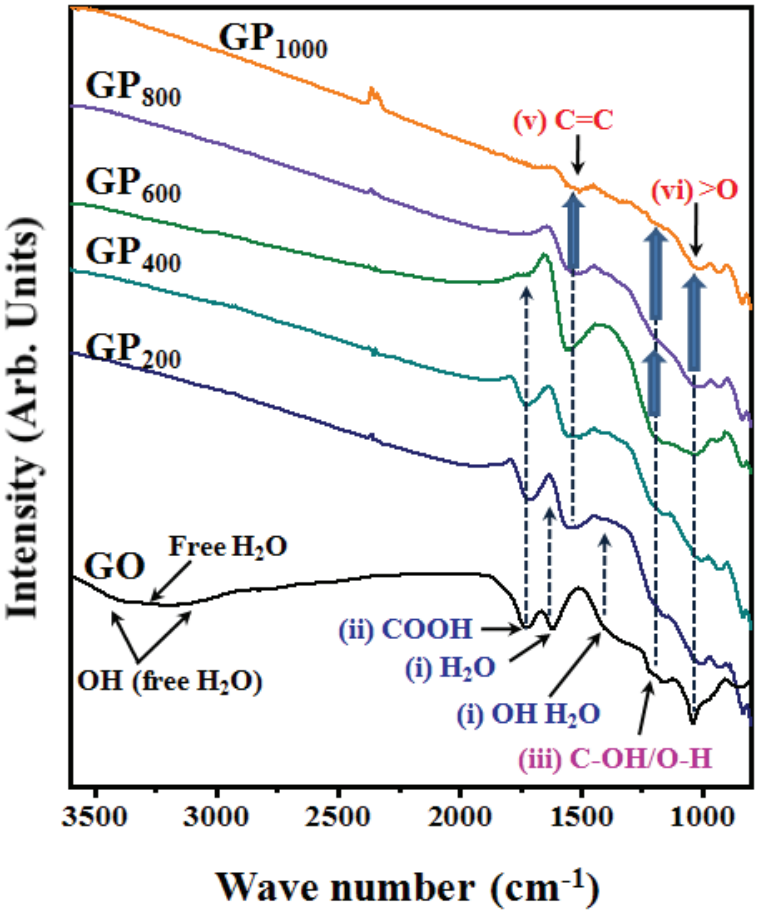

Fig. 8. FT-IR spectra for GO, GP_{200}, GP_{400}, GP_{600}, GP_{800}, and GP_{1000} samples.

affected by the layered stacking structure. GP_{800} has poorer crystallinity than GP_{600} (see the d_{002} and FWHM values). However, Raman data shows that both GP_{600} and GP_{800} have a similar D/G ratio as well as a similar Raman pattern. The combined XRD and Raman data in the range of 600–800°C are very abstruse. To solve this problem, two combination effects are supposed: a lattice relaxation mechanism and the detachment of disordered carbon. At 600–800°C, residual carboxyl groups and a partial hydroxyl group are detached.

Although the carboxyl groups do not require an additional carbon source to decompose into CO_2, the hydroxyl groups need a carbon source to yield CO gas (Figueiredo et al., 1999). If the carbon in CO gas comes from an ordered aromatic C=C structure, the D/G ratio will increase. If the carbon in CO gas comes from a disordered C–C structure, the D/G ratio will be unchanged. Many disordered carbons already exist in GO and $GP_{200–600}$ as shown in the Raman spectra (D/G = ~1.5). Therefore, the probable explanation for the unchanging Raman spectra of GP_{600} and GP_{800} is that the carbon in CO gas is produced from disordered carbon located at the edges and boundaries of nanoholes and empty spaces. The reason for

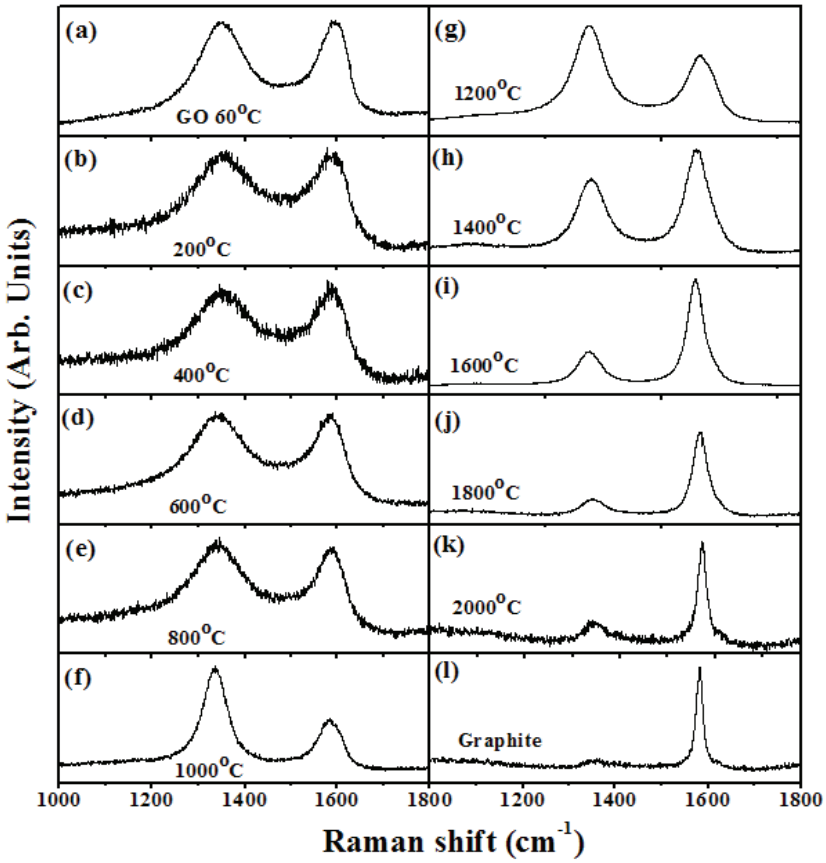

Fig. 9. Corresponding Raman spectra samples for XRD patterns of Fig. 6.

degradation of crystalline quality as $GP_{600} \rightarrow GP_{800}$ is explained by the lattice relaxation mechanism of GP_{600}; CO_2 and CO gases produced from the removal of residual carboxyl and partial hydroxyl groups, respectively, have high vibration and kinetic energy and pass through stable layers of GP_{600}. However, GP_{800} is considered to be a relatively good GP species because it has the smallest amount of oxide under an unchanging number of defects. As shown in a representative image of a Cs-corrected FE-TEM, a six-layered structure is observed at the edge of GP_{800} (Fig. 11a), and in-plane ordered lattice structures in the flat zone between the microfolding areas are also observed (Fig. 11b).

GP_{1000} has the largest amount of disordered carbon as shown in the Raman spectra. This is explained by the cracking of two bonds of >O, which causes the simultaneous destruction of adjacent C=C aromaticity, as shown in the FT-IR spectrum. Furthermore, broad D and G Raman peaks sharpen above 1000°C because of the thermal annealing effect. Between 1000 and 2000°C, the D/G ratio is continuously decreased, and it then approaches raw graphite material, which is in accord with XRD data on the basis of the fact that the crystalline quality increases and the crystal growth of GP layers is very effective owing to the thermal annealing effect, implying an accompaniment with the removal of d_{Ox} and D_{Df} (Fig. 1).

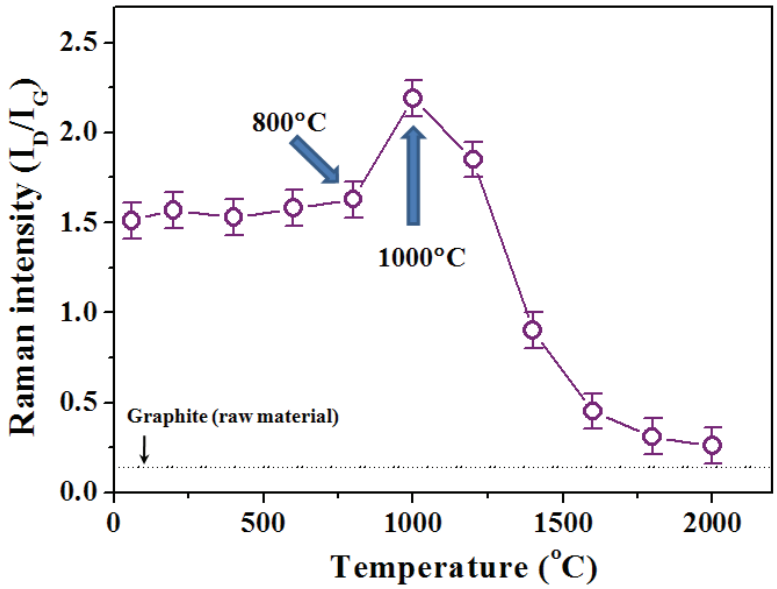

Fig. 10. Plot of Raman intensity ratio, I_D/I_G, of Fig. 9.

Based on equation 3, if the defects are offset for $GP_{200–800,1400–2000}$, the numbers of layers of GP_{200}, GP_{400}, GP_{600}, GP_{800}, GP_{1400}, GP_{1600}, GP_{1800}, and GP_{2000} are estimated to be 4.1, 5.5, 8.3, 6.1, 9.3, 12.3, 14.0, and 16.3, respectively. In this estimation, GP_{1000} and GP_{1200} are exceptions because of the existence of disordered carbon in an amount larger than the base GO powder. Further, we supposed that residual oxide groups do not exist in a well-developed interlayer space, but rather at the edges or nanoholes. This supposition is reasonable given that the maximum gap of 0.3 Å between $d_{200–800,1400–2000}$ = 3.390–3.747, and $d_{graphite}$ = 3.348 Å is too small to contain the ~1.25-Å minimum epoxy group (Giordano et al., 1988; Mkhoyan et al., 2009) or the ~2.75-Å of H_2O molecules (Graziano, 1998). However, various interlayer distances are explained by the contribution of d_{Df} and d_{Ox}, as shown in Fig. 1. Furthermore, because the estimated number of layers in $GP_{1400–2000}$ is very large, they are considered to have intermediate properties between typical graphene (less than 10 layers) and graphite.

3.6 Folding and unfolding processes of GO and GP powders

It is noteworthy that from the FE-SEM (left) and FE-TEM images (right) (Fig. 12), we observed both folding and unfolding graphene: (1) $GP_{200–600}$ with severely wrinkled or folded structures in both macroscopic and microscopic views (Figs. 12a–12c) and (2) GP_{800} with slightly unfolded structures (Fig. 12d) and GP_{1000} with a considerably unfolded and flat structure except for microwrinkling (Fig. 12e).

$GP_{200–600}$ have crater-like macropores surrounding the thick folded sheets owing to the vaporization of intercalated H_2O molecules, as shown in Figs. 12a–12c. It is possible that during the drastic exfoliation of AB-stacked GO, individually exfoliated GO sheets are unstable owing to a large number of defects (D/G = ~1.5), surface/edge dangling bonds, high surface-to-volume ratio, and thermodynamic instability as intrinsic properties of two-dimensional crystal; subsequently, for better stability, they tend to be coupled with each

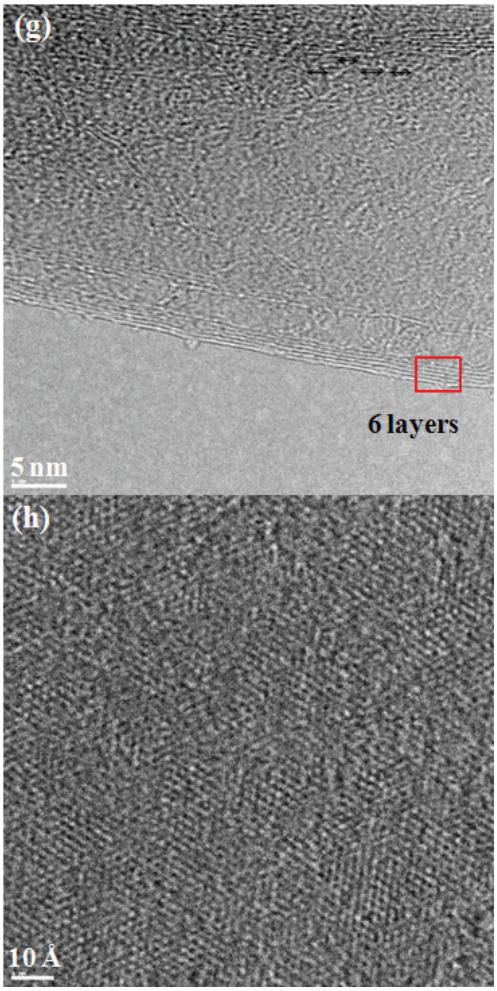

Fig. 11. Cs-corrected, high-resolution FE-TEM images for thermally reduced GP_{800} powder: six-layered structures located at the edge (a) and in-plane ordered carbon structure (b).

other through a van der Waals interaction. In this layer-coupling process, interlayer partial chemical or hydrogen bonds may be formed because of a large number of defects, dangling bonds, and O/H atoms, which are the driving force behind microscopic and macroscopic folding (Figs. 12a–12c). It should be noted that microscopic folding is an intrinsic characteristic of GP layer produced via chemical reduction and top-down physical exfoliation. Severely macrofolded $GP_{200-600}$ with porous structures are partially unfolded during the formation of GP_{800} (Fig. 12d) and largely unfolded at 1000°C. The unfolding process of GP_{1000} may be attributed to the coincident detachment of interlayer chemical and hydrogen bonds owing to both the effects of thermal annealing and the removal of C/O species. A schematic of the folding and unfolding processes during the thermal reduction of GO is summarized in Fig. 13.

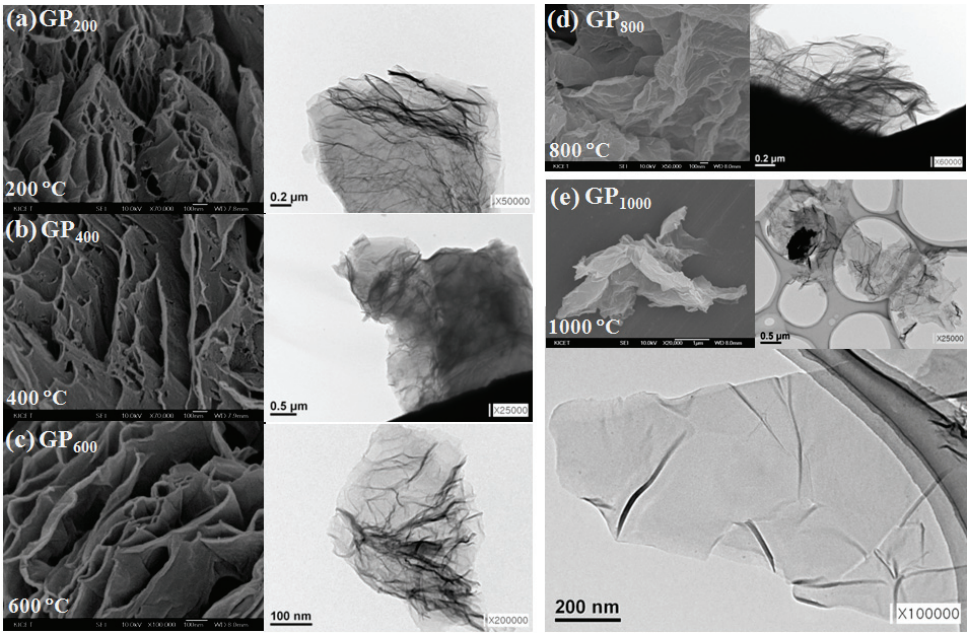

Fig. 12. FE-SEM (left) and FE-TEM images (right) for GP_{200} (a), GP_{400} (b), GP_{600} (c), GP_{800} (d), and GP_{1000} (e).

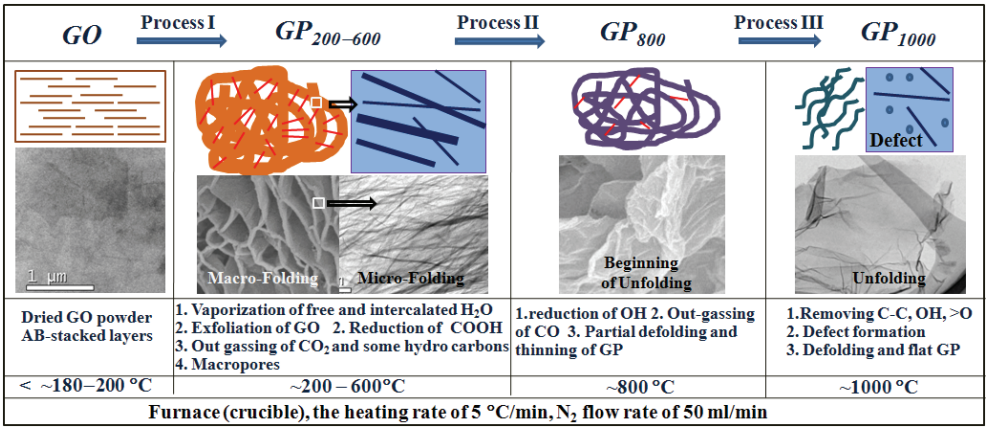

Fig. 13. Schematic diagram of folding and unfolding processes of $GP_{200–600}$, GP_{800}, and GP_{1000}.

3.7 Proposed model for thermal reduction of GO film and powder

From the XRD, FT-IR, Raman, FE-SEM, and FE-TEM results for GO/GP films and powders, a thermal reduction process for GO using five critical temperatures of 140, 180, 600, 800, and 1000°C is proposed, as shown in the schematic diagram of Fig. 14. In this model, the d_{002} value of large-sized GO crystal is gradually contracted within the range of RT–130°C during mild vaporization of intercalated H_2O molecules ($\mathbf{S_1}$ state). However, the d_{002} value is

greatly reduced within 140–180°C owing to a drastic vaporization of intercalated water molecules (**S_2**), along with a partial exfoliation of GO sheets (**S_7**). The GO (**S_2**) and exfoliated GO (**S_7**) gradually reduce their lattices in the range 180–600°C because of the removal of the main carboxyl groups (**S_3**). Within 600–800°C, a partial lattice relaxation with a broadening FWHM occurs owing to out-gassing formed from residual carboxyl and partial hydroxyl groups (**S4**). Within 800–1000°C, a large number of defects are produced during the removal of the epoxide group, along with in-plane C=C cracking (**S5**). Within 1000–2000°C, bottom-up layer stacking as crystal growth occurs with a decreasing number of defects (**S6**). However, the thermal reduction processes for the GO films and powders always yield small amounts of amorphous-like structures around 2θ = ~23–25° within 140–2000°C, which is explained by the complex folding structures, defects, impurities, and sp^1, sp^2, and sp^3 hybridization. Furthermore, folding and unfolding processes occur between $GP_{200–600}$ and $GP_{800–1000}$ depending on the presence of interlayer partial chemical and hydrogen bonds.

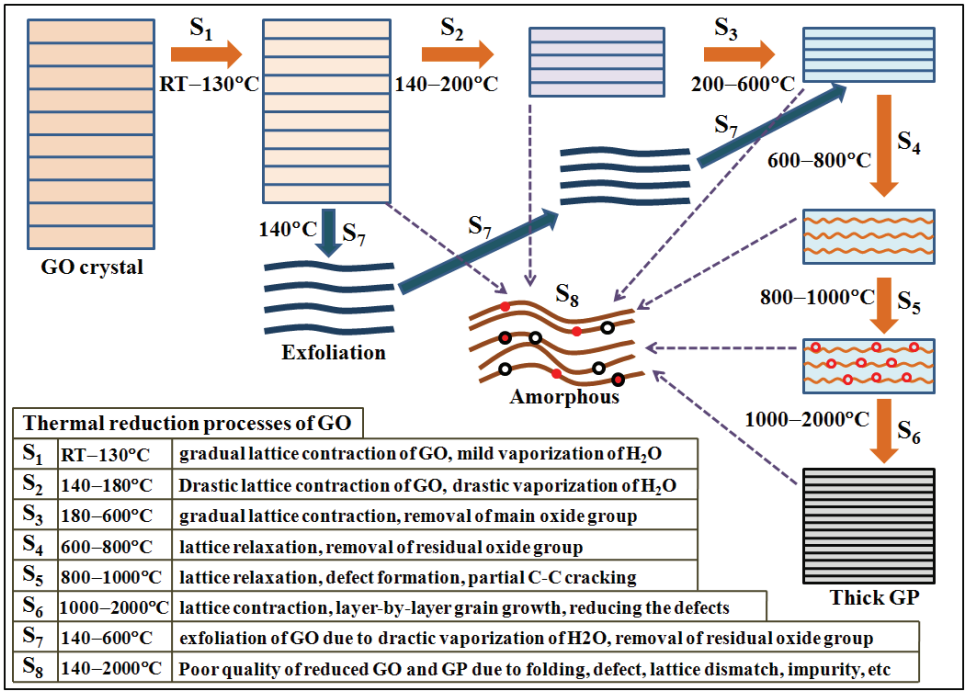

Thermal reduction processes of GO		
S_1	RT–130°C	gradual lattice contraction of GO, mild vaporization of H_2O
S_2	140–180°C	Drastic lattice contraction of GO, drastic vaporization of H_2O
S_3	180–600°C	gradual lattice contraction, removal of main oxide group
S_4	600–800°C	lattice relaxation, removal of residual oxide group
S_5	800–1000°C	lattice relaxation, defect formation, partial C-C cracking
S_6	1000–2000°C	lattice contraction, layer-by-layer grain growth, reducing the defects
S_7	140–600°C	exfoliation of GO due to dractic vaporization of H2O, removal of residual oxide group
S_8	140–2000°C	Poor quality of reduced GO and GP due to folding, defect, lattice dismatch, impurity, etc

Fig. 14. Schematic diagram of thermal reduction process of GO in the range of RT to 2000°C.

3.8 Application of partially reduced GO film for dye-sensitized solar cell

Graphene oxide cannot be used as a catalytic film in a dye-sensitized solar cell (DSSC), because it is hydrophilic and water-soluble. A pure hydrophobic GP film is also not a good candidate for a catalytic film in a DSSC, because it is easily destroyed during the forced electric-field-induced penetration of iodide (I) ions. However, partially reduced GO shows a relatively good catalytic property. Figure 15a shows an XRD pattern for a partially reduced GO film with a partially reduced GP structure, which is produced by careful heating on a hot plate at ~250–300°C for a short duration of around 2 min in air. The partially reduced

GO film has an intermediate contact angle of α = 59° (water droplet film) (Fig. 15b) between GO of α = 7° (Fig. 15c) and GP_{600} of α = 85° (Fig. 15d). Although this film maintains the hydrophilic property caused by a partial GO structure, it is water-insoluble owing to sections of reduced GP. We obtained a solar power conversion efficiency (η) of more than 2%. Although η is relatively lower than that of a DSSC with a platinum catalytic thin film (6.0%) under the conditions of this experiment, it is higher than that of a DSSC without a catalysis (0.74%) and those of other reported types of DSSC (0.84%) (Liu et al., 2009) and organic solar cell (1.1%) with conductive graphene electrode (Wang et al., 2008). The catalytic effect is explained by the effect of the ion channel through the sections of hydrophilic GO. This result implies that as an alternative to an expensive Pt catalyst, partially reduced GOs have the potential for use in a DSSC as a cheap catalytic thin film.

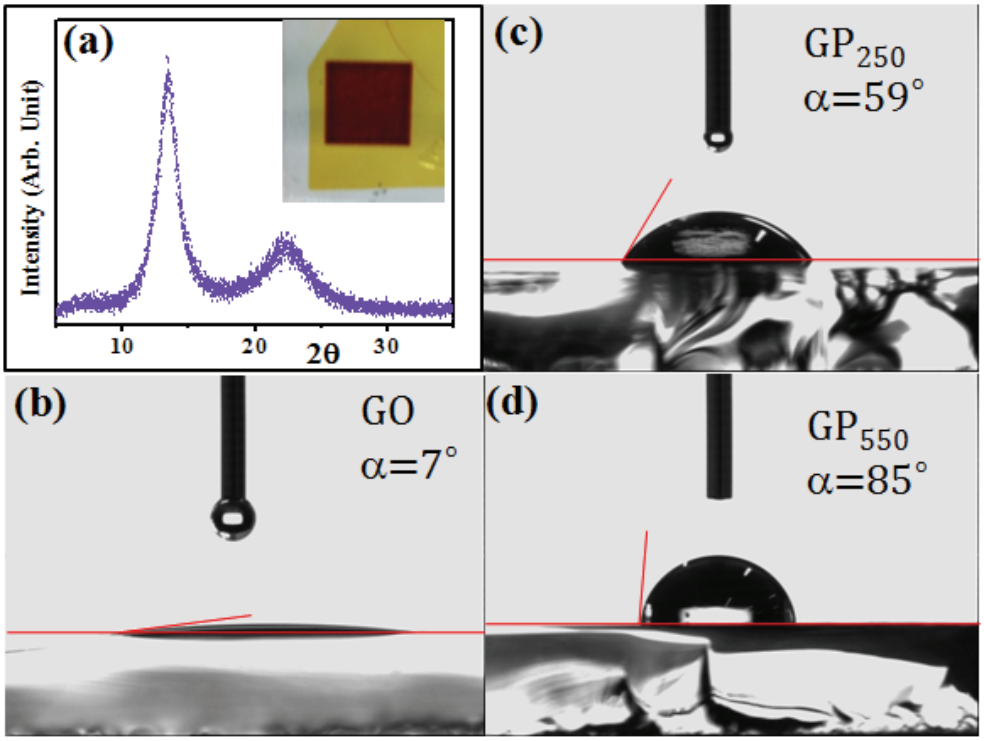

Fig. 15. XRD pattern of partially reduced GO film (a) used as a catalytic film of a DSSC (inset). Digital images of contact angles between water droplets and GO film (b), partially reduced GO (c), and GP (d).

4. Conclusion

Using XRD, Raman, FT-IR, FE-SEM, and FE-TEM results, a thermal reduction process of graphene oxide within a temperature range of RT to 2000°C was investigated in detail. The thermal reduction process has six important temperature zones, RT–130°C, 140–180°C, 180–600°C, 600–800°C, 800–1000°C, and 1000–2000°C. Within a temperature range of RT–130°C,

continuous lattice contraction of GO crystal occurs extensively owing to a mild vaporization of intercalated H_2O molecules. Within the range of 140–180°C, GO crystals are partially exfoliated because of the drastic vaporization of intercalated H_2O molecules. Within the 180–600°C temperature range, the interlayers for all GO and GP types are contracted with the removal of the main carboxyl groups. Within 600–800°C, a lattice relaxation of GP occurs owing to out-gassing generated from the residual carboxyl and partial hydroxyl groups, along with a broadening in FWHM. Within the 800–1000°C range, a large number of defects are generated owing to in-plane C=C cracking during the removal of the residual hydroxyl and partial epoxide groups. Within 1000–2000°C, a bottom-up layer stacking of GP as a crystal growth is observed with a decrease in the number of defects. The folding and unfolding processes of GO and GP are also observed at the boundaries of 140–600° and 800–1000°C, respectively. Furthermore, a partially reduced GO thin film can be applied as a catalytic thin film for a DSSC. These experimental results will be useful for the fundamental understanding of GO and GP, including the thickness control of GP and bottom-up layer stacking toward bulk graphite.

Appendix 1

XRD data for the GO/GP films and GO/GP powders

GO and GP thin films					Go and GP powders		
	Peak I		Peak II				
In situ measuring T(°C)	[a]d_{002} (Å)	[b]FWHM (°)	[c]d_{002} (Å)	[d]FWHM (°)	Annealing T(°C) (RT measuring)	[e]d_{002} (Å)	[f]FWHM (°)
25	8.071	1.16			60	7.131	1.03
50	7.864	1.20			200	3.747	5.30
100	7.611	1.22			400	3.605	4.05
140	7.259	1.35	4.034	4.9	600	3.392	2.68
150	6.920	1.51	3.999	5.96	800	3.432	3.89
160	6.576	1.78	3.945	5.08	1000	3.498	4.60
170	6.053	2.32	3.903	5.16	1200	3.434	3.37
180	5.254	2.55	3.886	5.19	1400	3.427	1.65
190	4.990	1.93	3.829	5.17	1600	3.396	1.25
200	4.851	1.58	3.828	5.16	1800	3.393	1.10
250	4.553	1.49	3.791	5.05	2000	3.390	0.95
300	4.326	1.48	3.752	4.93			
400	4.029	1.41	3.666	4.62			
500	3.782	1.32	3.602	4.1			
600	3.593	1.2					
700	3.485	1.28					
800	3.433	1.55					
900	3.415	1.95					
1000	3.453	2.53					
25 after cooling	3.385	2.35					

error: [a](±0.005), [b](±0.2), [c](±0.05), [d](±0.3), [e](±0.01), and [f](±0.5).

5. Acknowledgements

This work was supported by a Korea Institute of Ceramic Engineering and Technology (KICET) project (09-224c0001).

6. References

Brodie, B. C. (1859). *Phil. Trans. R. Soc. A*. 149, 249–259.
Cullity, B. D. (1978). *Elements of X-ray diffraction*, 2nd Ed. Addison-Wesley.
Figueiredo, J. L.; Pereira, M. F. R.; Freitas, M. M. A. & Órfão, J. J. M. (1999). *Carbon* 37, 1379–1389.
Fujimoto, H. (2003). *Carbon* 41, 1585–1592.
Gao, W.; Alemany, L. B.; Ci, L. & Ajayan, P. M. (2009). Nature *Chemistry* 1, 403-408.
Geim, A. K. & Novoselov, K. S. (2007). *Nature Materials* 6, 183–191.
Giordano, F; Graziano, M. L. & Lesce, M. R. (1988). *J. Chem. Soc. Perkin Trans II* 5, 773–775.
Gosselin, P.; Bérard, A.; Mohrbach, H. & Ghosh, S. (2009). *Eur. Phys. J.* C 59, 883–889.
Graziano, G. (1998). *J. Chem. Soc. Faraday Trans* 94, 3345–3352.
Hirata, M.; Gotou, T.; Horiuchi, S.; Fujiwara, M. & Ohba, M. (2004). *Carbon* 42, 2929–2937.
Hummers, W. S. & Offerman, R. E. (1958). *J. Am. Chem. Soc.* 80, 1339–1339.
(a) Jeong, H. K.; Lee, Y. P.; Jin, M. H.; Kim, E. S.; Bae, J. J. & Lee, Y. H. (2009). *Chem. Phys. Lett.* 470, 255–258.
(b) Jeong, H. K.; Lee, Y. P.; Lahaye, R. J. W. E.; Park, M. H.; An, K. H.; Kim, I. J.; Yang, C. W.; Park, C. Y.; Ruoff, R. S. & Lee, Y. H. (2008). J Am Chem Soc 130, 1362–1366.
Ju, H. M.; Huh, S. H.; Choi, S. H. & Lee, H. L. (2010). *Mater. Lett.* 64, 357–360.
Kim, K. S.; Zhao, Y.; Jang, H.; Lee, S. Y.; Kim, J. M.; Kim, K. S.; Ahn, J.-H.; Kim, P.; Choi, J.-Y. & Hong, B. H. (2009). *Nature* 457, 706-710
Lee, C.; Wei X. D.; Kysar, J. W. & Hone, J. (2008). *Science* 321, 385–388.
Li, Z. Q.; Lu, C. J.; Xia, Z. P.; Zhou, Y. & Luo, Z. (2007). *Carbon* 45, 1686–1695.
Liu, Q.; Liu, Z.; Zhang, X.; Yang, L.; Zhang, N.; Pzn, G.; Yin, S.; Chen, Y. & Wei, J. (2009). *Adv. Funct. Mater.* 19, 894–904.
Lotya, M; Hernandez, Y.; King, P. J.; Smith, R. J.; Nicolosi, V.; Karlsson, L. S.; Blighe, F. M.; Zhiming Wang, S. D.; McGovern, I. T.; Duesberg, G. S. & Coleman, J. N. (2009). *J. Am. Chem. Soc.* 131, 3611–3620.
McAllister, M. J.; Li, J-L.; Adamson, D. H.; Schniepp, H. C.; Abdala, A. A.; Liu, J.; Herrera-Alonso, M.; Milius, D. L.; Car, R.; Prud'homme, R. K. & Aksay, I. A. (2007). *Chem. Mater.* 19, 4396–4404.
Mkhoyan, K. A.; Contryman, A. W.; Silcox, J.; Stewart, D. A.; Eda, G.; Mattevi, C. ; Miller, S. & Chhowalla, M.(2009). *Nano Letters* 9, 1058–1063.
Obraztsov, A. N. (2009). *Nature Nanotechnology* 4, 212–213.
Stankovich, S.; Dikin, D. A.; Piner, R. D.; Kohlhaas, K. A.; Kleinhammes, A.; Jia, Y.; Wu, Y.; Nguyen, S. T. & Ruoff, R. S. (2007). *Carbon* 45, 1558–1565.
Stoller, M. D.; Park, S. J.; Zhu,Y.; An, J. H. & Ruoff, R. S. (2008). *Nano Lett.* 8, 3498–3502.
Titelman, G. I.; Gelman, V.; Bron, S.; Khalfin, R. L.; Cohen, Y. & Bianco-Peled ,H. (2005) *Carbon*, 43, 641–649.
Wang, X.; Zhi, L. & Mullen, K. (2008). *Nano Lett* 8, 323–327.

6

Graphene Etching on Well-Defined Solid Surfaces

Toshio Ogino and Takahiro Tsukamoto
Yokohama National University,
Japan

1. Introduction

Graphene is a two-dimensional material with hexagonal carbon network, and multilayer of graphene has been well-known as graphite. In 2004, it was reported that single-layer graphene can be exfoliated from graphite and observed using an optical microscope when a graphene sheet is attached on a 300 nm-thick SiO_2/Si wafer (Novoselov et al., 2004). Graphene exhibits an extremely high mobility, 200,000 cm^2/Vs, which is 200 times as fast as that of Si. This high mobility was theoretically expected and then a mobility of 230,000 cm^2/Vs was experimentally observed in a suspended graphene sheet (Bolotin et al., 2008). Since the sp^2 bonding of carbon is very strong, a mechanically and chemically stable two-dimensional network with few defects is realized in spite of an expectation that an atomic layer would be intrinsically unstable (Stolyarova et al., 2007). Owing to the small weight of carbon atom and the strong bonding between the atoms, thermal conductivity of graphene is in the highest group in the materials (Balandin et al., 2008). These features are effectively utilized when graphene is applied to electronic devices. Up to now, many reports have shown that graphene electronics is very promising for post-Si devices, but serious problems are also pointed out. For example, compatibility of high-quality graphene and wafer-scale processing is a big challenge. Although high-quality graphene can be obtained by exfoliation of graphene flakes from graphite, its size is small and the position control is almost impossible. Wafer-scale preparation of graphene sheets and their processing can be realized by epitaxial graphene on SiC (Berger, et al., 2004), chemical vapour deposition of graphene on a metal substrate (Sutter et al., 2008; Bae et al., 2010; Li et al., 2009), or coating of graphene oxide (Eda et al., 2008; Li et al., 2008). However, the quality of those graphene is not sufficient for high-performance devices.

In this article, we show our recent results about substrate engineering toward graphene integrated devices. We first describe properties and features of graphene on solid surfaces and then show strategy about etching of graphene, where "etching" is used for cutting of graphene sheets through chemical reactions. Based on this background, we show our experimental results about tight attachment of graphene onto oxide substrates, such as sapphire and titania, and characterize the interface properties between the graphene sheet and the substrate surface. Finally, we show processing of graphene sheets attached on the sapphire surfaces using the atomic structures on the substrate surface as templates. Here, we would like to emphasize that the interface properties between the graphene sheet and the substrate is particularly important and that etching and local properties of the graphene

sheets can be controlled by utilizing the atomic structure of the substrate surface because graphene consists of a single-atomic layer and, therefore, their shape and properties are strongly influenced by the substrate structure and properties.

2. Substrate strategy in graphene devices

Silicon integration technology has been exponentially developed according to the well-known Moore's law (Moore, 1998), but it is now expected that such trend will be saturated in the near future. To keep the present trend, there are two approaches: one is improvement of the conventional technology by introducing new materials and processing, and the other employment of completely different concept of device architecture. The former category called "more Moore" is based on down-scaling of the device processing. Silicon on insulator (SOI) (Yoshimi, 2002) has a long history and started with silicon on sapphire (SOS), in which a silicon thin layer is epitaxially grown on a sapphire surface. After the proposal of SOS, SIMOX (separation by implanted oxygen) and direct wafer bonding techniques have been developed. The SOI devices exhibit small parasitic capacitance and facile availability of full-depletion operation mode in MOSFET (metal-oxide-semiconductor field effect transistor). Therefore, device performance using SOI is almost equal to that of down-scaled devices fabricated by the next generation processing. On the other hand, concept of the latter class called "more than Moore" has not been established, but nanocarbon is one of the promising candidates of the materials for future electronic devices. Carbon nanotubes (CNTs) (Iijima, 1991) have been attracting great interest as alternative materials of Si because of its high electron mobility, thermal stability, high durability against a high electric current density. Though CNT-FETs have been developed for last 15 years and their high potential performance has been reported (Tan et al., 1998; Collins et al., 2001), reliable handling and position control are still difficult towards integrated devices. Moreover, separation of semiconducting CNTs from metallic ones is required. Therefore, industrialization of CNT FETs in the near future is thought to be questionable.

Graphene possesses compatibility with the planar technique that has been playing a principal role in the Si integration technology. It means that we can utilize the sophisticated technology, such as lithography, in fabrication of graphene devices, though the concrete image of the graphene device is still ambiguous at this moment. Since there is no structural variation in graphene, electronic structure is uniquely controlled within the two-dimensional plane (Stolyarova et al., 2007). As can be seen in graphene separated from natural graphite, atomic network of graphene is almost defect-free. We can conclude that graphene is a suitable material for integrated electronic devices. Graphene is flexible and deformed by a small external force though the bonding between individual atoms is extremely strong. Moreover, the electronic properties of graphene strongly depend on its shape, size, and deformation (Geim, 2009; Ertler et al., 2009). Therefore, graphene should be tightly fixed on the substrate in device applications that require a high reliability. For example, electrical conductivity of epitaxial graphene on SiC single crystal depends on the direction with respect to the atomic steps on the SiC surfaces (Yakes et al., 2010; Odaka et al., 2010). In the actual devices, graphene should be attached on an insulating substrate, which we call graphene on insulator, GOI. Requirements to GOIs are atomically defined surfaces to obtain a flat graphene without deformation and tight attachment between the graphene sheet and the substrate, so that variety of device processing can be utilized. In addition to the compatibility with the conventional technology, a new processing with atomic level

resolution is desired to effectively utilize the mono-atomic scale of graphene. Finally, wafer-scale GOIs are required in the industrialization stage. A wafer-scale integration of graphene devices has already been proposed (Lee et al., 2010). Though this requirement is indispensable, we focus on the interface control in small-size GIOs and etching to obtain various patterns of graphene sheets in this article.

Concerning adhesivity between graphene sheets and solid surfaces, it is well-known that apparent height of graphene attached on the SiO_2/Si substrate is much greater than the interlayer spacing of graphite, 0.34 nm, in air (Stolyarova et al., 2007; Ishigami et al., 2007; Geringer et al., 2009). Since chemical bond is not formed between graphene and SiO_2, atomic-scale roughness on the SiO_2 surface seems to prevent tight attachment at the interface. To form a device-level interface with non-covalent bonding, atomically flat substrate surface is required. Under this condition, Van der Waals force effectively works and adhesivity similar to that in epitaxial growth can be obtained, as appears in graphite. This requirement can be realized by using single crystals with atomically flat terraces and regularly ordered atomic steps. Techniques to well-ordered atomic steps have been developed in semiconductor technology, such as Si and GaAs.

Fig. 1 shows our substrate strategy towards GOI devices. From the above discussion, it can be concluded that the materials for GOI substrate should be highly insulating, and their surfaces are covered with flat terraces accompanied with well-ordered step arrangement. Some metal oxides satisfy these requirements, such as sapphire (Al_2O_3), titania (TiO_2), quarts (SiO_2). In particular, sapphire is highly insulating and chemically stable. On sapphire surfaces, step arrangement can be well-controlled, which means that atomically flat terraces can be obtained on the entire substrate surface. Since sapphire is an oxide crystal, no further oxidation occurs and, therefore, terraces can be kept atomically flat through processing in air and in solution. Another important advantage of sapphire is that production technique of high-quality large-scaled wafers has been established in SOS using Si and light-emitting devices using nitride semiconductors. In this article, we use sapphire as the most suitable substrate for GOIs and briefly show results of graphene attachment on titania and quartz surfaces.

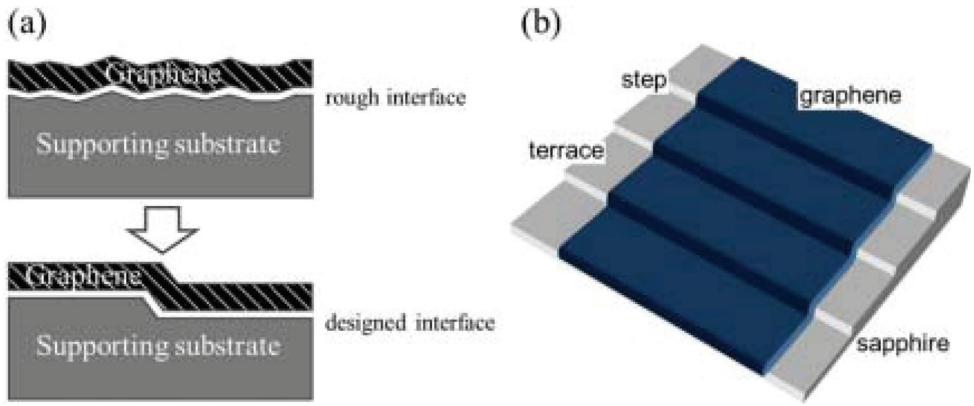

Fig. 1. Substrate strategy towards graphene-on-insulator devices. (a) Cross-sectional views of the interfaces and (b) GOI using substrates that exhibit well-ordered step/terrace structure.

3. Processing strategy in graphene devices

Si-MOSFETs have been developed with down-scaling that includes reduction of channel depth and the gate oxide thickness. Graphene is originally single-atomic layer and has no room for further reduction. In other word, reduction of lateral size to atomic level is required to make full use of the features of graphene. Because conventional lithography uses thick polymer resist masks, etching of graphene using such masks cannot be applied to atomic-scale processing. The processing strategy based on the substrate engineering may be divided into two methods. One consists of incorporation of strain distribution into the graphene sheet by locally bending the sheet using substrate patterns and modulation of the electrical, mechanical and chemical properties of the graphene sheet. The other is cutting graphene to separate individual device areas without thick resist masks. The former strategy has recently been proposed, where topographic patterns on the substrate is used to locally deform the graphene sheets (Pereira & Neto, 2009). This strategy is promising because graphene can be easily deformed owing to its flexibility and the properties can be controlled by the deformation. In other techniques for functionalization of graphene sheets, cutting accompanied with bond breaking or chemical termination accompanied with defect formation is used. The former strategy based on deformation of graphene also has advantage that the whole process can be done only by patterning of the substrate without handling graphene itself. However, the isolation between individual devices, which is one of the important elements in the integrated devices to avoid crosstalk, is not perfect. In the etching, a couple of technique has been proposed. One is crystallographic etching where metal nanoparticles, such as Fe, Co, and Ni, placed on a graphene surface are used as catalyst (Datta et al., 2008). The graphene sheet is located in H_2 or H_2-containing flow at elevated temperatures. Carbon of graphene is reacted with hydrogen gas and CH_4 gas forms by the following reaction:

$$C + 2H_2 -> CH_4 . \quad (1)$$

Since CH_4 gas is quickly released to the vapour phase, graphene etching proceeds. The notable feature of this etching mode is that the etching occurs along the zigzag edge of graphene because the energy required for removal of the carbon atoms along the zigzag edge is much larger than that along the armchair edge (Ci et al., 2008). As a result, crystallographic etching occurs and atomically straight trenches directed to one of three zigzag edges form. The movement of the metal nanoparticles is sensitive to deformation of graphene (Campos et al., 2009). For example, when a metal nanoparticle approaches a trench formed in advance, its movement direction is changed because graphene lattice near the pre-existing trench is deformed owing to instability of graphene edges. This is a remarkable feature because graphene nanoribbon, which is one of the methods to open bandgap in graphene electronic structure (Han et al., 2007), can be self-assembled. Moreover, since the etching begins from the graphene edge, etching patterns can be controlled by the arrangement of the nanoparticles (Ci et al., 2009). Another proposal to cut graphene is oxidation of graphene in O_2 atmosphere at elevated temperatures using Ag nanoparticle as catalyst by the following reaction (Severin et al., 2009):

$$C + O_2 -> CO_2 . \quad (2)$$

In this technique, crystallographic etching does not occur and irregular trench forms. However, this technique has an advantage that the reaction temperature is lower than that in the hydrogenation reaction shown in the reaction (1).

Fig. 2 shows our processing strategy for graphene devices. First, we employ etching mode based on the reaction expressed by eq. (1) and Fe nanoparticles are used as catalyst. In the application of graphene to electronic devices, graphene should be tightly attached on the substrate surface. Since the etching of graphene is strongly influenced by the externally introduced deformation, we can use the deformation patterns introduced by the topography of the substrate surface. In this strategy, atomic structures, even a single-atomic step, can produce an abrupt deformation in graphene when the graphene film is tightly attached to the terraces on both side areas of the atomic step. As shown later, we have developed etching of few-layer-graphene (FLG) utilizing deformation introduced into graphene from atomic structure of the substrate surface. Another factor of the etching based on atomic structure of the substrate surface is interaction between the metal nanoparticles and specific structure on the substrate surface. Directional control of the etching is also shown in section 6.

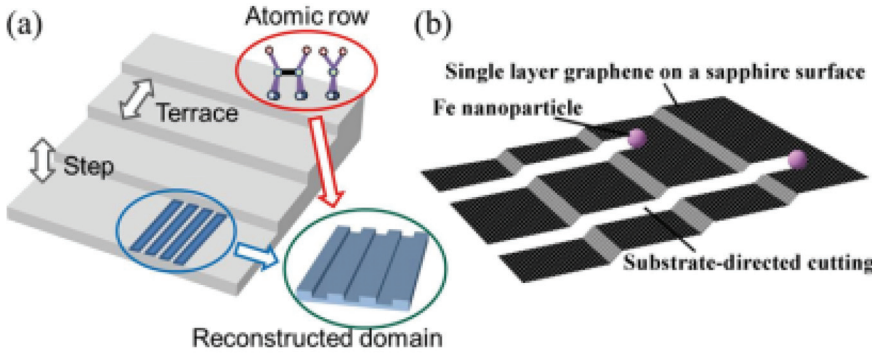

Fig. 2. Processing strategy of graphene -on-insulator. (a) Atomic structure control on substrate surface and (b) etching controlled by the substrate.

4. Graphene on single crystalline oxides

We show morphology and interface characterization of FLG or graphene on single crystalline sapphire surfaces (Tsukamoto & Ogino, 2009). In this study, we used (0001) and (1-102) surfaces, and atomic step arrangement is controlled in advance of the attachment process. Fig. 3 shows AFM iamges of typical step arrangement on a sapphire (0001) surface. Just after polishing and chemical etching, the atomic steps are randomly distributed, as shown in Fig. 3(a). After annealing in air at 1000 °C, regularly ordered atomic steps are obtained, as shown in Fig 3(b). In the equilibrium state, single height atomic steps are separated by terraces with similar width that is uniquely determined by the macroscopic miscut angle of the substrate. Upon annealing at 1400 °C, a couple of atomic steps are gathered and form step bunches, as shown in Fig. 3(c). This is one of the powerful tool to control deformation in the attached graphene sheets because the number of steps in step-bunches, which is controlled by the annealing temperature, directly determines the magnitude of deformation introduced into the attached graphene sheet. Similarly, step arrangement can be controlled also on sapphire (1-102) surface.

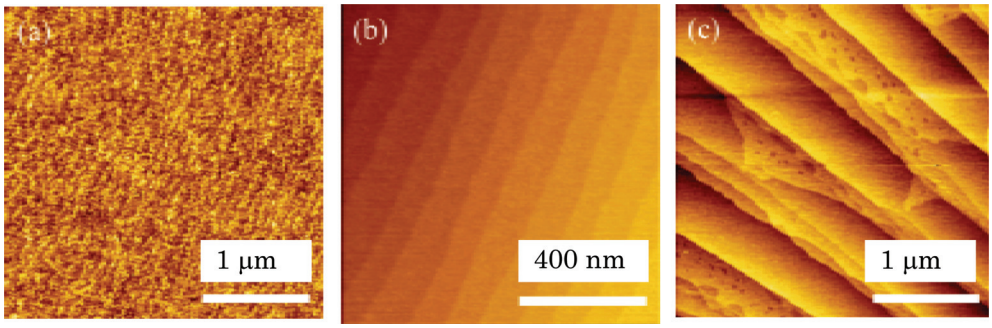

Fig. 3. AFM images of typical step arrangement on sapphire surfaces. (a) Randomly distributed steps, (b) uniformly distributed single-atom steps, and (c) bunched steps.

Fig. 4 shows atomic force microscopy (AFM) images of graphene on a sapphire (1-102) surface, where graphene flakes were mechanically exfoliated from highly oriented pyrolysis graphite (HOPG) and attached on the sapphire surface. Fig. 4(a) shows topography and Fig. 4(b) frictional force image. Before graphene attachment, the sapphire surface was annealed at 1000 °C in air and atomically flat terraces separated by ordered step arrays were formed. Just before the attachment, sapphire surface was cleaned using a H_2SO_4-H_2O_2 solution. Height of the graphene flake in Fig. 4(a) is 0.35 – 0.38 nm, which is similar to the layer spacing in HOPG. As previously reported, when graphene flakes were attached on amorphous SiO_2 layer prepared by thermal oxidation of Si, heights of 0.6 – 0.8 nm were observed (Stolyarova et al., 2007; Ishigami et al., 2007; Geringer et al., 2009). This means that atomically uniform contact is not obtained in the graphene/SiO_2 system. Since integrated electronic devices are fabricated through hundreds of processing including wet cleaning, thermal process and etching, atomically uniform contact is required. Our experimental results show that single crystalline insulating substrate is much more suitable than amorphous substrates, though generally SiO_2 is an ideal insulator. Frictional force image shown in Fig. 4(b) was taken simultaneously with topographic image, where the brightness corresponds to magnitude of the frictional force. In this operation mode, the cantilever of AFM is laterally scanned, and topographic and frictional force images are taken from the vertical bending and the lateral torsion of the cantilever, respectively. Figure 5(a) shows origin of the frictional force in AFM observation in air. The frictional force on solid surfaces exposed to air is usually determined by the resistance to the cantilever movement induced by the meniscus formed between the cantilever tip and the surface. Therefore, the observed frictional force is larger when the surface is more hydrophilic. In our experiment, the cantilever tip is made by Si_3N_4, which is hydrophilic. Since the sapphire surface used in our experiment was treated by acid, it is terminated with OH group generated by the acid treatment. Both the sapphire and the cantilever surfaces are hydrophilic, and a large meniscus forms. Therefore, the bserved frictional force on sapphire surface is relatively large, as shown in Fig. 5(b). Graphene, on the other hand, is an extremely hydrophobic material and, therefore, exhibit a low frictional force, as shown in Fig. 5(b). Thus, we can easily distinguish the graphene surface from the substrate. This is a useful tool particularly in graphene etching, because we can directly determine whether the bottom of the trench is sapphire surface or remaining graphene layer surface. Moreover, the spatial resolution of hydrophilic areas inside a large hydrophobic area is higher than the topographic image

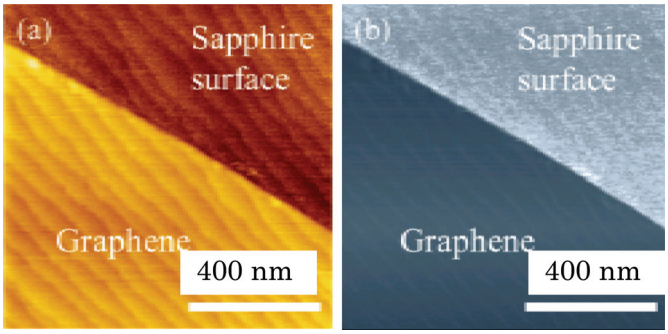

Fig. 4. Atomic force microscopy (AFM) images of graphene attached on a sapphire surface. (a) Topography and (b) frictional force image.

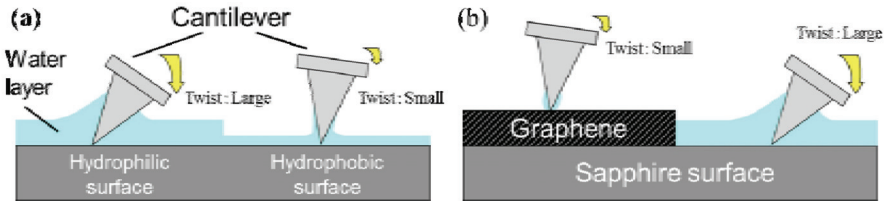

Fig. 5. Origin of the frictional force in AFM observation. (a) General explanation and (b) sapphire surface partially covered with graphene.

because frictional force is generated even on an area smaller than radius of the tip apex. From the above discussion, we can conclude that the top-right area in Fig. 4, which exhibits a larger frictional force, is a sapphire surface and the bottom-left a graphene flake one.

In Fig. 4(a), the step/terrace structure on the substrate surface is almost exactly reproduced on the graphene surface. This means that, owing to atomically uniform contact of graphene on single-crystalline sapphire surfaces, atomic-level topography can be precisely transferred to the graphene surface. Topographic control of the suspended graphene surface is almost impossible owing to its large flexibility. On the other hand, atomic-level control on solid surfaces has been highly developed mainly in semiconductor surfaces. On Si surfaces, formation mechanism of atomic-step arrangement was intensively studied (Ogino et al., 1999a) and artificial positioning of steps is realized. One example is a wafer-scale control of atomic steps on Si(111) surface where position of atomic-steps or step bunches can be uniquely determined (Ogino et al., 1995). When small hole arrays are pre-patterned on Si(111) surfaces, atomic steps on the surface are rearranged according to the hole pattern during high-temperature annealing. By utilizing these techniques, arrangement of self-assembled nanostructures, such as Ge quantum dots, is also controlled because nucleation of nanostructures is often initiated at the steps (Ogino et al., 1999b). In GOI, however, Si substrate is not suitable because Si itself is semiconducting. Although thermally grown SiO_2 layer on Si is a good insulator, it is amorphous and does not possess well-defined atomic structures. On the other hand, sapphire is an insulating oxide and exhibits well-ordered atomic steps. Wafer-scale control of atomic step arrangement was also demonstrated, as shown in Fig. 6. Atomic structure on sapphire surfaces is preserved in air or in water as well as in vacuum because no further oxidation occurs. We, therefore, can transfer topography of well-controlled sapphire surface to graphene surface attached on insulating substrate.

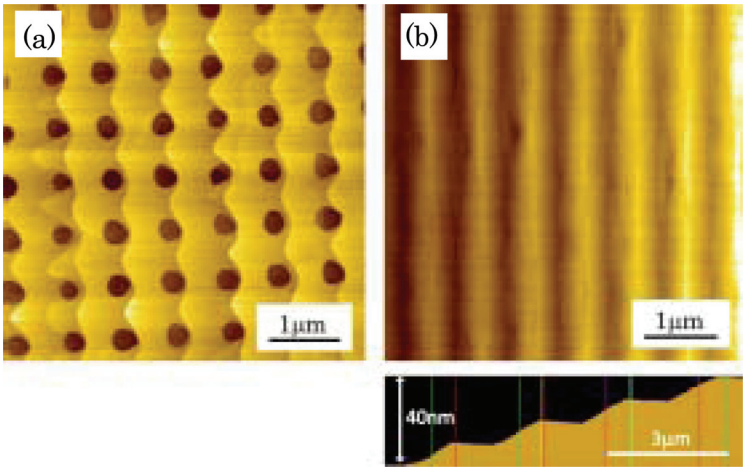

Fig. 6. Artificial control of step arrangement on sapphire surface using small hole arrays on the substrate. (a) Step rearrangement during annealing and (b) final step arrangement.

As previously described, sapphire is the best candidate for GOI substrate. However, some other oxides are possibly useful for specific applications. We attached graphene on titania (TiO_2) or quarts (SiO_2) single-crystal surfaces and observed the surface morphology. Fig. 7 shows topography of graphene flakes attached on (a) a TiO_2(001) surface and (b) a SiO_2(100) surface. On both surfaces, buried atomic-steps appear on the graphene flake surfaces. TiO_2 is well known as a catalytic material of photochemical reaction. It was reported that graphene oxide can be effectively reduced on TiO_2 particle surfaces (Williams et al., 2008) and it suggests that graphene on TiO_2 single crystal has potential applications in functional devices equipped with photochemical reactivity. Quarts is also a good material for radio frequency oscillator and graphene modification of quarts surface may have potential applications to specific oscillation functionality. Mica is a layered crystalline material similar to graphite and a large area of atomic-level flatness is obtained. Using mica, flat graphene surfaces can be obtained (Lui et al., 2009).

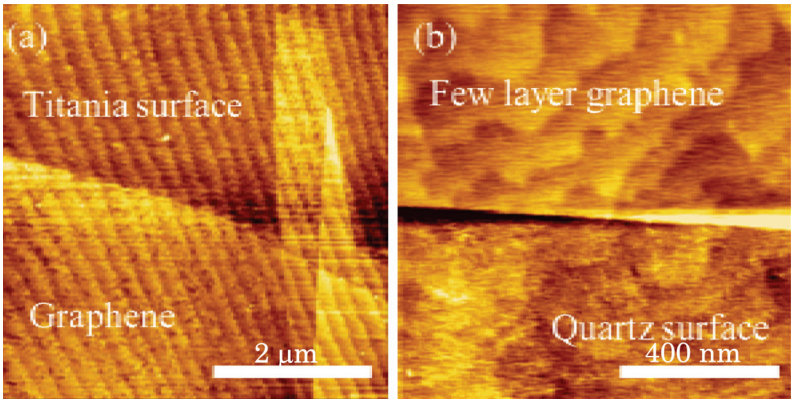

Fig. 7. AFM images of topography on graphene flakes on single crystalline (a) TiO_2(001) and (b) SiO_2(100) surfaces.

We have described physical properties of graphene-substrate interfaces. Another important factor is chemical properties of the interface. Here, we demonstrate a chemical effect of the sapphire substrate on graphene bonding using phase- separated sapphire (0001) surface (Isono et al., 2010). Generally, atomic steps originating from miscut of the surface exist even when the surface is carefully flattened. When a sapphire (0001) surface is annealed at high temperatures above 1300 °C, steps on the surface are gathered and form step bunches. If the miscut direction is rotated from the direction that would generate crystallographically straight steps, step arrangement consists of straight step bunches and crossing steps that is required to keep the macroscopic miscut direction, as shown in Fig. 8(a). We call this type of surface a cross-stepped surface. In the case of sapphire (0001) surface, the most stable crystallographic step direction is that perpendicular to [1-100] and the second that to [1-102]. Fig. 8(b) shows an AFM image of cross-stepped sapphire surface in air. On this surface, ellipsoidal domains, which we call domain A, are observed inside terraces surrounded by step bunches and crossing steps. Fig. 8(c) shows frictional force image of the same area as that shown in Fig. 8(b), where domain A exhibits lower frictional force than the other terrace areas, which we call domain B. This means that domain A is more hydrophobic than domain B. According to previously published papers, sapphire (0001) surface is terminated with Al atoms (Hass et al., 1998) and those Al atoms are terminated with OH groups after the acid treatment, which we used to clean the surface. Therefore, sapphire surface after the acid treatment is generally hydrophilic, as experimentally observed. However, the chemical properties of domain A are much different. We think that domain A is, at least partially, terminated with epoxy groups, and OH group termination, which makes the surface hydrophilic, is suppressed. Domain A grows upon high temperature annealing and the growth is saturated owing to increase in the peripheral stress energy. This kind of phase separation on a solid surface has been reported on other systems (Jones et al., 1996; Komeda & Nishioka, 1997), and it is widely accepted that this occurs to minimize the surface energy.

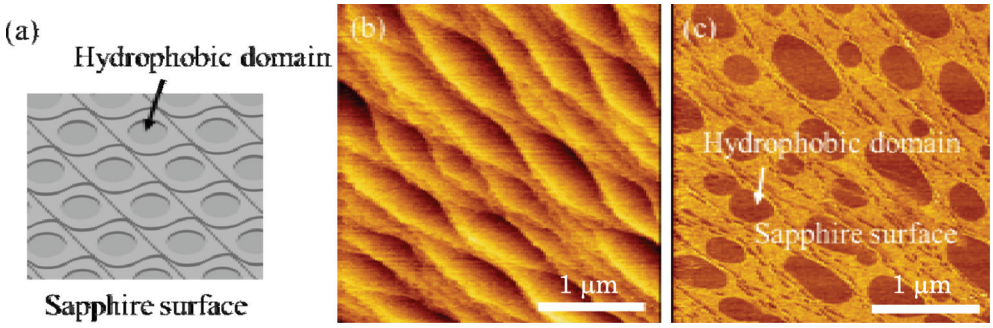

Fig. 8. Cross-stepped sapphire (0001) surface. (a) Schematic view, (b) AFM topographic image, and (c) frictional force image.

Fig. 9(a) shows surface topography of an as-deposited FLG flake on a phase-separated sapphire (0001) surface. On the domain A, flat FLG surface is observed whereas roughness at atomic-level height appears on domain B. Fig. 9(b) is a model for the surface topography. Although domain A is relatively hydrophobic, low-density of water molecules still exist. Since graphene is strongly hydrophobic, graphene and domain A are bonded by a hydrophobic interaction. Therefore, residual water molecules at the interface are swept out

and move to the interface between graphene and relatively hydrophilic domain B. Therefore, the amount of interface water in domain B, which is originally larger than that in domain A, further increases. In a recent paper, observation of single- or few-layer of water molecules was reported between graphene and mica surfaces (Xu et al., 2010). In our case, water layer thickness is probably larger than monolayer of water molecule, and water droplets are also observed. It is known that graphene is impermeable even for He gas (Bunch et al., 2008). In Fig. 9(a), a hydrophobic domain is surrounded by hydrophilic domains. If also opposite domain pattern is obtained, we can confine any species of atom or molecule beneath a graphene flake and directly observe single molecule behaviour because graphene deforms even on a single molecule, as shown in Fig. 9(a). Therefore, graphene on a phase-separated sapphire surface is a good stage to observe single atom or molecule dynamics using a scanning probe. In the case of GOI, confinement of any molecules at the interface should be avoided.

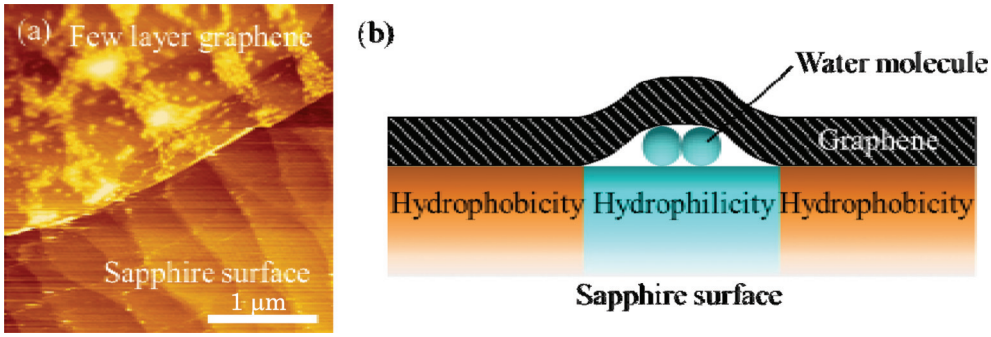

Fig. 9. Graphene on phase-separated sapphire (0001) surface. (a) AFM topographic image, and (b) interface model.

5. Etching of graphene on sapphire substrate

In this section, we show our experimental results about graphene or FLG etching using the reaction expressed by eq. (1) (Tsukamoto & Ogino, 2010). First, sapphire (1-102) substrates were thermally annealed above 1000 °C to obtain well-defined step-terrace structure, and then graphene or FLG exfoliated from HOPG was attached on the substrate. Fe nanoparticles as catalyst were prepared from isopropanol solution of $Fe(NO_3)_3/9H_2O$. The solution was spin-coated on the graphene-attached substrate and then inserted in a furnace after drying. Fe oxide nanoparticles were formed during raising temperature and then reduced to metal nanoparticles by H_2 gas at the initial stage of etching. Graphene etching was performed at 900°C for 10 or 45 min, and the surface morphology was observed by AFM.

Fig. 10(a) shows AFM image on a 30 nm thick FLG surface after etching, where a wide trench (trench A) and a narrow one with a turning point (trench B) are observed. From the cross sectional profiles, etching depth was found to be only monolayer of graphene. A nanoparticle, probably a Fe nanoparticle, is observed at the etching front of the trench A. The trench A clearly demonstrates that the etching proceeds with movement of the metal nanoparticles, and initial position and movement direction of the metal nanoparticles are essential for designing etching patterns. Since the FLG shown in Fig. 10(a) is enough thick,

the buried step-terrace structure is hidden under the FLG surface. Therefore, the substrate surface exhibits almost no effect on the etching mode, and crystallographic etching, which has already been reported, dominantly occurs. However, the trench B changes its etching direction by 120 degree around the deformation of the surface layer indicated by a white broken circle. This suggests that the etching direction, therefore the movement of the catalytic nanoparticles, is strongly affected even by small deformation of the top graphene layer. Fig. 10(b) shows an AFM image on which triangular graphene islands are regularly ordered. In this case, the FLG is enough thick for crystallographic etching to occur. First, a graphene belt was formed by parallel crystallographic etching and another Fe nanoparticle moved inside the belt. The Fe nanoparticle is reflected by 60 degree when it reaches the trench. Therefore, multiple reflection occurs and triangle islands are sequentially formed. The present etching mode is useful to fabricate regular patterns though the shape and direction are limited to triangle and three crystallographic directions, respectively.

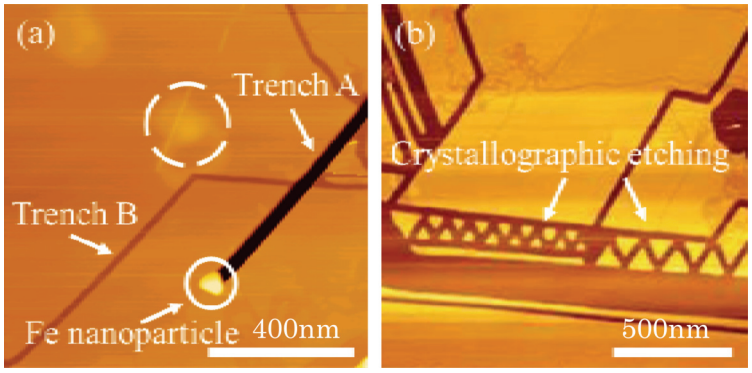

Fig. 10. (a) Etching processes of few-layer-graphene (FLG) along the crystallographic directions, (b) example of regular pattern formation.

Fig. 11(a) shows an AFM image of etching features on 6 nm thick FLG on a sapphire surface, where the etching conditions were same as those for Fig. 10. In this image, etching directions are roughly determined by the crystallographic orientations, but the formed trenches are not straight but fluctuated. This suggests that the etching mode in Fig. 11 was affected by two factors: crystallographic orientations of graphene and atomic roughness on the substrate surface. Fig. 11(b) shows an etching pattern of 3 nm thick FLG on a sapphire surface on which step/terrace structure appears. On this surface, trenches along crystallographic orientation are observed. The whole etching pattern was formed by reflection of Fe nanoparticles at both a pre-existing trench edge indicated by white arrows A and buried steps indicated by white arrows B. Since FLG is tightly attached on the sapphire surface with regularly ordered steps, large strain is locally introduced just above the atomic steps. The observed fluctuation in Fig. 11(a) is attributed to the strain induced by the roughness of the substrate surface and its major contribution is atomic steps. In Fig. 11(a), we observe some characteristic etching patterns. The Fe nanoparticles turn their moving direction at a pre-existing trench, as indicated by (A) in Fig 11(a), and never cross the trench. When there is no catalytic particle inside a triangular island surrounded by trenches, no further etching occurs, as indicated by (B). On the other hand, if catalytic nanoparticles remain inside the triangular island, they continue to divide the triangular island and, in some cases, triangular

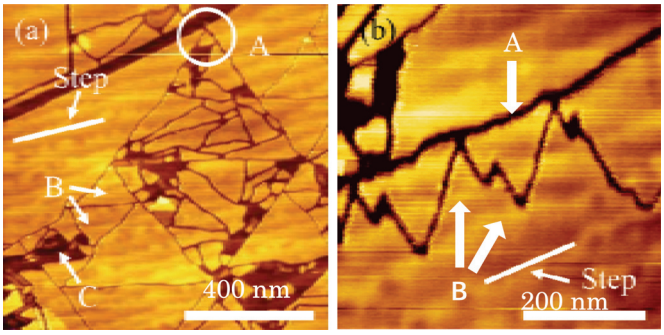

Fig. 11. Etching mode of a FLG, in which crystallographic etching is modified by atomic structure on the substrate surface. (a) Various patters in this etching mode and (b) reflection of Fe nanoparticles at buried steps.

voids are finally formed, as indicated by (C) in Fig. 11(a). These results show that initial arrangement of catalytic nanoparticles is the key factor to design the FLG island patterns.
Fig. 12(a) shows another AFM image of etching pattern on 6 nm thick FLG attached on a sapphire surface. On this surface, two trenches are observed. The relatively wide trench indicated by A is confined in an area above single buried terrace and consequently the macroscopic direction is parallel to the steps. However, the local direction of the trench A is fluctuated according to the crystallographic orientations inside the terrace. In Fig. 12(a), trench B with relatively narrow width is also observed. This is almost completely straight, which means trench B follows one of the crystallographic orientations though the FLG thickness is same as trench A. This suggests that influence of buried atomic steps on the etching shape is larger for larger Fe nanoparticles than for a smaller one, or that movement of a smaller nanoparticle is more strongly subject to crystallographic orientation. Fig. 12(b) shows an AFM image on another area on the same sample, where an almost straight trench along a single step is observed. From the above experimental results, we can conclude that the FLG etching is controlled by two factors; crystallographic orientations of the FLG and atomic structure on the substrate surface. As previously mentioned, we have a variety of techniques to artificially design atomic structures, in particular step arrangement, which has been developed in semiconductor surfaces. Therefore, the patterning technique of FLG based on substrate engineering is promising for future integration of graphene or FLG devices.

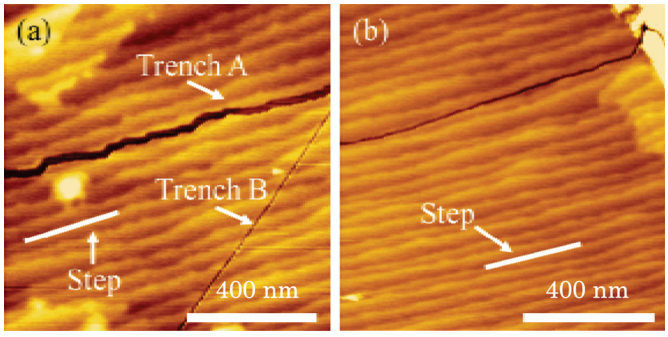

Fig. 12. Graphene etching subject to buried steps. (a) Etching confined in an area above single terrace, (b) etching along a single step.

In the etching of FLG, only the topmost layer of FLG flake is etched and the trench depth is a single layer of graphene. This is because etching is always initiated from graphene edge and never on the FLG terrace, at least within our experiment. Next, we describe etching mode of single layer of graphene on sapphire (1-102) surfaces that exhibits wide terraces. Upon annealing at 1000 °C for 3 h in air, a comb-shaped pattern appeared on the terraces, as shown Fig. 13(a), where the sample was cleaned using H_2SO_4 and H_2O_2 mixed acid. From the cross-sectional profile of this pattern, we found that the boundaries between bright (high) and dark (low) areas are not atomic steps, but the height difference is smaller than the unit step height. In the frictional force image, difference in the hydrophilicity is clearly observed. This means that the stripe domains exhibit different surface chemistry from each other. This is similar to the phase separation that we previously found on sapphire (0001) surfaces shown in Fig. 8, where there are two chemically different domains (Isono et al., 2010). Because the surface was treated with acid, it is more or less hydroxylated. The observed difference in hydrophilicity is attributed to a difference in OH group density. This means that the atomic structures, or bonding configurations of surface termination, on these domains are different and therefore exhibit different reactivity for acid. Generally, surface reconstruction induces surface strain. If two possible bonding configurations that exhibit different surface strain, phase separation occurs to reduce the strain energy. On a Si(001) surface, stripe domain structure similar to the comb-shaped pattern shown in Fig. 13(a) is observed (Jones et al., 1996; Komeda & Nishioka, 1997). Therefore, the comb-shaped pattern is attributed to a difference in atomic structure on the surface. Fig. 13(b) shows an AFM image of an etching pattern of single layer of graphene attached on the phase-separated sapphire surface, where the etching procedure using Fe nanoparticles was same as the previously-described experiments. On this surface, etching mode controlled by the crystallographic orientations or step of the substrate is not observed. However, a new etching mode appears, where the etching direction is almost perpendicular to the steps. There are two possible explanations for this etching mode. Since the graphene is a single-atomic layer, Fe nanoparticles move directly on the sapphire surface and the movement is possibly controlled by the interaction between the Fe nanoparticles and the substrate surface. In this explanation, Fe nanoparticles interact with the sapphire surface through comb-shaped domain pattern itself or atomic structure along the comb-shape. Another explanation is based on the strain induced into the graphene layer from the comb-shaped surface. In this case, etching direction is determined by the strain distribution on the graphene layer. We speculate that the comb-shaped pattern is directed to a particular crystallographic orientation and the movement of the Fe nanoparticles is controlled by the atomic structure along the same direction as comb-shaped pattern. This is similar to directional growth of carbon nanotubes (CNTs) on the sapphire surface, where CNTs recognize the atomic structure on the sapphire surface and grow along specific directions (Han et al., 2005; Ago et al., 2006).

In Fig. 13(b), two trenches parallel to each other are observed in the bottom area as well as an isolated trench in the top area. In the application of graphene to electronic devices, bandgap opening is thought to be crucial, and nanoribbon formation is one of the most promising approaches for it. Moreover, functional devices utilizing graphene edges have been proposed (Barone et al., 2006; Yan et al., 2007). The directional etching observed in Fig. 13(b) can be applied to formation of graphene nanoribbons. In this application, site and density control of catalytic nanoparticles again plays an important role.

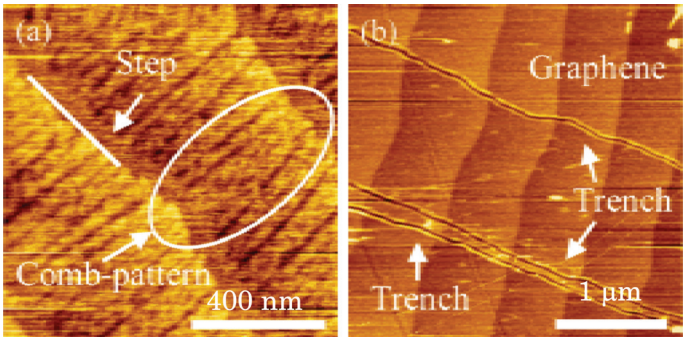

Fig. 13. AFM images of (a) phase separation on sapphire surface and (b) etching pattern of graphene attached on the phase-separated surface.

6. Summary

Graphene possesses tremendous potential for electronic devices owing to its high carrier mobility, high thermal conductivity, and large mechanical strength in spite of a single atomic layer material. In the application of graphene to reliable devices, graphene, which is too flexible for its devices to keep the stable performance, should be tightly fixed on a solid surface. Since such graphene sheet is single or few atomic layer, atomic-level structure and chemistry on the substrate surface directly influences the properties of the attached graphene sheets. Therefore, the selection of substrate is one of the important issues in graphene devices. We proposed sapphire as a substrate for integrated graphene devices because of its excellent insulating properties, high quality developed in the production of various devices using nitride semiconductors, and atomic level controllability of the surface. We have demonstrated that graphene or FLG can be tightly attached on the sapphire surface. Similar results have been obtained also on other single-crystalline oxides, such as quarts and titania surfaces, thought their application targets are probably different from integrated electronic devices. Graphene on these well-defined surfaces exhibits buried step/terrace structures. Modulation of graphene shape using atomic structures on the substrate surface is promising as an alternative approach to functionalize the graphene layers. Development of graphene processing is also required for realization of the integration. We have demonstrated that etching using catalytic nanoparticles is powerful tool for graphene tightly attached on the well-defined substrates. In this technique, we can utilize etching mode using surface structures of the substrate in addition to crystallographic etching, which has been already proposed. Before concluding this chapter, we have to refer to large-scale formation of graphene layer on an insulating substrate, which is believed to be a critical issue toward wafer-scale processing of graphene. Since large-scale high-quality graphene sheet formation is a challenge, we also have to search another approach in the integration strategy. One possible approach is self-arrangement of well-shaped graphene flake on specific sites on the substrate. Since the expected scale of graphene devices is 10 nm or smaller, large area will not be required for individual device areas. The important factor is precise arrangement of the graphene, and surface design of the substrates will be a key technique in this alternative approach.

7. Acknowledgement

This work was partially supported by Grant-in-Aid for Scientific Research from the Ministry of Education, Culture, Sports, Science and Technology and CREST/JST. We also would like to thank T. Isono and H. Komurasaki for the discussion about control of surface structure on sapphire substrates. Sapphire substrates were supplied from Namiki Precision Jewel Co., Ltd. Fig. 6 was obtained by research done by Ms. Takeuchi, et al, Namiki Precision Jewel Co., Ltd. The author would like to thank them for giving us the permission to use Fig. 6.

8. References

Ago, H.; Uehara, N.; Ikeda, K.; Ohdo, R.; Nakamura, K. & Tsuji, M. (2006). Synthesis of horizontally-aligned single-walled carbon nanotubes with controllable density on sapphire surface and polarized Raman spectroscopy. *Chem. Phys. Lett.* Vol. 421, (April 2006) 399-403, ISSN 0009-2614

Bae, S.; Kim, H.; Lee, Y.; Xu, X.; Park, J.-S.; Zheng, Y.; Balakrishnan, J.; Lei, T.; Kim, H. R.; Song, Y. I.; Kim, Y.-J.; Kim, K. S.; Özyilmaz, B.; Ahn, J.-H.; Hong, B. H. & Iijima, S. (2010). Roll-to-roll production of 30-inch graphene films for transparent electrodes. *Nature Nanotech.* Vol. 5, (June 2010) 574-578, ISSN 1748-3387

Balandin, A. A.; Ghosh, S.; Bao, W.; Calizo, I.; Teweldebrhan, D.; Miao, F. & Lau, C. N. (2008). Superior Thermal Conductivity of Single-Layer Graphene. *Nano Lett.*, Vol. 8, (February 2008) 902-907, ISSN 1530-6984

Barone, V.; Hod, O. & Scuseria, G. E. (2006). Electronic Structure and Stability of Semiconducting Graphene Nanoribbons. *Nano Lett.*, Vol. 6, (November 2006) 2748-2754, ISSN 1530-6984

Berger, C.; Song, Z.; Li, T.; Li, X.; Ogbazghi, A. Y.; Feng, R.; Dai, Z.; Marchenkov, A. N.; Conrad, E. H.; First, P. N. & de Heer, W. A. (2004). Ultrathin Epitaxial Graphite: 2D Electron Gas Properties and a Route toward Graphene-based Nanoelectronics. *J. Phys. Chem.* B, Vol. 108, (December 2004) 19912-19916, ISSN 1089-5647

Bolotin, K. I.; Sikes, K. J.; Jiang, Z.; Klima, M.; Fudenberg, G.; Hone, J.; Kim, P. & Stormer, H. L. (2008). Ultrahigh electron mobility in suspended graphene. *Solid State Commun.*, Vol. 146, (June 2008) 351-355, ISSN 0038-1098

Bunch, J. S.; Verbridge, S. S.; Alden, J. S.; van der Zande, A. M.; Parpia, J. M.; Craighead, H. G. & McEuen, P. L. (2008). Impermeable Atomic Membranes from Graphene Sheets. *Nano Lett.*, Vol. 8, (July 2008) 2458-2462, ISSN 1530-6984

Campos, L. C.; Manfrinato, V. R.; Sanchez-Yamagishi, J. D.; Kong, J. & Jarillo-Herrero, P. (2009). Anisotropic Etching and Nanoribbon Formation in Single-Layer Graphene. *Nano Lett.*, Vol. 9 (June 2009) 2600-2604, ISSN 1530-6984

Ci, L.; Song, L.; Jariwala, D.; Elías, A. L.; Gao, W.; Terrones, M. & Ajayan, P. M. (2009). Graphene Shape Control by Multistage Cutting and Transfer. *Adv. Mater.*, Vol. 21 (November 2009) 4487- 4491, ISSN 0935-9648

Ci, L.; Xu, Z.; Wang, L.; Gao, W.; Ding, F.; Kelly, K. F.; Yakobson, B. I. & Ajayan, P. M. (2008). Controlled Nanocutting of Graphene. *Nano Res.*, Vol. 1 (August 2008) 116-122, ISSN 1998-0124

Collins, P. G.; Hersam, M.; Arnold, M.; Maetel, R. & Avouris, Ph. (2001). Current Saturation and Electrical Breakdown in Multiwalled Carbon Nanotubes. *Phys. Rev. Lett.* Vol. 86, (April 2001) 3128-3131, ISSN 0031-9007

Datta, S. S.; Strachan, D. R.; Khamis, S. M. & Johnson, A. T. C. (2008). Crystallographic Etching of Few-Layer Graphene. *Nano Lett.*, Vol. 8, (June 2008) 1912-1915, ISSN 1530-6984

Eda, G.; Fanchini, G. & Chhowalla, M. (2008). Large-area ultrathin films of reduced graphene oxide as a transparent and flexible electronic material. *Nature Nanotech.* Vol. 3, (April 2008) 270–274, ISSN 1748-3387

Ertler, C.; Konschuh, S.; Gmitra, M. & Fabian, J. (2009). Electron spin relaxation in graphene: The role of the substrate. *Phys. Rev.* B, Vol. 80, (July 2009) 041405, ISSN 1098-0121

Geim, A. K. (2009). Graphene: Status and Prospects. *Science,* Vol. 324, (June 2009) 1530-1534, ISSN 0036-8075

Geringer, V.; Liebmann, M.; Echtermeyer, T.; Runte, S.; Schmidt, M.; Rückamp, R.; Lemme, M. C. & Morgenstern, M. (2009). Intrinsic and extrinsic corrugation of monolayer graphene deposited on SiO_2. Phys. Rev. Lett., Vol. 102, (February 2009) 076102, ISSN 0031-9007

Han, M. Y.; Özyilmaz, B.; Zhang, Y. & Kim, P. (2007). Energy Band-Gap Engineering of Graphene Nanoribbons. *Phys. Rev. Lett.*, Vol. 98 (May 2007) 206805, ISSN 0031-9007

Han, S.; Liu, X. & Zhou, C. (2005). Template-Free Directional Growth of Single-Walled Carbon Nanotubes on a- and r-Plane Sapphire. *J. Am. Chem. Soc.* Vol. 127, (March 2005) 5294-5295, ISSN 0002-7863

Hass, K. C.; Schneider, W. F.; Curioni, A. & Andreoni, W. (1998). The Chemistry of Water on Alumina Surfaces: Reaction Dynamics from First Principles. *Science* Vol. 282, (October 1998) 265-268, ISSN 0036-8075

Iijima, S. (1991). Helical microtubules of graphitic carbon. *Nature*, Vol. 354 (November 1991) 56-58, ISSN 0028-0836

Ishigami, M.; Chen, J. H.; Cullen, W. G.; Fuhrer, M. S. & Williams, E. D. (2007). Atomic Structure of Graphene on SiO2. *Nano Lett.*, Vol. 7, (May 2007) 1643-1648, ISSN 1530-6984

Isono, T.; Ikeda, T. & Ogino, T. (2010). Evolution of Supported Planar Lipid Bilayers on Step-Controlled Sapphire Surfaces. *Langmuir*, Vol. 26, (March 2010) 9607-9611, ISSN 0743-7463

Isono, T.; Ikeda, T.; Aoki, R.; Yamazaki K. & Ogino, T. (2010). Structural- and chemical-phase-separation on single crystalline sapphire (0001) surfaces. *Surf. Sci.* Vol. 604, (August 2010) 2055-2063, ISSN 0039-6028

Jones, D. E., Pelz, J. P., Hong, Y., Bauer, E. & Tsong, I. S. T. (1996). Striped Phase and Temperature Dependent Step Shape Transition on Highly B-Doped Si(001)-(2×1) Surfaces. *Phys. Rev. Lett.*, Vol. 77, (July 1996) 330-333, ISSN 0031-9007

Komeda, T. & Nishioka, Y. (1997). Comb-shape step formation on Si(001)-2×1 surface. *Appl. Surf. Sci.*, Vol. 117/118, (May 1997) 20-25, ISSN 0169-4332

Lee, Y.; Bae, S.; Jang, H.; Jang, S.; Zhu, S.-E.; Sim, S. H.; Song, Y. I.; Hong, B. H. & Ahn, J.-H. (2010). Wafer-Scale Synthesis and Transfer of Graphene Films. *Nano Lett.*, Vol. 10, (January 2010) 490-493, ISSN 1530-6984

Li, D; Müller, M. B.; Gilje, S. Kaner, R. B. & Wallace G. G. (2008). Processable aqueous dispersions of graphene nanosheets. *Nature Nanotech.* Vol. 3, (February 2008) 101-105, ISSN 1748-3387

Li, X.; Cai, W.; An, J.; Kim, S.; Nah, J.; Yang, D.; Piner, R.; Velamakanni, A.; Jung, I.; Tutuc, E.; Banerjee, S. K.; Colombo, L. & Ruoff, R. S. (2009). Large-Area Synthesis of High-Quality and Uniform Graphene Films on Copper Foils. *Science* Vol. 324, (June 2009) 1312-1314, ISSN 0036-8075

Lui, C. H.; Liu, L.; Mak, K. F.; Flynn, G. W. & Heinz, T. F. (2009). Ultraflat graphene. *Nature*, Vol. 462, (November 2009) 339-341, ISSN 0028-0836

Moore, G. E. (1998). Cramming More Components onto Integrated Circuits. *Proc. IEEE*, Vol. 86, (January 1998) 82-85, ISSN 0018-9219

Novoselov, K. S.; Geim, A. K.; Morzov, S. V.; Jiang, D.; Zhang, Y.; Dubonos, S. V.; Grigorieva, I. V. & Firsov, A. A. (2004). Electric Field Effect in Atomically Thin Carbon Films. *Science,* Vol. 306, (October 2004) 666-669, ISSN 0036-8075

Odaka, S.; Miyazaki, H.; Li, S.-L.; Kanda, A.; Morita, K.; Tanaka, S.; Miyata, Y.; Kataura, H.; Tsukagoshi, K. & Aoyagi, Y. (2010). Anisotropic transport in graphene on SiC substrate with periodic nanofacets. *Appl. Phys. Lett.*, Vol. 96, (February 2010) 062111, ISSN 0003-6951

Ogino, T.; Hibino, H. & Homma, Y. (1995). Patterning-assisted control for ordered arrangement of atomic steps on Si(111) surfaces. *Jpn. J. Appl. Phys. Lett.*, Vol. 34, (June 1995) L668-L670, ISSN 0021-4922

Ogino, T.; Hibino, H. & Homma Y. (1999a). Kinetics and thermodynamics of surface steps on semiconductors. *Critical Reviews in Solid State and Materials Science*, Vol. 24 (September 1999) 227-263, ISSN 1040-8436

Ogino, T.; Hibino, H.; Homma, Y.; Kobayashi, Y.; Prabhakaran, K.; Sumitomo, K. & Omi H. (1999b). Fabrication and integration of nanostructures on Si surfaces. *Acc. Chem. Res.*, Vol. 32 (February 1999) 447-454, ISSN 0001-4842

Pereira, V. M. & Neto, A. H. C. (2009). Strain Engineering of Graphene's Electronic Structure. *Phys. Rev. Lett.*, Vol. 103, (July 2009) 046801, ISSN 0031-9007

Severin, N.; Kirstein, S.; Sokolov, I. M. & Rabe, J. P. (2009). Rapid Trench Channeling of Graphenes with Catalytic Silver Nanoparticles. *Nano Lett.*, Vol. 9, (January 2009) 457-461, ISSN 1530-6984

Stolyarova, E.; Rim, K. T.; Ryu, S.; Maultzsch, J.; Kim, P.; Brus, L. E.; Heinz, T. F.; Hybertsen, M. S. & Flynn, G. W. (2007). High-resolution scanning tunneling microscopy imaging of mesoscopic graphene sheets on an insulating surface. *PNAS*, Vol. 104, (May 2007) 9209-9212, ISSN 0027-8424

Sutter, P. W.; Flege, J.-I. & Sutter, E. A. (2008). Epitaxial graphene on ruthenium. *Nature Mater.* Vol. 7, (May 2008) 406-411, ISSN 1476-1122

Tan, S. J.; Vershueren, A. R. M. & Dekker, C. (1998). Room-temperature transistor based on a single carbon nanotube. *Nature*, Vol. 393, (May 1998) 49-52, ISSN 0028-0836

Tsukamoto, T. & Ogino, T. (2009). Morphology of Graphene on Step-Controlled Sapphire Surfaces. *Appl. Phys. Express*, Vol. 2, (June 2009) 075502, ISSN 1882-0778

Tsukamoto, T. & Ogino, T. (2010). 'Graphene-on-insulator' fabricated on atomically controlled solid surfaces. *J. Phys. D: Appl. Phys.,* Vol. 43, (September 2010) 374014, ISSN 0022-3727

Williams, G.; Seger, B. & Kamat, P. V. (2008). TiO2-Graphene Nanocomposites. UV-Assisted Photocatalytic Reduction of Graphene Oxide. *ACS Nano*, Vol. 2, (July 2008) 1487-1491, ISSN 1936-0851

Xu, K.; Cao, P. & Heath, J. R. (2010). Graphene Visualizes the First Water Adlayers on Mica at Ambient Conditions. *Science*, Vol. 329, (September 2010) 1188-1191, ISSN 0036-8075

Yakes, M. K.; Gunlycke, D.; Tedesco, J. L.; Campbell, P. M.; Myers-Ward, R. L.; Eddy Jr., C. R.; Gaskill, D. K.; Sheehan, P. E. & Laracuente, A. R. (2010). Conductance Anisotropy in Epitaxial Graphene Sheets Generated by Substrate Interactions. *Nano Lett.*, Vol. 10, (April 2010) 1559-1562, ISSN 1530-6984

Yan, Q.; Huang, B.; Yu, J.; Zheng, F.; Zang, J.; Wu, J.; Gu, B.-L.; Liu, F. & Duan, W. (2007). Intrinsic Current-Voltage Characteristics of Graphene Nanoribbon Transistors and Effect of Edge Doping. *Nano Lett.*, Vol. 7, (April 2007) 1469-1473, ISSN 1530-6984

Yoshimi, M. (2002). Current status and future directions of SOI technology. *Solid-State Electron.*, Vol. 46, (July 2002) 951-958, ISSN 0038-1101

7

Transparent and Electrically Conductive Films from Chemically Derived Graphene

Siegfried Eigler
DIC Berlin GmbH
Germany

1. Introduction

The research interest in graphene based materials, especially for high quality graphene emerged due to its unique electronic and mechanical properties. Some exceptional properties are the high charge carrier mobility at room temperature of 2.5×10^5 $cm^2V^{-1}s^{-1}$, the thermal conductivity of 5000 $WK^{-1}m^{-1}$ and the mechanical stiffness of 1 TPa. Moreover, in electronic devices graphene will open up the possibility for a post silicon age. These properties are valid for graphene with a defect-free structure. For large-scale preparation of graphene a processible and versatile precursor called graphene oxide is utilized. (Compton & Nguyen, 2010).
In this article, a historical overview will be given to elucidate the development of graphene and especially the precursor graphene oxide, its structure in the oxidized and reduced state. Moreover the synthetic methods for graphene preparation will be contemplated. One discipline in graphene research is the preparation of transparent and electrically conductive coatings for the substitution of commonly used transparent conductors as indium tin oxide (ITO), which is currently used for touch screen applications and transparent electrodes. One essential disadvantage of ITO is its brittleness that excludes applications in flexible or wearable electronics.
Furthermore, the performance of such potentially flexible transparent and conductive coatings in dependants of its preparation method will be reviewed using graphene as the reference material. Besides, graphene based transparent coatings will be compared with other suitable transparent coatings.

2. Historical overview – the development to graphene

2.1 The first expansion of graphite

When did the story begin that resulted in the tremendous interest in the study of the properties and the rich chemistry of graphene? Certainly, it was the group of Geim in Manchester that succeeded to promote the outstanding properties and the research in the field of graphene. Their groundbreaking experiments were honoured 2010 with the nobelprize in physics. So this beginning was in 2004 (Novoselov et al., 2004).
Graphite itself is known for a long time and the name originates from the greek *graphein* what means to draw or write and was named by A. G. Werner in 1789. At this time the chemical structure of graphite was unknown and it took almost 130 years to clarify that structure. It was K. E. von Schafhaeutl in the 19th century who was a universal scholar and a

professional in physics, geology, chemistry and music. In 1840 he described an experiment where he observed the exfoliation of graphite. He placed graphite in hot sulphuric acid and added nitric acid that decomposed by the dropwise addition. After the complete decomposition he observed an increased volume of graphite by its expansion or exfoliation to assumedly few layer graphite. Moreover, he repeated that procedure four times until the acid became clear, possibly due to oxidative decomposition of graphite. With the description of these experiments he became a pioneer for modern chemistry on graphite, its intercalated compounds and finally exfoliated graphite (Schafhaeutl, 1840).

2.2 The synthesis of graphite oxide – from Brodie to Staudenmaier

A key for the rich chemistry especially on graphene oxide today is the earning of Brodie who discovered the oxidation of graphite to a stable solid product for the first time (Brodie, 1855). Before his discovery of now called graphite oxide, only the impact of sulphuric acid on graphite was studied (Marchand, 1845) and it was known that graphite can be completely oxidized to CO_2 by potassium dichromate in sulphuric acid (Rogers & Rogers, 1850). Brodie used potassium chlorate in nitric acid for the oxidation of graphite and found after repeated treatments a yellow dispersion of transparent particles that he termed graphitic acid. Gottschalk studied the synthesis and properties of that new substance in 1865. He described the stages of oxidation after each oxidation procedure and described the colour change from black over greens to yellow within five repeated oxidation procedures using Brodies method. Moreover, he recognized the darkening of yellow graphite oxide by the exposure of sunlight what can be ascribed to partial reduction of graphite oxide (Gottschalk, 1865).

At the end of the 19th century, Staudenmaier essentially enhanced the preparation procedure to graphite oxide. The advantage was not only a faster procedure but also a much saver one. The problem that caused unpredictable explosions was the formation of accumulative amounts of chlorine dioxide (ClO_2) that decompose at a temperature of about 60 °C when a certain concentration is reached. That danger was much lower for the two-step procedure developed by Staidenmaier. In the first step graphite is treated with a mixture of sulphuric and nitric acid and potassium chlorate at ambient conditions. In the second step graphite oxide is yielded by a final oxidation with potassium permanganate (Staudenmaier, 1898). Moreover, it is interesting to note that he described a small-scale lecture experiment for the preparation of graphite oxide (Staudenmaier, 1899). So, the Staudenmaier method rendered possible the preparation of graphite oxide on large scale minimizing the danger of explosions. Further, the preparation time was much lower compared to Brodies method. Instead of several weeks only several days were necessary.

Within the first 50 years of oxidizing graphite to graphite oxide the method could be dramatically enhanced and Staidenmaier pointed out that graphite oxide is not a uniform substance as others thought before, according to elemental analysis. As a consequence no chemical formula can be given for graphite oxide, as others tried before (Staudenmaier, 1899). Nevertheless, the oxygen content of yellow graphite oxide is about 40 % and a simple average formula might be given as $C_{6n}(OH)_{3n}$ without a valid claim.

2.3 From oxidized graphite to its structure

In the following years the aim was to identify the structure of graphite. For this purpose the reaction products of oxidized graphite were analyzed. Mellitic acid (benzene-1,2,3,4,5,6-

hexacarboxylic acid) was identified as one oxidation product of graphite, if the degree of oxidized graphite is higher than graphite oxide but lower than CO_2 (Dimroth & Kerkovius, 1913).

So, it was assumed that C_6 is the building block of graphite. Then, in 1917 Debye and Scherrer used x-ray methods to clarify the structure of graphite and diamond and they brought their experiments in the context of chemical oxidation results (Debye & Scherrer, 1917). Now, the structure of graphite is well-known and common knowledge. The C-C bond length is 1.42 Å and the structure consists of graphene layers that are stacked in an AB sequence. The sheet distance between two layers is 3.35 Å (Chung, 2002).

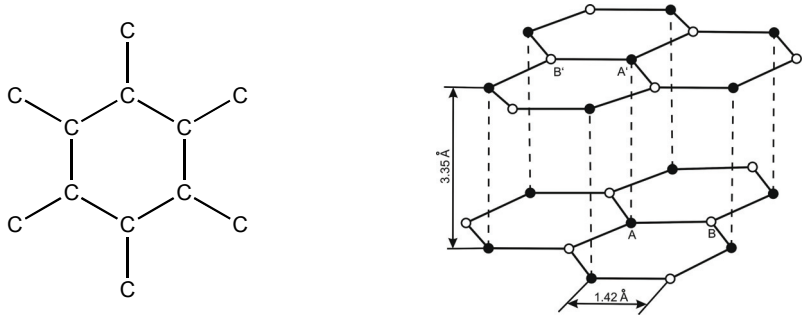

Fig. 1. A) C_6-structure motive – a first hint for the structure of graphite as a result of oxidizing graphite (Dimroth & Kerkovius, 1913); B) reproduced and simplified crystal structure of graphite; C-C bond length is 1.42 Å; AB stacking of graphene sheets (Chung, 2002).

2.4 Adsorption properties of graphite oxide

After the structure of graphite was known the development on the chemistry of graphite and graphite oxide was much faster. Researchers determined the chemical properties of graphite oxide in the following decades. E.g. Thiele analysed amongst other things the base exchange with graphite oxide (Thiele, 1937). It was recognized that a dispersion of graphite oxide changes its pH from neutral to acid upon the addition of ions, as Na^+, K^+, Ba^{2+}, NH_4^+ and others accompanied with an increase in the sheet distance of the graphene oxide sheets in graphite oxide. Generalized the data say, that one mol of graphite oxide with the generalized formula $C_6(OH)_3$ can adsorb about 1-2 equivalents. A curiosity was the usage of graphite oxide as a model substance for humic acid and lignin because of a similar basic structure, even if graphite oxide exhibits a sheet structure contrary to the others. So, Hamdi generated a tremendous work with the detailed analysis of the adsorption behaviour of graphite oxide. E.g. amino acids, as leucine was determined to be adsorbed to graphite oxide at pH=6, better than valine, alanine or NH_4^+. Moreover it is interesting to note that he could not find any toxicity of graphite oxide towards the fungi Oospora lactis (Hamdi, 1942).

2.5 Modern preparation procedures of graphite oxide

It was in 1957 when Hummers published a patent for the preparation of graphite oxide. There he claimed a simple scalable and innocuous synthetic procedure. He used sulphuric

acid and sodium nitrate to disperse graphite and potassium permanganate was used as the oxidant. The temperature was kept below 45 °C and the reaction time was only one hour. This procedure is now called Hummers method. Basically, besides a pre-treatment step of graphite, the procedure did not change any more and the aqueous work-up procedure followed by the addition of hydrogen peroxide to make metal salts removable is easy as well (Hummers, 1957).
Before, it was already known since 1909 that potassium permanganate in sulphuric acid can oxidize graphite at ambient temperature and it was determined that CO_2 is formed at a temperature higher than 45 °C (Charpy, 1909). Nevertheless, it was also described that it is difficult to separate metal salts from the oxidation mixture (Ruess, 1947).
These days, Hummers method or the modified Hummers method is the most commonly used procedure for the synthesis of graphite oxide. Modifications were done by Kovtyukhova et al. using phosphorus pentoxide and potassium peroxydisulfate in sulphuric acid to pre-oxidize graphite to make the subsequent oxidation of graphite according to Hummers method complete (Kovtyukhova et al., 1999). Another method is to use elongated reaction times up to about five days as described by Hirata et al. (Hirata et al., 2004).

2.6 The chemical structure of graphite oxide

Even if the structure of graphite oxide was not known for a long time chemical modifications and modern analytical methods elucidated the structure of graphite oxide. According to the latest analytical results the Lerf-Klinowski model describes best the structure of graphite oxide (Lerf et al., 1998; Casabianca et al., 2010).
The structure of graphite-oxide according to the Lerf-Klinowski model can be described as a CHO macromolecule with aromatic and aliphatic regions. The first ones are untouched and not oxidized. The latter consist mainly of epoxy- and hydroxyl-groups. The amount of these regions depends on the oxidative treatment method. So, on the one hand there are almost flat regions that consist of annulated aromatics, double bonds and epoxy groups. On the other hand there are hydroxyl-groups that cause wrinkles. There are also carboxylic acid groups at the edges of the sheets that can introduce charge in the graphite plane in their deprotonated state. Moreover, this model describes the low reactivity of epoxy-groups that was discussed in former times. Due to the negatively charged sheets and the oxygen functionalities on both sides of the sheets, a reaction with nucleophiles is almost not possible.

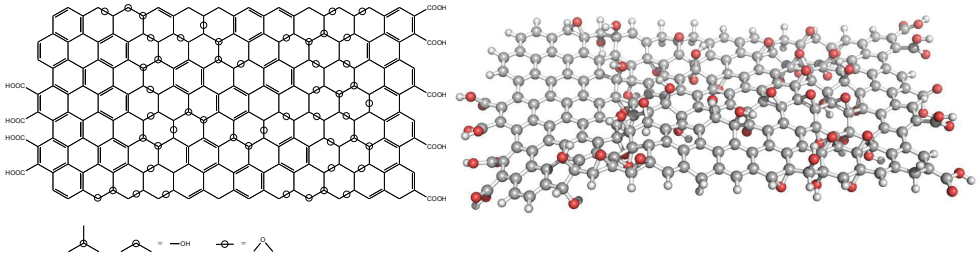

Fig. 2. A) Lerf-Klinowski structure model of graphite oxide; this model is supported by current investigations, reproduced (Lerf et al., 1998). B) Semiempirical AM1-optimized 3D-Lerf-Klinowski model.

2.7 The way to graphene oxide, reduced graphene oxide and graphene

When one considers the development of oxidized graphite, the question is at what time the transition from graphite oxide to graphene oxide and finally to isolated graphene happened. It was noted that solvent molecules can intercalate graphite oxide which leads to an expansion of the layers. Thereby the sheet distance can increase up to 15 Å for dioxane intercalated graphite oxide. Moreover, water at basic pH can further increase the sheet distance and it was supposed that graphite oxide exfoliates to single sheets, now called graphene oxide, a two dimensional macromolecule (Ruess, 1947).

The next step to graphene sheets was the thermal decomposition of graphite oxide at a rapid temperature increase to 300 °C. A volume increase by a factor of 500 was described and that material was further cocked to yield a carbon material of more than 99 % purity. It was concluded from electron microscopy that the yielded material consists of few layers only (Ruess & Vogt, 1948). Such a material is now named reduced graphene oxide.

Then, it were Boehm, Clauss, Fischer and Hofmann who did experiments with graphite oxide, that was exfoliated in diluted alkaline solution. Such conditions lead to graphene oxide, and they used hydrazine hydrate as reducing agent to yield reduced graphene oxide that consisted of 2-3 layers in average according to their analysis. This does not exclude single layers and single reduced graphene oxide was very likely observed by electron microscopy. Further their preparation method is now known to yield single sheets of reduced graphene oxide. But reduced graphene oxide is graphene with a variety of defects and only graphene free from defects exhibits exceptional physics (Boehm et al., 1962).

The next step was made by the group of Ruoff in 1999, who manipulated graphite islands by atomic force microscopy and they dangled the isolation of graphene (Lu et al., 1999). In 2003 it were Gan et al. in Beijing who exfoliated the single layer graphene from graphite by STM and verified it (Gan et al., 2003). In 2004 few layer graphene, about three layers, was grown from SiC and the beginning was laid for the application of graphene and few layer graphene in electronic devices (Berger et al., 2004).

The simplest method for preparing high quality graphene and the breakthrough for the discovery of the properties of graphene was published in 2004 by the Group of Geim in Manchester. They used adhesive tape to exfoliate graphene from graphite (Novoselov et al., 2004). Now it is possible to identify single sheets even by optical methods using e.g. 300 nm SiO_2 dielectric on Si substrates (Casiraghi et al., 2007; Roddaro et al., 2007).

3. Preparation methods for graphene

In the literature, it is not strictly separated between graphene, few layer graphene, reduced graphene oxide, graphene with a certain amount of defects and perfect graphene. The term graphene is generally used for one layer of carbon with a high carbon content, generally higher than 90 %.

3.1 Mechanical cleavage

One of the best qualities of isolated graphene is yielded by mechanical exfoliation using adhesive tape to overcome the van der Waals interaction energy for exfoliation. This exfoliation process must be repeated several times to obtain few layered graphene sheets that can be transferred on the desired substrate by gently pressing the tape. This method suffers from scaling problems and only μm^2 pieces can be prepared but this method is essential for fundamental studies. Besides, the obtained graphene is contaminated by the glue and must be removed before usage.

3.2 Decomposition of silicon carbide

A high temperature process is described using silicon carbide wafer in high vacuum. At about 1300 °C silicon sublimates and graphitization of the remaining carbon can take place to form graphene. At higher temperatures of about 1650 °C the decomposition takes also place in an argon atmosphere and graphene can be obtained. The quality is slightly worse than for mechanically processed material as it was judged from charge carrier mobility (Soldano et al., 2010).

3.3 Graphitization of small molecules

Another method is the growth of graphene on metal surfaces from small molecules. Mostly used molecules are methane and acetylene. Platinum, ruthenium, iridium, nickel or copper are suitable substrates. This method also needs high temperatures in the range of 900-1100 °C. There is also a strong interaction between graphene and the metal surface, making an etching process necessary to remove the metal and make it possible to transfer graphene to another substrate (Soldano et al., 2010). In a recent approach copper with large grain was used as the substrate and a 30-inch graphene sheet was prepared (Bae et al., 2010). A methane/hydrogen mixture was used to grow graphene at 1000 °C. Several transfer steps were necessary to isolate graphene. First, a transfer tape was applied on graphene and then copper was etched away. Second, graphene was transferred to a PET substrate at elevated temperatures. This process can be repeated to prepare few layer graphene on arbitrary substrates.
In the group of Muellen graphenes are prepared in a bottom-up approach by chemical total synthesis. These nano-graphenes are processible, e.g. hexadodecyl-substituted super-phenalene C_{96}-C_{12}. In a second step, annealing at 1100 °C is necessary for graphitization to gain an electrically conductive material (Wang et al., 2008b).

3.4 Exfoliation of graphite

In another approach graphite is the starting material and in the first step an intercalation compound is prepared. Commonly, nitric or sulphuric acid are suitable for the intercalation of graphite. As a consequence, the sheet distance increases and it becomes easier to intercalate other reagents that make the exfoliation possible. A thermal shock, heating to 800-1100 °C, causes the decomposition of the intercalated acid and the exfoliation takes place. Such materials can be dispersed as single layers in suitable solvents, as N-methyl-2-pyrrolidon, dimethylformamide, 1,2-dichloroethane or chloroform. Some examples are available were polymeric stabilizer or surfactants (e.g. sodium dodecylbenzenesulfonate) were used to increase the concentration of dispersed graphene. In almost all examples the dispersions are sonicated to increase single layer yield or to prevent aggregation (Compton & Nguyen, 2010; Cravotto & Cintas, 2010; Soldano et al., 2010).
Besides, potassium intercalated graphite KC_8 is a prominent stage-1 intercalation compound that readily exfoliates in N-methyl-2-pyrrolidon without sonication to form stable dispersions (Vallés et al., 2008). Sonication is also not necessary if graphite is treated with chlorosulfonic acid for several days. That solvent turned out to be a suitable solvent that causes spontaneous exfoliation to graphene sheets (Behabtu et al., 2010).

3.5 Reduction of graphene oxide

Another precursor compound of graphene is graphene oxide. The oxidation of graphite to graphene oxide provides the possibility of applying a rich chemistry to that class of material

that is not possible in other methods. Another advantage is the possibility for processing graphene oxide or chemically functionalized graphene oxide dispersions from solution to match common coating techniques. In addition, using graphene oxide makes large-scale production of electroactive materials possible. Graphene oxide itself is not electrically conductive and a further processing step is necessary to recover the conductivity. A broad set of reductive agents is available for the reduction or deoxygenatation of graphene oxide derivatives. Examples are hydrazine, hydrazine monohydrate, dimethylhydrazine, sodium boron hydride, sodium hydride, hydrochinone, p-phenylene diamine, strongly alkaline solution, supercritical water, H_2-plasma, electrochemical reduction, photocatalytic reduction and others (Eda & Chhowalla, 2010). In addition, it is possible to reduce graphene oxide in solution, e.g. water. Since reduced graphene oxide aggregates in aqueous solution a stabilizer is necessary to form reduced graphene dispersions. That can be achieved by adding surfactants, e.g. sodium 4-styrenesulfonate or ionic liquids (Zhang et al., 2010). The addition of base to deprotonate carboxylic acids of graphene oxide causes electrostatic repulsion and thus stabilization during reduction. Non-covalent interactions of aromatic molecules can also be used to stabilize reduced graphene oxide, e.g. pyrene-1-sulfonic acid. Furthermore, graphene oxides functional groups can react with a variety of reagents to form covalent bonds to amines, alcohols and others. These new functional groups remain stable during reduction and help stabilizing dispersions (Compton & Nguyen, 2010; Loh et al., 2010).

3.6 The structure of reduced graphene oxide

The oxidation/reduction process of graphene oxide is not a reversible one and the honeycomb lattice is not recovered. Amongst other properties, the electrical conductivity of reduced graphene oxide lags behind graphene prepared by mechanical cleavage or chemical vapour deposition (CVD). The reason for this is the defective structure of reduced graphene oxide. Gómez-Navarro et al. utilized high-resolution transmission electron microscopy at 80 keV to visualize the structure of reduced graphene oxide at atomic resolution. In this case hydrogen plasma was used for the reduction followed by annealing.

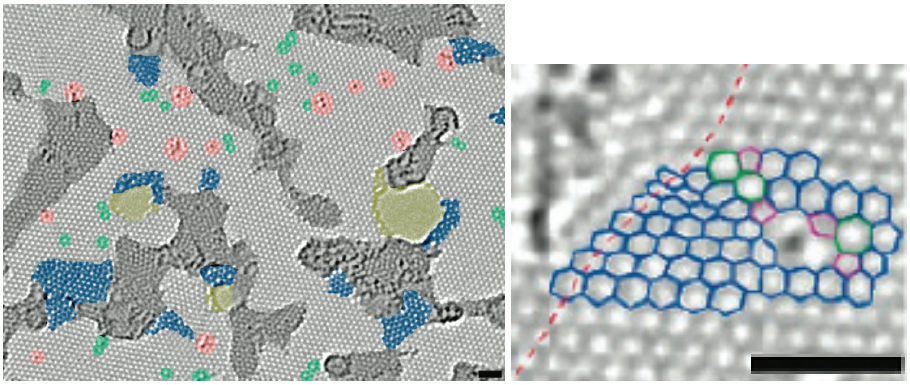

Fig. 3. A) Structure of reduced graphene oxide; grey: preserved structure, dark grey: contaminated area, yellow: holes with edge reconstructions, blue: distorted region, red: added or substituted atoms, green: isolated single bond rotations or dislocation cores. B) distorted region; scale bar 1 nm (Gómez-Navarro et al., 2010). Reprinted with permission from Gómez-Navarro et al., 2010. Copyright 2010 American Chemical Society.

Hence, different types of defects can be distinguished. Beside holes and reorganized edges (yellow) preserved regions of the original graphene lattice (grey) could be identified. These regions are sometimes disturbed by adjacently defects due to isolated pentagon/heptagon defects (green) and isolated defects caused by added or substituted atoms (red). Moreover, there are contaminated regions (dark grey) and distorted regions (blue). Especially these distorted regions cause strain combined with in- and out-of-plane defects. In addition, the Bernal AB stacking is not preserved and turbostratic stacking is favoured for few layer reduced graphene oxide (Gómez-Navarro et al., 2010).
Keeping the different preparation methods in mind, it is conceivable that the electrical properties of the obtained graphene are different. Hence, the quality of graphene and few layer graphene is dependent on the number and type of defects. One can image the manifold possibilities for oxidation and reduction procedures and the involved electrical conductivity. The described preparation methods are used for transparent and electrically conductive thin films (TCFs). The performance of these thin films is very different with respect to transparency and sheet resistance. Because of that, methods were developed to characterize the electrical performance of reduced graphene oxide, graphene and other electrically conductive and transparent materials.

4. Characterization of transparent and electrically conductive thin films

4.1 Determination of the electrical conductivity and transparency

For the characterization of electrically conductive materials it is necessary to measure current and voltage at a given distance to determine the resistance of the sample. The two-point probe measurement uses this method but the measured value includes e.g. the contact resistance between the metal electrode and the sample. To eliminate such uncertainties the four-point probe method is used (Topsoe, 1968).

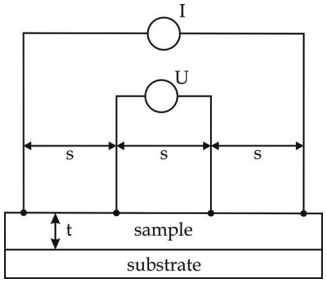

U: measured voltage
I: measured current
s: probe distance
t: thickness of the sample

Fig. 4. Illustration of the four-point probe measurement setup

If the four probes are equal in distance and the sheet thickness is much smaller than the probe distance, the sheet resistance can be expressed with the following term:

$$R_s = \frac{\pi}{\ln 2} \cdot \frac{U}{I} \tag{1}$$

R_s: sheet resistance; U: voltage; I: current.
With the help of the sheet resistance and measurement of the thickness of the sample it is possible to calculate the electrical conductivity. It is the reciprocal of the product of the sheet resistance and the thickness of the sample given in S/cm.

$$\sigma = \frac{1}{R_s \cdot t} \tag{2}$$

σ: electrical conductivity; R_s: sheet resistance; t: thickness of the sample.
For characterizing electrically conductive and transparent materials it is certainly necessary to determine the transparency what is accomplished by UV-Visible spectroscopy. For optical applications it is reasonable to measure the transparency in the visible region. Hence, it is best measured at the wavelength where the human eye is most sensitive, at 550 nm.

4.2 Comparing the performance of transparent and conductive materials

On the one hand the sheet resistance is measured in Ω or in Ω/sq to illustrate the given surface resistance. On the other hand the transparency is given in % or %T. It is obvious to combine both independent parameters to get one value for comparison. In 1972 Fraser & Cook prepared ITO coatings and introduced a figure of merit (FOM) to compare the performance of differently prepared coatings (Fraser & Cook, 1972).

$$FOM_1 = \frac{T}{R_s} \tag{3}$$

The disadvantage of this definition is that the performance is the same for a coating of 95 %T/95 Ω and 85 %T/85 Ω. The determined FOM_1 is 1 in both cases but certainly it is not. Spath et al. described a further improvement in 2006. The advantage is using the logarithm of the transparency for the determination of the figure of merit (Spath et al., 2006). Budhadipta et al. described a similar method in 2009. In this case the sheet resistance and the logarithm of the transmission are multiplied.

$$FOM_2 = -\ln\left(\frac{I}{I_0}\right) \cdot R_s = \rho\varepsilon \tag{4}$$

ε: extinction coefficient; ρ: material resistivity.
This FOM is the product of the material resistivity and the extinction coefficient of the material and both of them are generally not known.
For the example above this means a FOM_2=4.87 for 95 %T/95 Ω and a FOM_2=13.8 for 85 %T/85 Ω. In this case the smaller the value of the FOM the higher is the performance and the better performance of the first example becomes evident.
The "conductivity of transparency" or "transparence conductance" was defined in 2009, a similar approach compared to Budhadipta et al. but utilizing the transparency of a reference material to determine an ideal thickness of the sample (Eigler, 2009).
In 2008, Nair et al. published the transparency of single and few layer graphene. Each layer absorbs 2.3 % of white light and the Lambert–Beer law is fulfilled, even if it is defined for low concentrations where molecules do not interact with each other. According to equation 2 and using graphene as the ideal reference material the conductivity of transparency can be defined as the reciprocal of the sheet resistance and the ideal thickness of the sample.

$$\sigma_{gt} = \frac{1}{R_s \cdot t_{ideal}} \tag{5}$$

σ_{gt}: conductivity of transparency based on graphene at 550 nm; R_s: sheet resistance of a transparent conductive sample; t_{ideal}: thickness of the sample based on the transparency of the sample and the ideal sheet distance in graphite.
The ideal thickness is that one that corresponds to the transparency of graphene.
Differently prepared coatings consisting of different qualities of graphene should become comparable, even if the thickness of the sample is unknown. First of all, the absorption coefficient is calculated using the Bouguer–Lambert law that is given by:

$$\lg\left(\frac{I}{I_0}\right) = \varepsilon ct; \quad \varepsilon^* c = \varepsilon_{graphene} \tag{6}$$

ε^*: extinction coefficient; c: concentration; t: pathway of the light; $\varepsilon_{graphene}$: absorption coefficient of graphene; I: transmission in %; I_0: transmission (100%: no absorption).
The absorption coefficient is dependent on the intensity change of the light, the length of the pathway, and the concentration. For graphene the concentration is constant. In this case there is no dependence on the concentration because the perfect graphene structure has no variable concentration. Further, the sheet distance of graphite is well known to be 335 pm. From these data it is possible to calculate the absorption coefficient of graphene to 301655 cm^{-1} by Eq. (7):

$$\varepsilon_{graphene} = \frac{-\lg\left(\frac{I}{I_0}\right)}{t_{graphite}} = \frac{-\lg\left(\frac{97.7\%}{100\%}\right)}{3.35 \cdot 10^{-8} cm} = 301655 cm^{-1} \tag{7}$$

Even if the examined transparent sample is not perfect an ideal thickness can be calculated from Eq. (8):

$$t_{ideal} = \frac{-\lg\left(\frac{I}{I_0}\right)}{\varepsilon_{graphene}} \tag{8}$$

It corresponds to the thickness of ideal graphene sheets and in the case of several sheets they are also packed perfectly. Finally, the conductivity of transparency of a transparent sample can be calculated by the combination of equation 6 and 9:

$$\sigma_{gt} = \frac{\varepsilon_{graphene}}{-\lg\left(\frac{I}{I_0}\right) \cdot R_s} = \frac{301655 cm^{-1}}{-\lg\left(\frac{I}{100\%}\right) \cdot R_s} \tag{9}$$

It should be noted that σ_{gt} differs from the conductivity σ due to imperfections, e.g. interlayer distance, defects, intercalation of impurities or doping that can generally influence optical and electrical properties. Nevertheless, from a practically point of view, the real thickness of a transparent coating is not so important. For the example above this means σ_{gt} =1.4x10^5 S/cm for 95 %T/95 Ω and σ_{gt} =5.0x10^4 S/cm for 85%T/85 Ω.
For comparing different electrically conductive and transparent thin films the figure of merit approach using the logarithm of the transparency is sufficient. In our example it is clear that

the performance of the first one is almost three times higher compared to the second one. The advantage of using graphene as the reference material is to get a conductivity value that can be compared with graphene.
Blake et al. specify the sheet resistance of undoped graphene to about 6000 Ω, which results from one conductivity quantum per species of charge carrier (Blake et al., 2008). Moreover one sheet absorbs 2.3 % of white light. From these values σ_{gt} can be calculated to 5000 S/cm. The σ_{gt} is not limited to this value, e.g. if any coating absorbs 2.3 % of light but the sheet resistance is 500 Ω a σ_{gt} of 6.0×10^4 S/cm is obtained, which means that the conductivity of that coating is 12 times higher than that of a single graphene sheet. Because of that, the conductivity of transparency based on graphene is not limited to carbon materials. It can be extended to all transparent and conductive materials. As a consequence their conductivity is based on the conductivity and transparency of graphene and that is true at least for carbon-based materials that derive from graphene. Now it is possible to obtain not only a figure of merit but also a conductivity that can be compared with the bulk conductivity of other materials with knowing the transparency of the sample and without knowing the thickness.
In the following, this concept is applied to several recently published examples dealing with graphene and other transparent materials.

4.3 Correlation between the bulk conductivity and the conductivity of transparency for chemically derived graphene

In Table 1 typical values of σ_{gt} are summarized that result from 80, 90, and 98 %T at different sheet resistances to illustrate σ_{gt} values. E.g. a σ_{gt} of about 3000 S/cm is necessary to prepare coatings with a sheet resistance of 1000 Ω with 80 %T.

R_s (Ω)	10	100	500	10^3	10^4	10^5	10^6	10^7
σ_{gt} (S/cm) at 80 %T	3.1×10^5	3.1×10^4	6.2×10^3	3.1×10^3	3.1×10^2	31	3.1	0.31
σ_{gt} (S/cm) at 90 %T	6.6×10^5	6.6×10^4	1.3×10^4	6.6×10^3	6.6×10^2	66	6.1	0.61
σ_{gt} (S/cm) at 98 %T	3.4×10^6	3.4×10^5	6.9×10^4	3.4×10^4	3.4×10^3	3.4×10^2	34	3.4

Table 1. σ_{gt} at a transparency at 80, 90 and 98 %T in dependence of R_s.

Becerril et al. published a study of differently treated graphene oxide (Table 2). Graphene oxide itself is highly transparent and $\sigma_{gt} = 5.7 \times 10^{-5}$ S/cm that is about one order of magnitude higher than the bulk conductivity $\sigma_{gt} = 3.7 \times 10^{-6}$ S/cm. If graphene oxide is reduced with hydrazine, the conductivity increases by four orders of magnitude and σ_{gt} increases about three orders of magnitude. After treatment with hydrazine at 400 °C the conductivity and σ_{gt} differ by a factor of about 3. After heating GO in vacuum at 1100 °C the conductivity increases to 1.7×10^2 S/cm and the σ_{gt} is 6.5 times higher. In general the σ_{gt} values are higher than the σ values, possibly due to an increased transparency caused by, e.g. residual functional groups or possibly doping (Becerril et al., 2008).
According to investigations from Mattevi et al. the transparency of graphene oxide changed from 87 to 84 % during annealing between 200 and 1000 °C, a change of about 4 % (Mattevi et al., 2009). Assumedly, the difference between the bulk conductivity and the conductivity

of transparency for few layer coatings of reduced graphene oxide is attributed to the non-ideal sheet distance. It is well known that the sheet distance for reduced graphene oxide is higher, about 0.8 nm, due to residual functional groups or impurities, compared to few layer graphene (0.34 nm). So, the difference in the sheet distance should correlate well to the difference between bulk conductivity and the conductivity of transparency.

GO treated	not reduced	hydrazine	hydrazine 400 °C	vacuum 1100 °C
t (nm)	9	5	3	8
%T (550 nm)	96	92	93	92
R_s (Ω)	3.0×10^{11}	1.4×10^{8}	2.6×10^{5}	7400
σ (S/cm)	3.7×10^{-6}	1.4×10^{-2}	13	170
σ_{gt} (S/cm)	5.7×10^{-5}	5.9×10^{-2}	37	1100

Table 2. Comparison of the thickness, transparency, sheet resistance, conductivity and conductivity of transparency of differently treated graphene oxide (Becerril et al., 2008).

5. The performance of chemically derived graphene

Since 2008 the interest in conductive and transparent materials based on graphene increased and several preparation methods were developed. In many cases reduced graphene oxide was used. Moreover, chemical vapour deposition techniques and dispersed graphene are described and graphene was prepared from small molecules. Besides, graphene material was combined with several other materials to enhance the conductivity of transparency. In this chapter the performance of coatings derived from these materials will be compared with other materials as poly(3,4-ethylenedioxythiophene)/poly(4-styrenesulfonate) (PEDOT/PSS), single wall carbon nanotubes (SWCNTs), multi wall carbon nanotubes (MWCNTs), silver nanowires (AgNWs) and indium tin oxide (ITO).

5.1 The performance of reduced and low temperature annealed graphene oxide

Graphene oxide is a long known material and the preparation is well controlled. The great advantage of graphene oxide over other materials is its versatility that is reflected in more

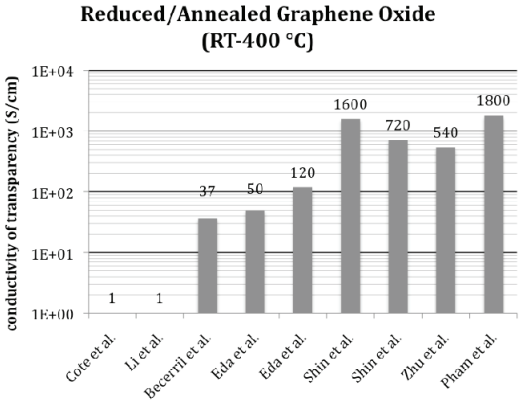

Fig. 5. Comparison: conductivity of transparency for reduced and annealed graphene oxide below 550 °C.

than thousand publications since 2009 from many disciplines. One discipline is its possibility of processing graphene oxide in thin films with a thickness from one layer to few layers that remain transparent upon reduction.

Thin films of graphene oxide can be deposited on transparent substrates, as glass by common techniques, e.g. by spin- or bar-coating, drop-casting, dipping, filtration and transfer printing.

In 2008 Cote et al. prepared Langmuir-Blodgett monolayer films from graphene oxide. Moreover they succeeded in preparing an overpacked film to provide a conduction pathway and reduced it by hydrazine vapour to yield a conductive film with a transparency of more than 95 % (Cote et al., 2009).

Reference	%T (550 nm)	R_s (Ω)	σ_{gt} (S/cm)
Cote et al.	95	$1.9x10^7$	1
Li et al.	96	$2.0x10^7$	1
Becerril et al.	93	$2.6x10^5$	37
Eda et al.	87	$1.0x10^5$	50
Eda et al.	65	$1.4x10^4$	120
Shin et al.	83	2300	1600
Shin et al.	83	5200	720
Zhu et al.	96	$3.2x10^4$	540
Pham et al.	84	2200	1800

Table 4. Comparison: transparency, sheet resistance and conductivity of transparency for reduced and annealed graphene oxide below 550 °C.

The conductivity of transparency was about 1 S/cm. Li et al. who reduced graphene oxide in an alkaline dispersion achieved a similar performance and spray coated reduced graphene oxide on glass (Li et al., 2008a). Becerril et al. deposited graphene oxide on glass slides and used hydrazine vapour for the reduction and annealed at 400 °C. As a consequence, the conductivity of transparency increased to 37 S/cm (Becerril et al., 2008). Eda et al. also used the combination of hydrazine reduction and thermal annealing and achieved 50 S/cm. A subsequent $SOCl_2$ p-type doping procedure increased the performance to 120 S/cm (Eda et al., 2008a; Eda et al., 2008b). Shin et al. utilized sodium boron hydride as reducing agent. They dipped coated glass in a solution of the reducing agent for several days and they achieved a σ_{gt} of 720 S/cm, which could be improved to 1600 S/cm by adding a layer of $AuCl_3$ as dopant (Shin et al., 2009a; Shin et al., 2009b). An assumedly highly ordered film was obtained by Zhu et al. who utilized the air-liquid interface to isolate few layer hydrazine reduced graphene oxide from the liquid surface and transferred it on glass. Despite the low temperature process the conductivity of transparency is about 500 S/cm (Zhu et al., 2009). An even better performance was achieved in 2010 by Pham et al. who described a spray-coating procedure for the coating of preheated glass. Hence, glass slides were heated to 240 °C and a hydrazine treated graphene oxide dispersion diluted in water/ethanol was sprayed on it. The conductivity of transparency can be calculated to 1800 S/cm, one of the highest values for reduced graphene oxide treated at a moderate temperature (Pham et al., 2010).

These examples demonstrate the increasing performance of reduced graphene oxide as transparent and conductive coatings. This development just started a few years ago and

there is currently tremendous research done. But even if the performance increase from 1 to almost 2000 S/cm is impressive it becomes evident that the chemical distortions caused by the oxidation and reduction procedure limits the performance. Moreover the charge transport is certainly another one compared to graphene obtained by mechanical cleavage. Using such coatings e.g. for touch screen application the minimum demands are 3000 S/cm or even more. To further improve the quality of graphene derived from graphene oxide a high temperature-annealing step is often desired.

5.2 The performance of reduced and annealed graphene oxide

To enhance the properties of reduced graphene oxide a high temperature-annealing step is often involved in the preparation of transparent and conductive coatings. In most cases quartz glass is necessary to apply temperatures within the range of 700-1100 °C.

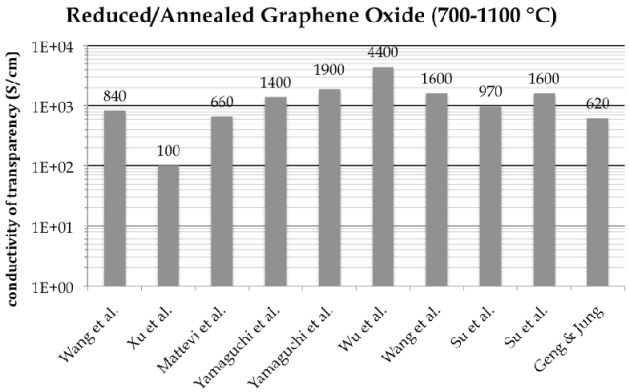

Fig. 6. Comparison: conductivity of transparency for reduced and annealed graphene oxide between 700 and 1100 °C.

Reference	%T (550 nm)	R_s (Ω)	σ_{gt} (S/cm)
Wang et al.	63	1800	840
Xu et al.	69	$1.8x10^4$	100
Mattevi et al.	84	6000	660
Yamaguchi et al.	81	2400	1400
Yamaguchi et al.	70	1000	1900
Wu et al.	82	800	4400
Wang et al.	80	2000	1600
Su et al.	70	2000	970
Su et al.	68	1100	1600
Geng & Jung	80	5000	620

Table 4. Comparison: transparency, sheet resistance and conductivity of transparency for reduced and annealed graphene oxide between 700 and 1100 °C.

In 2007/2008 Wang et al. published a transparent and conductive electrode with the scope of using it for solar cells. Therefore graphene oxide was annealed at 1100 °C (Wang et al., 2008a) and the conductivity increased five times during heating from 700 to 1100 °C and a final conductivity of transparency of 840 S/cm was obtained. However Xu et al. annealed hydrazine reduced graphene oxide at 700 °C and a moderate σ_{gt} of 100 S/cm was obtained (Xu et al., 2010). In 2009 Mattevi et al. annealed graphene oxide coatings at 1100 °C in a reducing atmosphere (H_2/Ar) and achieved 660 S/cm (Mattevi et al., 2009). A better performance was obtained in 2010 from Yamaguchi et al. for spin-coated graphene oxide on 300 mm wafers followed by either hydrazine reduction and thermal annealing or thermal annealing only. It was stated that a similar performance is obtained and the conductivity of transparency can be calculated to 1400 and 1900 S/cm, respectively for different samples. A much higher performance of 4400 S/cm was achieved by Wu et al. after annealing graphene oxide three hours at 1100 °C. It seems that a certain amount of defects could be repaired during that elongated thermal annealing procedure (Wu et al., 2010). Next, Wang et al. first reduced graphene oxide in alkaline solution by hydrazine and prepared thin films by filtration followed by transferring them on quartz glass and subsequent annealing at 1100 °C for 30 minutes. In this case the conductivity of transparency was 1600 S/cm (Wang et al., 2010). Another approach was to reduce a mixture of graphene oxide and pyrene-1-sulfonic acid sodium salt prior to hydrazine reduction followed by thermal annealing of thin films at 1000 °C. The anionic pyrene derivative acts first as a stabilizing agent and during thermal annealing as a nonographene material that can be graphitized. Indeed an increased performance from 970 to 1600 S/cm is found due to the addition of a nanographene derivative (Su et al., 2009). A similar approach is described by Geng & Jung who used the tetrasulfonated porphrin (TPPS) as stabilizing agent. Their transparent films were annealed at 800 °C resulting in a conductivity of transparency of 620 S/cm (Geng & Jung, 2010).
In every case slightly different preparation conditions for graphene oxide are described and there are many parameters altered from example to example. Some of the approaches exhibit advantages in terms of processing others benefit from an increased performance. Evident is the high performance from Wu et al. who annealed for three hours and yielded a performance close to pristine undoped graphene. The performance of the other examples is similar to reduced graphene oxide that was processed at a much lower temperature.

5.3 The performance of graphene obtained from graphite

The processing of graphene oxide is a versatile method, but due to imperfections occuring during oxidation and reduction the performance lags behind prisitine graphene. Hence, researcher try to avoid oxidation of graphite and prefer direct processing. One essential challenge is the solubilization and exfoliation of graphite to single layers.
Blake et al. did not solubilize graphite and their approch is not a chemical one, but they used mechanical exfoliation to obtain graphene directly from graphite. For undoped graphene σ_{gt} of about 5000 S/cm was found and they demonstrated a dramatically increased performance to 8.6×10^4 S/cm due to doping by polyvinyl alcohol (Blake et al., 2008). These promising results make it attractive to utilize graphite without oxidation. The drawback is the insolubility of graphite in water and common organic solvents that has to be overcome.
In 2008 Hernandez et al. demonstrated the dispersibility of graphite in *N*-methyl-2-pyrrolidone (NMP) upon sonication and they yielded graphene and few layer graphene.

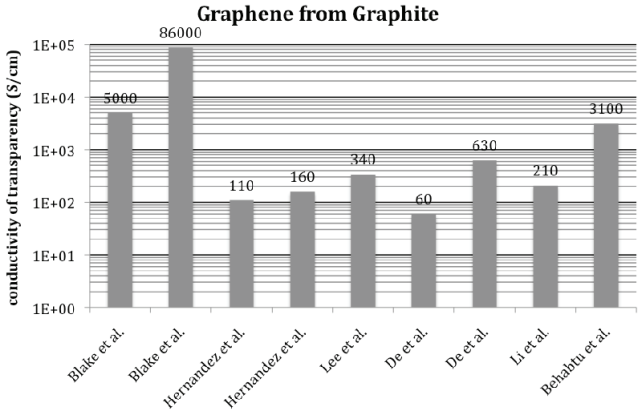

Fig. 7. Comparison: conductivity of transparency for transparent coatings derived from exfoliated graphite.

Reference	%T (550 nm)	R_s (Ω)	σ_{gt} (S/cm)
Blake et al.	98	6000	5000
Blake et al.	98	400	$8.6x10^4$
Hernandez et al.	42	7100	110
Hernandez et al.	42	5100	160
Lee et al.	79	8500	340
De et al.	68	$3.0x10^4$	60
De et al.	76	4000	630
Li et al.	85	$2.0x10^4$	210
Behabtu et al.	80	1000	3100

Table 5. Comparison: transparency, sheet resistance and conductivity of transparency of transparent coatings derived from exfoliated graphite.

Despite the concentration of graphene in NMP was 0.01 mg/ml only, it was possible to prepare films. After annealing these films at 300 °C or in a reductive atmosphere at 250 °C the performances were 110 and 160 S/cm, respectively. Even if the quality of the deposited graphene and few layer graphene was high the performance was expected to be better and NMP trapped between the sheets was likely the reason for it (Hernandez et al., 2008). In 2010 Lee et al. described a procedure to exfoliate graphite by thermal shock at 700 °C from ClF_3 intercalated graphite. In a second step that material could be dispersed in NMP and thin films were formed by filtration and a subsequent transfer process yielded thin films on the transparent substrate. In this case a conductivity of transparency of about 300 S/cm can be calculated (Lee et al., 2010). Sodium cholate was used by De et al. as a surfactant for

graphite and after sonication stabilized graphene and few layer graphene were obtained. Transparent and conductive films were obtained by a filtration method as well. The conductivity of transparency for as prepared films was 60 S/cm and the performance could be enhanced to 630 S/cm by thermal treatment at 500 °C due to assumedly reorganization (De et al., 2009b). A more sophisticated approach was done by Li et al. who used thermal shock exfoliated graphite and intercalated it with oleum. After removal of the acid the pretreated graphite was reinercalated with terabutyl ammonium ions (TBA^+) in DMF with the aid of sonication. Predominantly single layers were finally obtained by sonication with a pegylated phospholipid. Transparent films were obtained with the help of Langmuir-Blodgett techniques, providing a σ_{gt} of 210 S/cm (Li et al., 2008b). Behabtu et al. describe the best performance for transparent and electrically conductive coatings in 2010. They used chlorosulphonic acid as the solvent and observed intercalation and spontaneous exfoliation of graphite. Moreover they succeeded in preparing transparent coatings by a filtration method and the conductivity of transparency is 3100 S/cm, at least five times better compared to the other examples (Behabtu et al., 2010).
It can be seen from these examples, even if graphite is not oxidized the performance in transparent and conductive films is not much better, or even worse compared to films obtained by processing graphene oxide.

5.4 The performance of graphene from small molecules and hybrid materials

As described before, graphene can be obtained from graphene oxide by high temperature processes as decomposition product. Not only graphene oxide can be used as precursor compound but also other small molecules. Moreover, the combination of graphene with carbon nanotubes provides materials of very high performance.

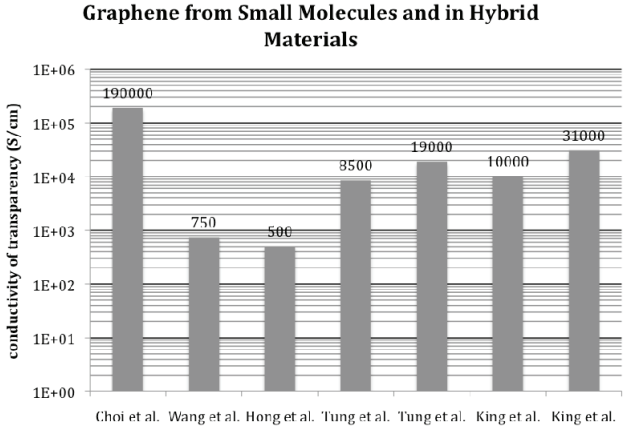

Fig. 8. Comparison: conductivity of transparency for transparent coatings derived from small molecules or hybrid materials.

Reference	%T (550 nm)	R_s (Ω)	σ_{gt} (S/cm)
Choi et al.	92	43	$1.9x10^5$
Wang et al.	56	1600	750
Hong et al.	84	8000	500
Tung et al.	86	240	$1.9x10^4$
Tung et al.	88	636	8500
King et al.	80	300	$1.0x10^4$
King et al.	80	100	$3.1x10^4$

Table 6. Comparison: transparency, sheet resistance and conductivity of transparency of transparent coatings derived from small molecules or hybrid materials.

One exceptional example was described in 2009 by Choi et al. who used Langmuir-Blodgett techniques to prepare thin films of oleic acid. These films were deposited on substrates coated with a nickel catalyst for graphitization. The thin oleic acid films were graphitized at 500 °C and a coating with a sheet resistance of 43 Ω at a transparency of 92 % was obtained, what corresponds to σ_{gt}=1.9x10^5 S/cm (Choi et al., 2009). The performance of that coating is up to 40 times better compared to undoped graphene and more than two times better compared to doped graphene flakes described by Blake et al. earlier. Wang et al. used the processible nanographenemolecule hexadodecyl-substituted superphenalene C_{96}-C_{12} as precursor molecule for thin coatings. They prepared an electrode for solar cells by annealing at 1100 °C with a conductivity of transparency of 750 S/cm (Wang et al., 2008b).

Another approach is to use a combination of several transparent and conductive materials. Thus, Hong et al. combined multi wall carbon nanotubes (MWCNTs) with reduced graphene oxide. They used layer-by-layer assembly to make sheets from cationic functionalized MWCNTs and negatively charged graphene sheets with σ_{gt}=500 S/cm (Hong et al., 2010). Instead of MWCNTs Tung et al. used single wall carbon nanotubes (SWCNTs) in combination with hydrazine reduced graphene oxide and they prepared coating with a performance of 8500 S/cm and 1.9x10^4 S/cm, respectively for doped coatings (Tung et al., 2009). King et al. used SWCNTs in combination with 3 % graphene obtained from sodium cholate exfoliated graphite. They prepared transparent films with a performance of about 1.0x10^4 and 3.1x10^4 S/cm for acid treated films, respectively (King et al., 2010).

5.5 The performance of graphene from chemical vapour deposition

As shown before, it is possible to use several types of precursor molecules for graphene, as graphene oxide, nanographenes or oleic acid. CVD utilizes even smaller molecules, mostly a mixture of methane and hydrogen. Additionally, a catalyst is necessary and nickel or copper turned out to work well between 900 and 1000 °C. The advantage of CVD is the preparation of continuous graphene and few layer graphene films instead of graphene flakes as it is the case for other methods.

The CVD method is not compatible with temperature sensitive substrates, so the prepared graphene film is transferred on the desired substrate. In some cases the graphene films are not perfect and additional cracks are formed during procesing. Juang et al. described a roll-to-roll process and finally a randomly stacked graphene structure is obtained with a conductivity of transparency of only 390 S/cm (Juang et al., 2010). Park et al. describe a

procedure that yields contineous inhomogeneous films with a flake structure and σ_{gt}=5000 S/cm (Park et al., 2010b). Similar results are described by Reina et al. with a conductivity of transparency of 7800 S/cm. Kim et al. and Choi et al. describe a better performance of 1.1x10^4 and 1.2x10^4 S/cm, respectively (Kim et al., 2009; Choi et al., 2010).

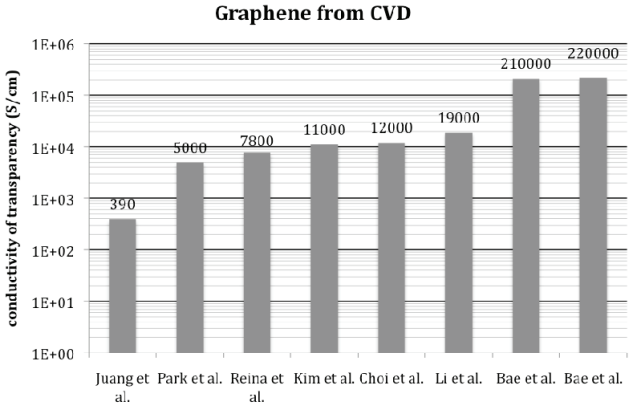

Fig. 9. Comparison: conductivity of transparency for transparent coatings from chemical vapour deposition.

These examples demonstrate the performance of the method. Even better results are obtained by switching from nickel to copper substrates. Li et al. demonstrate the crack free transfer of grown graphene films from copper to PMMA and from PMMA to the desired transparent substrate. These films with an area of 20 cm^2 are highly uniform and the conductivity of transparency is 1.9x10^4 S/cm (Li et al., 2009). Bae et al. described the largest 30-inch uniform nitric acid doped graphene films with a performance of 2.1 and 2.2x10^5 S/cm, about one order of magnitude better compared to previously described results (Bae et al., 2010).

Reference	%T (550 nm)	R_s (Ω)	σ_{gt} (S/cm)
Juang et al.	53	2800	390
Park et al.	84	800	5000
Reina et al.	88	700	7800
Kim et al.	80	280	1.1x10^4
Choi et al.	75	200	1.2x10^4
Li et al.	90	350	1.9x10^4
Bae et al.	90	30	2.2x10^5
Bae et al.	97	125	2.1x10^5

Table 7. Comparison: transparency, sheet resistance and conductivity of transparency of transparent coatings derived from chemical vapour deposition.

5.6 The conductivity of transparency of competing materials

Several groups already demonstrated the superior conductivity of transparency of graphene thin films. But graphene thin films are in competition with other materials, as electrically conductive polymers derived from PEDOT, MWCNTs, SWCNTs and AgNWs.

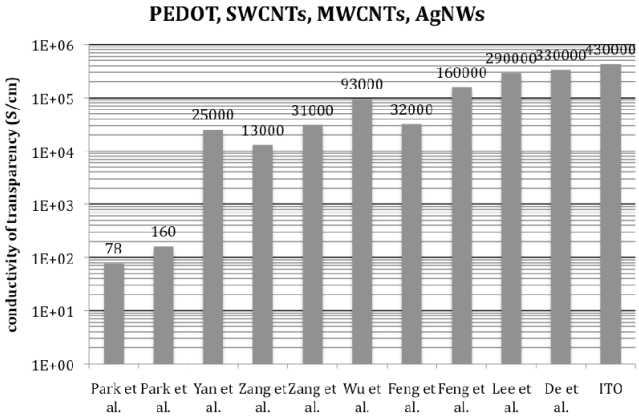

Fig. 10. Comparison: conductivity of transparency of with graphene competing transparent and conductive materials.

MWCNTs lag behind other transparent and conductive materials. Park et al. demonstrated their performance. The conductivity of transparency is 78 S/cm (Park et al., 2010a). Even if these nanotubes are coated by Au (10 nm), the performance doubles to only 160 S/cm. PEDOT/PSS is a bluish coloured conductive polymer and manifold used e.g. for electrostatic coatings, OLEDs or other devices. For very thin coatings the polymer appears almost colourless and transparent with a high conductivity of transparency of 2.5×10^4 S/cm (Yan et al., 2009). A well-competing material are SWCNTs those quality varies due to the synthetic preparation method. Zhang et al. demonstrated coatings with $\sigma_{gt}=1.3 \times 10^4$ S/cm and 3.1×10^4 S/cm for doped SWCNT coatings (Zhang et al., 2006). An even higher performance of 9.3×10^4 S/cm was already demonstrated in 2004 (Wu et al., 2004). A notable approach was described by Feng et al. who built touch-screens from superaligned carbon nanotubes. They enhanced the transparency by laser-trimming and applied thin metal layers of typically nickel as wetting layer and gold as additional conductive layer. The performance of coatings with about 90 % transparency still provide σ_{gt} values of 3.2×10^4 S/cm and can be improved up to impressive 1.6×10^5 S/cm (Feng et al., 2010). Another suitable class of materials for transparent and conductive coatings are AgNWs. Silver nanowire have a typical length of 7 μm and a diameter of about 100 nm and they can form a conductive mesh. The performance was demonstrated to be 2.9×10^5 and 3.3×10^5 S/cm (Lee et al., 2008; De et al., 2009a). These values are extremely high but one must keep in mind that AgNWs form mesh-electrodes and not a uniform hole-free coating. Nevertheless, the performance is comparable to commercially available indium tin oxide (ITO) with a conductivity of transparency of 4.3×10^5 S/cm (Sigma–Aldrich® catalog no. 576360).

Reference	%T (550 nm)	R_s (Ω)	σ_{gt} (S/cm)
Park et al.	80	$4.0x10^4$	78
Park et al.	80	$1.9x10^4$	160
Yan et al.	89	240	$2.5x10^4$
Zang et al.	87	380	$1.3x10^4$
Zang et al.	87	160	$3.1x10^4$
Wu et al.	78	30	$9.3x10^4$
Feng et al.	90	210	$3.2x10^4$
Feng et al.	83	24	$1.6x10^5$
Lee et al.	86	16	$2.9x10^5$
De et al.	85	13	$3.3x10^5$
Sigma–Aldrich® no. 576360	85	10	$4.3x10^5$

Table 8. Comparison: transparency, sheet resistance and conductivity of transparency of transparent coatings with graphene competing transparent and conductive materials.

6. Summary and outlook

It has been demonstrated that the definition of σ_{gt} provides helpful values to compare transparent and conductive coatings on the basis of graphene as a reference material. Moreover, the common preparation methods for graphene were summarized and the performance of graphene in transparent and electrically coatings was compared. Graphene oxide is available on a large scale and the coating procedures are versatile. The modification methods for that material are manifold and upon reduction a conductive graphene based material is yielded. Anyhow, the performance lags behind graphene prepared by other preparation methods if graphene oxide is processed at temperatures compatible with plastic substrates. State of the art performance is below 2000 S/cm (conductivity of transparency). A thermal annealing step up to 1100 °C can increase the performance that is comparable to undoped graphene (about 4500 S/cm). Another approach, the dispersion of graphene obtained from graphite flakes can provide a conductivity of transparency up to about 3000 S/cm. Further, graphene or reduced graphene oxide were combined with other potential materials as carbon nanotubes and promising results up to $3x10^4$ S/cm are described. A lot of research was already done for doped carbon nanotubes and in dependence of their quality conductivities of transparency of $3x10^4$ to $9x10^4$ S/cm are possible. The best quality to date was obtained by graphitization of molecular films, as oleic acid with a quality equal to films prepared by chemical vapour deposition. As a consequence doped graphene films with a conductivity of transparency of $2x10^5$ S/cm are possible, about three orders of magnitude better than for reduced graphene oxide. The quality is high enough to compete with commonly used indium tin oxide with a performance of $4x10^5$ S/cm. But other materials are also promising, as single wall carbon nanotubes especially combined with thin gold film and silver nanowires are mentioned with

2-3x10^5 S/cm. Besides touch screen applications that will come to marked within the next few years, graphene can be used as transparent electrode for solar cells or thin film transistors. One must keep in mind the research on graphene just started and we will see which applications will become economically worthwhile but it is conceivable that graphene based technology will become an invisible part in our daily life.

7. References

Bae, S., et al. (2010). Roll-to-roll production of 30-inch graphene films for transparent electrodes, *Nature Nanotechnology*, 5, 8, pp. 574-578.

Becerril, H. A., et al. (2008). Evaluation of solution-processed reduced graphene oxide films as transparent conductors, *ACS Nano*, 2, 3, pp. 463-470.

Behabtu, N., et al. (2010). Spontaneous high-concentration dispersions and liquid crystals of graphene, *Nature Nanotechnology*, 5, 6, pp. 406-411.

Berger, C., et al. (2004). Ultrathin Epitaxial Graphite: 2D Electron Gas Properties and a Route toward Graphene-based Nanoelectronics, *The Journal of Physical Chemistry B*, 108, 52, pp. 19912-19916.

Blake, P., et al. (2008). Graphene-Based Liquid Crystal Device, *Nano Letters*, 8, 12, pp. 1704-1708.

Boehm, H. P., et al. (1962). Dünnste Kohlenstoff-Folien, *Zeitschrift für Naturforschung*, 17b, 150-153.

Brodie, B. C. (1855). Note sur un nouveau procédé pour la purification et la désagrégation du graphite, *Ann. Chim. Phys.*, 45, pp. 351-353.

Casabianca, L. B., et al. (2010). NMR-Based Structural Modeling of Graphite Oxide Using Multidimensional ^{13}C Solid-State NMR and ab Initio Chemical Shift Calculations, *Journal of the American Chemical Society*, 132, 16, pp. 5672-5676.

Casiraghi, C., et al. (2007). Rayleigh imaging of graphene and graphene layers, *Nano Letters*, 7, 9, pp. 2711-2717.

Charpy, G. (1909). Lur sar formation de l'oxyde graphitique et la définition du graphite, *Comptes rendus hebdomadaires des séances de l'Académie des sciences*, 148, pp. 920-923.

Choi, D., et al. (2010). Fully Rollable Transparent Nanogenerators Based on Graphene Electrodes, *Advanced Materials*, 22, 19, pp. 2187-2192.

Choi, J.-Y., et al. (2009). Transparent electrode comprising graphene sheet, and display and solar cell including electrode, US2009071533.

Chung, D. D. L. (2002). Review Graphite, *Journal of Materials Science*, 37, 8, pp. 1475-1489.

Compton, O. C. & S. T. Nguyen (2010). Graphene oxide, highly reduced graphene oxide, and graphene: versatile building blocks for carbon-based materials, *Small*, 6, 6, pp. 711-723.

Cote, L. J., et al. (2009). Langmuir-Blodgett Assembly of Graphite Oxide Single Layers, *Journal of the American Chemical Society*, 131, 3, pp. 1043-1049.

Cravotto, G. & P. Cintas (2010). Sonication-Assisted Fabrication and Post-Synthetic Modifications of Graphene-Like Materials, *Chemistry - A European Journal*, 16, 18, pp. 5246-5259.

De, S., et al. (2009a). Silver Nanowire Networks as Flexible, Transparent, Conducting Films: Extremely High DC to Optical Conductivity Ratios, *ACS Nano*, 3, 7, pp. 1767-1774.

De, S., et al. (2009b). Flexible, Transparent, Conducting Films of Randomly Stacked Graphene from Surfactant-Stabilized, Oxide-Free Graphene Dispersions, *Small*, 6, 3, pp. 458-464.

Debye, P. & P. Scherrer (1917). Über die Konstitution von Graphit und amorpher Kohle, *Nachrichten von der Gesellschaft der Wissenschaften zu Göttingen, Mathematisch-Physikalische Klasse*, 1917, 2, pp. 180-188.

Dimroth, O. & B. Kerkovius (1913). Zur Kenntnis der Konstitution der Kohle, *Justus Liebigs Annalen der Chemie*, 399, 1, pp. 120-123.

Eda, G. & M. Chhowalla (2010). Chemically Derived Graphene Oxide: Towards Large-Area Thin-Film Electronics and Optoelectronics, *Advanced Materials*, 22, 22, pp. 2392-2415.

Eda, G., et al. (2008a). Large-area ultrathin films of reduced graphene oxide as a transparent and flexible electronic material, *Nature Nanotechnology*, 3, 5, pp. 270-274.

Eda, G., et al. (2008b). Transparent and conducting electrodes for organic electronics from reduced graphene oxide, *Applied Physics Letters*, 92, pp. 233305.

Eigler, S. (2009). A new parameter based on graphene for characterizing transparent, conductive materials, *Carbon*, 47, 12, pp. 2936-2939.

Feng, C., et al. (2010). Flexible, Stretchable, Transparent Conducting Films Made from Superaligned Carbon Nanotubes, *Advanced Functional Materials*, 20, 6, pp. 885-891.

Fraser, D. B. & H. D. Cook (1972). Highly Conductive, Transparent Films of Sputtered $In_{2-x}Sn_xO_{3-y}$, *Journal of the Electrochemical Society*, 119, 10, pp. 1368-1374.

Gan, Y., et al. (2003). STM investigation on interaction between superstructure and grain boundary in graphite, *Surface Science*, 539, 1-3, pp. 120-128.

Geng, J. & H.-T. Jung (2010). Porphyrin Functionalized Graphene Sheets in Aqueous Suspensions: From the Preparation of Graphene Sheets to Highly Conductive Graphene Films, *Journal of Physical Chemistry C*, 114, 18, pp. 8227-8234.

Gómez-Navarro, C., et al. (2010). Atomic Structure of Reduced Graphene Oxide, *Nano Letters*, 10, 4, pp. 1144-1148.

Gottschalk, F. (1865). Beiträge zur Kenntniss der Graphitsäure, *Journal für Praktische Chemie*, 95, 1, pp. 321-350.

Hamdi, H. (1942). Zur Kenntnis der kolloidchemischen Eigenschaften des Humus - Dispersoidchemische Beobachtungen an Graphitoxyd, *Kolloid-Beihefte*, 54, 10-12, pp. 554-634.

Hernandez, Y., et al. (2008). High-yield production of graphene by liquid-phase exfoliation of graphite, *Nature Nanotechnology*, 3, 9, pp. 563-568.

Hirata, M., et al. (2004). Thin-film particles of graphite oxide 1: High-yield synthesis and flexibility of the particles, *Carbon*, 42, 14, pp. 2929-2937.

Hong, T.-K., et al. (2010). Transparent, Flexible Conducting Hybrid Multilayer Thin Films of Multiwalled Carbon Nanotubes with Graphene Nanosheets, *ACS Nano*, 4, 7, pp. 3861-3868.

Hummers, W. S. (1957). Pereparation of graphitic acid, US2798878.

Juang, Z.-Y., et al. (2010). Graphene synthesis by chemical vapor deposition and transfer by a roll-to-roll process, *Carbon*, 48, 11, pp. 3169-3174.

Kim, K. S., et al. (2009). Large-scale pattern growth of graphene films for stretchable transparent electrodes, *Nature*, 457, 7230, pp. 706-710.

King, P. J., et al. (2010). Improvement of Transparent Conducting Nanotube Films by Addition of Small Quantities of Graphene, *ACS Nano*, 4, 7, pp. 4238-4246.

Kovtyukhova, N. I., et al. (1999). Layer-by-Layer Assembly of Ultrathin Composite Films from Micron-Sized Graphite Oxide Sheets and Polycations, *Chemistry of Materials*, 11, 3, pp. 771-778.

Lee, J. H., et al. (2010). The Superior Dispersion of Easily Soluble Graphite, *Small*, 6, 1, pp. 58-62.

Lee, J. Y., et al. (2008). Solution-processed metal nanowire mesh transparent electrodes, *Nano Letters*, 8, 2, pp. 689-692.

Lerf, A., et al. (1998). Structure of Graphite Oxide Revisited, *Journal of Physical Chemistry B*, 102, 23, pp. 4477-4482.

Li, D., et al. (2008a). Processable aqueous dispersions of graphene nanosheets, *Nature Nanotechnology*, 3, 2, pp. 101-105.

Li, X., et al. (2008b). Highly conducting graphene sheets and Langmuir–Blodgett films, *Nature Nanotechnology*, 3, 9, pp. 538-542.

Li, X., et al. (2009). Transfer of Large-Area Graphene Films for High-Performance Transparent Conductive Electrodes, *Nano Letters*, 9, 12, pp. 4359-4363.

Loh, K. P., et al. (2010). The chemistry of graphene, *Journal of Materials Chemistry*, 20, 12, pp. 2277-2289.

Lu, X., et al. (1999). Tailoring graphite with the goal of achieving single sheets, *Nanotechnology*, 10, 3, pp. 269-272.

Marchand, R. F. (1845). Ueber die Einwirkung des Schwefelsäure auf die Holzkohle, *Journal für Praktische Chemie*, 35, 1, pp. 228-231.

Mattevi, C., et al. (2009). Evolution of Electrical, Chemical, and Structural Properties of Transparent and Conducting Chemically Derived Graphene Thin Films, *Advanced Functional Materials*, 19, 16, pp. 2577-2583.

Novoselov, K. S., et al. (2004). Electric Field Effect in Atomically Thin Carbon Films, *Science*, 306, 5696, pp. 666-669.

Park, H., et al. (2010a). Sonochemical hybridization of carbon nanotubes with gold nanoparticles for the production of flexible transparent conducing films, *Carbon*, 48, 5, pp. 1325-1330.

Park, H. J., et al. (2010b). Growth and properties of few-layer graphene prepared by chemical vapor deposition, *Carbon*, 48, 4, pp. 1088-1094.

Pham, V. H., et al. (2010). Fast and simple fabrication of large-scale transparent chemical converted graphene film by spraying deposition, *Carbon*, 48, 7, pp. 1945-1991.

Roddaro, S., et al. (2007). The optical visibility of graphene: interference colors of ultrathin graphite on SiO_2, *Nano Letters*, 7, 9, pp. 2707-2710.

Rogers, R. E. & W. B. Rogers (1850). Oxydation von Graphit und Diamant auf nassem Wege, *Journal für Praktische Chemie*, 50, 1, pp. 411-413.

Ruess, G. (1947). Über das Graphitoxyhydroxyd (Graphitoxyd), *Monatshefte für Chemie*, 76, 3-5, pp. 381-417.

Ruess, G. & F. Vogt (1948). Höchstlamellarer Kohlenstoff aus Graphitoxyhydroxyd, *Kolloid Zeitschrift*, 78, 3-4, pp. 222-242.

Schafhaeutl, C. (1840). Ueber die Verbindungen des Kohlenstoffes mit Silicium, Eisen und andern Metallen, welche die verschiedenen Gattungen von Gusseisen, Stahl und Schmiedeeisen bilden., *Journal für Praktische Chemie*, 21, 1, pp. 129-157.

Shin, H.-J., et al. (2009a). Reduced graphene oxide doped with dopant, thin layer and transparent electrode, US20090146111.

Shin, H.-J., et al. (2009b). Efficient Reduction of Graphite Oxide by Sodium Borohydride and Its Effect on Electrical Conductance, *Advanced Functional Materials*, 19, 12, pp. 1987-1992.

Soldano, C., et al. (2010). Production, properties and potential of graphene, *Carbon*, 48, 8, pp. 2127-2150.

Spath, T. M., et al. (2006). Touchscreen with conductive layer comprising carbon nanotubes, WO2008013517.

Staudenmaier, L. (1898). Verfahren zur Darstellung der Graphitsäure, *Berichte der deutschen chemischen Gesellschaft*, 31, 2, pp. 1481-1487.

Staudenmaier, L. (1899). Verfahren zur Darstellung der Graphitsäure, *Berichte der deutschen chemischen Gesellschaft*, 32, 2, pp. 1394-1399.

Su, Q., et al. (2009). Composites of Graphene with Large Aromatic Molecules, *Advanced Materials*, 21, 31, pp. 3191-3195.

Thiele, H. (1937). Über Salzbildung und Basenaustausch der Graphitsäure, *Kolloid Zeitschrift*, 80, 1, pp. 1-20.

Topsoe, H. (1968). Geometric factors in four point resistivity measurement, http://www.four-point-probes.com/haldor.html.

Tung, V. C., et al. (2009). Low-Temperature Solution Processing of Graphene-Carbon Nanotube Hybrid Materials for High-Performance Transparent Conductors, *Nano Letters*, 9, 5, pp. 1949-1955.

Vallés, C., et al. (2008). Solutions of Negatively Charged Graphene Sheets and Ribbons, *Journal of the American Chemical Society*, 130, 47, pp. 15802-15804.

Wang, S. J., et al. (2010). Fabrication of highly conducting and transparent graphene films, *Carbon*, 48, 6, pp. 1815-1823.

Wang, X., et al. (2008a). Transparent, conductive graphene electrodes for dye-sensitized solar cells, *Nano Letters*, 8, 1, pp. 323-327.

Wang, X., et al. (2008b). Transparent Carbon Films as Electrodes in Organic Solar Cells, *Angewandte Chemie International Edition*, 47, 16, pp. 2990-2992.

Wu, J., et al. (2010). Organic Light-Emitting Diodes on Solution-Processed Graphene Transparent Electrodes, *ACS Nano*, 4, 1, pp. 43-48.

Wu, Z., et al. (2004). Transparent, Conductive Carbon Nanotube Films, *Science*, 305, 5688, pp. 1273-1276.

Xu, Y., et al. (2010). Polymer photovoltaic devices with transparent graphene electrodes produced by spin-casting, *Carbon*, 48, 11, pp. 3308-3311.

Yan, H., et al. (2009). Highly Conductive and Transparent Poly (3,4-ethylenedioxythiophene)/Poly(4-styrenesulfonate) (PEDOT/PSS) Thin Films, *Polymer Journal*, 41, 12, pp. 1028-1029.

Zhang, B., et al. (2010). Stable dispersions of reduced graphene oxide in ionic liquids, *Journal of Materials Chemistry*, 20, 26, pp. 5401-5403.

Zhang, D., et al. (2006). Transparent, conductive, and flexible carbon nanotube films and their application in organic light-emitting diodes, *Nano Letters*, 6, 9, pp. 1880-1886.

Zhu, Y., et al. (2009). Transparent self-assembled films of reduced graphene oxide platelets, *Applied Physics Letters*, 95, 10, pp. 103104.

8

Graphene-Based Nanocomposites

Xin Wang and Sheng Chen
Key Laboratory for Soft Chemistry and Functional Materials,
Nanjing University of Science and Technology, Ministry of Education,
China

1. Introduction

Since the historical observation of single layer graphene by Germ and his co-workers in 2004, this atomically thin carbon film has received ever-increasing attention and become a rapidly rising star on the horizon of materials science and condensed-matter physics (Novoselov et al., 2004). Graphene exhibits many unusual and useful properties such as a large theoretical specific surface area (2630 m^2 g^{-1}) (Stoller et al., 2008), high values of Young's modulus (~1.1 Tpa), excellent thermal conductivity (~5000 W m^{-1} s^{-1}) (Park & Ruoff, 2009), and amazing intrinsic mobility (200 000 cm^2 v^{-1} s^{-1}). Moreover, the extraordinary transport phenomena of graphene have also been well documented, including massless Dirac fermions (Novoselov et al., 2005), ambipolar field effect (Novoselov et al., 2004), room-temperature quantum Hall effect (Zhang et al., 2005), etc. These fascinating performances have attracted extensive concern in recent years with ever-increasing scientific and technological impetus. Among the numerous methods for harnessing these peculiar properties, one possible route would be to incorporate graphene sheets into composite materials (Stankovich et al., 2006). The easy synthesis, low cost and non-toxicity of graphene make this material a promising candidate for many technological applications (Geim & Novoselov, 2007; Allen et al., 2010). For example, graphene sheets are excellent nanoscale substrates for the formation of silver-nanoparticle films. These silver-nanoparticle films assembled on the single-layer sheets are flexible and can form stable suspensions in aqueous solutions (Xu et al., 2009). They can be processed facilely into paper-like materials and flexible electronic materials to satisfy different requirements for many products, such as membranes, anisotropic conductors, biological sensors and optoelectronic nano-devices, etc. Graphene sheets and exfoliated graphene oxide possess large surface areas and thus may be excellent support materials to disperse and stabilize inorganic nanoparticles, such as Pt, Co_3O_4, CuO, MnO_2, MnOOH, $Co(OH)_2$, etc., effectively inhibiting the aggregation in post-synthesis and thereby giving a relatively higher utilization of the active material. Decoration of graphene sheets with nanoparticles has been demonstrated to reveal special features in new hybrids that can be widely utilized in catalysts, supercapacitors, Li-ion batteries, etc. It was found that the introduction of less amount of graphene oxide into PANI could induce a synergistic effect, greatly enhancing the electrochemical performance of PANI as a supercapacitor electrode material (Wang et al., 2009a).

The intent of this chapter is to provide a basic overview of graphene-based nanocomposites. The emphasis is primarily on the different synthetic strategies that have been pursued so far

for the preparation of graphene supported inorganic nanoparticles and graphene-doped polymers, as well as the concerted effect of the properties of the individual components in the new hybrid materials that will present special features for catalysts, electrochemical materials and nanotechnology. Additionally, the prospective applications of these graphene-based materials will also be presented.

2. Graphene-based nanocomposites

2.1 A general method for preparing graphene-based nanocomposites

As a basic building block for graphitic materials of all other dimensionalities (Geim & Novoselov, 2007), graphene has suffered from a problem that was in the early days of nanotube and fullerene research. A prerequisite for exploiting most proposed applications for graphene is the availability of processable graphene sheets in large quantities. Until recently, two main routes are fully exploited: large-scale growth and large-scale exfoliation. Some techniques, such as liquid-phase exfoliation of graphite (Hernandez et al., 2008; Lotya et al., 2009), chemical vapour deposition (Lo´pez et al., 2010; Park et al., 2010), helium arc-discharge (Wu et al., 2010), large growth or self-assembly approach (Weixia et al., 2009; Li et al., 2009) and chemical reduction of GO (Li et al., 2008; Williams et al., 2008), have taken us a step closer to real-world applications of this intriguing material.

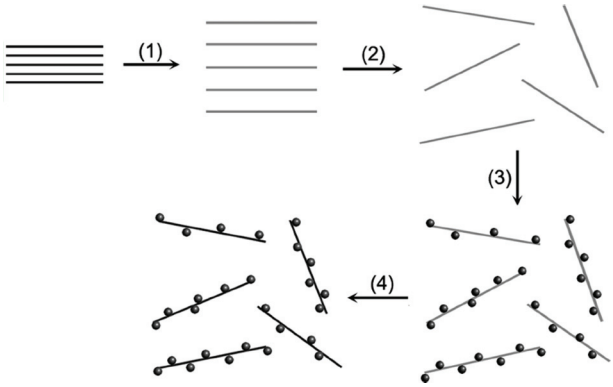

Fig. 1. A schematic route for anchoring nanoparticles onto graphene sheets. (1) Oxidation of graphite (black lines) to GO (gray lines) with greater interlayer distance. (2) Exfoliation of GO to graphene oxide sheets by sonication in water solution. (3) Attachment of metal particles on the graphene oxide sheets. (4) Formation of graphene-supported metal particles composites by reduction of the graphene oxide sheets. The distorted carbon sheets are simplified to an idealized planar model (Xu et al., 2008a).

Among above-mentioned strategies for manufacturing graphene-based nanocomposites, which requires not only that graphene sheets be made on a large scale but that they should be homogeneously distributed, chemical reduction of GO seems to be a much more efficient, low-cost, and bulk production pathway to incorporate graphene sheets into hybrids. As shown in Figure 1, the current main interests in preparing graphene-based nanocomposites are concentrated on exfoliating graphene through a combination of oxidation and sonication procedures, followed by reduction through chemical methods (Xu et al., 2008a). The GO is heavily oxygenated graphene bearing carbonyl, hydroxyl, and

epoxy groups on the basal planes as well as carboxylic groups on the edges of the carbon sheets (Boukhvalov & Katsnelson, 2008). The functional groups on GO can serve as anchor sites and consequently make the in situ formed nanoparticles attach on the surfaces and edges of GO sheets. It should be mentioned that GO is gradually lost its excellent electrical properties and eventually becomes electrically insulated owning to the transformation of carbon atoms from a planar sp^2-hybridized geometry to a distorted sp^3-hybridized geometry (Stankovich et al., 2006). To recover electrical conductivity, eliminating most of the oxygen-containing functional groups of GO to restore the aromatic graphene networks is necessary.

2.2 Flexible metal-nanoparticle films

Flexible paper-shaped materials are of great importance in our technological society. Their typical utilizations include chemical filters, adhesive layers, molecular storage, and batteries and supercapacitors films (Dikin et al., 2007). In the past several years, metal nanoparticles, in particular noble metal nanoparticles (e.g., Au and Ag) have generated extensive interest due to their unique electronic, optical, and catalytic properties. Alignment of metal nanoparticles into thin films is of great importance for diversified applications The substrate is a necessary to prepare nanoparticle films, for example, metal foils, glass plate, polymer films, silicon wafers, and so on have been widely used as substrates for nanoparticle assembling. Unfortunately, most of these substrates are bulk materials with rigid morphology, making the post-processing of as-synthesized nanoparticle films remain an insurmountable challenge. It is desirable to explore a flexible nanoscale substrate for assembling nanoparticles, thereby forming the flexible nanoparticle films.

Graphene sheets are attractive recently as excellent nanoscale building blocks for producing new composites. GO is heavily oxygenated graphene that is readily exfoliated in water to yield stable dispersions consisting mostly of single-layer sheets. In view of the pliable nature of graphene and GO, the preparation of graphene oxide paper and graphene sheets films have been reported, which have shown a combination of both macroscopic flexibility and stiffness, and has found use in many fields (Dikin et al., 2007; Li et al., 2008). Commonly, the silver mirror reaction has been used as an efficient method for preparing silver nanoparticles films using GO as substrates (Xu & Wang, 2009). It is known that silver-nanoparticle films are easily coated on bulk substrates by simply dipping these substrates in the reaction solutions. Because the hydrophilic GO can be exfoliated in water to form stable single-layer sheets, which can be regarded as immersed substrates, accordingly, it is possible that silver-nanoparticle films may form on the nanoscale 2D carbon sheets when dipping these exfoliated GO sheets, instead of bulk substrates, in the reaction solution. Therefore, an idea of using graphene oxide sheets as the nanoscale substrates for the formation of silver-nanoparticle films is examined.

Fig. 2 displays the typical TEM and FESEM images of silver nanoparticles on graphene oxide sheets. In Fig. 2a, the almost transparent 2D carbon sheets were thickly decorated by the silver particles. The monolayer carbon nanosheets were so thin that it was difficult to distinguish them with the carbon-supported films on the copper grid. However, the edges and crumpled silk waves of these carbon sheets lead us to believe that these nanoparticles are indeed deposited on supports. Moreover, as shown in Figure 2c and d, it can be clearly observed that these as-synthesized silver nanoparticle films can restack and large amounts of silver nanoparticles assembled on the 2D substrates. Commonly, the graphene oxide bears functional groups on the basal planes and edges. These negative charged functional

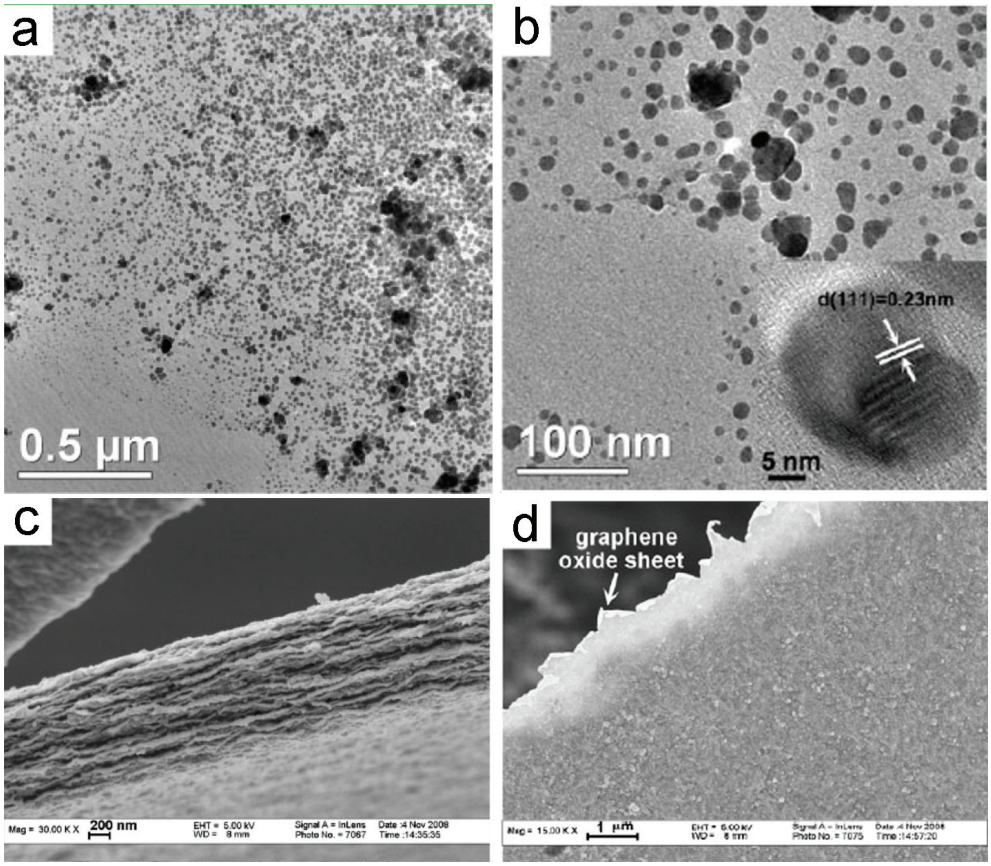

Fig. 2. TEM (a, b) and FESEM (c, d) images of silver nanoparticles on graphene oxide sheets (Xu & Wang, 2009).

groups can be used as anchors to adsorb polar materials and inorganic nanoparticles. Accordingly, $Ag(NH_3)^{2+}$, as a positive ion, can easily interact with these negative graphene sheets through electrostatic forces. The in situ reduction of these ions by glucose allows these silver nanoparticles to anchor onto the graphene oxide sheets. Some of the nanoparticles deposited onto the surface of the graphene oxide sheets, and some anchored onto the edges.

It has been well documented that the stable graphene-based sheets aqueous solution can be readily processed into films and paper-like materials (Stankovich et al., 2006; Li et al., 2008). When drying on a substrate, the silver-coated graphene oxide sheets have also easily assembled to form a macroscopic film with a shiny metallic luster that exhibited mirror-like properties (Figure 3). Nevertheless, the film consisting of individual graphene oxide sheets was dim and possessed poor reflectivity. It is believed that the silver-mirror films are usually originating from the assembly of silver nanoparticles on bulk substrates. In this system, the macroscopic mirror-like films obtained can be attributable to the restacking of silver nanoparticle films (Fig. 2c).

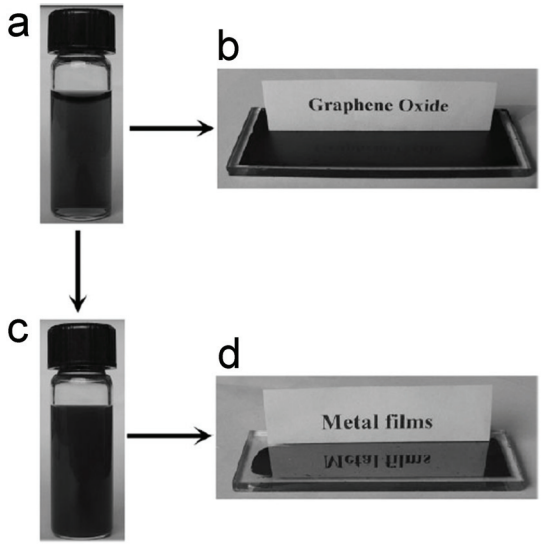

Fig. 3. Photos of graphene oxide and Ag–GO composite in water solution and dried. (a) A vial containing a suspension (0.25 mg mL^{-1}) of graphene oxide in water; (b) the graphene oxide film obtained by drying 60 mL of the dispersion on glass; (c) after coating by silver nanoparticles, the Ag–GO composite can form a stable suspension in a water solution with 0.25 mg mL^{-1} of graphene oxide; (d) The mirror-like film obtained by drying the suspensions of composite on glass (Xu & Wang, 2009).

Traditionally, the substrates for particle films are bulk materials. Free-standing films without any supports have also been prepared, but further processing of these films meets difficulties. Therefore, the nanoscopic substrates with flexible properties are beneficial for the use of particle films in practical technologies. The idea of using pliable graphene oxide sheets as substrates to prepare nanoparticle films can also be extended to other materials, such as metal and semiconductor particles. These flexible and adjustable nanoparticle films may show promising application in optics, sensors, catalysis, etc., broadening the horizon for the vast use of particle films.

2.3 Catalysis

Catalysis, an integral part in our daily life, has extensively utilized in a variety of technological fields. Recent studies continuously concentrate on the preparation and applications of nanoscale particles of metal or metal oxides, owning to their large specific surface area and high activity in most catalytic processes. Ammonium perchlorate (AP) is one of the main oxidizing agents that is widely used in various propellants (Boldyrev, 2006). The burning behaviour of propellants is highly relevant to the thermal decomposition of AP. Development of novel catalysts with high decomposition efficiency to produce large amount of energy as far as possible and to decrease the burning temperature for easy operation and control is of great significance for its practical applications. Generally, the thermal decomposition of AP takes place in three steps: the endothermic phase transition at around 240 ^{o}C, the low-temperature decomposition at around 316 ^{o}C (LTD) and the high-temperature decomposition at around 460 ^{o}C (HTD). To increase the exothermic heat and bring down the temperatures of decomposition are very important. It is demonstrated that metal oxide and hydroxide nanoparticles, like

Co_3O_4, CuO, and MnOOH, could promote the heterogeneous decomposition of deprotonized $HClO_4$ gas on the solid surface in the high-temperature decomposition, which will reduce the HTD and increase exothermic quantity in the decomposition process. However, in the post-synthesis of these materials, aggregation occurs when they were dried in air, resulting in a decrement of the catalytic capability. Considering the large specific area of graphene sheets or GO, which is desirable to disperse and stabilize the inorganic nanoparticle, the combination of graphene or GO with nanoparticles may effectively inhibit the aggregation and consequently give a higher catalytic performance.

Fig. 4 shows the TEM, FESEM, and DSC characterization of as-prepared GO-Co_3O_4 nanocomposites (Xu et al., 2008b). From Fig. 4a-c, it is clearly seen that the exfoliated GO sheet was decorated randomly by uniform spherical particles of about 100 nm in size. These in situ formed particles could result in exfoliating the layered GO. In Fig. 4c of the dark field TEM images of GO-Co_3O_4 nanocomposites, it is interesting that some of the Co_3O_4 nanoparticles are brighter than the ones which seem to be enveloped by a thin film. This may be attributed to the fact that the functional groups, especially hydroxyl and epoxy groups appear on both sides of the graphene oxide sheet, and thereby in situ formed Co_3O_4 could on anchor on both sides of the supports.

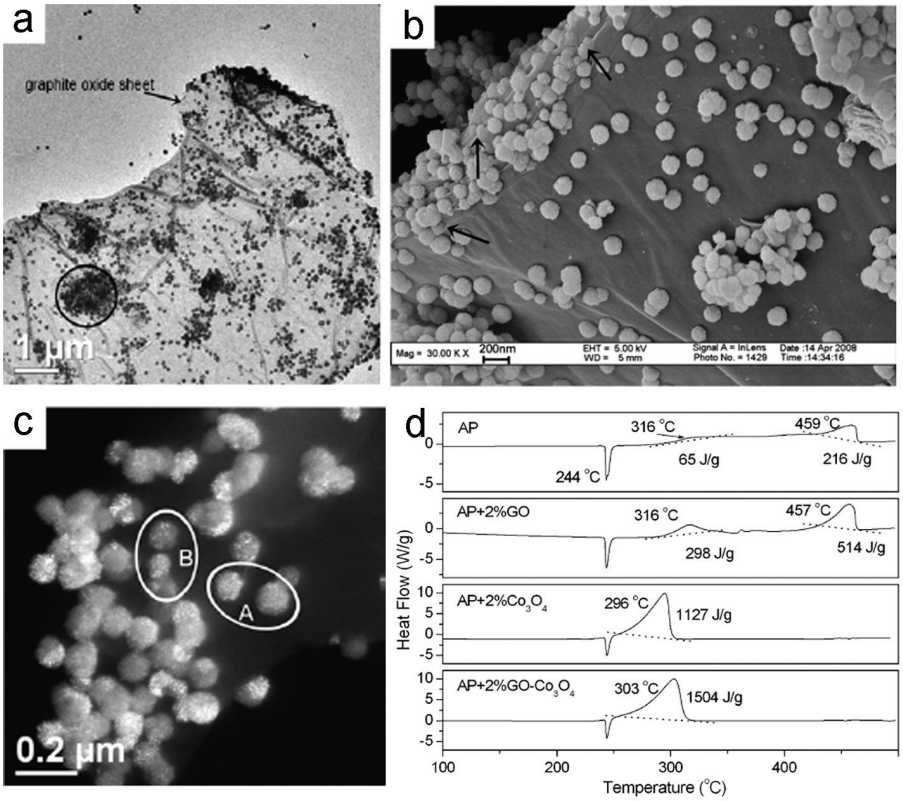

Fig. 4. TEM (a, c), FESEM (b) images of GO-Co_3O_4 nanocomposites; (d) DSC curves for the decomposition of AP, AP with 2% GO, AP with 2% Co_3O_4 and AP with 2% Co_3O_4-GO nanocomposite (Xu et al., 2008b).

To explore the catalytic effect of this nanocomposite on thermal decomposition of AP, DSC measurement is conducted. Figure 4d displays that when individual GO was added, two exothermic peaks of AP became apparent, along with a new exothermic peak centred at around 360 °C, and the exothermic heat of the two steps was larger than that of AP. This may be due to the catalytic effect of GO in the system. The introduction of Co_3O_4 and GO-Co_3O_4 reduced temperature of both LTD and HTD and made the two steps blend almost into one process. The decomposition temperature of AP with 2% Co_3O_4 (296 °C) was close to that of AP with 2%GO-Co_3O_4 (303 °C); however, the former exothermic quantity (1127 J/g) was much lower than that of the latter (1504 J/g). Therefore, owning to the concerted effect of the individual components for the catalysis of decomposition of AP, the addition of GO-Co_3O_4 not only brought down the decomposition temperature, but also increased the exothermic heat of AP, exhibiting good catalytic properties.

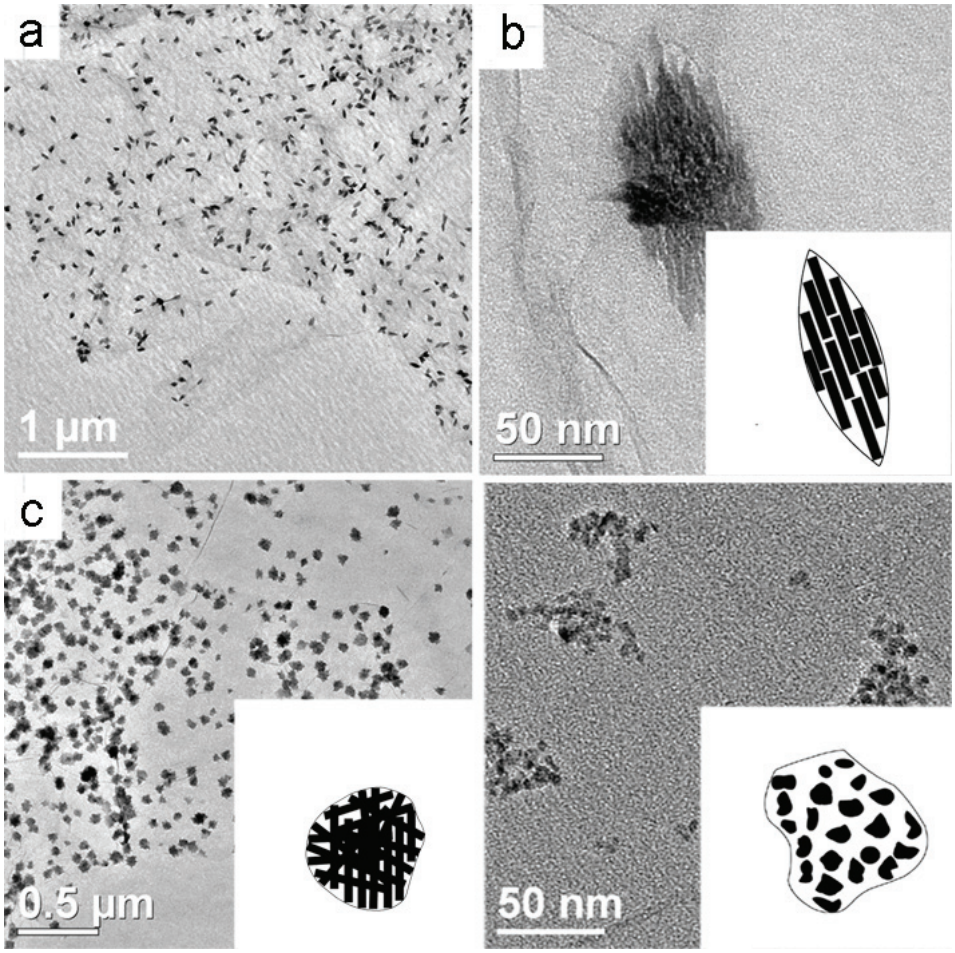

Fig. 5. TEM images of GO decorated CuO nanoparticles with different morphologies. (a-b) spindle-like CuO; (c) spherical CuO; (d) CuO nano-aggregates (Zhu et al., 2010).

Moreover, the composite of GO support CuO nanoparticles has been synthesized for the first time (Zhu et al., 2010). It should be mentioned that we can tune the catalytic performances by shape-controlled synthesis of different morphological nanoparticles on GO sheets. As displayed in Fig. 5, by varying the volume ratios of the added water and isopropanol and mass ratios of CuO/GO, the composite of CuO nanoparticles with different morphologies, including spindles, spheres, and nano-aggregates, on exfoliated GO sheets have been dramatically obtained. DSC tests display discrepant catalytic effects of these composites on AP. The HTD and exothermic quantity of AP mixed with 2% spindle-like CuO-GO, spherical CuO-GO, and CuO nano-aggregates-GO are 330 ^{o}C (1056 J g^{-1}), 315 ^{o}C (1347 J g^{-1}) and 321 ^{o}C (1297 J g^{-1}), respectively. The spherical CuO nanocrystals on GO sheets have shown the best catalytic action. In addition, the introduction of pure CuO and the composite of spherical CuO nanocrystals on GO sheets could both decrease the temperatures. However, the HTD and exothermic quantity of AP mixed with 2% spherical CuO-GO composites (315 ^{o}C, 1347 J g^{-1}) was much competitive than that of pure CuO (334 ^{o}C, 1093 J g^{-1}), suggesting the catalytic properties of the nanocomposites are enhanced by the concerted effect between GO and CuO.

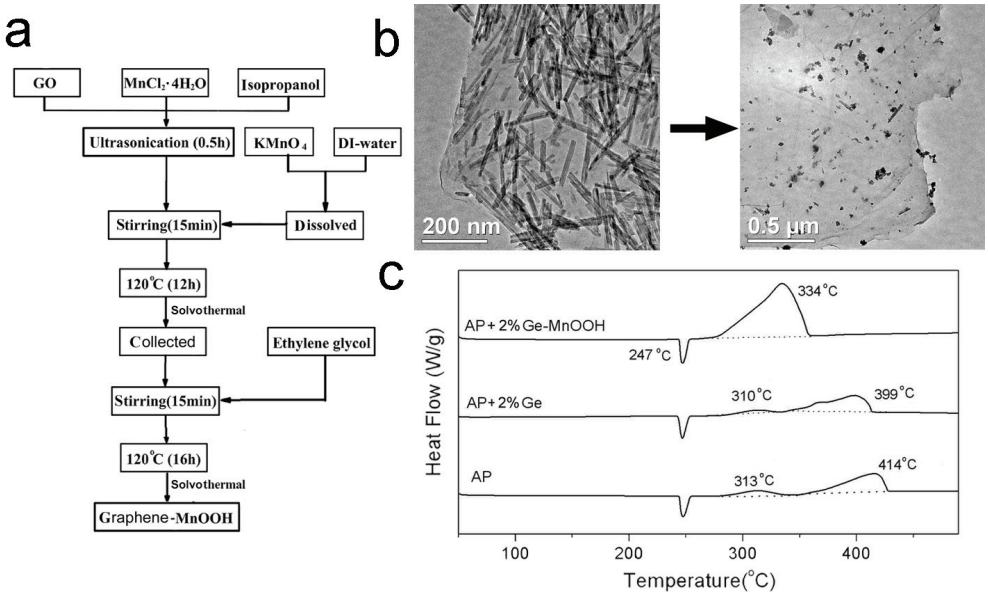

Fig. 6. (a) Preparation procedure of graphene-MnOOH nanocomposites; (b) TEM images of GO-MnO_2 and graphene-MnOOH nanocomposites; (c) DSC curves for the thermal decomposition of AP, AP with 2% graphene, and AP with 2% graphene-MnOOH nanocomposites (Chen et al., 2010a).

Generally, GO is insulated owning to the introduction of large amounts of functional groups, eliminating most of the oxygen-containing functional groups of GO to restore the aromatic graphene networks is necessary for obtaining graphene sheets. In Figure 6a, a two-step solvothermal procedure was developed to synthesize graphene-MnOOH nanocomposites through reducing GO-MnO_2 using ethylene glycol (Chen et al., 2010a). Initially, GO sheets

were decorated randomly by the rod-like MnO_2 (the left image in Figure 6b), where a significant morphological transformation is observed after solvothermal treatment with ethylene glycol. The rod-like MnO_2 transfers to particulate MnOOH with diameters ranging from 20 to 80 nm. The dissolution-crystallization mechanism is speculated to be responsible for this process. Additionally, the catalysis of as-obtained graphene-MnOOH nanocomposite on the decomposition of AP was displayed in Fig. 6c. With the addition of 2% graphene into the system, the LTD and HTD decreased to 310 and 399 ^{o}C, respectively, probably due to the catalytic action of graphene. However, when graphene-MnOOH nanocomposites were added, the two steps (LTD and HTD) blended into one process at 334 ^{o}C with the exothermic heat (1392 J g^{-1}) much larger than that of net AP and AP-graphene composites (590 and 540 J g^{-1}), revealing a good catalytic effect. Although in the actual process the decomposition of AP would involve many additional steps, the results of graphene (GO)-MnOOH (Co_3O_4, CuO) calculated from the DSC measurements are still believed of great significance for material investigation.

2.4 Surface-enhanced Raman scattering

Raman spectroscopy is a powerful technique that is nondestructive, fast, and could provide detailed information as to molecular structures. However, recent Raman researches are limited by its low sensitivity. Raman scattering (SERS) is able to overcome this obstacle and provide a spectral intensity often enhanced by many orders of magnitude for molecules adsorbed on a properly fabricated metal (e.g., Ag, Au, and Pt) surface. This offers the opportunities for SERS to facilitate the study of structural and electronic information of molecules with high resolution (Ferrari, 2007).

It is generally accepted that two mechanisms are contributable to the SERS: the electromagnetic and the charge transfer mechanisms (Fu et al., 2010a). Another enhancement can also be acquired from molecular resonances, but they are only considered in specific system. The electromagnetic enhancement usually can contribute factors of about 10^4–10^6 to the Raman enhancement. While the charge transfer enhancement involves the chemisorption interaction and the metal–adsorbate charge transfer, and is usually said to contribute factors of about 10–100 of the observed enhancement.

The typical features for graphene or GO in Raman spectra are the D band around 1360 cm^{-1} and the G band around 1600 cm^{-1}, corresponding to the breathing mode of κ-point phonons of A_{1g} symmetry and the first-order scattering of the E_{2g} phonons, respectively. Absorption of noble metallic-nanoparticles, like Ag, Au, and Pt, onto graphene or GO sheets is a feasible way to study of graphene sheets in detail. As mentioned in chapter 3.2, silver nanoparticles can form flexible film on GO sheets. On the contrary, we can also regard these one-atom-thick 2D nanostructures as monolayer molecules adsorbed on silver-nanoparticle films (Xu & Wang, 2009). The energy-dispersive X-ray spectrometry (EDS) analysis in Figure 7d indicated that the surface of the film was almost completely covered by elemental silver, which consequently enabled such macroscopic films to display a metallic luster (Figure 7c). Therefore, the as-synthesized silver-nanoparticle films in this system may also display SERS activity. It is obvious in Fig. 7a that the intensities of the D and G bands of GO are enhanced in comparison with those of the original GO. The level of enhancement factor of the Raman scattering is calculated to be about one order of magnitude. Thus, the SERS in this sample may originate from the chemical effect. Additionally, the degree of enhancement of Raman spectra in the system can be controlled by adjusting the quantity of silver particles. As shown in Fig. 7b, the intensities of D and G bands increase along with the incremental

density of the coating silver particles and gradually become stable. This phenomenon may be explained by the fact that the number densities of the anchor sites between the GO and silver nanoparticles are constant. Consequently, when saturation of the charge-transfer complexes is reached, further elevated quality of silver may have little influence on the intensities of the D and G bands.

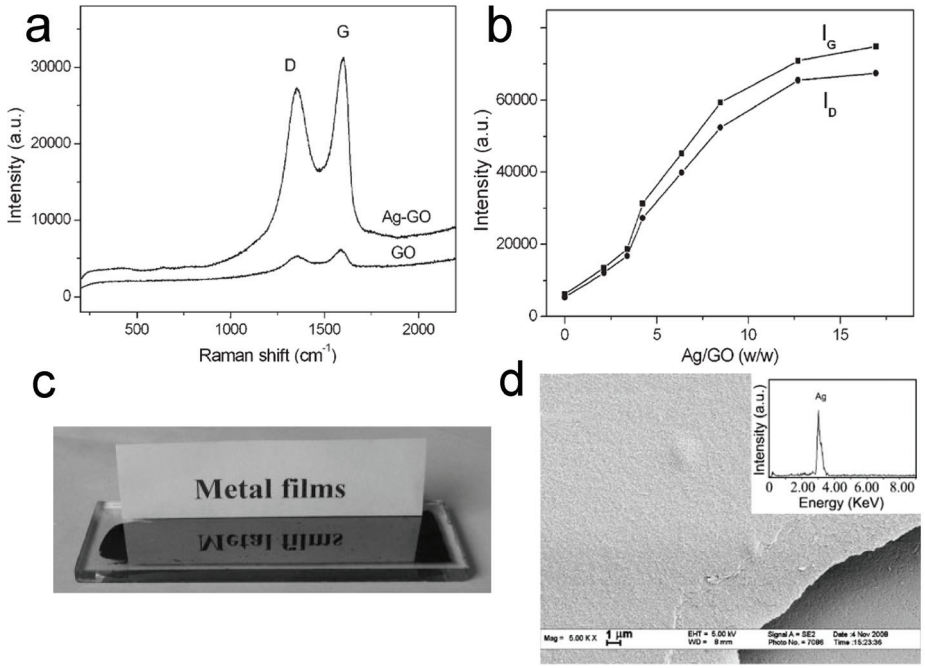

Fig. 7. (a) Raman spectra of GO and SERS spectra of Ag–GO composites with 80 wt% Ag; (b) The relationships between the intensity of the D and G bands of GO and the quality of silver in the composites; (c) the mirror-like film obtained by drying Ag-GO suspensions on glass; (d) FESEM images and EDS spectrum of the Ag–GO hybrid films (Xu & Wang, 2009).

To better understand the energy transfer mechanisms in graphene-based composites, which can provide a template for creating novel nanostructured derivatives, the graphene–Au sheets were fabricated (Xu & Wang, 2009). The composite was then removed to the surface of Si wafer pre-cleaned with ethanol and water to give high quality SERS spectra. By varying the excitation wavelength of lasers, the SERS excitation profile of graphene-Au was acquired.

The morphologies of the graphene-Au nanocomposites was obtained using TEM and SEM as shown in Fig. 7a and b. It is clearly seen that most metal nanoparticles distribute randomly on the supports. Despite there are some large triangular gold particles on the sheets, most are nano-spheres. In Fig. 7b, the sheets become more corrugated after the attachment of gold nanoparticles. The upper inset EDS images show that graphene-Au contain mainly the element Au, apart from the initial C and O. Additionally, the ratio of the contents (O/C) is lower compared to that of GO, suggesting the deoxygenation of GO to form graphene.

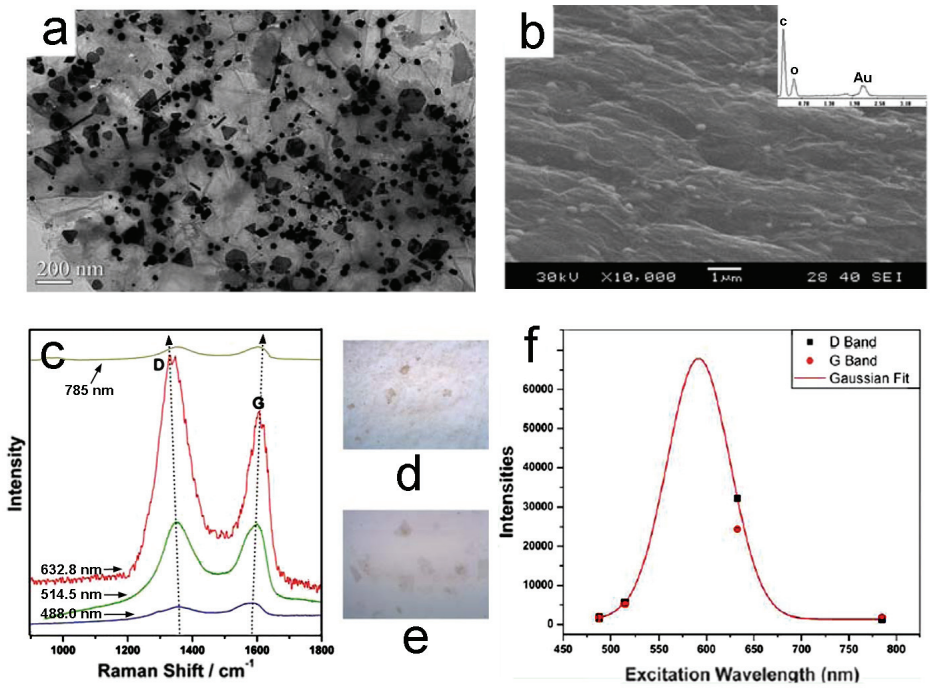

Fig. 8. (a) TEM (b) SEM images of graphene-Au nanocomposites; the inset of (b) is EDS images; (c) Raman spectra of G-Au at excitation wavelengths of 785, 632.8, 514.5, 488 nm; (d) G-Au (e) GO on the Si wafer that were observed under Raman microscopy and taken for the Raman measurements; (f) excitation profile of the D and G bands of graphene enhanced with Au nanoparticles (Fu et al., 2010a).

Raman spectra of graphene-Au at different excitation wavelengths are shown in Fig. 8c. To the right of the Raman spectra, Figure 8d and 8e show the images of graphene-Au and GO on the Si wafer that were observed under Raman microscopy and taken for the Raman measurements. The sheets of G-Au and GO seem to be one or two layers on Si wafer, and the sheets are smaller after decorated with Au nanoparticles. Similar to the Raman spectrum of pure GO (Fig. 6a), the G-Au Raman line at 488 nm, also contains both D and G bands however, with an increased D/G intensity ratio. Specifically, the peak intensity ratio (ID/IG) decreases from approximately 1.0 for GO to about 0.75 for the reduced sample. This observation makes sense regarding to the formation of more extended networks of conjugated sp^2 carbons, towards a more locally ordered graphene lattice.

In addition, Fig. 8c displays that at different wavelengths, the intensity of the D band was enhanced ~5 times when we measured with 514.5 nm excitation wavelength compared to that of GO, and ~27 times for 632.8 nm excitation wavelength. For the G band, enhanced factor is 3 for 514.5 nm and 16 for 632.8 nm excitation, respectively, in comparison with that of GO. However, the intensity decreased considerably in the case of excitation wavelength changed to 785 nm. In Fig. 8d, we provide an excitation profile of the D and G bands. Note that this profile indicates a resonance. A Gaussian fit to the D band profile gives a maximum of 2.09 eV (593 nm) and a width of 0.30 eV.

Commonly, the plasmon resonance of Au is ~548 nm, at some distance from the excitation profile maximum of about 593 nm. Aggregation of gold nanoparticles can lead to a red shift of the plasmon resonance. Although the TEM images show a significant fraction of larger nanoparticles, seldom shift was observed in the absorption spectrum, nor any other significant maximum besides that at 548 nm, even at higher concentrations. It is common in SERS to observe a difference between the plasmon resonance and the maximum of the excitation profile. The discrepancy was mainly due to contributions from charge transfer transitions between the molecule and metal. It should be mentioned that the work function of Au is -5.3 eV (relative to the vacuum level) and that of graphite (presumably close to that of the nanotubes) is -4.5 eV, therefore, a charge transfer from the graphite to the metal is expected to occur with ease at a Raman excitation wavelengths of 514.0 nm, resulting in the Fermi level shift.

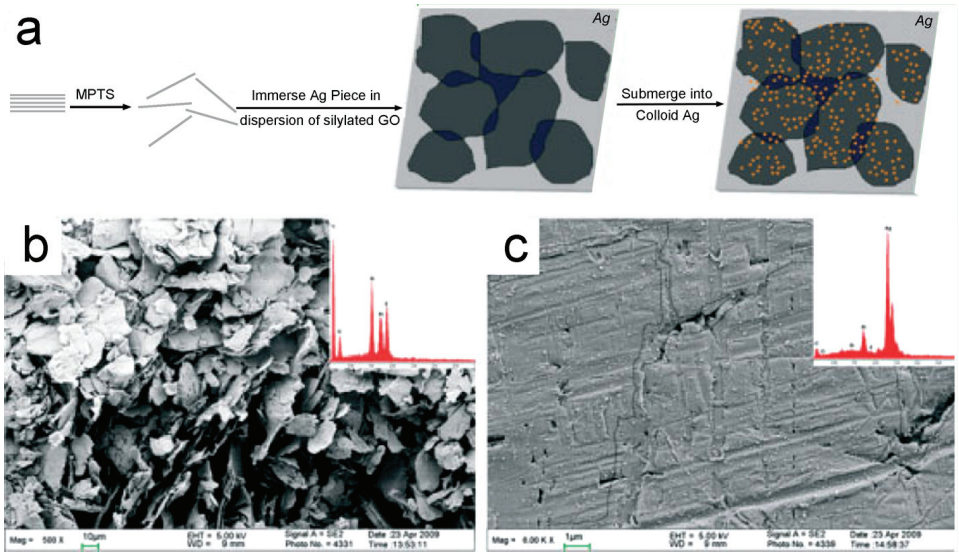

Fig. 9. (a) Scheme showing a proposed formation processes of Ag piece/GO/colloidal Ag sandwiches. SEM images of (b) MPTS-GO and (c) Ag piece/GO/colloidal Ag sandwiches. The inset shows the EDS image (Fu et al., 2010b).

To get a large enhancement, a structure of Ag piece/GO/colloidal Ag sandwiches is devised (Fu et al., 2010b). The typical route involves self-assembly of silylated GO sheets on a silver piece and then submerges the piece into colloidal Ag (Fig. 9a). It is seen from TEM, SEM and EDX analyses that the lamellar structures of GO sheets and the size of Ag particles remained, although the GO layers were exfoliated and destroyed after silylation (Fig. 9b and c). Remarkably, the enhanced factor of GO in this system is estimated to be about 10^4. The large enhancement of the SERS spectrum of silylated GO sheets can be attributed to the electromagnetic coupling of the colloidal Ag nanoparticles and the surface of the Ag piece, most probably due to the interactions of the localized surface plasmon of colloidal Ag nanoparticles and the surface plasmon polariton of the Ag piece. This research extends the capability of SERS investigations to GO products and points to a promising future for the fabrication of thin films with smart properties.

2.5 Methanol fuel cells

In recent years, fuel cells have been extensively considered as very promising devices, which convert the chemical energy of a fuel (hydrogen, natural gas, methanol, gasoline, etc.) and an oxidant (air or oxygen) into electricity. Among them, the direct methanol fuel cel1 (DMFC) has been developed for portable devices, such as mobile phones and laptops owning to its simple design and operation. The direct oxidation of methanol is a key step during DMFC operation and has been extensively investigated. Platinum is taken as the most active metal for methano1 oxidation. However, individual Pt particles for methanol adsorption has subjected to 1ow DMFC power density, low CO toleration, and short cycle life. Therefore, on one hand, Pt-based multiple alloys have been explored, for example the binary Pt-Ru alloy is generally accepted as the most promising candidate for improving DMFC performance. On the other hand, to improve deposition of Pt alloys nanoparticles onto carbon supports are demonstrated as an effective pathway. Given the cost-effectiveness, good conductivity and large specific surface area, graphene is undoubtedly the most intriguing nanoscale substrate.

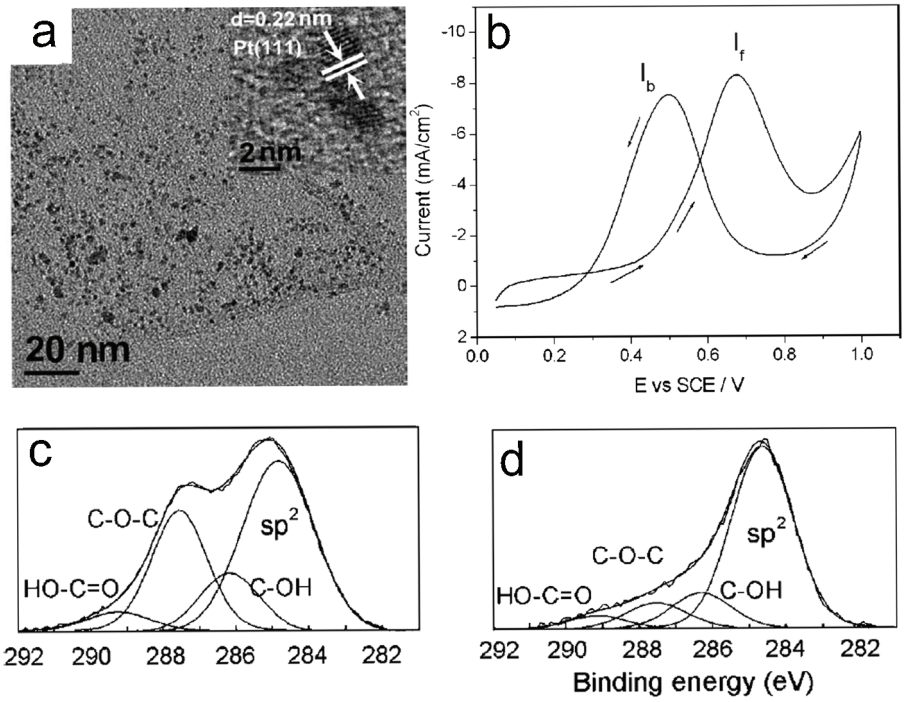

Fig. 10. (a) TEM images of graphene-Pt nanocomposites; (b) Cyclic voltammogram (20 mV s^{-1}) of methanol oxidation at graphene-Pt in 2 M CH_3OH + 1 M H_2SO_4 solution at room temperature. C1s XPS spectra of GO and graphene-Pt composite; (c) The C1s XPS spectrum of GO clearly indicates oxidation with four components that correspond to carbon atoms in different functional groups: the sp^2-hybridized C-C, the C in C-OH bonds, the epoxy C, and the carboxylate carbon; (d) the intensities of these groups in Pt-C become weak as a result of the deoxygenation, indicating the reduction of GO (Xu et al., 2008a).

Fig. 10 is the TEM, XPS and CV analyses of as-prepared graphene-Pt nanocomposites. It has been found that a water-ethylene glycol mixture is a very useful system to synthesize carbon-noble metal particle nanocomposites. Considering the facile exfoliation nature of GO in water, and the mild reducibility of the ethylene glycol for GO sheets, a water-ethylene glycol system was employed (Xu et al., 2008a). It is clearly seen in Fig. 10a that the almost transparent carbon sheets were decorated randomly by the nano-sized Pt particles. Because the monolayer carbon nanosheets were extremely thin, it was hard to make a distinction between them and the carbon-supported films on the copper grid. The crumpled silk waves of these carbon sheets leads us to believe that these nanoparticles indeed deposited on the supports. In addition, high-resolution TEM (HRTEM) images shown in the insets of Fig. 10a suggests the anchored crystal metal particles distributed uniformly on these single carbon sheets without obvious aggregations. The lattice fringes with interplanar distances of approximately 0.22 nm correspond to the nearest (111) plane of Pt.

The reduction of GO in water-ethylene glycol system can be verified by XPS analyses. The XPS spectrum of graphene-Pt composite indicates that the sample contains C, O and Pt as the main elements. The deconvolution of the C1s peak of graphene-Pt in Fig. 10d shows there are four types of carbon bonds: C-C (284.5 eV), C-OH (286.3 eV), C-O-C (287.5 eV), and HO-C= O (289.1 eV), respectively. By integrating the area of the deconvolution peaks, the following approximate percentages with respect to C-C bonds were obtained: C-C, 100; C-OH, 19; C-O-C, 14; HO-C=O, 6. The amount of incorporated functional groups in graphene-Pt is much lower than that of the unreduced GO as shown in Fig, 9c, where the approximate percentages of carbon atoms with respect to C-C bonds is C-C, 100; C-OH, 28; C-O-C, 59; HO-C=O, 11. The results of the XPS implied the decrease tendency of oxygen content in the composite. The intensity of some oxygenated functional groups on carbon sheets in the as-synthesized composites was obviously reduced, indicating the deoxygenation of GO. Specifically, the epoxy groups underwent considerable deoxygenation on the carbon sheets in these composites compared with the starting GO. The intensity of hydroxyl groups were also reduced to some extent.

The electrochemical performance of the graphene-Pt composite was tested for methanol oxidation, which is closely related to applications in DMFC. Figure 10b shows representative cyclic voltammetry plots of a graphene-Pt composite in CH_3OH solution, in which the typical methanol oxidation current peaks (I_f, 0.68 V) and the residual carbon species oxidation peaks (I_b, 0.53 V) appeared. The ratio of I_f/I_b is high (1.35), suggesting the good CO toleration of the catalyst. Moreover, there is seldom change of I_f/I_b even after 50 cycles, indicating good stability in the electrochemical cycling process.

To further verify that graphene is a promising candidate as supports of high-loading metal catalyst in fuel cells, a composite of highly loaded 80 wt.% Pt-Ru on graphene sheets was prepared using colloidal method, using Vulcan XC-72R (a kind of active carbon with a surface area of ~250 $m^2\ g^{-1}$) for comparison (Bong et al., 2010). As displays in Fig. 11a, the TEM analyses were conducted to verify dispersion degree, particle size distribution, alloy state and average particle size of the catalyst. It is clearly seen that the almost transparent graphene sheets were decorated homogeneously by the nanoscale Pt-Ru alloy particles with excellent dispersion. The size of Pt-Ru particle on graphene sheets ranges from 1 to 3.5 nm with an average particle size of 2.5 nm (inlet of Fig. 11a). XRD data in Fig. 11b present Pt (1 1 1) peak observed from all alloy catalysts shifts slightly towards the higher values compared with the pure Pt. This shift means that the alloy is formed between Pt and Ru.

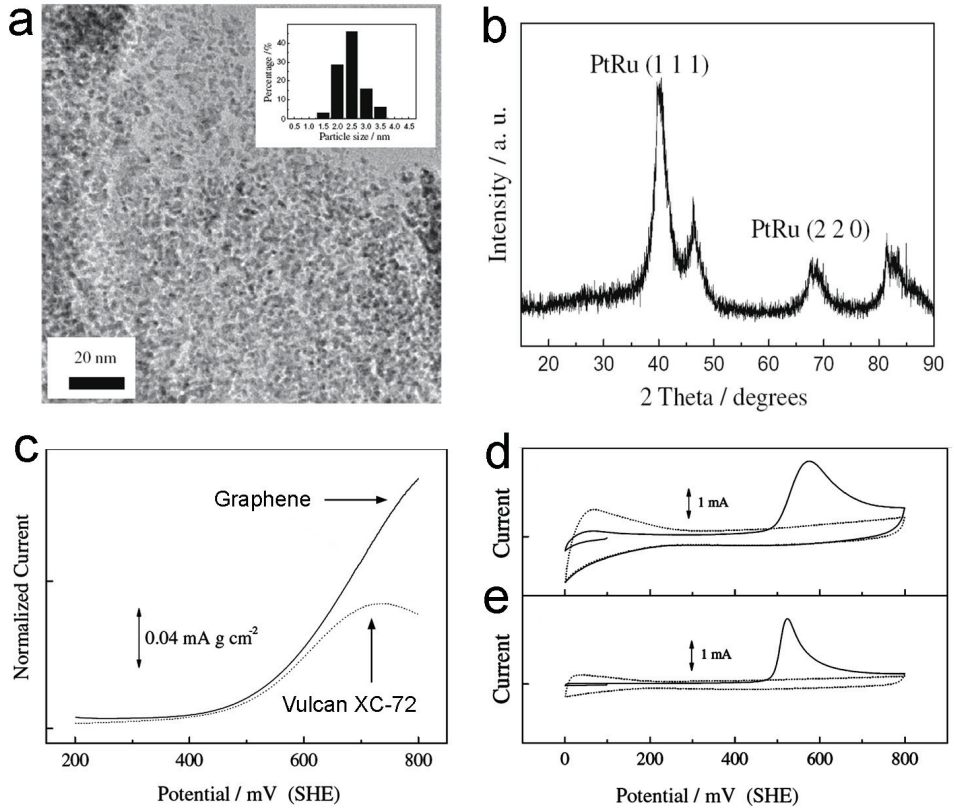

Fig. 11. (a) TEM images of Pt-Ru nanoparticles anchored on graphene sheets, and inlet graph is particle size distribution of Pt-Ru/graphene; (b) XRD profile of Pt-Ru/graphene catalyst; (c) normalized linear sweep Voltammograms obtaining of graphene nanosheets and Vulcan XC-72 supported Pt-Ru catalyst in 1 M H_2SO_4 and 1 M CH_3OH at 25 ^oC at a scan rate of 20 mV s^{-1}; (d) CO_{ad} stripping voltammograms of Pt-Ru/graphene and Pt-Ru/Vulcan XC-72 recorded in 1 M H_2SO_4 at a scan rate of 20 mV s^{-1} (Bong et al., 2010).

The electrochemically active surface area (ESA) is an effective manner to evaluate the number of available active sites. Fig. 11d and 11e shows the CO_{ad} stripping voltammograms of Pt-Ru/graphene and Pt-Ru/Vulcan recorded in 1 M H_2SO_4 at a scan rate of 20 mV s^{-1}. The ESA was determined assuming a monolayer of linearly adsorbed CO requires 420 μC cm^{-2} for its oxidation interesting to note that graphene catalyst (47.9 m^2 g^{-1}) exhibits larger electrochemical surface area than Vulcan catalyst value (28.3 m^2 g^{-1}) and it is attributable to the size of Pt-Ru particles well anchored on graphene sheets. The difference of the ESA values is related to the difference in the particle size in inverse proportion. The electrocatalytic activity for methanol oxidation was evaluated by linear sweep voltammetry. Fig. 11c represents the linear sweep voltammogram of the Pt-Ru/graphene and Pt-Ru/Vulcan in 1M CH_3OH and 1 M H_2SO_4 and the voltammogram displays that the Pt-Ru/graphene catalysts exhibit almost four times higher geometric anode peak current than that of Pt-Ru/Vulcan. In addition, these results can be transferred into normalized current

density (mAg m^2). Considering the electrochemical surface area and those of Pt-Ru/graphene and Pt-Ru/Vulcan are 0.113 and 0.0812 mAg m^{-2} at 700 mV, respectively. The enhancement of electrochemical activity of Pt-Ru/graphene could originate from highly dispersed particle size effect and large electrochemical surface area.

2.6 Supercapacitors

In recent years, due to environmental issues and depleting fossil fuels, interest in the development of alternative energy storage/conversion devices with high power and energy densities catering to the present day demands has increased to a great extent. Supercapacitors, also named electrochemical capacitors (ECs) or ultracapacitors, is a novel, low-cost and environmentally friendly energy storage systems. One of its advantage is that it can store and release energy at relatively higher rates than those accessible with batteries because its mechanisms for energy storage. In addition, they have several orders of magnitude higher energy density than that of conventional dielectric capacitors. They can complement or replace batteries in electrical energy storage and harvesting applications, when high power delivery or uptake is needed. Since 1957, when the practical utilization of electrochemical capacitors for the storage of electrical charge was demonstrated and patented by General Electric, supercapacitors are ideal for any application having a short load cycle and high reliability requirement, such as energy recapture sources including load cranes, forklifts, and electric vehicles.

Commonly, a supercapacitor unit cell is composed of two porous electrodes that are isolated from electrical contact by a separator (Fig. 12a). Current collectors of metal foil or carbon impregnated polymers are employed to conduct electrical current from each electrode. The separator and the electrodes are impregnated with an electrolyte, which allows ionic current to flow between the electrodes while preventing electronic current from discharging the cell. A packaged supercapacitor module, depending upon the desired size and voltage, is constructed of multiple repeating unit cells (Stoller et al., 2008). To approach the real application, the coin-shaped supercapacitors have been fabricated. An optical image of a real coin-shaped graphene-based supercapacitor device is displayed in Figure 12c (Wang et al., 2009b).

Generally, there are two kinds of supercapacitors based on the electrode materials: (1) high surface area, inert and conductive materials that store and release energy by nanoscopic charge separation at the electrochemical interface between an electrode and an electrolyte; (2) some redox active materials that use fast, reversible redox reactions at the surface of active materials which is known as the pseudo-capacitance. The carbonaceous nanostructures (like CNTs, active carbon and graphene) are commonly studied as electrodes for electrochemical double layer capacitors (EDLCs); while transition metal oxides or hydroxides (such as RuO_2, MnO_2, $Ni(OH)_2$, etc,) and conducting polymers (like polyaniline), are promising material for pseudocapacitors.

Considering that graphene sheets have high electrical conductivity and large specific surface area (calculated value, 2630 m^2 g^{-1}), which is substantially higher than values derived from BET surface area measurements of other carbon supports (such as activated carbons, carbon fibers, and CNTs), these peculiar characters may beneficial for insertion/desertion between ions of electrolyte and electrode material, giving rise to the good electrochemical performance of the material. The utilization of individual graphene sheets as electrode material for supercapacitors has been reported. Fig. 12b is the TEM images of graphene sheets prepared from a solution reduction process. It is interesting that this unique structure

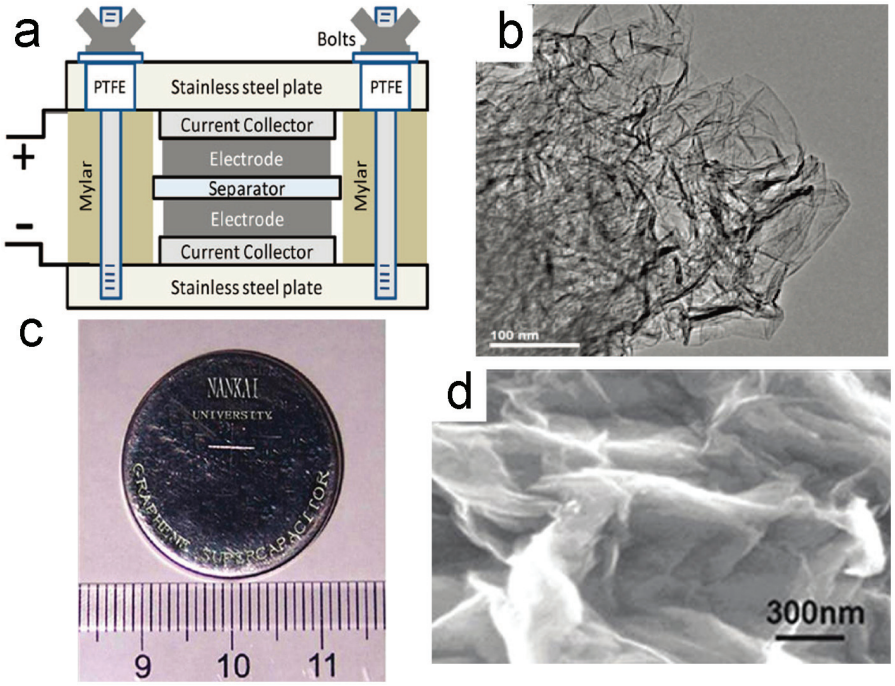

Fig. 12. (a) Schematic of test cell assembly of supercapacitors (Stoller et al., 2008); (b) TEM images of graphene sheets prepared from a solution reduction process (Stoller et al., 2008); (c) An optical image of an industry-grade coin-shaped graphene-based supercapacitor device (Wang et al., 2009b); (d) Scanning electron microscopy (SEM) image graphene sheets prepared from gas-based hydrazine reduction (Wang et al., 2009b).

gives graphene a consistently good performance over a wide range of voltage scan rates in the electrochemical testing (Stoller et al., 2008). In addition, Wang et al proposed a procedure for preparing graphene from gas-based hydrazine reduction of GO, which could restore the conducting carbon network without yielding much aggregation. SEM image of as-obtained graphene sheets is shown in Figure 12b. Notably that the graphene material exhibit excellent stability, with specific capacitance remaining ~90 % after 1200 cycles (Wang et al., 2009b).

Despite these advantages, graphene, being a kind of carbon material and charged-discharged mainly by EDLC, is also subjected to the problems that have emerged in other carbon-based materials for supercapacitors. The utilization of strong alkaline electrolyte is less eco-friendly. The specific capacitance of the pure graphene-based devices is relatively low in comparison with that of other pseudocapacitive materials, resulting in a low energy density. For example, the specific capacitance of graphene ranges from 100 to 200 F g^{-1}, while as a typical metal oxide, hydrate RuO_2, has a specific capacitance of 720 F g^{-1}. A notable improvement in performance may be achieved through the advances in understanding charge storage mechanisms and the development of advanced nanostructured materials. In view of large specific area, good conductivity and excellent electrochemical stability of graphene, and high power density of pseudo-captive materials,

one possible route to acquire high-performance electrochemical materials is the combination of graphene and the pseudocapacitive materials. Moreover, it should be mentioned that due to the low natural abundance and the requirement of highly acidic solutions in operation (such as sulfuric acid) as electrolyte have limited wide spread usage of RuO_2, and therefore, the development of novel electrode materials will accelerate the supercapacitor having an energy density as high as a secondary battery.

2.6.1 Graphene-inorganic nanoparticles composites

Manganese dioxide (MnO_2) is one of the most stable manganese oxides with excellent physical and chemical properties under ambient conditions. Because of its rich polymorphism and structural flexibility, this oxide has wide applications in catalysis, ion exchange, molecular absorption, microwave absorption, biosensors, and energy storage. As a potential excellent electrode material for the alternation of RuO_2 in supercapacitors, MnO_2 has received considerable attention in recent years owning to its abundant availability on the earth. Besides, MnO_2 shows good electrochemical performance in a neutral electrolyte (such as Na_2SO_4, K_2SO_4, and LiCl), which would be noteworthy when focused on eco-friendly point of view. As recently demonstrated, the electrochemical performance of MnO_2 critically depends on their crystallographic forms and then on their textural properties including morphology, surface area, pore volume, pore dimension, etc (Devaraj & Munichandraiah, 2008).

Considering the abundant functional groups of GO which can be regarded as anchor sites, a study on using GO as nanoscale supports to stabilize MnO_2 particles is examined (Chen et al., 2010d). Take the composite of CMG_3 (chemically synthesized GO-MnO_2 nanocomposites when the feeding ratio of MnO_2/GO is 3/1; the mass of MnO_2 is calculated by $MnCl_2$ according to the reaction: $2KMnO_4 + 3MnCl_2 + 2H_2O \rightarrow 5MnO_2 + 2KCl + 4HCl$) as an example. The results of nanocomposites with other feeding ratios are similar. The heterostructure of the composite is shown in Fig. 13. The GO sheets are multi-layers with diameters of a few micrometers, while the nano-MnO_2 shows needle-like morphology with typical diameters of 20-50 nm and lengths of 200-500 nm. It can be clearly seen from Figure 13c that the GO sheets were exfoliated and decorated randomly with the needle-like MnO_2. Comparing the bright- and dark-field TEM images in Figure 13c and d, the single layered graphene oxide sheet can be clearly distinguished from the background. The tip of a MnO_2 nanoneedle is shown in Figure 13e and f. It can be clearly seen from Figure 13e that the nanoneedle is actually composed of a few primary nanorods aggregated along the lateral faces. The nanorods of the center portions are longer than others, giving an indication that the oriented attachment mechanism played an important role in the formation of the nanoneedles. Additionally, the lattice fringes with interplanar distances of approximately 0.7 nm shown in Figure 13f correspond to the (110) plane of the tetragonal α-MnO_2 structure.

To test the electrochemical properties of GO-MnO_2 composites, the samples were fabricated into electrodes and characterized with CV and galvanostatic charge-discharge measurements. CV response carried out at a scan rate of 5 mV s^{-1} in 1 M Na_2SO_4 aqueous electrolyte solution is shown in Figure 14. The rectangular and symmetric CV curves of nano-MnO_2 indicate the ideal pseudo-capacitive nature of the fabricated electrode, while the lack of symmetry in $CMG_{0.5}$, CMG_3, and CMG_{15} is probably due to combined double-layer and pseudo-capacitive contribution to the total capacitance. Interestingly, with the feeding ratio of MnO_2/GO increasing from 0.5 to 15, CV plots of CMG_{ratio} became more close to that of the nano-MnO_2, which can be attributed to the increment of pseudo-capacitive contribution to the overall capacitance.

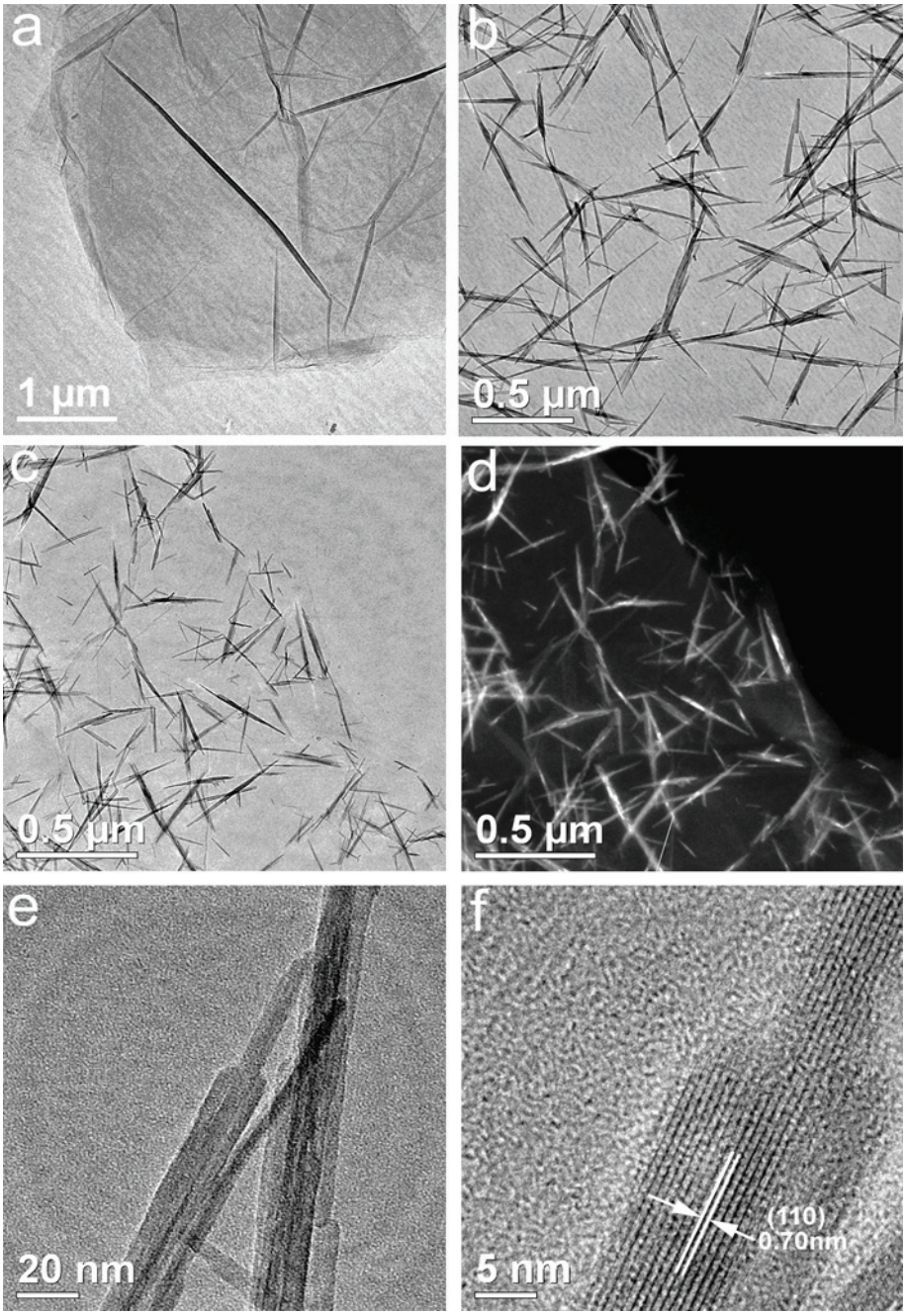

Fig. 13. (a, b) TEM images of GO and nano-MnO_2; (c, d) Bright and dark field images of CMG_3; (e, f) the HRTEM images of a MnO_2 nanoneedle (Chen et al., 2010d).

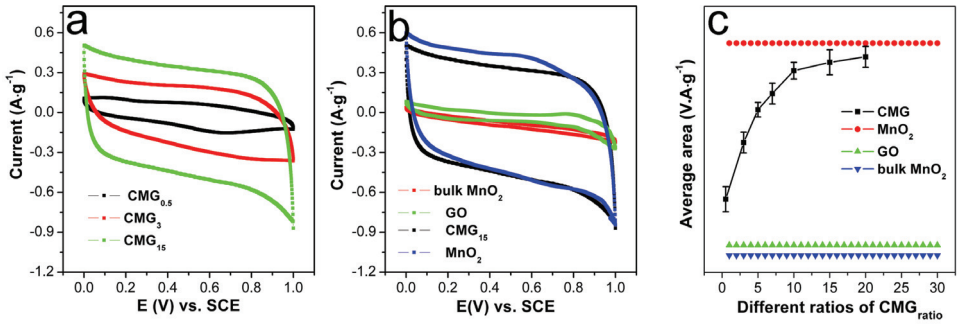

Fig. 14. CVs of (a) $CMG_{0.5}$, CMG_3, CMG_{15}; (b) bulk MnO_2, GO, CMG_{15} and nano-MnO_2 at 5 mV s^{-1} in 1 M Na_2SO4 solution; (c) Plot of average area of CV curves as a function of different ratios of CMG_{ratio}, with the average area of CV curves of nano-MnO_2, GO, and bulk MnO_2 for comparison (Chen et al., 2010d).

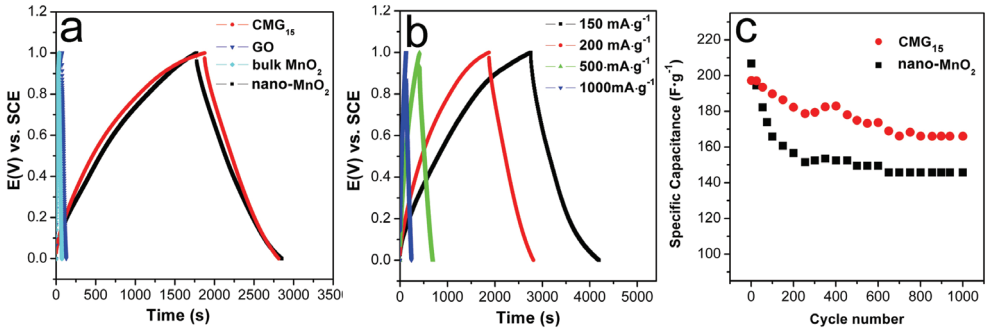

Fig. 15. CVs of (a) CMG0.5, CMG3, CMG15; (b) bulk MnO2, GO, CMG15 and nano-MnO2 at 5 mV s-1 in 1 M Na2SO4 solution; (c) Plot of average area of CV curves as a function of different ratios of CMGratio, with the average area of CV curves of nano-MnO2, GO, and bulk MnO2 for comparison (Chen et al., 2010d).

Galvanostatic charge-discharge measurements were carried out in 1 M Na_2SO_4 at a current density of 200 mA g^{-1}. As illustrated in Figure 15a, during the charging and discharging steps, the charge curve of CMG_{15} is almost symmetric to its corresponding discharge counterpart with a slight curvature, indicating the pseudo-capacitive contribution along with the double layer contribution. The C_s is calculated according to $C_s = I \times \Delta t / \Delta V \times m$ from the discharge curves, where I is the constant discharge current, Δt is the discharge time, ΔV is the potential drop during discharge; the C_s values of CMG_{15}, nano-MnO_2, GO and bulk MnO_2 are 197.2, 211.2, 10.9, and 6.8 F g^{-1}, respectively. These values are mainly consistent with the order indicated by the CVs.

Furthermore, the electrochemical stability of CMG_{15} and nano-MnO_2 is investigated in the range of 0 to 1 V at 200 mA g^{-1} in 1 M Na_2SO_4 aqueous solution (Figure 14c). It is found that the CMG_{15} electrode retained about 84.1 % (165.9 F g^{-1}) of initial capacitance after 1000 cycles, while that of the nano-MnO_2 retained only about 69.0 % (145.7 F g^{-1}). The discrepant electrochemical stability between CMG_{15} and nano-MnO_2 may be attributable to the different double-layer and pseudo-capacitive contributions. As well known, the double-

layer process only involves a charge rearrangement, while pseudo-capacitive is related to a chemical reaction, and the double-layer capacitors have a better electrochemical stability but lower C_S as compared with those of pseudo-capacitators. Accordingly, the as-synthesized CMG_{15}, making more double-layer contribution compared to that of nano-MnO_2 owning to the effect of GO, have a slightly lower C_s than the later; however, the electrochemical stability is obviously enhanced.

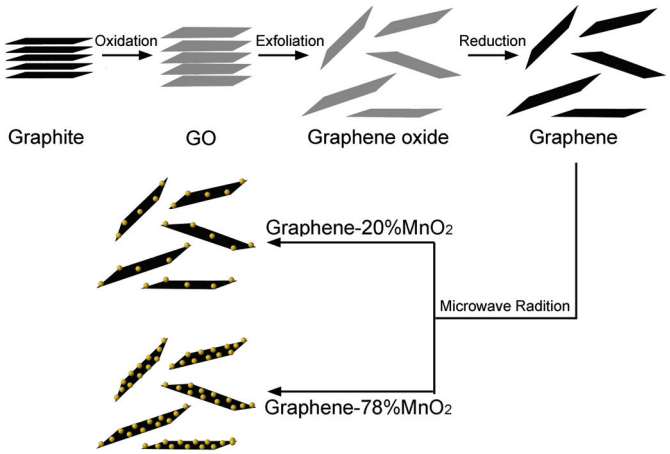

$$4MnO_4^- + 3C + H_2O \rightleftharpoons 4MnO_2 + CO_3^{2-} + 2HCO_3^-$$

Fig. 16. Schematic illustration and possible reactions for the synthesis of graphene-20% MnO_2 and graphene-70% MnO_2 composites (Yan et al., 2010).

As mentioned in chapter 3.3, the deoxygenation of GO-MnO_2 by reducing agent (like ethylene glycol) only produces graphene-MnOOH composites. To prepare the hybrid of graphene supported MnO_2 nanoparticles, the redox reaction between graphene sheets and $KMnO_4$ by microwave irradiation was reported (Yan et al., 2010). The schematic illustration and possible reactions for the synthesis of graphene-20% MnO_2 and graphene-70% MnO_2 composites are shown in Fig. 16. It can be seen from SEM and TEM images that graphene nanosheets can serve mainly as a highly conductive support, which can also provide a large surface for the deposition of nanoscale MnO_2 particles of about 5–10 nm (not shown). The large surface of graphene has been preserved by the products. The excellent interfacial contact and increased contact area between MnO_2 and graphene can significantly promote the electrical conductivity of the electrode due to the high electrical conductivity of graphene. Besides, the easy surface accessibility of this composite by the electrolyte, and the improved electrochemical utilization of MnO_2, resulted from the small particle size and high surface/area of the oxides, could provide both the high reversible pseudo-capacity and excellent capacitive retention ratio at high charge–discharge rate. In addition, the electrochemical tests of the as-obtained products show excellent performances. Graphene–78 wt.% MnO_2 composite displays the specific capacitance as high as 310 F g^{-1} at 2 mV s^{-1}, which is almost three times higher than that of pure graphene (104 F g^{-1}) and birnessite-type MnO_2 (103 F g^{-1}). The capacitance retention ratio is highly kept over a wide range of scan rates (88% at 100 mV s^{-1} and 74% at 500 mV s^{-1}). Moreover, the electrode material has a low ESR of ~0.66 Ω and good stability.

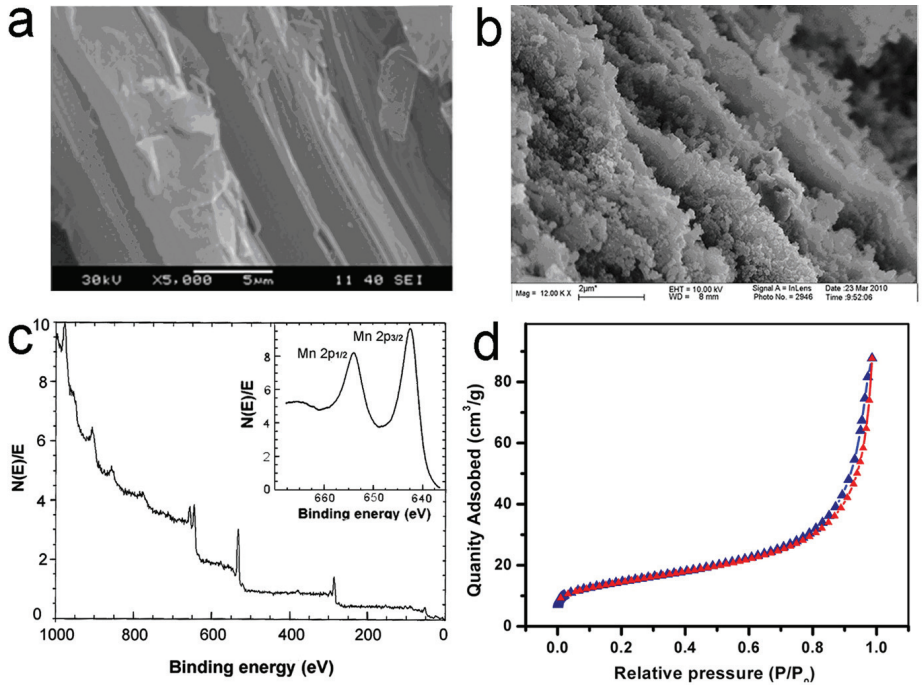

Fig. 17. (a) FESEM images of graphene sheets; (b) FESEM (c) XPS (d) Nitrogen adsorption/desorption isotherm of the as-obtained MnO_2-lamellas. The inset of (a) is the digital image of graphene dispersion; the inset of (c) is Mn (2P) peaks of MnO_2 nano-lamellas in XPS analyses (Chen et al., 2010c).

To further enrich potential applications of graphene, a facile procedure to explore the framework substitution of graphene by MnO_2 is investigated (Chen et al., 2010c). Single-layer-graphene and few-layer-graphene structures have been predicted to have high specific surface area. Recent research has focused largely on utilizing the intriguing morphology of graphene as building blocks or substrates, keeping the structure undisturbed. Therefore, a procedure for morphology transmission from graphene to MnO_2 nano-lamellas by in situ replacement with the framework of graphene is examined. The approach involves using graphene sheets as the starting reagent, thereby transmitting the morphology of layered structure from graphene to as-prepared MnO_2 product.

The definitive evidence that almost all the carbon atoms of graphene can be replaced by MnO_2 to form nano-lamellas was obtained with FESEM. It can be seen in Fig. 17 that the lamellar structure of graphene was indeed transmitted to the products. The brinks of the sheets can be clearly discerned; the lamellar structures of the products are fully seen. XPS results (Fig. 17c) indicate that the product contains Mn and O as the main components, while C and K are impurities. The binding energy of Mn 2p1/2 and Mn 2p3/2 is 642.4 and 654.2 eV, respectively. The splitting of the Mn 2p peak (11.8 eV) is very close to that of manganese (+4), suggesting the MnO_2 nature of the product. Surface area measurements indicate that the MnO_2 nano-lamellas have a Brunauer-Emmett-Teller (BET, nitrogen, 77 K) surface area of 50.3 m2 g-1, with pore volume of 0.135 cm^2 g^{-1}, and BJH desorption average

pore diameter of 14.4 nm. Remarkably, this value is much higher than the MnO_2 produced by traditional co-precipitation of $KMnO_4$ and Mn^{2+}. A large surface area suggests wider utilization of the as-prepared material.

The as-prepared products were fabricated to electrodes and tested using CV and galvanostatic charge/discharge measurements in 1 M Na_2SO_4 aqueous electrolyte (Figure 17). The rectangular and symmetric CV curves of MnO_2 nano-lamellas in Figure 15a indicate the ideal pseudo-capacitive nature of the as-fabricated electrode, while the lack of symmetry in graphene can be attributed to its double-layer capacitance in neutral electrolyte. Specific capacitance of MnO2 calculated at 150, 200, 500, 1000 and 2000 mA g-1 from the discharge curves is 206.2, 200.1, 191.0, 165.8 and 149.7 F g-1, respectively (Figure 18b-c). About 72.6 % specific capacitance was retained even with the current density increasing from 150 to 2000 mA g^{-1}. Consistently good performance of MnO_2 nano-lamellas over a wide range of current densities suggests this material is promising as supercapacitor electrodes. Additionally, when the charge-discharge was cycled at 500 mA g^{-1} as shown in Figure 18d, there is only a slight decrease in capacitance of less than 10 % even after 3000 cycles, demonstrating a great stability.

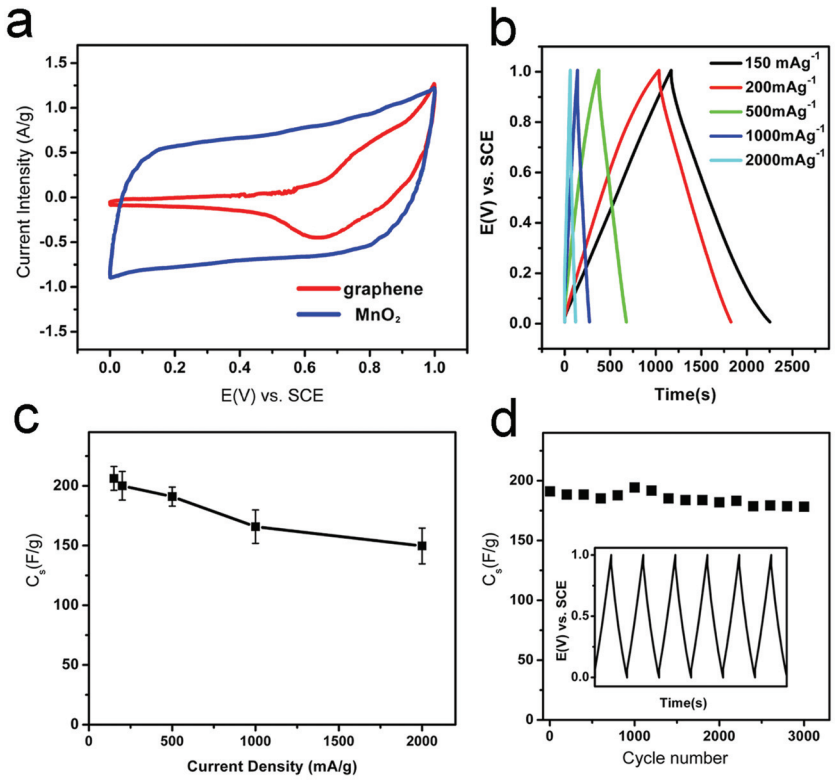

Fig. 18. (a) CV plots of graphene and MnO_2 at 5 mV s^{-1}; (b) Galvanostatic charge/discharge measurements of MnO_2 nano-lamellas at different current densities; (c) Plot of specific capacitance (C_s) as a function of current density of MnO_2 lamellas; (d) Cycle life of MnO_2 lamellas at 500 mA g^{-1} (Chen et al., 2010c).

Besides MnO_2, It has been demonstrated that some other metal oxides, such as SnO_2, ZnO (Lu et al., 2010) and Mn_3O_4 (Wang et al., 2010) etc., are also promising candidates as electrode material for supercapacitors. Specifically, recent studies suggest transitional metal hydroxides, such as $Co(OH)_2$ or $Ni(OH)_2$, have shown advanced electrochemical behaviors. Cobalt Hydroxide ($Co(OH)_2$) is an attractive material in recent years on account of their layered structure with large interlayer spacing and their well-defined electrochemical redox activity. Being an important electrochemical active material, a great deal of interest has been centered on the utilizations of $Co(OH)_2$ material in alkaline batteries, fuel cells and supercapacitors. Previous reports have shown that the film of $Co(OH)_2$ material has a higher specific capacitance than that of RuO_2. Taking into account the high specific area of graphene which be serve as excellent building blocks for nanocomposites, and the fact that graphene is a promising supercapacitor electrode material, consistently giving good electrochemical performance in strong alkaline electrolytes, the combination of $Co(OH)_2$ and graphene may produce synergistic results, giving the overall system enhanced electrochemical properties.

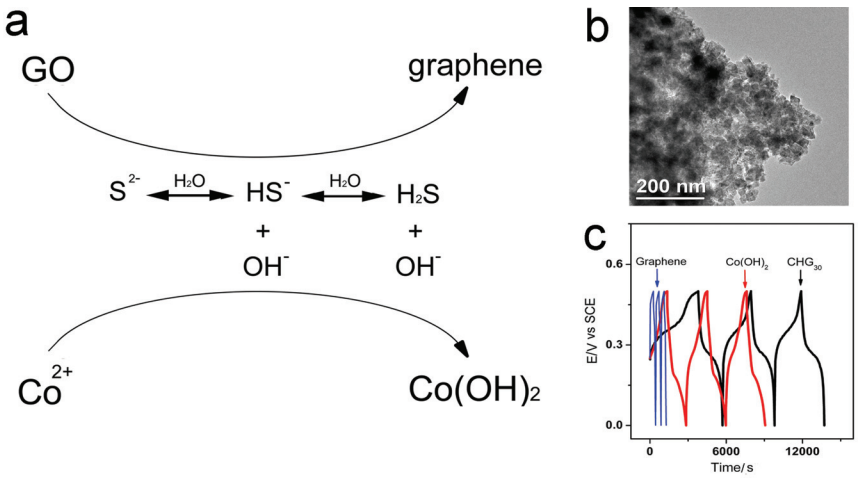

Fig. 19. (a) Proposed reactions for the formation of graphene-$Co(OH)_2$ nanocomposites; on one hand deoxygenate GO by S^{2-}, HS^-, H_2S, and OH^- from hydrolyzation of Na_2S in aqueous solution, on the other hand deposit Co^{2+} by OH^- (Chen et al., 2010b).

A typical procedure of depositing $Co(OH)_2$ onto graphene sheets is depicted in Fig. 19a. One essential characteristic of this procedure is the utilization of in situ hydroxylation of Na_2S aqueous solutions (Chen et al., 2010b). Due to the strong inclination of Na_2S to be hydrolyzed in aqueous solutions, the deposition of Co^{2+} and deoxygenation of GO occur in one step. Specifically, the negatively charged GO sheets, which have a high capability of absorbing dissolved Co^{2+} ions via electrostatic interactions, were first suspended in isopropanol. Subsequently, Na_2S aqueous solution was introduced rapidly into the above system. Due to the formation of large amounts of OH^- produced by the hydrolysis of Na_2S, Co^{2+} was precipitated easily in the form of $Co(OH)_2$. The exhaustion of OH^- provides a strong driving force for the further hydrolysis of Na_2S, which leads to the releasing of H_2S in large amounts. On the other hand, the produced H_2S, along with HS^-, S^{2-} and OH^- provide a great boost to the deoxygenation of GO.

Figure 19b displays a high density of $Co(OH)_2$ on graphene sheets for CHG_{30} (chemically synthesized from graphene-$Co(OH)_2$ nanocomposites at a feeding ratio of 30/1 for $Co(OH)_2$/GO; $Co(OH)_2$ is calculated on the basis of the amount of $CoCl_2 \cdot 6H_2O$ utilized according to the reaction: $Co^{2+} + 2OH^- \rightarrow Co(OH)_2$), and it looks like the particles are enveloped by a thin film. Notably, the graphene sheets are exfoliated and serve as excellent substrates to stabilize $Co(OH)_2$.
Figure 19c shows galvanostatic charge-discharge curves of CHG_{30}, $Co(OH)_2$, and graphene at 500 mA g^{-1}. The C_s of CHG_{30}, $Co(OH)_2$, and graphene at 500 mA g^{-1} are calculated to be 972.5, 726.1, and 137.6 F g^{-1}, respectively. The higher C_s of CHG_{30} than that of individual $Co(OH)_2$, and graphene suggests an elevated electrochemical performance of the overall system. Notably, the C_s value of CHG_{30} (972.5 F g^{-1}) is obviously higher than the typical electrode material of supercapacitors (RuO_2, 720 F g^{-1}), implying good electrochemical capacitance behaviors of the as-prepared nanocomposite.
Additionally, as reported by Wang et al. (Wang et al., 2010a), Single-crystalline $Ni(OH)_2$ hexagonal nanoplates directly grown on lightly oxidized, electrically conducting graphene sheets has exhibited exhibit advanced electrochemical performances, with high specific capacitance of ~1335 F g^{-1} at a charge and discharge current density of 2.8 A g^{-1} and ~953 F g^{-1} at 45.7 A g^{-1} with excellent cycling ability. It is highlighted the importance of direct growth of nanomaterials on graphene to impart intimate interactions and efficient charge transport between the active nanomaterials and the conducting graphene network. Considering the low cost of Mn, Co and Ni in comparison with noble metals (Ru), the advancement in these fields has stimulated significant progresses in supercapacitors.

2.6.2 Graphene-poly aniline (PANI) composites

Among the families of electrode materials for supercapacitors, conductive polymers have been extensively studied in recent years. Owning to the pseudocapacitive behaviors in doping and dedoping process, these materials could give large specific capacitance, high power and energy density. The main conductive polymer materials that have been investigated for the supercapacitor electrode are polyaniline (PANI), polypyrrole (PPy), polythiophene (PTH) and their derivatives, and so on. Polyaniline (PANI) is a popular due to its ease of synthesis, environmental stability, and simple acid-doping/base-dedoping chemistry. However, the relative poor cycling life restricts its practical applications. Taking into the good electrochemical stability of carbons (like graphene), the combination of graphene with PANI may provide improved performances as electrode materials for supercapacitors.
Considering the hydrophilic nature of GO, a simple in situ polymerization method in water system was reported to synthesize the nanocomposites of GO-doped PANI (GP) which were used as electrode materials (Wang et al., 2009a). The nanocomposites, signed as PG_{ratio}, like $PG_{100:1}$, $PG_{61:1}$, represent the feeding ratios of PANI: GO.
SEM and TEM images in Fig. 20e and f demonstrate the fibrillar morphology of the prepared nanocomposite $PG_{100:1}$, with the dimension of about 300 nm in diameter and 2-3 μm in length, compared with the granular aggregate structure for the pure PANI (not shown). These fibers are in fact built from many smaller nanofibers about 30 nm in diameter and 100-150 nm in length on the surface, and nanosheets in the backbone of the fibers.
Fig. 20a and b illustrates the cyclic voltammograms (CVs) and EIS plots of PANI, GO, $PG_{61:1}$ and $PG_{100:1}$ electrode. Compared with the GO and PANI electrodes, the nanocomposites exhibit larger current density response in A g^{-1} at 10 mV s^{-1} and less estimated charge-transfer resistances. This means that the electrochemical performances of the nanocomposites are enhanced due to the synergistic effect between GO and PANI.

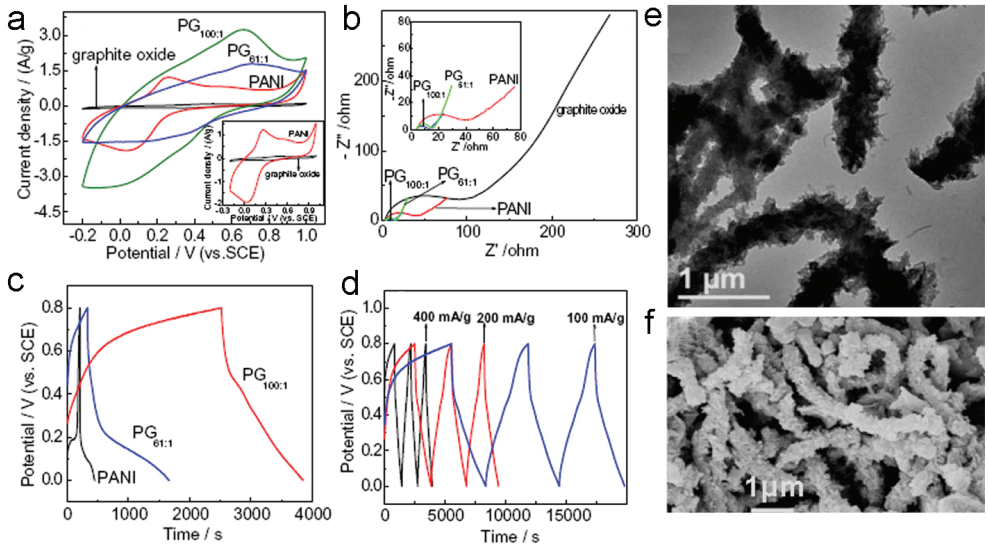

Fig. 20. CVs (a) at 10 mV s^{-1} (b) EIS of GO, PANI, $PG_{61:1}$, $PG_{100:1}$; (c) galvanostatic charge-discharge curves of PANI, $PG_{61:1}$, $PG_{100:1}$ at 200 mA g^{-1}; (d) galvanostatic charge-discharge curves of $PG_{100:1}$ at 100, 200, and 400 mA g^{-1}, respectively; TEM (e) and SEM (f) images of $PG_{100:1}$ (Wang et al., 2009a).

The specific capacitance (C_s) was calculated from the charging and discharging curves (Fig. 20c). The high C_s values were evaluated as 216, 284 and 531 F g^{-1} at 200 mA g^{-1} in the range from 0 to 0.45 V, for PANI, $PG_{61:1}$ and $PG_{100:1}$, respectively. Remarkably, the capacitance of the polymeric material is critically enhanced by the GO sheets. Moreover, the nanocomposites demonstrate good capacitive behavior and charge-discharge property at a current density of 100-500 mA g^{-1}. C_s of $PG_{100:1}$ is higher and that of $PG_{61:1}$, implying that the feeding ratio of the nanocomposite influences its electrochemical capacitance greatly.

The possible combinding mode of GO/PANI composite is investigated using Raman, FTIR, UV-vis and XPS, which is proposed including: (a) π-π stacking (b) electrostatic interactions, and (c) hydrogen bonding, as presented in Fig. 21 (Wang et al., 2010b).

Because the reaction parameters exert a great influence on the electrochemical performances of the composite, in order to get a higher specific capacitance, the effect of raw graphite material sizes and feeding ratios on the electrochemical properties of such composites have been systematically investigated (Wang et al., 2010b). Specifically, The GO/PANI composite was prepared by an in situ polymerization using a mild oxidant. The composites are synthesized under different mass ratios, using graphite as start material with two sizes: 12 500 and 500 mesh. The result shows that the morphology of the prepared composites is influenced dramatically by the different mass ratios. The highest initial specific capacitances of 746 F g^{-1} (12 500 mesh) and 627 F g^{-1} (500 mesh) corresponding to the mass ratios 1:200 and 1: 50 (GO/aniline) are obtained, compared to PANI of 216 F g^{-1} at 200 mA g^{-1} by charge-discharge analysis between 0.0 and 0.4 V. The improved capacitance retention of 73 % (12 500 mesh) and 64 % (500 mesh) after 500 cycles is obtained for the mass ratios 1:23 and 1:19 compared to PANI of 20%. The enhanced specific capacitance and cycling life implies a synergistic effect between two components.

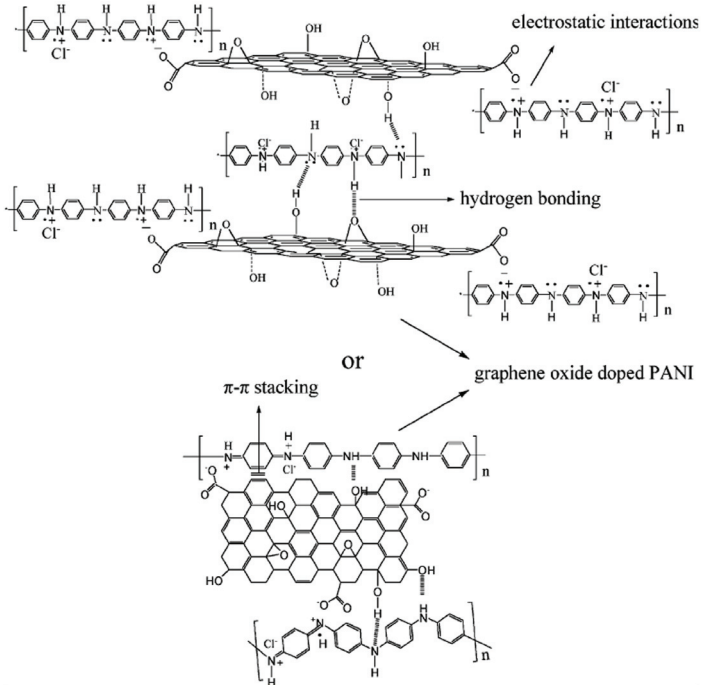

Fig. 21. Proposed possible combinding mode of GO/PANI Composite (Wang et al., 2010b).

To prepare graphene-PANI composites, a simple three-step synthesis method was presented by an in situ polymerization-reduction/dedoping-redoping process (Wang et al., 2010c). This method greatly improves the specific capacitance, retention time, energy density, and power density of the composite as electrode material for supercapacitors.

The formation process of the GEP composite is depicted in Fig. 22. The multilayer GO is extensively exfoliated into GEO nanosheets with abundant oxygen containing groups on both face and edges under ultrasonication in ethylene glycol. Such GEO nanosheets facilitate the uniform adsorption of aniline molecules under stirring. When APS and hydrochloric acid are added into the suspension under ice bath, the aniline molecules absorbed on the sheets are initiated to polymerize just from the absorbed sites on the surface, and then the structure of PANI covering nano-sheet slowly forms. This structure of the hybrid material maintains unaltered when GEO sheets are reduced and PANI are dedoped by sodium hydroxide at the temperature of 90 ^{o}C for 5 h, and it keeps steady even when PANI nanoparticles are redoped in hydrochloric acid solution. In addition, the morphology of the prepared hybrid material is quite uniform and no individual graphene or PANI agglomerates can be observed, suggesting that graphene sheets are covered by nanostructured PANI granules completely and successfully. It is noteworthy that the hybrid nanosheets can be convoluted freely without being splitting into pieces (Fig. 22, see blue lines in GEOP-1 and GEP-3 in the TEM images), further indicating the flexibility of the composites. The perfect coverage of PANI on graphene makes full use of the large specific area of graphene and could be favorable for the enhancement of electrochemical properties of the composite materials.

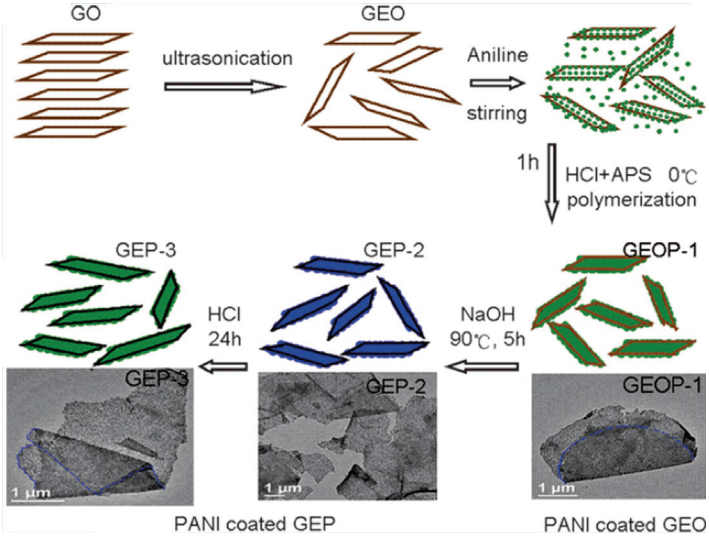

Fig. 22. A scheme illustrating the preparation process of GEP hybrid materials (Wang et al., 2010c).

The electrochemical performance of the electrode materials was analyzed using CV and galvanostatic charge-discharge. Fig. 23a shows the CV curves of the pristine graphene, PANI, GEOP-1, GEP-2 and GEP-3 at a scan rate of 1 mV s^{-1} in 1 M H_2SO_4 electrolyte in the potential range from -0.2 to 0.6 V. Both PANI and the composite electrodes show a pair of redox peaks. The peak positions of individual components are very close to each other and nearly merge into one peak. The specific capacitance was calculated. The pristine graphene electrode exhibits an approximated rectangular shape that is characteristic of an electric double layer capacitance (EDLC) with a specific capacitance of 316 F g^{-1}. The PANI electrode shows a pair of redox peak that is characteristic of pseudo-capacitance with the specific capacitance 777 F g^{-1}. On the other hand, the CV curves of GEOP-1, GEP-2 and GEP-3 electrodes show a behavior of a combination of both EDLC and redox capacitance with the specific capacitance of 827, 1126 and 1079 F g^{-1}, respectively. The specific capacitance changes with different samples were illustrated in Fig. 23b. The GEOP-1 electrode exhibits a sharply increased electrochemical capacitance compared to the graphene electrode. After treating with sodium hydroxide, the specific capacitance of GEP-2 electrode goes as high as 1126 F g^{-1}. Although the redoping process leads to a little decrease of the capacitance, the specific capacitance of 1079 F g^{-1} for GEP-3 is still higher than GEOP-1 and much better than each component of the hybrid material.

The cycling performance is shown in Fig. 23c and d. Fig. 23c gives a non-linear galvanostatic charge-discharge curve of GEP-2 for the first 1–5 cycles, which presents an evident pseudo-capacitance character. After 1000 cycles the bending extent of the curve becomes weak and the curve tends to linear, but still non-linear. This indicates the contribution of pseudo-capacitance in GEP hybrid materials decreases, and the EDLC effect becomes evident. The CV curves before charge-discharge test and after 1000 cycles are shown in Fig. 23d (inset). A large and wide area of the CV curve with a pair of evident redox peaks can be seen before charge–discharge test, indicating both EDLC and pseudo-capacitance performance of the

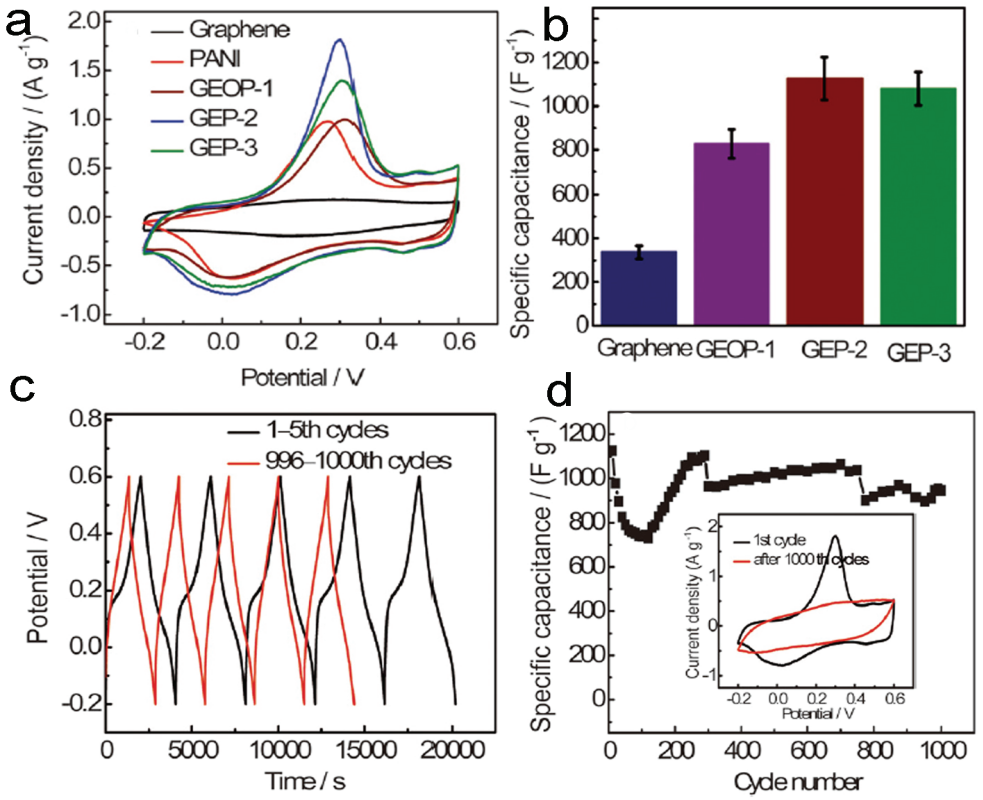

Fig. 23. (a) CV curves of graphene, PANI, GEOP-1, GEP-2 and GEP-3 at 1 mV s^{-1} in 1 M H_2SO_4 in the potential range from -0.2 to 0.6 V; (b) specific capacitance changes with different samples; (c) comparison of galvanostatic charge–discharge curves of GEP-2 between 1–5th and 996–1000th cycles at 200 mA g^{-1} in 1 M H_2SO_4 in the potential range from -0.2 to 0.6 V; (d) specific capacitance as a function of cycle number. (Inset: comparison of the CV curves before charge-discharge test and after 1000 cycles for charge–discharge test) (Wang et al., 2010c).

electrode. After 1000th cycles, the redox peaks become weak and nearly disappear. This results from the reduced pseudo-capacitance of PANI. The specific capacitance as a function of cycle number is shown in Fig. 23d. It is interesting that the specific capacitance sharply decreases first for the 1–100 cycles and increases rapidly for 100–200 cycles and then maintain approximately steady after 200 cycles around 900 F g^{-1}. The specific capacitance for GEP-2 after 1000 cycles still maintains 946 F g^{-1}, corresponding to 84% of the initial cycle. This result is better than that reported for the composites of graphene and PANI with capacitance retention of 84% after only 40 cycles; when the capacitance retention of GEOP-1 after 1000 cycles is 59%. The enhanced retention life for GEP-2 is mainly due to the change from GEO to graphene in the hybrid material, leading to the improvement of mechanical properties of the composite.

2.7 Other potential applications

The integration of graphene with other materials has also exhibited additional peculiar properties. For example, a composite of graphene–cuprous oxide has found to be an anode material in lithium ion batteries, giving a high capacity of ca.1100 mAh g^{-1} in the first charge–discharge cycle (Xu et al., 2009); the graphene–CdS quantum dot nanocomposite has shown promising optoelectronic performance and may be a potential material in novel semiconductor hybrid system (Cao et al.). Moreover, single-layer graphene can be modulated with various aromatic molecules to be an n- and p-doped type for tailoring its transistor devices (X.Dong et al., 2009); metal particles (Au, Au-Pt alloy, etc.) decorated graphene nanosheets can be used as immobilization matrix for amperometric glucose biosensor (Baby et al., 2010). In addition, Kuc et al. pointed out that the composite of fullerene intercalated graphene sheets has promising applications in hydrogen sieving and storage (Kuc et al., 2006).

3. Conclusion and perspectives

During the past few years, significant efforts have been directed toward the preparation of graphene-based nanocomposites, and the highly unique properties of these materials have been demonstrated for a variety of catalysts, supercapacitors and fuel cell batteries. It is indubitable that utilizing graphene-based nanocomposites in either of these technologies is a new endeavor, indicating that future research efforts will be abundant. One of the future challenges is to maintain the excellent physical properties of graphene in the process for synthesizing nanocomposites. It should be pointed out that GO sheets are indisputably effective precursors for bulk production of hybrid materials currently and the major shortcoming of this approach is the loss of conductivity. A seemingly obvious prediction is that a more straightforward route can be developed *via* direct oxidation of pristine graphene in soft manners, so that relatively low amount of functional groups is produced as the anchor sites to decorate graphene with nanoparticles. One feature of such process is that there is no need to reduce the composites because of the low oxidation degree, leading to lower defected frameworks of graphene. Notable is the progress in the area of graphene-based nanocomposites and hybrids. However, much more remains to be done, especially when considering the practical application of these materials in catalysts and electrochemical devices. The opportunities and challenges that rest on these targets should attract the efforts of many scientists and engineers in this important and fantastic field.

4. References

Allen, M. J., Tung, V. C. & Kaner, R. B. (2010). Honeycomb Carbon: A Review of Graphene. *Chem. Rev.,* 110, 1, (Feb-2010), page numbers (132-145), 0009-2665

Baby, T. T., Aravind, S. S. J., Arockiadoss, T., Rakhi, R. B. & Ramaprabhu, S. (2010). Metal Decorated Graphene Nanosheets as Immobilization Matrix for Amperometric Glucose Biosensor. *Sensors Actuat. B-Chem.,* 145, 1, (Mar-2010), page numbers (71-77), 0925-4005

Boldyrev, V. V. (2006). Thermal Decomposition of Ammonium Perchlorate. *Thermochim. Acta,* 443, 1, (Apr -2006), page numbers (1-36), 0040-6031

Bong, S., Kim, Y.-R., Kim, I., Woo, S., Uhm, S., Lee, J. & Kim, H. (2010). Graphene Supported Electrocatalysts for Methanol Oxidation. *Electrochem. Commun.,* 12, 1, (Nov-2010), page numbers (129-131), 1388-2481

Boukhvalov, D. W. & Katsnelson, M. I. (2008). Modeling of Graphite Oxide. *J. Am. Chem. Soc.,* 130, 32, (Jul-2008), page numbers (10697-10701), 0002-7863

Cao, A., Liu, Z., Chu, S., Wu, M., Ye, Z., Cai, Z., Chang, Y., Wang, S., Gong, Q. & Liu, Y. (2010). A Facile One-step Method to Produce Graphene–CdS Quantum Dot Nanocomposites as Promising Optoelectronic Materials. *Adv. Mater.,* 22, 1, (Jan-2010), page numbers (103-106), 1521-4095

Chen, S., Zhu, J., Huang, H., Zeng, G., Nie, F. & Wang, X. (2010a). Facile Solvothermal Synthesis of Graphene-MnOOH Nanocomposites. *J. Solid State Chem.,* In Press, DOI: 10.1016/j.jssc.2010.08.026, 0022-4596

Chen, S., Zhu, J. & Wang, X. (2010b). One-Step Synthesis of Graphene-Cobalt Hydroxide Nanocomposites and Their Electrochemical Properties. *J. Phys. Chem. C,* 114, 27, (Jun-2010b), page numbers (11829-11834), 1932-7447

Chen, S., Zhu, J. & Wang, X. (2010c). From Graphene to Metal Oxide Nanolamellas: A Phenomenon of Morphology Transmission. *ACS Nano*, In Press, DOI: 10.1021/nn101857y, 1936-0851

Chen, S., Zhu, J., Wu, X., Han, Q. & Wang, X. (2010d). Graphene Oxide-MnO_2 Nanocomposites for Supercapacitors. *ACS Nano,* 4, 5, (Apr-2010d), page numbers (2822–2830), 1936-0851

Devaraj, S. & Munichandraiah, N. (2008). Effect of Crystallographic Structure of MnO_2 on Its Electrochemical Capacitance Properties. *J. Phys. Chem. C,* 112, 11, (Feb-2008), page numbers (4406-4417), 1932-7447

Dikin, D. A., Stankovich, S., Zimney, E. J., Piner, R. D., Dommett, G. H. B., Evmenenko, G., Nguyen, S. T. & Ruoff, R. S. (2007). Preparation and Characterization of Graphene Oxide Paper. *Nature,* 448, 7152, (Jul-2007), page numbers (457-460), 0028-0836

Ferrari, A. C. (2007). Raman Spectroscopy of Graphene and Graphite: Disorder, Electron–phonon Coupling, Doping and Nonadiabatic Effects. *Solid State Commun.,* 143, 1-2, (Jul-2007), page numbers (47-57), 0038-1098

Fu, X., Bei, F., Wang, X., O'Brien, S. & Lombardi, J. R. (2010a). Excitation Profile of Surface-Enhanced Raman Scattering in Graphene-Metal Nanoparticle Based Derivatives. *Nanoscale,* 2, 8, (Jun-2010a), page numbers (1461-1466), 2040-3364

Fu, X., Bei, F., Wang, X., Yang, X. & Lu, L. (2010b). Surface-Enhanced Raman Scattering of Silylated Graphite Oxide Sheets Sandwiched between Colloidal Silver Nanoparticles and Silver Piece. *J. Raman Spectrosc.,* 41, 4, (Apr-2010b), page numbers (370-373), 1097-4555

Geim, A. K. & Novoselov, K. S. (2007). The Rise of Graphene. *Nat. Mater.,* 6, 3, (Mar-2007), page numbers (183-191), 1476-1122

Hernandez, Y., Nicolosi, V., Lotya, M., Blighe, F. M., Sun, Z., De, S., McGovern, I. T., Holland, B., Byrne, M., Gun'Ko, Y. K., Boland, J. J., Niraj, P., Duesberg, G., Krishnamurthy, S., Goodhue, R., Hutchison, J., Scardaci, V., Ferrari, A. C. & Coleman, J. N. (2008). High-Yield Production of Graphene by Liquid-Phase

Exfoliation of Graphite. *Nat. Nanotechnol.,* 3, 9, (Sep-2008), page numbers (563-568), 1748-3387

Kuc, A., Zhechkov, L., Patchkovskii, S., Seifert, G. & Heine, T. (2006). Hydrogen Sieving and Storage in Fullerene Intercalated Graphite. *Nano Lett.,* 7, 1, (Jan-2006), page numbers (1-5), 1530-6984

Li, D., Muller, M. B., Gilje, S., Kaner, R. B. & Wallace, G. G. (2008). Processable Aqueous Dispersions of Graphene Nanosheets. *Nat. Nanotechnol.,* 3, 2, (Jan-2008), page numbers (101-105), 1748-3387

Li, X., Cai, W., An, J., Kim, S., Nah, J., Yang, D., Piner, R., Velamakanni, A., Jung, I., Tutuc, E., Banerjee, S. K., Colombo, L. & Ruoff, R. S. (2009). Large-Area Synthesis of High-Quality and Uniform Graphene Films on Copper Foils. *Science,* 324, 5932, (May-2009), page numbers (1312-1314), 0036-8075

Lo´pez, V., Sundaram, R. S., Go´mez-Navarro, C., Burghard, D. O. M., Go´mez-Herrero, J., Zamora, F. l. & Kern, K. (2010). Chemical Vapor Deposition Repair of Graphene Oxide: A Route to Highly Conductive Graphene Monolayers. *Adv. Mater.,* 21(Aug-2010), page numbers (4683–4686), 1521-4095

Lotya, M., Hernandez, Y., King, P. J., Smith, R. J., Nicolosi, V., Karlsson, L. S., Blighe, F. M., De, S., Wang, Z., McGovern, I. T., Duesberg, G. S. & Coleman, J. N. (2009). Liquid Phase Production of Graphene by Exfoliation of Graphite in Surfactant/Water Solutions. *J. Am. Chem. Soc.,* 131, 10, (Feb-2009), page numbers (3611-3620), 0002-7863

Lu, T., Zhang, Y., Li, H., Pan, L., Li, Y. & Sun, Z. (2010) Electrochemical behaviors of graphene-ZnO and graphene-SnO_2 composite films for supercapacitors. *Electrochim. Acta* 55, 13, (May-2010), page numbers (4170-4173), 0013-4686

Novoselov, K. S., Geim, A. K., Morozov, S. V., Jiang, D., Zhang, Y., Dubonos, S. V., Grigorieva, I. V. & Firsov, A. A. (2004). Electric Field Effect in Atomically Thin Carbon Films *Science,* 306, 5696, (Oct-2004), page numbers (666-669), 0036-8075

Novoselov, K. S., Geim, A. K., Morozov, S. V., Jiang, D., Katsnelson, M. I., Grigorieva, I. V., Dubonos, S. V. & Firsov, A. A. (2005). Two-dimensional Gas of Massless Dirac Fermions in Graphene. *Nature.,* 438, 7065, (Nov-2005), page numbers (197-200), 0028-0836

Park, H. J., Meyer, J., Roth, S. & Ska´kalova´, V. (2010). Growth and properties of few-layer graphene prepared by chemical vapor deposition. *Carbon,* 48, 4, (Apr-2010), page numbers (1088-1094), 0008-6223

Park, S. & Ruoff, R. S. (2009). Chemical Methods for the Production of Graphenes. *Nat. Nanotechnol.* 4, (Mar-2009), page numbers (217-224), 1748-3387

Stankovich, S., Dikin, D. A., Kohlhaas, K. M., Zimney, E. J., Stach, E. A., Piner, R. D., Nguyen, S. T. & Ruoff, R. S. (2006). Graphene-Based Composite Materials. *Nature* 442, 7100, (Jul-2006), page numbers (282-286), 0028-0836

Stoller, M. D., Park, S., Zhu, Y., An, J. & Ruoff, R. S. (2008). Graphene-Based Ultracapacitors. *Nano Lett.* 8, 10, (Sep-2008), page numbers (3498-3502), 1530-6984

Wang, B., Park, J., Wang, C., Ahn, H. & Wang, G. Mn_3O_4 Nanoparticles Embedded Mn_3O_4 into Graphene Nanosheets: Preparation, Characterization, and Electrochemical

Properties for Supercapacitors. *Electrochim. Acta,* 55, 22, (Sep-2010), page numbers (6812-6817), 0013-4686

Wang, H., Hao, Q., Yang, X., Lu, L. & Wang, X. (2009a). Graphene Oxide Doped Polyaniline for Supercapacitors. *Electrochem. Commun.,* 11, 6, (Jun-2009a), page numbers (1158-1161), 1388-2481

Wang, H., Casalongue, H. S., Liang, Y. & Dai, H. (2010a). $Ni(OH)_2$ Nanoplates Grown on Graphene as Advanced Electrochemical Pseudocapacitor Materials. *J. Am. Chem. Soc.,* 132, 21, (May-2010a), page numbers (7472-7477), 0002-7863

Wang, H., Hao, Q., Yang, X., Lu, L. & Wang, X. (2010b). Effect of Graphene Oxide on the Properties of Its Composite with Polyaniline. *ACS Applied Mater. Interf.* 2, 3, (Mar-2010b), page numbers (821-828), 1944-8244

Wang, H., Hao, Q., Yang, X., Lu, L. & Wang, X. (2010c). A Nanostructured Graphene/Polyaniline Hybrid Material for Supercapacitors. *Nanoscale,* In Press, DOI: 10.1039/C0NR00224K, 2040-3364

Wang, Y., Shi, Z., Huang, Y., Ma, Y., Wang, C., Chen, M. & Chen, Y. (2009b). Supercapacitor Devices Based on Graphene Materials. *J. Phys. Chem. C,* 113, 30, (Jul-2009b), page numbers (13103–13107), 1932-7447

Weixia, Z., Jiecheng, C., Cheng-an, T., Yiguang, W., Zhanping, L., Li, M., Yuquan, W. & Guangtao, L. (2009). A Strategy for Producing Pure Single-Layer Graphene Sheets Based on a Confined Self-Assembly Approach. *Angew. Chem. Int. Ed.,* 48, 32, (Jul-2009), page numbers (5864-5868), 1521-3773

Williams, G., Seger, B. & Kamat, P. V. (2008). TiO_2-Graphene Nanocomposites. UV-Assisted Photocatalytic Reduction of Graphene Oxide. *ACS Nano* 2, 7, (Jul-2008), page numbers (1487-1491),

Wu, C., GuofaDong & LunhuiGuan. (2010). Production of Graphene Sheets by a Simple Heliumarc-Discharge. *Physica E: Low-Dimensional Systems and Nanostructures* 42, 5, (Mar-2010), page numbers (1267–1271), 1386-9477

X.Dong, D., Dongliang, F., Wenjing, F., Yumeng, S., Peng, C. & Lain-Jong, L. (2009). Doping Single-Layer Graphene with Aromatic Molecules. *Small* 5, 12, (Jun-2009), page numbers (1422-1426), 1613-6829

Xu, C., Wang, X. & Zhu, J. (2008a). Graphene & Metal Particle Nanocomposites. *J. Phys. Chem. C* 112, 50, (Nov-2008a), page numbers (19841-19845), 1932-7447

Xu, C., Wang, X., Zhu, J., Yang, X. & Lu, L. (2008b). Deposition of Co_3O_4 nanoparticles onto exfoliated graphite oxide sheets. *J. Mater. Chem.,* 18, 46, (Sep-2008b), page numbers (5625-5629), 0959-9428

Xu, C. & Wang, X. (2009). Fabrication of Flexible Metal-Nanoparticle Films Using Graphene Oxide Sheets as Substrates. *Small,* 5, 19, (Aug-2009), page numbers (2212-2217), 1613-6829

Xu, C., Wang, X., Yang, L. & Wu, Y. (2009). Fabrication of a Graphene-Cuprous Oxide Composite. *J. Solid State Chem.,* 182, 9, (Sep-2009), page numbers (2486-2490), 0022-4596

Yan, J., Fan, Z., Wei, T., Qian, W., Zhang, M. & Wei, F. (2010). Fast and Reversible Surface Redox Reaction of Graphene-MnO_2 Composites as Supercapacitor Electrodes. *Carbon* 48, 13, (Nov-2010), page numbers (3825-3833), 0008-6223

Zhang, Y., Tan, Y.-W., Stormer, H. L. & Kim, P. (2005). Experimental Observation of the Quantum Hall Effect and Berry's Phase in Graphene. *Nature* 438, 7065, (Nov-2005), page numbers (201-204),

Zhu, J., Zeng, G., Nie, F., Xu, X., Chen, S., Han, Q. & Wang, X. (2010). Decorating Graphene Oxide with CuO Nanoparticles in a Water-isopropanol System. *Nanoscale,* 2(Apr-2010), page numbers (988-994), 2040-3364

9

Graphene-Based Polymer Nanocomposites

Horacio J. Salavagione, Gerardo Martínez and Gary Ellis
Institute of Polymer Science and Technology, Spanish National Research Council (CSIC)
Spain

1. Introduction

Materials science continues to occupy a central place in our lives primarily through the design and creation of new materials, and our quality of life has improved over time thanks to the discovery of new materials. Major milestones in the advancement of our society are intimately associated with materials throughout history: the stone age, bronze age, iron age, steel age (industrial revolution), silicon age and silica age (telecom revolution) all reflect the important impact materials have in our civilization, and our daily life in the 21st century depends on an unlimited variety of materials of varying degrees of sophistication. Also, since our world is dominated by a consumer market, the demands to improve our lifestyle are without limit. Materials are fundamental to the technology that adds convenience to our lives, examples being laptop computers, digital cell phones, touch screens, and so on. Therefore, the challenge of creating new, more useful and diverse materials grows with the needs of society, and the limitations for covering needs such as sustainable energy, affordable health care, personal protection, etc., are closely related to constraints in the properties of materials.

One critical aspect for achieving materials with new improved properties is imaginative molecular design, synthesis and preparation of new materials. Materials chemistry focuses on understanding the relationships between the arrangement of atoms, ions or molecules comprising a material and its overall bulk structural/physical properties. Thus, it consists in the study of the structure and properties of existing materials, the synthesis and characterization of new or improved materials, and the use of advanced computational techniques to predict structures and properties of materials that have not yet been made. Since our demands are renewed continuously and new needs emerge daily, for further progress to meet present and future requirements a thorough understanding of existing materials and the tailor-making of new functional materials must be continued with increasing vigour.

Nowadays, in the frontiers of materials technology the concept of combining various types of materials through synergy is one of the most successful approaches to achieve specific goals with the greatest efficiency in properties and cost effectiveness. In this respect, polymers are one of the most successfully exploited classes of materials due to the incredible variety of chemical structures available and their subsequent compendium of properties, along with their relatively low cost, facile processing, and their possible recyclability and applicability as sustainable materials. The area of polymer nanocomposites (PNCs) has grown to represent one of the largest classes within the scope of materials science, becoming

a key area in nanoscience and nanotechnology offering significant potential in the development of advanced materials in numerous and diverse application areas (Ajayan et al. 2000, Thostenson et al. 2001, Ray and Okamoto 2003). Polymer nanocomposites are commonly defined as the combination of a polymer matrix and additives that have at least one dimension in the nanometre range. The additives can be one-dimensional, such as nanotubes and fibres, two-dimensional, which include layered clay minerals or graphene sheets, or three-dimensional, including spherical particles.

PNCs attract considerable interest due to the outstanding mechanical, optical, electrical, and thermal properties encountered with only a small quantity of nanofiller incorporated to the polymer matrix. This is caused by the large surface area to volume ratio of fillers when compared to micro- and macro-scale additives. The field of polymeric nanocomposites has evolved significantly from the earliest clay reinforced thermosetting resin *Bakelite* (Baekland 1909) developed at the beginning of the 20th century. New nanoscale materials are employed to reinforce polymers almost as soon as they have been discovered or developed, and continuing interest in the most widely used successful examples of nanofillers such as layered silicate clay-based nanocomposites and carbon nanotube-based nanocomposites have evolved more recently towards graphene-based nanocomposites.

The specific development of polymeric nanocomposites based on conventional polymers and conductive carbonaceous materials has drawn much attention as a route to obtain new materials with new structural and functional properties superior to those of the pure components and of previous nanocomposite systems with other fillers. Control of the size, shape and surface chemistry of the reinforcement materials are essential in the development of materials that can be used to produce devices, sensors and actuators based on the modulation of functional properties. At present, nanocomposites employing carbon-based reinforcement materials are dominated by carbon nanotubes (CNTs). However, the development of CNT-reinforced composites has been impeded by both their difficult dispersion in the polymer matrix and their high cost. A detailed analysis of CNTs-reinforced nanocomposites is beyond the scope of this chapter and several excellent books and reviews have been published (Ajayan et al 2000, Thostenson et al. 2001, Krueger 2010).

The discovery of graphene (Novoselov, et al 2004) and the subsequent development of graphene-based polymer nanocomposites is an important addition in the area of nanoscience, poised to play a key role in modern science and technology. Compared to carbon nanotubes, as well as its high aspect ratio and low density graphene has attracted considerable attention because of its unique and outstanding mechanical, electrical and electronic properties, which result in it being one of the most popular candidates for the development of functional and structural graphene-reinforced composites. Indeed, graphene-based PNCs is a rapidly growing area of nanoengineered materials, providing lighter weight alternatives to CNTs-based nanocomposites with additional functionality associated with nanoscale specific, value-added properties.

As clearly explained in previous chapters, graphene is an atomically thick, two-dimensional (2-D) sheet composed of sp^2 carbon atoms arranged in a honeycomb structure, viewed as the building block of all other graphitic carbon allotropes of different dimensionality, such as graphite, CNTs and fullerene (Geim and Novoselov, 2007). Graphene sheets have higher surface-to-volume ratios than CNTs owing to the inaccessibility of the inside surface of the nanotubes to the polymer molecules. This makes graphene sheets potentially more favourable for altering all matrix properties—such as the mechanical, rheological and

permeability properties, and thermal stability. Further, graphene is obtained from naturally occurring graphite implying that lighter nanocomposites can be produced at lower costs.
Tailor-made graphene-based nanocomposites which exploit the superlative properties of both graphene filler and polymer host can show enhanced performance in a large number of applications ranging from flexible packaging, semi-conductive sheets in transistors, memory devices, hydrogen storage, printable electronics, etc.
As occurred with other nanofillers, the maximum improvements in final properties can be achieved when the graphene is homogeneously dispersed in the matrix and the external load is efficiently transferred through strong filler/polymer interfacial interactions. However the nature of graphene makes it hard to disperse within the majority of polymers since it can only interact efficiently with a limited group of polymers typically containing aromatic rings. In addition, the low solubility of pristine graphene also limits its applications. In order to make graphene dispersible in - or compatible with - a variety of polymer matrices, as well as to maximize the interfacial interactions, chemical modification is generally required, introducing functional moieties that confer other properties to the pristine material.
This chapter will focus on functionalized graphene derivatives that have been employed in polymer nanocomposites obtained by solution intercalation. Although two more general methods for graphene dispersion in polymers exist, such as in-situ intercalative polymerization and melt intercalation, the area is overwhelmingly dominated by those prepared in solution. Some examples dealing with in-situ intercalative polymerization will be given, however, only a few examples of melt intercalation can be found. Whilst melt processing is one of the most important and widespread processing techniques in polymer materials production, it is generally not recommended because high-temperature mechanically driven processing can fragment the graphene sheets significantly decreasing the aspect ratio.
In spite of the fact that graphene is the youngest carbon allotrope, the exploration of its chemistry is rapidly advancing (Loh et al. 2010) and this chapter represents an updated panorama of the developments in the field of graphene based PNCs.

2. Discussion

2.1 Graphite oxide (GO) and Reduced graphite oxide (r-GO)

Graphite oxide (GO) is chemist's principal tool to modify graphene. It is obtained from the exhaustive oxidation of graphite, and contains a range of oxygen functional groups with specific chemistry, rendering it a good candidate for further functionalization (Dreyer et al. 2010). In addition currently the most promising methods for large scale production of graphene are based on exfoliation that generates graphene oxide, and its subsequent reduction.
Today there is no unambiguous model to describe the exact structure of graphite oxide because authors from different laboratories use different preparative methods and there is no single definitive analytical technique available to characterize the material. Even though there is some controversy and debate about the structure of GO, there seems to be consensus that the carboxylic groups are mainly located at the edge, while the rest of functional groups (hydroxyl, epoxide, etc.) are located in the basal planes of the graphitic layers. For better understanding and a deeper view on the chemical structure of GO the reader can visit other chapters in this book and an interesting review by the group of Prof. R. Ruoff (Dreyer et al. 2010).

The dispersability of GO depends on the extent of surface oxygenated groups as well as on the chosen solvent. However, it can be dispersed in a wide range of the same solvents in which the principal soluble polymers can be dissolved. Thus graphite oxide is dispersed in a solvent common to a specific polymer and then reduced to r-GO in presence of the polymer, with the aim of restoring the sp^2 network. The effective interaction between functional groups in GO and those in the polymers avoid the re-stacking of the graphitic layers after the reduction step. This constitutes the first type of example we shall describe in this chapter: the use of graphite oxide without further functionalization.

Poly(vinyl alcohol) (PVA) has been one of the preferred polymers to address this strategy. The high capacity of PVA to simultaneously form both intra- and interchain hydrogen bonding makes it an interesting polymer which could interact with GO in the same way and could be used as a model for understanding the interaction of graphite oxide with other polar polymers. For example, the synthesis of PVA/r-GO nanocomposites by chemical reduction of water-dispersed graphite oxide in presence of PVA has been reported (Salavagione et al. 2009). It has been proposed that some interactions occur between the polymer and the reduced graphite oxide layers, mainly by hydrogen bonding. These interactions are responsible for a remarkable change in the thermal behaviour of the nanocomposites. In addition, the electrical properties of the nanocomposites were superior not only with respect to the parent polymer but also compared with PVA/CNT nanocomposites. They show the typical insulating-conductive percolation behaviour (Figure 1). That is, conductivity remains at very low values (10^{-13} to 10^{-14} $S.cm^{-1}$) until a critical loading content is achieved. Then, it increases quickly by several orders of magnitude up to ca. 10^{-5} $S.cm^{-1}$. The percolation threshold for r-GO/PVA nanocomposites observed, between 0.5 and 1 wt%, was one order of magnitude lower than that reported for PVA/CNTs (Shaffer et al. 1999).

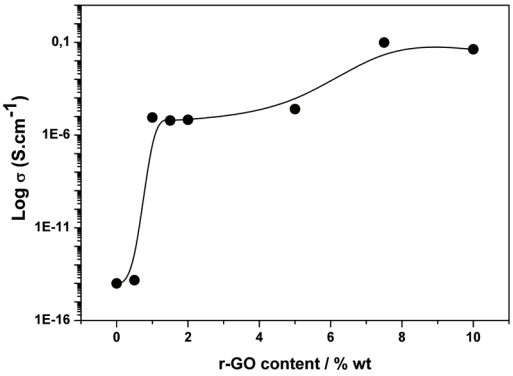

Fig. 1. Plot of the electric conductivity of PVA/RGO nanocomposites as a function of the RGO content (Reprinted with permission of The Royal Society of Chemistry, 2009).

In another example, the same procedure excluding the reduction step was employed to prepare PVA/GO nanocomposites (Liang et al. 2009). These nanocomposites showed enhanced mechanical performance due to the large aspect ratio of the graphene sheets, the molecular-level dispersion of the graphene sheets in the PVA matrix, and mainly due to strong interfacial adhesion due to hydrogen-bonding between graphene and the PVA matrix. For example, with only 0.7 wt% GO the tensile strength increased by 76% from 49.9

to 87.6MPa and the Young's modulus increased by 62% from 2.13 to 3.45G Pa with respect to the parent polymer.

Recently a similar procedure using sodium dodecylbenzene sulphonate (SDBS) as a surfactant has been reported (Zhao et al. 2010). The nanocomposites were prepared by chemical reduction of GO in an aqueous solution containing PVA and the stabilizing SDBS. The final products displayed significant enhancement of mechanical properties at low graphene loading: a 150% improvement of tensile strength and a nearly 10 times increase of Young's modulus were achieved at a graphene loading of only 1.8 vol %. Also the value of the elongation at break decreased from 220% for the polymer to 98% for the composite with the same loading, which was attributed to a large aspect ratio and the interaction between graphene and the matrix, which restricts the movement of the polymer chains.

Another remarkable study reported the fabrication of graphene–polymer nanocomposites with three-dimensional architectures (Vickery et al. 2009), where template-directed methods were employed to obtain higher-order architectures. Sponge-like macroporous scaffolds were generated by ice-segregation-induced self-assembly (ISISA) by freezing aqueous dispersions that contained homogeneous mixtures of polystyrene sulfonate-stabilized graphene sheets (PSS-G) and PVA (Figure 2).

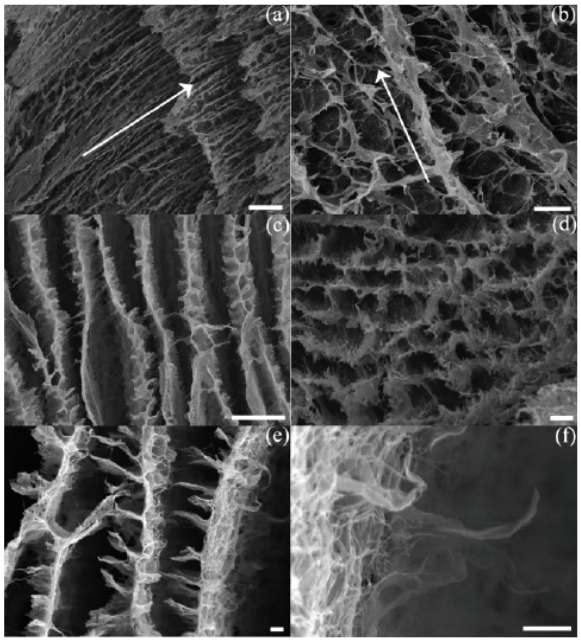

Fig. 2. SEM images of (a),(b) longitudinal sections, and (c),(d) cross sections of a PSS-G/PVA freeze-dried monolith (1:10 wt. ratio). Arrows in (a) and (b) indicate direction of freezing. Images (a),(c) show a layered structure, (b),(d) show a macroporous architecture. Image (e) is a higher-magnification image of the layered structure showing interlamellar cross links, and (f) shows an image of a single wall with loosely packed graphene sheets. Scale bars: 10 μm for (a),(c), and (d); 5 μm for (b); and 1 μm for (e) and (f). (Reprinted with permission of Willey-VCH, 2009).

In addition, hollow micrometer-sized PSS-G spheres or PSS-G coated polymer microparticles were prepared by the aqueous deposition of negatively charged PSS-G dispersions on the positively charged polymer bead surfaces (Figure 3).

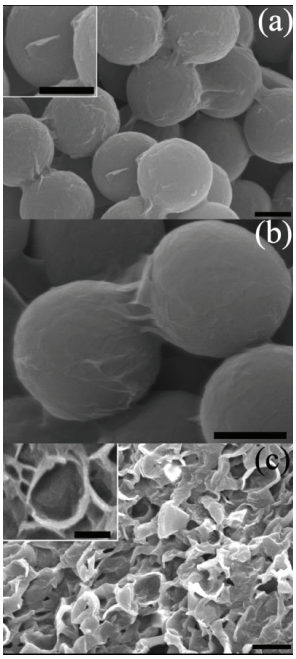

Fig. 3. SEM images of PSS-G-coated PAH-functionalized polystyrene beads: (a) Coated beads with surface textures. The inset shows the curled edge of an adsorbed PSS-G sheet, (b) High-magnification image showing overlapping PSS-G sheets on neighbouring beads, and (c) Sample after treatment with toluene showing aggregated film of deflated and fractured hollow graphene microspheres. The inset shows a single deflated hollow graphene microsphere. Scale bars: (a),(b) = 500 nm, (c) = 1μm. (Reprinted with permission of Willey-VCH, 2009).

Finally, GO/PVA hydrogel nanocomposites have been recently prepared (Bai et al. 2010). The formation of the hydrogels relied on the assembly of GO sheets and the cross-linking effect of PVA chains. The GO/PVA hydrogels exhibited pH-induced gel–sol transition and they were tested for loading and selectively releasing drugs at physiological pH.

Although here we only give a few representative examples on PVA/GO nanocomposites, a wide number of other studies can be found in the literature.

GO has also been employed in epoxy nanocomposites. In the first example, the materials were prepared by mixing adequate amounts of a GO aqueous solution with epoxy resin (Yang et al. 2009). Significant improvements in mechanical properties were achieved for the graphene oxide/epoxy resin for a 0.0375 wt% loading of chemically converted graphene oxide sheets, with an increase of 48.3% and 1185.2% in compressive failure strength and toughness, respectively.

In another study, GO was thermally reduced before mixing with the epoxy resin (Yu et al. 2007). Thermal conductivity measurements indicated that four layer GO, with a thickness of ca. 2 nm acts as a very efficient filler for epoxy composites. When embedded in an epoxy matrix, these graphite nanoplatelets provide a thermal conductivity enhancement of more than 3000% at a loading of 25 vol %, and a thermal conductivity k = 6.44 W/mK, which far surpasses the performance of conventional fillers that require loadings of around 70 vol % to achieve these values. The thermal conductivity using graphite nanoplatelets was higher than that using other carbon allotropes (Figure 4). This improvement in the properties was ascribed to the favourable combination of the high aspect ratio, two-dimensional geometry, stiffness, and low thermal interface resistance of the graphene nanoplatelets.

The above strategy relies on the fact that thermally or chemically reduced graphite oxide retains specific amounts of oxygenated groups, primarily as carboxylic moieties in the edge planes. This material is known as functionalized graphene sheets (FGS) (Li et al. 2008). Similarly, FGS was used as filler for poly(methyl methacrylate) (PMMA)] (Ramanathan, et al. 2007). The authors concluded that the reduced particle size, high surface area, and increased surface roughness significantly alter the filler/polymer interface enhancing the mechanical, thermal and electrical properties of the polymer matrix. In addition, an unprecedented shift in the glass transition temperature of over 40 ^{o}C was obtained for poly(acrylonitrile) (PAN) with 1 wt% of functionalized graphene sheet, and with only 0.05 wt% there is still an improvement of nearly 30 ^{o}C. Modulus, ultimate strength and thermal stability followed a similar trend, with values for functionalized graphene sheet–PMMA composites rivalling those for single-walled carbon nanotube–PMMA composites (Ramanathan et al. 2008).

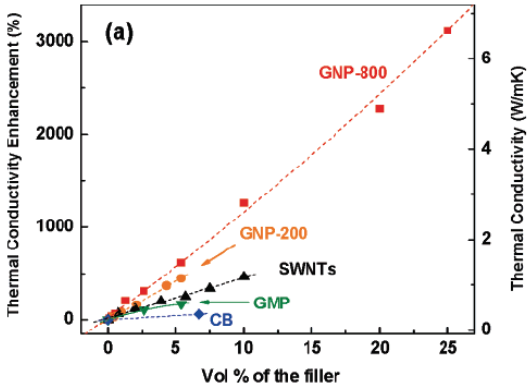

Fig. 4. Thermal conductivity enhancement of epoxy-based composites at 30 °C, using various graphitic fillers: graphitic microparticles (GMP), graphite nanoplatelets exfoliated at 200 °C (GNP-200) and 800 °C (GNP- 800), carbon black (CB), and purified SWNTs (Reprinted with permission of The American Chemical Society, 2007)

In another interesting example graphene nanosheets in the form of chemically reduced GO have been prepared in organic media (Villar-Rodil et al. 2009). The ability to prepare graphene dispersions in organic media facilitated their combination with polymers, such as PAN and PMMA, to yield homogeneous composites. Copolymers have been also employed to prepare nanocomposites with graphene. For instance, a stable aqueous graphene sheet

dispersion was prepared via the chemical reduction of exfoliated GO in the presence of a pluronic copolymer (poly-(ethylene oxide)-block-poly(propylene oxide)-block-poly-(ethylene oxide) triblock copolymer, PEO-b-PPO-b-PEO) (Zu and Han, 2009). Using this system the hydrophobic PPO segments bind to the surface of graphene via a hydrophobic effect, whereas the hydrophilic PEO chains extend into the water. The authors used the pluronic-graphene nanocomposites to prepare supramolecular hydrogels of the resulting graphene dispersion upon addition of R-cyclodextrin (R-CD) since the PEO chain can penetrate into the R-CD cavity. Potential applications in drug delivery are envisaged.

On the other hand, nanocomposites of r-GO with intrinsically conductive polymers have been reported (Zhao et al. 2009). A thin film of GO was deposited on indium tin oxide (ITO) electrodes, thermally reduced and covered with a layer of polyaniline (PANI). The PANI on graphene exhibited much higher electrochemical stability than PANI-ITO in aqueous acidic electrolytes and the performance of the electrochromic devices with graphene electrodes exhibited only slight decrease upon voltage switching while that of the devices with conventional ITO electrodes decreased considerably (Figure 5).

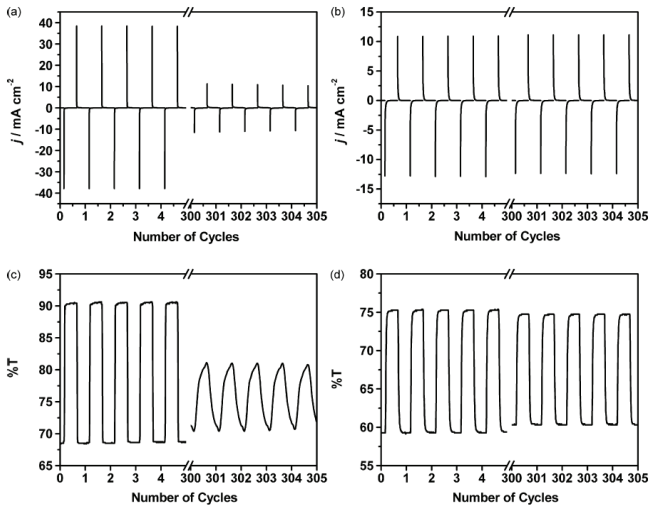

Fig. 5. Chronoamperometry (a and b) and transmittance curves at 700 nm (c and d) of the PANI-ITO (a and c) and PANI-Graphene (b and d) electrodes in 1 mol. L^{-1} H_2SO_4 for the first 5 and the 301st–305th cycles when an anodic potential was switched between −0.1 V and 0.5 V vs. Ag/AgCl for 10 s at each step (Reprinted with permission of Elsevier, 2009).

Also r-GO/polyelectrolyte nanocomposites have been prepared (Ansari et al. 2010). In this case well-dispersed nanocomposites with highly aligned graphene nanosheets in a polyelectrolyte (Nafion) matrix were described. By adapting experimental protocols originally developed for clay nanocomposites, highly oriented GO-Nafion nanocomposites were prepared by casting from an aqueous suspensión. Subsequent exposure of the GO–Nafion nanocomposites to hydrazine reduced the GO platelets *in-situ* producing well-aligned graphene–Nafion nanocomposites. The α relaxation of Nafion shifted to higher temperatures in the nanocomposites by as much as 50 ºC in the sample containing 7 wt% of GO. The modulus of the same sample was about a factor of two higher compared to that for

neat Nafion. Both of these effects was directly related to the molecular confinement in the vicinity of the organic/inorganic interface that drastically hinders the mobility of the polymer chains. Finally, after reduction with hydrazine, a conductivity value of 1.3 $S.m^{-1}$ was observed.

Ionic liquid polymers have also been employed to stabilize graphene dispersions (Kim et al. 2010). Briefly, the ionic liquid polymers were dissolved in water and added to an aqueous GO dispersion. This mixture was then reduced with hydrazine monohydrate to obtain r-GO sheets decorated with ionic liquid polymers that were well-dispersed in the aqueous phase and stable to chemical reduction. The authors demonstrated that hydrophilic-to-hydrophobic reversible switching of graphene sheets was possible by simply exchanging the anions associated with polymeric ionic liquids (PIL)(Figure 6).

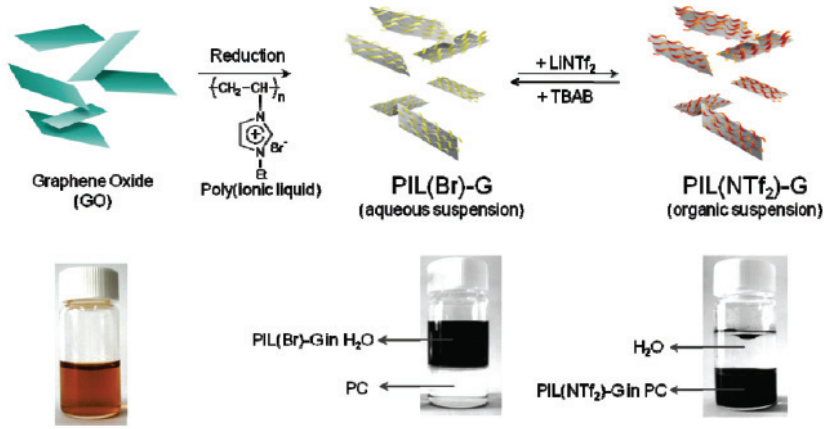

Fig. 6. Schematic illustration of synthetic process for the PIL-modified graphene sheets. (Reprinted with permission of American Chemical Society, 2010).

Finally, graphene-based nanocomposites have also been produced by *in-situ* intercalative polymerization. GO was employed in the polymerization of PVA (Liu et a 2000), PMMA (Jang et al. 2009), epoxy (Wang et al. 2009), poly(arylene disulphide) (Du et al.2005), and PANI (Wang et al. 2009; Zhang et al. 2010), while FGS were employed in the polymerization of silicone foams (Verdejo, et al. 2008) and poly(urethane) (Lee et al. 2009).

2.2 Functionalized graphite oxide (f-GO)

The reactive groups in GO offer the possibility of further modification rendering a more versatile filler for polymer nanocomposites. In principle, the chemistry of carboxylic, hydroxyl and epoxy groups can be extended to GO.

A complete study on the functionalization of GO with a wide number of organic isocyanates has been reported (Stankovich et al. 2006) (Figure 7). Exfoliation in polar aprotic solvents of isocyanate-treated GOs (iGOs) produced functionalized graphene oxide nanoplatelets that form stable colloidal dispersions. The authors concluded that the isocyanate treatment results in the derivitization of the carboxyl and hydroxyl groups on GO via the formation of

amides and carbamate esters, respectively. They proposed that the extent of functionalization can be controlled either by the reactivity of the isocyanate or the reaction time, and GO nanoplatelets with different surface functional groups have been prepared using this methodology.

The iGOs ensure molecular-level dispersion of individual, chemically modified graphene sheets within polymer hosts such as polystyrene (PS) (Stankovick et al. 2006). Briefly, PS was added to stable dispersions of phenyl isocyanate-treated GO materials and dissolved by stirring. Reduction of the dispersed material was accomplished with dimethylhydrazine at 80 ^{o}C for 24 h. The resulting PS–graphene nanocomposite displayed good electrical conductivity with a percolation threshold of 0.1 vol.%. The authors attributed this striking result to the extremely high aspect ratio of the graphene sheets and their excellent homogeneous dispersion in the PS matrix. It is probable that individual graphene sheets interact with the aromatic matrix through π-π interactions avoiding aggregation or re-stacking after the reduction step.

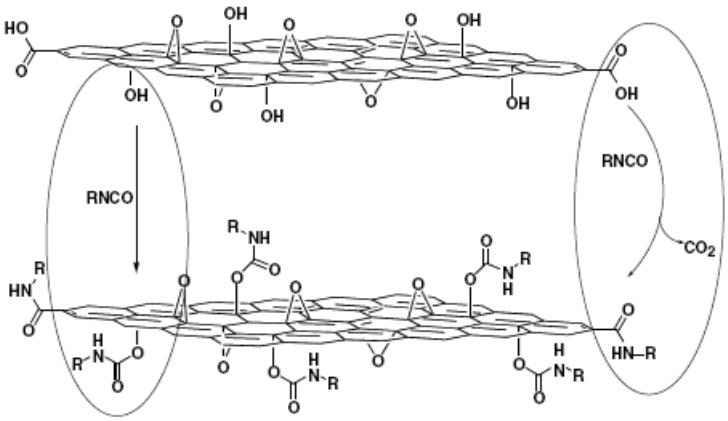

Fig. 7. Proposed reactions during isocyanate treatment of GO. Organic isocyanates react with hydroxyl (left) and carboxyl groups (right) of GO sheets to form carbamate and amide functionalities, respectively (Reprinted with permission of Elsevier, 2006).

In another study, r-GO-PS nanocomposites prepared using the above procedures were tested for electronic devices (Figure 8) (Eda et al. 2009). The authors demonstrated ambipolar field effect characteristics in transistors made from graphene-based composite thin films, and suggested that transport takes place via percolation between the functionalized graphene sheets in the insulating polymer matrix. Further, they showed that the highest mobility values were obtained in devices fabricated using the largest sized functionalized graphene sheets.

The same procedure was carried out to prepare r-GO/PS nanocomposites for field emission (Eda et al. 2008). Field emission from graphene is challenging because current deposition methods produce sheets that lie flat on the substrate surface, resulting in limited field enhancement. The authors described a simple and general solution-based approach for the deposition of field emitting graphene/polymer composite thin films, where angular orientation of the graphene sheets with respect to the substrate surface lead to field emission at low threshold fields in the order of 4 $V.\mu m^{-1}$

iGOs have also been used as reinforcements in thermoplastic polyurethane (Kim et al. 2010). An almost 10-fold increase in tensile stiffness and 90% decrease in nitrogen permeation were observed in thermoplastic polyurethane (TPU) with only 3 wt. % iGO, and was related to the high aspect ratio of exfoliated platelets. By real- and reciprocal- space morphological characterization the authors determined that thin exfoliated sheets can be more effectively distributed in the polymer matrix by solvent-based blending techniques than by melt processing.

Similarly iGOs together with sulphonated graphene and r-GO were used in TPU nanocomposites (Liang et al. 2009). Especially interesting were the results on sulphonated-graphene/polyurethane nanocomposites showing excellent light-triggered actuation with significantly enhanced mechanical properties. Actuators with 1 wt % of sulphonated functionalized graphene sheets exhibited repeatable infrared triggered actuation performance with remarkable levels of contraction able to lift a 21.6 g weight 3.1 cm with 0.21 N of force on exposure to infrared light. Furthermore, a dramatic improvement in mechanical properties was also obtained for the graphene nanocomposites with a homogeneous dispersion. As the concentration of -sulphonated -graphene increased, its nanocomposites showed significantly enhanced mechanical properties, i.e. the Young's modulus increased by 120% at only 1 wt. % loading. Moreover, through a comparative study of three kinds of graphene materials, it was found that this infrared-triggered actuation property was mainly dependent on the integrity of the aromatic network of graphene and on its level of dispersion within the matrix.

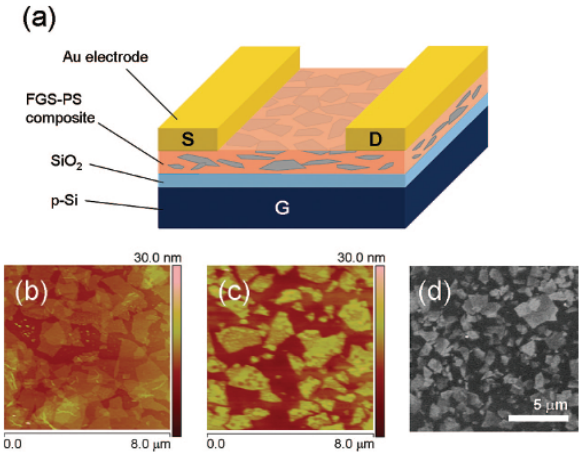

Fig. 8. (a) Schematic of functionalized graphene sheets-PS composite thin film field effect devices. Atomic force microscopies of (b) phenyl-isocyanate treated GO and (c) functionalized graphene sheets-PS composite thin films. (d) SEM of typical as-deposited functionalized graphene sheets-PS composite thin films. Contrast can be seen between conductive functionalized graphene sheets (light) and insulating PS matrix (dark) (Reprinted with permission of The American Chemical Society, 2009).

GO has also been functionalized to synthesize a polymerization-initiator covalently bonded to the GO surface. PS-graphene nanocomposites have also been prepared by grafting the polymer from an initiator-modified graphene (Fang et al. 2009). In this case the initiator molecules were covalently bonded to the graphene surface via a diazonium addition reaction

and the subsequent atom transfer radical polymerization (ATRP) linked the PS chains. Briefly, r-GO was treated with 2-(4-aminophenyl) ethanol and isoamyl nitrite at 80 ºC (diazonium functionalization) (Figure 9). This modified r-GO was then reacted with 2-bromopropionyl bromide and the resulting product used as the initiator for styrene polymerization. The prominent confinement effect arising from the incorporation of nanosheets resulted in a 15 ºC increase in the glass transition temperature of PS compared to that of the pure polymer. The resulting PS nanocomposites with 0.9 wt% graphene nanosheets showed around 70% and 57% increases in tensile strength and Young's modulus, respectively.

PS-grafted graphene has been employed as a filler in PS nanocomposites (Fang et al. 2010). Specific amounts of PS-grafted graphene were dispersed in toluene and mixed with the pristine polymer, and nanocomposite films were prepared by drop-casting. The nanocomposites showed better thermal conductivity than the parent polymer. For a nanocomposite containing only 2 wt% of graphene the thermal conductivity at 35 ºC increased from 0.18 W m^{-1} K for PS to 0.413 W m^{-1} K, higher than that obtained for PS-single walled nanotubes nanocomposites with a 5wt% loading. Again the higher aspect ratio of graphene emerges as the origin of these improvements. Furthermore, effective polymer/filler interfacial interactions play a key role since a lower degree of improvement in the thermal conductivity was obtained for graphite-filled nanocomposites.

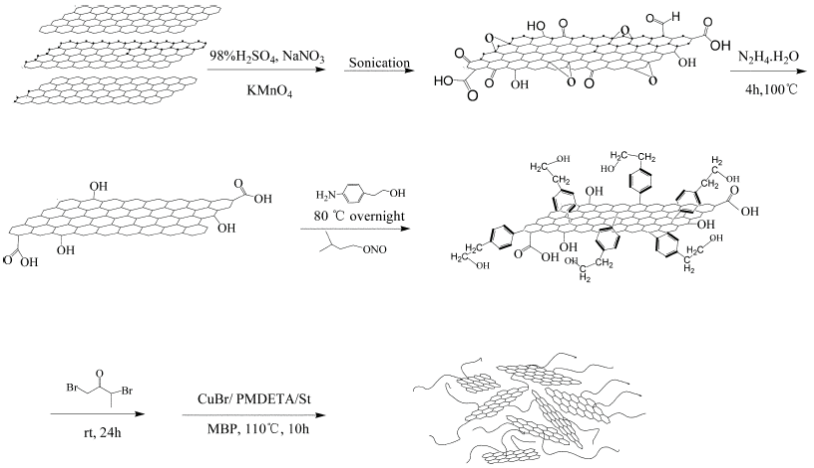

Fig. 9. Synthesis route of polystyrene-functionalized graphene nanosheets (Reprinted with permission of The Royal Society of Chemistry, 2009).

Although PS and PU dominated this section there are also interesting examples using other polymers. Polypropylene (PP) has been grafted from surface modified GO (Huang et al. 2010). Briefly, GO was modified to give a GO-supported Ziegler-Natta catalyst, and subsequent polymerization of propylene led to the *in situ* formation of a PP matrix accompanied by nanoscale exfoliation of GO, and consequently its gradual dispersion. Morphological examination of the PP/GO nanocomposites obtained by transmission electron microscopy (TEM) and scanning electron microscopy (SEM) demonstrated effective dispersion at the nanoscale of GO in the PP matrix. In addition, the GO/PP nanocomposites were demonstrated to be electrically conductive.

The ATRP method has also been employed to graft poly(tert-butyl acrylate) (PtBA) from GO (Li et al. 2010). The GO was reacted with trichloro(4-chloromethylphenyl) silane to prepare the ATRP initiator-coupled GO nanosheets. The modified-GO particles were then used as the initiator in the polymerization of PtBA to give GO nanosheets with covalently grafted PtBA. The grafted hydrophobic polymer brushes obtained produed a substantial enhancement of GO solubility in organic solvents, and the GO-*g*-PtBA nanosheets formed a stable dispersion in toluene. The functionalized GO nanosheets were successfully integrated into an electroactive polymer matrix and subsequently a composite material based on a thin film of poly(3-hexylthiophene) (P3HT) containing 5 wt % GO-*g*-P*t*BA in an Al/GO-*g*-P*t*BA+P3HT/indium tin oxide (ITO) sandwich structure, where bistable electrical conductivity switching behavior and a nonvolatile electronic memory effect were observed. Finally, water-dispersible GO-*g*-poly(acrylic acid) (PAA) nanosheets were prepared by hydrolysis, allowing gold nanoparticle-decorated GO-*g*-PAA nanofilms to be prepared from aqueous dispersions (Figure 10).

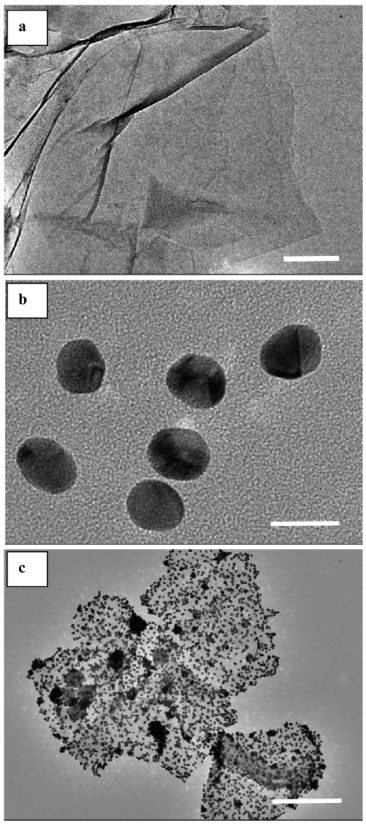

Fig. 10. TEM images of (a) GO-g-PAA nanosheets, (b) Au NPs of 18 nm in diameter and (c) GO-*g*-PAA nanosheets decorated with 18 nm Au NPs processed from aqueous dispersions. The respective scale bars for a, b, and c are 200, 20, and 500 nm (Reprinted with permission of The American Chemical Society, 2010).

Finally, fibres of poly(vinyl acetate) (PVAc) with GO and functionalized GO, which find application as light absorbers in ultrafast photonics, were prepared by electrospinning (Bao et al. 2010). The authors used GO and three types of functionalized GO as fillers. Firstly, GO was non covalently modified with a poly[(m-phenylenevinylene)-co-(2,5-dioctoxy-p-phenylenevinylene)], denominated PPV-GO. In the second example, GO was non-covalently modified with 1-pyrenebutanoic acid, succinimidyl ester and reduced with hydrazine, giving a stable r-GO dispersion (denominated G-PBASE). Eventually, r-GO was covalently modified by diazonium coupling followed by the Heck reaction to give a dye-covalent modified graphene (called G-dye). The author reported improvements in the mechanical, thermal, and optical properties of PVAc. G-PBASE and G-dye enhanced the Young's modulus, and the ultimate strength increases by 102% from 6.13 to 12.39MPa with only 0.07 wt% of G-PBASE. The authors attributed this enhancement to the good molecular-level dispersion of G-PBASE and G-dye in the PVAc matrix. The oxygen atoms in G-PBASE and the pyridinium nitrogen in G-dye provide hydrogen bonding interactions with the PVAc chains. Regarding the optical properties the graphene-based nanocomposites displayed enhanced absorbance in the region typically employed for telecommunications (around 1550 nm) compared to the parent PVAc, making it a promising candidate as saturable absorber with wideband tuneable absorption and an efficient photonic material for generating ultrashort pulses in fiber lasers.

2.3 Polymer-covalent functionalization of graphitic layers

Usually to achieve stable dispersions of graphene and control of the microstructure of nanocomposites, polymer covalent-functionalization of graphene is necessary. The direct modification of graphene laminates with polymer matrices by using the oxygenated groups in GO represents an interesting strategy. Thus, polymers with adequate functional groups can be covalently linked to graphene sheets. This issue refers to previously prepared polymers reacting with GO or graphene, and different procedures described previously involving the polymer grafting from initiator-modified graphene.

The covalent attachment of graphene to polymer chains can generate both positive and negative effects in the final properties. The fixation of graphene can limit the conductivity, increasing the percolation threshold. However, this confinement can also significantly improve other properties such as the mechanical properties.

As an example, soluble graphene covalently functionalized with PVA has been synthesized by a simple esterification reaction of carboxylic groups in GO (Salavagione et al. 2009). The esterification reaction of GO and PVA was undertaken in dimethylsulfoxide (DMSO) using a typical catalytic system composed of *N,N*-dicyclohexylcarbodiimide (DCC) and 4-dimethylaminopyridine (DMAP). The product was soluble in water and DMSO as was the parent PVA. Surprising results were obtained by ^{1}H NMR in the hydroxyl proton resonances which are resolvable in terms of configurational sequences, providing important information on the reaction mechanism. Since hydrogen bonding leads to downfield shifts, the chemical shifts of hydroxyl sequences resonances increase when passing from iso (4.7 ppm) to hetero (4.5 ppm) and from hetero to syndio (4.2 ppm) triads. By a simple inspection of the evolution of the ^{1}H spectrum, an increase in the syndiotactic signal to the detriment of the isotactic signal was seen for the esterified product, suggesting that the esterification reaction occurs at the isotactic configuration. Surprisingly, a new signal at 4.2 ppm upfield, very close to the syndiotactcic triads of unmodified PVA, was clearly observed in spite of the low degree of esterification. This signal can be related to hydroxyl protons next to

acetate groups as reported for the esterification of PVA. The authors concluded that the esterification of PVA with GO proceeds through a stereoselective mechanism, which is striking regarding the incorporation of huge graphitic laminates into free-voids of the polymer. The esterified polymer showed dramatic changes in the thermal and crystalline parameters as well as in the thermal stability (Figure 11). It was observed that the melting temperature (T_m) and the melting enthalpy (ΔH_m) were dramatically influenced by the presence of the graphitic layers. In the modified products the melting peaks disappeared, and the semicrystalline PVA (Xc=0.51) became totally amorphous, supporting the existence of covalent linkages between the PVA and the graphene laminates. In addition, the mobility of the polymer chains was strongly affected. The dramatic shift in T_g of 35 ^oC for the esterified polymer is particularly striking, and was similar to the best available data obtained for polymer composites using individual functionalized graphene sheets (FGS) as fillers at the same composition, and the thermal stability was significantly improved. Finally, the immobilized GO laminates were reduced with hydrazine in aqueous medium to give water soluble r-GO covalently bound to the polymer matrix.

This approach has also been extended to the covalent bonding of graphene to a conveniently modified poly(vinyl chloride) (PVC) (Salavagione et al. 2011). Here graphene soluble in common organic solvents was prepared by covalent attachment of a PVC derivative, resembling earlier work using multi walled carbon nanotubes (Salavagione et al. 2010). Dynamic mechanical measurements revealed a significant increase in the storage modulus (E´) of the GO-PVC with respect to the parent PVC. The evolution of tan δ (ratio of the loss to storage modulus) as a function of temperature showed that all relaxation peaks broadened and shifted to higher temperature. This indicated that GO-fillers efficiently restrict the mobility of the PVC chains thereby increasing the stiffness of the matrix, which was also reflected in higher transition temperatures.

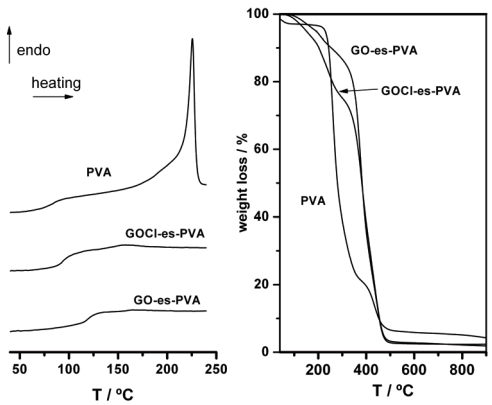

Fig. 11. Thermal behaviour of PVA, and its product of esterification with GO and thionyl chloride treated GO: DSC heating scans at 10 $^oC.min^{-1}$ (left) and thermogravimetric curves (right) (Reprinted with permission of The American Chemical Society, 2009).

Although the initial focus of the graphene community is on the wonderful electronic properties of graphene, the optical applications of graphene composites may emerge in the market sooner since the optical properties can be also tuned with polymers linked to

graphite oxide. The photoluminescence properties of GO have been employed for cellular imaging (Sun et al. 2008). GO was modified with an amine-terminated polyethylene glycol using *N*-(3-dimethylaminopropyl-*N'*-ethylcarbodiimide) hydrochloride catalyst. The modified GO sheets were found to be soluble in buffers and serum without agglomeration and displayed photoluminescence in both the visible and infrared regions. The intrinsic photoluminescence of this material was used for live cell imaging in the near-infrared (NIR). In addition, this study demonstrated that simple physisorption via π-π stacking can be used for loading doxorubicin, a widely used cancer drug onto functionalized GO with antibodies for the selective killing of cancer cells *in vitro*.
In another work toluene-2,4- diisocynate-modified GO was used to prepare a new soluble donor-acceptor type poly(*N*-vinylcarbazole)-covalently functionalized graphene oxide (GO-PVK) (Zhang et al. 2010). The intensity of the emission band of GO-PVK at 437 nm was slightly quenched when compared with that of S-1-Dodecyl-S´-(α,α´-dimethyl-α´´-aceticacid) trithio carbonate (DDAT)-PVK, suggesting intramolecular quenching from PVK to GO. Such intramolecular quenching processes may involve energy and electron transfer between the excited singlet states of the PVK moiety and the GO moiety.

2.4 Non-covalent functionalization

Other alternative procedures lie in non-covalent modification. Non-covalent functionalization is preferable for solubilisation, because it enables attachment of molecules through π-π stacking or hydrophobic (van der Waals) interactions, preserving the intrinsic electronic properties of graphene. The advantage is that this does not disrupt the extended π conjugation, unlike covalent functionalization which creates defects on the graphene sheet. Pyrene derivatives have a strong affinity with the basal plane of graphene via π-π interaction and this helps to stabilize graphene in aqueous solutions (Xu et al. 2008). Graphene has been modified with pyrene-terminated polymers, and pH sensitive graphene-polymer composites have been prepared by the non-covalent modification of graphene basal planes with pyrene-terminated poly(2-*N,N´*-(dimethyl amino ethyl acrylate) (PDMAEA) and PAA (Liu et al. 2010). The graphene-polymer composites were found to demonstrate phase transfer behaviour between aqueous and organic media at different pH values. Self-assembly of the two oppositely charged graphene-polymer composites generated layer-by-layer (LbL) structures (Figure 12). SEM images show that most graphene polymer nanosheets are flat after self-assembly and the LbL structure was clearly observed. Self-assembly, monitored with a quartz crystal microbalance (QCM), showed that when the negatively charged graphene-PAA composites and the positively charged graphene-PDAMEA suspensions were injected consecutively, a dramatic decrease in frequency was observed, demonstrating self-limiting assembly in intervals of around 20 min.
In another study stable dispersions of graphene in organic solvents were achieved by non-covalent functionalization of graphene with amine-terminated polymers (Choi et al. 2010). To obtain a stable dispersion in the evaluated non-solvents, amine-terminated PS was non-covalently functionalized to graphene, while graphene sheets were phase transferred via sonication from the aqueous phase to the organic non-solvent phase, including the amine-terminated polymers (Figure 13). Briefly, end-functionalized PS was dissolved in organic solvents (dichloromethane, o-xylene, benzene, and hexane) and the organic polymer solution was added to the vial containing an aqueous dispersion of reduced graphene. Then the vial including phase-separated organic and aqueous phases was subjected to sonication

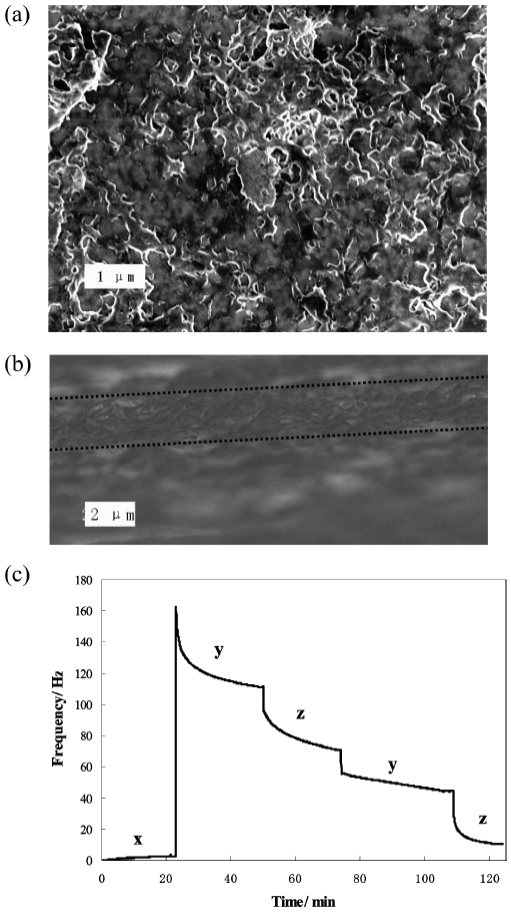

Fig. 12. High-resolution SEM images of LbL self-assembled graphene composites of PDMAEA and PAA from six self-assembly steps: (a) normal and (b) section view. (c) Quartz crystal microbalance monitorization of layer-by-layer self-assembly of positive charged (graphene-PDAMEA) and negatively charged (graphene-PAA) composites. x represents the immobilization of cystamine on gold coated crystal, y the self-assembly of negatively charged graphene-PAA, and z the self-assembly of positive charged graphene-PDAMEA (Reprinted with permission of The American Chemical Society, 2009).

to produce the non-covalent functionalization and phase transfer of graphene. In Figure 13 the dark phase corresponds to the aqueous dispersion of reduced graphene and the transparent phase corresponds to amine-terminated PS. After sonication the reduced graphene was transferred from aqueous to organic phase via non covalent (ionic) interaction between the protonated terminal amine groups (NH_3^+) of amine-terminated PS and the remaining carboxylate groups (COO-) of reduced graphene. After phase transfer, the Raman G band of reduced graphene markedly shifted from 1589 cm^{-1} to 1596 cm^{-1} indicating improved exfoliation of the graphene layers, as occurred with GO.

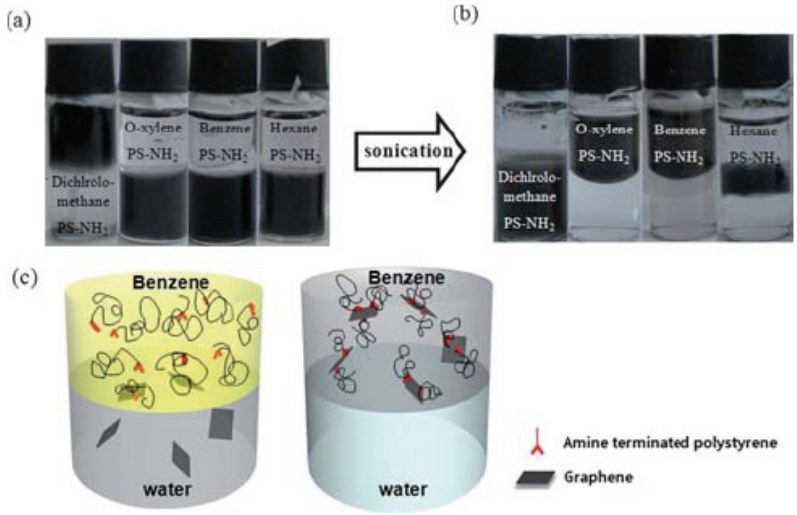

Fig. 13. Phase transfer of reduced graphene from the aqueous phase to the organic phase via PS–NH_2 functionalization. (a) Before sonication. Dark phases = aqueous dispersions of reduced graphene; transparent phases = PS–NH_2 dissolved in organic solvents. (b) After 5 h sonication. Phase transfer occurred. (c) Schematic illustration of phase transfer via non-covalent functionalization (Reprinted with permission of The Royal Society of Chemistry, 2010).

Recently, graphene was also non-covalently modified with a conducting polymer, sulfonated polyaniline (SPANI) (Bai et al. 2009). SPANI, is soluble in water in neutral or alkaline media. Here it was expected that SPANI dispersed graphene sheets via π-π interactions resembling a surfactant-assisted solubilisation, since SPANI can be considered a surfactant with a hydrophobic aromatic main chain and hydrophilic pendant sulfonate groups. GO was reduced in an aqueous solution of SPANI to give a homogeneous stable black dispersion. The SPANI-r-GO nanocomposites showed improved electrochemical stability and enhanced electrocatalytic activity.

The idea of using a polymeric surfactant to induce the solubility of graphene emerges as an interesting alternative. The dispersion of graphene within soluble polymeric matrices is fundamental for practical applications since it combines the superlative properties of both components. Polymer-dispersed graphene films can find applications as flexible conductors, transparent conductive coatings for optoelectronic devices, and/or photonics materials. A polymeric surfactant has been prepared by covalent attachment of a perylene derivative, *N*-(carboxyphenyl)-*N'*-(8-pentadecyl)perylene-3,4:9,10-bis(dicarboximide) (PDI-COOH), to PVA through esterification (Salavagione et al. 2010). The perylenediimide (PDI)-modified PVA polymers were soluble in water and DMSO. This solubility was conferred to the insoluble perylene derivative by the water-soluble polymer. This polymeric surfactant has been employed to induce the water solubility of graphene (Salavagione et al. 2011) giving a

stable graphene dispersion. The presence of dispersed few layer graphene sheets was demonstrated by UV-visible, Raman and Fluorescence spectroscopy, and indirect evidence for the strong interaction between the perylene and the graphene was obtained from the analysis of polymer parameters, such as the crystallinity that completely disappeared and the remarkable decrease in segmental motion reflected by a shift of upto 70 ^{o}C in the T_g. In addition, the graphene used in this study was obtained by reductive intercalation and microwave assisted expansion of graphite (Morales et al, 2010). This method did not use r-GO and avoided the creation of specific amounts of defects worsening the properties of graphene. To date the use of a polymeric surfactant has not been extensively studied and may be interesting to pursue this route for the preparation of graphene nanocomposites in the near future.

Although we have addressed many representative examples, this chapter is by far comprehensive, and works on other polymers such as polyethylene therephthalate (PET) (Zhang et al. 2010), polcarbonate (PC) (Kim and Macosko, 2009), poly(vinilydene fluoride)(PVDF) (Ansari and Giannelis, 2009) and poly(3,4-ethyldioxythiophene) (Xu et al. 2009), for example, can also be found in the literature.

3. Conclusions

Graphene is a cheap and multifunctional material that improves electrical, thermal, mechanical, optical, and gas barrier properties of polymer matrices, reuniting the laminar properties of layered silicates with the unique characteristics of carbon nanotubes. At very low filler contents most of these properties were better for graphene than those observed for other carbon-based reinforced nanocomposites due to the higher aspect ratio of graphene.

The versatility of graphene polymer nanocomposites suggests their potential application in automotive, electronics, aerospace and packaging. However the development and applicability of graphene-based PNCs will be intimately related to the limitations of graphene such as the lack of effective methods for scalable graphene production, which translates as higher costs, difficult manipulation of graphene sheets in processing due to its extremely low bulk density, and the lack of local sites or tensioned bonds on the graphene sheets to anchor functional moieties to make it more processable and compatible with other materials. In fact, so far only research on polymer nanocomposites using defect rich GO but not intact graphene itself have been published. Clearly the main drawback of GO is the disruption of the sp^2 network that can transform it into a completely insulating material. The sp^2 network is not totally recovered after thermal or chemical reduction since irreversible sp^3 defects are created under strongly oxidizing conditions, worsening the final properties of graphene. In fact, an alternative to modified graphene involves the modification by diazonium salts, but, usually diazonium salts are reacted with expandable graphite, by thermal expansion of GO. Therefore, efforts have to be made in the functionalization of pristine graphene and/or expanded graphite obtained avoiding the oxidation step for polymer nanocomposites in order to obtain materials with higher performance.

As described before, numerous efforts to prepare useful graphene-based nanocomposites have been made and important improvements achieved. However, in spite of the considerable advances, excitement and promise of exfoliated graphene-based polymeric

nanocomposites, substantial fundamental research is still necessary to provide a basic understanding of these materials to enable full exploitation of their nanoengineering potential. Despite the large number of combinations of matrices and potential reinforcing nano-elements with different chemistry, size, shape and properties, all graphene-based nanocomposites share common features with regard to fabrication methodologies, processing, morphology characterization and fundamental physics.

Thus, the key to prepare advanced graphene-based nanocomposites is the engineering at the polymer-graphene interface. Usually surfactant molecules have been employed to improve interface interactions. Developing an understanding of the characteristics of this interphase region, its dependence on the graphene surface chemistry, the relative arrangement of constituents and its relationship to the nanocomposite properties is a current research frontier in nanocomposites that unites the interest of scientists in physical chemistry, materials science and engineering. In the very near future, it is expected that a large number of new graphene-based nanocomposites using different polymer hosts (thermoplastic, thermosetting, and especially commodity polymers) and a wide range of graphene nanoelements (with different functionalities, size and shape) will be published. For instance the imaginative molecular design of polymeric surfactants has not yet been explored, and can circumvent the problem of solubility, dispersion in polymers and the film forming ability of graphene.

However, we are far from the end of the tunnel in terms of understanding the mechanisms of the enhancement effect in graphene nanocomposites. Thus, the challenge to reach the "graphene age" continues...

4. References

Ajayan, P. M. (2000). Single-walled carbon nanotube-polymer composites: Strength and weakness. *Advanced Materials,* vol. 12, No.10, (May 2000) 750–753, ISSN: 0935-9648.

Ansari, S. (2009). Functionalized graphene sheet-poly(vinylidene fluoride) conductive nanocomposites. *Journal of Polymer Science Part B: Polymer Physics*, Vol. 47, No. 9 (May 2009) 888-897, ISSN: 0887-6266.

Ansari, S. (2010). Oriented Arrays of Graphene in a Polymer Matrix by in situ Reduction of Graphite Oxide Nanosheets. *Small*, Vol. 6, No. 2, (January 2010) 205-209, ISSN: 1613-6810.

Baekland, L. H. (1909). The synthesis, constitution, and uses of bakelite. *Journal of Industrial and Engineering Chemistry-US*, Vol. 1 (March 1909) 149-161, ISSN: 0095-9014

Bai, H. (2009). Non-covalent functionalization of graphene sheets by sulfonated polyaniline. *Chemical Communications*, Vol. 45, No. 13, (April 2009), 1667–1669, ISSN: 1359-7345

Bai, H. (2010). A pH-sensitive graphene oxide composite hydrogel. *Chemical Communications*, Vol. 46, No. 14, (April 2010) 2376–2378, ISSN: 1359-7345.

Bao, Q. (2010). Graphene-Polymer Nanofiber Membrane for Ultrafast Photonics. *Advanced Functional Materials*, vol. 20, No. 5, (March 2010) 782-791, ISSN: 1616-301X.

Choi, E. (2010). Noncovalent functionalization of graphene with end-functional polymers. *Journal of Materials Chemistry*, Vol. 20, No 10, (March 2010) 1907-1912, ISSN: 0959-9428.

Dreyer, D. R. (2010). The chemistry of graphene oxide. *Chemical Society Reviews*, Vol. 39, No. 1, (January 2010) 228–240, ISSN: 0306-0012 .

Du, X. S. (2005). Direct synthesis of poly(arylenedisulfide)/carbon nanosheet composites via the oxidation with graphite oxide. *Carbon*, Vol 43, No 1, (January 2005) 195–213, ISSN: 0008-6223.

Eda, G. (2009). Graphene-based Composite Thin Films for Electronics. *Nano Letters*, Vol. 9, No 2, (February 2009) 814-818, ISSN: 1530-6984.

Eda, G. (2009). Transparent and conducting electrodes for organic electronics from reduced graphene oxide. *Applied Phisics Letters*, Vol 92, No. 23, (June 2008) 23305-1-23305-3, ISSN: 0003-6951.

Fang, M. (2009). Covalent polymer functionalization of graphene nanosheets and mechanical properties of composites. *Journal of Materials Chemistry*, Vol. 19, No. 38, (October 2009) 7098-7105, ISSN: 0959-9428.

Fang, M. (2010). Single-layer graphene nanosheets with controlled grafting of polymer chains. *Journal of Materials Chemistry*, Vol. 20, No. 10, (March 2010) 1982-1992, ISSN: 0959-9428.

Geim, A. K. (2007). The rise of graphene. *Nature Materials*, Vol. 6, No 3, (March 2007) 183-191, ISSN: 1476-1122.

Huang, Y. (2010). Polypropylene/Graphene Oxide Nanocomposites Prepared by In Situ Ziegler-Natta Polymerization. *Chemistry of Materials*, Vol. 22, No. 13, (July 2010) 4096-4102, ISSN: 0897-4756.

Jang, J. (2009). Graphite oxide/poly(methyl methacrylate) nanocomposites prepared by a novel method utilizing macroazoinitiator. *Composites Science and Technology*, Vol. 69, No. 2, (February 2009) 186–191, ISSN: 0266-3538.

Kim, H. (2009). Processing-property relationships of polycarbonate/graphene nanocomposites. *Polymer*, Vol. 50, No. 3, (January 2009) 797-809, ISSN:0032-3861

Kim, H. (2010). Graphene/Polyurethane Nanocomposites for Improved Gas Barrier and Electrical Conductivityl. *Chemistry of Materials*, Vol. 22, No. 11, (June 2010) 3441-3450, ISSN: 0897-4756.

Kim, T. (2010). Synthesis of Phase Transferable Graphene Sheets Using Ionic Liquid Polymers. *ACS Nano*, Vol. 4, No. 3 (March 2010) ▪ 1612–1618, ISSN: 1936-0851.

Krueger, A. (2010). *Carbon Materials and Nanotechnology*, Wiley-VCH, ISBN: 978-3-527-31803-2, Weinheim.

Lee, Y. R. (2009). Properties of Waterborne Polyurethane/Functionalized Graphene Sheet Nanocomposites Prepared by an in situ Method. *Macromolecular Chemistry and Phisics*, Vol. 210, No. 15, (August 2009) 1247–1254, ISSN: 1521-3935.

Li, M. B. (2008). Processable aqueous dispersions of graphene nanosheets. *Nature Nanotechnology*. Vol. 3, No. 2, (February 2008) 101–105, ISSN : 1748-3387.

Li, G. L. (2010). Organo- and Water-Dispersible Graphene Oxide-Polymer Nanosheets for Organic Electronic Memory and Gold Nanocomposites. *The Journal of Physical Chemistry C*, Vol. 114, No. 29, (June 2010) 12742–12748, ISSN 1932-7447.

Liang, J. (2009) Infrared-Triggered Actuators from Graphene-Based Nanocomposites. *The Journal of Physical Chemistry C*, Vol. 113, No. 22, (June 2009) 9921–9924, ISSN 1932-7447.

Liang, J. (2009). Molecular-level dispersion of graphene into poly(vinyl alcohol) and effective reinforcement of their nanocomposites. *Advanced Functional Materials*, Vol. 19, No. 14, (July 2009) 2297-2302, ISSN: 1616-301X.

Liu, P. (2000). Preparation and characterization of poly(vinyl acetate)-intercalated graphite oxide nanocomposite. *Journal of Materials Chemistry*, Vol. 10, No. 4, (February 2000) 933-935, ISSN: 0959-9428.

Liu, J. (2010). Synthesis, characterization, and multilayer assembly of pH sensitive graphene-polymer nanocomposites. *Langmuir*, Vol. 26, No. 12, (June 2010) 10068–10075, ISSN: 0743-7463.

Loh, K. P. (2010). The chemistry of graphene. *Journal of Materials Chemistry*, Vol. 20, No 12, (March 2010) 2277-2289, ISSN: 0959-942.

Morales, G. M. (2010). High-Quality Few Layer Graphene Produced by Electrochemical Intercalation and Microwave-Assisted Expansion of Graphite. Unpublished results.

Novoselov, K. S. (2004). Electric Field Effect in Atomically Thin Carbon Films". *Science,* Vol. 306, No 5696 (October 2004) 666-669, ISSN: 0036-8075

Ramanathan, T. (2007). *Journal of Polymer Science Part B: Polymer Physics*, Vol. 45, No. 11 (June 2007) 2097-2112, ISSN: 0887-6266.

Ramanathan, T. (2008). Functionalized graphene sheets for polymer nanocomposites. *Nature Nanotechnology*, Vol. 3, No. 6, (June 2008) 327-331, ISSN: 1748-3387.

Ray, S. S. (2003). Polymer/layered silicate nanocomposites: a review from preparation to processing. *Progress in Polymer Science*, Vol. 28, No. 11, (November 2003) 1539–1641, ISSN: 0079-6700.

Salavagione, H. J. (2009). Synthesis of poly(vinyl alcohol)/reduced graphite oxide nanocomposites with improved thermal and electrical properties. *Journal of Materials Chemistry*, Vol. 19, No. 28, (July 2009) 5027-5032, ISSN: 0959-9428.

Salavagione, H. J. (2009) Polymeric Modification of Graphene through Esterification of Graphite Oxide and Poly(vinyl alcohol). *Macromolecules*, Vol. 42, No. 17 (September 2009) 6331-6334, ISSN: 0024-9297.

Salavagione, H. J. (2010). Synthesis of water-soluble perylenediimide-functionalized polymer through esterification with poly(vinyl alcohol). *Journal of Polymer Science A: Polymer Chemistry*, Vol. 48, No. 16, (August 2010) 3613-3622, ISSN: 1099-0518.

Salavagione H. J (2010). Functionalization of multi-walled carbon nanotubes by stereoselective nucleophilic substitution on PVC. *Macromolecules*, Vol. 43, No. 23 (December 2010) 9754-9760, ISSN: 0024-9297

Salavagione, H. J. (2011). Graphene Water Dispersions Induced by a Conjugate Dye-Modified Polymer Surfactant. . Unpublished results.

Salavagione, H. J. (2011).When covalent linkages are essential to prepare effective reduced graphene oxide-based nanocomposites. The case of Poly(vinyl chloride). Unpublished results 2011.

Shaffer, M. S. P. (1999). Fabrication and characterization of carbon nanotube/poly(vinyl alcohol) composites. *Advanced Materials*, Vol. 11, No. 11, (August 1999) 937–941, ISSN: 0935-9648

Stankovich, S. (2006). Graphene-based composite materials. *Nature*, Vol. 442, No. 7100, (July 2006) 282 -286, ISSN: 0028-0836.

Stankovich, S. (2006). Synthesis and exfoliation of isocyanate-treated graphene oxide nanoplatelets. *Carbon*, Vol. 44, No. 15, (December 2006) 3342-3347, ISSN: 0008-6223.

Sun, X. M. (2008). Nano-Graphene Oxide for Cellular Imaging and Drug Delivery. *Nano Research*, Vol. 1, No. 3, (September 2008) 203-212, ISSN: 1998-0124.

Thostenson, E. T. (2001). Advances in the science and technology of carbon nanotubes and their composites: a review. *Composites Science and Technology*, Vol. 61, No. 13, (October 2001) 1899–1912, ISSN: 0266-3538.

Verdejo, R. (2008). Functionalized graphene sheet filled silicone foam nanocomposites. *Journal of Materials Chemistry*, Vol. 18, No. 19, (May 2008) 2221-2226, ISSN: 0959-9428.

Vickery, J. L. (2009). Fabrication of Graphene-Polymer Nanocomposites With Higher-Order Three-Dimensional Architectures. *Advanced Materials*, Vol. 21, No. 21, (June 2009) 2180–2184, ISSN: 0935-9648.

Villar-Rodil, S. (2009). Preparation of graphene dispersions and graphene-polymer composites in organic media. *Journal of Materials Chemistry*, Vol. 19, No. 22, (June 2009) 3591-3593, ISSN: 0959-9428.

Wang, S. (2009). Thermal Expansion of Graphene Composites. *Macromolecules*, Vol. 42, No. 14, (July 2009) 5251–5255, ISSN: 0024-9297.

Wang, D. W. (2009). Fabrication of Graphene/Polyaniline Composite Paper via In Situ Anodic Electropolymerization for High-Performance Flexible Electrode. *ACS Nano*, Vol. 3, No. 7, (July 2009) 1745-1752, ISSN: 1936-0851.

Xu, Y. (2008). Flexible graphene films via the filtration of water-soluble noncovalent functionalized graphene sheets. *Journal of the American Chemical Society*, Vol. 130, No. 18, (May 2008) 5856-5857 ISSN: 0002-7863.

Xu, Y. F. (2009). A hybrid material of graphene and poly(3,4-ethyldioxythiophene) with high conductivity, flexibility, and transparency. *Nano Research*, Vol.2, No. 4, (April 2009) 343-348, ISSN: 1998-0124.

Yang, H. F. (2009). Convenient preparation of tunably loaded chemically converted graphene oxide/epoxy resin nanocomposites from graphene oxide sheets through two-phase extraction. *Journal of Materials Chemistry*, Vol. 19, No. 46, (December 2009) 8856-8860, ISSN: 0959-9428.

Yu, A. (2007). Graphite nanoplatelet-epoxy composite thermal interface materials. *Journal of Physical Chemistry C*, Vol. 111, No. 21 (May 2007) 7565-7569, ISSN: 1932-7447.

Zhang, B. (2010). Poly(*N*-vinylcarbazole) chemically modified graphene oxide. *Journal of Polymer Science A: Polymer Chemistry*, Vol. 48, No. 12, (June 2010) 2642-2649 ISSN: 1099-0518.

Zhang, H. B. (2010). Electrically conductive polyethylene terephthalate/graphene nanocomposites prepared by melt compounding. *Polymer*, Vol. 51, No. 5 , (March 2010) 1191-1196, ISSN: 0032-3861.

Zhang, K. Graphene/Polyaniline nanofiber composites as supercapacitor electrodes. *Chemistry of Materials*, Vol. 22, No. 4, (February 2010) 1392-1401, ISSN: 0897-4756.

Zhao, L. (2009). Polyaniline electrochromic devices with transparent graphene electrodes. *Electrochimica Acta*, Vol. 55, No. 2, (December 2009) 491–497, ISSN: 0013-4686.

Zhao, X. (2010). Enhanced Mechanical Properties of Graphene-Based Poly(vinyl alcohol) Composites. *Macromolecules*, Vol. 43, No. 5, (March 2010) 2357-2363, ISSN: 0024-9297.

Zu, S. Z. (2009). Aqueous dispersion of graphene sheets stabilized by pluronic copolymers: formation of supramolecular hydrogel. *Journal of Physical Chemistry C*, Vol. 113, No. 31, (August 2009) 13651-13657, ISSN: 1932-7447.

10

Functionalized Graphene Sheet / Polyurethane Nanocomposites

Hyung-il Lee and Han Mo Jeong
Department of Chemistry, University of Ulsan, Ulsan 680-749, Republic of Korea

1. Introduction

One of an integral aspect of polymer nanotechnology is precise synthesis of polymer nanocomposites. [1-6] Small insertion of nanosized inorganic compounds usually improves the properties of polymers in a great deal, which makes many of the most important application areas possible depending on the inorganic material present in polymers. [7] Specially, polymer composites which contain electrically conducting inorganic fillers, such as natural graphite, carbon black and metal powders, have been extensively investigated in the past few decades for their potential applications in antistatic coatings, electromagnetic shielding and corrosion-resistant coatings, etc. [8-10] Sometimes, in order to obtain an electrical conductivity of 10^{-4} S cm^{-1} required for commercial uses, these composites often contain as much as 15 wt% filler, which in turn causes deterioration of mechanical properties and poor processability. It is, therefore, important to use a small amount of filler to retain the stretchability or transparency of a matrix polymer.

Graphene is essentially an isolated atomic plane of graphite, which is composed of a single layer sheet of sp^2-bonded carbon atoms that are densely packed in a honeycomb crystal lattice with large specific surface area. [11,12] Single-layer graphene sheet have been of great interest for their unique properties, including not only excellent mechanical properties but thermal conductivity and stiffness. Given these unique properties, graphene has been considered as an ideal reinforcing agent for high strength polymer composites. [13,14] In addition, the elusive two-dimensional structure of graphene has a number of unusual electronic and robust transport properties that may be useful in the electronics or in the related regions. [15-17]

The properties of polymer nanocomposites depend strongly on how well inorganic fillers are dispersed in the polymer matrix. A great deal of nanocomposite research using carbon nanotubes (CNT) as nanosize conductive fillers has focused on finding better methods for dispersing nanotubes into polymers since pristine carbon nanotubes have poor compatibility with most organic solvents and polymers. For this reason, additional surface treatment is necessary for CNT based nanocomposites to allow better compatibility. [18] Though surface modification via acid modification and polymer grafting improves solubility of CNT in solvents and polymers somehow, the extent of disentanglement of the CNT bundles into polymers is low, and severe sonication often leads to disruption of the CNT. In case of graphene, during the synthesis of graphene from graphite oxide (GO)[19] some epoxide and hydroxyl groups remain, which greatly facilitate dispersion. [20] There

could be minor issues related to restacking of the flat graphene sheets after chemical or thermal reduction, which might decrease dispersion efficiency. However, small addition of surfactants can efficiently prevent individual graphene sheets from restacking with each other by stabilizing the reduced particle suspensions. By virtue of these benefits, it is considered that graphene-based nanocomposites have better performance than their CNT-based counterparts.

While composites with graphene have been prepared with a number of polymers, polyurethane (PU) was one of the mostly studied polymers [21]. PU can provide properties covering from a high performance elastomer to tough thermoplastic with excellent physical properties, including high tensile strength, abrasion and tear resistance, and solvent resistance. In addition, high versatility in chemical structures originated from a wide range of monomeric materials affords tailor-made properties with well-designed combinations of these monomers. As a result, PU can be easily manipulated to satisfy the highly diversified demands of modern technologies.

Driven by modern requirements to decrease emissions of volatile organic compounds, the development of environmentally friendly waterborne polyurethane (WPU) has been increasing, especially in the field of coating industry where the reduction of evolution of volatile organic compounds during the drying process is critical. [22-24] In addition, WPU offers many advantages such as low viscosity at high molecular weight and good applicability, which cannot be realized with conventional solvent-borne systems. They could be also utilized effectively in electronic devices as coatings for antistatic or electromagnetic shielding if they could be modified for improved conductivity. This can be achieved with nanosize conductive fillers that can possibly make a percolative network at an extremely low loading. [25]

The first area covered will pertain to general preparation of graphite oxide (GO) and functionalized graphene sheets (FGS) with a focus on methods suitable for polymer composite applications. Several examples of graphene-based nanocomposites with various polymers are also discussed. Secondly, the preparation and physical properties of functionalized graphene sheet (FGS)/PU nanocomposites are highlighted.

2. Preparation of FGS

Graphenes can be made by two methods; bottom-up and top-down. Chemical vapor deposition (CVD)[26], arc discharge[27], and epitaxial growth on SiC[28] are usually employed to synthesize graphenes in the bottom-up approaches. In most cases, a variety of graphene preparations rely on the top-down approaches that utilize a cheap and commercially available graphite as a starting material. In this section, the top-down approaches are focused.

Synthetically, a variety of top-down approaches have been adopted to allow the preparation of graphenes. Generally, there are three methods for the synthesis of graphenes: “direct exfoliation of graphite”, “chemical reduction of GO”, and “thermal reduction of GO”. The “direct exfoliation of graphite” route involves micromechanical cleavage of graphite. This method allows graphenes with large-size and high-quality. It is difficult, however, to separate the exfoliated graphene sheets from the bulk graphite. In the “chemical reduction of GO” method, the starting material is graphite oxide (GO) produced by oxidation of graphite. GO is not completely exfoliated and contain extensive domains of stacked graphitic layers. The resulting GO is dispersed in solvent and chemically reduced to graphene sheets by reducing agents such as hydrazine, dimethylhydrazine, hydroquinone,

etc. "Thermal reduction of GO" strategy also begins with the preparation of GO. It is generally believed that each layer of GO consists of randomly distributed unoxidized aromatic regions and six-member aliphatic regions with polar groups, such as hydroxyl, epoxide, ether, and carboxylate groups, originated from oxidation. When a sufficiently oxidized GO is heated in an inert environment over 1000 ^{o}C, it can be exfoliated into a few layered graphene sheets, that is, functionalized graphene sheets (FGSs). This step accompanies pressure build-up which stems from CO_2 evolution due to the decomposition of the epoxy and hydroxyl groups that bridges each GO sheet. [29-31] As a result, an exfoliated GO, in which the inter-graphene spacing associated with GO and the graphite is almost completely excluded after thermal expansion, has an affinity for polar solvents and polymers, as well as good conductivity. These properties stem from the fact that the completely exfoliated GO is composed of a few layered FGSs that still contain the polar functional groups that remain after thermal treatment.[32] In addition, from the industrial point of view, this method is preferred since large scale bulk production of FGS is possible.
In this chapter, we confine our focus to thermally exfoliated FGSs since polymer/graphene composites that we will discuss are based on them. The following section coverd will briefly survey various types of polymers that have been used for nanocomposites with graphenes. Among them, poly(methyl methacrylate) (PMMA)/graphene nanocomposites are focused.

3. PMMA/graphene nanocomposites

Generally, FGS-based polymer composites benefit their excellent performance from graphene's thermal, mechanical and electrical properties. These composites are electrically conducting and have higher thermal stability than polymer alone. In addition, incorporation of a small amount of graphene into polymer matrix offers a great opportunity to make tough and lightweight materials as long as graphenes are homogeneously distributed in polymer matrices. There have been numerous reports on preparation of polymer/graphene nanocomposites with different kinds of polymer materials, including polystyrene (PS)[33], polycarbonate (PC)[34], PMMA[35-37], and PU.[38,39]

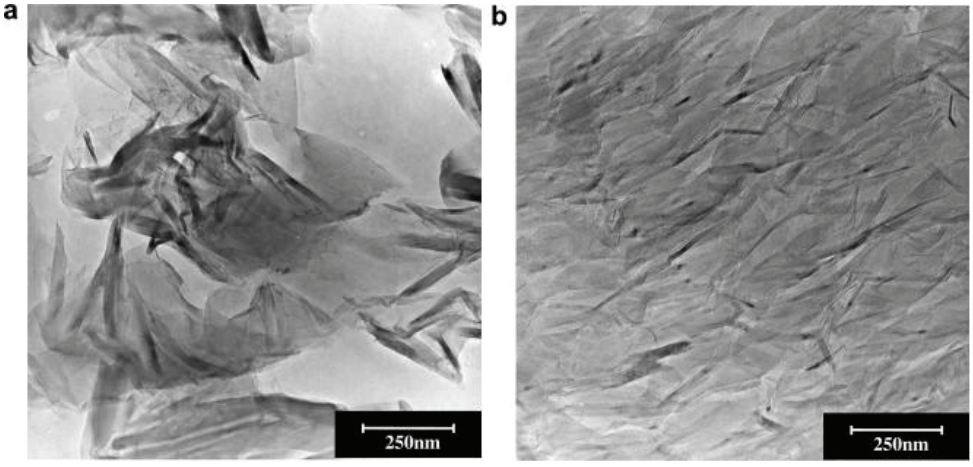

Fig. 1. TEM micrographs of PMMA/GO nanocomposites: (a) a PMMA/GO composite with 6.7 parts of GO, (b) a PEO-PMMA multi-block copolymer/GO composite with 6.7 parts of GO. Adapted with permission from Ref. [36]. Copyright 2005 Elsevier Ltd.

In our group, we began to examine PMMA as a matrix polymer material in which GO or FGS were incorporated. In the first study, PMMA/GO nanocomposites were prepared by in situ polymerization of methyl methacrylate (MMA) in the presence of GO. A the macroazoinitiator (MAI) containing a poly(ethylene oxide) (PEO) segment that was employed for this polymerization, was intercalated between the lamellae of GO to induce the inter-gallery polymerization of MMA and exfoliate the GO.[36] The morphological, conductivity, thermal, mechanical and rheological properties of these nanocomposites were examined and compared with those of intercalated nanocomposites prepared by polymerization with the normal radical initiator, 2,2'-azobisisobutyronitrile. Since it has been reported that PEO can be easily intercalated at the GO gallery[40,41], it is expected that the polymerized PEO-PMMA multi-block copolymer will have an affinity to GO due to the presence of PEO block, which cannot be easily achieved with a composite prepared by a conventional small molecular weight initiator. As shown in Fig 1, PEO-PMMA multi-block copolymer/GO composites have the finer dispersion than PMMA/GO composites due to PEO being easily intercalated at the GO gallery. It was also evident that conductivity of PEO-PMMA multi-block copolymer/GO composites was increased compared to that of PMMA/GO composites. For example, a conductivity of 1.78×10^{-7} S/cm was attained in the exfoliated PEO-PMMA multi-block copolymer/GO composites prepared with 2.5 parts GO per 100 parts MMA, which was about 50-fold higher than that of intercalated PMMA/GO composites.

Secondly, compatibilizing effect of GO in PMMA/FGS nanocomposites has been investigated.[37] While we have prepared and examined FGS nanocomposites with various polymers, it was found that the dispersability of FGS in a polymer matrix can be improved when GO was used as a compatibilizer. The compatibilizing effect of GO is originated from its chemical resemblance to FGS as well as polar functional groups that can interact with matrix PMMA. An PMMA/FGS nanocomposite containing 1 part FGS has a conductivity of 1.89×10^{-7} S/cm, more than 10^7-fold better than pristine PMMA. This conductivity was enhanced a further 100-fold by addition of 1 part GO. These results were ascribed to compatibilizing ability of GO to allow the fine dispersion of FGS in a PMMA matrix.

4. PU/FGS nanocomposites

Generally, PU/graphene nanocomposites can be prepared by two methods: "mechanical mixing method" and "in situ polymerization method". The "mechanical mixing method" includes solvent and melt process. Solvent process is usually used such that graphenes were mixed with a PU matrix via blending with solvents followed by solvent removal. It is often advantageous to employ "mechanical mixing" approach that can offer simple and facile preparation of nanocomposites. It is, however, less efficient to achieve uniform dispersion of graphenes in a polymer matrix. "In situ polymerization method" involves intercalative polymerization of monomers in the presence of graphenes. It is considered that it is a better approach for dispersing graphenes into polymers. However, this approach is limited to solvent process due to the high viscosity of even dilute dispersion of graphene.

4.1 Preparation of FGS/PU nanocomposites.

As discussed briefly in the previous section, various types of graphene-based polymer composites have been investigated. Extensive literature on graphene-based polymer composites is beyond the scope of discussion in this chapter. The representative examples

illustrating approaches to preparing FGS/PU nanocomposites are presented. Different aspects of FGS/PU nanocomposites, including electrical conductivities, thermal properties, and mechanical properties, will be thoroughly discussed based on our published results. As mentioned above, FGSs that were used to prepare PU/graphene composites were thermally exfoliated. Two different types of PU, organic solvent borne TPU and WPU, were employed to make four different kinds of nanocomposites with combination with two different processing methods, mechanical mixing and in situ polymerization.

1. FGS/organic solvent borne TPU nanocomposites prepared by mechanical mixing (TPUN).[42]
2. FGS/organic solvent borne TPU nanocomposites prepared by in situ polymerization (TPUNC).[43]
3. FGS/water-borne PU nanocomposites prepared by mechanical mixing (WPUN).[44]
4. FGS/water-borne PU nanocomposites prepared by in situ polymerization (WPUCL, WPUMG).[21]

4.1.1 FGS/organic solvent borne TPU nanocomposites prepared by mechanical mixing (TPUN)

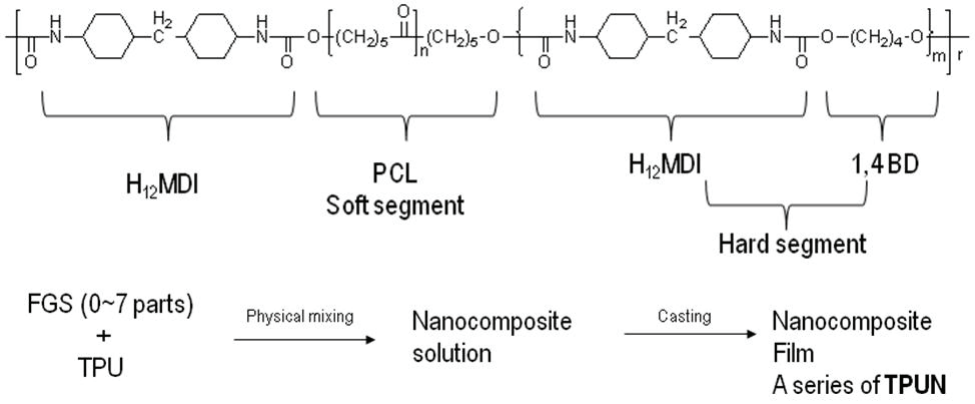

Fig. 2. A chemical structure of TPU (Up) and the preparation of nanocomposite films by a mechanical method (Down).

Fig 2 shows the structure of TPU that was used in this work. TPU/FGS nanocomposite solution was obtained by mixing different amounts of FGS in the presence of TPU in methylethylketone (MEK). Sample designation codes provide information regarding the amount of FGS included in the TPU samples. For example, TPUN-5 contains 5 parts of FGS per 100 parts of polymer.

4.1.2 FGS/organic solvent borne TPU nanocomposites prepared by in situ polymerization (TPUNC)

To prepare the TPU/FGS nanocomposite by the in situ polymerization method, the FGS was immersed in MEK where polymerization was performed (Fig 3). The TPU/FGS nanocomposites were prepared by using 0 to 3 parts of FGS per 100 parts TPU since flexible cast films were unachievable when the content of FGS was more than 3 parts per 100.

Sample designation codes were given by the amount of FGS included in the TPU samples. For example, TPUNC-3 contains 3 parts FGS per 100 parts TPU.

Fig. 3. The preparation of FGS/TPU nanocomposite films by in situ polymerization method.

4.1.3 FGS/water-borne PU nanocomposites prepared by mechanical mixing (WPUN)

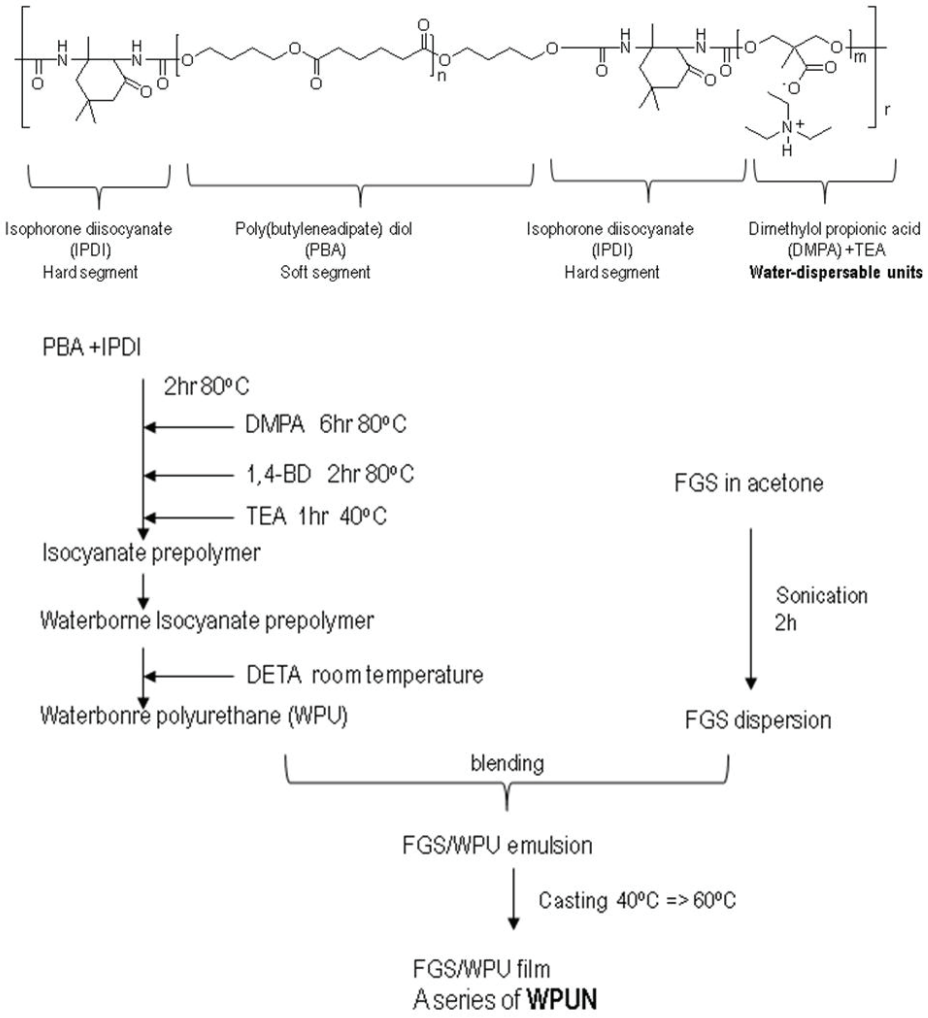

Fig. 4. A chemical structure of WPU (Up) and the preparation of nanocomposite films by a mechanical method (Down).

As schematically presented in Fig 4, the structure of WPU includes water-dispersable units (salt of DMPA and TEA). WPU/FGS nanocomposite solution was obtained by mixing different amount of FGSs (0 to 6 parts) in acetone with WPU in water. Sample designation codes were given by the amount of FGS included in the TPU samples. For example, WPUN-5 contains 5 parts of FGS per 100 parts of WPU.

4.1.4 FGS/water-borne PU nanocomposites prepared by in situ polymerization (WPUCL, WPUMG)

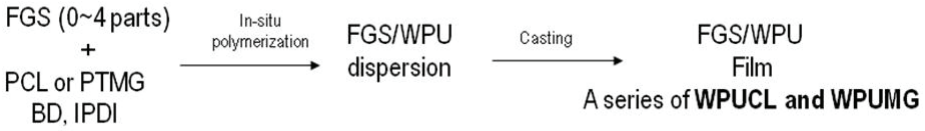

Fig. 5. The preparation of FGS/WPU nanocomposite films by in situ polymerization method.

Basically, the structure of WPU is the same as one that used in mixing method except that poly(tetramethylene glycol) (PTMG) was used along with PCL as a soft segment. FGS/WPU nanocomposites were made by in situ polymerization in the presence of FGS (Fig 5). Sample designation codes were given by the amount of FGS included in the WPU samples. For example, WPUCL-2 and WPUMG-2 contain 2 parts of FGS per 100 parts of WPU based on PCL and PTMG, respectively, as a soft segment.

4.2 Characterization of FGS/PU nanocomposites.

Characterization of successful preparation of FGS/PU nanocomposites rely on a variety of instruments such as transmission electron microscopy (TEM), FT-IR, and XRD. It is often difficult to characterize FGS/PU nanocomposites quantitatively by TEM due to wrinkled nature and small thickness of graphenes. Nonetheless, TEM has been one of the most widely used imaging techniques to visualize layered structures of graphenes. As shown in Fig 6, FGSs are finely dispersed in the PU matrices with subnano-sized thicknesses and high aspect ratios, demonstrating the good compatibility between the FGS and TPU. According to these images that show well dispersion of FGS, it is expected that effective conductive channels can be created for all cases of FGS/PU nanocomposites.

Figure 7 shows the wide-angle XRD patterns of the graphite, GO and FGS specimens. The diffractogram of graphite shows a very intense and narrow peak at 2θ = 26.5°, which corresponds to the X-ray reflection on the (002) planes of well-ordered graphenes with interlayer spacing, I_c, between the well ordered graphenes being 3.35 Å. GO has a broad peak at 2θ = 14.1° due to I_c being expanded to 6.27 Å by the accommodation of various functional groups on the graphene surface. However, FGS has no visible peak at the range of $2\theta > 2°$, which indicates the notable expansion and sufficient disorder of the graphene layers.

It is also possible to characterize FGS/PU nanocomposites with XRD patterns. Generally, one can attain very important information from XRD patterns of nanocpmposites: "extent of dispersion of FGS in a polymer matrix", which can be evaluated in two ways. Firstly, whether or not there exist visible peaks at the range of $2\theta > 2°$ due to long range order of the stacked FGSs. Secondly, whether or not peaks of crystalline segments of PU decrease upon

increased addition of FGSs. For example, the dispersed FGS does not give rise to any new wide-angle XRD peak at the range of $2\theta > 2^{\circ}$ (Fig 8). This suggests that either (1) the distance between the FGSs is far enough or (2) no long-range order exists even when the FGS has a stacked structure. Fig 8 also shows that the diffractogram of TPUN-0, which doesn't contain FGSs, has two peaks at $2\theta = 21.1^{\circ}$ and 23.3°. These peaks are attributed to the reflections on the (110) plane and the (200) plane of the PCL crystal, respectively. The intensity of these peaks decreases as the content of FGS increased due to the frustrated crystallization of the PCL phase by increasing amounts of FGS.

Sample codes		Tensile properties			Conductivity (S/cm)
		Modulus (MPa)	Tensile strength (MPa)	Elongation at break (%)	
TPUN	TPUN-0	458±23	20.0±0.1	814±64	4.58×10^{-11}
	TPUN-0.5	559±113	18.8±0.1	779±40	8.37×10^{-11}
	TPUN-1	557±85	17.8±0.3	693±34	4.62×10^{-10}
	TPUN-2	639±70	13.4±0.1	686±43	5.41×10^{-4}
	TPUN-3	657±157	15.5±0.3	693±52	5.88×10^{-4}
	TPUN-4	636±47	17.0±0.1	517±13	8.54×10^{-4}
	TPUN-5	351±2	18.8±0.9	347±73	9.16×10^{-4}
	TPUN-7	357±43	18.9±0.2	245±22	4.92×10^{-4}
TPUNC	TPUNC-0	59±19	7.4±0.5	1368±55	2.85×10^{-11}
	TPUNC-1	138±5	4.3±0.4	898±7	6.81×10^{-10}
	TPUNC-2	150±28	4.8±0.4	653±73	2.07×10^{-3}
	TPUNC-3	171±9	3.7±0.4	428±15	2.77×10^{-3}
WPUN	WPUN-0	66.2±9.0	29.6±0.9	478±44	1.34×10^{-10}
	WPUN-0.5	38.9±7.6	35.8±8.8	551±185	1.57×10^{-10}
	WPUN-1	54.7±6.1	40.0±4.6	590±88	1.90×10^{-10}
	WPUN-2	55.9±4.8	36.2±1.0	457±43	1.31×10^{-5}
	WPUN-3	53.6±11.5	32.5±3.3	458±83	2.24×10^{-4}
	WPUN-4	48.1±13.1	38.9±8.3	452±110	2.53×10^{-4}
	WPUN-5	56.9±3.8	31.2±6.4	402±97	5.47×10^{-4}
	WPUN-6	72.9±2.5	26.2±2.2	290±1	2.75×10^{-4}
WPUCL	WPUCL-0	79.6±4.9	21.6±6.8	553±91	8.84×10^{-11}
	WPUCL-1	87.5±20.9	11.9±4.3	448±77	4.14×10^{-11}
	WPUCL-2	99.9±15.6	7.5±0.4	415±19	7.03×10^{-10}
	WPUCL-3	115.2±23.7	7.1±0.6	374±26	1.20×10^{-5}
	WPUCL-4	345.5±102.2	5.9±4.8	46±10	7.87×10^{-4}
WPUMG	WPUMG-0	80.5±9.1	27.9±7.3	638±61	1.68×10^{-11}
	WPUMG-1	85.8±2.9	20.9±3.0	688±38	2.00×10^{-11}
	WPUMG-2	93.8±17.0	13.4±0.3	586±40	2.76×10^{-10}
	WPUMG-3	1009.9±9.7	7.4±1.5	409±117	3.17×10^{-4}
	WPUMG-4	145.5±7.0	5.1±0.6	151±32	1.91×10^{-3}

Table 1. Physical properties of PU/FGS nanocomposites.

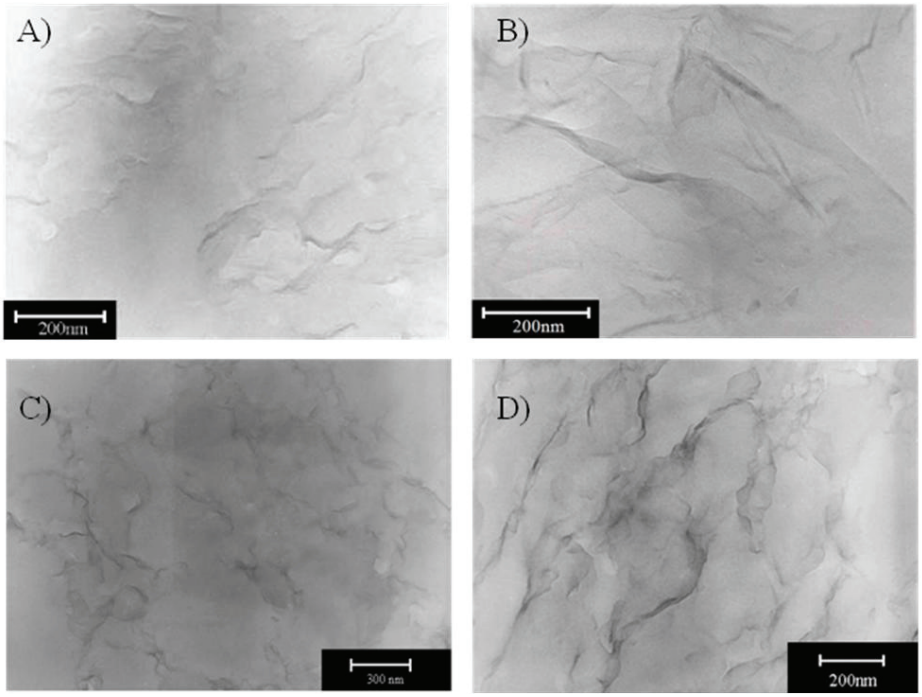

Fig. 6. TEM micrographs of FGS/PU nanocomposites: (A) TPUN-4, (B) TPUNC-3, (C) WPUN-3, (D) WPUCL-4. Adapted with permission from Ref. [42] and [21]. Copyright 2009 Wiley-VCH Verlag GmbH & Co. KGaA.

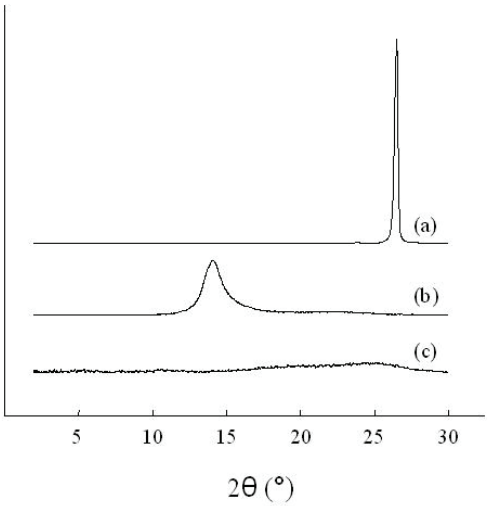

Fig. 7. XRD patterns of graphite, GO, and FGS. Adapted with permission from Ref. [42]. Copyright 2009 Wiley-VCH Verlag GmbH & Co. KGaA.

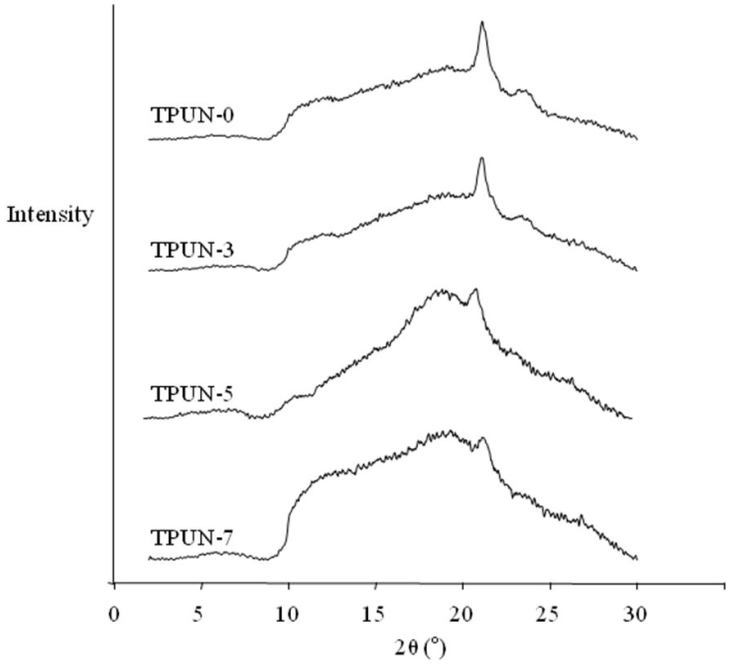

Fig. 8. XRD patterns of a series of TPUN. Adapted with permission from Ref. [42]. Copyright 2009 Wiley-VCH Verlag GmbH & Co. KGaA.

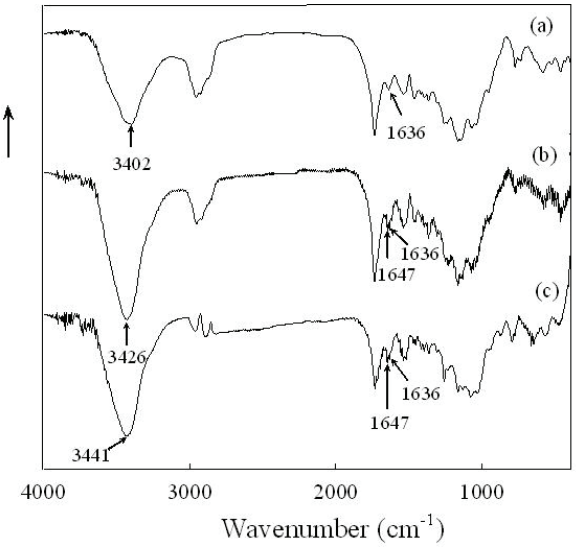

Fig. 9. FTIR spectra of (a) WPUN-0, (b) WPUN-3, and WPUN-6. Adapted with permission from Ref. [44]. Copyright 2008 Wiley-VCH Verlag GmbH & Co. KGaA.

FT-IR is another important tool to evaluate even dispersion of FGSs in a PU matrix. Specifically, by monitoring the intensity of hydrogenbonded N-H absorption band of urethane linkage, one can have an idea on the extent of dispersion of FGS. For example, the N–H stretching vibration of polyurethane in the range of 3,300~3,600 cm^{-1} is highly sensitive to hydrogen bond distribution. Absorption bands of hydrogenbonded and free N–H are located at 3,330 and 3,400 cm^{-1}, respectively. WPUN-0 (pristine WPU without addition of FGSs) has an absorption band at 3,402 cm^{-1}, which moves to a higher wavenumber with increased FGS content (Fig 9). This demonstrates that the high contents of FGSs weakened the interaction of hydrogen bonding between urethane linkages.
Overall, it is concluded that the extent of dispersion of FGSs in a PU matrix can be effectively evaluated by TEM, XRD, and FT-IR. In the following section, we discuss thermal properties of FGS/PU nanocomposites.

4.3 Thermal properties of FGS/PU nanocomposites.

Number of washing	Residue (wt%)	
	Physical mixing method	*In situ* polymerization method
1	32.7	26.5
2	38.7	33.9
3	43.4	37.3
6	46.5	39.3
9	50.3	41.1

Table 2. Residual weights of washed FGS after thermal degradation.[43]

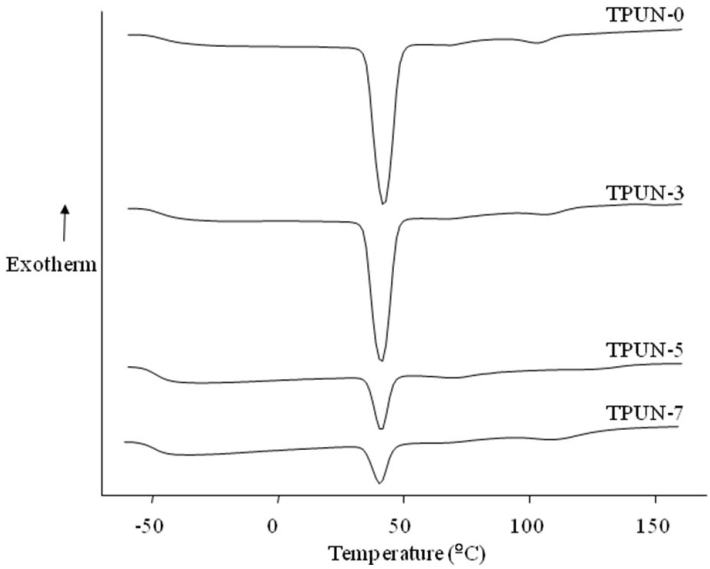

Fig. 10. DSC thermograms of a series of TPUN. Adapted with permission from Ref. [42]. Copyright 2009 Wiley-VCH Verlag GmbH & Co. KGaA.

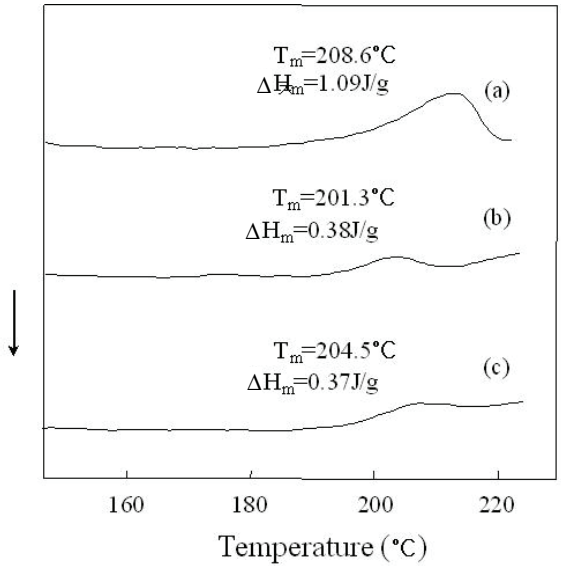

Fig. 11. DSC thermograms obtaind on heating of (a) WPUN-0, (b) WPUN-3, and (c) WPUN-6. Adapted with permission from Ref. [44]. Copyright 2008 Wiley-VCH Verlag GmbH & Co. KGaA.

As with the above three characterization tools, DSC and TGA can also provide useful information on how well FGSs are distributed in a PU matrix. Both TPU and WPU that were employed for the preparation of nanocomposites have soft and hard crystalline segments. By observing changes of glass transition temperature (T_g), crystalline melting temperature, and heat of fusion of each crystalline domain that are induced by added FGSs, one can assess how thermal properties are affected by addition of FGSs. For example, for a series of TPUNC prepared by in situ polymerization, the chemical and/or physical interactions between FGS and TPU were enhanced, as compared to a series of TPUN prepared by the physical mixing method. That is, gravimetry showed that the amount of TPU adhered onto FGSs increased when the nanocomposite was prepared by the in situ polymerization method (Table 2).[43] From the DSC thermogram of TPUN-0, one can see a sharp melting endothermic peak of the soft segment (T_{ms}) and a small endothermic melting peak of the hard segment (T_{mh}) at 41.8 and 103.2 °C, respectively (Fig 10). As the amount of FGS in the nanocomposites increased, the heat of fusion at T_{ms} (ΔH_{ms}) decreased and dropped abruptly at higher contents of FGS. This suggests that the crystallization of the PCL segment is inhibited by the FGS, more evidently at higher contents of FGS. This decrease in the crystallinity also seems to cause a decrease in T_g with increasing contents of FGS. Similar behaviors were observed for a series of WPUN systems in which melting of hard segments is more evident than that of soft segments (Fig 11). The melting endothermic peak (T_m) 200 °C and the heat of fusion (ΔH_m) of the hard segment decreased as contents of FGS increased, indicating that the crystallization of the hard segment was inhibited by FGSs.

4.4 Mechanical properties of FGS/PU nanocomposites.

Graphene is the one of the stiffest material with high intrinsic strength. When it is used as a filler, it is expected that a reinforced composite can have superior mechanical properties.

Moreover, one can further increase mechanical properties of the composite by employing different processing techniques. Here, we compare two processing methods, mechanical mixing and in situ polymerization, in detail and how mechanical properties of the resulting composites are affected by how they were made. As shown in Table 1, tensile modulus was enhanced with increasing amount of FGS for the series of TPUN and TPUNC. However, tensile strength and elongation at break gradually decreased with increase of the content of FGS, which is due to inhibition of molecular rearrangement and orientation with respect to the tensile axis during deformation. The reduced crystallinity of the soft segment can also contribute to these reductions of tensile strength and elongation at break. For the cases of TPUN and TPUNC, if TPUs are highly elongated, hard segments break apart when phase mixed with soft segments; the hard and soft segments orient in the direction of elongation, resulting in maximum intermolecular interaction. The evident lowering of tensile properties measured at large deformation suggested that these molecular rearrangements were interrupted in the presence of FGSs. This behavior became more evident for a series of TPUNC. When TPU was physically mixed with 3 parts of FGS (TPUN-3), the increase of modulus and the decrease of tensile strength and elongation at break were 43%, 23%, and 15%, respectively, of that of TPUN-0. In contrast, these respective changes, compared to TPUNC-0, are 190%, 50%, and 69% in the nanocomposites made by the in situ polymerization method (TPUNC-3). These results suggest that the interactions between FGS and TPU increased when prepared by the in situ polymerization method, and that the increased interactions reduce the chain mobility for realignment.

For the series of WPUCL and WPUMG, one can see that the modulus of WPU is effectively improved by the addition of FGS. For a series of WPUN, which were prepared by a simple physical mixing method, modulus decreased by the addition of FGSs. The interactions between hard segments were suppressed by the presence of FGSs, which overwhelmed the reinforcing effect of FGS. For the series of WPUCL, however, the reinforcing effect of FGS itself and the increased crystallinity of the soft segment in the presence of FGS overshadowed the effect on the modulus of decreased interactions between hard segments by FGSs. The interaction between the FGS and WPU molecules are stronger in the nanocomposites prepared by the in situ method than those made by a simple mixing method, and this consequently enhanced the reinforcing effect of FGS.

Overall, performance of FGS as s mechanical reinforcement material is as competitive as over existing carbon fillers such as carbon black and CNT. For all of FGS/PU composites, enhancement of modulus with better graphene dispersion is clearly demonstrated. Tensile strength and elongation at break dropped significantly with the addition of rigid fillers. In addition, modulus is greatly influenced by the interaction between FGS and PU. The modulus improvement of FGS/PU composites made by in situ polymerization is more evident than those made by a physical mixing method, supporting our reasoning that the interaction between FGS and WPU gets stronger when made by an in situ polymerization method.

4.5 Electrical conductivities of FGS/PU nanocomposites.

Due to conjugated nature of flat graphene sheets, the composites are electrically conductive through percolated channels generated for electron transfer. Moreover, graphene-based nanocomposites have very low percolation threshold, which allows the efficient preparation of the nanocomposite with high electrical conductivity at significantly low loading. The

extent of graphene dispersion can be estimated by the onset concentration for electrical percolation. For example, in case of TPUN-2, the 2 part addition of FGSs improved electrical conductivity by 10^7 times compared with TPUN-0 (Table 1). Evenly distributed FGSs with nano-sized thicknesses and high aspect ratios (Figure 6) can create an effective conductive channel. For the same amount of FGS loading, the conductivities of a series of TPUNC made by in situ polymerization method is slightly higher than those of a series of TPUN made by physical mixing, indicating that the dispersion of FGS in a TPU matrix is improved by in situ polymerization method (Fig 12).

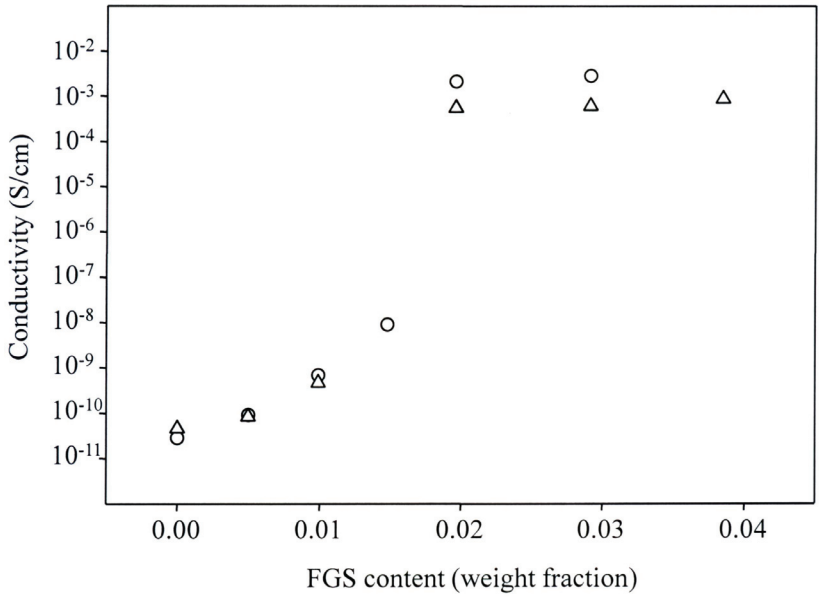

Fig. 12. Conductivities of TPU/FGS nanocomposites made by the in situ polymerization method (○) and by the physical mixing method (Δ)[43]

When preparing a series of WPUN, emulsion stability should be considered since high loading of FGSs might cause FGS/WPU emulsion unstable. Therefore, sufficiently high electrical conductivity and enough emulsion stability must be balanced for successful nanocomposite films. As expected, the conductivity of WPU increased drastically by the addition of FGS. The addition of two parts FGS per 100 parts of WPU (WPUN-2) led to about a 10^5-fold increase in conductivity. However, the conductivity of nanocomposite did not rise evidently above WPUN-3 while the emulsion stability decreased with increasing contents of FGS. WPUN-3 was optimal for the commercial production of WPU/FGS nanocomposites with excellent balance between electrical conductivity and emulsion stability.

5. Conclusions

With benefits arising from a variety of excellent properties of the FGS, FGS-based novel nanocomposites are constantly being developed. Especially, FGS/PU nanocpmposites

covered here exhibit excellent thermal, mechanical, and electrical properties. These properties can significantly vary with a processing method which determines the extent of dispersion and interaction of FGSs with PU matrices. We compared two processing methods, mechanical mixing and in situ polymerization, in detail and how properties of the resulting composites are affected by how they were made. It was observed that the modulus improvement by the reinforcing effect of FGS and high electrical conductivities were more evident when the nanocomposites of WPU with FGS were prepared by an in situ method, which suggested that the interaction between FGS and PU was stronger when made by an in situ method.

6. Acknowledgement

This work was supported by Priority Research Centers Program through the National Research Foundation of Korea (NRF) funded by the Ministry of Education, Science and Technology (2009-0093818).

7. References

[1] Du, M.; Guo, B.; Jia, D. *Polym. Int.* 2010, *59*, 574-582.
[2] Kiliaris, P.; Papaspyrides, C. D. *Prog. Polym. Sci.* 2010, *35*, 902-958.
[3] Sahoo, N. G.; Rana, S.; Cho, J. W.; Li, L.; Chan, S. H. *Prog. Polym. Sci.* 2010, *35*, 837-867.
[4] Shanmuganathan, K.; Capadona, J. R.; Rowan, S. J.; Weder, C. *Prog. Polym. Sci.* 2010, *35*, 212-222.
[5] Spitalsky, Z.; Tasis, D.; Papagelis, K.; Galiotis, C. *Prog. Polym. Sci.* 2010, *35*, 357-401.
[6] Djokovic, V.; Radhakrishnan, T.; Nair, P. S.; Comor, M. I.; Nedeljkovic, J. M. *Recent Adv. Polym. Nanocompos.* 2009, 227-268.
[7] Osman, M. A.; Mittal, V.; Suter, U. W. *Macromol. Chem. Phys.* 2007, *208*, 68-75.
[8] Kalaitzidou, K.; Fukushima, H.; Drzal, L. T. *Compos. Sci. Technol.* 2007, *67*, 2045-2051.
[9] Li, J.; Sham, M. L.; Kim, J.-K.; Marom, G. *Compos. Sci. Technol.* 2007, *67*, 296-305.
[10] Sandler, J. K. W.; Kirk, J. E.; Kinloch, I. A.; Shaffer, M. S. P.; Windle, A. H. *Polymer* 2003, *44*, 5893-5899.
[11] Kim, H.; Abdala, A.; Macosko, C. W. *Macromolecules* 2010, *43*, 6515-6530.
[12] Kim, J.; Kim, F.; Huang, J. *Mater. Today* 2010, *13*, 28-38.
[13] Fang, M.; Wang, K.; Lu, H.; Yang, Y.; Nutt, S. *J. Mater. Chem.* 2009, *19*, 7098-7105.
[14] Vickery, J. L.; Patil, A. J.; Mann, S. *Adv. Mater.* 2009, *21*, 2180-2184.
[15] Zhang, H.; Bao, Q.; Tang, D.; Zhao, L.; Loh, K. *Appl. Phys. Lett.* 2009, *95*, 141103/1-141103/3.
[16] Bao, Q.; Zhang, H.; Yang, J.-x.; Wang, S.; Tang, D. Y.; Jose, R.; Ramakrishna, S.; Lim, C. T.; Loh, K. P. *Adv. Funct. Mater.* 2010, *20*, 782-791.
[17] Liu, J.; Tao, L.; Yang, W.; Li, D.; Boyer, C.; Wuhrer, R.; Braet, F.; Davis, T. P. *Langmuir* 2010, *26*, 10068-10075.
[18] Chen, J.; Liu, H.; Weimer, W. A.; Halls, M. D.; Waldeck, D. H.; Walker, G. C. *J. Am. Chem. Soc.* 2002, *124*, 9034-9035.
[19] Dreyer, D. R.; Park, S.; Bielawski, C. W.; Ruoff, R. S. *Chem. Soc. Rev.* 2010, *39*, 228-240.
[20] Wiemann, K.; Kaminsky, W.; Gojny, F. H.; Schulte, K. *Macromol. Chem. Phys.* 2005, *206*, 1472-1478.

[21] Lee, Y. R.; Raghu, A. V.; Jeong, H. M.; Kim, B. K. *Macromol. Chem. Phys.* 2009, *210*, 1247-1254.
[22] Kim, B. K.; Seo, J. W.; Jeong, H. M. *Eur. Polym. J.* 2003, *39*, 85-91.
[23] Jeong, H. M.; Lee, S. H. *J. Macromol. Sci., Phys.* 2003, *B42*, 1153-1167.
[24] Jeong, H. M.; Jang, K. H.; Cho, K. *J. Macromol. Sci., Phys.* 2003, *B42*, 1249-1263.
[25] Wang, D.; Choi, D.; Li, J.; Yang, Z.; Nie, Z.; Kou, R.; Hu, D.; Wang, C.; Saraf, L. V.; Zhang, J.; Aksay, I. A.; Liu, J. *ACS Nano* 2009, *3*, 907-914.
[26] Li, X.; Cai, W.; An, J.; Kim, S.; Nah, J.; Yang, D.; Piner, R.; Velamakanni, A.; Jung, I.; Tutuc, E.; Banerjee, S. K.; Colombo, L.; Ruoff, R. S. *Science* 2009, *324*, 1312-1314.
[27] Karmakar, S.; Kulkarni, N. V.; Nawale, A. B.; Lalla, N. P.; Mishra, R.; Sathe, V. G.; Bhoraskar, S. V.; Das, A. K. *J. Phys. D: Appl. Phys.* 2009, *42*, 115201/1-115201/14.
[28] Rollings, E.; Gweon, G. H.; Zhou, S. Y.; Mun, B. S.; McChesney, J. L.; Hussain, B. S.; Fedorov, A. V.; First, P. N.; de Heer, W. A.; Lanzara, A. *J. Phys. Chem. Solids* 2006, *67*, 2172-2177.
[29] Schniepp, H. C.; Li, J.-L.; McAllister, M. J.; Sai, H.; Herrera-Alonso, M.; Adamson, D. H.; Prud'homme, R. K.; Car, R.; Saville, D. A.; Aksay, I. A. *J. Phys. Chem. B* 2006, *110*, 8535-8539.
[30] McAllister, M. J.; Li, J.-L.; Adamson, D. H.; Schniepp, H. C.; Abdala, A. A.; Liu, J.; Herrera-Alonso, M.; Milius, D. L.; Car, R.; Prud'homme, R. K.; Aksay, I. A. *Chem. Mater.* 2007, *19*, 4396-4404.
[31] Kudin, K. N.; Ozbas, B.; Schniepp, H. C.; Prud'homme, R. K.; Aksay, I. A.; Car, R. *Nano Lett.* 2008, *8*, 36-41.
[32] Velasco-Santos, C.; Martinez-Hernandez, A. L.; Fisher, F. T.; Ruoff, R.; Castano, V. M. *Chem. Mater.* 2003, *15*, 4470-4475.
[33] Liu, N.; Luo, F.; Wu, H.; Liu, Y.; Zhang, C.; Chen, J. *Adv. Funct. Mater.* 2008, *18*, 1518-1525.
[34] Kim, H.; Macosko, C. W. *Polymer* 2009, *50*, 3797-3809.
[35] Ramanathan, T.; Abdala, A. A.; Stankovich, S.; Dikin, D. A.; Herrera-Alonso, M.; Piner, R. D.; Adamson, D. H.; Schniepp, H. C.; Chen, X.; Ruoff, R. S.; Nguyen, S. T.; Aksay, I. A.; Prud'Homme, R. K.; Brinson, L. C. *Nat. Nanotechnol.* 2008, *3*, 327-331.
[36] Jang, J. Y.; Kim, M. S.; Jeong, H. M.; Shin, C. M. *Compos. Sci. Technol.* 2009, *69*, 186-191.
[37] Jang, J. Y.; Jeong, H. M.; Kim, B. K. *Macromol. Res.* 2009, *17*, 626-629.
[38] Lee, H. B.; Raghu, A. V.; Yoon, K. S.; Jeong, H. M. *J. Macromol. Sci., Part B: Phys.* 2010, *49*, 802-809.
[39] Liu, J.; Yang, W.; Tao, L.; Li, D.; Boyer, C.; Davis, T. P. *J. Polym. Sci., Part A: Polym. Chem.* 2009, *48*, 425-433.
[40] Matsuo, Y.; Tahara, K.; Sugie, Y. *Carbon* 1996, *34*, 672-674.
[41] Matsuo, Y.; Tahara, K.; Sugie, Y. *Carbon* 1997, *35*, 113-120.
[42] Nguyen, D. A.; Lee, Y. R.; Raghu, A. V.; Jeong, H. M.; Shin, C. M.; Kim, B. K. *Polym. Int.* 2009, *58*, 412-417.
[43] Jeong, H. M. *Polym. Polym. Compos.* 2010, 18, 351-358.
[44] Raghu, A. V.; Lee, Y. R.; Jeong, H. M.; Shin, C. M. *Macromol. Chem. Phys.* 2008, *209*, 2487-2493.

11

Equilibrium Nucleation, Growth, and Thermal Stability of Graphene on Solids

E.V.Rut'kov and N.R.Gall
Ioffe Physico-Technical Institute of Russian Academy of Sciences, St.Petersburg, Polytechnicheskaya, 26, 194021, Russia

1. Introduction

Graphene and graphite films form on the surface of many metals: Pt(100) [1], Pt(111) [2], Ru(001) [3], Ni(111) [4--6], Pd(100), Pd(111), Co(0001) [7], Mo(110) [8], Mo(100) [9], Fe(100) [10]. Re(1010) [11], Rh(111) [12], Ir(111), Ir(100) [13--15], on polycrystalline Pd [16], and carbides of a number of metals [17, 18].

The simplest way of producing graphene on the surface of a variety of metals consists in exposing a heated metal sample to an atmosphere of hydrocarbons C_xH_y---in most cases, this is benzene C_6H_6. A critical step in these experiments is to choose correctly the temperature of the heated metal, which, as a rule, should be not below 900--1000 K. C_xH_y molecules striking the heated metal dissociate intensively, with H_2 desorbing, and carbon remaining stuck onto the metal surface; its subsequent fate depends essentially on the actual type of the metal involved. This exposure to hydrocarbons culminates in formation of a continuous two-dimensional film of carbon with graphite structure, i.e., a graphene film. The physics underlying these processes differs radically among different Me-C systems. Consider several characteristic metal-graphene systems which were studied thoroughly under identical conditions.

A. Graphene on Ir(111) and Ir(100) [13—15]

The samples used most frequently in our experiments were thin textured metallic ribbons measuring (50 x 0.02 x 1) mm^3, with the surface uniform in work function $e\varphi$ = 5.75 eV, which corresponds to the closely packed (111) face [19]. While the experiments performed with iridium single crystals with (111) and (100) faces did not reveal any radical differences in the results obtained, thin ribbons prove to be much more convenient for the experimentalist.

The major attractive feature of iridium consists in that carbon, unlike other metals, does not dissolve in its bulk, thus simplifying considerably interpretation of the results obtained.

Figure 1 plots the variation of carbon and iridium Auger signal intensity with the time of exposure to benzene vapor at T = 1650 K. The Auger signal of carbon is seen to grow until it reaches saturation. Scanning tunneling microscopy demonstrates convincingly formation on the surface of a continuous graphene layer (Fig. 2) [20-23]. Graphene features valence-saturated, passive surface, which effectively terminates dissociation of C_6H_6 molecules.

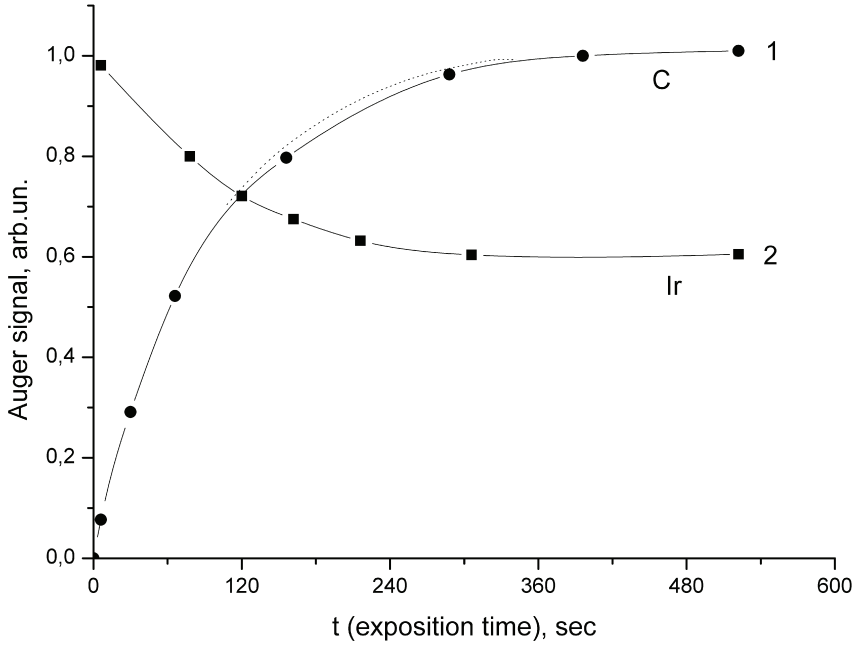

Fig. 1. Auger intensities versus deposition time for iridium ribbon exposure by benzene vapor at 1600 K and ~7*10^{-7} Torr; 1 – carbon at E -272 eV, 2 – iridium at E = 176 eV; solid – experimental data, dashed – calculations.

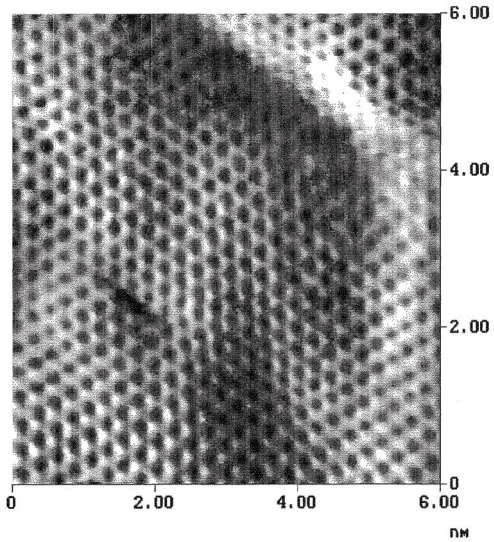

Fig. 2. STM image of a single grapene layer on Ir(111). the image was got using current mode. The layer was intercalated with Cs to saturation. The image size is 10 x 10 nm. The graphitic structure can be clearly seen.

Experiments revealed the growth of a graphene film to proceed through the following stages: adsorbed carbon "gas" → graphene islands in equilibrium with this gas → growth of islands in area → coalescence of the islands to form a continuous graphene layer (see **§** 5). Graphene islands being catalytically passive, the kinetics of their growth can be described by the equation

$$\frac{dN_c(t)}{dt} = N_{cm}\left(1 - S_0\right)\cdot \nu_c \cdot \eta\,, \tag{1}$$

where S_0 is the relative area covered by the islands, with $S_0 = 1$ corresponding to a continuous layer (**§** 2); $N_c(t)$ is the concentration of carbon atoms on the surface; N_{cm} is carbon concentration in a graphene layer, $N_{cm} = 3.56\ 10^{15}$ at/cm^2; ν_c is the carbon atom flux incident on the surface; and η is the sticking coefficient of benzene molecules to a graphene-free surface.
In our experiments, the concentration of carbon in the chemisorbed "gas" phase could be neglected [**§** 5]; therefore, $\frac{dN_c(t)}{dt} = N_{cm}\left(\frac{dS_0}{dt}\right)$, thus yielding the solution to Eq. (1) in the form

$$N_c(t) = N_{cm}\left[1 - \exp\left(-\frac{\nu_c \cdot \eta}{N_{cm}}\right)\cdot t\right] \tag{2}$$

The dashed line in Fig. 1 plots relation (2) calculated assuming the carbon Auger signal intensity $I \sim N_c$. The calculated curve is seen to fit nicely to experimental data. Similar results were obtained for other hydrocarbons as well, among them isoprene (C_5H_6), acetylene (C_2H_2), and limonene ($C_{10}H_{10}$), as well as for single-crystal (100) iridium [**§** 15]. The region within which high-quality graphene films can be obtained on iridium is confined to the 1400--1900-K interval; for T < 1500 K, one may suggest an increase of the concentration of as-formed graphene islands, with an ensuing growth of defects in the layer produced in the coalescence of these islands (**§** 11), while for T > 1900 K, desorption of carbon from iridium sets in [14].

B. Graphene on Pt(III), Rh(III), Re(1010) [11, 12, 24]

The above metals do not form bulk carbides [25], and at T > 1000--1100 K carbon atoms start to dissolve intensively in the bulk of the metal. To obtain graphene on Pt(III), both benzene and a calibrated carbon atom flux were employed [26]. Figure 3 displays graphically the variation of carbon Auger signal intensity with the time of carbon atom adsorption at T = 1475 K. We readily see that during ~120 s carbon atoms do not accumulate on the surface of platinum (the Auger signal is below the noise level) but dissolve instead actively in its bulk; indeed, desorption can be excluded from consideration because carbon atoms desorb from metal surfaces at high temperatures T > 1900 K [27]. After the amount of in-diffused carbon has reached the limit of its solubility in platinum, graphene islands will start to form on the surface of the latter, to coalesce finally into a continuous graphene layer (t = 400 s, Fig. 3). Significantly, carbonization in contact with benzene vapor produces automatically one graphene layer, just as in the case of iridium. By contrast, the thickness of a film formed under an atomic flux of carbon atoms grows without limit.
Figure 4 presents an Auger spectrum of carbon from graphene atop platinum (1) confronted by that from a graphite film on platinum (2). The Auger spectra displayed exhibit a classical "graphitic" signature (see **§** 3). In view of the large scatter among available published data, we used a calibrated carbon flux to determine for the Pt--C system the dependence of the

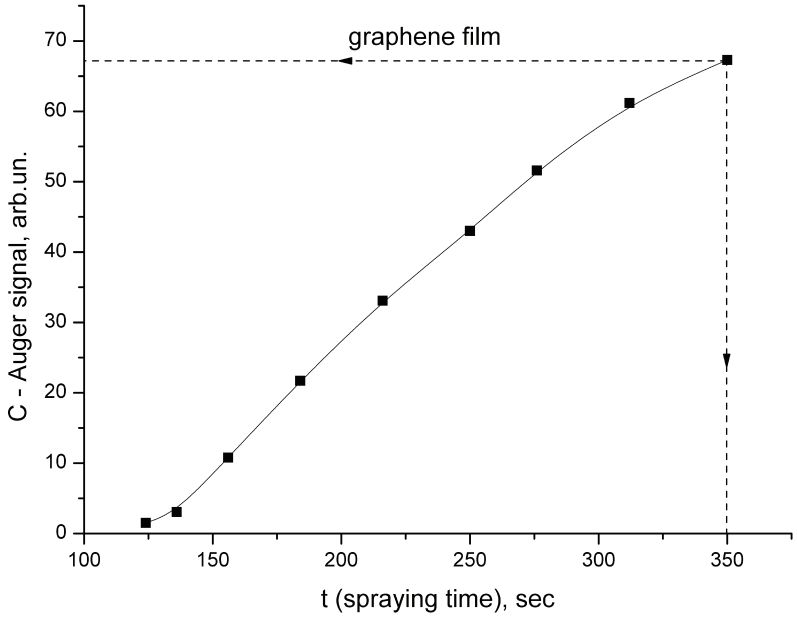

Fig. 3. Carbon Auger signal versus deposition time in atomic carbon deposition onto Pt(111) surface at 1465 K. 67 a.u. corresponds to a single grapheme layer. The deposition flux is v_C = 3.2 *10^{13} cm^{-2}*s^{-1}.

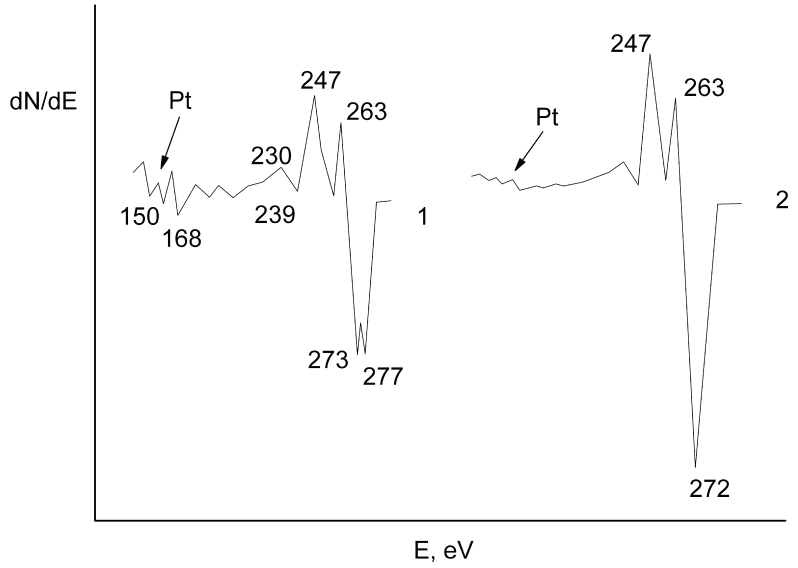

Fig. 4. Carbon KVV Auger spectra for a single graphene layer (1) and 4-layer graphite film (2) on Pt(111). the covers were got using carbon precipitation from the metal bulk at 1300 K. Peaks with energies 150 – 168 eV correspond to Pt Auger transitions.

limiting carbon solubility N_{lim} on substrate temperature from the beginning of appearance of graphene islands on the surface [24]

$$\lg N_{\lim}(at.\%) = 2{,}6 - \frac{7200}{T[K]} \tag{3}$$

Note the low solubility limit of carbon in Pt; indeed, at T = 1475 K, N_{lim} = 2.7 10^{-3} at. %. Interestingly, although carbon deposition was performed on one side of the platinum ribbon only, on the other side a symmetric pattern was observed, which suggests fast transport of carbon atoms across the bulk of the platinum. Heating of a carbonized sample up to T = 1800 K, followed by lowering its temperature to T = 1475 K, brings about again fast growth of the graphene layer from the "excess" carbon atoms that have out-diffused from the bulk of the metal onto its surface (§ 8). The operating temperature interval within which graphene can be obtained on platinum is 1000--1900 K. Significantly, if it is needed to "freeze" a graphene layer by dropping sharply the temperature down to room level, one will have to choose the lowest possible carbonization temperature. Otherwise, during the cooling of the ribbon several graphene layers may form from the carbon leaving the metal (§ 8).

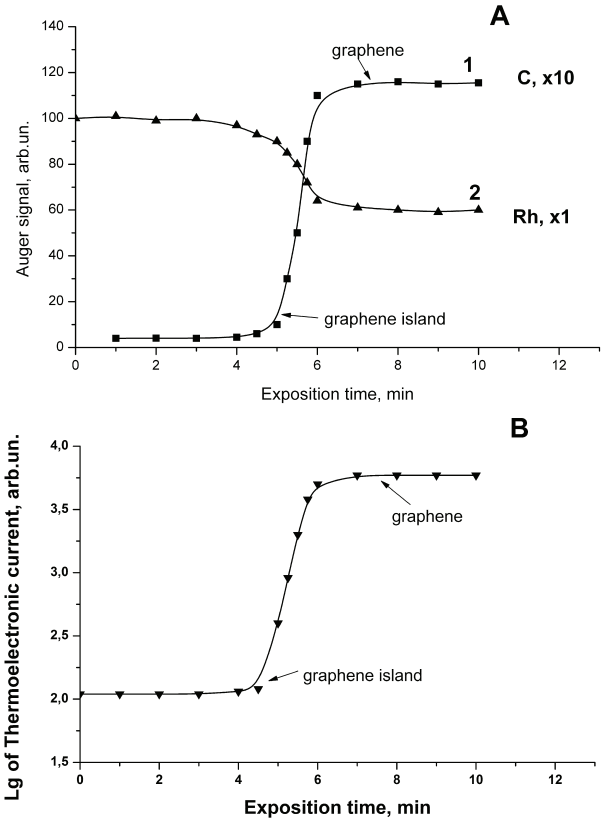

Fig. 5. A: Auger signals of carbon (curve 1), Rh (curve 2); and Fig.5B: thermionic current versus exposition time.

The time needed to load rhodium with carbon at the same temperatures and benzene vapor pressures as in the case of platinum is noticeably longer. Figure 5A demonstrates graphically the variation of the carbon and rhodium Auger signal intensities in the course of carbonization at T = 1360 K, and Fig. 5B traces the variation of the thermionic current under the same conditions. The sharp rise of the thermionic current should be ascribed to the formation and growth of graphene islands whose work function $e\varphi_1$ = 4.35 eV, to be contrasted with parts of the surface free of islands, where $e\varphi_1$ = 4.95 eV (Fig. 5B) [28]. The processes evolving on Rh are similar to those observed on Pt, namely, dissolution of carbon atoms in the bulk of rhodium and their buildup on the surface of the metal → formation of graphene islands in equilibrium with the chemisorbed carbon "gas" → growth of islands in area culminating in coalescence with eventual formation of a continuous graphene layer, and the carbon Auger signal intensity reaching saturation (Fig. 5A). In contrast to platinum, Auger spectroscopy probes already the carbon "gas" on the surface, whose concentration, for instance, at T = 1360 K is ~1 10^{14} at/cm^2.

We have succeeded in tracing, just as with platinum, the behavior with temperature of the solubility limit N_{lim} of carbon in rhodium in the 1000--1800-K range:

$$\lg N_{\lim}(at.\%) = 2{,}2 - \frac{4600}{T[K]}. \qquad (4)$$

Figure 6 shows graphically the variation of the carbon and rhodium Auger signal intensities with the temperature of a sample carbonized at T_c = 1400 K. One could isolate conveniently a few regions in the graph which are of special interest.

A. On the surface-- low-density chemisorbed carbon "gas", which does not affect the rhodium work function $e\varphi$ = 4.95 eV. Dissolved carbon dose not contribute to the Auger signal intensity of carbon.

B. Nucleation and growth of graphene islands. The surface becomes nonuniform in work function.

C. Termination of formation of a continuous graphene layer on rhodium has come to the end. The surface is again uniform in work function, with $e\varphi$ = 4.35 eV. The region of existence of a graphene layer is $\Delta T \sim 50^{o}$.

D. Growth of a thick graphite film on Rh through segregation of carbon out of the supersaturated Rh-C solid solution, with the substrate Auger signal intensity dropping below the instrument noise level.

The graph displayed in Fig. 6 is characteristic of nearly all Me-graphene systems, with the exclusion of iridium. It repeats over and over again under increasing or decreasing temperature, without noticeable time delays, which should be assigned to the small thickness of the metal samples used and fast volume diffusion of carbon in metals for T > 1000 K.

Regrettably, the strong Auger peak of rhodium at E = 302 eV is superimposed on the carbon Auger peak and distorts its shape (Fig. 7, spectrum 1). Therefore, the carbon Auger spectrum assumes a distinct graphitic shape only on formation of several layers of graphene on the surface of rhodium (Fig. 7, spectrum 3).

Formation of a graphene film on Re(1010) takes up still longer metal exposure times in benzene vapor, than is the case with Rh and Pt under the same experimental conditions. Figure 8 displays the kinetics of variation of the Auger spectrum of carbon (1) and rhenium (2) observed under carbonization of a ribbon sample at T = 1700 K, The process starts with

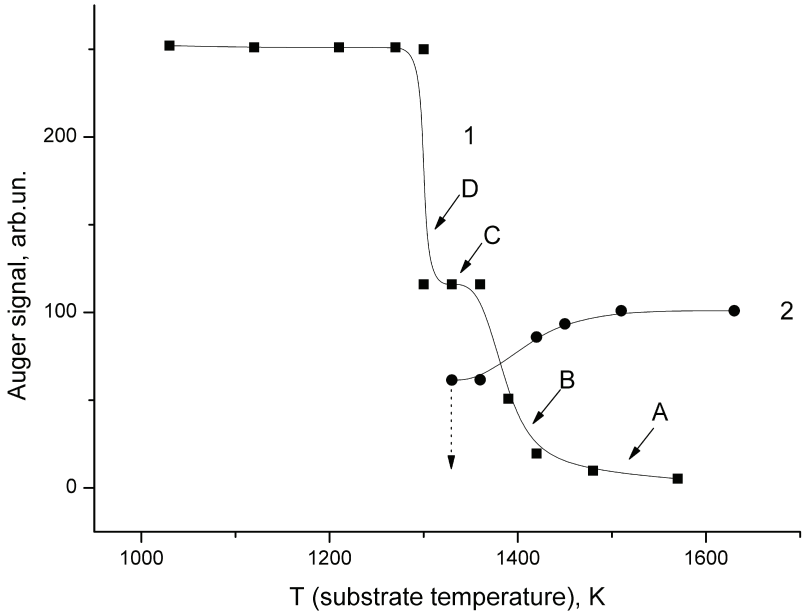

Fig. 6. Auger signals of carbon (1) and Rh (2) versus temperature in sequential annealing of carbonated Rh. Carbonization temperature is T_C = 1400 K; time delay at each temperature point is 30 s.

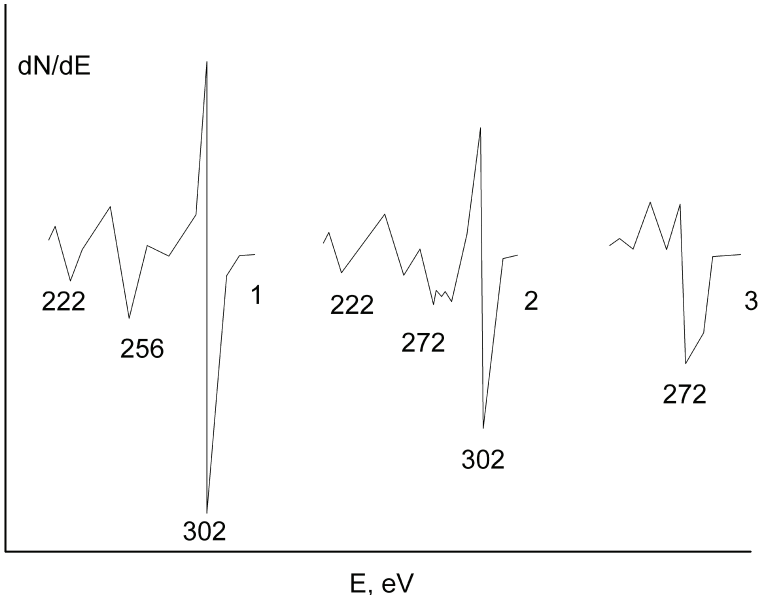

Fig. 7. Auger spectra for pure Rh (1), for Rh with a single grapheme layer (2), and for polylayer (n~8) graphite film on Rh.

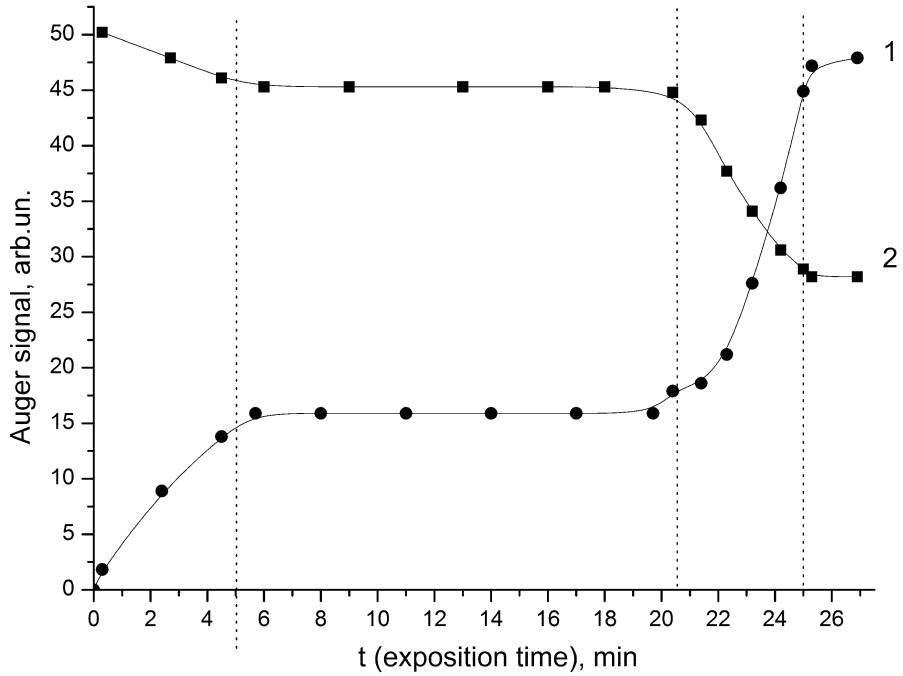

Fig. 8. Auger signals of carbon (1) and Re (2) versus exposure time in carbonization of Re in benzene vapor. Carbonization temperature is T_C = 1700 K; benzene pressure is ~1*10^{-5} Torr

dissolution of carbon in the bulk of the metal, accompanied by its accumulation on the surface. As seen from the graphs, the time t = 5 min can be identified with formation on the surface of a stationary carbon coating. Consider some properties of this carbon coating.

1. Concentration of carbon is consistent with the ReC stoichiometry.
2. As carbon deposition continues, the surface concentration N_s = 1.4 10^{15} at/cm^2 does not change for a long time because of all of the evaporated carbon dissolving in the bulk of rhenium.
3. Changing the sample temperature in the 300--1700-K range does not affect the surface concentration of carbon.
4. The Auger spectrum of this coating has a typical "carbidic" shape (spectrum 1 in Fig. 9), a feature characteristic of strong Me-C bonding [27]. This coating suppress the substrate Auger signal intensity only by 10—20%.

We have called this surface compound "surface rhenium carbide"---ReC. According to the diagram of state, volume rhenium carbide should not exist [25]; this restriction does not, however, extent to an interface state. Obviously enough, the surface rhenium carbide resides in dynamic equilibrium with carbon atoms dissolved in the bulk of the metal, so that this carbon phase can likewise be called chemisorbed carbon "gas". Surface chemical compounds were a subject of a number of our earlier publications [29--33]. For $t \geq 20$ min (Fig. 8), the carbon Auger signal grows somewhat in amplitude to match the coverage

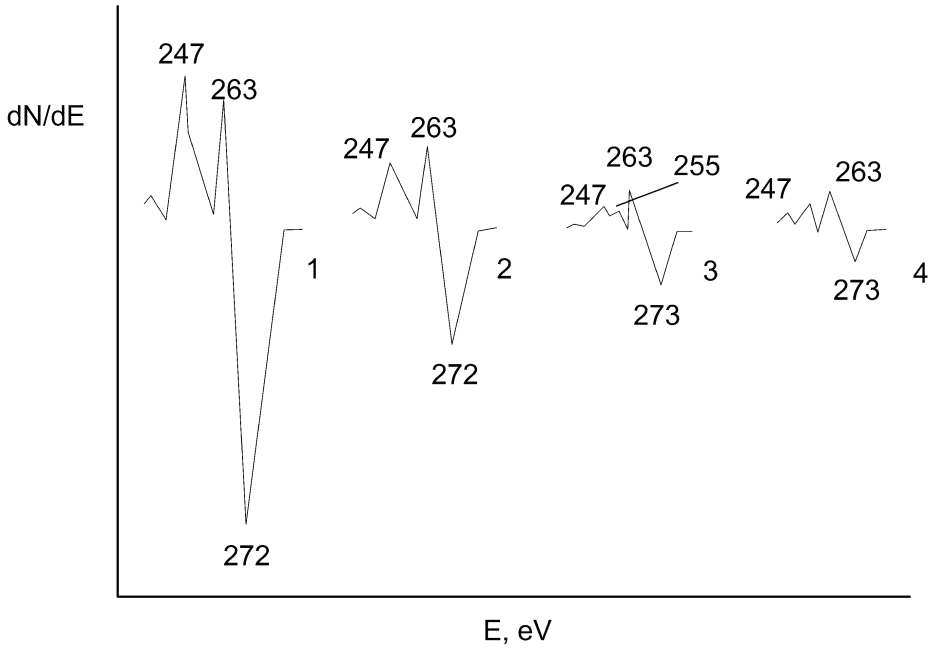

Fig. 9. Carbon KVV Auger spectra for: 1 – Re surface carbide with $N_C = 1.4*10^{15}$ cm^{-2}; 2 – Re surface carbide with $N_C = 2*10^{15}$ cm^{-2}; 3 -- a single graphene layer on Re with the surface carbide behind it; 4 - 7-layer graphite film on Re.

N_s =2 10^{15} at/cm^2, accompanied by a change in the shape of the Auger spectrum of carbon which remains "carbidic" (spectrum 2 in Fig. 9). For t > 21 min, the Auger signal of carbon increases noticeably, while that of the substrate decreases by a factor 1.6. For $t \geq 25$ min, the Auger signals of carbon and of the substrate change no longer. This stage should be identified with formation of a continuous graphene film on the surface of rhenium, with the carbon Auger spectrum becoming close to "graphitic" in shape (spectrum 3 in Fig. 9); the carbon "gas" confined under the graphene layer amplifies additionally the positive surge of the carbon Auger peak with E = 263 eV; it is to be confronted with spectrum 4 corresponding to a thick graphite film on rhenium which was obtained through precipitation of carbon from the supersaturated solid solution Re-C by lowering its temperature down to T = 1300 K.

The process of rhenium carbonization can be visualized not only by AES. Figure 10 displays graphically the variation with temperature of the thermionic current (1) and of pressure (2) in the chamber during carbonization of rhenium at T = 1780 K. The sharp drop of pressure in the chamber (curve 2) measured by an ionization pressure gauge was caused, as revealed by mass spectrometric measurements, by a change in the composition of the gas atmosphere, because the breakup of benzene molecules on heated rhenium brings about out-diffusion of carbon into the bulk of the metal accompanied by desorption of hydrogen molecules. It is the difference between the ionization coefficients of benzene and hydrogen that accounts for the pressure drop. Interestingly, if, following admission of benzene vapors

into the chamber, one shuts off the pumping and heats rhenium to T = 1700--2000 K, the benzene vapor in the chamber will become "replaced", as it were, by hydrogen molecules, a convenient method of obtaining pure hydrogen for experimental purposes indeed! Measurements of thermionic current (curve 1 in Fig. 10) offers a straightforward way to fixing the moment when the limiting concentration of rhenium has been reached and formation of graphene islands has started. Indeed, the start of graphene island formation (t > 16 min) is signaled by a sharp increase of the thermionic emission, because the chemisorbed carbon "gas" raises the rhenium work function from 5.15 to 5.25 eV, while graphene islands lower it strongly to 4.25 eV (§ 7). For t > 25 min, the surface is uniform in work function again, with $e\varphi$ = 4.25 eV.

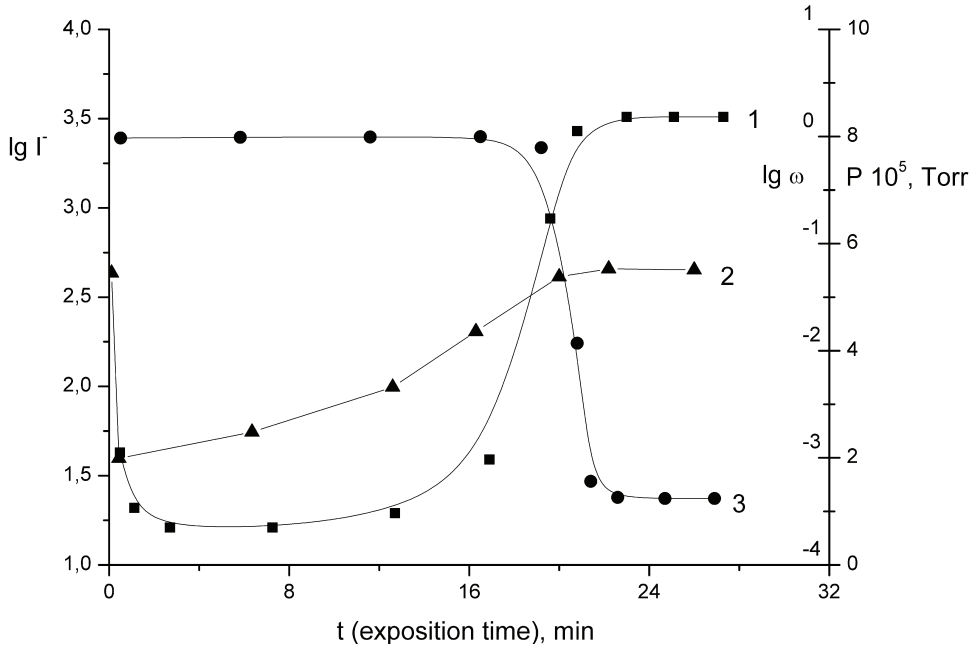

Fig. 10. Thermionic current (1) and lgω for CsCl molecules (3) and the pressure (2) as functions of the exposure time for Re carbonization in benzene vapor at 1780 K. The pressure was measured by ionization manometer calibrated for dry nitrogen.

Just as other Me-C systems, carbonized rhenium can be manipulated purposefully at will by varying its temperature. If the temperature of rhenium carbonized at T_n is raised to T ≈ T_n + 100°, the graphene layer breaks up in no time and carbon from the graphene phase dissolves in the bulk of the metal leaving on the surface carbon "gas" with a concentration N_c = 2 10^{15} at/cm^2. Lowering the temperature down to $T = T_n$ gives rise to a fast recovery of the graphene layer. Reducing the temperature still lower, to 1100 K ≤ $T \le T_n$, will drive the Re-C solid solution to supersaturation, and carbon will precipitate on the surface forming a graphite film tens of atomic layers thick (spectrum 4 in Fig. 9).

If the temperature of carbonized rhenium T_n = 1600--1700 K, turning off the ribbon heating current will leave the graphene layer "frozen" on the surface. Carbonization of rhenium at moderate temperatures of 1200--1500 K can hardly be recommended, because it will result

in formation in the very early stages of graphene islands which will suppress dissociation of benzene molecules, with the ensuing drop of carbon atom flux into the bulk of the metal. Therefore, the process of carbonization may take up several hours [11]. On the other hand, at T_c = 1100--1200 K one may turn off the ribbon heating current after the benzene inlet and prepare a graphene layer with the bulk of the metal remaining practically free of carbon.

A. Graphene on Mo(100) [9, 34]

It is instructive to study the processes involved in graphene formation on carbide-forming metals, for instance, molybdenum. As with rhenium, carbonization of molybdenum passes through a stage of formation of the surface carbide. Figure 11 plots the variation of surface carbon concentration in the course of adsorption of carbon atoms from a calibrated flux striking Mo at T = 1400 K. As follows from the overall particle balance, part of the incident carbon atoms dissolve in the bulk of the metal, while the other part remains on the surface. For a total evaporation dose $N = v_c t$ = 6 10^{15} at/cm^2, surface coverage reaches a level N_c = 1 10^{15} at/cm^2, to remain constant thereafter. Knowing the ribbon parameters (40 x 0.03 x 1) mm^3, one readily finds that each atomic plane of the molybdenum ribbon contains dissolved carbon in a concentration ~6 10^{10} at/cm^2; such low concentrations of carbon in the bulk of a molybdenum sample, just as of other Me-C systems, cannot contribute to Auger spectra which originate from surface carbon. All of the newly arriving carbon becomes dissolved in the bulk of molybdenum (Fig. 11). This surface coating has MoC stoichiometry, thus giving us grounds to call it the surface molybdenum carbide, whose Auger spectrum has a "carbidic" shape (spectrum 1 in Fig. 12). Variation of the temperature of a molybdenum sample within the 300--1500-K range does not affect in any way the surface concentration of carbon. The chemisorbed carbon atoms from the surface carbide phase are in equilibrium with the atoms of carbon dissolved in the bulk. Surface molybdenum carbide increases noticeably the molybdenum work function from 4.45 to 5.25 eV.

Let us follow the processes occurring on molybdenum surface exposed for a long time to benzene vapors at T = 1600 K (Fig. 13). In region I, surface carbide of molybdenum is forming with $e\varphi$ = 5.25 eV. Interestingly, this value of $e\varphi$ persists in region II too, which suggests that the surface carbide is sustained there as well. After the carbon solubility limit in the bulk of molybdenum has been reached, in region II starts formation in the near-surface layer of bulk molybdenum carbide, apparently of the Mo_2C composition, as can be inferred from the diagram of state [35]. Bulk molybdenum carbide evolves into the ribbon toward its center. This is what accounts for the variation of the carbon and molybdenum Auger signal stopping in t > 14 min, because Auger spectroscopy is capable of probing 3--5 surface layers. That penetration of carbon into the bulk of the ribbon is deep is corroborated by the growth of its resistance and increase by ~200° of its radiance temperature. Formation of a volume Mo_2C carbide "poor" in carbon compared with the "carbon-rich" surface carbide MoC was suggested also by experiments on ion etching of carbonized molybdenum, in which after sputtering of the surface carbide the Auger peak of carbon decreased in intensity, whereas that of molybdenum grew to reach new steady-state values identifiable with the volume carbide. Evaluation of the total dose of carbon absorbed by the sample in region II by the time volume carbide evolved to the ribbon center suggests Mo_2C stoichiometry for the volume carbide.

Ion etching revealed that the thickness of the volume carbide layer is > 10^3 Å. Formation under the surface carbide in the metal of the volume carbide produces only a weak impact on the "carbidic" shape of the Auger peak (compare spectra 1 and 2 in Fig. 12).

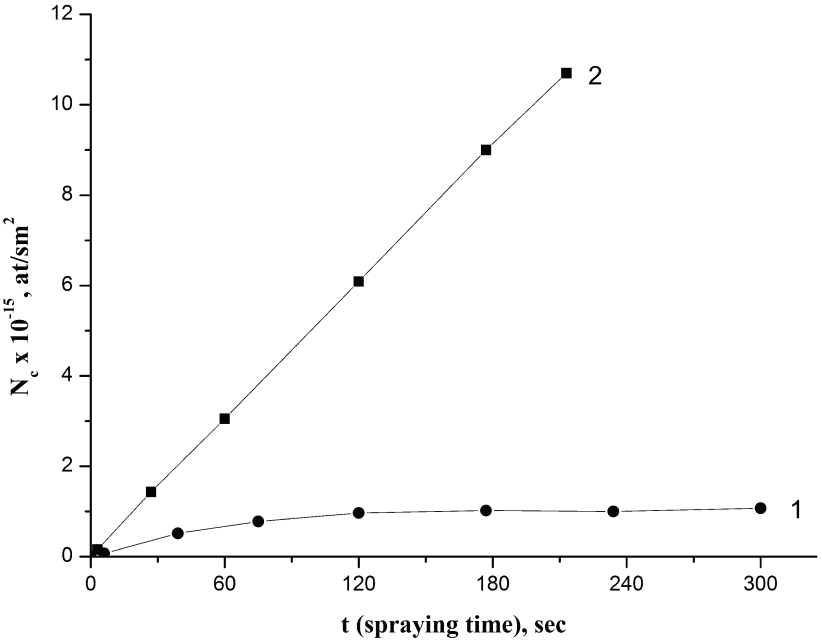

Fig. 11. Carbon surface concentration (1) and the total amount of deposited carbon $N_{tot} = \nu_C * t$ (2) in atomic carbon deposition on heated Mo at 1400 K.

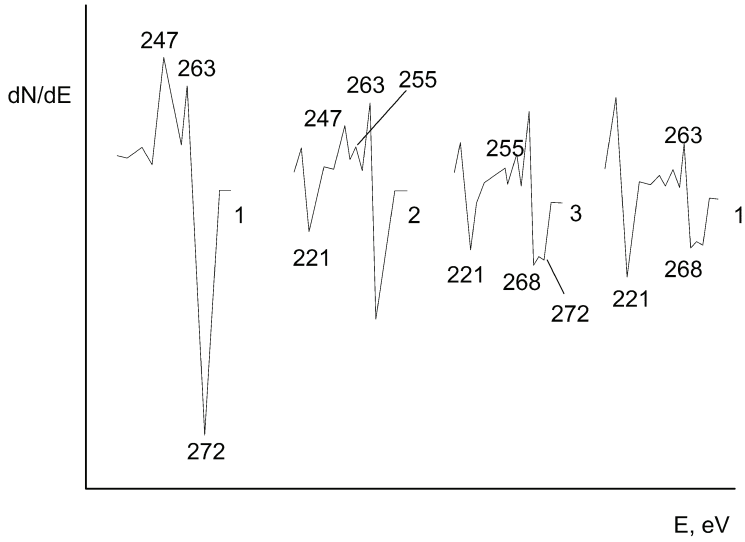

Fig. 12. Auger spectra of various carbon forms on Mo(100) surface: 1 – surface carbide MoC; 2 – bulk carbide MoC_2; 3 -- a single graphene layer with the bulk carbide MoC_2 behind it; 4 - 8-layer graphite film.

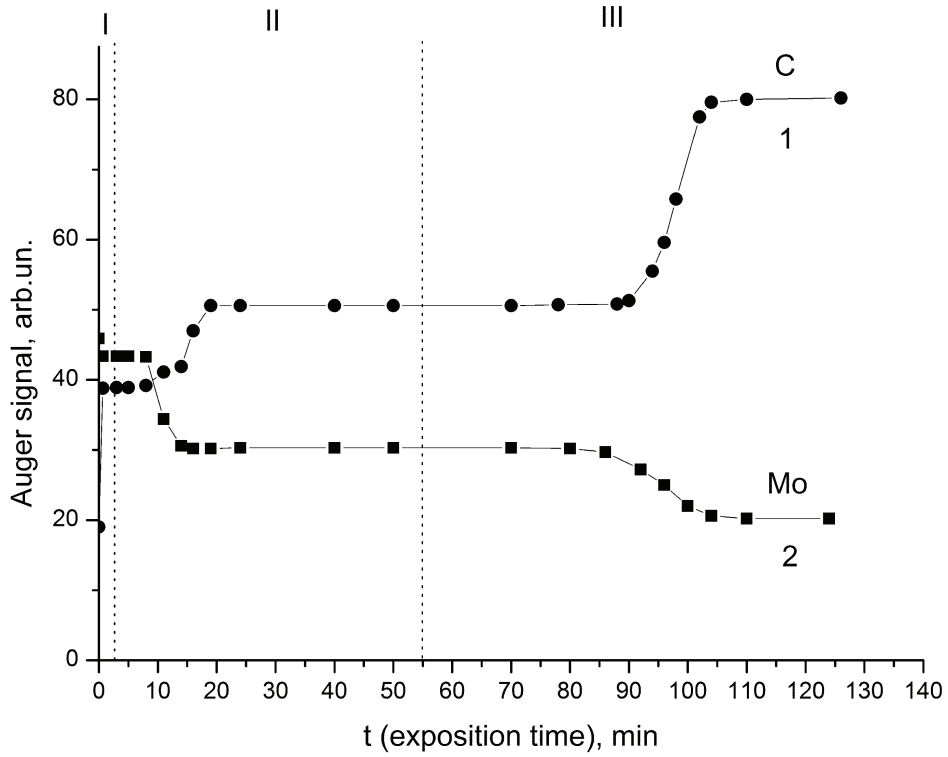

Fig. 13. Auger signals of carbon (1) and Mo (2) versus exposure time in carbonization of Re in benzene vapor. Carbonization temperature is T_C = 1700 K; benzene molecular flux is ~$2*10^{15}$ $cm^{-2}*s^{-1}$

Interestingly, if the volume carbide formed in the near-surface region of the ribbon at a low temperature, for instance, at T = 1000 K, is heated to $T \geq 1300$ K, it breaks down, and the excess carbon becomes incorporated in the Mo-C solid solution, with the surface carbide remaining on the surface.

If we continue the exposure of the molybdenum ribbon to benzene vapors after the volume carbide Mo_2C has formed throughout the bulk of the sample, a graphene layer will grow above the surface carbide (region III in Fig. 13). This is accompanied by a decrease of the molybdenum Auger signal by a factor 1.6, a feature characteristic of screening by one graphene layer (see **§** 4).

Spectrum 3 in Fig. 12 was obtained in Auger probing of a graphene film on molybdenum. We note immediately an unusual shape of the carbon Auger peak, which is actually a superposition of the Auger peaks of graphene and the signal of surface (MoC) and volume (Mo_2C) carbides.

Molybdenum carbonized at T_c was subjected to different heat treatments. When heated to $T > T_c + 70^o$, graphene was found to dissolve in the bulk of the metal. Subsequent lowering of the temperature down to $T < T_c - 30^o$ initiated growth on the surface of a thick graphite film,

the molybdenum Auger peak disappears, and the Auger peak assumes the "graphitic" shape (spectrum 4 in Fig. 12). For T ≤ 1100 K, carbon stops to evolve because of the diffusion becoming "frozen".

Dissolution of carbon from graphene in molybdenum at temperatures T rising above T_c and its precipitation below T_c resemble very much similar processes occurring in the Re-C, Pt-C, and Rh-C systems. The MoC system differs essentially only in that rhenium, platinum, and rhodium do not support carbide formation, while molybdenum has the volume carbide, which is the first to become augmented by carbon following formation of the surface carbide MoC.

It thus appears proper to expect that after formation of the volume carbide carbon will dissolve in it just as it does in the metal, up to the solubility limit. Then lowering of the temperature to $T < T_c$ will bring about supersaturation of the solid solution of carbon in the volume carbide, while the excess carbon atoms will start construction of a graphene film on the surface without involvement of carbon atoms from the volume carbide.

D. Graphene on Ni(III)

Unlike the Re-C and Mo-C systems, nickel can be readily carbonized at comparatively low temperatures T = 1100—1400 K, despite the high solubility limit of carbon in this metal (0.3 to 3 at. % in the temperature region specified). This should be assigned to the diffusion of adatoms from the surface into the bulk of nickel being a process fast enough to preclude formation of a "protective" graphene film, as this is observed to occur in the Re-C system. To estimate the average depth x of penetration of carbon atoms from nickel into the ribbon in time t, we use the relation $\bar{x} = \sqrt{2Dt}$ [37], in which $D = D_0 \exp[-E/kT]$ is the diffusion coefficient, and E is diffusion activation energy. It is known that for volume diffusion of carbon in nickel $E \approx 1.5$ eV, and $D_0 \approx 0.1$ cm^{2}s^{-1} [36]. Then for T = 1200 K and the exposure time of nickel to benzene vapors t = 100 s we obtain

$$\bar{x}(\text{cm}) = \sqrt{2D_0 t \exp(-E/kT)} = 3 \cdot 10^{-3} \text{cm},$$

a value close to one half the thickness of the ribbon used in the experiments. Just as in the Ir-C, Re-C, Mo-C, Pt-C, and Rh-C systems, carbonization culminates in formation of a graphene film. That the film formed is indeed graphene, is attested by the "graphitic" shape of the carbon Auger spectrum (spectrum 2 in Fig. 14), by characteristic splittings of the Auger spectrum of carbon initiated by intercalation of cesium atoms under graphene (spectrum 5 in Fig. 14) – see below **§** 7, as well as by the good fit of the calculated to experimentally observed drop of the substrate Auger signal intensity by a factor ~ 2 for E_{Ni} = 61 eV caused by one graphene layer.

The variation in intensity of the carbon and nickel Auger peaks brought about by heating and cooling of nickel carbonized at T_c = 1365 K is shown graphically in Fig. 15. If the ribbon temperature is increased, at $T > T_c + 40^o$ graphene breaks down and escapes from the surface altogether, leaving a small carbidic Auger peak of carbon (spectrum 1 in Fig. 14), whose intensity and shape practically do not vary with further increase of temperature. The concentration of carbon in this state $N_c \approx$ (2--3) 10^{14} at/cm^2; this may be the Ni_6C surface carbide, because for the Ni(III) face N_{Ni} = 1.86 10^{15} at/cm^2. Obviously enough, surface carbide of nickel resides in equilibrium with the carbon dissolved in the bulk of the metal, as is the case with other systems forming surface carbides (WC, MoC, ReC). After the

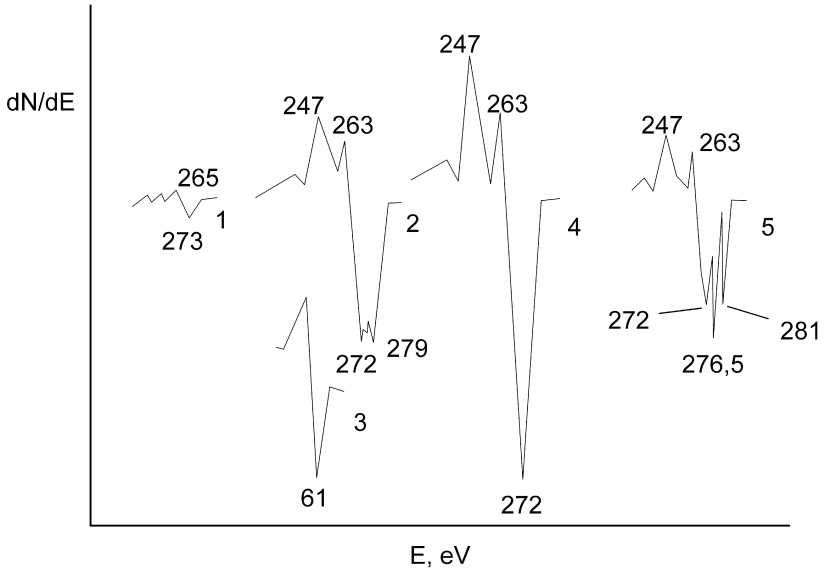

Fig. 14. Auger spectra of various carbon forms on Ni(111) surface: 1 – surface carbide of Ni; 2 –a single graphene layer; 3 Ni Auger peak at E= 61 eV under it; 4 – 6-layer graphite film; 5 – the spectrum of a graphene layer after intercalation with Cs.

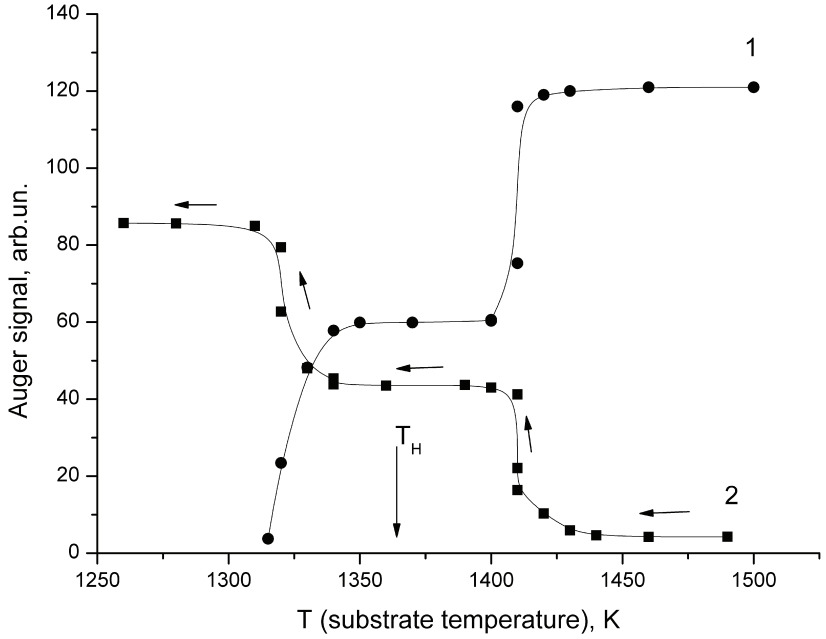

Fig. 15. Auger signals of Ni (1) and carbon (2) versus temperature in temperature decreasing. Carbonization temperature is T_C = 1375 K; time delay at each temperature is 30 s.

temperature has been lowered down to $T = T_c = 1365$ K, a layer of graphene forms again on the surface. As the temperature is lowered down to $T < T_c - 30^o$, a thick graphite film starts to grow, with its thickness clearly larger than 6--7 layers, because Auger spectroscopy does not sense the substrate (Fig. 15). The Auger spectrum of carbon exhibits a distinct "graphitic" shape (4 in Fig. 14).

Because the solubility limit N_{lim} of carbon in nickel is well known [35], for instance, at T = 1365 K it is $N_{lim} \approx 2$ at. %, while at T = 900 K, $N_{lim} \approx 0.15$ at. %, one readily finds that at T = 900 K a graphite film about 100 atomic layers thick should form on each side of a nickel ribbon 30 μm thick through segregation on the surface of "excess" carbon atoms.

We did not study the low-temperature (T < 900 K) region of volume nickel carbide formation.

§ 2. Probing a surface with CsCl molecule flux

A simple method is proposed for detection of graphene on a metal and determination of the relative area occupied by graphene islands

It was shown [27] that a graphene film is valence-saturated and passive, and that it suppresses dissociation of a variety of molecules which on a clean metal proceeds very efficiently (see **§** 7). If we direct a flux of CsCl molecules on a metal heated above 900 K, the molecules will dissociate, with one of the products of this reaction, the cesium atoms, desorbing from the surface as Cs^+ ions with a 100% probability; indeed, on all the metals under study here the cesium ionization potential V = 3.89 eV is much lower than the surface work function φ, i.e., $V << \varphi$ – the case of "easy" surface ionization indeed [39]. On a continuous graphene film, only residual dissociation is observed, at a level of 0.01--0.1 %, depending on the metal, and it originates apparently from substrate defects or edges of the merged graphene islands. Therefore, by measuring the cesium ion current I_0^+ from a clean metal surface and the ion current I^+ from a surface coated by islands one can readily find the fraction n of the surface occupied by graphene islands:

$$n = \left(1 - \frac{I^+}{I_0^+}\right). \quad (1)$$

Experiments revealed that only graphene is capable of reducing radically the dissociation efficiency of CsCl molecules. On a clean metal, on surface and volume metal carbides, and on continuous carbon films formed at T < 900 K (see **§** 11) the dissociation efficiency is 100%. As this should be expected, n does not depend on substrate temperature, and the effects associated with CsCl molecules sliding off the edges of graphene islands onto the metal could be neglected because of the migration path length of CsCl molecules in their lifetime on graphene is extremely short [40]. Besides, as demonstrated for the Ir(III)-graphene system, the carbon Auger signal intensity for graphene islands growing at T = 1600 K is directly proportional to the fraction n of the area occupied by the islands.

In addition to CsCl, the island-occupied fraction n of the area can be derived by probing the surface by a variety of atoms, for instance, by K and Na. On the iridium surface coated by chemisorbed carbon "gas" with $e\varphi \approx 6.0$ eV, K and Na desorb only in the form of ions---another illustration of "easy" ionization; in this case, the measured I_0^+ ion current will be [39]

$$I_0^+ = e \cdot \nu \cdot s\,, \tag{2}$$

Where e is the electronic charge, ν is the density of the atom flux, and s is the area is the emitting surface of the sample; in our experiments, s = 0.005 cm².
For atoms desorbing from a surface bearing graphene islands the measured current I^+ can be written as [39]

$$I^+ = e \cdot \nu \cdot s \cdot (1-n) + \frac{e \cdot \nu \cdot s \cdot n}{1 + A \cdot \exp\left(\frac{e(V-\varphi)}{kT}\right)} = I_0^+(1-n) + \frac{I_0^+ \cdot n}{1 + A \cdot \exp\left(\frac{e(V-\varphi)}{kT}\right)}\,, \tag{3}$$

where A is the ratio of the partition functions of the atomic and ionic states of the ionizing atoms, V is the ionization potential of K or Na atoms, φ is the work function of graphene islands on iridium (eφ = 4.45 eV), k the Boltzmann constant, and n is fraction of surface area occupied by graphene islands.
Having measured I_0^+ and I^+, one can find from Eqs. (2) and (3) n, i.e., the fraction of iridium surface area occupied by graphene islands.
These two methods correlate well with one another, with the data scatter not over 10%, thus providing support for the physical model reproducing the relations in the metal-graphene islands system.
The first method is certainly simpler and can be realized readily with any high-vacuum equipment; significantly, it allows one to follow in real time the nucleation, growth, and destruction of graphene islands on various metals.
Note also one more significant aspect of the method based on probing the surface with CsCl molecules, more specifically, the high sensitivity to the integrity of a graphene film; indeed, a film rupture of only ~0.1% of the total graphene area is signaled reliably by a growth of the Cs^+ ion current. Apart from this, residual dissociation of CsCl molecules on thick graphite films decreases still more by a hundred times compared with graphene. This may be considered as one more evidence in support of the assumption of residual dissociation of molecules occurring at the edges of merged islands in the graphene layer.
For illustration, curve 3 in Fig. 10 plots the variation of the dissociation efficiency of CsCl molecules (logω) in the course of rhenium carbonization (ω = I^+/I_0^+). The steep growth of the thermionic current, which signals the appearance of graphene islands, is seen to coincide with the sharp drop of the CsCl dissociation efficiency.

§ 3. Electronic Auger spectroscopy of carbon

The rich variety of chemical realizations of carbon exhibits an astounding diversity of its Auger spectra, both in shape and energy position, which is revealed most clearly by high-resolution Auger spectroscopy.

Our studies have amassed a vast collection of Auger spectra of carbon in its various chemical states [41]. The experiments were conducted under identical conditions with a high-resolution prism electronic Auger spectrometer ($\Delta E/E \le 0.1\%$). The characteristic features and the main parameters of the instrument were basically determined by the prism type of its energy analyzer, more specifically, a prism analyzer with deflecting electric field [42]. As a rule, the primary electron beam with a current ~5 μA bombarded the operating

surface of a sample, 1 mm² in area, from which the Auger electrons were collected. The large distance (~ 74 mm) between the sample and the energy analyzer permitted obtaining, without any loss in sensitivity, carbon Auger spectra of ribbon samples heated up to T = 2500 K, an aspect which in more than one case turned out to be of crucial significance for correct unraveling of the physical-chemical processes occurring in a Me-C system. For instance, if we carbonize rhenium at T = 1850 K and measure the carbon Auger spectrum directly at this temperature, the spectrum will have a typically graphitic shape (Fig. 9, spectrum 3). By contrast, if the ribbon is temperature is lowered down to room level, a layer of graphite will form on the surface during the cooling (Fig. 9, spectrum 4). Now if we measure the Auger spectrum at T = 1900 K, the shape of the Auger spectrum will be purely carbidic due to the chemisorbed carbon "gas' involved (Fig. 9, spectrum 2).

Figure 16 displays some carbon Auger spectra obtained both from pure carbon materials and from carbon in its various chemical compounds. We see that even morphologically close forms of carbon, single-crystal and polycrystals of graphite, differ markedly in the shape of their Auger spectra. A fullerite film produces a spectrum approaching that of graphite polycrystals while differing strongly in the position of the negative spike of the carbon Auger peak, 272 eV for the graphite polycrystals, to be contrasted with 269 eV for the fullerite (spectra 2 and 7 in Fig. 16).

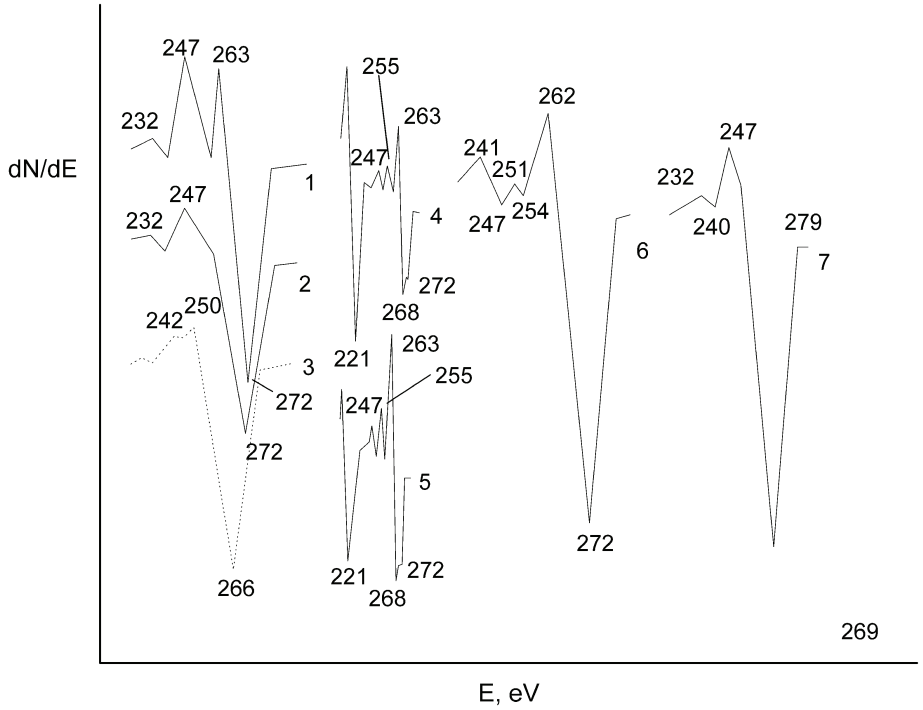

Fig. 16. Carbon KVV Auger spectra for various chemical forms of carbon: 1 – graphite single crystal, 2 –polycrystalline graphite; 3 – diamond, 4 – surface carbide MoC; 5 – bulk carbide MoC_2; 6 -- silicon carbide SiC; 7 – fullerit.

A continuous graphene film formed on Ir(III) in exposure to benzene vapors at T_c = 1600 K offers a convenient means of calibration relating the Auger peak intensity of carbon with its amount present on the surface. A convenient reference for calibration of carbon in the carbide state is the readily obtained surface tungsten carbide WC containing N_c = 1 10^{15} at/cm^2 [43]. The two calibrations correlate nicely with one another as well.
Summing up, we can say that high-resolution Auger spectroscopy is a valuable complementary tool in diagnostics of surface processes evolving in a carbon layer on metals (see the subsequent Sections).

§ 4. The structure and two-dimensional pattern of graphene films on metals

A graphene film on a metal is indeed two-dimensional!

There can be no doubt whatsoever that a carbon film prepared by exposing a heated metal to hydrocarbon vapors does indeed have graphite structure; this can be readily demonstrated in a direct experiment with the use of scanning tunneling microscopy (Fig. 2, **§** 2). Indirect supportive evidence for this comes from Auger electron spectroscopy measurements, as well as from a number of properties of graphene films correlating closely with those of graphite single crystals, in particular, valence bond saturation of a layer of graphene, its chemical passivity [27], and the possibility of intercalating the film with foreign atoms [13].
One can hardly question the statement that the graphene films obtained in this way are continuous---this is argued for by scanning tunneling microscopy measurements [20-23] and probing the surface with CsCl molecules. Besides, the graphene surface is uniform in work function (**§** 7).
Consider some evidence for the graphene film being indeed two-dimensional:

1. Figure 17 plots the variation of the carbon Auger peak intensity with the relative area of graphene islands, with carbon atoms deposited on the iridium (III) face at T = 1500 K. At this temperature, carbon adatoms are confined primarily to graphene islands.

   We readily see that the carbon Auger peak intensity is directly proportional to the relative area of graphene islands. This suggests convincingly that the incident carbon does not form a three-dimensional structure, and that it is distributed in one layer, i.e., that the graphene islands are actually two-dimensional. The two-dimensionality of graphene islands was demonstrated in a similar way for the Pt-C and Ni-C systems.
2. Compare now the experimentally observed attenuation of the iridium Auger peak produced by graphene-initiated screening with the corresponding calculations. We assume that the Auger electron emission is isotropic, and that the attenuation of the primary electron beam intensity by graphene may be neglected. Then the attenuation of the iridium Auger peak by a graphene film with thickness x can be derived readily from the relation

$$\frac{1}{\delta(\mathrm{Ir,C})} = \frac{I'_{\mathrm{Ir}}}{I_{\mathrm{Ir}}} = \exp\left[-\frac{x}{\lambda(E_{\mathrm{Ir}})}\cdot\frac{1}{\cos\theta}\right], \qquad (1)$$

   where $\lambda(E_{Ir})$ is the average mean free path length of the iridium Auger electrons with the energy E = 171 eV in graphite, and $\theta = 10^{o}$ is the angle between the energy analyzer

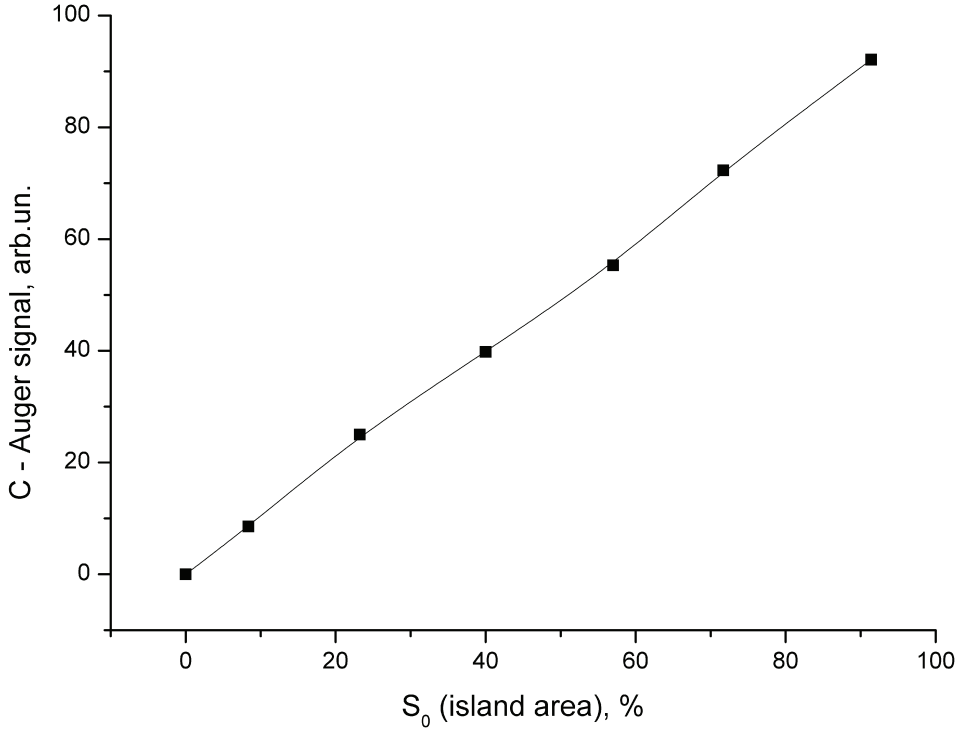

Fig. 17. Carbon KVV Auger signal versus relative area of grapheme islands in deposition of atomic carbon onto Ir(111) surface at 1500 K. The deposition flux is $\nu_C = 3.2 * 10^{13}$ cm^{-2}*s^{-1}.

axis and normal to the sample surface. Putting x = 3.35 Å, which is the interplanar distance in graphite and deriving $\lambda(E_{Ir}) = 5.0$ Å from the $\lambda = f(E)$ relation constructed for a number of materials including graphite, we come to δ(Ir, C) = 1.8. The experimentally found attenuation of a factor 1.6 turns out to be close to the calculated value. We may add that for a graphite film two monolayers thick the same calculation yields a factor 3 for the attenuation.

A comparison of the values of attenuation of the substrate Auger signal intensity by a graphene layer performed for other Me-C systems with close Auger peak energies of the metal (Re, Mo, Pt) yields an experimental value $\delta = 1.6 \pm 0.1$. We note also that one layer of C_{60} fullerene molecules on Ir(III) with a concentration $N_{C60} = 2*10^{14}$ mol/cm^2 reduces the substrate Auger signal ~4 times [44].

3. That the graphene layer on iridium is monatomic is argued for also by a comparison of Auger peak intensities from a graphene film, I_c', and graphite, I_c'' obtained under identical experimental conditions with calculations. Neglecting the dependence of electron backscattering from the material and setting $\cos\theta = I$, we come for a thick film of graphite on iridium to

$$I_c'' = \kappa \int_0^h \exp\left[-\frac{x}{\lambda(E_c)}\right] dx = \kappa\lambda(E_c), \quad (2)$$

where $\lambda(E_c)$ = 6.2 Å is the average mean free path length of carbon Auger electrons with E_c = 272 eV in graphite [44]. For the carbon Auger peak intensity from a graphite monolayer h = 3.35 Å thick we obtain

$$I_c^{'} = \kappa \int_0^h \exp\left[-\frac{x}{\lambda(E_c)}\right] dx = 0{,}42\kappa\lambda(E_c)\,. \tag{3}$$

The calculated ratio $I_c^{''}/I_c^{'}$ = 2.4 is close to the experimental value 2.5. It is worth reiterating that a continuous graphene film on a metal can be obtained in any high-vacuum instrument without any effort expended, without special diagnostics of the surface---indeed, all one needs to do is expose the metal heated enough to benzene vapors. Table 1 presents for illustration the time needed for a graphene layer to form on various metals at T = 1700 K and P_{C6H6}~ 1*10−6 Torr for thin metal ribbons 20—30 μm thick.

Me	Ir(III)	Pt(III)	Rh(III)	Re(I0I0)	Mo(I00)
t, c	~ 10	~ 20	~ 300	~ 1500	70000

Table 1

Figure 18 plots the times needed for formation of a graphene layer on rhenium heated to T_c = 1730 K; at each point, the temperature was first raised to 1900 K, and lowered

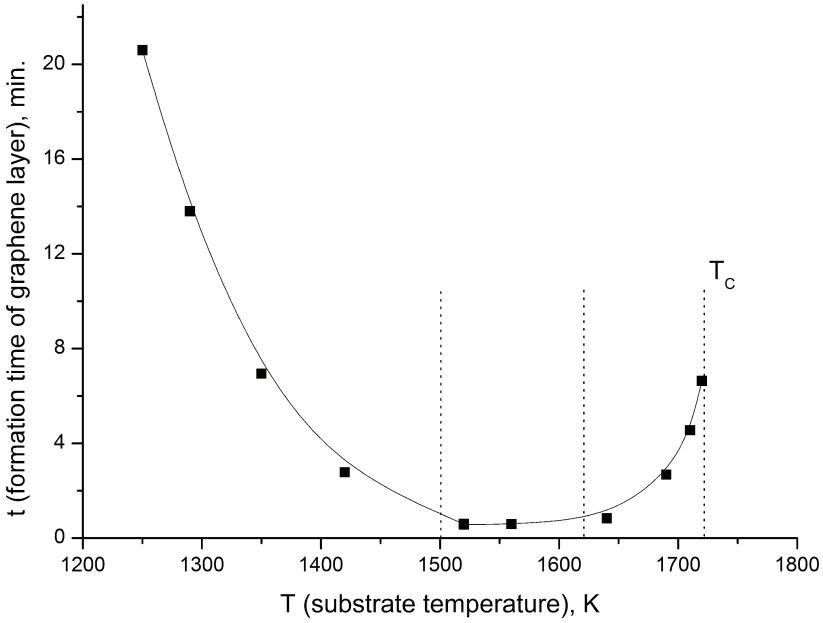

Fig. 18. Time of single graphene layer formation on Re due to carbon precipitation from the metal bulk versus surface temperature. Carbonization temperature is T_C = 1730 K; The layer was considered as completed when the thermionic current become corresponded to the work function eφ = 4.25 eV

subsequently to the required level. The growth of the formation time at low temperatures should be assigned to freezing of the volume diffusion of carbon atoms, and its increase at high temperatures can be traced to intensive dissociation of graphene islands.

§ 5. Two-dimensional phase transition in a carbon layer on metals

A graphene film on a metal grows by formation of graphene islands, which expand in area and coalesce to produce a continuous layer.

It is known that many films coating the surface of solids undergo first-order phase transitions. In the course of such a phase transition, the originally uniform adsorbate layer becomes nonuniform, with the surface breaking up to form islands containing adsorbate with different adatom densities. An apparently pioneering experimental study [45] based on the use of an ion projector revealed the presence on a tungsten surface of two-dimensional Zr islands produced in a phase transition in the adfilm, with the same process observed to occur [46--48] in zirconium, hafnium, and platinum films coating the surface of a number of refractory metals. The theory of the phase transition involved and a review of the experimental studies amassed was dealt with in Ref. [49]. Phase transitions were observed to evolve in platinum metal-carbon systems [50--52], in sodium adlayers on W(I00) [53], in barium adlayers on metal substrates [54], and, probably, in gold and copper films grown on single-crystal graphite [55]. Even in two-dimensional films of charged adatoms one may expect, despite the repulsive character of their interaction, a first-order phase transition, including a condensation-type one, as this was shown theoretically [56--57]. Phase transitions in such systems set in as the density of the film increases, thus reducing the effective charge of the adatoms.

A first-order phase transition in a carbon adlayer on a metal was first observed in the iridium-carbon system [50--52], the associated ideology having been underpinned by statistical theory of lattice gas and exposed in considerable detail in Ref. [27]. The onset of a phase transition depends essentially on several factors, among them the nature of the adsorbate and substrate atoms, the strength of lateral interaction among the adatoms, and charge state of the adatom. For carbon atoms having electronegativity close in magnitude to that of substrate atoms of transition metals (W, Ir, Re) one may expect the carbon adatom to either be uncharged or have a weak negative charge. On the other hand, the binding energy coupling carbon atoms is high, for instance, in molecules of organic compounds the energy of a single C-C bond is 3.6 eV, that of the double C=C bond, 6.32 eV, that of the ternary bond C≡C, 8.65 eV, and the sublimation heat of carbon is also large---7.44 eV [59]. Assuming a noticeable migration mobility of carbon adatoms, one may therefore expect formation of closely packed carbon islands. A condensation-type first-order phase transition would make a Me-C film system nonuniform in its emission characteristics. Therefore, phase transitions can be revealed by methods sensitive to nonuniformities in emission, such as field-emission microscopy, low-energy electron diffraction, and a method combining thermionic emission with surface ionization of hard-to-ionize elements (TESI).

A study of high-temperature (T ~ 1600 K) adsorption of carbon atoms on iridium made by TESI [50--52] reported on a first observation on a metal surface of a first-order phase transition of the two-dimensional condensation type which gives rise to coexistence on the surface of two carbon phases, more specifically, two-dimensional graphene islands and

chemisorbed carbon atoms (two-dimensional carbon "gas"). For the substrate the above authors conveniently chose iridium, a metal which does not dissolve carbon in its bulk, a factor which alleviated markedly interpretation of the results obtained.

The phase transition in a carbon adlayer on metals having presently become universally recognized, it deserves a particular place in our analysis here. The TESI method, first proposed in Ref. [60] and developed in a later publication [27], is based essentially on determination of the work function from measurement of the thermionic and ion currents generated through surface ionization of the probing atomic beam [39]. By measuring the thermionic and ion currents at a constant emitter temperature and different coverages of the substrate by carbon, one can readily calculate by the total current method the variation of the thermionic, $\Delta\varphi_e$, and ionic, $\Delta\varphi_i$, work functions. A comparison of $\Delta\varphi_e$ with $\Delta\varphi_i$ provides a good means to judge the nonuniformity of the carbon layer. Indeed, thermionic current I_e from a uniform emitter is given by the Richardson relation [60]

$$I_e = A_0\left(1-\overline{R}\right)\cdot S\cdot T^2\exp\left[-\varphi_e / kT\right], \tag{1}$$

where A_0 is a universal constant, R is the coefficient of thermoelectron reflection from the potential barrier on the sample surface, S is the emitting surface area, and k is the Boltzmann constant.

The positive ion current from a surface produced by surface ionization is given by the Saha—Langmuir relation [39]

$$I_i^+ = \frac{eS\nu}{1+A\cdot\exp\left[\dfrac{V-\varphi_i}{kT}\right]}, \tag{2}$$

where ν is the density of the flux of atoms with ionization potential V striking the surface, and A is the partition function ratio of the atomic and ionic states of the ionizing atoms.

Examining Eqs. (1) and (2), we see that thermionic emission "senses", as it were, the surface areas with the lowest work function, while the ion current produced by the atomic flux probing the surface is, by contrast, sensitive to those with the highest work function. When $\varphi_e = \varphi_i$, we infer that the sample surface is uniform in the work function.

Figure 19 displays graphically the variation of the φ_e and φ_i work functions in the case of carbon atoms adsorbed on Ir(III) at T = 1700 K with the surface coverage by carbon θ (θ = 1 corresponds to a carbon concentration N_{cm} = 3.56*10^{15} at/cm^2). Three regions stand out in the graph:

I--- the surface is uniform in work function, $\varphi_e = \varphi_i$;

II---the surface is nonuniform in emission, and $\varphi_e < \varphi_i$;

III---the surface is again uniform in work function, $\varphi_e = \varphi_i$.

The presence in the carbon adlayer of regions with different work functions (region II in Fig. 19) is attributed [50--51] to a first-order two-dimensional phase transition. In region I in Fig. 19, carbon resides in the phase of two-dimensional chemisorbed "gas", i.e., it is spread uniformly over the surface, and $\varphi_e = \varphi_i$. In region II, a phase of condensed carbon (graphite islands with θ_c = 1), which is in dynamic equilibrium with the carbon "gas", is forming on the iridium surface. The nonuniformity of the surface in work function in region II finds convincing support in the strong anomalous electronic Schottky effect. As the total carbon concentration on the iridium surface increases, the different adsorbate phases undergo

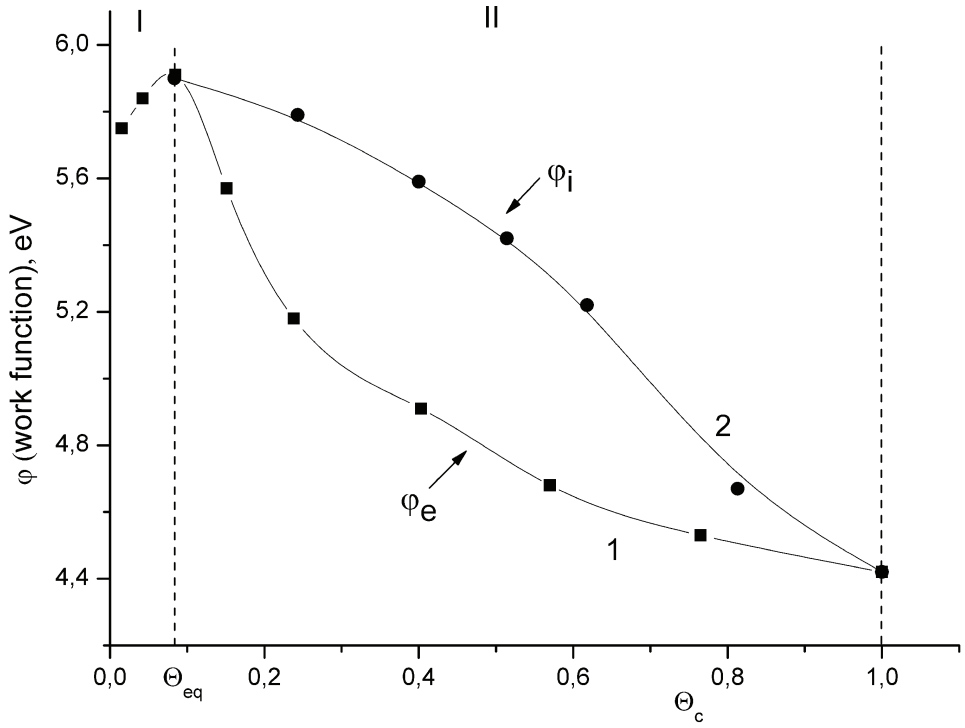

Fig. 19. Variations of 'electron' φ_e (1) and 'ionic' φ_I (2) work functions measured from thermionic current and from In+ ion probing respectfully, with surface carbon cover θ_C. θ_C = 1 corresponds to a continuous grapheme layer; T = 1700 K

redistribution in occupied area, with the graphene islands growing in area, thus reducing the area covered by the carbon "gas". Merging islands produce a graphene film---region III in Fig. 19---which is uniform in work function. Obviously enough, the ratio of the areas occupied by the different carbon phases depends not only on the amount of the adsorbate present but on the substrate temperature as well.

A two-dimensional phase transition was subsequently found to occur in the Ni-C system [5] and explored in detail in our studies of the growth of graphene films on Ir, Pt, Ni, Rh, Re, and Mo [41].

For the first time in Me-C systems, the equilibrium carbon coverage θ_{eq} (T) in the state of chemisorbed carbon "gas" on Ir(III) was determined in the phase transition in a carbon layer which involved formation of graphene islands [14]. Consider two methods of θ_{eq} (T) determination.

Determination of $\theta_{eq}(T)$ by Auger electron spectroscopy. Chemisorbed carbon "gas" is known to increase the work function of the iridium surface; indeed, at T = 1800 K the work function grows from 5.75 to 5.95 eV (Fig. 19). The maximum in the $\varphi = f(\theta_c)$ plot signifies reaching a critical coverage by carbon θ_c which initiates a phase transition with formation of graphene islands residing in dynamic equilibrium with their carbon "gas" whose coverage $\theta_{eq} = \theta_c$. Formation of graphene islands with $e\varphi$ = 4.45 eV brings about a sharp growth (by

orders of magnitude) of the thermionic current. To determine $\theta_{eq}(T)$, carbon atoms were deposited at different iridium temperatures in the 1600--1900-K region until φ_{max} was reached, which was signaled by the thermionic current, and the carbon concentration N_c on the surface was found by AES, with subsequent calculation of $\theta_{eq} = N_c/N_{cm}$ (N_{cm} = 3.56*10^{15} at/cm^2). The measurements were performed repeatedly at each T. The averaged values of $\theta_c = \theta_{eq}$ are plotted vs. temperature in Fig. 20.

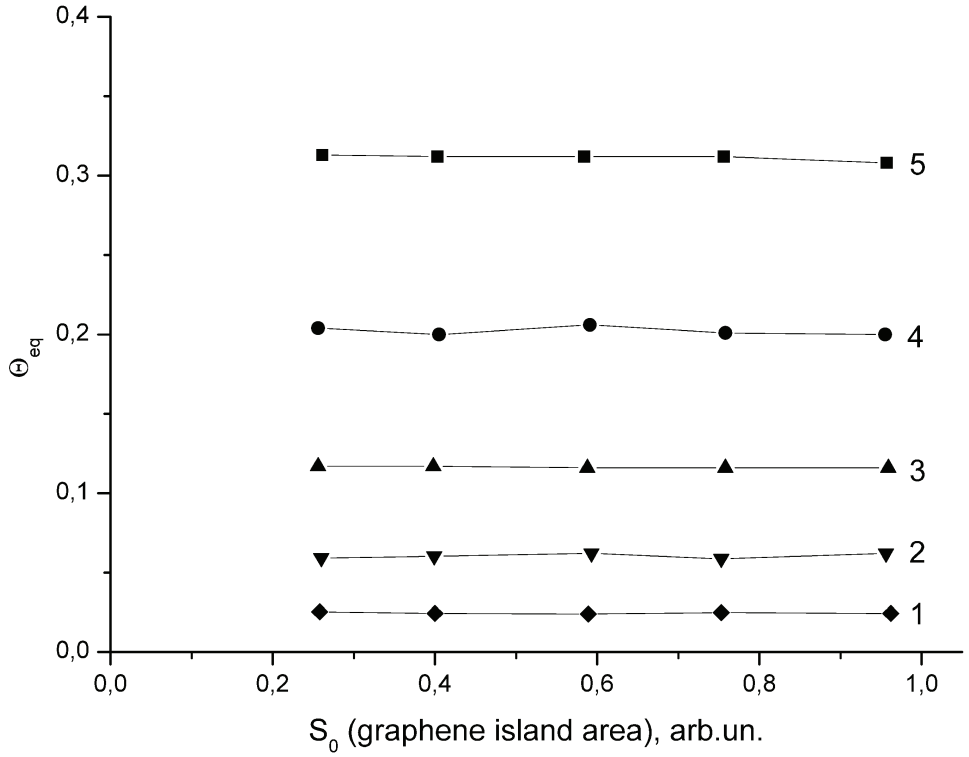

Fig. 20. Equilibrium surface carbon covers θ_{eq} as functions of relative grapheme area S_0 for Ir-C system at various temperatures (K): 1 – 1670; 2 – 1760; 3 – 1840; 4 – 1915; 5 – 1975.

Determination of $\theta_{eq}(T)$ from dissociation of CsCl molecules. The method draws essentially from the possibility of deriving the relative area of graphene islands from dissociation of CsCl molecules (see **§** 2). Graphite islands with a relative area $S_0(T_C)$ were produced at T_C = 1600 K on the surface of an iridium ribbon by exposing it to benzene vapors. At T_C = 1600 K, θ_{eq} ~ 0.01, and carbon adatoms are concentrated primarily within graphene islands; therefore, lowering the temperature below T_C does not change the relative area of the graphene islands. After this, benzene vapors were pumped out, and the temperature of iridium was raised in steps to T_1, T_2, …, T_i. As the temperature increased, the graphene islands dissociated, and their relative area decreased, while the chemisorbed carbon "gas" became, accordingly, denser. The graphene islands recovered finally their area after the temperature had been lowered down to T_C.

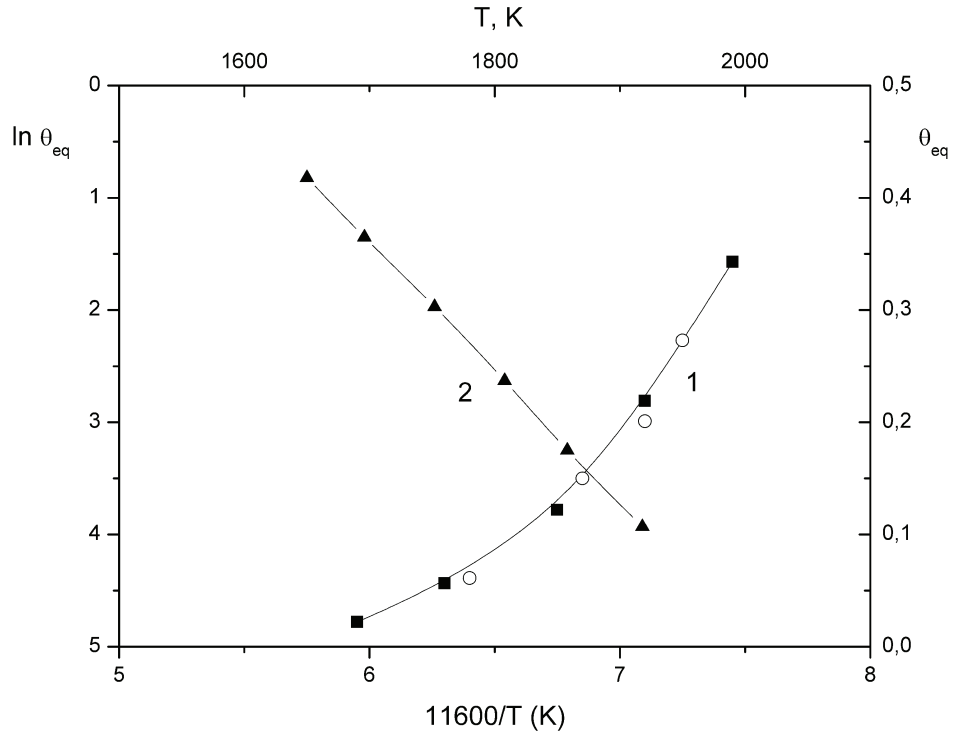

Fig. 21. Equilibrium carbon cover θ_{eq} as function of T (1) and $\ln\theta_{eq}$ as function of 1/kT (2) for 2D carbon gas in equilibrium with grapheme islands. black dots – by CsCl dissociation, light dots – by AES.

It was demonstrated convincingly [14] that the carbon "gas" covers the total surface, i.e., that it resides under the graphene islands as well. But then $\theta_{eq}\,(T_i) - \theta_{eq}\,(T_C) = S_0(T_C) - S_0(T_i)$, and, recalling the small value of $\theta_{eq}\,(T_C)$, we come to

$$\theta_{eq}\,(T_i) \approx S_0(T_c) - S_0(T_i). \tag{3}$$

Figure 20 illustrates the experiments performed at different T_i within the 1670--1970-K region, as well as for different original values of $S_0(T_C)$ in the 0.25--0.95 interval. It was found that the magnitude of $\theta_{eq}\,(T_i)$ does not depend on the initial relative area of graphene islands. The $\theta_{eq}\,(T_i)$ plot is displayed in Fig. 21, curve 1. The results of θ_{eq} determination by this method and with the use of AES are seen to correlate closely. If we construct the in $\theta_{eq} = f(1/kT)$ plot using experimental data, the result will be a straight line (Fig. 21, curve 2)

$$\theta_{eq} = D \cdot \exp\left(-\frac{\Delta E}{kT}\right) = 2 \cdot 10^5 \exp\left(-\frac{2{,}3eV}{kT}\right). \tag{4}$$

Consider now this relation. Let N_1 be the linear concentration of carbon along the perimeter of the graphene islands. Then for the carbon atom flux from the island into the adsorbed "gas" phase outside the island we obtain

$$\nu_1 = N_1 \cdot W_0 \cdot \frac{1}{2} = \frac{1}{2} N_1 \cdot C \exp\left(-\frac{E_{\text{det}}}{kT}\right), \tag{5}$$

where $W_0 = C \cdot \exp(-E_{\text{det}}/kT)$ is the probability for an edge carbon atom to become detached from the island, C is the prefactor, E_{det} is the binding energy of the edge carbon atom with the island, and the coefficient 1/2 reflects the probability for the carbon atom that has been detached from the island to end up either outside the graphene island or under it. Assuming dynamic equilibrium, for the flux of carbon atoms from the adsorbed "gas" phase outside the graphene islands onto the island we obtain

$$\nu_2 = N_1 \cdot \theta_{eq} \cdot W_{tr} \cdot \frac{1}{4} = \frac{1}{4} N_1 \cdot \theta_{eq} \cdot A \exp\left(-\frac{E_{tr}}{kT}\right), \tag{6}$$

where $W_{tr} = A \exp(--E_{tr}/kT)$ is the probability for a carbon adatom to transfer (or better to say, to be reattached) from the phase of surface "gas" to that of the graphene island, A is the prefactor, and E_{tr} is the binding energy for activation of this transition, and the 1/4 coefficient accounts for possible adatom migration hops in the four equally probable directions.
At equilibrium, $\nu_1 = \nu_2$, and

$$\theta_{eq} = 2 \cdot \frac{C}{A} \cdot \exp\left[-\frac{(E_{\text{det}} - E_{tr})}{kT}\right] \tag{7}$$

Confronting now Eq. (7) with (4), we obtain $E_{det} - E_{tr} = 2.3$ eV, and $(C/A) \sim 10^5$. Equation (7) deserves a careful study because it provides an insight into the actual meaning of the quantities entering it for determination of $\theta_{eq}(T)$. Indeed, knowing the energy of detachment of an edge carbon atom from a graphene island on iridium, $E_{det} = 4.5$ eV (**§** 7), one immediately comes to $E_{tr} = E_{det} - 2.3 = 4.5 - 2.3 = 2.2$ eV. A question arises now as to why we have obtained such a large value of $E_{tr} >> E_M$, where E_M is the activation energy for carbon adatom migration over iridium equal to 0.7 eV [27]. To get an answer to this question, consider Fig. 22. For a newly arrived carbon atom to become incorporated into a graphene island, the edge atom has to transfer from the chemisorbed state I (B) to the physisorbed state II (C) identifying incorporation into the graphene island; said otherwise, this atom has to rupture its bonds to the surface atoms of iridium. In this case, $E_{tr} = 2.2$ eV is the energy which has to be expended to transfer a carbon atom from the state of surface "gas" to its "just" position in the graphene island, while $E_{det} = 4.5$ eV is the energy required to detach an edge carbon atom from an island accompanied by its transition to the "adsorbed gas state" (Fig. 22). The position of a metal-linked edge carbon atom in an island is nothing more than an intermediate state of an adatom in the process of growth or dissolution of graphite islands.
Regrettably, attempts at studying the two-dimensional phase transition in a carbon layer in other Me-graphene systems to the extent this was done for the iridium substrate failed, because the processes involved in carbon dissolution in the bulk of a metal play a substantial role. Nevertheless, for some temperatures it was found possible to derive by AES the concentration of chemisorbed carbon "gas" at which graphene islands start to nucleate on other metals as well (Table 2). We readily see that the carbon concentration depends crucially on the substrate material used; indeed, the highest density has the carbon "gas" on Re(1010), while on Pt(III) AES does not sense the carbon "gas", because its concentration is below the Auger spectrometer sensitivity to carbon.

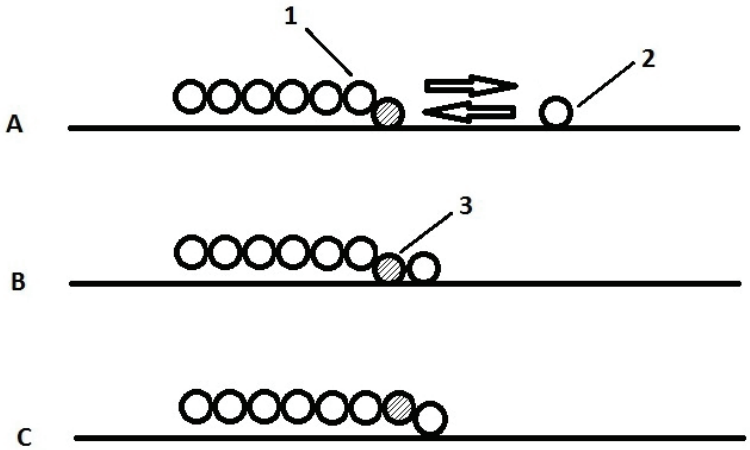

Fig. 22. A model scheme showing graphene island growth on metal surface by attaching a chemisorbed carbon atom form 2D carbon 'gas': 1 – carbon atom in the grapheme island; 2 – chemisorbed carbon atom; 3 – edge carbon atom.

Подложка	Ni (111)	Re(I0-I0)	Pt(III)	Rh(III)	Ir(III)
T, K	1370	1700	1700	1400	1700
at/cm^2	(2÷3) ·10^{14}	2 ·10^{15}	< 5 ·10^{13}	~ 6 ·10^{14}	~ 7 ·10^{13}

Table 2

Chemisorbed carbon "gas" is involved in two extremely essential operations in the adlayer. First, it participates actively in the dissolution and growth of graphene islands. Second, it acts as an intermediate link in the transport of carbon between the surface and the bulk of the metal where carbon atoms are dissolved. If there were no carbon "gas" on the surface, carbon atoms dissolved in the bulk of the metal just could not diffuse over its surface.

High-temperature, high-resolution AES offers a possibility of visualizing the process of the phase transition in the carbon adlayer on iridium. As shown above, this possibility rests on the extremely high sensitivity of the shape of the carbon Auger spectrum to the phase in which adatoms reside on the surface. Figure 23 illustrates the reversible transformation in a heating-cooling cycle of the Auger peak of carbon adsorbed on iridium, which is initiated by the substrate temperature variation in the 1600--1960-K interval. The total carbon concentration on the surface is N_c = 1.2 10^{15} at/cm^2 ($\theta_c \approx 0.3$). At T = 1600 K, virtually all of the carbon on the surface is confined to graphene islands, and the carbon Auger peak approaches the shape characteristic of graphene. At T = 1950 K (θ_{eq} = 0.27), a sizable part of carbon is bound in chemisorbed "gas", and its Auger peak is close to being "carbidic"; there is nothing strange in it, because the activation energy for desorption of a carbon atom from the surface of iridium, which is 6.3 eV (see **§** 7) testifies to strong metal-carbon bonding.

Literature has virtually neglected a relevant problem of paramount importance, namely, the very beginning of nucleation of graphene islands. Indeed, the transition from a single chemisorbed carbon atom to a graphene island should contain an intermediate stage of clustering of two, three and so on carbon atoms together. It appears reasonable to expect

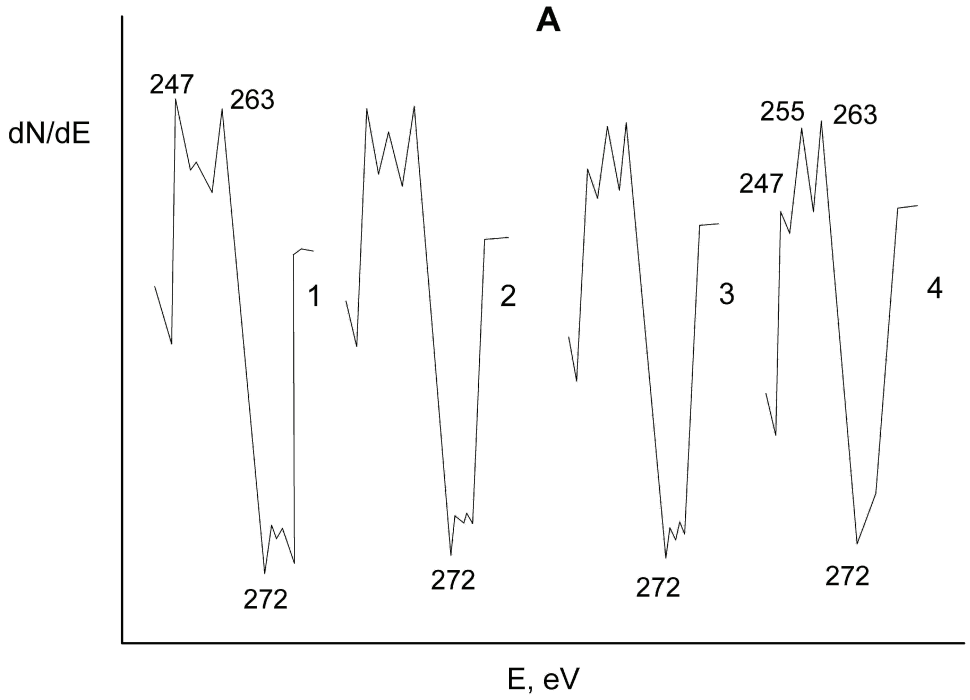

(a)

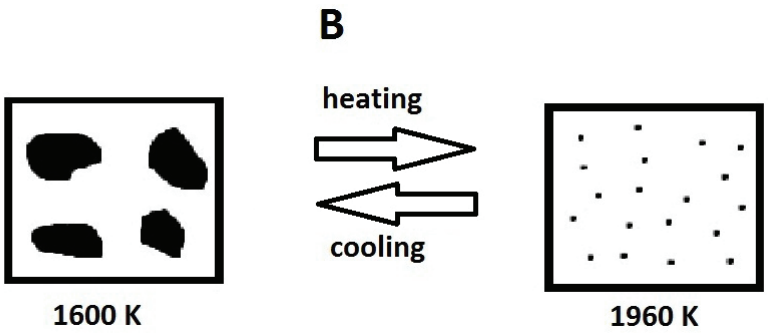

(b)

Fig. 23. Phase transition between grapheme and carbon chemisorbed 2D 'gas' on Ir (111). The total amount of carbon on the surface N_C = 1.2 *10^{15} cm^{-2} is unchanged. A – transformation of carbon KVV Auger spectra with temperature T (K): 1 – 1600; 2 – 1800; 3 – 1850; 4 – 1960. B – a model scheme illustrating the process.

that a cluster will acquire the right to be called a graphene island after it has combined several tens of carbon atoms together. Relevant theoretical calculations do indeed yield for such a cluster a figure of ~50 atoms, of which only its central part will be a proper graphene island [61]. While visualize the process of growth of carbon cluster structures would not be an easy thing to do, that they should exist cannot probably be questioned.

Another, and possibly not less serious, problem is how to deal with the edges of graphene islands, on which the carbon atoms have dangling bonds. It appears reasonable to suggest that edge carbon atoms form strong chemical bonding to the surface atoms of metals. This is suggested by the following observations. First, thermal stability of graphene islands is different and lies in the 900--1600-K interval for various metals (**§** 7); bonding of an edge carbon atom in an island to the metal weakens its coupling to the "parent" island, and it is this that brings about its destruction. To cite just one example, on nickel graphene islands break up already at T ~ 900 K, while the most heat-resistant islands turned out to be those on iridium, with their temperature of destruction being above 1600 K (**§** 7). It is pertinent to note here that a thick (more than 3 layers) graphite film on iridium dissolves at T > 2300 K, because the three edges of the top graphene layer do not bond chemically to the metal, and the binding energy of the edge carbon atom to its parent layer is ~6 eV [27].

Second, intercalated cesium, i.e., cesium located under a graphene island, for instance, on rhenium, desorbs only for T > 2200 K (sic !), because it remains imprisoned under the graphite traps---islands whose edges are coupled to the metal (**§** 7). By contrast, cesium present on the surface of graphene or a metal can be readily removed at T ~ 800 K [62].

The various chemical states of carbon translate into varying patterns of the Auger spectrum of carbon as it is adsorbed, for instance, on iridium at T = 1950 K (Fig. 24). The spectra are seen to change, which reflects the constantly changing carbon redistribution among its different states. For a relative island surface area S_0 = 0.3--0.4, the shape of the carbon Auger

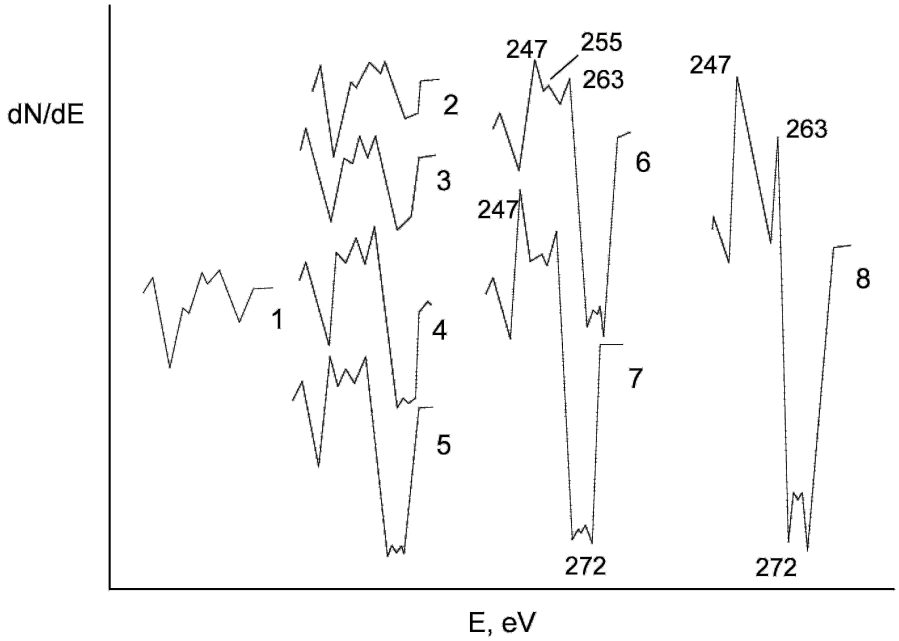

Fig. 24. Carbon KVV Auger spectrum transformation in deposition of atomic carbon on the Ir(111) at 1950 K for various covers of 2D carbon 'gas' θ_C and relative grapene areas S_0 (relative un.):

No	1	2	3	4	5	6	7	8
θ_C	0.12	0.24	0.21	0.27	0.27	0.27	0.27	0.27
S_0	0	0	0	0.11	0.27	0.33	0.43	0.73

All Auger spectra were measured at 1900K.

spectrum is still not pure graphene-like. Even after the temperature has been lowered down to $T \leq 1600$ K, with practically all of the carbon "gas" confined to the islands, the Auger spectrum of carbon will not have the pure graphenic shape, which should be assigned to the graphene island edges being bound chemically to the substrate. In some simpler cases, for instance, with surface carbides of the metal present, the shape of the carbon Auger peak does not change, and only the intensity of the carbon Auger signal undergoes variation.

§ 6. The nature of graphene island coupling to the metal

The central part of the islands is coupled to the metal
by weak van der Waals-type forces,
and the island edges are coupled to the metal.

As already mentioned, graphene films form on many metals and their carbides with strongly different crystal geometries of their surfaces. There is an intriguing point, however: only the crystal geometry of the Ni(III) face coincides perfectly with the structure of graphene layers [56]. We are thus facing a paradoxical situation: formation of a chemisorbed graphene layer on metal surfaces should be an extremely uncommon event. This point was discussed in Ref. [27] where it was suggested that because of the graphene layer being valence saturated, it should be physisorbed on a metal surface, i.e., coupled to it only by the van der Waals forces of polarization nature, without electron exchange, and, hence, should be separated from the surface by a resultant distance characteristic of these forces.

This suggestion is corroborated by our studies of intercalation of graphene layers on a metal with foreign atoms and C_{60} fullerene molecules [41], the situation where adatoms build up spontaneously, and in sizable amounts, under the graphene layer, and, thus, force the layer away from the surface of the metal to a distance comparable with the diameter of the intercalated atoms or molecules. Apart from this, experimental studies of surface migration of Si atoms on Ir(III) revealed that the kinetics of surface diffusion under a graphene layer remains the same as on a pure metal [63].

Graphite is known to have layered structure with a large interplanar distance, $2R_{vdW} = 3.35$ Å, accounted for by van der Waals coupling without electron exchange. Within a layer, carbon atoms are coupled by strong covalent bonding, with the distance between atoms $2R_c = 1.42$ Å. Treated in the context of the ideology developed in Ref. [27], the layered structure of graphite suggests that the graphite layer is valence-saturated. In a graphite crystal, by contrast, each layer is permanently in contact with an identical valence-saturated layer. The situation is radically different with a graphite layer forming on a metal whose surface atoms have many free electrons capable of forming chemical bonding with graphite. If a graphite layer is physisorbed on a metal surface, there is no electron exchange between them, and the layer should evolve in the way it would on the surface of a graphite single crystal, i.e., exist in the form of a "plate" $2R_{vdW} = 3.35$ Å thick (Fig. 25) whose central plane is spaced from the plane passing through the centers of the metal surface atoms of radius R_M by a distance

$$L_{\text{phys.}} = R_{vdW} + R_{\text{M}}. \quad (1)$$

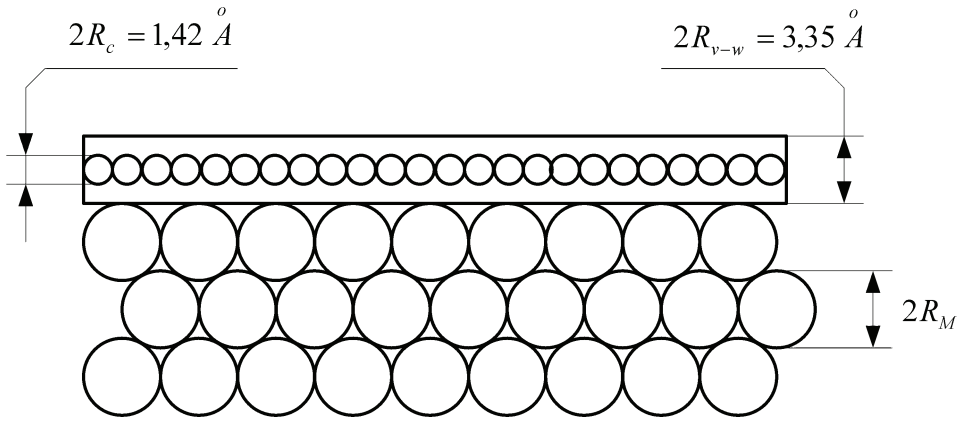

Fig. 25. A model scheme showing the structure of a graphene layer on a metal: R_C - carbon atomic radius, R_m – metal atomic radius, $2R_{VW}$ – interlayer distance in graphite.

In the case of chemisorption, i.e., in the presence of electron exchange, the graphite layer would be pressed to the metal surface, with the distance between the center of carbon atom of radius R_C in the island and that of the surface metal atom

$$L_{\text{chem.}} = R_c + R_M. \tag{2}$$

There are three publications of interest in this respect. The first study [64] used SEELFS (surface-extended energy-loss fine-structure spectroscopy) to investigate the structure of a graphene film on the Ni(III) face whose crystal geometry matches nicely that of graphene. From SEELFS measurements one has succeeded in deriving an essential distance L_{exp} = 2.80 ± 0.08) Å. Significantly, the physical meaning of L_{exp} is, however, not disclosed in the paper. Let us analyze now this quantity following the review of A. Ya. Tontegode [27]. The author of the review estimated and compared the distances involved in chemisorption, L_{chem}, and physisorption, L_{phys}, with the experimental value L_{exp} = 2.80 Å reported in Ref. [64]. The distance L_{chem} was estimated from geometric parameters, with carbon atoms placed into the hollows separating nickel atoms, with due account taken for the known radii R_C = 0.71 Å and R_{Ni} = 1.24 Å [65]. The calculations yielded $L_{chem} \leq 1.6$ Å. For physisorption we have

$$L_{phys.} = R_{vdW} + R_{Ni} = \frac{3{,}35}{2} + 1{,}24 = 2{,}91 \text{ A} \tag{3}$$

Because $L_{exp} \sim L_{phys}$ and considerably larger than L_{chem}, a conclusion was drawn [27] that a graphene layer is physisorbed on nickel. That the Ni--Ni distance in an atomic surface layer is constant, an observation made by LEEDS, likewise argues for the absence of electron exchange between a graphite layer and a metal surface. The physisorptive nature of the graphite-metal coupling is corroborated by another study [6] which shows that the best agreement between the dependences of diffraction intensities on electron energy obtained experimentally and by calculation performed under certain assumptions is reached for a separation of graphene from the nickel surface of 3.4 Å. Strange though as this may seem, the paper that reported this result did not comment on this either.

The third study [66] probed the system consisting of a graphene film on Pt(III) by a LEED method developed to study structures of incommensurate adlayers. The analysis offered three interplanar spacings: L_1 = (3.70 ± 0.05) Å, L_2 = 2.45 Å, and L_3 = 1.25 Å, as well as the metal-carbon bond length L_4 = (2.03 ± 0.07) Å. It was found possible to interpret these results by assuming that sandwiched between the graphite monolayer and platinum there are chemisorbed carbon atoms; indeed, the distance $R_{Pt} + R_C$ = 1.38 + 0.71 Å = 2.09 Å [66], which is close to L_4; L_3 can be identified with the distance between the centers of chemisorbed carbon atoms sitting in the hollows between platinum atoms and the centers of surface Pt atoms. The distance L_2 = 2.45 Å approaches the sum $R_C + R_{vdW} = R_C + R_{vdW} = 0{,}71\overset{\circ}{A} + \frac{3{,}35\overset{\circ}{A}}{2}$ = 2.39 Å, and the distance L = 3.70 Å, equal to the sum ($L_2 + L_3$), is then the separation between the centers of platinum surface atoms and those of carbon atoms in the graphene film. Drawing from these data, A. Ya. Tontegode [27] came to the conclusion that the good agreement between L_2 and the sum $R_C + R_{VdW}$ gives one solid enough grounds to suggest that the graphite-metal bonding is actually physisorptive in character. The conclusion drawn in Ref. [66] assumes this bonding to be rather intermediate in character between "chemisorption" and "physisorption". But if this coupling is indeed of a mixed nature, valence electrons of carbon atoms chemisorbed on platinum should have been able to penetrate into the π electron zone of graphene, with the result that the distance L_2 should be smaller than the sum $R_C + R_{vdW}$.

Obviously enough, the physisorptive character of coupling between the graphene film and the surface of a metal should produce a substantial impact on the various physico-chemical processes occurring in an adlayer, more specifically, segregation of atoms from the bulk of the metal onto the surface, migration-based processes in the adlayer, in the initial stages of growth of carbon films, adsorption-desorption phenomena, and chemical reactions. A physisorbed graphite monolayer, i.e., a graphene film on a metal, may be identified, in a certain sense, with a graphite cell (a two-dimensional graphite "plate"). This novel approach has revealed a new intriguing direction in the investigation of intercalation, namely, study of the relations governing intercalation in the metal-graphene system.

Thus, the above experimental findings suggest the following simplified model representation of the processes evolving in the Me-graphene system (Figs. 26A and 26B).

1. Chemisorbed carbon "gas" increasing the work function of the metal surface by a few tenths of an eV. Carbon atoms of this phase are coupled to the metal by a strong covalent bonding ≥6 eV (**§** 7)---see item 1 in Fig. 26A.
2. Chemisorbed carbon "gas" under the graphene islands [15]---item 2 in Fig. 26A; if present in a high enough concentration, this "gas" distorts the shape of the Auger spectrum of carbon of the graphene films (see, e.g., spectra 3 and 4 in Fig. 9).
3. Graphene island whose central part is coupled to the metal by weak, van der Waals-type forces; this is what makes it possible, for instance, for foreign atoms to penetrate easily under a graphene film---item 3 in Fig. 26A.
4. Edge, non-graphite carbon atoms chemically bound to the metal surface; on iridium, for instance, this energy is ~2.2 eV (**§** 5). Different binding energies coupling edge atoms in an island to different metals account for the strongly different temperatures at which graphene islands break up (**§** 7)---item 4 in Fig. 26A.
5. Carbon atoms dissolved in the bulk of the metal; as a rule, at T > 900--1000 K diffuse easily over the bulk of the metal---item 5 in Fig. 26A.

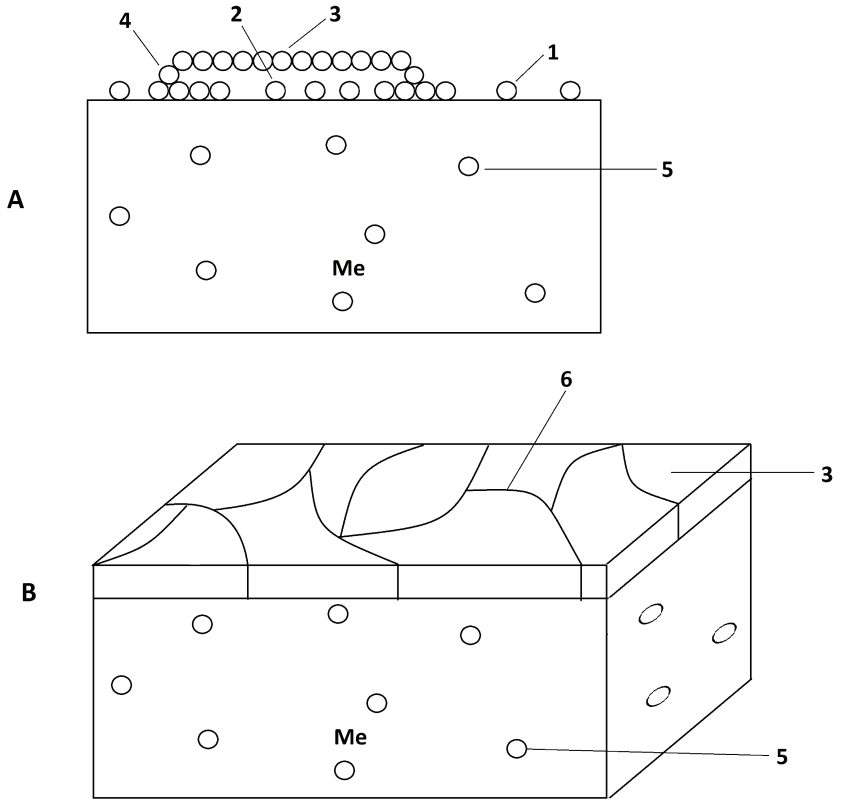

Fig. 26. A model scheme showing the grapheme layer on a metal: 1 – chemisorbed carbon 'gas' upon the metal and under the grapheme layer (2); 3 – carbon atom in the grapheme island; 4 – non-graphitic edge carbon atom; 5 atomic carbon dissolved in the metal bulk; 6 – edges of the merged graphene islands.

Figure 26B displays a model representation of formation of a continuous graphene film from merged islands. It is assumed that the edges of coalesced islands are actually layer defects which are responsible for residual dissociation of CsCl molecules, and that through these defects foreign atoms penetrate under the layer; and it is at the defect edges that nucleation of the second layer of graphene is initiated when carbon atoms segregate onto the surface from the supersaturated Me-C solid solution (**§** 9).

§ 7. Properties of graphene films on metal surfaces

Valence saturation and passivity of graphene
give rise to some intriguing properties.

1. Concentration of graphene islands on iridium

As derived from graphene island oxidation. Oxidation of carbon in its various chemical states on the surface of iridium was studied in considerable detail in Ref. [67]. It was shown that at

300 K only the edges of graphene islands become decorated; in fact, oxygen does not adsorb to the passive surface of the central part of an island. As the temperature increases, the edge atoms of carbon in an island escape from the surface in the form of CO and CO_2. Consider the results obtained in Ref. [67]. At $\theta_c = 0.5$, i.e., at $S_0 = 0.5$, the total concentration of carbon atoms in the islands is $N_c(\text{tot}) = N_{cm}\,\theta_c = 1.8\ 10^{15}$ at/cm^2. One temperature flash produced after a sample with graphite islands has been maintained in an oxygen atmosphere at 300 K removes $N_c(\text{edge}) \approx 1.7\ 10^{14}$ at/cm^2 atoms from the surface. Assuming graphene islands to have a simple, e.g., circular shape of radius R, we come to

$$N_c(tot) = \frac{\pi R^2}{a^2} \cdot f\ , \tag{1}$$

$$N_c(edge) = \frac{2\pi \mathrm{R}}{a} \cdot f\ , \tag{2}$$

where $S \approx a^2$ is the area occupied by a carbon atom with a diameter a, and f is the graphene island concentration on the surface. Solving Eqs. (1) and (2), we obtain

$$f = \frac{N_c^2(edge)}{N_c(\mathrm{tot})4\pi}\ . \tag{3}$$

Substitution of the above experimental data yields an estimate for the island concentration $f \approx 3\ 10^{12}$ cm^2. In the case under consideration, the number of carbon atoms in an island will be ~$7\ 10^2$. Straightforward calculation shows that 13 adsorption-desorption cycles would be required to "consume" such islands with the use of oxygen. This number 13 matches very well with the estimate [67] that 12 ÷ 13 cycles should suffice to clean completely the iridium surface of graphene islands covering an initial relative area $S_0 = 0.5$.

As derived from potassium atom adsorption. The idea underlying the method involves adsorption of potassium atoms at 300 K on an iridium surface with graphite islands to saturation. A temperature flash (Fig. 27) desorbs first potassium atoms from the central part of graphene islands (T_{max} ~ 700 K), followed by desorption from the parts of uncovered metal areas (T_{max} ~ 800 K), and only after that, at comparatively high temperatures, from the edges of graphene islands (T_{max} ~ 1100 K) (for more details, the Reader can be referred to Ref. [62]). The adsorption capacity of phase "2" in Fig. 27 associated with decoration of graphene island edges by potassium atoms depends on the area of graphene islands. Figure 28 displays in graphical form the dependence of the maximum filling of this phase by potassium atoms on the relative area occupied by the graphene islands. Assuming in a first approximation the maximum concentration of potassium atoms along the island periphery to be equal to the concentration of edge carbon atoms, one may safely use Eq. (3) to estimate f. It turned out that $f \approx 3*10^{11}$ cm^{-2} for $S_0 = 0.4$--0.6. As the relative island area increases, f decreases. Indeed, for $S_0 = 0.8$ we obtain $f \approx 1\ 10^{10}$ cm^{-2}, which should probably be assigned to coalescence of the islands setting in as their relative area becomes large enough.

Experiments revealed that the concentration of graphene islands on iridium does not depend on the intensity of the carbon atom flux striking the surface. This suggests that the nucleation is not homogeneous. There are firm grounds to believe that graphene islands nucleate at defects in the iridium substrate, e.g., at the edges of atomic steps.

Thus estimation of the concentration of graphene islands on iridium for the case of the islands occupying a relatively small part of the total surface area yields $f \approx 10^{11}$ --10^{12} cm^{-2}.

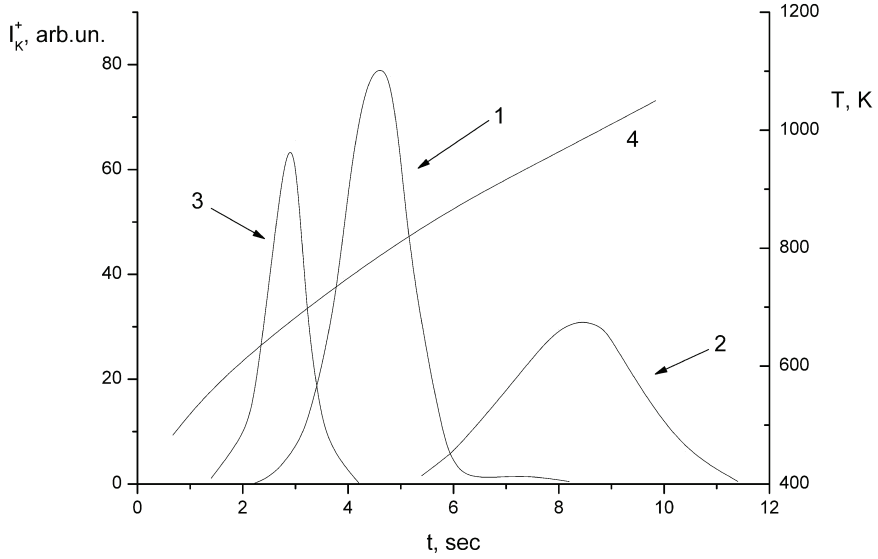

Fig. 27. Thermal desorption spectra for K+ ions from Ir(111) (1); from Ir covered with graphene islands at S_0 = 0.5 (2), and from grapheme (3). the substrate was pre-exposed to atomic K with the flux ν_K = 2.8 *10^9 $cm^{-2}*s^{-1}$ for 30 sec. 4 – temperature versus time dependence.

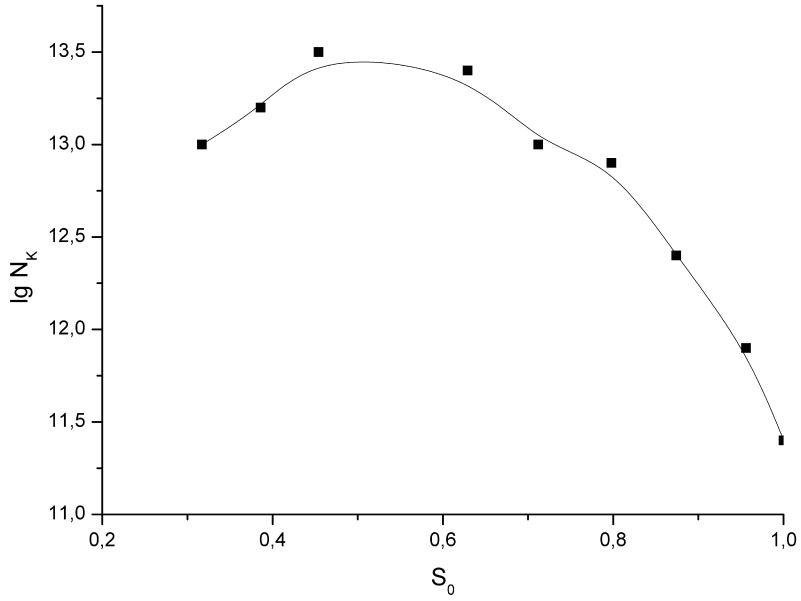

Fig. 28. The maximal concentration of the atomic K on the periphery of the graphite islands as function of relative grapheme area on Ir(111). the temperature of K adsorption is 960 K, ν_K = 1 *10^{12} $cm^{-2}*s^{-1}$, exposition time is 10 min for each point.

2. Specific features of exchange and catalytic reactions on graphene

The activity of catalysts in heterogeneous reactions involved in dissociation of molecules is intimately related with the valence state of atoms in the surface layer of a metal. In the representation adopted in Refs. [27], in order for an adsorbed molecule on the surface of a solid to be capable of dissociating, the atoms making up the molecule should bond to the atoms of the surface catalyst, which reduces the dissociation energy and increases the reaction rate. While the dissociation energy of a CsCl molecule, for instance, is E_v = 4.56 eV in free space, on the surface of metals (Ir, W, Re and others) it decreases strongly down to E_v < 0.3 eV [27].

The surface of a clean metal has a large number of valence bonds, which makes metals efficient catalysts in dissociation reactions. One may expect the efficiency of such reactions to drop markedly (catalyst poisoning) when an adsorbate film of an element of Subgroup IV÷VIIb of the Periodic System forms on the metal surface [27].

Indeed, heterogeneous catalytic reactions of dissociation of As, Sb, P, Se, Te films were found to exhibit poisoning [68].

Deposition of carbon on the metal surface is a widely recognized process. There were reports of the poisoning effect a carbon film produces in a catalytic reaction of ammonium decomposition on platinum [69, 70], as well as on other metals (Ni, Rh, Ta, W) [70], when carbon is adsorbed in large amounts.

While the poisoning effect of carbon was pointed out in many publications, nevertheless, a systematic study of the effect exerted by controllable amounts of carbon on metal surfaces on the efficiency of heterogeneous reactions of dissociation of a number of salt molecules did not appear until a series of publications [50,71,72], as well as of reviews [27]. An approach most widely used in the above studies involves application of surface ionization (SI) techniques to probe one of the dissociation products of MX molecules. SI of a MX molecule proceeds in two stages:

1. Catalytic dissociation of the molecule, MX → M + X;
2. Ionization of the metal atom M → M^+ + *e*.

(Here M stands for the atom of the metal, and X, for that of a halogen).

The easily measurable current of the M^+ ions (with the mass spectrometric technique employed) provides information on the process of catalytic dissociation of MX molecules on the surface. The above publications made use of the degree of dissociation ω as a quantitative characteristic of the catalyst (metal) activity:

$$\omega = \frac{\nu_{MX} - \nu'_{MX}}{\nu_{MX}}, \tag{4}$$

where ν_{MX} is the flux density of MX molecules striking the substrate surface, ν'_{MX} is the density of the desorbing molecule flux, and (ν_{MX} --ν'_{MX}) is the fraction of the flux of molecules that has dissociated on the surface. It is assumed that the experimental conditions are stationary, with the flux of molecules incident on the surface equal to that desorbing from it, and no elastic scattering of molecules from the surface present, the points borne out in a special experiment [72].

The role played by the two carbon phases on iridium surface in dissociation of CsCl molecules was studied in Ref. [51]. It was demonstrated that carbon present in the phase of two-dimensional chemisorbed "gas" does not affect in any way the efficiency of the CsCl dissociation reaction, and that ω = 1 just as in the case of clean iridium. Carbon present in

the phase of two-dimensional graphene islands reduced drastically the efficiency of CsCl dissociation, the degree of dissociation decreasing after formation of a graphene film down to $\omega = 10^{-3}$ (at $T = 1700$ K) or $\omega = 10^{-5}$ (at $T = 900$ K). That it was the poisoning action of the graphene phase of carbon on the CsCl dissociation reaction was corroborated by studies of both with carbon layers on other substrates---Rh [27], Pt [73], Pd [74], Re [74], and with other salts---KNO_3, KCl, K_2SO_4, RbCl, HCOOK [27].

The virtually total suppression of dissociation of CsCl molecules on graphene islands, combined with their complete dissociation on surface areas of either a clean metal or a metal containing chemisorbed carbon "gas" suggested a simple method of determining the relative area of two-dimensional graphene islands by measuring the current of Cs^+ ions produced in SI of one of the dissociation products, namely, Cs atoms (**§** 2).

TDS, AES, and LEED were applied to probe the role played by the carbide and graphene carbon phases in the breakup of molecules of the HCOOH and DCOOH formic acid [75]. The carbon was deposited on the surface by exposing heated nickel to C_2H_4 vapor. It was found that exposure to C_2H_4 vapor at $P_{C2H4} \sim 10^{-7}$ Torr and $T = 525$ K produced surface nickel carbide with the (2 x 1)C structure as revealed by LEEDS, and at $T = 600$ K, the (4 x 5)C surface carbide. The concentration of surface carbon was estimated as $\sim 9\ 10^{14}$ at/cm^2, a figure fairly close to that of surface nickel atoms on (110). It was demonstrated that surface carbide did not poison the catalyst; indeed, HCOOH (or DCOOH) molecules dissociated, which was inferred from the release of the various reaction products: H_2, CO_2, CO and H_2O. By contrast, formation of graphene on nickel in C_2H_4 vapor at $T \sim 800$ K reduced dramatically the probability of dissociation of HCOOH molecules, which implies poisoning of the catalyst.

The part played by the same, carbide and graphite, phases of carbon on Ni(100) in the kinetics of hydrogenation of CO ($CO + 3H_2 \rightarrow CH_4 + H_2O$) was studied in Ref. [76]. It was found that carbon is produced at $T = 600$ K in the surface carbide phase in the $2CO \rightarrow CO_2 + C$ reaction, and that it plays a major role in the reaction involved in methane formation. The carbide-contained carbon is chemically active and could be readily removed from the sample by heating it up to 700 K in a hydrogen atmosphere ($P_{H2} \sim 100$ Torr). Surface graphite was produced by exposing nickel heated to 700 K to a CO atmosphere (($P_{CO} \sim 24$ Torr). The graphite film completely poisoned the catalyst, with the methane production reaction becoming suppressed.

One studied also [77] hydrogenation of CO on Fe(110) which contained carbon deposits of different origin, among them a CH_x phase, carbon-hydrogen carbide phase, and graphite phases differing in the content of intercalated hydrogen. It was found that the CH_x and carbide-carbon phases participated actively in hydrogenation. The graphite phase suppressed the hydrogenation process completely.

An interesting analysis reported in Ref. [78] provided an explanation for the observation that palladium membranes used to prepare chemically pure hydrogen lost their hydrogen permeability after carbonization. Penetration of hydrogen through a membrane involves the stage of H_2 dissociation at the front face of the palladium membrane, followed by dissolution of H atoms in the bulk of the metal, after which the H atoms associate on the rear side of the membrane, to be desorbed in the form of H_2 molecules. It appeared only reasonable to suggest [72] that suppression of hydrogen permeability of the palladium membrane is initiated by termination of the dissociation of H_2 molecules at the front side of the membrane, when it becomes coated by a valence-saturated graphite film.

As pointed out in the review article [27] and suggested by the results of the above studies, it is only in the form of graphite that carbon poisons the metal catalysts used in dissociation-based catalysis.

The graphene surface on metals turned out a convenient substrate for studying exchange chemical reactions. The Ir-graphene system appears to be a particularly suitable combination, because the properties of graphene on iridium are both well studied and readily controllable.

Interaction among particles of different origin on the surface of solids has become a subject of considerable interest. These studies, besides being very instrumental in development of the theory of elementary processes on the surface, pave a way to emerging applications. It is known, for instance, that deposition of a small amount of an alkali metal onto the surface of metal catalysts enhances considerably the yield of products of molecule dissociation.

The favorable effect of atoms of alkali elements adsorbed on metals is attributed to the change in elementary properties the adsorbed molecules undergo when close to alkali atoms [ ].

For adsorbents with a passive surface, the corresponding aspects have been studied to a considerably lesser extent, although substrates used intensively in heterogeneous catalysis are passive toward dissociation of molecules. The first observation of the substitution reaction K + RbCl → KCl + Rb taking place on the carbonized surface of the Pt + 8%W under combined adsorption of K and RbCl molecules was announced in Ref. [79]. The exchange reaction initiated by combined adsorption of CsCl and Na on the same surface and the kinetics of this process were described in Ref. [80].

The results reported in [79,80] are complicated by superposition on the substitution reactions of a quite pronounced intrinsic dissociation of CsCl or RbCl molecules on the heavily defected alloy surface coated by a carbon film.

A study was made of the role played by the properties of an alkali metal (Na, Li and K), as well as of atoms in different valence states (Ba, Tm, Pt) in the reaction with CsCl molecules on the surface of graphene on iridium (Ir-C) [81--84]. Carbon in the graphene layer does not react chemically with atoms of alkali metals and molecules of alkali halide salts. It can be added than within the operating temperature range background dissociation of CsCl molecules on graphene is low ($\omega \approx 10^{-5}$).

The interaction of CsCl molecules with Ir-C was studied in considerable detail [27]; it was shown that the molecules do not scatter elastically from Ir-C [72]. Cs atoms released in exchange reactions of dissociation are detected by the surface ionization technique with the highest possible sensitivity; indeed, virtually each Cs atom desorbing thermally from Ir-C becomes ionized [39]. This offers a possibility of studying elementary events of interaction at low coverages of the adsorbent by reagents.

In the above studies, the surface was bombarded by stationary fluxes of particles of a variety of compositions, and from the surface desorbed fluxes of reacted and unreacted particles. The total number of atoms in the incident fluxes is equal to their total number in the desorbing fluxes. Significantly, at a constant T the coverage by each species of particles is constant. The surface is hit by fluxes of molecules, ν_{CsCl}, and atoms, ν_z, where z stands for K, Na, Li etc. Part of the particles can desorb in the neutral and charged states (ν'_{CsCl}, ν'_z, ν'_{z+}). Chemical interaction among the particles may bring about either catalytic dissociation of CsCl molecules at active z centers

$$CsCl + z \leftrightarrow Cs + Cl + z, \quad (5)$$

or a substitution reaction

$$CsCl + z \leftrightarrow zCl + Cs. \quad (6)$$

For direct determination of reaction type on the surface, introduce a characteristic κ which is actually the coefficient of utilization of z atoms:

$$\kappa = \frac{\nu'_{Cs^+}(T)}{\nu_z} \ . \quad (7)$$

In the reaction of type (5), the active z centers are not expended , so that $\kappa_{max} = 1$. In the case of z atoms in the valence state m, the limiting value of κ will be $\kappa_{max} = m$, because mCsCl + z ↔ zCl_m+ mCs. Thus, to determine the type of the reaction, one has to measure the ν'_{CsCl} and ν'_z, ν_z fluxes.

To study the reaction kinetics and compare the efficiencies of the reactions between CsCl molecules and z atoms, introduce the efficiency of interaction η

$$\eta(T) = \frac{\nu_{CsCl} - \nu'_{CsCl}(T)}{\nu_{CsCl}} = \frac{\nu'_{Cs^+}(T)}{\nu_{CsCl}} \ , \quad (8)$$

η(T) defines the fraction of the molecules taking part in the reaction. The quantities η(T, ν_z, ν_{MX}) are calculated theoretically [85], so that the parameters of exchange interaction can be derived from η(T) relations for the given ν_z and ν_{MX}.

Studies of reactions within a broad interval of substrate temperatures and a wide range of fluxes of interacting particles revealed that the Z atoms and CsCl molecules adsorbed on a graphene layer on iridium are involved in an exchange reaction; in the case of Na, K, and Li it is one-stage with $\kappa_{max} = 1$, for Ba it is two-stage with $\kappa_{max} = 2$, and for Tm, a three-stage one with $\kappa_{max} = 3$ (Tm is in this case in the highest possible valence state of 3). Experiments with all alkali metals were conducted in not very different conditions:

Reaction	T, K	ν_{CsCl}, $sm^{-2} \cdot s^{-1}$	ν_z, $sm^{-2} \cdot s^{-1}$
K + CsCl	760 – 1050	$5 \cdot 10^{11}$ – $4 \cdot 10^{13}$	$1 \cdot 10^{10}$ – $2 \cdot 10^{13}$
Li + CsCl	800 – 1000	$3 \cdot 10^{11}$ – $2 \cdot 10^{13}$	$1 \cdot 10^{11}$ – $5 \cdot 10^{12}$
Na + CsCl	750 – 950	$5{,}3 \cdot 10^{11}$ – $3{,}4 \cdot 10^{13}$	$3 \cdot 10^{10}$ – $9 \cdot 10^{12}$

Table 3

Experimental studies permitted one to obtain log η(T) and κ(T) relations for different fluxes of atoms and molecules incident on the surface. Figure 29 plots typical log η(T) and κ(T) graphs for the case of potassium atoms. The growth of η observed to occur with decreasing T is initiated by the increase of particle concentration on the surface and of the migration path lengths during their lifetime in adsorbed state (the fluxes striking the surface are constant).

The kinetics of the exchange reaction was considered in terms of the model describing formation of activated MXZ complexes in encounters of adsorbed particles migrating over the surface, and subsequent breakup of these complexes

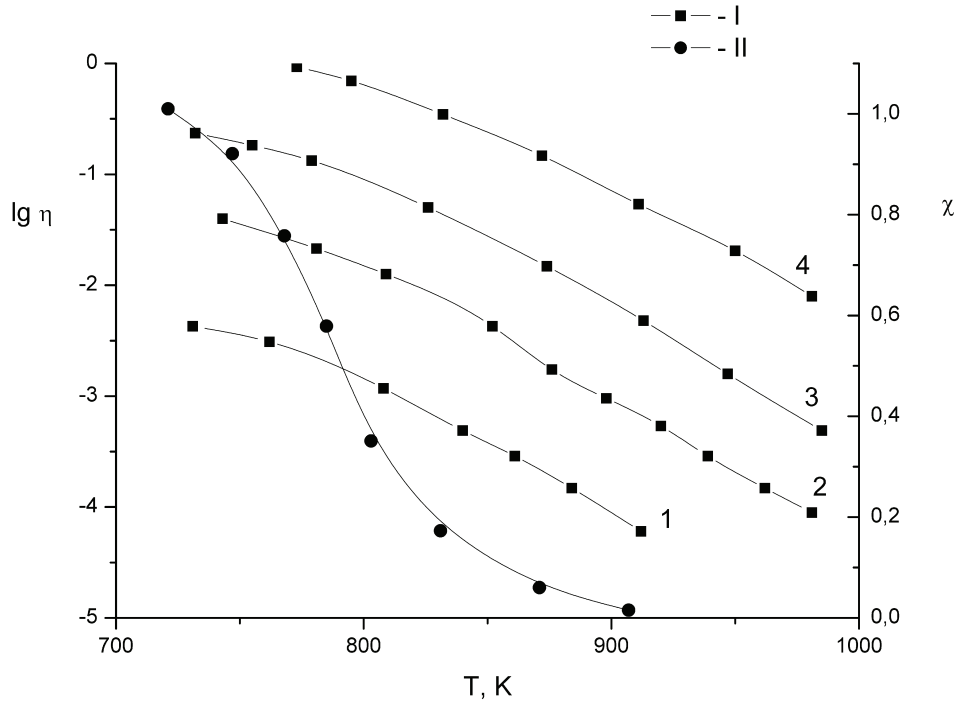

Fig. 29. The dependencies of lgη (I) and η (II) for the reaction K + CsCl. The fluxes were ν_{CsCl} = 3.2 *10^{12} $cm^{-2}*s^{-1}$ and ν_K ($cm^{-2}*s^{-1}$): 1 – 1.3 *10^{10}: 2 - 1.4 *10^{11}; 3 – 7.5 *10^{11}; 4 - 8 *10^{12}. Dots show experimental data, solid lines are calculated.

$$MX + Z \xrightarrow{K_1^a} MZX \begin{array}{l} \xrightarrow{K_1^g} M + ZX \xrightarrow{K_1^a} MXZ \\ \xrightarrow{K_2^g} MX + Z \end{array}, \qquad (9)$$

where k_1^a and k_2^a are the rate constants for association of particles into an activated complex MXZ, and k_1^g and k_2^g, those for its dissociation over all possible channels.

One succeeded in deriving analytical expressions for the reaction efficiencies that account for the experimental results obtained [81]. The observed increase in the efficiency of the reactions between Li, Na, K atoms and CsCl molecules in the Li → Na → K sequence matches with the model of local interaction between alkali metal atoms and MX molecules, which provides a reasonable description for the promoting effect alkali metals exhibit in heterogeneous catalytic reactions [81].

We note that the phase state of particles on the surface is essential not only for the kinetics of the reactions proceeding on the surface but for the character of the reaction itself. For instance, in the case of two-dimensional barium islands it was found that the reaction with CsCl molecules involves edge barium atoms only; interestingly, in some temperature regimes one observes not an exchange catalytic reaction but rather catalytic dissociation of CsCl molecules, with the magnitude of κ becoming as large as a few hundred [84]. By properly applying "chemical surface ionization" on passive surfaces with the use of

exchange reactions, one can increase the sensitivity of surface-ionization detection of atoms of a variety of elements. A major requirement is that these atoms are chemisorbed rather than physisorbed on the passive surface of graphene.

3. Thermionic properties of graphene films

It appears only natural to expect that studies of thermal emission from graphene films should reveal the specific characteristics of the metal, which would become manifest, for instance, in the work function of graphene. The work function of graphene films on metals was derived from thermionic emission both by the total current technique and from Richardson graphs [60], as well as by probing the surface with a beam of K, Na, Ba, In atoms [39]. The ribbon temperature was chosen such that its decrease would not initiate growth of the second layer of graphene through segregation of carbon from the bulk of the metal. The results obtained are summarized in Table 4. On all substrates, the graphene surface was uniform in work function. $Re(10\bar{1}0)$

Substrate	Ir(111)	Pt(111)	Rh(111)	$Re(10\bar{1}0)$
ΔT, K	1800÷1200	1500÷1200	1300÷1150	1700÷1150
(φ ± 0,05) eV	4,45	4,55	4,35	4,25

Table 4.

Apart from this, for the Rh-graphene and Re-graphene systems one determined the work function by measuring the total thermionic current from graphene islands as a function of their relative area S_0, which was derived by the well-known method involving probing the surface with a flux of CsCl molecules (§ 2). As expected, the work function of islands remained constant with variation of their area from $S_0 = 0.1$ to $S_0 = 1$ (monolayer coverage).
Interestingly, the work function of graphene on a metal is affected by atoms of alkali and alkaline-earth metals buried under the graphene film in intercalated state. Indeed, a monolayer of K or Cs adatoms confined under a graphene film on Ir(111) reduces the graphene work function by $\Delta\varphi \approx 0.3$--0.4 eV; by contrast, the same amount of K or Cs on the surface of graphene lowers the work function by $\Delta\varphi \approx 2.0$--2.5 eV. A barium monolayer buried under graphene reduces the work function by $\Delta\varphi \approx 0.65$ eV.

4. Thermal stability of graphene films

It appears only natural to expect that as the temperature is increased, graphene islands that formed on a metal surface at T will start to break up eventually at some higher temperature $T_d > T$. Experiments showed that for the four metals studied (Re, Ir, Ni, Pt) the temperature interval within which the graphene islands break up, ΔT_d, lies substantially lower than the temperature of mechanical disintegration of the substrate or of the onset of noticeable desorption T_{des} of carbon atoms from the surface of refractory metals (usually, $T_{des} \geq 2000$ K). On platinum, nickel and rhenium breakup of graphene islands brings about a decrease of the total amount of carbon on the surface. This should apparently be attributed to dissolution of the carbon atoms that have broken off the edge of a graphene island in the bulk of the metal. The only exclusion is iridium, in which carbon practically does not dissolve for $T \leq 200$ K, with the carbon material produced in the breakup of islands persisting on the surface in the form of chemisorbed carbon "gas" [41].

We believe that the elementary event involved in the breakup of a graphene island consists in detachment of a single carbon atom from the edge of this island, followed by its transition to the chemisorbed state on the metal surface. Simplifying the real pattern, we are going to assume that the graphene islands are disc-shaped and have equal areas S_1. Then the number n_1 of carbon atoms confined to a single island will decrease with time with the temperature increasing up to $T > T_d$ by the law

$$-\frac{dn_1(t)}{dt} = n_b(t) * W = n_b(t)C\exp\left[-E_{\text{det}} / kT\right], \tag{10}$$

where $n_b(t)$ is the number of carbon atoms in the boundary layer of the island at time t, W is the probability of two-dimensional sublimation, C is the prefactor, and E_{det} is the activation energy for two-dimensional sublimation, or, said otherwise, the energy required to detach an edge carbon atom from the island.

We also assume for the sake of simplicity that the packing of carbon atoms in an island does not differ from that in the basal plane of graphite and that it is independent of the island size, in which case $S_1 \approx an_1$, where a is the area per one carbon atom. Assuming further that $n_b = 2\pi r/d$, where r is the radius of the disc-shaped carbon island, and d is the effective carbon-atom diameter in the graphene lattice, $d = \sqrt{4a/\pi}$, and taking into account that

$$r = \sqrt{\frac{n_1 a}{\pi}} = \sqrt{\frac{aN}{\pi m}},$$

where N is the total number of carbon atoms in all islands per 1 cm², and m is the island concentration, we come to

$$n_b = \frac{\pi}{\sqrt{m}}\sqrt{N(t)}\,.$$

Now we use Eq. (10) to obtain

$$\frac{dN}{\sqrt{N}} = -\pi\sqrt{m}C\exp\left[-E_{\text{det}} / kT\right]dt\,. \tag{11}$$

Equation (11) can be solved for an arbitrary t subject to the initial condition that at $t = 0$, $N = N_0$

$$1 - \sqrt{\frac{N}{N_0}} = -\frac{\pi\sqrt{m}C\exp\left[-\dfrac{E_{\text{det}}}{kT}\right]}{2\sqrt{N_0}} \cdot t\,. \tag{12}$$

The ratio $N/N_0 = S(t)/S_0$, where S_0 is the area occupied by islands at $t = 0$, is found experimentally by the CsCl dissociation method described above. Having now a set of relations $\left(1 - \sqrt{S(t)/S_0}\right) = f(t)$, one can find from the $\log t = f(1/kT)$ equation the energy required to detach a carbon atom from a graphene island for each value S = const. Now knowing E_{det}, one readily derives from Eq. (12) the value of $\sqrt{mC}$.

As an illustrative case, consider the process of breakup of graphene islands on Re(10-10). A clean rhenium sample was exposed for a short time (t ~ 10--30 s) to benzene vapor (P_{C6H6} ~ 1 10^{-7} Torr) at T = 1050 K. This initiated fast formation of graphene islands on the surface,

while the bulk of the metal remained practically free of carbon. Experiments demonstrated that carbon resides at this temperature on the surface in graphene islands only, because single carbon atoms dissolve rapidly in the bulk of the metal [41]. Nevertheless, to make the experiment as pure as possible, the sample was annealed for several minutes at T = 1050 K after the benzene had been pumped off; in this process, the island did not break up, and the small amount of carbon that could build up in the near-surface region was dispersed throughout the volume of the metal, thus reducing the probability of segregation of carbon from the bulk back onto the surface. After this, the rhenium temperature was raised to $T_d \geq$ 1200 K and one measured the kinetics of island breakup, i.e., determined the $S/S_0 = f(t)$ relation. The islands broke up completely (Fig. 30). Note that the breakup curves reproduced well enough from one experiment to another although the volume of the sample was not freed from the carbon that had accumulated there. This suggests that at the temperatures ΔT chosen the carbon concentration in the bulk of rhenium is far from the solubility limit, carbon diffuses freely over the metal lattice, and the reverse flux of carbon from the bulk onto the surface may be neglected.

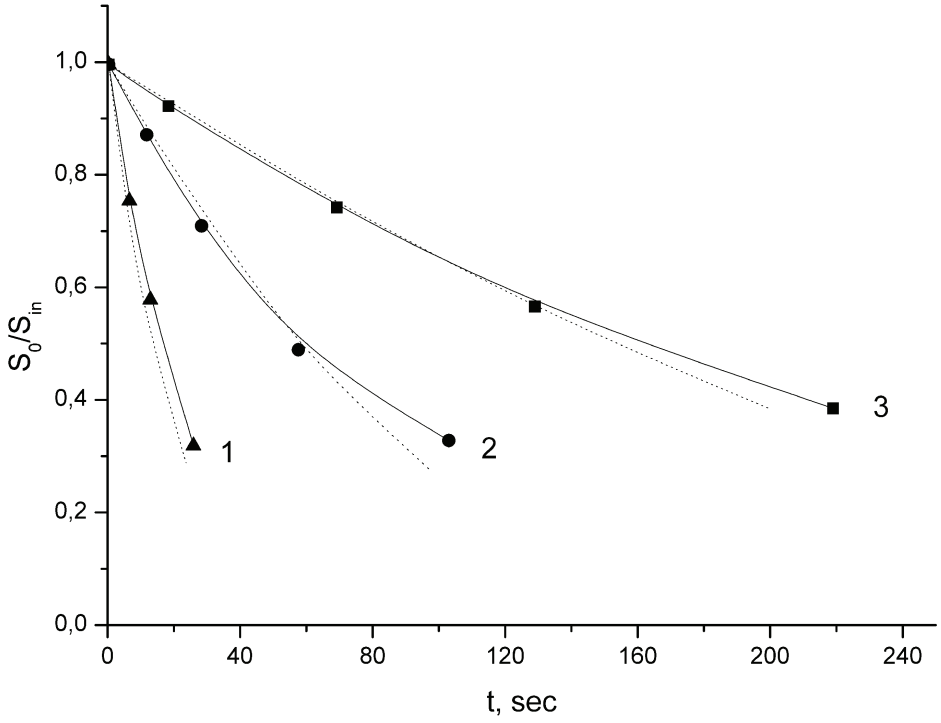

Fig. 30. Equilibrium relative areas of grapheme islands versus annealing time at Re surface at annealing temperatures (K): 1 – 1280; 2 – 1240; 3 – 1215. The value $S_0 / S_{in} = 1$ corresponds to the initial area of grapheme islands S_{in} = 30%. Dots show experimental data, solid lines are calculated.

The experimental data were treated in the following way. The curves of Fig. 30 were used to construct log $t = f(1/kT)$ curves for different S = const, whence one could derive the carbon

detachment energy from the island, E_{det} = (3.0 ± 0.2) eV. We note that S/S_{tot} varied in the experiments within the 0.2--0.6-interval, and S/S_{tot} = 1 correspond to a graphene film with N_c = 3.56 10^{15} cm^{-2}. Next one constructed the graph

$$S(t) / S_0 = \left(1 - Bt\right)^2 ,$$

where

$$B = \frac{\pi\sqrt{m}C\exp\left[-E_{\det} / kT\right]}{2\sqrt{N_0}} . \tag{13}$$

The value of B was chosen so as to fit the calculated $S/S_0 = f(t)$ relations to experiment (dotted line in Fig. 30). The knowledge of B permitted one now to find from Eq. (13) the product of the prefactor by the root of the number of islands $\sqrt{m}C$ = 3 10^{18} $cm^{-1}s^{-1}$. Our studies of the topography of the graphene film on Re(10-10) made by scanning tunneling microscopy permitted estimation of the concentration of graphene islands at close to monolayer coverages, which turned out to be $m \sim 10^{12}$ cm^{-2} [86]. Knowing m, one can readily estimate $C \sim 10^{12}$ s^{-1}.

In a similar way we studied the breakup of graphene islands on Ni(111) and Pt(111). The only difference consisted in the temperature interval ΔT_d within which the islands broke up. The results of the experiments are summed up in Table 5. The values of $\sqrt{m}C$ thus obtained were found to be of the same order of magnitude as those derived for the rhenium sample.

Me	$E_{\det}$, eV	ΔT_d, K
(111)Ni	2.5	950–1050
(1010)Re	3.0	1200–1300
(111)Pt	3.2	1300–1400
(111)Ir	4.5	1650–1850

Table 5

Graphene islands on iridium start to break up at $T_d \geq 1600$ K, which suggests a substantially stronger binding energy of the edge carbon atom to the island compared with the substrates considered earlier. Because the carbon atoms that have detached from the island do not dissolve in the bulk of iridium and do not desorb, the total carbon concentration on the surface does not change, so that as the area of the graphene islands decreases as a result of their thermal destruction, the concentration of carbon atoms in the chemisorbed carbon "gas" phase grows. This, in its turn, gives rise to an increase of the flux of carbon atoms from the chemisorbed "gas" phase to graphene islands. Therefore destruction at a given T_d = const culminates in the onset of dynamic equilibrium, in which the flux produced in two-dimensional sublimation becomes equal to that of carbon deposited on the islands from the chemisorbed "gas" phase. After this, the island area will no more change (Fig. 31) staying at a certain level depending on T_d. If we reduce the temperature to $T < 1600$ K, the island area recovers to the former level $S = S_0$, with all of the carbon "gas" transferring again to the graphene islands. To be able to neglect the reverse flux of carbon from the chemisorbed "gas" phase, only the very beginning of the $S/S_0 = f(t)$ curves was taken into account. The results of these experiments are also listed in Table 5.

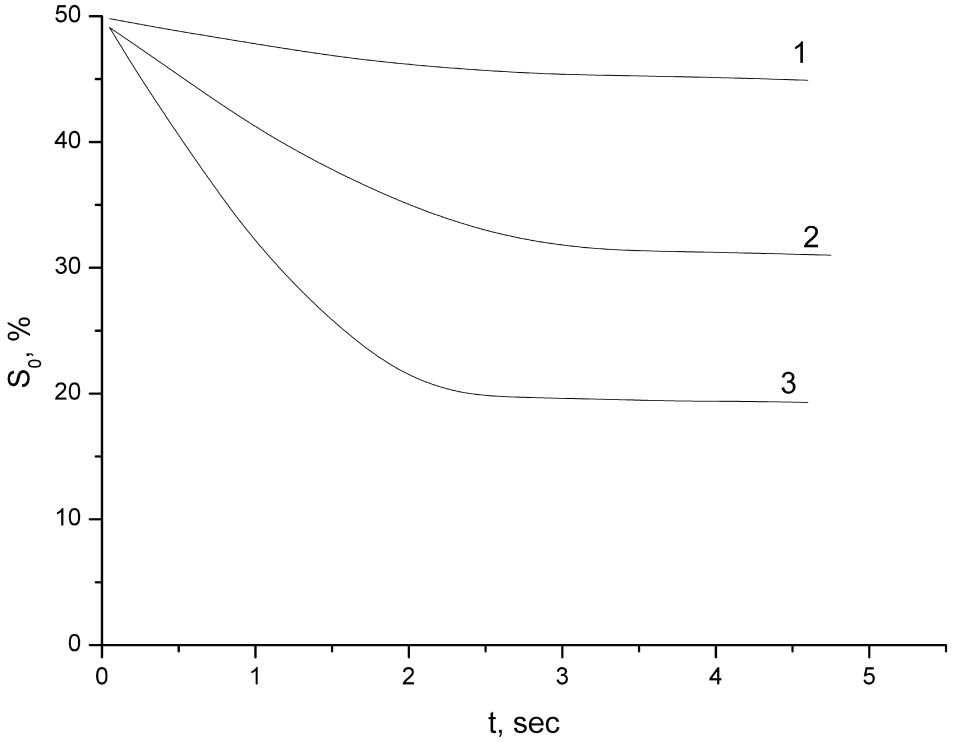

Fig. 31. The dependence of relative graphene island area on Ir versus annealing time at various T, K: 1 - 1715; 2 - 1840; 3 - 1940.

As seen from the table, in contrast to bulk graphite, for which the detachment energy of an edge carbon atom in a layer is ~6 eV (T_d > 2300 K) [27], in the case of graphene islands adsorbed on metallic surfaces the detachment energy can be markedly lower. It appears reasonable to assume that the valence-active edges of graphite islands form strong chemisorption bonding with atoms of the metallic substrate, which weakens the C--C bonds of an edge carbon atom to neighboring atoms and weakens strongly, in its turn, the destruction temperature of graphene islands on a metal (see Table 5). Experiments show that the easiest to destroy are graphene islands on nickel; this correlates with the observation the nickel, of all the substrates studied, is the only carbide-forming metal. The most thermally stable turned out to be graphene islands on iridium; iridium does not form carbides, practically does not dissolve carbon in its bulk, and, apparently, is the least capable of forming C-Me chemical bonds. Interestingly, if one forms, for instance, on Ir(111) a graphite film a few atomic layers thick by deposition from an atomic flux at $T \approx 1700$ K (Fig. 32), the temperature at which a graphite layer breaks up and, accordingly, carbon escapes from the surface, grows to T_d > 2300 K, which corresponds to E_{det} ~ 6 eV, a value identified with thermal destruction of bulk graphite. Indeed, in this case no edge atom of the top graphite layer can contact the metal and, hence, there are no grounds to expect that active C-Me chemisorption bonds will reduce the activation energy for detachment of an edge atom from the graphite island.

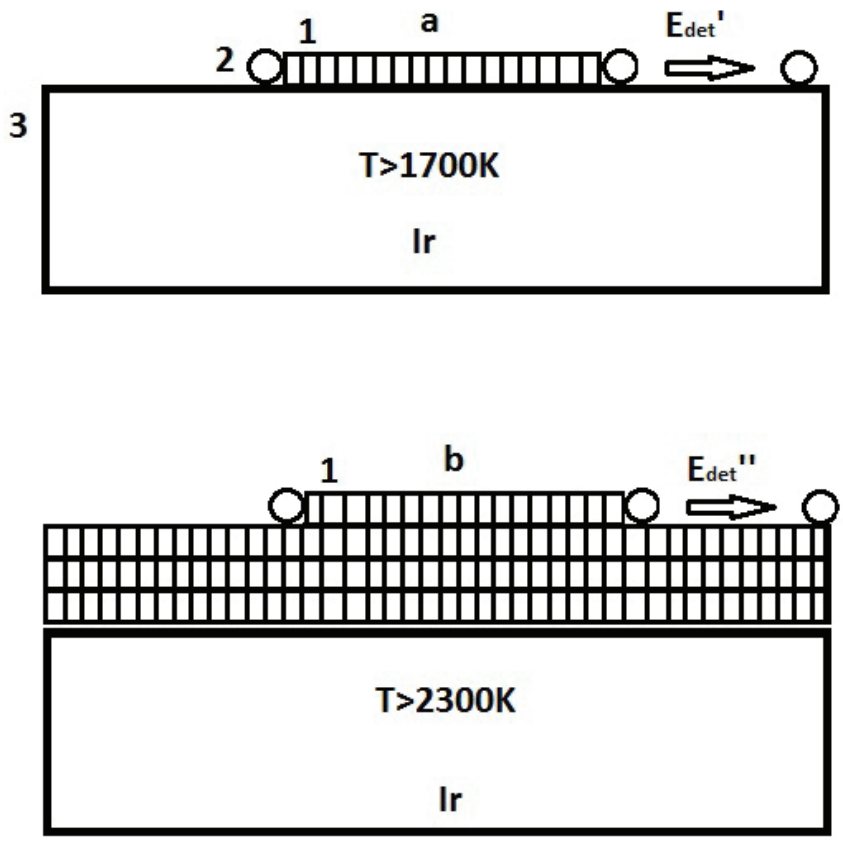

Fig. 32. Schematic representation of atomic carbon interaction with a graphene island on metal surface (a) and on graphite (b). 1 – graphene; 2 – atomic carbon; 3 – substrate.

It appears pertinent to point out here the following significant aspect. The above results relate to the case of the bulk of the metal being practically free of carbon. As carbon is dissolving in the bulk of the metal, the flux of carbon atoms segregating onto the surface increases. This flux enhances noticeably the thermal "lifetime" of the island. To cite an example, on Rh(111) graphene islands start to break up at $T \geq 1000$ K, with the bulk free of carbon. On carbonization of Rh at $T_C = 1800$ K, however, one obtains a continuous graphene film, which persists at such high T assisted by a strong carbon flux from the volume of the metal.

5. Adsorption, desorption, and migration on graphene

Valence-bond saturation in the surface layer of a solid should affect noticeably such characteristics as the binding energy of adsorbed particles with the surface, sticking coefficients, adsorption capacity etc. The valence bonds of surface atoms being not saturated, the binding energies of foreign atoms of metals and molecules with atoms of the near-surface metal layer are quite large.

Graphite samples may serve as a good illustrative example of solids with a valence-saturated (passive) surface. Beitel [87] studied adsorption of CO and H_2 on graphite samples. It was demonstrated that the sticking coefficients of CO and H_2 molecules to graphite are very small and decrease with increasing coverage. For instance, at low coverages ($\theta < 10^{-4}$) the sticking coefficients of CO and H_2 molecules to graphite were the highest, (1--5) 10^{-5}. The sticking coefficient was found to decrease rapidly with increasing coverage. Significantly, the number of CO and H_2 molecules chemisorbed on graphite turned out to be ~0.01 of the number of molecules chemisorbed on the surface of tungsten. The sticking coefficient of atomic hydrogen to graphite was measured by the same author and found to be $5\ 10^{-3}$--$1\ 10^{-2}$ [10].

It is essential that the sticking coefficients of CO and H_2 to pyrolytic graphite ribbons with a precisely adjusted orientation of the (0001) plane of graphite on the surface were smaller than those to other, poorer quality graphite samples. It is suggested [10, 87] that the observed adsorption of gases occurs actually only at defects of the graphite lattice (corner atoms, plane edges, steps, impurity atoms) near which there are empty valence orbitals. Precisely-oriented surface of pyrolytic graphite ribbons containing less structure defects, they are characterized by smaller sticking coefficients than samples of fine-grained graphite. Interestingly, the sticking coefficient of H_2 to graphite heated to $T \sim 1850$ K was $\sim 4\ 10^{-5}$, while that to graphite heated to $T \sim 2400$ K was smaller than 10^{-8}. Quite possibly, high-temperature treatment of graphite samples gave rise to enhanced graphitization, i.e., an increase in the density of surface defects and of the fraction of surface area occupied by them, and this is what caused the decrease of the sticking coefficient. This conclusion matches with our results on graphitization of carbon films on metals studied as a function of sample annealing temperature (§ 11).

Lander and Morrison [88-90] conducted a LEEDS study of the adsorption of O_2, J_2, Br_2, CO, and H_2O molecules on the (0001) face of single-crystal graphite, the most perfect surface of all. It was shown [90] that admission of these gases to pressures $p \leq 1\ 10^{-4}$ Torr and exposure at these pressures of a single crystal for tens of minutes at $T \sim 300$ K did not bring about any change in the diffraction patterns obtained from a clean crystal face. Studies of adsorption of the same gases on other surfaces revealed that a monolayer of gas is easily detectable. The authors offer a conclusion that the substances studied are not chemisorbed on the basal plane of graphite; as for physisorption, it certainly should take place, but at lower substrate temperatures. It was also demonstrated [88,89] that molecules of a number of compounds ($FeCl_3$, GeI_4, GeI_2, C_6H_6, Xe, ZnI_2) are only physisorbed on the basal plane of single-crystal graphite.

The study of Arthur and Cho [55] occupies a particular place among works dealing with adsorption on the (0001) face of graphite. They investigated the adsorption and desorption kinetics of Cu and Au atoms on this surface. The flash heating method used by them permitted obtaining some quantitative characteristics of desorption. It was shown, for instance, that the coefficient of condensation of Cu and Au increases from ~0.05 for $\theta \rightarrow 0$ to 1 for $\theta = 1$. Measurements of the accommodation coefficient of Cu and Au revealed that the small value of the condensation coefficient for a clean surface of the graphite (0001) face is not related in any way with elastic scattering of Cu and Au atoms from the surface; said otherwise, Cu and Au atoms reach thermal equilibrium with the surface prior to desorption.

The authors offered the following model to account for the results obtained. Metal atoms reaching the surface of single-crystal graphite have a high mobility and a short average lifetime against desorption. The value of τ determined in the study is in actual fact nothing

else than the upper limit to average lifetime; both for Cu and Au, τ measured at T = 300 K and θ ≈ 0 was found to be less than 10^{-2} s. Accepting the prefactor in the expression for the lifetime of particles on the surface to be 10^{-13} s, the authors obtained for an estimate of the binding energy of adatoms to the substrate $E_b \leq 0.65$ eV. Such low binding energies should apparently be assigned to the van der Waals character of adatom interaction with the surface, which is possible under valence-band saturation of the graphite surface. This should be contrasted with the activation energy for desorption of Cu and Au atoms from the (110) and (100)W faces, which is (3 ÷ 5) eV at low coverages [91]. The low binding energy of adatoms with the substrate suggests also a small activation barrier E_{dif} for surface diffusion (estimated by the authors as $E_{dif} \sim kT$), which accounts for the high mobility of the two-dimensional Cu and Au "gas" on graphite. Colliding with one another or with valence-unsaturated surface defects, Cu and Au adatoms can form centers of growth of two- or three-dimensional islands. This is what can underlie the decrease of desorbing flux with time, because islands of adsorbate act as traps for adatoms. The observed increase of the condensation coefficient with increasing atom evaporation time or coverage is attributed by the authors to adatoms escaping from the two-dimensional "gas" phase into close-packed islands, where the lifetime of adatoms exceeds by far the average lifetime in the adsorbed "gas" phase; indeed, the binding energy of a Cu adatom with a copper island was found to be ~2.1 eV, and that of Au adatoms with their island, ~2.5 eV.

The above data suggest a reasonable conclusion that under the conditions of valence bond saturation in the surface layer of a solid and weak binding of particles with the substrate, particles with free orbitals can form strong bonds with one another. These conditions are conducive to formation of close-packed adsorbate islands, provided the particle mobility on the surface is high enough. An electron microscope study revealed growth of three-dimensional islands of Ag, Au, Pb, Cd, and Zn on amorphous carbon [92-94]. It suggested a conclusion that condensed phase islands nucleate at "particularly active spots" on the surface, i.e., apparently, at valence-active edges of graphite scales on which carbon layers had formed. This suggestion is corroborated by the concentration of adsorbate islands being found independent of the density of the atom flux striking the surface, which appears to indicate that there is no homogeneous nucleation. Growth of three-dimensional Ag and Au islands was observed also on another valence-saturated surface, molybdenum disulfide (MoS_2) [95,96].

Unlike valence-bond-saturated surfaces, adsorption of foreign metal atoms on the surface of metals does not, as a rule, bring about formation of close-packed adsorbate islands [97-99].

It should be noted that amorphous carbon is not a very good model object of valence-bond-saturated surface, because it has a large number of valence-unsaturated defects whose number depends strongly on sample prehistory. Thin carbon films on a metal surface are more stable samples with a reliably controllable surface. McCarthy and Madix [100] studied adsorption of gases and vapors on the surface of a metal coated by a carbon film. Adsorption of CO, H_2, CO_2, and H_2O on clean Ni(110), on carbidized nickel, and on the surface of the Ni(110) face coated by a carbon film of graphitic structure was probed by three methods---LEEDS, AES, and heat flashing. Nickel was carbidized by cracking of ethylene on the surface at 600 K. The carbon layer on nickel underwent graphitization either under heating of carbidized nickel at 775 K, or in ethylene cracking at T = 700--800 K, a finding corroborated by other authors as well, e.g., in Refs. [4,5]. In summing up available data, the authors of Ref. [100] came to the conclusion that CO, H_2, CO_2, and H_2O undergo physisorption on a graphite surface, because the heats of adsorption turned out to be too low; for CO_2 and H_2O, for instance, they were found to be ~0.35 eV.

Iridium, which does not dissolve carbon, turned out irreplaceable in probing carbon films on metals. Abdullaev *et al*. [101,102] reported on a TESI investigation of the adsorption and initial stages in samarium condensation on iridium ((111)-texture ribbons) and on iridium coated by graphene. The heats of adsorption of Sm atoms on these surfaces at low coverages were found to be 6.0 eV and ~1.9 eV, respectively. The large difference between the heats of desorption was attributed to a decrease of the covalent component of adsorption bonding on the passive substrate. The comparatively high desorption heat of ~1.9 eV could be assigned to a noticeable contribution to the heat of desorption of the ionic component acting against the mirror image forces [49]. Measurements performed on the same surface [102] demonstrated that the average lifetime of NaCl molecules on graphene-coated iridium, $\tau < 1\ 10^{-5}$ s, even at 300 K, whence for the binding energy of the molecules with the substrate one comes immediately to $E < 0.5$ eV.

It was shown [103] that after formation of graphene on Pt(111) has terminated, the surface becomes passive with respect to adsorption of CO, H_2, and C_6H_6 at $T = 300$ K.

Measurements were conducted [104] of the kinetics of desorption of a number of atoms---Cs. K, Na, Ba, Sr (Table 6)---from both the clean Ir(111) metal and from a graphene film on its surface. It was found that the valence-bond-saturated graphene film on iridium modifies the heats of desorption of particles; in particular, the heats of evaporation E^+ of the monovalent atoms Cs^+, K^+, Na^+ change very little, primarily as a result of a decrease of the polarization

Element	Desorption characteristic $E_{+,0}$ (eV) C, D (s^{-1})	Iridium	Graphene on iridium	V (eV)
Cs	E_+	2,1 ± 0,1	1,8 ± 0,1	3,89
	E_0	4,0 ± 0,1	2,4 ± 0,1	
	C	$1{,}7 \cdot 10^{12}$	$2 \cdot 10^{12}$	
	D	$3{,}4 \cdot 10^{12}$	$4 \cdot 10^{12}$	
K	E_+	2,4 ± 0,1	2,2 ± 0,2	4,34
	E_0	3,8 ± 0,1	2,4 ± 0,2	
	C	$4 \cdot 10^{12}$	$1 \cdot 10^{14}$	
	D	$8 \cdot 10^{12}$	$2 \cdot 10^{14}$	
Na	E_+	3,0 ± 0,1	2,9 ± 0,1	5,14
	E_0	3,6 ± 0,1	2,2 ± 0,1	
	C	$1 \cdot 10^{13}$	$3 \cdot 10^{11}$	
	D	$2 \cdot 10^{13}$	$6 \cdot 10^{11}$	
Ba	E_+	5,2 ± 0,1	2,6 ± 0,1	5,21
	E_0	5,8 ± 0,1	1,9 ± 0,1	
	C	$2 \cdot 10^{12}$	$1{,}8 \cdot 10^{10}$	
	D	$1 \cdot 10^{12}$	$0{,}9 \cdot 10^{10}$	
Sr	E_+	4,8 ± 0,1	~ 2,7	5,70
	E_0	4,9 ± 0,1	~ 1,5	
	C	$6 \cdot 10^{12}$	–	
	D	$3 \cdot 10^{12}$	$\sim 10^{13}$	

Table 6.

interaction between the ion and the metal; indeed, E^+(Cs) = 2.1 eV for Ir(111) and E^+(Cs) = 1.8 eV for Ir(111)-graphene (see Table 6). For the divalent atoms of Ba and Sr, the heats of desorption of Ba^+ and Sr^+ ions decrease strongly, primarily because of the weakening covalent binding forces acting between the *s* electron of the ion and atomic electrons in the surface layer of the adsorbent. For instance, E^+(Ba) = 5.2 eV from Ir(111) and E^+(Ba) = 2.6 eV from Ir(111)-graphene (Table 6). The large value of E^+(Ba) from graphene should be assigned in the first place to the large "ionic" component of the heats of desorption of alkaline-earth atoms. The Guerney representation was used [104] to find that the covalent component of the barium heat of desorption decreases from ~2.7 eV for clean iridium to a few tenths of eV in the case of graphene coating.

The effect of graphene formation on Ir(111) on the migration characteristics of Cs and Ba was investigated in Ref. [105].The method was based essentially on continuous irradiation of a ribbon emitter by a flux of atoms on one side only, with detection by surface ionization techniques of the adatoms that have migrated during their lifetime to the other side of the ribbon.

The results of the experiments are presented in Table 7 listing the temperature interval within which the quantities under consideration were measured.

	$E_м$, eV	Interval of T, K	D_0, cm^2/s
Ir(111)-Cs	0,6 ± 0,1	860 – 1140	0,23
Ir(111)-C-Cs	0,5 ± 0,1	860 – 1300	0,23
Ir(111)-Ba	1,0 ± 0,1	1980 – 2200	$2{,}2 \cdot 10^{-2}$
Ir(111)-C-Ba	~ 0,5	950 – 1135	–

Table 7.

We readily see that graphene affects only weakly the migration characteristics of Cs (just as the heats of desorption of Cs^+ ions). The explanation lies in that Cs adatoms on both surfaces reside primarily in ionic state and are constrained mainly by polarization forces, with the influence of the graphene film being very weak. Therefore, the material of the metallic ribbons practically does not

affect the migration characteristics of Cs adatoms; indeed, in the case of Cs diffusion over a tungsten ribbon with uniform emission characteristics, $D = 0.23 \exp^{-0,57/kT}$ cm^2s^{-1} [23] (the study was conducted by the photoemission technique).

Migration of Ba over iridium requires higher temperatures than that of Cs (Table 7). Just as the heat of desorption of Ba^+ ions, the activation energy for migration of Ba adatoms residing primarily in ionic state is higher than that for Cs, which implies the existence, besides the bonding forces of the polarization nature, of covalent forces as well. It turned out that formation of graphene lowers noticeably the temperature region where migration operates, which practically coincides with that for cesium atoms (Table 7), with E_m decreasing down to 0.4--0.5 eV.

Thus, by reducing strongly the covalent components of the binding forces coupling particles to the surface, graphene on iridium gives rise to a substantial decrease of the activation energy for surface migration of polyvalent atoms.

The above literature data on the adsorption of atoms and molecules on valence-saturated surfaces of single-crystal graphite, polycrystalline graphite, graphitized nickel, and graphene on iridium, platinum and other metals suggest a conclusion that the binding

energy of adsorbed particles with atoms of the surface layer is small, which in some cases may give rise to growth of two- or three-dimensional close-packed islands of adsorbate on such surfaces even for submonolayer coverages.

Our studies reveal formation on graphene/iridium of condensed close-packed Pt, Th, Ni, Mo islands [41], tower islands built of fullerene molecules [107], and two-dimensional islands of CsCl molecules [40]. Investigation of the growth and dissolution of CsCl islands, for instance, permitted determination of the migration length $\lambda(T)$ of CsCl molecules during their lifetime on graphene

$$\lambda(T) = B\exp^{\Delta E/kT} = 10\exp\left[\frac{0{,}13}{kT}\right].$$

For instance, at T = 300 K, λ = 1500 Å, while at T = 1500 K, λ = 27 Å. We succeeded in determining also the difference E_{des} -- E_{migr} = 0.25 eV between the activation energies for desorption and migration. It may be added that CsCl molecules desorb easily from the graphene surface even at T = 300 K, with their lifetime being <0.01 s [40].

6. Metal-graphene thermal equilibrium

A. Specific features of carbon atom diffusion between the surface and bulk of a metal

Many studies deal with diffusion of carbon atoms in the bulk of solids; see, for instance, Refs. [108-110]. At the same time, literature practically does not contain any reports on such an essential subject as diffusion of atoms between the surface and the bulk of a metal.

Exchange of atoms between the surface and the bulk of a solid is an important aspect of all physico-chemical problems associated with processes occurring on the surface, when the channels involved in dissolution and segregation of atoms operate efficiently. Mass transport of atoms between the surface and the bulk of the metal defines the activation energies for dissolution, E_{S1}, and segregation, E_{lS}; the latter may differ slightly from E_0, the activation energy for volume diffusion (Fig. 33). Consider the relevant relations for the fluxes of dissolution, ν_{Sl}, and segregation, ν_{1S}, presented in Refs. [27]

$$\nu_{S1} = N_S\left(1 - N_1 / N_{1\lim}\right)\cdot W_{S1} = N_S\left(1 - N_1 / N_{1\lim}\right)\cdot C_{S1}\exp^{-E_{S1}/kT} \quad (1)$$

$$\nu_{1S} = N_1\left(1 - N_S / N_{Sm}\right)\cdot W_{1S} = N_1\left(1-\theta\right)\cdot C_{1S}\exp^{-E_{1S}/kT}, \quad (2)$$

where N_S and N_{SM} are the concentrations of atoms on the surface, both running and in a monolayer (the physical meaning of a monolayer may differ depending on the actual Me-C system discussed); N_1 and $N_{1lim}(T)$ are the concentrations of atoms diffusing in the site plane adjoining the surface, running and at the solubility limit, W_{S1} and W_{1S} are the probabilities of dissolution and segregation, E_{S1} and E_{1S} are the corresponding activation energies, and C_{S1} and C_{1S} are the prefactors. Because desorption involves rupture of all bonds of an adparticle with the surface, and dissolution, of a part of them only, it appears reasonable to expect that $E_{des} > E_{S1}$.

Despite the fairly obvious significance, both for basic science and for the field of applications, of studying diffusion of atoms between the surface and the bulk of a metal, we are aware only of one publication [111] reporting on a quantitative investigation of dissolution of surface carbon in single-crystal W(100) with interesting results, namely, the

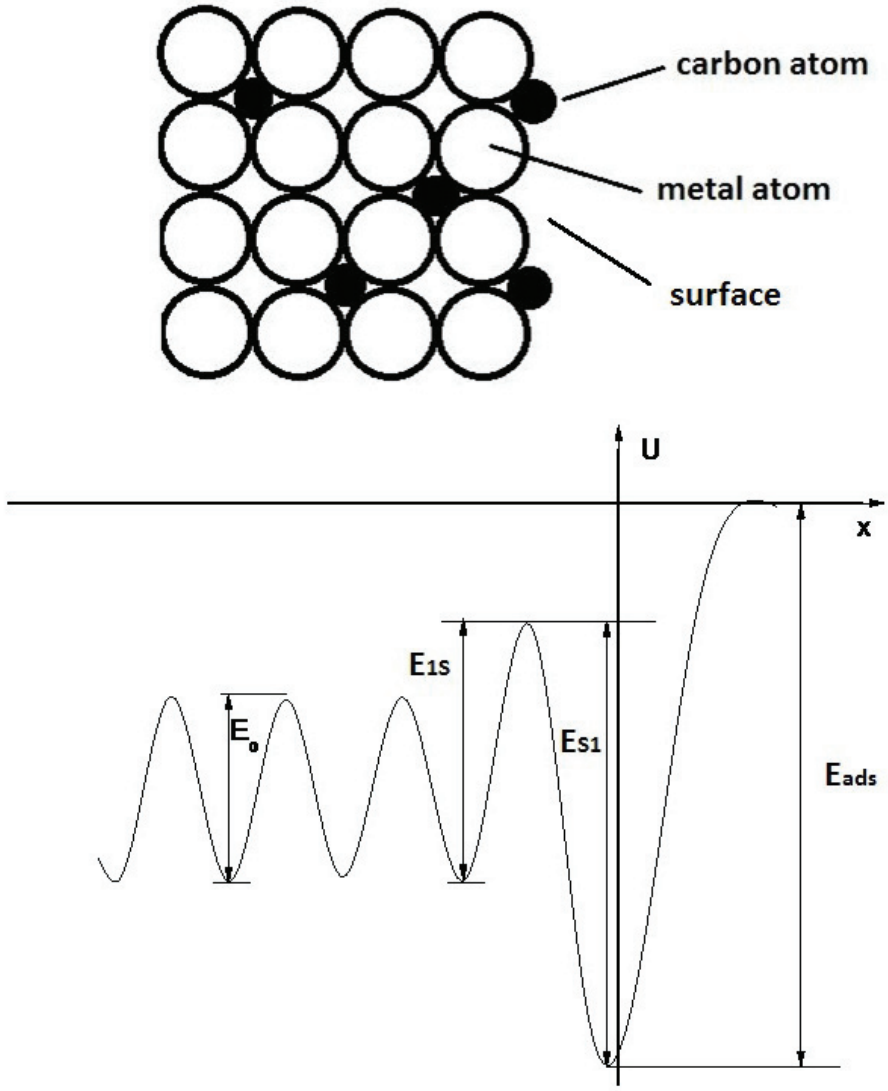

Fig. 33. A model scheme for the surface-bulk interface with diffusing atomic carbon and activation energy barriers for desorption and diffusion:
E_{ads} - for desorption, E_{s1} - for dissolution into te bulk; E_{1s} - for segregation onto the surface, E_0 - for bulk diffusion.

activation energy for dissolution was found to be high, E_{S1} = 5.0 eV, which exceeds by far that of volume diffusion of carbon in tungsten E_0 = 2.56 eV. This implies that knowledge of the activation energy for volume diffusion E_0 is not enough by far for adequate description of the diffusion of atoms between the surface and the bulk of a metal; one would need instead the knowledge of E_{S1} and E_{1S}, which should be derived from direct experiments and found readily, besides the energy E_0, in handbooks on the physics of metals.

The lack of literature data on such a new direction of research as transport processes at the surface/bulk of metal interface can be traced to the following circumstances. To begin with, in order to obtain quantitative data, one has to know exactly the concentration of dissolved carbon in the metal and be able to vary it in a controllable manner. We tackled this problem by employing an absolutely calibrated carbon atom flux and purifying on a qualitative scale the volume of the metal under study from all impurities, including carbon. Apart from this, the use in our experiments of thin (20--50 μm) textured metal ribbons permits one to spread carbon, rapidly and uniformly, over the volume of the metal, as well as to reach in acceptable times equilibrium between the surface carbon and carbon in the bulk of the ribbons; indeed, for a ribbon length of 40--60 mm and a carbon evaporation zone ~30 mm long, the effects associated with escape of carbon to cold ends of the ribbons may be neglected. Significantly, we could evaporate carbon onto either side of the ribbon, a factor which in many cases provided supportive evidence for the physical pattern of the processes under study in the Me-C system.

Consider the factors governing diffusion of carbon atoms between the surface and the bulk in the particular case of the (100)Mo-C system.

Distribution of carbon between the surface and volume in a molybdenum ribbon. We have earlier discussed in some detail the physical pattern of the processes involved in the interaction of carbon with heated molybdenum. We recall that if one evaporates carbon atoms on the heated surface of a molybdenum ribbon, say, at T = 1400 K, carbon dissolves rapidly in the bulk of the metal, accompanied by a buildup of carbon on the surface in the form of chemisorbed "gas". After carbon has accumulated in the ribbon volume up to a concentration $N_1 \approx 8\ 10^{10}$ at/cm^2 in each site plane, a carbon film of chemisorbed atoms with $N_c = 1\ 10^{15}$ at/cm^2 forms on the surface, the surface carbide MoC. One can accumulate SC MoC on the front side of the ribbon by adsorbing carbon at T = 1400 K on the rear side of the molybdenum ribbon to the same concentration. But this implies that at $T \geq 1400$ K carbon atoms cross rapidly the thin ribbon. Incidentally, our data fit to the information available in the literature. For instance, it was found [112] that the coefficient of volume diffusion in Mo can be written as $D(\text{cm}^2/\text{s}) = 3{,}4 \cdot 10^{-2} \cdot \exp\left(-\frac{1{,}78 \cdot 11600}{TK}\right)$. It is known that the length λ of the diffusion front in the case of diffusion in one direction is related with the diffusion time t through the expression $\lambda = \sqrt{2Dt}$. [37]. Setting ε = h = 20 μm = 2 10^{-3} cm at T = 1450 K, we come to the time t = 100 s required for carbon to traverse the ribbon from one side to the other, a figure which fits well to the time experimentally observed in our experiments performed at the same temperature.

Interestingly, it is probably for the first time that one had determined for a Me-C system the carbon distribution between the volume and the surface in molybdenum; it is presented in Table 8. It lists N_{front} and N_{rear}, the carbon concentrations on the surface of the front and rear sides of the ribbon, $N_v = N_{dep} - N_{front} - N_{rear}$, the amount of carbon that dissolved from 1 cm^2 of the surface into the bulk of the ribbon containing 7*10^4 atomic planes;as well as the

carbon concentration in one site layer $N_1 = \frac{N_v}{n}$ (with the diameter of the Mo atom taken to be 3 Å). N_{dep} is the total amount of the deposited atomic carbon.

N_{dep}, cm^{-2}	N_{front}, cm^{-2}	N_{rear}, cm^{-2}	$N_v = N_{dep} - N_{front} - N_{rear}$, cm^{-2}	$N_1 = N_v/n$, cm^{-2}
$5 \cdot 10^{14}$	$1 \cdot 10^{14}$	$1 \cdot 10^{14}$	$4 \cdot 10^{14}$	$6 \cdot 10^{9}$
$1 \cdot 10^{15}$	$2{,}5 \cdot 10^{14}$	$2{,}5 \cdot 10^{14}$	$5 \cdot 10^{14}$	$7 \cdot 10^{9}$
$3 \cdot 10^{15}$	$7 \cdot 10^{14}$	$7 \cdot 10^{14}$	$1{,}6 \cdot 10^{15}$	$2{,}3 \cdot 10^{10}$
$4{,}5 \cdot 10^{15}$	$9 \cdot 10^{14}$	$9 \cdot 10^{14}$	$2{,}7 \cdot 10^{15}$	$4 \cdot 10^{10}$
$7{,}5 \cdot 10^{15}$	$1 \cdot 10^{15}$	$1 \cdot 10^{15}$	$5{,}5 \cdot 10^{15}$	$8 \cdot 10^{10}$
$8 \cdot 10^{16}$	$1 \cdot 10^{15}$	$1 \cdot 10^{15}$	$7{,}8 \cdot 10^{16}$	$1{,}1 \cdot 10^{12}$

Table 8

Consider now these results (Table 8) in more detail. At low concentrations of evaporated carbon, $N_{dep} \leq 5\ 10^{14}$ at/cm^2, the major part of carbon is confined to the volume of the ribbon, and $N_{front} = N_{rear} < 1\ 10^{14}$ at/cm^2. At higher concentrations, for instance, for $N_{dep} \leq 1\ 10^{15}$ at/cm^2, the amount of carbon on the surface of the ribbon grows to $N_{front} = 2.5\ 10^{14}$ at/cm^2, and that in its bulk, to $N_1 = 7\ 10^9$ at/cm^2. At still higher concentrations, $N_{dep} = 7.5\ 10^{15}$ at/cm^2, the carbon concentration on the surface increases to its maximum value $N_{front} = N_{rear} = 1\ 10^{15}$ at/cm^2, with the attendant formation on the surface of the SC MoC, and carbon in the bulk present in a concentration $N_1 = 8\ 10^{10}$ at/cm^2. Interestingly, increasing the concentration of evaporated carbon by one more order of magnitude, to $N_{dep} = 8\ 10^{16}$ at/cm^2, *does not* initiate growth of surface carbon concentration; indeed, the SC MoC with $N_{front} = N_{rear} = 1\ 10^{15}$ at/cm^2 persists, while the C concentration in the ribbon bulk grows to $N_1 \approx 1\ 10^{12}$ at/cm^2.

Diffusion of carbon into molybdenum at surface concentrations $N_S \leq 1\ 10^{15}$ at/cm^2. A molybdenum ribbon was cleaned thoroughly of impurities by annealing in an oxygen atmosphere ($P_{O2} \approx 1\ 10^{-5}$ Torr) at $T = 1400$ K, and subsequently, in ultrahigh vacuum at 2200 K to free it of oxygen; thereafter the only peaks left in Auger spectra were those due to molybdenum. Next, carbon was evaporated on the ribbon at 600 K up to the concentration $N_S = 1\ 10^{15}$ at/cm^2, i.e., to the concentration corresponding to the SC MoC, at which carbon atoms occupy apparently deep hollows between the 4 surface molybdenum atoms. As demonstrated by experiments, heating of such a carbon film to $T \leq 1250$ K does not initiate dissolution of surface carbon. Noticeable dissolution of C in (100)Mo was observed to occur only at $T = 1350$ K, which took a characteristic time of ~1 min. This time was found not to depend on the surface concentration of carbon for $N_S < 1\ 10^{15}$ at/cm2. Figure 34 shows a typical curve of the kinetics of carbon dissolution in molybdenum for $N_S \approx 6\ 10^{14}$ at/cm^2. The kinetic parameters describing dissolution of surface carbon can be found using the results published in Ref. [113]. The decrease dN of the surface carbon concentration occurring in a time dt is related with the dissolution flux ν_{nl} and the average lifetime $\tau_{S1} = \tau_o \exp^{E_{S1}/kT}$ of C adatoms with respect to dissolution in the metal through

$$dN = -\nu_{S1} dt = -\frac{N dt}{\tau_{S1}} \ . \tag{3}$$

Integration of Eq. (3) in the time t in which the surface concentration of carbon decreases from N_0 to N yields

$$N = N_o \exp^{-t/\tau_{S1}} . \quad (4)$$

Equation (4) can be used to derive the activation energy for dissolution E_{nl} of surface carbon into the molybdenum

$$E_{S1} = kT\ln\left(\frac{t}{\tau \ln N_o / N}\right). \quad (5)$$

Upon substitution in Eq. (5) of $\tau_0 = 10^{-13}$s, $kT(\text{eV}) = \frac{1350\ K}{11600\ \text{K/eV}}$, and analysis of the initial parts of the dissolution curves, we come to E_{S1} = 3.9 eV.

We wish to note the large magnitude of the activation energy for dissolution of surface carbon in (100)Mo, E_{S1} = 3.9 eV, which exceeds by far, by ~ 2 eV, that for volume diffusion E_0 = 1.78 eV [112]. A similarly large difference between E_{S1} and E_0 was obtained [111] for W-C(100), which is apparently characteristic of such Me-C systems.

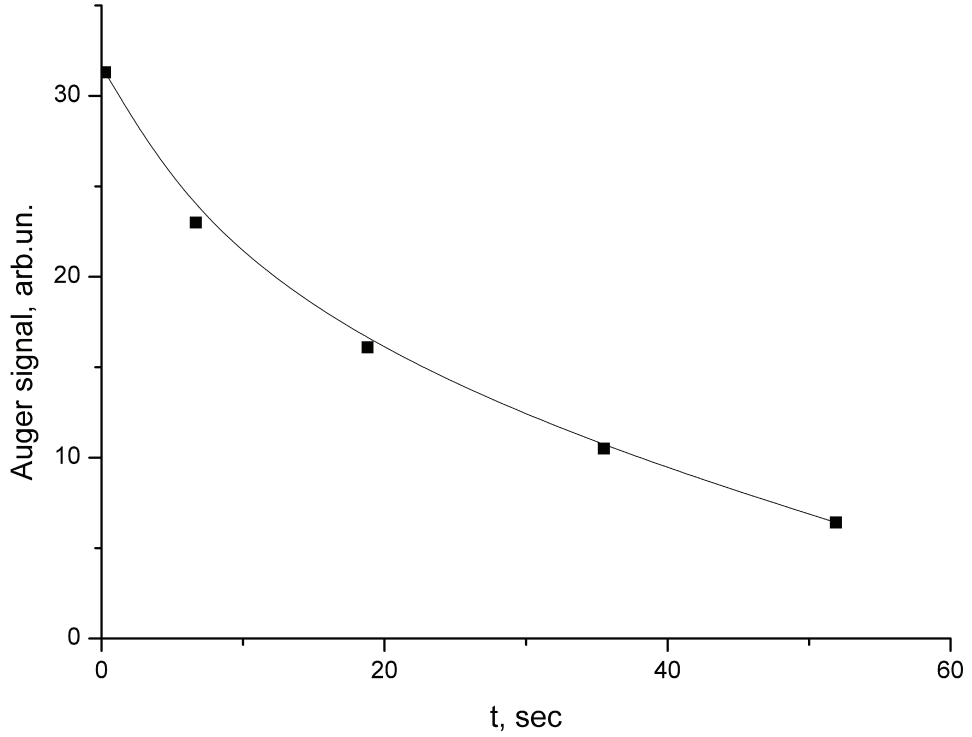

Fig. 34. Carbon Auger signal versus heating time in annealing of carbon film on pure Mo(100) at 1350 K. the film was got by atomic carbon deposition at 300 K using the flux ν_C = 6 *10^{14} cm^{-2}*s^{-1}.

Diffusion into molybdenum of carbon for surface concentrations N_c > 1 10^{15} at/cm². It appeared interesting to learn how carbon would dissolve in molybdenum at concentrations higher than that in the SC, when all sites between 4 surface molybdenum atoms are occupied. The study was started by preparing at T = 1400 K Mo SC on both sides of the ribbon, as this was described earlier (in the volume, the concentration N_1 = 8 10^{10} at/cm²---see Table 8). After this, carbon was evaporated in an atomic flux on SC MoC at = 300 K to N_c = 1.5 10^{15} at/cm², and the ribbon thus treated was annealed at a number of temperatures (Fig. 35). It is seen that now noticeable diffusion of carbon into the bulk of molybdenum occurs at markedly lower temperatures, T ~ 900--1000 K, with all *excess* carbon present above that bound in the MoC SC diffusing into the bulk. The dissolution temperature T = 900 K was used to estimate the activation energy for dissolution of carbon from centers other than those in SC (we shall refer to them as weakly bound ones). Recalling the relation of Frenkel for average particle lifetimes with respect to dissolution, $\tau = \tau_o \exp^{E_{S1}/kT}$, accepting $\tau_0 = 10^{-13}$ s and setting for the time of the experiment τ ~ 10 s (at T = 1000 K), we come to E_{S1} = 2.5 eV.

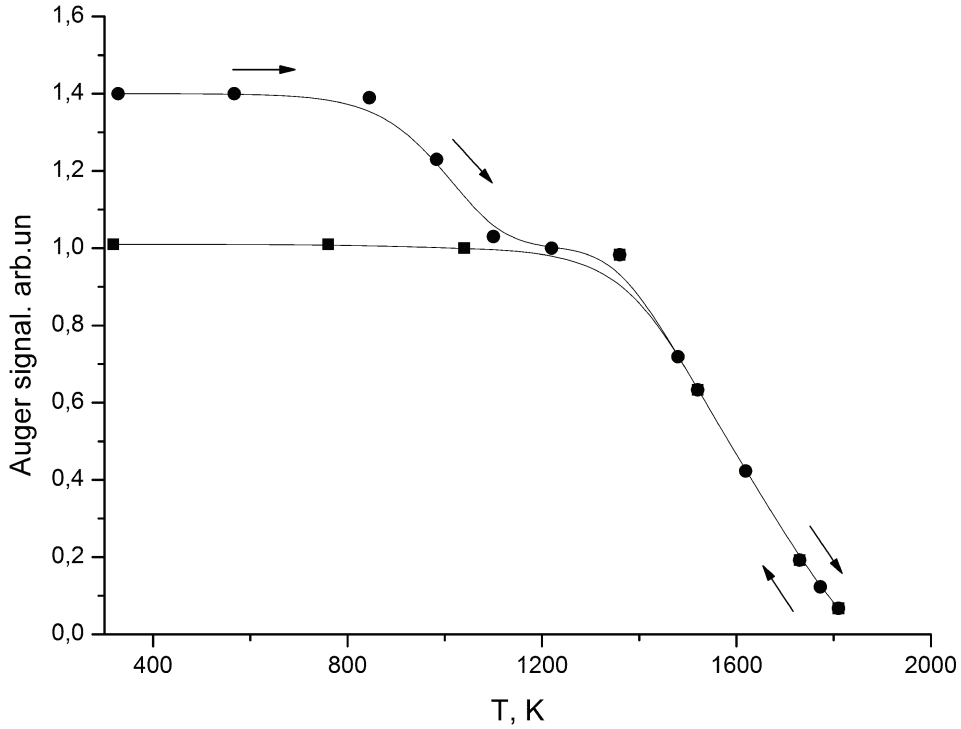

Fig. 35. Carbon Auger signal versus temperature in in annealing of carbon film with N_C = 1.5 * 10^{15} cm^{-2}, deposited onto Mo(100) with surface carbide at 300 K. Dissolved carbon presented in the substrate bulk in concentration of N_C = ~2 * 10^{11} cm^{-2}, at each interstitial plane.

Consider now the possible nature of these weakly bound dissolution centers. The carbon in SC occupies all deep hollows between the 4 surface Mo atoms, from which it dissolves into the bulk with a high activation energy E_{S1} = 3.9 eV. Because C atoms are small, so that the surface area occupied by them is small, ~2 Å, at a concentration of such atoms in MoC SC N_c = 1 10^{15} at/cm^2 they will cover a surface area of ~2 10^{15} Å^2, which corresponds, for the total area of 1 cm^2, only 20%. Therefore, the dissolution energy E_{S1}' = 2.5 eV relates to adsorption of carbon atoms located closely to the weakly bound MoC SC centers, and it is from here that they apparently diffuse into the metal. We note that the observed strong dependence of the activation energy for dissolution of surface carbon into molybdenum on the nature of adsorption centers has apparently been established for the first time, and that it should be characteristic of other Me-C systems as well.

Interestingly, if one replaces all strongly bound centers on molybdenum by other atoms, e.g., by sulfur or silicon, then the carbon arriving from the outside at T = 1000 K will, rather than building up on the surface, dissolve completely in the bulk of the metal [43].

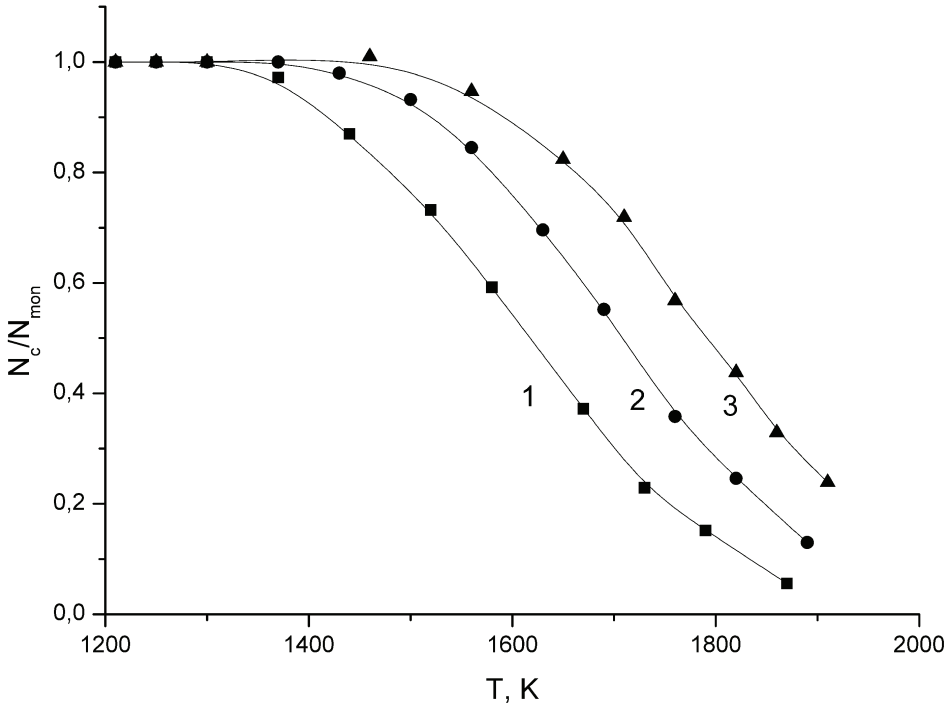

Fig. 36. Equilibrium carbon relative surface concentration (N_C /N_{mon}) versus temperature in Mo-C system. The concentration of dissolved carbon at each interstitial plane is, cm^{-2}: 1 - 2*10^{11}; 2 - 4*10^{11}; 3 - 8*10^{11}. N_{mon} = 1 *10^{15} cm^{-2}.

Equilibrium between the fluxes of dissolution and segregation of carbon in the Mo-C system. An intriguing pattern is observed for many Me-C systems on carbonized metal samples at moderate temperatures. Figure 36 plots the variation of the Auger signal intensity due to surface carbon (or, said otherwise, of the surface concentration) with the

temperature of the Mo-C solid solution. Each point on the curve corresponds to equilibrium between the segregation and dissolution fluxes, i.e., $\nu_{S1} = \nu_{1S}$, with the surface concentration of carbon being totally independent of the time the sample was kept at the given T = const. The curves obtained under increasing and decreasing temperature are reproducible with a high accuracy. An increase in the concentration of carbon dissolved in the bulk of the molybdenum ribbon brings about an increase of N_1 and, accordingly, as follows from (2), initiates growth of ν_{S1}, i.e., of the segregation flux. This is accompanied by growth of the surface concentration N_n of carbon as well (see curves 1--3 in Fig. 36) obtained for $T > 1400$ K, where the carbon concentration in the bulk of the metal serves as a parameter. Crossing these curves by a straight line for N_S = const and using Eqs. (1) and (2), we obtain, for instance, for curves 1 and 2 the following equilibrium of fluxes for two temperatures, T_1 and T_2:

$$N_S\left(1-\frac{N_1(T_1)}{N_{1\lim}(T_1)}\right)\cdot C_{S1}\cdot\exp^{-E_{S1}/kT_1} = N_1(T_1)(1-\theta)C_{1S}\exp^{-ES/kT_1}, \tag{6}$$

$$N_S\left(1-\frac{N_1(T_2)}{N_{1\lim}(T_2)}\right)\cdot C_{S1}\cdot\exp^{-E_{S1}/kT_2} = N_1(T_2)(1-\theta)C_{1S}\exp^{-E_{1S}/kT_2}. \tag{7}$$

Assuming C_{1S} and C_{S1} to be temperature independent, and accounting for the volume concentrations of carbon being far from the solubility limit $N_1(T) << N_{1lim}(T)$, an inference drawn from direct experiments on additional adsorption of carbon atoms, we obtain from Eqs. (6) and (7)

$$\exp^{E_{S1}\left(1/kT_2-1/kT_1\right)} = \frac{N_1(T_1)}{N_1(T_2)}\exp^{E_{1S}\left(1/kT_2-1/kT_1\right)}$$

or

$$\exp^{\Delta E\left(1/kT_2-1/kT_1\right)} = \frac{N_1(T_1)}{N_1(T_2)}$$

or again

$$\Delta E = \frac{\ln\dfrac{N_1(T_1)}{N_1(T_2)}}{1/kT_2-1/kT_1} \tag{8}$$

Thus, $E_{S1} - E_{1S} = 2.0$ eV. Because $E_{S1} = 3.9$ eV, $E_{1S} = 3.9 - 2.0 = 1.9$ eV, a point appearing reasonable enough and matching the magnitude of $E_o = 1.8$ eV reported in Ref. [111]. The relative similarity of the energies $E_{1S} = 1.9$ eV and $E'_{1S} = 2.5$ eV for the surface concentration of carbon $N_S > 1\ 10^{15}$ at/cm^2 accounts for the weak growth of the surface concentration of carbon for $T < 1400$ K considered against the large "base" of the surface carbide MoC; this is why the Auger signal intensity of carbon at $T < 1400$ K is practically constant (Fig. 36). Thus, the energies mediating transport processes in the Mo-C system could be arranged in the following way:

1. Activation energy for dissolution E_{1S} of carbon atoms in Mo(100) for surface concentrations $N_S \le 1\ 10^{15}$ at/cm^2: $E_{1S} = 3.9$ eV.

2. Activation energy for dissolution E'_{1S} of carbon atoms in (100)Mo for surface concentrations N_S > 1 10^{15} at/cm², when all the strongly bound centers are already occupied: E'_{1S} = 2.5 eV.
3. Activation energy for carbon segregation E_{1S} from the near-surface region: E_{1S} = 1.9 eV,
4. Activation energy for volume diffusion E_0 of carbon in molybdenum: E_0 = 1.8 eV [112].

The very close values of E_{1S} and E_0 do not give us sound grounds to consider these quantities as radically different. It appears reasonable presently to accept $E_0 \approx E_{1S}$.

Dissolution of carbon in (1010)Re. Carbon atoms dissolve actively in rhenium which contains carbon neither on the surface nor in the bulk of the metal at T ~ 1000 K. Study of the kinetics of dissolution provided an estimate $E_{S1} \approx$ 2.6 eV for low carbon surface concentrations $N_c \approx 5\ 10^{14}$ at/cm². Formation of rhenium SC with $N_c \approx 1.4\ 10^{15}$ at/cm², when the concentration of carbon in the bulk of rhenium is far from the solubility limit, displaces the threshold of active carbon diffusion into the bulk of the metal to T ~ 800 K, which matches with the estimated activation energy for dissolution for the case of N_c > 1.4 10^{15} at/cm², $E'_{S1} \approx$ 2.2--2.4 eV. Literature suggests E_0 = 2.3 eV for volume diffusion of carbon in the unsaturated Re-C solid solution [114]. The closeness of the E_{1S} and E_0 values implies virtual independence of the equilibrium surface concentration of carbon on temperature in the Re-C system after the formation of rhenium SC (T > 1800 K) and accounts for the weak temperature dependence of the equilibrium carbon concentration on the rhenium surface N_c in the high temperature domain (T > 1900 K), when N_c < 1.4 10^{15} at/cm², which should be contrasted, for instance, with the Mo-C system, with $Nc \sim \exp^{\Delta E/kT}$, where $\Delta E = E_{S1} - E_0$.

B. Equilibrium of graphene islands in the Me-graphene system

The two-dimensional phase transition in a carbon layer on Me involving formation of graphene islands (**§** 5) at moderate and high temperatures assumes dynamic equilibrium between the chemisorbed carbon "gas" and graphene islands. Incidentally, the equilibrium of the islands rests on the peripheral, edge carbon atoms of the islands.

Figure 37 displays an equilibrium curve of the dependence of the relative area of graphene islands S_0 on substrate temperature for Ir(111). The curve does not change shape with the temperature increased to T = 1950 K followed by its decrease; equilibrium obtains on a time scale of a few seconds to a few tens of seconds. For T > 1950 K, the S_o = f(T) curve becomes irreversible, because of noticeable desorption of carbon atoms from iridium setting in.

Figures 38 and 39 present similar S_o = f(T) curves for the Re(1010)-graphene and Rh(111)-graphene systems. The parameter of the curves is the amount of carbon in the bulk of the metal; for better visualization, the concentration of carbon dissolved in the bulk is given for each atomic plane of the metal (in at/cm²). The curves reflect strict equilibrium, because maintaining the sample for a long time at each T = const does not result in a change of the graphene island area. Obviously enough, the lifetime of graphene islands at high T depends directly on the carbon flux from the bulk of the metal to the surface; as the concentration of dissolved carbon increases, the flux to the surface grows, with equilibrium shifting to higher temperatures (Figs. 38 and 39).

One can readily estimate that, for instance, for the Re-graphene system at T = 1400 K the islands would have broken up in a few hundredths of a second without adequate supply from the chemisorbed "gas" phase [115].

The equilibrium in the Me-graphene case resembles that in a vapor-liquid system (Fig. 40). There is, however, a radical difference also in that in the Me-graphene case there is the metal

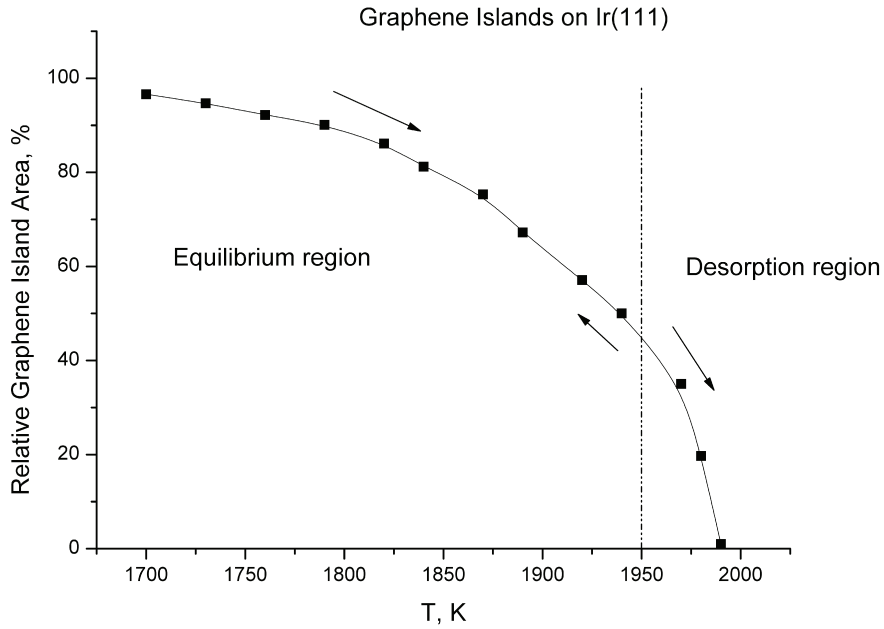

Fig. 37. Relative graphene island area versus annealing temperature for Ir(111).

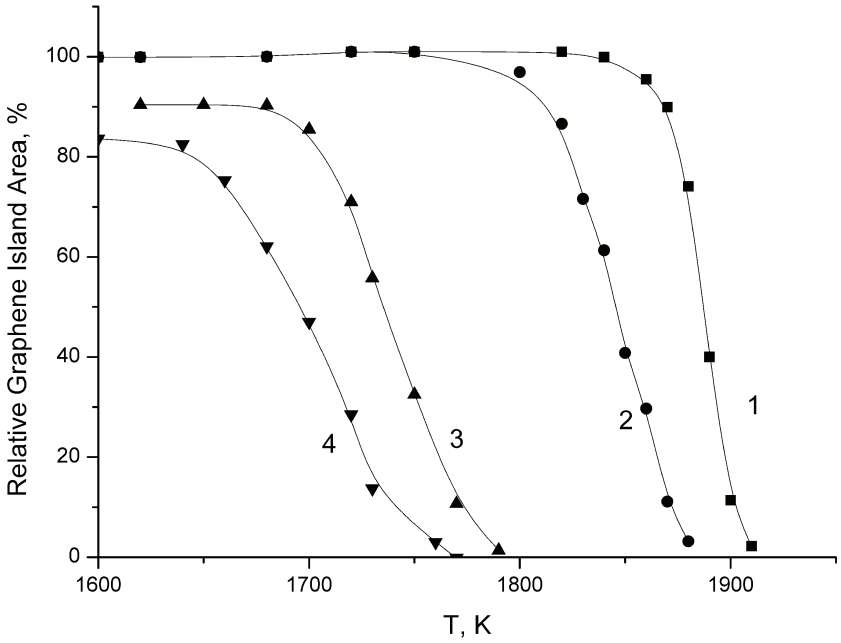

Fig. 38. Equilibrium relative graphene island area versus annealing temperature for Re (10-10). Carbonization temperature T_C, K: 1 - 1840, 2 - 1790, 3 - 1670, 4 - 1640.

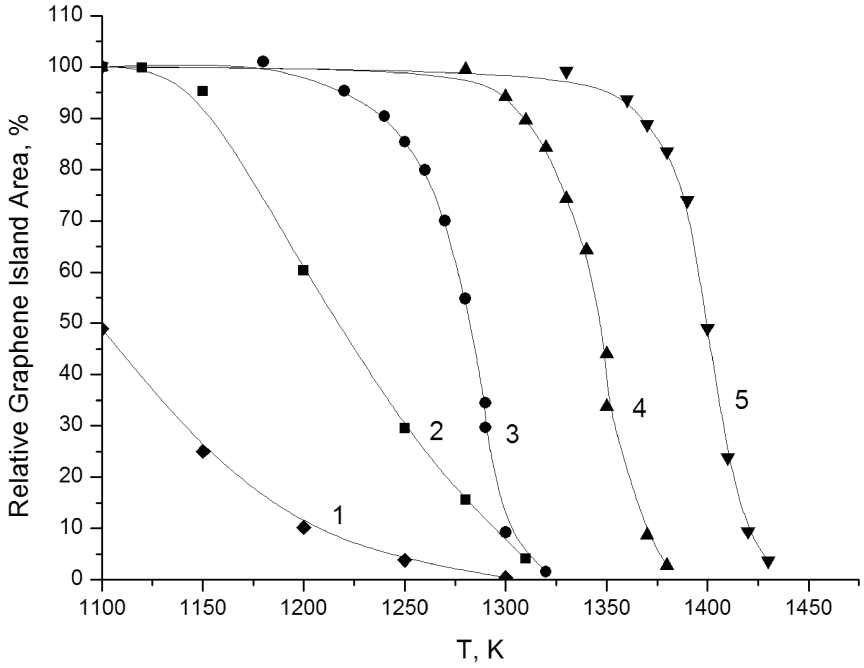

Fig. 39. Equilibrium relative graphene island area versus annealing temperature for Rh(111). The concentration of dissolved carbon at each interstitial plane is, at.%: 1 - 0.035; 2 - 0.045; 3 - 0.06; 4 - 0.075

surface separating the two phases of carbon (Fig. 40). In this case, the equilibrium is mediated by the chemisorbed carbon "gas" on the metal surface and edge carbon atoms in the graphene islands.

Consider the extent to which the concepts developed here agree with the universally accepted thermodynamic description of equilibrium systems, in particular, with the Gibbs phase rule. The rule postulates that W=U+2-V, where W is the number of phases, U is the number of components, and v is the number of thermodynamic degrees of freedom.

At zero pressure and a fixed component composition, the conditions corresponding to the standard experimental arrangements, when carbon neither enters the system not leaves it, V = 1, because the only thermodynamic degree of freedom is here the temperature. Apart from this, one may consider the above system as a single-component one (U = 1); indeed, the metal itself is not involved in any chemical transformation and is not modified in the course of experiments, so that it may be considered as just an external limitation similar, say, to walls, flasks etc. With this in mind, we come to W = 2, i. e., one can expect that TWO volume phases can be in equilibrium here. And we have here indeed TWO such phases---carbon dissolved in the metal (metal-C solid solution) and GRAPHENE (graphite).

It appears, however, that, staying in the context of phase equilibrium, graphene should be considered not as an independent chemical form of carbon bur rather as the initial stage of growth of the volume phase, which is graphite. This approach is attested by its being virtually impossible to locate the point in an experiment where growth of a graphene film

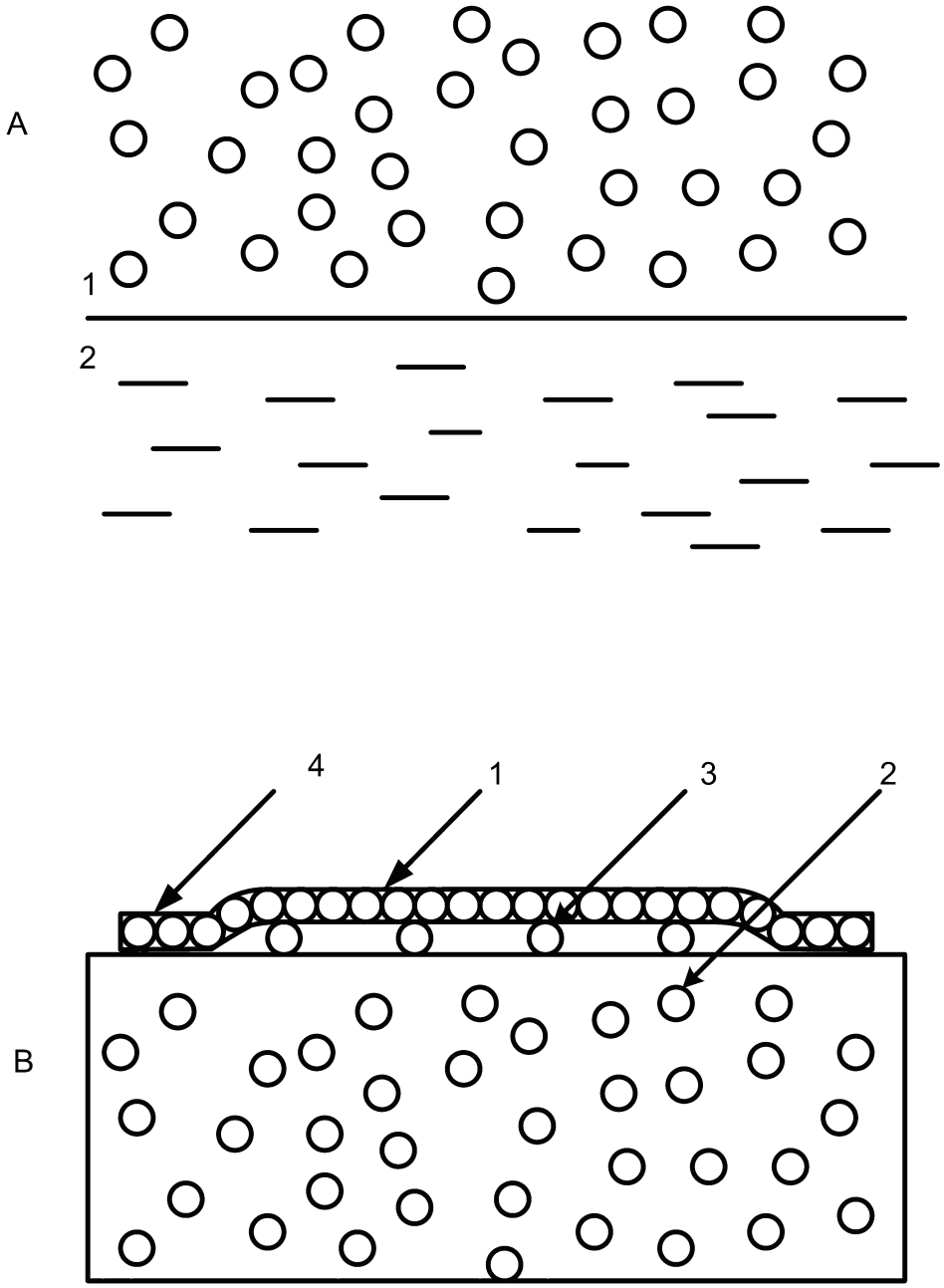

Fig. 40. A model scheme illustrating details of the phase transition for graphene - metal system: A – vapor (1) over the substrate (2); B – graphene (1); dissolved atomic carbon (2); chemisorbed atomic carbon (3); chemisorbed graphene island edges (4).

transforms to that of a multilayer graphite film. We showed [11] that the reason for it is rooted in the mechanism itself of nucleation and growth of the second and subsequent layers.
In the above consideration we have missed, however, a very important phase, namely, that of carbon atoms chemisorbed on the surface. It might seem at first glance that its existence is in contradiction with the Gibbs phase rule. This is, however, not so. Indeed, accepted in its classical form, this rule relates only to volume phases. To take due account of the part played by the surface, one has to add to the number of independent degrees of freedom also surface tension, a two-dimensional analog of pressure. With this correction included, it is THREE surface or volume phases that can be in equilibrium, a conclusion corroborated by experiment.

§ 8. Growth of graphite on a metal surface

A graphene film of a given thickness can be
readily produced by segregation of carbon
from a Me-C solid solution onto the surface of a metal.

1. Segregation of carbon onto the nickel surface [36]

The solubility limit of carbon in nickel is high [114]. For instance, at T = 1170 K, N_{lim} = 1 at. %, to be contrasted with rhenium, in which at the same temperature N_{lim} < 0.01 at. %. Figure 41 visualizes the kinetics of carbon segregation on the surface of nickel at T = 900 K obtained by AES; the carbonization temperature T_c = 1100 K. Interestingly, accepting the reference of nickel substrate screening (E_{Ni} = 61 eV) by a graphene (~ a factor two), we come to the conclusion that assuming layer-by-layer film growth the time taken by each layer to form is the same (Fig. 41). This means that the flux of carbon atoms arriving from the bulk of nickel onto its surface is constant, ν_c = const = 2.4 10^{13} at/cm^2 s. The constancy of the flux suggests both fast migration of carbon from central regions of the ribbon to its surface and a large amount of carbon accumulated in the bulk of nickel. For $T \le 800$ K, diffusion of carbon in Ni freezes out, with no carbon segregation to the surface of nickel observed.
Figure 15 in **§** 1 visualizes the behavior of nickel carbonized at T_c = 1375 K at different T translated by AES (equilibrium curve). The initial state is a graphene layer at $T = T_c$ = 1375 K. Now if we raise the temperature to $T > T_c + 15^o$, graphene breaks down, and the carbon left on the surface at $T \ge T_c + 40^o$ will be surface carbide with $N_c \approx (2 \div 3)\ 10^{14}$ at/cm^2. If we lower the ribbon temperature, it is only a graphene layer which will grow at $(T_c - 40^o) \le T \le T_c$ (Fig. 15, **§** 1). One can readily see in Fig. 15 a small, but well reproducible wing in the temperature region $T_c \div (T_c - 40^o)$ which can be identified with one graphene layer. A similar wing is observed in spectra of many metal-carbon systems: Re-C, Rh-C, Mo-C.
One may forward the following assumption as a reasonable explanation. The conditions in which the first and the subsequent graphene layers grow are essentially different. Indeed, while the first layer grows on a metal, the second layer, while it has been nucleated on the metal too, but it was under the first graphene layer (the physical processes involved in the growth of thick graphite layers are discussed at length in **§** 9). It appears that in order for the second layer to start growing, the concentration of surface carbon should be higher by some amount than θ_c, which is made possible by setting the temperature of the ribbon below the carbonization temperature. For $T < T_c - 40^o$, a thick film of graphite grows; in our case, its thickness can be readily estimated knowing the dependence of the limiting solubility of carbon on temperature and the ribbon thickness [36].

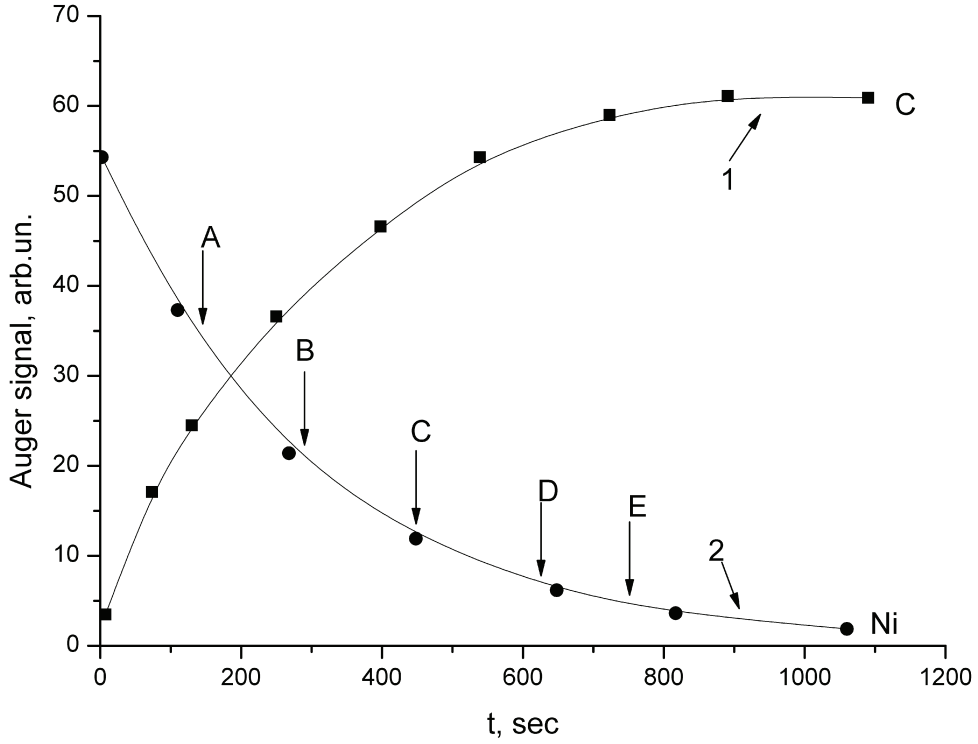

Fig. 41. Auger signals of carbon (1) and Ni (2) versus time in carbon precipitation from the Ni-C solid solution at 900 K. Carbonization temperature is 1100 K, initial carbon concentration in the substrate bulk is $N_C = 4 * 10^{12}$ cm^{-2} per each interstitial plane. A, B, C, D, E – correspond to the formation of the first, second, etc. graphene layer

2. Segregation of carbon onto the surface of rhodium, rhenium, and platinum [27,41]

If rhodium is carbonized in the region of moderate and high temperatures, T_c = 1400--1800 K, and thereafter the temperature is lowered, for instance, down to T = 1100 K, a graphite film will also grow on the surface of rhodium, with its thickness depending on T_c. Figure 6 (§ 1) plots the behavior of the intensity of the Auger signal of carbon and rhodium under decreasing temperature of a sample carbonized at T = 1400 K. As with the Ni-C system, one observes an equilibrium wing $\Delta T \approx 50^o$ wide corresponding to one graphene layer, for $T \le T_c$ -- 50^o, a thick graphite film grows rapidly and the Auger signal of rhodium melts into background noise, with the Auger spectrum of carbon acquiring the typically "graphitic" shape (spectrum 3 in Fig. 7).

A similar wing in the behavior of the carbon Auger signal intensity with temperature of a carbonized sample is observed with the Re-carbon system as well (Fig. 42). At T < 1710 K, intensive growth of a thick graphite film becomes evident.

For the Pt-carbon system, however, there is no wing, and the intensity of the carbon Auger signal grows monotonically with decreasing temperature (Fig. 43).

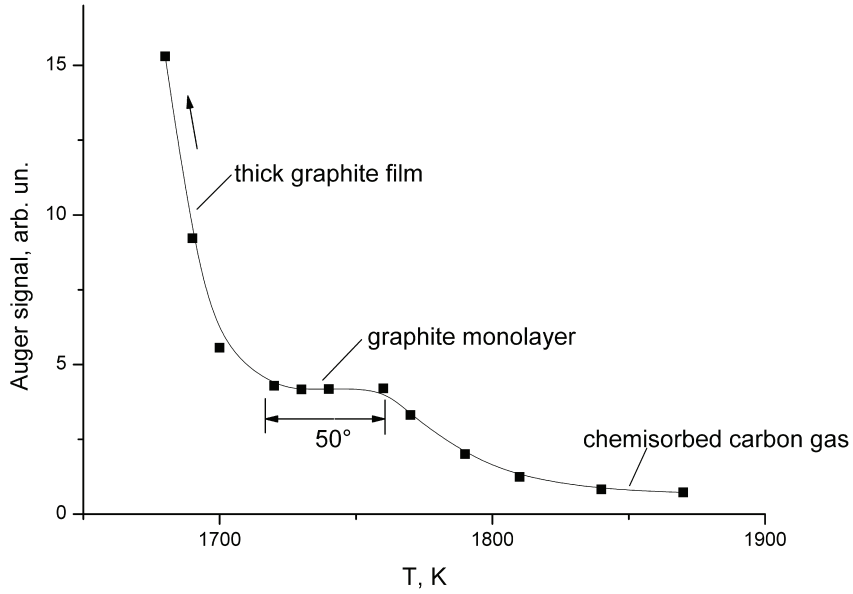

Fig. 42. Carbon Auger signal versus heating time in annealing of polylayer graphite film of about 8 layer thick. Carbonization time is 1770 K, time delay at each temperature is 5 min.

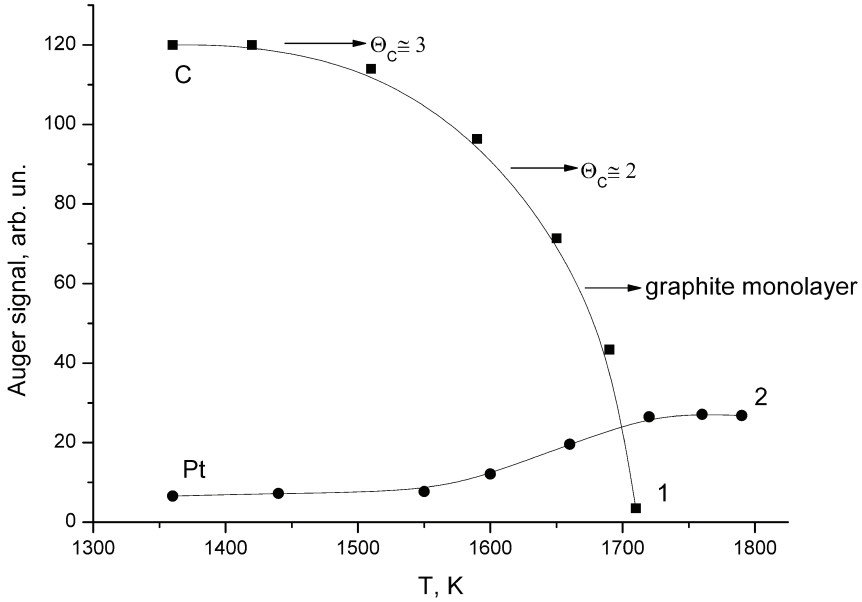

Fig. 43. Auger signals of carbon (1) and Pt (2) versus annealing temperature in carbon precipitation from the solid solution Pt-C. Carbonization temperature is 1670 K, initial carbon concentration in the substrate bulk is $N_C = 1 * 10^{11}$ cm^{-2} per each interstitial plane. $I_C = 55$ a.u. corresponds to the graphene layer with the surface carbon concentration $N_C \sim 3.5 * 10^{15}$ cm^{-2}.

3. Carbon segregation onto the surface of molybdenum [9]

In contrast to rhenium, rhodium, and nickel, carbon segregates to molybdenum surface only after formation of the Mo_2-C volume carbide has come to an end over all of the ribbon thickness (§ 1). Therefore, in this case we deal actually with a solid solution of carbon in the Mo_2C volume carbide. The kinetics of carbon segregation at T = 1200 K to the surface of molybdenum (T_c = 1670 K) obtained by AES at T = 1200 K is visualized in Fig. 44. The falloff of the molybdenum Auger signal intensity down to background level implies growth of a thick graphite film.

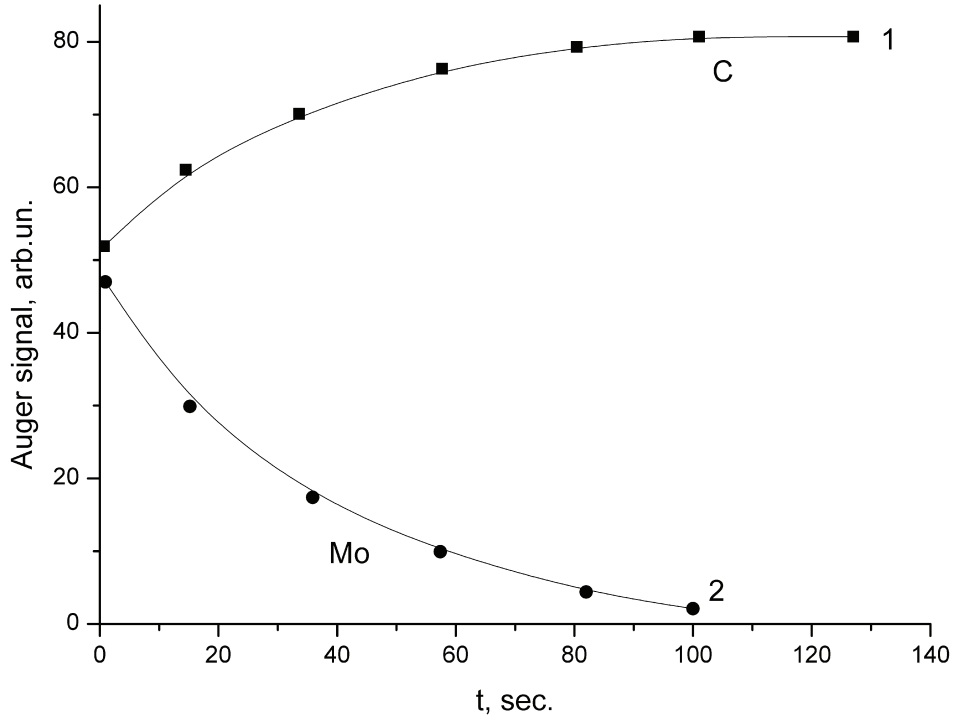

Fig. 44. Auger signals of carbon (1) and Mo (2) versus heating time in annealing of the carbonated Mo at 1200 K. Carbonization temperature is 1670 K.

4. Formation of thick graphite films on iridium [41]

As already pointed out, exposure of heated iridium samples to benzene vapor brings about formation of one graphene layer only. Experiments revealed that a thick film of carbon grows under incidence of a flux of carbon atoms. Figure 45 displays graphs relating the Auger peak intensities of carbon and iridium with the time of evaporation of carbon atoms at T = 1600 K. We readily see that the iridium Auger peak intensity falls by a factor of 16 for t = 600 s, to melt into the background for t > 800 s. The Auger spectrum of carbon obtained from a thick (θ_c ~ 4) graphite film presented in Fig 46 (spectrum1) is completely similar in shape to that of single-crystal graphite. Close results are obtained when carbon atoms are evaporated onto iridium in the 1100--1900-K region.

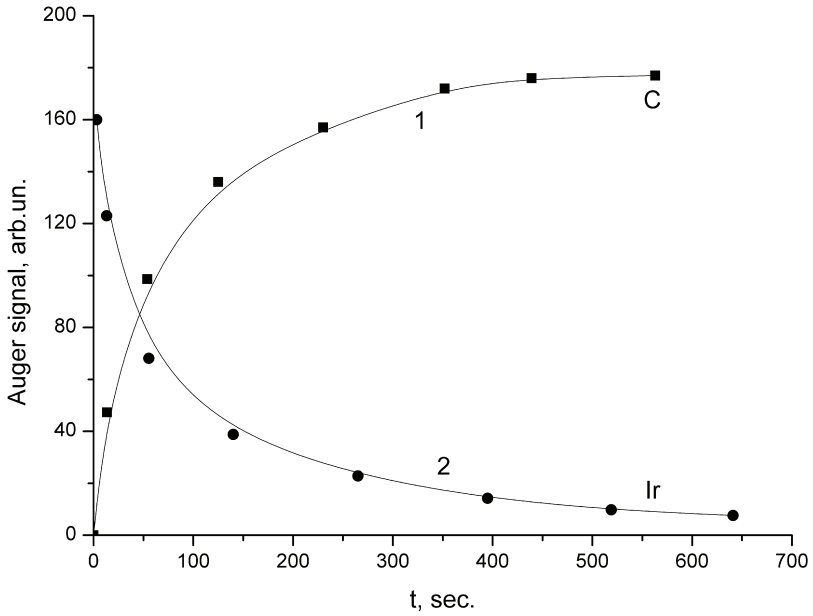

Fig. 45. Auger signals of carbon (1) and Ir (2) versus deposition time in atomic carbon deposition on Ir(111) at 1600 K. The deposition flux is $\nu_C = 7 * 10^{13}$ $cm^{-2}*s^{-1}$, $I_C = 85$ a.u. corresponds to the graphene layer.

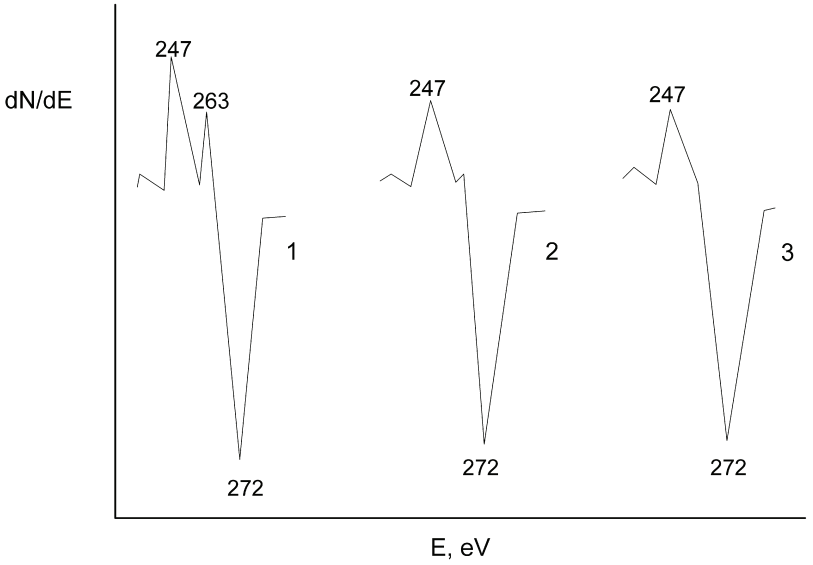

Fig. 46. Carbon KVV Auger spectra for carbon films of about 4 layer thick, deposited onto Ir(111) at the various temperatures, K: 1- 1800, 2 - 900, 3 - 300. the spectra are identical for the range 1100 - 1800 K.

Evaporation of carbon on graphene-coated Ir(111) at T < 1000 K initiates growth of a disordered carbon film atop the graphene, with the carbon Auger spectrum acquiring the typical shape of pyrographite (spectra 2 and 3 in Fig. 46).
When carbon is evaporated at $T \geq 1100$ K, its atoms migrate actively under the graphene film to form the second layer of graphene on the surface of iridium. In this case, the growth rate of graphene layers at ν_c = const falls off with increasing thickness of the graphene film, because the probability for a carbon atom to be desorbed from the surface of the graphite film increases progressively compared with that to migrate under the film down to the metal.
For $T \leq 1000$ K, the rate of growth of a carbon layer is constant for ν_c = const.

§9. Mechanism of growth of a thick graphite film on the surface of supersaturated solid solution of carbon in a metal

The graphene film "raised over" the metal
does not interfere with nucleation and growth of
subsequent layers through segregation of carbon
from a supersaturated Me-C solid solution.

It is common knowledge that such atoms as C, Si, B, P, S, H, N, O diffuse over the volume of the metal by migrating over the interstitial sites of the metal lattice [117]. Segregation of "non-gas" atoms from the volume onto the surface culminates most frequently by formation of a diffusant monolayer. Then why do we observe on the surface of carbon-containing metals and alloys whose volume is supersaturated with carbon formation of a thick graphite film?
Information on the structure of a carbon adlayer on metals accumulated recently provide an explanation for the anomalous behavior of carbon. We are going to use also present concepts of the first-order phase transition of the type of two-dimensional condensation in a carbon adlayer on metals, which suggests the possibility of coexistence on the surface of two carbon phases, more specifically, of chemisorbed "gas" and two-dimensional graphene islands. In the initial stage of film growth on a heated metal, as long as the critical coverage θ_c has not been reached, carbon resides on the surface in the form of chemisorbed "gas" (A in Fig. 47a). For $\theta > \theta_c$, close-packed carbon islands form and attain equilibrium with the chemisorbed carbon "gas" (B in Fig, 47a). A small enough carbon island may not have yet graphitic structure and rests chemisorbed on the surface. On reaching a certain critical size, the island acquires graphitic structure and becomes coupled to the metal by van der Waals forces (C in Fig. 47a). Therefore, the adlayer under the graphite islands becomes filled by chemisorbed carbon "gas" through diffusion of carbon from the bulk of the metal until second-layer islands start to grow on having reached a certain coverage (D in Fig. 47a). The central part of such an island rises from the metal surface up to the equilibrium height defined by van der Waals forces. A first-layer graphene island may interfere with this process, and the second-layer island will try to force it out of the way (E in Fig. 47b). As a result, the first-layer graphene island will be acted upon by two forces, namely, that of expulsion $F_{ex} \sim R^2$ (R is the island radius) and the other, from attraction from the side of the metal $F_{att} \sim R$, which acts along the island periphery. As the area of the second-layer island grows, the expulsive force may become larger than the attractive one, which will culminate in the first-layer graphene island tearing away from the metal surface (F in Fig. 47), Thus, this mechanism operating on the metal surface may give rise to growth of a thick graphite film through segregation of carbon out from the bulk of the metal.

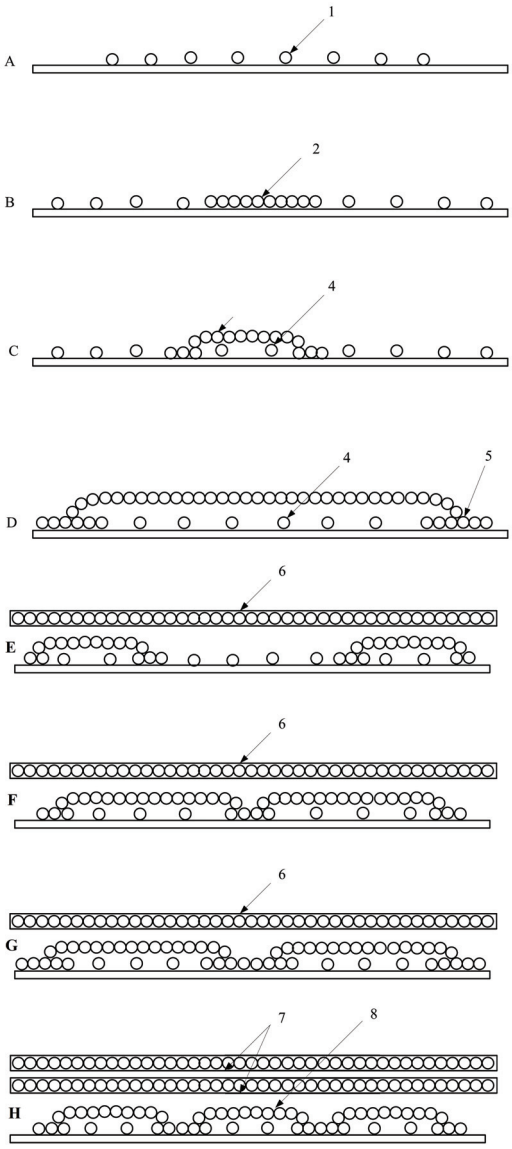

Fig. 47. A model scheme showing sequential growth of a polylayer graphite film on a metal by carbon precipitation from the substrate bulk: 1 - chemisorbed 2D carbon 'gas'; 2 - nucleation of a carbon island; 3 - graphene island; 4 - carbon 2D 'gas' under the graphene island; 5 - non-graphitic edge of the island; 6 - finalization of the first layer growth and nucleation of the second layer; 7 - finalization of the two graphene layers and nucleation of the third layer; 8 – graphene islands of the third layer.

This mechanism is supported by the observation of the edges of first-layer graphene islands detaching from the surface during carbon segregation from a supersaturated Re-C solid solution. In this experiment, rhenium was carbonized in benzene vapor at T_c = 1800 K up to formation of graphene on its surface, after which it was cooled rapidly down to 300 K, Cesium atoms were adsorbed to saturation on the graphene film at 300 K, with the cesium becoming distributed equally between the α-phase (atop graphene) and γ-phase (cesium buried under the graphene film), with $N_\alpha = N_\gamma \approx 5\ 10^{14}$ at/cm^2 (see below). After this, the rhenium ribbon was heated rapidly to $T = T_c$ = 1800 K. It was found that all of the cesium desorbed from the α phase, leaving cesium buried in the γ phase under the graphene layer with a concentration $N_\gamma \approx 8\ 10^{13}$ at/cm^2. This cesium could be removed in one of two ways. In the first way, the ribbon temperature was raised to T = 2200 K, where the graphene film broke down completely. Incidentally, if one intercalates a thick graphene film on a metal at 300 K with Cs atoms and raises thereafter the temperature to $T \sim 1000$ K, all of the intercalated cesium will end up desorbed, as this was observed with single-crystal graphite [62]; in this case, the graphene layer edges will not close onto the surface. Cesium will remain buried under the graphene islands only in the lowest layer contacting the metal. In the second approach, cesium could be removed completely from the surface by lowering T below T_c! In this case, at $T < T_c$, the Re-C solid solution supersaturates, thus initiating carbon segregation to the surface, which brings about detachment of the edges of first-layer graphene islands, with the attendant escape of cesium atoms from under the graphene traps and desorption from the surface (Fig. 48). The desorption of cesium was followed by measuring the Cs^+ ion current, a highly sensitive method, because each cesium atom desorbed in the form of the Cs^+ ion as a result of surface ionization [39]. Figure 48 displays in graphical form the dependence of the Cs ion current on time after the lowering of T from T_c = 1800 K to T = 1570 K. This procedure removes all of cesium from the γ phase, and the variation of the Auger peak intensities of carbon and rhenium visualized growth of the graphite film thickness.

The proposed mechanism of growth of a thick graphite film on the surface of a metal rests on a number of conditions. First, carbon islands growing in the adlayer should have graphitic structure, because only graphite is a valence-saturated state of carbon, in contrast, for instance, to chemisorbed atoms and clusters or carbides. Second, for a thick graphite film to grow, the edges of first-layer graphene islands should be able to break off the surface of the metal. If the island edges detach at $\theta_c < 1$, a multilayer graphite "tower" will grow over each graphene island, with the result that the graphite film will not be continuous in the initial stages of its growth. Incidentally, in Me-C systems two types of carbon segregatation on the surface were observed. In segregation of the first type, the dependence of the carbon Auger signal on substrate temperature T has three characteristic regions (Fig. 49A). In region "A", the Me-C solid solution is not saturated, with chemisorbed carbon "gas' present on the surface. In region "B" ($T < T_c$), extending over ~ 40--70°, the surface is coated by a graphene layer (see, e.g., Fig. 49A). In this region, the solid solution becomes supersaturated with decreasing temperature, and the graphite film will not grow above one monolayer thickness. It appears reasonable to assign the absence of growth of a graphite film above monolayer thickness to the observation that in order for the second-layer graphene islands to nucleate, the coverage θ_c should exceed a critical level which is larger than that required for the first layer to form. Therefore with T decreasing still more, supersaturation grows to an extent where the required coverage θ_c is reached, at which the second-layer islands grow, $F_a > F_b$, and the edge of a first-layer graphene island detaches from the surface. Therefore, in region "C" in Fig. 49A a multilayer graphite film grows layer by layer.

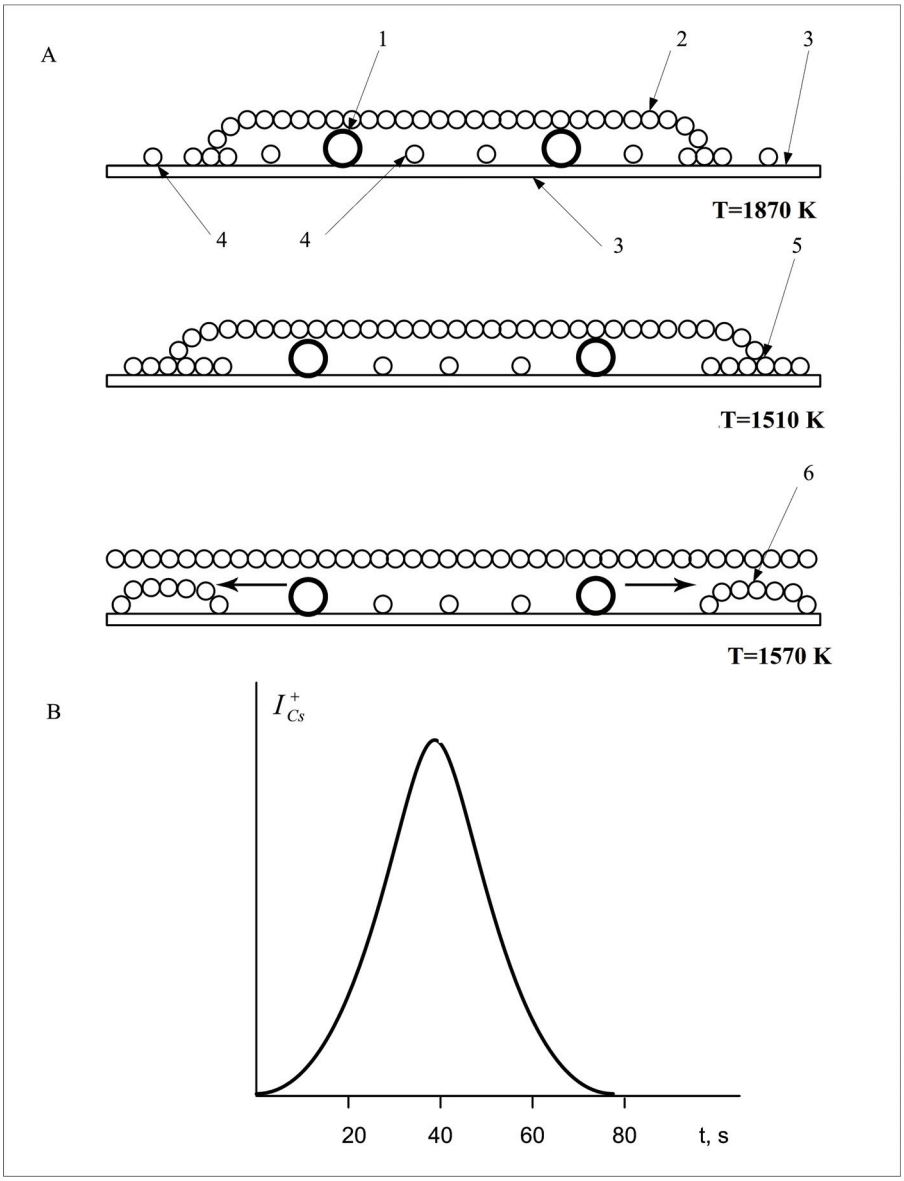

Fig. 48. Desorption of Cs^+ ions in their release from the graphite island at temperature decrease from 1870 K to 1570 K. A - thermal desorption spectrum. B - A model scheme showing oversaturation of the solid solution Me-C, carbon precipitation onto the surface and Cs^+ release. 1 – Cs atom under a layer of graphene – the output of cesium from the islands is difficult; 2 – graphene island; 3 – rhenium substrate; 4 – carbon atoms in the phase of two-dimensional "gas"; 5 – carbon atoms at the edges of graphene islands; 6 – graphene islands of the second layer – the output of cesium greatly facilitated.

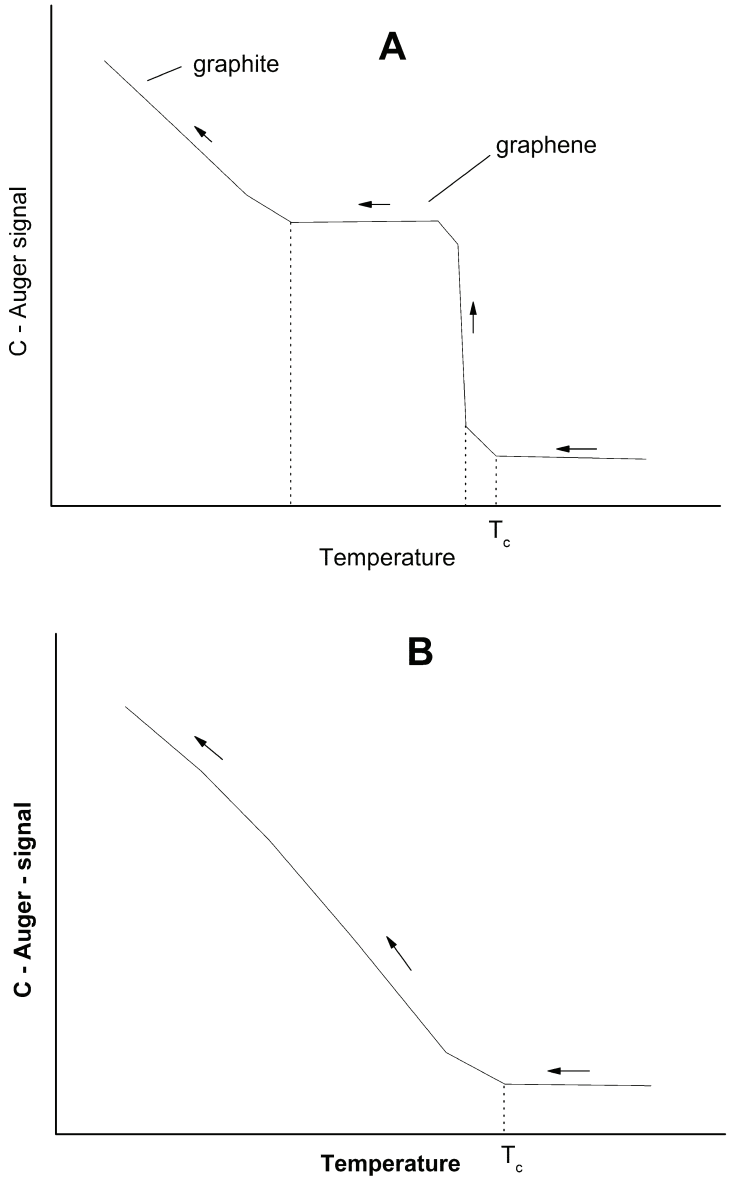

Fig. 49. A model carbon Auger signal versus temperature and film structure for two possible variants of carbon precipitation form the substrate bulk onto the surface: A - the first type; B - the second type.

Carbon segregation of the first type from supersaturated Me-C solid solutions was observed on Ni(111) [118], Pd(100) [7], Pd(111) [7], polycrystalline Pd [16], Co(0001) [7], Mo(100) [8], Re(1010) [11], polycrystalline Re [119], and Rh [27].
The dependence of the carbon Auger signal intensity on T in segregation of the second type is displayed graphically in Fig. 49B. The carbon signal continues to grow as T decreases, because in these conditions multilayer graphite towers surrounded by chemisorbed carbon "gas" grow on the metal surface. Film growth does not pass here through the stage of formation of a graphene film. This growth may be expected if the $F_a > F_b$ condition is reached before the formation of the graphene film came to an end. Segregation of the second type was observed to take place on Pt(100) [7], Fe(100) [120], and Pt(111) [2].

§10. Three-dimensional phase transition in the Me-graphite system

This transition gives rise to growth of
the volume graphite phase, i.e., polylayer graphite films.

The two-dimensional phase transition in a carbon layer on a metal was studied in considerable detail for the Ir(111)-C system (§5). It appeared reasonable to expect that under certain conditions a three-dimensional phase transition would occur, in which volume graphite phase of carbon would form. As pointed out in §8, many Me-C systems exhibit a stable temperature interval $\Delta T \approx 40$--70^{o} within which a continuous graphene film can exist (Figs. 6 and 15 in §1). Further cooling of the carbonized metal initiates intense growth of graphite films. For illustration, consider the physical processes occurring in the Rh(111)-C system as visualized by studying thermionic emission. Rhodium was carbonized at T_c = 1720 K, after which the temperature was increased to T = 1820 K, and lowered subsequently in small temperature steps. Figure 50 plots variation of the thermionic current in logI^-vs. ribbon heating current coordinates, with the top scale referring to the sample temperature. Now what do we see? In region AB, the low-density chemisorbed carbon "gas" covering the surface practically does not change the surface work function $e\varphi$ = 4.95 eV, and the current I^- falls off in accordance with Eq. (1) of §5. Point B identifies the two-dimensional phase transition, graphene islands form and thermionic emission rises, because for graphene islands $e\varphi$ = 4.35 eV.
In region BC, islands grow in area and coalesce to form a continuous graphene layer (C in Fig. 50).In region BC, equilibrium obtains among the graphene islands (§7, item 6).
In region DC, the graphene layer is stable, with AES producing a wing (Figs. 6 and 15 in §1).
An intriguing and important feature is awaiting us at point D: lowering the temperature by 3--5^{o} brings about a drop of the thermionic current by nearly four orders of magnitude! Auger electron spectroscopy reveals a thick graphite film to have grown on the surface, which suppresses the strong rhodium Auger signal. In region DE, the brightness temperature of the sample decreases by $\Delta T \sim 300^{o}$ too (sic!); this effect is seen by naked eye. A sharp decrease of the brightness temperature was observed for the Rh-C and Re-C systems earlier [121,122] and attributed to formation of a thick graphite film, which reduces markedly the spectral coefficient of emissivity from $\varepsilon_\lambda = 0.24$ characteristic of clean rhodium to $\varepsilon_\lambda \approx 0.8$ for graphite [123]. Now the true ribbon temperature decreases strongly too, which initiates a drop in thermionic emission by several orders of magnitude. Therefore the ribbon temperature for region EF in Fig. 50 is not specified. Nevertheless, if we repeat a pyrometric measurement of ribbon temperature in region EF with due account of $\varepsilon_\lambda = 0.8$ and construct a Richardson graph, the graphite work function can be found, which turned out to be 4.65 eV (§7).

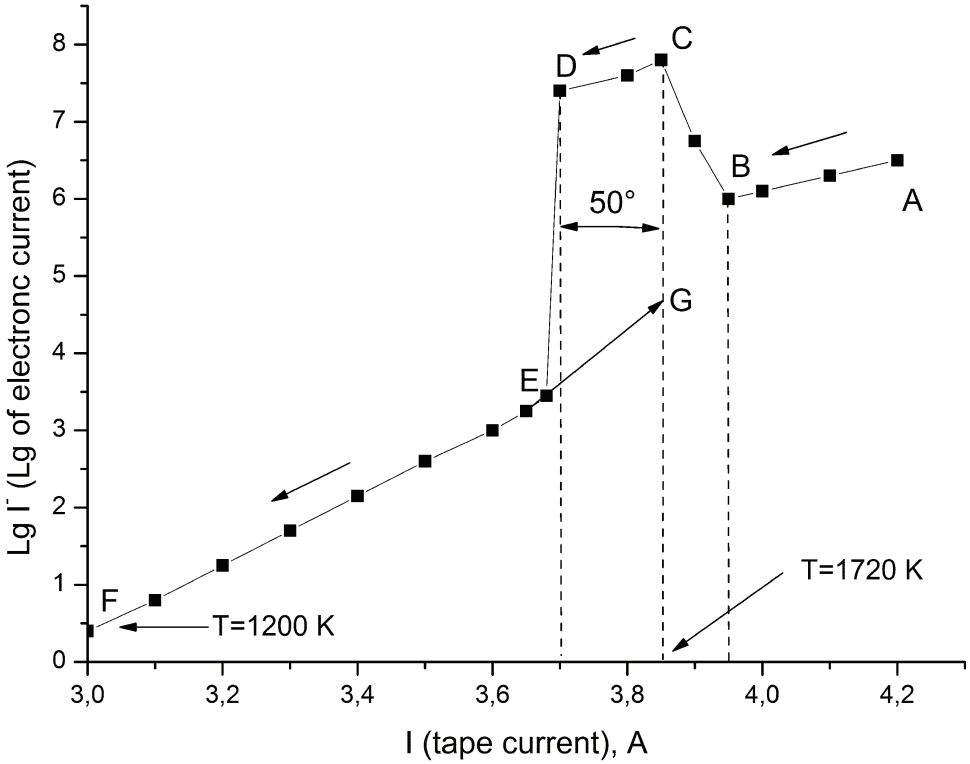

Fig. 50. Thermionic current from the surface of carbonated Rh (T_C = 1720 K) in decreasing of the current heating the ribbon.

Reverse heating (F → E) reveals a noticeable hysteresis, with the curve choosing region EG, because the true temperature at point E is lower now by a few hundred degrees than the former value of T = 1680 K, and additional heating is required to destroy the graphite film. Knowing the solubility limit of carbon in rhodium and varying properly the carbonization temperature T_c (**§**1), one can readily calculate the number of "excess" carbon atoms freed by the decrease of temperature ($T < T_c$) and determine the effect of the thickness of a graphite layer on variation of the brightness temperature. Experiments showed that for thicknesses below 10 layers the sample temperature does not change. For thicknesses above 40--50 layers, the emissive optics of the system is governed by the graphite film.

§11. Graphitization of carbon films on a metal surface

Temperature is a major factor
mediating graphitization

Significantly, adsorption of carbon on a metal at low T either does not initiate formation of graphene films or such films turn out to be heavily defective. This should apparently be attributed to the large number of carbon clusters in the layer and the islands being too small and not graphitic yet. Consider an illustrative example of graphitization of carbon films

adsorbed at a low temperature on Ir(111) [114]. Obviously enough, these conditions depend strongly on carbon layer thickness.

Recall, necessarily briefly, the methods used to detect the presence of graphene on the surface of a metal.

1. ***Through catalytic dissociation of CsCl molecules.*** This method, proposed by A. Ya. Tontegode [27], consists in probing the surface with a flux of CsCl molecules. One of the products of dissociation of these molecules are cesium atoms. On the surface of refractory metals, graphite, and other carbon films the relation $V_{Cs} < \varphi$ holds, and, therefore, each cesium atom desorbs from a heated surface in the form of the Cs^+ ion, which facilitates markedly detection of one of the products of dissociation and makes the method highly sensitive.

As shown earlier, it is only carbon present in the form of graphite that reduces markedly the efficiency of dissociation of CsCl molecules. Therefore, the degree of dissociation $\omega = I^+/I_0^+$ can be found by measuring the total cesium current from a clean iridium surface, $I_0^+ = e\nu S$, and the current $I^+ = e\nu S\omega$ from the surface of iridium coated by a carbon film (ν is the CsCl flux density). On clean metals, a chemisorbed carbon film, carbon clusters, and surface carbide $\omega \sim 1$. By contrast, on the graphene phase of carbon $\omega = 10^{-3}$--10^{-5}, thus making it possible not only to detect the presence itself of graphite on the surface but to determine the relative area occupied by this phase. The shortcoming of this method is its becoming inapplicable at $T < 900$ K, when cesium atoms no longer desorb from a metal coated by a carbon film.

2. ***From the shape of the carbon Auger spectrum.*** The shape of the Auger spectrum of carbon is extremely sensitive to the chemical state in which it resides on the surface (**§**3). This method is applicable over a wide range of temperatures (in the present study, 300--2500 K).

3. ***From a change in the shape of carbon Auger spectrum in adsorption of alkali metals.*** It was shown that adsorption of Cs, K, and Na on a graphene film atop a metal modifies strongly the shape of the high-energy part of the carbon Auger spectrum, more specifically, the negative spike in the spectrum splits into three peaks located energy-wise at 272, 276.5, and 281 eV (Fig. 14, spectrum 5). At the same time, adsorption of alkali metals on a monolayer of chemisorbed (non-graphite) carbon does not initiate such changes. This method turned out fruitful in detection of the graphite phase.

4. ***By application of TDS.*** It is known that cesium present on refractory metals desorbs completely from the surface at $T \leq 900$ K. Cesium atoms adsorbed on carbon (non-graphite) films are desorbed totally in the 900--1100-K interval. If, however, cesium atoms are adsorbed at 300 K on graphene-coated iridium to saturation, the TD spectrum will reveal two phases: a low-temperature (~900 K) and a high-temperature (~2000 K) ones, the latter being associated with cesium escaping from under the graphene film in the course of its destruction. Thus the presence in a TD spectrum of the high-temperature phase implies unambiguously the presence of the graphene phase of carbon on the metal surface in submonolayer coverages.

5. ***From the work function.*** The work function of a chemisorbed carbon film, for instance, on iridium is larger by 0.3 eV than that of graphene film. Therefore, graphitization should be accompanied here by a decrease of the work function.

Graphitization of a film evaporated on iridium. Carbon atoms were evaporated at 300 K on iridium up to $\theta \approx 1.5$; this coverage implies complete filling of the first layer with carbon, the second layer containing carbon to $\theta = 0.5$. At $\theta = 1.5$, the surface work function varying from 5.75 eV to 4.75 eV becomes stabilized. Tests for graphite (involving cesium adsorption)

demonstrated that the film prepared by this method is non-graphitic (Fig. 51, spectrum 2). After this, the carbon film was annealed for 10 min at each temperature point and analyzed again. It was found that only after annealing at T = 1300 K did adsorption of cesium atoms initiate noticeable appearance of a fine structure in the carbon Auger spectrum (3 in Fig. 51). The degree of graphitization increased with increasing temperature, until at T = 1500 K graphitization of the carbon film came to completion; indeed, adsorption of Cs atoms brought about now the appearance of a fine structure in the Auger spectrum of carbon like that from a graphene film (Fig. 51, spectrum 5). The onset of complete graphitization is corroborated also by a decrease of the surface work function from 4.75 down to 4.45 eV.

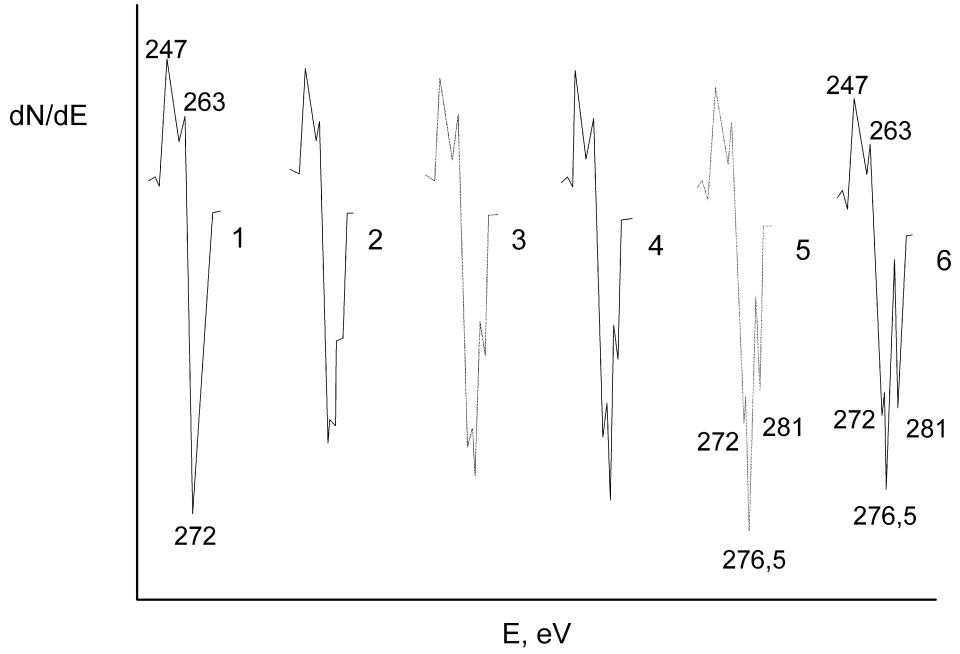

Fig. 51. Transformation of carbon KVV Auger spectra in adsorption of atomic Cs to saturation. The carbon film was got by atomic carbon deposition at 300 K (θ_C ~ 1.5) with sequential annealing at various temperatures, K: 1- 300, 2 - 800, 3 - 1300, 4 - 1400, 5 - 1500, 6 - 1600. The total amount of the adsorbed Cs in saturation for the spectrum 6 is twice as high as for the spectrum 2.

The processes involved in graphitization can be studied through dissociation of CsCl molecules too. Figure 52 plots the variation of the degree of dissociation ω with the heating time of a chemisorbed carbon layer (θ ~ 1.5--2) for two substrate temperatures. We readily see that the major changes take place during $t \approx 30$ s of heating, while subsequent heating (~ 10 min) produces very little effect. At T = 1300 K, ω drops to ω = 0.1 only, which suggests incomplete graphitization. At T = 1600 K, the graphitization comes to completion, with ω = 10^{-3}, which corresponds to a graphene film. Figure 53 illustrates the behavior of the ω(T) relation for a carbon film with θ = 1.5 chemisorbed at 300 K, which was studied under stepped heating from 1200 to 1600 K (at each point, ω was measured 30 s after the

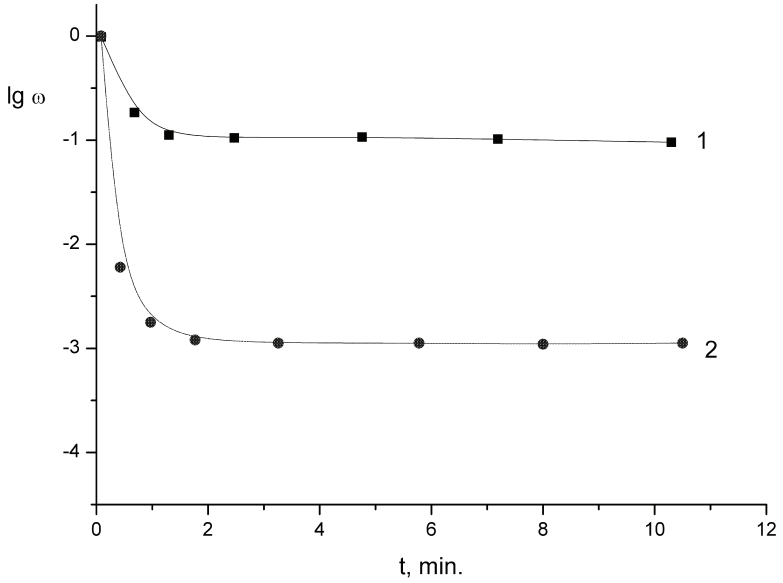

Fig. 52. The dependence of lgω for molecular CsCl from annealing time of the carbon layer deposited at 300 K with $\theta_C \sim 1.5$ for two substrate temperatures, K: 1 - 1300; 2 - 1600. The deposition flux of molecular CsCl is $\nu_{CsCl} = 1 * 10^{12}$ cm^{-2}*s^{-1}.

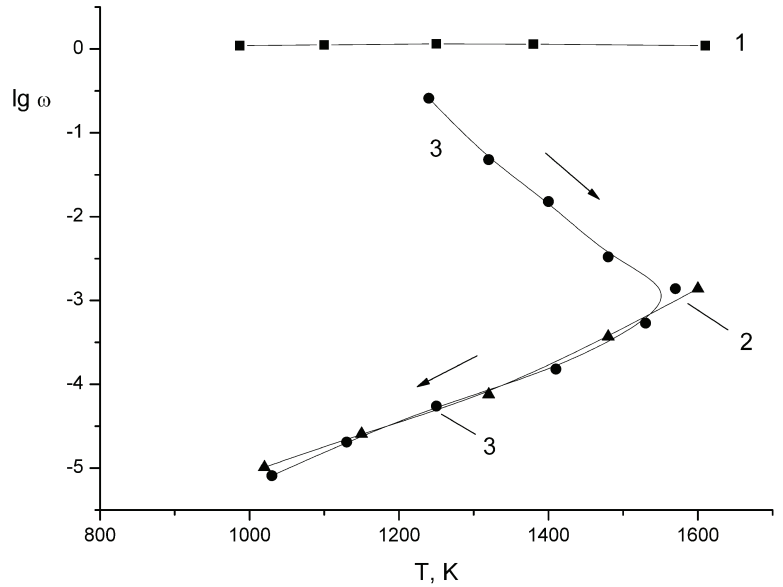

Fig. 53. The dependence of lgω for molecular CsCl from temperature for three surfaces: 1 - pure Ir(111); 2 - graphene single layer on Ir(111); 3 - carbon layer deposited at 300 K with $\theta_C \sim 1.5$ Exposure at each point is 10 s; $\nu_{CsCl} = 1 * 10^{12}$ cm^{-2}*s^{-1}.

temperature had been raised). On reaching complete graphitization, decrease of temperature reproduces the ω(*T*) relation obtained with a graphene film (Fig. 53). This suggests that graphitization of a carbon film with θ = 1.5 chemisorbed at 300 K occurs in the 1300--1500-K temperature interval. Interestingly, evaporation of carbon atoms on heated iridium affects favorably graphitization, in that its temperature interval shifts toward lower temperatures, 950--1100 K, and comes to completion at 1100 K.

One can reasonably suggest that carbon atoms adsorbing on a heated substrate at $T \sim 1000$ K fit immediately into the thermally favorable graphite phase. In the case of a carbon film chemisorbed at 300 K, a variety of different carbon structures form on the surface, and, therefore, graphitization requires expending an activation energy to break different C-C bonds, a factor that curtails graphitization.

Graphitization of a carbon layer formed on a graphene film atop iridium. The experiment was started by producing a graphene film on iridium at T = 1700 K in benzene vapor, after which carbon was evaporated at 300 K on the graphene to $0.1 \le \theta \le 150$. The graphitization of the carbon films thus formed was studied at T = 1300 K by CsCl dissociation (Fig. 54). We readily see that evaporation on a graphene film of carbon atoms stimulates growth of ω, which is the more pronounced, the larger the evaporated carbon dose. For instance, for $\theta \sim 100$, ω = 0.6, and this carbon film approaches in its catalytic properties a metal, for which ω = 1. To make graphitization of thick carbon films with $\theta \approx 100$ complete, temperatures in excess of 2200 K were required.

The decrease of ω(*T*) for *T*= const evident in Fig. 54 can be assigned to partial graphitization of carbon films.

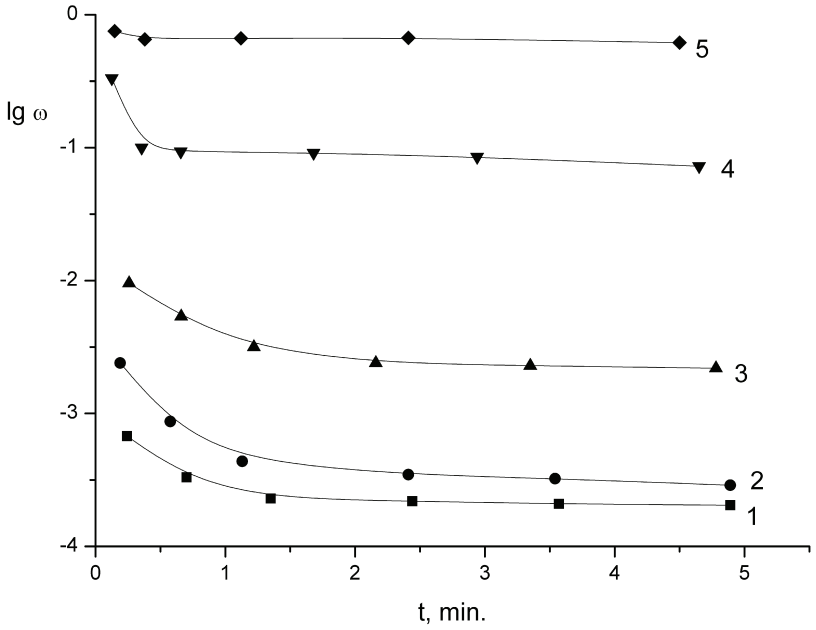

Fig. 54. The dependence of lgω for molecular CsCl from annealing time of the carbon layer deposited at 300 K with θ_C, arb.un.: 1 - 1.1; 2 - 1.4; 3 - 2.6; 4 - 9, 5 - 100. Annealing temperature is 1300 K; $\nu_{CsCl} = 1 * 10^{12}$ cm^{-2}*s^{-1}.

Graphitization of carbon films on iridium prepared by adsorption of benzene molecules. Experiments demonstrated adsorption of benzene vapors on a heated iridium surface at high temperatures, 1500--1800 K, to culminate in formation of a graphene film. At lower temperatures, the carbon film prepared by adsorption of benzene undergoes graphitization in the temperature region $1100 < T < 1400$ K, with the process being only partial at $T < 1400$ K, to become complete for $T \geq 1400$ K (the test for graphite was effected by adsorption at 300 K of Cs atoms which brought about the change of the carbon Auger peak shape, namely, the appearance of "splitting").

It is instructive to follow the process of graphitization occurring in adsorption of benzene molecules on iridium at 300 K to saturation, with subsequent annealing of the film. Spectrum 1 in Fig. 55 corresponds to a benzene monolayer. At $T \sim 800$ K, desorption of hydrogen [124] produced in the breakup of benzene molecules on iridium sets in, and a carbon film, consisting apparently of carbon cores of benzene molecules and their cluster fragments, forms on the surface. Tests on graphite performed after the annealing of such a film at 900 and 1000 K (spectra 2 and 3) showed the film to be non-graphitic. Graphitization starts at anneal temperatures $T > 110$ K, with the process coming to completion at $T = 1400$ K. The end result is formation on the surface of graphene islands over a relative area $s_0 \sim 0.5$. The graphitization is accompanied by a slight modification of the carbon Auger peak shape (spectra 4 and 5 in Fig. 55).

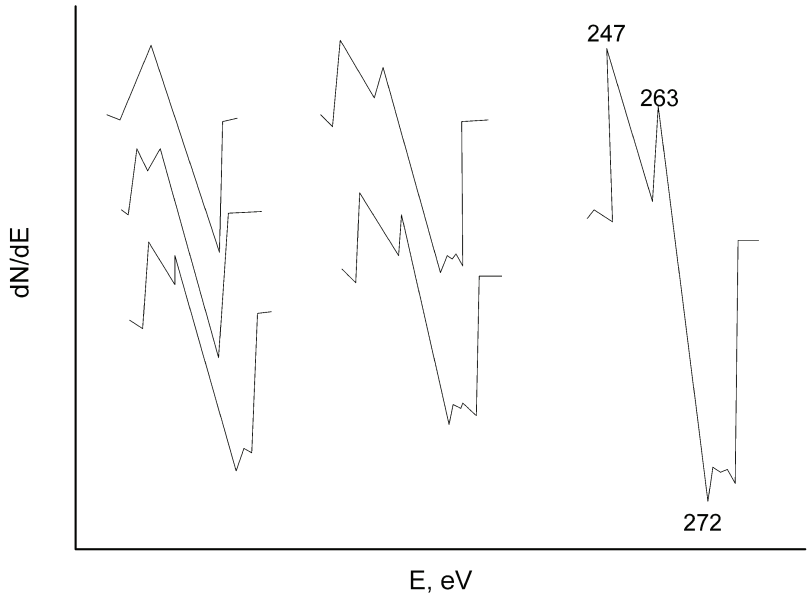

Fig. 55. Transformation of carbon KVV Auger spectra for benzene vapor adsorbed to saturation onto Ir(111) at 300 K in surface heating at various temperatures, K: 1 - 300 (spectrum remains unchanged up to 600 K); 2 - 900; 3 - 1040; 4 - 1280; 5 - 1400 (spectrum remains unchanged up to 1850 K). the spectrum 6 corresponds to the single graphene layer on Ir(111).

Significantly, the high temperature ($T \approx 1400$ K) required for complete graphitization of carbon films prepared by low-temperature adsorption of benzene suggests that it is indeed rupture of C-C bonds in carbon clusters that is the limiting stage of the process, because complete graphitization of films of atomic composition takes place at $T \approx 1100$ K. Clusters may form on the surface through adsorption of already existing clusters in evaporation, say, of carbon from pyrographite ribbons, association of carbon atoms in the layer, and adsorption and breakup of molecules of hydrocarbons producing cluster fragments.

A. Ya. Tontegode [27] and N. R.Gall, E. V. Rut'kov and A. Ya. Tontegode [41] studied the conditions favoring graphitization on other substrates as well, namely, Re, Pt, and Ni, which are among the most widely used industrial catalysts. It was shown that thin carbon films (one to two layers thick) undergo graphitization at moderate temperatures $T \sim (1100 \pm 250)$ K. Listed below in Table 9 are the temperature intervals within which one layer of carbon chemisorbed at 300 K on different metals can be graphitized, with the upper T referring to the onset of graphitization, and the lower one, to complete graphitization of the layer.

Examining the table shows that the conditions favoring graphitization are different for different metals. On nickel, graphitization occurs at the lowest temperatures of all.

Me	Ir(111)	Re(1010)	Pt(111)	Ni(111)
	1200	1100	950	750
T, K	1500	1500	1100	850

Table 9.

12. References

[1] Palmberg P.W. In: The Structure and Chemistry of Solid Surfaces. Eds. G.A. Somorjai, J. Wiley. N.Y., 1969.
[2] Hamilton J.C., Blakely J.M. J. Vacuum Sci. Technol. 1978. V.15. P. 559-562.
[3] Grant J.T., Haas T.W. Surf. Sci. 1970. V. 21, P. 76-85.
[4] Coad J.P., Riviere J.C. Surf. Sci. 1971. V. 25. P. 609-624.
[5] Shelton J.C., Patil H.R, Blakely J.M. Surf. Sci. 1974. V. 43. P. 493-503.
[6] Eizenberg M., Blakely J.M. Surf. Sci. 1979.V. 82(1). P. 228-236.
[7] Humilton J.C., Blakely J.M. Surf. Sci. 1980. V. 91(1). P. 199-217.
[8] Gillet E.J. Less-Common. Met. 1980. V. 71(1). P. 277-291.
[9] Rut'kov E.V., Tontegode A.Ya., Usufov M.M., Gall N.R. ЖТФ. 1992. V. 62(10). P. 148-153.
[10] Beitel G.A. J. Vac. Sci. and Technol., 1969. V. 6. P. 224-228.
[11] Gall N.R., Mikhailov S.N., Rut'kov E.V., Tontegode A.Ya. Surf. Sci. 1987. V. 191. P.185-202.
[12] Rut'kov E.V., Gall N.R., Physics of the Solid State, 2009, Vol. 51, No. 8, pp. 1738–1743
[13] Kholin N.A., Rut'kov E.V., Tontegode A.Ya. Surf. Sci. 1984. V.139. P. 155-172.
[14] Tontegode A.Ya., Rut'kov E.V. Surf. Sci. 1985. V. 161. P. 373-389.
[15] Ageev V.N., Rut'kov E.V., Tontegode A.Ya., Kholin N.A. Fiz. Tverd. Tela, 1982. V. 24(3). P. 780-786.
[16] Abdullaev R.M., Tontegode A.Ya. Zh.Tech. Fiz. 1980. V. 50. P. 577-581.
[17] Tilley B., Aizava T., Souda R., Hayami W., Otani S., Ishizava Y. Solid State Communications. 1995. V. 94. P. 685.
[18] Nagashima A., Itoh H., Ishinokava T.,.Oshima C, Otani S. Phys. Rev. B. 1994. V. 50. P. 4756.
[19] M.W.Roberts, C.S.McKee "Chemistry of the metal-gas interface", Clarendon Press, Oxford, 1978, pp.300-331

[20] Gall N.R., Makarenko I.V., Titkov A.N., Waqar Z., Rut'kov E.V., Tontegode A.Ya., Usufov M.M., Poverhnost, 1999. V. 7. P. 39-42.
[21] Waqar Z., Makarenko I.V., Titkov A.N., Gall N.R., Rut'kov E.V., Tontegode A.Ya. J. of Materials Research (JMR). 2004. V 19(4). P. 1058-1061.
[22] Klusek Z., Kozlowski W., Waqar Z., Patta S., Buenell-Gray J.S., Makarenko I.V., Gall N.R., Rut'kov E.V., Tontegode A.Ya., Titkov A.N. Applied Surface Science. 2005. V. 252. P. 1221-1227.
[23] Makarenko I.V., Titkov A.N., Rut'kov E.V., Gall N.R. Izvestia RAN (Seria fizicheskays) 2007. V. 71(1). P. 57-60.
[24] Rut'kov E.V., Tontegode A.Ya. Fiz. Tverd. Tela, 1996. V. 38(2). P. 635-639.
[25] E.Fromm, E.Gebhardt "Gase und Kohlenstoff in Metallen", Springer-Verlag, Berlin, 1976
[26] Gall N.R., Rut'kov E.V., Tontegode A.Ya., Kuznetsov P.B., Gall R.N. J. Chemical Vapor. 1997. V. 6(10. P. 72-75.
[27] Tontegode A.Ya. Progress in Surface Science. 1991. V. 38(3-5). P. 429.
[28] Fomenko V.S. Electronic properties of materials. Reference-book, Kiev< Naukova Numka, 981, 336 c.
[29] Gall N.R., Rut'kov E.V., Tontegode A.Ya. Rossiiski Himichesky Zurnal, 2003. V. 47(2). P. 13-22.
[30] Ageev V.N., Afanasieva E.Yu., Gall N.R., Mikhailov S.N., Rut'kov E.V., Tontegode A.Ya. Poverkhnost. 1987. V. 5. P. 7-14 (in Russian).
[31] Gall N.R., Rut'kov E.V., Tontegode A.Ya. Zh.Tech. Fiz., 1990. V. 60(4). P. 125-130.
[32] Gall N.R., Rut'kov E.V., Tontegode A.Ya., Usufov M.M. Pisma v Zh.Tech. Fiz., 1994. V. 20(18). P. 65.
[33] Gall N.R., Rut'kov E.V., Tontegode A.Ya., Usufov M.M. Applied Surface Science. 1996. V. 93. P. 353-358.
[34] Gall N.R., Rut'kov E.V., Tontegode A.Ya., Usufov M.M. Applied Surface Science. 1994. V. 78. P. 179-184.
[35] Shank F.A. Structure of Binary Alloys Moscow, Metallurgia, 1973, 568 p. (in Russian)
[36] Rut'kov E.V., Tontegode A.Ya., Usufov M.M. Известия РАН (серия физическая). 1994. V. 58. P. 102-105.
[37] Schulze G. Metallophysika. M.: Mir, 1971. 404 p. (in Russia)
[38] Anderson J. Structure of Metal catalysts, Mocsow, MIR, 1978. 482 p (in Russian).
[39] Zandberg E.Ya. and Ionov N.I. Surface Ionization. Israel Program for Scientific Translation. Jerusalem, 1971.
[40] Nasrullaev N.M., Rut'kov E.V., Tontegode A.Ya. Zh.Tech. Fiz.. 1987. V. 57(2). P. 353-356.
[41] Gall N.R., Rut'kov E.V., Tontegode A.Ya. Int. J. of Modern Physics B. 1997. V. 11(16). P. 1865-1911.
[42] Ageev V.N., Rut'kov E.V., Tontegode A.Ya., Kholin N.A. Fiz. Tverd. Tela, 1981. V. 23(8). P. 2248-2254.
[43] Gall N.R., Rut'kov E.V., Tontegode A.Ya., Usufov M.M. Zh.Tech. Fiz. 1997. V. 67(7). P. 137-140.
[44] Methods of Surface Analysys, ed. by A.W.Zanderna, N.Y., 1975.
[45] Shrednik V.N. ФТТ. 1961. V. 3. P. 1750-1761.
[46] Shrednik V.N., Odishariya G.A. Izvestia AN USSR (Seria fizicheskays). 1969. V. 33. P. 536-543.
[47] Odishariya G.A., Shrednik V.N. Dokladi AN USSR, 1968. V. 182. P. 542-544.
[48] Shrednik V.N., Odishariya G.A. Fiz. Tverd. Tela, 1969. V. 11. P. 1844-1853.
[49] Shrednik V.N. Cristal Growth and Field Ion Microscopy, Moscow, Nauka, 1975. P. 150-171. (in Russian)

[50] Zandberg E.Ya., Tontegode A.Ya., Yusifov F.K. Zh.Tech. Fiz.. 1971. V. 41. P. 2420-2427.
[51] Zandberg E.Ya., Tontegode A.Ya., Yusifov F.K. Zh.Tech. Fiz.. 1972. V. 42(1). P. 171-174.
[52] Potekhina N.D., Tontegode A.Ya. Zh.Tech. Fiz. 1972. V. 42. P. 162-170.
[53] Medvedev V.K., Naumovets A.G., Fedorus A.G. Fiz. Tverd. Tela, 1970. V. 12. P. 375-385.
[54] Vedula Yu.S., Naumovets A.G., Ukrainski Fizicheski Zurnal, 1973. V. 18. P. 1000-1007.
[55] Arthur J.R., Cho A.Y. Surf. Sci. 1973. V.36. P. 641-660.
[56] Bol'shov L.A., Napartovich A.P. Fiz. Tverd. Tela, 1971. V. 13. P. 1679-1684.
[57] Bol'shov L.A., Napartovich A.P. Zh. Exp. Tech. Fiz. 1973. V. 64. P. 1404-1413.
[58] R.Defay, I.Prigogine, A.Bellmans, D.H.Everett Surface tension and Adsorption, N-Y, Willey and Son, 1966, 274 p..
[59] Thermodynamic constants of matter, V. IV, part I. M. Ussr Academy of Sciences. 1970. 383 p (in Russian).
[60] Dobretsov L.N. Zh.Tech. Fiz.,. 1934. V. 4. P. 783-795.
[61] Potehina N.D. Poverhnost, 1987, No 4, P. 14- 21
[62] Rut'kov E.V., Tontegode A.Ya. Uspekhi Fiz. Nauk. 1993. V. 163. P. 57.
[63] Gall N.R., Rut'kov E.V., Tontegode A.Ya. Pisma v Zh.Tech. Fiz., 1988. V. 14(6). P. 527-532.
[64] Rosei R., De Cresceczi M., Sette F., Quaresima C., Savoia A., Perfetti P. Phys. Rev. 1983. V. 28. P. 1161-1164.
[65] Efimov A.I., Belorukova L.P., Basil'kova I.V., Chechev V.P. "Properties of Nonirganic Compounds", Handbook, Leningrad , Khimia, 1983 (in Russian)
[66] Zi-Pu Hu, Ogletree D.F., Van-Hove M.A., Somorjai G.A. Surf. Sci. 1987. V.180. P. 433-459.
[67] Ageev V.N., Soloviev S.N., Tontegode A.Ya. Fiz. Tverd. Tela, 1981. V. 23. P. 2280-2289.
[68] Meksted E.B. in Problems of catalysis, Moscow, Inostrannaia Literatura, 1955. 100 p.(in Russian)
[69] Fogel Ya.M., Nadytko V.T., Rybalko V.F., Slabospitsky R.P., Korobchanskaya I.E. ДАН СССР. 1962. V.147. P. 414-417.
[70] Wilhoff M.A. Trahs. Farad. Soc. 1968. V.64. P. 1925-1933.
[71] Zandberg E.Ya., Tontegode A.Ya. Zh.Tech. Fiz.. 1970. V. 40. P. 626-630.
[72] Zandberg E.Ya., Tontegode A.Ya., Yusifov F.K. Fiz. Tverd. Tela, 1970. V. 12. P. 1740-1744.
[73] Zandberg E.Ya., Tontegode A.Ya. Zh.Tech. Fiz. 1968. V. 38. P. 763-766.
[74] Abdullaev R.M. "Growth of carbon films on Ir, Re, and Pd, and its role in their adsorption, catalytic, and emission properties". Kandidate thesis, Leningrad, 1983. 194 p (in Russian).
[75] Mc Carty J.G., Madix R.J. J. of Catalysis. 1975. V. 38. P. 402-409.
[76] Goodman D.W., Kelley R.D., Madey T.E., Yates J.T. J. of Catalysis. 1980. V. 63. P. 226-231.
[77] Bonzel H.P., Krebs H.J. Surf. Sci. 1980. V. 91. P. 499-513.
[78] Tontegode A.Ya. Pisma v Zh.Tech. Fiz., 1977. V. 3. P. 635-639.
[79] Bonzel H.P. J. Vacuum Sci. Technol. 1984. V. A2(2). P. 866-872.
[80] Holmlid L. J. Chem. Phys. 1974. V. 61. P. 1244-1245.
[81] Zandberg E.Ya., Nasrullaev N.M., Potekhina N.D., Rut'kov E.V., Tontegode A.Ya. Kinetika i Kataliz. 1991. V. 32(1). P. 92-97.
[82] Zandberg E.Ya., Nasrullaev N.M., Rut'kov E.V., Tontegode A.Ya. Kinetika i Kataliz. 1986. V. 27(5). P. 1170-1173.
[83] Zandberg E.Ya., Nasrullaev N.M., Rut'kov E.V., Tontegode A.Ya. Dokladi AN USSR. 1987. V. 295(3). P. 633-636.
[84] Zandberg E.Ya., Nasrullaev N.M., Rut'kov E.V., Tontegode A.Ya. Himicheskaya Fizika. 1988. V. 7(7). P. 962-969.
[85] Potekhina N.D. Kinetika i Kataliz. 1990. V. 31. P. 72-78.

[86] Wakar Z., Gall N.R., Makarenko I.N., Rut'kov E.V., Titkov A.N., Tontegode A.Ya., Usufov M.M. ФТТ. 1998. V. 40(8). P. 1570-1573.
[87] Beigel G.A. J. Vac. Sci. and Technol. 1972. V. 9. P. 370-372.
[88] Lander J.J., Morrison J. Surf. Sci. 1966. V. 4. P. 103-107.
[89] Morrison J., Lander J.J. Surf. Sci. 1966. V. 5. P. 163-169.
[90] Lander J.J., Morrison. J. Appl. Phys. 1964. V.35. P. 3593-3599.
[91] Baner E., Bonczek F., Poppa H., Todd G. Surf.. Sci. 1975. V. 53. P. 87-109.
[92] Hamilton J.F., Logel P.C., Baetzold R.C. Thin Solid Films. 1976. V. 32. P. 233-236.
[93] Hamilton J.F., Logel P.C. Thin Solid Films. 1974. V. 23. P. 89-100.
[94] Hamilton J.F., Logel P.C., Baetzold R.C. Thin Solid Films. 1973. V. 16. P. 49-63.
[95] Pashley P.W., Stowell M.F., Jacobs M.H., Law T.J. Phil. Mag. 1964. V. 10. P. 127-158.
[96] Corbett J.M., Baswell F.W. J. Appl. Phys. 1969. V. 40. P. 2663-2669.
[97] Fedorus A.G. "Electromic and adsorption properties and the structure of Cs and Na films on W surface" Doctor thesis, Kiev, 1970. 160 p.
[98] I.F.Luksutov, A.G.Naumovetz, V.L.Pokrovsky, "Two-Dimensional Cristals", Kiev, Naukova Dumka, 1988, p.20. (in Russian)
[99] Ionov N.I., Mittsev M.A. Fiz. Tverd. Tela, 1975. V. 17. P. 1607-1612.
[100] Mc Carty J.G., Madix R.J. Surf. Sci. 1976. V. 54. P. 121-138.
[101] Abdullaev R.M., Tontegode A.Ya., Yusifov F.K. Fiz. Tverd. Tela, 1978. V. 20. P. 2343-2356.
[102] Abdullaev R.M., Tontegode A.Ya., Yusifov F.K. Fiz. Tverd. Tela, 1978. V. 20. P. 3217-3224.
[103] Abon M., Billy J.C., Bertolini J.C., Jardy B. Surf. Sci. 1986. V. 167. P. L187-L193.
[104] Zandberg E.Ya., Rut'kov E.V., Tontegode A.Ya. Zh.Tech. Fiz. 1975. V. 45. P. 1884-1891.
[105] Zandberg E.Ya., Potekhina N.D., Rut'kov E.V., Tontegode A.Ya. Zh.Tech. Fiz. 1982. V. 52. P. 2398-2404.
[106] Love H.M., Wiederick H.D. Canad. J. Phus. 1969. V. 47. P. 657-663.
[107] Rut'kov E.V., Tontegode A.Ya., Usufov M.M. Phys. Rev. Letters. 1995. V. 74(5). P. 758-760.
[108] Burrer R.M. Diffusion in and through Solid. Cambridge. 1941.
[109] Shumon P. Diffusion in Solids. Moscow, Metallurgia, 1966. 195 p. (in Russian)
[110] Seach M.P. In: Practical Surface Analysis by Auger and X-ray Photoelectron Spectroscopy. John Willey&Sons Ltd., 1983. P. 277-317.
[111] Rawlings K.J., Foulias S.D., Hopkins B.J. Surf. Sci. 1981. V. 109. P. 513-521.
[112] Rudman P.S. TMS-AIME. 1967. V. 239. P. 1949.
[113] Tontegode A.Ya., Yusifov F.K. Poverhnost, 1994. V. 4. P. 20-24.
[114] Samsonov G.V., Vanitsky I.M. Refractory Compounds, Reference-book, Moscow, Metallurgia, 1976, 558 p.
[115] Gall N.R., Lavrovskaya N.P., Rut'kov E.V., Tontegode A.Ya. Phys. Rev. Letters. 1995. V. 74(5). P. 758-760.
[116] Rut'kov E.V., Gall N.R. Fiz. Tverd. Tela, 2008.
[117] Goldschmodt H.J. Interstitial Alloys, Moscow, MIR, 1971. 424 p. (in Russian)
[118] Shelton J.C., Patil H.R., Blakely J.M. Surf. Sci. 1974. V. 43. P. 493-505.
[119] Tontegode A.Ya., Abdullaev R.M., Yusifov F.K. Zh.Tech. Fiz.. 1975. V. 45. P. 1904-1914.
[120] Panzner G., Diekmann W. Surf. Sci. 1985. V. 160. P. 253-270.
[121] Tontegode A.Ya., Yusifov F.K. Zh.Tech. Fiz.. 1973. V. 43. P. 1106.
[122] Pallmer P.G., Jr., Gordon R.L. J. Appl. Phys. 1980. V. 51(3). P. 1798-1801.
[123] Espe V. Technogy of electronic vacuum materials, Moscow, State Elekctronics Publishiong, 1962. V. 1. 631 p. (in Russia)
[124] Gall N.R., Mikhailov S.N., Rut'kov E.V., Tontegode A.Ya. Kinetika i Kataliz. 1988. V. 29. P. 1196-1201.

12

Intercalation of Graphene Films on Metals with Atoms and Molecules

E.V.Rut'kov and N.R.Gall
Ioffe Physico-Technical Institute of Russian Academy of Sciences, Russia

1. Introduction

Our studies [1--3] resulted in a first observation of intercalation of graphene films on metal surfaces, which consists essentially in penetration (diffusion) of foreign atoms and molecules between the surface of a metal and the graphene film. The fact of intercalation itself implies a weak binding of graphene to the metal surface (**§** 6) and finds a reasonable explanation in the graphene layer being valence saturated. Intercalation is usually observed to occur in layered solids (graphite, MoS_2) whose interlayer space may become occupied by some penetrating atoms and molecules. For instance, exposing a heated graphite crystal to cesium vapor initiates spontaneous penetration of cesium atoms between the graphite layers to form the C_8Cs intercalation compound, in which graphite layers with concentration N_c = $3.56\ 10^{15}$ cm^{-2} alternate with cesium layers with $N_{Cs} = 5\ 10^{14}$ cm^{-2}, and the distance between neighboring graphite layers increases from 3.35 Å in a graphite single crystal to 5.94 Å in C_8Cs [4, 5]. Interestingly, intercalation leaves the structure and lattice constant of the graphite layer and, hence, its individual features unchanged.
Our research group has studied in considerable detail the various aspects of intercalation of graphene films on metals with a range of atoms, more specifically, K, Cs, Na, Ba, Sr, Pt, Si, C, Ag, Al, Ir, Cu, Mo, as well as with molecules of the C_{60} fullerenes [1--3].

2. Intercalation with atoms of alkali metals (K, Cs, Na) [1--3, 6]

2.1 Adsorption of potassium atoms on graphene-coated iridium

Potassium atoms were adsorbed at 300 K on a graphene film atop iridium to saturation, i.e., until a reverse flux of potassium atoms desorbing from the surface became equal to the incident flux. Next the surface was flash-heated. Three phases were observed in the thermal desorption spectrum (Fig. 1). The potassium atoms in the α phase desorbing completely at T < 850 K are produced by desorption of potassium from graphene; indeed, the temperature of potassium desorption from the α phase matches nicely with the lifetime of potassium adatoms on graphene. The β phase having a low adsorption capacity (~10^{11} at/cm^2) is attributed to the potassium adatoms decorating defects in graphene films (for a more detailed account of the β phase, see [2]). The adsorption capacity of the β phase grows strongly with removal of a part of carbon atoms from the graphene film [7]. Particularly interesting is the γ phase, with potassium desorbing from this state at $T \geq 2000$ K (sic!) when the graphene film breaks up. This desorption phase is associated with the release of

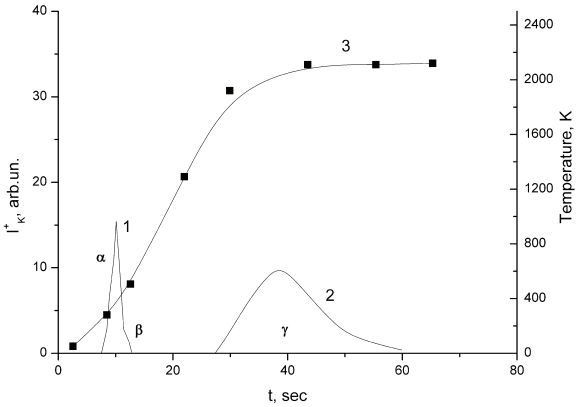

1, 2 - α- and γ- are desorption phases, 3 - the temperature - time dependence T(t).

Fig. 1. Thermal desorption spectra of K+ ions in heating of a graphene layer on Ir(111). K was deposited at 300 K with the flux ν_K = 1.0 *10^{11} cm^{-2}*s^{-1} for 40 s.

potassium atoms buried under the graphene film. Figure 2 illustrates filling of the γ phase with potassium for υ_K = 6 10^{11} $cm^{-2}s^{-1}$ reached in 10 min for different substrate temperatures in the 300 ≤ *T* ≤ 900 K region, and the kinetics of this process in the 300--670 K interval is plotted in Fig. 3.

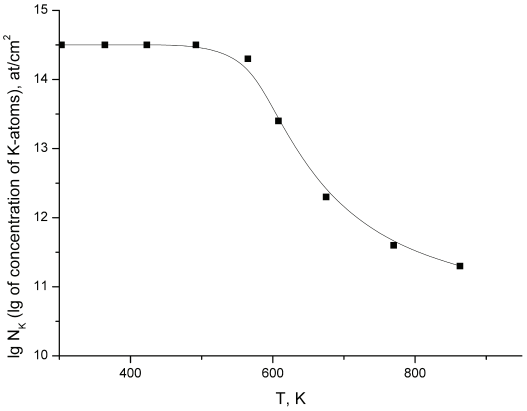

Fig. 2. K atomic concentration in logarithmic scale for K stored behind the graphene layer on Ir(111). K was deposited at various temperatures with the flux ν_K = 6.0 *10^{11} cm^{-2}*s^{-1} for 10 min at the each temperature.

In the 300 ≤ *T* ≤ 550-K region, the γ phase was filled in 10 min to its maximum possible level of $N_\gamma \approx$ (2--3) 10^{14} at/cm^2, which did not change during subsequent exposure to a potassium atom flux. There is more than one experimental verification of the potassium in the γ phase residing indeed under the graphene film [6]. Consider only two of them.

Verified by the work function. Potassium present with a concentration N_K ~ (2--3) 10^{14} at/cm^2 on the surface of graphene was experimentally shown by CPD to reduce the surface work function by close to 2 eV. The potassium in the γ phase adsorbed to the same concentration reduces the work function by 0.3 eV only.

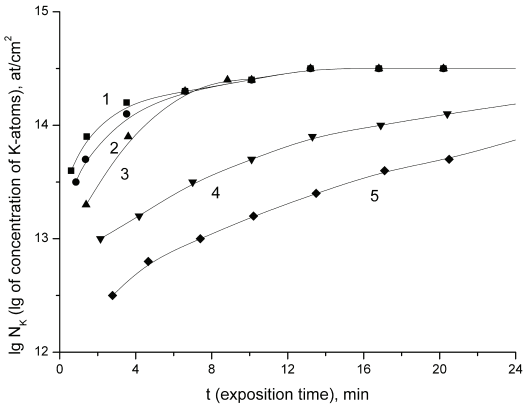

Fig. 3. K atomic concentration for K stored behind the graphene layer on Ir(111). K was deposited versus exposure time at various temperatures T (K): 1 - 300; 2 - 530; 3 - 590; 4 - 630; 5 - 670. The K flux was $\nu_K = 6.0 * 10^{11}$ cm^{-2}*s^{-1}.

Verified by AES. This is probably the most direct method of all, because it was found that filling of the γ phase with potassium to $N_\gamma \approx$ (2--3) 10^{14} at/cm^2 (following desorption of potassium from the α phase) reduces the intensity of the iridium Auger peak by a factor 1.4, although that of the carbon Auger peak does not change, thus implying that potassium is sandwiched between metal and the graphene film, i.e., resides in the intercalated state. The presence of potassium in the γ phase suggests that the graphene film is physisorbed on iridium, and that after intercalation with potassium it rose above iridium by a considerable distance, because the diameter of the potassium atom d_0 = 4.72 Å, and that of the potassium ion, d_+ = 2.66 Å [6].

It is common knowledge that graphite can be intercalated with atoms and molecules. Obviously enough, insertion of foreign atoms between layers should increase the interplanar distance *h*. This is evidenced by the data [4] listed below in Table 1.

Intercalant	Cs	K	Li	Rb	Br	HNO_3	HCl_3	$FeCl_3$
h, Å	5,94	5,35	3,71	5,65	7,04	7,84	7,94	9,37

Table 1.

Similar results are obtained in adsorption at 300 K of Cs and Na atoms on Ir(111)-graphene.

2.2 Adsorption of potassium atoms on iridium with graphene islands

The transition from a continuous film to graphene islands brings about appearance of a number of features in thermodesorption spectra. The first of them is the sharp increase of the capacity of the β phase, which should be assigned to potassium atoms decorating the edges of graphene islands.

Second, as the area of the islands S_0 decreases, the time lag t^* in filling of the γ phase after the beginning of potassium evaporation grows rapidly. Figure 4 displays graphs illustrating γ phase filling for different S_0. We readily see that t^* grows strongly with increasing area free of graphene islands.

Assuming all potassium atoms to roll off the graphene islands onto iridium, we find that for all S_0 filling of the γ phase starts at the same concentration of potassium on iridium, ~2.5 10^{14}

at/cm^2. Significantly, in the case of a continuous graphene film on iridium, filling of the γ phase with potassium comes to completion after the concentration of atoms on the graphene surface has reached ~5 10^{13} at/cm^2.

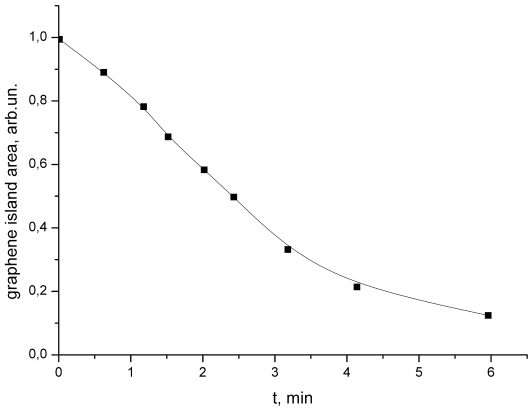

Fig. 4. Dependence of the initial time of K penetration into the γ-phase t* versus the relative graphene island area on iridium S_0. K was deposited at 300 K with the flux ν_K = 8.4 *10^{11}cm^2*s^1.

Figure 5 plots the dependence of the maximum filling by potassium of the γ phase on the relative area of graphite islands. We see N_γ to scale directly proportional to S_0.

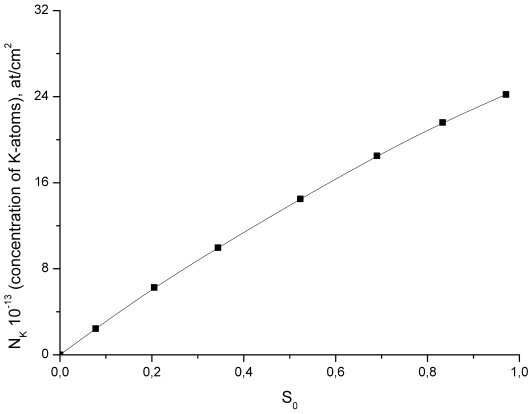

Fig. 5. Maximal K concentration under graphene (in the γ-phase) N_K versus the relative island area on Ir(111). K was deposited at 300 K with the flux ν_K = 2.0 *10^{12} cm^{-2} *s^{-1}. N_K was determined by TDS method.

Consider now how could one explain these results. Obviously enough, the first centers to be filled by adsorbing potassium atoms should be those with strong binding; here they would be edges of the graphite islands (the β phase). The next to be filled are less energetically favorable centers; potassium adsorbs on iridium. For θ > 0.1, a substantial part should be played by Coulomb repulsion among positively charged potassium adatoms, and it is apparently this repulsion that prevents complete filling of the potassium monolayer on

iridium, so that for $N_K \geq 2.5\ 10^{14}$ at/cm^2 potassium atoms acted upon by Coulomb forces will start occupying the free surface of graphene islands. This is followed by effective filling of the γ phase. Just as in the case of a continuous graphene film, potassium from the γ phase for graphene islands desorbs from the surface at high temperatures ($T \geq 1900$ K). That potassium persists for a long time at high temperatures in the γ phase suggests that valence-non-saturated carbon atoms at the edges of graphene islands are chemically bound to atoms in the surface layer of iridium. It is the closed island edges that prevent potassium from escaping from under the islands ("bottom-up saucer" island, Fig. 6).

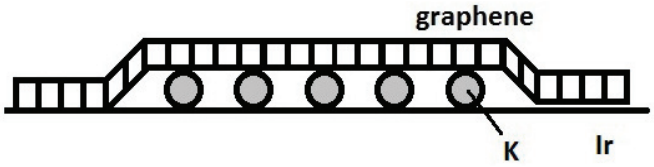

Fig. 6. Schematic graphene island on a metal with atomic K in the γ-phase.

5.3 Adsorption of cesium atoms on graphene atop rhenium [7--11]

One more example of a substrate metal, rhenium, may be in order here to demonstrate that graphene islands are physisorbed in this case too. A rhenium ribbon was carbonized in benzene vapor at T_c = 1700 K up to formation of a graphene film, after which the temperature was lowered to 300 K by turning off the heating current. Experiments showed that in this way one can preserve a graphene layer on iridium at temperatures of 300--1100 K, because volume diffusion becomes frozen at these temperatures. Thereafter, cesium atoms were adsorbed at 300 K on the graphene layer atop iridium in a constant flux $\upsilon_{Cs} = 2\ 10^{12}$ cm^{-2}s^{-1} to saturation, i.e., until the reverse flux became equal to the incident one. After this, the temperature was flashed (Fig. 7). We readily see that cesium desorption occurs in two phases, with the first of them (α phase) observed at $T \sim 900$ K, and the second (γ phase), at high temperatures, $T \geq 2100$ K (sic!). The temperature of cesium desorption from the α phase matches with the lifetime of cesium on a graphene film (**§** 7) and can be identified with cesium escaping from the surface of the graphene film. The high temperatures of cesium desorption from the γ phase are associated with cesium becoming freed from under the graphene film when it breaks up. The maximum adsorption capacity of cesium in the γ phase, $N_\gamma \approx 8\ 10^{13}$ at/cm^2. Significantly, in these experiments the adsorption capacity of the β phase of cesium (similar to the potassium β phase for the iridium-graphene system), which is related with graphene defects, was at a level of $N_\beta \sim 10^{11}$ at/cm^2, and is not reflected in Fig. 7. Just as for the Ir-C system, we are going to present here two arguments in support of cesium in the γ phase being buried under the graphene film.

1. The work function of the surface of a graphene film decreases after maximum filling by cesium of the γ phase by ~0.25 eV, although the same amount of cesium present in the α phase causes a decrease of the work function by ~1.25 eV.
2. After desorption of the cesium α phase, the Auger peak intensity of carbon recovers to the level corresponding to a clean graphene film, whereas the rhenium peak intensity is found to be lower by a factor ~1.3 than that before the beginning of cesium adsorption. This implies that cesium in the γ phase is sandwiched between the graphene film and the metal.

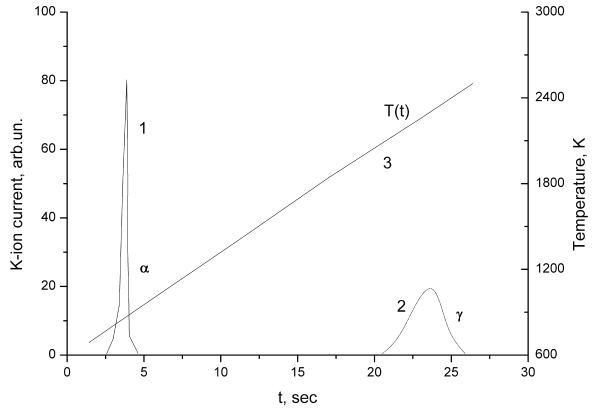

Fig. 7. Thermal desorption spectra for Cs+ ion after Cs deposition on a graphene layer on Re. Cs was deposited at 300 K with the flux ν_K = 8.5 *10^{11} cm^{-2}*s^{-1} for 15 min. 1, 2 - α- and γ-desorption phases, 3 the temperature - time dependence T(t).

Figure 8 illustrates filling of the γ phase by evaporation of cesium atoms for υ_{Cs} = 3.3 10^{12} cm^{-2}s^{-1} during 10 min, measured for different substrate temperatures within the interval 300 ≤ *T* ≤ 900 K. Examining Fig. 8, we see that intensive filling of the γ phase by cesium starts at *T* ≤ 800 K. Just as in the case of potassium atoms, the maximum adsorption capacity of the cesium γ phase does not depend on the sample exposure time to the flux of cesium atoms.

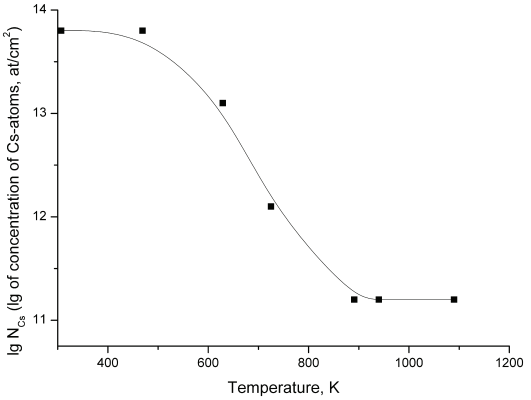

Fig. 8. Cs atomic concentration in logarithmic scale for Cs stored behind the graphene layer on Ir(111) versus temperature. Cs was deposited at various temperatures with the flux ν_{Cs} = 3.3 *10^{12} cm^{-2}*s^{-1} for 10 min at the each temperature.

Thus, the assumption of a graphene film on a metal being physisorbed is valid not only for iridium but for rhenium as well. Similar experiments on adsorption of K, Na, and Cs atoms performed on graphene grown atop other metals as well---rhodium, molybdenum, platinum, and nickel, provide convincing support for the general physisorptive character of graphene bonding with a metal surface.

2.4 Intercalation of graphene on a metal with alkali atoms [2, 3, 12, 13]

Application of TDS (in studies of adsorption of Cs atoms on graphene atop rhenium) involving detection of the ions released in surface ionization increased strongly the sensitivity of the method in the initial stages of adsorption, when the surface work function does not yet change and each desorbing Cs atom escapes in the form of the Cs^+ ion.

The following features observed at T = 300 K appear noteworthy.

1. At cesium concentrations on graphene atop rhenium below $N_{Cs} \approx 1\ 10^{12}$ at/cm^2, cesium atoms reside only in the α phase, i.e., on the surface of the graphene film.
2. For $N_{Cs} > 1\ 10^{12}$ at/cm^2, surface migration of cesium atoms sets in (rather of cesium ions, because cesium on the surface is positively charged), which is apparently initiated by Coulomb repulsion. In the process, cesium transfers to the back side of the ribbon to the α state, which is corroborated by the observation that the thermodesorption spectrum contains only the α phase with the cesium concentration $N_{Cs} = ½\upsilon_{Cs}t_{exp}$.
3. After the cesium concentration on both sides of the rhenium ribbon has reached the level $N_{Cs} \geq 1\ 10^{13}$ at/cm^2, cesium atoms start to diffuse actively into the space under graphene, signaling filling of the γ phase. The total concentration of cesium on the surface becomes $N_{Cs}(tot) = ½\upsilon_{Cs}t_{exp}$, because half of the material (cesium) escapes to the back side of the ribbon (this is why the α and β phases of cesium on the front side of the ribbon are easy to fill by evaporating it on the back side of the sample). It is apparently only at noticeable cesium concentrations (≥1 10^{13} at/cm^2) that the forces of electrostatic repulsion among cesium adatoms with a charge close to 1 become strong enough to overcome an activation barrier and start to diffuse under the graphene film. The nature of this activation barrier remains unclear, but it could be related, for instance, with the Coulomb repulsion of the cesium adatom from a positively charged defect in a graphene film, and it is possibly this defect that mediates efficiently the escape of charged adatoms migrating over the surface.

The process of filling of the γ phase by the other alkali atoms, sodium and potassium, exhibits basically the same features as that of the filling by cesium, which should be assigned to these alkali atoms having a noticeable positive charge on the graphene surface.

Cs, Na, and K atoms fill actively the γ phase in the 300--700-K temperature interval, where evaporation of atoms can result in building up on the surface of a certain "critical" concentration of adatoms which would initiate filling up of the γ phase. For T > 700 K, the lifetimes of alkali metals on graphene become too short (§7), which reduces the equilibrium surface concentration, with the result that the migration transfer under the graphite layer drops sharply (Figs. 2 and 8).

2.5 Why do Cs atoms find it easy to diffuse under the graphene film but hard to escape from under it?

There are presently no grounds to doubt that adatoms of alkali metals are "pushed" under the graphene film by their electrostatic repulsion. It was observed that for the intercalation of single-crystal graphite by alkali metals to begin, they should first build up to a certain concentration on the crystal faces [14]. This reminds one of the problem where one should force into a rubber tube balls of a slightly larger diameter; it can be solved by applying a certain force F (Fig. 9A). As the pushing "finger" acts in our case repulsion among positively charged adatoms (Fig. 9B). The above is supported by experiments aimed at studying Cs migration under the graphene islands; indeed, single Cs adatoms were found to practically not migrate under graphene at all [15].

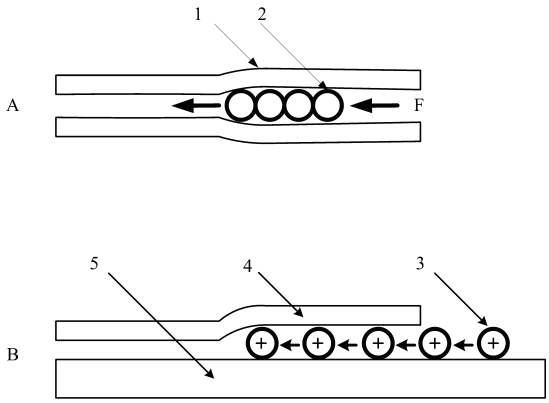

Fig. 9. **A**. Schematic structure of solid balls movement inside a ribbon tube under the action of an external force: 1 – ribbon tube, 2 – solid ball. **B.** Schematic structure for electropositive atomic metal penetration between the graphene layer and metal substrate: 3 – adsorbed Cs, 4 – graphene layer, 5 – metal substrate.

Now about the question of why it is easy (T = 300 K) for atoms of alkali metals to transfer under a graphene film but difficult (at $T \geq 2000$ K!) to escape from under it, i.e., why the entry--escape ways are so strongly asymmetric.

Studies of the intercalation of graphene on Rh(111) with Cs atoms revealed that after desorption of the Cs α phase from the graphene surface, the cesium intercalant emerges partially from under the graphene film and desorbs likewise at low temperatures, 900--1000 K. The emergence of cesium from under graphene is signaled by the formation of diffusion "tails" in thermodesorption spectra (Fig. 10).

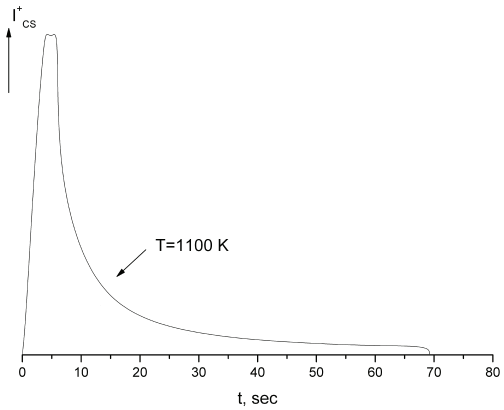

Fig. 10. Thermal desorption spectroscopy for Cs+ ions from the graphene layer on Rh(111) in the temperature increase form 300 to 1100 K. Cs was deposited at 300 K up to the concentration $N_{Cs} = \nu_{Cs}*t = 4.4 *10^{14}$ cm^{-2}.

Significantly, the larger was the amount of Cs adsorbed into the α phase, the deeper penetrated Cs atoms and in larger numbers under the graphene layer, and the longer was the diffusion "tail" in the TDS spectra.

Thus, as *T* increases, Cs emergence from under the layer is initially not blocked in any way, which makes it difficult to separate the α phase of the Cs emergence from the onset of the Cs escape from the γ phase. We are turning now to the second question of what forced adatoms to stay in intercalated state, so that they escape from under the graphene film only when it breaks up, and this may require quite high temperatures, often above 2000 K (sic!).
The answer to this question may be contained in Fig. 11. As *T* increases, Cs escapes from the α phase, i.e., from the graphene surface (1 in Fig. 11A), the next to desorb is Cs from the defects in the layer (2 in Fig. 11B), and it is through them that adatoms penetrate under the layer in the first place. The turn to emerge comes after that to Cs adatoms bound close to graphene island edges (3 in Fig. 11C). The Cs adatoms left far from the layer edge do not have time enough to migrate to the edge closing to the metal (4 in Fig. 11D). These adatoms remained trapped under the "bottom-up saucer" islands (Fig. 6).

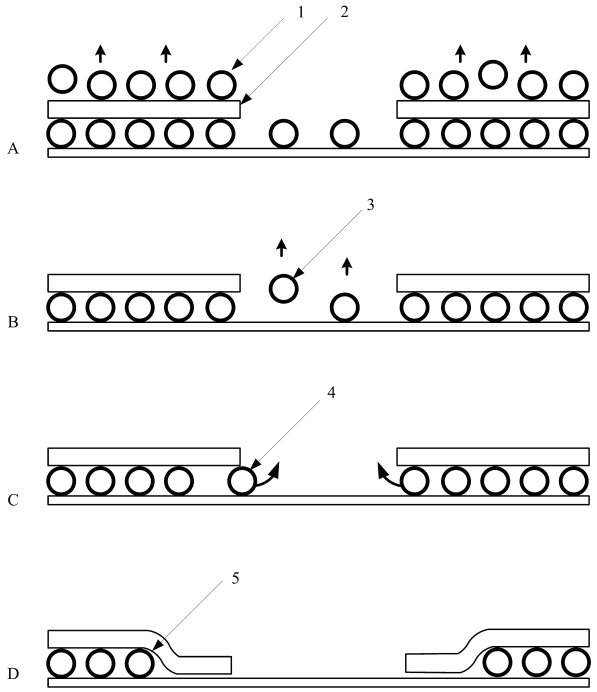

Fig. 11. Schematic model (A – D) showing the process of Cs liberation from the γ-phase and the island edge closure to the metal substrate after the temperature increase for the intercalation system Me-Cs-graphene. 1 - atomic Cs above the graphene layer, α- phase; 2 – graphene; 3 - atomic Cs desorbing from the layer defect; 4 - intercalated Cs near the island edge; 5 - 'locked' atomic Cs under the layer; graphene traps.

2.6 Excitation of edges of graphene islands

Under certain temperatures, the graphene island edges bound to metal should open periodically stimulated by thermal excitation. Rupture of the Me-C chemical bond may open the way for a part of the intercalant cesium to escape from under the graphene film and desorb. This accounts for a certain, albeit low-density, flux υ_{Cs} of Cs atoms leaving at *T* >

1000 K. For instance, for the Ir(111)-graphene system with a cesium concentration under graphene $N_\gamma \sim 2\ 10^{14}$ at/cm^2 and T = 1100 K, $\upsilon_{Cs} \sim 10^9$--10^{10} cm^{-2}s^{-1}. The Cs flux decreases with time, primarily because of the edge region becoming depleted in cesium, which makes it ever more difficult for the remaining adatoms to reach the island edge. Experiments demonstrate that removing Cs from under a graphene film without destroying it takes up several hours at $T \sim 1100$ K on Ir(111), although the lifetime of Cs, both on graphene and on iridium, at this temperature is only ~ 0.01 s (**§** 7).

Figure 12 plots the variation of the flux of Cs atoms emerging from under graphene on Rh(111) with the substrate temperature varied from T_1 = 1300 K to T_2 = 1350 K, for the Cs concentration under the graphene islands $N_{Cs}(\gamma) = 5\ 10^{13}$ at/cm^2.

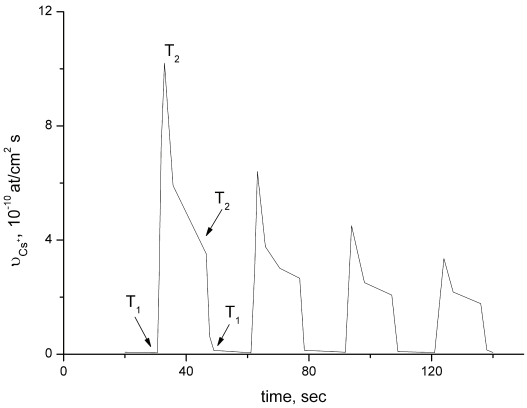

Fig. 12. The flux of Cs^+ ions out of graphene islands in their thermal excitation. The temperature was T_1 = 1300 K and T_2= 1350 K, relative island area was s_0~15%. The islands were grown on Rh(111), and Cs was intercalated to saturation at 300 K.

We immediately see a sharp rise of the cesium flux with increasing temperature associated with the increase of thermal excitation of graphene. As the temperature returns to its initial level T_1, the cesium flux density falls off rapidly too. Experiments with cyclic variation of temperature $T_1 \rightarrow T_2 \rightarrow T_1$ can be performed many times, and the results will be the same, except for the gradual decrease of the burst in the flux density of Cs atoms escaping from under the graphene (Fig. 12).

Knat'ko *et al.* [1989] showed that illumination with light or electron bombardment of a graphene film on Cs-intercalated iridium heated to ~900 K initiates emergence of these adatoms from under the graphene islands, which was visualized by monitoring the Cs^+ current. This effect was observed at photon energies varied from 2.3 to 1.5 eV, with the low-energy threshold remaining not quantified. It was assumed that the adatoms escape from under the graphene islands through some "valves" forming in the rupture of bonding of island-edge C atoms with iridium initiated by irradiation by light or electrons. The transport of particles taking place in the absence of external stimulating factors was explained as due to diffusion via defects present in the graphene film. The kinetics of these processes stimulated by light and electrons was studied, and a model reproducing them proposed [15]. It was shown that the burst of the Cs^+ ion current can be attributed to the emergence of adatoms buried under graphene close to the island edges. Filling of the near-edge region after its having being depleted by irradiation is a very slow process, which sets in probably

following formation of a compact Cs cluster diffusing as a whole to the edge of an island from its central region. Thus Knat'ko *et al.* [1989] established an unusual pattern of migration of intercalated Cs atoms, in that they move in compact clusters rather than singly, with the rate of migration growing with increasing concentration of the intercalated atoms.
Besides the edges of graphene islands, thermal excitation may set in in any part of an island, accompanied by the appearance of a graphene hillock and increase of the graphene-metal distance at this point [16].
Even at T = 300 K, one may expect excitation of any part of graphene islands bound with the metal by weak van der Waals forces; indeed, such bubbles form and disappear all the time over the film. It appears reasonable to assume that from time to time, each carbon atom in the graphene network, is capable, while participating in thermal random motion, of building up on the bond with the surface an energy high enough to be able, in moving away from the surface, to drag along its nearest neighbors and form a graphene "bubble".
A graphene film could be said to remind one, as a suitable figure of speech, the surface of a rough sea, with crests and hollows coming to life and disappearing continuously, with the sea roughness becoming the stronger, the stronger is the gale (the temperature in the case of graphene).
Tontegode (1985) [16] resorted to the relation of Frenkel $\tau = \tau_0 \exp(E/kT)$ to estimate the kinetic energy E building up on a particle bond in random thermal motion in a given observation time τ at a temperature T, which is expended in formation of a "bubble". In this sense, the motion of a carbon atom over the network on the surface resembles largely the process of desorption, the only difference being that the graphene network itself, not unlike a spring, restores the carbon atom to its original position.
Estimates show that for a binding energy of a carbon atom with the metal in a graphene film of ~0.2 eV, a graphene "bubble" should accumulate four atoms in a time τ =1 s (for $\tau_0 = 10^{-13}$ s) at T = 300 K, while at T = 1500 K the "bubble" will be quite large and contain ~20 atoms. Formation of graphene "bubbles" facilitates migration of intercalated atoms.

2.7 Compression of a layer of Cs atoms under graphene islands

The first successful monitoring of the area of graphene islands with carbon atoms trapped underneath was made in the course of their destruction. The experiment started with intercalation of a graphene film on rhodium at 300 K with cesium atoms. Next the cesium was removed from the surface at ~900 K, after which the temperature was raised to T_1 > 1250 K, and the relative island area S_{01} was determined. Next the surface was flash heated, and the amount of cesium N_1 under the islands of area S_{01} deduced. The experiment was repeated from the very beginning, but now the temperature was raised to $T_2 > T_1$, the magnitude of $S_{02} < S_{01}$ found, and N_2 derived. The results obtained are summarized graphically in Fig. 13A, in which each data point is essentially a separate experiment.
We readily see that a decrease of the relative island area from 100% (continuous layer) to ~20% (curve 1 in Fig. 13A) does not actually entail a noticeable decrease of the total number of cesium atoms on the surface (curve 2 in Fig. 12A). This implies that while the islands may shrink markedly in area, they do not "let go" the cesium atoms buried under them (Fig. 13B). It is as obvious also that although the number of cesium atoms under the islands remains unchanged, their concentration grows through the decrease of islands in area (curve 3 in Fig. 13A for T = 1150--1270 K).
We note also that for T > 1300 K graphene islands become so small that they can possibly no longer keep trapped the cesium atoms confined under them, with the result that the average concentration of intercalated cesium will start to decrease. Apart from this, the concentration

A.

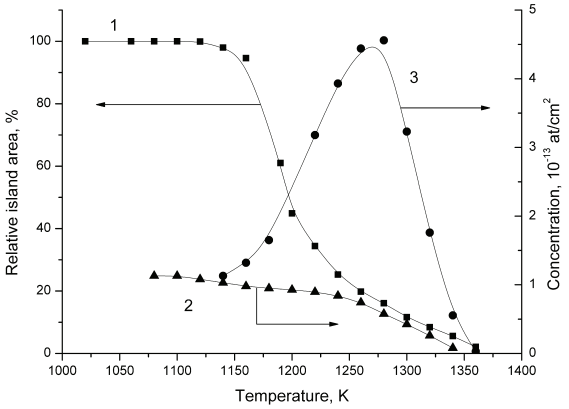

B.

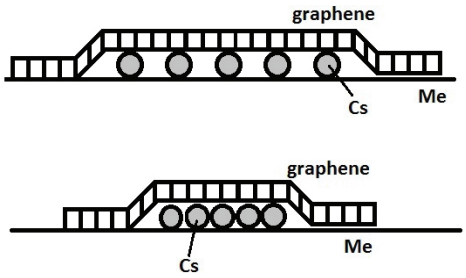

Fig. 13. Compression of graphene islands with intercalated Cs. **A**. Temperature dependences of: 1 - relative graphene island area; 2 - Cs concentration relative the total surface area; 3 - calculated Cs concentration relative to the actual area occupied by graphene. **B**. Schematic structure of the process:

of the graphene islands themselves will decrease as they break up with increasing temperature. Recalling the well known expression for particle lifetime on the surface, $\tau = \tau_0 \exp(E/kT)$ (τ_0 is the prefactor, E, the desorption energy, is in our case $E \sim 2$ eV [17]), we come readily to the estimate that graphene traps increased the lifetime of cesium adatoms on rhodium surface ~10^6 times.

Thus, we have revealed a new effect inherent in intercalation of an alkali metal under graphene films and consisting in a substantial increase of its concentration in the intercalated state under heating of the adlayer. While annealing reduces the graphene island area, their edge atoms bound with the metal by chemisorption forces do not let cesium emerge from under the graphene; this gives rise to compression of the cesium layer, and it is under the islands that its surface concentration exhibits a noticeable increase.

3. Intercalation with barium [18, 19]

It was found that Ba intercalates under graphene on iridium and rhenium, but the pattern of the processes involved depends essentially on the temperature of the substrate metal. We are going therefore to consider these processes separately for $T < 1000$ K and $T > 1000$ K.

3.1 Adsorption of Ba on Ir-C for $T < 1000$ K

In the case of Ba adsorbed on iridium at 300 K intercalation does not seem to occur, which can be deduced from a characteristic change in shape of the carbon C_{kvv} Auger peak (to be discussed in detail below), but because of strong Ba-Ba bonding on the graphene surface Ba undergoes condensation, which complicates monitoring the intercalation process. Adsorption of Ba on iridium at 300 K does not probably result in intercalation, which is suggested by a characteristic change in the shape of the C_{kvv} Auger peak of carbon (to be discussed in detail below), but strong Ba-Ba binding gives rise to condensation of Ba on graphene surface, which makes difficult monitoring the intercalation processes. These difficulties are sidestepped by invoking adsorption of Ba on heated Ir-C. Consider Fig. 14A,a displaying the dependence of the Ba, Ir, and C Auger peak intensities observed in Ba adsorption on Ir-C at 880 K. In the course of adsorption, the Auger peak of Ba grows in amplitude and that of iridium falls off, while the carbon Auger peak does not change. This implies that barium accumulates only under the graphene as intercalant (Fig. 14B). For $t \geq 150$ s, the concentration of intercalated Ba becomes as high as $5\ 10^{14}$ cm^{-2} (which is close to its monolayer concentration on the surface of transition metals) and changes no more. The efficiency of intercalation is ~0.3, in other words, 30% of the Ba flux striking the Ir-C surface becomes intercalated, with the remaining 70% desorbing. If we heat now this system, approximately 50% of the intercalated barium desorb at $T \leq 1300$ K, while the barium left under the graphene with the concentration of $2\ 10^{14}$ cm^{-2} leaves the surface only at $T > 2000$ K, when the islands break up. This experiment provides one more argument for the absence of any "blocking" of Ba escape from under graphene in the initial stage, as this was observed in the case of cesium.

A.

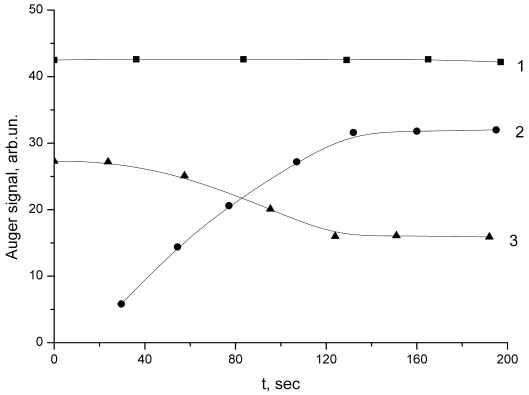

B.

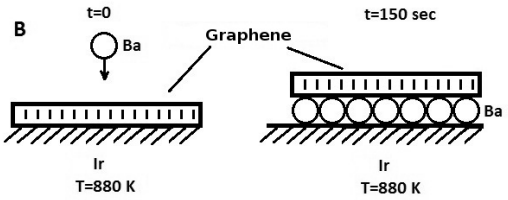

Fig. 14. Ba intercalation under a graphene layer on Ir(111). **A**. Auger signals of carbon (1), barium (2), and iridium (3) versus total amount of deposited Ba onto Ir-C at 880 K. The deposition flux is $\nu_{Ba} = 3.2 * 10^{12}$ cm^{-2}*s^{-1}. **B.** Schematic structure of the process:

3.2 Adsorption of barium on Ir-C at 1000 < *T* < 1500 K

Ba atoms with activation energy for desorption E = 1.9 eV desorb intensively from graphene on iridium at 880 K. Therefore observation of existence of barium islands on Ir-C at substantially higher temperatures, 1000 < T < 1500 K, came as a total surprise [19]. One studied the specific features of growth and dissolution of two-dimensional barium islands on Ir-C [17, 21]. Barium in these islands was bound strongly with the substrate with an energy of 3.4 eV and was present in a concentration of 2 10^{14} cm^{-2}, which means that the Ba islands were not close packed. In this temperature region, Ba did not intercalate with graphene. One had to account for the high binding energy of barium with the substrate in an island, 3.4 eV, which exceeds substantially the energy required for Ba sublimation, ~1.8 eV, and that for desorption of a Ba atom from Ir-C, which is 1.9 eV. We assumed that Ba adatoms are adsorbed at the centers of benzene rings in the graphene film, so that when the latter performs random thermal vibrations, they come closer to the surface atoms of iridium and compress slightly the graphene film to form an electron bond with iridium with a binding energy increased from 1.9 to 3.4 eV (Fig. 15). It appears actually a reasonable assumption, because the energy of desorption of a Ba atom from the iridium surface is high, 5.7 eV. If such a Ba monolayer is heated to T ~ 1600 K, about half of the barium will desorb, while the other half will migrate under the film to become an intercalant. If now we adsorb Ba again at 1000 < T < 1500 K on graphene confining intercalated barium in a concentration of 5 10^{13} cm^{-2}, strongly bound Ba islands do form, but only on a part of the surface [18]. It appears probable that the intercalated Ba is distributed nonuniformly in these experiments, so that regions with its maximum concentration of 5 10^{14} cm^{-2} border areas with no intercalated Ba present, but it is in these regions that strongly bound Ba islands form on graphene (Fig. 16). At concentrations of intercalated Ba in excess of 2 10^{14} cm^{-2}, strongly bound islands do not form at all. Neither do they form on the surface of a graphene film on iridium at film thicknesses above two monolayers. Similar results were obtained by us in studies of strontium adsorption on Ir-C [18--21].

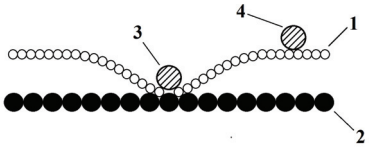

Fig. 15. Schematic structure of the graphene layer (1) on iridium (2) with strongly (3) and weakly (4) bonded atomic Ba.

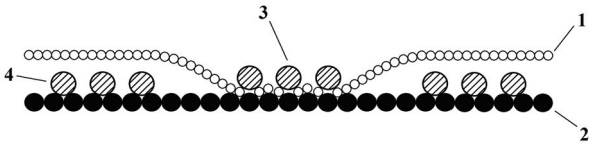

Fig. 16. Schematic structure of the graphene layer (1) on iridium (2) with 2D Ba island (3) and intercalated Ba (4).

4. Intercalation with platinum [22]

It was found that a graphene film on a metal is intercalated efficiently with atoms having low ionization potentials (Cs, K, Ba,…), which are positively charged on graphene and are strongly

bound with it by mirror image forces. An intriguing question arises immediately of whether atoms with high ionization potentials, which are not charged on a graphene film and bound with it only weakly by van der Waals forces of polarization origin, would intercalate a graphene film on a metal. In an attempt at finding an answer to this question, we studied adsorption and intercalation of Ir-C with atoms of Pt, Si, and C.

Platinum was evaporated by sublimation from heated Pt ribbons. Pt adsorbed on Ir-C at 300 K grew to form a thick film on the graphene film. It was found that Pt atoms adsorbing on a graphene film atop iridium heated to 1000 K intercalate with Ir-C with an efficiency $\kappa = 1$. This intriguing result implies that *each* Pt atom incident at 1000 K on a graphene film penetrates under it to become an intercalant species. Figure 17A shows how the Auger peaks of carbon, platinum and iridium vary as a result of adsorption of Pt on Ir-C at a higher $T = 1200$ K, when the intercalation efficiency is slightly lower ($\kappa < 1$), and part of Pt atoms desorb from the graphene film. Interestingly, in contrast to Cs, K, and Ba atoms which form in intercalated state a monatomic film, Pt grows under the graphene in a thick, *multilayer* film, which, on the one hand, is strongly chemically bound with iridium, while on the other is coupled weakly, probably by van der Waals forces, to the graphene film (Fig. 17B). This is probably what accounts for our observation [2, 3] of the effect of *bi-intercalation*, in which consecutive adsorption first of Pt atoms, and subsequently, by atoms of Cs, brings about growth under the graphene film of a thick Pt film, with a Cs monolayer forming on top of it (Fig. 18).

A.

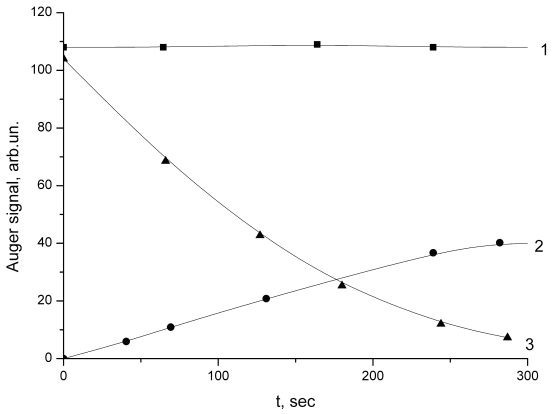

B.

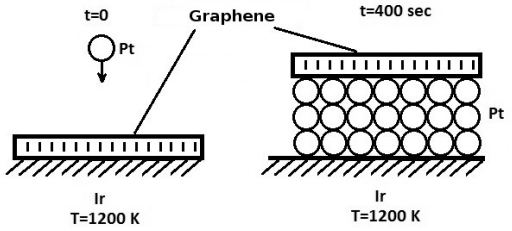

Fig. 17. Pt intercalation under a graphene layer on Ir(111). **A.** Auger signals of carbon (1), Pt (2), and iridium (3) versus Pt deposition time onto Ir-C at 1200 K. The deposition flux is $v_{Pt}=1\cdot10^{13}$ cm$^{-2}\cdot$s^{-1}. **B.** Schematic structure of the process:

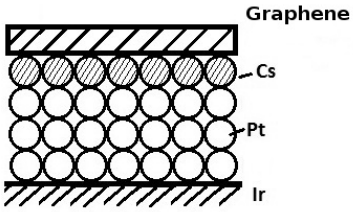

Fig. 18. Schematic structure of the layer in bi-intercalation: first Pt is deposited onto the graphene layer on Ir(111) at 1000 K; than Cs was deposited at 300 K and the system was annealed at 800 K to remove α-phase Cs.

The condition $\kappa = 1$ means that a Pt atom physisorbed on graphene can migrate in its lifetime against desorption from the center of the island to its edge, which is possible if migration over graphene is very efficient. For the process to be efficient enough, the graphene film should be smooth, and the potential relief for migration, fine; also, the graphene islands should not be very large. Because Pt adatoms on graphene residing atop iridium are electrically neutral, decoration of the graphene island edges by them leaves it neutral, as a result of which intercalation with Pt occurs without the concentration threshold characteristic of the intercalation with Cs, K, and Ba; this means that already the very first Pt atoms adsorbing on graphene with iridium heated to 1000 K penetrate under the film. Interesting data were obtained on the efficiency of intercalating Ir-C with Pt atoms at lower temperatures, $300 < T < 1000$ K, as well. For instance, if platinum is evaporated on a graphene film on iridium at 300 K, then at room temperature no intercalation is observed; instead, Pt is adsorbed to form a monolayer (with $N_{Pt} \sim 1\ 10^{15}$ cm^{-2}, which reduces the Auger peak of carbon (with $E = 272$ eV) by a factor 1.5, and that of iridium ($E = 54$ eV), ~ 3 times. After this, the temperature was raised in steps of 100°, with exposure of the sample for 30 s at each temperature. As the temperature increased, the Auger peak of iridium was found not to change, while that of carbon grew by a factor 1.5. This means that as the temperature was raised, all of the adsorbed Pt monolayer became intercalated, apparently already at $T < 1000$ K, when Pt does not yet start to desorb.

5. Intercalation with silicon [2, 3, 22]

Silicon was deposited by sublimation from heated ribbons. Si adsorbed on Ir-C at 300 K grows to form a thick film which reduces the Auger peaks of carbon and iridium until they melt into the background. As T increases, the pattern of carbon film growth changes substantially, Figure 19A plots the variation of the intensities of Auger peaks of carbon, silicon, an iridium in the course of Si adsorption on Ir-C at 1000 K. The growth of the silicon Auger peak suggests that silicon builds up in the near-surface region, and the constancy of the carbon peak, that silicon accumulates under the graphene film. After 150 s of deposition, the Auger peaks of silicon and iridium stop to change, hence, stops to change also the composition of the near-surface region ≥(10--15) Å thick, which is accessible for AES. Studies of silicon adsorption on clean iridium [23] revealed that up to the concentration $N_{Si} \sim 3\ 10^{14}$ cm^{-2} all of the silicon incident on the surface accumulates in the form of a surface chemical compound, surface silicide. Silicon atoms arriving onto the surface after this state has been filled diffuse into the bulk of iridium to form in its near-surface region volume silicide (Fig. 19B). It was found that the curves plotting the variation of the silicon Auger peak intensities

vs. deposition time of the same silicon flux on iridium and iridium coated by a graphene film at 1000 K practically coincide (if one accounts for the attenuation of the silicon Auger peak intensity by the graphene film). This means that silicon intercalates into Ir-C at 1000 K with an efficiency $\kappa \sim 1$. When Si adsorbs on Ir-C at higher temperatures $T \geq 1300$ K, a sizable part of it becomes bound in the intercalated state, with the remainder desorbing.

A.

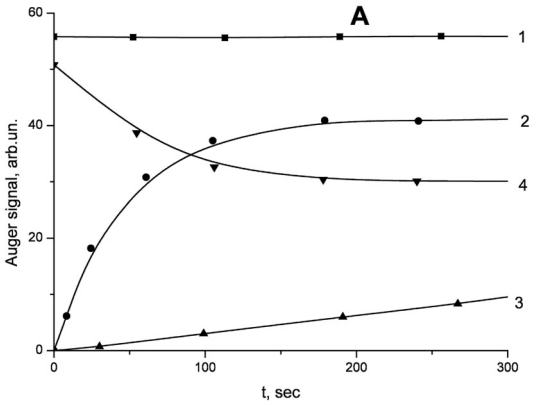

B.

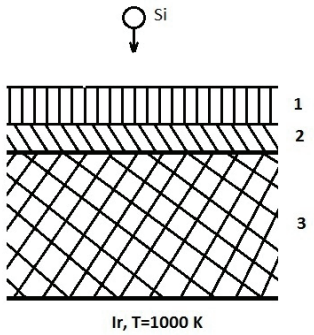

Fig. 19. Si intercalation under a graphene layer on Ir(111). **A**. Auger signals of carbon (1), Si (2), and iridium (4) versus Si deposition time onto Ir-C at 1000 K. (2) - Si Auger signal in its deposition onto Ir-C at 1500 K. The deposition flux is $\nu_{Si} = 1 * 10^{13}$ cm^{-2}*s^{-1}. **B.** Schematic structure of the process: 1 - graphene layer; 2 - surface silicide; 3 - bulk silicide

6. Intercalation with carbon [2, 3]

The experiments which demonstrated that atoms of Pt and Si intercalate with an efficiency $\kappa = 1$ under a graphene film adsorbed on iridium heated to $T = 1000$ K stimulated interest in looking for other atoms which could be intercalated with intrinsic carbon atoms. In these experiments, carbon atoms (emitted by a source developed by us and not producing C clusters [24]) were deposited at $300 < T < 1800$ K on a graphene film atop iridium, with the film thickness probed by AES. At all these temperatures, a thick carbon film was observed to

grow, but its nature (graphitic or non-graphitic) and the growth mechanism involved were found to depend strongly on T.

Adsorption of C atoms on a graphene film atop iridium heated to $T \leq 700$ K produces a thick carbon film of non-graphitic structure (Fig. 20), which is evidenced by some of its characteristics. First, the shape of the C_{kvv} Auger peak becomes non-graphitic (the spectrum contains one peak at 247 eV, while graphite features two peaks at 247 and 263 eV). Second, adsorption of Cs atoms on such a film does not demonstrate a characteristic splitting of the C_{kvv} Auger peak (a point to be discussed below), which is observed when Cs atoms are adsorbed on a graphite film. Third, the work function increases from 4.45 eV, a figure typical of graphite, to 4.75 eV, an energy identified with chemisorbed carbon. And finally, fourth, the degree of dissociation of CsCl molecules increases from 10^{-4} on graphene to 10^{-1} in the case of a thick carbon film. From this we can infer that adsorption of C atoms on graphene atop iridium heated to 700 K translates into formation of a thick non-graphitic carbon film, which grows on graphene with no intercalation mechanism involved.

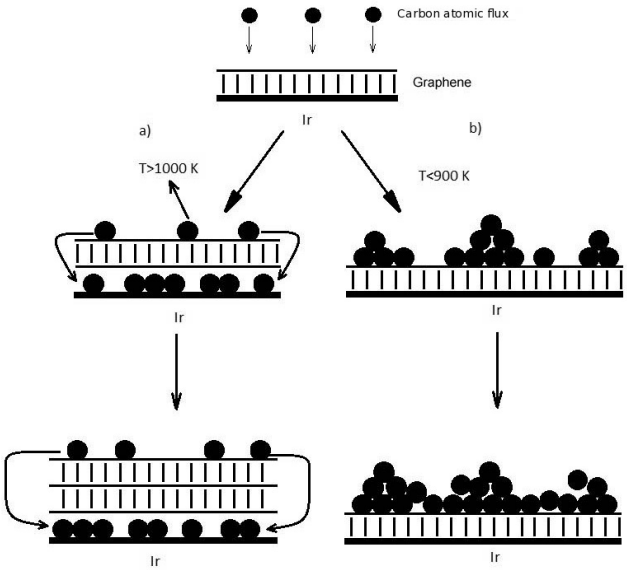

Fig. 20. A scheme of carbon film structure in atomic carbon deposition onto the graphene layer on Ir(111) at various temperatures: (a) - T > 1000 K; (b) - T < 900 K.

The situation is radically different for the formation of a carbon film when C atoms adsorb on graphene atop iridium heated to higher temperatures, $T \sim 1100$ K (see Fig. 20). Accumulation of carbon in the adlayer likewise was not observed, with all the C atoms striking the surface either intercalating under the graphene islands or desorbing. Intercalation started with formation under the graphene film of graphite islands, and after their coalescence, of a second graphene film above the first one. It was found that after the growth of the second graphene layer has come to completion, the rate of growth of the third graphene layer drops by a few times. This finds a ready explanation in that C atoms have to diffuse from the top of the film to its base, i.e., the iridium surface, where graphene islands of the next layer nucleate; this brings about loss of C atoms because of the increasing

probability of their desorption and of decreasing film growth rate. We note that at $T \leq 700$ K the rate of film growth in thickness is constant for υ_C = const. Thus, in adsorption of C atoms on Ir-C at 1100 K carbon accumulates not in the adlayer but rather in intercalated state under the graphene film, where a thick carbon film with graphitic structure grows.

7. Intercalation with silver [25, 26]

Ag was evaporated by sublimation of Ag wires wound on a heated W spiral. Adsorption of silver onto graphene atop iridium did not result in intercalation at any temperature; indeed, at $T < 900$ K, a thick silver film grew, while at $T > 900$ K, silver atoms desorbed. It is possibly because of their tendency to aggregation that Ag atoms form at the edge of a graphite island, a place best suited for starting intercalation, Ag_2 and Ag_3 clusters, which interfere with penetration of silver under the island.

If, however, one intercalates Ir-C preliminarily with Cs atoms to $N \sim 2\ 10^{14}$ cm^{-2}, and only after this deposits a thick silver film at 300 K and raises then the temperature to 1000 K, then silver will effectively roll off under the graphene in an amount of ~ 1 monolayer, the remaining silver desorbing. It appears reasonable to suggest that silver penetrates under the graphite islands when their edges are raised; it was found that it expels the intercalated cesium.

8. Intercalation with aluminum [27]

Evaporation of aluminum on graphene atop iridium or rhenium at room temperature brings about growth of three-dimensional aluminum islands on graphite. There is no noticeable intercalation of aluminum under the film, which is evidenced by the Auger signal intensities of carbon and the substrate being attenuated by the growing adsorbate film to the same extent.

The results obtained in annealing of three-dimensional aluminum islands ($N_{Al} \sim$ cm^{-2}) adsorbed on graphene atop iridium are presented in Fig. 21A. We readily see that up to ~700 K the system remains practically unchanged. At high temperatures, the Auger signal of aluminum begins to fall off, and that of carbon, to rise, with the substrate (iridium) signal remaining initially constant, to increase slightly afterwards. For $T > 1200$ K, all the three Auger signals reach constant levels remaining unchanged up to 1500 K. At high temperatures, the aluminum signal drops to zero, that of iridium grows almost twofold, and that of carbon, remains unchanged.

To gain understanding of the observed variation of Auger signals, consider Fig. 21B. At T = 700 K we see the onset, and at 1200 K, completion of a rearrangement of the adsorption layer, in which three-dimensional aluminum islands adsorbed on top of the graphene layer, dissolve, and the Al atoms released in the process partially evaporate, and partially intercalate under the graphene. For $T > 1200$ K, there is no aluminum on the outer side of the graphene, and the Auger signal of carbon has the same intensity as before the beginning of aluminum evaporation. By contrast, the Auger signal of the substrate became substantially smaller in amplitude as a result of its being screened both by the graphite layer and by the intercalated aluminum; indeed, its intensity is close to one half the initial (before Al evaporation) level (we used the iridium Auger signal with E = 54 eV).

With the heating continued ($T > 1500$ K), aluminum escapes from the adlayer, apparently through thermal desorption and, possibly, by partial dissolution in the bulk of the substrate, and its Auger peak drops to zero. By contrast, the Auger peak of iridium grows to its initial level, and that of carbon retains its initial amplitude (Fig. 21A).

A.

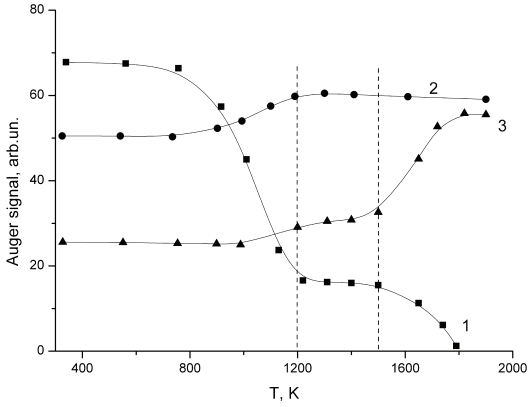

B.

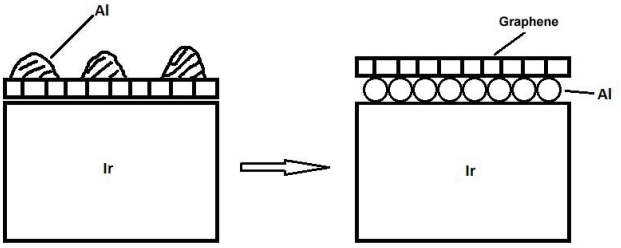

Fig. 21. Al intercalation under a graphene layer on Ir(111). **A**. Auger signals of Al (1), carbon (2), and iridium (3) versus temperature in a stepwise annealing of the Al film deposited onto Ir-C at 300 K. Initial Al surface concentration was ~2*10^{15} cm^{-2}. **B.** Schematic structure of the process: at 300 K (left) and at 1200 K (right).

The absolute amount of aluminum intercalated under the film was found to be N_{Al} ~ 5 10^{14} cm^{-2} [27].

The net result of direct evaporation of aluminum on graphene at T > 950 K is that it ceases to accumulate on top of the graphene layer but intercalates under it instead. This is evidenced by Auger signal of carbon remaining unchanged whereas that of aluminum grows, and the signal of iridium, falls off, albeit insignificantly. This suggests that the aluminum entering the adlayer does not build up on top of the graphite layer and, hence, does not reduce its Auger signal but rather accumulates sandwiched between the graphite film and the metal surface.

An experiment was conducted [27] to measure the efficiency of aluminum intercalation under graphene on (111) iridium, i.e., the fraction of particles penetrating under the film relative to the total number of atoms incident on the surface. Estimates showed the intercalation efficiency to be ~14% at 1000 K, to fall off to 7% at 1100 K. The same figures are obtained when using rhenium as a substrate metal, thus supporting the earlier conclusion of the properties of graphene being practically independent of the nature of the metal it was formed on. The limiting concentration of aluminum accumulating in intercalated state on the surface of rhenium also matches with the composition of the surface aluminide ReAl.

The low efficiency of intercalation should apparently be assigned to desorption of the larger part of the aluminum incident on the surface of graphene. It appeared worthwhile to see whether the aluminum intercalation efficiency would change if graphene covered not all of

the metal surface. For this purpose, we grew successively on a rhenium sample a graphene film of area s covering 40, 70, and 90% of the metal surface, and studied the process of intercalation. The fraction of the substrate surface coated by graphite was assumed to be proportional to the carbon Auger signal intensity from the graphene film.

As follows from these experiments, within experimental error the intercalation efficiency is practically independent of the amount of aluminum that has already penetrated under the film, while remaining dependent on the fraction of the surface coated by the island, to increase at T = 1100 K from W ~ 0.35--0.1 for s = 90% to W ~ 1 for s < 70%. Significantly, the figures obtained exceed by far the efficiency of intercalation of aluminum atoms under a continuous graphene film.

While it would appear reasonable to assume that the quality of the graphene film itself does not depend on whether it is continuous or not, in the second case the number of island boundaries would certainly increase, as would possibly decrease their size. Indeed, the island breakup starts from the edges [3], which is not strange at all, particularly if we remember that the binding energy of a single carbon atom within the layer is ~9 eV [28], and at the island edges, substantially lower, ~3 eV on rhenium [10] and ~4.5 eV on iridium [3]. It may be that the noticeable difference between the efficiencies of intercalation under a monolayer and a submonolayer film suggests that it is the edges of graphene islands that are the defects involved in intercalation of particles under graphene, as was supposed in Ref. [2]. After the islands had coalesced to form a continuous monolayer, the penetration with respect to intercalating particles decreases. And conversely, the increase of the efficiency to a value approaching unity means that the islands have become close in size to the migration path lengths of aluminum atoms they can travel in their lifetimes over graphite surface at a given temperature. Scanning tunneling microscopy suggests that the island size is 3000--8000 Å, and, hence, the migration path lengths of aluminum atoms at 1000--1100 K should be of the same order of magnitude.

The above increase in the intercalation efficiency is very likely of a universal nature, so that it will be characteristic of many types of intercalating particles.

9. Intercalation with iridium [29]

Adsorption of iridium atoms on graphene. Iridium atoms were provided by a second evaporating iridium ribbon, which was freed thoroughly of impurities and heated to ~2400 K. The expected flux of Ir atoms subliming from the ribbon was ~10^{15} $cm^{-2}s^{-1}$ [30], a level high enough to provide formation of several layers of iridium atoms on graphene surface in a reasonable time.

The main difficulty of the experiment consisted in the need to discriminate by AES the evaporated iridium from the iridium of the substrate. To overcome it, formation of the graphene film was preceded by evaporation on iridium of molybdenum atoms to a concentration of ~0.1 of monatomic density (molybdenum is identified adequately by AES). Molybdenum atoms were provided by well cleaned molybdenum ribbons heated to high temperatures. Thus, already after formation of graphene, AES offered a possibility of probing carbon in the form of graphene (E = 272 eV), molybdenum (E = 221 eV), and iridium (E = 176 eV) (Fig. 22a). In these conditions, the intensities of the molybdenum and iridium Auger signals decreased ~1.6 times, a figure characteristic of screening by a graphene film [31]. Next, 2--3 layers of iridium were evaporated on graphene at 300 K; this resulted in a decrease of the Auger signal intensities of carbon and molybdenum by about a factor 3 (Fig. 22b).

a.

b.

c.

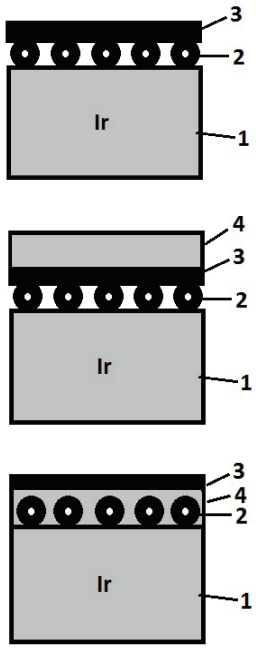

Fig. 22. A model scheme for the adsorption system Ir - graphene with intercalated atomic Mo as an inner standard: **a** - Ir substrate (1) with chemisorbed Mo (2) under graphene (3). Mo surface concentration is ~0.1 ML; **b** - the same system with Ir film of ~2 ML thickness (4) deposited above the graphene at 300 K; **c** - the result of the system annealing at 1200 K.

Annealing of the Ir(111)-Mo-graphene system. Figure 23 illustrates the results of annealing of an iridium film on graphene obtained by AES. The intensity of the carbon Auger signal at T = 1100 K was found to recover to the initial level corresponding to a clean graphene surface. At the same time, the molybdenum Auger signal intensity did not change. This can be understood by examining Fig. 22c. The evaporated iridium has diffused under heating of the sample under the graphene; the graphene surface became free of the adsorbate, with the intensity of the carbon Auger signal growing back to the original level (Fig. 23). At the same time, the iridium film confined under graphene continues to screen the layer of molybdenum, and its Auger signal intensity remains unchanged (Fig. 22c). The decrease of the iridium Auger signal in intensity should apparently be attributed to transition of Ir atoms to the intercalated state and to their screening by the graphene film (Fig. 23).

Direct experiments with evaporation of Ir atoms on graphene performed at moderate temperatures of 1100--1300 K suggest accumulation of iridium under the graphene; indeed, the molybdenum Auger signal intensity decreases, while the surface of graphene remains free of the adsorbate. For $T \geq 1300$ K, desorption of iridium atoms from the heated passive graphene surface begins to play a prominent part, with the result that buildup of Ir atoms in intercalated state decreases strongly.

Experiments with intercalation of graphene with iridium atoms provided supportive evidence for the overall pattern of this process for polyvalent atoms, namely, intensive

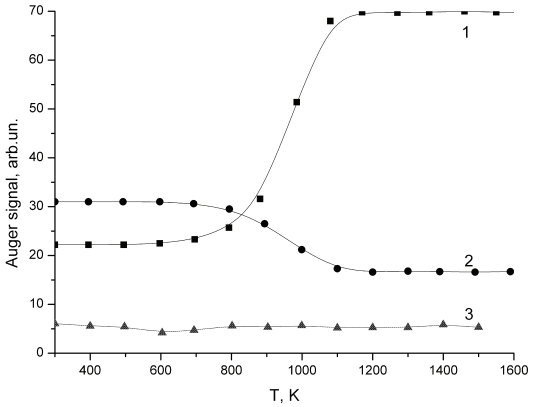

Fig. 23. Carbon (1), Ir (2), and Mo (3) Auger signals versus annealing temperature in a stepwise, within 100 K, heating of the Mo film initially deposited onto graphene at 300 K.

penetration of the adsorbate under the graphene is observed to occur at moderate and high temperatures (1000--1500 K). Recall that atoms with low ionization potentials (primarily the alkali metals) intercalate under graphene at low temperatures, $T \leq 700$ K; also, the lower the temperature, the more efficient is the diffusion of adatoms under the graphene film.

10. Intercalation with copper [32]

Evaporation and annealing of a copper film on iridium. Copper atoms were evaporated on an iridium surface at 300 K until the Auger signal intensity of the substrate dropped to one half its original level, which we estimated as corresponding to a copper concentration of about two monolayers. The main events occurring under stepped annealing of such a film are observed at $T \sim 1100$ K; more specifically, within a narrow temperature interval of the order of 50 K, the Auger signal of copper drops sharply in intensity to melt into the background noise, whereas that of iridium recovers to the original level identified with a clean surface. The most probable mechanism accounting for the surface cleaning is desorption of copper from the iridium surface. While this experiment does not permit us to exclude completely the possibility of copper dissolution in the bulk of the substrate, later experiments with graphene (see below) make this assumption highly unlikely.

Evaporation and annealing of a copper film on graphene atop iridium. Two copper monolayers were evaporated at 300 K on graphene (Fig. 24a), after which the system was annealed in steps at a number of temperatures. The variation of Auger signal intensity from the iridium substrate (E = 176 eV), copper (E = 60 eV), and carbon (E= 272 eV) is displayed in graphical form in Fig. 25. We readily see that at the transition from 1100 to 1200 K the Auger signal of carbon increased sharply to become equal to that from clean graphene surface. There still remains a noticeable Auger signal of copper, though; and since the Auger signal intensity of the substrate is substantially lower than that of the initial, copper-free "graphene on iridium" system, the only reasonable interpretation of the above observations appears to be that copper atoms escaped from the surface under the graphene film to become an intercalant (Fig. 24b). The graphene-involved decrease of the Auger signal of copper (E = 60 eV) to about one half its original value suggests that practically all of the

a.

b.

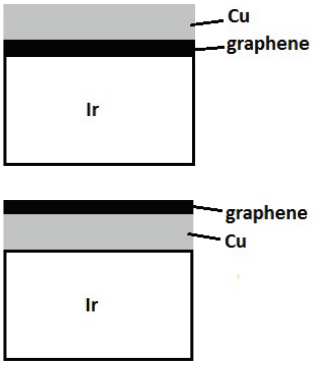

Fig. 24. Schematic structure of the layer transformation for the system Ir(111) - graphene - Cu: (**a**) - Cu film of ~2 ML thickness is deposited upon graphene on Ir(111) (T=3000K); (**b)** - the same layer after annealing at 1200 K.

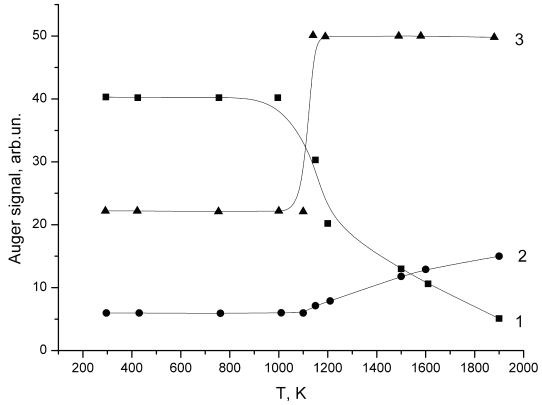

Fig. 25. Cu (1), Ir (2), and carbon (3) Auger signals versus annealing temperature in a stepwise, within 100 K, heating of the Cu film initially deposited onto graphene at 300 K. Time delay is 30 s at each temperature.

copper atoms initially adsorbed on graphene ended with being confined under it [32]. Further annealing brought about one more intriguing observation, namely, the Auger signal of copper is observed now under annealing up to ~1700 K, i.e., a temperature 500 K (sic!) higher than that in the case of clean iridium surface.

This seems to imply that in the first experiment copper atoms mostly desorbed from the clean surface of iridium, whereas in the second experiment the graphene "roof" interferes with this process, with copper atoms left confined to the surface up to high temperatures. Obviously enough, the channel of copper dissolution in the bulk of the metals (if it does exist) remains available in the presence of a graphene film too; moreover, the graphene "roof" which confines Cu atoms at high temperatures (≥1700 K) enhances the probability for adatoms to dissolve in the bulk of the substrate metal, as this was observed [33] to occur for cesium atoms intercalated in the same iridium-graphene system.

Thus, graphene adsorption on iridium surface acts as a kind of a trap for intercalated copper atoms by increasing substantially the temperature at which the sample is freed completely of the adsorbed atoms.

Graphene acts as a trap for atoms with both high and low ionization potentials, for instance, Cs, K, Na [2, 3, 32]. These two types of systems differ, however, radically from one another. First, atoms of alkali metals intercalate actively under graphene only at low temperatures, $T \leq 700$ K. Second, such atoms can be freed completely from under graphene only if all of the graphene islands break up under heating; the temperatures involved may, however, be quite high indeed---for instance, intercalated cesium escapes from under graphene islands on Re(10-10) at $T \sim 2200$ K (sic!) [2].

In the case of polyvalent atoms and atoms with high ionization potentials, breakup of graphene islands is not required altogether; indeed, the intercalant can escape from under a continuous graphene film through the same defects that were possibly instrumental in its penetration there in the first place (Fig. 26).

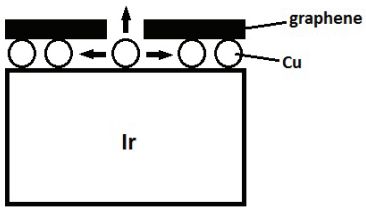

Fig. 26. A model scheme for atomic Cu thermal desorption from the intercalated state.

Now we are turning to the question of why atoms of copper or of other polyvalent high-ionization potential metals diffuse readily under a graphene film on a metal at $T \sim 1100$--1200 K, whereas their total removal from the intercalated state requires substantially higher temperatures. It might appear strange that the graphene film behaves in such a, say, anisotropic manner, namely, it is easy to penetrate when atoms transfer from the adsorbed to intercalated state, i.e., from the outer surface inward, but is difficult to cross in the opposite direction,

Let us turn to Fig. 26. As demonstrated by direct studies of migration of Si adatoms on Ir(111), silicon adatoms migrate freely both over a clean iridium surface by wandering from one side of the ribbon to the other (originally clean) in the 1200 K--1500 K temperature interval, and over iridium with the graphene layer forming [2, 3]; in other words, graphene does not interfere with the migration of adatoms over the metal surface. The same results can be expected with other polyvalent atoms as well (Pt, Cu, Al, etc.); indeed, they migrate easily and uniformly under the graphene film on a metal at temperatures of 1100--1200 K.

But then how can an intercalated atom leave an adsorption system? Adatoms in intercalated state get a chance to desorb when two events coincide. First---adatom occurs close to a defect in the graphene film, i.e., on the open surface, as it were, without a graphene roof overhead (Fig. 26). Second---if the adatom receives at exactly this instant a heat pulse from the substrate strong enough to desorb or transfer to the graphene film with subsequent desorption. Otherwise, the adatom will continue its migration further under the graphene film and, even if it is hit by a thermal pulse from the substrate strong enough to break the adsorption bond, will not leave the system, because it will be repelled back from the graphene film. Obviously enough, in this case desorption will become strongly complicated, so that atoms confined under the graphene will be forced to stay in the system up to very

high temperatures. For illustration, Table 3 lists for the Ir(111)-graphene system the temperatures required for the adatoms to escape from a clean metal surface, T_1, and from the intercalated state, T_2.

Element	Cs	K	Al	Cu	Ag
T_1, K	900	900	1500	1250	1000
T_2, K	2000	2000	1900	1900	1900

Table 3.

Now atoms with low ionization potentials (Cs, K, Na) behave in a radically different way. Diffusion under the graphene film, migration under it and escape from under the graphene are essentially cooperative effects involving electrostatic repulsion of charged adatoms [2, 3]. It can be maintained with confidence that migration of single adatoms of alkali metals under a graphene film is all but suppressed [15].
Thus, the graphene "roof" reduces by many orders of magnitude the probability of desorption of adatoms from the surface compared with that from the open surface of a metal (Table 3).

11. Intercalation with fullerene molecules [34--36]

The density of the flux of C_{60} molecules was estimated from the time taken up by formation of a fullerene monolayer N_M on clean iridium at T = 300 K, when the Auger signal intensity of the substrate dropped to one fourth of its initial level, with $\upsilon_{C60} = N_M/t_M$, where $N_M \approx 2$ 10^{14} mol/cm^2.
If a fullerene monolayer is evaporated at 300 K on graphene atop iridium, the Auger signal intensity of the substrate drops practically down to background level. Heating such a film to T = 800 K brings about complete desorption of C_{60} molecules, because one observes recovery of the Auger signals of the graphene film and iridium. Thus, C_{60} molecules do not dissociate on the passive Ir-C surface and do not intercalate with it.
After this, a thick fullerite film (~ $3N_M$) was produced on the graphene (Fig. 27a). The intensity of the iridium Auger signal passes into background noise, while the carbon Auger peak took on "fullerene" shape with an energy of 269 eV. The results produced by heating of such a film to 800 K were as follows: only part of the C_{60} molecules desorbed, while a sizable part of C_{60} molecules diffused under the graphene film to become intercalated (Fig. 27b). The disappearance of the iridium Auger signal after the substrate had been heated to 800 K implies that C_{60} molecules had diffused under the graphene in an amount equivalent to not less than one monolayer. The Auger spectrum of carbon was in this case actually a superposition of the Auger spectra of graphene and a fullerene monolayer, with an energy of 271 eV. Experiments on adsorption of C_{60} on clean iridium demonstrated dissociation of C_{60} molecules within the $900 \le T \le 1200$ K [37] (Fig. 27C).
In the $1400 \le T \le 1600$ K interval, the carbon Auger signal falls off somewhat in intensity, and the substrate Auger signal becomes visible (Figs. 27 c and d). This temperature interval, 1400--1600 K, is associated with active migration of carbon over the surface involving transfer onto the back side of the ribbon (Fig. 27 d), which was supported by direct evidence in studies of migration on clean iridium. For $T > 1600$ K, the carbon film under the graphene undergoes intensive graphitization which changes the C_{kvv} Auger spectrum shape to "graphitic". At T = 1600--2100 K, the intensity of the Auger signal of carbon can be

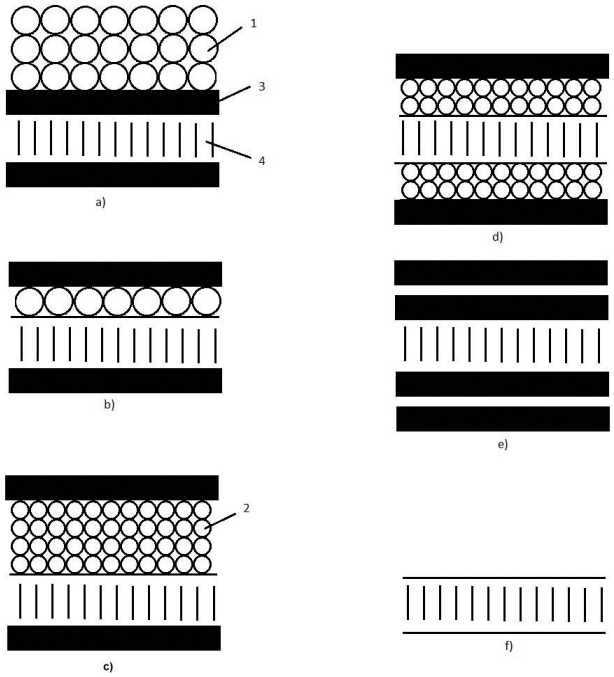

Fig. 27. Schematic representation for intercalation of the graphene layer on Ir(111) by molecular C_{60}. 1 - deposited polylayer film of molecular C_{60}; 2 - single carbon atom; 3 - graphene layer; 4 - iridium substrate. Temperature, K: (a) - 300; (b) - 800, (c) - 1200; (d) - 1600; (e) - 1900; (f) - 2200.

explained as due to screening by ~ two graphite monolayers (Fig. 27,e). Heating the substrate at temperatures above T ~ 2200 K cleaned efficiently the surface of carbon.
Thus, C_{60} molecules adsorbed in the form of a thick fullerite film (unlike a C_{60} monolayer) intercalate under the graphene atop iridium. This might be because the C_{60} molecules at the "bottom" of the fullerite film cannot desorb fast enough at T = 800 K and do not break up on the passive graphite surface, but rather transfer by diffusion to the intercalated state.
Graphene on rhenium can be intercalated with fullerene molecules just as this is done with iridium [36].

12. Electronic properties of graphene on metals with adsorbed and intercalated atoms [38--42]

As shown by calculations [43, 44] corroborated by experimental studies of the valence band of single-crystal graphite by photoelectron [45] and Auger electron [46] spectroscopy, the densities of both filled and empty electronic states of two-dimensional graphite drop dramatically close to the Fermi level.
In describing the interaction of particles with the metal surface, we shall follow the scheme suggested by Gurney [47]. As a single atom approaches the surface of a metal, interaction with it broadens the discrete level of the valence electron of the atom into a quasi-level and displaces it from its original position (Fig. 28). In this schematic description, one species of

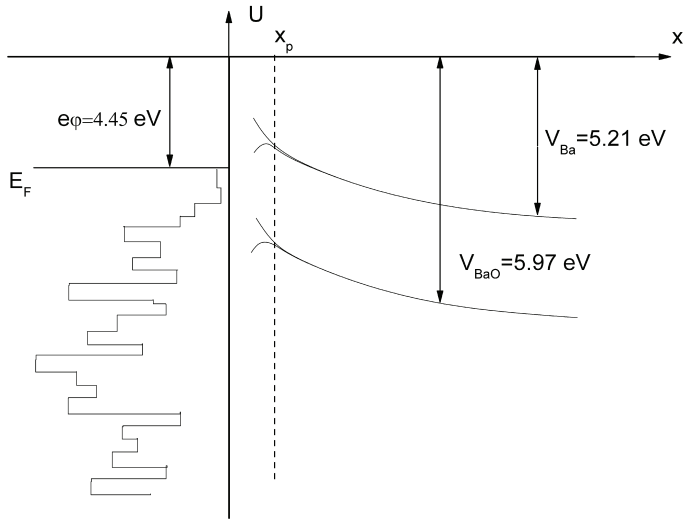

Fig. 28. Schematic transformation of the valence electron level of atomic Ba and molecular BaO in their moving towards the graphene layer on a metal. eφ is the graphene work function, V - atomic particle ionization potential.

adatoms differs from another in the shape and position of the quasi-level only. The adatom charge is determined both by the position of the center of the quasi-level relative to the Fermi level and its width. For the transfer of valence electrons from Cs and Ba adatoms to the valence band of graphite to be efficient, a sizable part of the quasi-level should be located in both cases above the Fermi level. Adsorption and intercalation with both Cs and Ba adatoms brings about filling of the empty band in the valence band of graphite lying above the Fermi level by depersonalized electrons. It thus appears reasonable to expect that the C_{kvv} Auger transition in two-dimensional graphene involving two electrons from the valence band should be sensitive to its filling. Discussion of the electronic properties of Re-C and Ir-C containing Cs and Ba can be found in Refs. [38--42].

Graphene residing on a metal is made up of atoms of two kinds, adsorbed and intercalated ones, albeit in somewhat different conditions. We start with experiments [28] in which adsorption of Ba atoms on graphene atop iridium heated to 900 K was performed by high-resolution ($\Delta E/E \approx 0.1\%$) AES. It was found that Ba fills only the intercalated state up to high concentrations, ~5 10^{14} cm^{-2}, at saturation. As evident from Fig. 29, before the intercalation the C_{kvv} Auger peak has a characteristic graphitic shape with energies 247 and 263 eV in the positive part of the spectrum, but no carbidic peak at the energy 255 eV (spectrum 1). We see that intercalation with Ba does not affect the "graphitic", positive part of the spectrum, while in its negative part, as the Ba concentration increases, first a peak at 276.5 eV (spectra 2 and 5), and after that, a second peak with an energy of 281 eV (spectra 3 and 4) appears on the high-energy side. One may thus conclude that the intercalated Ba is in the charged state, with its valence electron donated to the valence band of graphene to fill the levels adjoining the Fermi level, which is evidenced by the change in the high-energy part of the C_{kvv} Auger peak, because the transition in carbon is the *kvv*-type, and it involves two electrons of the graphite valence band. A similar pattern was observed in intercalation of HOPG graphite

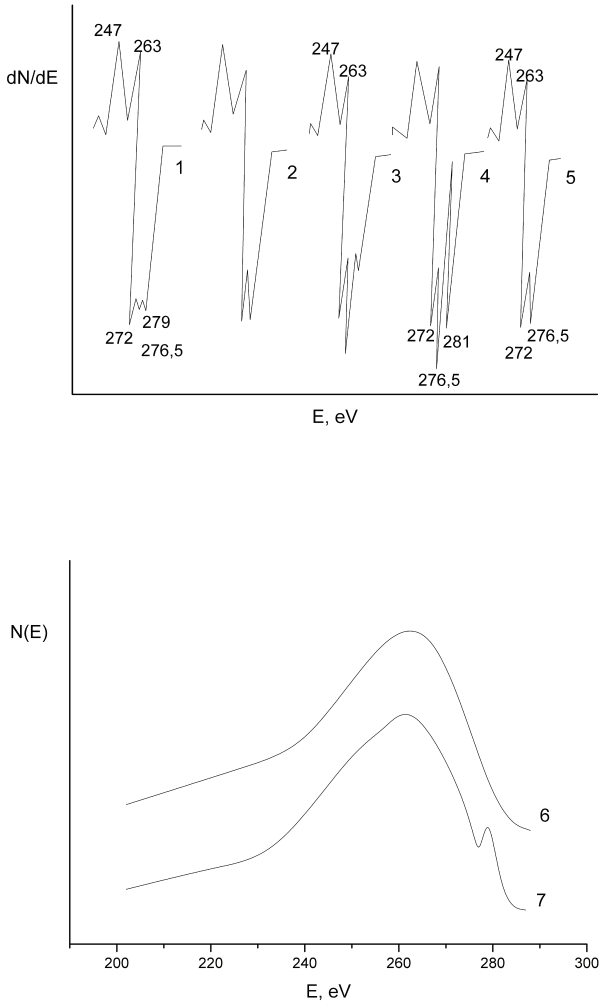

Fig. 29. Carbon KVV differential Auger spectra for sequential stages of Ba adsorption on the graphene layer on Ir(111) at 900 K. Ba concentration under the layer, 10^{14} cm^{-2}: 1 - 0; 2 - 1.5; 3 - 2.5; 4 - 5.0 (saturation). 5 - C_{KVV} Auger spectrum after system annealing at 1600 K (N_{Ba} ~ $2*10^{14}$ cm^{-2}). 6; 7 - integral C_{KVV} Auger spectra for pure grapene (6) and for the state 4: Ba adsorption to saturation (7).

with atoms of alkali metals [46, 48]. Heating an Ir-C ribbon to 1600 K forces part of the intercalated Ba to desorb, with the remaining Ba with a concentration of 2 10^{14} cm^{-2} being identifiable with the Auger peak at 276.5 eV (spectrum 5).

Figure 30 [41] presents C_{kvv} Auger spectra obtained in adsorption of Cs on Re-C. This process is paralleled by simultaneous filling of the adsorption (to a concentration N_α) and intercalation (to a concentration N_γ) states, and at the completion of adsorption, to saturation $N_\alpha \sim N_\gamma \sim 4$

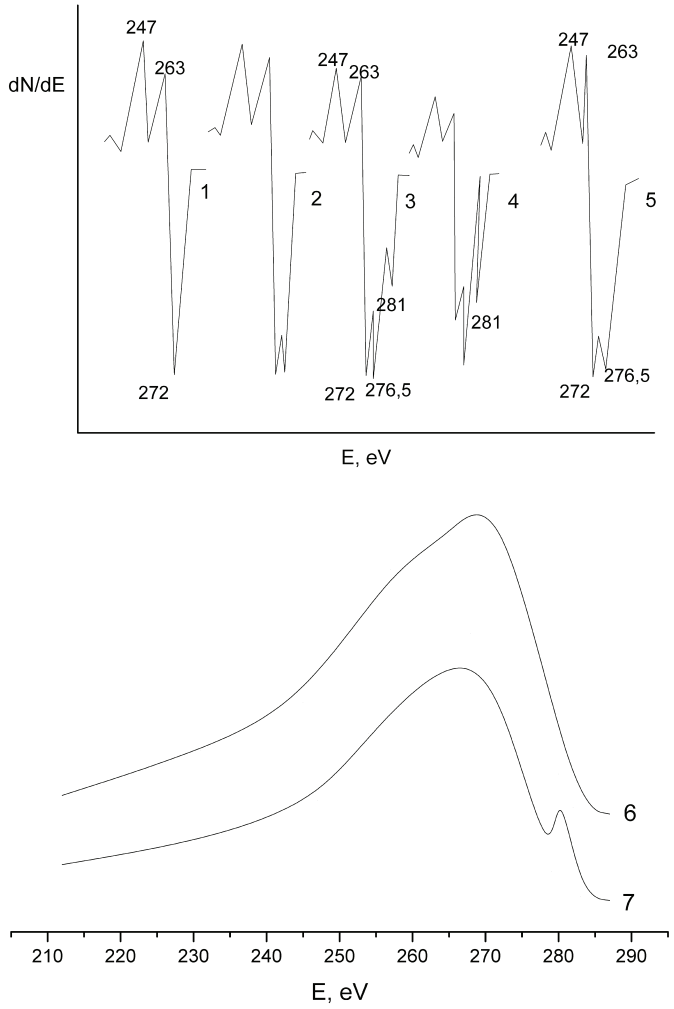

Fig. 30. Carbon KVV differential Auger spectra for sequential stages of Cs adsorption on the graphene layer on Re(10-10) at 300 K. Total Cs concentration over and under the layer, 10^{14} cm^{-2}: 1 - 0; 2 - 1.0; 3 - 2.0; 4 - 7.5 (saturation). 5 - C_{KVV} Auger spectrum after system annealing at 850 K (N_{Cs} ~ 1*10^{14} cm^{-2}). 6; 7 - integral C_{KVV} Auger spectra for pure grapene on Re (6) and for the state 4 - Cs adsorption to saturation (7).

10^{14} cm^{-2}. We readily see that the valence-band electrons of Cs fill the same levels in the graphite valence band as in adsorption of Ba, with peaks at 276.5 eV and 281 eV appearing successively, besides the one at 272 eV, in the negative part of the spectrum.

Interesting relevant information on the behavior of intercalated Cs and Ba with oxygen admitted to the instrument can be found in Ref. [42]. In this experiment, Re-C containing only intercalated Cs, and adsorbed and intercalated Cs was exposed at 300 K to O_2 (with a

dose of 10^{-6} Torr x 60 s = 60 Langmuirs), and C_{kvv} Auger spectra were recorded (Fig. 31). It turned out that at 300 K the concentration of surface-adsorbed carbon on graphene is as low as to be undetectable by AES (O_2 is only physisorbed on the basal plane of crystalline graphite). Exposure to oxygen did not affect the shape of the C_{kvv} Auger peak of intercalated Cs, wherefrom we can infer that oxygen does not diffuse under the graphite islands on rhenium. Interestingly, the shape of the C_{kvv} peak of adsorbed Cs did change; indeed, the peak at 281 eV disappeared, which implies that as a result of oxidation part of the Cs valence electrons returns from the valence band of graphite into the oxide molecule. Figure 28 illustrates this in the particular example of Ba, in which case oxidation of Ba adatoms on graphene results in formation of a BaO admolecule with its inherent system of electronic levels. It is a safe guess that because of the high ionization potential of the BaO molecule (V_{BaO} = 6.97 eV, to be contrasted with V_{Ba} = 5.21 eV for the Ba atom) the quasi-level of the valence electron in the BaO admolecule lies below the graphite Fermi level and, thus, will be filled in oxidation by electrons leaving the valence band of graphite.

A.

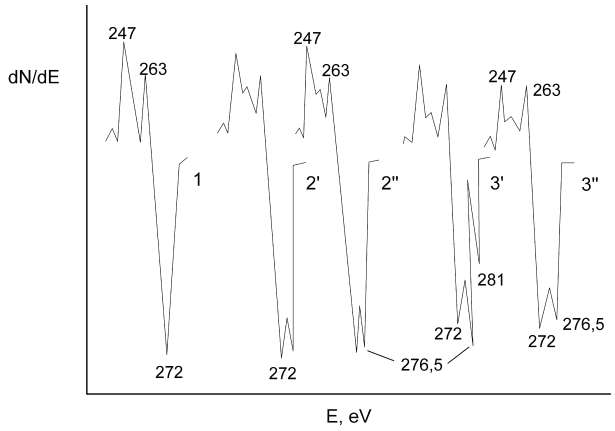

B.

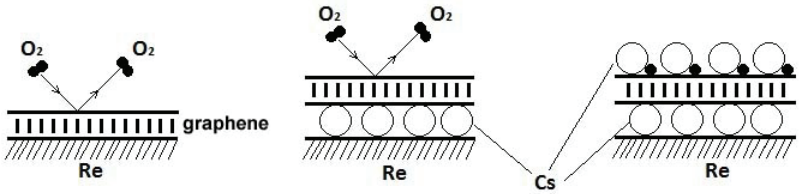

Fig. 31. Cs adsorption on the graphene layer on Re(10-10) at 300 K with subsequent oxidation at P_{O2} = 1*10^{-5} Torr. **A.** Carbon KVV differential Auger spectra. Total Cs concentration over and under the layer, 10^{14} cm^{-2}: 1 - 0; 2′ and 2′′ - 1.5; 3′ and 3′′ - 7.0; (saturation). The spectra 2′ and 3′ are taken before exposure to oxygen; the spectra 2′′ and 3′′ - after the exposure. **B**. Schematic representation of the process.

An interesting study [42] compared the possibilities of intercalating with cesium the surface of iridium with graphene and a monolayer of chemisorbed carbon with a concentration N_C ~ 3.9 10^{15} cm^{-2} produced by adsorption of C atoms on iridium at 300 K. It was found that, in

contrast to graphite, Cs does not intercalate under the monolayer of chemisorbed carbon; indeed, there is no characteristic splitting of the C_{kvv} Auger peak and no high-temperature ($T \geq 2000$ K) γ phase in the TD spectrum.

Another study [41] covered intercalation not only of graphene films on metals with Cs and Ba, but that of thick graphite films on rhenium with cesium at 300 K. Figure 31 presents Auger spectra of graphite on rhenium taken before (spectrum 1) and after (spectrum 2-4a) intercalation with cesium. We readily see that intercalation of both graphene and graphite with cesium atoms initiates similar changes in the shape of the carbon Auger spectrum. As already pointed out, in the case of graphene the strong changes in the shape of carbon Auger peak stem from its unique electronic properties, namely, the layer being two-dimensional, there are many electrons in the valence band, and the levels are widely separated. The same explanation can apparently be assigned to a thick graphite film, because graphene layers are not coupled by electron exchange, and they are bound by van der Waals forces. Incidentally, studying an Auger spectrum of carbon of a similar shape in the case of intercalation into a thick graphite film required a substantially longer exposure time than in the case of one graphene layer. There is nothing strange in it, because as the number of graphite layers increases, the adsorption capacity of the system with respect to cesium which intercalates between all graphite layers increases proportionally. Significantly, heating a graphite film intercalated with cesium to $T \sim 1000$ K removes completely the intercalated cesium (except for the first graphene layer on the metal). We may infer that this heating temperature is high enough to remove cesium both from the surface and from the bulk of graphite, because the edges of graphite "plates" in a thick film are not closed and, thus, do not interfere with diffusion of Cs adatoms with their subsequent desorption.

If a thick, cesium-intercalated graphite film (its Auger spectrum is 4a in Fig. 31) is exposed to oxygen, the Auger peak of cesium decreases by about a factor 5 (from 5a to 5b in Fig, 31), and a high Auger peak of oxygen (6 in Fig. 31) appears in the spectrum. Explanation to this interesting observation can be readily found in that the charged cesium adatoms residing on the outer side of the graphite film become neutralized in the course of oxidation, and, thus, will not interfere with the release of cesium sandwiched inside the graphite film, where cesium adatoms are charged and, hence, repel one another. Thus, a layer of oxide of the alkali metal grows on the surface of the graphite film, whose thickness is large enough to bring about an increase of the Auger peaks of cesium and oxygen and a decrease of that of oxygen. Experiments showed that the thickness of the oxide layer grows with that of the graphite film intercalated with cesium.

13. References

E.V. Rut'kov, A.Ya. Tontegode Pisma Zhur. Tekh. Fiz., 7(18), 1122, (1981)

A.Ya. Tontegode, E.V. Rut'kov. Usp. Fiz. Nauk, 163(11), 57, (1993)

N.R. Gall, E.V. Rut'kov, A.Ya. Tontegode. Modern Phys. B., 11(16), 1765, (1997)

Graphite Intercalation compounds eds. H.Zabel, S.A.Solin, Springer Ser.Mater.Sci., 1990, v.14; 1992, v.18.

N.A. Kholin, E.V. Rut'kov, A.Ya. Tontegode. Surf. Sci., 139, 155, (1984)

J.E.Fischer, R. Thomson, Phys.Today, 1978, v.31, N.7, p.363.

N.R. Gall, E.V. Rut'kov, S.N. Mikhailov, A.Ya. Tontegode Fiz. Tverd. Tela. 27(8), 2351, (1985)

N.R. Gall, S.N. Mikhailov, E.V. Rut'kov, A.Ya. Tontegode Zhur. Tekn. Fiz., 56, 732, (1986)
N.R. Gall, S.N. Mikhailov, E.V. Rut'kov, A.Ya. Tontegode Surf. Sci, 191, 185, (1987)
N.R. Gall, S.N. Mikhailov, E.V. Rut'kov, A.Ya. Tontegode Fiz. Tverd. Tela, 28, 2521, (1986)
N.R. Gall, S.N. Mikhailov, E.V. Rut'kov, A.Ya. Tontegode Synthetic Metals, 34, 497, (1989)
E.V. Rut'kov, N.R. Gall, Fiz. Tverd. Tela 51(8), 1639 (2009)
E.V. Rut'kov, N.R. Gall. Pisma Zhur. Eksp. Tekn. Fiz. 88(4), 308, (2008)
M.S. Dresselhaus, G. Dresselhaus. Advan. Phys. 30, 139, (1981)
M.V. Knat'ko, V.I. Paleev, N.D. Potehina Zhur. Tekn. Fiz. 59, 154, (1989)
A. Ya. Tontegode Pisma Zhur. Tekn. Fiz., 15, 57, (1989)
E.V. Rut'kov, A.Ya. Tontegode Zhur. Tekn. Fiz., 45(9), 1884, (1975)
E.V. Rut'kov, A.Ya. Tontegode Fiz. Tverd. Tela, 32(10), 2960, (1990)
E.V. Rut'kov, A.Ya. Tontegode Materials Science Forum, (91-93), 709, (1992)
E.Y. Zandberg, E.V. Rut'kov, A.Ya. Tontegode Pisma Zhur. Tekn. Fiz., 1(16), 741, (1975)
E.Y. Zandberg, E.V. Rut'kov, A.Ya. Tontegode, N.D. Potehina Fiz. Tverd, Tela, 19(2), 1665, (1997)
N.R. Gall, E.V. Rut'kov, A.Ya. Tontegode, Pisma Zhur. Tekn. Fiz. 14(6), 527, (1988)
N.R. Gall, E.V. Rut'kov, A.Ya. Tontegode Povrkhnost, 10, 47, (1989)
N.R. Gall, E.V. Rut'kov, A.Ya. Tontegode J. Chemical Vapor Deposition, July, 6(1), 72, (1997)
N.R. Gall, E.V. Rut'kov, A.Ya. Tontegode Pisma Zhur. Eksp. Tekn. Fiz., 75(1), 28, (2002)
N.R. Gall, E.V. Rut'kov, A.Ya. Tontegode Phys Solid State, 46(2), 371, (2004)
N.R. Gall, E.V. Rut'kov, A.Ya. Tontegode Semiconductors. 36(3), 276, (2002)
A.R.Ubbelohde, F.A.Lewis, "Graphite and its Crystal compounds", Oxford, Clarendon Press, 1960.
E.V. Rut'kov, N.R. Gall Pisma Zhur. Tekn. Fiz.35 (16), 1 (2009)
N.A.Nesmeianov "Vapor pressure of chemical elements", Academia Nauk Publ., Moscow, 1961. (in Russian)
V.N. Ageev, E.V. Rut'kov, A.Ya. Tontegode, N.A. Kholin Fiz. Tverd. Tela, 23(8), 2248, (1981)
E.V. Rut'kov, N.R. Gall Fiz. Tekn. Poluprovodnikov, 43(10), 57 (2009)
A.Ya. Tontegode, F.K. Yusifov Fiz. Tverd. Tela, 35, 987, (1993)
E.V. Rut'kov, A.Ya. Tontegode, M.M. Usufov, Yu.S. Grushko Mol. Mat., 4, 217, (1994)
E.V. Rut'kov, A.Ya. Tontegode, M.M. Usufov Phys. Rev. betters 74(5), 758, (1995)
N.R. Gall, E.V. Rut'kov, A.Ya. Tontegode, M.M. Usufov, Mol. Mat., 7, 187, (1996)
E.V. Rut'kov, A.Ya. Tontegode, Yu.S. Grushko Pisma Zhur. Eksp. Tekn. Fiz. 57(11), 712, (1993)
N.R.Gall, S.N. Mikhailov, E.V. Rut'kov, A.Ya. Tontegode Poverkhnost, 12, 14, (1986)
N.R.Gall, S.N. Mikhailov, E.V. Rut'kov, A.Ya. Tontegode Fiz. Tverd. Tela, 28(8), 2521, (1986)
N.R.Gall, S.N. Mikhailov, E.V. Rut'kov, A.Ya. Tontegode Poverkhnost, 4, 22, (1987)
N.R.Gall, S.N. Mikhailov, E.V. Rut'kov, A.Ya. Tontegode Synthetic Metals, 34(1-3), 447, (1989)
N.R.Gall, S.N. Mikhailov, E.V. Rut'kov, A.Ya. Tontegode Surf. Sci., 226, 381, (1990)
R.F. Willis, B.E. Fitton, G.S. Painter Phys. Rev., 9, 1926, (1974)
G.S. Painter, D.E. Ellis Phys. Rev. 1, 4797, (1970)
P. Murchand, G. Fretigny, M. Lagies and al. Phys. Rev., 30, 4788, (1984)
P. Oelhafen, P. Pfluger, H.I. Grüntherodt Solid State Commun., 32, 885, (1975)

R. Gurney Phys. Rev., 47, 479, (1935)
P. Pfluger, P. Oelhafen, N.H. Künzi, R. Ieker, E. Hauser, K.P. Ackermann, M. Müller, H.I. Cüntheoront Physica B+C, 99, 395, (1980)

Part 2

Electronic Properties

13

Electronic and Magnetic Properties of the Graphene-Ferromagnet Interfaces: Theory vs. Experiment

Elena Voloshina[1] and Yuriy Dedkov[2]
[1]*Physikalische und Theoretische Chemie, Freie Universität Berlin*
[2]*Fritz-Haber-Institut der Max-Planck-Gesellschaft, Berlin*
Germany

1. Introduction

Graphene is a two-dimensional sheet of carbon atoms arranged in a honeycomb lattice with two crystallographically equivalent atoms (C1 and C2) in the unit cell [Geim (2009); Geim & Novoselov (2007); Neto et al. (2009)] [Fig. 1(a)]. The sp^2 hybridization between one $2s$ orbital and two $2p$ orbitals leads to a trigonal planar structure with a formation of a σ bonds between carbon atoms that are separated by 1.42 Å. These corresponding σ bands have a filled shell and, hence, form a deep valence band. The half-filled $2p_z$ orbitals, which are perpendicular to the planar structure, form the bonding (π) and antibonding (π^*) bands in the electronic structure of graphene [Fig. 1(b)]. The π and π^* bands touch in a single point exactly at the Fermi energy (E_F) at the corner of the hexagonal graphene's Brillouin zone (K-points). Close to this so-called Dirac point (E_D) the bands display a linear dispersion and form perfect Dirac cones [Neto et al. (2009)] [Fig. 1(c)]. Thus, undoped graphene is a semimetal ("zero-gap semiconductor"). The linear dispersion of the bands mimics the physics of quasiparticles with zero mass, so-called Dirac fermions [Geim (2009); Geim & Novoselov (2007); Neto et al. (2009)].

The unique "zero-gap" electronic structure of graphene leads to some limitations for application of this material in real electronic devices. In order, for example, to prepare a practical transistor, one has to perform a "doping" of a graphene layer inducing electrons or holes in the electronic structure [Fig. 1(d)]. There are several ways of the modification of the electronic structure of graphene with the aim of doping. Among them are: (i) incorporation in its structure of nitrogen [Wang et al. (2009)] and/or boron [Dutta & Pati (2008)] or transition-metal atoms [Mao et al. (2008)]; (ii) using different substrates that influence the electronic structure of the graphene layer, e. g. metallic substrates for the graphene growth [Wintterlin & Bocquet (2009)]; (iii) intercalation of different materials underneath graphene grown on different substrates [Dedkov et al. (2008a; 2001); Enderlein et al. (2010); Gierz et al. (2008; 2010); Shikin et al. (2000)]; (iv) deposition of atoms or molecules on top [Boukhvalov & Katsnelson (2009); Coletti et al. (2010)]; etc.

The exceptional transport properties of graphene [Geim & Novoselov (2007)] make it a promising material for applications in microelectronics [Morozov et al. (2008); Novoselov et al. (2005)] and sensing [Schedin et al. (2007)]. This has recently led to a revival of interest

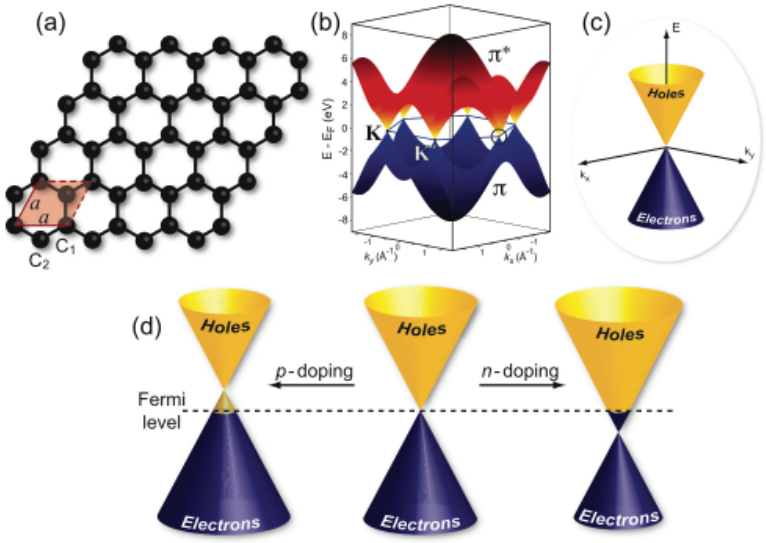

Fig. 1. (a) Crystal structure of the graphene layer where carbon atoms are arranged in the honeycomb lattice. Unit cell of graphene with lattice constant a has two carbon atoms per unit cell, C1 and C2. (b) Electronic dispersion of π and π^* states in the honeycomb lattice of free-standing graphene obtained in the framework of tight-binding approach. These branches have linear dispersion (c) in the vicinity of the K points of the Brillouin zone of graphene. (d) Position of the Dirac point and the Fermi level as a function of doping for the free-standing graphene.

in graphene on transition metal surfaces [Coraux et al. (2008; 2009); Dedkov et al. (2008a;b); Gamo et al. (1997); Hu et al. (1987); Land et al. (1992); Martoccia et al. (2008); N'Diaye et al. (2006); Sasaki et al. (2000); Sutter et al. (2009); Wang et al. (2008)], as large area epitaxial graphene layers of exceptional quality can be grown, which might be an alternative to micromechanical cleavage for producing macroscopic graphene films [Bae et al. (2010); Kim et al. (2029)].

The electronic interaction of graphene with a metal is both of fundamental and technological interest in view of possible device applications. Recent theoretical calculations by V. M. Karpan and co-workers [Karpan et al. (2007; 2008)] for graphene/metal interfaces imply the possibility of an ideal spin-filtering in the current-perpendicular-to-the-plane configuration (CPP) for the ferromagnet/graphene/ferromagnet sandwich-like structures. The close-packed surfaces of Co and Ni were considered as ferromagnetic (FM) electrodes, which perfectly coincide with graphene from the crystallographic point of view. The spin-filtering effect originates form the unique overlapping of the electronic structures of the graphene monolayer and close-packed surfaces of ferromagnetic Ni and Co. As discussed earlier, graphene is a semimetal with electronic density in the vicinity of E_F at corners (K points) of the hexagonal Brillouin zone of graphene. If the Fermi surface projections of ferromagnetic metals, fcc Ni or Co, on the (111) close-packed plane are considered, then in both cases one finds only minority electron density around the K points of the surface Brillouin zone. In this case, it is expected that the preferential transport of only minority electrons and

perfect spin-filtering will appear in a FM/graphene/FM stack [Karpan et al. (2007; 2008)], because graphene has electronic states only around K. The interaction between graphene and ferromagnetic material will however change the electronic properties of the interface partially quenching the spin-filtering effect in the sandwich-like structure, but a sizable effect can still be detected by choosing the proper combination of FM materials [Yazyev & Pasquarello (2009)] and this effect is predicted to increase strongly when multilayers of graphene are used [Karpan et al. (2007; 2008)].

Besides spin-filtering, graphene might be the best material for the realization of spintronic devices. Such systems usually require the effective injection of the spin-polarized electrons in the conductive channel which can be made from graphene [Tombros et al. (2007)]. However, prior to being able to implement graphene/ferromagnet systems in any kind of spintronic unit, a study of their electronic, magnetic, and interfacial properties has to be performed.

In the present chapter the electronic and magnetic structures of the graphene/FM interface will be discussed. From the theoretical side the different interfaces will be analyzed: graphene/Ni(111), graphene/Co(0001), graphene/1 ML Fe/Ni(111). Here the electronic structure of the interface as well as effect of induced magnetism in the graphene layer are discussed. As for experiment, the crystallographic structure, morphology, electronic and magnetic properties of a graphene/ferromagnet interface are considered for the case of the Ni(111) close-packed surface. Electronic structure studies of this interface reveal the existence of interface states, which originate from the strong hybridization of the graphene π and Ni $3d$ valence-band states leading to the appearance of the induced magnetic moment on the carbon atoms in the graphene layer that is confirmed by both x-ray magnetic circular dichroism (XMCD) and spin-resolved photoemission (PES). Detailed analysis of the Fermi surface of the graphene/Ni(111) system is performed via comparison of experimental and theoretical data for this interface.

2. Methods of investigations of graphene on ferromagnetic surfaces

2.1 Methods of calculation of the electronic and magnetic structure

Binding between graphene and metallic surface can be either chemical or physical in nature. Chemical binding typically implies a strong interaction through a charge sharing between the substrate and the adsorbate, yielding modification of their electronic structures. Physisorption, on the other hand, arises due to classical electrostatic or dispersion (van der Waals) interactions. The latter ones are the long-range correlation effects, which are not captured in the density functional theory (DFT) calculations because of the local character of standard functionals. In such cases, local density approximation (LDA) is known to give rather good results due to error cancellation. This is the reason of using for the graphene-containing systems the LDA, instead of generalized gradient approximation (GGA). Clearly, this is not a proper solution of the problem, and a better way would be to resort to methods beyond the DFT approach, either phenomenological or quantum-chemical post-Hartree-Fock correlation methods (see, e. g. [Paulus & Rosciszewski (2009); Pisani et al. (2008)]). An alternative approach is an inclusion of the dispersion correction to the total energy obtained with standard DFT approximation explicitly by hand with DFT-D method, that is atom pair-wise sum over C_6R^{-6} potentials (see, e. g. [Grimme (2004)]). High accuracy is accessible with a new exchange-correlation functional named van der Waals-density functional (vdW-DF), recently developed by Dion *et al.* [Dion et al. (2004)]. This functional is parameter free and therefore is considered *ab initio* in true spirit of DFT as it depends only on the total electron density.

The latter approach is shown to be working well for graphene/metal interface, where weak interaction between graphene and substrate is observed [Brako et al. (2010)].
In the previous theoretical studies on graphene/FM interface, the strong interaction for FM = Ni(111) or Co(0001) was found [Bertoni et al. (2005); Karpan et al. (2007; 2008)]. While existence of a non-magnetic configuration of graphene/Ni(111) interface, where graphene is weakly bound with substrate, was theoretically predicted, this structure was shown to be energetically unfavourable. The purpose of the present work is a comparison between theory and experiment, therefore the most stable configurations will be in the focus of the study. For them, standard GGA functionals are supposed to give reasonable result.
In our DFT studies, the electronic and structural properties of the graphene-substrate system are obtained using the Perdew-Burke-Ernzerhof (PBE) functional [Perdew et al. (1996)]. For solving the resulting Kohn-Sham equation we have used the Vienna Ab Initio Simulation Package (VASP) [Kresse & Furthmuller (1996a;b)] with the projector augmented wave basis sets [Blochl (1994)]. The plane-wave kinetic energy cutoff is set to 500 eV. The supercell used to model the graphene-metal interface is constructed from a slab of 13 layers of metal atoms with a graphene sheet adsorbed at both sides and a vacuum region of approximately 14 Å. When optimizing the geometry, the positions (z-coordinates) of the carbon atoms as well as those of the top two layers of metal atoms are allowed to relax. In the total energy calculations and during the structural relaxations the k-meshes for sampling the supercell Brillouin zone are chosen to be as dense as 24×24 and 12×12, respectively.

2.2 Experimental methods of investigation

The presented experimental studies of the graphene/Ni(111) interface were performed in different experimental stations in identical experimental conditions allowing for the reproducible sample quality in different experiments. In all experiments the W(110) single crystal was used as a substrate. Prior to preparation of the graphene/Ni(111) system the well-established cleaning procedure of the tungsten substrate was applied [Dedkov et al. (2008)]: several cycles of oxygen treatment with subsequent flashes to 2300°C. A well-ordered Ni(111) surface was prepared by thermal deposition of Ni films with a thickness of more than 200 Å on to a clean W(110) substrate and subsequent annealing at 300°C. An ordered graphene overlayer was prepared via thermal decomposition of propene (C_3H_6) according to the recipe described elsewhere [Dedkov et al. (2008;a;b; 2001); Nagashima et al. (1994)]. The quality, homogeneity, and cleanliness of the prepared graphene/Ni(111) system was verified by means of low-energy electron diffraction (LEED), scanning tunneling microscopy (STM), and core-level as well as valence-band photoemission.
STM experiments were carried out in an ultra-high vacuum (UHV) system (base pressure 8×10^{-11} mbar) equipped with an Omicron variable temperature scanning tunneling microscope. All STM measurements were performed in the constant-current-mode at room temperature using electrochemically etched polycrystalline tungsten tips cleaned in UHV by flash-annealing. The sign of the bias voltage corresponds to the voltage at the sample. Tunneling parameters are given separately for each STM image: U_T for tunneling voltage and I_T for tunneling current.
Near-edge absorption spectroscopy (NEXAFS) and XMCD spectra were collected at the D1011 beamline of the MAX-lab Synchrotron Facility (Lund, Sweden) at both Ni $L_{2,3}$ and C K absorption edges in partial (repulsive potential $U = -100$ V) and total electron yield modes (PEY and TEY, respectively) with an energy resolution of 80 meV. Magnetic dichroism spectra were obtained with circularly polarized light (degree of polarization is $P = 0.75$)

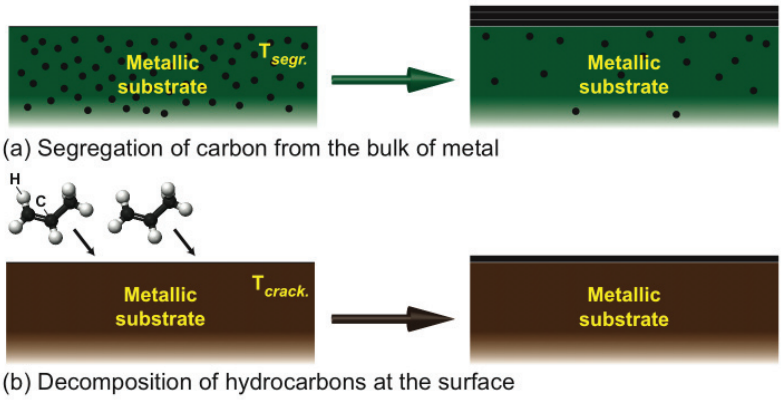

Fig. 2. Two ways of the graphene preparation on metal surfaces: (a) Segregation of bulk-dissolved carbon atoms to the surface at high temperature T_{segr}; (b) Decomposition (cracking) of hydrocarbon molecules at the surface of transition metals at high temperature T_{crack}.

in the remanence magnetic state of the graphene/Ni(111) system after applying of an external magnetic field of 500 Oe along the $< 1\bar{1}0 >$ easy magnetization axis of the Ni(111) film. All absorption measurements were performed at 300 K. The base pressure during the measurements did not exceed 1×10^{-10} mbar.

Angle-resolved PES (ARPES) experiments were performed at the UE56/2-PGM-1 beam-line at BESSY (Berlin, Germany). The photoemission intensity data sets $I(E, k_x, k_y)$ were collected with a PHOIBOS 100 energy analyzer (SPECS) while the graphene/Ni(111)/W(110) sample was placed on a 6-axes manipulator (3 translation and 3 rotation axes). The temperature of the sample during the measurements was kept at 80 K or 300 K. The energy/angular resolution was set to 80 meV/0.2°. In case of the spin-resolved PES experiments the mini-Mott-spin-detector (SPECS) was used instead of the 2D CCD detector. The spin-resolved spectra were collected in the remanent magnetic state of the graphene/Ni(111) system (see above) in normal emission geometry. The effective Sherman function was estimated to be $S_{eff} = 0.1$ and instrumental asymmetry was accounted via measuring of spin-resolved spectra for two opposite directions of the sample magnetization. The base pressure during all photoemission measurements was below 7×10^{-11} mbar.

3. Methods of graphene preparation on metallic surfaces

There are two common methods of the graphene preparation on metallic surfaces: (i) Segregation of the carbon atoms at the surface of bulk metallic sample, which was previously doped with carbon [Fig. 2(a)] and (ii) Decomposition of the carbon-containing molecules on the surface of transition metal [Fig. 2(b)]. In the first method the transition metal sample with some amount of carbon impurities or the bulk crystal, which was preliminary loaded by carbon (via keeping the sample at elevated temperature in the atmosphere of CO or hydrocarbons) is annealed at higher temperatures. This procedure leads to the segregation of carbon atoms at the surface of metal. The careful control of the temperature and the cooling rate of the sample allows to obtain the different thicknesses of the grown graphene layer: mono- vs. multilayer growth. In the second method the decomposition (cracking)

of carbon-containing molecules at the particular temperatures is used. Here, mostly light hydrocarbon molecules, like ethylene or propene, are used, but the decomposition of CO, acetylene, and of heavy hydrocarbon molecules, like cyclohexane, *n*-heptane, benzene, and toluene, also was successfully applied [Wintterlin & Bocquet (2009)]. In this method molecules could be adsorbed on the surface of metal at room temperature and then annealing of the sample leads to the molecule decomposition and hydrogen desorption; or molecules could be directly adsorbed on the hot sample. The recent experiments demonstrate that both methods, segregation and decomposition, practically lead to the graphene layers of the same quality. In case of segregation the kinetic of single graphene layer formation is defined by the careful controlling of the annealing temperature (but multilayers of graphene could be also prepared). In the second method the restriction to the formation of only single-layered graphene is defined by the fact that in this case the chemical reaction on the catalitically active metallic surface takes the place. Here the speed of hydrocarbon decomposition drops down by the several order of magnitude as soon the first grapehen monolayer is formed [Nagashima et al. (1994)]. List of metal surfaces, which were used for the preparation of graphene layers is compiled in Ref.[Wintterlin & Bocquet (2009)], where methods of preparation (segregation vs. decomposition), main experimental method, and corresponding reference are presented for different metallic surfaces (lattice-matched and lattice-mismatched).

4. Structure and bonding of graphene on ferromagnetic surfaces: Theory

The surface lattice constants of Ni(111), Co(0001), and the 1 ML Fe/Ni(111) system match the in-plane lattice constants of the graphene layer almost perfectly (compare: $a_{\mathrm{Ni}}/\sqrt{2} = 2.49$ Å, $a_{\mathrm{Co}} = 2.51$ Å, $a_{1\,\mathrm{ML\,Fe/Ni(111)}} = 2.52$ Å, and $a_{\mathrm{graphene}} = 2.46$ Å), that leads to the perfect crystallographic order at the interface between considered FM substrates and graphene. Several possible atomic configurations are usually considered for the interface between graphene and close-packed FM surface. Three "high-symmetry" structures, which preserve $3m$ symmetry, are known as $fcc-hcp$, $top-hcp$, and $top-fcc$. The latter one is schematically shown in Fig. 3: the C atoms are arranged above the Ni atoms of the first and third (fcc) layers. In the $top-hcp$ configuration, the C atoms are placed directly above the Ni atoms of the first layer (top site) and the second layer (hcp site). In the $fcc-hcp$ configuration, the C atoms are placed above fcc and hcp sites. Three additional configurations were considered recently, which were called $bridge-top$, $bridge-fcc$, and $bridge-hcp$. In these structures, one of the carbon atoms is not placed in top, fcc or hcp sites but in-between [Fuentes-Cabrera et al. (2008)].

In the present studies the electronic and magnetic structures of the graphene/Ni(111), graphene/Co(0001), and graphene/1 ML Fe/Ni(111) systems were calculated for the slab consisting of the graphene layer and 13 layers of FM material (in case of the latter system, 1 ML Fe was placed on the both sides of the 11-layers Ni slab in fcc stacking). As a first step the energy minimization for different structural arrangements of carbon atoms on FM surface was carried out. The results of these calculations are compiled in Table 1.

It has been found that the lowest energy configuration for FM = Ni or Co corresponds to a $top-fcc$ geometry in which one carbon atom is positioned above a surface FM atom (C-top) while the second carbon atom is situated above a third layer FM atom (C-fcc). This is in agreement with other previously published first-principles calculations [Bertoni et al. (2005); Eom et al. (2009); Karpan et al. (2007)] as well as with experiments for graphene on the Ni(111) surface [Gamo et al. (1997)]. In contrary to the latter result, where LEED $I-V$-curve analysis has been used in order to determine the interface arrangement, in experiments of C. Klink *et al.*

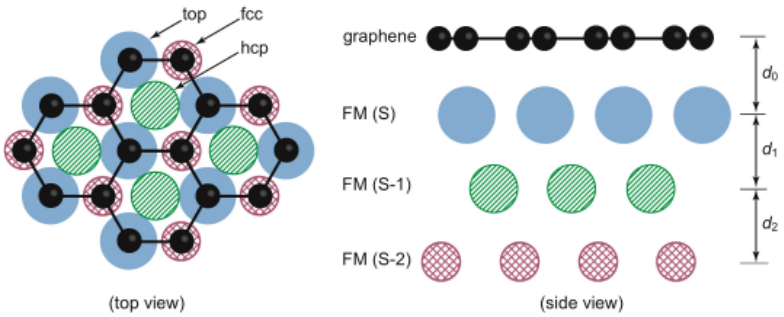

Fig. 3. Top- and side-view of a ball model of one of a possible arrangements of carbon atoms in a graphene layer on the lattice matched (111) surface. The different positions of carbon atoms in the graphene layer above FM interface atom (S) and on the hollow places above FM atoms in the second (S-1) as well as third layer (S-2) are marked as top, hcp, and fcc, respectively. d_{0-2} are distances between layers in the system.

[Klink et al. (1995)], involving combined STM and LEED studies, the $fcc - hcp$ configuration is shown to be the most stable one. The same conclusion was made by R. Rosei *et al.* [Rosei et al. (1983)], when using the extended-energy-loss fine-structure spectroscopy method. The calculations including three additional "low symmetry" configurations showed that within DFT employing GGA-PBE, none of the structures is stable at the experimentally relevant temperatures; with local-density approximation (LDA), the $bridge - top$ configuration was found to be the most energetically favorable one [Fuentes-Cabrera et al. (2008)].
The situation is different in the case of the graphene/1 ML Fe/Ni(111) system where the lowest-energy configuration was found to be $top - hcp$ with one carbon atom staying above Fe interface atom and the second one in the hollow hcp cite of the structure. The available experimental data [Dedkov et al. (2008a)] confirms the three-fold symmetry of this system, but cannot give any additional information about the stacking of the graphene and metallic layers. Structural studies by means of, e. g. LEED $I - V$-curve-analysis or x-ray diffraction, are necessary for this system.
The presented results (Table 1) demonstrate the reduction of the magnetic moment of the surface atoms of FM material upon adsorption of graphene on top. This reduction originates from the strong interaction between graphene π states and the 3d states of the FM interface layer. Such interaction leads to the noticeable modification of the graphene and metal valence band states, which will be discussed further in the text.
The electronic structure of a graphene sheet depends on its interaction strength with the ferromagnetic substrate. Clearly, the stronger bonding between graphene and underlaying metal, the shorter equilibrium distance d_0 between graphene and FM interface layer. As expected, this calculated distance is nearly the same for $top - fcc$ and $top - hcp$ arrangements, where one carbon atom of the graphene unit cell sits on top of a metal atom. But the energy difference found between these two models shows that FM atoms of the second and third layers also interact with the graphene layer. For the less strongly bound $fcc - hcp$ configurations of graphene on FM, the equilibrium separation is rather large, comparable to the layer spacing of 3.35 Å in bulk graphite (note: in our calculations, d_0 is slightly larger than can be expected due to the inability to describe dispersion interactions by PBE functional), indicating physisorption, and the characteristic band structure of an isolated graphene sheet is clearly recognizable.

	FM	Structure of the graphene/FM interface		
	Ni(111)	*top-fcc*	*top-hcp*	*fcc-hcp*
d_0 (Å)		2.135/2.133	2.145/2.146	3.540/3.540
d_1 (Å)	2.005	2.020	2.020	2.020
d_2 (Å)	2.031	2.017	2.015	2.036
ΔE (eV)		0.000	0.049	0.054
m_{FM} (μ_B)	−0.030/0.710	−0.025/0.543	−0.026/0.514	−0.029/0.669
m_{C} (μ_B)		−0.019/0.031	−0.019/0.027	0.000/0.000
	Co(0001)	*top-fcc*	*top-hcp*	*fcc-hcp*
d_0 (Å)		2.155/2.137	2.155/2.138	3.639/3.639
d_1 (Å)	1.954	1.963	1.956	1.952
d_2 (Å)	2.046	2.035	2.043	2.046
ΔE (eV)		0.000	0.017	0.090
m_{FM} (μ_B)	−0.053/1.784	−0.060/1.600	−0.059/1.583	−0.055/1.771
m_{C} (μ_B)		−0.043/0.038	−0.048/0.044	0.000/0.000
	1ML Fe/Ni(111)	*top-fcc*	*top-hcp*	*fcc-hcp*
d_0 (Å)		2.117/2.092	2.114/2.089	3.487/3.487
d_1 (Å)	2.039	2.029	2.019	2.028
d_2 (Å)	2.061	2.044	2.057	2.062
ΔE (eV)		0.021	0.000	0.104
m_{FM} (μ_B)	−0.028/2.622	−0.034/2.486	−0.035/2.469	−0.022/2.616
m_{C} (μ_B)		−0.048/0.040	−0.050/0.039	0.000/0.000

Table 1. Results for the atomic structure of the three graphene/FM interface models and for the clean FM surface: d_0 is the distance between the graphene overlayer and the interface FM layer (the two values for the two nonequivalent carbon atoms are indicated); d_1 is the distance between the interface FM layer and the second FM layer; d_2 is the distance between the second and third FM layers; ΔE is the energy difference between the energy calculated for the different slabs and the energy calculated for the most stable geometry; m_{FM} is the interface/surface FM spin magnetic moment (the two values for the sp and d magnetizations are indicated); m_{C} is the interface carbon spin magnetic moment (the two values for the two nonequivalent carbon atoms are indicated).

We consider the case of the graphene/Ni(111) as a representative one for the description of general features of the electronic structure of the graphene/FM interface with the analysis of the region around the Fermi level further in the text. The majority and minority spin band structures of the graphene/Ni(111) system (13 ML of Ni in the slab) with the $top - fcc$ arrangement of the carbon atoms are shown in Fig. 4. Due to the strong interaction between carbon layer and FM substrate, noticeable modification of the both graphene and FM band structure is observed. First of all, this is a nonrigid downward shift of the occupied graphene bands compare to those in pure graphene: at the Γ point, the π band is shifted by 2.25 eV while the σ band is only shifted by 1.15 eV. The unoccupied σ^* band is also shifted by 1.01eV. The interaction between graphene and metal layers implies a hybridisation of the graphene π bands with the nickel (cobalt, iron) 3d bands (and, in the second turn, with the FM 4s and 4p bands).

Strong hybridization of the graphene π and FM substrate 3d valence band states results in three occupied and two unoccupied hybridized states, with a strong contribution of the carbon p_z orbitals (see Fig. 5 for details). Four of them are clearly visible near the K point: $HS1$,

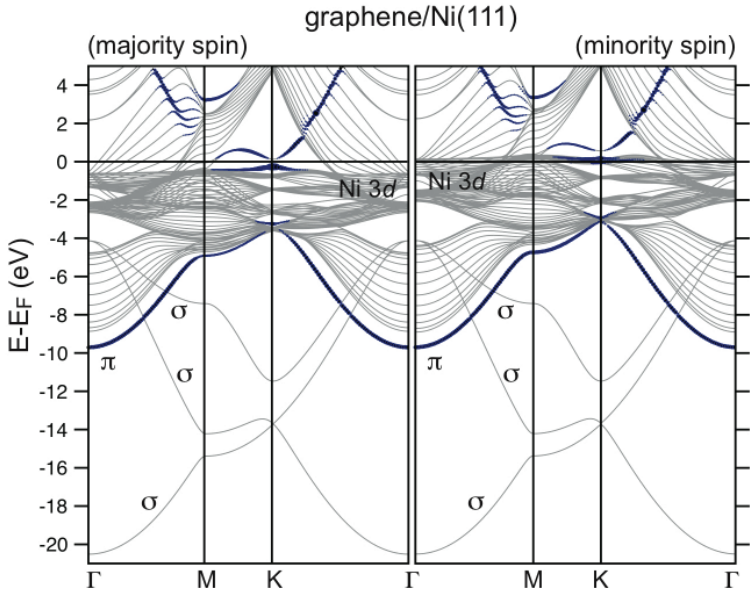

Fig. 4. Calculated majority and minority spin band structures for a slab terminated by graphene/Ni(111) interface for a most energetically favorable $top - fcc$ configuration. For the blue (darker) lines, the carbon p_z character is used as a weighting factor.

$HS2$, $HS3$, and $HS4$, respectively (Tab. 2). The states $HS2$ and $HS4$ can be attributed to the carbon atoms just above the interface nickel atoms, while the states $HS1$ and $HS3$ only involve the carbon atoms occupying the fcc hollow sites (Fig. 5). A 0.40 eV gap opening between the graphene occupied π and unoccupied π^* bands at the K point for the graphene/Ni(111) system is related to the $HS3$ and $HS4$. One more hybrid state $HS5$, observed near the M point of the Brillouin zone, results from a hybridisation of the interface nickel p_x, p_y, and d orbitals with carbon p_z orbitals (Fig. 5).

The resembling situation is observed for the graphene/Co(0001) and graphene/ 1 ML Fe/Ni(111) interfaces where similar hybridized states can be clearly identified in the calculated electronic structure (Fig. 5). The results of the analysis are summarized in Table 2. In the row Ni(111), Co(0001), 1 ML Fe/Ni(111) one can clearly identify increasing the exchange splitting between spin-up and spin-down counter-parts for every interface state, that can be assigned to increasing the magnetic moment of the underlying FM substrate. The interesting case is observed for graphene/1 ML Fe/Ni(111) where two Fe 3d quantum-well states of the minority character exist in the energy gap above the Fermi level around the K point [M. Weser, E.N.Voloshina, K.Horn, Yu.S.Dedkov (submitted)]. These states are strongly hybridized with C p_z states of C-top and C-hcp atoms that leads to increasing the magnetic moments of carbon atoms compared to those in the graphene/Ni(111) system (Table 1).

The calculated magnetic moment of the FM substrate for three systems, which are considered here are presented in Table 1. In all cases the deposition of the graphene layer on FM surface leads to the reduction of the magnetic moment of the interface FM atoms and appearing the induced magnetism of carbon atoms of graphene. For example, in the case of the most stable $top - fcc$ arrangement of the graphene/Ni(111) interface the magnetic moment of

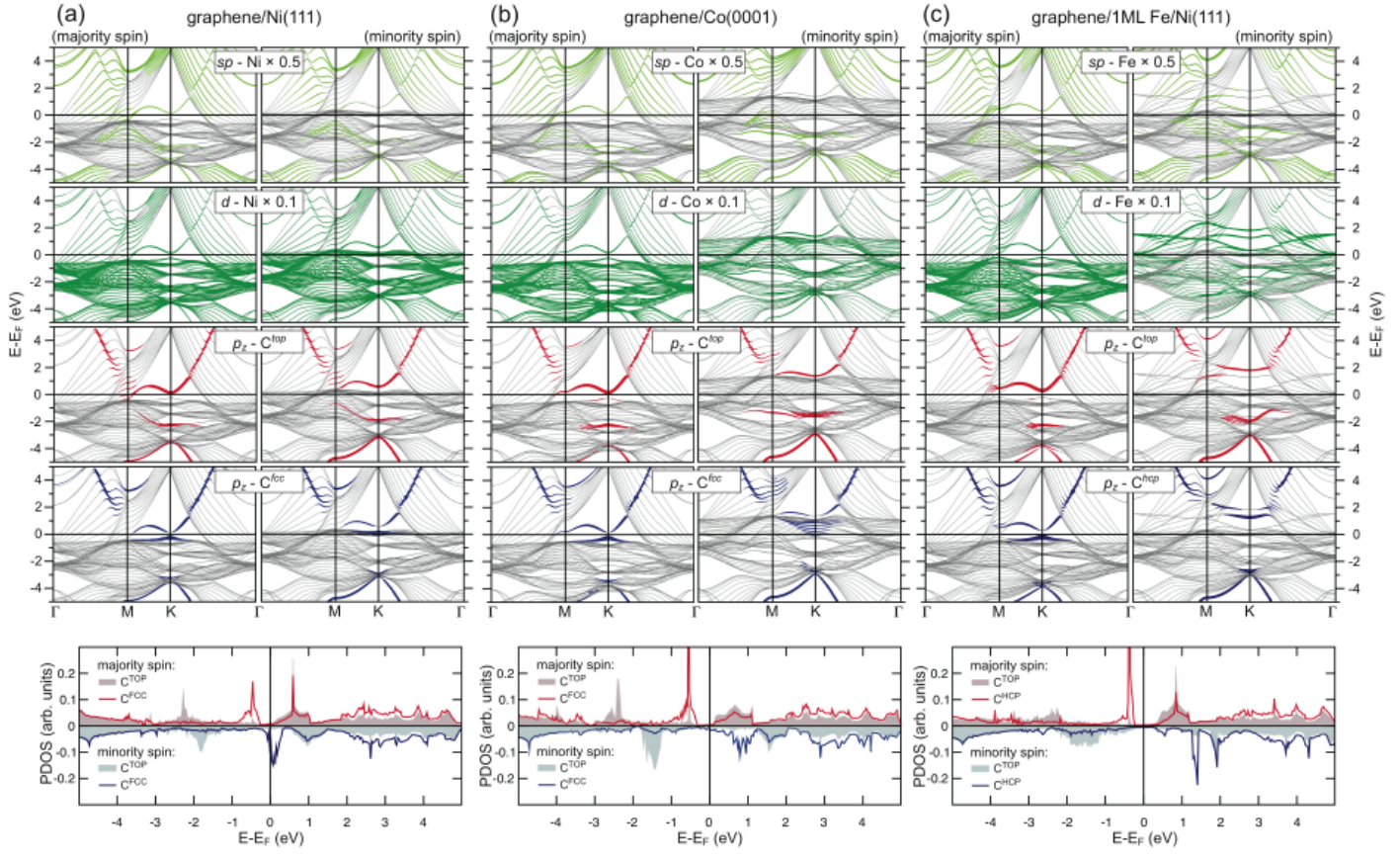

Fig. 5. Calculated majority and minority spin band structures for a slab terminated by: (a) graphene/Ni(111) interfaces ($top - fcc$ arrangement); (b) graphene/Co(0001) interfaces ($top - fcc$ arrangement); (c) graphene/1 ML Fe/Ni(111) interfaces ($top - hcp$ arrangement). The radius of the circles is proportional to the partial density of states at the interface between FM or C atoms (see legend). The corresponding calculated majority and minority partial p_z density of states of graphene is shown for every example in the lower panel of the figure.

State	FM = Ni(111)		FM = Co(0001)		FM = 1ML Fe/Ni(111)	
	spin ↑	spin ↓	spin ↑	spin ↓	spin ↑	spin ↓
$HS5$	−3.20	−3.32	−3.51	−4.01	−3.56	−4.05
$HS4$	−0.12	−0.55	−0.12	−1.27	−0.28	−1.72
$HS3$	0.28	−0.16	0.27	−0.95	0.26	−1.19
$HS2$	2.28	1.93	2.26	1.63	2.32	1.99
$HS1$	3.27	2.93	3.44	2.81	3.75	2.77

Table 2. Binding energies (in eV) (positive sign for states below the Fermi level and negative sign for states above the Fermi level) of the interface hybrid states (HS) extracted from the calculated band structures of the graphene/FM system at the K and M points (see text for details).

Ni interface atoms shows a reduction by about 20 % for 3d electrons. Our DFT calculations predict an induced magnetic moment of the carbon atoms in the graphene layer, which is equal to $-0.019\mu_B$ and $0.031\,\mu_B$ depending on the position of the carbon atom on the Ni(111) surface, due to the different behavior of the majority and minority spin interface states. The same behavior is also observed for the graphene/Co(0001) and graphene/1 ML Fe/Ni(111) interfaces where significantly large induced magnetic moments of carbon can be observed (Table 1).

5. Electronic and magnetic structure of graphene on ferromagnetic substrates: experiment

5.1 Growth and surface structure of graphene on Ni(111)

The quality of the samples at each preparation step was checked with LEED and STM. Since Ni(111) and graphene have the nearly similar lattice parameters (the lattice mismatch is of only 1.3 %), graphene forms the hexagonal (1×1) structure. Fig. 6(a) shows an overview of a graphene domain on Ni(111) after thermal decomposition of propene. The graphene layer is continuous and exhibits a highly ordered crystallographic structure without any visible defects even over large areas. Fig. 6(b) represents a magnified topographic image of the graphene lattice together with a typical LEED pattern of monolayer graphene on Ni(111) [inset of Fig. 6(b)]. A higher magnification STM image of the graphene surface is shown in Fig. 6(c) with the graphene hexagonal unit cell marked in the image.

So far several possible atomic configurations were considered for the graphene/Ni(111) intrface. Three "high-symmetry" structures are known as $hcp-fcc$, $top-hcp$, and $top-fcc$ and they are discussed in the previous section. In our case, graphene terraces have a peak-to-peak roughness of 0.2 Å and show a honeycomb structure with a lattice constant of 2.4 ± 0.1 Å [Fig. 6(b,c)], which agrees well with the expected 2.46 Å lattice spacing of graphene. STM images show that in the honeycomb unit cell carbon atoms corresponding to different sites appear with a different contrast, which can be attributed to the differences in the local stacking of the graphene sheet and the Ni(111) substrate. Therefore we interpret our STM images in the following way: Fig. 6 shows a single layer graphene, where carbon atoms most possibly occupy positions corresponding to one of the two non-equivalent configurations – $top-fcc$ or $top-hcp$. However, it turns to be impossible to directly identify which of the sites are occupied.

Additionally, some different orientations of the graphene relative to the Ni(111) substrate could be observed [Dedkov & Fonin (2010); Dedkov et al. (2008b)]. These observations show

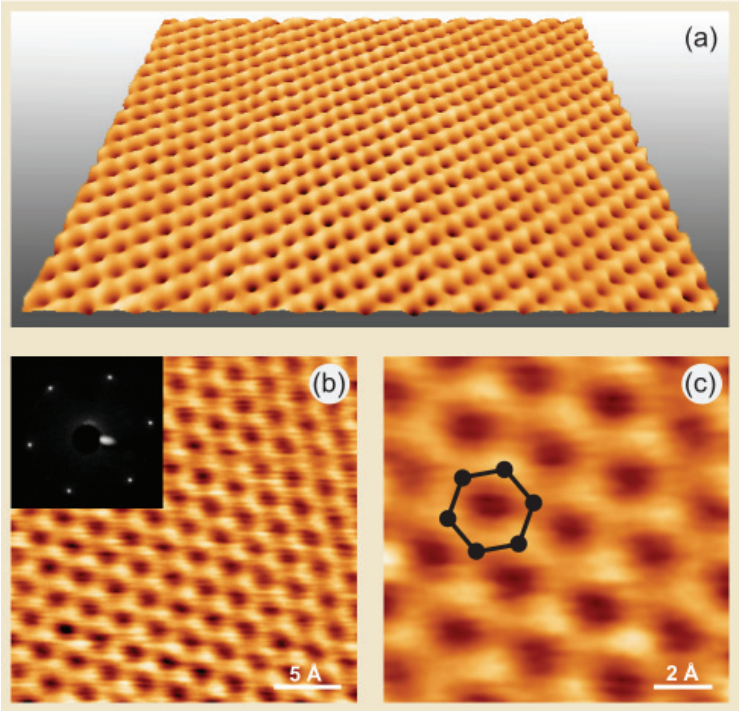

Fig. 6. High-quality graphene/Ni(111) system. (a) Large scale constant current STM image of the graphene/Ni(111) surface. Tunneling parameters: $U_T = 0.002\,\mathrm{V}$; $I_T = 48\,\mathrm{nA}$. (b) Magnified STM image of the perfect graphene lattice. The inset shows a LEED image obtained at 63 eV. (c) High magnification STM image showing atomic structure of the graphene monolayer. Tunneling parameters: $U_T = 0.002\,\mathrm{V}$; $I_T = 48\,\mathrm{nA}$. Graphene hexagonal unit cell is marked in (c).

that although the interaction between nickel and graphene is relatively strong, different adsorption geometries are locally possible.

5.2 Bonding and magnetism at the graphene/Ni(111) interface

In order to address the average spatial orientation of selected molecular orbitals (for example π or σ) at the graphene/Ni(111) interface, we vary the sample orientation with respect to the wave vector of the linearly polarized x-ray light and monitor the NEXAFS intensity. The observed changes of the NEXAFS lineshape at the C *K* edge in the graphene/Ni(111) system represent a nice example demonstrating the so-called *search-light*-like effect [Stöhr & Samant (1999)]. In such an experiment, the absorption intensity associated with a specific molecular orbital final state has a maximum if the electric field vector is aligned parallel to the direction of maximum charge or hole density, i. e. along a molecular orbital, and the intensity vanishes if the electric field vector is perpendicular to the orbital axis. The detailed description of the angular dependence of NEXAFS intensities can be found elsewhere [Stöhr (1999); Stöhr & Samant (1999)].

Figure 7 shows NEXAFS spectra of the graphene/Ni(111) system recorded at the C K absorption edge as a function of the angle, θ, between the direction of the incident linearly polarized x-ray light and the sample surface, e. g. between the electrical field vector of light and the sample surface normal (see the insets of Fig.7). The reference NEXAFS spectrum of the highly-oriented pyrolitic graphite (HOPG) crystal measured at $\theta = 30^\circ$ is shown in the upper part of the figure. The spectral features in the two broad regions $283 - 289$ eV and $289 - 295$ eV can be ascribed to C $1s \rightarrow \pi^*$ and C $1s \rightarrow \sigma^*$ transitions of core electrons into unoccupied states (π^*, σ_1^*, and σ_2^*), respectively. Upon the comparison of the NEXAFS C $1s \rightarrow \pi^*, \sigma^*$ spectrum of the graphene/Ni(111) system with the reference graphite spectrum, considerable changes in the spectral shapes are observed, which can be attributed to a strong chemisorption. A broadening of the π^* and σ^* resonances gives an evidence for a strong orbital mixing at the graphene/Ni interface, indicating a strong delocalization of the corresponding core-excited state. The characteristic double-peak structure at 285.5 and 287.1 eV can be qualitatively understood already with the ground-state DFT calculations (see present calculations discussed in the previous section and Ref. [Bertoni et al. (2005)]), while the dynamics of core-hole screening has to be considered for correct reproducing of the spectral profile [Rusz et al. (2010)]. In the ground-state approximation the first π^* resonance can be roughly associated with the unoccupied C $2p$ density of states located at the C atoms on top of Ni atoms, while the second π^* peak is mainly due to the C $2p$ density of states on the C atoms located at fcc hollow sites. However, in a real experiment individual contributions are considerably mixed and further affected by the core hole and its dynamical screening. The σ^* resonances are also influenced by the interaction with the substrate: they are visibly broadened and shifted by 0.6 eV to lower energies. The broadening is a result of the increased screening by the substrate electrons. The reduction of the $\pi^* - \sigma^*$ separation reflects the reduced anisotropy of the potential for outgoing electrons due to the slight ripple in the graphene layer on Ni(111) accompanied by a softening of the C-C bonds. A comparison of the present NEXAFS results for graphene on Ni(111) with those recently obtained for graphene/Rh and graphene/Ru [Preobrajenski et al. (2008)] indicates the existing of a very strong covalent interfacial bonding between carbon atoms in the graphene layer and Ni atoms of the substrate.

In the following we would like to compare our NEXAFS results with the recently calculated C K-edge electron energy-loss spectra (EELS) for the graphene/Ni(111) interface [Bertoni et al. (2005)]. In this case, experimental NEXAFS spectra taken at $\theta = 10^\circ$ and $\theta = 90^\circ$ correspond to the calculated EELS spectra for the scattering vector $\mathbf{q}$ perpendicular and parallel to the graphene layer, respectively. The calculated EELS spectra are found to agree well with the experimental NEXAFS data: (i) the spectra show the same angle (scattering vector) dependence and (ii) the experimentally observed NEXAFS features are well reproduced in the calculated EELS spectra. For example, two peaks in the NEXAFS spectra in the $1s \rightarrow \pi^*$ spectral region at 285.5 eV and 287.1 eV of photon energy can be assigned to the double-peak structure in the calculated EELS spectrum at 0.8 eV and 3.0 eV above the Fermi level [Bertoni et al. (2005)]. According to the theoretical calculations [Bertoni et al. (2005)], the first sharp feature in the NEXAFS spectrum is due to the transition of the electron from the $1s$ core level into the interface hybridized state HS_4 above the Fermi level (around the K point in the hexagonal Brillouin zone), which originates from the C p_z–Ni $3d$ hybridization and corresponds to the antibonding orbital between a carbon atom C-top and an interface Ni atom. The second peak in the NEXAFS spectrum is due to the dipole transition of an electron from the $1s$ core level into the interface hybrid state HS_5 above the Fermi level (around the M point in the hexagonal Brillouin zone), which originates from C p_z–Ni $p_x, p_y, 3d$ hybridization and

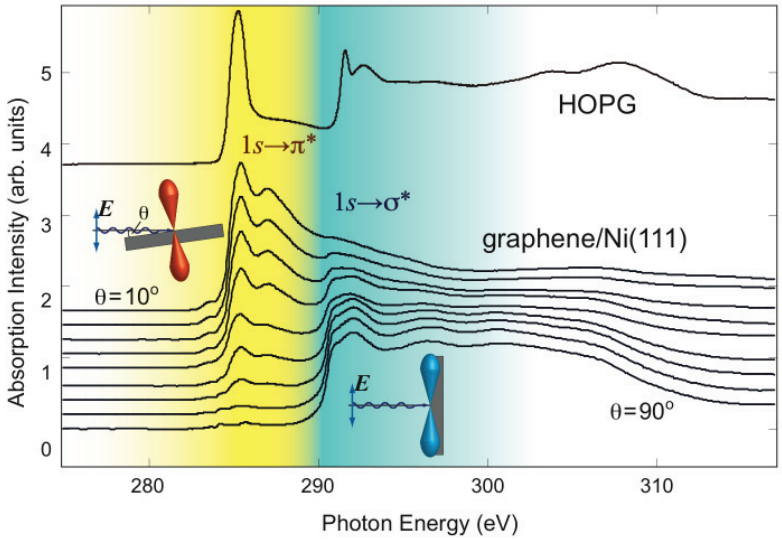

Fig. 7. Angular dependence of the absorption signal at the C *K* edge of the graphene/Ni(111) system measured as a function of angle, θ, between polarization vector of incoming linearly polarized light and the surface normal of the sample. Spectra were collected in the partial electron yield mode and angle was changed with a step of 10° from top to bottom. The reference spectrum of HOPG is shown in the upper part of the panel for comparison.

corresponds to a bonding orbital between C-*top* and C-*fcc* atoms, involving a Ni interface atom (see discussion about interface hybrid states in the previous section). In case of the NEXAFS C $1s \rightarrow \sigma^*$, the theory also correctly describes the shape of the absorption spectra [Bertoni et al. (2005)].

The strong hybridization between graphene π and Ni $3d$ valence band states at the graphene/Ni(111) interface leads to the partial charge transfer of the spin-polarized electrons from Ni onto C with the appearance of an induced effective magnetic moment of carbon atoms (Section 4), which can be detected in an experiment sensitive to the magnetic state of particular element, like XMCD. Figure 8 shows NEXAFS spectra of the graphene/Ni(111) system obtained for two opposite magnetization directions with respect to the polarization of the incident X-ray beam (upper panels) together with the resulting XMCD signal (lower panels). The spectra collected at the Ni $L_{2,3}$ edge in TEY mode and at the C *K* edge in PEY mode are presented in the left-hand panel and in the right-hand panel, respectively. The Ni $L_{2,3}$ XMCD spectrum (white line as well as fine structure behind the absorption edge) is in perfect agreement with previously published spectroscopic data [Dhesi et al. (1999); Nesvizhskii et al. (2000); Srivastava et al. (1998)]. The quantitative analysis of the absorption spectra obtained on a magnetic sample with circularly polarized light can be performed with the help of the so-called sum rules for spin- and orbital-magnetic moments [Carra et al. (1993); Thole et al. (1992)]. The intensities of L_3 and L_2 absorption lines and their differences for the parallel and anti-parallel orientations of the projection of photon spin on the sample magnetization direction are quantitatively related by the sum rules to the number of $3d$ holes in the valence band of the ferromagnetic material and the size of the spin and orbital magnetic moments.

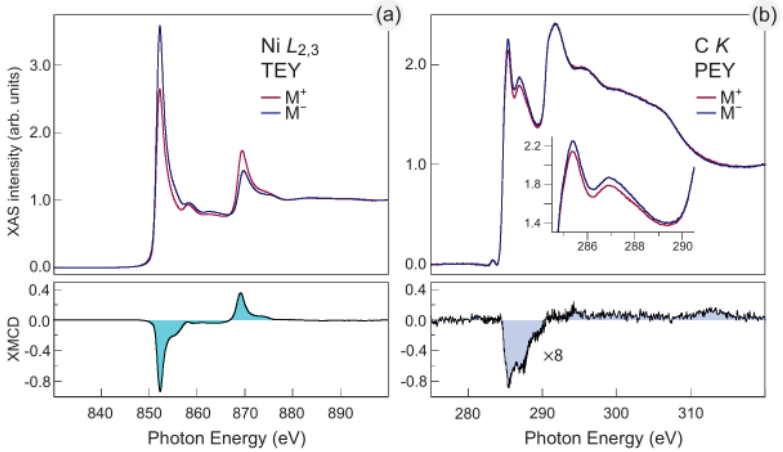

Fig. 8. XMCD spectra of the graphene/Ni(111) system: absorption spectra measured with circularly polarized light for two opposite orientations of the sample magnetization are shown in the upper part for the Ni $L_{2,3}$- (a) and C K-edges (b). The corresponding differences reflecting the strength of the dichroic signal are shown in the lower part of the respective figures.

From the experimental Ni $L_{2,3}$ TEY NEXAFS data [Fig. 8(a)] the bulk values of Ni $3d$ magnetic moments were derived, using a number of $3d$ holes in the valence band of Ni $n_h = 1.45$ [Sorg et al. (2004)] and polarization of light $P = 0.75$. At room temperature and in TEY mode (more bulk sensitive), Ni provides a spin moment of $3d$ electrons of $\mu_S = 0.69\,\mu_B$ and an orbital moment of $\mu_L = 0.07\,\mu_B$, respectively. These values coincide with the previously published experimental results [Baberschke (1996); Srivastava et al. (1998)]. The experimentally obtained spin-magnetic moment is very close to the calculated bulk value of $\mu_S = 0.67\,\mu_B$ for the graphene/Ni(111) system (Section 4). For the most energetically favorable configuration of carbon atoms on Ni(111), $top - fcc$, the calculations predict a reduction of the spin-magnetic moments of Ni interface atoms by 16 % down to $0.52\,\mu_B$ (Section 4). The experimental data collected at the Ni $L_{2,3}$ absorption edge in the PEY mode (more surface/interface sensitive) also shows a slight reduction of the spin moment to $\mu_S = 0.63\,\mu_B$. However, the observed decreasing is not so pronounced as yielded by the theoretical calculation, which can be explained by the large contribution of the bulk-derived signal to the XMCD spectra.

The most important and interesting results of these XMCD experiments on the graphene/Ni(111) system is the observation of the relatively large dichroic contrast at the C K absorption edge [Fig. 8(b)]. In order to magnify the measured magnetic contrast at the $1s \rightarrow \pi^*$ absorption edge, these XMCD spectra were collected in the PEY mode with the circularly polarized light at an angle of $\theta = 20^\circ$. We note that the observed differences in the NEXAFS spectra collected at this angle visible in Figs. 7 and 8 are due to the different polarization of light: in Fig. 7(a) the data are obtained with the linearly polarized x-rays, i. e. the strong angular dependence of the absorption signal is due to the different graphene's orbital orientation; whereas the data in Fig. 8 are taken with the circularly polarized light, i. e. both $1s \rightarrow \pi^*$ and $1s \rightarrow \sigma^*$ transitions are nearly equivalently possible. The C K XMCD spectrum reveals that the major magnetic response stems from transitions of the $1s$ electron onto the π^*-states, while transitions onto the σ^*-states yield very weak (if any)

magnetic signal. These results indicate that only the C $2p_z$ orbitals of the graphene layer are magnetically polarized due to the hybridization with the Ni $3d$ band. The sharp structure at the $1s \rightarrow \pi^*$ absorption edge originates from hybridized C p_z–Ni $3d$ and C p_z–Ni p_x, p_y $3d$ states (see earlier discussion and Section 4).

The appearance of XMCD signal at the C K-edge shows that indeed the Ni film induces a magnetic moment in the graphene overlayer. However, at the C K absorption edge, the electron transitions occur from the non-spin-orbit split $1s$ initial states to the $2p$ final states and thus, in the analysis of the dichroism effect at the K edge one equation in the selection rules is missed. This means that the XMCD signal at K edges provides the information only on the orbital magnetic moment μ_{orb} [Carra et al. (1993); Huang et al. (2002); Thole et al. (1992)]. The partial charge transfer from Ni to C atoms in the graphene/Ni(111) system was calculated for the 22-atom (graphene)/Ni cluster [Yamamoto et al. (1992)] yielding $0.205e^-$ per C atom in graphene, which leads to the $2p$-orbital occupation number of $n_p = 2.205e^-$. Using the C K NEXAFS spectra the procedure described in work [Huang et al. (2002)], the orbital magnetic moment of $\mu_{orb} = 1.8 \pm 0.6 \times 10^{-3}\,\mu_B$ per C atom was extracted. The relatively large uncertainty arises mainly from the estimation of the number of C $2p$ holes, the background subtraction of NEXAFS spectra, and from the error for the degree of circular polarization of light.

The theoretical calculations presented in Section 4 also give the values for the spin magnetic moment of $-0.019\,\mu_B$ and $0.031\,\mu_B$ for C-top and C-fcc atoms, respectively. However, the magnetic splitting of the majority and minority parts of the interface hybrid states HS_3 and HS_4 was found between 0.44 and 0.43 eV, respectively, which may yield higher values for the magnetic moment. Due to the impossibility to directly extract the value of the spin magnetic moment form the K edge XMCD spectra, we apply a simple comparison with the magnetic measurements on similar systems in oder to estimate the average μ_S value for the carbon atoms at the graphene/Ni(111) interface. For the Fe/C multilayers clear magnetic signals of carbon were obtained by using the resonant magnetic reflectivity technique [Mertins et al. (2004)]. Hysteresis loop recorded at C K absorption edge gave a clear proof of ferromagnetism of carbon atoms at room temperature with a measured spin magnetic moment of $\mu_S = 0.05\,\mu_B$ induced by adjacent Fe atoms. The observed ferromagnetism of carbon in the Fe/C multilayered system was related to the hybridization between the Fe $3d$ orbitals and the C p_z orbitals, which are normal to the graphene-type layered sp^2-coordination. The second comparison can be performed with carbon nanotubes on ferromagnetic Co substrate [Céspedes et al. (2004)]. Carbon nanotubes were shown to become magnetized when they are in contact with magnetic material. Spin-polarized charge transfer at the interface between a flat ferromagnetic metal substrate and a multiwalled carbon nanotube leads to a spin transfer of about $0.1\,\mu_B$ per contact carbon atom. Additionally, a comparison of the XMCD spectra obtained at the C K edge in graphene/Ni(111) (present work) and at the O K edge in O/Ni(100) [Sorg et al. (2006)], reveals the approximately same magnitude of the XMCD signal. For the O/Ni(100) system, where the induced spin-magnetic moment of $0.053\,\mu_B$ on oxygen atom was calculated, the theoretically simulated NEXAFS and XMCD spectra agree well with the experimental data. Considering these analogous systems, we estimate the induced magnetic moment for graphene on Ni(111) to be in the range of 0.05-0.1 μ_B per carbon atom.

The experimentally observed effective magnetic moment of carbon atoms of the graphene layer on Ni(111) was recently confirmed by spin-resolved photoemission measurements [Dedkov & Fonin (2010)]. These data present the clear spin-contrast in the valence band region and a spin polarization value of about -60% at the Fermi level for the pure Ni(111)

surface. The presence of graphene on Ni(111) strongly modifies the valence band spectrum of Ni indicating the strong interaction between valence band states of graphene and Ni. In the graphene/Ni(111) system the spin polarization of Ni 3*d* states at E_F is strongly reduced to about -25%. The significant modifications of the spin-resolved structure of Ni 3*d* states as well as the reduction of the spin polarization at E_F is considered as an indication of decreasing the magnetic moment of Ni atoms at the graphene/Ni(111) interface. These spin-resolved photoemission measurements demonstrate the clear spin contrast for the graphene π states with the maximum spin-polarization of $P = -12 \pm 2\,\%$ at room temperature. The two spin-resolved π components are clearly resolved giving the exchange splitting of about 34 ± 9 meV for these states, which agrees well with the value extracted from theoretical calculations (Section 4).

5.3 Electronic properties of graphene on Ni(111)

Fig. 9(a) shows a series of angle-resolved photoemission spectra measured along the $\Gamma - K$ direction of the hexagonal Brillouin zone of the graphene/Ni(111) system. This series is extracted from the 3D sets of data of photoemission intensity $I(E_B, k_x, k_y)$, where E_B is the binding energy and k_x, k_y are the orthogonal components of the in-plane wave vector. For the graphene/Ni(111) system the K and M points of the Brillouin zone are reached at $1.7\,\text{Å}^{-1}$ and at $1.4\,\text{Å}^{-1}$, respectively. The presented photoemission data are in very good agreement with previously published results [Dedkov et al. (2008b; 2001); Grüneis & Vyalikh (2008); Nagashima et al. (1994); Shikin et al. (2000)]. In Fig. 9(a) one can clearly discriminate dispersions of graphene π- and σ-derived states in the region below 2 eV of the binding energy (BE) as well as Ni 3*d*-derived states near E_F. The binding energy of the graphene π states in the center of the Brillouin zone (in the Γ point) equals to 10.1 eV which is approximately by 2.4 eV larger than the binding energy of these states in pure graphite. The shift to larger binding energy is different for σ and π valence band graphene-derived states. This behavior can be explained by the different hybridization strength between these states and Ni 3*d* valence band states, which is larger for the out-of-plane oriented π states compared with the one for the in-plane oriented σ states of the graphene layer as discussed in Section 4. The binding energy difference of ≈ 2.4 eV for the π states and ≈ 1 eV for the σ states between graphite and graphene on Ni(111) is in good agreement with previously reported experimental and theoretical values [Bertoni et al. (2005); Dedkov et al. (2008b)]. The effect of hybridization between Ni 3*d* and graphene π states can be clearly demonstarted in the region around the K point of the Brillouin zone: (i) one of the Ni 3*d* bands at 1.50 eV changes its binding energy by ≈ 150 meV to larger BE when approaching the K point; (ii) a hybridization shoulder is visible in photoemission spectra, which disperses from approximately 1.6 eV to the binding energy of the graphene π states at the K point [see also Fig. 9(b,c) for a detailed view]. The strong hybridization observed in PES spectra underlines the fact that the π states might become spin-polarized and might gain a non zero-magnetic moment due to charge transfer from the Ni atoms to the carbon atoms.

Considering the electronic band structure of the graphene/Ni(111), the region around the K point delivers the most interesting and important information with respect to the possible spin-filtering effects in the graphene/ferromagnet or ferromagnet/graphene/ferromagnet sandwich-like structures. This part of the electronic structure measured with two different photon energies ($h\nu = 70$ eV and 100 eV) is shown in Fig. 9(b,c) as color maps (upper panels) together with the corresponding intensity profiles directly at the K point (lower panels). Firstly, the spectral function of the graphene layer on Ni(111) is characterized by the absence of

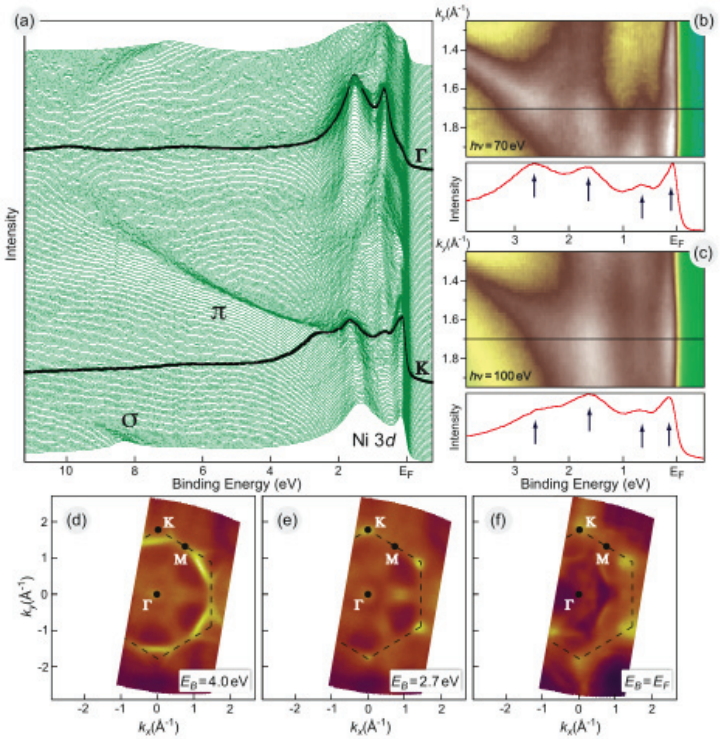

Fig. 9. (a) Series of the angle-resolved photoemission spectra of the graphene/Ni(111) system recorded along the Γ − K direction of the hexagonal Brillouin zone at 100 eV of photon energy. Spectra corresponding to Γ and K points are marked by thick black lines. (b,c) Regions around the K point of photoemission intensity of the graphene/Ni(111) system measured at 70 eV and 100 eV of photon energy. The corresponding intensity profiles at the K point are shown in the lower panels with arrows indicating the main photoemission features discussed in the text. (d-f) Constant energy cuts of the 3D data sets in the energy-wave vector space at 4 eV, 2.7 eV of BE, and at E_F.

well-ordered structure of the graphene π-bands in the vicinity of the Fermi level and secondly, the Dirac-cone is not preserved. Both observations can be attributed to a strong interaction between graphene layer and metallic substrate leading to a strong hybridization between the graphene π and the Ni 3*d* valence band states. In the vicinity of the K point a number of photoemission peaks can be clearly distinguished: (i) a sharp peak about the Fermi level at 0.1 − 0.2 eV BE, (ii) a graphene π-states-related peak at 2.65 eV BE, (iii) two peaks at 0.7 eV and 1.65 eV BE.

In the following we perform a detailed analysis of the experimentally obtained electronic structure relying on electronic structure calculations for the graphene/Ni(111) system discussed in Section 4. These calculations predict the existence of three interface hybrid states below the Fermi level originating from the strong hybridization between the Ni 3*d* and the graphene π states and corresponding to: (HS_1) bonding between C-*fcc* and interface Ni atoms; (HS_2) bonding between C-*top* and interface Ni atoms; (HS_3) antibonding between

C-fcc and interface Ni atoms. From the analysis of the experimental data in the region around the K point of the hexagonal Brillouin zone we could distinguish a number of flat bands, which are clearly separated from each other.

The interpretation of the experimentally observed photoemission features around the Fermi level could be performed as presented in the following. The photoemission peak close to the Fermi level (0.1-0.2 eV BE) could be considered as a combination of the interface hybrid state HS_3 (both spins) with a large contribution of the graphene π-character and the Ni $3d(\downarrow)$-band. The second peak at 0.7 eV BE could be assigned to the combination of the Ni $3d(\uparrow)$- and Ni $3d(\downarrow)$-bands present calculations. The feature at 1.65 eV could be considered as a combination of Ni $3d(\uparrow)$-band and $HS_2(\downarrow)$-state with a large graphene π-character. The last photoemission peak (2.65 eV BE) could be assigned to the interface hybrid state $HS_2(\uparrow)$ with large contribution of the graphene π-character.

In order to check the theoretical predictions concerning the spin-dependent electronic transport properties of the ideal graphene/Ni(111) interface, we perform a careful analysis of the constant energy photoemission maps close to the Fermi level. We would like to admit that such an analysis can be rather complicated due to the fact that Ni $3d$ bands, which dominate the photoemission intensity around the Fermi level, are very flat in the vicinity of E_F. Figure 9(d-f) shows the constant energy cuts of the 3D data set obtained at $h\nu$=100 eV for the graphene/Ni(111) system. These energy cuts were taken at (a) 4 eV and (b) 2.7 eV of BE as well as at (c) the Fermi level. The energy cut at $E_B = 4$ eV shows characteristic photoemission intensity patterns of the graphene layer, which reflect the symmetry of the system. Below the Dirac point (crossing of straight dispersion lines of π states in free-standing graphene) the graphene π bands are visible in the first Brillouin zone whereas no bands can be seen in the second one. Additionally several energy bands are present in the middle of the Brillouin zone, which also show hexagonal symmetry. These bands originate from the hybridization of the Ni and graphene valence band states. The constant energy cut taken in the region of the minimal binding energy of the graphene π states ($E_B = 2.7$ eV) is shown in Fig. 9(e). In the case of graphene/Ni(111) the Dirac point is not preserved due to the strong hybridization of Ni $3d$ and graphene π states around the K point. This can also be directly recognized at this energy cut where graphene π states produce broad intensity spots instead of sharp points in the wave-vector space. As in the previous case, we observe a number of valence band states in the middle part of the Brillouin zone, which again could be assigned to the hybridization-derived states.

The most interesting and important information in view on the spin-dependent transport properties of the graphene/Ni(111) system can be extracted form the constant energy cut obtained at the Fermi energy, which is presented in Fig. 9(f). Already the analysis of Fig. 9(a-c) shows that the photoemission intensity is increased around the K point and along the $\mathrm{K}-\mathrm{M}$ direction of the hexagonal Brillouin zone, that correlates with the increased photoemission intensity observed in the energy cut shown in Fig. 9(f) for the Fermi energy. Additionally, a number of arcs surrounding the K points and weak (but distinguished) diamond-shape regions of increased intensity is clearly visible in the middle part and around the M points of the Brillouin zone, respectively. Upon the comparison of the obtained photoemission results for the graphene/Ni(111) system [Fig. 9(a-f)] with the band structure calculations for this system (Section 4), we find very good agreement between theory and experiment. Particularly, the region around the Fermi level for the ideal graphene/Ni(111) system is well reproduced in the experiment, confirming the main predictions of the theory. Unfortunately, at the present

stage of the experiment, we can not specify the spin-character of energy bands, which should be the subject of future spin- and angle-resolved photoemission investigations.

6. Conclusions and outlook

In conclusion, the electronic structure and magnetic properties of the graphene/ferromagnet interface were investigated via combination of theoretical and experimental methods: DFT calculations, NEXAFS, XMCD, and mapping of the band structure by means of ARPES. From the theoretical side the different interfaces were analyzed: graphene/Ni(111), graphene/Co(0001), and graphene/1 ML Fe/Ni(111). Here the electronic structure of the interface as well as the effect of induced magnetism in graphene layer were discussed. In all cases a strong modification of the electronic structure of the graphene layer and FM substrate upon graphene adsorption were detected in theoretical calculations and confirmed by spectroscopic methods. This modification is due to the considerable hybridization of the graphene π and FM 3*d* valence band states accompanied by the partial charge transfer of spin-polarized electrons from FM onto C atoms leading to the appearance of the effective magnetic moment in the graphene layer. The presence of an effective magnetic moment on carbon atoms of the graphene layer was unambigously proven by XMCD and spin-resolved photoemission measurements for the graphene/Ni(111) system. The experimentally obtained electronic structure of occupied and unoccupied states of graphene/Ni(111) was compared with band structure calculations allowing the clear assignment of spectral features in the NEXAFS and ARPES data. The good agreement between theory and experiment was also found upon the analysis of the Fermi energy cuts, that give us an opportunity to confirm the main statements of the theoretical works predicting the spin-filtering effects of the graphene/Ni(111) interface. However, the clear assignment of the spectroscopic valence band features have to be performed in future spin-resolved photoemission experiments.

7. Acknowledgements

We would like to thank K. Horn, M. Weser, S. Böttcher, M. Fonin, and B. Paulus. We are also grateful to P. Kelly and L. Calmels for fruitful discussions. This work has been supported by the European Science Foundation (ESF) under the EUROCORES Programme EuroGRAPHENE (Project "SpinGraph"). E. V. appreciate the support from the German Research Foundation (DFG) through the Collaborative Research Center (SFB) 765 "Multivalency as chemical organisation and action principle: New architectures, functions and applications". Y. D. acknowledges the financial support by the DFG under project DE 1679/2-1. We would like to acknowledge our co-workers in Max-lab (Lund) and BESSY (Berlin) synchrotron facilities for the technical assistance during experiment. We appreciate the support from the HLRN (High Performance Computing Network of Northern Germany) in Berlin.

8. References

Baberschke, K. (1996). The magnetism of nickel monolayers, *Appl. Phys. A* 62(5): 417–427.

Bae, S., Kim, H., Lee, Y., Xu, X., Park, J.-S., Zheng, Y., Balakrishnan, J., Lei, T., Kim, H. R., Song, Y. I., Kim, Y.-J., Kim, K. S., Ozyilmaz, B., Ahn, J.-H., Hong, B. H. & Iijima, S. (2010). Roll-to-roll production of 30-inch graphene films for transparent electrodes, *Nature Nanotech.* 5(8): 574–578.

Bertoni, G., Calmels, L., Altibelli, A. & Serin, V. (2005). First-principles calculation of the electronic structure and eels spectra at the graphene/Ni(111) interface, *Phys. Rev. B* 71(7): 075402 1–8.

Blochl, P. (1994). Projector augmented-wave method, *Phys. Rev. B* 50(24): 17953–17979.

Boukhvalov, D. W. & Katsnelson, M. I. (2009). Chemical functionalization of graphene, *J. Phys.: Condens. Matter.* 21(34): 344205 1–12.

Brako, R., Sokcevic, D., Lazic, P. & Atodiresei, N. (2010). Graphene on Ir(111) surface: From van der Waals to strong bonding, *arXiv:1006.1280v1 [cond-mat.mes-hall]*. URL: *http://arxiv.org/abs/1006.1280*.

Carra, P., Thole, B., Altarelli, M. & Wang, X. (1993). X-ray circular-dichroism and local magnetic-fields, *Phys. Rev. Lett.* 70(5): 694–697.

Céspedes, O., Ferreira, M. S., Sanvito, S., Kociak, M. & Coey, J. M. D. (2004). Contact induced magnetism in carbon nanotubes, *J. Phys.: Condens. Matter.* 16: L155–L161.

Coletti, C., Riedl, C., Lee, D. S., Krauss, B., Patthey, L., von Klitzing, K., Smet, J. H. & Starke, U. (2010). Charge neutrality and band-gap tuning of epitaxial graphene on SiC by molecular doping, *Phys. Rev. B* 81(23): 235401 1–8.

Coraux, J., N'Diaye, A. T., Busse, C. & Michely, T. (2008). Structural coherency of graphene on Ir(111), *Nano Lett.* 8(2): 565–570.

Coraux, J., N'Diaye, A. T., Engler, M., Busse, C., Wall, D., Buckanie, N., zu Heringdorf, F.-J. M., van Gastel, R., Poelsema, B. & Michely, T. (2009). Growth of graphene on Ir(111), *New J. Phys.* 11(2): 023006 1–22.

Dedkov, Y. S. & Fonin, M. (2010). Electronic and magnetic properties of the graphene-ferromagnet interface, *New J. Phys. (accepted)* .

Dedkov, Y. S., Fonin, M. & Laubschat, C. (2008). A possible source of spin-polarized electrons: The inert graphene/Ni(111) system, *Appl. Phys. Lett.* 92(5): 052506 1–3.

Dedkov, Y. S., Fonin, M., Rüdiger, U. & Laubschat, C. (2008a). Graphene-protected iron layer on Ni(111), *Appl. Phys. Lett.* 93(2): 022509 1–3.

Dedkov, Y. S., Fonin, M., Rüdiger, U. & Laubschat, C. (2008b). Rashba effect in the graphene/Ni(111) system, *Phys. Rev. Lett.* 100(10): 107602 1–4.

Dedkov, Y. S., Shikin, A. M., Adamchuk, V. K., Molodtsov, S. L., Laubschat, C., Bauer, A. & Kaindl, G. (2001). Intercalation of copper underneath a monolayer of graphite on Ni(111), *Phys. Rev. B* 64(3): 035405 1–6.

Dedkov, Y., Vyalikh, D., Holder, M., Weser, M., Molodtsov, S., Laubschat, C., Kucherenko, Y. & Fonin, M. (2008). Dispersion of 4f impurity states in photoemission spectra of Yb/W(110), *Phys. Rev. B* 78(15): 153404 1–4.

Dhesi, S., Dürr, H., van der Laan, G., Dudzik, E. & Brookes, N. (1999). Electronic and magnetic structure of thin Ni films on Co/Cu(001), *Phys. Rev. B* 60(18): 12852–12860.

Dion, M., Rydberg, H., Schroder, E., Langreth, D. & Lundqvist, B. (2004). Van der Waals density functional for general geometries, *Phys. Rev. Lett.* 92(24): 246401 1–4.

Dutta, S. & Pati, S. K. (2008). Half-metallicity in undoped and boron doped graphene nanoribbons in the presence of semilocal exchange-correlation interactions, *J. Phys. Chem. B* 112(5): 1333–1335.

Enderlein, C., Kim, Y. S., Bostwick, A., Rotenberg, E. & Horn, K. (2010). The formation of an energy gap in graphene on ruthenium by controlling the interface, *New J. Phys.* 12: 033014 1–9.

Eom, D., Prezzi, D., Rim, K. T., Zhou, H., Lefenfeld, M., Xiao, S., Nuckolls, C., Hybertsen, M. S., Heinz, T. F. & Flynn, G. W. (2009). Structure and electronic properties of graphene nanoislands on Co(0001), *Nano. Lett.* 9(8): 2844–2848.

Fuentes-Cabrera, M., Baskes, M. I., Melechko, A. V. & Simpson, M. L. (2008). Bridge structure for the graphene/Ni(111) system: A first principles study, *Phys. Rev. B* 77(3): 1–5.

Gamo, Y., Nagashima, A., Wakabayashi, M., Terai, M. & Oshima, C. (1997). Atomic structure of monolayer graphite formed on Ni(111), *Surf. Sci.* 374(1-3): 61–64.

Geim, A. (2009). Graphene: Status and prospects, *Science* 324(5934): 1530–1534.

Geim, A. K. & Novoselov, K. S. (2007). The rise of graphene, *Nature Mater.* 6: 183–191.

Gierz, I., Riedl, C., Starke, U., Ast, C. & Kern, K. (2008). Atomic hole doping of graphene, *Nano Lett.* 8(12): 4603–4607.

Gierz, I., Suzuki, T., Weitz, R. T., Lee, D. S., Krauss, B., Riedl, C., Starke, U., Hoechst, H., Smet, J. H., Ast, C. R. & Kern, K. (2010). Electronic decoupling of an epitaxial graphene monolayer by gold intercalation, *Phys. Rev. B* 81(23): 235408 1–6.

Grimme, S. (2004). Accurate description of van der waals complexes by density functional theory including empirical corrections, *J. Comput. Chem.* 25(12): 1463–1473.

Grüneis, A. & Vyalikh, D. (2008). Tunable hybridization between electronic states of graphene and a metal surface, *Phys. Rev. B* 77(19): 193401 1–4.

Hu, Z., Ogletree, D., van Hove, M. & Somorjai, G. (1987). LEED theory for incommensurate overlayers - application to graphite on Pt(111), *Surf. Sci.* 180(2-3): 433–459.

Huang, D., Jeng, H., Chang, C., Guo, G., Chen, J., Wu, W., Chung, S., Shyu, S., Wu, C., Lin, H. & Chen, C. (2002). Orbital magnetic moments of oxygen and chromium in CrO_2, *Phys. Rev. B* 66(17): 174440 1–5.

Karpan, V. M., Giovannetti, G., Khomyakov, P. A., Talanana, M., Starikov, A. A., Zwierzycki, M., van den Brink, J., Brocks, G. & Kelly, P. J. (2007). Graphite and graphene as perfect spin filters, *Phys. Rev. Lett.* 99(17): 176602 1–4.

Karpan, V. M., Khomyakov, P. A., Starikov, A. A., Giovannetti, G., Zwierzycki, M., Talanana, M., Brocks, G., Brink, J. V. D. & Kelly, P. J. (2008). Theoretical prediction of perfect spin filtering at interfaces between close-packed surfaces of Ni or Co and graphite or graphene, *Phys. Rev. B* 78(19): 1–11.

Kim, K. S., Zhao, Y., Jang, H., Lee, S. Y., Kim, J. M., Kim, K. S., Ahn, J.-H., Kim, P., Choi, J.-Y. & Hong, B. H. (2029). Large-scale pattern growth of graphene films for stretchable transparent electrodes, *Nature* 457(7230): 706–710.

Klink, C., Stensgaard, I., Besenbacher, F. & Lægsgaard, E. (1995). An STM study of carbon-induced structures on Ni(111) - evidence for a carbidic-phase clock reconstruction, *Surf. Sci.* 342(1-3): 250–260.

Kresse, G. & Furthmuller, J. (1996a). Efficiency of ab-initio total energy calculations for metals and semiconductors using a plane-wave basis set, *Comp. Mater. Sci.* 6(1): 15–50.

Kresse, G. & Furthmuller, J. (1996b). Efficient iterative schemes for ab initio total-energy calculations using a plane-wave basis set, *Phys. Rev. B* 54(16): 11169–11186.

Land, T., Michely, T., Behm, R., Hemminger, J. & Comsa, G. (1992). STM investigation of single layer graphite structures produced on Pt(111) by hydrocarbon decomposition, *Surf. Sci.* 264(3): 261–270.

Mao, Y., Yuan, J. & Zhong, J. (2008). Density functional calculation of transition metal adatom adsorption on graphene, *J. Phys.: Condens. Matter.* 20(11): 115209 1–6.

Martoccia, D., Willmott, P. R., Brugger, T., Bjorck, M., Gunther, S., Schleputz, C. M., Cervellino, A., Pauli, S. A., Patterson, B. D., Marchini, S., Wintterlin, J., Moritz, W. & Greber, T.

(2008). Graphene on Ru(0001): A 25 × 25 supercell, *Phys. Rev. Lett.* 101(12): 126102 1–4.

Mertins, H., Valencia, S., Gudat, W., Oppeneer, P., Zaharko, O. & Grimmer, H. (2004). Direct observation of local ferromagnetism on carbon in C/Fe multilayers, *Europhys. Lett.* 66: 743–748.

Morozov, S. V., Novoselov, K. S., Katsnelson, M. I., Schedin, F., Elias, D. C., Jaszczak, J. A. & Geim, A. K. (2008). Giant intrinsic carrier mobilities in graphene and its bilayer, *Phys. Rev. Lett.* 100(1): 016602 1–4.

Nagashima, A., Itoh, H., Ichinokawa, T., Oshima, C. & Otani, S. (1994). Change in the electronic states of graphite overlayers depending on thickness, *Phys. Rev. B* 50(7): 4756–4763.

Nagashima, A., Tejima, N. & Oshima, C. (1994). Electronic states of the pristine and alkali-metal-intercalated monolayer graphite/Ni(111) systems, *Phys. Rev. B* 50(23): 17487–17495.

N'Diaye, A., Bleikamp, S., Feibelman, P. & Michely, T. (2006). Two-dimensional Ir cluster lattice on a graphene moiré on Ir(111), *Phys. Rev. Lett.* 97(21): 215501 1–4.

Nesvizhskii, A., Ankudinov, A., Rehr, J. & Baberschke, K. (2000). Interpretation of x-ray magnetic circular dichroism and x-ray absorption near-edge structure in Ni, *Phys. Rev. B* 62(23): 15295–15298.

Neto, A. C., Guinea, F., Peres, N., Novoselov, K. & Geim, A. (2009). The electronic properties of graphene, *Rev. Mod. Phys.* 81(1): 109–162.

Novoselov, K., Geim, A., Morozov, S., Jiang, D., Katsnelson, M., Grigorieva, I., Dubonos, S. & Firsov, A. (2005). Two-dimensional gas of massless dirac fermions in graphene, *Nature* 438(7065): 197–200.

Paulus, B. & Rosciszewski, K. (2009). Application of the method of increments to the adsorption of h2s on graphene, *Int. J. Quantum. Chem.* 109(13): 3055–3062.

Perdew, J., Burke, K. & Ernzerhof, M. (1996). Generalized gradient approximation made simple, *Phys. Rev. Lett.* 77(18): 3865–3868.

Pisani, C., Maschio, L., Casassa, S., Halo, M., Schuetz, M. & Usvyat, D. (2008). Periodic local MP2 method for the study of electronic correlation in crystals: Theory and preliminary applications, *J. Comput. Chem.* 29(13): 2113–2124.

Preobrajenski, A. B., Ng, M. L., Vinogradov, A. S. & Mårtensson, N. (2008). Controlling graphene corrugation on lattice-mismatched substrates, *Phys. Rev. B* 78(7): 073401 1–4.

Rosei, R., Decresceni, M., Sette, F., Quaresima, C., Savoia, A. & Perfetti, P. (1983). Structure of graphitic carbon on Ni(111) - a surface extended-energy-loss fine-structure study, *Phys. Rev. B* 28(2): 1161–1164.

Rusz, J., Preobrajenski, A. B., Ng, M. L., Vinogradov, N. A., Mårtensson, N., Wessely, O., Sanyal, B. & Eriksson, O. (2010). Dynamical effects in x-ray absorption spectra of graphene and monolayered h-BN on Ni(111), *Phys. Rev. B* 81(7): 073402 1–4.

Sasaki, M., Yamada, Y., Ogiwara, Y., Yagyu, S. & Yamamoto, S. (2000). Moire contrast in the local tunneling barrier height images of monolayer graphite on Pt(111), *Phys. Rev. B* 61(23): 15653–15656.

Schedin, F., Geim, A. K., Morozov, S. V., Hill, E. W., Blake, P., Katsnelson, M. I. & Novoselov, K. S. (2007). Detection of individual gas molecules adsorbed on graphene, *Nature Mater.* 6(9): 652–655.

Shikin, A., Prudnikova, G., Adamchuk, V., Moresco, F. & Rieder, K. (2000). Surface intercalation of gold underneath a graphite monolayer on Ni(111) studied by angle-resolved photoemission and high-resolution electron-energy-loss spectroscopy, *Phys. Rev. B* 62(19): 13202–13208.

Sorg, C., Ponpandian, N., Bernien, M., Baberschke, K., Wende, H. & Wu, R. Q. (2006). Induced magnetism of oxygen in surfactant-grown Fe, Co, and Ni monolayers, *Phys. Rev. B* 73(6): 064409 1–7.

Sorg, C., Ponpandian, N., Scherz, A., Wende, H., Nunthel, R., Gleitsmann, T. & Baberschke, K. (2004). The magnetism of ultrathin Ni films grown with O surfactant, *Surf. Sci.* 565(2-3): 197–205.

Srivastava, P., Wilhelm, F., Ney, A., Farle, M., Wende, H., Haack, N., Ceballos, G. & Baberschke, K. (1998). Magnetic moments and curie temperatures of Ni and Co thin films and coupled trilayers, *Phys. Rev. B* 58(9): 5701–5706.

Stöhr, J. (1999). Exploring the microscopic origin of magnetic anisotropies with x-ray magnetic circular dichroism (xmcd) spectroscopy, *J. Magn. Magn. Mat.* 200(1): 470–497.

Stöhr, J. & Samant, M. (1999). Liquid crystal alignment by rubbed polymer surfaces: a microscopic bond orientation model, *J. Electr. Spectr. Rel. Phenom.* 98-99: 189–207.

Sutter, P., Hybertsen, M. S., Sadowski, J. T. & Sutter, E. (2009). Electronic structure of few-layer epitaxial graphene on Ru(0001), *Nano Lett.* 9(7): 2654–60.

Thole, B., Carra, P., Sette, F. & van der Laan, G. (1992). X-ray circular-dichroism as a probe of orbital magnetization, *Phys. Rev. Lett.* 68(12): 1943–1946.

Tombros, N., Jozsa, C., Popinciuc, M., Jonkman, H. T. & van Wees, B. J. (2007). Electronic spin transport and spin precession in single graphene layers at room temperature, *Nature* 448(7153): 571–574.

Wang, B., Bocquet, M. L., Marchini, S., Guenther, S. & Wintterlin, J. (2008). Chemical origin of a graphene moire overlayer on Ru(0001), *Phys. Chem. Chem. Phys.* 10(24): 3530–3534.

Wang, X., Li, X., Zhang, L., Yoon, Y., Weber, P. K., Wang, H., Guo, J. & Dai, H. (2009). N-doping of graphene through electrothermal reactions with ammonia, *Science* 324(5928): 768–771.

Wintterlin, J. & Bocquet, M. L. (2009). Graphene on metal surfaces, *Surf. Sci.* 603(10-12): 1841–1852.

Yamamoto, K., Fukishima, M., Osaka, T. & Oshima, C. (1992). Charge-transfer mechanism for the (monolayer graphite)-Ni(111) system, *Phys. Rev. B* 45(19): 11358–11361.

Yazyev, O. V. & Pasquarello, A. (2009). Magnetoresistive junctions based on epitaxial graphene and hexagonal boron nitride, *Phys. Rev. B* 80(3): 035408 1–5.

14

Electronic Properties of Graphene Probed at the Nanoscale

Filippo Giannazzo, Sushant Sonde and Vito Raineri
Consiglio Nazionale delle Ricerche, Istituto per la Microelettronica e Microsistemi, Catania, Italy

1. Introduction

Graphene is a two-dimensional (2D) crystal made out of carbon atoms arranged on a hexagonal (honeycomb) structure, as shown schematically in Fig. 1(a). Although it has been experimentally isolated only recently (2004) [1], graphene has been the object of theoretical investigations for more than 60 years, because it represents the simplest structure to understand the electronic properties of all other allotropes of carbon with sp^2 hybridisation.

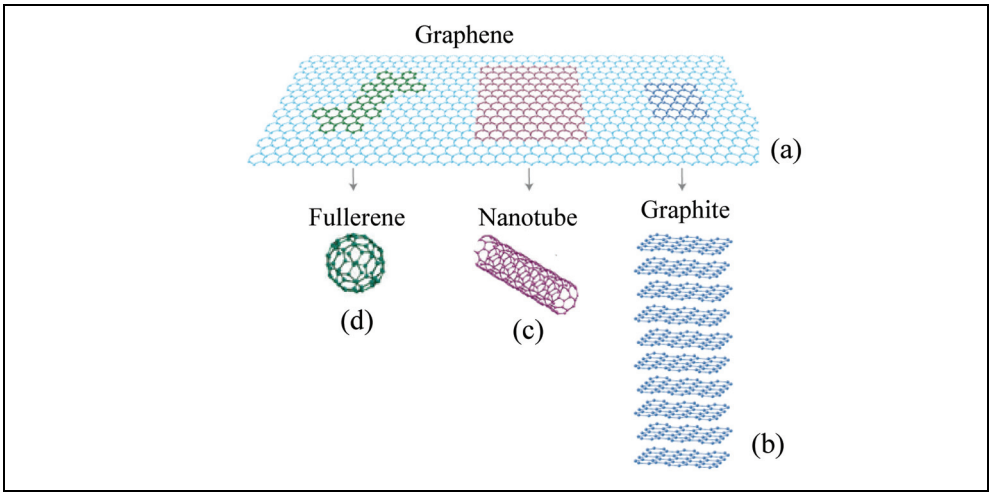

Fig. 1. Schematic structure of graphene (a), graphite (b), carbon nanotube (c) and fullerene (d).

In fact, fullerenes [2] are molecules where carbon atoms are arranged spherically (Fig.1(d)), and hence, from the physical point of view, are zero-dimensional (0D) objects with discrete energy states. Carbon nanotubes [3,4] are one-dimensional (1D) objects (Fig.1(c)) , and can be modelled as a rolled graphene sheet along a given direction with reconnected carbon bonds. Graphite, the three dimensional (3D) allotrope of sp^2 carbon, can be modelled as the stacking of graphene sheets (Fig.1(b)).

The graphene lattice structure is characterized by two types of C–C bonds (σ, π) constructed from the four valence orbitals (2s, $2p_x$, $2p_y$, $2p_z$), where the z-direction is perpendicular to

the sheet. Three σ-bonds join a C atom to its three neighbours. They are quite strong, leading to optical-phonon frequencies much higher than observed in diamond. In addition, the C–C bonding is enhanced by a fourth bond associated with the overlap of p_z (or π) orbitals. The electronic properties of graphene are determined by the bonding π- and antibonding π*-orbitals, that form electronic valence and conduction bands. Fig.2(a) shows a stereoscopic graph of the graphene valence (π) and conduction (π*) bands in the first Brillouin zone, while Fig.2(b) shows the energy of the π (π*) and σ (σ*) band along the high symmetry directions in the first Brillouin zone.

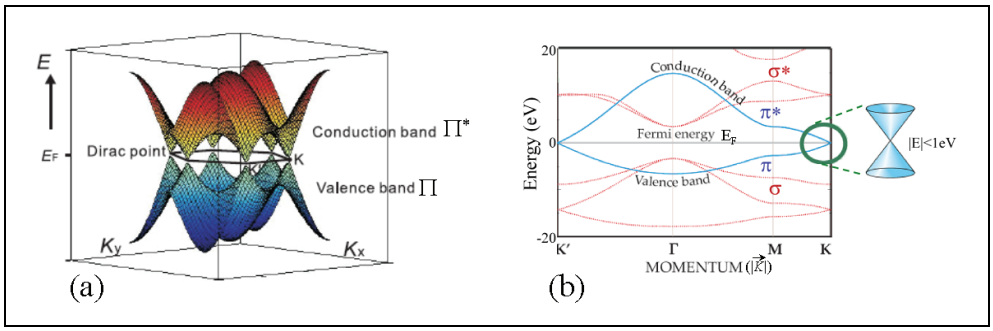

Fig. 2. Electronic bandstructure of graphene in the first Brillouin zone.

According to this bandstructure, graphene can be described as a zero-gap semiconductor. The π-band electronic dispersion for graphene at the six corners of the 2D hexagonal Brillouin zone is found to be linear,

$$E = \hbar v_F k. \quad (1)$$

where ħ is the reduced Planck's constant and v_F (≈10^6 m/s) is the electron Fermi velocity in graphene.

The linear electronic band dispersion leads to the description of carriers in graphene as "massless Dirac fermions". The six points where the cones touch are referred to as the "Dirac" points, and Fermi energy crosses these points in neutral graphene.

Graphene is a true 2D electron system. There are, broadly speaking, four qualitative differences between 2D graphene and 2D semiconductor systems found in Si inversion layers in MOSFETs, GaAs-AlGaAs heterostructures, quantum wells, etc.

i. First, 2D semiconductor systems typically have very large (> 1 eV) bandgaps so that 2D electrons and 2D holes must be studied using completely different electron-doped or hole-doped structures. By contrast, graphene is a gapless semiconductor with the nature of the carrier system changing at the Dirac point from electrons to holes (or vice versa) in a single structure. A direct corollary of this gapless (or small gap) nature of graphene, is of course, the "always metallic" nature of 2D graphene, where the Fermi level is always in the conduction or the valence band. By contrast, the 2D semiconductor becomes insulating below a threshold voltage, as the Fermi level enters the bandgap.
ii. Graphene systems are chiral, whereas 2D semiconductors are non-chiral. Chirality of graphene leads to some important consequences for transport behavior. For example, $2k_F$ -backscattering is suppressed in single layers of graphene at low temperature.

iii. Monolayer graphene dispersion is linear, whereas 2D semiconductors have quadratic energy dispersion. This leads to substantial quantitative differences in the transport properties of the two systems.

iv. Finally, the carrier confinement in graphene is ideally 2D, since the graphene layer is precisely one atomic monolayer thick. For 2D semiconductor structures, the quantum dynamics is two dimensional by virtue of confinement induced by an external electric field, and as such, 2D semiconductors are quasi-2D systems, and always have an average width or thickness $<t>$ (≈ 5 nm to 50 nm) in the third direction with $<t> \leq \lambda_F$, where λ_F is the 2D Fermi wavelength (or equivalently the carrier de Broglie wavelength). The condition $<t> < \lambda_F$ defines a 2D electron system. In particular, for graphene, we have $\lambda_F \approx (2\times10^7\sqrt{\pi}/\sqrt{n})$ nm, where n is the carrier density in cm^{-2}, and since t ≈ 0.1 nm to 0.2 nm (the monolayer atomic thickness), the condition $\lambda_F > t$ is always satisfied, even for an unphysically large $n=10^{14}$ cm^{-2}.

The classic technique to verify the 2D nature of a particular system is to show that the orbital electronic dynamics is sensitive only to a magnetic field perpendicular to the 2D plane of confinement. Therefore, the observation of magnetoresistance oscillations (Shubnikov-de Hass effect) proves the 2D nature. The most definitive evidence for 2D nature, however, is the observation of the quantum Hall effect, which is a quintessentially 2D phenomenon. Any system manifesting an unambiguous quantized Hall plateau is 2D in nature, and therefore the observation of the quantum Hall effect in graphene in 2005 by Novoselov et al. [5] and Zhang et al. [6] is an absolute evidence of its 2D nature. In fact, the quantum Hall effect in graphene persists to room temperature [7], indicating that graphene remains a strict 2D electronic material even at room temperature.

1.1 Graphene for electronic applications: opportunities and challenges

Graphene has been adopted as a material of choice by researchers involved in many fields. In particular, simultaneous observation of high mobility, sensitivity to field effect and ease of contacting made graphene an appealing candidate for field-effect transistor devices. A lot of progress has been made in that direction. Manufacturability of graphene transistor operating at 100 GHz has been demonstrated on wafer-scale [8]. Moreover, chemically stable, robust and foldable graphene sheets possess enough optical transparency to be considered as transparent conductors in applications as coatings for solar cells, liquid crystal displays etc. for the replacement for indium tin oxide [9].

However some open issues still remain and are currently the object of intense research activity.

i. Although the "intrinsic" mobility of graphene has been estimated to be $>2\times10^5$ $cm^2V^{-1}s^{-1}$, the mobility values commonly reported in the literature span a wide range, from $\sim10^2$ to $\sim10^4$ $cm^2V^{-1}s^{-1}$, depending on the synthesis method used to obtain graphene, on the kind of substrate where it is deposited, etc… It is evident that the intrinsically outstanding transport properties of this material are limited by extrinsic mechanisms. However, there is no consensus about the scattering mechanism that currently limits the mobility in graphene devices;

ii. Due to the zero bandgap of graphene electronic structure, it is not possible to reach high values of the ratio I_{on}/I_{off} between the on state and off state current in graphene field effect devices. To date several strategies have been developed to open a gap in graphene electronic bandstructure. Among them, the following must be cited.

a. The inclusion of sp^3 hydrocarbon defects in the sp^2 lattice [10],
b. The distortion of the graphene lattice under uniaxial strain [11],
c. The application of a transversal electric field to a bilayer graphene [12],
d. The influence of the SiC substrate on the epitaxial graphene on Si face of hexagonal SiC has also been shown to induce substantial band gap [13],
e. Moreover, a bandgap can also be induced in semimetallic graphene if it is shaped in nanoribbons by a direct consequence of the lateral confinement of the 2DEG [14]. However, this points to extremely challenging need to perform atomically precise tailoring of graphene over long distances for advanced graphene electronic architectures.

1.3 Need for a nanoscale control of graphene electronic properties

As ongoing efforts to incorporate graphene into electronic applications, attempts are already being made to gain consistent control over electronic properties in graphene down to nanometer scale so as to explore its possibility as a complementary material to Silicon for prospective nanoelectronics. Notable amongst these include intentional control of the density and character of its charge carriers by doping [15], and confining charge carriers to nanometer constrictions [14]. Typically, most experiments probe the global electrical response of graphene devices thus yielding properties averaged over the whole device. As a consequence, local properties and their distributions within the sample are inaccessible with standard electron transport measurements. In low dimensional electronic systems, like graphene, the local phenomenona/effects might have much stronger impact than previously believed. Hence, naturally, developing techniques to analyse and/or control the local effects in graphene has attracted wide interests. Consequently, such local probing techniques have helped gain significant insights into various aspects of functioning graphene devices. Notably, scanning probe microscopy (SPM) based measurements have provided the most direct probe of local electronic properties. For example, Scanning Photocurrent Microscopy [16] has been used to probe the 'electrostatic potential landscape' of graphene in view of analyzing the local changes in the electronic structure of the graphene sheets introduced by their interaction with deposited metal contacts and by local symmetry breaking/ disorder at the sheet edges. On the other hand Raman microscopy has been used to probe mesoscopic inhomogeneity in the doping [17], due, possibly, to the presence of charged impurities. Formation of sub-micron (resolution limited) electron and hole charge puddles near Dirac point in graphene, has been demonstrated by Martin et. al. [18] using Scanning Single Electron Transistor microscopy where they gauged the intrinsic size of the puddles to be ~30 nm. Atomic Force Microscope based scanning microscopy techniques have also been significantly used to get better insights in graphene electronic properties. For example, high-resolution scanning tunneling microscopy (STM) [19] experiments have directly imaged charge puddles of ~10 nm in size and suggested they originate from individual charged impurities underneath graphene.

In the wake of such proven local inhomogeneity in electrical properties of graphene the work presented in this *chapter* focuses on local evaluation of transport properties in substrate-supported graphene by the use of scanning probe microscopy based methods with nanometer scale lateral resolution.

In particular Section 2 deals with the most common graphene synthesis methods and, in particular, on those used in this study, i.e. mechanical exfoliation of HOPG and epitaxial

growth by thermal treatments on hexagonal SiC. The characterization methods used for the identification and morphological and structural analyses of the produced graphene layers are also illustrated

Section 3 is focused on the evaluation of the local transport properties, electron mean free path and mobility, in graphene on insulating and semiconducting substrates. In particular the role of the interaction of 2DEG in graphene with the substrate (in particular, the role of dielectric environment) is discussed.

2. Graphene synthesis methods

Graphene has been adopted as a material of interest quite widely. This had led to many motivations for material synthesis. To date, the synthetic techniques fall into two categories. In the first approach the weak bonding between the graphene layers in HOPG is exploited and single or few layers of graphene are separated from the parent crystal either by mechanical [1] or chemical exfoliation [20]. Mechanical separation, the technique used to obtain and study graphene in the laboratory for the first time [1], is a simple, inexpensive method, yielding graphene flakes of very high crystalline quality. However, the yield of graphene production is extremely low and the flakes have small dimension (from 1 μm to 100 μm lateral size), so that this approach lacks the scalability required by mass device production. Exfoliation of graphene in solution from HOPG by chemical methods allows to improve the yield, but the size of the flakes remains too small and the crystalline quality is worse than in mechanically exfoliated graphene.

The second approach is based on the epitaxial growth of graphene on substrates. In particular, graphene has been obtained by chemical vapour deposition on catalytic metal films (Ni, Cu,..) from hydrocarbon precursors [21,22], or by controlled thermal decomposition of SiC [23]. This second approach has the potential of producing large-area lithography-compatible films and is rapidly advancing at the moment. The crystalline quality of epitaxial graphene is typically lower than in mechanically exfoliated graphene flakes, but it could be improved by improving the growth methods. In the case of graphene grown on metal substrates, the grown film needs to be transferred to an insulating substrate, to be useful in electronic applications. On the contrary, epitaxial graphene obtained by thermal treatments of SiC grows directly on a semiconducting or semiinsulating substrate, and is expecially suitable for electronic applications.

In the present study, the used graphene samples were obtained by mechanical exfoliation of HOPG and by epitaxial growth on hexagonal SiC substrate. The sample preparation and graphene identification for the two methods are discussed in the following.

2.1 Mechanical exfoliation of HOPG

Mechanical exfoliation, developed by Novoselov and Geim [1], involves a topdown approach to get graphene from highly oriented pyrolitic graphite (HOPG). Using a common adhesive tape a thin graphite layer is peeled off from HOPG. With an inter-layer van der Waals interaction energy of about 2 eV/nm^2, the force required to exfoliate graphite is extremely weak, about 300 nN/μm^2. After repeated thinning the flakes are transferred by gently pressing the tape onto suitable substrate. We used extensive characterization by Optical contrast microscopy imaging (OM), TappingMode AFM (t-AFM), and microRaman (μR) spectroscopy to analyze/identify manolayer flakes.

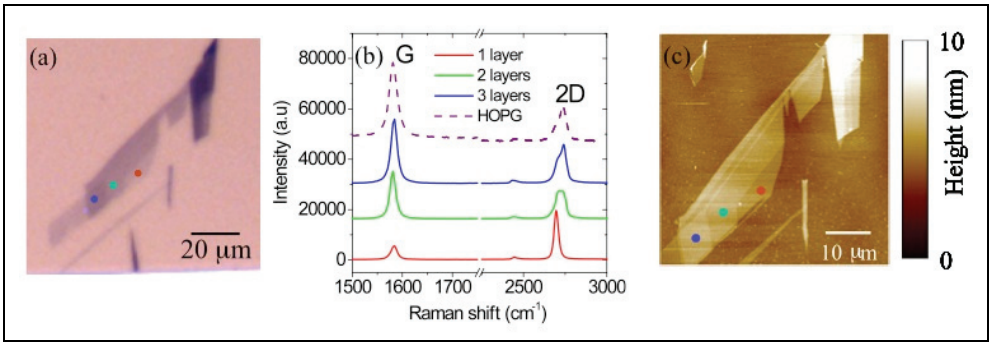

Fig. 3. Optical microscopy image (a), micro-Raman spectra (b) and atomic force microscopy (c) image of few layers of graphene obtained by mechanical exfoliation of HOPG (Data from Ref. [24].)

In Fig. 3(a), an OM image of a FLG sample is reported [24]. The variable contrast in the image is indicative of a variable number of layers in the different regions of the sample. In particular, a lower contrast is associated to thinner layers. After an appropriate calibration, optical contrast variations can be used for a quantitative determination of the number of layers. In Fig.3(b), μR spectra measured on some selected positions indicated by the red, green and blue dots in the OM of Fig. 3(a) are shown. As a reference, the spectrum obtained from HOPG is also reported. Raman spectroscopy is a very powerful method for the characterization of HOPG and FLG. In particular, it allows an unambiguous distinction between single layer, bilayer and multilayers in the case of graphene obtained by exfoliation of HOPG [25]. This is possible through a comparison of the relative intensity of the characteristics G peak (appearing at ~1580 cm^{-1}) and 2D peak (appearing at ~2680 cm^{-1}) and from the symmetry of the 2D peak in the Raman spectra. As it is evident from Fig.3(b), the spectrum measured in the flake region with the lowest optical contrast (position indicated by a red point in Fig.3(a)), exhibits a symmetric 2D peak with very high intensity compared with the G peak. These characteristic spectroscopic features have been associated uniquely to a graphene single layer. As it is evident, the relative intensity of the two peaks is very different in the case of a graphene bilayer, for which the 2D peak is not symmetric. For a number of layers larger than three the Raman spectrum becomes qualitatively similar to that of HOPG.

In Fig.4(a), an AFM morphological image on the same sample region as in Fig.3(a) is reported. In order to obtain quantitative information on the number of graphene layers from these morphological image, a height profile along the dashed line indicated in Fig.4(a) is reported in Fig.4(b). The zero height value is represented by the SiO_2 surface level. Hence, from the profile in Fig.4b it is possible to deduce the height associated to the single layer, bilayer and trilayer of graphene previously identified by Raman spectroscopy.

Interestingly, the measured height of a single layer with respect to the SiO_2 is ~0.7 nm, while the relative heights of the second layer with respect to the first one and that of the third layer with respect to the second are both ~0.35 nm. The latter thickness value is very close to the interlayer spacing between graphene planes within HOPG. Hence, it seems that the measured step-height for a single layer of graphene is affected by an "offset". This means that, in order to use AFM to determine the number of graphene layer in a sheet, it is

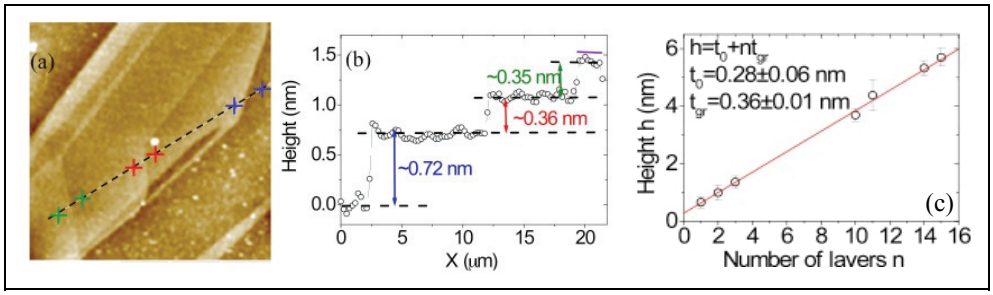

Fig. 4. AFM morphological image of a FLG (a) and height profile along the indicated dashed line (b). Average height h as a function of the estimated number of layers n (c). The data have been fitted with the linear relation, $h=t_{gr}\times n+t_0$, with the interlayer spacing t_{gr} and the offset t_0 fitting parameters. The best fit with the experimental data obtained for the values of $t_{gr}=0.36\pm0.01$ nm and $t_0=0.28\pm0.06$ nm (Data from Ref. [24]).

necessary to have an accurate estimate of this value. To do this, the step height with respect to SiO_2 was measured on a large number of flakes with variable number of layers, and with a "staircase" structure similar to that illustrated in Fig.4(b). For each flake, the single layer region was unambiguously determined by μR measurements. The number of layers for thicker regions could be obtained by counting the number of subsequent steps with ~0.35 nm height. In Fig.4c, the average height h is reported as a function of the estimated number of layers n. These data have been fitted with the linear relation, $h=t_{gr}\times n+t_0$, where the interlayer spacing t_{gr} and the offset t_0 are the fitting parameters. The best fit with the experimental data has been obtained for the values of $t_{gr}=0.36\pm0.01$ nm and $t_0=0.28\pm0.06$ nm. Based on such calibration curve (measured height versus number of layers), it is possible to determine in an accurate and straightforward way the number of layers in a multilayer sheet deposited on thermal SiO_2 by an AFM analysis. However, this calibration procedure has to be repeated if the substrate material is changed, since the offset t_0 depends on the specific substrate.

Quantitative information on number of graphene layers deposited on a substrate can also be obtained from optical images, if an accurate analysis of the contrast is carried out. The optical contrast C can be quantitatively defined as,

$$C = (R_{sub} - R_{gr}) / R_{sub} \tag{2}$$

where R_{gr} is the reflected light intensity by FLG and R_{sub} the reflected intensity by the substrate[26]. Typically a SiO_2/Si substrate with 100 or 300 nm thick SiO_2 is chosen, since for these thicknesses optical contrast is maximized for light wavelengths in the visible range (400-700 nm), due to a constructive interference effect.

Fig. 5(a) and (b) illustrate the procedure to extract the optical contrast from an OM on a single layer of graphene flake deposited on 100 nm thick SiO_2 and illuminated with light of 600 nm wavelength [24]. Based on this procedure, the optical contrast can be determined for flakes of different thickness. The number of layers in the flakes can be independently determined by AFM according to the calibration curve in Fig.4 (c). In Fig.5(c), the symbols represent the contrast as a function of the flake thickness (and the number of graphene

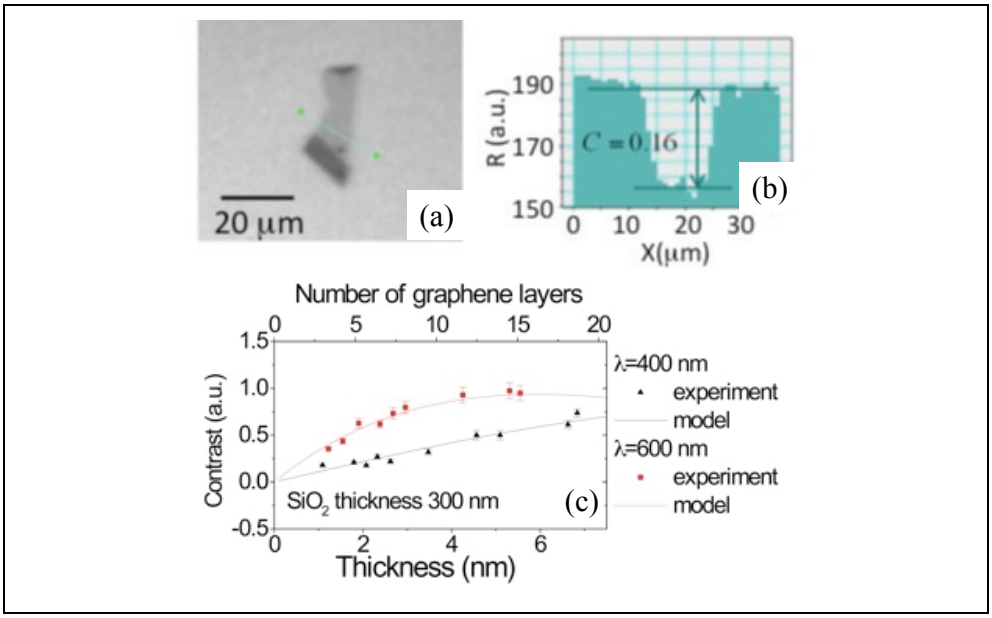

Fig. 5. Optical image of a SLG (a), reflected intensity profile along the dashed line (b) and optical contrast versus the number of graphene layers for two different incident light wavelengths (c) (Data from Ref. [24]).

layers) for samples deposited on 300 nm SiO_2 and illuminated with light of 400 nm (black triangles) and 600 nm (red squares) wavelengths. The lines represent the calculated contrast as a function of the number of layers. The reflected light intensities R_{sub} and R_{gr} are calculated using the Fresnel equations. The literature values of the complex refraction index of Si and SiO_2 as a function of the wavelength were used.

For graphene, the real and imaginary part of the refraction index n_{gr} were calculated starting from its noticeable absorption properties in the wavelength range of visible light. In fact, recently, it has been shown that a single layer of graphene absorbs a fixed percentage ($\pi\alpha$= 2.3%, where α is the fine structure constant) of the intensity of incident visible light [27]. Moreover, for few layers of graphene, the absorbance increases linearly with the number of layers. Based on these properties, refraction index values of graphene for the two considered wavelengths were calculated to be:

$$n_{gr}(400nm) = 2.57 - i0.81 \quad (3.a)$$

$$n_{gr}(600nm) = 2.53 - i1.21 \quad (3.b)$$

2.2 Epitaxial growth of graphene of SiC

Graphene growth during annealing of SiC relies on the interplay of two different mechanisms: (i) the preferential Si sublimation from SiC surface, which leaves an excess of C atoms in the near surface region, and (ii) the diffusion of these C atoms on the SiC surface

and their reorganization in the two dimensional graphene lattice structure. Both mechanisms depend in a complex way both on the annealing conditions (temperature T_{gr}, ramp rate, pressure in the chamber) and on the initial surface conditions of SiC wafers, e.g. the termination (Si or C –face), the miscut angle, the defectivity. It has been shown that the rate of Si evaporation can be strongly reduced by performing the annealing in inert gas ambient at atmospheric pressure instead than in vacuum [28]. This results in the possibility to raise the growth temperature, from typical values of T_{gr}~1300°C in vacuum to T_{gr}>1600°C at atmospheric pressure [29]. This has, in turns, beneficial effects on the crystalline quality of the EG layers, since at higher temperature a higher diffusivity of the C atoms on the surface is achieved. It has been also observed that graphene growth starts from the kinks of terraces on the SiC surface or from defects (e.g. pits or threading dislocations) [30]. This means that, for fixed annealing conditions, a higher growth rate is expected on vicinal, i.e. off-axis, SiC surfaces than on on-axis ones, since the spacing between terraces kinks is reduced. Most of the studies on EG growth reported in the literature were carried out on on-axis hexagonal SiC substrates.

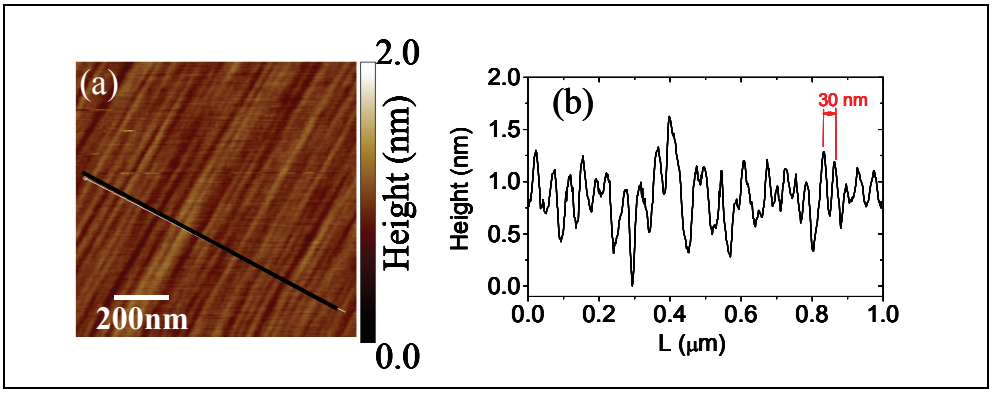

Fig. 6. AFM morphological image of a virgin 4H-SiC (0001), 8° off-axis surface (a) and linescan (b), showing the parallel terraces with a mean width of ~30 nm (Data from Ref. [31]).

The results here reported concern EG grown on the Si face of 8° off-axis 4H-SiC by annealing in inert gas (Ar) ambient in a wide range of temperatures (T_{gr} from 1600°C to 2000°C) [31]. A morphological AFM image of the virgin 4H-SiC (0001) surface is reported in Fig.6, showing the parallel terraces oriented in the <00-10> direction and with a mean width of ~30 nm. AFM images of the surface morphology for the samples annealed at 1600, 1700 and 2000 °C are reported in Fig.7(a), (b) and (c), whereas the corresponding phase maps on the same samples are reported in Fig.7(d), (e) and (f). Annealed samples show wide terraces (average width of ~150-200 nm) running parallel to the original steps in the virgin sample.

Such large terraces are the result of the step-bunching commonly observed on off-axis SiC substrates after thermal treatments at temperatures >1400°C. Interestingly, a network of nanometer wide linear features is superimposed to these large terraces. These features are particularly evident in the phase images of the surfaces.

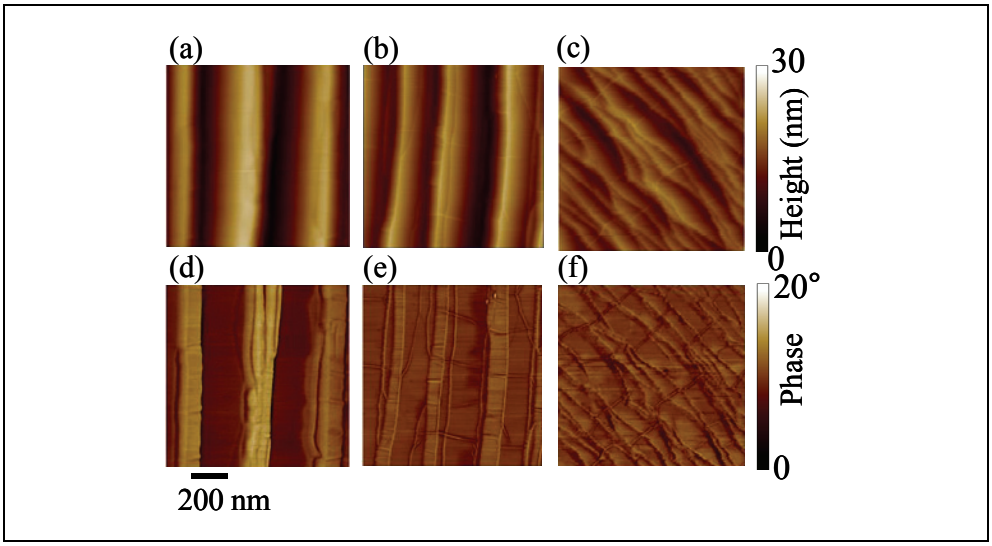

Fig. 7. AFM images of the surface morphology for the samples annealed at 1600 (a), 1700 (b) and 2000 °C (c). The corresponding phase maps on the same samples are reported in (d), (e) and (f). (Data from Ref. [31]).

Fig.8 shows two representative linescans taken in the direction orthogonal (b) and parallel (c) to the terraces length obtained from the morphology map of the sample annealed at 1700°C. In the orthogonal direction, it is worth noting very small steps with nm or sub-nm height, which are overlapped to the large terraces of the SiC substrate. The height of these steps is always a multiple of 0.35 nm, the height value corresponds the interlayer spacing between two stacked graphene planes in HOPG. As an example a ~0.35 nm and a ~1.1 high step are indicated in Fig.8(b), associated, respectively, to one and three graphene layers over the substrate or stacked over other graphene layers.
From the linescan in the direction parallel to the terraces length (c), peculiar corrugations with ~2 nm typical height can be observed.

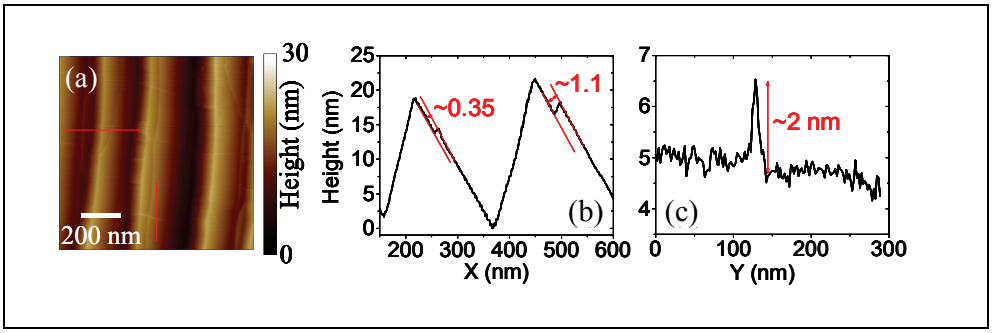

Fig. 8. Two representative linescans from the morphology map (a) of a sample annealed at 1700°C taken in the direction orthogonal (b) and parallel (c) to the steps. (Data from Ref. [31]).

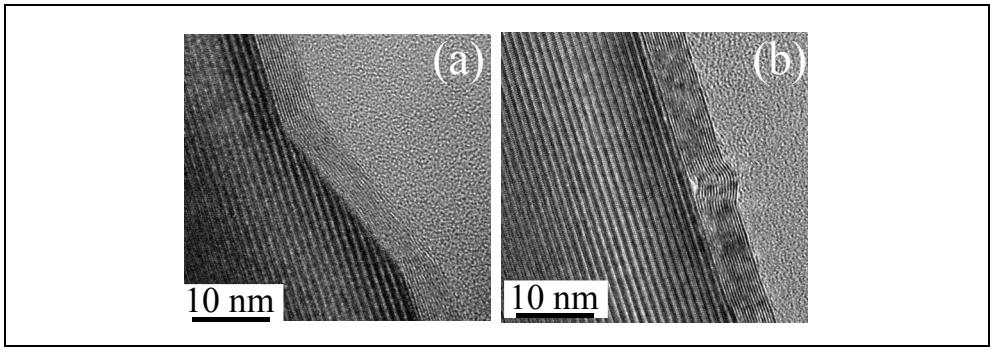

Fig. 9. Two representative HRXTEM images for 8° off-axis 4H-SiC (0001) annealed at 2000 °C. (Data from Ref. [31]).

HRXTEM analyses allowed to get further insight on the structural properties of the graphene films grown at the different temperatures and to clarify the nature of these peculiar corrugations.

In Fig.9(a) and (b) two representative HRXTEM images for a sample annealed at 2000 °C are reported. From Fig.9(a), it is evident that a graphene multilayer uniformly covers the SiC surface also on the terrace step edges. From Fig.9(b), the structure of one of the peculiar corrugations running orthogonal to the steps is reported. This cross sectional image unambiguously demonstrate that those features are wrinkles in the multilayer graphene film. These peculiar defects have been observed also by other authors in the case of few layers of graphene grown on the C face [32] or on the Si face [33] of hexagonal SiC, on-axis. However, in that case wrinkles do not exhibit any preferential orientation with respect to the steps, but form an isotropic mesh-like network on the surface, where wrinkles are interconnected into nodes (typically three wrinkles merge on a node and the angles subtended by the wrinkles are ~60° or 120 °C [32]). The formation of that mesh-like network of wrinkles was attributed to the release of the compressive strain which builds up in FLG during the sample cooling due to mismatch between the thermal expansion coefficients of graphene and the SiC substrate [32]. Comparing the morphology and phase images in Fig.7 for the samples annealed at the different temperatures, it is easy to observe that the density of wrinkles increases with temperature.

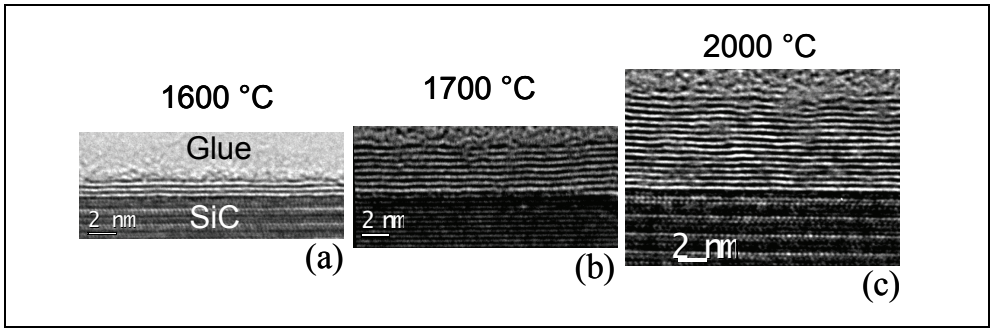

Fig. 10. HRXTEM images on the samples annealed at 1600 (a), 1700 (b) and 2000°C (c) are reported, showing 3, 8 and 18 layers on the surface of 4H-SiC. (Data from Ref. [31]).

In Fig.10(a), (b) and (c), HRXTEM images on the samples annealed at 1600, 1700 and 2000°C are reported, showing 3, 8 and 18 layers on the surface of 4H-SiC. These cross-sectional analyses give a direct measure of the number of grown layers, but only on a very local scale. Lateral variation of the FLG thickness on different sample positions cannot be determined by such a method. To get an estimation of the number of layers at selected surface positions and with higher statistics, AFM can be used to measure the depth of selectively etched stripes in FLG by O_2 plasma. This plasma treatment is known to remove efficiently carbonaceous species through a chemical reaction leading to the formation of CO_2.

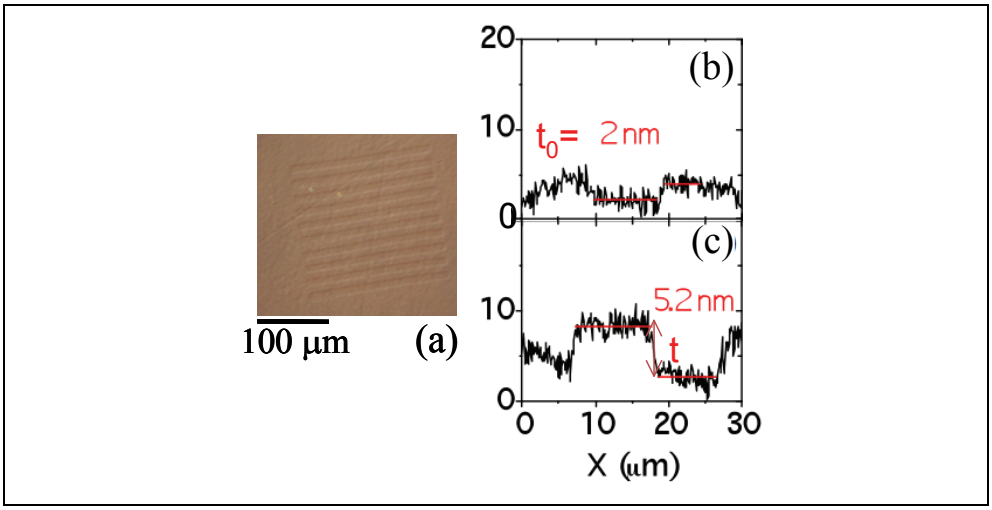

Fig. 11. Optical image of the etched graphene stripes by O_2 plasma treatment in multilayer graphene grown on SiC at 1700 °C (a). To estimate the graphene thickness, a lithographically patterned pristine SiC was simultaneously etched together with the graphitized SiC sample, and the etched SiC depth was measured. AFM Height profiles taken on a etched stripe on pristine SiC (b) and on the sample annealed at 1700 °C (c), respectively. (Data from Ref. [31]).

In Fig. 11(a), an optical image of the etched stripes in on the sample annealed at 1700 °C is reported. To obtain an accurate estimation, we checked if the SiC substrate is slightly etched by the used plasma processing. To this aim, a lithographically patterned pristine SiC substrate was simultaneously etched together with the graphitized SiC samples. Fig. 11(b) and (c) show the height profile taken on a stripe on pristine SiC and on the sample annealed at 1700 °C, respectively. From Fig. 11(b), it is clear that a thickness t0~2 nm of SiC is etched during the plasma treatment, due to the physical action of the plasma. This depth must be subtracted while evaluating the number of layers on graphitized SiC. Hence the number of layers can be estimated according to the relation n=(t-t0)/tgr, being tgr the interlayer separation between to stacked graphene layers (tgr≈0.35 nm). The average number of grown layers as a function of the growth temperature Tgr is reported in Fig.12, where the error bars represent the standard deviations obtained from a large statistics on the number of layers determined at several sample positions.

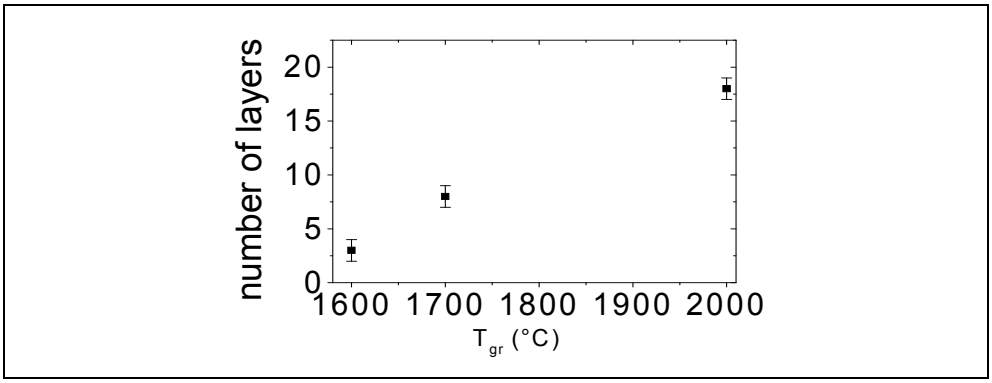

Fig. 12. Average number of grown layers on 4H-SiC (0001), 8° off, as a function of the growth temperature (T_{gr}). The error bars represent the standard deviations obtained from a large statistics on the number of layers at several sample positions. (Data from Ref. [31]).

3. Local transport properties of graphene by scanning probe microscopy

One of the main issues in the research on graphene is to understand how the various scattering mechanisms limit the transport properties, i.e. the electron mean free path and the mobility. Ideally, in a very clean graphene sheet (i.e. with no adsorbed impurities) sufficiently isolated from its environment to be considered free standing, charge carriers can exhibit a giant intrinsic mobility [34] and can travel for micrometers without scattering at room temperature. Indeed, very high values of mobility (>2×10^5 $cm^2V^{-1}s^{-1}$) and electron mean free path have been observed in vacuum and at low temperature (5K) in 'suspended' graphene, obtained by locally etching the substrate under the sheet, after a cleaning by current-induced heating [35]. However, graphene for electronics applications is commonly supported by a dielectric substrate (typically SiO_2 or high-*k* dielectrics) or by semi-insulating SiC. The values of the electron mean free path and mobility observed in supported graphene layers are usually significantly lower than in suspended ones. So far, graphene on a substrate has shown field-effect mobility ranging from 10^2 to 2×10^4 $cm^2V^{-1}s^{-1}$, depending on the kind of substrate and on the graphene synthesis method.

Several factors that can affect the transport of carriers in graphene and degrade its electron mean free path and mobility have been identified and are still under active debate. Carrier scattering with charged impurities [36] (either adsorbed on graphene surface or trapped at the interface with the substrate) is typically indicated as one of the main mechanisms limiting mobility of graphene two-dimensional-electron-gas (2DEG). Since charged impurities interact with graphene 2DEG by a screened Coulomb potential, the strength of the interaction is expected to decrease significantly with increasing the permittivity of the substrate and/or of the dielectric layer deposited on graphene. Experimental results by different authors suggest that scattering by charged impurities is not the only mechanism that limits the mean free path attainable for substrate-supported graphene. Inelastic scattering by surface polar phonons (SPP) of the substrate [37] has been indicated as an additional mechanism limiting the carrier mobility in graphene. It has been shown theoretically that, due to the polar nature of the substrates commonly used for graphene (like SiO_2 and SiC), a long-range polarization field is associated to the thermally induced

lattice vibrations at the surface of the substrate (i.e. the SPP). This field electrostatically couples with the 2DEG, resulting in a sizeable degradation of mobility at room temperature. Recently, the experimental evidence of such SPP scattering at room temperature has been reported, based on temperature dependent transport measurements performed on devices in graphene deposited on SiO_2 substrate [34]. It has also been predicted that for graphene on SiC, the SPP scattering has a weaker effect on the electron mobility than for graphene on SiO_2, due to weaker polarizability of SiC and relatively high phonon frequencies associated with the hard Si-C bonds [37].
As a matter of fact, charged impurities are randomly distributed on the graphene surface. The random distribution of these scattering sources causes local inhomogeneities in the transport properties, which adversely influence the reproducible operation of graphene nanodevices. Under this point of view, nanoscale resolution methods are required to probe the lateral homogeneity of the transport properties in graphene sheets.

3.1 Local electron mean free path

Recently, scanning capacitance spectroscopy (SCS) on graphene was applied to determine the "local" electron mean free path *l* (defined as the average of the distances traveled by electrons between "few" subsequent scattering events) and mobility μ [38,39]. A schematic representation of the SCS measuring setup is reported in Fig.13(a). The graphene/insulator/semiconductor backgate system can be described as a metal-insulator-semiconductor (MIS) capacitor. Under electric fields, graphene does not behave as a "classical" metal film, but manifests itself as a capacitor, whose capacitance (the quantum capacitance C_q) adds in series to the insulator and semiconductor capacitance contributions [40].

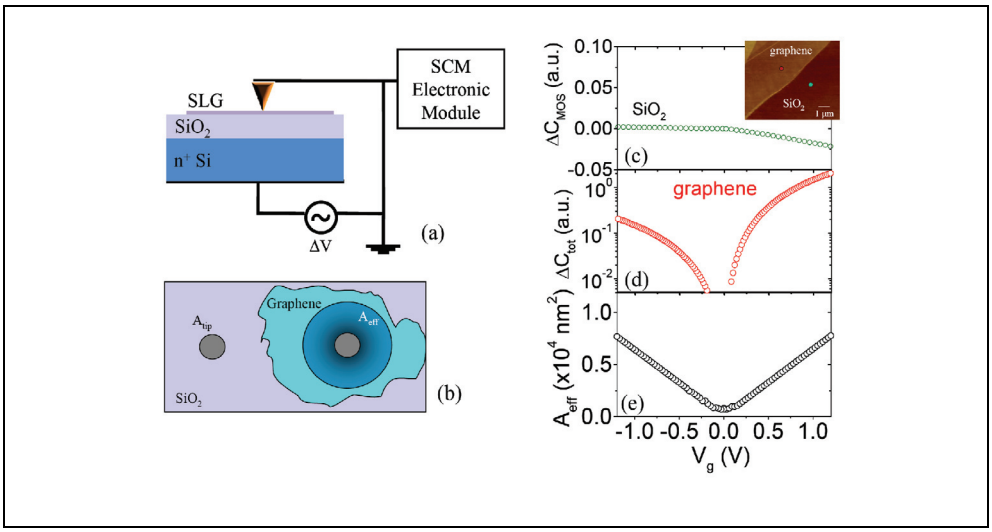

Fig. 13. Schematic representation of the scanning capacitance spectroscopy (SCS) measuring setup (a) and of the effective area in graphene (b). Representative □C-Vg characteristics measured with the tip in contact on 100 nm SiO2 on n+ Si (c) and with the tip on graphene coated SiO2 (d). Experimental dependence of the effective area on the gate bias (e), obtained from the ratio of the curves in (d) and (c). (Data from Ref. [39]).

Local measurements were carried out by an AFM, using Pt coated n^+-Si tips as probes. A modulating bias $\Delta V = \frac{V_g}{2} + \frac{V_g}{2}\sin(\omega t)$ with amplitude V_g and frequency ω=100 kHz was applied between the Si n^+ backgate and the probe. An ultra-high-sensitive (10^{-21} $F/Hz^{1/2}$) capacitance sensor connected to the conductive AFM tip allowed to measure, through a lock-in system, the capacitance variation $\Delta C(V_g)$ induced by the modulating bias.

The AFM tip in contact with bare SiO_2 forms a MOS capacitor with capacitance $A_{tip} \times C'_{MOS}$, where C'_{MOS} is the per unit area capacitance of the MOS system and $A_{tip} = \pi r_{tip}^2$ is the tip contact area with tip radius r_{tip}. When the tip is in contact with graphene, a positive gate bias causes the accumulation of electrons in graphene to screen the positively charged uncompensated ions in the depletion layer at the SiO_2/Si interface. On the contrary, a negative gate bias induces the accumulation of holes in graphene to screen the electrons at the SiO_2/Si interface. In both cases, the induced carriers in graphene are distributed over an effective area A_{eff} [40,41] This is schematically illustrated in Fig. 13(b). The total capacitance, when the tip is on graphene, is $C_{tot}=A_{eff} \times C'_{tot}$, where C'_{tot} is the series combination of C'_{MOS} and C'_q, the per unit area quantum capacitance of graphene. Since $C'_q >> C'_{MOS}$ for the typical thicknesses (~100 or ~300 nm) of the adopted SiO_2 layers, C_{tot} can be expressed as $C_{tot}=A_{eff} \times C'_{MOS}$. Hence, $C_{tot}/C_{MOS} = A_{eff}/A_{tip}$.

Fig.13(c) and 13(d) show two representative ΔC-V_g characteristics measured with the tip in contact on two distinct positions on a sample with graphene deposited on 100 nm SiO_2. The curve in Fig.13(c) was measured with the tip on bare SiO_2 and exhibits the typical behavior observed for a MIS capacitor on a n-type semiconductor. The curve in Fig.13(d), measured with the tip on graphene, has a minimum value close to V_g=0 and increases both for negative and positive V_g values. The experimental dependence of the effective area on the gate bias can be obtained from the ratio of the curves in Fig.13(d) and (c), i.e.

$$A_{eff} = A_{tip} \frac{|\Delta C_{tot}|}{|\Delta C_{MOS}|} \tag{4}$$

As shown in Fig.13 (e), A_{eff} exhibits a minimum at V_g~0 and increases linearly with V_g in a symmetric way for both bias polarities. $A_{eff}=\pi L_{eff}^2$ represents the effective area of the graphene capacitor responding to the AC bias, i.e. L_{eff} is the distance from the tip contact where the induced screening charges (electrons/holes) spread in graphene. A_{eff} is much smaller than the area of the entire graphene sheet (~100 μm^2 in this specific case).

In the following, it is shown that L_{eff} corresponds to the local electron mean free path in the probed graphene region. The induced charge carriers diffuse over a length L_{eff} from the tip contact, traveling at velocity v_F. Their diffusivity in graphene can be expressed as $D=v_F L_{eff}/2$. On the other hand, the diffusivity D can be related to electron mobility μ by the generalized Einstein relation $D/\mu = n/(q\partial n/\partial E_F)$, being q the electron charge, n the electron density and E_F the Fermi energy in graphene. The concepts of mobility and carrier density in graphene are meaningful when the Fermi level is far from the Dirac point but is still in the linear region of the dispersion relation. In these conditions, the density of states is linearly dependent on E_F. As a consequence, the carrier density can be expressed as $n=E_F^2/(\pi\hbar^2 v_F^2)$, and $D/\mu = E_F/2q$. Furthermore, far from the Dirac point, Boltzmann transport theory can be used to describe the electronic transport in graphene and μ can be expressed in terms of l as $\mu = q v_F l / E_F$. As a consequence, L_{eff} measured by SCS correponds to l. This continuum treatment, using the concepts of diffusivity and mobility and the Einstein relation, is

justified on the "mesoscopic" length scale investigated by SCS (from 10 to 100 nm). A quantum mechanical treatment of electron scattering phenomena, based on the interference of incident and reflected electron wavefunctions by a single scattering center, is required on a length scale of ~1 nm, as recently demonstrated in some investigations by scanning tunneling microscopy [42].

3.2 Role of graphene/substrate interface on the 2DEG transport properties

In this section, 'local' measurements of the electron mean free path are reported in graphene on most relevant substrates for electronic applications: (i) graphene exfoliated and deposited on 4H-SiC(0001) (DG-SiC), (ii) graphene epitaxially grown on 4H-SiC(0001) (EG-SiC), and (iii) graphene deposited on SiO_2 (DG-SiO_2) [43].

In the case of DG-SiO_2, the SiO_2 film works as the gate dielectric and the n^+ Si substrate works as the semiconductor of a metal-insulator-semiconductor (MIS) capacitor. Similarly, both in the case of DG-SiC and of EG-SiC, the very lowly doped SiC film works as the gate dielectric, whereas the n^+ SiC substrate works as the semiconductor back gate of the capacitor. Bias amplitude V_g was varied from 0 to 10V at bias frequency of ω = 100kHz.

In Fig.14 are reported representative capacitance-voltage characteristics obtained on DG-SiC (a), EG-SiC (b) and DG-SiO_2 (c) on arrays of 5×5 tip positions with an inter-step distance of 1μm×1μm. For reference, SCS measurements were carried also on bare SiO_2 and SiC regions of the samples.

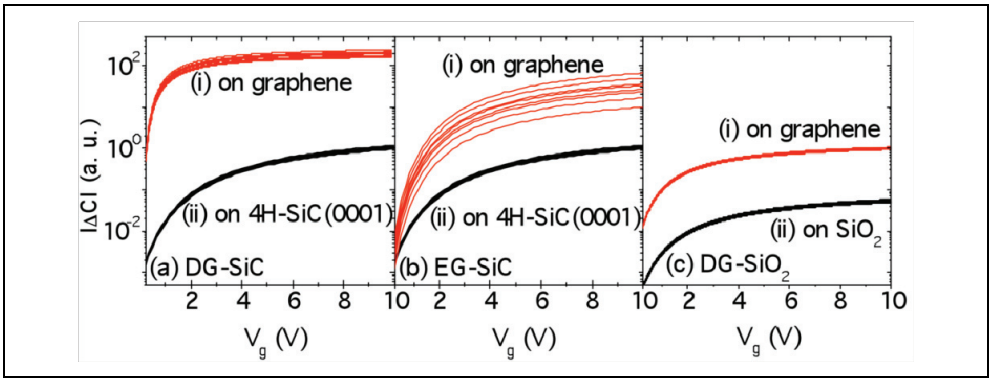

Fig. 14. Representative capacitance-voltage characteristics obtained on DG-SiC (a), EG-SiC (b) and DG-SiO_2 (c) on arrays of 5×5 tip positions with an inter-step distance of 1μm×1μm. (Data from Ref. [43]).

Fig.15(a) shows the evaluated l_{gr} for DG-SiC, EG-SiC and DG-SiO_2. l_{gr} is reported versus n_{Vg}-n_0, being n_{Vg} the carrier density induced in graphene by the gate bias V_g and n_0 the carrier density at V_g=0. The values of n_{Vg}-n_0 are obtained as

$$n_{Vg} - n_0 = e_0 e_{ins} V_g / q t_{ins} \quad (5)$$

where ε_{ins} and t_{ins} are the relative dielectric constant and the thickness of the insulating layer under graphene and ε_0 is the vacuum absolute dielectric constant. The histograms of the l_{gr} values at a fixed value of n_{Vg}-n_0=1.5×10^{11}cm^{-2} are reported in Fig.15(b) for DG-SiC (i), EG-SiC (ii) and DG-SiO_2 (iii).

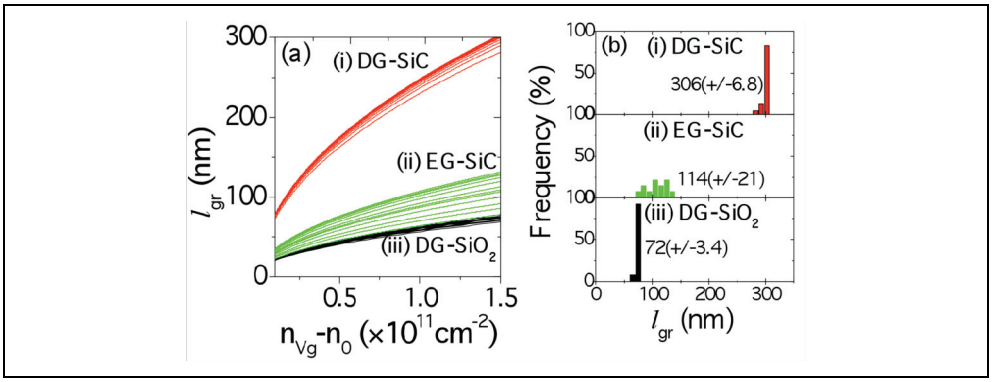

Fig. 15. Evaluated l_{gr} for graphene exfoliated and deposited on 4H-SiC(0001) (DG-SiC), for graphene epitaxially grown on 4H-SiC(0001) (EG-SiC), and for graphene deposited on SiO_2 (DG-SiO_2) (a). l_{gr} is reported versus n_{Vg}-n_0, being n_{Vg} the carrier density induced in graphene by the gate bias V_g and n_0 the carrier density at V_g=0.

It is worth noting that l_{gr} in EG-SiC is on average 37% of l_{gr} in DG-SiC, but the spread of the l_{gr} values in EG-SiC is much larger than in DG-SiC. These differences can be explained in terms of the peculiar structure of EG/4H-SiC (0001) interface, as discussed in the following section.

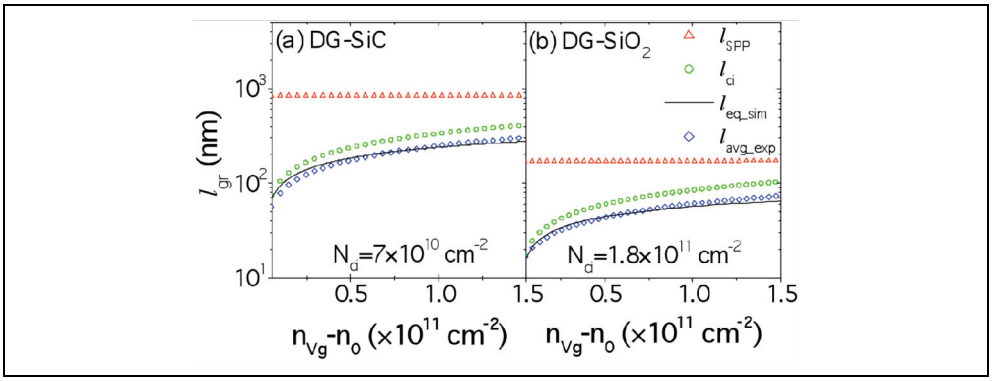

Fig. 16. Average of the l_{gr} vs n_{Vg}-n_0 curves measured on different tip positions on DG-SiC (a) and DG-SiO_2 (b). Data from Ref. [43].

It is also worth noting that l_{gr} on DG/SiC is on average ~4× than on DG/SiO_2 and the spread of the l_{gr} values are comparable in the two cases. This difference can be explained in terms of the higher permittivity of SiC (ε_{SiC}=9.7) than SiO_2 (ε_{SiO2}=3.9) and of the lower coupling of the 2DEG with surface polar phonons in SiC than in SiO_2. This is better discussed in the following. The electron mean-free path limited by scattering on charged impurities (l_{ci}) in graphene could be expressed as a function of the carrier density as [44],

$$l_{ci}(n) = \frac{16\varepsilon_0^2\varepsilon^2\hbar^2 v_F^2}{Z^2 q^4 N_{ci}}\left(1+\frac{q^2}{\pi\hbar v_F\varepsilon_0\varepsilon}\right)^2\sqrt{\pi n} \tag{5}$$

where Z is the net charge of the impurity (assumed to be 1 for this study), N_{ci} is the impurity density and ε is the average between the relative permittivity of the substrate (ε_{ins}) and of vacuum permittivity (ε_{vac}=1). The electron mean free path limited by scattering with a SPP phonon mode of characteristic frequency ω_υ can be expressed as [45]

$$l_{SPP,\upsilon} = \sqrt{\frac{\beta}{\hbar\omega_\upsilon}} \frac{\hbar v_F 4\pi\varepsilon_0}{q^2} \frac{q v_F}{F^2_\upsilon} \frac{\exp(k_0 z_0)}{N_{SPO,\upsilon}} \frac{\hbar\sqrt{\pi}}{q} \tag{6}$$

where

$$k_0 \approx \sqrt{\left(\frac{2\omega_{SO,\upsilon}}{v_F}\right)^2 + \chi n} \tag{7}$$

$\chi \approx 10.5$, $\beta \approx 0.153\times10^{-4}$ eV and $z_0 \approx 0.35$ nm is the separation between the polar substrate and graphene flake. $N_{SPP,\upsilon}$ is SPP phonon occupation number. The magnitude of the polarization field is given by the Fröhlich coupling constants, F^2_υ [46].
In Fig.16(a) and (b) the average of the l_{gr} vs n_{Vg}-n_0 curves measured on different tip positions on DG-SiC and DG-SiO_2 are fitted with the equivalent mean free path obtained by,

$$l_{gr\_eq}^{-1} = l_{gr\_ci}^{-1} + \sum_\upsilon l_{gr\_SPO,\upsilon}^{-1} \tag{8}$$

The characteristic SPP frequencies and the corresponding Fröhlich coupling constants for SiO_2 and 4H-SiC substrate are listed in Table 1 .

	SiO_2	4H-SiC
$\hbar\omega_{SO1}$ (meV)	58.9	116.0
$\hbar\omega_{SO2}$ (meV)	156.4	-
F^2_1 (meV)	0.237	0.735
F^2_2 (meV)	1.612	-

Table 1. Characteristic surface polar phonons frequencies and corresponding Fröhlich coupling constants for SiO_2 and 4H-SiC substrate.

The only fitting-parameter is N_{ci}. The charged-impurity density limiting the mean free path was found to be ~7×10^{10} cm^{-2} for DG-SiC, and ~1.8×10^{11} cm^{-2} for DG-SiO_2 [43]. The calculated l_{SPP} and l_{ci} versus n_{Vg}-n_0 curves are also reported in both cases. It is worth noting that l_{SPP} for DG-SiC is more than five times l_{SPP} for DG-SiO_2. As a result, scattering by charged impurities is the limiting scattering mechanism in DG-SiC (see Fig.16(a)), whereas a significant contribution is played by scattering with SPP in the case of DG-SiO_2, especially at higher carrier densities (see Fig. 16(b)).

3.3 Electronic properties of the graphene/4H-SiC(0001) interface.

As shown in Fig.15(a), the interface between epitaxial graphene and 4H-SiC (0001) strongly affects the overall electronic and transport properties of the 2DEG in EG.
Both experimental and theoretical studies have shown that EG synthesis on the (0001) face of SiC, occurs through a series of complex surface reconstructions [47]. This starts from an

initial (Si-rich) $(\sqrt{3}\times\sqrt{3})R30°$ phase which rapidly converts into a second (C-rich) $(6\sqrt{3}\times6\sqrt{3})R30°$ reconstruction when the temperature increases. This layer may be more or less defective with more or less dangling bonds at the interface with the Si face. Angle resolved photoemission spectroscopy (ARPES) measurements indicate that its electronic structure is not that of graphene single layer, i.e. no linear dispersion is observed. This layer is simply an intermediate (buried) buffer layer (zero layer, ZL) with a large percentage of sp^2 hybridization. The first graphene layer which forms on the ZL (see schematic in Fig.17(a)) exhibits, instead, a linear dispersion relation. The presence of the ZL makes EG n-type doped and causes an overall degradation of the carrier mobility.

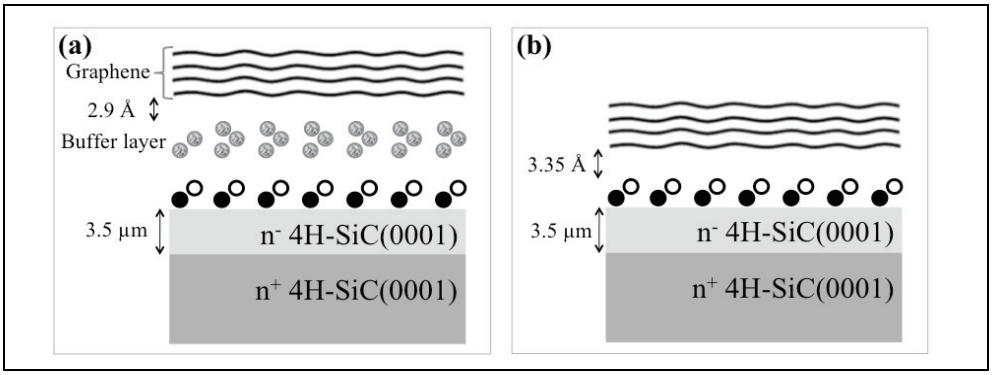

Fig. 17. Schematic representation of the interface between epitaxial graphene grown 4H-SiC (0001) and the substrate (a) and of the deposited graphene/4H-SiC (0001) interface (b).

Recently, the properties of the interface between EG and the zero layer have been investigated with nanoscale lateral resolution and compared with those of graphene mechanically exfoliated from HOPG and deposited on 4H-SiC (0001) [48].

In fact, in the case of deposited graphene (DG) no zero layer is present at the interface. EG was grown on n^+-doped (0001) 4*H*-SiC substrate, 8° off axis, with a weakly doped *n*-epitaxial layer on top, in an inductively heated reactor at a temperature of 2000 °C and under 1 atm Ar pressure [29]. A piece of the same 4*H*-SiC wafer (not subjected to annealing) was used as the substrate for DG. This local investigation has been performed by measuring the current flowing across the interface using torsion resonance conductive atomic force microscopy (TR-CAFM) and scanning current spectroscopy (SCS).

TR-CAFM (see schematic in Fig.18(a)) is a dynamic scanning probe method which allows nondestructive electrical measurements from a conductive tip oscillating in a torsional or twisting mode in close proximity to the sample surface (0.3–3 nm). When a bias is applied between the tip and the sample backside, a map of the current flowing from the tip to sample surface is acquired. This noncontact method has a distinct advantage over the conventional conductive atomic force microscopy performed in contact mode because of the absence of shear forces that can damage the graphene sheets. Commercially available Si n^+-doped probes with platinum (Pt) coating were used, with a typical radius of the apex of 10–20 nm. TR-CAFM was used to measure, simultaneously, topographic and current maps on the sample surface. Fig.18(b) shows a TR-CAFM current map taken on DG at tip bias of 1 V. The brighter portions in the current map (region carrying a higher current) correspond to graphene. After identifying the SiC regions coated with DG, local *I-V* measurements were

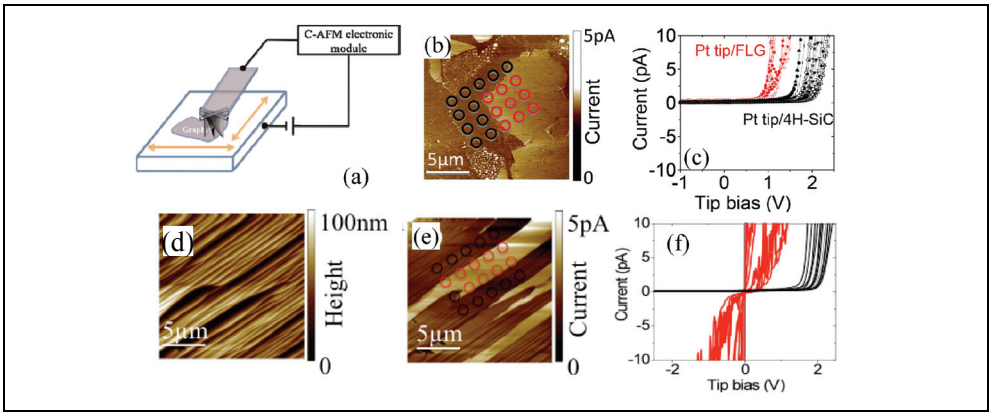

Fig. 18. Schematic representation of the Torsion Resonant–Conductive Atomic Force Microscopy (TR-CAFM) setup (a). TR-CAFM current map taken at tip bias of 1 V on deposited graphene on SiC (b). The brighter portions in the current map (region carrying a higher current) correspond to graphene coated regions. Local *I-V* curves measured on the indicated tip positions (c). TR-CAFM morphology (d) and current (e) maps collected on EG on SiC. The investigated sample region is only partially covered with a single layer of epitaxial graphene. Local *I-V* characteristics collected in the same sample region (f). (Data from Ref. [48]).

carried out by scanning current spectroscopy (SCS). In SCS the conductive tip is placed in contact on a discrete array of positions on the sample surface non invasively, lifting the tip by 20 nm at every interval. A swift transition between TR-CAFM and SCS is possible without altering the sample position. The representative positions of the tip during the SCS scan are depicted in Fig.18(b) and the recorded *I-V* curves are shown in Fig.18(c). All *I-V* curves exhibit a rectifying behavior, with a low leakage current under reverse bias and a sudden increase in the current for positive bias higher than a threshold voltage. It is worth noting that the acquired curves can be divided in two groups, which correspond to the tip positions on DG and bare SiC substrate. It is clear that DG forms a Schottky contact on top of the 4*H*-SiC layer.
Based on these results on DG, TR-CAFM was used to get local information on the graphene coverage on EG. Fig.18(e) shows a typical TR-CAFM current map along with the morphology collected on EG (Fig.18(d)). By comparing the morphology and current maps, brighter regions in the current map appear evident, corresponding to areas covered by a few MLs of graphene. The *I-V* characteristics collected by SCS in the same sample region are reported in Fig.18(f).
Similarly to the sample with DG, the *I-V* curves on the sample with EG can be divided into two distinct families: the curves acquired on an area covered with graphene and those acquired on an area free of graphene. The *I-V* characteristics on the graphene-free regions remained similar to those measured on the bare 4*H*-SiC surface in the sample not subjected to thermal treatment (see Fig.18(c)). The curves obtained on the regions coated with EG show completely different *I-V* characteristics. The leakage current is now very large with, in some cases, a clear Ohmic behavior. This is a direct evidence that the Schottky barrier height (SBH) at the EG/4*H*-SiC interface has been reduced with respect to DG/4*H*-SiC with, in some cases, a possibility of direct tunnel injection.
These SBH values have been evaluated for each of the *I-V* curves in Figs.18 (c) and (f), using the procedure of Refs. [49,50].
The histograms of the corresponding values have been reported in Figs.19(a) and (b), respectively. While the SBHs for Pt-tip/4*H*-SiC remain similar for both samples, the average

SBH value for EG on 4*H*-SiC appears very much reduced (Φ_{EG}=0.36±0.1 eV) with respect to DG (Φ_{DG}=0.85±0.06 eV). This fact is especially interesting considering that the SBHs on positions uncovered with graphene remain similar. The SBH difference must then be explained in terms of the band diagrams schematically drawn in Figs.19(c) and (d). Here, E_C is the energy of the conduction band edge, E_F is the Fermi energy at the bulk 4*H*-SiC, $E_{F,DG}$ is the Fermi energy of DG, and $E_{F,EG}$ the Fermi energy of EG. Due to the weak (van der Waals-like) interaction with the substrate, DG can be considered neutral (or close to neutral) in the absence of external bias. In this case, $E_{F,gr}$ should (more or less) coincide with the Dirac point energy (E_{Dirac}). Hence, in the first approximation, the SBH between DG and the *n*-type 4*H*-SiC epilayer should be given by the difference between the neutral graphene work function (W_{gr}≈4.5 eV) and the 4*H*-SiC electron affinity ($\chi_{4H\text{-}SiC}$≈3.7 eV). The value of Φ_{DG} is in good agreement with the value predicted by the simple model, i.e. 0.8 eV. The SBH in the case of EG can be explained in terms of a pinning of $E_{F,EG}$ at an average value ΔE_F≈0.49 eV higher than $E_{F,DG}$, as shown in Fig.19(d). This pinning is a direct evidence of the presence of positively charged states located at the interface between the Si face of 4*H*-SiC and the zero layer. The spread of SBH values for EG/4*H*-SiC is an evidence of a non uniform density of the interface states.

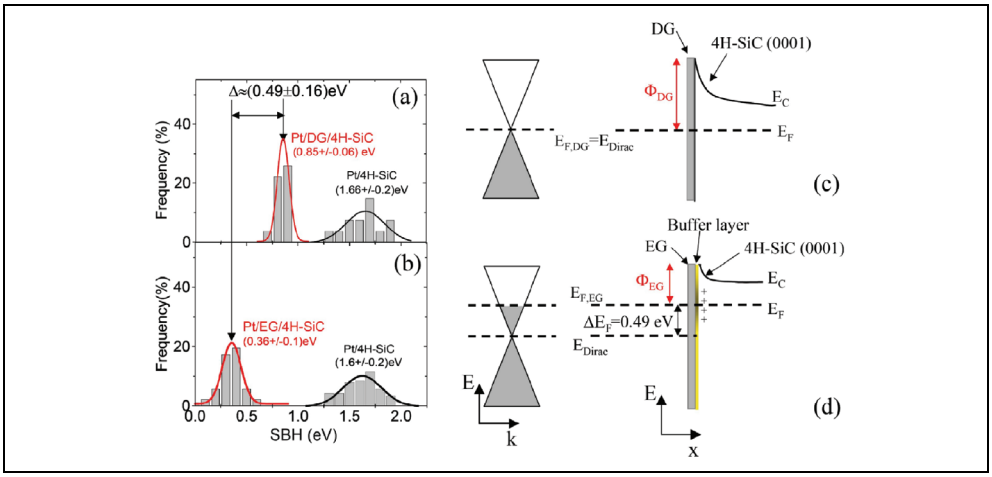

Fig. 19. Histograms of the local Schottky barrier height at DG/4H-SiC (a) and at EG/4H-SiC (b). The SBH difference is explained in terms of the band diagrams schematically drawn in (c) and (d). (Data from Ref. [48]).

3. Summary

After discussing two of the main graphene synthesis routes (mechanichal exfoliation of HOPG and thermal decomposition of SiC), the local characterization of graphene electronic properties by recently demonstrated scanning probe microscopy techniques has been presented. In particular, the lateral inhomogeneity of the electron mean free path has been determined, in relation to the graphene/subtrate interface and to the substrate dielectric properties. The peculiar electrical properties of epitaxial graphene/4H-SiC (0001) interface have been discussed.

The results of these measurements will allow to explain some peculiar aspects of the electrical behavior of macroscopic devices fabricated on graphene.

4. Acknowledgment

This work has been supported, in part, by the European Science Foundation (ESF) under the EUROCORE program EuroGRAPHENE, within GRAPHIC-RF coordinated project.

5. References

[1] Novoselov, K. S.; et al. (2004). Electric Field Effect in Atomically Thin Carbon Films. Science, Vol. 306, pp. 666.

[2] Andreoni, W., 2000, The Physics of Fullerene-Based and Fullerene-Related Materials (Springer, Berlin).

[3] Saito, R., G. Dresselhaus, and M. S. Dresselhaus, 1998, Physical Properties of Carbon Nanotubes, Imperial College Press, London.

[4] Charlier, J.-C.; Blase, X. & S. Roche. (2007). *Rev. Mod. Phys.* Vol. 79, pp. 677.

[5] Novoselov, K. S.; Geim, A. K.; Morozov, S. V.; Jiang, D.; Zhang, Y.; Katsnelson, M. I.; Grigorieva, I. V.; Dubonos, S. V. & A. A. Firsov. (2005). Two-dimensional gas of massless Dirac fermions in graphene, *Nature* Vol. 438, pp. 197– 200.

[6] Zhang, Y.; Tan, Y.-W.; Stormer, H. L. & P. Kim. (2005). Experimental observation of the quantum hall effect and Berry's phase in graphene, *Nature* Vol. 438, pp. 201–204.

[7] Novoselov, K. S.; Jiang, Z.; Zhang, Y.; Morozov, S. V.; Stormer, H. L.; Zeitler, U.; Maan, J. C.; Boebinger, G. S.; Kim, P.; and & Geim, A. K. (2007). Room-Temperature Quantum Hall Effect in Graphene. *Science* Vol. 315, pp. 1379–.

[8] Lin, Y.-M.; Dimitrakopoulos, C.; Jenkins, K. A.; Farmer, D. B.; Chiu, H.-Y.; Grill, A.; Avouris, Ph. (2010). 100-GHz Transistors from Wafer-Scale Epitaxial Graphene. Science, Vol. 327, pp. 662.

[9] Wang, X.; Zhi, L.; Tsao, N.; Tomovic, Z.; Li, J.; Mullen, K. (2008). Transparent Carbon Films as Electrodes in Organic Solar Cells. *Angew. Chem.,* Vol. 120, pp. 3032-3034.

[10] Elias, D. C.; Nair, R. R.; Mohiuddin, T. M. G.; Morozov, S. V.; Blake, P.; Halsall, M. P.; Ferrari, A. C.; Boukhvalov, D. W.; Katsnelson, M. I.; Geim, A. K.; Novoselov, K. S. (2009). Control of Graphene's Properties by Reversible Hydrogenation: Evidence for Graphane. Science, Vol. 323, pp. 610-613.

[11] Ni, Z. H.; Yu, T.; Lu, Y. H.; Wang, Y. Y.; Feng, Y. P.; & Shen, Z. X. (2008). Uniaxial Strain on Graphene: Raman Spectroscopy Study and Band-Gap Opening, *ACS Nano*, Vol. 2, pp. 2301–2305.

[12] Zhang, Y.; Tang, T.-T.; Girit, C.; Hao, Z; Martin, M.C.; Zettl, A.; Crommie, M. F.; Shen, R. Y. & Wang, F. (2009). Direct observation of a widely tunable bandgap in bilayer graphene. *Nature Letters*, Vol. 459, pp.820-823.

[13] Rotenberg, E.; Bostwick, A.; Ohta, T.; McChesney, J. L.; Seyller, T. & Horn, K. (2008). Origin of the energy bandgap in epitaxial graphene, Nature Materials, Vol. 7, pp. 258 – 259.

[14] Han, M. Y. ; Ozyilmaz, B.; Zhang, Y.; Kim, P. (2007). Energy Band-Gap Engineering of Graphene Nanoribbons. *Phys. Rev. Lett.* 98, 206805.

[15] Wang, X.; Li, X.; Zhang, L.; Yoon, Y.; Weber, P. K.; Wang, H. & Dai, H. (2009). N-Doping of Graphene Through Electrothermal Reactions with Ammonia. *Science*, Vol. 324, pp. 768-771.

[16] Lee, E. J. H.; Balusubramanian, K.; Weitz, R. T.; Burghard, M. & Kern, K. (2008). Contact and edge effects in graphene devices. *Nat. Nanotechnol.* Vol. 3, pp. 486-490.

[17] Casiraghi, C.; Pisana, S.; Novoselov, K. S.; Geim, A. K.; & Ferrari, A. C. (2007). Raman fingerprint of charged impurities in graphene. *Appl. Phys. Lett.* Vol. 91, 233108.

[18] Martin, J.; Akerman, N.; Ulbricht, G.; Lohmann, T.; Smet, J.; Klitzing, K. V. & Yacoby, A. (2008). Observation of electron–hole puddles in graphene using a scanning single-electron transistor. *Nature Phys.* Vol. 4, pp. 144-148.

[19] Zhang, Y.; Brar, V. W.; Girit, C.; Zett, A.; Crommie, M. F. (2009). Origin of spatial charge inhomogeneity in graphene. *Nature Phys.* Vol. 5, pp. 722-726.

[20] Hernandez, Y.; Nicolosi, V.; Lotya, M.; Blighe, F. M.; Sun, Z.; De, S.; McGovern, I. T.; Holland, B.; Byrne, M.; Gun'Ko, Y. K.; Boland, J. J.; Niraj, P.; Duesberg, G.; Krishnamurthy, S.; Goodhue, R.; Hutchison, J.; Scardaci, V.; Ferrari, A. C. & Coleman, J. N. (2008). High-yield production of graphene by liquid-phase exfoliation of graphite, Nature Nanotechnology, *Vol.* 3, pp. 563 - 568.

[21] Li, X.; et al. (2009). Large-Area Synthesis of High-Quality and Uniform Graphene Films on Copper Foils. *Science,* Vol. 324, pp. 1312.

[22] Lee, Y.; Bae, S.; Jang, H.; Jang, S.; Zhu, S.-E.; Sim, S. H.; Il Song, Y.; Hong, B. H.; Ahn, J.-H. (2010). Wafer-Scale Synthesis and Transfer of Graphene Films, *Nano Lett.* Vol. 10, pp. 490.

[23] Berger, C.; Song, Z.; Li, X.; Wu, X.; Brown, N.; Naud, C.; Mayou, D.; Li, T.; Hass, J.; Marchenkov, A. N.; Conrad, E. H.; First, P. N. & de Heer, W. A. (2006). Electronic Confinement and Coherence in Patterned Epitaxial Graphene, *Science* Vol. 312, pp. 1191.

[24] Giannazzo, F.; Sonde, S.; Raineri, V.; Patanè, G.; Compagnini, G.; Aliotta, F.; Ponterio, R.; & Rimini, E. (2010). Optical, morphological and spectroscopic characterization of graphene on SiO_2, *Phys. Status Solidi* C Vol. 7, pp. 1251.

[25] Ferrari, A. C.; Meyer, J. C.; Scardaci, V.; Casiraghi, C.; Lazzeri, M.; Mauri, F.; Piscanec, S.; Jiang, D.; Novoselov, K. S.; Roth, S.; & A. K. Geim. Raman Spectrum of Graphene and Graphene Layers, (2006). *Phys. Rev. Lett.* Vol. 97, pp. 187401

[26] Blake, P.; Hill, E. W.; Castro Neto, A. H.; Novoselov, K. S.; Jiang, D.; Yang, R.; Booth, T. J.; & Geim, A. K. (2007). Making graphene visible, Appl. Phys. Lett. Vol. 91, pp. 063124.

[27] Nair, R. R.; Blake, P.; Grigorenko, A. N.; Novoselov, K. S.; Booth, T. J.; Stauber, T.; Peres, N. M. R.; Geim, A. K. (2008). Fine Structure Constant Defines Visual Transparency of Graphene. *Science* Vol. 320, 1308.

[28] Emtsev, K. V.; Bostwick, A.; Horn, K.; Jobst, J.; Kellogg, G. L.; Ley, L.; McChesney, J. L.; Ohta, T.; Reshanov, S. A.; Rohrl, J.; Rotenberg, E.; Schmid, A. K.; Waldmann, D.; Weber, H. B.; & Seyller, T. (2009). Towards wafer-size graphene layers by atmospheric pressure graphitization of SiC(0001). *Nature Materials.* Vol. 8, pp. 203.

[29] Virojanadara, C.; Syvajarvi, M.; Yakimova, R.; Johansson, L.; Zakharov, I. & T. Balasubramanian. (2008). Homogeneous large-area graphene layer growth on 6H - SiC(0001). *Phys. Rev. B* Vol. 78, 245403.

[30] Bolen, M. L.; Harrison, S. E.; Biedermann, L. B.; & Capano, M. A. (2009). Graphene formation mechanisms on 4*H*-SiC(0001). *Phys. Rev. B* Vol. 80, pp. 115433.

[31] Vecchio, C.; Giannazzo, F.; Sonde, S. ; Bongiorno, C. ; Rambach, M.; Yakimova, R.; Rimini, E.; Raineri, V. (2010). Nanoscale structural characterization of epitaxial graphene grown on off-axis 4H-SiC (0001). *Nanoscale Research Letters*, in press.

[32] Prakash, G.; Capano, M. A.; Bolen, M. L.; Zemlyanov, D.; Reifenberger, R. G. (2010). AFM study of ridges in few-layer epitaxial graphene grown on the carbon-face of 4H–SiC (000-1). *Carbon.* Vol. 48, pp. 2383-2393.

[33] Sun, G. F.; Jia, J. F.; Xue, Q. K. & Li, L. (2009). Atomic-scale imaging and manipulation of ridges on epitaxial graphene on 6H-SiC(0001). *Nanotechnology*, Vol. 20, pp. 355701.

[34] Chen, J.H.; Jang, C.; Xiao, S.; Ishigami, M. & Fuhrer, M.S. (2008). Intrinsic and extrinsic performance limits of graphene devices on SiO_2. *Nature Nanotechnology,* Vol. 3, pp. 206-209.

[35] Bolotin, K. I.; Sikes, K. J.; Jiang, Z.; Klima, M.; Fudenberg, G.; Hone, J.; Kim P. & Stormer, H. L. (2008). Ultrahigh electron mobility in suspended graphene. *Solid State Commun.* Vol. 146, pp. 351-355.

[36] Hwang, E. H.; Adam, S.; & Das Sarma, S. (2007). Carrier Transport in Two-Dimensional Graphene Layers. *Phys. Rev. Lett.* Vol. 98, pp. 186806.

[37] Fratini, S.; & Guinea, F. (2008). Substrate-limited electron dynamics in graphene. *Phys. Rev. B* Vol. 77, pp. 195415.

[38] Giannazzo, F.; Sonde, S.; Raineri, V.; & Rimini, E. (2009). Irradiation damage in graphene on SiO_2 probed by local mobility measurements, *Appl. Phys. Lett.* Vol. 95, pp. 263109.

[39] Giannazzo, F.; Sonde, S.; Rimini, E. & Raineri, V. (2010). Lateral homogeneity of the electronic properties in pristine and ion irradiated graphene probed by scanning capacitance spectroscopy, *Nanoscale Research Letters*, in press.

[40] Giannazzo, F., Sonde, S., Raineri, V., & Rimini, E. (2009). Screening Length and Quantum Capacitance in Graphene by Scanning Probe Microscopy. *Nano Letters* Vol. 9, pp. 23

[41] Sonde, S.; Giannazzo, F.; Raineri, V.; & Rimini, E. (2009). Dielectric thickness dependence of capacitive behavior in graphene deposited on silicon dioxide. *J. Vac. Sci. Technol. B*. Vol. 27, pp. 868

[42] Rutter, G. M.; Crain, J. N.; Guisinger, N. P.; Li, T.; First, P. N.; & Stroscio, J. A. (2007). Scattering and Interference in Epitaxial Graphene. *Science* .Vol. 317, 219-222.

[43] Sonde, S.; Giannazzo, F.; Vecchio, C.; Yakimova, R.; Rimini, E.; & Raineri, V. (2010). Role of graphene/substrate interface on the local transport properties of the two-dimensional electron gas, *Appl. Phys. Lett.* Vol. 97, pp. 132101

[44] Stauber, T.; Peres, N. M. R.; & Guinea, F. (2007). Electronic transport in graphene: A semiclassical approach including midgap states, *Phys. Rev. B* Vol. 76, pp. 205423

[45] Perebeinos, V.; & Avouris, Ph. (2010). Inelastic scattering and current saturation in graphene, *Phys. Rev. B* Vol. 81, pp. 195442.

[46] Wang, S. Q.; & Mahan, G. D. (1972). Electron Scattering from Surface Excitations. *Phys. Rev. B*. Vol. 6, pp. 4517-4524.

[47] Emtsev, K. V.; Speck, F.; Seyller, Th.; Ley, L.; Riley, J. D. (2008). Interaction, growth, and ordering of epitaxial graphene on SiC{0001} surfaces: A comparative photoelectron spectroscopy study. *Phys. Rev. B* Vol. 77, pp. 155303.

[48] Sonde, S.; Giannazzo, F.; Raineri, V.; Yakimova, R.; Huntzinger, J.-R.; Tiberj, A. & Camassel, J. (2009). Electrical properties of the graphene/4H-SiC (0001) interface probed by scanning current spectroscopy, *Phys. Rev. B* Vol. 80, pp. 241406(R).

[49] Giannazzo, F.; Roccaforte, F.; Raineri, V. & Liotta, S. F. (2006). Transport localization in heterogeneous Schottky barriers of quantum-defined metal films, *EuroPhysics Letters* Vol. 74, pp. 686.

[50] Giannazzo, F.; Roccaforte, F.; Iucolano, F.; Raineri, V.; Ruffino, F. & Grimaldi, M. G. (2009). Nanoscale current transport through Schottky contacts on wide bandgap semiconductors, *J. Vac. Sci. Technol.* B 27, pp. 789.

15

Scanning Transmission Electron Microscopy and Spectroscopy of Suspended Graphene

Ursel Bangert[1], Mhairi Gass[2], Recep Zan[1] and Cheng Ta Pan[1]
[1]*The University of Manchester,*
[2]*SuperSTEM Laboratories, CCLRC Daresbury Laboratory,*
UK

1. Introduction

Transmission electron microscopy is the only technique by which freely suspended graphene can be scrutinised for nano-scale topography and chemistry occurring in micromechanically exfoliated graphene or having been introduced by production methods, e.g., by growth on Ni-subtsrates, or as a result of functionalistaion, e.g., upon hydrogenation. Investigations on this scale require atomic resolution, which can be catered for by electron microscopy; indeed several impressive studies have been conducted. In this chapter we summarise reports on scanning transmission electron microscopy and spectroscopy investigations, conducted with aberration corrected probes, especially recent results of atomic resolution high angle dark field microscopy, by which chemical information about atoms in graphene that are heavier then carbon can be obtained. By combining this with ultra-high spatially resolved electron energy loss spectroscopy to reveal the nature of elements, particularly those with lower atomic number (e.g., boron and hydrogen), which do not show up in high angle dark field images, one obtains an invaluable and powerful tool for graphene reserach; added to this is the information about the electronic bandstructure that can be obtained on a highly spatially resolved scale through monitoring the plasmon behaviour of graphene.

Paragraph 2 briefly describes the scanning transmission electron microscopy (STEM) technique employed for imaging and chemical analysis, and how free-standing membranes of graphene, required for these measurements, are obtained. Paragraph 3 deals with high resolution imaging of the atomic structure and configuration of intrinsic defects and paragraph 4 with stabilisation issues of single and bi-layer membranes: rippling effects in the graphene lattice are revealed. In free-standing CVD-grown graphene the membranes are an intricate patchwork of mono- and bi-layers, the latter being AB stacked or rotated at various angles to each other. In paragraph 5 atomic resolution HAADF and ultra-high spatially resolved electron energy loss spectroscopy are used to identify atomic sites and chemical nature of metal impurity atoms Au, Ni and Fe, as well as of B, intentionally introduced into graphene as electronic dopant via ion implantation. It is highly desirable to be able to reveal the presence and distribution of hydrogen in order to assess the success of H-dosing for the purpose of bandgap tailoring; we investigate the applicability of energy loss spectrum imaging for this purpose. Paragraph 6 scrutinises plasmon characteristics of graphene. Plasmon behaviour is sensitive to electron densities and electronic structure of

solids; the graphitic σ-plasmon undergoes typical changes in few-layer structures and provides an unambiguous fingerprint for single layer graphene, whilst the graphitic π-plasmon can give valuable information about changes in the π-electron system upon doping and dosing. In combination with DFT calculations we test the scope of plasmon spectroscopy in assessing, especially, H-induced graphene morphologies.

2. Microscopy methods and TEM sample preparation techniques

2.1 Microscopy methods

Electron microscopy studies of graphene so far have been conducted in a transmission electron microscope (TEM), using a stationary electron beam. Here we use an aberration corrected (AC) transmission electron microscope (STEM) (Goodhew & Bleloch, 2003) with a cold field emission gun and added, analytical facilities. In a STEM a focussed electron probe is scanned in a pixelated raster over a pre-defined sample area. The benefits of this microscope are the very bright (100 pA) and very fine (≤0.1 nm diameter) probe, which, due to the small depth of focus (8nm) provides an image- (pixel-) resolution of better then 0.1 nm, allowing atomic-scale imaging to be carried out in bright field (BF) and, very importantly, in high angle annular dark field (HAADF) mode. A further benefit is the variable operating voltage from 100 down to 60 kV, ensuring measurements below the displacement threshold of C (at ~80 keV).

In BF mode electrons from the central diffraction disk are collected over an angular range of 0-6 mrad. Diffraction disks (rather then spots) are formed because of the high beam convergence angle (~24 mrad). The occurrence of atomic lattice images at high resolution arises from coherence (phase) effects in overlapping diffraction disks. In HAADF mode electrons scattered to high angles are collected in an annular detector with an angular range of 70-210 mrad. These electrons have undergone incoherent elastic scattering (Rutherford scattering), the strength (or probability) of which is approximately proportional to the square of the atomic number of the scattering element (Z-contrast), and therefore this imaging method can be used for chemical identification (Pennycook & Boatner, 1988). At high magnifications, due to the fine probe and employing sub-Å scan point separation, individual atoms can be 'lined-out', giving rise to atomic resolution HAADF images. Such images can be interpreted rather straight forwardly and much more easily than BF phase contrast images.

Chemical/elemental analysis using electron energy loss spectroscopy (EELS) (Brydson, 2003; Egerton, 1986) can be conducted with high sensitivity at the same spatial resolution as obtained in images. Inelastic scattering events can be detected with collection angles of up to 19 mrad over an energy range of 0-2000 eV, covering energy losses from valence band to K-shell core loss excitations of elements spanning the periodic table from H to noble metals (using an 'Enfina' energy loss spectrometer). The combination of the ~0.3 eV energy resolution and energy dispersions of up to 0.01 eV/channel provides access to absorption events in the 1 eV loss regime, thus enabling electronic bandstructure studies. Energy loss spectra can be obtained as individual spectra in single locations on the sample or as collective data sets along predefined lines (line scans) or in predefined image areas (spectrum images (Hunt & Williams, 1991)). The small probe size enables EELS to be carried out even on single atoms (Browning & Pennycook 1994). Image acquisition and processing as well as EELS measurements and evaluation were conducted with the Gatan Digital Micrograph software and its various 'plug-ins'; data analysis using special programs is described in the respective paragraphs.

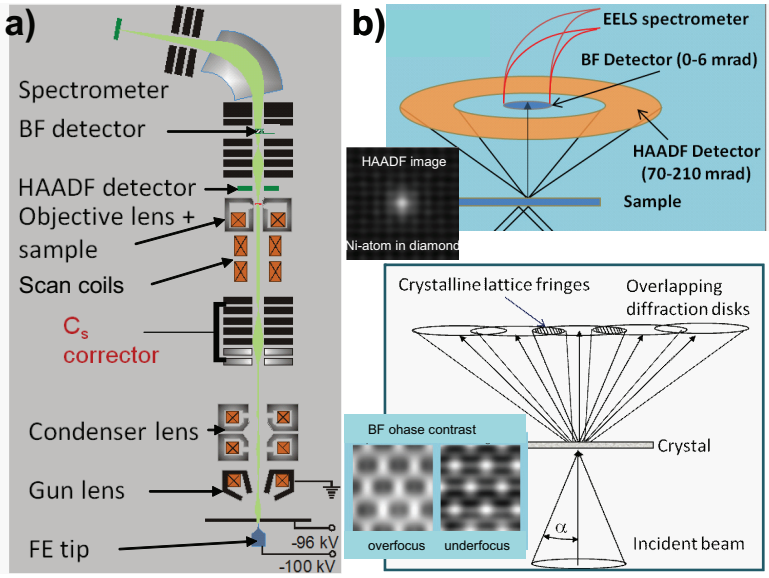

Fig. 1. a) Schematics of the STEM, b) enlarged detail of detector configuration with schematic HAADF image inset (top panel) and schematics of origin of phase contrast on the BF detector with inset showing lattice images in overfocus and underfocus (bottom panel).

The Daresbury SuperSTEMs (the UK's first aberration corrected STEMs) were used for STEM imaging and analysis. TEM results, which are also presented in this chapter, were obtained with a Tecnai F30.

2.2 TEM sample preparation

There are several methods to acquire suspended graphene layers, initially such layers were obtained by micro-mechanical cleaving and exfoliation (Booth et al, 2008). After repeated cleaving of graphite by using adhesive tape, thin flakes are transferred to an oxidised Si wafer on which few-layer graphene flakes can be identified by their colour using a light microscope. Selected flakes are then made to adhere to a TEM sample grid; this is facilitated by using, e.g., sticky grids (Quantifoil), and employing the surface tension of a drop of evaporating IPA, dripped onto the graphene flakes.

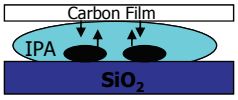

Another frequently used method employs embedding of graphene flakes in PMMA or CAB (Cellulose Acetate Butyrate) for protection, and subsequent lift off the substrate (e.g., by etching the substrate), and floating the PMMA (or CBA) containing the graphene flakes off. The details of this procedure can vary; the steps outlined in the sketch below entail for example applying a sticky tape (blue) with a window (step 2) to make a 'frame' for easier handling of the PMMA/graphene film during the transfer to the TEM grid. This sticky tape is later removed by scribing the PMMA around the target area (step 5)

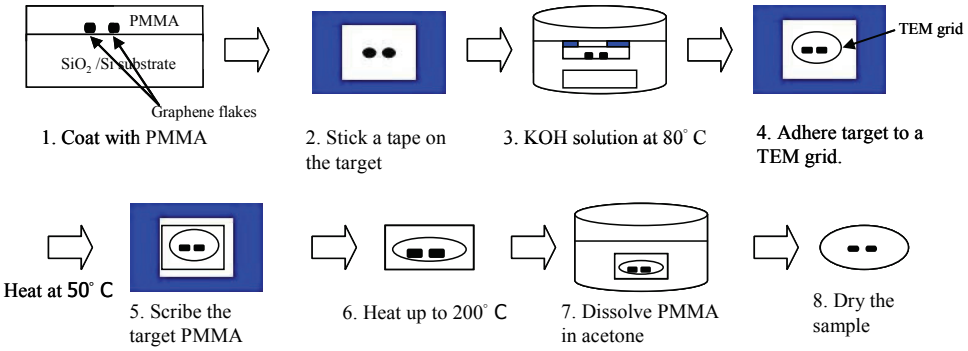

Figure 2a) shows an optical micrograph of graphene flakes obtained by micromechanical cleaving and deposition across a crack (induced by cleaving) in an oxidised Si wafer. The darkish blue graphene areas are identified as single or bi-layers. The graphene is freely suspended, where it lies across the gap and hence could be directly imaged in a TEM using the Si as sample support. Figures 2b-d are TEM BF images of the suspended flake at increasing magnification. Figure 2c shows that the graphene surface has significant contamination; 2d) shows the atomic lattice in an uncontaminated patch. Figure 2e) is a HAADF STEM image at low magnification with contamination, most likely hydrocarbon deposits, presenting them selves as whitish contrast. These deposits are interrupted by dark patches, representing uncontaminated parts of single layers. In the following paragraph it is the atomic scale topography of uncontaminated patches that we will concern ourselves with. Figures 2e&f are views at increased magnification. Figure 2g), although noisy, as it represents scattering of one single atomic layer, shows the graphene lattice. Much of the work in the following paragraphs will focus on HAADF studies, which we have carried out in the SuperSTEM; a number of papers have dealt with transmission electron microscopy (TEM) of graphene (Meyer et. al., 2007a; Meyer et. al., 2008a; Meyer et. al., 2008b) however HAADF studies have not been amongst these.

3. Atomic scale topography: defects and ad-atoms

3.1 Defects

In the case of graphene with the electron beam focussed onto the sheet, the rare occasions occurs, where electron microscopy lattice images can be seen as a direct depiction of the ball-and-stick model of an atomic lattice structure. These images are directly interpretable: bright contrast corresponds to atoms and dark contrast to the gaps in between. Effects of atomic structure extending in direction of the electron beam, resulting in de-channelling of the beam on atomic columns and hence inducing contrast changes etc, cannot occur in mono-layer structures. Moreover, the atomic arrangements of atomic-scale defects can be straight forwardly deduced. HAADF can furthermore reveal the atomic nature of species at single-atom level through the approximate Z^2-dependence of the scattering probability. It is thus feasible for detection of atom species on/in graphene of Z equal to and larger then carbon. Graphene has provided the basis for elegant theoretical calculations and predictions of defect structures alongside their effects on the physical, chemical and electronic properties (Duplock, Scheffer & Lindan, 2004; Crespi, Scheffler & Rubio, 1997; Charlier, 2002). Structural observations on suspended graphene, on the other hand, are still relatively scarce, and, as

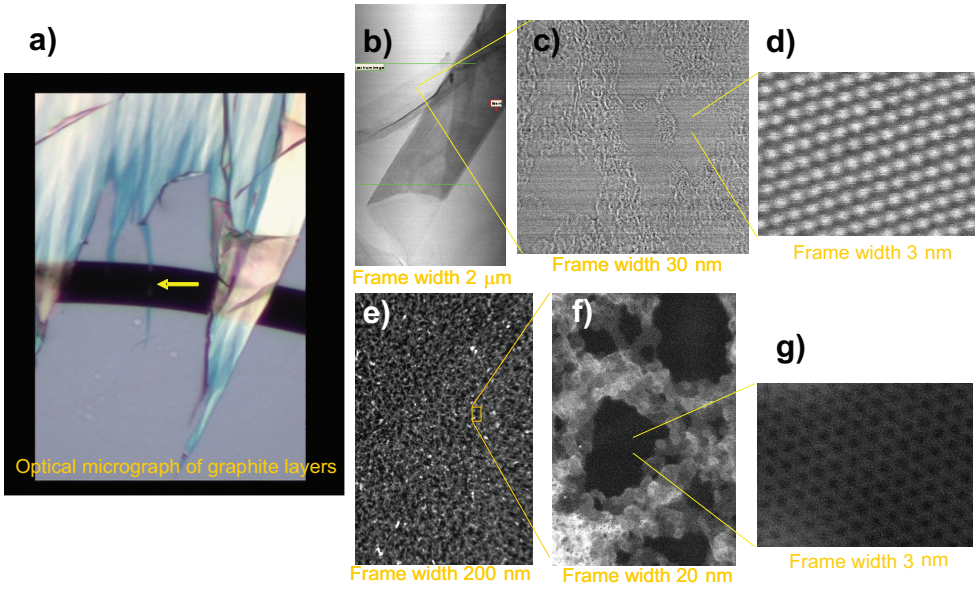

Fig. 2. a) optical micrograph of graphene flake deposited across a gap in an oxidised Si-wafer, b), c) and d) BF TEM images and e), f) and g) HAADF STEM images of the flake at increasing magnification.

noted earlier, HAADF studies are non-existent. Here we reveal directly atomic scale topological features of free standing graphene.

Electron beam energies of 100 keV, used for some of the following studies are just around the displacement threshold for atoms in carbon structures. Hence it is difficult to judge, whether defects occurring during the first image scan are radiation induced, or whether they were already present. However, changes in the films occurring over multiple scans were carefully monitored (and captured in movies), and on the basis of this it appears that discernible changes took place only after ~2 minutes of repeated scanning, and that the defect numbers during the first few scans are very small and stay constant, with the defects well separated (although some movement / reconstruction was observed even between initial scans). It is of interest to follow in-situ defect formation in the STEM, captured in sequential scans, each scan lasting no longer then 10 s. Figure 3 shows the 1st, 17th, 18th and 19th image of a 20-images series of STEM high resolution BF images. Only in the later scans, after ~2 min irradiation, does e-beam defect formation become a distinctive feature. At that stage a large number of single point defects- seen here are vacancies- suddenly appears (fig. 3c, red circle). These aggregate to form larger clusters (fig. 3d, red circle) and, eventually, holes. We emphasise we are dealing with BF-phase contrast images; these are not as directly interpretable as their HAADF counterparts. Nevertheless, since the images here were taken at ~1nm overfocus, the centre of the 6-rings, and also vacancies, will appear darker then the atoms, similar to dark field images. The delay in the apparent setoff of the beam damage may indicate that a small number of defects are already present in graphene sheets, and almost all of these are single vacancies. However, this contradicts STM studies of graphene obtained by micro-cleavage, in which the authors were unable to detect one single vacancy

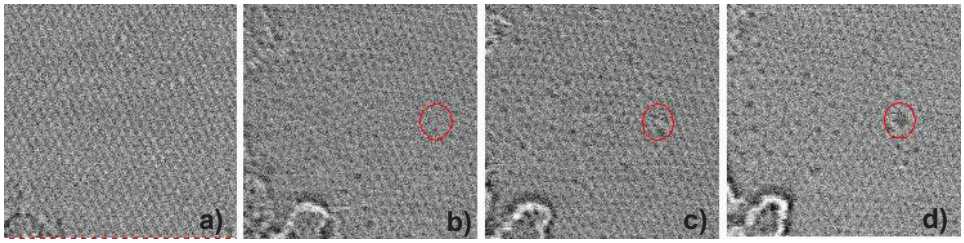

Fig. 3. Snapshots of a BF image series demonstrating development of radiation induced defects in the STEM. The darks spots are vacancy related defects. a) frame 1, b) frame 17 c) frame 18, d) frame 19; the scan time per frame was ~10 s.

(Stolyarova, 2007). Alternatively, the electron beam can radicalize molecules absorbed on the surface, which react with carbon leading to broken bonds.

Figure 4a) depicts a single-layer area imaged in HAADF. Although the lattice is visible in the raw HAADF images, it is feasible to reduce the noise by applying either a deconvolution routine based on maximum entropy image reconstruction (HREM Research Inc., 2009) or a low pass Fourier filtering method. The former sharpens features by deconvolving the images with a simulated electron probe function having a Gaussian or Lorentzian profile (or a combination of both), thus constituting a software C_s corrector, the latter improves visibility of spatial frequencies by applying a mask to the Fourier transformed (FFT) image, which includes the spatial frequencies right up to the lowest order *a*-plane diffraction spots, as well as the *a*-plane ([100], [010] and [-110]) reflections themselves (inset top left), and then obtaining the inverse Fourier transform (IFFT).

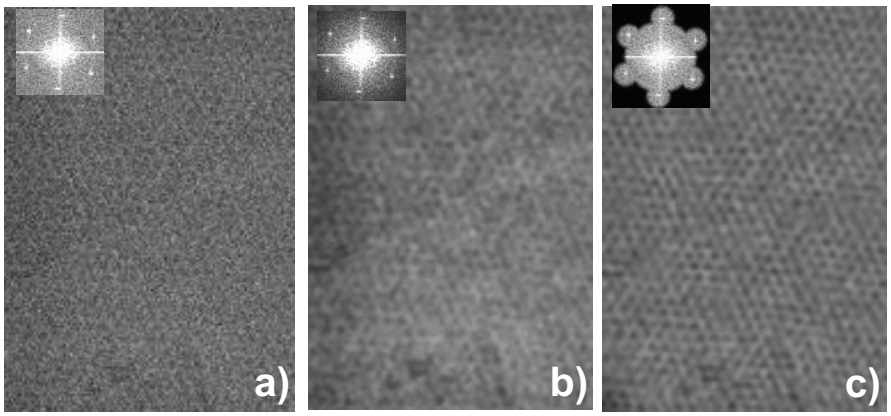

Fig. 4. a) raw HAADF image of single graphene sheet with FFT as inset, b) same HAADF image after deconvolution; the FFT in the inset is clearer as a result of noise reduction, c) IFFT of area in (a) having applied the band pass filter in the inset.

Noise reduction using deconvolution is shown in fig.4b. The low pass filter (fig.4c) achieves noise reduction by cutting out high frequencies; it preserves the information of all direct space distances larger then the a-lattice plane spacing and additionally superimposes a 'directional' component as frequencies between diffraction spots are masked out, thus enhancing the graphene lattice. In the following this latter filter is used. In order to

investigate possible artefacts introduced into the IFFT, i.e., into the end image, by the mask edges and the background noise, we subtracted a filtered Fourier transformed vacuum image from the filtered graphene Fourier space image, before we applied the inverse transform. However, this showed insignificant change in the case of this particular filter.
The vast majority of defects are vacancies. The HAADF lattice images in figures 5a and 5b are filtered in the described fashion, showing enlarged lattice structure surrounding a mono- and a di-vacancy with overlaid model structure (Gass et al., 2008). These are easy to discern, whereas Stone-Wales defects (Terrones & Terrones, 1996), constituting a reconfigured, rotated bond have not been identified so far.

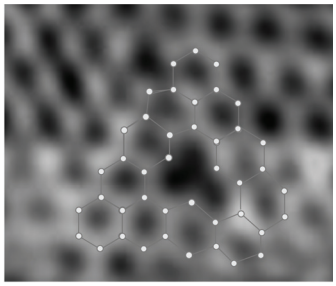

(a)

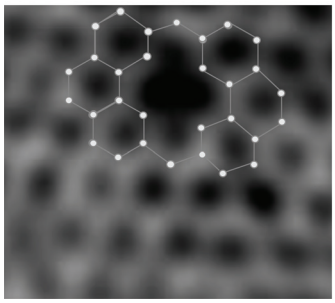

(b)

Fig. 5. a) and b): enlarged areas in HAADF images after low pass filtering showing a single vacancy and a di-vacancy with overlaid ball and stick models

There is a wealth of literature dealing with defects in HPO graphite [e.g. Hahn & Kang, 1999; Bourelle, Konno & Inagaki, 1999, Telling & Heggie 2007; Krasheninnikov et. al. 2001]. Isolated point defects on the surface of graphite are exlusively reported in connection with irradiation damage or ion bombardment, this might indicate that even the defects seen in the very first scan occur due to electron bombardment.
However, we also observe a second type of defect, related to the termination of a row of hexagons, and hence representing the 2-D or mono-layer equivalent of a dislocation (Gass et al., 2008). There are two species of unit c-axis edge dislocation in graphitic materials [Jenkins, 1969], depending on whether their glide plane cuts between atoms closely spaced in this direction or between atoms separated by a full bond length (defined as 'shuffle' and 'glide' plane respectively [Ewels, 2002]). After bond reconstruction, these two dislocation cores consist of either a pentagon-heptagon pair (5-7 defect, 'glide plane' dislocation core),

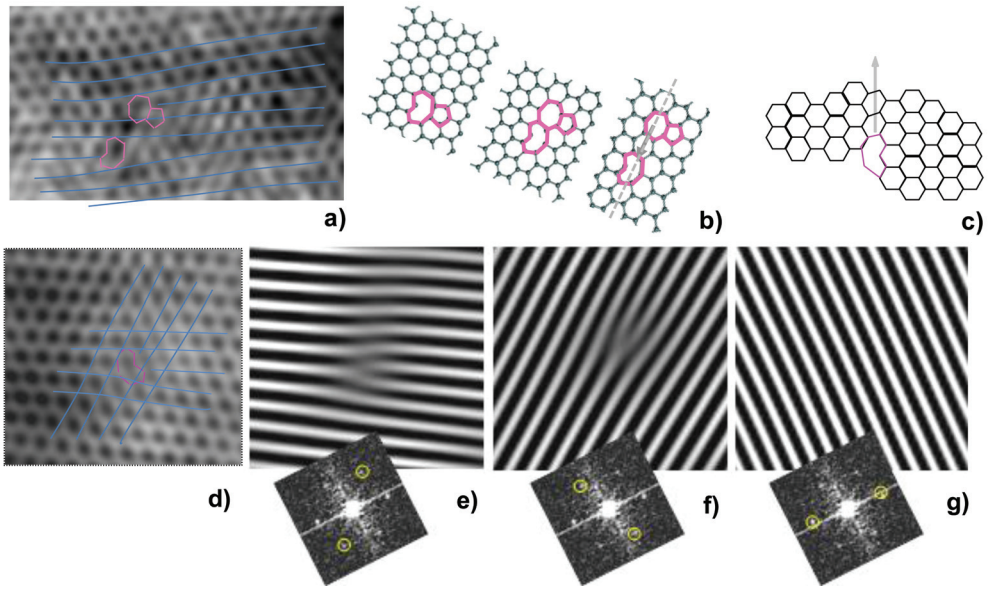

Fig. 6. a) HAADF image of dissociated shuffle-glide dipole (purple) with lattice 'planes' indicated in blue, b) model of an undissociated dipole (purple), formed by only one vacancy (leftmost panel), and subsequent separation into glide and shuffle defect via glide of the shuffle segment along the plane indicated by the dashed grey line (rightmost panel), c) formation of a shuffle defect by bond reconstruction at the edge of a graphene sheet; glide inwards along the grey arrow might be achieved by shear stress, leading as in (b) to the termination of a row of atoms, d) HAADF image of a single defect, which could have formed according to (c), e), f) and g) IFFTs obtained by masking the respective diffraction spots in the FFTs of (d), revealing termination of two different rows of atoms at the defect.

or a pentagon-heptagon pair with a 2-fold coordinated ad-atom carbon in the central bond ('shuffle' plane dislocation core; see figure 6b, e.g., 3rd schematic). These two dislocations were shown to migrate with radically different activation barriers, namely, 7.64eV for the glide core, 2.22eV for the shuffle core [Ewels, 2002]. This difference was explained in terms of the mechanism of motion. Motion occurs through a 90° rotation of a C-C bond along one side of the heptagon. For the glide dislocation core this requires breaking two C-C bonds, whereas in the shuffle dislocation core the same effect can be achieved through breaking and formation of just one bond. Thus the additional atom at the core of the shuffle dislocation is able to catalyse the motion of the dislocation [Ewels, 2002]. The glide dislocation core is essentially immobile. A single vacancy can be considered a dislocation dipole, with the two dislocations of opposite sign facing each other on neighbouring glide planes, as shown in fig. 6b (1st schematic). The 2nd and 3rd schematic in fig. 6b show dissociation of the dipole along the glide plane. The 3rd schematic depicts indeed the situation in the HAADF image of such a dissociated shuffle-glide dipole in fig. 6a.

Another possible route to create a shuffle core is through reconstruction of the edge of a graphene layer, which exhibits a distortion, as shown in fig. 6c (see row of sheared hexagons). Here an 8-atom ring defect bridges a corner. Under shear stress along the grey arrow, the defect could glide into the layer. This requires neither formation of a dipole nor vacancies, and each glide step, i.e., moving the defect by one hexagon along the grey line, only requires reconstruction of one bond. The HAADF image in figure 6d shows a single shuffle dislocation core with a clearly visible under-coordinated carbon atom in the defect core. We have demonstrated in fig. 3 that vacancies move easily under electron beam irradiation, so the e-beam facilitates glide. The presence of residual stresses (e.g., originating from micromechanical cleaving and exfoliation of the graphene) might be an additional source for glide of 8-atom ring defects formed at graphene edges.

3.2 Adatoms

Lattice resolution HAADF images of uncontaminated patches in single layer graphene films show contrast variations in the benzene rings. This can be observed in the previous figures. The area in figure 7a) is part of a clean patch and has been Fourier filtered, using a low pass filter (like this in figure 4). It becomes clear that the graphene lattice is not of uniform contrast; some of the bridges between atoms are significantly brighter. The ball and stick model, overlaid in the top right indicates the bright regions as ad-atoms. To the left of the overlaid model there is a vacancy (marked 'V'). We suggest that the regions of enhanced brightness found in fair numbers are due to C-adatoms, forming bridges above the in-plane C-C bonds. We derive this from a quantitative evaluation of the HAADF contrast (Bangert et al., 2009b). Examples of the quantification are shown in fig 7b, which includes intensity profiles (blue curves) that had been taken in *raw*, i.e., unfiltered HAADF images; the scan lines are marked in 7a) to indicate the corresponding scan locations in the filtered image. The red curves in the two panels are intensity scans across a vacuum image. They show the counts arising from camera shot noise and electron background when the beam is not on the specimen. The base line in the graphene is higher then in the vacuum image due to scattering from a single atomic layer; the high frequency variations in the intensity in the curves are of statistical nature, but it has to be noted that a lower frequency pattern with troughs and peaks modulates the noise around the base line intensity in the blue curves; this pattern reflects the periodicity of the atom array, as the 1-Å probe causes higher intensities on then between atoms. Distinctively above the graphene layer intensity are 'spikes' (orange arrows) of just below twice the intensity. These correlate with positions of the brighter 'bridges', indicated by corresponding orange arrows in the low pass filtered image. The HAADF contrast scales near linearly with the material thickness, i.e., with the number of atomic layers traversed by the e-beam. It scales, however, approximately with the square of the atomic number: measured ratios of HAADF signals from C-atoms in graphene and single atoms of Si or Cu contaminants, the nature of which was confirmed by EELS, revealed a power dependence of slightly less then 2. The HAADF intensity on the ad-atoms increases by a factor of just less then 2, whereas it should increase by 2½ or 3 times if these atoms were N or O; such an increase would lie outside the statistical error interval. In addition, highly localised core loss spectra (not shown) encompassing the range from C to O showed no sign of N and O.

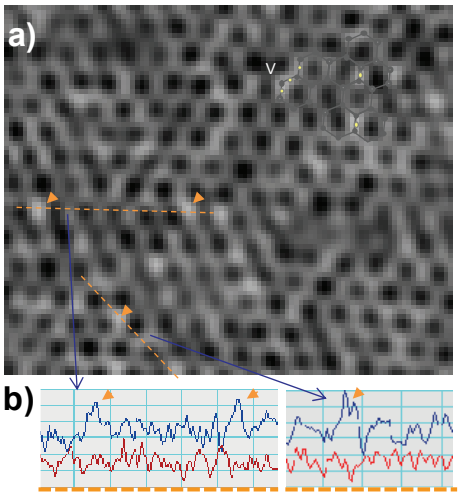

Fig. 7. a) Enlarged region from the filtered HAADF image in figure 4c with ball-and-stick model overlaid in the top right corner and a vacancy V indicated. Shown also are lines along which the intensity profiles displayed in b), blue curves, were taken. Intensity line-profiles from vacuum images are in red. Spikes of ~2x the graphene intensity are indicated with orange arrows. Enhanced intensity in the corresponding locations is emphasised and arrowed in (a). All intensity profiles were taken on raw, unprocessed images.

Carbon ad-atoms on graphene have previously been suggested (Meyer et. al. 2008b; Nordlund, Keinonen & Mattila, 1996). However, from HAADF contrast it cannot be excluded that H-atoms, too, are bound to C-adatoms or, indeed, directly to graphene C-atoms. Their Z-contrast would be lost in the noise.

4. Nano-scale topography: ripples in monolayers and turbostratic arrangements in bi-layers

4.1 Ripples

The stability of extended two-dimensional (2D) structures has been the subject of a long-standing theoretical debate, with previous suggestions that 2D films embedded in three-dimensional 3D space are crinkled. It was then countered that crinkles can be suppressed by anharmonic coupling between bending and stretching modes, such that a 2D membrane can exist but will nevertheless exhibit height fluctuations (Nelson, Piran & Weinberg, 2004; Gass et. al. 2008; Meyer et. al. 2007a&b;). The mechanical behavior of graphene can have profound impact on its extraordinary electronic properties. Recent observations suggest that suspended graphene is not perfectly flat, but rather exhibits microscopic corrugations (ripples) which can be not only dynamic (that is, through flexural phonons) but also static (Gass et. al., 2008; Booth et. al. 2008; Meyer et. al. 2007b). In those observations, large-scale ripples (>15 nm) were visualized directly (Nordlund, Keinonen & Mattila, 1996) whereas ripples on a nanoscopic scale (<15 nm) were only identified from the broadening of diffraction spots (Meyer et. al., 2007b) which prevents static bending from being distinguished from dynamic bending. Furthermore, it was argued that scaffolds supporting

graphene crystals and contamination by adsorbed hydrocarbons, can induce an external compression resulting in ripples especially on the large scale, or films remember the initial non-flat configuration induced by a silicon oxide substrate used for sample preparation. In either instance, the observed ripples would not be intrinsic. The difficulty with directly imaging ripples in a transmission electron microscope arises from their small amplitude: the defocus, even with aberration-correction, is not precise enough to reliably detail changes in contrast which would arise from height differences less than a few nanometers, let alone one nanometer.

Observing perpendicularly onto an undulating plane of atoms, the bond inclination will cause variations in the projected bondlength. For example, inclinations of ~5° from the horizontal flat sheet will give rise to a change in the projected C-C bond lengths of ~1 %. Ripples possessing a wavelength of 5 nm, thus have an amplitude of 0.25 nm (this value being derived from electron beam diffraction (Meyer et al., 2007a)). However, such bond length changes are not easily observed in raw or even low-pass filtered HAADF lattice images, as seen using the filter detailed in fig. 4b and c. As FFTs of nano-scale areas, like in our case, are embedded in significant noise, the error in positioning the diffraction spot maxima gives rise to a bond length error of ~±2% in BF images, and slightly less in HAADF images. Applying a narrow annular band pass filter, with a band width corresponding to ~0.04 Å, i.e., imposing a narrow ring mask on the Fourier transform (FFT) of the raw images, passes spatial frequencies within ~2% of a selected frequency corresponding to a real space distance. The inverse transform (IFFT) reveals locations of atoms with such spacings, although with possible rotations, through intense lattice fringes. For graphene, the color coding is selected such that atoms possessing the correct bond length appear orange. Should the projected bond length change by as little as 2% owing to out-of plane bending of the atoms, the lattice periodicity will become less visible in the IFFT, and blurred patches will occur at such locations. Such regions appear blue. An example of this procedure shows ring filter and the resultant IFFT, respectively, in fig. 8a) and 8b). The latter is the projected bond length visualization; atomic scale detail can be seen as a fine raster superimposed on the colors. To better reveal the sheet rippling effect, the atomic detail has been removed by a Gaussian blurring function in the image in fig. 8d). In the Gaussian filtered images again, orange (blue) regions correspond to areas of small (large) deviations from the graphitic ***a***-plane distance of pristine and perfectly flat graphene sheets. Any spatial frequencies outside an annular mask diameter corresponding to the graphitic ***a***-plane spacing, will possess significantly weaker intensity; the color-coded IFFT resulting from both, a smaller or larger band pass would therefore be expected to exhibit more bluish colors. Since flanks of undulations reduce the projected bond length, they become visible as bluish regions in IFFTs obtained with a narrow ring mask.

We have obtained IFFTs of a number graphene images, using a series of filter diameters in each case, with increments corresponding to 0.02 Å (such an increment would arise from an inclination of ~5°), and with the above bandwidth of 0.04 Å. Although the ring mask increment lies within the error of measurement, it is still possible to follow gradual changes in contrast. In such a series of IFFT images, the spacing range covers ±10% variation of the graphitic ***a***-plane distance. In each IFFT image, a different projected lattice spacing is passed by the respective filter and comes 'into focus'; this is equivalent to observing the lattice in slices 'cut' through the crumpled 3D graphene sheet at different distances parallel to the flat sheet reference plane. In figure 9a and b, selected images from a series of IFFTs using ring mask diameter increments as described are detailed, the masks were applied to raw, single

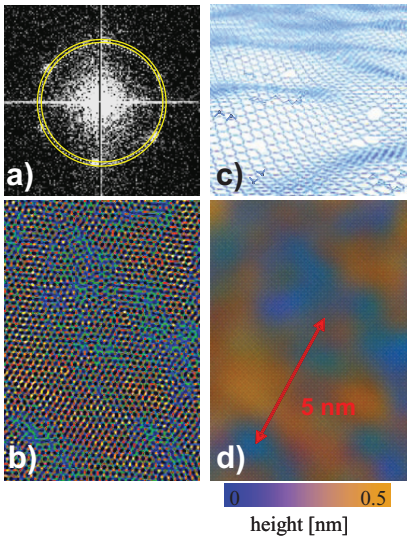

Fig. 8. a) A ring mask typically used to construct the IFFTs in (b), which is the inverse FFT of a raw HAADF image. c) Model of graphene, with undulations and defects. d) Gaussian-blurred image of (b) with the atomic detail removed, to highlight larger scale structure (flanks of undulations appear blue, approximate height scale given underneath in colour with flank inflection points set at zero).

layer images, i.e. allowing spatial frequencies both below and above the first order diffraction spot distance to pass. Fig. 9 (uppermost and middle rows) detail identical features imaged in BF and HAADF, with their associated IFFTs. BF IFFTs for the same band pass are very similar in their overall pattern to those of HAADF images, taking into account that the color scheme is slightly different in both cases. This lends credibility to the method being applied to HAADF images with weak intensities. The strongest intensity variations (orange to blue) can be observed in Fig. 9 columns iv-vii, where the ***a***-plane frequency has filtered through, whilst deviations from this band pass result in images of overall lower contrast (bluish colors, columns ii, iii and viii). In row c, the same method is applied to a 5-layer graphene sample, (the number of graphene layers was determined using the procedures described in chapter 6 and also in (Eberlein et. al., 2008). The breadth of images exhibiting the brown-orange colors (columns iv-vii) suggests flatter sheets, but also reflects the accuracy limit of the measurement; however, the radius of the ring filter used in column v (blue arrow) corresponds most closely to the ***a***-plane spacing. We note that pattern changes with band passes larger than the graphitic *a*-plane frequency (right of arrow, i.e. in columns vi and vii.) arise from a reduction in the bond length projection. For example, the circled locations mark contrast inversions, where the lattice at the flank of a ripple comes into focus, and then goes out of focus. In a simplistic picture, the peaks / troughs of ripples should be 'in focus' at the same band pass as the flat sheet, and the flanks should then be 'out of focus'. The increment in the annular filter radius required to change the color from brown to blue (images in rows a and b, columns vi and vii, circled area), allows one to deduce the inclination angle as ~12°. The ripple width of ~5 nm yields a height of ~0.5 nm. Although this is slightly greater than the value reported (Meyer et. al., 2007b; Fasolino, Los

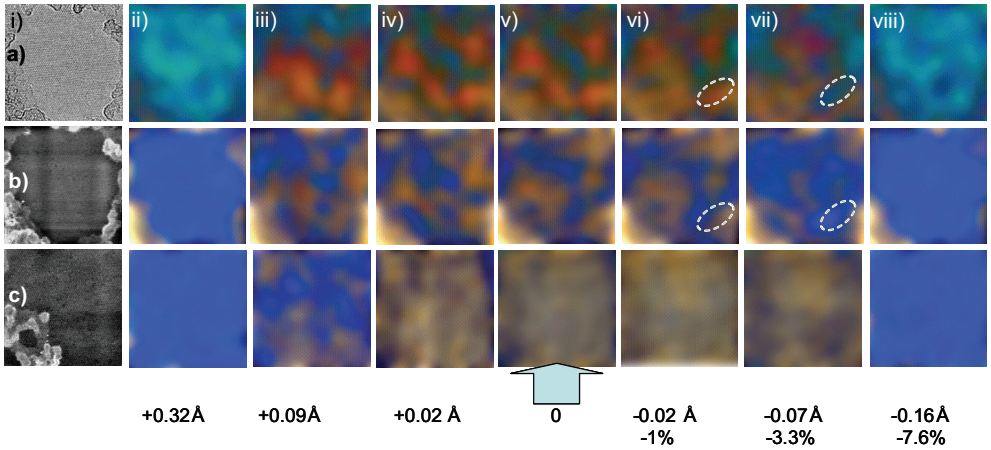

Fig. 9. In a) image (i) is a BF lattice image of a clean patch in a single graphene sheet, from which the IFFTs in (ii) to (viii) are obtained. All IFFT images have undergone Gaussian blurring. The arrow in column (v) marks the image corresponding to the correct graphitic lattice spacing. Bandpass deviations from the graphitic ***a***-plane spacing, and hence from the C-C bond length are, (ii) +15%, (iii) +4.3%, (iv) +1%, (v) none, (vi) -1%, (vii) -3.3% and (viii) -7.6%. In b) (i) represents the HAADF lattice image of the same area as in (a), and in c) (i) is the HAADF image of a 5-layer graphene patch. (ii) to (viii) in (b) and (c) represent IFFTs of the respective images in (i) with the same band pass filters as detailed for (a) above. The frame width of panels is 15 nm.

& Katnelson, 2007), ripples of this height are frequent in occurrence and pronounced in our samples. Ripples of lesser height are most likely present too, but they are concealed by larger undulations and are also close to the resolution limit of the present method: the smallest increment in Fig. 9 corresponds to 1% change in spatial frequency equivalent to ~6° inclination. The contrast variations reflect the complex and intricate sheet buckling, which is quite severe in certain regions. Additionally, topography on a larger scale arising from thin hydrocarbon deposits, as can be seen bordering 'clean' areas' in all lower magnification images of graphene, also affects the IFFT image: such deposits introduce some amorphicity, hence many spatial frequencies are present in such locations, ranging from the lattice frequency down to low frequencies representing local, large scale disturbances. This accounts for the pink coloration occurring at such locations at all band passes.

Although undulations are observed in every clean graphene 'patch' (graphene area free from hydro-carbon deposit that is) in the absence of visible topological defects, we observe that the ripple patterns can, however, be influenced by the latter. Further results on this are given in Bangert et al. (2009a).

4.2 Turbostratic graphene

All results shown so far were obtained of micro-mechanically cleaved and exfoliated graphene. Electron microscopy investigations were also carried out on graphene grown by chemical vapour deposition (CVD) on nickel and copper substrates and lifted off these substrates via aforementioned procedures. We note that hydrocarbon contamination is generally more extensive and more finely dispersed on all such samples.

The images in figure 10, in contrast to the STEM images of the previous figures, are high resolution phase contrast images, obtained in a transmission electron microscope, a Tecnai F30. Ni-grown samples consisted of large films (10's to 100's of μm), partially consisting of single layer, but in the main of few-and bi-layers, either in graphitic AB stacking or in turbostratic arrangements (de-coupled layers, rotated at various angles with respect to each other). Figure 10a) depicts suspended CVD-graphene extracted from a Ni substrate. The small omni-present worm-like contrast arises from molecular hydrocarbons, presumably in form of chains, on the surface of bi- or triple-layer graphene. This contrast is present on all such CVD sample surfaces, uncontaminated surface areas are only of the order of few nm; upon closer inspection (fig. 10a might have to be viewed with slight enlargement) the underlying graphene lattice becomes obvious. The inset in the left hand top corner is an electron diffraction pattern of the image area, revealing the turbostratic nature by the two hexagonal spot patterns rotated with respect to each other (12 spots instead of 6). The right hand bottom inset is the FFT of the image, showing the same orientation relationship of the sheets as the diffraction pattern. Areas with apparent AB stacking can also be found (not shown here). This might, however, arise from differences in the rotation angle across the film: fig 10c) shows a schematics of graphene sheet rotated with respect to each other with different rotation angles, leading to varying Moiré patterns and different atomic lattice appearances within.

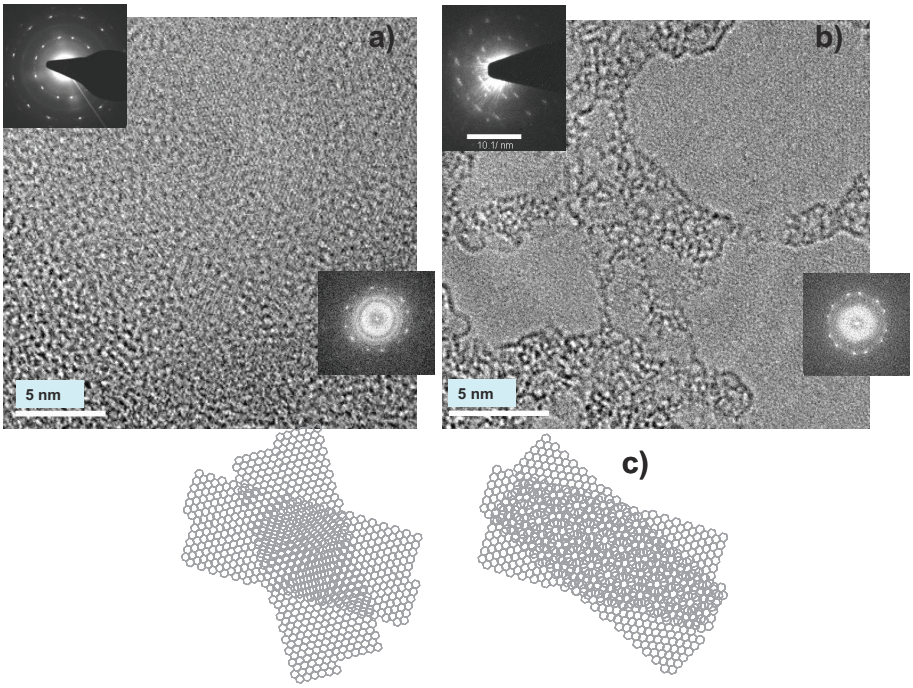

Fig. 10. HREM phase contrast images of suspended graphene grown by CVD after lift-off from a) a nickel and b) a copper substrate. Insets in both cases are the experimental diffraction pattern (top left in each image) and the Fast Fourier Transform (FFT; bottom right) of the image areas shown; c) schematics of turbostratic arrangements leading to different appearances of the atomic-scale structure.

Figure 10b) shows an image of suspended CVD-graphene grown on copper. Regions of larger uncontaminated areas (some 10s of nm) are found in these samples, however, the films consist in large, like in the Ni-substrate case, of turbostratic graphene. The insets show again the electron diffraction pattern (left top) and the FFT (right bottom) of the image area. Close inspection of the lattice structure reveals a Moiré pattern similar to the right-hand schematics in fig.10c).
Hence micromechanically exfoliated and CVD-grown graphene have quite different topographies, larger single-layer areas appear to be rare in the latter.

5. Atomic scale chemical information: impurities- native, dosed and doped

5.1 Impurities with Z ≥ 6

We have explained and demonstrated in paragraphs 1-3 that HAADF is the prime tool for pinpointing impurities with Z ≥6 on graphene. We cannot identify hydrogen attached to C-atoms via HAADF, but we will show other means of detecting H in paragraphs 5 and 6. We can identify extensive C-adatom coverage (paragraph 3), and although HAADF contrast evaluation gives strong evidence that the ad-atoms are indeed C (the HAADF signal strength in respective locations is twice that of graphene), due to the error in quantifying weak HAADF signals, we do not want to exclude oxygen atoms as being part of the ad-atom population (although the signal strength in locations of O-adatoms should be ~3x that of pure graphene), nor do we want to exclude, at this stage, the existence of OH-groups. However, we should be able to identify fluorine with a Z number of 9, giving a theoretical HAADF signal ratio F:C of 81:36 and hence an expected HAADF signal strength, in places of F-adatoms, of ~4x that of pure graphene). We have dosed graphene with F (details not given here), however, we could not detect any F retention on pristine graphene patches.
Extensive HAADF investigations, in which we have scrutinised many clean single-layer graphene patches for foreign atoms have revealed it is free of impurities with Z≥9. Graphene investigated for residual impurities was exfoliated by micromechanical cleavage as well as from CVD grown layers on Ni and Cu. Included were also attempts to dope/dose graphene with impurities via metal deposition (Au and Cr).
It should be emphasised that the above said applies strictly to clean, single layer graphene; we have never observed impurity atoms of any kind attached to such sheets. However, we observed many types of impurities in the hydrocarbon contamination on single and multiple sheets, and we did also observe impurity atoms on clean areas in multi-layer graphene.
Transition, noble, and group IV ad-atoms are predicted to modify the graphene electronic states to a large degree indicating covalent bonding with strong hybridization between ad-atoms and graphene. Metal-graphene interactions have been much studied by means of Density Functional Theory (DFT) calculations. H-sites (see fig.12e) are predicted as preferred location for most metals (e.g., Ti, Fe), T-sites for Sb, Sn and Ni, whereas Pd, Cr and Pt are expected to bind strongly to B sites (Suarez-Martinez et al, 2009; Uchoa, Lin & Neto, 2008; Chan, Neaton & Cohen, 2008; Mao, Juan & Zhong, 2008; Sevincli et al, 2008). Experimental exploration of the metal-graphene systems is still limited, especially TEM observations are practically non-existent. Such observation would be of great interest, as calculations have lead to discrepancies in the site of metal atoms: the two common approximation for the calculations, local density approximation and generalized gradient

approximation –the latter does not represent Van-der-Waals forces very well (Leenaerts, Partoens & Peeters, 2008)-, lead to different binding energies and thereby to different sites for Au atoms, T-sites for the former and B-sites for the latter method (Aktürk & Tomak., 2009). In addition, arbitrary variables used in the calculation, such as cut-off energy (Varns & Strange, 2008) and size of the supercell (Leenaerts, Partoens & Peeters, 2009) can affect the result of DFT calculations. It was furthermore found, theoretically and experimentally, that point defects in graphene provide nucleation sites and even further substitutional incorporation of metals (Charlier et al., 2009; Boukhvalov & Katsnelson, 2009; Gan., Sun & Banhart, 2008; Krasheninnikov et al., 2009; Zhou, Gao & Goodman, 2010).

Gold atoms and its dimers on the graphene surface have been studied by using first-principles calculation with the local density approximation (Varns & Strange, 3008). The results show that the gold–gold interaction is significantly stronger than the gold–graphene interaction (for this reason gold is highly mobile on graphene) as is experimentally confirmed by Gan., Sun & Banhart (2008) with observation of gold clusters –rather then atoms- on the graphene sheet. For a single gold atom the favourable energy configuration is found to be directly above a carbon atom. We have evaporated 0.1 nm of gold onto graphene. Figures 11a) and b) show results of such deposition: indeed on single or de-coupled (turbostratic) layers gold atoms do not remain dispersed, but cluster into nano-crystals, and notably, are exclusively located in the hydrocarbon contamination. This demonstrates the extreme mobility of gold on pure graphene. Only in stacked few-layer films (here: exfoliated by cleaving) can single gold atoms be observed: it appears that atoms in sub-surface layers are needed to contribute to the bonding with surface gold atoms in order to prohibit dissociation and diffusion. Figure 11c) is a BF STEM image, and represents phase contrast (like an HREM image). The beam is focussed on the exit surface of the sample; this is the surface, on which the gold is evaporated. So the electron beam proceeds through the graphene layers before it encounters the gold atoms. The aggregate of gold atoms is so thin, that it is invisible in phase contrast, however, the graphene in the BF image exhibits strong contrast and relatively little noise, and shows the lattice periodicities well. This means that for BF analysis the raw (unprocessed) image can be used. Figure 11d) is the corresponding HAADF image, and is obtained simultaneously with the BF image. The image intensity arising from incoherent elastic scattering of few atom layers is very much lower than in BF, and the noise is so high that the benzene rings are barely recognisable. However, the gold atoms are clearly visible. They have formed a loose aggregate with single atoms dotted around the aggregate, some of which we have numbered. We note that comparing identical positions in images (c) and (d), the benzene ring centres, known to be black in HAADF images, correspond to bright patches in the BF images; this can be seen from the schematic benzene rings (red) overlaid on the HAADF image and positioned in identical locations in the BF image. Hence the C-atoms surrounding the black centres in HAADF images, constituting bright contrast, correspond to dark contrast in BF images. Due to the weak contrast and the noise of the raw HAADF image, although gold atoms can be located rather accurately, it would be near impossible to assign them exact sites on the benzene rings. However, the benzene ring shape is clearly discernible in the BF image, and by locating the exact corresponding position here (circled), the sites can be identified. It thus occurs that all gold atoms sit on T-sites. This is in agreement with theoretical predictions.

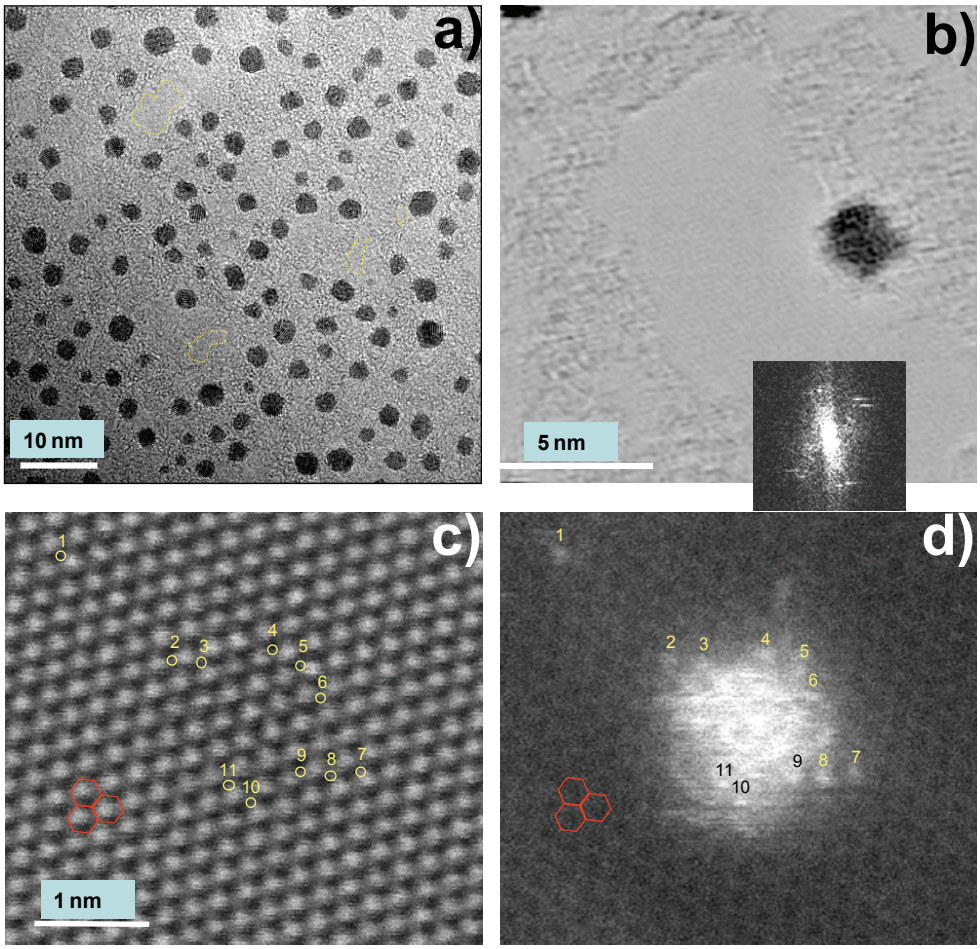

Fig. 11. a) TEM image of 0.1 nm gold evaporated on mono-layer graphene, b) BF STEM image of 0.1 nm gold evaporated on 2-layer turbostratic graphene with FFT of the image as inset to show, by the double spots, that the two layers are rotated with respect to each other, c) and d) BF and HAADF STEM lattice image of the same area in few-layer graphene. Here individual gold atoms can bee seen separated from the small cluster in the middle. Identical positions of the benzene rings are marked in red, showing that bright contrast in the BF image corresponds to the dark, hollow centres of benzene rings in the HAADF image. Single atoms 1-11 are marked with the numbers occurring just above the atoms in the HAADF image; identical places are marked by yellow circles in the BF image, showing that Au-atoms sit on T-sites (see fig. 12e) on the sample surface. All images represent raw, unfiltered data.

Iron-atoms have not been deliberately deposited, but reside as impurities on many samples, presumably as a result of chemical processing. The graphene sample in the here presented results was obtained by micromechanical exfoliation. Figure 12a) shows again that on uncontaminated single layer areas (black patches) the sticking probability is very small: all Fe clusters and single atoms (white spots) are located on hydrocarbon contamination (greyish areas). On the surfaces of multi-layer graphene on the other hand individual atoms can be seen. Figures 12c) and d) are HAADF and BF images of 1-4-layer staggered graphene sheets; with the sheet number increasing from the right to the left (i.e., on the right edge of the image is one sheet). Fe-atoms are clearly visible in (c) and corresponding positions have been circled in (d). The spectrum on the right of fig. 12c) is an energy loss spectrum taken on an individual Fe-atom, showing the characteristic $L_{2,3}$ absorption edge of Fe at ~708 eV. In fig.12b) the areas around two Fe-atoms are enlarged with a model of the AB-stacked graphene lattice overlaid. From this it becomes clear that the Fe-atoms in both cases sit on B-sites. This contradicts calculations, which predict H-sites.

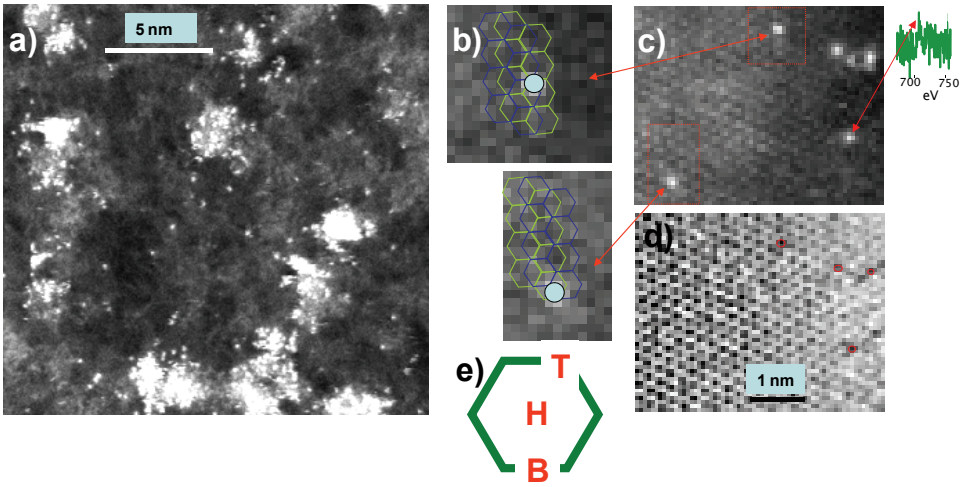

Fig. 12. a) Fe-atom contamination on single layer graphene, showing that all Fe- impurities sit on hydrocarbon contamination and not on clean graphene patches, b) enlargement of the red framed areas in the atomic resolution HAADF image of few-layer AB-stacked graphene in (c). The model of the lattice and positions of the Fe-impurity atoms are overlaid, c) HAADF image of larger area showing individual Fe-atoms on few-layer AB-stacked graphene. The inset on the right hand side of (c) shows an EEL spectrum with Fe $L_{2,3}$ absorption peak, taken on the arrowed atom. d) BF STEM lattice image of the same area as in (c); positions identical to those of atoms in the HAADF image in (c) are circled in red. The graphene sheets are staggered starting with a single sheet with on the right, followed by a second, third and fourth sheet towards the left with edges running parallel to the sides of the frame. e) model of benzene ring with sites of impurity atoms.

Nickel-atom contamination is shown in figure 13. The graphene film in this case was grown by CVD on Si with a sacrificial Ni-layer on top of the Si-substrate. Ni-atoms have remained 'stuck' to the film after lift-off. The image in this example is a low-pass filtered HREM phase contrast image taken in a TEM. The large underlying image shows mono-layer Ni-atom islands or –rafts on top of graphene, which itself consists of a patchwork of 1 and 2 layers and more.

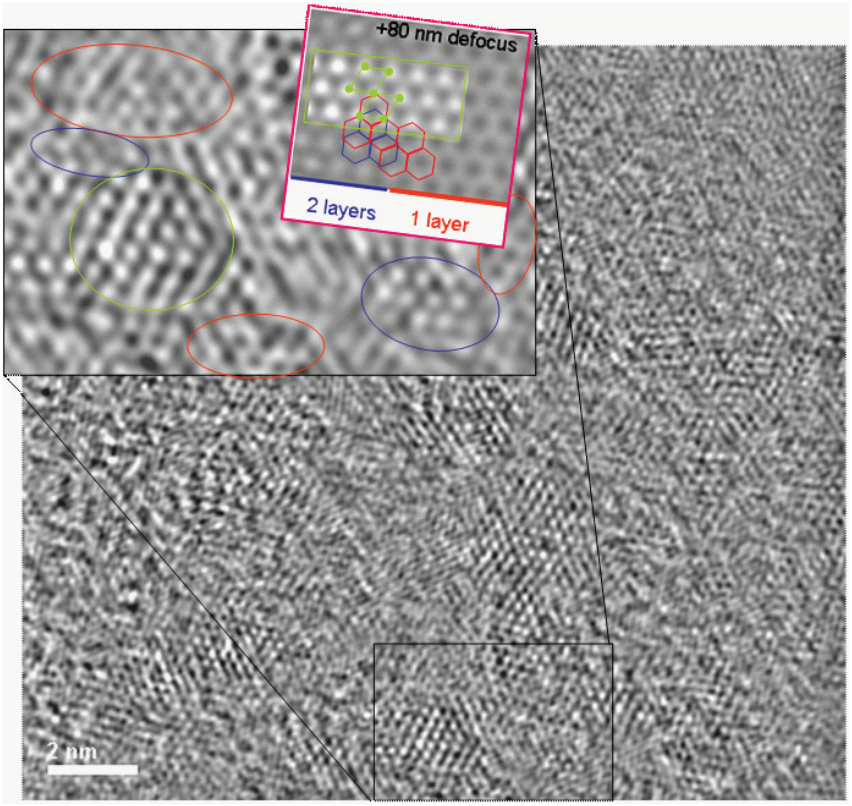

Fig. 13. Low pass filtered HREM image, taken in a TEM, of graphene grown by CVD on a sacrificial Ni-layer on Si. The area in the image consists of patches of mainly mono- and bi-layers, as well as of mono-layer Ni-islands. The larger inset is an enlargement of the black-framed area, the smaller inset is an image simulation, using the TEMSIM program, of mono- and bi-layer graphene with a mono-layer island of Ni stretching over both. Features with similar contrast in the experimental image in the larger inset are circled with the respective colours. The focus value of +80 nm achieves strongest contrast of Ni and graphene simultaneously.

The contrast in phase contrast images is not straight-forwardly interpretable and depends on sample lens aberrations, sample thickness and defocus, and it is common practice to run image simulation., if information other then that about lattice periodicities and perfection is to be extracted. We have used the TEMSIM code (Kirkland, 2005). The small inset shows simulated HREM contrast for 1 and 2 layers and a Ni-atom island covering parts of both, the single and the bi-layer. The model lattice for the graphene layers (red and blue) and a Ni-atom raft (green) is overlaid. The simulations were run for a series of focus values; we have depicted the simulation for 80 nm defocus, as this focus condition achieved the strongest contrast (best visibility) in the simulated images, so this value would be 'automatically' tuned to in the experiment. It should be noted that in overfocus conditions Ni-atoms have bright contrast similar to the centres of benzene rings in 2-layer graphene, whereas in 1-layer graphene the

centres of benzene rings are dark. Comparing this to the larger inset, which in turn is an enlargement of the black famed area in the underlying image, we can then identify single layer (circled in red) and bi-layer (circled in blue) patches. Atoms constituting a Ni-island (circled in green) can be recognised by their strong, bright contrast (like in the image simulation). In relationship to the C-hexagons the position of these Ni-atoms can be assigned T-sites in benzene ring in agreement with above mentioned calculations.

5.2 Impurities with Z≤ 6

Interesting potential electronic dopants in graphene, such as nitrogen and ***boron***, due to the similarity in atomic number with carbon, cannot easily be detected in HAADF images. However, their presence, and even local bonding environment, should be accessible via core loss EELS. With probe aberration corrected STEM it is possible to detect EEL signals and positions of single atom (we have already shown an example of this in fig. 12c). Boron was ion implanted at 100 eV to a level giving on average one atom per nm^2 (10^{14}cm^{-2}) (Bangert et al., 2010a) Figure 14a) is an atomic resolution STEM BF image of few-layer graphene. A spectrum image was taken over the whole image area, and pixels, in which B K-edge signals were detected, are filled in yellow. Although the dopants appear dispersed the retention is less then 10%. We do presently not have an explanation as to why the retention is so small, other then that the implantation energy might not have been large enough to incorporate B in the lattice. This might have been the case, since Pomoell et al. (2003) estimate that ions ranging from carbon to xenon loose on average 300 eV when penetrating a single walled CNT, i.e., 150 eV per graphene sheet. Figure 14f) shows EEL spectra of the B K-edge, extracted from the yellow pixels. Although noisy, the spectra exhibit a sharp peak at 192 eV, which very much resembles the π*-peak spectra of boron-doped carbon nanotubes measured by Fuentes et al. (2003), indicative for substitutional boron.

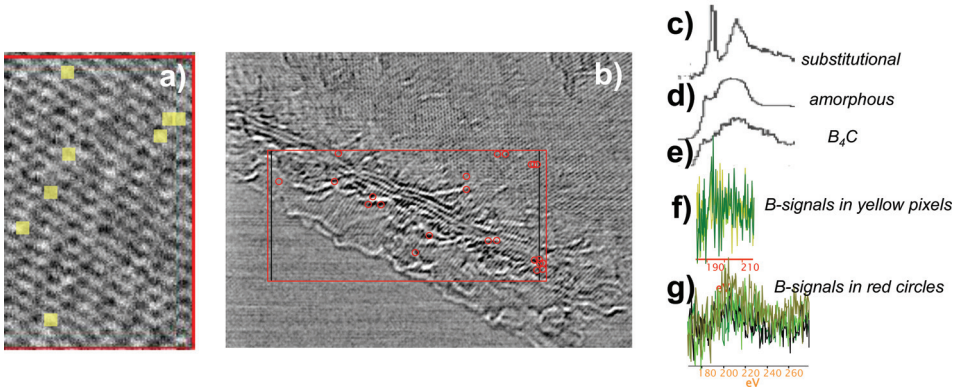

Fig. 14. a) STEM BF image of few-layer graphene and b) of staggered graphene sheets, starting with a single sheet, whose edge runs diagonally from left side to bottom right, implanted with B to a dose of 10^{14} atoms cm^{-2} at an energy of 100 eV. Positions were B K-edge EEL signals were recorded in spectrum images (area indicated by red frames) are indicated by yellow squares (a) or red circle (b), c) literature reference spectrum of BN (Gatan EELS atlas), d) of amorphous B, e) of B_4C, f) spectra extracted from yellow pixels in (a), g) spectra extracted from red circles in (b).The spectra in (f) and (g) indicate that B assumes substitutional positions in multilayers, and attaches along graphene edges in form of few-atom clusters.

Interestingly, the rather strong B-signal obtained from staggered graphene sheets in fig. 14g) does not exhibit the π*-peak. Signal positions are indicated by red circles in fig.14b); they coincide in most cases with the edge of graphene sheets: the leftmost portion of the image in 14b) represents a single layer, followed (towards the right) by the 'frayed' edge of a second sheet along which a number of signal positions are marked. This edge is followed by, to a large part, straight edges of four further graphene sheets, with a cluster of boron signal positions marked at the bottom left hand corner of the image, and two further positions higher up along these edges. Typical spectra of the boron K-edge in red-circled pixels are shown in fig. 14g). Comparison with spectra of amorphous boron (fig.14d) and B_4C (fig.14e) suggests that small few-atom boron clusters have formed attached to sheet edges or mono-atomic steps. Hence, although there is indication of substitutional B-incorporation via low energy ion implantation in few and many-layer samples (as in the case of carbon nanotubes (Bangert et al., 2010a), B does not seem to substitute atoms in single, bi- or triple-layers, nor does it appear bound to the surface. As in the case of metal impurities in previous examples mobilities of single-atom species on graphene surfaces seem very high.

The possibility for ***atomic hydrogen*** to be chemi- or physisorbed on graphite surfaces (Jeloaica & Sidis, 1999) and graphene has been researched theoretically and experimentally (e.g., Ito, Nakamura & Takayama, 2009; Elias et al., 2009), and direct experimental observation has been attempted via transmission electron microscopy imaging (Meyer et al., 2008b). H-dosing appears promising for band-gap engineering of graphene. In order to carry out investigations of the effect of hydrogen on the graphene atomic and electronic structure we have dosed graphene with hydrogen by exposure to a hydrogen plasma, described in Elias et al., (2009).

H cannot be revealed in HAADF images, so in order to assess H adsorption on graphene we have carried out EELS. Figure 15a) shows low loss spectra, which were obtained of uncontaminated graphene patches, typically a few 10 nm^2 in size. The blue spectrum in (a) is a reference spectrum taken of pristine, hydrogen-free graphene. To ensure that we have hydrogen-free surface areas few-layer graphene regions were repeatedly scanned in the STEM. The scan raster was successively decreased, and HAADF images in combination with EEL measurements revealed material being peeled off layer-by-layer, until finally a hole appeared. The blue spectrum is from the last remaining layer after such a repeat-scan procedure; the Lorentzian fit curve (red dotted line) was obtained from least squares fitting, and was used as fit for the rise of the σ+π plasmon. Spectra of such freshly revealed areas did not show the bump at 13 eV like in the orange spectrum above, which was obtained from a deliberately hydrogen dosed sample.

We applied the spectrum imaging method (Jeanguillaume & Colliex, 1989), and scrutinised entire EEL-spectrum images for occurrence of the ~13 eV core-level excitation signal of hydrogen. Spectrum images were obtained in the following way: a raster was defined over an area of an uncontaminated patch and in each pixel (typically 0.3x0.3nm^2) of this raster a spectrum was taken. Intensity maps, extracted from these spectrum images are shown in figs 15b) and c). These maps were obtained by displaying in each pixel the intensity of the respective spectrum integrated over an energy window ~12-14 eV, after having subtracted the plasmon background determined by the Lorentzian fit. These maps represent the distribution and relative amount of hydrogen on the graphene surface. Since spectra from individual pixels display a great deal of noise, we carried out Principle Component Analysis (PCA) on the spectrum images prior to background subtraction (e.g., Borglund, Astrand & Csillag, 2005). This reduces the noise significantly, and clearly reveals the bump on the rise of the σ+π plasmon at ~ 13.2 eV as seen in the orange curve in fig.15a).

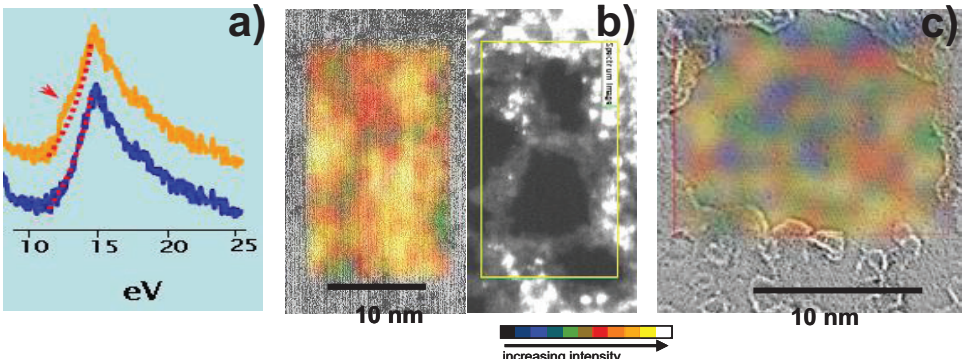

Fig. 15. a) low loss EEL spectra showing the π+σ-plasmon of ***H-free*** (electron beam 'zapped') single layer graphene with Lorentzian fit (blue spectrum) and of hydrogen-dosed graphene with the same Lorentzian fit-curve (orange spectrum), b) EEL intensity map of hydrogen-dosed graphene, showing the integrated intensity –after Lorentzian background subtraction- in the energy region 12-14 eV; the map is overlaid on the respective STEM BF image area (left); the corresponding HAADF image is shown on the right, c) EEL intensity map of pristine, i.e., undosed graphene, obtained with the same procedure as in (b), overlaid on the respective STEM BF image area.

Figure 15b) shows an EEL intensity map of the H-core loss signal of hydrogen-dosed graphene. The intensity map is overlaid on the BF STEM image area where the spectrum image was taken. The corresponding HAADF image is also shown. It reveals a hydrocarbon 'net' (greyish contrast), bordering uncontaminated single layer graphene patches (black), as well as contaminants of higher atomic number (white dots) on top of hydrocarbons. The intensity map shows highest H-signals (yellow/orange) in regions free of hydrocarbons, whereas hydrocarbon contamination shows up with lower intensity values (green). The reason for this is that hydrocarbons with longer chains have a distribution of energies of the molecular orbitals causing a spread in the H-core level energies with a shift towards lower values (Murell & Schmidt, 1972). These will not have been picked up in the energy window set for the intensity map in (b). Figure 15c) shows an intensity map obtained with the same energy window of 12-14 eV in an uncontaminated region in pristine graphene, revealing that hydrogen is present on clean graphene even without hydrogenation. Again the map is overlaid on the STEM BF image. The amount of hydrogen, however, is significantly lower (by 2-3 times) then in the dosed sample, as evidenced by the colour-scale. A detailed discussion of hydrogenation studied by EELS can be found in (Bangert et al., 2009b).
The question about coverage, detailed atomic structure and bonding arrangements of the hydrogenated areas poses itself. We can get a fair insight into this via highly spatially resolved valence band EELS, i.e., EELS in the extreme low loss regime in combination with DFT calculations; an introduction into this will be given in paragraph 6.

6. Plasmons in graphene: indicators of local electronic bandstructure

6.1 Pure graphene

From an experimental viewpoint, an essential task in the research into 2D structures is to provide evidence that they do indeed exist. This is especially important, because theory does not allow the existence of perfect crystals in 2D space. STM-, AFM- and Raman studies have

given indirect proof of the existence of single-layer graphene. The most conclusive evidence for the existence of *free-standing* graphene, except for the HAADF studies reported in Bangert et al. (2009b) and Gass et al. (2008), a resumé of which has been given in paragraph 3, has been obtained from electron diffraction experiments (Meyer et al., 2007a).

By carrying out highly spatially resolved electron energy loss spectroscopy (EELS), we observe significant red-shifts in the frequency of plasmons in sample positions concomitant with single graphene sheets (Eberlein et al. 2008), very similar to those observed in SWCNTs (Stéphan et al., 2002). Surface plasmon behaviour in thin metal sheets is well documented experimentally and explained using dielectric theory (Raether, 1977; Otto, 1967). There are also numerous reports on surface plasmons in graphite and carbon nanotubes (Annet, Palmer & Willis, 1988; Laitenberger & Palmer, 1996; Perez & Que, 2006; Kociak et al., 2001).

A characteristic of thin foils is the vanishing of the bulk plasmon mode, leaving only the surface plasmon mode; the out-of-plane and in-plane contributions of the latter split in energy when the product of foil thickness d and plasmon momentum q, tends to zero; in graphite the maximum/minimum energy of the π -> π^* transition tends to roughly 7 and 5 eV, and of the σ-> σ^* transition to 20 and 15 eV, respectively (Stéphan et al., 2002). The $\boldsymbol{E}$-field of a fast moving particle is elongated along its direction of travel, therefore, when passing perpendicularly through a graphene foil mainly the out-of plane mode, with momentum $\boldsymbol{q}$ parallel to $\boldsymbol{E}$, should be excited. However, these modes are forbidden in a single layer (Eberlein et al. 2008), and they have weak intensity in graphite. In an EELS experiment carried out in a STEM, although the momentum transfer is close to zero, nonetheless, $\boldsymbol{q}$ has a considerable in-plane component (along $\boldsymbol{a}$, the in-plane spacing) because the collection angle is several mrad. For this reason we will observe surface and bulk plasmons excited with $\boldsymbol{E}$ (or $\boldsymbol{q}$) parallel to $\boldsymbol{a}$.

Graphene samples for the plasmon studies were obtained by exfoliation after micromechanical cleavage. An HAADF image of a region including one to up to a few graphene layers is shown in Fig. 16a), top panel; the narrow, rectangular bar shows the line along which the intensity (overlaid profile), integrated over the width of the bar, is traced. The step heights in the contrast profile are multiples of the smallest height at position 1 (to the right of which is vacuum), confirming that the contrast in this location arises from one single graphene sheet.

Plasmon spectra taken in positions near the edges of one, two, three and several sheets (fig.16a, bottom panel) show that the π-mode, at 7 eV in graphite, has shifted to 4.8 eV at position 1 relating to single graphene layer. Furthermore, the spectrum here exhibits only the $\pi+\sigma$ -surface mode at 15 eV and the 26 eV bulk mode of graphite is not present. The shape and intensity of the one-layer plasmon structure was repeatedly measured in different places on the same sample, in different samples and even in different experimental sessions. Given the same acquisition conditions (e.g., energy dispersion, electron beam current and dwell time), nearly identical spectra were obtained, which at the same time, constituted the lowest plasmon signal measured overall. For two sheets the triangular shape of the $\pi+\sigma$ resonance gives way to a plateau and the integrated intensity under the peak approximately doubles, for three layers it triples; this linear relationship carries on up to ~8 layers, but for increasing numbers of sheets, features above 15 eV start to appear and the plasmon maximum moves to higher energies accompanied by further broadening. The multi-layer plasmon structure in fig.16a) strongly resembles that of graphite. The plasmon characteristics are thus supreme indicators for the presence of single layers.

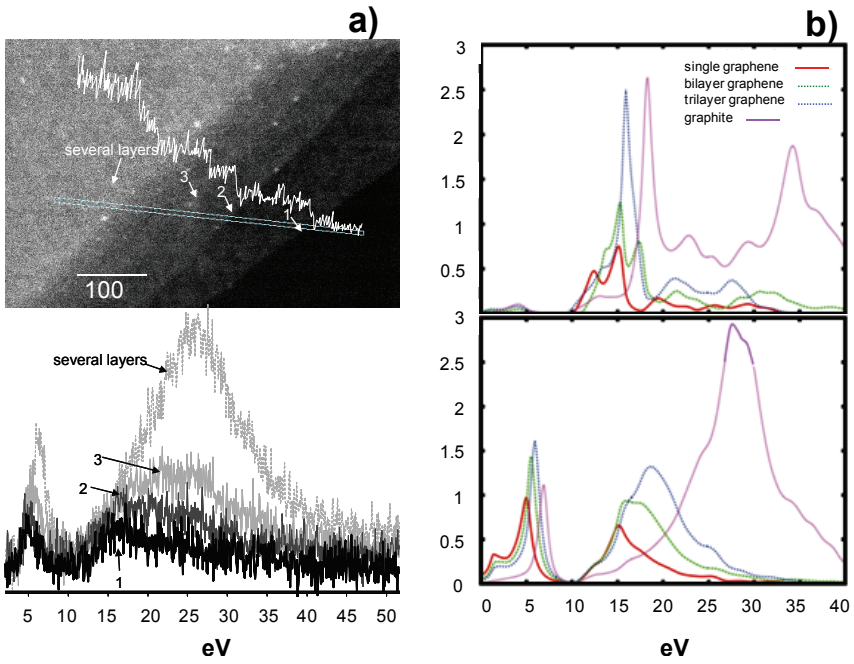

Fig. 16. a) top panel: HAADF image of staggered graphene layers with overlaid intensity profile, which was taken in the turquoise box. The arrows indicate the positions of the edges of new layers, the bottom right corner is vacuum; bottom panel: b) EEL spectra taken of one, two, three and six layers, showing the π- and the π+σ-plasmon shifting to higher energies with increasing layer number; b) AIMPRO calculations of EEL spectra of single, bi- and triple-layer graphene and of graphite for ***E***-fields (plasmon ***q***-vectors) parallel to the ***c***-axis (top panel) and parallel to the graphene sheet (bottom panel). The latter spectra show good agreement with the experimental spectra, indicating that the plasmons in graphitic structures are in-plane plasmons.

In support of the experimental results we have carried out EEL spectra calculations using the AIMPRO local density functional code (Jones et al., 2000; Fall et al., 2002) to evaluate the imaginary part of the dielectric tensor for q=0 and use the Kramers-Kronig relations to derive its real part. The loss function is then found for graphite, graphene and bi- and tri-multilayers. We have also carried out density functional calculations using the WIEN2K code (Nelhiebel et al., 1999), (results of this are shown in the last part), and, after optimising the input parameters and obtaining convergence, acquired identical results as with AIMPRO.

In modelling physical properties of extended periodic (e.g., crystalline) structures the desired process is applied to a unit cell of the structure and the 'outcome' for the entire sample obtained by assembling unit cells in a 3D repeat operation. The representation of nano-objects by repetition of a crystallographic unit cell within the nano-object is inappropriate (the object itself may only consist of few unit cells), here the usual approach is to build large 'supercells' with the entire structure of the nano-object placed in the middle surrounded by vacuum. A repeat structure of these supercells is then obtained and the

calculations carried out as described above. If the supercell is large enough, the calculations of individual unit cells do not impact on each other and the modelled physical property represents that of the supercell alone. To find the required size of such a supercell is tricky, and often a series of calculations for increasing size is carried out until the 'outcome' converges.

Graphene, was modelled by expanding the lattice parameter along ***c*** (Eberlein et al., 2008); convergence occurs at around 20 lattice parameters in this direction, but qualitative changes in the low loss spectra already cease to happen at 5 ***c***-parameters. Figure 16 b) shows calculated spectra for single, bi- and triple-layer graphene for plasmon propagation (momentum vectors) ***q*** along the ***c***-axis (top panel) and in-plane (bottom panel). Notably in single layers (red line) the loss for $\boldsymbol{q} \| \boldsymbol{c}$ is almost zero up to 12 eV, and after this the onset occurs at a similar energy to graphite. However, the peak heights are very different from graphite. The disappearance of the 4 eV peak can be explained by a selection rule. As stated above the peak is due to a transition between occupied and unoccupied π * bands at the M (1/2,0,0) point of the Brillouin zone. (Inspection of the wave functions for these two states shows that both transform as ***pz,*** and are odd under the reflection symmetry present in the basal plane of graphene, but not AB graphite, and hence the dipole matrix element between them vanishes for transitions for which ***q*** is parallel to ***c,*** although the transition is allowed for ***q*** parallel to ***a***.) This shows that the dielectric constant of graphene is not the same as graphite. Fig. 16b), bottom panel, compares the loss function for $\boldsymbol{q} \| \boldsymbol{a}$ for graphite and graphite. We note there are substantial red-shifts of the peaks found in graphite (Eberlein et al., 2008). The 7 eV plasmon peak has shifted downwards to about 4.8 eV while the broad peak around 27 eV has sharpened and shifted to 14 eV just as seen in the experimental spectra; in fact the latter seem to be entirely dominated by the in plane plasmon component ($\boldsymbol{q} \| \boldsymbol{a}$). The loss functions for bi-layers, triple-layers stacked as in graphite, and graphite itself are shown as green, blue and purple curves. The separation between periodically repeated multilayers was chosen as 5 times the separation in graphite. The supercell containing the trilayer for example, has three layers of graphene separated by the interlayer separation found in graphite, but the separation of these planes from similar planes in adjacent unit cells along the c-axis is now 5 times the separation in graphite. The peak positions depend on the number of layers. There is an increasing red shift of the π+σ plasmon resonance as the number of layers decreases. Markedly, there is also a red-shift to ~4.7eV in the graphitic π-plasmon, the latter only occurs for $\boldsymbol{q} \| \boldsymbol{c}$ (see bottom panel 16b). The relative amplitudes of the two plasmon peaks here for the different layers seem roughly consistent with experimental spectra in Fig.16a).

It is the π-plasmon, which bears significant information about electronic properties of graphene and is especially sensitive to modifications of graphene. In the last sub-paragraph we will give a glimpse of the wealth of properties of graphene that can be deduced from the π-plasmon.

6.2 π-plasmon in modified graphene

To give an example of the sensitivity of the low loss region to modification of graphene we return to the hydrogenation issue. In paragraph 5 we observed presence and distribution of hydrogen atoms by their core level excitation, but the detail of the atomic-scale structure was not revealed; questions concerning issues that might have implications for electronic properties include: Is hydrogenation complete? If not, is there ordering of H-atoms? Is H

bonded on both sides? If not, does this induce strain (Xue & Xu, 2010)? Does hydrogenation induce diamond-like, corrugated atomic stucture (Sofo, Chaudhari & Barber, 2007; Elias et al. 2009)?

In all spectra, which showed the H-core loss signal, additional structure was found in the low loss region on the high energy tail of the π-plasmon. Experimental low loss spectra of pure and of hydrogenated graphene, including the π-plasmon, can be seen in figures 17a) (purple curve) and 17c) (orange curve). An extra peak at ~7eV has occurred in the latter, whereas the pre-plasmon peak at ~2eV in pure graphene has vanished. EEL intensity maps of the integrated intensity (after subtraction of a fitted plasmon tail) in the 6-8 eV region, from the same area as in fig. 15b show identical intensity distributions as seen in the latter figure. This suggests that the 7-eV feature is induced by hydrogen. More interestingly, the π-plasmon remains present throughout the spectrum image, in co-existence with the new feature, which is similar to a feature occurring on unpassivated, reconstructed diamond surfaces (Bangert et al., 2006), which have undergone reconstruction of their dangling bonds into π-bonded chains. Hydrogenation ought to passivate the π-bonds, and cause formation of sp^3 bonds instead, and hence dramatically diminish the occurrence of the π-plasmon. However, the π-plasmon in graphene exposed to a hydrogen plasma is nearly undiminished in areas, which, at the same time, show the H-ground state excitation. Co-existence of the π-plasmon and the 13.2 eV signal suggests that hydrogenation is not complete, i.e., not every C-atom is bonded to an H-atom.

In order to support the above interpretation of the EELS observations and to reproduce the EEL spectra theoretically, DFT calculations using the WIEN 2K code, have been performed. WIEN 2K is an all-electron code and uses the General Gradient Approximation with a mixed linearized augmented plane basis set of wave functions (Nelhiebel et al. 1999; see also Blaha et al. 2010). There is a fair number of bandstructure calculations of hydrogenated graphene in the recent literature, predicting the opening of a band-gap of ~3.7 eV and C atoms displaced from planar geometries by H atoms (e.g., Haberer et al., 2010), optimum corrugation angles and resulting bandstructure (Sofo, Chaudhari & Barber, 2007), and influence of hydrogenation on strain and corrugation angle (Xue & Xu, 2010).

As mentioned before WIEN2K calculations carried out on graphite and pure graphene show identical results to those from ab-initio calculations using the AIMPRO code, which reproduces measured spectra very well (Eberlein et. al. 2008) This gives us confidence in using WIEN calculations –not previously applied to graphene- on hydrogenated structures. It is beyond the scope of this chapter to go into detailed discussion of the input parameters and how they were established; it suffices to say here that all parameters (k-point number, maximum g-vector, muffin tin potential radius) were the minimum value requirements for convergence of the calculations to occur, and that a detailed discussion of the procedures and the results of WIEN calculations of hydrogenated graphene can be found in Bangert et al. 2010b.

Also shown in figure 17a) is a calculated EEL spectrum for single-layer graphene. It matches the experimental spectrum very well. Surprisingly flat and corrugated unhydrogenated graphene both produce similar π-plasmons, indicating the presence of a π-electron system even in corrugated graphene. Figure 17b) shows the evolution of the π-plasmon in fully hydrogenated graphene (also termed graphane) with increasing corrugation angle. Interestingly, flat graphane, similar to graphene, possesses a π-plasmon. However, its energy is slightly higher then experimentally observed. The π-plamon has nearly vanished

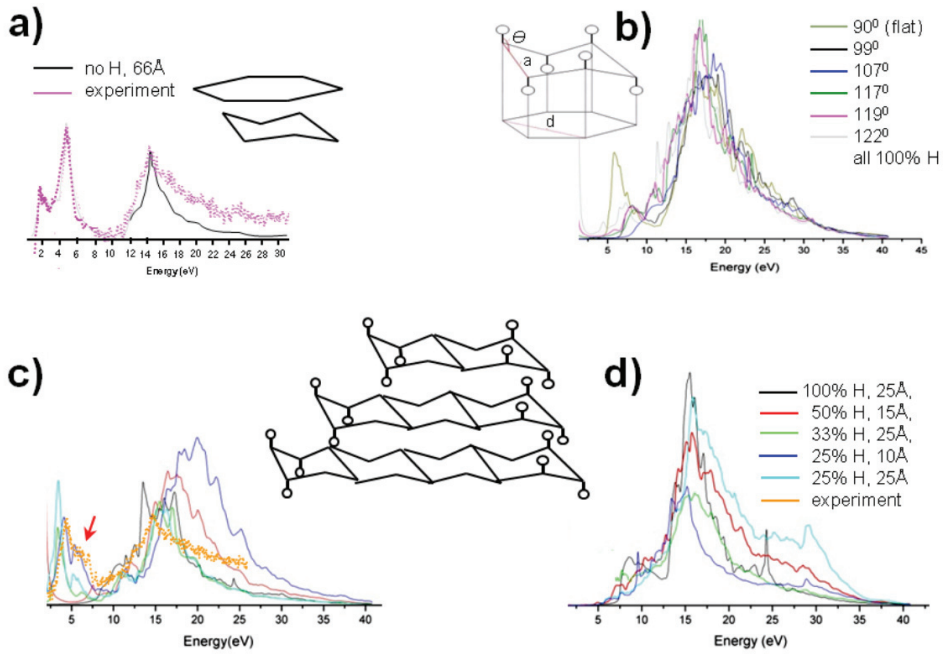

Fig. 17. WIEN 2K calculations of low loss EEL spectra for a) non hydrogenated graphene in flat and corrugated geometry for the in-plane plasmon component ($\boldsymbol{q}||\boldsymbol{a}$) with overlaid experimental spectrum. Note the agreement in the pre-plasmon structure; b) fully hydrogenated graphene with varying corrugation angle Θ, again, for ($\boldsymbol{q}||\boldsymbol{a}$). c) and d) show calculated in-plane and out-of-plane ($\boldsymbol{q}||\boldsymbol{c}$) plasmon components for corrugated graphene (Θ=114^0) with different hydrogen content (given in % in the legend; model structures are shown in the sketch). The orange spectrum overlaid in (c) is an experimental spectrum of a hydrocarbon-free region in H-dosed graphene. Note the disappearance of the pre-plasmon feature and the occurrence of an extra peak at ~7eV. The distances given in Å in the legends are the separation distances of the graphene sheets, or the supercell dimension along the c-axis. Further detail and fuller explanation of the input parameters (k-point number, muffin-tin radii etc) are given in Bangert et al. 2010b.

for 10^0 out-off-plane bending of bonds, and has disappeared for 22^0 bond bending. A feature at ~6-7 eV emerges at the rise of a (presumably) pure σ-plasmon, which sits at slightly higher energy then the π+σ-plasmon in graphene. Hence sp^3 character does become established in corrugated graphene, when all bonds are used. It should be noted that (a) and (b) show the in-plane plasmon component. Figures 17c) and d) show plasmon calculations of the in-plane and the out-off-plane plasmon component for different hydrogen coverages for a sheet corrugation angle of 114^0 (as deduced from diffraction experiments (Elias et al, 2009)). The overlaid experimental spectrum fits the >25% hydrogenation cases rather well. The out-off plane component does not have a π-plasmon for any hydrogen coverage. Models to describe possible structural scenarios are shown as inset. It becomes clear that corrugation is essential to produce the ~7eV feature, as is occurrence of sp^3-character. In order be preserve π-bonding, however, the corrugation angles have either to be small (as

would be the case for strained graphene, if it is hydrogenated mainly on one surface (Xue & Xu, 2010)) or unhydrogenated areas have to be present,. Alternatively or simultaneously, hydrogenated patches could be interleaved with pure graphene areas. The low loss region thus provides a wealth of information, which we have only just started to explore.

7. Acknowledgements

We gratefully acknowledge our colleagues from the University of Manchester, A. Geim and K. Novoselov for stimulating discussions and R. R. Nair for provision and hydrogenation of samples. We thank Q. Ramasse from the SuperSTEM for conducting the Au-on-graphene STEM measurements and J. Vandenberg from Salford University for the low energy ion-implantations.

8. Conclusions

Combined HAADF/BF imaging in an AC STEM has proven a most powerful method to 'see' directly the atomic-scale landscapes of graphene; the former imaging mode provides chemical information and position of atoms, the latter, due to the stronger contrast, helps relate positions of ad-atom/ impurities with sites on benzene rings. Ultra-high resolution EELS has proven an invaluable add-on to identify the chemical nature of individual atoms, especially those with $Z \leq 6$, and to gain information about local bonding and electronic bandstructure.

The imaging studies revealed extensive hydrocarbon contamination on every single graphene sample, independent of growth method or fabrication procedure, as well as a fair proportion of multiple layers and –in CVD grown samples- predominance of turbostratic arrangements. Here we present facts concerning uncontaminated ('model') graphene, which exists in patches of only few 10s of nm in diameter interspersed with extended chain-like adsorbate networks. In 'model' graphene we have shown existence of nanometer-size ripples, point- and ring defects and omnipresence of C-adatoms above C-C bonds. We have identified metal impurity sites and found Au- and Ni-atoms taking up T-sites on benzene rings, and Fe-atoms to occupy B-sites; the former in agreement with and the latter contradicting theoretical predictions. H can be found on clean graphene, and to a much larger extent on hydrogen-dosed graphene. EELS in combinations with DFT WIEN calculations shows the structure of the latter is concomitant with corrugated graphene possessing partial H-coverage and small corrugation angles, or/and co-existence of unhydrogenated areas. Plasmons in graphene show unique behaviour and can be used to identify single layers.

9. References

Annet, J. F., Palmer, R. B & Willis, R. F., 'Surface dielectric response of a semimetal- electron energy loss spectroscopy of graphite', *Phys. Rev. B* 37, 2408-2414 (1988)

Aktürk, O.Ü. & Tomak, M., 'AuPt clusters adsorbed on graphene studied by first-principles calculations', *Phys. Rev. B* 80, 085417 (2009)

Bangert, U., Barnes, R., Hounsome, L. S., Jones, R., Blumenau, A. T., Briddon, P. R., Shaw, M. J. & Öberg, S., 'Electron energy loss spectroscopic studies of brown diamonds' *Phil Mag* 86 (29-30), 4757-4779 (2006)

Bangert, U., Eberlein, T., Nair, R. R., Jones, R., Gass, M. H., Bleloch, A. L., Novoselov, K. S., Geim, A., Briddon P. R., 'STEM plasmon spectroscopy of free standing graphene', *phys. stat. sol. A* 205 (9), 2265-2269 (2008)

Bangert, U., Gass, M. H., Bleloch, A. L., Nair, R. R. & Geim, A. K., 'Manifestation of ripples in free-standing graphene in lattice images obtained in an aberration-corrected scanning transmission electron microscope', *phys. stat. sol. A* 206 (6), 1117-1122 (2009a)

Bangert, U., Gass, M. H., Bleloch, A. L., Nair, R. R. & Eccles, J., 'Nanotopography of graphene' *phys. stat. sol. A,* 206 (9), 2115-2119 (2009b)

Bangert, U., Bleloch, A. L., Gass, M. H., Seepujak, A. & Vandenberg, J., 'Doping of few-layered graphene and carbon nanotubes using ion implantation', *Phys. Rev. B* 81(24), 245423 (2010a)

Bangert, U., Pan, C.-T., Nair, R. R. & Gass, M. H., 'Atomic structure and low electron loss characteristics of hydrogen-dosed graphene deduced from STEM experiments and DFT-WIEN calculations', *Appl. Phys. Lett.*, 97, 253118 (2010b)

Batson, P. E., 'Simultaneous STEM imaging and electron-energy-loss-spectroscopy with atomic-column sensitivity' *Nature* 366 (6457), 727-728 (1993)

Blaha, P., Schwarz,K., Madson, G., Kvasnicka D. & Luitz, J, *User's guide WIEN 2k_10.1* at www.wien2k.at/reg_user/textbooks/usersguide.pdf

Booth, T. J., Blake P., Nair, R. R., Jiang, D., Hill, E.W. , Bangert, U., Bleloch, A. L., Gass, M., Novoselov, K. S. M., Katsnelson , I. & Geim , A. K., 'Macroscopic graphene membranes and their extraordinary stiffness', *Nano Lett.,* 9 (4), 1433-1441 (2008)

Borglund, N., Astrand, P.-G. & Csillag, S., 'Improved background removal method using principal components analysis for spatially resolved electron energy loss spectroscopy' *Microsc. Microanal.* 11(1), 88-96 (2005)

Browning, N. & Pennycook, S., 'Atomic-resolution electron energy-loss spectroscopy in the scanning transmission electron microscope', *J. Microsc.-Oxford* 180, 230-237 (1995)

Brydson, R., *Electron Energy Loss Spectroscopy*, Garland Science, England (2003)

Boukhvalov, D.W. & Katsnelson, M.I., 'Destruction of graphene by metal adatoms', *Appl. Phys. Lett.* 95 (2), 023109 (2009)

Bourelle, E., Konno, H. & Inagaki, M., 'Structural defects created on natural graphite surface by slight treatment of oxygen plasma - STM observations', *Carbon* 37 (12), 2041-2048 (1999)

Chan, K. T., Neaton, J. B. & Cohen, N. L., 'First-principles study of metal adatom adsorption on graphene', *Phys Rev B* 77 (23), 235430 (2008)

Charlier, J.-C., 'Defects in carbon nanotubes', *Acc. Chem. Res.* 35 (12), 1063-1069 (2002)

Charlier, J.-C., Arnaud, L. , Delgado, M., Demoisson, F., Espinosa, E. H., Ewels, C. P., Felten, A., Guillot, J., Ionescu, R., Leghrib, R., Llobet, EMansour, A., Migeon, H-N, Pireaux, J-J., Reniers, F., Suarez-Martinez, I., Watson, G. E. & Zanolli, Z., 'Carbon nanotubes randomly decorated with gold clusters: from nano(2)hybrid atomic structures to gas sensing prototypes', *Nanotechnology* 20 (37), 375501 (2009)

Crespi, V. H., Cohen, M. L. & Rubio, A., 'In situ band gap engineering of carbon nanotubes', *Phys Rev Lett* 79 (11), 2093-2096 (1997)

Duplock, E. J., Scheffler, M. & Lindan, P. J. D, 'Hallmark of perfect graphene', *Phys Rev Lett* 92 (22), 225502 (2004)

Eberlein, T., Bangert, U., Nair, R. R., Jones, R., Gass, M., Bleloch, A. L., Novoselov, K. S., Geim, A. K. & Briddon, P. R., 'Plasmon spectroscopy of free-standing graphene films', *Phys Rev B* 77, 233406 (2008)

Egerton, R. F., *Electron Energy Loss Spectroscopy in the Electron Microscope'*, Plenum Press N.Y. (1986)

Elias, D. C., Nair, R. R., Mohiuddin, T. M. G., Morozov, S. V., Blake, P.,. Halsall, M. P., Ferrari, A. C., Boukhvalov, D. W., Katsnelson, M. I.,Geim, A. K. & Novoselov, K. S., 'Control of Graphene's Properties by Reversible Hydrogenation: Evidence for Graphane', *Science* 323 (5914), 610-613 (2009)

Ewels, C. P., Heggie, M. I. & Briddon, P. R., 'Adatoms and nanoengineering of carbon', *Chem. Phys. Lett.* 351, 178 (2002)

Fall, C. J., Blumenau, A. T., Jones, R., Briddon, P. R., Frauenheim, T.,Gutiérrez-Sosa, A., Bangert, U., Mora, A. E., Steeds, J. W. & Butler, P. E., 'Dislocations in diamond: Electron energy-loss spectroscopy', *Phys. Rev. B* 65 (24), 205206 (2002)

Fasolino, A., Los, J. H. & Katnelson, M. I., 'Intrinsic ripples in graphene', *Nature Materials 6* (11), 858-861 (2007)

Fuentes, G. G., Borowiak-Palen, E., Pichler, T., Liu, X., Graff, A., Behr, G., Kalenczuk, R. J., Knupfer, M. & Fink, J., 'Electronic structure of multiwall boron nitride nanotubes', *Phys. Rev. B* 67 (3), 035429 (2003)

Gan, Y., Sun, L.T, & Banhart F., 'One- and two-dimensional diffusion of metal atoms in graphene', *Small* 4 (5), 587–591 (2008)

Gass, M. H., Bangert, U., Bleloch, A. L., Wang, P., Nair R. R. & Geim, A. K., 'Free-standing graphene at atomic resolution', *Nature Nanotechnology* 3 (11), 676-681, (2008)

Goodhew, P. & Bleloch, A. L., 'SuperSTEM - the microscope with glasses', Mater. World 11 (3), 23-24 (2003)

Haberer, D., Vyalikh, D. V., Taioli, S., Dora, B., Farjam, M., Fink, J., Marchenko, D., Pichler, T., Ziegler, K., Simonucci, S., Dresselhaus, M. S., Knupfer, M., Büchner B.& Grüneis, A., 'Tunable Band Gap in Hydrogenated Quasi-Free-standing Graphene', *Nano Lett.* 10, 3360-3366 (2010)

Hahn, R. & Kang, H., 'Vacancy and interstitial defects at graphite surfaces: Scanning tunneling microscopic study of the structure, electronic property, and yield for ion-induced defect creation', *Phys. Rev. B* 60 (8), 6007-6017 (1999)

HREM Research Inc., DeConvHAADF User's Guide (2009)

Hunt, A. & Williams, D. B., 'Electron energy-loss spectrum imaging', Ultramicroscopy 38 (1), 47-73 (1991)

Ito, A., Nakamura, H. & Takayama, A., 'Molecular Dynamics Simulation of the Chemical Interaction between Hydrogen Atom and Graphene', *J. Phys. Soc. Jpn* 77 (11), 114602 (2008)

Jenkins, G. M., 'Basal plane distortion in pyrolytic carbon', *Carbon* 7, 9 (1969)

Jeanguillaume, C. & Colliex, C., 'Spectrum image- the next step in EELS digital acquisition and processing', *Ultramicroscopy* 28 (1-4), 252-257 (1989)

Leenaerts, O., Partoens, B., Peeters, F. M., 'Adsorption of H_2O, NH_3, CO, NO_2, and NO on graphene: A first-principles study', *Phys. Rev. B* 77 (12), 125416 (2008)

Leenaerts, O., Partoens, B., Peeters, F. M., 'Adsorption of small molecules on graphene', *Microelectronics Journal* 40 (4-5), 860–862 (2009)

Jeloaica, L. & Sidis, V., *Chem. Phys. Lett.* 300, 157 (1999)

Jones, R., Coomer, B. J., Goss, J. P., Hourahine, B. & Resende A., 'The interaction of hydrogen with deep level defects in silicon' in: *Special defects in semiconducting materials,* Volume 71 of *Solid State Phenomena*, Chapter 173-248. Scitech Publications Ltd., Zuerich-Uetikon, Switzerland, (2000)

Kirkland, E., *Advanced Computing in Electron Microscopy*, New York: Plenum (2005)

Kociak, M., Stéphan, O., Henrard, L., Charbois, V., Rothschild, A., Tenne, R. & Colliex, C., 'Experimental evidence of surface-plasmon coupling in anisotropic hollow nanoparticles', *Phys. Rev. Lett.* 87 (7), 077501 (2001)

Krasheninnikov, A. V., Nordlung, K., Sirviö, M., Salonen, E. & Keinonen, J., 'Formation of ion-irradiation-induced atomic-scale defects on walls of carbon nanotubes', *Phys Rev B* 63 (24), 245405 (2001)

Krasheninnikov, A. V., Lehtinen, P. O., Foster, A. S., Pyykko, P., Nieminen, R. M., 'Embedding transition-metal atoms in graphene: structure, bonding, and magnetism', *Phys. Rev. Lett.* 2 (12), 126807 (2009)

Laitenberger, P. & Palmer, R. B., 'Plasmon dispersion and damping at the surface of a semimetal', *Phys. Rev.Lett.* 76 (11), 1952-1955 (1996)

Mao, Y., Juan, J. & Zhong, J., 'Density functional calculation of transition metal adatom adsorption on graphene', *J Phys: Condens Matter* 20 (11), 115209 (2008)

Meyer, J. C., Geim, A. K., Katsnelson, M. I., Novoselov, K. S., Booth, T. J. & Roth, 'The structure of suspended graphene sheets,' *Nature* 446, 60-63 (2007a)

Meyer. J. C., Geim, A. K., Katsnelson, M. I., Novoselov, Obergfell, D., Roth, S., Girit, C. & Zettl, A., 'On the roughness of single- and bi-layer graphene membranes', *Solid State Commun.* 143, 101-109 (2007b)

Meyer, J. C., Kisielowski, C., Erni, R., Rossell, M. D., Crommie, M F & Zettl, A., 'Direct imaging of lattice atoms ond topological defects in graphene membranes' *Nano Lett.* 8(11), 3582 (2008a)

Meyer, J. C., Girit, C. O., Crommie, M. F. & Zettl, A., 'Imaging and dynamics of light molecules on graphene', *Nature* 454, 319-322 (2008b)

Murrell, J. N.& Schmidt, W., *J.* 'Photoelectron spectroscopic correlation of molecular-orbitals of methane, ethane, propane, isobutane and neopentane', *Chem. Soc.-Faraday Trans.II,* 68 (10) 1709-1718 (1972)

Nelhiebel, M., Louf, P. H., Schattschneider, P, Blaha, P, Schwarz, K.& Jouffrey, B., 'Theory of orientation-sensitive near-edge fine-structure core-level spectroscopy', *Phys. Rev. B* 59 (20), 12807-12814 (1999)

Nelson, N. D., Piran T. & S. Weinberg, (eds.) *Statistical Mechanics of Membranes and Surfaces* , World Scientific, Singapore, (2004).

Nordlund, K., Keinonen, J. & Mattila, T., 'Formation of ion irradiation induced small-scale defects on graphite surfaces', *Phys. Rev. Lett.* 77 (4), 699-702 (1996)

Otto, A., 'Theory of plasmon excitations in thin films by electrons of non-normal incidence', *phys. stat. sol.* 22 (2), 401-406 (1967)

Pennycook, S., & Boatner, L.A., 'Chemically sensitive structure-imaging with a scanning transmission electron microscope', *Nature* 336 (6199), 565-567 (1988)

Perez, R. & Que, W., 'Plasmons in isolated single-walled carbon nanotubes', *J. Phys: Condens. Matter* 18 (12), 3197-3216 (2006)

Pomoell, J., Krasheninnikov, A. V., Nordlund, K. & Keinonen, J., 'Stopping of energetic ions in carbon nanotubes', *Nucl. Instr. Meth. in Phys. Res. B* 206, 18-21 (2003).

Raether, H.,' Surface plasma oscillations and their applications' in: *Physics of Thin Films*. Vol 9, p 145ff, Academic Press, New York - London (1977)

Sevincli, H., Topsakal, M., Durgun, E. & Ciraci, S., 'Electronic and magnetic properties of 3d transition-metal atom adsorbed graphene and graphene nanoribbons *Phys Rev B* 77 (19), 195434 (2008)

Sofo, J. O., Chaudhari, A. S. & Barber, G. D., ,Graphane: A two-dimensional hydrocarbon', *Phys. Rev.* B 75 (15), 153401 (2007)

Stéphan, O., Taverna, D., Kociak, M., Suenaga, K., Henrard, L. & Colliex, C., 'Dielectric response of isolated carbon nanotubes investigated by spatially resolved electron energy-loss spectroscopy: From multiwalled to single-walled nanotubes', *Phys. Rev. B* 66 (15), 155422 (2002)

Stolyarova, E., Rim, K.- T., Ryu, S. M., Maultzsch, J., Kim, P., Brus, L. E., Heinz, T. F., Hybertsen, M. S. & Flynn, G. W., 'High-resolution scanning tunneling microscopy imaging of mesoscopic graphene sheets on an insulating surface', Proceedings of PNAS of the U. S. A, 104 (22), 9209-9212, May 2007

Suarez-Martinez, I., Felten, A., Pireaux, J. J., Bittencourt, C. & Ewels, C. P., 'Transition Metal Deposition on Graphene and Carbon Nanotubes' *J Nanosci. Nanotechnol*. 9 (10), 6171-6175 (2009)

Telling, R. H. & Heggie, M. I., 'Radiation defects in graphite', *Phil Mag* 87 (31), 4797-4846 (2007)

Terrones, M. & Terrones, H., 'The role of defects in graphitic structures', *Fullerene Sci and Tecnol* 4 (3), 517-533 (1996)

Uchoa, B., Lin, C.-Y. & Neto, A. H. C, 'Tailoring graphene with metals on top' *Phys Rev B* 77 (3), 35420 (2008)

Varns, R. & Strange, P., 'Stability of gold atoms and dimers adsorbed on graphene', *J. Phys.: Condens. Matter* 20 (22), 225005 (2008)

Xue, K. & Xu, Z.-P., 'Strain effects on basal-plane hydrogenation of graphene: A first-principles study', *Appl. Phys. Lett.* 96 (6), 063103 (2010)

Zhou, Z.-H., Gao, F. & Goodman, D. W., 'Deposition of metal clusters on single-layer graphene/Ru (0001): Factors that govern cluster growth', *Surface Science* 604 (13-14), L31–L38 (2010)

16

Electrical Conductivity of Melt Compounded Functionalized Graphene Sheets Filled Polyethyleneterephthalate Composites

Haobin Zhang[1], Shunlun He[2*], Cao Chen[1],
Wenge Zheng[1*] and Qing Yan[1]
[1]*Ningbo Key Laboratory of Polymer Materials, Division of Polymers and Composites, Ningbo Institute of Material Technology & Engineering, Chinese Academy of Sciences,*
[2]*Orinko Plastics Group,*
China

1. Introduction

Graphene, monolayer of carbon atoms arranged in a honeycomb network, has recently gained revolutionary aspirations (Novoselov et al., 2005; Novoselov et al., 2007; Heersche et al., 2007; Zhang (a) et al., 2005; Stankovich et al., 2006) because of its remarkable electronic properties (Zhang (b) et al., 2005; Berger et al., 2004), unusual thermal properties (Balandin et al., 2008) and good mechanical properties (Lee et al., 2008). These extraordinary properties make it an excellent choice as inorganic fillers to substantially improve electrical, thermal and mechanical properties of composite materials (Stankovich et al., 2006; Ramanathan et al., 2008). Several effective techniques have been developed for preparing graphene nanosheets, including chemical (Stankovich et al., 2006) and mechanical exfoliation (Novoselov et al., 2004), alkali metals intercalation and expansion (Viculis et al., 2003), microwave chemical vapor deposition (Wang et al., 2009), substrate-based thermal decomposition (Berger et al., 2004), and thermal exfoliation of graphite oxide (GO) (McAllister et al., 2007). Among them, chemical reduction of exfoliated graphite oxide in the presence of a surfactant or polymer is a relatively new method to prepare electrically conductive individual graphene sheets. Stankovich (Stankovich et al., 2006) put forward a new process to produce polystyrene/graphene nanocomposites via ultrasonic exfoliation and chemical reduction of graphite oxide and molecular-level dispersion of chemically modified graphene nanosheets. In addition, the thermal exfoliation and in situ reduction method can conveniently produce graphene nanosheets for mass production. As confirmed by Aksay and co-workers (McAllister et al., 2007), in situ reduction reaction took place during the thermal exfoliation process, which converted insulating graphite oxide to conducting graphene. More importantly, the graphene resulted through thermal exfoliation still contained some oxygen-containing groups. The oxygen functionalities on the graphene nanosheets will facilitate their dispersion in polar polymers (Ramanathan et al., 2008). Effective medium approximation indicated that graphene is more effective in improving conductivity of composites than carbon nanotubes (Xie et al., 2008). The polystyrene/graphene nanocomposites prepared by chemical modification and reduction in

solution exhibited a percolation threshold in electrical conductivity as low as 0.1 vol%, comparable to those observed in single-walled carbon nanotubes (SWCNT) based nanocomposites (Grossiord et al., 2005; McLachlan et al., 2005); The electrical conductivity was as high as 1 S/m at 2.5 vol% of graphene content. Kim and Macosko (Kim & Macosko, 2008) compared the effect of graphene nanosheets and graphite on conductivity of polyester-based composites, and the results revealed that graphene gave a much lower percolation threshold (0.3 vol%) than graphite (3.0 vol%). Recently, Liang et al. (Liang et al., 2009) prepared epoxy/graphene nanocomposites via in situ process, which showed a small percolation threshold of 0.52 vol% and an electromagnetic interference shielding efficiency of 21dB with 8.8 vol% of graphene over 8.2~12.4 GHz. In contrast, unfully exfoliated graphite led to a much higher threshold (> 0.6 vol%) and a much lower electrical conductivity (< 10-2 S/m) even at high loading of 6.0 vol% (Kalaitzidou et al., 2007; Weng et al., 2005; Zheng et al., 2002).

Compared to in situ polymerization and solution mixing, melt compounding using conventional compounding devices such as mixers and commercial resins is more attractive because this approach provides manufacturers many degrees of freedom with regard to the selection of polymer grades and choice of graphene content. It is believed that melt compounding would be more economical and simple than in situ polymerization processes. Actually, melt compounding has been successfully used to prepare conductive polymeric composites by using conducting fillers such as carbon nanotubes (CNTs) (Li et al., 2006), carbon black and expanded graphite (Lagreve et al., 2006; Zhang et al., 2008). It has been confirmed that CNTs can substantially increase the electrical conductivity of PET nanocomposites with low loading of CNT, but it is expensive. As for cheap carbon black, higher loading is usually required to make a polymer conductive. Due to the low price and availability of pristine graphite in large quantities, graphene nanosheets can be an ideal choice as conductive fillers in the preparation of conductive PET nanocomposites. To the best of our knowledge, few papers have been published on PET/graphene nanocomposites prepared by conventional melt compounding. In this study, Graphene nanosheets were prepared by complete oxidation of pristine graphite followed by thermal exfoliation and reduction. Subsequently, polyethylene terephthalate/graphene nanocomposites were prepared by melt compounding. The microstructure of graphene, its dispersion in PET matrix, and the electrically conductive behavior of the resulting nanocomposites were studied.

2. Experimental

2.1 Materials

PET pellets were purchased and dried in vacuum oven at 150 oC for 5 h before use. Flaky pristine graphite with a mean size of 45 μm was bought from Qingdao Huatai Lubricant Sealing S&T (China). Graphene density is assumed to be equal to the theoretical graphite density of 2.28 g/cm3 (Kelly, 1981), and PET density is 1.34 g/cm3 (Cobbs & Burton, 1953). Fuming nitric acid (63%), sulfuric acid (98%), potassium chlorate (98%) and hydrochloric acid (37%) were obtained from Sinopharm Chemical Reagent (China).

2.2 Preparation of graphene

A technique, similar to that of Aksay and co-workers (Schniepp et al., 2006), was used to prepare bulk quantities of graphene nanosheets. Graphite oxide (GO) was prepared according to Staudenmaier method (Staudenmaier, 1898). First of all, the reaction flask was

purged with nitrogen and immersed in an ice bath, 40 g graphite was then added to the homogeneous mixture of concentrated nitric acid (270 ml) and sulfuric acid (525 ml) under vigorous stirring. After uniform dispersion of the graphite powder, 330 g potassium chlorate was added slowly to minimize the risk of explosion. The reaction was then allowed to last for 120 h at room temperature. After reaction, the slurry resultants were filtered and washed with excess deionized water and 5% HCl solution to remove the sulfuric ions (SO_4^{2-}), then GO aqueous solution was neutralized with potassium hydroxide solution. GO powder was separated from the solution by using GQ75 high-speed centrifuge, and dried in an air-circulating oven at 135°C for 24 h followed by another 24 h at 135°C in a vacuum oven. As confirmed by Aksay and co-workers (McAllister et al., 2007), 1050°C was adequate for thermal exfoliation and in situ reduction of GO, this temperature was also adopted in the present work to thermally exfoliate GO. The dried GO powder was quickly inserted into a muffle furnace preheated to 1050 oC and held in the furnace for 30s.

2.3 Fabrication of PET composites

PET/graphene nanocomposites were prepared by melt compounding at 285°C using a Brabender mixer. Compounding was performed with an initial screw speed of 50 rpm/min for 4 minutes; then the screw speed was raised to 100 rpm/min within 1 min and the compounding was conducted at this speed for 5 min. The samples for microscopy and electrical conductivity analysis were prepared by pressing the composites at 275°C under a pressure of 15 MPa.

2.4 Characterization

The volume conductivity of moderately conductive composites (Conductance $>10^{-6}$ S·m) was measured with a Agilent 34401A digital multimeter and a YOKOGAWA 7651 voltage source by the two-probe method. For PET and composites with low conductivity (Conductance $\leq 10^{-6}$ S·m), the conductivity testing was performed using a EST121 ultrahigh resistance and micro current meter (Beijing EST Science & Technology CO. LTD) according to National Standard of China GB/1410-1989. A three-terminal fixture (two electrodes plus guard), similar to that proposed by the ASTM D257 standard for volume conductance determination of flat specimens, was selected for the measurement of low conductance. The guard electrode connected to the earth was used to eliminate the leakage current along specimen surface. In addition, the testing fixture was embedded in a metal shield box to minimize external interference. Circular plates with 7 cm in diameter and 2.5 mm in thickness were fabricated for conductivity measurement. Sample surfaces were coated with silver paste to reduce contact resistance between sample and electrodes. For specimens with low conductivity, the side contacting with the unguarded electrode was wholly painted with silver paste while the other side only partly painted, the painted area was in accordance with the cross-section of the guarded cylinder electrode. Three specimens of each sample were tested and the average value was reported as volume electrical conductivity. The resistance R can be obtained directly from the multimeter, and thus the electrical conductivity σ can be calculated by using Eq. (1)

$$\sigma = \frac{1}{\rho} = \frac{t}{RS} \tag{1}$$

where ρ is electrical resistivity, t is thickness of sample between electrodes, and S is cross-sectional area of the guarded cylinder electrode.

The microstructures of graphene and its PET nanocomposites were characterized using a Tecnai G2 F20 TEM at an accelerating voltage of 100 kV. Graphene sheets were dispersed in methanol by ultrasonication and some pieces were collected on carbon-coated 300-mesh copper grids for observation. While for PET/graphene nanocomposites, the samples were embedded in epoxy resin, and cured at 80 oC for 6 h, and then ultrathin sections of thinner than 100 nm were cryogenically cut with a diamond knife using a microtome and collected on 300-mesh copper grids. SEM observation of PET composites was performed using an FEI scanning electron microscope (Hitachi, S-4800) with an accelerating voltage of 5 kV. PET composites were freeze-fractured in liquid nitrogen and the fractured section was coated with a thin layer of platinum before observation.
The diffraction behavior of pristine graphite, GO and graphene were studied using a Bruker AXS X-ray diffractometer with CuKα radiation at a generator voltage of 40 kV and a generator current of 40 mA. The scans were carried out in the reflection mode at a scan rate of 10°/min. Laser granularity analyzer (Malven, Zeta sizer Nano ZS) was used to determine the lateral dimension of graphene in alcohol solution.

3. Results and discussion

3.1 Characterization of graphene

Figure. 1 shows the XRD spectra of pristine graphite, graphite oxide and graphene. The strong and sharp diffraction peak of pristine graphite at 26.6o completely disappeared after oxidization and instead a new peak at 13.9° appeared, indicating a complete oxidization of graphite (Wang et al., 2008), which is a prerequisite to obtain exfoliated graphene nanosheets by ultrasonication or thermal expansion. After thermal exfoliation of the completely oxidized graphite (GO), there was no apparent diffraction peak detected, which means the periodic structure of GO was eliminated and graphene nanosheets were formed.

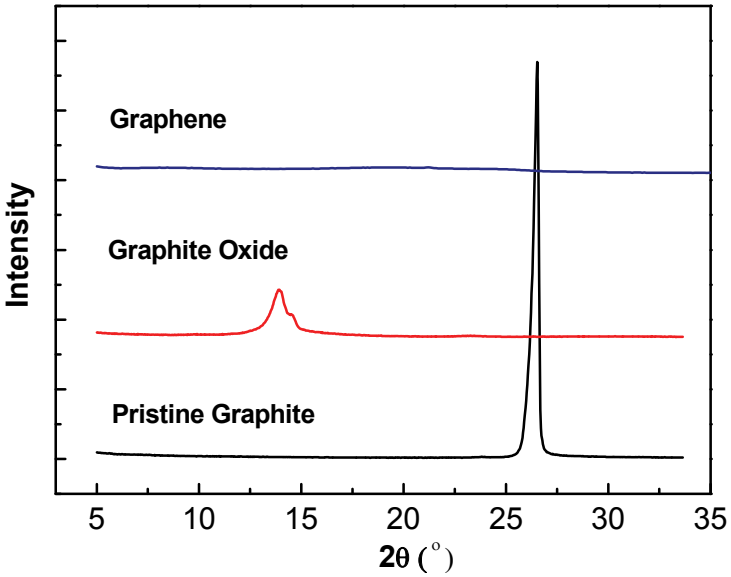

Fig. 1. X-ray diffraction patterns of pristine graphite, graphite oxide and graphene.

Figure 2 shows TEM images of the graphene under low and high magnifications. Under low magnification, graphene looks like a transparent ultrathin film with a few thin ripples within the plane (Figure. 2a), quite different from the opaque and smooth feature of pristine graphite flakes. It is known that perfect two-dimensional graphene crystal was thermodynamically unstable (Meyer et al., 2007), therefore corrugations and ripples in the two dimension were formed for thermodynamic stability (Carlsson, 2007). Thereby the transparency and rippled feature of graphene, in turn, suggests a fact that graphene sheets prepared in this study are wafer thin and consists of few-layer or even monolayer graphene. Furthermore, stacks of graphene sheets arranged with a roughly parallel structure can be clearly observed in the high-magnification TEM image from an edge-on view (Figure. 2b).

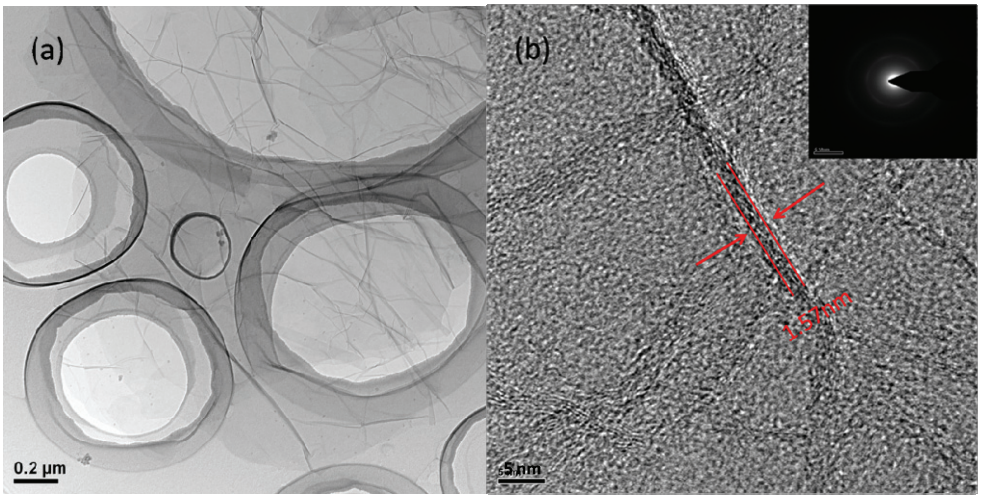

Fig. 2. TEM images of graphene under low (a) and high (b) magnifications. The scale bars are (a) 0.2 μm and (b) 5 nm. The inset is selected area electron diffraction (SAED) pattern of graphene.

The thickness of graphene sheets can thus be measured. Statistical results from many TEM images give an average thickness ~ 1.57 nm of the graphene sheets prepared in this study. In addition, the weak and diffuse selected area electron diffraction (SAED) pattern (the inset of figure. 2b) also indicates the loss of long range ordering between graphene sheets and the ultrathin feature of the graphene. However, it should be mentioned that the specific surface area of the graphene sheets measured with BET method is 555 m2/g , much smaller than the theoretical value (2630 m2/g) of single graphene sheet (Peigney et al., 2001), indicating that existence of agglomerated and overlapped parts of the graphene sheets. In spite of this, a high aspect ratio (lateral dimension to thickness) of 146 for the graphene sheets is obtained based on the results from laser granularity analyzer. In contrast, pristine graphite flake has a lower aspect ratio (~36) and smaller specific surface area (< 10 m2/g).

3.2 Microstructure of PET/graphene nanocomposites

To clearly reveal the dispersion of graphene in PET matrix, Figure 3 shows the microstructure of PET nanocomposite with 3 vol% graphene. Graphene nanosheets were

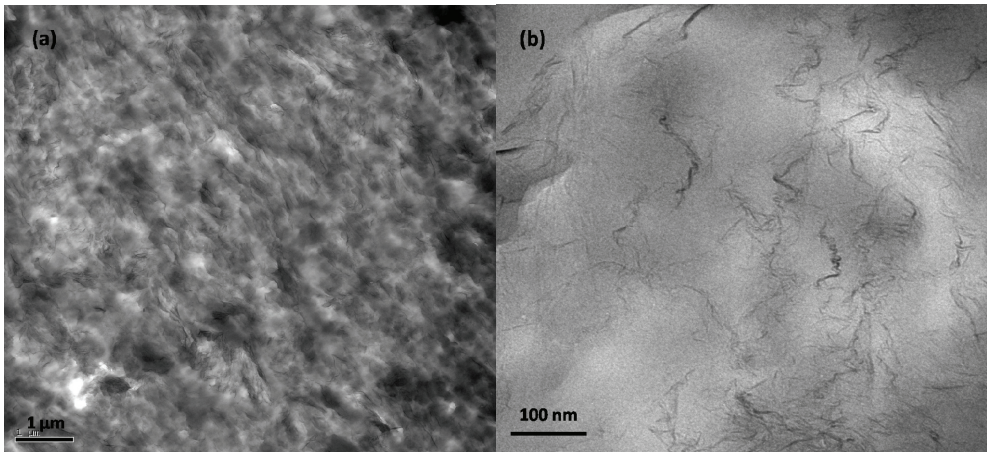

Fig. 3. Low (a) and high (b) magnification TEM micrographs of PET nanocomposite with 3 vol% graphene. The scale bars are (a) 1 µm and (b) 100 nm.

homogeneously dispersed in PET matrix and there are almost no large agglomerates observed (Figure. 3a).

The good dispersion of graphene sheets should be due to the good interaction between the oxygen and hydroxyl functional groups on the surface of graphene and the polar groups of PET. In addition, a compact continuous network throughout the matrix is also observed (Figure. 3a). As proposed by Alig et al (Alig et al., 2007), this conductive network can be considered as a network built by conductive fillers which are separated by local contact regions with polymer chains in-between, also improving electron mobility and interface polarization via tunneling (Yao et al., 2007). High magnification image (Figure. 3b) indicates that the network is composed of abundant thin stacks of a few sheets of monolayer graphene (black curly thin lines), which are bridged by the crumpled or overlapped graphene sheets (slightly thicker lines) (Figure. 3b). These wrinkled and overlapped graphene sheets can effectively link individual graphene sheets and carry high density of current, resulting in high electrical conductivity (Halperin et al., 1985).

To demonstrate the strong interaction between the oxygen and hydroxyl functional groups on the surface of graphene and the polar groups of PET, Figure 4 shows SEM image of cryo-fractured surface of PET nanocomposite with 1.2 vol% graphene. It is seen that the graphene sheets were encapsulated by PET and the thickness of the sheets increased from 1.57 to ~ 50 nm (see the inset of Fig. 4). This confirms the strong interaction between graphene and PET. Due to the large specific surface area of the graphene nanosheets, the area of interface between graphene and PET is huge, providing numerous tunneling sites for electron transport (Steinert & Dean, 2009).

3.3 Electrical properties of PET/graphene nanocomposites

Figure. 5 shows plots of electrical conductivity versus filler content for PET/graphene nanocomposites and PET/pristine graphite composites.

The PET/graphene nanocomposites exhibit a sharp transition from insulator to semiconductor with a small percolation threshold of 0.47 vol%. With a small increase of graphene content from 0.47 to 1.2 vol%, the electrical conductivity of the PET

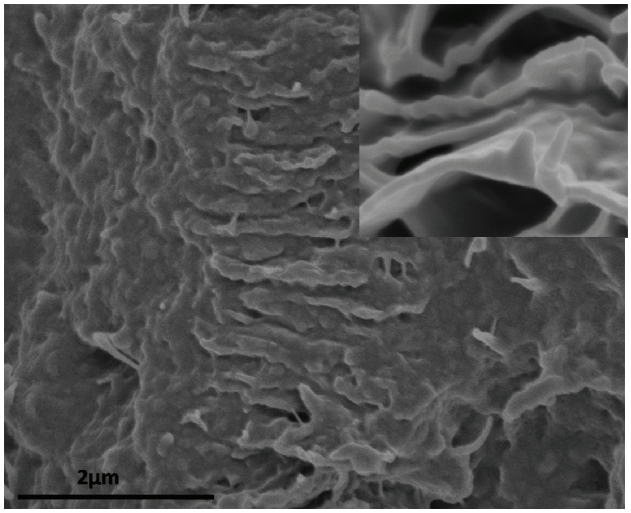

Fig. 4. SEM images of fractured surface of PET nanocomposite with 1.2 vol% of graphene. The insert is a high-magnification SEM image of the same nanocomposite.

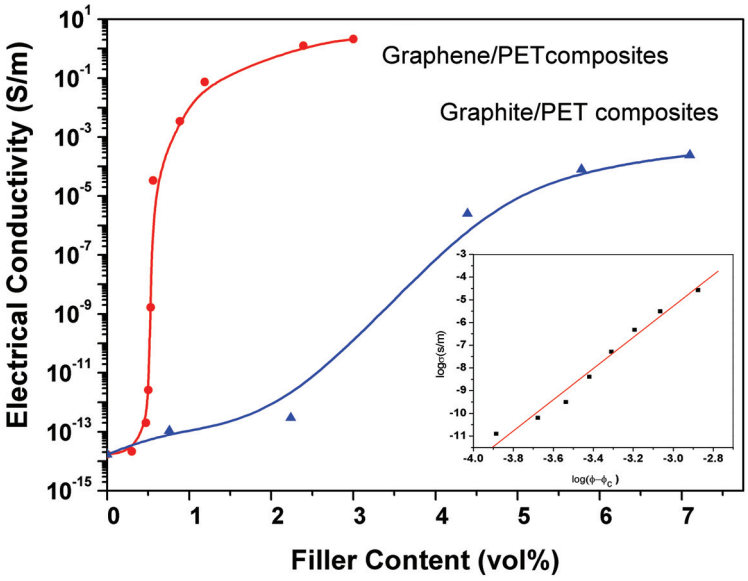

Fig. 5. Plots of electrical conductivity versus filler content for PET/graphene nanocomposites and PET/graphite composites. The inset is double-logarithmic plot of volume electrical conductivity versus (φ-φc).

nanocomposites increased quickly from 2.0×10^{-13} to 7.4×10^{-2} S/m. Actually, at 0.56 vol% of the graphene content, the conductivity the PET nanocomposite is 3.3×10^{-5} S/m, which is higher than antistatic criterion of 10^{-6} S/m. With only 3.0 vol% graphene, the conductivity of

PET nanocomposite is as high as 2.11 S/m. On the contrary, PET/graphite composites show a much higher percolation threshold of 2.4 vol% and a very broad percolation transition within a range of graphene content from 2.4 to 5.8 vol%. More interestingly, graphene is more efficient in improving electrical conductivity of PET than pristine graphite. For instance, the conductivity of PET/graphene nanocomposite with 0.92 vol% of graphene is 3.46×10^{-3} S/m, even higher than that of PET/pristine graphite composite with 7.1 vol% of graphite (2.45×10^{-4} S/m).

According to the percolation theory (Stauffer, 1985), the relationship of composite conductivity (σ) with filler volume content (φ) follows the below scaling law near the percolation threshold (φc):

$$\sigma \propto \sigma_0(\varphi - \varphi_c)^{\upsilon} \tag{2}$$

Where σo is the bulk electrical conductivity of the fillers and υ is the critical exponent describing the rapid variation of σ near φc. The percolation threshold is the critical content above which a continuous connected network is formed for the transport of electrons throughout the matrix. The inset in figure. 5 shows the double-logarithmic plot of electrical conductivity of PET/graphene nanocomposites versus (φ-φc), and an "anomalous" critical exponent (4.22) was obtained from the slope of linear fit curve, much larger than the theoretically predicted value (~ 2) for three-dimensional system (Balberg, 1987).

To predict the electrical percolation threshold in theory, filler shape must be first considered in view of its strong influence on the electrical properties of composites (Ma & Gao, 2008). However, the electrical percolation threshold cannot be directly related to filler morphology, fortunately, geometrical percolation threshold (pc) provides some insight into the former although cannot be simply identified as it. Therefore, several models were developed to explore the percolative properties of oblate objects in respect of their aspect ratio (Ambrosetti et al., 2008; Garboczi et al., 1995; Yi & Tawerghi, 2009). Recently, Ambrosetti and coworkers (Ambrosetti et al., 2008) proposed a model consisting of isotropically distributed hard oblate spheroids of identical dimensions with soft shell, more fits the system of conducting spheroids dispersed in an insulating continuum host, and the shell thickness can be interpreted as a typical tunneling length between the particles, governing the electrical connectivity of composite. The percolation threshold, pc, for infinite system was obtained by extrapolating that for finite systems through the following scaling relations (Rintoul & Torquato, 1997):

$$\Delta(L) \propto L^{-1/\delta} \tag{3}$$

$$p_c^{eff} - p_c \propto L^{-1/\delta} \tag{4}$$

where δ is the correlation length exponent, Δ represents the width of the percolation transition, pceff is the effective percolation threshold for a system of linear size L. The value of correlation exponent δ is calculated as around 0.9 from thousands of simulations for variously sized lattices, and then pc can be consequently estimated from Eq. (4) by plotting pceff against L-δ for selected values of cell size L. The simulation results, for oblate ellipsoids with various aspect ratio and penetrable shell thickness, indicated that high aspect ratio entails a lower percolation threshold and this effect is also dependant on the shell

thickness, consistent with the behavior observed in our study and other composites containing oblate objects as conducting fillers. Therefore, the small φc of PET/graphene nanocomposites mainly owes to the high aspect ratios of graphene nanosheets.

Moreover, if neglecting the limiting interaction distances to a shell of constant thickness from the presence of the hard core, the model will evolve to an idealized model consisting of completely permeable ellipsoids randomly dispersed in a matrix, as Garboczi and coworkers (Garboczi et al., 1995) suggested. From this model, pc can be predicted as 1.27 α/β where β is the radius of revolution and α is the semiaxis length in the extreme oblate limit. Therefore, pc can be easily calculated as 0.87 vol% for PET/graphene nanocomposites and 3.34 vol% for PET/graphite composites if graphene and graphite considered as permeable oblate particles. These values are higher than that of φc obtained experimentally from curves of Figure 5. This difference between pc and φc may be, in part, due to the assumption that graphite and graphene were permeable, and in part, to the fact that Eq. (2) did not consider tunneling mechanism. The permeable assumption allows regions of space to be occupied by parts of more than one sheet and thereby the critical volume of fillers is overestimated. In addition, the unfavorable geometries of oblate particles also tend to reduce the interparticle connectivity and increase the percolation point. Finally, it is noticed that physically contacted network is adequate but not absolutely necessary for current flow in insulator-conductor composites, since electrons can transmit between isolated particles by tunneling through thin polymer layer (Quivy et al., 1989; Toker et al., 2003).

From above experimental results, it is can be seen that the efficiency of graphene in improving conductivity of PET is comparable to or even better than CNTs. Hu (Hu et al., 2006) reported a low electrical percolation threshold (0.9 wt%) in PET/MWCNT nanocomposites fabricated via coagulation, and the electrical conductivity reached 10-2 S/m at higher filler loading (~5 wt%). A small percolation threshold was reported by Steinert and coworkers in PET/SWCNT nanocomposite films prepared using a solution mixing and casting method. It was shown that sufficient conductivity for antistatic and electrostatic dissipation purposes was achieved at 0.5 wt% SWCNT, which was easily understood because solution casting of a film is efficient to form a conductive network due to the 2-dimentional distribution of CNT and less serious damage of CNT length. However, melt compounding like twin-screw extrusion would inevitably shorten CNT and thus reduce its aspect ratio, which is not beneficial for achieving small percolation thresholds and high conductivity. For example, CNTs-based composites prepared by melt blending with coupling agent only leads to a moderate conductivity of 0.1S/m with 2.48 vol% CNTs (Li et al., 2006). Fortunately, the electrical percolation threshold (φc = 0.47 vol %) obtained in this study is also one of the lowest values for graphite-based composites (Chen et al., 2003; Zheng & Wong, 2003) although slightly higher than that observed in polystyrene/graphene composites prepared by solution mixing (Stankovich et al., 2006). This low percolation threshold and the good conductivity are attributed to the high aspect ratio, large specific surface area and the good dispersion of graphene in PET matrix.

In addition, we found the anomalous exponent of 4.22 for the PET/graphene nanocomposites. Indeed, nonuniversal values (≥ 3) of the critical exponent were reported in many systems (Celzard et al., 1996; Carmona et al., 1984; Ezquerra et al., 1990). To explain this phenomenon, the tunneling conduction mechanism is repeatedly proposed. Balberg proposed a model based on the interparticle tunneling in percolation network. The conductance distribution function of the network, f(g), was related to the tunneling

conductance, g, between two impermeable spherical particles with a radius of b and an average interparticle distance a by:

$$f(g) \propto \ln(g_0 / g) g^{(d_0/a)-1} \tag{5}$$

where g_0 is a constant and d_0 is the characteristic distance for tunneling (usually several nanometers). Percolation network and tunneling conductance are two competitive mechanisms in conductive composites, and the configuration of conductive fillers in polymer matrix determines the competition of these two mechanisms. Fillers existing as large and complicated aggregates (i.e. high structured carbon blacks) in composites are easy to cause much narrower distribution of interparticle tunneling distances than that of the distances between two adjacent particles, namely, the case of d0 > a, for small g values, the conductance function can account for the network and a universal behavior will be obtained (Balberg & Binenbaum, 1985). Whereas, smaller and less agglomerated filler structure (low structure carbon blacks) can provide a wide-enough distribution of the distances between particle surfaces, d0 < a, it can be seen that the essential part of the conductance distribution is determined and given by Eq. (6), which is well known to yield a anomalous behavior (Kogut & Straley, 1979).

$$g^{(d_0/a)-1} \equiv g^{-a} \tag{6}$$

Thus, an anomalous critical exponent of 4.0 was found in the composites filled with uniformly dispersed carbon blacks. Notice that the relationship given by Eq. (6) can be extended to general case of a ≥ 2b. For our PET/graphene nanocomposites, the evenly dispersed monolayer graphene or very small aggregates would also result in wide distribution of the interparticle distances similar to that derived from the above low structure carbon blacks in polyvinylchloride. Therefore, Eq.s (5) and (6) can be applied to interpret the nonuniversal conductivity in PET/graphene nanocomposites. Additionally, the vast nanosheet-polymer interface provides abundant potential sites for tunneling conductance, thereby an anomalous critical exponent of 4.22 was found in PET/graphene nanocomposites.

The nonuniversal behavior can also be associated with the anisotropy (Smith & Lobb, 1979) of conductive fillers and the neck-like bonds in the percolation backbone. Both experimental and theoretical results indicate that geometrical and electrical anisotropy degree is expected to influence the percolation threshold and critical exponent.

4. Conclusions

Graphene sheets were prepared by chemical oxidation of pristine graphite flakes followed by thermal exfoliation and reduction of graphite oxide. PET/graphene nanocomposites prepared by melt compounding exhibit superior electrical conductivity with a small percolation threshold of 0.47 vol%. A high electrical conductivity of 2.11 S/m of PET nanocomposite was achieved with only 3.0 vol % of graphene, which is even adequate for EMI shielding. Additionally, an anomalous critical exponent of 4.22 for PET/graphene nanocomposites can be ascribed to the tunneling conduction and conductivity anisotropy of graphene. Compared to expensive CNTs, graphene is cheaper and it is more effective in making insulating polymers electrically conductive due to its higher specific surface area than CNTs.

5. References

Alig I., Lellinger D., Dudkin S.M. & Potschke P. (2007). *Polymer*, 48(4):1020-1029.

Ambrosetti G., Johner N., Grimaldi C., Danani A. and Ryser P. (2008). *Phys Rev E*, 78(6), 061126.

Balandin A.A., Ghosh S., Bao W.Z., Calizo I., Teweldebrhan D., Miao F. & Lau C.N. (2008). *Nano Letters*, 8(3):902-907.

Balberg I. & Binenbaum N. (1985). *Phys Rev A*, 31(2):1222-1225.

Balberg I. (1987). *Phys Rev Lett*, 59(12):1305-1308.

Berger C., Song Z.M., Li T.B., Li X.B., Ogbazghi A.Y., Feng R., Dai Z.T., Marchenkov A.N., Conrad E.H., First P.N. & de Heer W.A. (2004) *J Phys Chem B*, 108(52):19912-19916.

Carmona F., Prudhon P. & Barreau F. (1984). *Solid State Commun*, 51(4):255-257.

Carlsson J.M. (2007). *Nature Materials*, 6(11):801-802.

Celzard A., Furdin G., Mareche J.F., McRae E., Dufort M. & Deleuze C. (1994). *Solid State Commun*, 92(5):377-383.

Celzard A.M.E., Mareche J.F., Furdin G., Dufort M. & Deleuze C. (1996). *J Phys Chem Solids*, 57(6-8):715-718.

Chen G.H., Weng W.G., Wu D.J. & Wu C.L. (2003). *Eur Polym J*, 39(12):2329-2335.

Cobbs W.H. & Burton R.L. (1953). *J Polym Sci*, 10(3):275-290.

Ezquerra T.A., Kulescza M., Cruz C.S. & Baltacalleja F.J. (1990). *Adv Mater,* 2(12): 597-600.

Garboczi E.J., Snyder K.A., Douglas J.F. & Thorpe M.F. (1995). *Phys Rev E*, 52(1):819-828.

Grossiord N., Loos J. & Koning C.E. (2005). *J Mater Chem*, 15(24):2349-2352.

Halperin B.I., Feng S. & Sen P.N. (1985). *Phys Rev Lett*, 54(22):2391-2394.

Heersche H.B., Jarillo-Herrero P., Oostinga J.B., Vandersypen L.M.K. & Morpurgo A.F. (2007). *Nature*, 446(7131):56-59.

Hu G.J., Zhao C.G., Zhang S.M., Yang M.S. & Wang Z.G. (2006). *Polymer*, 47(1):480-488.

Kalaitzidou K., Fukushima H. & Drzal L.T. (2007). *Carbon*, 45(7):1446-1452.

Kelly B. (1981). *Physics of graphite*, London Englewood N.J: Applied science publishers, pp. 267-361.

Kim H. & Macosko C.W. (2008). *Macromolecules*, 41(9):3317-3327.

Kogut P.M. & Straley J.P. (1979). *J Phys C- Solid State Phys*, 12(11):2151-2159.

Lagreve C. Feller J.F., Linossier I. & Levesque G. (2001). *Polym Eng Sci*, 41(7): 1124-1132.

Lee C., Wei X.D., Kysar J.W. & Hone J. (2008). *Science*, 321(5887):385-388.

Li Z.F., Luo G.H., Wei F. & Huang Y. (2006). *Compos Sci Technol*, 66(7-8):1022-1029.

Liang J.J., Wang Y., Huang Y., Ma Y.F., Liu Z.F., Cai F.M., Zhang C.D., Gao H.J. & Chen Y.S. (2009). *Carbon*, 47(3):922-925.

Ma H.M. & Gao X.L. (2008). Polymer, 49(19):4230-4238.

McAllister M.J., Li J.L., Adamson D.H., Schniepp H.C., Abdala A.A., Liu J., Herrera-Alonso M., Milius D.L., Car R., Prud'homme R.K. & Aksay I.A. (2007). *Chem Mater*, 19(18): 4396-4404.

McLachlan D.S., Chiteme C., Park C., Wise K.E., Lowther S.E., Lillehei P.T., Siochi E.J. & Harrison J.S. (2005). *J Polym Sci Pol Phys*, 43(22):3273-3287.

Meyer J.C. Geim A.K., Katsnelson M.I., Novoselov K.S., Booth T.J. & Roth S. (2007). *Nature*, 446(7131):60-63.

Novoselov K.S., Geim A.K., Morozov S.V., Jiang D., Zhang Y., Dubonos S.V., Grigorieva I.V. & Firsov A.A. (2004). *Science*, 306(5696):666-669.

Novoselov K.S., Geim A.K., Morozov S.V., Jiang D., Katsnelson M.I., Grigorieva I.V., Dubonos S.V. & Firsov A.A. (2005). *Nature*, 438(7065):197-200.

Novoselov K.S., Jiang Z., Zhang Y., Morozov S.V., Stormer H.L., Zeitler U., Maan J.C., Boebinger G.S., Kim P. & Geim A.K. (2007). *Science*, 315(5817):1379-1379.

Peigney A, Laurent C, Flahaut E, Bacsa RR, & Rousset A. *Carbon,* 2001; 39(4): 507-514.

Quivy A., Deltour R., Jansen A.G.M. & Wyder P. (1989). *Phys Rev B*, 39(2):1026-1030.

Ramanathan T., Abdala A.A., Stankovich S., Dikin D.A., Herrera-Alonso M., Piner R.D., Adamson D.H., Schniepp H.C., Chen X., Ruoff R.S., Nguyen S.T., Aksay I.A., Prud'homme R.K. & Brinson L.C. (2008). *Nature Nanotechnology,* 3(6):327-331.

Rintoul M.D. & Torquato S. (1997). *J Phys A-math Gen,* 30(16):L585-L592.

Schniepp H.C., Li J.L., McAllister M.J., Sai H., Herrera-Alonso M., Adamson D.H., Prud'homme R.K., Car R., Saville D.A. & Aksay I.A. (2006). *J Phys Chem B,* 110(17): 8535-8539.

Smith L.N. & Lobb C.J. (1979). *Phys Rev B,* 20(9):3653-3658.

Stankovich S., Dikin D.A., Dommett G.H.B., Kohlhaas K.M., Zimney E.J., Stach E.A., Piner R.D., Nguyen S.T. & Ruoff R.S. (2006). *Nature*, 442(7100):282-286.

Staudenmaier L. (1898). *Ber Dtsch Chem Ges*, 31:1481-1499.

Stauffer D. (1985). *An introduction to percolation theory*, Landon and Philadephia: Taylor and Fansis, 325-355.

Steinert B.W. & Dean D.R. (2009). *Polymer*, 50(3):898-904.

Toker D., Azulay D., Shimoni N., Balberg I. & Millo O. (2003). *Phys Rev B,* 68: 041403.

Viculis L.M., Mack J.J. & Kaner R.B. (2003). Science, 299(5611):1361-1361.

Wang G.X., Yang J., Park J., Gou X.L., Wang B., Liu H. & Yao J. (2008). *J Phys Chem C*, 112(22):8192-8195.

Wang X.B., You H.J., Liu F.M., Li M.J., Wan L., Li S.Q., Li Q., Xu Y., Tian R., Yu Z.Y., Xiang D. & Cheng J. (2009). *Chem Vapor Depos,* 15(1-3):53-56.

Weng W.G., Chen G.H. & Wu D.J. (2005). *Polymer*, 46(16):6250-6257.

Xie S.H., Liu Y.Y. & Li J.Y. (2008). *Appl Phys Lett*, 92(24):243121.

Yao S.H., Dang Z.M., Jiang M.J. & Xu H.P. (2007). *Appl Phys Lett*, 91(21):042914.

Yi Y.B. & Tawerghi E. (2009). *Phys Rev E,* 79: 041134.

Zhang M., Li D.J., Wu D.F., Yan C.H., Lu P. & Qiu G.M. (2008). *J Appl Polym Sci,* 108(3):1482-1489.

Zhang Y.B., Tan Y.W., Stormer H.L. & Kim P. (2005). *Nature*, 438(7065):201-204.

Zhang Y.B., Small J.P., Amori M.E.S. & Kim P. (2005). *Phys Rev Lett*, 94(17): 178603.

Zheng W.G., Wong S.C. & Sue H.J. (2002). *Polymer*, 43(25):6767-6773.

Zheng W. & Wong S.C. (2003). *Compos Sci Technol*, 63(2):225-235.

17

Non-Volatile Resistive Switching in Graphene Oxide Thin Films

Fei Zhuge, Run-Wei Li,* Congli He, Zhaoping Liu and Xufeng Zhou
Ningbo Institute of Materials Technology and Engineering,
Chinese Academy of Sciences,
People's Republic of China

1. Introduction

The semiconductor industry has long been seeking a high-density, high-speed, and low-power memory technology that retains its data even when the power is interrupted (Meijer, 2008). Though static random access memory (SRAM) and dynamic random access memory (DRAM) are very fast, both of them are volatile, which is a huge disadvantage, costing energy and additional periphery circuitry. Si-based Flash memory devices represent the most prominent nonvolatile data memory (NVM) because of their high density and low fabrication costs. However, Flash suffers from low endurance, low write speed, and high voltages required for the write operations. In addition, further scaling, i.e., a continuation in increasing the density of Flash is expected to run into physical limits in the near future. Ferroelectric random access memory (FeRAM) and magnetoresistive random access memory (MRAM) cover niche markets for special applications. One reason among several others is that FeRAM as well as conventional MRAM exhibit technological and inherent problems in the scalability, i.e., in achieving the same density as Flash today. In this circumstance, a renewed nonvolatile memory concept called resistance-switching random access memory (RRAM), which is based on resistance change modulated by electrical stimulus, has recently inspired scientific and commercial interests due to its high operation speed, high scalability, and multibit storage potential (Beck et al., 2000; Lu & Lieber, 2007; Dong et al., 2008). The reading of resistance states is nondestructive, and the memory devices can be operated without transistors in every cell (Lee et al., 2007; Waser & Aono, 2007), thus making a cross-bar structure feasible. A large variety of solid-state materials have been found to show these resistive switching characteristics, including solid electrolytes such as GeSe and Ag_2S (Waser & Aono, 2007), perovskites such as $SrZrO_3$ (Beck et al., 2000), $Pr_{0.7}Ca_{0.3}MnO_3$ (Liu et al., 2000; Odagawa et al., 2004; Liao et al., 2009), and $BiFeO_3$ (Yang et al., 2009; Yin et al., 2010; Li et al., 2010), binary transition metal oxides such as NiO (Seo et al., 2004; Kim et al., 2006; Son & Shin, 2008), TiO_2 (Kim et al., 2007; Jeong et al., 2009; Kwon et al., 2010), ZrO_2 (Wu et al., 2007; Guan et al., 2008; Liu et al., 2009), and ZnO (Chang et al., 2008; Kim et al., 2009; Yang et al., 2009), organic materials (Stewart et al., 2004), amorphous silicon (a-Si) (Jo and Lu, 2008; Jo et al., 2009), and amorphous carbon (a-C) (Sinitskii & Tour, 2009; Zhuge et al., 2010).

In last decades, carbon-based materials have been studied intensively as a potential candidate to overcome the scientific and technological limitations of traditional

semiconductor devices (Rueckes et al., 2000; Novoselov et al., 2004; Avouris et al., 2007). It is worthy mentioning that most of the work on carbon-based electronic devices has been focused on field-effect transistors (Wang et al., 2008; Burghard et al., 2009). Thus, it would be of great interest if nonvolatile memory can also be realized in carbon so that logic and memory devices can be integrated on a same carbon-based platform. Graphene oxide (GO) with an ultrathin thickness (~1 nm) is attractive due to its unique physical-chemical properties. A GO layer can be considered as a graphene sheet with epoxide, hydroxyl, and/or carboxyl groups attached to both sides. GO can be readily obtained through oxidizing graphite in mixtures of strong oxidants, followed by an exfoliation process. Due to its water solubility, GO can be transferred onto any substrates uniformly using simple methods such as drop-casting, spin coating, Langmuir-Blodgett (LB) deposition and vacuum filtration. The as-deposited GO thin films can be further processed into functional devices using standard lithography processes without degrading the film properties (Eda et al., 2008; Cote et al., 2009). Furthermore, the band structure and electronic properties of GO can be modulated by changing the quantity of chemical functionalities attached to the surface. Therefore, GO is potentially useful for microelectronics production. Considering that although a large variety of solid-state materials have been found to show resistive switching characteristics, none of them can fully meet the requirements of RRAM applications, exploration of new storage media is still a key project for the development of RRAM. Therefore, in this chapter, the resistive switching effect in GO thin films has been investigated and the possibility of GO used as a potential storage medium for RRAM has been discussed.

2. Experiments

The oxidation of graphite was carried out following the Hummer's method (Hummers & Offeman, 1958). In a typical procedure, KNO_3 (1.2 g) and graphite (1.0 g) was added into 46 mL of concentrated H_2SO_4 (98%) under stirring. After 10 mins 6.0 g of $KMnO_4$ was added slowly. The mixture was then heated to 35 °C and stirred for 6 hours. Subsequently, 80 mL of water was added dropwise under vigorous stirring, resulting in a quick rise of the temperature to ~80 °C. The slurry was further stirred at this temperature for another 30 mins. Afterwards 200 mL of water and 6 mL of H_2O_2 solution were added in sequence to dissolve insoluble manganese species. The resulting graphite oxide suspension was washed repeatedly by a large amount of water until the solution pH reached a constant value at ~4.0, and finally the suspension was diluted to 600 mL with water. 200 mL of the diluted graphite oxide suspension was transferred into a conical beaker with a volume of 500 mL. Then the suspension was gently shaken in a mechanical shaker at a speed of 160 rpm for ~6 hours. To remove the small amount of unexfoliated particles, the resulting viscous suspension was centrifuged at 2,000 rpm for 10 mins, producing a brown, homogeneous colloidal suspension of GO sheets. The colloidal suspension could be further concentrated by centrifugation at 8,000 rpm. Then GO thin films of ~30 nm in thickness were prepared at room temperature by the vacuum filtration method. 50 g of GO suspension with a concentration of 6 mg/L was filtered through a cellulose ester membrane to achieve uniform GO thin films. The film thickness could be well controlled by tuning the GO concentration or filtration volume. The as-filtered GO flakes were then transferred from the filter membrane onto commercial $Pt/Ti/SiO_2/Si$ substrates.

Atomic force microscopy (AFM) characterization was conducted by a Veeco Dimension 3100V scanning probe microscope at ambient conditions using a tapping or conductive-

AFM (CAFM) mode. Scanning electron microscopy (SEM) images were taken by a Hitachi S-4800 Field Emission Scanning Electron Microscope. Specially, a low accelerating voltage of 1.0 kV and high current of 20 μA were applied for the graphene oxide sheets on silicon substrates. In order to measure the electrical properties, metal (Cu, Ag, and Au etc.) top electrodes with a thickness of 200 nm and diameter of 100 μm were deposited at room temperature by electron beam evaporation with an in-situ metal shadow mask. The *I-V* characteristics of metal/GO/Pt structures were measured at room temperature by Keithley 4200 semiconductor characterization system with voltage sweeping mode. During the measurement, a bias voltage was applied between the top (Cu, Ag, and Au etc.) and bottom (Pt) electrodes with the latter being grounded. The schematic structure of the sandwiched devices is depicted in Fig. 1(a). In the local leakage current measurement by CAFM, the conductive tip was grounded and directly touched the GO films, as shown in Fig. 1(b). The resistances in the low resistance state and high resistance state of the metal/GO/Pt structures were measured as a function of temperature by a physical property measurement system (PPMS, Quantum Design).

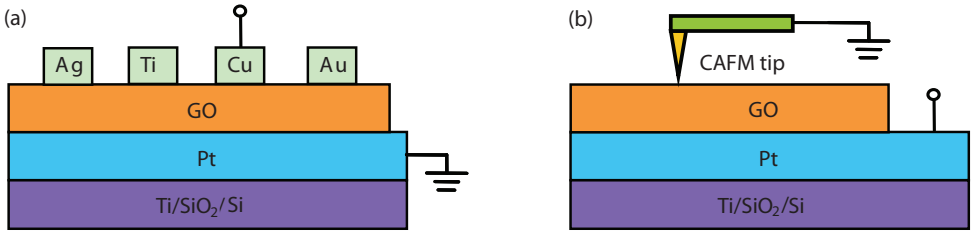

Fig. 1. Schematic configuration (a) of the metal/GO/Pt sandwiched structures, and (b) for the conductive-AFM measurements.

3. Results and discussions

3.1 Morphology of GO sheets and thin films

A typical SEM image of the GO sheets is shown in Fig. 2(a). As can be seen, the sheets have a lateral size, dominantly, in the order of 100 μm, and some of them even possess a size as large as 200 μm. To the best of our knowledge, there have been no reports on GO sheets with such a huge size. Besides the large sheets, fragments with sizes of only a few micrometres can also be observed in a small amount. These fragments might be derived from micrometre-sized graphite flakes or by inevitable breakage during the delamination process. Figure 2(b) displays an AFM image of a GO sheet which has a size far beyond the AFM scan range. The height profile denoted in Fig. 2(b) demonstrates a mean thickness of ~1 nm, indicative of a unilamellar nature of the sheet. It is worth mentioning that the sizes of the exfoliated GO sheets are closely associated with those of the starting graphite flakes. For example, if the graphite flakes of 500 mesh size (~25 μm in mean size) were used, the exfoliated GO sheets had a lateral size around 15 μm. This result indicates that the sheet sizes can be easily controlled through the size selection of the graphite material. Figure 2(c) shows an AFM image of a GO thin film of ~30 nm in thickness deposited at room temperature by the vacuum filtration method. From Fig. 2(c), we see that the as-grown GO film is not smooth and there are a large amount of protuberances on the film surface. These observed protuberances are most likely to be the gauffers of GO sheets formed during the film preparation process (Zhou & Liu, 2010).

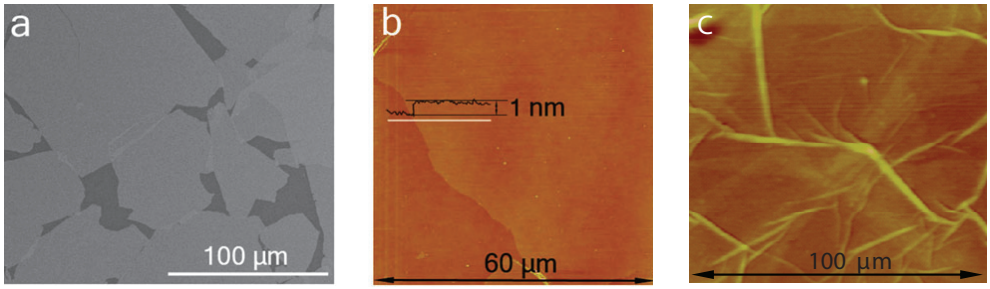

Fig. 2. (a) SEM and (b) AFM images of GO sheets that were deposited on a Si substrate by Langmuir-Blodgett assembly at a constant surface pressure of 10 mN m^{-1}. (c) AFM image of GO thin films of ~30 nm in thickness prepared at room temperature by the vacuum filtration method

3.2 Nonvolatile resistive switching in GO thin films

Metal/GO/Pt sandwiched structures show the bipolar resistive switching behavior (He et al., 2009). The *I-V* characteristics of the Cu/GO/Pt memory cell are studied by dc voltage sweep measurements to evaluate the memory effects of the obtained devices. Figure 3(a) plots a typical *I-V* curve of a Cu/GO/Pt cell. Figure 3(b) shows the same *I-V* curve in a semilogarithmic scale. During the measurement, the voltage is swept in a sequence of 0 V → 1 V → 0 V → –1 V → 0 V with a sweeping step of 0.01 V. While increasing the positive voltage steadily, the current jumps abruptly at a voltage value of about 0.8 V. The device switches from the high resistance state (HRS or Off state) to a low resistance state (LRS or On state), which is called the "Set" process. A current compliance (10 mA in this work) is usually needed during the Set process to prevent the sample from a permanent breakdown. By sweeping the voltage from 1 V to –0.4 V, the device holds on the LRS, and starts switching from the LRS to the HRS ("Reset" process) from –0.4 V. At the voltage of –0.75 V, the cell recovers to the HRS, and holds until next Set process. The *I-V* characteristics exhibit a typical bipolar switching behavior. The device yield of the Cu/GO/Pt structure is more than 50%.

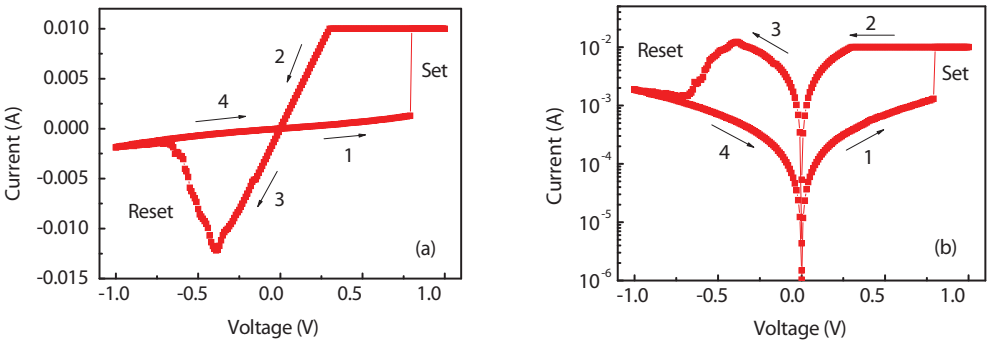

Fig. 3. Typical *I-V* characteristics of the Cu/GO/Pt sandwiched structure shown in (a) linear scale, and (b) semilogarithmic scale. The voltage is swept in the direction as follows: 0 V → 1 V → 0 V → –1 V → 0 V

In order to investigate the endurance performance of the Cu/GO/Pt memory device, cyclic switching operations are conducted. Figure 4(a) shows the evolution of resistance of the two well-resolved states in 100 cycles. The statistical distribution of the resistances in HRS and LRS is shown in Fig. 4(b). The resistance values are read out at –0.1 V in each dc sweep. Although the resistance values of both HRS and LRS show some fluctuations, the On/Off ratios are about 20 without any obvious degradation within 100 cycles. The endurance measurements ensured that the switching between On and Off states is controllable, reversible, and reproducible. After the device was switched On or Off, no electrical power was needed to maintain the resistance within a given state. The distribution of the programming voltages (V_{Set} and V_{Reset}), another critical parameter to evaluate the memory device, is shown in Fig. 4(c). Figure 4(d) shows The statistical distribution of the programming voltages. As can be seen, V_{Set} and V_{Reset} distribute in a range of 0.3 V to 1 V and –0.3 V to –0.9 V, respectively. The switching threshold voltages of the Cu/GO/Pt sandwiched structure are lower than those of most reported RRAM devices (Szot et al., 2006; Tsubouchi et al., 2007; Guan et al., 2007; Fujiwara et al., 2008; Li et al., 2008).

The retention performance of the Cu/GO/Pt memory cell at room temperature is shown in Fig. 5. The device is switched On or Off by dc voltage sweeping. Then the resistance of LRS or HRS is read out at a reading voltage of 0.1 V. The reading of the resistance state is nondestructive, and no electrical power is needed to maintain the resistance within a given state (LRS or HRS). As can be seen in Fig. 5, the LRS and HRS resistances are kept stable for more than 10^4 s, indicating that the memory device is nonvolatile and stable at room temperature.

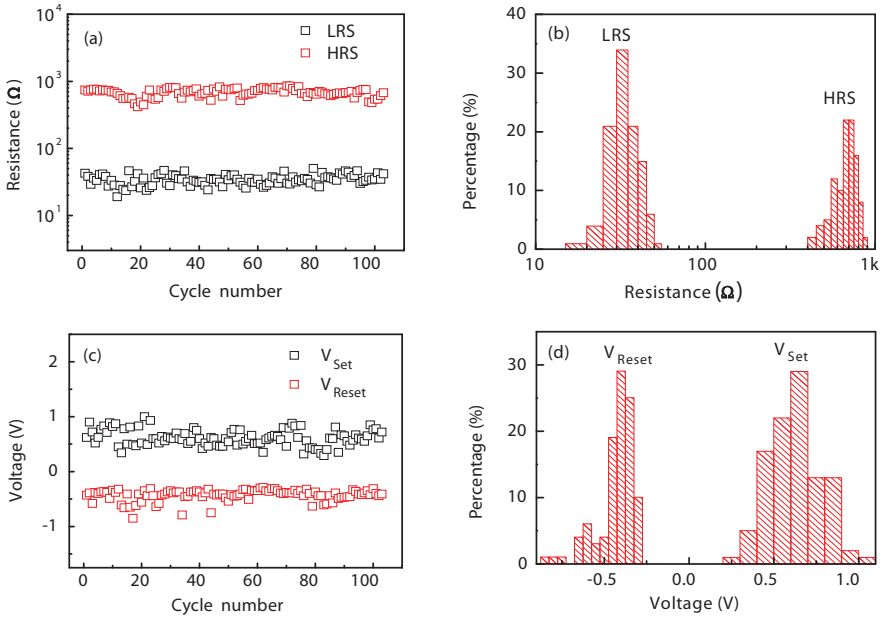

Fig. 4. (a) Endurance performance of the Cu/GO/Pt memory cell. The resistance values are read out at 0.1 V in each sweep. (b) Statistical distribution of the resistances in HRS and LRS. (c) Evolution of V_{Set} and V_{Reset} of the Cu/GO/Pt device as a function of the switching cycle. (d) Statistical distribution of V_{Set} and V_{Reset}

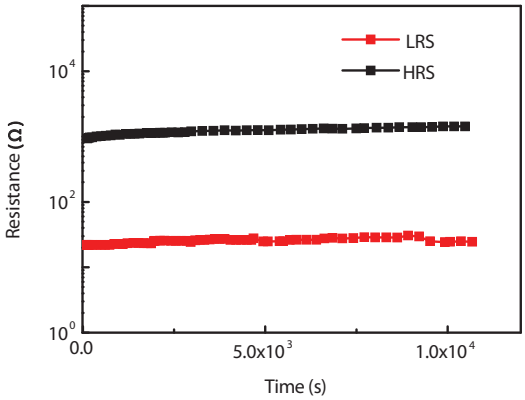

Fig. 5. Retention performance for the LRS and HRS of the Cu/GO/Pt memory cell at room temperature

To understand the conduction mechanisms of the Cu/GO/Pt memory cell, the *I-V* curves are replotted in a log-log scale. Figures 6(a) and (b) show the logarithmic plot and linear fitting of the previous *I-V* curve for the positive and negative voltage sweep regions, respectively. As shown in Fig. 6, the *I-V* curve of LRS exhibits a linearly Ohmic behavior with a slope of ~1. However, the conduction mechanisms of HRS are much more complicated. Fitting results for HRS suggest that the charge transport behavior is in good agreement with a trap-controlled space charge limited current (SCLC), which consists of two portions: the Ohmic region ($I \propto V$) and the Child's law region ($I \propto V^2$) (Strukov et al., 2008; Kim et al., 2007; Son & Shin, 2008; Chen et al., 2008). The different conduction behaviors in HRS and LRS suggest that the high conductivity in On-state cell is likely to be a confined effect rather than a homogenously distributed one (Zhuge et al., 2010).

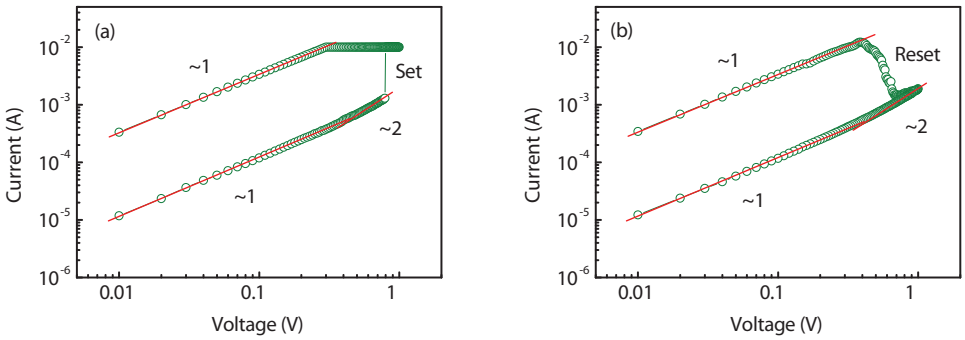

Fig. 6. *I-V* curves of the the Cu/GO/Pt memory cell plotted in log-log scale and the linear fitting results in both LRS and HRS: (a) positive voltage region and (b) negative voltage region. Also shown are the corresponding slopes for different portions

3.3 Top electrode material dependence of resistive switching of metal/GO/Pt sandwiches

Various metals (Cu, Ag, Au, and Ti) as top electrodes are deposited on GO films and the *I-V* characteristics of the corresponding metal/GO/Pt memory cells are investigated. The

similar bipolar switching behaviors are observed in these four types of metal/GO/Pt sandwiched structures. Actually, a Forming process, which is the first transition from fresh state to low resistance state, is always needed before such sandwiches show good resistive switching characteristics. However, this is not desired in practical applications because the Forming voltage is usually much higher than the Set voltage of the device. Most materials, for example, NiO, TiO_2, ZnO, CuO, and $SrTiO_3$ etc. (Kinoshita et al., 2006; Do et al., 2008; Chang et al., 2008; Fujiwara et al., 2008; Oligschlaeger et al., 2006), have already been reported to be in need of Forming process. It is necessary to find some solutions to overcome this difficulty. Kinoshita et al. developed a NiO_y film (y=0.88±0.05) free from Forming process, where a grain structure was found with conductive atomic force microscopy and most current flows through grain boundaries to obviate the requirement of Forming (Kinoshita et al., 2006). Herein, the effect of top electrode materials on the Forming process in GO thin films is investigated.

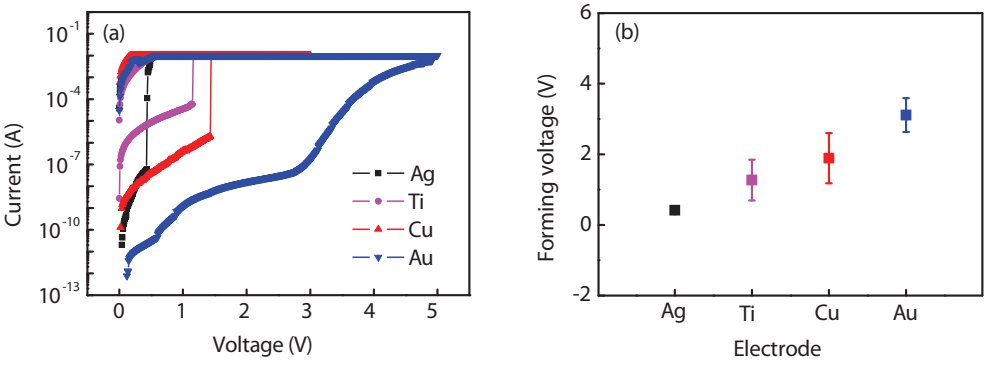

Fig. 7. (a) *I-V* curves of Forming processes of GO-based memory cells using different metals (Ag, Ti, Cu, and Au) as top electrodes. (b) Forming voltages of different metal/GO/Pt sandwiches

Figure 7(a) shows the *I-V* properties of Forming processes of Ag/GO/Pt, Ti/GO/Pt, Cu/GO/Pt, and Au/GO/Pt sandwiched structures. The Forming voltages of different metal/GO/Pt memory cells are shown in Fig. 7(b). As can be seen from Fig. 7, the Ag/GO/Pt structures have the lowest Forming voltages of about 0.4 V, while the Au/GO/Pt sandwiches show the highest Forming voltages of about 3 V. The Forming voltage of the metal/GO/Pt memory cell varies as follows: $V_{Ag}<V_{Ti}<V_{Cu}<V_{Au}$. It has been reported that solid electrolyte memory devices based on silver ions generally show low switching voltages (Kund et al., 2005; Schindler et al., 2007; Tsunoda et al., 2007). Banno et al. further clarified that the switching voltage for turn-on in RRAM devices based on solid electrolyte such as $Cu_{2-a}S$ and Ta_2O_5 could be strongly affected by the ion flux which is proportional to the product of the diffusion coefficient and the concentration of ions (Banno et al., 2008). Therefore, we can infer that a large ion diffusion coefficient can lead to a large ion flux and thus a low switching voltage. Govindaraj et al. have reported that Ag has a large diffusion coefficient in oxide films (Govindaraj et al., 2001). The Ag/ZrO_2/Au structure shows low switching voltages of <1 V without any Forming process (Li et al., 2010). In our case, it is likely that Ag also has a large diffusion coefficient in GO thin films, resulting in low Forming voltages for Ag/GO/Pt memory cells. The high Forming voltages

for Au/GO/Pt structures are likely due to gold's chemical inertness. Compared to other top electrode metals (i.e. Ag, Ti, and Cu), Gold is very difficult to be oxidized to the ions. High voltages are necessary for the activation of Au/GO/Pt memory cells.

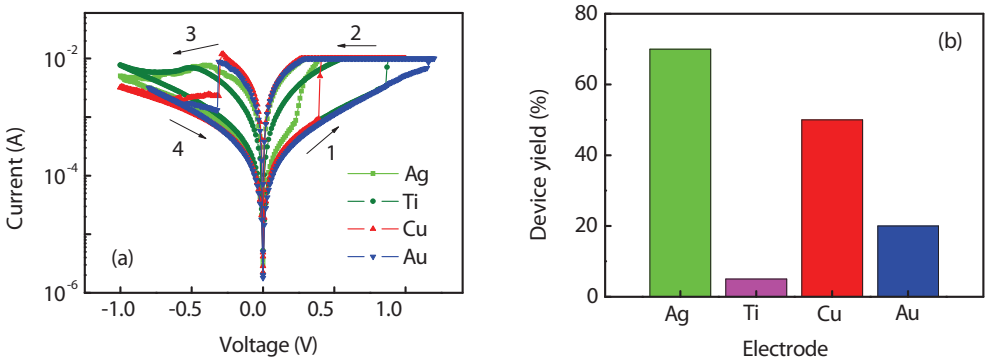

Fig. 8. (a) Typical *I-V* characteristics of GO-based memory cells using different metals (Ag, Ti, Cu, and Au) as top electrodes shown in semilogarithmic scale. (b) Device yields of different metal/GO/Pt sandwiches

Figure 8(a) shows the typical *I-V* characteristics of Ag/GO/Pt, Ti/GO/Pt, Cu/GO/Pt, and Au/GO/Pt sandwiched structures after Forming processes. Similar to the Forming processes, the Ag/GO/Pt structures have the lowest Set voltages of about 0.25 V, and the Au/GO/Pt sandwiches show the highest Set voltages of about 1.2 V. Figure 8(b) shows the top electrode dependence of device yields of metal/GO/Pt memory cells. As can be seen from Fig. 8(b), the device yield (Y) of the metal/GO/Pt memory cell varies as follows: $Y_{Ag}>Y_{Cu}>Y_{Au}>Y_{Ti}$. The Ag/GO/Pt structure has the highest device yield of about 70%. The strong top electrode material dependence of the switching characteristics is helpful for speculating about the resistive switching mechanism in GO thin films. It will be discussed later.

3.4 GO film thickness dependence of resistive switching of metal/GO/Pt sandwiches

Figure 9(a) shows the *I-V* characteristics of Forming processes of Cu/GO/Pt memory cells using GO films with different thicknesses, i.e. 15 nm, 30 nm, 60 nm, and 90 nm. The GO film thickness dependence of Forming voltages of Cu/GO/Pt memory cells is shown in Fig. 9(b). Obviously, the voltage required for the initial Forming process increases with the thickness of GO, indicating that the electric field inside the bulk GO is the controlling factor of the Forming. The similar experiment results have been also obtained in some oxides, for example, Fe_2O_3 (Inoue et al., 2008). Therefore, to reduce the Forming voltage or even entirely remove the Forming process of the metal/GO/Pt memory cell, an appropriate thickness of the GO thin film should be considered.

The resistances of the high resistive state and low resistive state after the Forming process for Cu/GO/Pt memory cells are shown in Fig. 10, as a function of the thickness of GO. No obvious variation can be observed for both HRS resistance and LRS resistance as the GO thickness changes from 15 nm to 90 nm. The thickness-insensitive property of HRS resistance and LRS resistance indicates that once the Forming process is completed, it is unlikely that the bulk region of GO contributes to the resistive switching effectively. This also underpins that the switching phenomenon occurs at the interface rather than the bulk region.

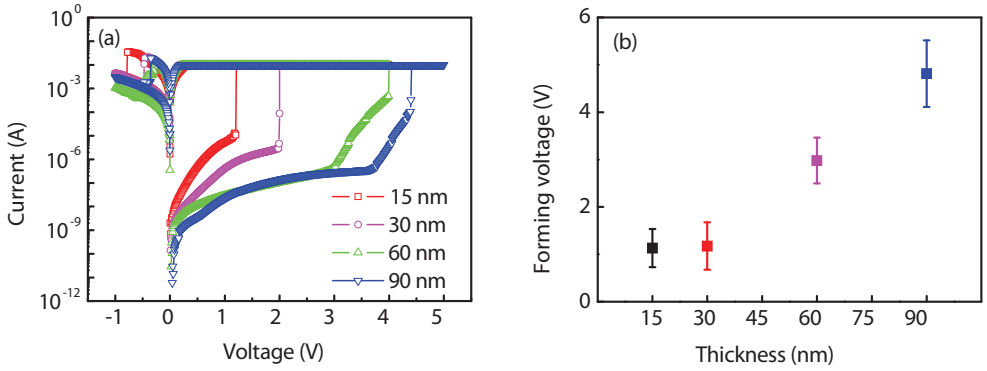

Fig. 9. (a) *I-V* curves of Forming processes of Cu/GO/Pt memory cells using GO films with different thicknesses, i.e. 15 nm, 30 nm, 60 nm, and 90 nm. (b) GO film thickness dependence of Forming voltages of Cu/GO/Pt memory cells

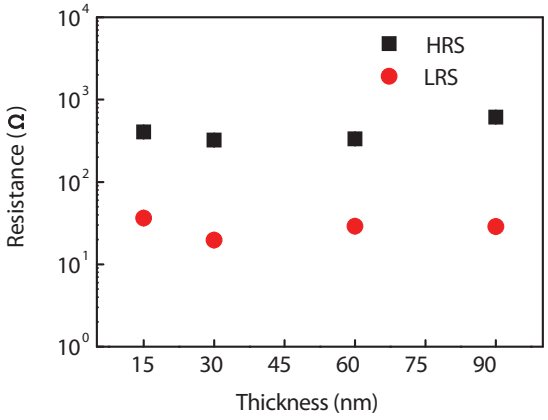

Fig. 10. Resistances of the high resistive state and low resistive state for Cu/GO/Pt memory cells, plotted against the thickness of GO

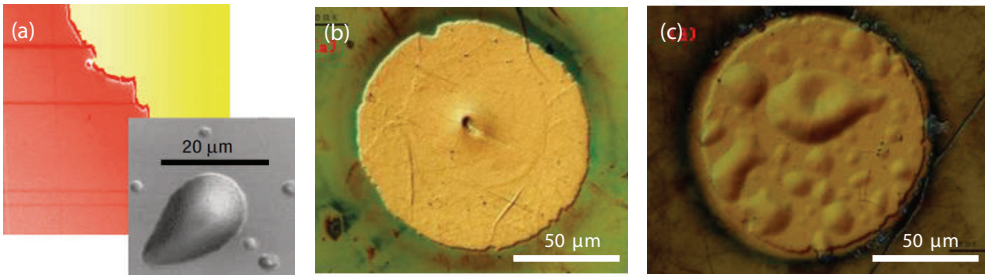

Fig. 11. Gas bubbles under the electrodes formed during the Forming processes of (a) the Pt/single crystalline $SrTiO_3$/Pt memory cell (Szot et al., 2006), (b) Cu/GO/Pt memory cell with a GO thickness of 90 nm, and (c) Au/GO/Pt memory cell with a GO thickness of 30 nm

Szot et al. investigated the resistive switching of the Pt/single crystalline $SrTiO_3$/Pt memory cell and found gas bubbles under the anode. This phenomenon was explained by the polyfilamentary models proposed in the context of amorphous-oxide films (Dearnaley et al., 1970; Rakhshani et al., 1976; Ray et al., 1990), namely the preferential diffusion of oxygen and solid-state electrolytic processes along a discrete set of filaments, which give rise to a located decomposition and subsequent accumulation of oxygen gas under the anode. In our case, such gas bubbles are also observed under the top electrodes for the Cu/GO/Pt memory cell with a GO thickness of 90 nm and Au/GO/Pt memory cell with a GO thickness of 30 nm. From Fig. 7, we see that for the Au/GO/Pt cell, the Forming voltage is more than 4 V. As can be seen from Fig. 9, the Cu/GO/Pt cell with a GO thickness of 90 nm needs a high Forming voltage of about 5V. Therefore, we infer that as the high Forming voltage is applied to the GO-based memory cell, a large amount of heat is generated in a confined region, resulting in an increase of temperature. Then, the high temperature in the confined region may cause the decomposition of epoxide, hydroxyl, and/or carboxyl groups in GO, resulting in water steam and CO_2 (Zhou et al., 2006).

3.5 Current compliance dependence of resistive switching of metal/GO/Pt sandwiches

A current compliance is usually needed during the Forming and Set processes to prevent the sample from a permanent breakdown. We find that the current compliance is another critical parameter to determine the resistive switching characteristics of metal/GO/Pt memory cells. Figure 12(a) shows the typical *I-V* characteristics of the Au/GO/Pt device with different current compliance (0.02 A, 0.04 A, and 0.07 A). Clearly, the Reset current (maximum current level before the Reset process) increases with increasing compliance current. As mentioned above, the different conduction behaviors in high and low resistance states suggest that the high conductivity in On-state cell is likely to be a confined effect rather than a homogenously distributed one. It is likely due to the formation of conducting filaments in GO (Yang et al., 2009). It is considered that stronger filaments with a higher density are formed at a larger current compliance (Rohde et al., 2005). The Reset process is also considered to be due to the rupture of the filaments due to the heat generated by the large current flow (Rohde et al., 2005). Thus, it can be imagined that a larger Reset current is necessary for the Reset process at the larger current compliance. The dependence of the Reset current and resistance in the low resistance state on current compliance applied in the Set process is shown in Fig. 12(b). We see that the Reset current has an approximate linear relationship to the current compliance. Thus, the power needed for the WRITE and ERASE operations in RRAM can be modulated by controlling the current compliance. As can be seen from Fig. 12(b), the resistance in the low resistance state decreases with increasing current compliance. Therefore, different resistance states can be achieved using different current compliances in the program process, showing good potential for multilevel storage (Wang et al., 2010). Figure 12(c) shows the current compliance dependence of the Set and Reset voltages. The Set voltage shows weak dependence on current compliance, whereas the Reset voltage increases obviously with increasing current compliance applied in the Set process.

3.6 Possible mechanisms of resistive switching in GO thin films

i. Filamentary model for metal/GO/Pt sandwiches

As mentioned above, the strong top electrode material dependence of the switching characteristics is helpful for speculating about the resistive switching mechanism in GO thin

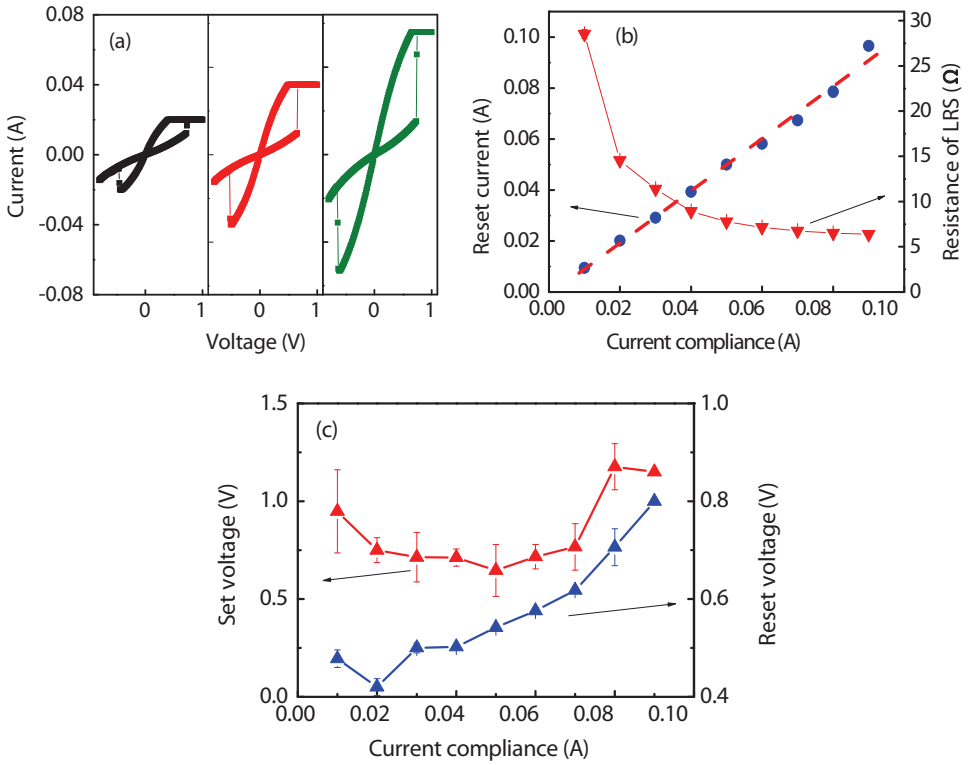

Fig. 12. (a) Typical *I-V* characteristics of the Au/GO/Pt device with different current compliance (0.02 A, 0.04 A, and 0.07 A). (b) Current compliance dependence of the Reset current and resistance of the low resistance state of the Au/GO/Pt device. (c) Current compliance dependence of the Set and Reset voltages of the Au/GO/Pt device.

films. Tokunaga et al. investigated the RS effect at the interface between metal electrodes (Pt, Au, Ag, Al, Ti, and Mg) and atomically flat cleaved (001) surfaces of $La_{1-x}Sr_{1+x}MnO_4$ (x=0−1.0) single crystals (Tokunaga et al., 2006). Hysteretic *I-V* characteristics were observed in the junctions for Mg, Al, and Ti, which have relatively shallow work functions (Φ). In our case, Ti, Cu, and Ag have a lower Φ of 3.98 eV, 4.35 eV, and 4.26 eV, respectively, whereas Au has a higher one of 5.1 eV. It indicates that the occurrence of the resistive switching in metal/GO/Pt structures is irrelevant to Φ of the top electrodes. Liao and co-workers studied the resistive switching characteristics of metal/$Pr_{0.7}Ca_{0.3}MnO_3$ (PCMO)/Pt devices and found that devices with top electrode made of Al, Ti, and Ta exhibit a bipolar resistive switching, but those with top electrode made of Pt, Ag, Au, and Cu do not (Liao et al., 2009). The resistive switching was attributed to a thin metal-oxide layer formed at the interface between the former group of top electrode and PCMO. In our work, the top electrode material includes both reactive metals such as Ti and inert metals such as Au. Therefore, the observed resistive switching is not due to the formation of a metal-oxide layer at the interface between the top electrode and GO. The strong top electrode material dependence of the resistive switching characteristics of GO thin films suggests that the resistive

switching effect may be attributed to the formation/rupture of metal filaments due to the diffusion of the top electrodes under a bias voltage. Briefly, a positive voltage (>V_{Set}) on the top electrodes generates a high electric field that drives metal (e.g., Ag) ions into the GO matrix and form conducting filaments inside the GO layer, and the device reaches the On state. After the Set process, the device retains the On state unless a sufficient voltage of opposite polarity (<V_{Reset}) is applied and the electrochemical dissolution of the metal filaments Resets the device, and the Off state is finally reached again (Jo et al., 2008; Zhuge et al., 2010).

To verify the physical nature of the resistive switching effect of the metal/GO/Pt structures, resistances in the low and high resistance states of the Cu/GO/Pt device are measured as a function of temperature. Figure 13(a) shows the typical metallic behavior of the resistance in the On state. In contrast, the resistance in the Off state shows a semiconducting behavior as displayed in the inset of Fig. 13(a). The metallic conducting behavior in the low resistance state indicates the formation of conducting filaments in the GO films. The temperature dependence of metallic resistance can be written as $R(T) = R_0[1 + a(T - T_0)]$, where R_0 is the resistance at temperature T_0, and a is the temperature coefficient of resistance. By choosing T_0 as 300 K, the temperature coefficient of resistance of the filaments is calculated to be 1.7×10^{-3} K^{-1}, which is similar to the value 2.5×10^{-3} K^{-1} for high-purity copper nanowires of diameter ≥15 nm (Bid et al., 2006), confirming that the filaments are composed of Cu in metallic states due to the diffusion of the top electrode under a bias voltage. The discrepancy of the temperature coefficient of resistance is attributed to inevitable defects in the Cu filaments, since the presence of defects can reduce the temperature coefficient of resistance by shortening the mean free path of electrons (Bid et al., 2006).

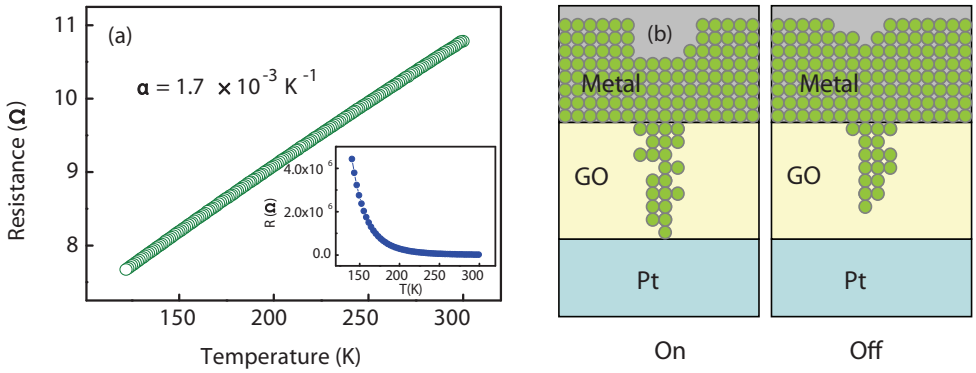

Fig. 13. (a) Temperature dependence of the resistance in the low resistance sate of the Cu/GO/Pt device. The inset shows the temperature dependence of the resistance in the high resistance state. Also shown is the temperature coefficient of resistance (a) of the conducting filaments. (b) A schematic diagram for the mechanism of resistive switching effects in metal/GO/Pt devices.

ii. Desorption/absorption of oxygen-related group on the GO sheets

Figure 14(a) shows the typical local *I-V* characteristics of GO films by the conductive atomic force microscopy measurements in which the AFM tip is in perpetual contact with the sample. The obvious bipolar resistive switching effect is also observed though the threshold

voltages are higher probably due to the nonideal contact between the AFM probe and GO films as well as very small contact area compared to the conventional *I-V* characterization (Yin et al., 2010). In this case, we intend to attribute the observed resistive switching to the desorption/absorption of oxygen-related groups on the GO sheets. As shown in Fig. 14(c), a GO layer can be considered as a graphene sheet with epoxide, hydroxyl, and/or carboxyl groups attached to both sides, and physical properties of GO can be modulated by those chemical functionalities on the surface (Yan et al., 2009). When there are an amount of epoxide, hydroxyl, and carboxyl groups on the GO surface, the conductance of GO is assumed to be low due to sp^3 bonding feature. As a negative voltage bias is applied on the bottom electrode (i.e., Pt), some oxygen-related functional groups inside the GO layers are removed, resulting in an amount of sp^2 bonds. The conductance of GO becomes higher due to an increase in the concentration of interlayer π electrons. As a result, the sample is switched to the low resistance state (On state). While sweeping the voltage to certain positive values, the oxygen-related groups diffuse toward GO sheets and attach to them again. Correspondingly, the sample returns to the high resistance state (Off state). Therefore, as schematically shown in Fig. 14(b), the desorption and absorption of the oxygen-related functional groups on the GO sheets correspond to the low and high resistive states, respectively.

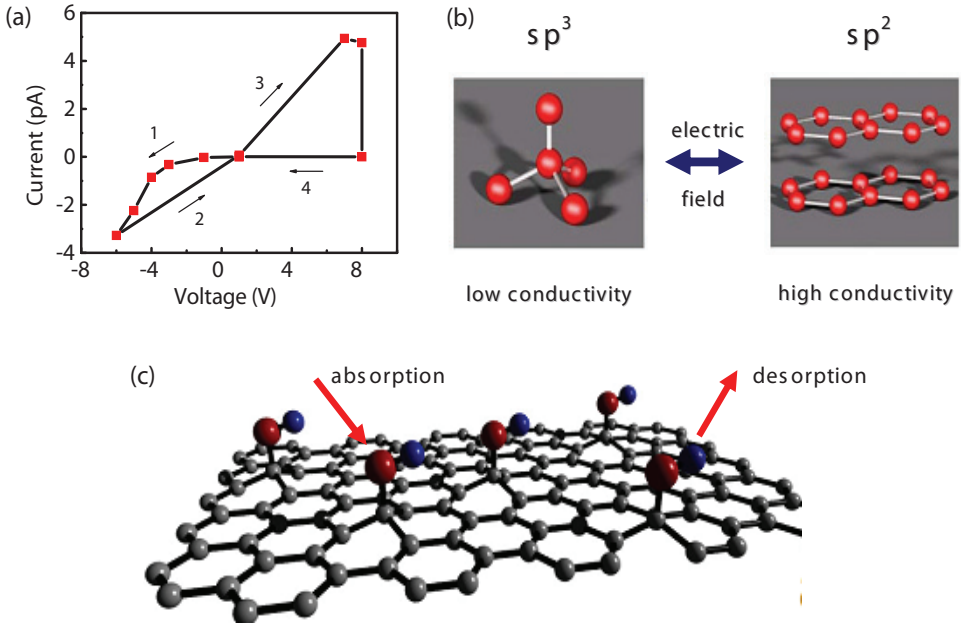

Fig. 14. (a) Typical local *I-V* characteristics of GO films measured by conductive atomic force microscopy. The voltage is swept in the direction as follows: 0 V → –6 V → 0 V → 8 V → 0 V. (b) Insulating carbon can be switched to conductive sp^2-rich carbon and conductive carbon can be switched to sp^3-rich carbon by applying appropriate electric fields (Kreupl et al., 2008). (c) Schematic of the desorption and aborption of hydroxyl or similar groups on the GO sheets (Echtermeyer et al., 2008).

4. Conclusion

Reliable and reproducible resistive switching behaviors are observed in GO thin films. The metal/GO/Pt structures exhibit an On/Off ratio of about 20, switching threshold voltages of less than 1 V, good retention and endurance performances. The Ag/GO/Pt structure has a low Forming voltage likely due to a large Ag ion diffusion coefficient in GO, whereas the Au/GO/Pt structure shows a high Forming voltage likely due to gold's chemical inertness. The Forming voltage increases with the thickness of GO, indicating that the electric field inside the bulk GO is the controlling factor of the Forming. The resistances of the high and low resistance states show weak dependence on the film thickness, demonstrating that the resistive switching occurs in a confined region. It is found that the resistance of the On state decreases with current compliance, whereas the Reset current and Reset voltage increase with current compliance. Therefore, by adjusting current compliance, the power consumption of RRAM can be modulated and multilevel storage can be realized. The resistive switching is also observed in micro-regions by conducting atomic force microscope. The dominant conduction mechanisms of low and high resistance states are Ohmic behavior and trap-controlled space charge limited current, respectively. Based on the experimental results, the possible physical mechanisms of resistive switching behaviors in GO thin films can be understood by considering the desorption/absorption of oxygen-related groups on the GO sheets as well as the formation/rupture of conducting filaments.

This work was supported by State Key Research Program of China (973 Program), National Natural Science Foundation of China, Zhejiang and Ningbo Natural Science Foundations, Chinese Academy of Sciences (CAS), Zhejiang Qianjiang Talent Project, and State Key Lab of Silicon Materials (China).

5. References

*Corresponding author. Electronic mail: runweili@nimte.ac.cn.

Avouris P.; Chen Z. H.; & Perebeinos V. (2007). Carbon-based electronics. *Nature Nanotechnology,* Vol. 2, No. 10, 605-615, ISSN: 1748-3387

Banno N.; Sakamoto T.; Iguchi N.; Sunamura H.; Terabe K.; Hasegawa T. & Aono M. (2008). Diffusivity of Cu ions in solid electrolyte and its effect on the performance of nanometer-scale switch. *IEEE Transactions on Electron Devices*, Vol. 55, No. 11, 3283–3287, ISSN: 0018-9383

Beck A.; Bednorz J. G.; Gerber Ch.; Rosse C.L. & Widmer D. (2000). Reproducible switching effect in thin oxide films for memory applications. *Applied Physics Letters*, Vol. 77, No. 1, 139-141, ISSN: 0003-6951

Bid A.; Bora A. & Raychaudhuri A. (2006). Temperature dependence of the resistance of metallic nanowires of diameter ≥15 nm: Applicability of Bloch-Gruneisen theorem. Physical Review B, Vol. 74, No. 3, 035426, ISSN: 1098-0121

Burghard M.; Klauk H.; & Kern K. (2009). Carbon-Based Field-Effect Transistors for Nanoelectronics. *Advanced Materials*. Vol. 21, No. 25-26, 2586-2600, ISSN: 0935-9648

Chang W. Y.; Lai Y. C.; Wu T. B.; Wang S. F.; Chen F. & Tsai M. J. (2008). Unipolar resistive switching characteristics of ZnO thin films for nonvolatile memory applications. *Applied Physics Letters*. Vol. 92, No. 2,022110, ISSN: 0003-6951

Chen X. M.; Wu G. H. & Bao D. H. (2008). Resistive switching behavior of $Pt/Mg_{0.2}Zn_{0.8}O/Pt$ devices for nonvolatile memory applications. *Applied Physics Letters,* Vol. 93, No. 9, 093501, ISSN: 0003-6951

Cote L. J.; Kim F. & Huang J. X. (2009). Langmuir−Blodgett Assembly of Graphite Oxide Single Layers. *Journal of the American Chemical Society,* Vol. 131, No. 3, 1043-1049, ISSN: 0002-7863

Dearnaley, G.; Morgan, D. V. & Stoneham, A. M. (1970). A model for filament growth and switching in amorphous oxide films. *Journal of Non-Crystalline Solids,* Vol. 4, 593–612, ISSN: 0022-3093

Dearnaley, G.; Stoneham, A. M. & Morgan, D. V. (1970). Electrical phenomena in amorphous oxide films. *Reports on Progress in Physics,* Vol. 33, No. 3, 1129–1191, ISSN: 0034-4885

Do Y. H.; Kwak J. S.; Hong J. P.; Jung K. & Im H. (2008). Al electrode dependent transition to bipolar resistive switching characteristics in pure TiO_2 films. *Journal of Applied physics*, Vol. 104, No. 11, 114512, ISSN: 0021-8979

Dong Y.; Yu, M G.; McAlpine C.; Lu W. & Lieber C. M. (2008). Si/α-Si core/shell nanowires as nonvolatile crossbar switches. *Nano Letters*, Vol. 8, No. 2, 386-391, ISSN: 1530-6984

Echtermeyer T. J.; Lemme M. C.; M. Baus et al. (2007). A grapheme-based electrochemical switch. arXiv:0712.2026v1

Eda G.; Fanchini G. & Chhowalla M. (2008). Large-area ultrathin films of reduced graphene oxide as a transparent and flexible electronic material. *Nature Nanotechnology*, Vol. 3, No. 5, 270-274, ISSN: 1748-3387

Fujiwara K.; Nemoto T.; Rozenberg M. J.; Nakamura Y. & Takagi H. (2008). Resistance Switching and Formation of a Conductive Bridge in Metal/Binary Oxide/Metal Structure for Memory Devices. *Japanese Journal of Applied Physics*, Vol. 47, No. 8, 6266-6271, ISSN: 0021-4922

Govindaraj R.; Kesavamoorthy R.; Mythili R. & Viswanathan B. (2001). The formation and characterization of silver clusters in zirconia. *Journal of Applied Physics*, Vol. 90, No. 2, 958–963, ISSN : 0021-4922

Guan W. H.; Long S. B.; Jia R.& Liu M. (2007). Nonvolatile resistive switching memory utilizing gold nanocrystals embedded in zirconium oxide. *Applied Physics Letters,* Vol. 91, No. 6, 062111, ISSN: 0003-6951

Guan W. H.; Liu M.; Long S. B.; Liu Q. & Wang W. (2008). On the resistive switching mechanisms of Cu/ZrO_2:Cu/Pt. *Applied Physics Letters* , Vol. 93, No. 22, 223506, ISSN: 0003-6951

He C. L.; Zhuge F.; Zhou X. F.; Li M.; Zhou G. C.; Liu Y. W.; Wang J. Z.; Chen B.; Su W. J.; Liu Z. P.; Wu Y. H.; Cui P. & Li R. W. (2009). Nonvolatile resistive switching in grapheme oxide thin films. *Applied Physics Letters*, Vol. 95, No. 23, 232101, ISSN: 0003-6951

Hummers W. S. & Offeman R. E. (1958). Preparation of Graphitic Oxide. *Journal of the American Chemical Society,* Vol. 80, No. 6,1339, ISSN: 0002-7863

Inoue I. H.; Yasuda S.; Akinaga H. & Takagi H. (2008). Nonpolar resistance switching of metal/binary-transition-metal oxides/metal sandwiches: Homogeneous/inhomogeneous transtion of current distribution. *Physical Review B*, Vol. 77, No. 3, 035105, ISSN: 1098-0121

Jeong D. S.; Schroeder H. & Waser R. (2009). Abnormal bipolar-like resistance change behavior induced by symmetric electroforming in Pt/TiO_2/Pt resistive switching cells. *Nanotechnology*, Vol. 20, No. 37, 375201, ISSN: 0957-4484

Jo S. H. & Lu W. (2008). CMOS Compatible Nanoscale Nonvolatile Resistance Switching Memory. *Nano Letters,* Vol. 8, No. 2, 392-397, ISSN: 1476-1122

Jo S. H.; Kim K. H. & Lu W. (2009). Programmable Resistance Switching in Nanoscale Two-Terminal Devices. *Nano Letters*, Vol. 9, No. 1, 496-500, ISSN: 1476-1122

Jo, S. H.; Kim K. H. & Lu W. (2009). High-Density Crossbar Arrays Based on a Si Memristive System. *Nano Letters*, Vol. 9, No. 2, 870-874 , ISSN: 1476-1122

Kim D. C.; Lee M. J.; Ahn S. E.; Seo S.; Park J. C.; Yoo I. K.; Baek I. G.; Kim H. J.; Yim E. K.; Lee J. E.; Park S. O.; Kim H. S.; In Chung U.; Moon J. T. & Ryu B. I. (2006). Improvement of resistive memory switching in NiO using IrO_2. *Applied Physics Letters*, Vol. 88, No. 23, 232106, ISSN: 0003-6951

Kim K. M.; Choi B. J.; Shin Y. C.; Choi S. & Hwang C. S. (2007). Anode-interface localized filamentary mechanism in resistive switching of TiO_2 thin films. *Applied Physics Letters*, Vol. 91, No. 1, 012907, ISSN: 0003-6951

Kim S.; Moon H.; Gupta D.; Yoo S. & Choi Y. K. (2009). Resistive Switching Characteristics of Sol–Gel Zinc Oxide Films for Flexible Memory Applications. *IEEE Transactions on Electron Devices*, Vol. 56, No. 4, 696-699 , ISSN: 0018-9383

Kinoshita K.; Tamura T.; Aoki M.; Sugiyama Y. & Tanaka H. (2006). Bias polarity dependent data retention of resistive random access memory consisting of binary transition metal oxide. *Applied Physics Letters*, Vol. 89, No. 10, 103509, ISSN: 0003-6951

Kinoshita K.; Yoshida C.; Aso H.; Aoki M. & Sugiyama Y. (2006). Thermal properties of NiO_y resistor practically free from the "forming" process, *Proceedings of International Conference on Solid State Devices and Materials*, pp. 570-571, Pacifico Yokohama Yokohama, Japan, Sept. 2006

Kreupl F.; Bruchhaus R.; Majewski P. et al. (2008). Carbon-based resistive memory. *Proceeding of IEEE Electron Devices Meeting*, pp. 521-524

Kund M.; Beitel G.; Pinnow C.U.; Röhr T.; Schumann J.; Symanczyk R.; Ufert K.D. & Müller G. (2005). Conductive bridging RAM (CBRAM): An emerging non-volatile memory technology scalable to sub 20 nm, *Electron Devices Meeting, 2005, IEDM Technical Digest, IEEE International*, pp. 754–757. ISBN: 0-7803-9268-x, Washington, DC, Dec. 2005, IEEE

Kwon D. H.; Kim K. M.; Jang J. H.; Jeon J. M.; Lee M. H.; Kim G. H.; Li X. S.; Park G. S.; Lee B.; Han S.; Kim M. & Hwang C. S. (2010). Atomic structure of conducting nanofilaments in TiO_2 resistive switching memory. *Nature Nanotechnology*, Vol. 5, No. 2, 148-153, ISSN: 1748-3387

Lee M. J.; Park Y.; Suh D. S.; Lee E. H.; Seo S.; Kim D. C.; Jung R.; Kang B. S.; Ahn S. E.; Lee C. B.; Seo D. H.; Cha Y. K.; Yoo I. K.; Kim, J. S. & Park B. H. (2007). Two Series Oxide Resistors Applicable to High Speed and High Density Nonvolatile Memory. *Advanced Materials*, Vol. 19, No. 22, 3919-3923, ISSN: 0935-9648

Li Y. B.; Sintskii A. & Tour J. M. (2008). Electronic two-terminal bistable graphitic memories. *Nature Materials*, Vol. 7, No. 12, 966 -971, ISSN: 1476-1122

Li M.; Zhuge F.; Zhu X. J.; Yin K. B.; Wang J. Z.; Liu Y. W.; He C. L.; Chen B. & Li R. W. (2010). Nonvolatile resistive switching in metal/La-doped $BiFeO_3$/Pt sandwiches. *Nanotechnology*, Vol. 21, No. 42, 425202, ISSN: 0957-4484

Li Y. T.; Long S. B.; Zhang M. H.; Liu Q.; Shao L. B.; Zhang S.; Wang Y.; Zuo Q. Y.; Liu S. & Liu M. (2010). Resistive switching properties of Au/ZrO_2/Ag structure for low-voltage nonvolatile memory applications. *IEEE Electron Device Letters*, Vol. 31, No. 2, 117-119, ISSN: 0741-3106

Liao Z. L.; Wang Z. Z.; Meng Y.; Liu Z. Y.; Gao P.; Gang J. L.; Zhao H. W.; Liang X. J.; Bai X. D. & Chen D. M. (2009). Categorization of resistive switching of metal-$Pr_{0.7}Ca_{0.3}MnO_3$-metal devices. *Applied Physics Letters*, Vol. 94, No. 25, 253503, ISSN: 0003-6951

Liu S. Q.; Wu N. J. & Ignatiev A. (2000). Electric-pulse-induced reversible resistance change effect in magnetoresistive films. *Applied Physics Letters*, Vol. 76, No. 19, 2749-2751, ISSN: 0003-695

Liu Q.; Long S. B.; Wang W.; Zuo Q. Y.; Zhang S.; Chen J. N. & Liu M. (2009). Improvement of Resistive Switching Properties in ZrO_2 -Based ReRAM With Implanted Ti Ions. *IEEE Electron Device Letters,* Vol. 30, No. 12, 1335-1337, ISSN: 0741-3106

Lu W. & Lieber C. M. (2007). Nanoelectronics from the bottom up. *Nature Materials*, Vol. 6, No. 11, 841-850, ISSN: 1476-1122

Meijer G. I. (2008). MATERIALS SCIENCE: Who Wins the Nonvolatile Memory Race?. *Science*, Vol. 319, No. 5870, 1625-1626, ISSN: 0036-8075

Novoselov K. S.; Geim A. K.; Morozov S. V.; Jiang D.; Zhang Y.; Dubonos S. V.; Grigorieva I. V.; & Firsov A. A. (2004). Electric field effect in atomically thin carbon films. *Science*, Vol. 306, No. 5696, 666-669, ISSN: 0036-8075

Odagawa A.; Sato H.; Inoue, I. H.; Akoh H.; Kawasaki M.& Tokura Y. (2004). Colossal electroresistance of a $Pr_{0.7}Ca_{0.3}MnO_3$ thin film at room temperature. *Physical Review B*, Vol. 70, No. 22, 224403, ISSN: 1098-0121

Oligschlaeger R.; Waser R.; Meyer R.; Karthauser S. & Dittmann R. (2006). Resistive switching and data reliability of epitaxial (Ba,Sr)TiO_3 thin films. *Applied Physics Letters*, Vol. 88, No. 4, 042901, ISSN: 0003-6951

Rakhshani, A. E.; Hogarth, C. A. & Abidi, A. A. (1976). Observations of local defects caused by electrical conduction through thin sandwich structures of Ag–SiO/BaO–Ag. *Journal of Non-Crystalline Solids,* Vol. 20, No. 1, 25–42, ISSN: 0022-3093

Ray, A. K. & Hogarth, C. A. (1990). Recent advances in the polyfilamentary model for electronic conduction in electro-formed insulating films. *International Journal of Electronics,* Vol. 69, No. 1, 97–107, ISSN: 0020-7217

Rohde C.; Choi B. J.; Jeong D. S.; Choi S.; Zhao J. S. & Hwang C. S. (2005). Identification of a determining parameter for resistive switching of TiO_2 thin films. *Applied Physics Letters*, Vol. 86, No. 26, 262907, ISSN: 0003-6951

Rueckes T.; Kim K.; Joselevich E.; Tseng G. Y.; Cheung C. L.; & Lieber C. M. (2000). Carbon nanotube-based nonvolatile random access memory for molecular computing. *Science*, Vol. 289, No. 5476, 94-97, ISSN: 0036-8075

Schindler C.; Meier M. & Waser R. (2007). Resistive switching in Ag-Ge-Se with extremely low write currents, *Proceedings of Non-Volatile Memory Technology Symposium*, pp. 82–85, Print ISBN: 978-1-4244-1361-4, Albuquerque, NM, Nov. 2007, IEEE

Seo S.; Lee M. J.; Seo D. H.; Jeoung E. J.; Suh D.S.; Joung Y. S.; Yoo I. K.; Hwang I. R.; Kim S. H.; Byun I. S.; Kim J.S.; Choi J. S. & Park B. H. (2004). Reproducible resistance switching in polycrystalline NiO films. *Applied Physics Letters*, Vol. 85, No. 23, 5655-5657, ISSN: 0003-6951

Son J. Y. & Shin Y. H. (2008). Direct observation of conducting filaments on resistive switching of NiO thin films. *Applied Physics Letters*, Vol. 92, No. 22, 222106, ISSN: 0003-6951

Stewart D. R.; Ohlberg D. A. A.; Beck P. A.; Chen Y.; Williams R. S.; Jeppesen J. O.; Nielsen K. A. & Stoddart J. F. (2004). Molecule-Independent Electrical Switching in Pt/Organic Monolayer/Ti Devices. *Nano Letters*, Vol. 4, No. 1, 133-136, ISSN: 1476-1122

Strukov D. B.; Snider G. S.; Stewart D. R. & Williams R. S. (2008). The missing memristor found. *Nature*, Vol. 453, No. 7191, 80 -83, ISSN: 0028-0836

Szot K.; Speier W.; Bihlmayer G. & Waser R. (2006). Switching the electrical resistance of individual dislocations in single-crystalline $SrTiO_3$. *Nature Materials* , Vol. 5, No. 4, 312-320, ISSN: 1476-1122

Tokunaga Y.; Kaneko Y.; He J. P.; Arima T.; Sawa A.; Fuji T.; Kawasaki M. et al. (2006). Colossal electroresistance effect at metal electrode/$La_{1-x}Sr_{1+x}MnO_4$ interfaces. *Applied Physics Letters,* Vol. 88, No. 22, 223507, ISSN: 0003-6951

Tsubouchi K.; Ohkubo I.; Kumigashira H.; Oshima M.; Matsumoto Y.; Itaka K.; Ohnishi T. et al. (2007). High-Throughput Characterization of Metal Electrode Performance for Electric-Field-Induced Resistance Switching in Metal/$Pr_{0.7}Ca_{0.3}MnO_3$/Metal Structures. *Advanced Materials*, Vol. 19, No. 13, 1711-1713, ISSN: 1476-1122

Tsunoda K.; Fukuzumi Y.; Jameson J. R.; Wang Z.; Griffin P. B. & Nishi Y. (2007). Bipolar resistive switching in polycrystalline TiO2 films. *Applied Physics Letters,* Vol. 90, No. 11, 113501, ISSN: 0003-6951

Wang X. R.; Ouyang Y. J.; Li X. L.; Wang H. L.; Guo J.; & Dai H. J. (2008). Room-Temperature All-Semiconducting Sub-10-nm Graphene Nanoribbon Field-Effect Transistors. *Physical Review Letters,* Vol. 100, No. 20, 206803, ISSN: 0031-9007

Waser R. & Aono M. (2007). Nanoionics-based resistive switching memories. *Nature Materials*, Vol. 6, No. 11, 833-840, ISSN: 1476-1122

Wu X.; Zhou P.; Li J; Chen, L. Y.; Lv H. B.; Lin Y. Y. & Tang T. A. (2007). Reproducible unipolar resistance switching in stoichiometric ZrO_2 films. *Applied Physics Letters*, Vol. 90, No. 18 ,183507, ISSN: 0003-6951

Yan J. A.; Xian L. & Chou M. Y. (2009). Structural and electronic properties of oxidized graphene, *Physical Review Letters*, Vol. 103, No. 8, 086802, ISSN: 0031-9007

Yang C. H.; Seidel J.; Kim S. Y.; Rossen P. B.; Yu P.; Gajek M.; Chu Y. H.; Martin L. W.; Holcomb M. B.; He Q.; Maksymovych P.; Balke N.; Kalinin S. V.; Baddorf A. P.; Basu S. R. et al. (2009). Electric modulation of conduction in multiferroic Ca-doped $BiFeO_3$ films. *Nature Materials*, Vol. 8, No. 6, 485-493, ISSN: 1476-1122

Yang Y. C.; Pan F.; Liu Q.; Liu M. & Zeng F. (2009). Fully Room-Temperature-Fabricated Nonvolatile Resistive Memory for Ultrafast and High-Density Memory Application. *Nano Letters*, Vol. 9, No. 4, 1636-1643, ISSN: 1476-1122

Yin K. B.; Li M.; Liu Y. W.; He C. L.; Zhuge F.; Chen B.; Lu W.; Pan X. Q. & Li R. W. (2010). Resistance switching in polycrystalline $BiFeO_3$ thin films. *Applied Physics Letters,* Vol. 97, No. 4, 042101, ISSN: 0003-6951

Zhou X. F. & Liu Z. P. (2010). A Scalable, Solution-phase Processing Route to Ultralarge Graphene Sheets. *Chemical Communications*, Vol. 46, No. 15, 2611-2613, ISSN: 1359-7345

Zhou Y. H.; Liu H. B.; Fu L.; Li B. & Chen Z. Z. (2006). Influence of pyrolytic temperature on structures and properties of graphite oxide. *Journal of the Chinese Ceramic Society*, Vol. 34, No. 3, 318-323, ISSN: 0454-5648

Zhuge F.; Dai W.; He C. L.; Wang A. Y.; Liu Y. W.; Li M.; Wu Y. H.; Cui P. & Li R. W. (2010). Nonvolatile resistive switching memory based on amorphous carbon. *Applied Physics Letters*, Vol. 96, No. 16,163505, ISSN: 0003-6951

18

Measuring Disorder in Graphene with Raman Spectroscopy

Ado Jorio[1], Erlon H. Martins Ferreira[2], Luiz G. Cançado[3], Carlos A. Achete[4] and Rodrigo B. Capaz[5]

[1,3]*Departamento de Física, Universidade Federal de Minas Gerais*
[2,4]*Instituto Nacional de Metrologia, Normalização e Qualidade Industrial*
[5]*Instituto de Física, Universidade Federal do Rio de Janeiro*
Brazil

1. Introduction

Since the experimental discovery of an easy method to produce graphene (Novoselov et al., 2004; 2005), there is a continuous rising of interest on this fascinating material. Due to its own peculiar electronic band structure, graphene is a promising material for the future electronic nanodevice industry. In any production process is of fundamental importance to control the quality of materials in a fast and non-destructive manner. Quantifying defects in graphene related systems is a major problem for the application of such materials (Neto et al., 2009).
In the field of carbon-based nanostructures, Raman spectroscopy has shown to be the most suitable technique since it accomplishes those desirable goals and also because it can be used to differentiate the many types of sp^2 carbon structures and to identify the presence of defects (Ferrari & Robertson, 2000; Pimenta et al., 2007). Defects are of great importance since they modify the electronic and optical properties of the system, sometimes in a desirable way. Raman spectroscopy is also one of the most sensitive techniques to probe disorder in carbon structures. The development of an accurate methodology to study disorder with Raman spectroscopy will certainly facilitate the control of the amount of induced disorder in a target system. By combining experiment and theory, a phenomelogical model has been established to explain the evolution of the Raman spectrum of graphene with increasing amount of disorder caused by low energy ion bombardment. Using this model one can extract information about the density of defects, the average defect size and also the Raman process relaxation length and its dependence with the laser excitation energy and temperature. How the ion bombardment procedure affects graphene samples with two or more layers and graphene read edges has also been studied.

2. Review of Raman spectroscopy in graphene-related systems

Graphene has two atoms in the unit cell and, therefore, six phonon branches. Three are acoustic branches and three are optical branches. From the three optical branches, one gives rise to an infra-red active mode at the Γ point, while the two other branches are degenerate at the Γ point and Raman active. Therefore, zone center ($q = 0$) phonons would generate a one peak Raman spectra. However, the electronic structure of graphene generates special

electron-phonon induced resonance conditions with non-zone center modes ($q \neq 0$), known in the literature as the double-resonance Raman scattering process. This double-resonance process is responsible for the graphene related systems to have a Raman spectra with many features (Saito et al., 2002; Thomsen & Reich, 2000).

Although the double resonance process can activate phonons from all the six branches, the main features in the Raman spectra of graphene come from the phonon branch related to the zone-center Raman-active mode, i.e. to the optical phonon branch related to in-plane stretching of the C-C bondings. The strongest Raman peaks in crystalline graphene are the so-called G (~1584 cm^{-1}) and G' (~2400-2800 cm^{-1}) bands. The first is the first-order Raman-allowed mode at the Γ point, and the second is a second-order Raman-allowed mode near the K point, activated by the double-resonance process. Furthermore, the presence of disorder in the crystalline lattice causes changes in the graphene Raman spectra, the most evident being the appearance of two new peaks, the so-called D (~1200-1400 cm^{-1}) and D' (1600-1630 cm^{-1}) bands. Both bands come from the in-plane optical branches (iTO and LO, respectively) and both are related to the double-resonance process. The D band comes from the iTO phonon near the K point, while the D' band comes from the LO phonon near the Γ point.

Since 1970, large efforts have been devoted to develop disorder-quantification methods using Raman spectroscopy for nano-graphite (Cançado et al., 2006; Ferrari & Robertson, 2000; Pimenta et al., 2007; Tuinstra & Koenig, 1970), carbon nanotubes (Chou et al., 2007; Hulman et al., 2005) and graphene (Jorio et al., 2010; Lucchese et al., 2010; Martins Ferreira et al., 2010; Teweldebrhan & Baladin, 2009). The most advanced protocols have been developed for the edge-defects in nano-graphite, where the in-plane crystallite dimensions ranging from $L_a = 20\,\text{nm}$ up to values larger than a microscope spot size can be obtained by measuring the intensity ratio between the disorder induced D band and the first-order allowed tangential G band, including the dependence of I_D/I_G with the excitation laser wavelength, as given by (Cançado et al., 2006)

$$L_a(\text{nm}) = (2.4 \times 10^{-10})\lambda_{laser}^4 (I_D/I_G)^{-1}. \quad (1)$$

Such behavior is shown in Figure 1. Equation 1 gives the state-of-the-art for using Raman spectroscopy to quantify nano-graphite crystallite sizes, which is related to a certain type of disorder that are the graphene edges. Of course the result given above is an averaged measure of all possible edge structures present in a bulk nanographite sample. It has been shown that the D band intensity depends on the atomic structure at the edge, and it is actually absent in graphite edges when the atomic structure exhibit the zigzag arrangement (Cançado et al., 2004). Figure 2 shows an example of a graphite edge. The atomic orientation of the lattice was identified with scanning tunnelling microscopy, thus showing that the armchair and zigzag orientations are parallel to edges 1 and 2 in Figure 2, respectively. This is consistent with the observed change in the D band intensity, but the observation of a small but non-null D band at edge 2 shows that the structure at the edge is not perfectly zigzag. This result has been used to identify zigzag vs. armchair edges in graphene as well (Neubeck et al., 2010), although up to date there is no evidence of perfect zigzag graphene edged. Such a perfect zigzag edge structure would be evidenced by the observation of a D' band in the Raman spectra with a complete absence of the D band (Cançado et al., 2004).

Finally, the picture discussed above does not hold for ion-bombarded induced defects in graphene samples, as shown by (Lucchese et al., 2010), because of the simple and fundamental geometric difference between defects related to the size of a nano-crystallite and point defects in the lattice, which changes the I_D/I_G dependence on the amount of disorder. Basically, the

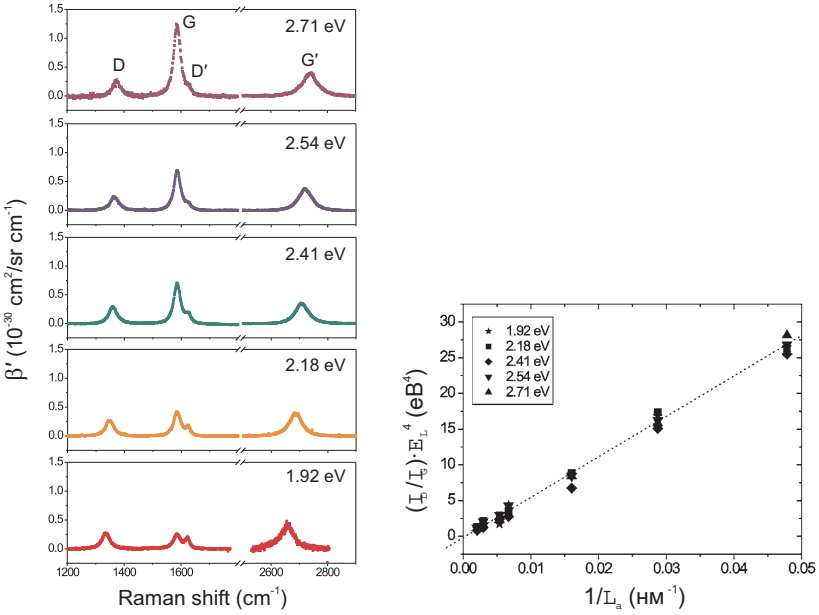

Fig. 1. (a) The spectral differential cross section β' of the D, G, D', and G' bands for the nanographite sample with $L_a = 35$ nm, using five different values of E_L, each indicated at the top of the respective spectrum. The same vertical scale was used for the five spectra for comparison. (Cançado et al., 2007) (b) The intensity ratio I_D / I_G for nanographite samples normalized by E_L^4, plotted versus $1/L_a$ using five different laser excitation energies (Cançado et al., 2006).

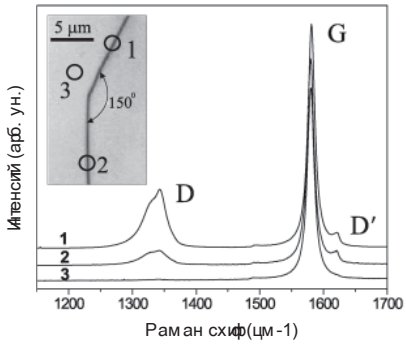

Fig. 2. Raman spectra obtained in three different regions of a highly oriented pyrolytic graphite (HOPG) sample. The inset shows an optical image of the step and the regions where spectra 1, 2, and 3 were taken (open circles). The atomic structure of the sample was identified using scanning tunneling microscopy, and the edges 1 and 2 were identified as parallel to the armchair and zigzag orientations, respectively. (Cançado et al., 2004)

disorder in a nano-crystallite can be quantified by the amount of border (one-dimensional defects) with respect to the total crystallite area, and this is a measure of the average inverse nano-crystallite size $1/L_a$. In ion bombarded graphene, the disorder is better quantified by the defect concentration, defined by $1/L_D^2$, where L_D is a typical interdefect distance, with the defect being a point-like (zero-dimensional) structure. In the following sections we will discuss these concepts in depth to develop the methods to quantify disorder in graphene related systems.

3. Creating defects on graphene by ion bombardment

There are many different techniques that could be used to investigate the amount of disorder in graphene, but Raman spectroscopy is certainly a fast and easy way to do it. However, to extract quantitative information from a Raman spectrum we need to calibrate the procedure. Such a calibration can be achieved with the help of a more direct technique such as scanning tunneling microscopy (STM), which can show the defects on the surface of a material. Doing STM on an exfoliated graphene is still a challenging task, since we need a graphene sample deposited on a conductive surface or make an electrical contact. The first method may complicate (if not prevent) to find the graphene on the surface and the second method can cause non-desirable defects on the sample (Ishigami et al., 2007; Neubeck et al., 2010). On the other hand, performing STM on graphite is a much simpler procedure, since the bulk graphite is conductive. One can then irradiate the graphite with low energy ions, do the STM image to count the number of defects per unit area and then perform the Raman measurement to correlate the relative intensity between the *D* and *G* bands with the measured ion dose. In a second step one can perform the same kind of irradiation on a graphene sample and use a HOPG flake as a reference for determining the actual ion dose (Lucchese et al., 2010).

Figure 3 shows STM images of a bulk HOPG surfaces, both pristine (a) and bombarded with 90 eV argon ions (b-e). Using the same parameters of current and ion energy, the increasing ion dose was obtained by increasing the bombardment time. From (b) to (e) the ion dose has been increased from 10^{11} Ar^+/cm^2 up to 10^{14} Ar^+/cm^2, which corresponds to an average distance between defects from $L_D = 32$ nm down to $L_D = 1$ nm. The right panel shows the Raman spectra measured for pristine HOPG and for the same HOPG right after each bombardment procedure shown in panels (b-e) (increasing bombardment dose from bottom to top). Although for the highest dose the HOPG surface seems already completely damaged, the Raman spectrum shows a well defined *G* band, indicating that the ions affect mostly the upper layers. To fully calibrate the bombardment procedure that is further going to be applied to the graphene samples, ion bombardment and consecutive Raman measurements on HOPG were performed three times, for up to eight different ion doses between 10^{11} and 10^{15} Ar^+/cm^2. The Raman response was measured at up to 7 locations within the HOPG specimen for each ion dose (Jorio et al., 2009).

Using this procedure, the same bombardment can be applied to a graphene sample. When obtaining a graphene sample by the micro-mechanical cleavage of graphite and further deposition on a SiO_2 substrate ("scotch tape" method), one can always find some bulk graphite flake next to a graphene sample. This small flake can then be used as a "standard" for the ion dose calibration by comparing its Raman spectrum with the previously HOPG measured spectrum discussed in Fig. 3. Thus one can skip the STM procedure on the graphene sample to actually count the number of defects on the sample. Figure 4(a) shows the Raman spectra of such a ion bombarded monolayer graphene subject to the same ion doses measured in the HOPG case. It is clear from those spectra that the graphene sample is much more

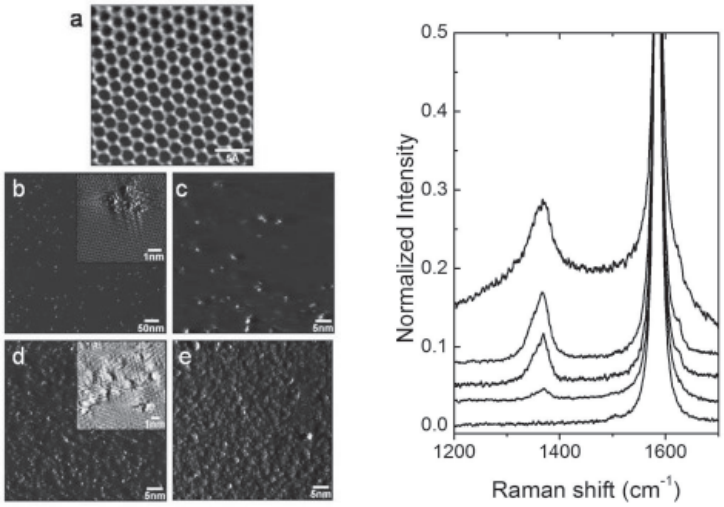

Fig. 3. Left panel are the STM images of (a) pristine HOPG surface and (b)–(e) after increasing ion bombardment showing how the defects are spread on the surface. (a) to (e) corresponds to zero, 10^{11}, 10^{12}, 10^{13}, 10^{14} Ar^+/cm^2 dose. Insets to (b) and (d) show some defects in detail. The right panel shows the Raman spectra of pristine HOPG and the same HOPG right after each bombardment in (a-e), increasing ion dose from bottom to top, showing the increasing *D* band.

sensitive to the ion bombardment procedure than the bulk graphite. Because it has just one layer, there is no extra contribution to the *G* band intensity as in the case of the inner layers of the HOPG sample. Then the relative intensity I_D/I_G increases up to ~ 3.5 in the monolayer case while it never reaches 1 in the HOPG sample, with an excitation laser energy of 2.41 eV ($\lambda = 514$ nm). A more complete behavior of those relative intensities can be seen in Figure 4(b). This graph shows the evolution of the relative intensity I_D/I_G with increasing ion dose (decreasing distance between defects) from 1.5×10^{11} to 2.5×10^{15} Ar^+/cm^2 (26 nm down to 0.63 nm) and compares with both the original Tuinstra-Koenig relation (Equation 1) for the graphite and a modified version introduced by (Lucchese et al., 2010). It is clear from the plot that Equation 1 does not hold for graphene because the topology of defects created by the ion bombardment is different from those boundaries defects. The relation introduced for point-like defects is (Lucchese et al., 2010).

$$\frac{I_D}{I_G} = \frac{C(\lambda)}{L_D^2}\,, \tag{2}$$

where, in this case, $C(514\text{ nm}) \sim 107\text{ nm}^2$. Still, the limit of validity of this relation is for the regime of low defect density (or $L_D > 6$ nm). In the graph we can see two well defined disorder regimes, one in the right side of the curve, which is the low disorder limit, and the one in the left side, which is typical of amorphous carbon structures. The complete model to describe the transition between the two regimes was described also in (Lucchese et al., 2010) and will be presented in Section 5.

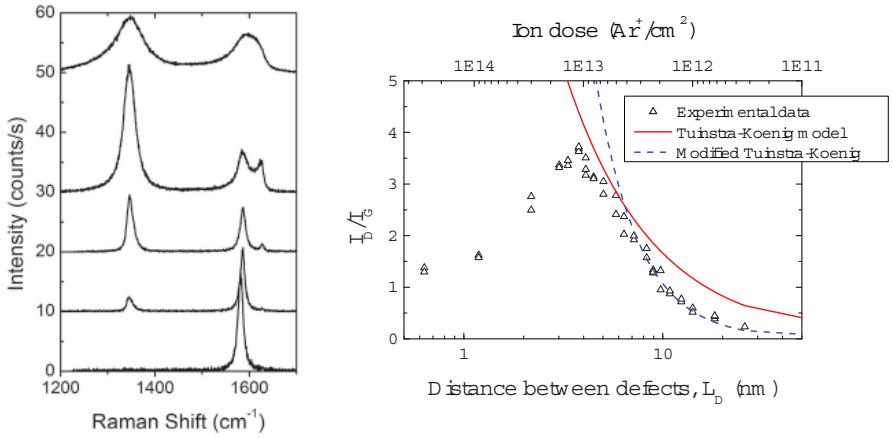

(a) (b)

Fig. 4. (a) Raman spectra of a monolayer graphene bombarded with low energy (90 eV) argon ions measured with a 514 nm laser. From bottom to top, curves correspond to zero, 10^{11}, 10^{12}, 10^{13} and 10^{14} Ar^+/cm^2 dose. (b) Comparison between experimental I_D/I_G data and both original and modified Tuinstra-Koenig relations for disorder in carbon structures (see text).

When studying disorder by means of Raman spectroscopy, the relative intensity between the D and G bands is the main feature that is taken into consideration. However, disorder is also responsible for the changes in the intensities of other bands, such as D' and G', and also affects the position and shape of the Raman peaks. Figure 5 plots the relative integrated areas of the main Raman bands, namely D, D' and G' with respect to G, and Figures 6(a) and 6(b) show the behaviour of the peak position and the full width at half maxium (FWHM) of those same bands for the same monolayer graphenes of Figure 4. A careful look at those plots shows that in the limit of low disorder (large L_D) there is no significant change in the peak position and just a slightly increase of the FWHM of all bands. However, for increasing disorder ($L_D \lesssim 4$ nm), there is an abrupt increase of the FWHM and also a small downshift in the peak positions. This suggests that even at moderately large disorder regimes, the C–C bonds are still sp^2 kind, with no significant strain in the bonds. When looking at the disorder in graphene, not only the ratio I_D/I_G must be considered, as it is clear that it is possible to have the same value of I_D/I_G for two different values of L_D. Therefore, it is important to look also at the values of the FWHM which can tell if the system is in lower or higher disorder regime.

4. Laser energy dependency

The experimental data presented in the previous Sections show that disorder introduced by a random distribution of defects causes significant changes in the relative intensities of the resonance Raman bands and it leads to broadening and shifting of those bands. Moreover, these effects appear to be strongly dependent on the laser excitation energy. It was a work by (Mernagh et al., 1984) that showed for the first time a strong dependency of the ratio I_D/I_G on the excitation laser energy E_L used in the Raman scattering experiment (Mernagh et al., 1984). Later on, (Cançado et al., 2006) measured the I_D/I_G ratio dependence on E_L for nanographites, and generated Equation 1.

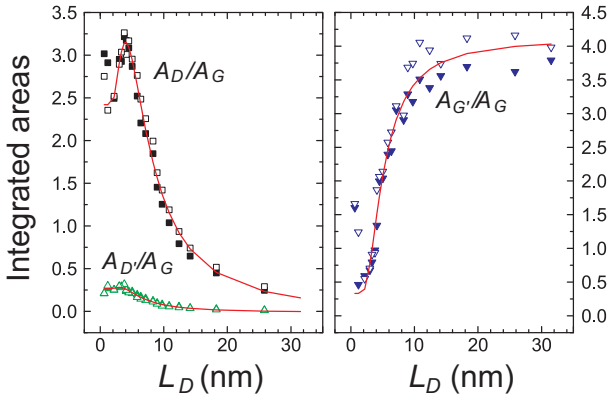

Fig. 5. Evolution of the integrated areas of the D, D' and G' bands normalized by the G band for a monolayer graphene bombarded with low energy argon ions. Symbols are the experimental data and the curves are the fitting with Equations 3 and 4. Open and filled symbols stand for two different graphene samples. (Martins Ferreira et al., 2010)

In this section we describe recent efforts to fully accomplish the protocol for quantifying the amount of point-like defects in graphene (or equivalently, L_D) (Cançado et al., 2011). For that, different excitation laser lines have been used for measuring the Raman spectra of ion bombarded samples with different L_D values and their respective I_D/I_G ratios.
Figures 7(a-c) show the Raman spectra of five distinct ion-bombarded graphene samples which were exposed to different ion bombardment doses in the range of 10^{11} Ar^+/cm^2 (one defect per 4×10^4 C atoms) to 10^{15} Ar^+/cm^2. The Raman spectra shown in panels (a), (b), and (c) were taken using the excitation laser energies (wavelengths) $E_L = 2.41$ eV ($\lambda_L = 514.5$ nm), $E_L = 1.96$ eV ($\lambda_L = 632.8$ nm), and $E_L = 1.58$ eV ($\lambda_L = 785$ nm), respectively. The samples have $L_D = 24$ nm, 14 nm, 7 nm, 5 nm and 2 nm. Figure 7(d) shows the Raman spectra of the ion-bombarded sample with $L_D = 7$ nm obtained using the three different laser energies. Notice that the ratio I_D/I_G decreases as the laser energy increases, showing that a complete analysis for the I_D/I_G ratio in graphene must take into account the excitation laser energy. However, before going into details, we have to introduce the model to analyse the evolution of the D and G peaks.

5. Theoretical model

5.1 The local activation model

A unified theoretical description of the disorder induced effects from a more fundamental point-of-view is still an open problem, although some advances have been made on the related problem of the D band arising from graphene edges (Basko, 2009; Casiraghi et al., 2009). Nevertheless, some understanding of the problem at hand has been achieved through phenomenological models, as we describe in this Section.
Both experiments (Cançado et al., 2006; Tuinstra & Koenig, 1970) and theory (Basko, 2009; Casiraghi et al., 2009) describe the D band as being "locally activated", i.e., it only becomes active in the near vicinity of an imperfection (such as an edge or a point defect). Therefore, for the specific case of disorder induced by impact of individual Ar^+ ions, we can associate a characteristic length scale r_A, measured from the impact point, as the typical decay distance

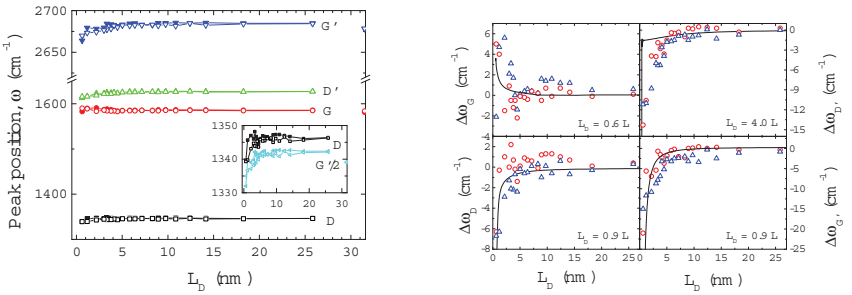

(a)

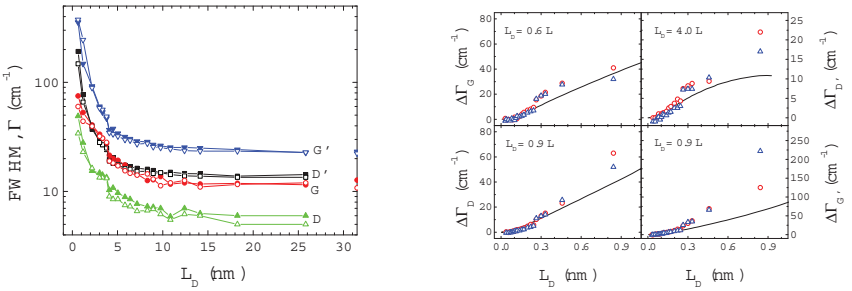

(b)

Fig. 6. Peak position (a) and full width at half maximum (b) of the four main Raman bands D, G, D' and G' of a monolayer graphene bombarded with low energy ions as a function of the average distance between the defects (L_D). Left panels show the absolute experimental data, and right panels the shifts in peak position and peak width with respect to the initial values (from the first bombardment). Symbols are experimental data and curves are the fitting from the theoretical model presented in Section 5. (Martins Ferreira et al., 2010)

of the D band intensity (green region in Figure 8). Another length scale is given by r_S, also measured from the impact points, which describes the region where the graphene sp^2 network disorganizes due to the ion impact (red region in Figure 8).

The activated region leads to an increase of the A_D/A_G ratio (equivalently on I_D/I_G), whereas the disorganized region reduces this ratio. By solving rate equations describing the evolution of the green and red regions with the ion dose, an analytical expression is obtained for A_D/A_G as a function of L_D (Lucchese et al., 2010; Martins Ferreira et al., 2010):

$$\frac{A_D}{A_G}(L_D) = C_A \frac{r_A^2 - r_S^2}{r_A^2 - 2r_S^2}\left[e^{-\frac{\pi r_S^2}{L_D^2}} - e^{-\frac{\pi(r_A^2 - r_S^2)}{L_D^2}}\right] + C_S\left[1 - e^{-\frac{\pi r_S^2}{L_D^2}}\right], \quad (3)$$

In this expression, the coefficients C_A and C_S correspond to the A_D/A_G ratio in two idealized limits. C_A refers to the situation in which the D band is activated in the whole of the graphene layer. Therefore, it embodies important information on the relative strengths

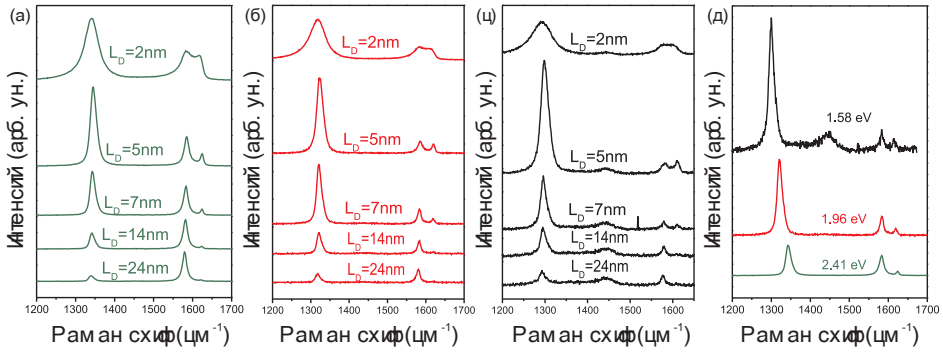

Fig. 7. (a-c) Raman spectra of five distinct ion-bombarded graphene samples using the excitation laser energies (wavelengths) E_L =2.41 eV (λ_L =514.5 nm), E_L =1.96 eV (λ_L =632.8 nm), and E_L =1.58 eV (λ_L =785 nm), respectively. (b) Raman spectra of an ion-bombarded sample with L_D = 7 nm obtained using the three different excitation laser energies. (Cançado et al., 2011)

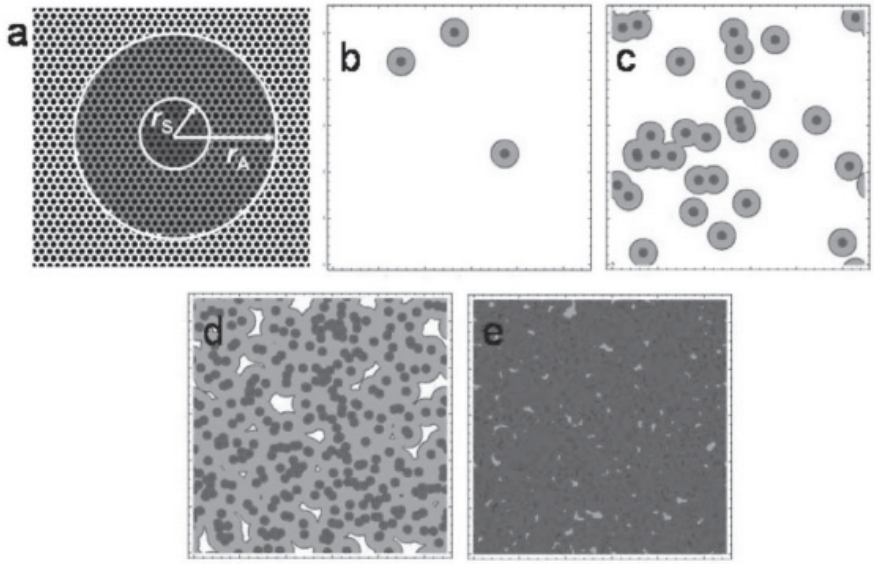

Fig. 8. (a) The two length scales (r_A and r_S) describing the evolution of the D band intensity with disorder induced by the impact of Ar^+ ions in graphene. Panels (b) to (e) correspond to the same ion doses in panels (b) to (e) in Figure 3. (Lucchese et al. (2010))

of the electron-phonon scattering near the Γ and K points in the Brillouin zone and on the electron-defect scattering cross-section for the D band. In particular, the strong energy dependence of C_A is revealing of the physics of Kohn anomaly near the K-point phonons in graphene (Piscanec et al., 2004) and of electron-defect scattering on short-range imperfections of graphene (Basko, 2008). The coefficient C_S corresponds to the A_D/A_G ratio in the highly disordered limit.

Notice from Figure 5 that this analytical function describes the experimental evolution of A_D/A_G with the amount of disorder, including its energy dependence. Moreover we can also extract physical meaning from the two length scales obtained from the fits. For instance r_S appears to be energy-independent, which is consistent with its interpretation as geometrical, structure-related length. The fitted values of r_S are in accordance with the typical defect-size estimates found from STM analysis (Martins Ferreira et al., 2010), which shows a sparse size distribution with an average value of 1.8 nm. The length $r_A - r_S$ is a rough measure of the length traveled over the lifetime of the electron-hole pair, v_F/ω_D, where v_F is the graphene Fermi velocity (Casiraghi et al., 2009). This length is energy-dependent, as imposed by the double-resonance condition and the strong phonon dispersion near the K point.

The analytical function in Equation 3 also describes the evolution of D' band integrated area with disorder (Martins Ferreira et al., 2010). Similar ideas can be applied for the $A_{G'}/A_G$ ratio. However, the G' band is already active for pristine graphene, so the integrated area ratio is only affected by the progressive disorganization of the graphene network, leading to:

$$\frac{A_{G'}}{A_G}(L_D) = \frac{A_{G'}}{A_G}(\infty) - B\left[1 - \mathrm{e}^{-\frac{\pi r_S^2}{L_D^2}}\right], \tag{4}$$

where $A_{G'}/A_G(\infty)$ is the area ratio for pristine graphene. The fitting of the experimental data also shows an excellent agreement in this case.

5.2 The excitation energy dependence

Now we can consider the excitation energy dependence in more depth. Figure 9(a) shows the I_D/I_G data (bullets) for all graphene samples and laser energies used in the experiment. The lines are the fitting curves following Equation 3. The C_A values obtained from the fitting shown in Figure 9(a) are plotted in the inset to Figure 9(a) (down triangles). Notice that C_A decrease as the laser energy increases. This behavior is ruled by a strong dependency of the strength of the D band on the wavevector of phonons involved in the double-resonance scattering process (Cançado et al., 2011). The solid line in the inset to Figure 9(a) is the fitting of the experimental data using an inverse fourth power dependence on the excitation laser energy, which gives $C_A = 140\,E_L^{-4}$, following the results on nanocrystallites (Cançado et al., 2006). This dependence is not yet understood and may be restricted to this energy range.

Although C_S could present some dependency with the excitation laser energy, our experimental data set does not allow us a clear determination of this dependency. In this case, we have considered $C_S = 0.9$ for all three excitation laser energies used in the experiment, in agreement with the more detailed results displayed in Figure 4(b). The fitting also gives $r_A = 3.1$ nm, and $r_S = 1$ nm, which is in excellent agreement with the values obtained by (Lucchese et al., 2010) and (Beams et al., 2010).

Figure 9(b) shows the plot of the product $E_L^4(I_D/I_G)$ versus L_D for the experimental data shown in Figure 9(a). It is clear from the plot depicted in Figure 9(b) that the data with $L_D > 10$ nm obtained with different laser energies collapse in the same curve. The same is not valid for

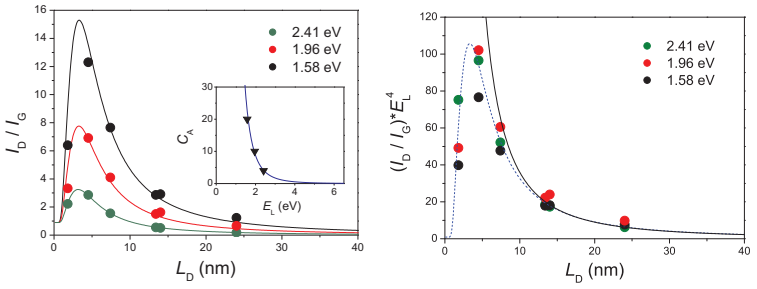

Fig. 9. (a) I_D/I_G data (bullets) for all graphene samples and laser energies used in the experiment. The solid lines are the fitting curves according to Equation 3. The inset shows the plot of C_A versus E_L. (b) Plot of the product $(I_D/I_G)E_L^4$ versus L_D for the experimental data shown in Figure 9(a). (Cançado et al., 2011)

$L_D < 10$ nm, indicating that C_S might also play a role in the E_L dependence. The dashed blue line is the plot obtained from the substitution of the relation $C_A = 140/E_L^4$ in Equation 3.
We now turn our attention to the low defect density regime ($L_D \geq 10$ nm). In this regime, for which $L_D > 2r_A$, the total area contributing to the D band scattering is simply proportional to the number of point defects, giving rise to $I_D/I_G \propto 1/L_D^2$ (see Equation 2). By considering large values of L_D, and also taking in account that $C_A(r_A^2 - r_S^2) \gg C_S r_S^2$, Equation 3 takes the form

$$\left(\frac{I_D}{I_G}\right) \simeq C_A \frac{\pi(r_A^2 - r_S^2)}{L_D^2}. \tag{5}$$

By taking the values $r_A = 3.1$ nm, $r_S = 1$ nm, and also the relation $C_A = 140/E_L^4$ obtained from the fit of the experimental data shown in Figure 9(a), Equation 5 can be rewritten as

$$L_D^2(\text{nm}^2) = \frac{3600}{E_L^4}\left(\frac{I_D}{I_G}\right)^{-1}. \tag{6}$$

The above relation is valid for Raman data obtained from graphene samples that present point defects with $L_D \geq 10$ nm using excitation laser lines in the optical range. In terms of the defect density $n_D(\text{cm}^{-2}) = 10^{-14}/L_D^2$, Equation 6 becomes

$$n_D(\text{cm}^{-2}) = (2.8 \times 10^{-18})E_L^4\left(\frac{I_D}{I_G}\right). \tag{7}$$

The solid dark line in Figure 9(b) is the plot of the product $E_L^4(I_D/I_G)$ versus L_D according to Equation 6. The plot shown in Figure 9(b) clearly validates this relation for samples with $L_D > 10$ nm.

5.3 Evolution of peak frequency and width

The evolution of the Raman FWHM and frequency shifts with increasing disorder in graphene can also be described by a phenomenological model, the so-called "spatial-correlation model". This model was originally developed to describe the evolution of the Raman spectra of disordered semiconductors (Richter et al., 1981; Tiong et al., 1984). In a crystalline system,

the Raman intensity $I_0(\omega)$ associated to a vibrational mode of wavevector $\mathbf{q}_0$ and frequency $\omega(\mathbf{q}_0)$ is described by a Lorentzian:

$$I_0(\omega) \propto \frac{1}{[\omega - \omega(\mathbf{q}_0)]^2 + [\Gamma_0/2]^2}, \tag{8}$$

where the FWHM Γ_0 is the inverse phonon lifetime. In a perfect system, Γ_0 has contributions from both electron-phonon and phonon-phonon (anharmonic effects) interactions. A disordered distribution of point defects will add a contribution to the FWHM by coupling phonons of different momenta, so the phonon wave packet in k-space can be described by a Gaussian function $\exp[-(\mathbf{q} - \mathbf{q}_0)^2 L^2/4]$ centered in $\mathbf{q}_0$ and having a width proportional to $1/L$. In real space, L is a measure of the phonon coherence length, which should be a good measure of the average distance between point defects. Then, the Raman intensity for the disordered graphene $I(\omega)$ is written as (Tiong et al., 1984):

$$I(\omega) \propto \int_{BZ} d^2q \frac{W(\mathbf{q}) \exp\left[\frac{-(\mathbf{q}-\mathbf{q}_0)^2 L^2}{4}\right]}{[\omega - \omega(\mathbf{q})]^2 + [\Gamma_0/2]^2}, \tag{9}$$

where, in our case, the integral is taken over the two-dimensional graphene Brillouin Zone and $W(\mathbf{q})$ is a weighting function that describes wavevector dependence of the electron-phonon coupling for the Raman process.

Within this phenomenological model, and using experimentally available phonon dispersion relations the full lineshape of $I(\omega)$ can be calculated, and from that the disorder-induced peak shifts $\Delta\omega_{\mathbf{q}_0}$ and the increase in FWHM $\Delta\Gamma_{\mathbf{q}_0}$ can be extracted. Details of the application of this model to specific Raman bands can be found in (Martins Ferreira et al., 2010). As seen in Figures 6(a) and 6(b), this simple model describes the main qualitative features of experimental data on the evolution of the FWHM and peak-frequency shifts of the D, D', G and G' bands with disorder. Notice that the agreement is better for large values of L_D, as expected. In the figures, we also show the best relationships between L and L_D in each case (obtained by the fits). Notice that L and L_D are similar to each other and this behavior arises naturally from the fitting procedure. That means the disordered-induced phonon coherence length is of the same order of the typical inter-defect distance, as we argued. Also, it seems that the D' modes are the most affected by disorder, showing a smaller coherence length than the other modes for the same amount of disorder. Finally, the model allows us to explain the greater increase in FWHM of the modes near K with respect to the modes near Γ as simply a consequence of the larger magnitude of phonon dispersions near K.

6. Effect of ion bombardment on few-layer graphenes

Differently from the monolayer, where the G' and D bands are described by a single Lorentzian function, in a graphene with 2 or more layers, those bands become more complex due to the interaction between the layers, and, therefore, a quantitative description of the evolution of the Raman bands with increasing disorder is a tougher task (Martins Ferreira et al., 2010). Figure 10 shows the Raman spectra of a bilayer and a trilayer graphene sample subjected to the same ion bombardment of the previously discussed monolayer sample. In comparison, the effect of ion bombardment in this sample is less pronounced than in monolayer. The I_D/I_G ratio grows faster and reaches a higher value for the monolayer than for the bilayer, and the same applies to the bilayer as compared to the trilayer. This behavior is a confirmation that the defects are mainly on the surface (Jorio et al., 2010). Since the Raman

signal gets the contribution of all the layers, the *G* band intensity must be stronger for the bilayer and trilayer, while the *D* band intensity, which depends mostly on the number of defects, must be approximately the same. This can explain the behavior of the intensity ratios I_D / I_G. As for the case of the monolayer, we see no significant change in the frequency of the *G* band, and we observe a broadening of the peaks for the higher ion doses (Martins Ferreira et al., 2010).

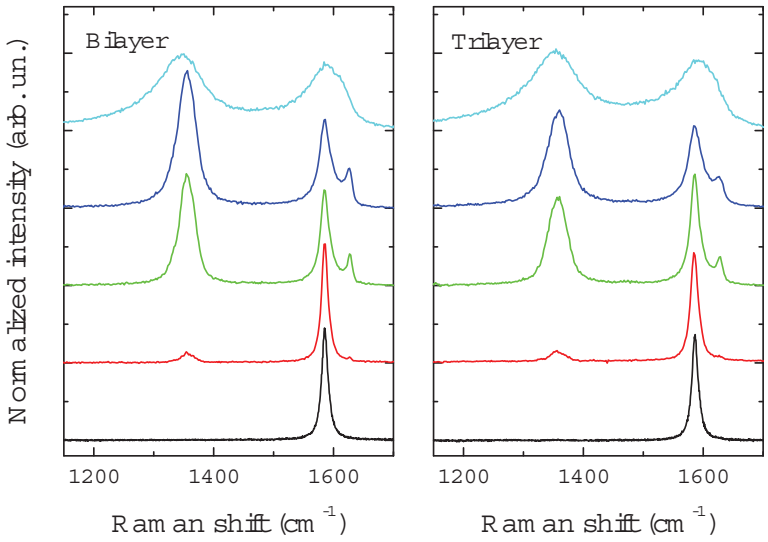

Fig. 10. Raman spectra of bilayer and trilayer graphenes bombarded with low energy (90 eV) argon ions. From bottom to top, curves correspond to zero, 10^{11}, 10^{12}, 10^{13} and 10^{14} Ar^+/cm^2 doses. (Jorio et al., 2010)

7. Raman at edges

The borders of a graphene sheet act like defects in the crystallographic structure and may have great impact in transport properties of graphene. As discussed in Section 2, previously studies on graphite edges have shown that the Raman *D* band intensity depends on the crystallographic orientation of the edge and the polarization of the laser beam (Cançado et al., 2004). Figure 11 shows the Raman mapping of the *D* band of a graphene sample showing the presence of defects at the borders (Carozo et al., 2011). For graphene, it has also been shown that the intensity of the *D* band is stronger for an incident light with polarization parallel to the border and is proportional to $\cos^2 \theta$, where θ is the angle between the polarization of incident light and the edge (Casiraghi et al., 2009; Gupta et al., 2009). Theoretically it is expected that the *D* band intensity would vanish for a perfectly oriented edge, such as armchair or zigzag, when the incident light polarization is perpendicular to the edge. However, both (Casiraghi et al., 2009) and (Gupta et al., 2009) failed to found a null *D* band intensity with

a perpendicular polarization and they could not tell the difference between the a zigzag and armchair borders by the evaluation of the relative intensity I_D / I_G, contrary to what have been found by (Cançado et al., 2004). The conclusion was that the edges were not a perfect zigzag or armchair, but a mix of them. A more recent work by (Neubeck et al., 2010) determined the crystallographic orientation of a graphene sheet by STM measurements and found that the intensity of the *D* band is higher for the armchair edge than for the zigzag edge when the polarization of the laser beam was parallel to the edges, in accordance with have been published by (Cançado et al., 2004). Yet, it is expected that a perfect zigzag border would not present a *D* band, due to phonon momentum conservation (Cançado et al., 2004). It is to conclude then, that although at a microscopy level the border may be mainly zigzag or armchair, at the atomic level it is not perfect.

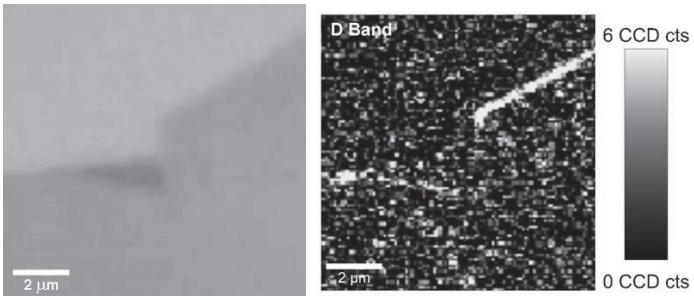

(a) (b)

Fig. 11. (a) Optical image of a monolayer graphene and (b) the Raman mapping of the *D* band of the same graphene sample showing the presence of the defects at the border (Carozo et al., 2011).

Finally, a theoretical work of (Sasaki et al., 2010) proposed that the intensity of the *G* band at the edges may be different depending on the orientation of the border, however no experimental data has corroborated it so far. The major difficulty in these studies to the moment is to obtain a perfect zigzag or armchair edge in sample produced by micro-mechanical cleavage. It is expected that graphene samples produced via chemical exfoliation may produce a much smoother edge and then those theories could be tested.

8. Conclusions and perspectives

The possibility of performing experiments on an isolated graphene sample improved substantially our understanding of disorder-induced effects in the Raman spectra of graphene related systems, even though such effects have been studied since 1970. Performing joint spectroscopy and microscopy experiments on a single layer of atoms allowed us to have a clear picture of the disorder effect in both real and reciprocal spaces, setting us free from volume-related aspects that were not easily addressable by microscopy and depend on light penetration depth. The parameters ruling the intensity of disorder-induced Raman bands, named r_A, r_S, C_A, C_S and defect topology, are now clearly established, so that accurate models can be developed for fully understanding the importance of electron-phonon and electron-defect interactions in this matter. The evolution of peak frequencies and linewidths are also clearly understood now for the low disorder limit, as discussed in this chapter. However, for understanding the peak behavior at the large disorder limit, more experimental

and theoretical developments are needed. Finally, all this development has shown that, up to date, no perfect zigzag graphene edge has been produced. Edge perfection will be important for the electronic properties of graphene nanoribbons, and Raman spectroscopy might play an important role on testing the development of such edges.

9. References

Basko, D. M. (2008). Resonant low-energy electron scattering on short-range impurities in graphene, *Phys. Rev. B* 78: 115432.

Basko, D. M. (2009). Boundary problems for dirac electrons and edge-assisted Raman scattering in graphene, *Phys. Rev. B* 79: 205428.

Beams, R., Cançado, L. G. & Novotny, L. (2010). Optical measurement of the phase-breaking length in graphene. arXiv:1008.1563v.

Cançado, L. G., Jorio, A., Martins Ferreira, E. H., Stavale, F., Achete, C. A., Moutinho, M. V. O., Capaz, R. B., Lombardo, A. & Ferrari, A. C. (2011). Laser energy dependency of the disorder-induced band in the Raman spectrum of graphene. Umpublished.

L. G., Takai, K., Enoki, T., Endo, M., Kim, Y. A., Mizusaki, H., Jorio, A., Coelho, L. N., Magalhães-Paniago, R. & Pimenta, M. A. (2006). General equation for the determination of the crystallite size L_a of nanographite by Raman spectroscopy, *Applied Physics Letters* 88(16): 163106.

Cançado, L. G., Jorio, A. & Pimenta, M. A. (2007). Measuring the absolute Raman cross section of nanographites as a function of laser energy and crystallite size, *Phys. Rev. B* 76(6): 064304.

Cançado, L. G., Pimenta, M. A., Neves, B. R. A., Dantas, M. S. S. & Jorio, A. (2004). Influence of the atomic structure on the Raman spectra of graphite edges, *Phys. Rev. Lett.* 93(24): 247401.

Carozo, V., Almeida, C. M., Martins Ferreira, E. H., Achete, C. A., Jorio, A. (2011). Raman Spectroscopy of Folded Graphene. Umpublished.

Casiraghi, C., Hartschuh, A., Qian, H., Piscanec, S., Georgi, C., Fasoli, A., Novoselov, K. S., Basko, D. M. & Ferrari, A. C. (2009). Raman spectroscopy of graphenes edges, *Nano Lett.* 9(4): 1433–1441.

Chou, S. G., Son, H., Kong, J., Jorio, A., Saito, R., Zheng, M., Dresselhaus, G., & Dresselhaus, M. S. (2007). Length characterization of DNA-wrapped carbon nanotubes using Raman spectroscopy, *Appl. Phys. Lett.* 90: 131109.

Ferrari, A. C. & Robertson, J. (2000). Interpretation of Raman spectra of disordered and amorphous carbon, *Phys. Rev. B* 61(20): 14095–14107.

Gupta, A. K., Russin, T. J., Gutiérrez, H. R. & Eklund, P. C. (2009). Probing graphene edges *via* Raman scattering, *ACS Nano* 3(1): 45–52.

Hulman, M., Skakalova, V., Roth, S. & Kuzmany, H. (2005). Raman spectroscopy of single-wall carbon nanotubes and graphite irradiated by γ rays, *J. of Appl. Phys.* 98(2).

Ishigami, M., Chen, J. H., Cullen, W. G., Fuhrer, M. S. & Williams, E. D. (2007). Atomic structure of graphene on SiO_2, *Nano Letters* 7(6): 1643–1648.

Jorio, A., Lucchese, M. M., Stavale, F. & Achete, C. A. (2009). Raman spectroscopy study of Ar^+ bombardment in highly oriented pyrolytic graphite, *Phys. Status Solidi B* 246(11–12): 2689–2692.

Jorio, A., Lucchese, M. M., Stavale, F., Martins Ferreira, E. H., Moutinho, M. V. O., Capaz, R. B. & Achete, C. A. (2010). Raman study of ion-induced defects in N-layer graphene, *J. Phys.: Condens. Matter* 22: 334204.

Lucchese, M. M., Stavale, F., Martins Ferreira, E. H., Vilani, C., Moutinho, M. V. O., Capaz, R. B., Achete, C. A. & Jorio, A. (2010). Quantifying ion-induced defects and Raman relaxation length in graphene, *Carbon* 48(5): 1592–1597.

Martins Ferreira, E. H., Moutinho, M. V. O., Stavale, F., Lucchese, M. M., Capaz, R. B., Achete, C. A. & Jorio, A. (2010). Evolution of the Raman spectra from single-, few-, and many-layer graphene with increasing disorder, *Phys. Rev. B* 82(12): 125429.

Mernagh, T. P., Cooney, R. P. & Johnson, R. A. (1984). Raman spectra of graphon carbon black, *Carbon* 22(1): 39–42.

Neto, A. C., Guinea, F., Peres, N. M. R. & Geim, K. S. N. A. K. (2009). The electronic properties of graphene, *Rev. Mod. Phys.* 81: 109–162.

Neubeck, S., You, Y. M., Ni, Z. H., Blake, P., Shen, Z. X., Geim, A. K. & Novoselov, K. S. (2010). Direct determination of the crystallographic orientation of graphene edges by atomic resolution imaging, *Appl. Phys. Lett.* 97(5): 053110.

Novoselov, K. S., Geim, A. K., Morozov, S. V., Jiang, D., Zhang, Y., Dubonos, S. V., Grigorieva, I. V. & Firsov, A. A. (2004). Electric field effect in atomically thin carbon films, *Science* 306(666–669).

Novoselov, K. S., Jiang, D., Schedin, F., Booth, T. J., Khotkevich, V. V., Morozov, S. V., & Geim, A. K. (2005). Two-dimensional atomic crystals, *Proc. Natl. Acad. Sci. USA* 102(30): 10451–10453.

Pimenta, M. A., Dresselhaus, G., Dresselhaus, M. S., Cançado, L. G., Jorio, A. & Saito, R. (2007). Studying disorder in graphite-based systems by Raman spectroscopy, *Physical Chemistry Chemical Physics* 9: 1276–1291.

Piscanec, S., Lazzeri, M., Mauri, F., Ferrari, A. C. & Robertson, J. (2004). Kohn anomalies and electron-phonon interaction in graphite, *Phys. Rev. Lett.* 93(18): 185503.

Richter, H., Wang, Z. P. & Ley, L. (1981). The one phonon Raman spectrum in microcrystalline silicon, *Solid State Commun.* 39: 625.

Saito, R., Jorio, A., Filho, A. G. S., Dresselhaus, G., Dresselhaus, M. S. & Pimenta, M. A. (2002). Probing phonon dispersion relations of graphite by double resonance Raman scattering, *Phys. Rev. Lett.* 88(02): 027401.

Sasaki, K., Saito, R., Wakabayashi, K. & Enoki, T. (2010). Indentifying the orientation of edge of graphene using G band Raman spectra, *J. of the Phys. Soc. of Japan* 79(4): 044603.

Teweldebrhan, D. & Baladin, A. A. (2009). Modification of graphene properties due to electron-beam irradiation, *Appl. Phys. Lett.* 94: 013101.

Thomsen, C. & Reich, S. (2000). Double resonant Raman scattering in graphite, *Phys. Rev. Lett.* 85(24): 5214.

Tiong, K. K., Amirtharaj, O. M., Pollak, F. H. & Aspnes, D. E. (1984). Effects of as^{+} ion implantation on the Raman spectra of GaAs: spatial correlation interpretation, *Appl. Phys. Lett.* 44: 122.

Tuinstra, F. & Koenig, J. L. (1970). Raman spectrum of graphite, *J. Chem. Phys.* 53(3): 1126–1130.

19

Superconductivity and Electron-Phonon Coupling in Graphite Intercalation Compunds

Tonica Valla and Zhihui Pan
Condensed Matter Physics and Materials Science Department, Brookhaven National Laboratory
USA

1. Introduction

In graphite intercalation compounds (GIC), the intercalation of various atomic or molecular species in between graphene layers in graphite leads to novel properties and a very rich physics, including superconductivity (Dresselhaus & Dresselhaus, 2002). In graphite intercalated with alkaline metals, superconductivity has been known for decades (Hannay et al., 1965), but after recent discovery of relatively high T_c superconductivity in CaC_6 (T_c = 11.5 K)(Emery et al., 2005; Weller et al., 2005) research in this field has been intensified. In conventional metals, the electron-phonon coupling has long been known to be the pairing interaction responsible for the superconductivity. The strength of this interaction essentially determines the superconducting transition temperature T_c. Even though the electron-phonon coupling is most likely responsible for pairing in GICs (Hinks et al., 2007; Kim et al., 2006; Lamura et al., 2006), it is still not clear what electronic states, intercalant- or graphene- derived ones, and what phonons are responsible for pairing (Boeri et al., 2007; Calandra & Mauri, 2005; Mazin et al., 2007; Mazin, 2005). Due to differences in structure and composition, no clear trends have been identified that could unambiguously resolve these issues. For example, KC_8 is a superconductor and LiC_6 is not. Further, in GICs intercalated with alkaline earths, T_c ranges from zero to 11.5K, even though they share the same chemical formula MC_6, where M is an alkaline earth atom. This obviously represents a serious problem to the proposal that superconductivity originates from graphene sheets and that the only role of intercalants is to provide the charge to the graphene bands. Further, band structure calculations show that in graphite and GICs, an interlayer state exists above π^* band (Holzwarth et al., 1984; Posternak et al., 1983), prompting some researchers to propose that its partial filling and coupling to soft intercalant phonons induces superconductivity in GICs (Csányi et al., 2005; Mazin, 2005). The experimental situation is still inconclusive, with strong advocates for intercalant (Hinks et al., 2007) and graphene dominated superconductivity (Dean et al., 2010; Grüneis et al., 2009; Kim et al., 2006; Pan et al., 2010; Valla et al., 2009). Recent angle resolved photoemission spectroscopy study on CaC_6 (Valla et al., 2009) reported that the electron-phonon coupling on graphene-derived Fermi surface to graphene phonons is strong enough to explain a T_c in the range of tens of Kelvin, indicating that graphene sheets provide crucial ingredients for superconductivity in GICs. However, to test this idea, it would be important to extend similar studies to GICs with different T_c.

One manifestation of electron-phonon coupling is a renormalization of the electronic dispersion or a "kink" at the energy scale associated with the phonons. This renormalization

is directly observable in a photoemission experiment, making photoemission spectroscopy an ideal probe of electron-phonon coupling. In this chapter, we present the angle resolved photoemission studies of the electronic structure and the electron-phonon coupling in the non-superconducting LiC_6 and in superconducting KC_8 ($T_c = 0.39$ K) and compare these materials with several other GICs. We find that the electron-phonon coupling on the graphene derived π^* states to the graphene derived phonons increases with the filling of π^* states in a sequence from LiC_6 to KC_8 to CaC_6, following the same trend as T_c. The positive correlation between these quantities implies that superconductivity originates in graphene sheets while the main role of intercalants is to provide the charge for filling of the graphene π^* states.

2. Photoemission and interactions

In photoelectron spectroscopy, a photon of known energy, $h\nu$, is absorbed and the outgoing electron's kinetic energy $E_K = h\nu - \phi - \varepsilon_k$ and angle are measured. These properties determine the binding energy ε_k and parallel momentum $k_\parallel$ of the hole left in the occupied valence bands (Kevan, 1992). Interaction effects, including for instance electron-phonon coupling, cause the infinitely sharp line spectrum of independent electron theory, $A_0(\mathbf{k},\omega)$ = Im $G_0(\mathbf{k},\omega)$ = Im $1/(\omega - \epsilon_{\mathbf{k}0} - i\eta)$, where $\epsilon_{\mathbf{k}0}$ represents a bare band dispersion, to evolve into Im $1/[\omega - \epsilon_{\mathbf{k}0} - \Sigma(\mathbf{k},\omega)]$ where the complex self-energy $\Sigma(\mathbf{k},\omega)$ contains the effects of the many body interactions. The spectral function of the photo-hole, $A(\mathbf{k},\omega)$, then takes the form

$$A(\mathbf{k},\omega) \propto \frac{\mathrm{Im}\Sigma(\mathbf{k},\omega)}{[\omega - \epsilon_{\mathbf{k}0} - \mathrm{Re}\Sigma(\mathbf{k},\omega)]^2 + (\mathrm{Im}\Sigma(\mathbf{k},\omega))^2} \tag{1}$$

The real part, $\mathrm{Re}\Sigma(\mathbf{k},\omega)$, gives a shift in energy and associated mass enhancement, while the imaginary part $\mathrm{Im}\Sigma(\mathbf{k},\omega)$ gives the lifetime broadening of a quasiparticle. The spectral function $A(\mathbf{k},\omega)$ is a fundamental quantity that determines all the properties of a many-body system. It can be directly measured in a photoemission experiment because the intensity of photoelectrons is given by $I(\mathbf{k},\omega) = |M|^2 A(\mathbf{k},\omega) f(\omega)$ where M represents the matrix element linking the initial and final states in the photoemission process, $A(\mathbf{k},\omega)$ is the single particle spectral function given in equation (2) and $f(\omega)$ is the Fermi function which enters because the photoemission process is restricted to excitation from occupied states.

2.1 Electron-phonon coupling in photoemission

We now focus on the electron-phonon coupling. The electron-phonon coupling contribution, $\Gamma_{e-ph} = 2\mathrm{Im}\Sigma_{e-ph}$, to the total scattering rate may be calculated via the Eliashberg equation such that (Mahan, 1990)

$$\Gamma_{e-ph}(\omega,T) = 2\pi\hbar \int_{-\infty}^{\infty} d\omega' \alpha^2 F(\omega') \left[2n(\omega') + f(\omega' + \omega) + f(\omega' - \omega)\right] \tag{2}$$

where $\alpha^2 F$ is the Eliashberg function and $f(\omega)$ and $n(\omega)$ are the Fermi and Bose-Einstein distribution functions, respectively. (Grimvall, 1981) $\Gamma_{e-ph}(\omega,T)$ monotonically increases with energy over the region $|\omega| < \omega_{max}$ (for T=0), where ω_{max} is the cutoff of the phonon spectrum. The exact functional form is slightly dependent on the phonon spectrum. The temperature dependence of Γ_{e-ph} is approximately linear at higher temperatures, with slope

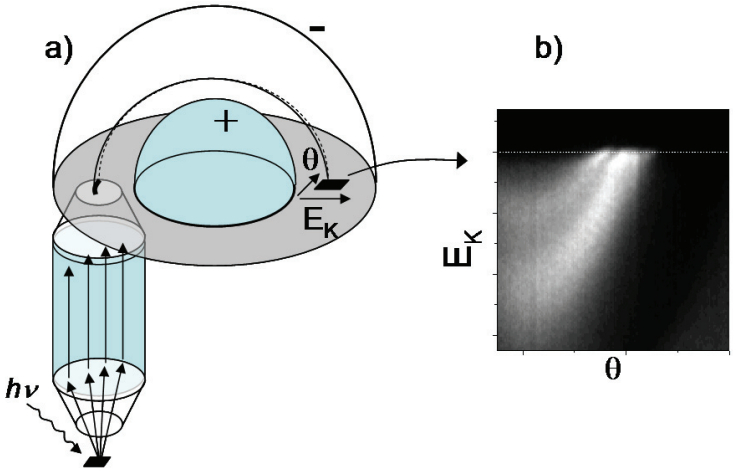

Fig. 1. Angle-resolved photoemission spectroscopy experiment. (a) Scienta hemispherical analyzer composes of a cylindrical lens, a hemispherical energy analyzer and a 2-dimensional detector (dark square). The entrance slit of the hemisphere selects a single angular line out of a finite solid angle collected by the lens. This defines a line in the inverse space over which the photoemission intensity is detected on a detector (b) Typical 2-dimensional photoemission intensity map as a function of kinetic energy E_K and angle θ from $NbSe_2$ sample (Valla et al., 2004). Bright (dark) represents high (low) photo-electron intensity.

$2\pi\lambda k_B$, where λ is the electron-phonon coupling constant given by (Grimvall, 1981)

$$\lambda = 2\int_0^\infty \frac{\alpha^2 F(\omega')}{\omega'} d\omega' \tag{3}$$

and k_B is Bolzman constant.
For most metals 10 meV $< \omega_{max} <$ 100 meV, and λ falls between 0.1 and 1.5. The electron-phonon coupling constant λ can be extracted directly from ReΣ as $\lambda = -[\partial(\mathrm{Re}\Sigma)/\partial\omega]_0$ by fitting the low energy part of ReΣ to a straight line. The scattering process is illustrated in Fig. 2 where we consider a coupling to a single phonon mode at energy Ω_0. Coupling to such a mode (at T = 0 K) will result in a step function in the scattering rate or ImΣ. The step function reflects the observation that when the photohole has enough energy to create the mode ($\omega \geq \Omega_0$), scattering from the mode opens up a decay channel, thereby limiting the lifetime. The real and imaginary parts of the self energy are related via causality through a Kramers Kronig transform. Thus the step function in ImΣ results in a cusp function for ReΣ. Such an energy dependence of Σ affects the measured spectra in two ways. Above and below the mode energy there will be a noticeable change in the quasiparticle width. Secondly, the measured dispersion will be given by $\epsilon_{\mathbf{k}0} + \mathrm{Re}\Sigma(\mathbf{k},\omega)$ and will display the mass enhancement observed immediately below the Fermi level as presented in Fig. 2(e).
Modern photoelectron spectrometers allow the simultaneous measurement of photoelectron intensities from a finite range in both energy and momentum space. A typical image is shown in Fig. 1. The ability to obtain such images has led to the development of new methodologies for the extraction of self-energies. The spectral response in Fig. 1(b) may be analysed by taking

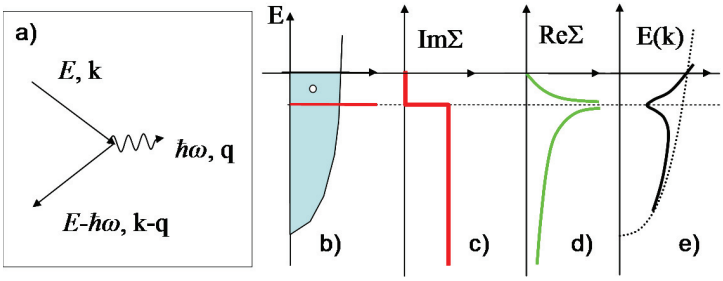

Fig. 2. Electron-phonon scattering (a) A Feynman diagram for the electron-phonon scattering. The straight lines represent the photo-hole states before and after scattering on a phonon (wiggly line). (b) The photo-hole created in photoemission (hollow circle) can emit a phonon only if it has enough energy. The red horizontal line indicates the energy of a phonon mode. (c) Imaginary part, ImΣ of the self-energy. The step function reflects the opening of a decay channel when the photohole has enough energy to create the mode ($\omega \geq \Omega_0$). (d) Real part, ReΣ of the self-energy. (e) The renormalized (observed) dispersion (thick solid line) is then obtained as a superposition of the bare dispersion (dotted line) and ReΣ.

an intensity cut at constant angle or momentum, the so called energy distribution curve or by taking an intensity cut at constant energy, a momentum distribution curve. In the limit of a momentum independent self-energy and a linear bare dispersion ($\epsilon_{k0} = v_0(k - k_F)$, where v_0 represents the bare velocity), the momentum distribution curve is a simple Lorentzian, centered at $k_m = k_F + [\omega_0 - \mathrm{Re}\Sigma(\omega_0)]/v_0$ and with the full width at half maximum $\Delta k = 2\mathrm{Im}\Sigma(\omega_0)/v_0$. The self-energy can thus be simply extracted from momentum distribution curve peaks at any binding energy, as has been discussed in several papers. (Kaminski et al., 2000; Kordyuk et al., 2005; LaShell et al., 2000; Valla et al., 2000) The same method of analysis has been employed here to study the electron-phonon coupling in GICs.

3. Photoemission from graphite intercalation compounds

The experiments were carried out on a Scienta SES-100 electron spectrometer operating in the angle resolved mode at the beamline 12.0.1 of the Advanced Light Source. The spectra were recorded at the photon energy of 50 eV with the combined instrumental energy resolution of 20-25 meV and the momentum resolution of 0.008 $\mathrm{Å}^{-1}$ in geometry where the polarization of light was perpendicular to the probed momentum line. The thin flake of pristine graphite was obtained by micromechanical exfoliation of HOPG on a SiO_2/Si substrate in air. From the optical contrast and from Raman data, the thickness of the flake was determined to be in the range of 7-9 graphene layers. The flake was annealed to 600 K in the ultra-high vacuum chamber before angle resolved photoemission studies. The LiC_6 and KC_8 samples were prepared by intercalating natural, single-crystal graphite flakes (Madagascan) as described in Ref. (Dresselhaus & Dresselhaus, 2002; Pruvost et al., 2004). The CaC_6 samples were prepared via immersion of a HOPG platelet or single-crystal graphite flake in a lithium/calcium alloy for 10 days. X-ray diffraction showed very high sample purity with no graphite or secondary stage phases. SQUID magnetometry revealed a sharp ($\Delta T \sim 0.3$K) superconducting transition at $\sim$ 11.6 K (onset) for CaC_6 samples. To avoid degradation, all samples were unsealed and glued to the sample holder with Ag- epoxy in an Ar filled glow box. Protected by the cured epoxy, they were then quickly transferred to the angle resolve photoemission prep-chamber,

and cleaved at low temperature (15-20 K) under ultra-high vacuum conditions (2×10^{-9} Pa). All data were collected at 15-20 K.

3.1 Electronic structure and charge transfer

Fig. 3 shows the angle resolved photoemission spectra near the K point in the graphene Brillouin zone for pristine graphite, LiC_6, KC_8 and CaC_6. The upper panels (a) - (d) show the contours of photoemission intensity as a function of binding energy for a momentum line going through the K point. The intensity from a narrow interval ($\pm$10 meV) around the Fermi level, representing the Fermi surface, is shown in the lower panels (e) - (h). The dispersing states are the graphene-derived π and π^* bands, as marked in Fig. 3(a) through (d). In KC_8 the low energy band structure is essentially graphene-like, with π and π^* bands touching at the Dirac point (Grüneis et al., 2009), shifted below the Fermi level due to the electron doping. In LiC_6 and CaC_6 a sizable gap exists between π and π^* bands. Dirac point is determined

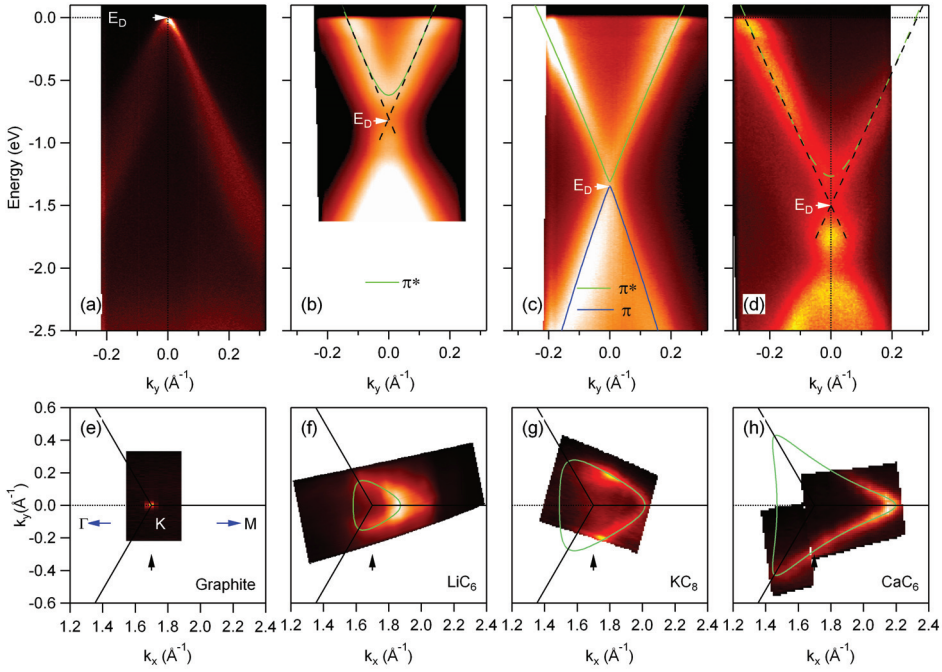

Fig. 3. Photoemission from pristine and intercalated graphite. Photoemission spectra from pristine graphite (a), LiC_6 (b), KC_8 (c) and CaC_6 (d) along the same momentum line in the graphene Brillouin Zone traversing the K point, as indicated by the black arrows in panels (e)-(h). Blue and green lines represent the π and π* bands. White arrows indicate position of Dirac point. (e)-(h) Photoemission intensity from a narrow energy interval around the Fermi level ($\omega = \pm 10$ meV), representing the graphene-derived π* Fermi surface, for graphite, LiC_6, KC_8 and CaC_6 respectively. The green lines represent tight-binding fits to the Fermi surface. All spectra were taken at T $\sim$ 15 K.

by extrapolating the linear part of π^* dispersion at low binding energies to the K point. The arrows indicate positions of Dirac point, (E_D), 0 eV, 0.825 eV, 1.35 eV and 1.5eV for pristine

graphite, LiC_6, KC_8 and CaC_6, respectively, indicating that the filling of the π^* band increases in that sequence. In particular, it appears that the π^* band is filled more in KC_8 than in LiC_6 and that it forms a larger Fermi surface in the former material. The area enclosed by the Fermi surface (lower panels in Fig. 3) is a direct measure of doping of graphene π^* states, i.e. of the charge transferred into the graphene sheets. The Fermi surface area is determined from peak positions of momentum distribution curves at Fermi level and compared to the 3^{rd} nearest neighbor hopping tight binding band structure. In pristine graphite, the Fermi surface is essentially a point, indicating nearly neutral graphene sheets. In the intercalated samples the Fermi surface grows from LiC_6 to KC_8 to CaC_6. Its area is 0.399 $Å^{-2}$ in KC_8, corresponding to 0.11 electrons per graphene unit cell, or 44% of the nominal value of 0.25 for the complete charge transfer. In LiC_6, the enclosed area is 0.125 $Å^{-2}$, corresponding to the doping of only 0.0344 electrons per graphene unit cell (GUC). This is far below the nominal value of 1/3 electrons per graphite unit cell expected for the complete intercalant ionization. For CaC_6 the complete charge transfer would involve a donation of 2 calcium electrons to the graphene sheets, equivalent of the doping of 1/3 electrons per C atom (or $2/3e^-$ per unit cell). Instead, the measured Fermi area gives approximately 0.18 electrons per C atom.

The incomplete charge transfer into the graphene π^* states would suggest that the remaining charge occupies the so-called interlayer band. There has been a substantial body of theoretical work that depicts the intercalant-derived interlayer states and phonons as main contributors to superconductivity in GICs. However, so far there has been no clear evidence of the intercalant-derived nearly free electron band in photoemission experiments. The occupation of the interlayer state has been recently reported in CaC_6 (Sugawara et al., 2008), but the observed feature was very weak and broad. There, even the graphene-derived π^* state was very broad and did not form an enclosed contour at the Fermi level, casting doubts on these results. Our experiments always show relatively sharp π^* band that forms a well defined Fermi surface. However, in MC_6(M=Li, Ca, Ba) materials, in addition to π^* band, we always see a broad feature at slightly higher binding energy that follows the π^* band, dispersing upward from K point (Fig. 3(b)and (d)). Further from the K point, it loses intensity and its dispersion cannot be precisely traced. In CaC_6, this feature is observable over larger region of k space (Valla et al., 2009). It is possible that this is a remnant of an interlayer band, smeared out by a disorder within the intercalant layers and folded into the K point of the graphene Brillouin zone. However, our measurements do not show any evidence of the interlayer band in the region from which it should be folded to the K point - the Γ point. Of course, the missing charge has to be somewhere and even if the state is completely incoherent it still can count for the missing charge. We note that in pristine graphite, the interlayer hopping $t_\perp$ splits both π and π^* bands into the bonding and antibonding counterparts due to the AB stacking of graphene sheets. It would be tempting to assign the broad feature to a bonding π^* state, due to similarities with π^* in initial dispersion. However, unlike the pristine graphite, all the first stage GICs have the AA stacking of graphene sheets and such assignment would be incorrect. On the other hand, in LiC_6 and CaC_6 the π^* band might be split due to the AB stacking of the intercalant (if there is not too much disorder in the intercalant sites). If this was indeed the case, we counted only a portion of charge transferred to graphene layers. The alternative charge counts would be in this case 0.0616 and 0.349 electrons per C atom, for LiC_6 and for CaC_6, respectively. We point out that, if this is indeed the case, only the antibonding counterpart, which appears more coherent, plays a significant role in superconductivity, because it is its filling and its coupling to phonons that determines T_c, as will be shown in the next section. Irrespective of these issues, our experimental observation that the doping of graphene sheets is larger in KC_8 than in LiC_6 is opposite of the expected nominal doping, but is in line with the existence of superconductivity in these materials: KC_8 is a superconductor and LiC_6 is

not. In the following, we identify the reason for the correlation between superconductivity and doping of the graphene sheets.

3.2 Electron-Phonon Coupling in Graphite Intercalation Compounds

It is evident from Fig. 3 that in all three intercalated materials, an anomaly or a kink in dispersion of the π^* band occurs at approximately 160 meV below the Fermi level. This is a hallmark of the interaction of the electronic states with phonons (Hengsberger et al., 1999; Valla et al., 1999) that has been attributed to a coupling to graphene in- plane high-frequency phonons(Grüneis et al., 2009; Pan et al., 2010; Valla et al., 2009). We now focus on CaC_6, a system in which these effects are the most pronounced. Fig. 4 shows the angle resolved

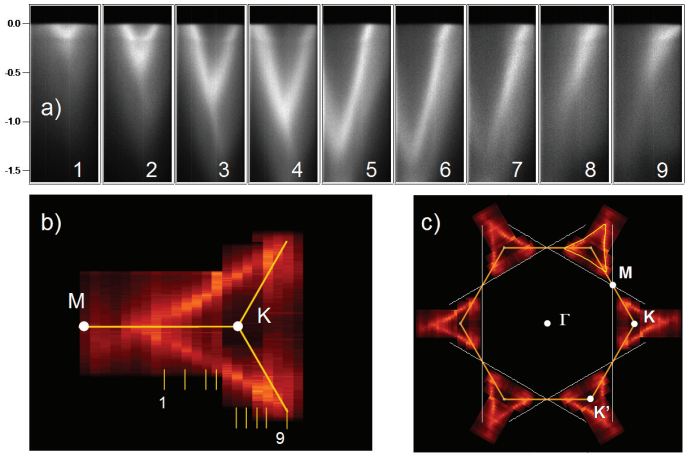

Fig. 4. Photoemission from CaC_6. (a) 1-9: photoemission spectra from CaC_6 along several momentum lines near the K point as indicated in (b). (b) Photoemission intensity from CaC_6 from a narrow energy interval around the Fermi level ($\omega = \pm 10$ meV) near the K point of the graphene Brillouin zone. Thin bars indicate momentum lines probed in (a). (c) Fermi surface of CaC_6 obtained by six fold symmetrization of intensity shown in (b). White lines correspond to the doping of 0.5 electrons per C atom, at which the van Hove singularity in the π^* band sits at the Fermi level.

photoemission spectra near the K point in the graphene Brillouin zone. The upper panel (a) shows the contours of photoemission intensity as a function of binding energy for several momentum lines in the vicinity of K point, while the intensity from a narrow interval ($\pm$10 meV) around the Fermi level is shown in the lower contours (b and c). All the spectra are shown on the same momentum and energy scales and all were taken in the normal state, at T=15 K. The Fermi surface of CaC_6 encloses a significant area and has a concave triangular shape centred at the K point of the Brillouin zone. The charge transfer from intercalant atoms fills the graphene bands and the Dirac point has moved to 1.5 eV below the Fermi level. White lines in Fig. 4c) correspond to the doping of 0.5 electrons per C atom, at which the van Hove singularity in the π^* band sits at the Fermi level. An important observation can immediately be made: in all the spectra from Fig. 4a), there is a renormalization of the quasiparticle dispersion at $\sim$160 meV below the Fermi level.

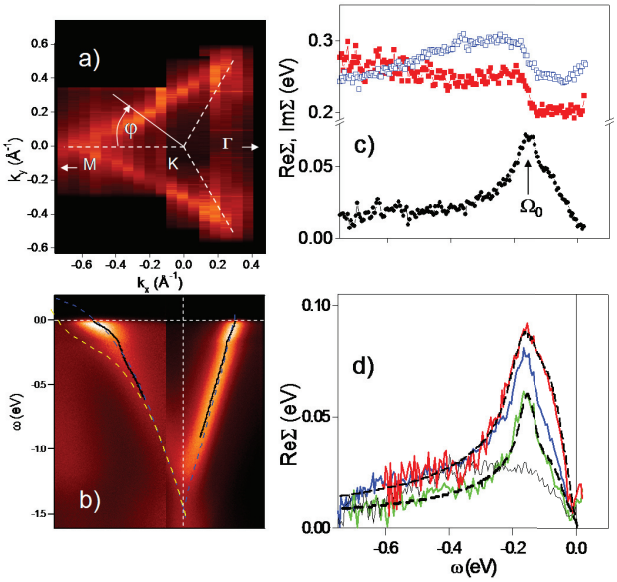

Fig. 5. Electron-phonon coupling in CaC_6. (a) Fermi surface of CaC_6. ϕ defines the polar angle around the K point, measured from the KM line. (b) Spectral intensity for $\phi = 60^\circ$ or KΓ line (right) and $\phi = 0^\circ$ or KM line (left). Black solid lines represent the momentum distribution curve derived dispersions. Dashed blue and yellow lines represent bands from Ref. (Calandra & Mauri, 2007), calculated for graphene and CaC_6 monolayer, respectively. (c) ReΣ (black circles) and ImΣ (red solid squares) for $\phi = 43^\circ$ and ImΣ for $\phi = 35^\circ$ (blue open squares). Peak (step) position in ReΣ (ImΣ) is labeled with Ω_0. (d) Real part of the self-energy for $\phi = 53^\circ$, 32° and 2° (bottom to top). Dashed lines represent the fits to the simple model self-energies as described in text. Thin black line is ReΣ of pristine graphite flake.

It is also apparent from Fig. 4 that the renormalization effects ("kinks) are not equally strong for all the points on the Fermi surface. Fig. 5 illustrates the anisotropy of the renormalization effects in CaC_6. We have extracted the dispersions and the linewidths of the quasiparticle states by fitting the spectral intensities at constant energies, or momentum distribution curves (Valla et al., 1999), with Lorentzian distributions. The real and imaginary components of the self-energy are then derived in the usual manner from the peak positions k_m and widths Δk of the momentum distribution curve peaks at each ω, as described in section 2.1, using the expressions

$$\mathrm{Re}\Sigma(\omega) = (k_m - k_0)v_0(\omega), \mathrm{Im}\Sigma(\omega) = \frac{\Delta k}{2}v_0(\omega) \quad (4)$$

where v_0 represents the bare band velocity at ω (LaShell et al., 2000; Valla et al., 2000). The starting approximation for the bare band was a tight binding dispersion which was then refined until the obtained ReΣ and ImΣ satisfied Kramers-Kronig transformations (Kordyuk et al., 2005). We note that the choice of the bare dispersion may play a significant role in determining the exact shape and magnitude of the self-energy (Valla et al., 2000). Therefore, the self-consistency check through the Kramers-Kronig criterion is important in getting the correct results. We note that the bands calculated for a CaC_6 monolayer (dashed blue line

in Fig. 5(b) (Calandra & Mauri, 2007) do not realistically represent the bare dispersions in our case. Instead, we have found that the bare dispersions calculated within 3^{rd} nearest neighbor tight binding approximation and appropriately filled, work well for the whole Fermi surface. The results for ReΣ and ImΣ corresponding to the azimuthal angle $\phi = 43^\circ$ and ImΣ for $\phi = 35^\circ$ are shown in Fig. 5(c). Fig. 5(d) shows ReΣ for different momentum lines corresponding, from bottom to top, to azimuthal angles $\phi = 53^\circ$, 32° and 2° . All the self-energies have a structure typical for the interaction with a well defined bosonic mode: the imaginary part has a sharp step-like feature, while the real part has a peak at the energy of the mode, Ω_0. Therefore, the mode energy can be read directly from the measured self-energy. In our case, the dominant structure occurs at $\sim$160 meV, with an additional feature at $\sim$75 meV. These features can be naturally attributed to the interaction with in-plane and out-of-plane phonons of the graphene sheets. We note that the finite energy resolution also affects the measured ReΣ near the Fermi level, within the resolution range, but with the tendency to underestimate the measured electron-phonon coupling (Valla, 2006). We have excluded the affected interval $|\omega| < 20$ meV from the considerations and any fine structure, related to a possible coupling to the intercalant modes, is out of our detection limits. At higher energies, we can model the measured self-energy at any ϕ with an Eliashberg function, $\alpha^2F(\omega)$ (see equation 2), consisting of two peaks: one fixed at 75 meV and the other ranging from 155 to 165 meV. The relative contribution of these two peaks increases from 1:5 to almost 1:1 on moving from $\phi = 60^\circ$ to $\phi = 0$. The modelled ReΣ are shown for these two limiting cases. Our model assumes a constant density of states (DOS), whereas a linear DOS would be a better approximation since the scattering is expected to reflect the density of final states. This is visible in Fig. 5(c), where ImΣ quickly acquires a slope as one moves from ΓK to KM. Fitting of measured ReΣ in the energy range $20 \leq |\omega| \leq 300$ meV to the model gives the energy of the high frequency mode Ω_0. In addition, the coupling strength, λ, can be extracted from the low energy slope of ReΣ, $\lambda = -[\partial(\mathrm{Re}\Sigma)/\partial\omega]_0$ by fitting the low energy part of ReΣ to a straight line. From Fig. 5(d) it is clear that the characteristic energy Ω_0 does not vary a lot, whereas the coupling strength λ displays a significant anisotropy. In Fig. 6(e-f), we plot both quantities as functions of azimuthal angle ϕ. The coupling constant ranges from 0.38 (for $\phi \approx 60^\circ$) to 0.89 (for $\phi \approx 0$), with the momentum averaged value of 0.53. The coupling constant in pristine graphite flake is much smaller ($\lambda = 0.16$) and does not show a significant anisotropy, in agreement with Leem et al. (Leem et al., 2008). The measured Fermi velocity on the graphene-derived Fermi surface is also very anisotropic: $v_F(\phi = 0) \approx 1.1$ eVÅ, $v_F(\phi = 60^\circ) \approx 4.1$eVÅ, with the momentum average $\langle v_F(k) \rangle \approx 2.5$ eVÅ. If the graphene electrons were responsible for superconducting properties, the in-plane coherence length, $\epsilon_{ab} = v_F/(\pi\Delta)$, would be in the range 200Å$< \epsilon_{ab} <$ 800 Å, if we take $\Delta \approx 1.6$ meV for the superconducting gap (Bergeal et al., 2006). $\langle v_F(k) \rangle$ gives $\epsilon_{ab} \approx$500 Å, in reasonable agreement with $\epsilon_{ab} \approx$350 Å reported in scanning tunneling microscopy (Park et al., 2007), specific heat (Kim et al., 2006) and magnetization (Emery et al., 2005; Lamura et al., 2006) studies. We also note that peculiar linearity in the upper critical filed, H_{C2}, at low temperatures, could also be explained by anisotropic Fermi velocity on the graphene-derived Fermi surface (Mazin et al., 2007). In contrast, the highly isotropic intercalant Fermi surface would not produce linear H_{C2}. Recent theoretical calculations suggest that in CaC_6, the crucial role is played by calcium, i.e. electrons on the intercalant-derived Fermi surface are strongly coupled to the intercalant vibrations (Boeri et al., 2007; Calandra & Mauri, 2005; Csányi et al., 2005; Mazin, 2005). Those calculations show nearly one order of magnitude weaker coupling of the graphene-derived electrons to the in-plane graphene phonons, with essentially no anisotropy (Park et al., 2008). The large calcium isotope effect also implies the dominant role of soft Ca vibrations

in superconductivity (Hinks et al., 2007). Our results, on the contrary, suggest that graphene sheets play the dominant role because the obtained electron-phonon coupling on graphene-derived Fermi surface with the in-plane and out-of-plane graphene phonons seems to be more than sufficient to give T_c ∼11.6 K in CaC_6.

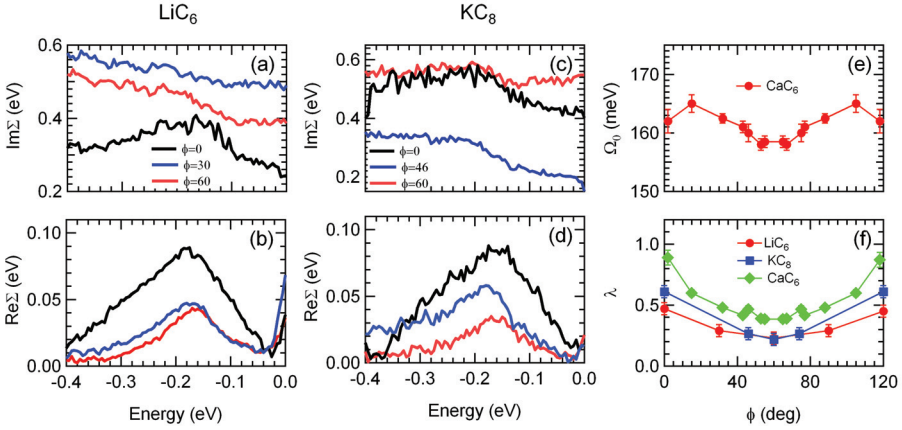

Fig. 6. Self-energy and electron-phonon coupling in graphite intercalation componds. $\mathrm{Im}\Sigma(\omega)$ (a) and $\mathrm{Re}\Sigma(\omega)$ (b) for LiC_6 and KC_8 ((c) and (d)) for several different points at the Fermi surface as indicated by the polar angle ϕ. (e) Characteristic energy Ω_0 of the maximum in $\mathrm{Re}\Sigma(\omega)$ of CaC_6 as a function of ϕ. (f) The electron phonon coupling constant λ in LiC_6, KC_8 and CaC_6 , extracted from $\mathrm{Re}\Sigma$ as a function of ϕ.

By extending similar analysis to a whole series of graphite intercalation compounds, including LiC_6, KC_8, KC_{24} (Camacho et al., n.d.; Pan et al., 2010), and BaC_6, we have been able to track certain trends and to get a better insight into the mechanism of superconductivity in the intercalated graphite. Fig. 6 shows the self-energies and the extracted electron-phonon coupling for the two most interesting members of the series: LiC_6, KC_8. The superconducting transition temperature, T_c, in these two materials is inverted from the expected trend in which the more charge nominally transferred to graphene sheets would mean the higher T_c. However, the actual charge transfer to graphene sheets measured in photoemission, is different from the nominal one dictated by the chemical formula (see Fig. 3) and, as previously discussed, it is actually larger in KC_8 than in LiC_6. Following the same procedure as for CaC_6, we have extracted the electron-phonon coupling from the self-energies. The coupling in both materials shows some anisotropy [Fig. 6(f)], with the maximum along the KM direction and the minimum along the ΓK direction, similar, but significantly weaker than in CaC_6(Valla et al., 2009) and what was recently reported for KC_8 (Grüneis et al., 2009). The most important observation, however, is that the momentum averaged $\langle\lambda_k\rangle$ is stronger in KC_8 than in LiC_6. The coupling constant and its anisotropy both increase from LiC_6 to KC_8 to CaC_6, exactly in the same sequence as the actual filling of the graphene π^* band and in previously established sequence for T_c. Strengthening of the electron-phonon coupling with the filling of the π^* band has also been observed in the epitaxial graphene (McChesney et al., 2007). This is not surprising, because the density of states near the Fermi level increases with the filling of the π^* band. Also, a larger Fermi surface makes an electron-phonon scattering process more probable as the phase space available for the scattering events grows. In the pristine graphite, the Fermi surface is nearly a point and the coupling is strongly suppressed (Leem et al.,

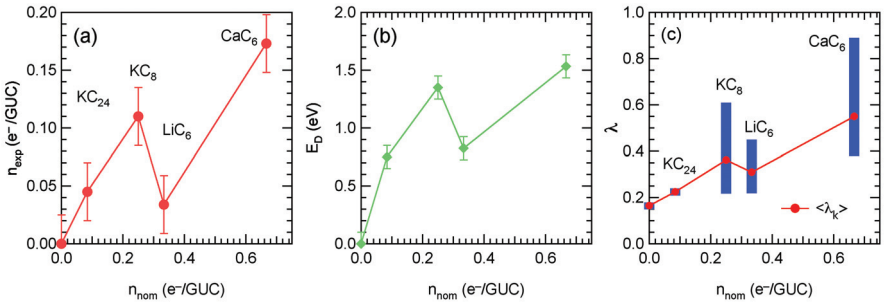

Fig. 7. Electron-phonon coupling and the filling of graphene states. (a) Measured charge transfer from the intercalant to the graphite π^* states. (b) Binding energy of Dirac point (chemical potential shift). (c) electron-phonon coupling, λ. The range of each vertical bar indicates the anisotropy with the maximum along the K-M line and minimum along the K-Γ line. Red circles represent the momentum averaged values, $\langle\lambda_k\rangle$.

2008; Valla et al., 2009). To better illustrate the positive correlation between the filling of the graphene π^* band and the coupling strength λ in different GICs, we plot these quantities in Fig. 7 as functions of nominal chemical composition for several different materials. The actual (measured) charge transfer (in electrons/GUC), obtained fom the Fermi surface area, is shown in Fig. 7(a). The increase in size of the Fermi surface is consistent with the energy of Dirac point [panel (b)] as the chemical potential, μ, shifts from the pristine graphite to CaC_6. It is interesting to note that $\mu \propto \sqrt{n_{exp}}$ still holds, regardless of the shape of Fermi surface and number of Fermi sheets in these five different materials. The coupling constant λ [panel (c)] follows the same trend as the filling of the π^* band. Note that this is the very trend of superconducting transition temperatures (T_c) in these materials, plotted in Fig. 8(c). This correlation suggests that the graphene π^* states and their coupling to graphene in-plane phonons is crucial for superconductivity in graphite intercalation compounds. The only role that the intercalants seem to play is to provide the charge for filling of the π^* states. As an additional test of this idea we have calculated the superconducting transition temperature, T_c, from McMillan's formula (McMillan, 1968), using the measured coupling constants $\langle\lambda_k\rangle$ and Coulomb pseudo-potential $\mu^* = 0.14$. The calculated T_c is compared with the experimental one in Fig. 8(b-c). It is clear not only that the calculated T_c follows the same trend, but even the absolute values are very close to the measured ones. This reinforces our conclusion that the graphene electronic states and graphene-derived phonons are crucial for superconductivity in GICs. Note that the threshold-like behavior near $\langle\lambda_k\rangle = 0.3$ places LiC_6 on one side and KC_8 on another side of a steep increase in T_c. We note that superconductivity in LiC_3 and LiC_2, materials in which more Li is pushed in under pressure, supports our picture where the electron-phonon coupling and superconductivity strengthen with the filling of graphene π^* states. The increase in T_c from 0.39 K for stoichiometric KC_8 to 0.55K in material with excess K is also in line with this picture. A further test would be a systematic photoemission study on alkaline-earth GICs (Ca, Sr, Ba) where T_c decreases with the atomic mass of alkaline-earth intercalant.

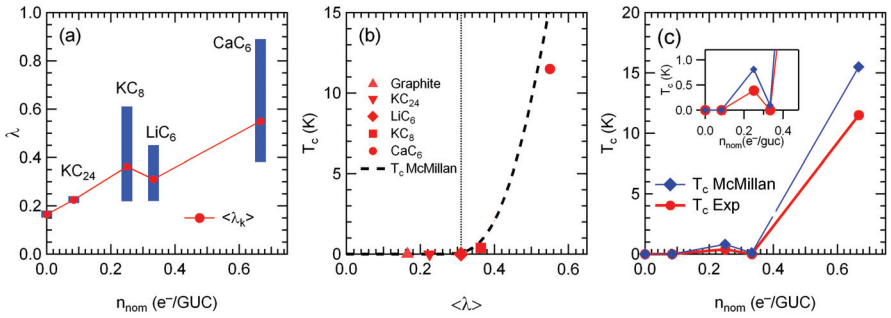

Fig. 8. Electron-phonon coupling and superconducting critical temperature (T_c) in graphite intercalation compunds. (a) Measured λ for several different GICs. The range of each vertical bar indicates the anisotropy with the maximum along the KM line and minimum along the KΓ line. The red circles and line represent the momentum averaged values $\langle\lambda_k\rangle$. (b) T_c as a function of $\langle\lambda_k\rangle$ calculated from measured $\langle\lambda_k\rangle$ using McMillan's formula (McMillan, 1968). The dashed line represents the calculated values while symbols represent experimental T_c values. (c) Comparison of calculated (blue diamond) and measured (red circle) values as functions of nominal chemical composition (electrons per graphene unit cell (GUC)) for measured GICs. Zero corresponds to the pristine graphite. The inset zooms in the low T_c values.

3.3 Enhancement of electron-phonon coupling via dynamical nesting

A huge discrepancy between the calculated and measured coupling, where the later one is almost one order of magnitude stronger, naturally provokes the question: Where is such strong and anisotropic coupling coming from? Similar anisotropy was recently reported for electron-phonon coupling in K and Ca doped graphene on SiC (McChesney et al., 2007). There, the proximity of van Hove singularity to the Fermi level was suggested to be an origin of the enhanced coupling. Even though the claim on very high anisotropy was subsequently retracted due to the erroneous procedure of extracting the coupling near the KM lines, the measured coupling on the unaffected portion of the Fermi surface was still significantly stronger than the calculated one (Park et al., 2008). In the case of CaC_6 we believe that we have found the likely mechanism of enhancement of the coupling: very favourable dynamical nesting conditions exist on the Fermi surface that may strongly enhance the inter-valley coupling.

This is illustrated in Fig. 9. In order to satisfy the energy conservation rule in an electron-phonon scattering event, the photohole created at ∼160 meV has to be scattered to the Fermi level after emission of a 160 meV phonon. To explore the allowed momenta in such a process, we plot the states at $\omega = -160$ meV at one corner of the Brillouin zone and the states at the Fermi level ($\omega = 0$) in another corner for two highly doped GICs: KC_8 (panel (a)) and CaC_6 (panel (b)). A wavevector connecting any pair of points on different contours represents an allowed scattering process. Note that in the case of intra-valley scattering, both contours would have to be centred at the same K point. However, from the measured phonon spectra in graphite (Maultzsch et al., 2004), and recent Raman experiments on CaC_6 (Hlinka et al., 2007), it is clear that there are no $q \approx 0$ modes at ∼160 meV and we have to consider inter-valley scattering.

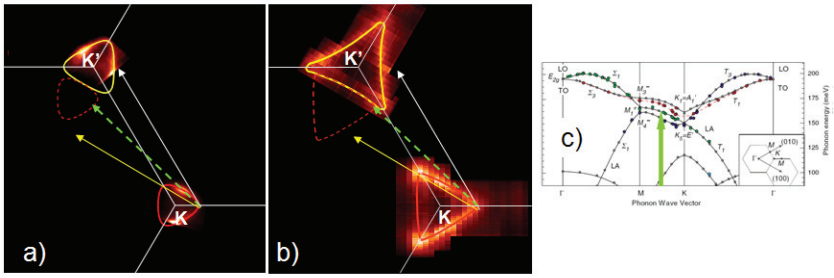

Fig. 9. Dynamical nesting of the Fermi surface in GICs. Contour of photoemission intensity from KC_8 (a) and CaC_6 (b) at ω = 0 meV (yellow contour) around K′ point and at the "kink" energy $\omega = -\Omega_0 = -160$ meV (red contour), in the vicinity of of K point of the Brillouin zone. White (yellow) arrow represents the ΓK (ΓM) wave vector, while the dashed green arrow represents the wave vector that "nests" the two contours. Evidently, the nesting is much more efficient in CaC_6 than in KC_8. (c) Phonon dispersions in pristine graphite (Maultzsch et al., 2004). The position of dynamical nesting wave vector for CaC_6 from(b) is marked with green arrow. Its length corresponds to the exchanged energy.

From Fig. 9, it appears that in the case of CaC_6, some wave-vectors are particularly efficient in connecting the two contours. As the $\omega = -160$ meV contour is slightly convex and the Fermi surface is slightly concave with essentially the same curvature, the green vector in Fig 9(b) effectively nests the whole side, or $\sim$ 1/3 of the length of the two contours. The tips of contours can be nested by two such vectors, which might explain a portion of the observed anisotropy in λ. The additional factor characterizing the tips is a gain in coupling to lower frequency phonons at $\omega \approx 75$ meV, as can be seen in Fig. 5d. We note that the observed "nesting" is not static: it involves emission/absorption of a high frequency phonon and would not produce the charge density wave instability. The dynamical nesting and resulting enhancement of the electron-phonon coupling is obviously very sensitive to the filling of graphene-derived bands. For lower doping levels, the nesting efficiency is quickly lost as both contours become convex, as is evident in the case of KC_8 (Fig. 9(a)). At even higher fillings, possibly realized under pressure (Gauzzi et al., 2007; Smith et al., 2006), the nesting conditions would likely improve further, but at some point, the coupling to lower frequency phonons near the KM lines might become too strong and eventually drive the system into the charge-density wave state.

4. Summary and outlook

In conclusion, we have performed angle resolved photoemission spectroscopy studies of the electronic structure in pristine graphite and several alkali and alkaline-earth GICs. We have measured the strength of the electron-phonon interaction on the graphene-derived Fermi surface to carbon derived phonons in these materials and found that it follows a universal trend where the coupling strength and superconductivity monotonically increase with transfer of electrons into the graphene-derived π^* states. This correlation between the filling of graphene π^* states, the strength of the electron-phonon coupling and superconductivity suggests that both graphene-derived electrons and graphene-derived phonons are crucial for superconductivity in GICs. We have also identified a possible mechanism of enhancement of the electron-phonon coupling in these materials that stems from the particular Fermi surface geometry. For highly doped systems (CaC_6), a concave triangular shape of the Fermi

surface perfectly matches the convex energy contour at the energy of the exchanged phonon, effectivley enhancing the electron-phonon coupling. Such mechanism is expected to be very sensitive on the occupation of the π^* band and might be used to fine-tune the coupling in order to reach a maximal T_c. Perhaps this is what is going on under pressure in some superconducting GICs (Gauzzi et al., 2007; Smith et al., 2006).
We note that similar results were obtained for graphene monolayers, epitaxially grown on SiC(0001) and Ir(111) and chemically doped by adsorbed (or subsurface) alkali and alkaline-earth atoms (Bianchi et al., 2010; McChesney et al., 2007; 2010). Due to the reduced dimensionality, we probably cannot expect these systems to be superconducting, but the ability to contionusly fill the π^* states and to fine tune the electronic structure in these films offers the opportunity of measuring the electron-phonon coupling in much finer steps of doping. Such studies might help in understanding the role of the Fermi surface topology in shaping the properties of graphite intercalation compounds and open the new avenues of designed synthesis of new intercalated materials with targeted properties.

5. Acknowledgments

We would like to acknowledge the many contributions of our collaborators on the work described here. These include T. Berlijn, J. Camacho, M. Dean, M. Ellerby, A. V. Fedorov, C. A. Howard, M. Khodas, W. Ku, M. Strongin, M. H. Upton, A.C. Walters and I. Zaliznyak. The research work described in this paper was supported by the Department of Energy under Contract No. DE-AC02-98CH10886.

6. References

Bergeal, N., Dubost, V., Noat, Y., Sacks, W., Roditchev, D., Emery, N., Hérold, C., Marêché, J.-F., Lagrange, P. & Loupias, G. (2006). Scanning tunneling spectroscopy on the novel superconductor CaC_6, *Phys. Rev. Lett.* 97(7): 077003.

Bianchi, M., Rienks, E. D. L., Lizzit, S., Baraldi, A., Balog, R., Hornekær, L. & Hofmann, P. (2010). Electron-phonon coupling in potassium-doped graphene: Angle-resolved photoemission spectroscopy, *Phys. Rev. B* 81(4): 041403.

Boeri, L., Bachelet, G. B., Giantomassi, M. & Andersen, O. K. (2007). Electron-phonon interaction in graphite intercalation compounds, *Phys. Rev. B* 76(6): 064510.

Calandra, M. & Mauri, F. (2005). Theoretical explanation of superconductivity in C_6Ca, *Phys. Rev. Lett.* 95(23): 237002.

Calandra, M. & Mauri, F. (2007). Electronic structure of heavily doped graphene: The role of foreign atom states, *Phys. Rev. B* 76(16): 161406.

Camacho, J., Upton, M., Pan, Z.-H., Howard, C., Ellerby, M. & Valla, T. (n.d.). unpublished.

Csányi, G., Littlewood, P. B., Nevidomskyy, A. H., Pickard, C. J. & Simons, B. D. (2005). The role of the interlayer state in the electronic structure of superconducting graphite intercalated compounds, *Nature Physics* 1(1): 42–45.
URL: *http://www.nature.com/doifinder/10.1038/nphys119*

Dean, M. P. M., Howard, C. A., Saxena, S. S. & Ellerby, M. (2010). Nonadiabatic phonons within the doped graphene layers of XC_6 compounds, *Phys. Rev. B* 81(4): 045405.

Dresselhaus, M. S. & Dresselhaus, G. (2002). Intercalation compounds of graphite, *Advances in Physics* 51(1): 1–186.
URL: *http://www.informaworld.com*

Emery, N., Hérold, C., d'Astuto, M., Garcia, V., Bellin, C., Marêché, J. F., Lagrange, P. & Loupias, G. (2005). Superconductivity of bulk CaC_6, *Phys. Rev. Lett.* 95(8): 087003.

Gauzzi, A., Takashima, S., Takeshita, N., Terakura, C., Takagi, H., Emery, N., Hérold, C., Lagrange, P. & Loupias, G. (2007). Enhancement of superconductivity and evidence of structural instability in intercalated graphite CaC_6 under high pressure, *Phys. Rev. Lett.* 98(6): 067002.

Grimvall, G. (1981). *The Electron-Phonon Interaction in Metals*, North-Holland, New York.

Grüneis, A., Attaccalite, C., Rubio, A., Vyalikh, D. V., Molodtsov, S. L., Fink, J., Follath, R., Eberhardt, W., Büchner, B. & Pichler, T. (2009). Angle-resolved photoemission study of the graphite intercalation compound KC_8 : A key to graphene, *Phys. Rev. B* 80(7): 075431.

Hannay, N. B., Geballe, T. H., Matthias, B. T., Andres, K., Schmidt, P. & MacNair, D. (1965). Superconductivity in graphitic compounds, *Phys. Rev. Lett.* 14(7): 225–226.

Hengsberger, M., Purdie, D., Segovia, P., Garnier, M. & Baer, Y. (1999). Photoemission study of a strongly coupled electron-phonon system, *Phys. Rev. Lett.* 83(3): 592–595.

Hinks, D. G., Rosenmann, D., Claus, H., Bailey, M. S. & Jorgensen, J. D. (2007). Large Ca isotope effect in the CaC_6 superconductor, *Phys. Rev. B* 75(1): 014509.

Hlinka, J., Gregora, I., Pokorny, J., Hérold, C., Emery, N., Marêché, J. F. & Lagrange, P. (2007). Lattice dynamics of CaC_6 by Raman spectroscopy, *Phys. Rev. B* 76(14): 144512.

Holzwarth, N. A. W., Louie, S. G. & Rabii, S. (1984). Interlayer states in graphite and in alkali-metal-graphite intercalation compounds, *Phys. Rev. B* 30(4): 2219–2222.

Kaminski, A., Mesot, J., Fretwell, H., Campuzano, J. C., Norman, M. R., Randeria, M., Ding, H., Sato, T., Takahashi, T., Mochiku, T., Kadowaki, K. & Hoechst, H. (2000). Quasiparticles in the superconducting state of $Bi_2Sr_2CaCu_2O_{8+\delta}$, *Phys. Rev. Lett.* 84(8): 1788–1791.

Kevan, E. (1992). *Angle-Resolved Photoemission*, Elsevier, Amsterdam.

Kim, J. S., Kremer, R. K., Boeri, L. & Razavi, F. S. (2006). Specific heat of the Ca-intercalated graphite superconductor CaC_6, *Phys. Rev. Lett.* 96(21): 217002.

Kordyuk, A. A., Borisenko, S. V., Koitzsch, A., Fink, J., Knupfer, M. & Berger, H. (2005). Bare electron dispersion from experiment: Self-consistent self-energy analysis of photoemission data, *Phys. Rev. B* 71(21): 214513.

Lamura, G., Aurino, M., Cifariello, G., Di Gennaro, E., Andreone, A., Emery, N., Hérold, C., Marêché, J.-F. & Lagrange, P. (2006). Experimental evidence of *s*-wave superconductivity in bulk CaC_6, *Phys. Rev. Lett.* 96(10): 107008.

LaShell, S., Jensen, E. & Balasubramanian, T. (2000). Nonquasiparticle structure in the photoemission spectra from the Be(0001) surface and determination of the electron self energy, *Phys. Rev. B* 61(3): 2371–2374.

Leem, C. S., Kim, B. J., Kim, C., Park, S. R., Ohta, T., Bostwick, A., Rotenberg, E., Kim, H. D., Kim, M. K., Choi, H. J. & Kim, C. (2008). Effect of linear density of states on the quasiparticle dynamics and small electron-phonon coupling in graphite, *Phys. Rev. Lett.* 100(1): 016802.

Mahan, G. (1990). *Many Particle Physics*, Plenum Press, New York.

Maultzsch, J., Reich, S., Thomsen, C., Requardt, H. & Ordejón, P. (2004). Phonon dispersion in graphite, *Phys. Rev. Lett.* 92(7): 075501.

Mazin, I., Boeri, L., Dolgov, O., Golubov, A., Bachelet, G., Giantomassi, M. & Andersen, O. (2007). Unresolved problems in superconductivity of CaC_6, *Physica C: Superconductivity* 460-462: 116–120.
URL: *http://dx.doi.org/10.1016/j.physc.2007.03.276*

Mazin, I. I. (2005). Intercalant-driven superconductivity in YbC_6 and CaC_6, *Phys. Rev. Lett.* 95(22): 227001.

McChesney, J. L., Bostwick, A., Ohta, T., Emtsev, K. V., Seyller, T., Horn, K. & Rotenberg, E. (2007). Massive enhancement of electron-phonon coupling in doped graphene by an electronic singularity, p. 8.
URL: *http://arxiv.org/abs/0705.3264*

McChesney, J. L., Bostwick, A., Ohta, T., Seyller, T., Horn, K., González, J. & Rotenberg, E. (2010). Extended van hove singularity and superconducting instability in doped graphene, *Phys. Rev. Lett.* 104(13): 136803.

McMillan, W. L. (1968). Transition temperature of strong-coupled superconductors, *Phys. Rev.* 167(2): 331–344.

Pan, Z.-H., Camacho, J., Upton, M. H., Fedorov, A. V., Walters, A. C., Howard, C. A, Ellerby, M. & Valla, T. (2010). Why is KC8 a superconductor and LiC6 is not? URL: http://arxiv.org/abs/1003.3903.

Park, C.-H., Giustino, F., Cohen, M. L. & Louie, S. G. (2007). Velocity renormalization and carrier lifetime in graphene from the electron-phonon interaction, *Phys. Rev. Lett.* 99(8): 086804.

Park, C.-H., Giustino, F., McChesney, J. L., Bostwick, A., Ohta, T., Rotenberg, E., Cohen, M. L. & Louie, S. G. (2008). Van hove singularity and apparent anisotropy in the electron-phonon interaction in graphene, *Phys. Rev. B* 77(11): 113410.

Posternak, M., Baldereschi, A., Freeman, A. J., Wimmer, E. & Weinert, M. (1983). Prediction of electronic interlayer states in graphite and reinterpretation of alkali bands in graphite intercalation compounds, *Phys. Rev. Lett.* 50(10): 761–764.

Pruvost, S., Herold, C., Herold, A. & Lagrange, P. (2004). Co-intercalation into graphite of lithium and sodium with an alkaline earth metal, *Carbon* 42(8-9): 1825–1831.
URL: *http://linkinghub.elsevier.com/retrieve/pii/S0008622304002106*

Smith, R. P., Kusmartseva, A., Ko, Y. T. C., Saxena, S. S., Akrap, A., Forró, L., Laad, M., Weller, T. E., Ellerby, M. & Skipper, N. T. (2006). Pressure dependence of the superconducting transition temperature in C_6Yb and C_6Ca , *Phys. Rev. B* 74(2): 024505.

Sugawara, K., Sato, T. & Takahashi, T. (2008). Fermi-surface-dependent superconducting gap in C_6Ca, *Nature Physics* 5(1): 40–43.
URL: *http://www.nature.com/doifinder/10.1038/nphys1128*

Valla, T. (2006). Comment on "Multiple bosonic mode coupling in the electron self-energy of $(La_{2-x}Sr_x)CuO_4$", *Phys. Rev. Lett.* 96(11): 119701.

Valla, T., Camacho, J., Pan, Z.-H., Fedorov, A. V., Walters, A. C., Howard, C. A. & Ellerby, M. (2009). Anisotropic electron-phonon coupling and dynamical nesting on the graphene sheets in superconducting CaC_6 using angle-resolved photoemission spectroscopy, *Phys. Rev. Lett.* 102(10): 107007.

Valla, T., Fedorov, A. V., Johnson, P. D., Glans, P.-A., McGuinness, C., Smith, K. E., Andrei, E. Y. & Berger, H. (2004). Quasiparticle spectra, charge-density waves, superconductivity, and electron-phonon coupling in 2H-$NbSe_2$, *Phys. Rev. Lett.* 92(8): 086401.

Valla, T., Fedorov, A. V., Johnson, P. D. & Hulbert, S. L. (1999). Many-body effects in angle-resolved photoemission: quasiparticle energy and lifetime of a Mo(110) surface state, *Phys. Rev. Lett.* 83(10): 2085–2088.

Valla, T., Fedorov, A. V., Johnson, P. D., Xue, J., Smith, K. E. & DiSalvo, F. J. (2000). Charge-density-wave-induced modifications to the quasiparticle self-energy in 2H-$TaSe_2$, *Phys. Rev. Lett.* 85(22): 4759–4762.

Weller, T. E., Ellerby, M., Saxena, S. S., Smith, R. P. & Skipper, N. T. (2005). Superconductivity in the intercalated graphite compounds C_6Yb and C_6Ca, *Nature Physics* 1(1): 39–41.
URL: *http://dx.doi.org/10.1038/nphys0010*

Part 3

Applications

20

Graphene Transistors

Kristóf Tahy, Tian Fang, Pei Zhao, Aniruddha Konar, Chuanxin Lian,
Huili (Grace) Xing, Michelle Kelly and Debdeep Jena
University of Notre Dame,
USA

1. Introduction

The recent discovery of graphene (Novoselov et al., 2004), a single atomic sheet of graphite, has ignited intense research activities to explore the electronic properties of this novel two-dimensional (2D) electronic system. Charge transport in graphene differs from that in conventional 2D electronic systems as a consequence of the conical energy dispersion relation near the charge neutrality (Dirac) point in the electronic band structure (Zhang et al., 2005). Field-effect mobility as high as 15 000 $cm^2/V{\cdot}s$ and a Fermi velocity of ~10^8 cm/s have been demonstrated at room temperature (Geim & Novoselov 2007). These properties make graphene a possible candidate for electronic devices in the future.

The major benefit of graphene frequently quoted is superior electron/hole mobility compared to other semiconductors, but as Fig. 1 shows, this is not experimentally the case *yet* when compared to narrow bandgap III-V semiconductors for comparable carrier densities. In addition, the lack of a bandgap limits the usage of two dimensional graphene for digital switching, where high on/off ratios are necessary. However, several potential advantages may be listed: the perfect 2D confinement of carriers, electron/hole symmetry originating from a conical bandstructure, and the possibility of opening bandgaps lithographically by fabricating graphene nanoribbons (GNRs). In Section 2, high field characteristics of 2D exfoliated graphene are reported on both short-channel and long-channel back gated field effect transistors (FETs). We will elaborate on the problem of metal contact formation and high field transport of 2D graphene. The comparison of fabricated devices based on exfoliated, epitaxial and chemical vapour deposited (CVD) graphene will follow. The large area graphene opens the possibility to make 2D graphene devices for RF/analog amplification (Lin et al., 2010). Superior frequency performance of such devices makes it a promising application of 2D graphene FETs.

The real advantage of graphene, however, can be highlighted from a novel proposed device architecture that is yet to be demonstrated (Zhang et al., 2008). If GNRs are made by lithographic patterning, and are either chemically or electrostatically doped into GNR p-n junctions, then the planar form yields to a tunnelling field-effect transistor (TFET). Towards the realization of the GNR TFET we designed a single but tuneable junction structure to demonstrate the operational principle. We discuss these GNR p-n junction transistors in Section 3 along with the developed analytical and device models used to explain the measured transistor characteristics.

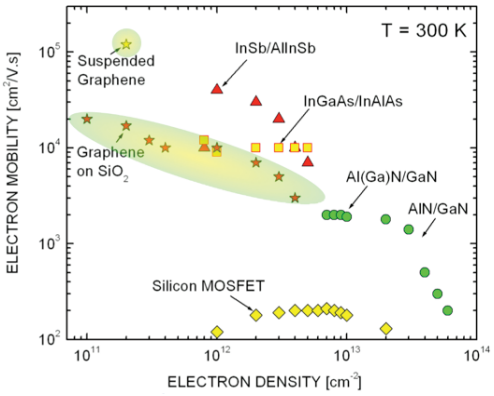

Fig. 1. 300 K electron mobility vs. 2DEG density for various semiconductor materials.

2. 2D graphene transistors

2.1 Device fabrication and characteristics of 2D exfoliated graphene transistors

Graphene offers advantages for interconnects due to high current carrying capacity despite its single layer nature (Murali et al., 2009) but more often graphene is being considered as a possible channel material for transistor technology. So far, graphene has been studied mostly at low biases, but for the application in practical devices, it is essential to investigate the high-field transport properties. High current drives were measured by pushing the devices up to breakdown. The saturation current density for many samples has been measured to be in the 1.5 – 2 A/mm range. Gate modulation of the drain current is found to depend strongly on the channel length. For comparable 2D carrier concentrations, saturation currents in 2D graphene are found to be higher than Si MOSFETs and III-V Nitride HEMTs – a feature that is attractive for various applications.

We first discuss 2D graphene FETs fabricated from exfoliated graphene and later we compare the results to graphene devices made of catalyzed CVD or epitaxial graphene. Exfoliated graphene flakes on heavily n-type doped silicon wafers with t_{ox} = 300 nm thick thermal oxide from Graphene Industries (for preparation of samples, see: Novoselov et al., 2004) were used for the experiments. Single layer graphene flakes were identified by Raman spectroscopy (inset of Fig. 2 (a)). The wafers were backside-metalized after oxide removal in HF to form back-gate contacts. E-beam evaporated Cr/Au (2/200 nm) was used to define the drain and source contacts, which were patterned by e-beam lithography. The source-drain separations ranged from L = 250 nm - 8 µm. After metal deposition and lift-off, the samples were annealed in forming gas at ~650 K for ~2 hours to remove the e-beam resist residue. The graphene flakes were then patterned by O_2 plasma reactive ion etch with PMMA masks to widths ranging from W = 1 - 10 µm. The SEM image (inset of Fig. 2 (b)) shows a typical FET. High current annealing was performed to drive off impurities for some FETs to recover their intrinsic performance. The devices were measured using a semiconductor parameter analyzer in ambient environment and in vacuum, at room temperature and at 77 K. The drain currents of the FETs were first measured at a low bias of V_{DS} = 20 mV, while the gate voltage was varied over a wide range. The gate leakage current was many orders of magnitude lower than the drain current.

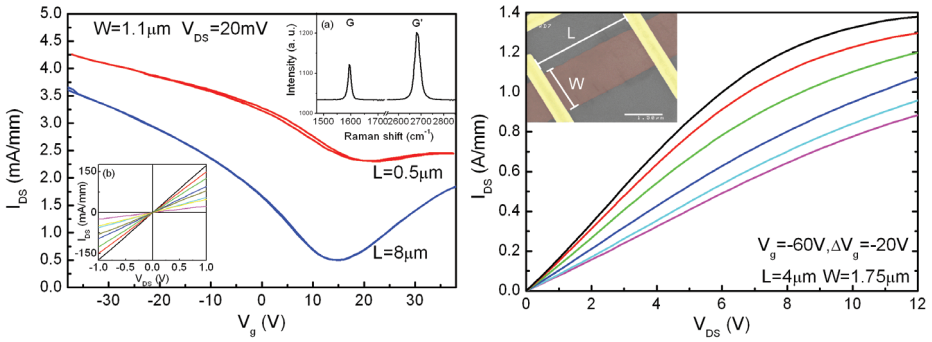

(a) (b)

Fig. 2. (a) I_{DS} as a function of V_G at V_{DS} = 20 mV for short-channel (0.5 μm) and long-channel (8 μm) back-gated graphene FETs. Inset (a) Raman spectrum of single layer graphene. Inset (b) Low field I-V curves of long-channel FETs with V_G = -35 V, ΔV_G = +10 V. (b) I-V curves of a long-channel FETs. Inset is a SEM image of this FET. The scale bar is 1.5 μm.

Fig. 2 (a) shows the representative transfer characteristics of a long- and a short-channel FET. Over the same range of gate overdrives, the long channel FET was observed to exhibit higher gate modulation (~8x) than the short-channel FETs (~2x). The field-effect mobilities were calculated to be ~2000 – 4000 $cm^2/V{\cdot}s$ for long-channel FET and ~200 $cm^2/V{\cdot}s$ for short-channel FET respectively. These characteristics remained similar at different pressures, as well as at lower temperature.

Recently, saturation of drain current at high source-drain biases has been reported, and theory of optical phonon emission limited saturation current has been proposed (Meric et al., 2008; Luo et al., 2008). In particular, back- and top-gated 2D graphene FETs showed saturation current densities in the 0.5 – 0.7 A/mm range as reported by Meric et al., 2008. In Fig. 2 (b), the high bias characteristics of a back-gated FET (W/L = 1.75/4 μm) are shown. A saturation current of 1.38 A/mm is measured for this device. Saturation current densities in the 1.5 – 2.0 A/mm range were measured on a number of devices, in agreement with another earlier report for back-gated devices (Luo et al., 2008). This is ~2x higher than the reported saturation current densities for dual-gate devices, indicating that the top-gate high-κ oxide lowers the current drive through graphene. The effective 2D carrier densities were in the $2 - 4{\cdot}10^{12}$ cm^{-2} range, as estimated from the effective gate voltage. The ~0.5 - 0.7 A/mm saturation current reported earlier has been attributed to substrate-induced optical phonon scattering. However the ~2x higher current drives measured here on SiO_2 substrates indicate that the lower current drives are due to the top gate high-κ oxide rather than the SiO_2 substrate. This conjecture will be discussed in detail in the next Section.

Such current drives can be obtained in Si MOSFETs and III-V HEMTs, but only with a) high 2DEG densities (>10^{13} cm^{-2}), and/or b) very short channel lengths taking advantage of ballistic transport. Our measurements show that graphene FETs are able to achieve these high current densities without these criteria, implying that even higher current drives are possible when they are met in the future. For a rough comparison, a carbon nanotube with diameter ~2 nm and a saturation current ~25 μA has an effective current per the circumferential width ~4 A/mm (Chen & Fuhrer, 2005), much higher than either graphene or other semiconductors. At high drain biases, the current saturates at more than 1 A/mm,

but with weak gate modulation. Graphene carries over the high current carrying capacity of carbon nanotubes, but the absence of an energy bandgap hampers the modulation of this high current density.

2.2 Graphene on high-κ dielectrics

In the last section, we discussed carrier mobility and current drive of graphene on SiO_2. Low-field mobility values for graphene on SiO_2 was 4000 $cm^2/V{\cdot}s$ at room temperature and the highest reported value at $>10^{13}$ cm^{-2} carrier concentration is around 9000 $cm^2/V{\cdot}s$ in literature (Novoselov et al., 2004). It is widely believed that ionized charged impurities at the graphene-oxide interface (Hwang et al., 2007) limits the carrier mobility in graphene. As electron-ionized charged impurity interaction $v_{cou} \approx \kappa^{-2}$, where κ is the average dielectric constant of graphene's environment, it seems that use of very high-κ substrate instead of SiO_2 can improve the carrier mobility of graphene at low fields. But use of high-κ dielectrics for graphene transistors comes with an extra scattering mechanism—the remote interface-phonon or surface optical phonon (SO) scattering. Most of the high-κ materials are polar in nature because of large difference in electronegativity of constituent atoms. At room temperature, the vibrating dipoles of the high-κ dielectric material create an electric field, which decays exponentially away from the graphene-dielectric interface. Due to the fact that graphene is an atomically thin (0.3 - 0.4 nm) membrane, the decaying polarization field (also known as surface-phonon field) can scatter the carriers in the graphene channel and limit the low-field mobility. The surface phonon energies can be calculated by solving Maxwell's equation in the dielectric continuum model.

	SiO_2	AlN	Al_2O_3	HfO_2	ZrO_2	SiC
κ^0_{ox}	3.9	9.14	12.53	22.0	24.0	9.7
κ^∞_{ox}	2.5	4.8	3.2	5.03	4.0	6.5
$\omega_{TO,1}$	55.6	81.4	48.18	12.4	16.67	-
$\omega_{TO,2}$	138.1	88.5	71.41	48.35	57.7	-
$\omega_{SO,1}$	59.98	83.60	55.01	19.42	25.02	116.0
$\omega_{SO,2}$	146.51	104.96	94.29	52.87	70.80	167.58

Table 1. Surface phonon energies of graphene/dielectric/air system for various dielectric materials.

In Table 1, we present the calculated values of surface-phonon energies for commonly used dielectrics in device-physics. Most binary dielectric compounds exhibit two surface-phonon modes corresponding to two bulk transverse phonon (TO) modes. It should be noted that, high-κ dielectric materials such as HfO_2 and ZrO_2 exhibit very low- energy SO modes. The surface-phonon modes are optical-like (dispersionless) as shown in Fig. 3 and cause inelastic scattering of carrier electrons in graphene. The electron-SO phonon scattering rates are calculated using second order perturbation theory and transport coefficient such as electron mobility have been calculated using the Boltzmann transport equation under the relaxation time approximation. When ionized impurity scattering is combined with SO-phonon scattering, a comprehensive picture of charge transport emerges. At low temperature, when SO-phonons are frozen, indeed electron mobility can be enhanced by a

factor of 3-4 by using ZrO_2 as the gate dielectric, but at room temperature, this dielectric enhancement is washed out by strong electron-SO phonon scattering. Fig. 3 (b) provides a relative assessment of electron mobility on different dielectrics. The curve represents the expected mobility enhancement by high-κ dielectrics, whereas the dots represent the effective mobility after inclusion of SO-phonon scattering rates. It is seen that there is not much room for improving carrier mobility with commonly available high-κ dielectrics at room temperature. In the future, high-κ dielectrics with high SO-phonon energies should be sought to achieve high mobility and speed in graphene.

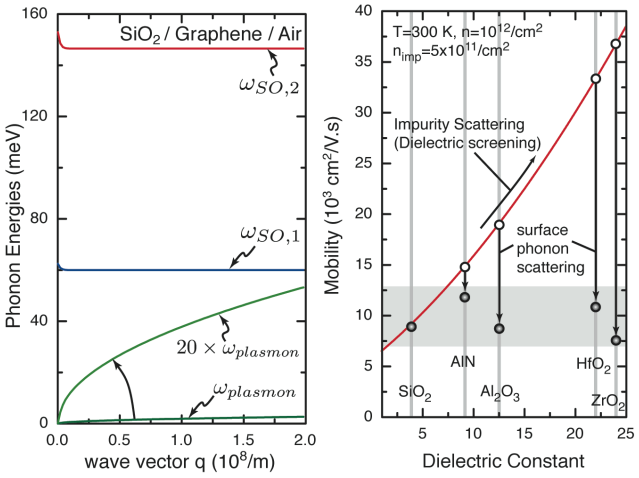

Fig. 3. (a) Dispersion of SO phonon and (b) mobility of graphene on common dielectrics.

2.3 Short channel and contact effects

The dependence of high bias drain currents and their modulation efficiency with the back-gate is observed to depend strongly on the channel length of graphene. In Fig. 4, the FET characteristics are shown for four different channel lengths, ranging from 0.5 to 8 μm. Two features are observed – a) for the same channel length, the gate modulation at higher drain biases is lower, as is expected from the saturation of the current, and b) for the same bias voltages (or fields), the gate modulation efficiency decreases sharply as the channel length reduces. As shown in Fig. 4, the gate modulation reduces from ~7 to ~1.4 as the source-drain separation is scaled from 8 μm to 0.5 μm.

Due to the absence of a bandgap in graphene, charge exchange is expected at the metal-graphene source/drain contacts owing to the work function differences. Considering the work function of Cr (W_{Cr} ~4.5 eV), and that of pristine graphene (W_{Gr} ~4.5 eV) one would expect them to form a flat-band (or 'neutral') contact without any charge transfer. However, recent calculations have shown that the necessary condition for the formation of a neutral contact with a metal (work function W_M) in intimate contact with graphene is W_M - W_{Gr} ~0.9eV (Giovannetti et al., 2008). Therefore, we expect that the graphene region adjacent to the Cr contact pad is effectively doped with excess carriers. The excess charge region extends over an effective Debye length from each contact resulting in source/drain extension regions. Quantitative modelling of this interesting phenomenon will be presented in detail in Section

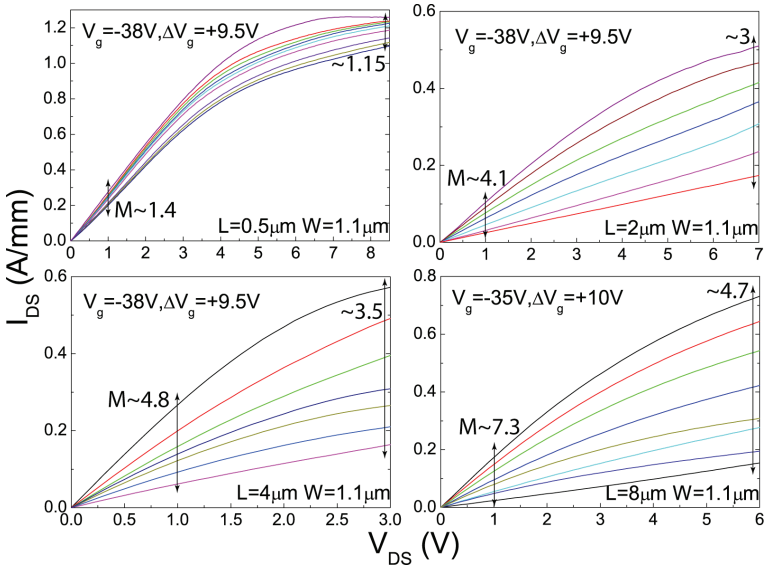

Fig. 4. Current density as a function of drain biases for FETs with different channel lengths varied from 0.5 μm to 8 μm. Clear loss of gate modulation is observed with the shrinking of the graphene channel length.

2.4. When the source/drain separation is smaller than twice the Debye length, the channel conductivity is controlled by the source/drain contacts, and the back-gate gradually loses the ability to modulate the current, as seen in the FET characteristics in Figs. 2 & 4.

2.4 Influence of metal/graphene coupling on 2D graphene transistor

Recently, many experimental studies point out that metal contacts could play a critical role on device performance of graphene transistors (Lee et al., 2008; Mueller et al., 2009). When graphene is covered by a metal electrode, the Fermi level of the underlying graphene will be shifted according to density functional theory calculations (Giovannetti et al., 2008) and have been observed in experiments (Huard et al., 2008; Nagashio et al., 2009). Here, we explore the effects of metal contacts on the operation and scalability of 2D graphene FETs using detailed numerical device simulations based on the non-equilibrium Green's function (NEGF) formalism in the ballistic limit. Our treatment of metal/graphene contacts captures (1) the doping effect due to the shift of the Fermi level at graphene contacts; (2) the Metal-Induced-States (MIS) in the graphene channel.

The modelled device is shown in the inset of Fig. 5 (left). The channel is assumed to be uniform graphene with width of 150 nm. At w = 150 nm, the current density is similar to analytical 2D results, which implies an effective 2D approximation. The contact regions are assumed to be semi-infinitely long. The top gate insulator is t_{ox} = 1.5 nm thick with a dielectric constant ε_{ox} = 20. The bottom gate dielectric SiO2 is 50 nm thick, and the Si substrate is connected to the ground. The simulated area is only the channel (dashed rectangle) with fixed boundary conditions at the source and the drain. The major challenge in experiments is the aforementioned degradation of graphene channel mobility due to the top high-κ gate dielectric; in this theoretical evaluation, a ballistic model has been assumed to describe the charge transport in the graphene channel for simplicity.

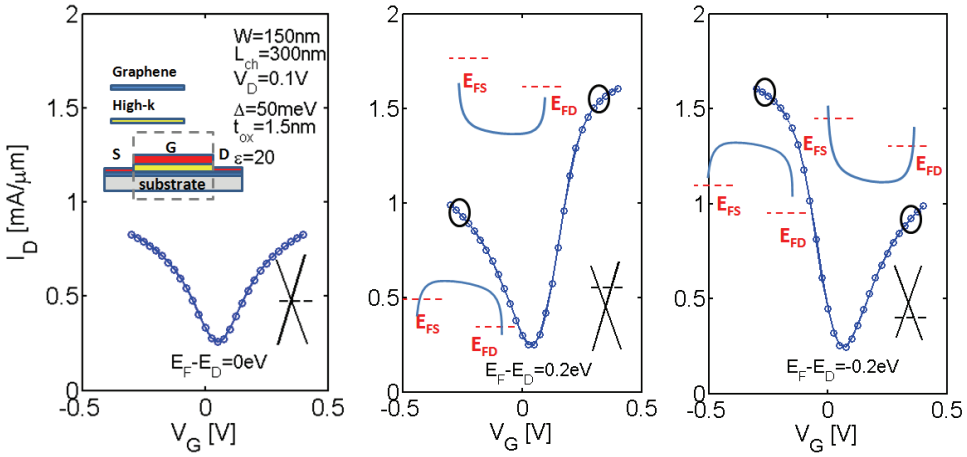

Fig. 5. (inset) Structure of the modelled device. (left) Without any shift of Fermi level in the contact region, symmetric transfer characteristics can be seen. When the Fermi level of contact regions of graphene is shifted due to the metal by E_F-E_D = 0.2 eV (center) and by E_F-E_D = -0.2 eV (right), asymmetric transfer characteristics are observed.

The channel transport is solved using a mode-space based non-equilibrium Green's function formalism. A mode space approach significantly reduces the computational cost while still maintaining the accuracy, as already demonstrated in simulations of silicon (Venugopal et al., 2002), carbon nanotube (Guo et al., 2004), and GNR (Zhao & Guo, 2009) FETs. In our calculation, we assume that the potential variation along the channel width is negligible. Based on this approximation, the electrostatics is solved in 2D, and the mode space method yields accurate results. The channel potential is computed using the 2D electrostatic solver, which also capture the shift of Fermi level at graphene contact. The details of the electrostatic solution procedure are discussed in Zhang et al., 2010. The effect of contacts on the channel is captured through the contact self-energy $\Sigma_{S,D} = \tau g_S \tau$, where τ is the coupling matrix between the contact and channel, and g_S is the surface Green's function of the contact, $g_S = [(E+i\eta+i\Delta)I-H_{contact}]^{-1}$ (Datta, 2005), where η is typically an infinitesimal quantity, and Δ describes the metal/graphene coupling (Golizadeh-Mojarad & Datta 2009; Nemec et al., 2008). By iterating between the NEGF transport solver to find the charge density and the 2D electrostatic solver to find the self-consistent potential, a self-consistent solution is obtained. The source/drain current is then computed from $I_{DS} = (2e/h)\int T(E)(f_S(E)-f_D(E))dE$, where T(E) is the source/drain transmission coefficient.

Fig. 5 shows the calculated transfer characteristics at V_{DS}=0.1 V with different Fermi level shifts of the contact regions of graphene. The metal/graphene coupling strength is Δ = 50 meV. The effects of different Δ's are discussed later. If the contact does not introduce any Fermi level shift as in Fig. 5 (left) E_F-E_D = 0 eV, the transfer curve is symmetric. The minimum conduction point locates at $V_{GS} = V_{DS}/2$. Fig. 5 (right) shows a typical case (Au contact), when the value of the Fermi level shift is E_F-E_D = -0.2 eV (Giovannetti et al., 2008). At negative V_G, carriers can directly go through the channel without experiencing any barriers (see schematic potential profile of Dirac point in Fig. 5 (right)). However at positive V_G, electron transport through the channel will be suppressed by the barrier. Thus the

positive current branch is reduced compared to the negative current branch. The complete transfer curve shows a clearly asymmetric behaviour. We point out that the minimum conduction point gate voltage is also shifted due to the barriers at contacts and I_{on} also increases with contact doping effect. When E_F-E_D = -0.2 eV as shown in Fig. 5 (center), an effective n-type doping is introduced by the metal contacts. A similar asymmetric behaviour with positive current branch larger than negative current branch is expected in that case. We point out that even though previous studies have described an asymmetric transfer characteristics in 2D FETs due to electrostatically doped graphene p-n junctions (Low et al., 2009), metal/graphene contacts themselves may also lead to asymmetric conduction as experiments have indicated (Huard et al., 2008; Nagashio et al., 2009).

Fig. 6 shows a comparison of the effect of different coupling strengths Δ at large drain bias (V_{DS}) voltages. The rigorous explanation of the values used for Δ is related to the metal/graphene hybrid system, which is beyond the focus of this study. For a comparison, we define three Δ values here, Δ = 0 eV for the intrinsic graphene case, Δ = 8 meV for weak metal-graphene coupling, and Δ = 50 meV for strong coupling. The first interesting feature that emerges is that the current drive *increases* as Δ increases. Higher Δ induced broadening

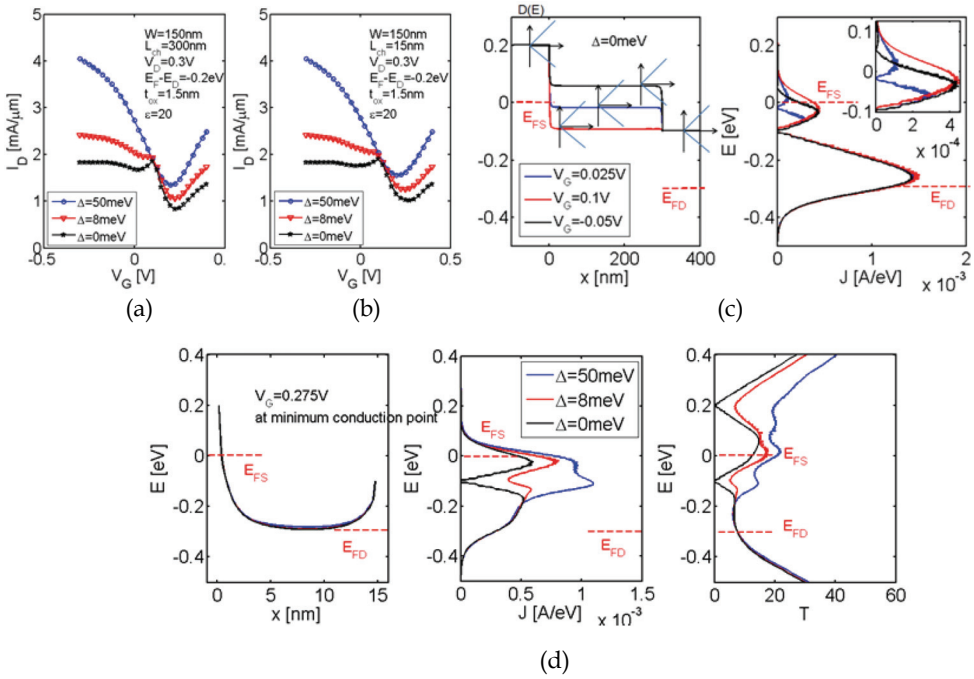

Fig. 6. (a) and (b) Effect of different coupling strength Δ at V_{DS} = 0.3 V. At about 0.2 V away from the minimum conduction point a distortion appears when metal/graphene coupling is weak (black and red lines). (c) shows S/D and channel DOS (cartoon) in series decide how total carriers transport through the channel. As Δ increases, DOS of graphene contact are broadened and distortion disappears. (d) For L_{ch} = 15 nm at V_G = 0.275 V, the drain Dirac point is between E_{FS} and E_{FD}, large Δ broaden DOS at drain contact, which increase the *T(E)*and total current.

of the DOS of graphene contacts increases the transmission coefficient $T(E)$. Larger $T(E)$ leads to higher on current. When $\Delta = 0$ eV (black curve in Fig. 6 (a)), beside the primary minimum conduction point, a distortion appears. The distortion corresponds with the minimum density-of-states (DOS) at the Dirac point of graphene. As shown in Fig. 6 (c), source, drain and channel contribute three cones in series, which decide states allowed for transport through the channel. At $V_G = 0.025$ V, both electron and hole cones of the channel graphene are involved, which gives a local minimum. When $V_G = -0.05$ V, carriers pass the channel through the channel hole half cone. In this case, the DOS minimum point of the channel is not in the transport energy windows between E_{FS} and E_{FD}, thus current increases compared with the local minimum case. When $V_G = 0.1$ V, carriers move through the channel electron half cone and current also increases. When the metal/graphene coupling strength increases, the DOS of the graphene contact regions are broadened. The current monotonically changes with V_G and the distortion disappears. A recent experimental work reports the presence of this type of distortion before annealing, and the disappearance of the distortion after annealing (Nouchi & Tanigaki, 2010). I_{min} also shows a dependence on Δ here. Fig. 6 (d) shows the minimum conduction point for $L_{ch} = 15$ nm. The drain Dirac point is between E_{FS} and E_{FD}. The broadened DOS at the drain contact increases the total current density. $T(E)$ along the channel Dirac point at about -0.3 eV does not show a dependence on different coupling strengths Δ. Thus the increase of I_{min} corresponds to DOS broadening in the contacts, and not the MIS in the channel. We point out that when $V_{DS} > -(E_F-E_D)/q$ the minimum current will increase with higher metal/graphene coupling.

The performance of the FET upon scaling of the channel length is a crucial point, which is discussed in Fig. 7. As mentioned earlier, our model assumed a high-κ insulator to avoid short channel effect. I_{on} remains almost the same at different channel lengths, but I_{min} increases with short L_{ch}. As discussed in Fig. 6, at short channel lengths, I_{min} is mainly decided by direct source/drain tunnelling and the effect of MIS in the channel is weak. Here, when L_{ch} is reduced from 150 nm to 40 nm, the slight increase of I_{min} corresponds to the increase in the probability of source/drain tunnelling. When $L_{ch} = 15$ nm, source/drain tunnelling becomes more severe, leading to higher I_{min}.

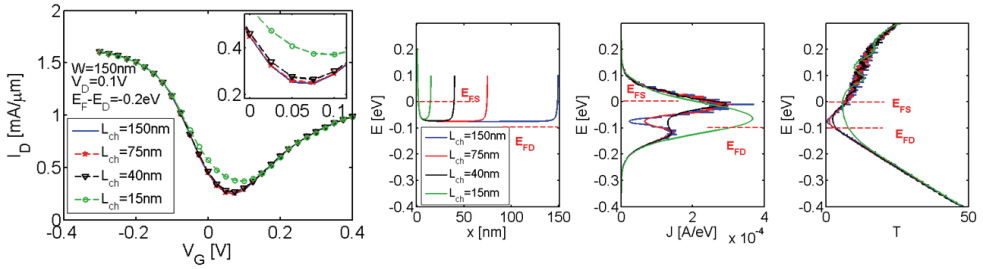

Fig. 7. Effect of channel length scaling at $V_{DS} = 0.1$ V. I_{on} stays the same when L_{ch} scaling down. As L_{ch} reduces I_{min} shows a slight increasing due to the direct source/drain tunnelling and at $L_{ch} = 15$ nm it becomes more severe thus I_{min} increase about 2 times.

2.5 High field transport model of 2D graphene

In this section, we will answer two questions: what is the value of the saturation velocity in graphene and what are the dominant scattering mechanisms under high field. We will

discuss the role of all scattering mechanisms in high field transport. Simple models are used to estimate the saturation currents in graphene and also compared with the Ensemble Monte Carlo simulation (EMC) results.

The scattering rates of both elastic and in-elastic mechanisms at 300 K are shown in Fig. 8 (a). Two dominant modes of SiO_2 SO phonons, 60 meV and 148 meV, are considered in the plot. In order to capture high field effects, the scattering rates for 0 to 1 eV electron energies are calculated for all the scattering mechanisms. At high field, electrons are accelerated by the electric field and populate high energy states. Thus, the scattering rates at high energy states determine the current saturation. The intrinsic optical phonon scattering rate increases linearly with energy, whereas SO phonon scattering rate 'saturates' for high energy states. The impurity scattering rate decreases with the energy and is negligible at high energy. Although the acoustic phonon scattering rate increases with energy, it is smaller than the optical phonon scattering at high energies. In Fig. 8 (a), the bar plot shows the relative magnitudes of scattering rates at E = 0.6 eV. From these observations, optical phonon scattering is dominant for graphene under high field. In exfoliated graphene the substrate temperature can be heated to as high as 1000 K so that the 60 meV mode SO phonon scattering is more than one magnitude higher than at room temperature. As a result, this low energy mode plays a dominant role in energy relaxation of electrons at high temperature. Optical phonon emission is not the dominant energy relaxation mechanism in those situations. On the other hand, in epitaxial graphene grown on SiC substrate, the lowest SO phonon mode energy is 116 meV (see Section 2.2), which is higher than that in SiO_2 and close to the intrinsic optical phonon energy of graphene**.** The scattering rate is also lower than that in SiO_2 due to the weak polarization of Si-C bonds. Furthermore, the thermal conductivity of SiC is much higher than SiO_2. Thus, the high field transport property in epitaxial graphene is limited by its intrinsic optical phonon scattering. From Fig. 8 (a), the phonon scattering at high energy is more than 10 ps^{-1}. Optical phonons generated by electrons have to relax to other phonon modes before the heat can propagate into the substrate or contacts. The characteristic lifetime of optical phonon decay into acoustic phonons is around 1 to 5 ps in carbon-based sp^2 crystals. Since optical phonon lifetime is much longer than phonon generation time (<1 ps), the optical phonon population in graphene is out of equilibrium. The fast generation rate and slow decay rate of optical phonons create the non-equilibrium phonon effect in graphene.

To begin, we assume the phonon scattering is instantaneous and ignore all other elastic scatterings. Under this assumption, two possibilities of electron distribution functions are shown in Fig. 8 (b). The first model assumes that the Fermi circle keeps the shape but drifts rigidly along the electric field direction. Optical phonon emission empties the high energy states and fills the low energy states. As such, the instantaneous phonon emission stops further movement of the Fermi circle and a steady state distribution is achieved. The difference of highest energy state (dotted circle) and lowest energy state (solid circle) is exactly the optical phonon energy $\hbar\omega_0$. Fig. 8 (b) shows another possibility of the steady state distribution function. The energy difference between these dotted and solid circles is the optical phonon energy. Optical phonon emission by electrons in states between the two circles is prohibited by the Pauli exclusive principle. Optical phonon emission is allowed only for electrons approaching the dotted energy circle. The optical phonon emission continues to scatter the electrons from high energy states back to the low energy states. As a result, the Fermi circle is squeezed due to the Pauli principle. Both of the models capture

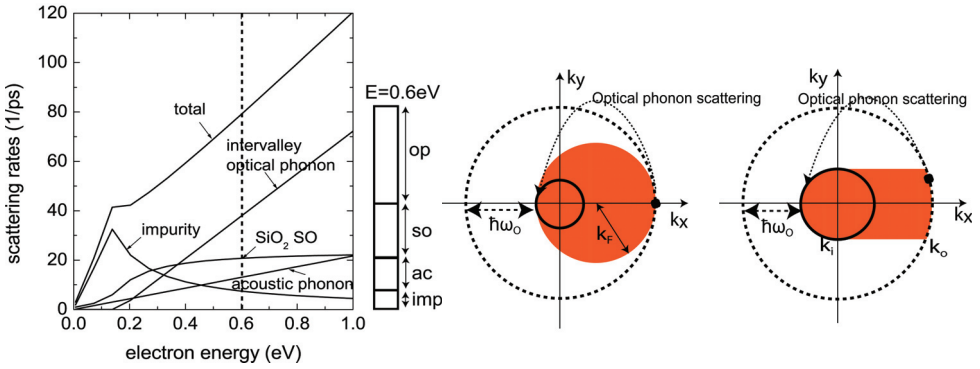

(a) (b)

Fig. 8. (a) Scattering rates vs. energy in 2D graphene: impurity density $n_{imp} = 5 \cdot 10^{11}$ cm^{-2}, T=300 K. The bar shows the relative scattering rates at an energy of 0.6 eV. (b) Current saturation model in 2D graphene: (left) The drift Fermi circle model. k_F is the Fermi wave vector. (right) Squeezed distribution function model. The outer circle radius is k_o and the inner circle radius is k_i.

the effect of carrier degeneracy, which has not been discussed in non-degenerate conventional semiconductors.

The calculated saturation currents versus carrier density for the two models are shown in Fig. 9 (a); the result of the two models are very similar. Both of the models give a roughly square root relation of saturation current versus carrier density. From $J_{sat} = en v_{sat}$, the ensemble saturation velocity v_{sat} is proportional to $n^{1/2}$. Saturation velocity in conventional semiconductors is typically a constant, e.g. $v_{sat} = 10^7$ cm/s in Si. The primary reason for the difference is the degeneracy of carriers and the Pauli principle. Non-degeneracy of carriers leads to constant saturation velocity and fully degenerate carrier leads to a square root relation for 2D systems. This theoretical model is in good agreement with the measurement for graphene on SiO_2 substrate (Dorgan et al., 2010). The agreement of the model and measurement results indicates that the carriers are degenerate in such graphene devices under high field.

The analytical models capture the carrier degeneracy effect but ignore the rise of carrier temperature due to the applied electric field. In reality, the optical phonon emission rate is not instantaneous, so that carriers have opportunities to populate high energy states giving rise to a tail of the distribution function at high energies. At the same time, other scattering mechanisms spread the carrier distribution over a wider range in k space. Moreover, electron electron (e-e) scattering is strong in graphene at high carrier densities, causing carriers to thermalize to a Fermi-Dirac distribution with a finite temperature. In order to capture all of these effects, we applied an electron temperature approximation to high field transport. Since the carriers are degenerate in graphene, a shifted Fermi-Dirac distribution function is assumed, rather than the Boltzmann distribution used for conventional semiconductors (Lundstrom, 2000).

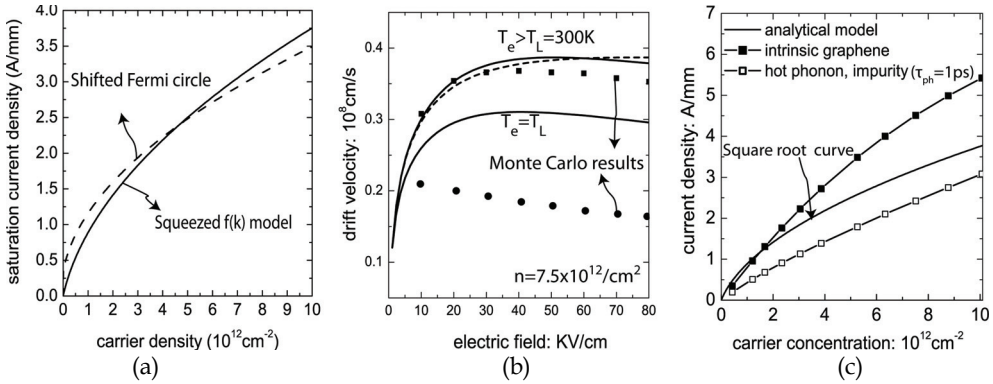

Fig. 9. (a) Current vs. carrier density of the two models. (b) Velocity vs. electric field based on electron temperature approximation. Solid lines: (upper) $T_e > T_L = T_{op}$ = 300 K and (lower) $T_L = T_e$, T_{op} = 300 K; Dashed line: $T_{op} = T_e$; T_L = 300 K; Squares: MC simulation, $T_{op} = T_L$ =300 K; Circles: MC simulation, with hot phonon τ_{ph} = 5 ps, T_L = 300 K. (c) Current vs. carrier density. Solid line: analytical current saturation model; Solid square: no hot phonon, $T_L = T_{op}$ = 300 K, F = $2{\cdot}10^4$ V/cm; Open square: with hot phonon, T_L = 300 K, F = $8{\cdot}10^4$ V/cm, τ_{ph} = 1 ps;

The 2D electron gas, acoustic phonon and optical phonon are not fully in thermal equilibrium with each other at high field. The acoustic phonon temperature T_L is the lattice temperature. The optical phonon temperature T_{op} describes the optical phonon vibrations. In Fig. 9 (b), the upper solid curve shows the currents by assuming lattice temperature is in equilibrium with environmental temperature, $T_e > T_L$ = 300 K. The current decreases if assuming the graphene lattice temperature increases with electron's temperature, $T_L = T_e$, which is shown in the lower solid curve. In these two curves, the optical phonon temperature is still assumed to be in equilibrium with room temperature, T_{op} = 300 K. From the comparison of the two solid curves, the current drops substantially due to lattice heating. This indicates that acoustic phonon scattering could limit the current if graphene is heated to high lattice temperature. The Monte Carlo simulation results (square and circle symbols) are also shown on Fig. 9 (b). The black square dots are in good agreement with the model prediction. This indicates that the electron temperature approximation is a reasonable model for high field transport in graphene. The optical phonon temperature T_{op} rises due to the emission of phonon by electrons. The effect of optical phonon temperature increase is considered in the dashed curve in Fig. 9 (b), in which the optical phonon temperature is in equilibrium with electron's temperature, $T_{op} = T_e$. However, the current does not show obvious degradation. This indicate that temperature rise of optical phonons has less impact on the current compared to lattice temperature. On the other hand, the squares considering non-equilibrium (hot) optical phonon show more degradation of the current. This finding indicates that the non-equilibrium phonon is dominant in high field transport in graphene.
In Fig. 9 (c), the saturation current versus carrier density curves are shown. The solid black curve shows the analytical result from the squeezed distribution function model for comparison. The square-line is the intrinsic saturation currents of grapheme without hot phonon effect. In the absence of hot phonons and impurity scattering, the current-field curves show strong negative differential resistance (NDR). The currents of the squares are at a field of

$F = 2 \cdot 10^4$ V/cm. The saturation current is lower than the analytical result (solid line) when hot phonon exists in grapheme (open square line). In MC simulation, we also find that the saturation currents vary with the phonon lifetime. The longer is lifetime of phonon the lower is the saturation current. At high field, the impurity scattering has an effect on saturation current, but it is minor compared to the hot phonon effect. Saturation current density around 3 A/mm has been measured in epitaxial graphene on SiC substrate ($n \sim 10^{13}$ cm^{-2}) (Moon et al., 2009), which is consistent with our simulation result considering hot phonon effect (open square line). At low carrier densities, J_{sat} as a function of n curves are approximately linear; the slopes correspond to the ensemble saturation velocities. The saturation velocity thus extracted for intrinsic graphene (neglecting charged impurity scattering and hot phonon effect) is $5.2 \cdot 10^7$ cm/s and $2.7 \cdot 10^7$ cm/s when hot phonons are considered. From the simulation results, the hot phonon effect determines the saturation currents in graphene on substrates without strong SO phonon coupling. The (semi-) analytical models best serve as a rough guideline, since elastic scattering processes, and especially the hot phonon effect are not captured in the model, which is done in the EMC approach.

2.6 2D graphene FETs based on CVD grown graphene on Cu

Availability of high-quality large-area graphene on suitable handling substrates will ultimately determine the success of graphene as a device platform. Recently, the formation of single layer graphene via catalyzed-chemical vapour deposition (CVD) on copper foils has generated a rapidly growing body of research (Li et al., 2009). A few groups have reported the CVD growth of graphene on copper, and transport properties including quantum Hall effect (Levendorf et al., 2009; Bae et al., 2010) in layers subsequently transferred to insulating substrates. So far, mobility in Cu-CVD based graphene transferred to SiO_2/Si wafers has been measured around 4 000 cm^2/Vs while mobility of exfoliated graphene on SiO_2/Si has been demonstrated to exceed 15 000 cm^2/Vs. The reduced mobility for Cu-CVD graphene could come from the quality of the graphene itself (eg. lower uniformity, defects, small domain size) or from contamination introduced during the wet transfer process. There have been no careful studies of FETs fabricated from CVD grown graphene. In this work, we report the characteristics of single-layer graphene FETs whose channels were grown by CVD on copper.

We grow Cu-catalyzed CVD graphene in a quartz tube furnace under flow of CH_4 and H_2 with an Ar background on copper foils and on evaporated copper films. Pre-growth chemical and thermal treatment of the copper catalyst material enables single layer graphene deposition at temperatures ranging from 800 - 1050 °C (Fig. 10). For our optimized growth step, the chamber conditions are: CH_4:H_2 gas flow of 100:20 sccm, pressure of 2 Torr, and a temperature of 1000 °C. The gas and pressure are kept at the growth conditions during cooldown until the system is below 500 °C when the growth gases are turned off and an Ar flow is introduced. Fig. 10 shows optical and SEM images of as grown graphene on a copper foil substrate. Following growth, graphene sheets are transferred to a range of host substrates (typically quartz or silicon) using wet etch methods similar to those described in other work (Li et al., 2009). Fig. 11 (a) shows an optical image of a graphene sheet following removal of the PMMA used to support the graphene during wet transfer. Large regions of clean graphene are apparent along with areas of visible contamination from processing. Improvement of the transfer process is underway to reduce contamination introduced during processing.

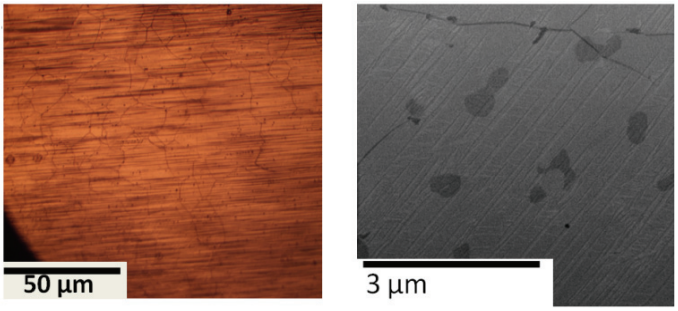

(a) (b)

Fig. 10. (a) Optical image and (b) SEM image of as grown graphene on Cu foil.

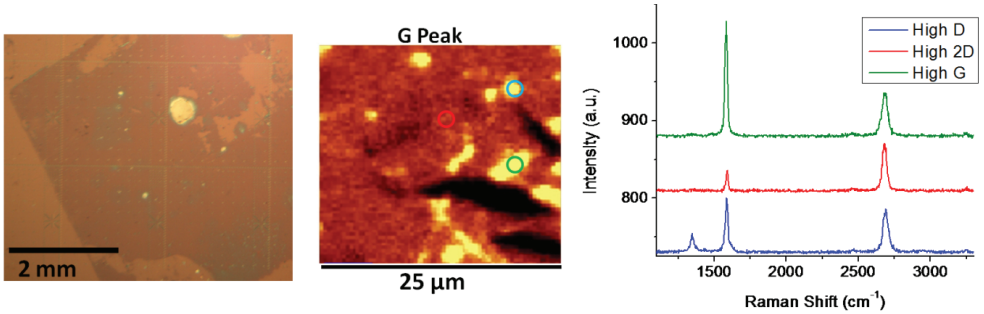

(a) (b) (c)

Fig. 11. (a) Optical image of as graphene following wet transfer to SiO_2/Si substrate. (b) Scanning Raman image of G peak of transferred graphene. (c) Raman spectra at indicated points from the G peak scan. The middle spectrum is representative of the main field of the graphene sample with characteristic 2D:G ratio of 2 of single layer graphene.

Following transfer, Raman mapping is used to determine the quality and uniformity of the CVD-graphene. Large area single-layer graphene regions are verified from the signature 2D:G peak ratio of ~2, that is uniform over large regions (Fig. 11 (a)). Complementary SEM and AFM characterization corroborate the Raman result. Fig. 11 (b) shows a map of the G peak intensity across a 25 µm x 25 µm field and the individual Raman spectra from the three circled locations are in Fig. 11 (c). The middle (red) spectrum is found in most of the graphene region consistent with the presence of high-quality single-layer graphene as indicated by the absence of a D peak at 1350 cm^{-1} and the characteristic 2D:G peak ratio > 2. The bright spots in the G peak scan have two types of associated spectra. The bottom (blue) spectrum is from a region with high defect peak intensity suggesting either contaminated or defective regions of graphene. The top (green) spectrum has a low defect peak intensity indicating high quality graphene, but has a low 2D:G peak ratio consistent with more than one layer of graphene.

Back-gated FETs were prepared by transferring the single-layer graphene to 300 nm SiO_2/conductive Si substrates, followed by conventional e-beam lithography, O_2 plasma etching of the graphene for device isolation, ohmic metal evaporation (Cr/Au), and lift-off.

The backside of the conductive Si wafer was metalized for back gating. The channel lengths of the FETs range from 1 – 8 μm and the channel widths vary between 1 – 4 μm. Based on the transfer characteristics (Fig. 12 (a)), the field-effect mobility is found to be ~4500 cm^2/Vs for electrons and slightly lower for holes. The Dirac point is at V_{BG} ~2 V, much closer to zero volt than in case of exfoliated graphene sheets, indicating close to equal amount of positive and negative charged contamination on the surfaces. The impurity concentration is estimated from the measurement to be ~$8 \cdot 10^{10}$ cm^{-2}. The devices exhibit field-effect current modulations of ~4 - 6 at 20 mV V_{DS} at gate sweeps of +/-30V (Fig. 12 (a)). Interestingly at very low applied source-drain bias (V_{DS} = 20 μV) the modulation increases significantly (Fig. 12 (b)). The current does not scale linearly; ~1000X lower bias causes less than ~10X smaller current. The apparent field-effect mobility is ~200 000 cm^2/Vs, but we stress that this is not a fundamental property of graphene, it just indicates the limitation of the traditional model to estimate the mobility of high purity graphene samples.

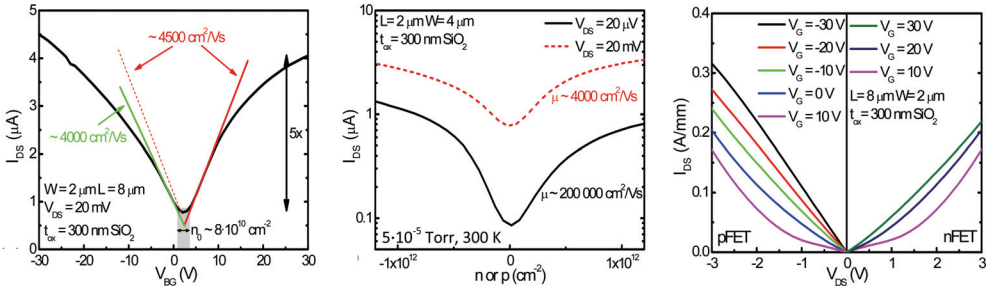

Fig. 12. (a) Transfer characteristic of a 2D graphene FET transferred to Si/SiO_2 substrate. The calculated impurity concentration is 8.10^{10} cm^{-2}. (b) Very low (V_{DS} = 20 μV) applied drain bias gives an extremely high apparent field-effect mobility. (c) High-field family I-V curves showing both sub-linear and super-linear behaviour.

At high drain bias voltages (Fig. 12 (c)), the DC output characteristics of the devices were linear up to ~1 V V_{DS}, and deviated significantly from linearity at higher drain biases. The super-linear behaviour is especially evident at gate biases close to the Dirac point, and is indicative of zero-gap single-layer graphene.

2.7 Epitaxial graphene RF FETs on SiC for analog application

While DC performance has been extensively studied just a few small signal characterizations have been done so far. The widely observed high carrier mobility naturally focuses our attention towards high frequency performance of graphene based devices. Gigahertz operation of exfoliated (Lin et al., 2009) and epitaxial (Moon et al., 2009) graphene FETs has been reported. Here we present the high frequency performance of graphene devices based on epitaxially grown graphene on SiC substrates. The measured $f_T \cdot L_G$ product of 8 GHz·μm and f_{max} of 16 GHz is in very good agreement with previously reported values (Moon et al., 2009). Surprisingly, in spite of the much lower electron mobility and transconductance, these FETs demonstrate remarkable small signal performance comparable to the small signal performance of higher mobility exfoliated graphene devices. Recently significant improvement was reported: device with $f_T \cdot L_G$ = 24 GHz·μm (Lin et al., 2010).

Epitaxial graphene FETs were fabricated on 2-3 layer graphene on Si-face 4H-SiC. According to AFM and LEEM characterization and Raman measurements the graphene thickness is 1.9 layers in average over the wafer (Luxmi et al., 2009). Graphene is patterned by optical lithography and etched it in O_2 plasma. Using the same resist-pattern the SiC is etched 100 nm deep in CF_4 plasma to facilitate the sticking of the metal contacts on the surface. Cr/Au source/drain contacts and e-beam evaporated Al_2O_3/Ti/Au top gate (t_{ox} = 15 nm) have been deposited to form field effect transistors (FETs). For increased RF performance short gates were fabricated using e-beam lithography. The channel lengths of the devices range from 1-4 μm and the gate length is 1 - 2 μm in optically defined and 40 - 500 nm in e-beam patterned devices. Standard ground-signal-ground probing pads are lithographically realized for the gate and drain. Open structures were used to de-embed the signals of the parasitic pad-capacitance.

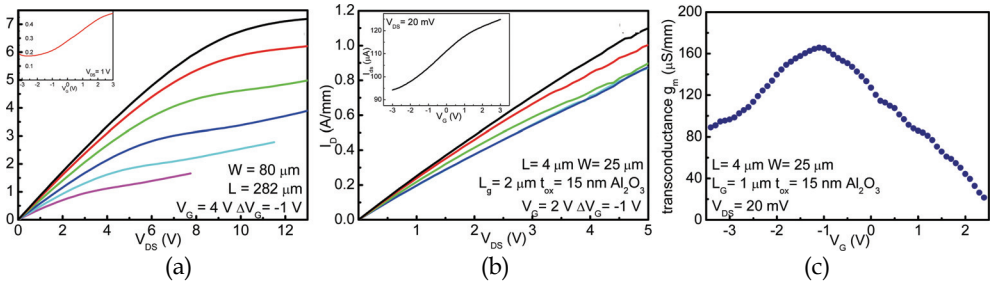

Fig. 13. Output characteristics of a saturating large area graphene transistor (a) and the graphene transistor (b), which RF characteristic is shown on Fig. 14. Insets: transfer characteristics at V_{DS} = 1 V (a) and at V_{DS} = 20 mV (b). (c) Transconductance as a function of gate voltage at V_{DS} = 20 mV.

Hall measurements reveal μ ~ 200 – 500 cm^2/Vs throughout the sample showing smooth variation and better performance in the middle of the wafer. The DC output characteristics of the devices were linear up to 5 V and slightly sublinear above 10 V. The drain current had a weak gate dependence as we swept the gate voltage between +/- 2.5 V. In the high source-drain bias range the gate modulation decreased indicating a non-reversible degradation mechanism by high electrical field. The transconductance of the devices varied between 120 – 400 μS/mm, which is significantly lower than in case of exfoliated devices having the same gate length. For very long gate lengths, reasonable current modulation and current saturation was observed as shown in Fig. 13 (a). However, with scaling of the gate length, the gate modulation and current saturation properties degraded substantially, indicating the need for improvement of material quality and gate material processing. In spite of the weak gate modulation, it is possible to envision usage of graphene FETs in low-noise amplifiers (LNAs) if RF performance improves. In addition, single layers of almost transparent graphene may be transferred to flexible insulating substrates, which can offer low-cost high frequency performance. Small signal performance of devices with gate-lengths between 2 μm and 0.5 μm on epitaxially grown graphene were measured. The used bias-conditions for the FETs are V_{DS} = 10 V and V_{GS} = 2 V.

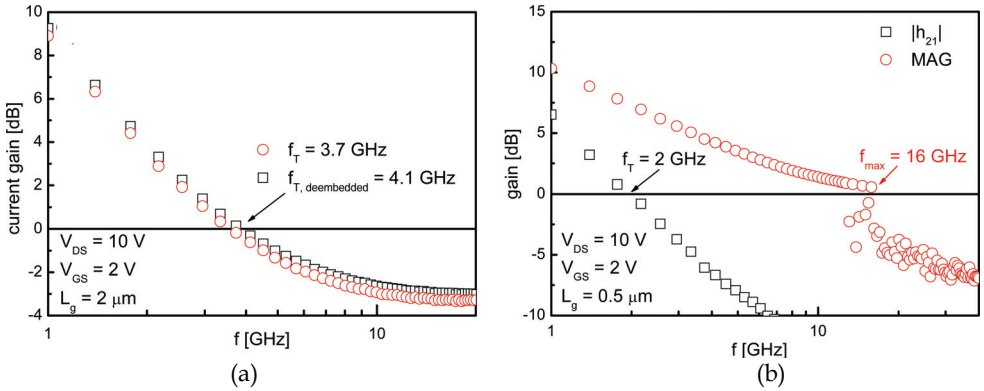

Fig. 14. (a) Current gain as function of frequency for a graphene FET with 2 μm long gate. (b) f_T and f_{max} of a graphene transistor with 0.5 μm long ebeam-defined gate.

A deembedded current gain cut-off frequency f_T of 4.1 GHz for devices with 2 μm long gates was achieved (Fig. 14 (a)). For a graphene FET with a 0.5 μm long gate an exceptional high power gain cut-off frequency f_{max} of 16 GHz is demonstrated. (Fig. 14(b)). These preliminary results are very encouraging and demonstrate the potential of the epitaxially grown graphene devices for high-frequency applications. As the quality of graphene on insulating substrates improved over time indeed cut-off frequency higher than 100 GHz was demonstrated (Lin et al., 2010). Moving from zero-bandgap single-layer 2D graphene to bilayer graphene or graphene nanostructures can enable controlled bandgaps. We present our efforts to date on the latter approach in the following section.

3. Graphene nanoribbon transistors

3.1 Band gap of graphene nanoribbons

Two-dimensional (2D) graphene sheets are nearly metallic, while ultrathin graphene nanoribbons (GNRs) can show semiconducting properties with the energy bandgap scaling inversely with the ribbon width. The achievable energy bandgap, superior transport properties, and the planar manufacturability establish GNRs as promising cornerstones beyond the Si CMOS technology (Zhang et al., 2008; Murali et al., 2009). Although sub−10 nm GNRs have been demonstrated by chemical approaches (Li et al., 2008; Jiao et al., 2009), the ability to form GNRs lithographically will facilitate the fabrication compatibility with the conventional planar integrated circuit (IC) manufacturing technology. GNRs were fabricated on exfoliated graphene flakes on SiO_2/Si. The oxide thickness is 300 nm and the Si substrate is heavily doped n-type. Al metal masks were patterned by EBL and e-beam deposition. The exposed graphene was removed by O_2 plasma etching and the metal masks were removed by Al etchant. GNRs connected to two 2D graphene sheets were thus achieved. Fig. 15 (a) shows the SEM images of a 29 nm wide Al strip mask (top) and a 21 nm wide GNR (bottom). The fact that the obtained GNR is thinner than the Al mask indicates the effect of lateral etching in O_2 plasma. Cr/Au was e-beam deposited as source (drain) contacts on the 2D graphene areas to reduce the contact resistance. Al/Au was used as the back-gate contact. The length of GNRs in this work is 2 μm. Current-voltage (I-V) measurements were performed in vacuum (~10^{-6} Torr) with the temperature ranging from 4.2 K to 300 K.

The temperature dependent transfer characteristics of GNRs at V_{DS} = 20 mV are shown in Fig. 15 (b). It is clearly seen that the minimum current decreases with decreasing temperature while the maximum current (due to the hole conduction) remains almost unchanged. As a result, the back-gate modulation increases from ~ 12 at room temperature to > 10^6 at 4.2 K, indicating the formation of energy bandgap. The positive Dirac point indicates the presence of holes, which can be induced by negatively charged impurities, at zero gate bias. It is worth noting that the transfer curve does not show the symmetric V shape, with the hole conduction much stronger than the electron conduction, a phenomenon often seen in GNRs (Chen et al., 2007). This is attributed to surface impurities based on the fact that surface passivation by Al_2O_3 grown by atomic layer deposition (ALD) was found to be able to improve the electron conduction. But the exact origin remains unclear currently and is under investigation. Fig. 15 (c) shows the high field (corresponding to 30 kV/cm at V_{DS} = 6 V) family I-Vs measured at 77 K. The drain current exhibits tendency to saturate at high drain bias and the maximum current density is ~1.4 A/mm. The inset shows I-Vs measured at 4.2 K. The maximum current density reaches 2 A/mm at V_{DS} = 15 V (equivalent electric field: 75 kV/cm), indicating high current drive capability of GNRs. The source and drain electrodes were found to be exchangeable as can be seen from the symmetric I-Vs in the first and third quadrant. This is not unexpected since the back gate controls the whole GNR channel universally.

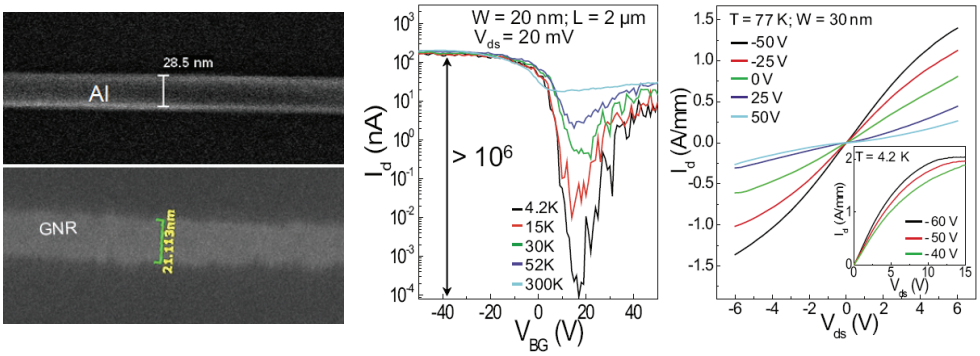

(a) (b) (c)

Fig. 15. (a) SEM image of an Al strip (top) and a GNR (bottom) formed using the Al strip as etching mask. (b) Temperature-dependent transfer characteristics at 20 mV drain bias and (c) high field family I-Vs measured at 77 K and 4.2 K (inset).

The quantum confinement in the quasi-1D GNR channel creates discrete subband energy levels, which are filled by carriers in sequence as the gate voltage increases. As a result, staircase-like features are expected in the transfer curve. Such quantum conductance was observed in the patterned GNRs. The conductance quantization was seen in different GNR devices and Fig. 16 (a) shows a typical transfer curve measured at 30 K plotted in the linear scale exhibiting conductance plateaus with roughly equal spacing. The conductance modulation by the back gate is about 200 at this temperature. GNRs with armchair edges have band structure expressed as:

$$E(k_n, k_y) = \hbar v_f \sqrt{k_n^2 + k_y^2} \quad (1)$$

where v_f (10^8 cm/s) is the Fermi velocity, $\hbar$ is the reduced Plank's constant, and k_y is the wave vector in the GNR length direction. The transverse wave vector k_n can only take allowed discrete values defined at $n\pi/3W$ (n is non-zero integer)(Fang et al., 2008). Therefore, perfect armchair GNRs should have quantized energy levels separated by:

$$\Delta E = \hbar v_f \pi / 3W \tag{2}$$

For GNRs with W = 20 nm, ΔE is calculated to be ~ 34 meV. At zero temperature, only the energy levels below the Fermi level E_f populated with electrons in the conduction band, or those above E_f populated with holes in the valence band, contribute to the conductance. Each 1D energy level (or mode) has a finite transmission probability. The overall device conductance at a finite temperature is the summation of all the available conducting modes, and is described by the well-known Landauer formula:

$$G = \left(\frac{2e^2}{h}\right)\sum_i t_i(E)\left(-\frac{\partial f}{\partial E}\right)dE \tag{3}$$

where t_i is the transmission probability of the i-th mode and f is the Fermi-Dirac statistics. The nearly equal spacing of the plateaus shown in Fig. 16 (a) reveals that each conduction mode should have similar transmission probability. To further analyze the measured conductance quantization using Landauer formula, the back-gate voltage needs to be correlated with the Fermi energy. The link between them is the carrier density in the channel:

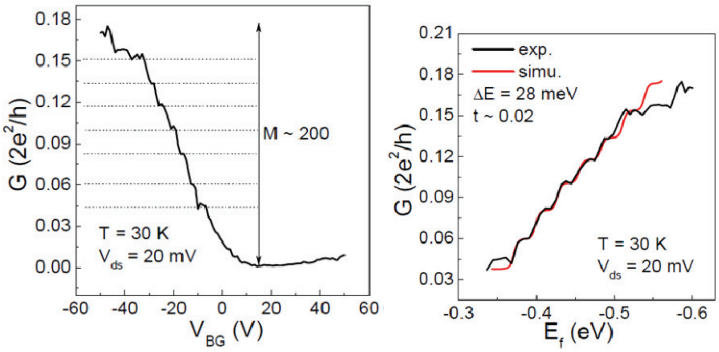

(a) (b)

Fig. 16. (a) a typical transfer curve measured at 30 K showing conductance plateaus and (b) fitting of the experimental data using Landauer formula.

$$C_g(V_{BG} - V_{Dirac}) = E_f^2 / \pi\hbar v_f^2 \tag{4}$$

where C_g is effective gate capacitance per area (F/cm²). Both sides of the above equation give the carrier sheet density (cm^{-2}) in the GNR channel (Fang et al., 2007). The experimental data were fitted using Eq. (3), with ΔE, t, and C_g as adjustable parameters. Excellent agreement was achieved as shown in Fig. 16 (b). The obtained subband energy separation from the fitting is 28 meV, close to the calculated value (34 meV) for W = 20 nm. The

discrepancy could be due to the likely existence of a mixture of both armchair and zigzag orientations in GNRs. The average transmission probability is $t \sim 0.02$, similar to that reported in (Lin et al., 2008). The very small t can be explained by the scattering due to GNR edge/bulk disorder which can severely suppress the conductance causing G much smaller than $2e^2/h$ (Mucciolo et al., 2009).

3.2 Low field transport in GNR

GNR with width down to 20 nm by lithography (see Section 3.1) or 2-5 nm by chemical preparation (Li et al., 2008) has been achieved. The measured carrier mobility (~200 cm^2/Vs) in the ultrathin GNRs are reported to be much lower than in corresponding 2D graphene sheets. GNR opens a bandgap by the edge confinement, but the edges induce line edge roughness (LER) scattering besides the normal scattering mechanisms present in 2D graphene. The LER scattering has W^{-4} dependence on the width of GNR, which is due to the linearity of graphene band structure (Fang et al., 2009). The effect of LER scattering depends on the width of GNR and the height of the roughness, which related to the fabrication processes. The mobility due to various scattering mechanisms was calculated in the Boltzmann transport scheme (Fang et al., 2009). Fig. 17 shows the mobility in a 3 nm wide GNR. The roughness height 0.5nm is used in the calculation. Scattering from surface impurity located at interface of GNR and substrate and line edge roughness (LER) are dominant at low carrier density shown in Fig. 17 (a). However, LER scattering becomes more important at higher carrier density (Fig. 17 (c)). This is due to the increasing of screening of the impurity charge in GNR at high carrier density. At the same time, acoustic phonon scattering also plays important role in limiting the mobility at 300K or higher temperature. The mobility from the theoretical calculation qualitatively explains the mobility measurement results in ultra-thin GNRs (Li et al., 2008).

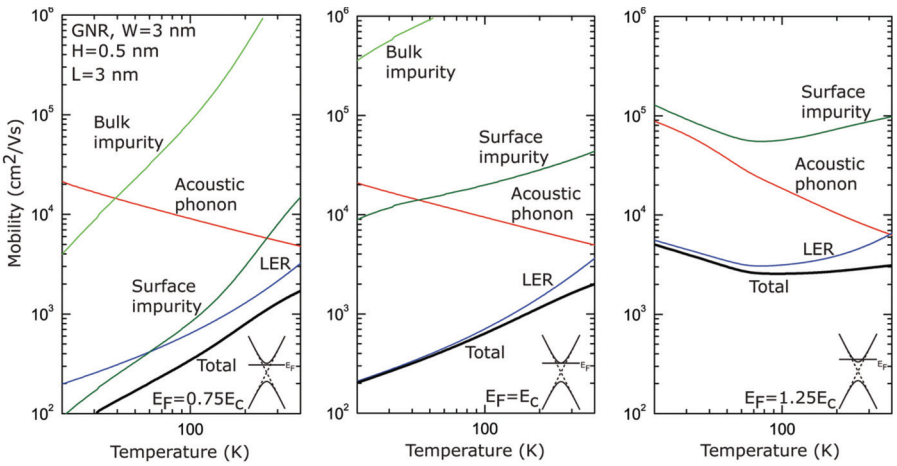

Fig. 17. Mobility in a GNR as a function of temperature for three distinct Fermi levels. The relative importance of the various scattering rates can be ascertained from the plots.

More recently, the LER scattering was investigated elaborately by measuring the carrier mobility in different width GNRs (Yand & Murali, 2010). The mobility is found to decrease

at rate W^{-4} when the width is narrower than 60 nm, which indicates the height of LER in GNR fabricated by lithography is larger than 0.5 nm. In SEM the height of LER is estimated to be 2~3 nm, so that the theoretical work and experimental measurements are in agreement. The LER also induces states in the band gap, which enhance the Zener tunnelling probability. This effect has been studied in the tunnelling field effect transistors structure by numerical simulations (Luisier & Klimeck, 2009). The LER increases the off state current, which degrades the performance of FETs by increasing the sub-threshold voltage. The experimental works to achieve thinner GNR with better edges are future tasks to realize devices based on GNRs.

3.3 Graphene nanoribbon p-n junction transistors

For the reason outlined above GNR FET devices with both top- and back-gates were fabricated. The fabrication started by back gated GNR FETs as described in Section 3.1. Then using 1 nm e-beam evaporated Al as a seed layer, 30 nm ALD Al_2O_3 was deposited. The channel length of the fabricated devices is 2 μm and the length of the top gate electrode is about 1 μm, covering half of the channel. The SEM image on Fig. 18 shows a typical FET.

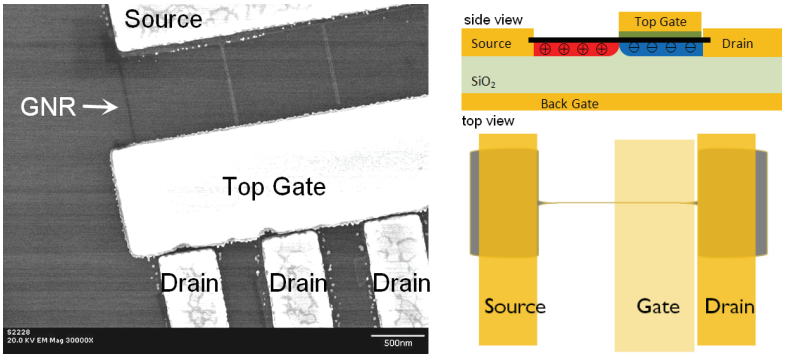

(a) (b)

Fig. 18. (a) SEM image and (b) schematics of the GNR FET. Half of the channel is top-gated, while the whole device is back-gated. Device parameters: L = 2 μm, L_G = 1 μm, W = 30 nm.

In this section the measurements of a representative device at room temperature will be presented. It is found that at high applied source drain current the temperature has very little effect on the device performance, namely at cryogenic temperature the high-field modulation is only ~10% more. Many similar devices were fabricated and similar characteristics were observed in all cases. Fig. 19 (a) and (b) shows the source-drain conductance at V_{DS} = 20 mV and at V_{DS} = 1 V respectively as a function of the top-gate and the back-gate voltage.

The back-gate capacitance is ~11 nF/cm² assuming κ = 3.9 and the top gate capacitance is 209 nF/cm² calculated based on the measurement of the minimum conductance (Dirac) point shown in Fig. 19 (b). The Dirac point is defined by the ratio of the applied voltages on both gates, the slope defining the value of C_{top}/C_{back} ~19. From either a constant back-gate or constant top-gate slice we can determine V_{TG}^0 = -6 V and V_{BG}^0 = -70 V, indicating strong n-type doping. While the devices before the top gate deposition were slightly p-type doped one can conclude that the strong n-doping is caused by trapped charges in the top gate oxide and other impurities on the graphene oxide interface.

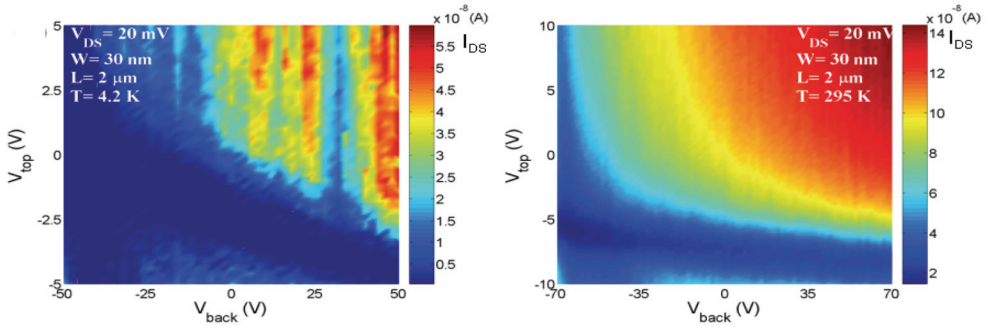

(a) (b)

Fig. 19. (a) Conductance steps at 4.2 K at low source-drain voltage (linear scale); (b) At room temperature the modulation is smaller even at low bias (V_{DS}= 20 mV).

Temperature dependent measurements have confirmed band-gap opening of >26meV depending on GNR widths, and result in 20x and 10^3x modulation at room temperature and 4 K, respectively, by varying the top gate potential between +/- 5V.

The source and drain contacts are in contact with a large 2D graphene region to ensure low contact resistance. The 2D graphene has no bandgap so the Cr/Au metal can form good ohmic contacts easily. The back-gate may vary the carrier concentration of the graphene at the contacts, but due to its large size it will always have much lower resistance than the GNR channel, always supplying the channel with enough carriers. Fig. 20 (a), (b) and (c) shows the measured I_{DS} for different top gate voltages at V_{back} = -70, 0 and +70 V respectively.

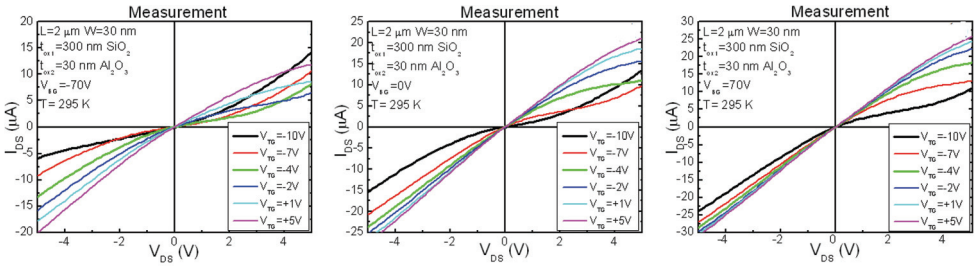

(a) (b) (c)

Fig. 20. I_{DS} versus V_{DS} of the GNR p-n junction FET at -70 V (a), 0 V (b) and +70 V (c) back gate bias. Plateauing of the IV characteristics can be observed in all three cases, but at different bias conditions.

To understand the device operation, examine the device model in detail. The channel of the devices can be separated into two distinct regions: one with a back-gate only, and the other with both top- and back-gates. A model have been developed to explain the transistor characteristics of the p-n channel GNR FET by extending the work of Meric et al., 2008. A field effect model was applied to both side of the junction, defining the only back-gated region similarly as the top-gate having V_{TG} = 0 V:

$$n(x) = \sqrt{n_0^2 + \left(\frac{C_{tg}}{q}(V_{tg} - V_{tg0} - V(x)) + \frac{C_{bg}}{q}(V_{bg} - V_{bg0} - V(x)) \right)^2}, \quad (5)$$

where is x is the distance along the channel and $V(x)$ is the potential in the channel due to the applied source-drain voltage. The current in the channel is expressed by:

$$J(x) = qn(x)\mu F(x), \tag{6}$$

where μ is the mobility and $F(x)$ is the electric field along the channel. The I-V characteristics are obtained by forcing current continuity in a self-consistent electrostatic and transport model:

$$I(V_{DS}) = q\frac{W}{L}\mu \int_0^{V_{DS}} n(x)dV(x), \tag{7}$$

where L is the channel length and W is the GNR width. Carrier drift velocity and mobility saturation is considered depending on the carrier concentration based on the work of Dorgan et al., 2010:

$$v_{sat} = \frac{\omega_{op}}{\sqrt{\pi n(x)}}, \tag{8}$$

where ω_{op} is the optical phonon wavelength of the dominant scattering phonons, which are surface optical phonons of the high-κ oxide. And

$$\mu = \frac{\mu_0}{\sqrt{1 + \left(\mu_0 V_{DS} / L v_{sat}\right)^2}}. \tag{9}$$

For simplicity, we assumed equal mobility and saturation velocity to describe both the electrons and holes. The solution not only provides the I-V characteristics of the device but detailed information about the carrier concentration under various bias conditions. Figs. 20 & 21 show the experimental and modelling data, displaying close agreement. As input parameters in the model we used mobility of 300 cm^2/Vs, a minimum carrier density of $5 \cdot 10^{11}$ cm^{-2} and source-drain series resistance of 0.5 Ω.mm. The saturation of current at high positive bias is caused by depletion of the carriers even in those cases when the gate biases set a high initial carrier concentration. At high negative drain bias on the other hand lack of saturation is observed. This is because the drain bias in this case further increases the carrier concentration instead of depleting. Depending on the gate bias conditions the flattening of the current occurs at different applied source-drain bias. Superlinear current increase is caused by the sharp increase of carrier concentration close to the Dirac point in conjunction with the increase of the accelerating field (V_{DS}).

In conclusion, p-n junction in GNR FETs has been experimentally demonstrated. The analysis of the device operation shows that sublinear and superlinear features observed in the I-V characteristics is caused by the device electrostatics. We point out here that the gate induced barrier at the source end of the GNR FET can be no more than the bandgap. Since the bandgap is small, interband tunnelling prevents the modulation of drain current at high drain biases. Though this is detrimental for a traditional FET, this problem can be turned around and actually used in a GNR based tunnelling FET. Such FETs have been modelled and have proposed GNR based TFETs, which is where current experimental effort is headed. (Zhang et al., 2008).

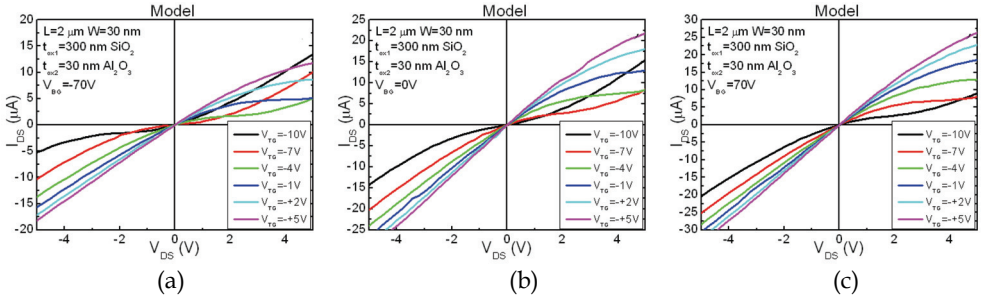

Fig. 21. Simulated device characteristic at the same bias conditions as the device shown in Fig. 20. I_{DS} versus V_{DS} at -70 V (a), 0 V (b) and +70 V (c) back gate bias.

3.4 Tunnelling in graphene and GNR p-n junction

Tunnelling in 2D graphene attracted a lot of attention due to the new phenomenon, Klein tunnelling of the massless Dirac particle (Stander et al., 2009). From an engineering point of view, graphene/GNR could provide higher tunnelling current if used as a channel in devices, e.g. tunnelling field-effect transistor. The current-voltage characteristics of GNR have been studied in (Low et al., 2009). The tunnelling probability in GNRs or in carbon nanotube (CNT) was found to be similar in magnitude with conventional parabolic semiconductors. However, two facts tilt the tunnelling currents decisively in favour of CNTs and GNRs. First is that the transverse kinetic energy of carriers can be large and leads to an exponential decrease in carrier tunnelling probability in bulk 3D p-n junctions, which is avoided in 1D structures. Second, if normal parabolic-bandgap semiconductors are shrunk to length scales comparable to those of CNTs and GNRs, their bandgaps and effective masses increase further due to quantum confinement. In 2D graphene, p-n junction has been realized in FETs with back and top gates. The conductance across such p-n junction has been studied both theoretically (Low et al., 2009) and experimentally (Huard et al., 2007). Here, we present the full I-V characteristics of p-n junction in 2D graphene. The tunnelling probability in 2D graphene is calculated by WKB approximation (Cheianov & Falko, 2006). At low temperature (T~ 0 K), the tunnelling current density in a biased p-n junction is calculated as

$$J_t = -\frac{e^2 V_a}{\pi^2 \hbar} \sqrt{\frac{E_{fn} + E_{fp} - qV_a}{\hbar \upsilon_F \lambda_{pn}}}, \tag{10}$$

where e is the electron charge, V_a is the applied voltage, E_{fn}/E_{fp} is the doping level at n/p region, λ_{pn} is the screening length of p-n junction (Low et al., 2009). Fig. 22 shows the full I-V characteristics of both abrupt and gradual p-n junctions. The screening length of gradual p-n junction is assumed to be λ_{pn} = 80 nm, which is achievable in real devices (Huard et al., 2007). The current includes both tunnelling and thermal emission parts. The analytical result shown in Eq. (10) gives a good estimation of the junction I-V curves. The tunnelling current is dominant at reverse bias. At high forward bias (>0.3 V) the current rises exponentially due to thermal emission. The full I-V curves show the current capability through graphene p-n junction has the magnitude around 1 A/mm, due to the zero band gap and high Fermi velocity (cm/s) in this material.

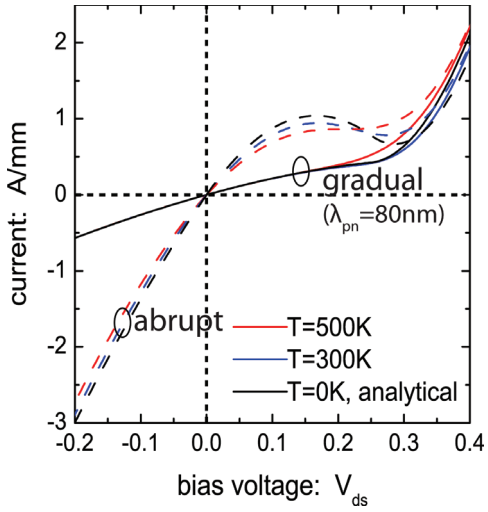

Fig. 22. I-V characteristics of graphene p-n junctions (n_1=n_2= cm^{-2}).

4. Summary

In summary, a wide variety of graphene devices and electronic device problems have been discussed. First 2D graphene transistors were made, which exhibited poor on/off ratio but promising mobility. Short channel effect has been observed, which invoked the detail exploration of the doping effect of the metal-graphene contacts. The poor saturation characteristics of the 2D graphene FETs led the attention toward the detailed study of the high field transport of graphene. The exfoliated graphene FETs were compared to CVD graphene based devices and were found to have similar performance but offering the advantage of wafer scale size. SiC based epitaxial graphene has the same size advantage along with the exceptional RF characteristics. For further improvement it became clear that band gap has to be opened by 1D confinement, which was experimentally demonstrated. The successful fabrication of p-n junction in GNR FET is a major achievement and an important step toward the realization of the GNR TFET.

5. References

Bae, S.; Kim, H.; Lee, Y.; Xu, X.; Park, J-S.; Zheng, Y.; Balakrishnan, J.; Lei, T.; Kim, H. R.; Song, Y. I. et al. (2010). Roll-to-roll production of 30-inch graphene films for transparent electrodes. *Nature Nanotechnology*, Vol. 5, pp. 574–578

Cheianov, V. V.; Falko, V. I. (2006). Selective transmission of Dirac electrons and ballistic magnetoresistance of np junctions in graphene. *Physical Review B,* Vol. 74, p. 041403

Chen, Y-F. & Fuhrer, M. (2005). Electric-Field-Dependent Charge Carrier Velocity in Carbon Nanotubes. *Physical Review Letters*, Vol. 95, pp. 236803

Chen, Z.; Lin, Y.; Rooks, M. J. & Avouris, P. (2007). Graphene nano-ribbon electronics. *Physica E*, Vol. 40, p. 228

Datta, S. (2005). *Quantum transport: atom to transistor*, Cambridge University Press, USA

Dorgan, V.; Bae, M-H. & Pop, E. (2010). Mobility and Velocity-Field Relationship in Graphene. *IEEE DRC Conf. Digest.*, Vol. 68, pp. 73-74

Fang, T.; Konar, A.; Xing, H. & Jena, D. (2007). Carrier statistics and quantum capacitance of graphene sheets and ribbons. *Applied Physics Letters,* Vol. 91, 092109

Fang, T.; Konar, A.; Xing, H. & Jena, D. (2008). Mobility in semiconducting graphene nanoribbons: Phonon, impurity, and edge roughness scattering. *Physical Review B,* Vol. 78, p. 205403

Geim, A. K. & Novoselov, K. S. (2007). The rise of graphene. *Nature Materials,* Vol. 6, p. 183

Giovannetti, G.; Khomyakov, P. A.; Brocks, G.; Karpan, V.; Brink, J. v d; & Kelly, P. J. (2008). Doping Graphene with Metal Contacts. *Physical Review Letters*, Vol. 101, p. 026803

Golizadeh-Mojarad, R. & Datta, S. (2009). Effect of contact induced states on minimum conductivity in graphene. *Physical Review B*, Vol. 79, p. 085410

Guo, J.; Datta, S.; Lundstrom, M. & Anantram, M. P. (2004). Towards Multi-Scale Modeling of carbon Nanotube Transistors. *The International Journal on Multiscale Computational Engineering*, Vol. 2, p. 257

Huard, B.; Sulpizio, J.A.; Stander, N.; Todd, K.; Yang, B.; Goldhaber-Gordon, D. (2007). Transport Measurements Across a Tunable Potential Barrier in Graphene. *Physics Review Letters,* Vol. 98, p. 236803

Huard, B.; Stander, N.; Sulpizio, J. A. & Goldhaber-Gordon, D. (2008). Evidence of the role of contacts on the observed electron-hole asymmetry in graphene. *Physical Review B*, Vol. 78, p. 121402

Hwang, E.; Adam, S.; & Das Sarma, S. (2007). Carrier Transport in Two-Dimensional Graphene Layers. *Physical Review Letters,* Vol. 98, p. 186806

Jena, D.; Fang, T.; Zhang, Q. & Xing, H. (2008). Zener tunneling in semiconducting nanotube and graphene nanoribbon p−n junctions. *Applied Physics Letters,* Vol. 93, p. 112106

Jiao, L.; Zhang, L.; Wang, X.; Diankov, G.; & Dai, H. (2009). Narrow graphene nanoribbons from carbon nanotubes. *Nature,* Vol. 458, p. 877

Levendorf, M. P.; Ruiz-Vargas, C. S.; Garg, S.; & Park, J. (2009). Transfer-Free Batch Fabrication of Single Layer Graphene Transistors. *Nano Letters*, Vol. 9, p. 4479

Lee, E. J. H.; Balasubramanian, K.; Weitz, R. T.; Burghard, M. & Kern, K. (2008). Contact and edge effects in graphene devices. *Nature Nanotechnology*, Vol. 3, pp. 486 – 490

Li, X.; Cai, W.; An, J.; Kim, S.; Nah, J.; Yang, D.; Piner, R.; Velamakanni, A.; Jung, I.; Tutuc, E. et al. (2009). Large-Area Synthesis of High-Quality and Uniform Graphene Films on Copper Foils. *Science,* Vol. 324, p. 1312

Li, X.; Wang, X.; Zhang, L.; Lee, and S.; & Dai, H. (2008). Chemically Derived, Ultrasmooth Graphene Nanoribbon Semiconductors. *Science,* Vol. 319, p. 1229

Lin, Y.; Perebeinos, V.; Chen, Z. & Avouris, P. (2008). Electrical observation of subband formation in graphene nanoribbons. *Physical Review B*, Vol. 78, p. 161409

Lin, Y.-M.; Jenkins, K. A.; Valdes-Garcia, A.; Small, J. P.; Farmer D. B.; & Avouris P. (2009). Operation of Graphene Transistors at Gigahertz Frequencies. *Nano Letters,* Vol. 9, pp. 422–426

Lin, Y.-M.; Dimitrakopoulos, C.; Jenkins, K. A.; Farmer, D. B.; Chiu, H.-Y.; Grill, A.; & Avouris, Ph. (2010). 100-GHz Transistors from Wafer-Scale Epitaxial Graphene. *Science*, Vol. 327, p. 662

Low, T.; Hong, S.; Appenzeller, J.; Datta, S. & Lundstrom, M. (2009). Conductance asymmetry of graphene pn junction. *IEEE Trans. on Electronic Devices,* Vol. 56, p. 129

Luisier, M. & Klimeck, G. (2009). Performance analysis of statistical samples of graphene nanoribbon tunneling transistors with line edge roughness. *Applied Physics Letter*s, Vol. 94, p. 223505

Luo, X.; Lee, Y.; Konar, A.; Fang, T.; Snider, G.; Xing, H.; & Jena, D. (2008). Current-carrying capacity of long and short-channel 2D graphene transistors. *IEEE DRC Tech. Digest*, Vol. 67, p. 29

Lundstrom, M. (2000). *Fundamentals of Carrier Transport.* Cambridge University Press.

Luxmi; Nie, S.; Fisher, P. J.; Feenstra, R. M.; Gu, G.; & Sun, Y. J. (2009). Temperature Dependence of Epitaxial Graphene Formation on SiC(0001). *Journal of Electronic Materials,* Vol. 38, p. 718

Meric, I.; Han, M. Y.; Young, A. F.; Oezyilmaz, B.; Kim P.; & Shepard, K. L. (2008). Current saturation in zero-bandgap, top-gated graphene field-effect transistors. *Nature Nanotecnology*, Vol. 3, pp. 654-659

Moon, J.S.; Curtis, D.; Hu, M.; Wong, D.; McGuire, C.; Campbell, P.M.; Jernigan, G.; Tedesco, J.L.; VanMil, B.; Myers-Ward, et al. (2009). Epitaxial-Graphene RF Field-Effect Transistors on Si-Face 6H-SiC Substrates. *IEEE Electron Device Letters,* Vol. 30, p. 650

Mucciolo, E. R.; Castro Neto, A. H. & Lewenkopf, C. H. (2009). Conductance quantization and transport gaps in disordered graphene nanoribbons. *Physical Review B,* Vol. 79, p. 075407

Mueller, T.; Xia, F.; Freitag, M.; Tsang, J. & Avouris, Ph. (2009). Role of contacts in graphene transistors: A scanning photocurrent study. *Physical Review B,* 79, 245430

Murali, R.; Brenner, K.; Yinxiao Yang; Beck, T.; & Meindl, J.D. (2009). Resistivity of Graphene Nanoribbon Interconnects. *IEEE Electron Device Letters,* Vol. 30, p. 611

Nagashio, K.; Nishimura, T.; Kita, K. & Toriumi, A. (2009). Metal Graphene Contact as a Performance Killer of Ultra-high Mobility Graphene a Analysis of Intrinsic Mobility and Contact Resistance. *IEEE IEDM Tech. Dig. , Baltimore, MD, Dec. 2009,* pp. 1-4

Nemec, N.; Tománek, D. & Cuniberti, G. (2008). Modeling extended contacts for nanotube and graphene devices. *Physical Review B*, Vol. 77, p. 125420

Nouchi, R. & Tanigaki, K. (2010). Charge-density depinning at metal contacts of graphene field-effect transistors. *Applied Physics Letters*, Vol. 96, p. 253503

Novoselov, K. S.; Geim, A. K.; Morozov, S. V.; Jiang, D.; Zhang, Y.; Dubonos, S. V.; Grigorieva, I. V. & Firsov, A. A. (2004). Electric field effect in atomically thin carbon films. *Science*, Vol. 306, pp. 666-669

Stander, N.; Huard, B. & Goldhaber-Gordon, D. (2009). Evidence for Klein Tunneling in Graphene p-n Junctions. *Physical Review Letters*, Vol. 102, p. 026807

Venugopal, R.; Ren, Z.; Datta, S.; Lundstrom, M. & Jovanovic, D. (2002). Simulating quantum transport in nanoscale transistors: Real versus mode-space approaches. *Journal of Applied Physics*, Vol. 92, p. 3730

Yand, Y. & Murali, R. (2010). Impact of Size Effect on Graphene Nanoribbon Transport. *IEEE Electron Device Letters*, Vol. 31, p.237

Zhang, Y.; Tan, Y.-W.; Stormer, H. L.; & Kim, P. (2005). Experimental observation of the quantum Hall effect and Berry's phase in graphene. *Nature*, Vol. 438, pp. 201-204

Zhang, Q.; Fang, T.; Seabaugh, A.; Xing, H.; & Jena, D. (2008). Graphene Nanoribbon Tunnel Transistors. *IEEE Electron Device Letters,* Vol. 29, pp. 1344-1346

Zhang, Q.; Lu, Y.; Xing, H.; Koester, S. & Koswatta, S. (2010). Scalability of Atomic-Thin-Body (ATB) Transistors Based on Graphene Nanoribbons. *IEEE Electron Device Letters,* Vol. 31, p. 531 – 533

Zhao, P. & Guo, J. (2009). Modeling edge effects in Graphene Nanoribbon FETs with real and mode space methods. *Journal of Applied Physics,* Vol. 105, p. 034503

21

Graphene Transistors and RF Applications

Jeong-Sun Moon[1], Kurt Gaskill[2] and Paul Campbell[2]
[1]*HRL Laboratories,*
[2]*United States Naval Research Laboratory,*
U.S.A

1. Introduction

Graphene is an atomically thin but stable layer form of hexagonal carbon and has attracted a lot of attention in the research community over the last few years because of its unique electronic properties [Geim & Novoselov, 2007; Guisinger and Arnold, 2010]. Graphene exhibits the highest carrier mobility: >100,000 $cm^2\ V^{-1}\ s^{-1}$ at room temperature [Morozov et al., 2008]. This is not only ~100 times greater than that of Si, but about 10 times greater than state-of-the-art semiconductors lattice-matched to InP, currently regarded the best high-speed materials. The saturation velocity (v_{sat}) of graphene has not been determined clearly yet, but it is estimated to be ~5 times greater than that for Si MOSFETs [Akturk and Goldsman, 2008]. With expected large on-state current density and transconductance per gate capacitance compared to Si, graphene has the potential to offer excellent switching characteristics (capacitance/on-state current) and short-circuit current gain cut-off frequency. Although it is too early to predict, graphene FETs could potentially be processed in a manner compatible with Si CMOS with desirable integration density for system-on-chip applications. While there are numerous challenges (including proper bandgap engineering) to be overcome for graphene to become a mature technology, this material offers unique device and circuit applications including ambipolar RF electronics [Moon et al., 2009].

2. Epitaxial graphene synthesis

Several epitaxial graphene synthesis approaches have been reported on the wafer-scale, including a Si sublimation method out of SiC substrates [Berger et al., 2004 & 2006], metal catalyst-based CVD growth [Sutter, 2008] and direct carbon deposition in MBE.

3. Epitaxial graphene transistors

Epitaxial graphene FETs on the wafer-scale are in early stages of development, although several key device parameters have been demonstrated. For example, epitaxial graphene RF FETs have been demonstrated in a top-gated layout with the highest ever on-state current density of 3 A/mm [Moon et al., 2009 #2]. In addition, the extrinsic speed performance (f_t/f_{max} of 5 GHz/14 GHz) is reported with a 2 μm gate length [Moon et al., 2009 #2]. On the other hand, the current-voltage characteristics are quasi-linear with weak saturation behaviors, yielding low transconductance (gm) per capacitance (i.e., <140 mS/mm at 3.4 $fF/\mu m^2$) and poor voltage gain (gm/G_{ds}). Also, the I_{on}/I_{off} ratio was ~4 with field-effect mobility below 200

cm^2/Vs. While graphene field-effect mobility as high as 5400 cm^2/Vs for electron has been demonstrated [Wu et al., 2008], it was achieved using six to seven layers of epitaxial graphene on C-face SiC substrates, resulting in an I_{on}/I_{off} ratio of <2. In the case of graphene FETs fabricated on the Si-face of SiC substrates, field-effect mobility has been limited to below 1200 cm^2/Vs, but with an improved I_{on}/I_{off} ratio of ~10 [Kedzierski et al., 2008].

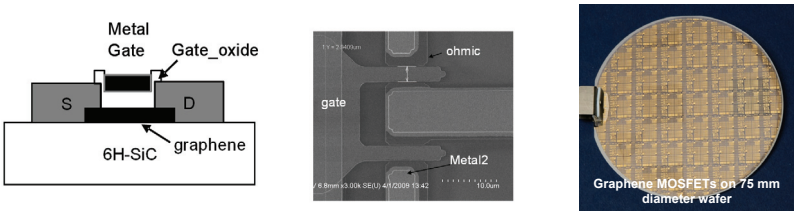

(a) (b) (c)

Fig. 1. (a) A schematic of the top-gated graphene FET. (b) A SEM photograph of 2f x 4 μm graphene FET. (c) A photograph of 75 mm graphene wafer.

In this section, we present top-gated graphene n-FETs and p-FETs from epitaxial graphene layers, where *excellent I-V saturation behaviors were observed in epitaxial graphene FETs* with a record peak extrinsic transconductance of 600 mS/mm [Moon et al., 2010]. Also, the effective mobility and field-effect mobility versus E_{eff} were characterized and compared with Hall mobility. The epitaxial graphene layers were grown on Si-face 6H-SiC substrates on 50-mm wafers via Si sublimation [Gaskill et al., 2009]. The sheet electron carrier density of the epitaxial graphene layer was typically 8.8 x 10^{12} cm^{-2} at room temperature and had electron mobility of ~1192 cm^2/Vs, characterized by non-contact Hall Lehighton 1600. The number of epitaxial graphene layers (nGL) was found to be one layer on the SiC terraces and two layers on the step edges over the entire 50-mm wafer as characterized by Raman analysis and transmission electron microscopy analysis.

Graphene FETs were fabricated using Ti/Pt/Au source and drain metal deposition and lift-off process. The non-alloyed ohmic metal yielded the contact resistivity of 10^{-6} – 10^{-7} $\Omega \cdot cm^2$ [Moon et al., 2009 #2]. The metal gates were processed via the Ti/Pt/Au metal deposition and lift-off process on top of a 35-nm-thick SiO_2 gate dielectric layer deposited by electron beam evaporation. The gate leakage current was in the range of ~nA/μm^2 or less, which is negligible in the device characterization presented here.

Figure 1 (a)-(c) shows the graphene FET processed in a layout, where the gate metal is aligned with respect to the ohmic metals in an under lap layout with a gate-to-source/drain separation of <100 nm to minimize the access resistance over a source-drain spacing (L_{sd}) of 3 μm. The source access resistance was <0.2 Ω·mm via the standard end-point measurements on transfer length method (TLM) structures. A graphene channel width of 4 μm was defined by O_2 plasma etching.

Figure 2 (a)-(b) shows measured room temperature, common-source, current-voltage characteristics of a two-gatefinger and 4-μm-wide n-channel graphene FET (denoted as 2f x 4 μm), in which excellent drain current saturation was observed. The source-to-drain voltage (Vds) increased to 3 V, where the gate-to-source (Vgs) voltage was stepped from 3 V (top-curve) in steps of -0.5 V. At Vds = 1 V, on-state current at Vgs = 3 V was 0.59 A/mm. The off-state current was 0.047 A/mm at Vgs = -1 V, yielding I_{on}/I_{off} ratio of 12.5. At Vds = 0.5 V, the I_{on}/I_{off} ratio increased to 19 with the on-state current of 0.31 A/mm. At Vds = 3 V, the on-state current at Vgs = 3 V was measured as high as 1.65 A/mm. The on-resistance was 1.6 Ω·mm.

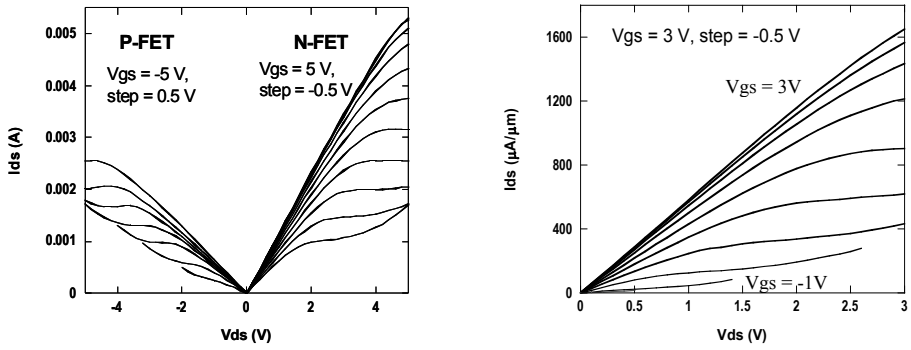

(a) (b)

Fig. 2. (a) Measured common-source current-voltage characteristics of 1f x 4 μm graphene FET. (b) Both p-channel and n-channel graphene MOSFET operations.

Figure 3 shows measured transconductance (gm) of a 2f x 4 μm graphene FET at different Vds, stepping from 1.05 to 3.05 V with a step of 0.5 V. The inset shows measured transfer curves. At Vds = 3.05 V, the Ids reached up to 1.1 A/mm at Vgs = 3 V. The ambipolar behavior was observed clearly at Vds >2 V, while the ambipolar behavior is not well-developed with a relatively flat region observed at low Vds such as Vds = 1.05 V. The peak extrinsic gm of 600 mS/mm was measured at Vds = 3.05 V, which is the highest ever, amongst epitaxial graphene FETs. The observed negative transconductance is due to a conversion of n-channel to p-channel. The effective mobility, μ_{eff}, was extracted using a formula: $\mu_{eff} = (L/W)\cdot Ids/[C_{ox}\cdot(Vgs-V_T)\cdot Vds]$. The C_{ox} is gate_oxide capacitance, $\varepsilon_0\cdot\varepsilon_{ox}/t_{ox}$, where ε_0 and ε_{ox} are permittivity of the free space and gate_oxide layer, respectively. Gate_oxide capacitance is measured using a metal-gate_oxide-metal (MOM) capacitor array with OPEN and SHORT calibration standards. The geometric scaling of the MOM capacitors is verified to eliminate fringe capacitances. The geometric oxide capacitances were measured at 1 fF/μm² or 1.7 fF/μm² from the two different wafers. The dielectric constant of the deposited SiO_2 films was determined to be 3.9, which is close to that of SiO_2. The field-effect mobility, μ_{FE}, defined by $\mu_{FE} = (L/W)\cdot gm/(C_{ox}\cdot Vds)$, was obtained from the transconductance (gm) at Vds = 50 mV. So, there is no ambiguity in μ_{FE} associated with the V_T unlike the case of μ_{eff}. The effective electric field is estimated using $E_{eff} = Q_{Gr}/(\varepsilon_0\cdot\varepsilon_{ox})$, where Q_{Gr} is the total charge in the graphene channel.

Figure 4 shows extracted μ_{eff} and μ_{FE} of graphene n-FETs versus the effective electric field, E_{eff}. In comparison, the universal and field-effect mobility of Si n-MOSFETs [Takagi et al., 1994] and strained Si n-MOSFETs on SiGe-on-oxide [Cheng et al., 2001] are shown. While both the μ_{eff} and μ_{FE} of the graphene n-FETs depend on E_{eff}, both values were higher than 1000 cm²/Vs over a wide range of the effective electric field up to 1.6 MV/cm. The peak field-effect mobility values ranged from 3200 cm²/Vs to 6000 cm²/Vs. A record field-effect mobility of 6000 cm²/Vs was obtained at an effective electric field of 0.27 MV/cm. The measured field-effect mobility of graphene n-FETs was at least seven times higher than that of ITRS Si n-MOSFETs and ~80 times higher than ultra-thin-body SOI n-MOSFETs. The peak field-effect mobility of graphene p-FETs was also determined to be 3200 cm²/Vs at an effective electric field of 0.2 MV/cm.

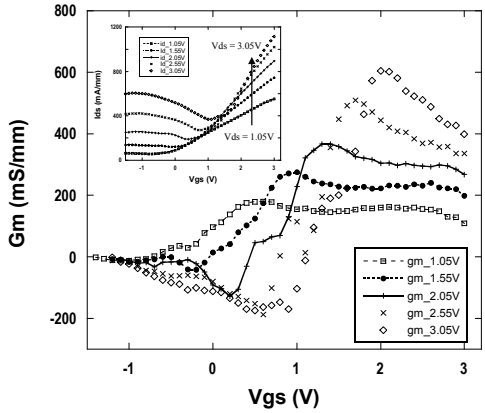

Fig. 3. Measured small-signal transconductance of 1f x 4 μm n-channel graphene FET at different Vds , from 1.05 V to 3.05 V in steps of 0.5 V. Peak extrinsic transconductance is as high as 600 mS/mm at Vds = 3.05 V. The inset shows measured transfer curves from 1.05 V to 3.05 V in steps of 0.5 V.

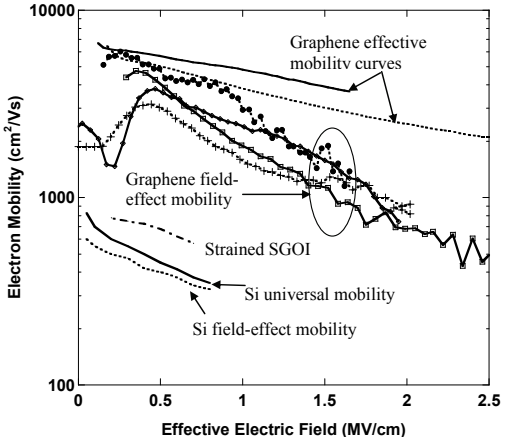

Fig. 4. Measured effective carrier mobility and field-effect mobility of graphene n-FETs compared with those of Si n-MOSFET and strained Si on SGOI MOSFET.

4. Wafer-scale graphene-on-Si transistors

Graphene synthesis directly on silicon substrates is highly attractive because graphene wafers can be scaled-up significantly larger than commercially available (4,6)H-SiC substrates; this technique is being evaluated either via a direct carbon deposition [Hackley et al., 2009] or via a growth of template layer such as 3C-SiC [Suemitsu et al., 2009]. Utilizing a 3C-SiC(111) template grown on Si(110), epitaxial graphene-on-Si FETs are reported with Ion of >0.03 μA/μm at V_{ds} = 1V in a top-gated layout [Kang et al., 2009]. The very low Ion was attributed to a hight sheet resistance of 129 kΩ/sq. Ambipolar current-voltage characteristics, unique to the graphene, were not clearly demonstrated.

In this section, we present top-gated graphene-on-Si FETs utilizing 3C- SiC(111) templates grown on 75 mm Si(111) substrates. The ambipolar characteristics were observed clearly for the first time, with Dirac points close to zero gate voltage. The Ion of 225 μA/μm was demonstrated, which is the highest for epitaxial graphene-on-Si FETs.

Figure 5 shows a schematic of top-gated and self-aligned, graphene-on-Si FETs with a SEM photograph of a 2 gatefinger graphene FET. These graphene-on-Si FETs were processed in a layout with a source-drain spacing (L_{sd}) of 1 or 3 μm; the gate metal is aligned with respect to the pre-defined ohmic metals in an under lap layout with a gate-to-source/drain separation of <100 nm. Graphene channel widths varied from 6 μm, 12 μm, and 25 μm, which were defined by O_2 plasma etching. Ohmic metals were fabricated with Ti/Pt/Au source and drain metal deposition and lift-off process. The non-alloyed ohmic metal yielded a contact resistance of 2.5 Ω·mm and a contact resistivity of ~10^{-5} Ω·cm^2 using the transmission line method (TLM). The contact resistivity was higher than that of ~10^{-7} Ω·cm^2 from graphene-on-SiC FETs [6]. The metal gates were processed with Ti/Pt/Au metal deposition and lift-off process on top of a 35-nm-thick SiO_2 gate dielectric layer deposited by electron beam evaporation. Figure 5(c) shows measured transfer curves of 25-μm-wide graphene-on-Si FETs with L_{sd} = 3 μm at a fixed V_{ds} = 2 V. The ambipolar behaviors were observed clearly with Dirac points closed to zero gate voltage. An I_{on} of 80-100 μA/μm was obtained at V_{gs} = 3 V.

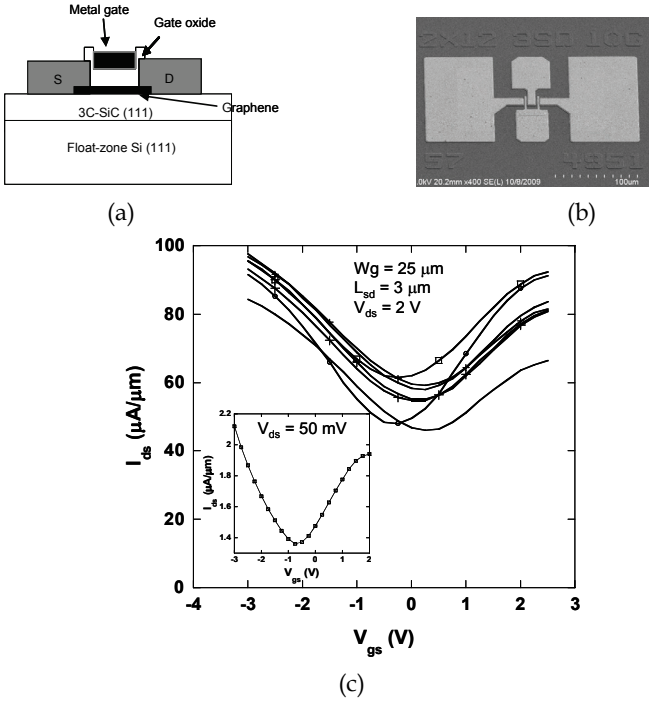

Fig. 5. (a) A schematic of the top-gated graphene FET. (b) A SEM photograph of two-gatefinger and 12-μm-wide graphene FET (denoted as 2f x 12 μm). (c) Measured transfer curve of 1f x 25 μm epitaxial graphene-on-Si FETs at V_{ds} = 2 V with ambipolar behaviors. The L_{sd} was 3 μm. The inset shows measured transfer curve at V_{ds} = 50 mV.

5. RF Applications

Figure 6(a) shows measured $|H_{21}|$ and unilateral gain (U) of the 2 x 12 μm graphene FETs at Vds = 5 V with source-drain spacing (Lds) of 3 μm. The extrinsic f_T and f_{max} are 2.7 GHz and 3.4 GHz, respectively. Figure 6(b) shows measured plots of magnitude of H_{21} ($|H_{21}|$) and unilateral gain (U) of the 2 x 12 μm graphene FETs with source-drain spacing (Lds) of 1 μm. The S-parameters were measured at Vds = 5 V and Vgs = -2.5 V. An extrinsic cut-off frequency (f_T) of 4.1 GHz was extracted, yielding an extrinsic $f_T \cdot L_g$ of 8.2 GHz·μm. The extrinsic gm was 195 mS/mm. A maximum oscillation frequency (f_{max}) of 11.5 GHz was extracted from the unilateral gain (U) with a slope of -20 dB/decade. Figure 7 shows a plot of extrinsic f_T and f_{max} measured from both of the graphene FETs. For graphene FET #1, the extrinsic gm improved to 148 mS/mm at Vds = 9 V, yielding the extrinsic f_T and f_{max} of 4.4 GHz and 6 GHz, respectively. For graphene FET #2, the f_T and f_{max} were 4.2 GHz and 14 GHz, respectively, at Vds = 7 V. With a source access resistance of 1.9 Ω·mm, the intrinsic gm becomes 205 mS/mm. This yields an intrinsic f_T of 5 GHz with an intrinsic $f_T \cdot L_g$ of 10 GHz·μm, which is slightly better than 8.9 GHz·μm from the bulk Si NMOS. At present, the RF performance of graphene FETs is not close to what had been predicted by the intrinisc saturation velocity of the graphene channel, 4-5E7 cm/sec. The $f_T \cdot L_g$ product of graphene FETs is expected to improve as the quality of the epitaxial graphene layer and transistor fabrication processing improve with reduced parasitic charging delay, such as (Rs +Rd)*Cgd [Moon e tal., 2008]. The unique ambipolar nature of graphene FETs can benefit various RF circuit applications, such as frequency multipliers, mixers and high-speed radiometers. The future success of the RF circuit applications depends on vertical and lateral scaling of graphene MOSFETs to minimize parasitics and improve gate modulation efficiency in the channel.

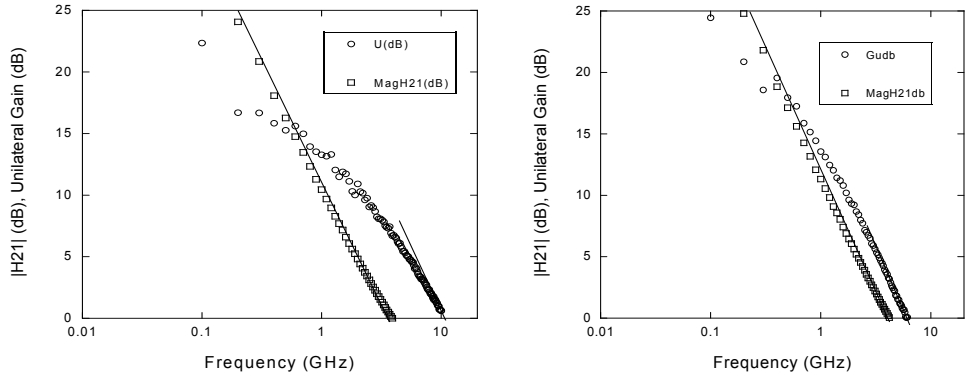

(a) (b)

Fig. 6. Measured $|H_{21}|$ and unilateral gain (U) are shown as a function of frequencies at Vds = 5 V and Vgs = -2.5 V of 2 x 12 μm graphene MOSFETs with (a) Lds = 3 μm and (b) Lds = 1 μm.

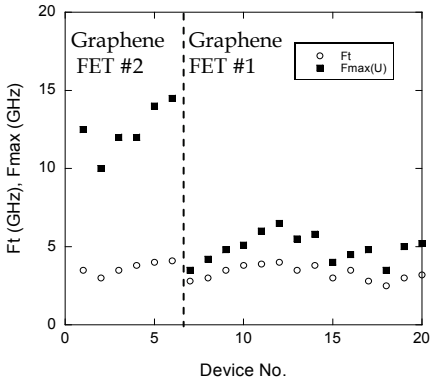

Fig. 7. A plot of measured extrinsic f_T and f_{max} of the graphene FETs is shown. The gate length is 2 μm. The highest ft and fmax are 4.1 GHz and 14 GHz, respectively.

This work was supported by the Defense Advanced Research Projects Agenecy (DARPA) and monitored by Dr. John Albrecht at DARPA under SPAWAR contract #N66001-08-C-2048. The views, opinions, and/or findings contained in this article/presentation are those of the author/presenter and should not be interpreted as representing the official views or policies, either expressed or implied, of the Defense Advanced Research Projects Agency or the Department of Defense.

6. References

A. K. Geim and K. S. Novoselov, "The rise of graphene", Nature Materials, vol. 6, pp 183-191, 2007.

N.P. Guisinger and M.S. Arnold, "Beyond Silicon: Carbon-based Nanotechnology", MRS Bulletin, vol. 35, April, 2010.

Morozov et al., "Giant Intrinsic Carrier Mobilities in Graphene and Its Bilayer", Phys. Rev. Lett., vol. 100, p 16602, 2008

A. Akturk and N. Goldsman, "Electron transport and full-band electron-phonon interactions in graphene", J. Appl. Phys., vol. 103, p 053702, 2008.

J. S. Moon et al.,"Development toward wafer-scale graphene electronics", First International Symposium on Graphene and Emerging Materials for Post-CMOS Applications in 215th Electrochemical Society meeting, 2009.

C. Berger et al., J. Phys. Chem. B 108, 19912 (2004).

P. W. Sutter, J.-I. Flege, E. A. Sutter, "Epitaxial graphene on ruthenium". Nat. Mater. *7*, 406–411, 2008.

C. Berger et al., "Electronic confinement and coherence in patterned epitaxial graphene," Science, vol. 312, pp. 1191–1196, 2006.

J. S. Moon et al., "Epitaxial Graphene RF Field-Effect Transistors on Si-face 6H-SiC Substrates", IEEE Electron Dev. Lett., vol. 60, pp 650-652, 2009.

Y. Q. Wu et al., "Top-gated graphene field-effect transistors formed by decomposition of SiC", Appl. Phys. Lett., vol. 92, p 092102, 2008.

J. Kedzierski et al., "Epitaxial Graphene Transistors on SiC Substrates", IEEE Trans. Electron Devices, vol. 55, pp 2078-2085, 2008.

J. S. Moon et al., " Top-gated Epitaxial Graphene FETs on Si-face SiC Wafers with a Peak transconductance of 600 mS/mm", IEEE Electron Dev. Lett., vol. 31, pp 260-262, 2010.

D. K. Gaskill et al., "Epitaxial Graphene Growth on SiC Wafers", ECS Transactions 19, p.117, 2009.

S. Takagi et al., "On the Universality of Inversion Layer Mobility in Si MOSFET's: Part I – Effects of Substrate Impurity Concentration", IEEE Trans. Electron Devices, vol. 41, pp 2357-2362, 1994.

Z.-Y. Cheng et al., "Electron Mobility Enhancement in Strained-Si n-MOSFETs Fabricated on SiGe-on-Insulator (SGOI) Substrates", IEEE Electron Dev. Lett., vol. 22, pp 321-323, 2001.

J. Hackley etal., "Graphitic carbon growth on Si(111) using solid source molecular beam epitaxy", Appl. Phys. Lett., vol. 95, p 133114, 2009.

M. Suemitsu et al., "Graphene formation on a 3C-SiC(111) thin film grown on Si(110) substrate", e-J Surf. Sci. Nanotech. vol. 7, pp. 311-313, 2009.

H-C Kang et al., "Epitaxial graphene top-gate FETs on silicon substrates", International Semiconductor Device Research Symposium, pp 1-2, 2009.

M. Fanton et al., "3C-SiC films grown on Si(111) substrates as a template for graphene epitaxy", First International Symposium on Graphene and Emerging Materials for Post-CMOS Applications in 215th Electrochemical Society meeting, 2009.

22

Chemical and Biosensing Applications Based on Graphene Field-Effect Transistors

Yasuhide Ohno, Kenzo Maehashi and Kazuhiko Matsumoto
The Institute of Scientific and Industrial Research, Osaka University
Japan

1. Introduction

Label-free electrical detection of biomolecule based on nano-meter size materials has attracted in many fields such as clinical diagnosis for health care, life science and practical pharmacy because they are expected for rapid and easy detection of various biological species at home. Chemical and biological sensors using silicon nanowires(Cui et al., 2001; Li et al., 2005; Zheng et al., 2005) and carbon nanotubes (CNTs)(Besteman et al., 2003; Chen et al., 2003; Ishikawa et al., 2010; Maehashi et al., 2007; Maehashi, Matsumoto, Kerman, Takamura & Tamiya, 2004; Martnez et al., 2009; Star et al., 2003) have been developed for the past decades. Especially, CNT field-effect transistors (CNT-FETs) are one of the strongest candidates for biosensing applications due to their high aspect ratio, high mechanical strength, large surface areas and outstanding electrical characteristics. These superior characteristics make CNTs ideal for nanoscale devices(Saito et al., 1998). There have been many reports about chemical and biological sensors using CNT-FETs such as proteins, glucose, DNA hybridizations and immunosensors(Besteman et al., 2003; Chen et al., 2003; Ishikawa et al., 2010; Maehashi et al., 2007; Maehashi, Matsumoto, Kerman, Takamura & Tamiya, 2004; Martnez et al., 2009; Star et al., 2003).

Although the CNT-FET based sensors have high potential, their electrical characteristics strongly depends on their chirality (diameter) and work function of the contact metal(Chen et al., 2005). Since the chirality control growth of CNTs has not been achieved, the reproducibility and stability of the CNT-FET based sensors have been major problem(Maehashi, Ohno, Inoue & Matsumoto, 2004). And the typical absolute value of the drain current (I_D) of a CNT-FET with one CNT channel in solution is several nA to several 10 nA because only small drain and gate voltages can be applied in solution due to the avoidance of solution electrolysis and oxidization of the electrodes, channel and analyte. To resolve these problems, aligned CNTs have been studied in recent years(Palaniappan et al., 2010). However, the separation between semiconductor and metallic CNTs is also very difficult problem.

Graphene, single layer hexagonal network of carbon atom, can modify these problems. Since they are ideal two-dimensional crystal with extremely high carrier mobility at room temperature without any sophisticated doping process and very stable materials, graphene field-effect transistors (G-FETs) have been expected for the next-generation practical devices(Geim & Novoselov, 2007; Novoselov et al., 2004). In recent years, sensing applications using graphene and graphene-like materials have been intensively studied because their electrical characteristics are very sensitive for the environmental conditions and

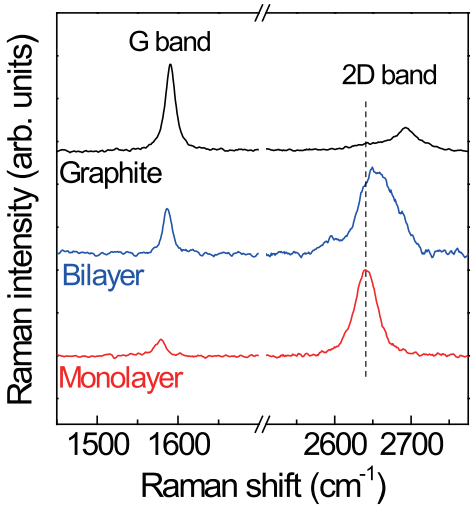

Fig. 1. Raman spectra of G- and 2D-bands for 1 and 2 layer(s) graphene and HOPG.

the surface-analyte or analyte-analyte bindings occur very close to the graphene channel(Yang et al., 2010). The mechanism of action for G-FET sensors is that chemical species adsorbed on the surface of the graphene act as electron donors or acceptors, resulting in conductance changes. Most of the graphene sensors have been used to detect gas molecules(Arsat et al., 2009; Dan et al., 2009; Fowler et al., 2009; Lu et al., 2009; Qazi et al., 2007; Robinson et al., 2008; Schedin et al., 2007). In addition, research on electrical detection of biomolecule detection using graphene has gradually increased over the last few years. Electrochemical detections of glucose and proteins have been investigated(Alwarappan et al., 2009; Lu et al., 2007; Shan et al., 2009; Shang et al., 2008; Wu et al., 2009). Field-effect transistors based on reduced graphene from graphene oxide or graphene amine have detected DNA hybridizations and negatively charged bacteria(Mohanty & Berry, 2008). In graphene, the highest carrier mobility is only achieved in single-layer graphene due to its linear energy dispersion at K point(Nagashio et al., 2008). Since the sensitivity using G-FET-based chemical and biological sensors depend on their transconductance ($= \partial I_D / \partial V_G = C_G V_D \mu$; where C_G, V_D and μ are the gate capacitance, drain voltage and field-effect mobility, respectively), G-FETs with single-layer graphene are thought to be suitable for the sensing devices.

In this chapter, we describe our attempts to apply G-FETs with single-layer graphene to chemical and biological sensors(Ohno et al., 2009). We investigated behavior of G-FETs immersed in an electrolyte and show that they have very good transfer characteristics compared with their characteristics in vacuum. They also exhibit clear pH-dependent I_D characteristics and could electrically detect surface-protein adsorption. Moreover, we demonstrate the achievement of electrical detection of biomolecules and their charge types by G-FETs.

2. Experimental

The G-FETs used in this study were fabricated on a 285-nm-thick thermally grown SiO_2 layer on a heavily *p*-doped silicon substrate ($\rho < 0.01\ \Omega$·cm). Single-layer graphene flakes were obtained by micromechanical exfoliation using natural graphite and clear adhesive tape. The graphene flakes were searched by an optical microscope after slowly peeling off the tape from the substrate. As a result of this procedure, various types of graphene layers (or thick graphite) were identified on the surface SiO_2/Si substrate. Single-layer graphene flakes were identified by analyzing the shift in green intensity under optical microscope observation and by Raman spectroscopy. Figure 1 compares the 632.8 nm Raman spectra of 1 and 2 layer(s) graphene and highly oriented pyrolytic graphite (HOPG). Two strong peaks with a G band at $\sim$1580 cm^{-1} and a 2D band at $\sim$2650 cm^{-1} could be observed. A single peak of the 2D can be observed for the single-layer graphene, while a much broader peak with some shoulders, shifted to a high-frequency, could be observed for the bilayer graphene. As shown in Figure 1, a single peak in the 2D band in the Raman spectrum is direct evidence of single-layer graphene(Ferrari et al., 2006). Ti (5 nm)/Au (30 nm) source and drain electrodes were formed by electron beam lithography and lift-off method. The degenerately doped silicon substrate was also used for the back gate. Typical optical microscope image of G-FET was shown in Fig. 2.

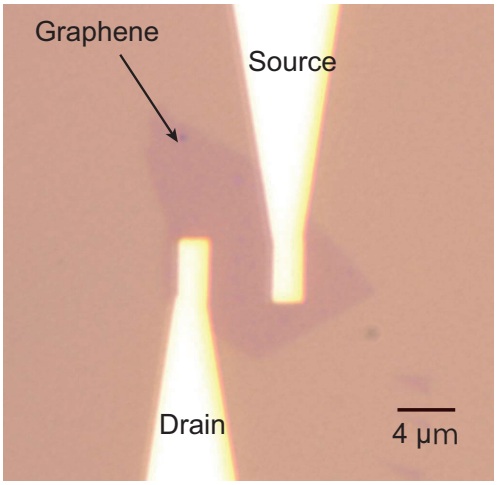

Fig. 2. Optical micrograph of a typical G-FET.

To measure the solution pH value and protein adsorption, the device was surrounded by a silicone rubber pool attached to the substrate. Then, the Ag/AgCl reference electrode was immersed into the solution contained within a silicone rubber barrier as shown in Fig. 3 and Fig. 4. The Ag/AgCl reference electrode was used as the top-gate electrode to minimize environmental effects(Minot et al., 2007). The electrical characteristics of the G-FETs were measured by a semiconductor parameter analyzer (4156C; Agilent technologies Inc., Santa Clara, CA), using two-terminal measurement. In the experiments, we drove the G-FETs under low voltage ($\leq$ 0.2 V) due to the avoidance of oxidization of electrodes and graphene channel. Natural graphite used in this work was kindly provided by Nippon Graphite Industries Ltd. (Shiga, Japan). 10 mM phthalate buffer solution of pH 4.0, phosphate buffer solution of pH 6.8 and 10 mM borate buffer solution at pH 9.3 were purchased from Horiba Ltd. (Kyoto, Japan).

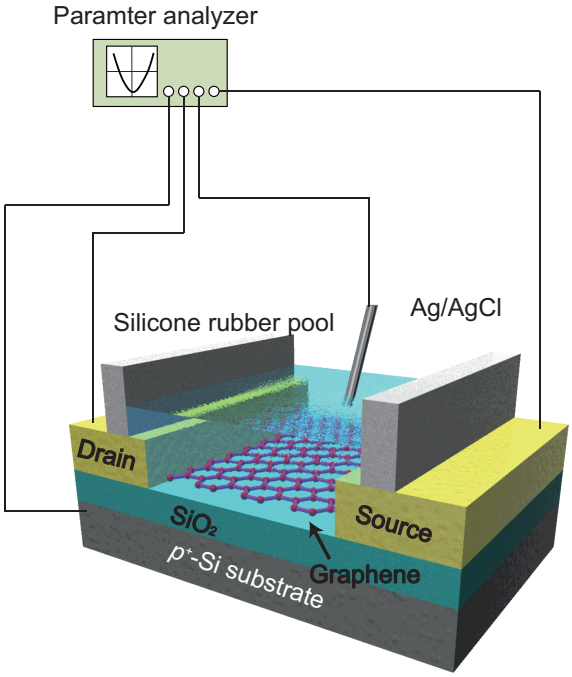

Fig. 3. Schematic illustration of experimental setup with G-FETs.

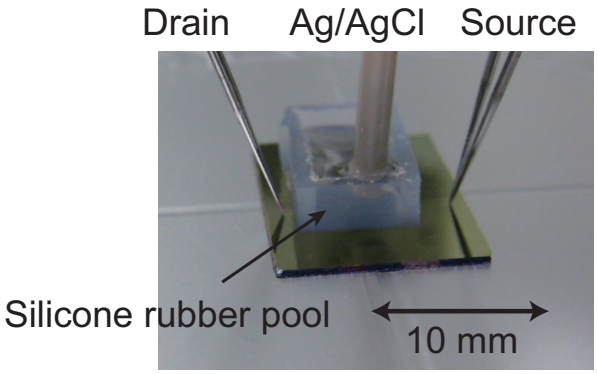

Fig. 4. Photograph of experimental setup with a G-FET.

Solutions of various pH values were prepared by mixing a 10 mM phthalate buffer solution of pH 4.0, a 10 mM phosphate buffer solution of pH 6.8 and a 10 mM borate buffer solution at pH 9.3. Bovine serum albumin (BSA), which was used as the target protein, was purchased from Sigma Aldrich Inc. (St Louis, MO).

3. Results and discussion

3.1 Transport characteristics in solution

At first, we investigated the transport characteristics of G-FETs in solution. In a solution or electrolyte, the electrical-double layer acts as a top-gate insulator, and the thickness of electrical-double layer is generally defined by the Debye-Hückel equation, which depends on the ionic strength and temperature, which is as small as 5 nm in the buffer solution with several ten mM. This value is very thin compared with the SiO_2 layer used as the back-gate insulator. For graphene devices, only 90 or 290 nm-thick SiO_2 can be used because single or a few layer graphene flakes on the 90 or 290 nm can be observed by a conventional optical microscope due to the refractive index of the graphene(Blake et al., 2007). Because of this thin gate insulator, the field-effect applied by the top-gate electrodes is very effective compared from the back gate. In fact, electrolyte-gated CNT-FETs and G-FETs have shown good electrical characteristics as thin top-gate insulators with high dielectric constants in ionic solutions(Das et al., 2008; Rosenblatt et al., 2002).

A typical plot of I_D as a function of back-gate voltage under reduced pressure (1×10^{-3} Pa) is shown in Fig. 5. Transconductance ($= \partial I_D / \partial V_G$) was estimated to be 0.13 μS and 30 μS for back-gate and top-gate operations, respectively. The transconductance was for top-gate operation was more than 200 times better than that of back-gate operation; thus, a thin electrical-double layer is formed on the graphene surface. This result shows that G-FETs can operate even in solution, and their electrical characteristics in solution are excellent.

To clarify the difference between the g_m values of the devices, back- and top-gate capacitances were estimated using a simple model. Assuming that graphene is equivalent to a metal disk placed on the insulator, the gate capacitance can be expressed by the equation below, (Gelmont et al., 1995)

$$C_G = \frac{2\pi\varepsilon_0(\varepsilon_r + 1)r}{\tan^{-1}\left[\frac{2h(\varepsilon_r + 1)}{r\varepsilon_r}\right]}, \tag{1}$$

where, r, h, ε_r and ε_0 are the radius of the metal disk (graphene), the thickness of the gate insulator, the relative permittivity and vacuum permittivity, respectively. For the electrolyte-gated G-FETs (with r=1.5 μm, h=1 nm and ε_r (H_2O)=80), the estimated electrostatic gate capacitance was C_{G_EL} ~500 nF cm^{-2}. In this case, if total top-gate capacitance (C_{TG}) is considered as a series of the C_{G_EL} and the quantum capacitance (C_Q), (Meric et al., 2008; Rosenblatt et al., 2002) then C_{TG}=$C_{G\_EL}C_Q/(C_{G\_EL} + C_Q)$. Because the C_Q of the graphene channel is approximately 2 μF cm^{-2}, (Meric et al., 2008) the C_{TG} is 400 nF cm^{-2}. This value is more than three orders of magnitude larger than the back-gate capacitance of 85 pF cm^{-2} (with r=1.5 μm, h=285 nm and ε_r (SiO_2)=3.9), given by the above equation. It can be concluded that this larger top-gated capacitance gave rise to better transfer characteristics of G-FETs in the electrolyte, indicating their high potentials for use in field-effect sensing applications.

3.2 pH dependence

The dependence of the transfer characteristics and conductance of G-FETs on pH were evaluated. Figure 6 shows I_D plotted as a function of V_{TGS} for a G-FET in various electrolytes at various pH values from 4.04 to 8.16. The Dirac points of the G-FET shifted in a positive detection with increasing pH. This behavior indicates that G-FETs can detect the pH value by the electrical characteristics. A plot of the time-dependent I_D for a G-FET at V_{TGS} =−80 mV in pH values from 4.0 to 8.2. is shown in Figure 7. Every 10 min, either a 10-mM phosphate buffer solution at pH 6.8 or a 10-mM borate buffer solution at pH 9.3 were added to increase

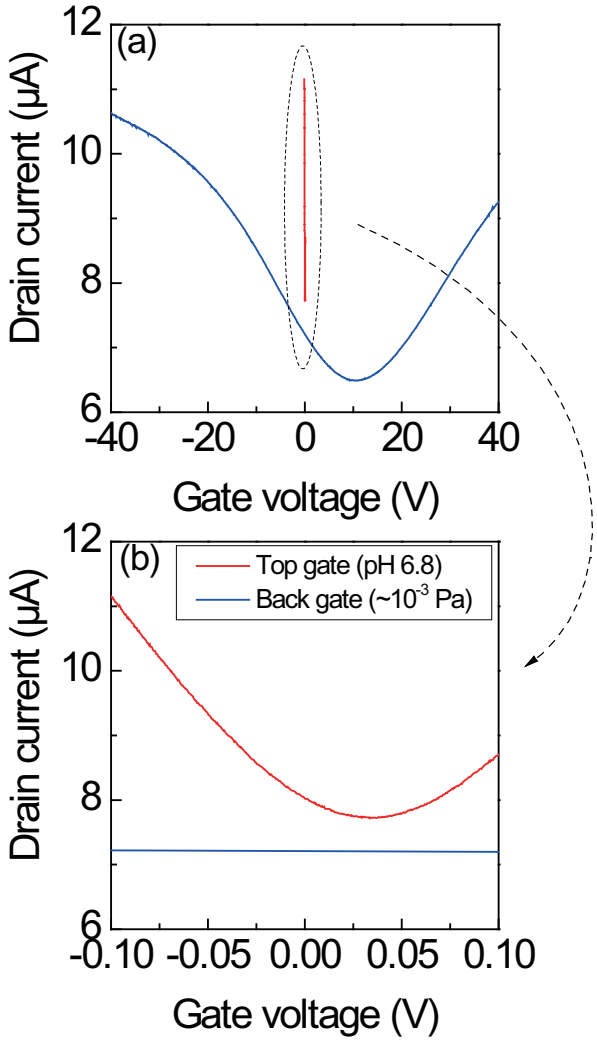

Fig. 5. (a) I_D as a function of back-gate voltage at 10^{-3} Pa and top-gate voltage in an solution at pH 6.8. (b) Enlarged view of I_D as a function of gate voltage.

the pH. The I_D increased stepwise with pH from 4.0 to 8.2, and the I_D at each pH value was virtually constant. The plot of the average I_D against pH values indicates that the relationship between pH and I_D is linear over the range from 4.0 to 8.2, as shown in Figure 8. Similar changes in gate transfer characteristics have been observed for a G-FET exposed to NO_2 and pH dependence of G-FETs with few-layer epitaxial graphene. It is concluded that the increased I_D can be attributed to the increased negative charge around the graphene channel, because the hole is the carrier in this condition. The origin of the increase in current is not clear at present. We speculate that hydrogen or hydroxide ions have some effect on the graphene surface. In case of the CNT-FETs, hydroxide ions bound to the carbon nanotube surface act as acceptors(Lee et al., 2007; Pan et al., 2004). As a nano-carbon material, graphene may exhibit chemical reactivity similar to carbon nanotubes. Further investigation is necessary to clarify this point.

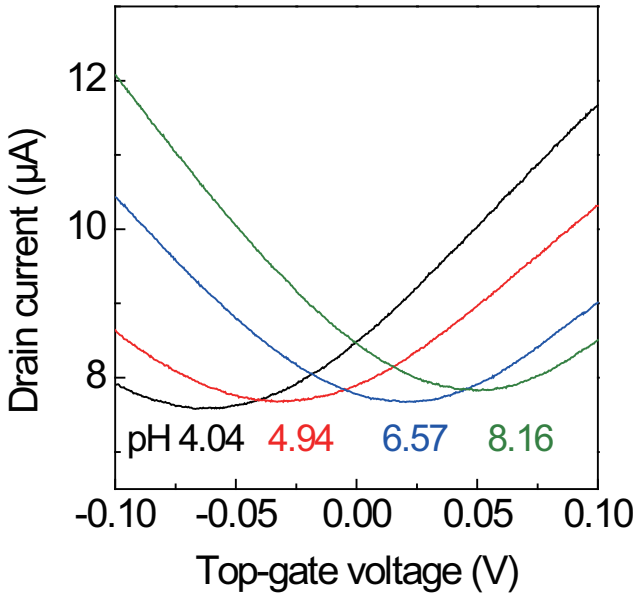

Fig. 6. I_D as a function of top-gate voltage of a G-FET at pH 4.04, 4.94, 6.57 and 8.16.

It should be noted that the Dirac point of G-FETs at a pH solution was not constant. Although the Dirac point = 0 V was realized at pH 5.8 in this device, other devices showed the Dirac point = 0 V at different pH values. One possible reason of the instability is due to charged impurities such as residual EB resist, defects or underlying SiO_2 and Si. Indeed, the solution pH slightly influenced the carrier mobility. Charged impurity scattering is major subject in the graphene technology. These uncontrollable charged impurities may lead the Dirac point instability.

The detection limit (=resolution, signal/noise=3) for changes in pH was estimated to be 0.025 in the pH range from 4.04 to 8.16. In this work, the signal and noise were defined by the average and standard deviation of the data, respectively. On the other hand, a pH sensor based on carbon nanotube FETs showed the detection limit of 0.67 due to the small drain current in

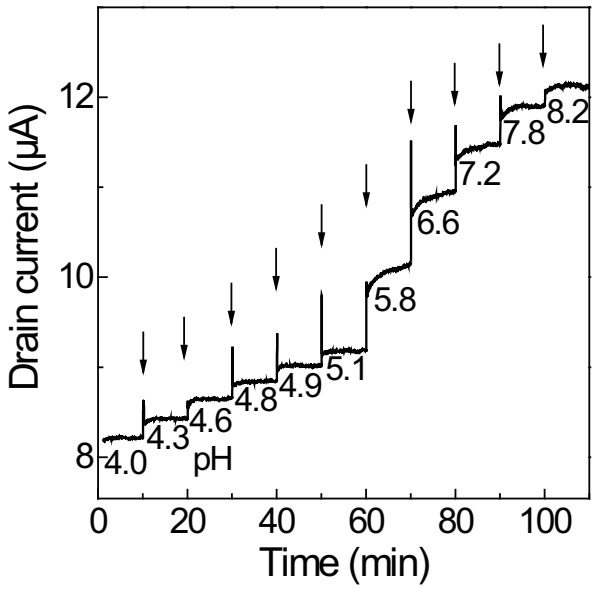

Fig. 7. I_D versus time data of a G-FET for pH values from 4.04 to 8.16. Arrows indicate the adding points of solution with different pH.

solution ($\sim$ 10 nA)(Yamamoto et al., 2009). Therefore, the G-FETs are useful as pH sensors for their stability. The pH dependence of the drain current was similar to that of few-layer epitaxial graphene.

3.3 Detection of protein adsorption

Finally, we demonstrated label-free biomolecule detection, based on electrolyte-gated G-FETs. A 10-mM phosphate buffer electrolyte solution at pH 6.8 was used, with a bovine serum albumin (BSA; Sigma Aldrich Inc., St Louis, MO) target biomolecule. The isoelectric point of BSA is 5.3, indicating that BSA molecules are negatively charged at the pH used for this measurement. Figure 9 shows the evolution of I_D of a G-FET for electronic monitoring of BSA adsorption on a graphene channel at $V_{TGS} = -0.1$ V and $V_{BGS} = 0$ V. Under this condition, the I_D was expected to be increased by the hole carrier when (negatively charged) BSA was attached to the graphene. Measurement began with a 10-mM pure phosphate buffer solution. After 10 min, further pure buffer solution was added and I_D was virtually unchanged. After 20 min, BSA concentration dependence of I_D was shown. Arrows in Figure 9 mark the points where solutions with various concentration of BSA were injected. The I_D clearly increased when BSA was introduced, indicating adsorption on the graphene surface. The drain current change (ΔI_D) is shown as a function of BSA concentration (C_{BSA}) in Figure 10. ΔI_D increased linearly at low concentrations and was saturated at higher concentrations. This result indicates that the adsorption of BSA molecules onto the graphene surface follows the Langmuir adsorption isotherm given by

$$\frac{C_{BSA}}{\Delta I_D} = \frac{C_{BSA}}{\Delta I_{DMax}} + \frac{K_d}{\Delta I_{DMax}}, \tag{2}$$

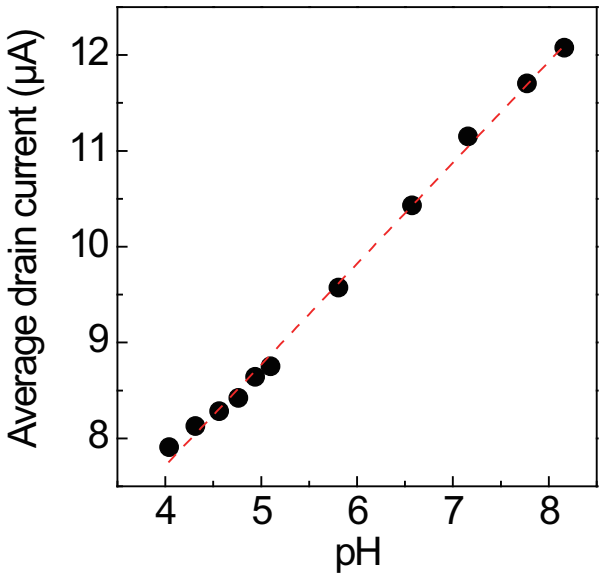

Fig. 8. Average I_D as a function of pH. The dashed line is a linear fit to the data points.

where K_d is the dissociation constant of the interaction between BSA molecules and graphene and ΔI_{DMax} is the drain current at saturation. The Langmuir adsorption isotherm fitted the experimental results well, as shown in Figure 10 (red dashed line). The K_d was estimated to be 1.5×10^{-8} M, which was comparable with the values obtained for Si nanowire(Cui et al., 2001) and CNT-FET biosensors(Abe et al., 2008; Maehashi et al., 2009) using antibody-antigen interactions, despite the fact that BSA molecules were considered to be directly adsorbed onto the graphene surface in this work rather than through a protein-protein interaction. Further experiments are needed to confirm the suitability of the Langmuir adsorption isotherm for these experimental results.

Moreover, adsorption of proteins with different charge types onto the graphene surface was detected. The isoelectric point of BSA is approximately 5.3; accordingly, BSA molecules are positively (negatively) charged in the 10-mM phthalate (phosphate) buffer solution. Four G-FETs were used in this experiment. Two of them were used in the phthalate buffer solution and others in the phosphate buffer solution. Figures 11 show the time course of normalized I_D at V_D and V_{TGS} of 0.1 and -0.1 V, respectively. The drain current decreased when 80 (red lines) and 100 (blue lines) nM BSA in 10 mM phthalate buffer solution (pH 4.0) was added, indicating that the graphene channel detected the positive charge. Conversely the drain current increased after adding negatively charged BSA in 10 mM phosphate buffer solution (pH 6.8). And the I_D changes seem to depend on the concentration of BSA. It should be noted that some I_D trends are unstable after adding the BSA as shown in Fig. 11. The origin of these unstable features may come from remote impurity in SiO_2 layer under the graphene channel. Very recent research showed that the existence of SiO_2 layer influenced the sensing properties for G-FETs.

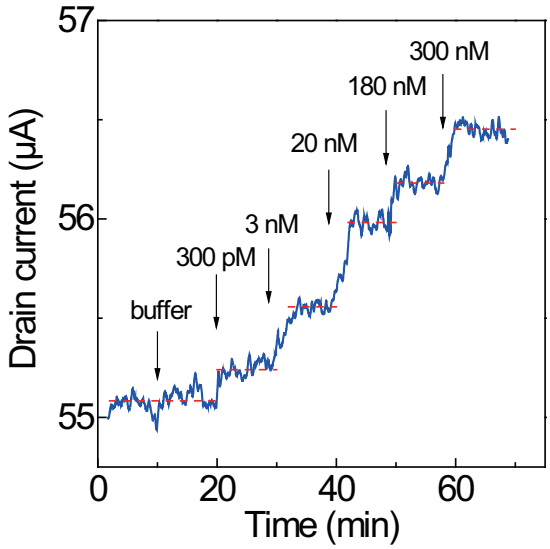

Fig. 9. I_D versus time for electrical monitoring of exposure to various BSA concentrations. Dashed lines indicate the average I_D.

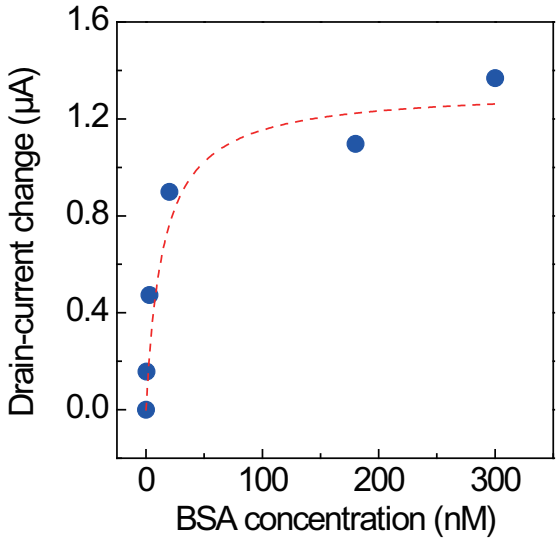

Fig. 10. Plot of the net I_D change of a G-FET versus BSA concentration. The dashed line is a fit to the Langmuir adsorption isotherm.

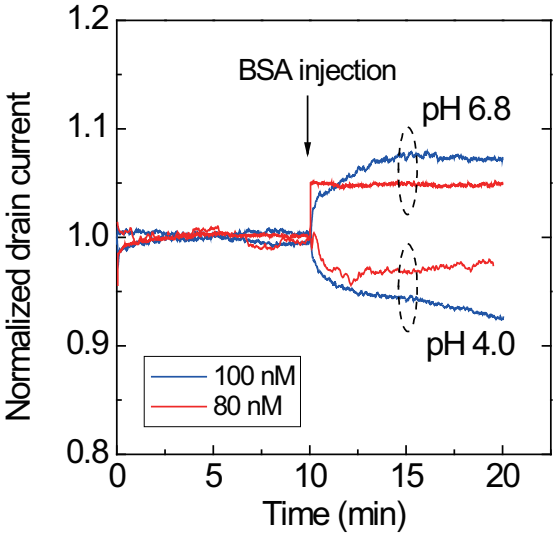

Fig. 11. Time course of normalized I_D for G-FETs at V_D and V_{TGS} of 0.1 and −0.1 V, respectively, in 10-mM phthalate and phosphate buffer solution. Red (blue) lines indicate that 80 (100) nM BSA was added at 10 min.

These results indicate that the graphene channel could detect the charge type of the adsorbed biomolecules. Under the experimental conditions, the carriers in the graphene channel were holes. Therefore, the decreased (increased) I_D observed for BSA in the phthalate (phosphate) buffer solution was a consistent result, because the hole carrier in the graphene channel decreased (increased) as a result of exposure to the positively (negatively) charged proteins. For biosensors based on CNT-FETs, only positive charged biomolecules can be detected, owing to their *p*-type semiconductor band characteristics(Yamamoto et al., 2010). In contrast, the G-FETs can detect positively and negatively charged biomolecules because a Schottky barrier does not form at the interface between the electrodes and graphene, owing to its the zero-gap semiconductor characteristics. Furthermore, the absolute value of the drain current is larger than that of carbon nanotube devices, indicating their robustness to noise.

In this work, the conductance changes by BSA adsorption were quite small. Three possible interpretations can be considered for the small conductance changes. One interpretation is due to the electrode-graphene contact resistance. Although two-terminal measurement was used in this experiment, four-terminal measurement is needed to ignore the contact resistance fluctuations. Another interpretation is due to desorption of the BSA molecules. Protein sensing using specific protein detection such as antigen-antibody effect is efficiency to interrupt the BSA desorption. The other interpretation is due to the difference between isoelectric point of the BSA (=5.6) and solution pH (=6.8) is relatively small. This small difference may lead some uncharged amino acid of the BSA molecules. Moreover, it is important to clarify where the charge transfer occurs and surface area dependence of the protein adsorption. These subjects should be investigated to develop the biomolecule detector using G-FETs.

The G-FETs can reuse after measuring of protein adsorption. Figure 12 shows the optical micrographs of a G-FET after exposing the several μM BSA (a) and after washing the proteins

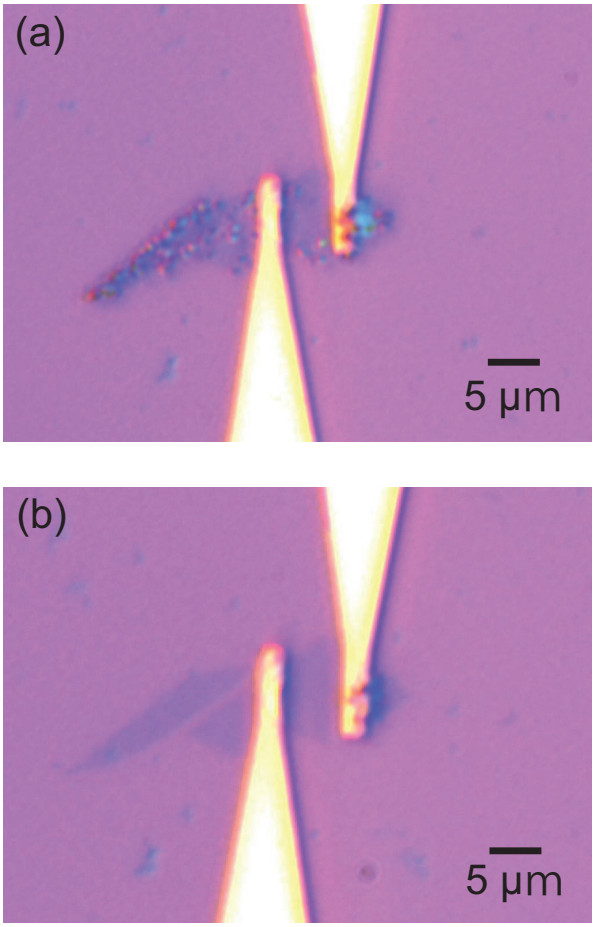

Fig. 12. Optical micrograph of a G-FET (a) after exposing proteins and (b) washing the proteins by acid and alkali solutions.

by acid and alkali solutions (b). Many bright points indicate the adsorbed proteins onto the graphene surface, and only these proteins disappeared after washing by sulfuric acid and sodium hypochlorite solution. The graphene flakes have not been broken by these solutions, indicating their high stability. And after the washing process, the G-FET can reuse as a sensor. These results indicate that the G-FETs have high potentials for the chemical and biological sensors.

3.4 Comparison of the CNT-FETs and G-FETs

Finally, comparison of the sensing characteristics of CNT-FETs and G-FETs are briefly described. The important requirements of materials for the sensing device are the charge sensitivity and stability. Since the charge sensitivity is strongly depends on the surface to volume ratio, it can be considered that the CNT-FETs have better charge sensitivity than G-FETs. On the contrary, the stability of G-FETs is superior to the CNT-FETs. Their absolute

value of the drain current is as high as several ten μA, which is more than 1000 times larger than those of CNT-FETs. This large drain current indicates the robustness for the noise during the sensing measurements. The stable devices carry more credibility. And chirality-controlled CNT growth technique, which leads the stable FET characteristics, has not been achieved at present. This problem makes it difficult to fabricate the integrated sensors based on CNT-FETs. In the case of G-FETs, the development of growth technique of graphene is the key technology. Very recent reports says the roll-to-roll production of 30-inch graphene films can be grown by CVD system(Bae et al., 2010). Such large-scale graphene growth technique will lead large-scale integrated and multiple sensors based on G-FETs. Because both CNT-FETs and G-FETs have superior characteristics for the sensing applications each other, it is important to use them according to the situations.

4. Conclusion

We have investigated chemical and biological sensors using G-FETs. Single-layer graphene was obtained by a micro-mechanical cleavage method. Changes in the solution pH were electrically detected with a lowest detection limit (signal/noise = 3) of the 0.025. Their I_D showed protein-concentration dependence and their I_D changes with BSA concentration were fitted well by the Langmuir adsorption isotherm. In addition, the G-FETs clearly detected the different charge types of a biomolecule owing to its isoelectric point. G-FETs are promising devices for highly sensitive chemical and biological sensors. In near future, we try to evaluate the selective protein sensing using the G-FETs.

5. References

Abe, M., Murata, K., Ataka, T. & Matsumoto, K. (2008). Calibration method for a carbon nanotube field-effect transistor biosensor, *Nanotechnology* 19: 045505.

Alwarappan, S., Erdem, A., Liu, C. & Li, C.-Z. (2009). Probing the Electrochemical Properties of Graphene Nanosheets for Biosensing Applications, *J. Phys. Chem. C* 113: 8853–8857.

Arsat, R., Breedon, M., Shafiei, M., Spizziri, P., Gilje, S., Kaner, R., Kalantar-zadeh, K. & Wlodarski, W. (2009). Graphene-like nano-sheets for surface acoustic wave gas sensor applications, *Chem. Phys. Lett.* 467: 344–347.

Bae, S., Kim, H., Lee, Y., Xu, X., Zheng, J.-S. P. Y., Balakrishnan, J., Lei, T., Kim, H. R., Song, Y. I., Kim, Y.-J., Kim, K. S., Özyilmaz, B., Ahn, J.-H., Hong, B. H. & Iijima, S. (2010). Roll-to-roll production of 30-inch graphene films for transparent electrodes, *Nat. Nanotechnol.* 5: 574–578.

Besteman, K., Lee, J.-O., Wiertz, F. G. M., Heering, H. A. & Dekker, C. (2003). Enzyme-Coated Carbon Nanotubes as Single-Molecule Biosensors, *Nano Lett.* 3: 727–730.

Blake, P., Hill, E. W., Neto, A. H. C., Novoselov, K. S., Jiang, D., Yang, R., Booth, T. J. & Geim, A. K. (2007). Making graphene visible, *Appl. Phys. Lett.* 91: 063124.

Chen, R. J., Bangsaruntip, S., Drouvalakis, K. A., Kam, N. W. S., Shim, M., Li, Y., Kim, W., Utz, P. J. & Dai, H. (2003). Noncovalent functionalization of carbon nanotubes for highly specific electronic biosensors, *Proc. Natl. Acad. Sci.* 100: 4984–4989.

Chen, Z., Appenzeller, J., Knoch, J., lin, Y. & Avouris, P. (2005). The Role of Metal-Nanotube Contact in the Performance of Carbon Nanotube Field-Effect Transistors, *Nano Lett.* 5: 1497–1502.

Cui, Y., Wei, Q., Park, H. & Lieber, C. M. (2001). Nanowire Nanosensors for Highly Sensitive and Selective Detection of Biological and Chemical Species, *Science* 293: 1289–1292.

Dan, Y., Lu, Y., Kybert, N. J., Luo, Z. & Johnson, A. T. C. (2009). Intrinsic Response of Graphene Vapor Sensors, *Nano Lett.* 9: 1472–1475.

Das, A., Pisana, S., Chakraborty, B., Piscanec, S., Saha, S. K., Waghmare, U. V., Novoselov, K. S., Krishnamurthy, H. R., Geim, A. K., Ferrari, A. C. & Sood, A. K. (2008). Monitoring dopants by Raman scattering in an electrochemically top-gated graphene transistor, *Nat. Nanotechnol.* 3: 210–215.

Ferrari, A. C., Meyer, J. C., Scardaci, V., Casiraghi, C., Lazzeri, M., Mauri, F., Piscanec, S., Jiang, D., Novoselov, K. S., Roth, S. & Geim, A. K. (2006). Raman Spectrum of Graphene and Graphene Layers, *Phys. Rev. Lett.* 97: 187401.

Fowler, J. D., Allen, M. J., Tung, V. C., Yang, Y., Kaner, R. B. & Weiller, B. H. (2009). Practical Chemical Sensors from Chemically Derived Graphene, *ACS Nano* 3: 301–306.

Geim, A. K. & Novoselov, K. S. (2007). The rise of graphene, *Nat. Mater.* 6: 183–191.

Gelmont, B., Shur, M. S. & Mattauch, R. J. (1995). Disk and Stripe Capacitances, *Solid-State Elec.* 38: 731–734.

Ishikawa, F. N., Chang, H.-K., Curreli, M., Liao, H.-I., Olson, C. A., Chen, P.-C., Zhang, R., Roberts, R. W., Sun, R., Cote, R. J., Thompson, M. E. & Zhou, C. (2010). Label-Free, Electrical Detection of the sars Virus N-Protein with Nanowire Biosensors Utilizing Antibody Mimics as Capture Probes, *ACS nano* 3: 1219–1224.

Lee, K., Kwon, J. H., Cho, S. M. W. S., Ju, B. K. & Lee, Y. H. (2007). pH sensitive multiwalled carbon nanotubes, *Mat. Lett.* 61: 3201–3203.

Li, C., Curreli, M., Lin, H., Lei, B., Ishikawa, F. N., Datar, R., Cote, R. J., Thompson, M. E. & Zhou, C. (2005). Complementary Detection of Prostate-Specific Antigen Using In_2O_3 Nanowires and Carbon Nanotubes, *J. Am. Chem. Soc.* 127: 12484–12485.

Lu, G., Ocola, L. E. & Chen, J. (2009). Gas detection using low-temperature reduced graphene oxide sheets, *Appl. Phys. Lett.* 94: 083111.

Lu, J., Drzal, L. T., Worden, R. M. & Lee, I. (2007). Simple Fabrication of a Highly Sensitive Glucose Biosensor Using Enzymes Immobilized in Exfoliated Graphite Nanoplatelets Nafion Membrane, *Chem. Mater.* 19: 6240–6246.

Maehashi, K., Katsura, T., Kerman, K., Takamura, Y., Matsumoto, K. & Tamiya, E. (2007). Label-Free Protein Biosensor Based on Aptamer-Modified Carbon Nanotube Field-Effect Transistors, *Anal. Chem.* 79: 782–787.

Maehashi, K., Matsumoto, K., Kerman, K., Takamura, Y. & Tamiya, E. (2004). Ultrasensitive Detection of DNA Hybridization Using Carbon Nanotube Field-Effect Transistors, *Jpn. J. Appl. Phys.* 43: L1558–L1560.

Maehashi, K., Matsumoto, K., Takamura, Y. & Tamiya, E. (2009). Aptamer-Based Label-Free Immunosensors Using Carbon Nanotube Field-Effect Transistors, *Electroanalysis* 21: 1285–1290.

Maehashi, K., Ohno, Y., Inoue, K. & Matsumoto, K. (2004). Chirality selection of single-walled carbon nanotubes by laser resonance chirality selection method, *Appl. Phys. Lett.* 85: 858–860.

Martnez, M. T., Tseng, Y.-C., Ormategui, N., Loinaz, I., Eritja, R. & Bokor, J. (2009). Label-Free dna Biosensors Based on Functionalized Carbon Nanotube Field Effect Transistors, *Nano Lett.* 9: 530–536.

Meric, I., han, M. Y., Young, A. F., Ozyilmaz, B., Kim, P. & Shepard, K. L. (2008). Current saturation in zero-bandgap, topg-ated graphene field-effect transistors, *Nat. Nanotechnol.* 3: 654–659.

Minot, E. D., Janssens, A. M., Heller, I., Dekker, H. A. H. C. & Lemay, S. G. (2007). Carbon nanotube biosensors: The critical role of the reference electrode, *Appl. Phys. Lett.* 91: 093507.

Mohanty, N. & Berry, V. (2008). Graphene-Based Single-Bacterium Resolution Biodevice and Dna Transistor: Interfacing Graphene Derivatives with Nanoscale and Microscale Biocomponents, *Nano Lett.* 8: 4469–4476.

Nagashio, K., Nishimura, T., Kita, K. & Toriumi, A. (2008). Mobility Variations in Mono- and Multi-Layer Graphene Films, *Appl. Phys. Express* 2: 025003.

Novoselov, K. S., Geim, A. K., Morozov, S. V., Jiang, D., Zhang, Y., Dubonos, S. V., Grigorieva, I. V. & Firsov, A. A. (2004). Electric Field Effect in Atomically Thin Carbon Films, *Science* 306: 666–669.

Ohno, Y., Maehashi, K., Yamashiro, Y. & Matsumoto, K. (2009). Electrolyte-gated graphene field-effect transistors for detecting ph and protein adsorption, *Nano Lett.* 9: 3318–3322.

Palaniappan, A., Goh, W. H., Tey, J. N., Wijaya, I. P. M., Moochhala, S. M., Liedberg, B. & Mhaisalkar, S. G. (2010). Aligned carbon nanotubes on quartz substrate for liquid gated biosensing, *Biosens. Bioelectron.* 25: 1989–1993.

Pan, H., Feng, Y. P. & Lin, J. Y. (2004). Ab initio study of OH-functionalized single-wall carbon nanotubes, *Phys. Rev. B* 70: 245425.

Qazi, M., Vogt, T. & Koley, G. (2007). Trace gas detection using nanostructured graphite layers, *Appl. Phys. Lett.* 91: 233101.

Robinson, J. T., Perkins, F. K., Snow, E. S., Wei, Z. & Sheehan, P. E. (2008). Reduced Graphene Oxide Molecular Sensors, *Nano Lett.* 8: 3137–3140.

Rosenblatt, S., Yaish, Y., Park, J., Gore, J., Sazonova, V. & McEuen, P. L. (2002). High Performance Electrolyte Gated Carbon Nanotube Transistors, *Nano Lett.* 2: 869–872.

Saito, R., Dresselhaus, G. & Dresselhaus, M. S. (1998). *Physical Properties of Carbon Nanotubes*, Imperial College Press, London.

Schedin, F., Geim, A. K., Morozov, S. V., Hill, E. W., Blake, P., Katsnelson, M. I. & Novoselov, K. S. (2007). Detection of individual gas molecules adsorbed on graphene, *Nat. Mater.* 6: 652–655.

Shan, C., Yang, H., Song, J., Han, D., Ivaska, A. & Niu, L. (2009). Direct Electrochemistry of Glucose Oxidase and Biosensing for Glucose Based on Graphene, *Anal. Chem.* 81: 2378–2382.

Shang, N. G., Papakonstantinou, P., McMullan, M., Chu, M., Stamboulis, A., Potenza, A., Dhesi, S. S. & Marchetto, H. (2008). Catalyst-Free Efficient Growth, Orientation and Biosensing Properties of Multilayer Graphene Nanoflake Films with Sharp Edge Planes, *Adv. Funct. Mater.* 18: 3506–3514.

Star, A., Gabriel, J.-C. P., Bradley, K. & Grüner, G. (2003). Electronic Detection of Specific Protein Binding Using Nanotube fet Devices, *Nano Lett.* 3: 459–463.

Wu, H., Wang, J., Kang, X., Wang, C., Wang, D., Liu, J., Aksay, I. A. & Lin, Y. (2009). Glucose biosensor based on immobilization of glucose oxidase in platinum nanoparticles/graphene/chitosan nanocomposite film, *Talanta* 80: 403–406.

Yamamoto, Y., Ohno, Y., Maehashi, K. & Matsumoto, K. (2009). Noise Reduction of Carbon Nanotube Field-Effect Transistor Biosensors by Alternating Current Measurement, *Jpn. J. Appl. Phys.* 48: 06FJ01.

Yamamoto, Y., Ohno, Y., Maehashi, K. & Matsumoto, K. (2010). Electrical Detection of Negatively Charged Proteins Using n-Type Carbon Nanotube Field-Effect Transistor Biosensors, *Jpn. J. Appl. Phys.* 49: 02BD10.

Yang, W., Ratinac, K. R., Ringer, S. P., Thordarson, P., Gooding, J. J. & Braet, F. (2010). Carbon Nanomaterials in Biosensors: Should You Use Nanotubes or Graphene?, *Angew. Chem., Int. Ed.* 49: 2114–2138.

Zheng, G., Patolsky, F., Cui, Y., Wang, W. U. & Lieber, C. M. (2005). Multiplexed electrical detection of cancer markers with nanowire sensor arrays, *Nat. Biotechnol.* 23: 1294–1301.

23

Graphene-Supported Platinum and Platinum-Ruthenium Nanoparticles for Fuel Cell Applications

Lifeng Dong[1,2], Qianqian Liu[1], Li Wang[2] and Kezheng Chen[2]
[1]*Department of Physics, Astronomy, and Materials Science, Missouri State University,*
[2]*College of Materials Science and Engineering,*
Qingdao University of Science and Technology,
[1]*U.S.A.*
[2]*P. R. China*

1. Introduction

As one of the most promising alternative energies, fuel cells have been receiving increased attention recently due to the depletion of fossil fuels and the increase in environmental pollution. Among different types of fuel cells, direct ethanol fuel cells (DEFCs) and direct methanol fuel cells (DMFCs) are excellent power sources due to their high energy density, low pollutant emission, low operating temperature, and ease of handling liquid ethanol/methanol fuel (Lamy et al., 2002; Long et al., 2000; Maillard et al., 2003). However, critical obstacles remain that inhibit broad applications of DEFCs and DMFCs, including low electrocatalytic activity of anode/cathode electrodes and the high cost of noble metal, platinum (Pt)-based catalysts. In order to enhance catalytic activity and to reduce the usage of Pt-based catalysts, one strategy is to explore novel carbon materials as catalyst supports and to effectively disperse Pt-based particles on these supports (Chen et al., 2007; Sanganna Gari et al., 2010; Girishkumar et al., 2006; Halder et al., 2009; Maiyalagan, 2008; Selvaraj & Alagar, 2007; Rajesh et al., 2003; Tang et al., 2004; Tsai et al., 2006; Zhao et al., 2004). Vulcan XC-72R carbon black has been the most widely-used catalyst support for the preparation of fuel cell catalysts because of its exceptional electronic conductivity and surface area (Guo et al., 2008; Lin et al., 2005; Maiyalagan et al., 2005). During the past several years, a few research groups have investigated graphene, one type of novel carbon nanostructures, as a catalyst support and have demonstrated that graphene can improve the electrocatalytic activity of Pt nanoparticles more effectively for methanol and ethanol oxidation than Vulcan XC-72R carbon black (Dong et al., 2010; Seger et al., 2009; Yoo et al., 2009).

In this chapter, a series of atomic force microscopy (AFM) and electron microscopy techniques, including scanning electron microscopy (SEM) and scanning transmission electron microscopy (STEM), were employed to characterize the morphology of Pt nanoparticles, platinum-ruthenium (Pt-Ru) nanoparticles, and graphene sheets as well as the distribution of Pt and Pt-Ru nanoparticles on the graphene supports. Effects of graphene supports on electrocatalytic activity of Pt and Pt-Ru nanoparticles for methanol and ethanol oxidations were investigated using cyclic voltammetry. In comparison to Vulcan XC-72R

carbon black, graphene-supported Pt and Pt-Ru catalysts demonstrate better electrocatalytic activities in terms of oxidation potential, forward oxidation peak current density, and the ratio of forward peak current density to reverse peak current density. This study indicates that graphene can serve as an effective catalyst support for both direct methanol and ethanol fuel cells. These systematic characterizations provide detailed information on the morphology and structures of Pt and Pt-Ru nanoparticles supported on graphene sheets, and this information will help to design and synthesize graphene-supported Pt/Pt-Ru nanoparticles for fuel cell applications.

2. Structural characterization and electrocatalytic measurements

2.1 Synthesis of Pt and Pt-Ru nanoparticles

For the synthesis of graphene-supported Pt and Pt-Ru catalysts, 1 g of graphene oxide powder was dispersed in 100 ml of ethylene glycol (EG) and sonicated for 30 min (Li et al., 2003). Graphene oxide was prepared from graphite powder in accordance with the Hummers-Offeman method (Hummers et al., 1958). Hexachloroplatinic EG solution (15 ml) (7.4 mg H_2PtCl_6 per ml of EG) was added into the graphene oxide solution and mechanically stirred for 2 h. Sodium hydroxide was added to adjust the pH of the solution to 11.0, and then the solution was fluxed under flowing argon at 130 °C for 3 h. The solid was filtered, washed with deionized water, and dried in an oven at 80 °C for 12 h. For the synthesis of graphene-supported Pt-Ru catalysts, the only difference was to add 15 ml of EG solution, including both H_2PtCl_6 and ruthenium chloride ($RuCl_3$) (7.4 mg H_2PtCl_6 and 7.4 mg $RuCl_3$ per ml of EG) into the graphene oxide solution. Similar procedures were used to prepare carbon black (Vulcan XC-72R) supported Pt and Pt-Ru catalysts.

2.2 Electron microscopy and microanalysis

The morphology of Pt and Pt-Ru nanoparticles and their distributions on carbon black and graphene were investigated using an FEI Quanta 200 field emission scanning electron microscope (FESEM). The FESEM system is equipped with an Everhart-Thornley secondary electron detector (SED), a low-vacuum SED, a gaseous SED, a backscattered electron detector (BSED), a scanning transmission electron microscopy detector (STEM), and an Oxford INCA 250 silicon drift X-ray energy dispersive spectrometer (EDS).

2.3 Atomic force microscopy

A Multimode Nanoscope IIIa atomic force microscopy (AFM) system was used to examine surface characteristics of graphene sheets and nanoparticles supported on the graphene sheets. The AFM system was equipped with an E-type scanner and a standard silicon cantilever with a length of 115-135 μm and a tip radius less than 10 nm. All images were obtained using tapping mode in air at room temperature with a 1.0 Hz scan rate, a 0^o scan angle, and a 261.0 Hz tapping frequency. Both topographical and phase images were captured for each real-time scan. Nanoscope III 6.13rl software was used for off-line image flattening and analysis.

2.4 Electrocatalytic activity measurements

Electrocatalytic activities of Pt and Pt-Ru nanoparticles on different supports (Vulcan XC-72R carbon black and graphene) were measured in a conventional three-electrode cell using a CHI

600C electrochemical work station. Ag/AgCl served as a reference electrode, Pt wire as a counter electrode, and glassy carbon coated with carbon black- and graphene-supported nanoparticles as a working electrode. For the preparation of a working electrode, 3.8 mg of catalyst powder was dispersed in 1 ml of ethanol solution and sonicated for 30 min; 30 μl of the suspension was placed onto the surface of a glassy carbon electrode and dried for 15 min; and 10 μl of 5% Nafion 117 solution was sequentially applied and dried for 15 min.
Electrocatalytic oxidation of methanol on graphene and carbon black-supported Pt and Pt-Ru nanoparticles was measured in 1 M CH_3OH + 0.5 M H_2SO_4 electrolyte by cyclic voltammetry between -0.3 V and 1.0 V. The potentials were measured and reported with respect to the Ag/AgCl electrode. After methanol oxidation measurements, the electrodes were stored in distilled water for 30 min prior to ethanol oxidation measurements. Electrocatalytic oxidation of ethanol was measured in 1 M CH_3CH_2OH + 0.5 M H_2SO_4 electrolyte by cyclic voltammetry between -0.3 V and 1.0 V. Prior to electrochemical characterizations, all electrolyte solutions were de-aerated under flowing nitrogen gas for 20 min. Electrical current density was calculated by normalizing electrical current on the surface of 3 mm diameter glassy carbon electrodes.
In order to ensure the reproducibility of experimental results, all electrocatalyst powders, including graphene- and carbon black-supported Pt and Pt-Ru nanoparticles, were synthesized three times; the same amount of catalytic powder was cautiously loaded onto the electrodes.

3. Electron microscopy study of Pt nanoparticles

Pt-Ru nanoparticles were synthesized using the same procedures and the same reaction parameters as for Pt nanoparticles, and thereby had similar morphology and similar distributions on catalytic supports (graphene and carbon black) compared to Pt nanoparticles. In this study, we report only the study of the morphology of Pt nanoparticles and their distributions on catalytic supports using electron microscopy and atomic force microscopy.

3.1 Scanning electron microscopy characterization

The Everhart-Thornley secondary electron detector and the solid state backscattered electron detector are the two most commonly-used detectors for a scanning electron microscope (SEM). Low energy SEs (less than 50 eV, with a most probable energy of 3 – 5 eV) are emitted from the surface and immediate sub-surface of a specimen and provide information regarding the surface topography of the specimen; high energy BSEs reveal areas having different chemical compositions because heavy elements with high atomic number backscatter incident electrons more strongly than light elements with low atomic number (Goldstein et al., 2003). For a sample characterization using SE/BSE detectors, nanoparticle powder was directly affixed onto the surface of double-stick conductive copper tape, which in turn was attached to an aluminum SEM sample stub.
Fig. 1a and Fig. 1c are SE images of Pt nanoparticles supported on graphene and carbon black, respectively. Graphene sheets are rippled and crumpled, with a dimension of several hundred nm to several μm; Vulcan XC-72R carbon black supports are spherical particles with a dimension of 30 nm to 100 nm. Few small particles exist on the surface of both graphene and carbon black supports, yet it is difficult to identify the locations of these particles due to weak contrast between small particles and their supports. However, simultaneously obtained BSE images (Fig. 1b and Fig. 1d) clearly reveal the dimension and

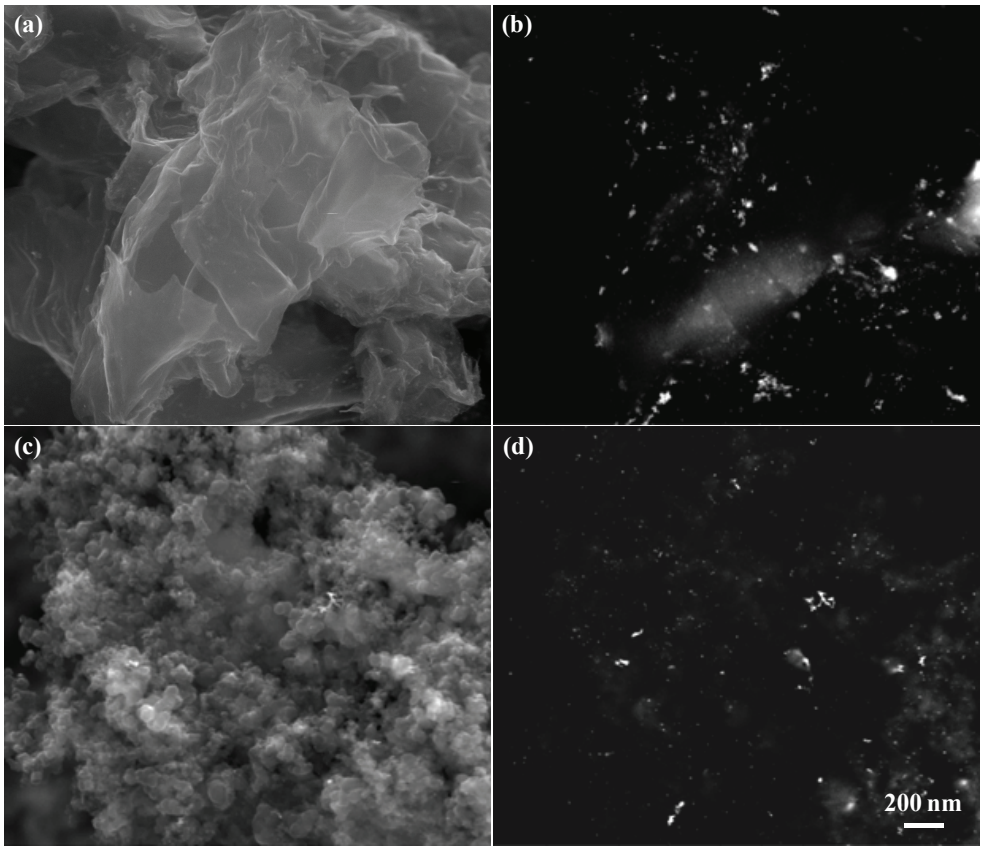

Fig. 1. SE (a, c) and BSE (b, d) images recorded simultaneously from Pt nanoparticles supported on graphene and carbon black, respectively. SE images demonstrate the surface morphology of graphene and carbon black, while the Z-contrast effect in the BSE imaging permits identification of Pt nanoparticles. All images were acquired at the same magnification for comparison.

distribution of those particles on the surface of graphene and carbon black, an observation which confirms that BSE imaging is a Z-contrast technique that yields compositional contrast information. Atomic numbers Z for Pt and C are 78 and 6, respectively. The signal from the BSE detector is proportional to the backscatter coefficient, which nearly monotonically increases with increasing Z. In Fig. 1b and Fig. 1d, the higher Z particles appear brighter than the lower Z background structures. The bright particles are Pt nanoparticles with a size of less than 10 nm. These nanoparticles are difficult to identify in SE images (Fig. 1a and Fig. 1c). SE images reveal the morphology and dimension of graphene and carbon black supports, while BSE images demonstrate the morphology and distribution of Pt nanoparticles associated with the surface of the graphene and carbon black support materials. SE and BSE imaging are complementary concurrent techniques for the characterization of Pt nanoparticles and supporting materials.

3.2 Scanning transmission electron microscopy characterization

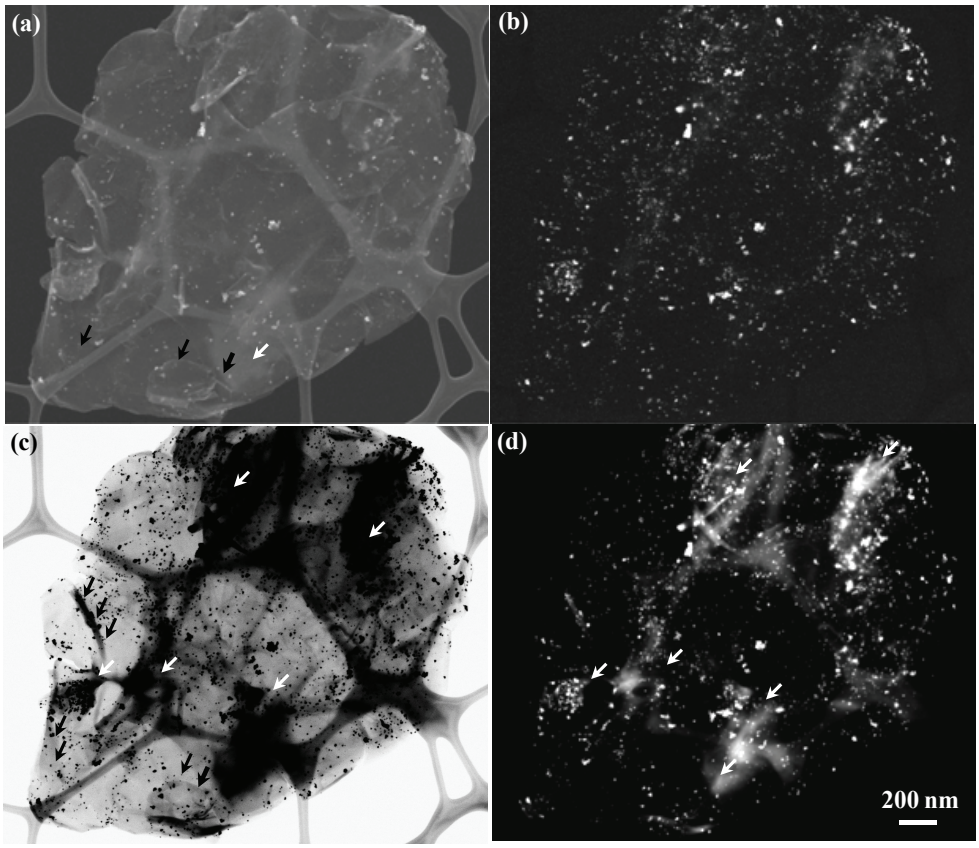

Fig. 2. Pt nanoparticles supported on graphene sheets were simultaneously imaged with SE (a), BSE (b), STEM-BF (c), and STEM-HAADF (d) detectors. Different detectors concurrently reveal different information regarding the morphology of graphene sheets and Pt nanoparticles as well as the distribution of Pt nanoparticles on the graphene sheets. Multiple graphene layers, white arrows; sheet folds and very few graphene layers, black arrows.

With the development of technology and improved manufacturing techniques, SEMs are more commonly equipped with a STEM detector for revealing internal structures of a specimen. A retractable STEM detector, attached to the FEI Quanta 200 FESEM system, consists of three different modes of detection: bright field (BF), dark field (DF), and high angle annular dark field (HAADF). The STEM-BF detector collects electrons transmitted through the specimen. Both mass-thickness and diffraction contrast contribute to the BF image formation; the STEM-DF detector gathers electrons diffracted in crystalline areas and incoherent Rutherford scattering electrons; and the STEM-HAADF detector collects electrons scattered to high angles (50 to 200 mrad) where the scattering is predominately incoherent Rutherford scattering and roughly proportional to the square of the atomic number (Z). SE and BSE in combination with STEM-BF/DF/HAADF provide information

about the surface and throughout the specimen at the same time. One prerequisite for STEM imaging is that the specimen needs to be thin enough to enable the transmission of incident electrons. Usually, the thickness of the specimen is less than 100 nm. For a sample characterization using SE/BSE/STEM-BF/STEM-HAADF, sample powder was dispersed in an ethanol solution and sonicated for 5 min. Several drops of suspension were transferred subsequently onto a holey carbon film supported on a 3 mm copper grid.

As given in Fig. 2, SE, BSE, STEM-BF, and STEM-HAADF images of Pt nanoparticles supported on graphene sheets demonstrate different characteristics of various imaging techniques. A graphene sheet is a single atomic layer of carbon, which is thin enough to allow incident electrons to pass completely through it (Girit et al., 2009; Novoselov et al., 2004; Novoselov et al., 2005; Zhang et al., 2005). All four images in Fig. 2, which are different from the images in Fig.1, illustrate the distribution of Pt nanoparticles on the surfaces of graphene sheets. Different imaging techniques have their unique advantages for morphology and structural characterization. For instance, an SE image (Fig. 2a) shows several small pieces of graphene sheets (200 nm to 500 nm) and some small particles that exist on the surface of a large piece of graphene sheet (around 2.5 μm). In comparison to Fig. 2a, Z-contrast BSE image (Fig. 2b) clearly demonstrates the dimension and distribution of Pt nanoparticles, but no information on graphene sheets. However, STEM-BF imaging (Fig. 2c) provides information on both graphene sheets and Pt nanoparticles' dimension and distribution. In addition, STEM-BF imaging qualitatively provides information on the thickness of those graphene sheets: some areas with dark contrast resulted from their large thickness. These areas were too thick to allow incident electrons to pass through them and thereby, no information on Pt nanoparticles could be revealed in these regions (marked by white arrows in Fig. 2c); graphene sheets with a few layers or folded layers show gray contrast (marked by black arrows in Fig. 2c). In comparison to BSE imaging (Fig. 2b), Z-contrast STEM-HAADF imaging (Fig. 2d) provides similar information on Pt nanoparticles but some additional information about the thickness of graphene sheets: some thick regions appear brighter than surrounding backgrounds due to multi-scattering of electrons in multi-layers of graphene sheets (marked by white arrows in Fig. 2d).

Therefore, in comparison to conventional SE/BSE imaging, STEM-BF/HAADF imaging in combination with SE/BSE detectors provides much more information on the morphology of graphene sheets and nanoparticles as well as the distribution of nanoparticles on the surface of graphene sheets and their inside layers. A next step for electron microscopy characterization is to explore interactions between Pt nanoparticles and graphene supports through atomic imaging of their interfaces using transmission electron microscopy (TEM)/STEM with a high acceleration voltage (e.g., 200 kV) or aberration-corrected TEM/STEM (Dong, 2009; Pennycook et al., 2009; Zhu et al., 2009).

4. Atomic force microscopy characterization of Pt nanoparticles

Tapping mode atomic force microscopy (AFM) provides information about surface structure of a sample through topographical imaging and phase imaging. As illustrated in Fig. 3a, some individual particles and small clusters consisting of several particles exist on the surfaces of graphene sheets. A height line profile (Fig. 3c), recorded along two nanoparticles (marked as a dashed line in Fig. 3a), shows the dimensions of Pt nanoparticles were approximately 6 nm to 8 nm. The dimension and distribution of nanoparticles on graphene sheets are consistent with those observed using SEM/STEM. Beyond topographical

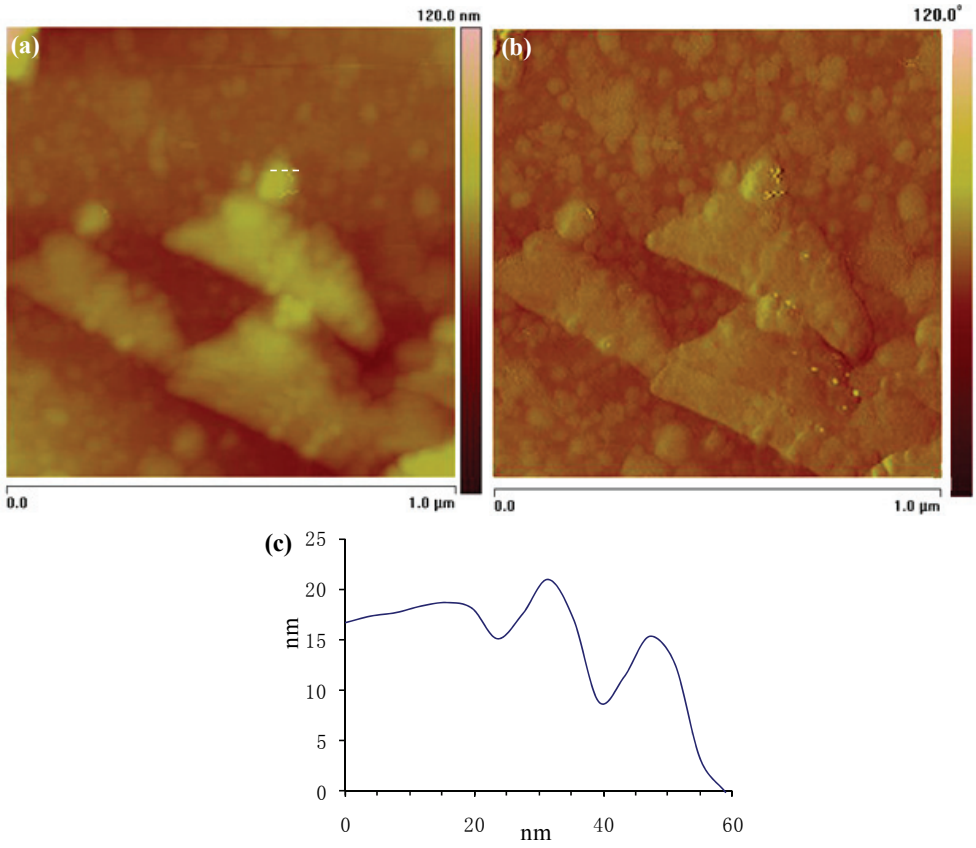

Fig. 3. AFM topography (a) and phase (b) images of Pt nanoparticles supported on graphene sheets. A line height profile (c), recorded along two nanoparticles (marked as a dashed line in Fig. 3a), shows that the dimensions of Pt nanoparticles were approximately 6 nm to 8 nm.

information, phasing imaging detects variations in composition, viscoelasticity, adhesion, and others, since these parameters affect the phase of the oscillation of a cantilever (Liu et al., 2009; Tamayo & Garcia, 1997). In comparison to topographical imaging (Fig. 3a), the phase imaging in Fig. 3b clearly provides more information on the morphology of Pt nanoparticles and their distribution on graphene sheets. Besides those nanoparticles observed in Fig. 3a, some individual particles with smaller dimensions were revealed through the phase imaging mode. However, it is challenging to obtain detailed information on large pieces of graphene sheets due to their intrinsic tendency to fold and crumple together. AFM also lacks depth of field, yet SEM can have a depth of field of several µm.

5. Electrocatalytic activity for methanol oxidation

The electrocatalytic activity of methanol oxidation on carbon black- and graphene-supported Pt and Pt-Ru nanoparticles was characterized by cyclic voltammetry in an electrolyte of 1 M CH_3OH and 0.5 M H_2SO_4 at 50 mV/s. The voltammograms of each sample

became stable after the fifth cycle. The resulting voltammograms from the fifth cycle are shown in Fig. 4. The efficiencies of the Pt and Pt-Ru nanoparticles on methanol oxidation were compared with regard to oxidation potential, forward oxidation peak current density, and the ratio of the forward peak current density to the reverse peak current density; these data are summarized in Table 1.

Electrode	Forward Sweep		Reverse Sweep		I_F/I_R Ratio
	E (V)	I_F (mA/cm^2)	E (V)	I_R (mA/cm^2)	
Pt-graphene	0.65	19.1	0.46	2.93	6.52
Pt-CB	0.59	9.76	0.43	7.01	1.39
Pt-Ru-graphene	0.50	16.5	-	-	-
Pt-Ru-CB	0.58	5.23	0.36	1.51	3.46

Table 1. Comparison of electrocatalytic activity of methanol oxidation on graphene and carbon black-supported Pt and Pt-Ru nanoparticles.

Graphene-supported Pt nanoparticles have a higher activity for methanol oxidation and a better tolerance to CO in comparison to carbon black-supported Pt nanoparticles (Fig. 4a). On the forward potential sweep, the current increases slowly at lower potentials, then quickly increases at potentials higher than 0.5 V, and oxidation occurs at approximately 0.65 V. The magnitude of the peak current density is directly proportional to the amount of methanol oxidized at the electrode. The peak current density observed with graphene is approximately 19 mA/cm^2, nearly two times the peak current density for carbon black (9.8 mA/cm^2); this result suggests that graphene plays a critical role in promoting methanol oxidation of Pt nanoparticles. In the reverse potential sweep, an oxidation peak is observed around 0.46 V, putatively associated with the removal of CO and other residual carbon species formed on the electrode in the forward sweep. The reverse anodic peak current density (2.93 mA/cm^2) is much lower than those measurements for carbon black (7.01 mA/cm^2). The ratio of the forward anodic peak current density (I_F) to the reverse anodic peak current density (I_R) can be used to describe the tolerance of Pt catalysts to CO and other carbonaceous species. Graphene-supported Pt nanoparticles have a ratio of 6.52, much higher than carbon black-supported Pt nanoparticles (1.39), a result which suggests that graphene-supported Pt nanoparticles generate a more complete oxidation of methanol to carbon dioxide.

As shown in Fig. 4c, the addition of Ru results in a negative shift of oxidation potential of methanol at all two electrodes with the decreasing of I_R and the increase of the I_F to I_R ratio. The oxidation peak potential of methanol was 0.50 V compared with an oxidation of 0.65 V for graphene-Pt nanoparticles. This observation suggests that the presence of Ru can significantly decrease the barrier to methanol oxidation and that Pt-Ru nanoparticles perform in a better fashion than Pt nanoparticles. Conversely, the oxidation potential of methanol at carbon black-supported Pt-Ru nanoparticles minimally shifts 0.02 V (0.58 V to 0.56 V). These data indicate that graphene-supported Pt-Ru may be an ideal candidate for direct methanol fuel cell electrodes. The above data also clearly support the proposition that Ru-Pt nanoparticles can effectively advance the oxidation of methanol to CO_2 and inhibit the accumulation of CO and other carbonaceous species formed on the graphene and carbon black electrodes. For graphene electrodes especially, there is no obvious reverse peak in Fig. 4b. Similar effects of Ru on other catalysts for methanol oxidation have been reported by a number of research groups (Long et al., 2000; Maillard et al., 2003).

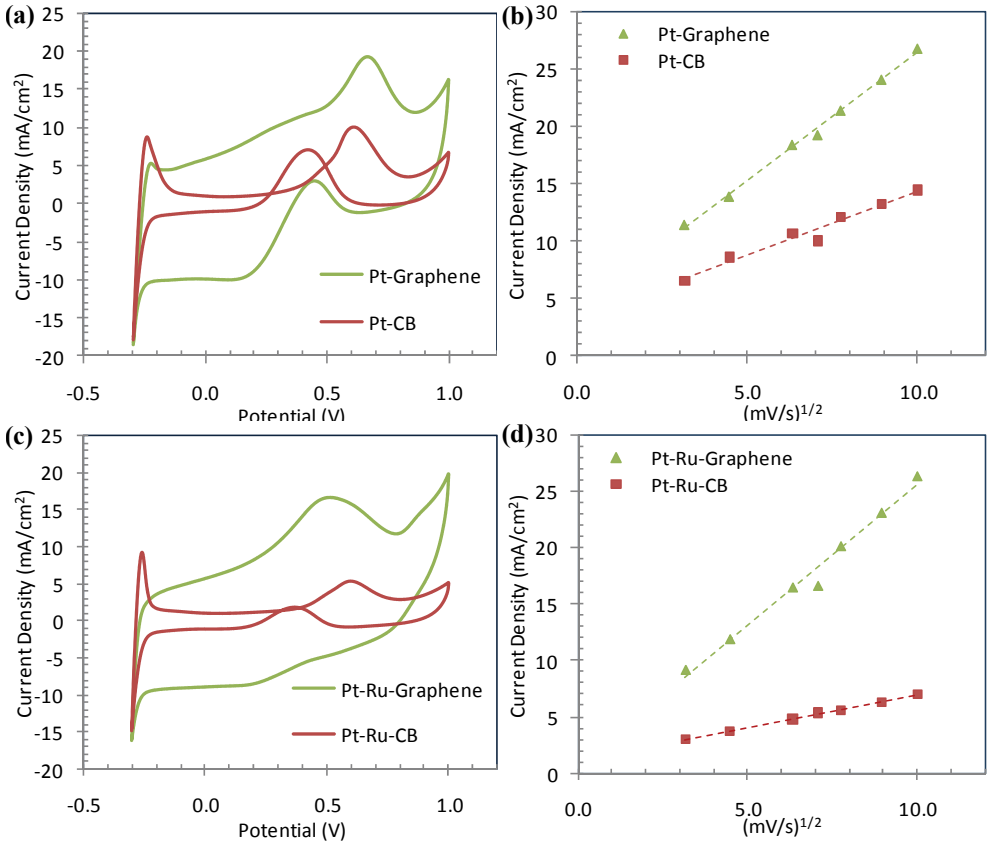

Fig. 4. Electrocatalytic activity of graphene and Vulcan XC-72R carbon black-supported Pt and Pt-Ru nanoparticles for methanol oxidation: cyclic voltammograms of Pt nanoparticles (a) and Pt-Ru nanoparticles (c) in 1 M CH_3OH/0.5 M H_2SO_4 at 50 mV/s between -0.3 V and +1.0 V vs. Ag/AgCl; and the relationship of peak current density vs. scan rate for Pt nanoparticles (b) and Pt-Ru nanoparticles (d).

As given in Fig. 4b and Fig. 4d, for all graphene- and carbon black-supported Pt and Pt-Ru nanoparticles, the forward oxidation current density (I_F) is proportional to the square root of the scan rate, suggesting that the oxidation behavior of methanol at all electrodes is controlled by diffusion processes. The slopes for graphene supports are larger than those for carbon black, indicative of a faster diffusion process of methanol on the surfaces of graphene sheets than that for methanol on the carbon black substrata.

Chronoamperometry was used to characterize the stability of the electrodes for methanol oxidation activity. The current density-time plots of graphene- and carbon black-supported Pt and Pt-Ru nanoparticles in 1 M CH_3OH/0.5 M H_2SO_4 at 0.4 V are shown in Fig. 5. During the 60-min test period, graphene-supported nanoparticles behave in a more stable fashion than those nanoparticles supported on carbon-black, and graphene-supported Pt-Ru nanoparticles were more stable than graphene-supported Pt nanoparticles. These results

suggest that the addition of Ru onto Pt nanoparticles lowers not only oxidation potential (0.65 V to 0.5 V), but also increases the tolerance of Pt nanoparticles to CO and thereby improves the stability of Pt nanoparticles for methanol oxidation.

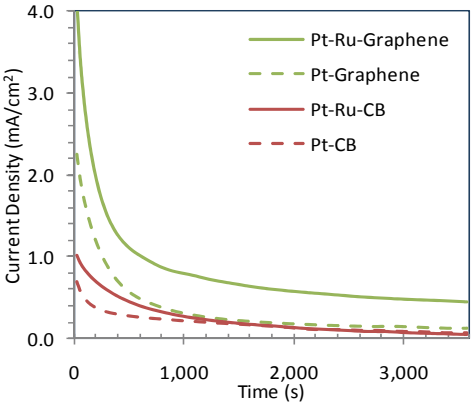

Fig. 5. Chronoamperogram curves for graphene- and carbon black-supported Pt and Pt-Ru nanoparticles in 1 M CH_3OH/0.5 M H_2SO_4. The potential was 0.4 V vs. Ag/AgCl.

6. Electrocatalytic activity for ethanol oxidation

In comparison to direct methanol fuel cells, fuel cells based on direct ethanol oxidation possess several advantages, such as demonstrating enhanced safety, having a higher energy density (8.01 vs. 6.09 kW/kg), and being more easily produced in large quantities from agricultural products and from the fermentation of biomass (Lamy et al., 2002). A complete ethanol electro-oxidation involves the release of 12 electrons per molecule and the cleavage of the C-C bond. Experimental studies have revealed that ethanol is largely and partially oxidized to acetaldehyde and acetic acid (two- and four-electron oxidation, respectively) instead of being fully oxidized (12-electron oxidation) (Wang & Liu, 2007). The ethanol electro-oxidation was considered more complicated than that for methanol, and consequently, needs more active and selective catalysts. In this study, we investigated effects of graphene as a catalyst support for ethanol electro-oxidation of Pt and Pt-Ru nanoparticles in comparison to the extensively-used Vulcan XC-72R carbon black.

Electrode	Forward Sweep		Reverse Sweep		I_F/I_R Ratio
	E (V)	I_F (mA/cm²)	E (V)	I_R (mA/cm²)	
Pt-graphene	0.72	16.2	0.48	4.43	3.66
Pt-CB	0.65	13.8	0.46	15.3	0.90
Pt-Ru-graphene	0.66	18.1	0.46	5.23	3.46
Pt-Ru-CB	0.64	7.50	0.36	4.93	1.52

Table 2. Comparison of electrocatalytic activity of ethanol oxidation on graphene and carbon black-supported Pt and Pt-Ru nanoparticles.

Compared with carbon black, graphene enhances considerably the electrocatalytic activity of Pt nanoparticles for ethanol oxidation by increasing the forward oxidation current density and decreasing the reverse peak current density (Fig. 6 and Table 2). As discussed above, the

I_F to I_R ratio describes the catalyst tolerance to CO-like intermediates formed on electrodes during the forward potential sweep. The high forward peak current density (16.2 mA/cm^2) and the high I_F to I_R ratio (3.66) for graphene-supported Pt nanoparticles indicate that graphene effectively enhances the complete oxidation of ethanol to CO_2, and fewer CO-like carbonaceous species accumulate on the electrode surface. The forward peak current density and the I_F to I_R ratio for carbon black-supported Pt nanoparticles were 16.2 mA/cm^2 and 0.9, respectively. As given in Fig. 6c, the addition of Ru effectively lowers the potentials for ethanol oxidations and increases the I_F to I_R ratios. The oxidation peak potential of ethanol was 0.66 V for graphene-supported Pt-Ru nanoparticles in comparison to an oxidation potential of 0.72 V for graphene-supported Pt nanoparticles, and the potential shift of ethanol oxidation is 0.06 V. However, no significant shifts of oxidation potential for ethanol were observed for carbon black-supported Pt nanoparticles (from 0.65 V to 0.64 V).

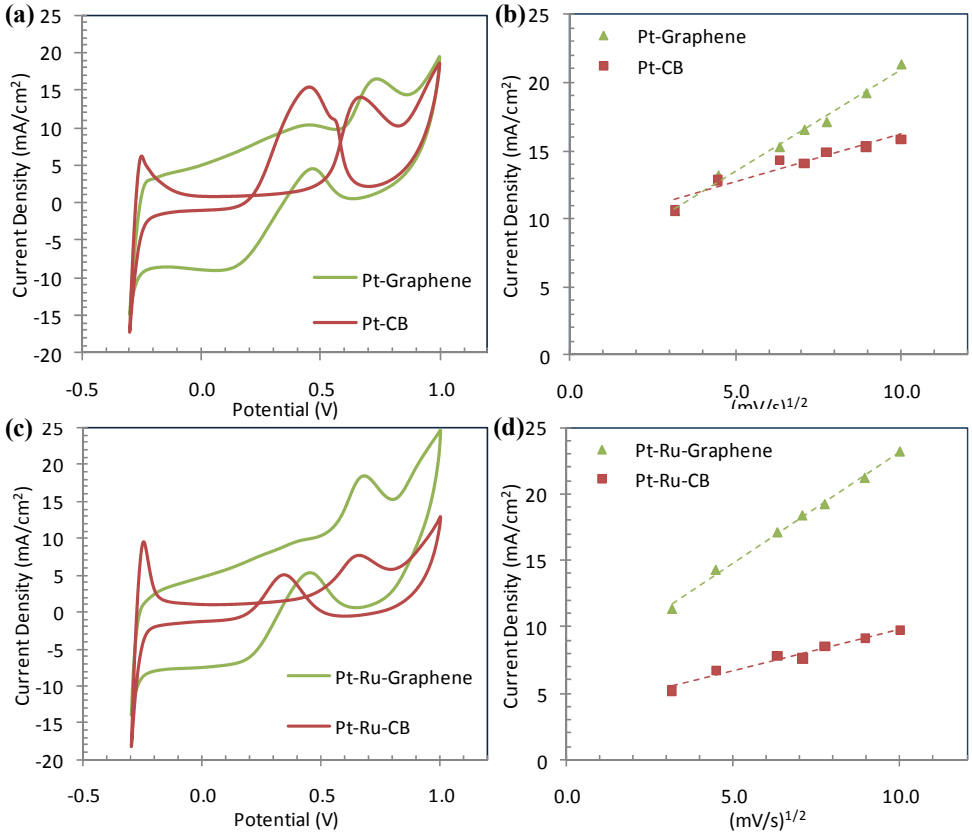

Fig. 6. Electrocatalytic activity of graphene- and Vulcan XC-72R carbon black-supported Pt and Pt-Ru nanoparticles for ethanol oxidation: cyclic voltammograms of Pt nanoparticles (a) and Pt-Ru nanoparticles (c) in 1M CH_3CH_2OH/0.5M H_2SO_4 at 50 mV/s between -0.3 V and +1.0 V vs. Ag/AgCl; the relationship of peak current density vs. scan rate for Pt nanoparticles (b) and Pt-Ru nanoparticles (d).

The forward peak potentials for ethanol oxidation are much higher in comparison to methanol oxidation. For example, the peak potentials for ethanol oxidations on graphene- and carbon black-supported Pt nanoparticles were 0.72 V and 0.65V, respectively; the peak potentials for methanol oxidations on graphene- and carbon black-supported Pt nanoparticles were 0.65 V and 0.59 V, respectively. These results suggest that ethanol oxidation needs more energy than does methanol oxidation. Similar phenomena occur on graphene- and carbon black-supported Pt-Ru nanoparticles (Table 1 and Table 2).

As shown in Fig. 6b and 6d, for both graphene and carbon black-supported Pt and Pt-Ru nanoparticles, the forward oxidation peak current density (I_F) is proportional to the square root of the scan rate, suggesting that the oxidation of ethanol at all electrodes is a diffusion-controlled phenomenon. Graphene has a larger slope than that for carbon black, suggesting that the diffusion efficiency of ethanol inside graphene sheets is higher than that inside carbon black and therefore, can enhance the efficiency and capacity of fuel cells.

The stability of the electrodes for ethanol oxidation was studied using chronoamperometry. The current density-time plots of graphene- and carbon black-supported Pt and Pt-Ru nanoparticles in 1 M CH_3CH_2OH/0.5 M H_2SO_4 at 0.4 V are shown in Fig. 7. Graphene-supported nanoparticles appear to be more stable than those nanoparticles supported on carbon-black, and graphene-supported Pt-Ru nanoparticles were more stable than graphene-supported Pt nanoparticles. Initial current density for carbon black-supported Pt-Ru nanoparticles was higher than that for graphene-supported Pt catalysts, but ethanol oxidation activity on carbon black supports deteriorated more rapidly than that on graphene. After 200 s, graphene-supported Pt nanoparticles demonstrated higher oxidation activity than those supported on carbon-black supports. These results indicate that the addition of Ru onto Pt nanoparticles lowers not only oxidation potential (0.72 V to 0.66 V), but also increases the tolerance of Pt nanoparticles to CO and thereby improves the stability of Pt nanoparticles for ethanol oxidation.

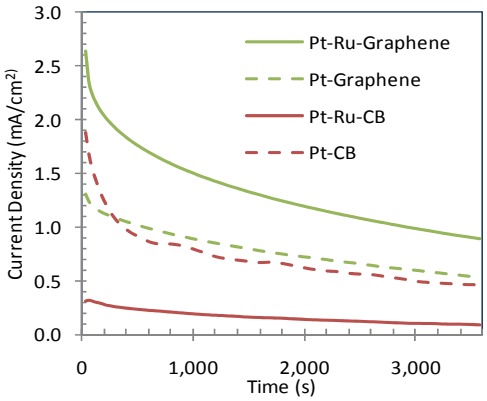

Fig. 7. Chronoamperogram curves for graphene- and carbon black-supported Pt and Pt-Ru nanoparticles in 1 M CH_3CH_2OH/0.5 M H_2SO_4. The potential was 0.4 V vs. Ag/AgCl.

Experimental results on electrocatalytic activity of both methanol and ethanol oxidations clearly demonstrates that graphene-supported Pt and Pt-Ru nanoparticles possess superior electrocatalytic activity compared to Vulcan XC-72R carbon black. Exceptional electrical conductivity and large surface area are two critical parameters for the development of novel

catalyst supports for direct methanol and ethanol fuel cells. Graphene sheets possess both advantages when compared to Vulcan XC-72R carbon black.

7. Conclusion

Different imaging techniques have their various unique advantages for morphology and structural characterization. AFM tapping mode imaging can clearly reveal the morphology of nanoparticles and their distributions on graphene supports; however, it is challenging to image folded or crumpled graphene sheets. In comparison to both AFM imaging and conventional SE/BSE SEM imaging, concurrent STEM/SEM imaging can provide much more detailed information on the morphology of graphene sheets and nanoparticles as well as the distribution of nanoparticles on graphene supports. Future work on electron microscopy characterization will explore interactions between Pt nanoparticles and graphene supports through atomic imaging of their interfaces using high resolution TEM/STEM techniques.

In comparison to Vulcan XC-72R carbon black as a catalyst support, graphene-supported Pt and Pt-Ru nanoparticles have lower oxidation potentials, higher forward oxidation peak current density, higher ratios of forward peak current density to reverse peak current density, and better stability for both methanol and ethanol oxidation. These findings clearly demonstrate that as catalyst supports, graphene can more effectively enhance electrocatalytic activity of Pt and Pt-Ru nanoparticles for the oxidation of methanol and ethanol into CO_2. A next step will be the exploration of a facile and efficient method to synthesize graphene-supported Pt and Pt-Ru nanoparticles with controlled properties, which includes the formation of nanoparticles on defined locations, the density of nanoparticles located on graphene sheets, the size of nanoparticles, and the size and thickness of graphene sheets (Dong, 2009).

8. Acknowledgments

The authors thank Dr. Michael M. Craig for helpful discussions and Raghavendar Reddy Sanganna Gari and Zhou Li for their help with some experiments. This work was partially supported by a Summer Faculty Fellowship from Missouri State University, the American Chemical Society Petroleum Research Fund (47532-GB10), the Cottrell College Science Award from Research Corporation for Science Advancement, and the National Science Foundation (DMR-0821159). L. F. Dong also acknowledges financial support by the Taishan Scholar Overseas Distinguished Professorship program from the Shandong Province Government, P. R. China.

9. References

Chen, C. C.; Chen, C. F.; Chen, C. M. & Chuang, F. T. (2007). Modification of multi-walled carbon nanotubes by microwave digestion method as electrocatalyst supports for direct methanol fuel cell applications. *Electrochemistry Communications,* 9, 159-163.

Dong, L. F. (2009). DNA-templated synthesis of Pt nanoparticles on single-walled carbon nanotubes. *Nanotechnology,* 20, 465602.

Dong, L. F.; Sanganna Gari, R. R.; Li, Z.; Craig, M. M. & Hou, S. F. (2010). Graphene-supported platinum and platinum-ruthenium nanoparticles with high electrocatalytic activity for methanol and ethanol oxidation. *Carbon*, 48, 781-787.

Girishkumar, G.; Hall, T. D.; Vinodgopal, K. & Kamat, P. V. (2006). Single wall carbon nanotube supports for portable direct methanol fuel cells. *Journal of Physical Chemistry B,* 110, 107-114.

Girit, C.; Meyer, J. C.; Erni, R.; Rossell, M. D.; Kisielowski, C.; Yang, L.; Park, C. H.; Crommie, M. F.; Cohen, M. L.; Louie, S. G. & Zettl, A. (2009). Graphene at the edge: stability and dynamics. *Science,* 323, 1705-1708.

Goldstein, J.; Newbury, D. E.; Joy, D. C.; Lyman, C. E.; Echlin, P.; Lifshin, E.; Sawyer, L. & Michael, J. R. (2003). *Scanning Electron Microscopy and X-ray Microanalysis*, Springer, New York.

Guo, Y. L.; Zheng, Y. Z. & Huang, M. H. (2008). Enhanced activity of PtSn/C anodic electrocatalyst prepared by formic acid reduction for direct ethanol fuel cells. *Electrochimica Acta*, 53, 3102-3108.

Halder, A.; Sharma, S.; Hegde, M. S. & Ravishankar, N. (2009). Controlled attachment of ultrafine platinum nanoparticles on functionalized carbon nanotubes with high electrocatalytic activity for methanol oxidation. *Journal of Physical Chemistry C*, 113, 1466-1473.

Hummers, W. S. & Offeman, R. E. (1958). Preparation of graphitic oxide. *Journal of the American Chemical Society,* 80, 1339-1339.

Lamy, C.; Lima, A.; LeRhun, V.; Delime, F.; Cutanceau, C. & Leger, J. M. (2002). Recent advances in the development of direct alcohol fuel cells. *Journal of Power Sources,* 105, 283-296.

Li, W. Z.; Liang, C. H.; Zhou, W. J.; Qiu, J. S.; Zhou, Z. H.; Sun, G. Q. & Qin, X. (2003). Preparation and characterization of multiwalled carbon nanotube-supported platinum for cathode catalysts of direct methanol fuel cells. *Journal of Physical Chemistry B,* 107, 6292-6299.

Lin, Y. H.; Cui, X. L.; Yen, C. H. & Wai, C. M. (2005). PtRu/carbon nanotube nanocomposites synthesized in supercritical fluid: a novel electrocatalyst for direct methanol fuel cells. *Langmuir*, 21, 11474-11479.

Liu, H.; Fu, S. Y.; Zhu, J. Y.; Li, H. & Zhan, H. Y. (2009). Visualization of enzymatic hydrolysis of cellulose using AFM phase imaging. *Enzyme and Microbial Technology,* 4, 274-281.

Long, J. W.; Stroud, R. M.; Swider-Lyons, K. E. & Rolison, D. R. (2000). How to make electrocatalysts more active for direct methanol oxidation avoid PtRu bimetallic alloys! *Journal of Physical Chemistry B,* 104, 9772-9776.

Maillard, F.; Gloaguen, F. & Leger, J. M. (2003). Preparation of methanol oxidation electrocatalysts: ruthenium deposition on carbon supported platinum nanoparticles. *Journal of Applied Electrochemistry,* 33, 1-8.

Maiyalagan, T. (2008) Synthesis and electro-catalytic activity of methanol oxidation on nitrogen containing carbon nanotubes supported Pt electrodes. *Applied Catalysis B: Environmental,* 80, 286-295.

Maiyalagan, T.; Viswanathan, B. & Varadaraju, U. V. (2005). Nitrogen containing carbon nanotubes as supports for Pt-alternate anodes for fuel cell application. *Electrochemistry Communications*, 7, 905-912.

Novoselov, K. S.; Geim, A. K.; Morozov, S. V.; Jiang, D.; Zhang, Y.; Dubonos, S. V.; Grigorieva, I. V. & Firsov, A. A. (2004). Electric field effect in atomically thin carbon films. *Science,* 306, 666-669.

Novoselov, K. S.; Geim, A. K.; Morozov, S. V.; Jiang, D.; Katsnelson, M. I.; Grigorieva, I. V.; Dubonos, S. V. & Firsov, A. A. (2005). Two-dimensional gas of massless Dirac fermions in graphene. *Nature,* 438, 197-200.

Pennycook, S. J.; Varela, M.; Lupini, A. R., Oxley, M. P. & Chisholm, M. F. (2009). Atomic-resolution spectroscopic imaging: past, present, and future. *Journal of Electron Microscopy,* 58, 87-97.

Rajesh, B.; Thampi, K. R.; Bonard, J. M.; Xanthopoulos, N.; Mathieu, H. J. & Viswanathan, B. (2003). Carbon nanotubes generated from template carbonization of polyphenyl acetylene as the support for electrooxidation of methanol. *Journal of Physical Chemistry B,* 107, 2701-2708.

Sanganna Gari, R. R.; Li, Z. & Dong, L. F. (2010). Effects of different carbon nanotube supported catalysts on methanol and ethanol electro-oxidation, In: *Nanomaterials for Polymer Electrolyte Membrane Fuel Cells*, Swider-Lyons, K. & Park, B. (Ed.), T08-17.1.-17.6., Materials Research Society, Warrendale, PA.

Seger, B. & Kamat, P. V. (2009). Electrocatalytically active graphene-platinum nanocomposites: role of 2-D carbon support in PEM fuel cells. *Journal of Physical Chemistry C*, 113, 7990-7995.

Selvaraj, V. & Alagar, M. (2007). Pt and Pt-Ru nanoparticles decorated polypyrrole/multi-walled carbon nanotubes and their catalytic activity towards methanol oxidation. *Electrochemistry Communications,* 9, 1145-1153.

Tamayo, J. & Garcia, R. (1997). Effects of elastic and inelastic interactions on phase contrast images in tapping-mode scanning force microscopy. *Applied Physics Letters,* 71, 2394.

Tang, H.; Chen, J. H.; Huang, Z. P.; Wang, D. Z.; Ren, Z. F.; Nie, L. H.; Kuang, Y. F. & Yao, S. Z. (2004). High dispersion and electrocatalytic properties of platinum on well-aligned carbon nanotube arrays. *Carbon,* 42, 191-197.

Tsai, M. C.; Yeh, T. K. & Tsai, C. H. (2006). An improved electrodeposition technique for preparing platinum and platinum-ruthenium nanoparticles on carbon nanotubes directly grown on carbon cloth for methanol oxidation. *Electrochemistry Communications*, 8, 1445-1452.

Wang, H. F. & Liu, Z. P. (2007). Selectivity of direct ethanol fuel cell dictated by a unique partial oxidation channel. *Journal of Physical Chemistry C,* 111, 12157-12160.

Yoo, E. J.; Okata, T.; Akita, T.; Kohyama, M.; Nakamura, J. & Honma, I. (2009). Enhanced electrocatalytic activity of Pt subnanoclusters on graphene nanosheet surface. *Nano Letters,* 9, 2255-2259.

Zhang, Y. B.; Tan, Y. W.; Stormer, H. L. & Kim, P. (2005). Experimental observation of the quantum Hall effect and Berry's phase in graphene. *Nature*, 438, 201-204.

Zhao, X. S.; Li, W. Z.; Jiang, L. H.; Zhou, W. J.; Xin, Q.; Yi, B. L. & Sun, G. Q. (2004). Multi-wall carbon nanotube supported Pt-Sn nanoparticles as an anode catalyst for the direct ethanol fuel cell. *Carbon,* 42, 3263-3265.

Zhu, Y.; Inada, H.; Nakamura, K. & Wall, J. (2009). Imaging single atoms using secondary electrons with an aberration-corrected electron microscope. *Nature Materials,* 8, 808-812.